

1 DRAFT 1.5  
2 Geneva, May 2, 2012  
3 CERN report  
4 ECFA report  
5 NuPECC report  
6 LHeC-Note-2011-003 GEN



# A Large Hadron Electron Collider at CERN

Report on the Physics and Design  
Concepts for Machine and Detector

LHeC Study Group



To be submitted for publication

<sup>13</sup> The Kandinsky painting is taken from a talk on gluon saturation and 5D black hole duality as presented  
<sup>14</sup> at the first CERN-ECFA-NuPECC Workshop on the LHeC held at Divonne near to CERN in September  
<sup>15</sup> 2008 [1].

## Abstract

17 The physics programme and the design are described of a new electron-hadron collider, the LHeC, in which  
18 electrons of 60 to possibly 140 GeV collide with LHC protons of 7000 GeV. With an  $ep$  design luminosity  
19 of about  $10^{33} \text{ cm}^{-2}\text{s}^{-1}$ , the Large Hadron Electron Collider exceeds the integrated luminosity collected at  
20 HERA by two orders of magnitude and the kinematic range by a factor of twenty in the four-momentum  
21 squared,  $Q^2$ , and in the inverse Bjorken  $x$ . The physics programme is devoted to an exploration of the  
22 energy frontier, complementing the LHC and its discovery potential for physics beyond the Standard Model  
23 with high precision deep inelastic scattering (DIS) measurements. These are projected to solve a variety of  
24 fundamental questions in strong and electroweak interactions. The LHeC thus becomes the world's cleanest  
25 high resolution microscope, designed to continue the path of deep inelastic lepton-hadron scattering into  
26 unknown areas of physics and kinematics. The physics programme also includes electron-ion (eA) scattering  
27 into a  $(Q^2, 1/x)$  range extended by four orders of magnitude as compared to previous lepton-nucleus DIS  
28 experiments. The LHeC may be realised either as a ring-ring or as a linac-ring collider. Optics and beam  
29 dynamics studies are presented for both versions, along with technical design considerations on the interaction  
30 region, magnets, cryogenics, RF, civil engineering and further components. A design study is also presented  
31 of a detector suitable to perform high precision DIS measurements in a wide range of acceptance using  
32 state-of-the art detector technology, which is modular and of limited size enabling its fast installation. The  
33 detector includes tagging devices for electron, photon, proton and neutron detection near to the beampipe.  
34 The LHeC is designed to be built and operated while the LHC runs. It is a major opportunity for progress  
35 in particle physics and further exploits the investment made in the LHC.



## 36 LHeC Study Group

37 J.L. Abelleira Fernandez<sup>10,15</sup>, C.Adolphsen<sup>39</sup>, S.Alekhin<sup>40,11</sup>, A.N.Akai<sup>01</sup>, H.Aksakal<sup>30</sup>, P.Allport<sup>17</sup>, J.L.Albacete<sup>37</sup>,  
38 V.Andreev<sup>25</sup>, R.B.Appleby<sup>23</sup>, E.Arikan<sup>30</sup>, N.Armesto<sup>38</sup>, G.Azuelos<sup>26</sup>, M.Bai<sup>47</sup>, D.Barber<sup>11,17,23</sup>, J.Bartels<sup>12</sup>,  
39 J.Behr<sup>11</sup>, O.Behnke<sup>11</sup>, S.Belyaev<sup>10</sup>, I.BenZvi<sup>47</sup>, N.Bernard<sup>16</sup>, S.Bertolucci<sup>10</sup>, S.Bettoni<sup>10</sup>, S.Biswal<sup>32</sup>, J.Bluemlein<sup>11</sup>,  
40 H.Boettcher<sup>11</sup>, H.Braun<sup>48</sup>, S.Brodsky<sup>39</sup>, A.Bogacz<sup>28</sup>, C.Bracco<sup>10</sup>, O.Bruening<sup>10</sup>, E.Bulyak<sup>08</sup>, A.Bunyatian<sup>11</sup>,  
41 H.Burkhardt<sup>10</sup>, I.T.Cakir<sup>54</sup>, O.Cakir<sup>53</sup>, R.Calaga<sup>47</sup>, E.Ciapala<sup>10</sup>, R.Ciftci<sup>01</sup>, A.K.Ciftci<sup>01</sup>, B.A.Cole<sup>29</sup>, J.C.Collins<sup>46</sup>,  
42 J.Dainton<sup>17</sup>, A.De.Roeck<sup>10</sup>, D.d'Enterria<sup>10</sup>, A.Dudarev<sup>10</sup>, A.Eide<sup>43</sup>, R.Enberg<sup>58</sup>, E.Eroglu<sup>45</sup>, K.J.Eskola<sup>14</sup>,  
43 L.Favart<sup>06</sup>, M.Fitterer<sup>10</sup>, S.Forte<sup>24</sup>, P.Gambino<sup>42</sup>, T.Gehrmann<sup>50</sup>, C.Glasman<sup>22</sup>, R.Godbole<sup>27</sup>, B.Goddard<sup>10</sup>,  
44 T.Greenshaw<sup>17</sup>, A.Guffanti<sup>09</sup>, V.Guzey<sup>28</sup>, C.Gwenlan<sup>34</sup>, T.Han<sup>36</sup>, Y.Hao<sup>47</sup>, F.Haug<sup>10</sup>, W.Herr<sup>10</sup>, B.Holzer<sup>10</sup>,  
45 M.Ishitsuka<sup>41</sup>, M.Jacquet<sup>33</sup>, B.Jeanerret<sup>10</sup>, J.M.Jimenez<sup>10</sup>, H.Jung<sup>11</sup>, J.M.Jowett<sup>10</sup>, H.Karadeniz<sup>54</sup>, D.Kayran<sup>47</sup>,  
46 F.Kocac<sup>45</sup>, A.Kilic<sup>45</sup>, K.Kimura<sup>41</sup>, M.Klein<sup>17</sup>, U.Klein<sup>17</sup>, T.Kluge<sup>17</sup>, G.Kramer<sup>12</sup>, M.Korostelev<sup>23</sup>, A.Kosmicki<sup>10</sup>,  
47 P.Kostka<sup>11</sup>, H.Kowalski<sup>11</sup>, D.Kuchler<sup>10</sup>, M.Kuze<sup>41</sup>, T.Lappi<sup>14</sup>, P.Laycock<sup>17</sup>, E.Levichev<sup>31</sup>, S.Levonian<sup>11</sup>,  
48 V.N.Litvinenko<sup>47</sup>, A.Lombardi<sup>10</sup>, C.Marquet<sup>10</sup>, B.Mellado<sup>07</sup>, K.H.Mess<sup>10</sup>, A.Milanese<sup>10</sup>, S.Moch<sup>11</sup>, I.I.Morozov<sup>31</sup>,  
49 Y.Muttoni<sup>10</sup>, S.Myers<sup>10</sup>, S.Nandi<sup>26</sup>, P.R.Newman<sup>03</sup>, T.Omori<sup>44</sup>, J.Osborne<sup>10</sup>, Y.Papaphilippou<sup>10</sup>, E.Paoloni<sup>35</sup>,  
50 C.Pascaud<sup>33</sup>, H.Paukkunen<sup>38</sup>, E.Perez<sup>10</sup>, T.Pieloni<sup>15</sup>, E.Pilicer<sup>45</sup>, B.Pire<sup>55</sup>, A.Polini<sup>04</sup>, V.Ptitsyn<sup>47</sup>, Y.Pupkov<sup>31</sup>,  
51 V.Radescu<sup>13</sup>, S.Raychaudhuri<sup>27</sup>, L.Rinolfi<sup>10</sup>, R.Rohini<sup>27</sup>, J.Rojo<sup>24</sup>, S.Russenschuck<sup>10</sup>, C.A.Salgado<sup>38</sup>, K.Sampe<sup>41</sup>,  
52 R.Sassot<sup>57</sup>, E.Sauvan<sup>19</sup>, M.Sahin<sup>01</sup>, U.Schneekloth<sup>11</sup>, T.Schoerner Sadenius<sup>11</sup>, D.Schulte<sup>10</sup>, A.N.Skrinsky<sup>31</sup>,  
53 W.Smith<sup>20</sup>, H.Spiesberger<sup>21</sup>, A.M.Stasto<sup>46</sup>, M.Strikman<sup>46</sup>, M.Sullivan<sup>39</sup>, B.Surrow<sup>05</sup>, S.Sultansoy<sup>01</sup>, Y.P.Sun<sup>39</sup>,  
54 L.Szymanowski<sup>56</sup>, I.Tapan<sup>45</sup>, P.Taels<sup>02</sup>, E.Tassi<sup>52</sup>, H.Ten.Kate<sup>10</sup>, J.Terron<sup>22</sup>, H.Thiesen<sup>10</sup>, L.Thompson<sup>23</sup>,  
55 K.Tokushuku<sup>44</sup>, R.Tomas.Garcia<sup>10</sup>, D.Tommasini<sup>10</sup>, D.Trbojevic<sup>47</sup>, N.Tsoupas<sup>47</sup>, J.Tuckmantel<sup>10</sup>, S.Turkoz<sup>53</sup>,  
56 K.Tywoniuik<sup>18</sup>, G.Unel<sup>10</sup>, J.Urakawa<sup>44</sup>, P.VanMechelen<sup>02</sup>, A.Variola<sup>37</sup>, R.Veness<sup>10</sup>, A.Vivoli<sup>10</sup>, P.Vobly<sup>31</sup>,  
57 R.Wallny<sup>51</sup>, S.Wallon<sup>59</sup>, G.Watt<sup>10</sup>, G.Weiglein<sup>12</sup>, C.Weiss<sup>28</sup>, U.A.Wiedemann<sup>10</sup>, U.Wienands<sup>39</sup>, F.Willeke<sup>47</sup>,  
58 B.-W.Xiao<sup>46</sup>, V.Yakimenko<sup>47</sup>, A.F.Zarnecki<sup>49</sup>, F.Zimmermann<sup>10</sup>, R.Zlebcik<sup>60</sup>, F.Zomer<sup>33</sup>

59 <sup>01</sup> *TOBB University of Economics and Technology, Ankara, Turkey*

60 <sup>02</sup> *University of Antwerpen, Belgium*

61 <sup>03</sup> *Univeristy of Birmingham, UK*

62 <sup>04</sup> *University of Bologna, Italy*

63 <sup>05</sup> *Massachusetts Institute of Technology, MIT, Boston, USA*

64 <sup>06</sup> *IIHE Brussels, Belgium*

65 <sup>07</sup> *Harvard University, Cambridge, USA*

66 <sup>08</sup> *Charkow National University, Ukraine*

67 <sup>09</sup> *Freiburg University, Germany*

68 <sup>10</sup> *CERN, Geneva, Switzerland*

69 <sup>11</sup> *DESY, Hamburg, Germany*

70 <sup>12</sup> *University of Hamburg, Germany*

71 <sup>13</sup> *University of Heidelberg, Germany*

72 <sup>14</sup> *Jyvaskyla University, Finland*

73 <sup>15</sup> *EPFL, Lausanne, Switzerland*

74 <sup>16</sup> *University of California in Los Angeles, UCLA, USA*

75 <sup>17</sup> *University of Liverpool, UK*

76 <sup>18</sup> *University of Lund, Sweden*

77 <sup>19</sup> *LAPP, Annecy, France*

78 <sup>20</sup> *University of Madison, Wisconsin, USA*

79 <sup>21</sup> *University of Mainz, Germany*

80 <sup>22</sup> *University of Madrid, Spain*

81 <sup>23</sup> *University of Manchester/Cockcroft Institute, UK*

82 <sup>24</sup> *INFN Milano, Italy*

83 <sup>25</sup> *LPI Moscow, Russia*

84 <sup>26</sup> *University of Montreal, Canada*

85 <sup>27</sup> *Tata Institute, Mumbai, India*

86 28 *Jefferson Laboratory, USA*  
87 29 *Columbia University, New York, USA*  
88 30 *Nigde University, Turkey*  
89 31 *Budker Institute of Nuclear Physics SB RAS, Novosibirsk, 630090 Russia*  
90 32 *Orissa University, India*  
91 33 *Orsay, LAL, France*  
92 34 *University of Oxford, UK*  
93 35 *University of Pisa, Italy*  
94 36 *University of Pittsburgh, USA*  
95 37 *IPhT Saclay, France*  
96 38 *University of Santiago de Compostela, Spain*  
97 39 *SLAC, Stanford Linear Accelerator Centre, Stanford, USA*  
98 40 *Serpukhov Institute, Russia*  
99 41 *Tokyo Institute of Technology, Japan*  
100 42 *University of Torino and INFN Torino, Italy*  
101 43 *NTNU, Trondheim, Norway*  
102 44 *KEK, Tsukuba, Japan*  
103 45 *Uludag University, Turkey*  
104 46 *Pennsylvania State University, USA*  
105 47 *Brookhaven National Laboratory, BNL, USA*  
106 48 *Paul Scherrer Institute, Villigen, Switzerland*  
107 49 *Faculty of Physics, University of Warsaw, Poland*  
108 50 *University of Zurich, Switzerland*  
109 51 *ETH Zurich, Switzerland*  
110 52 *INFN Gruppo Collegato di Cosenza and Universita della Calabria, Italy*  
111 53 *University of Ankara, Turkey*  
112 54 *SANAEM Ankara, Turkey*  
113 55 *CPHT, École Polytechnique, CNRS, 91128 Palaiseau, France*  
114 56 *National Center for Nuclear Research (NCBJ), Warsaw, Poland*  
115 57 *Universidad de Buenos Aires, Buenos Aires, Argentina*  
116 58 *Uppsala University, Sweden*  
117 59 *Laboratoire de Physique Théorique, Université Paris XI, Orsay, France*  
118 60 *Charles University, Praha, Czech Republic*

# Preface

120 Preparations for new, big machines take time. The idea of an electron-proton collider in the LEP-LHC  
 121 tunnel was discussed as early as 1984 [2], at the first LHC workshop at Lausanne. This was the time when  
 122 the first ever built  $ep$  collider, HERA, was approved by the German government. HERA was a machine of  
 123 about 30 GeV electron beam energy and nearly 1 TeV proton beam energy, a combination of a warm dipole  
 124 electron ring with a superconducting dipole proton ring, in a 6 km circumference tunnel. The machine  
 125 started operation 8 years after its approval. It reached luminosities of  $10^{31} \text{ cm}^{-2} \text{ s}^{-1}$  in its first phase of  
 126 operation which increased by about a factor of 4 in the subsequent, upgraded configuration. HERA never  
 127 attempted to collide electrons with deuterons nor with ions.

128 The realisation of HERA had followed a number of attempts to realise  $ep$  interactions in collider mode,  
 129 mainly driven by the unforgettable Bjoern Wiik: since the late 1960s, he and his colleagues had considered  
 130 such machines and proposed to probe the proton's structure more deeply with an  $ep$  collider at DORIS [3],  
 131 later at PETRA (PROPER) [4] and subsequently at the SPS at CERN (CHEEP) [5]. Further  $ep$  collider  
 132 studies were made for PEP [6], TRISTAN [7] and also the Tevatron (CHEER) [8].

133 In 1990, at a workshop at Aachen, the combination of LEP with the LHC was discussed, with studies [9–  
 134 11] on the luminosity, interaction region, a detector and the physics as seen with the knowledge of that  
 135 time, before HERA. Following a request of the CERN Science Policy Committee (SPC), a brief study of  
 136 the ring-ring  $ep$  collider in the LEP tunnel was performed [12] with the estimated luminosity of about  
 137  $10^{32} \text{ cm}^{-2} \text{ s}^{-1}$ .

138 At the end of the eighties it had been realised that there was a possible end to the increase of the energy  
 139 of  $ep$  colliders in the ring-ring configuration, because of the synchrotron radiation losses of an electron ring  
 140 accelerator. The classic SLAC fixed target  $ep$  experiment had already used a 2 mile linac. For  $ep$  linac-ring  
 141 collider configurations, two design sketches considering electron beam energies up to a few hundred GeV were  
 142 published, in 1988 [13] and in 1990 [14]. As part of the TESLA linear collider proposal, an option (THERA)  
 143 was studied [15] to collide electrons of a few hundred GeV energy with protons and ions from HERA at  
 144 DESY. Later, in 2003, the possibility was evaluated to combine LHC protons with CLIC electrons [16]. It  
 145 was yet realised, that the bunch structures of the LHC and CLIC were not compliant with the need for high  
 146 luminosities.

147 In September 2007, the SPC again asked whether one could realise an  $ep$  collider at CERN. Some of us  
 148 had written a paper [17] in the year before, that had shown in detail, for the first time, that a luminosity  
 149 of  $10^{33} \text{ cm}^{-2} \text{ s}^{-1}$  was achievable. This appeared possible in a ring-ring configuration based on the ultimate  
 150 LHC beam, with  $1.7 \cdot 10^{11}$  protons in bunches 25 ns apart. Thanks to the small beam-beam tune-shift, it was  
 151 found to be feasible to simultaneously operate  $pp$  in the LHC and  $ep$  in the new machine, which in 2005 was  
 152 termed the Large Hadron Electron Collider (LHeC) [18]. Thus it appeared possible to realise an  $ep$  collider  
 153 that was complementary to the LHC, just as HERA was to the Tevatron. The integrated luminosity was  
 154 projected to be  $O(100) \text{ fb}^{-1}$ , a factor of hundred more than HERA had collected over its lifetime of 15 years.

155 It was clear that with a centre-of-mass energy of about  $\sqrt{s} \simeq 1.5 \text{ TeV}$  an exciting programme of deep  
 156 inelastic scattering (DIS) measurements at the energy-frontier was in reach. This would comprise searches  
 157 and analyses for physics beyond the Standard Model, novel measurements in QCD and electroweak physics  
 158 to unprecedented precision, as well as DIS physics at such low Bjorken  $x$ , that all the known laws of parton  
 159 and gluon interactions would have to be modified to avoid violating unitarity. It had also been realised that

160 the kinematic region, in terms of four-momentum-transfer-squared,  $Q^2$ , and  $1/x$ , accessed in lepton-nuclear  
161 interactions could be extended by 4 orders of magnitude using the ion beams of the LHC. A salient theme  
162 of the LHeC therefore is the precise mapping of the gluon field, over six orders of magnitude in Bjorken  $x$ ,  
163 in protons, neutrons and nuclei, with unprecedented sensitivity.

164 In the autumn of 2007, (r)ECFA and CERN invited us to work out the LHeC concept to a degree,  
165 which would allow one to understand its physics programme, evaluate the accelerator options and their  
166 technical realisation. The detector design should be affordable and capable of realising a high precision,  
167 large acceptance experimental programme of deep inelastic scattering at the energy frontier. The electron  
168 beam energy range was set to be between about 50–150 GeV. The wall plug power consumed for the electron  
169 beam was limited to 100 MW.

170 For the installation of the LHC it had been decided to remove LEP from the tunnel and to re-use the  
171 injector chain. To realise an  $ep$  collider based on the LHC, a new electron accelerator has to be built. The  
172 following report details two solutions for the chosen default electron beam energy of  $E_e = 60$  GeV. One option  
173 is to build and install a new ring, with modern magnet technology, on top of the LHC, using a new 10 GeV  
174 injector. Alternatively, one can build a “linac”, actually two 10 GeV superconducting linacs in a racetrack  
175 configuration. By employing energy recovery techniques, this configuration could provide the equivalent of  
176 about 1 GW available power and reach  $10^{33} \text{ cm}^{-2}\text{s}^{-1}$  luminosity. The genuine linac would be of about the  
177 same length as the one used for the discovery of quarks at SLAC [19,20], the  $Q^2$ , however, with which parton  
178 interactions were studied at the LHeC exceeded that from 1969 by a factor of nearly  $10^5$ .

179 It was agreed early on to devote a few years to the report, also because none of the people involved  
180 could work anything near to full time for this endeavour. Three workshops were held in 2008-2010, that  
181 annually assembled about a hundred experts on theory, experiment and accelerator to develop the LHeC  
182 design concepts. The project was presented annually to ECFA and in 2008 to ICFA, see [21]. In view  
183 of the unique electron-ion scattering programme of the LHeC, the design effort became also supported by  
184 NuPECC, and the LHeC is now part of the NuPECC roadmap for European nuclear physics as released in  
185 2010 [22]. Following an intermediate report to the Science Policy Committee of CERN, in July 2010, the  
186 SPC considered the LHeC “an option for a future project at CERN”.

187 The LHeC by its nature is an upgrade of the LHC. It substantially enriches the physics harvest related to  
188 the gigantic investment in the LHC. Whatever the outcome of the searches at the LHC for physics beyond  
189 the Standard Model turns out to be, an  $ep$  collider operating at the energy frontier is guaranteed to deepen  
190 the understanding of TeV scale physics and thus will support the development of the theory of particles and  
191 their interactions.

192 The LHeC needs the LHC proton and ion beams to be operational and so the design is made for syn-  
193 chronous  $pp$  and  $ep$  operation, as well as  $AA$  and  $eA$ , including deuterons. Should the LHC eventually be  
194 upgraded to even higher beam energy, beyond 7 TeV per beam [23], it would open an even higher energy  
195 reach for  $ep$  also. There is a future for deep inelastic scattering at the energy frontier, beginning with the  
196 LS3 shutdown of the LHC, envisaged for 2022, likely leading into further decades. As Frank Wilczek put it,  
197 “one of the joys of our subject is the continuing of our culture that bridges continents and generations” [24].

198 Our science is driven by curiosity, by theoretical expectations, sometimes too great, but also by experiment  
199 and technology, and the authors of this study therefore hope that the LHeC may be given the chance to  
200 contribute to the common efforts of our community for a deeper understanding of nature.

201  
202 Max Klein (Chair of the LHeC Steering Committee)

203  
204 The current, preliminary version of this report, as of August 5<sup>th</sup>, is handed to the referees appointed by  
205 the CERN directorate. Following their reports, and also considering further developments and necessary  
206 updates of the current draft, the report will be handed to CERN, ECFA and NuPECC. It is thereby intended  
207 to become part of the European deliberations on the future directions of particle physics, which must be  
208 seen in the context of the LHC and the results now emerging at half its design energy.

# Contents

209

210	<b>I Introduction</b>	<b>14</b>
211	<b>1 Lepton-Hadron Scattering</b>	<b>16</b>
212	1.1 Development and Contributions . . . . .	16
213	1.2 Open Questions . . . . .	17
214	<b>2 Design Considerations</b>	<b>22</b>
215	2.1 DIS and Particle Physics . . . . .	22
216	2.2 Synchronous <b>pp</b> and <b>ep</b> operation . . . . .	22
217	2.3 Choice of Electron Beam Energy . . . . .	23
218	2.4 Detector Constraints . . . . .	25
219	2.5 Two Electron Beam Options . . . . .	25
220	2.6 Luminosity and Power . . . . .	26
221	<b>3 Executive Summary</b>	<b>29</b>
222	<b>II Physics</b>	<b>30</b>
223	<b>4 Precision QCD and Electroweak Physics</b>	<b>31</b>
224	4.1 Inclusive Deep Inelastic Scattering . . . . .	31
225	4.1.1 Cross Sections and Structure Functions . . . . .	31
226	4.1.2 Neutral Current . . . . .	32
227	4.1.3 Charged Current . . . . .	35
228	4.1.4 Cross Section Simulation and Uncertainties . . . . .	36
229	4.1.5 Longitudinal Structure Function $\mathbf{F_L}$ . . . . .	40
230	4.2 Determination of Parton Distributions . . . . .	44
231	4.2.1 QCD Fit Ansatz . . . . .	44
232	4.2.2 Valence Quarks . . . . .	45
233	4.2.3 Strange Quarks . . . . .	48
234	4.2.4 Top Quarks . . . . .	48
235	4.3 Gluon Distribution . . . . .	53
236	4.4 Prospects to Measure the Strong Coupling Constant . . . . .	55
237	4.4.1 Status of the DIS Measurements of $\alpha_s$ . . . . .	55
238	4.4.2 Simulation of $\alpha_s$ Determination . . . . .	56
239	4.5 Electron-Deuteron Scattering . . . . .	58
240	4.6 Charm and Beauty production . . . . .	59
241	4.6.1 Introduction and overview of expected highlights . . . . .	59
242	4.6.2 Total production cross sections for charm, beauty and top quarks . . . . .	62
243	4.6.3 Charm and Beauty production in DIS . . . . .	62
244	4.6.4 Intrinsic Heavy Flavour . . . . .	67



245	4.6.5	$D^*$ meson photoproduction study . . . . .	69
246	4.7	High $p_t$ jets . . . . .	70
247	4.7.1	Jets in $ep$ . . . . .	70
248	4.7.2	Jets in $\gamma A$ . . . . .	76
249	4.8	Total photoproduction cross section . . . . .	77
250	4.9	Electroweak physics . . . . .	78
251	4.9.1	The context . . . . .	78
252	4.9.2	Light Quark Weak Neutral Current Couplings . . . . .	80
253	4.9.3	Determination of the Weak Mixing Angle . . . . .	81
254	<b>5</b>	<b>Physics at High Parton Densities</b>	<b>88</b>
255	5.1	Physics at small $x$ . . . . .	88
256	5.1.1	High energy and density regime of QCD . . . . .	88
257	5.1.2	Status following HERA data . . . . .	95
258	5.1.3	Low- $x$ physics perspectives at the LHC . . . . .	102
259	5.1.4	Nuclear targets . . . . .	105
260	5.2	Prospects at the LHeC . . . . .	109
261	5.2.1	Strategy: decreasing $x$ and increasing $A$ . . . . .	109
262	5.2.2	Inclusive measurements . . . . .	109
263	5.2.3	Exclusive Production . . . . .	114
264	5.2.4	Inclusive diffraction . . . . .	134
265	5.2.5	Jet and multi-jet observables, parton dynamics and fragmentation . . . . .	146
266	5.2.6	Implications for ultra-high energy neutrino interactions and detection . . . . .	159
267	<b>6</b>	<b>New Physics at Large Scales</b>	<b>162</b>
268	6.1	New Physics in inclusive DIS at high $Q^2$ . . . . .	162
269	6.1.1	Quark substructure . . . . .	162
270	6.1.2	Contact Interactions . . . . .	163
271	6.1.3	Kaluza-Klein gravitons in extra-dimensions . . . . .	166
272	6.2	Leptoquarks and leptogluons . . . . .	166
273	6.2.1	Phenomenology of leptoquarks in $ep$ collisions . . . . .	166
274	6.2.2	The Buchmüller-Rückl-Wyler Model . . . . .	167
275	6.2.3	Phenomenology of leptoquarks in $pp$ collisions . . . . .	168
276	6.2.4	Current status of leptoquark searches . . . . .	169
277	6.2.5	Sensitivity on leptoquarks at LHC and at LHeC . . . . .	170
278	6.2.6	Determination of LQ properties . . . . .	170
279	6.2.7	Leptogluons . . . . .	174
280	6.3	Excited leptons and other new heavy leptons . . . . .	175
281	6.3.1	Excited Fermion Models . . . . .	176
282	6.3.2	Simulation and Results . . . . .	177
283	6.3.3	New leptons from a fourth generation . . . . .	179
284	6.4	New physics in boson-quark interactions . . . . .	181
285	6.4.1	An LHeC-based $\gamma p$ collider . . . . .	181
286	6.4.2	Anomalous Single Top Production at the LHeC Based $\gamma p$ Collider . . . . .	181
287	6.4.3	Excited quarks in $\gamma p$ collisions at LHeC . . . . .	184
288	6.4.4	Quarks from a fourth generation at LHeC . . . . .	185
289	6.4.5	Diquarks at LHeC . . . . .	185
290	6.4.6	Quarks from a fourth generation in $Wq$ interactions . . . . .	186
291	6.5	Sensitivity to a Higgs boson . . . . .	186
292	6.5.1	Higgs production at LHeC . . . . .	186
293	6.5.2	Observability of the signal . . . . .	187
294	6.5.3	Probing Anomalous <b>HW</b> Couplings at the LHeC . . . . .	189

296	<b>7 Ring-Ring Collider</b>	<b>196</b>
297	7.1 Baseline Parameters and Configuration . . . . .	196
298	7.2 Baseline Parameters and Configuration . . . . .	197
299	7.3 Geometry . . . . .	197
300	7.3.1 General Layout . . . . .	197
301	7.3.2 Electron Ring Circumference and e-p Synchronization . . . . .	197
302	7.3.3 Idealized Ring . . . . .	198
303	7.3.4 Bypass Options . . . . .	199
304	7.3.5 Bypass Point 1 . . . . .	200
305	7.3.6 Bypasses Point 5 . . . . .	200
306	7.3.7 Matching Proton and Electron Ring Circumference . . . . .	200
307	7.4 Layout and Optics . . . . .	201
308	7.4.1 Arc Cell Layout and Optics . . . . .	201
309	7.4.2 Insertion Layout and Optics . . . . .	201
310	7.4.3 Bypass Layout and Optics . . . . .	202
311	7.4.4 Chromaticity Correction . . . . .	202
312	7.4.5 Working Point . . . . .	203
313	7.4.6 Aperture . . . . .	203
314	7.5 Layout . . . . .	217
315	7.5.1 Beam Separation Scheme . . . . .	218
316	7.5.2 Crossing Angle . . . . .	220
317	7.5.3 Beam Optics and Luminosity . . . . .	222
318	7.6 Design Requirements . . . . .	223
319	7.6.1 Detector Coverage and Acceptance . . . . .	223
320	7.6.2 Lattice Matching and IR Geometry . . . . .	224
321	7.7 High Luminosity IR Layout . . . . .	225
322	7.7.1 Parameters . . . . .	225
323	7.7.2 Layout of the Electron Lattice . . . . .	225
324	7.7.3 Separation Scheme . . . . .	226
325	7.8 High Acceptance IR Layout . . . . .	226
326	7.8.1 Parameters . . . . .	226
327	7.8.2 Layout . . . . .	228
328	7.8.3 Separation Scheme . . . . .	229
329	7.9 Comparison of the two Layouts . . . . .	229
330	7.9.1 Crab Cavities . . . . .	230
331	7.10 Long Straight Section . . . . .	231
332	7.10.1 Dispersion . . . . .	231
333	7.10.2 Geometry . . . . .	231
334	7.10.3 Electron Optics in the LSS . . . . .	232
335	7.10.4 Synchrotron Radiation . . . . .	232
336	7.10.5 LHC Integration . . . . .	233
337	7.11 The Non-Colliding Proton Beam . . . . .	234
338	7.11.1 Design Elements . . . . .	234
339	7.11.2 Solution . . . . .	235
340	7.11.3 Summary . . . . .	237
341	7.12 Synchrotron radiation and absorbers . . . . .	238
342	7.12.1 Introduction . . . . .	238
343	7.12.2 High Luminosity . . . . .	240
344	7.12.3 High Detector Acceptance . . . . .	246
345	7.13 Beam-beam effects in the LHeC . . . . .	253

346	7.13.1	Head-on beam-beam effects . . . . .	253
347	7.13.2	Long range beam-beam effects . . . . .	256
348	7.14	Performance as an electron-ion collider . . . . .	257
349	7.14.1	Heavy nuclei, e-Pb collisions . . . . .	257
350	7.14.2	Electron-deuteron collisions . . . . .	258
351	7.15	Spin polarisation – an overview . . . . .	259
352	7.15.1	Self polarisation . . . . .	259
353	7.15.2	Suppression of depolarisation – spin matching . . . . .	262
354	7.15.3	Higher order resonances . . . . .	262
355	7.15.4	Calculations of the $e^\pm$ polarisation in the LHeC . . . . .	263
356	7.15.5	Spin rotator concepts for the LHeC . . . . .	265
357	7.15.6	Further work . . . . .	266
358	7.15.7	Summary . . . . .	267
359	7.16	Integration and machine protection issues . . . . .	268
360	7.16.1	Space requirements . . . . .	268
361	7.16.2	Impact of the synchrotron radiation on tunnel electronics . . . . .	274
362	7.16.3	Compatibility with the proton beam loss system . . . . .	274
363	7.16.4	Space requirements for the electron dump . . . . .	275
364	7.16.5	Protection of the p-machine against heavy electron losses . . . . .	275
365	7.16.6	How to combine the Machine Protection of both rings? . . . . .	276
366	7.17	LHeC Injector for the Ring-Ring option . . . . .	276
367	7.17.1	Injector . . . . .	276
368	7.17.2	Required performance . . . . .	277
369	7.17.3	Source, accumulator and acceleration to 0.6 GeV . . . . .	278
370	7.17.4	10 GeV injector . . . . .	279
371	<b>8</b>	<b>Linac-Ring Collider</b> . . . . .	<b>281</b>
372	8.1	Basic Parameters and Configurations . . . . .	281
373	8.1.1	General Considerations . . . . .	281
374	8.1.2	ERL Performance and Layout . . . . .	282
375	8.1.3	Polarization . . . . .	290
376	8.1.4	Pulsed Linacs . . . . .	290
377	8.1.5	Higher-Energy LHeC ERL Option . . . . .	292
378	8.1.6	$\gamma$ -p/A Option . . . . .	292
379	8.1.7	Summary of Basic Parameters and Configurations . . . . .	294
380	8.2	Interaction region . . . . .	294
381	8.2.1	Layout . . . . .	295
382	8.2.2	Optics . . . . .	295
383	8.2.3	Modifications for $\gamma$ p or $\gamma$ -A . . . . .	300
384	8.2.4	Synchrotron radiation and absorbers . . . . .	303
385	8.3	Linac Lattice and Impedance . . . . .	310
386	8.3.1	Overall Layout . . . . .	310
387	8.3.2	Linac Layout and Lattice . . . . .	311
388	8.3.3	Beam Break-Up . . . . .	315
389	8.3.4	Imperfections . . . . .	321
390	8.3.5	Touschek Scattering . . . . .	321
391	8.4	Performance as a Linac-Ring electron-ion collider . . . . .	322
392	8.4.1	Heavy nuclei, e-Pb collisions . . . . .	322
393	8.4.2	Electron-deuteron collisions . . . . .	322
394	8.5	Polarized-Electron Injector for the Linac-Ring LHeC . . . . .	322
395	8.6	Spin Rotator . . . . .	324
396	8.7	Positron Options for the Linac-Ring LHeC . . . . .	326

397	8.7.1	Motivation . . . . .	326
398	8.7.2	LHeC Linac-Ring $e^+$ Requirements . . . . .	328
399	8.7.3	Mitigation Schemes . . . . .	329
400	8.7.4	Positron Production Schemes . . . . .	332
401	8.7.5	Targets . . . . .	333
402	8.7.6	Conventional Scheme based on $e^-$ Beam Hitting Target . . . . .	333
403	8.7.7	Compton Sources . . . . .	336
404	8.7.8	Undulator Source . . . . .	341
405	8.7.9	Source based on Coherent Pair Creation . . . . .	342
406	8.7.10	Conclusions . . . . .	342
407	<b>9</b>	<b>System Design</b>	<b>343</b>
408	9.1	Magnets for the Interaction Region . . . . .	343
409	9.1.1	Introduction . . . . .	343
410	9.1.2	Magnets for the ring-ring option . . . . .	343
411	9.1.3	Magnets for the linac-ring option . . . . .	344
412	9.2	Accelerator Magnets . . . . .	350
413	9.2.1	RR option, dipole magnets . . . . .	350
414	9.2.2	RR option, quadrupole magnets . . . . .	353
415	9.2.3	LR option, dipole magnets . . . . .	358
416	9.2.4	LR option, quadrupole magnets . . . . .	358
417	9.2.5	LR option, corrector magnets for the two 10 GeV linacs . . . . .	362
418	9.3	Ring-Ring RF Design . . . . .	363
419	9.3.1	Design Parameters . . . . .	363
420	9.3.2	Cavities and klystrons . . . . .	363
421	9.4	Linac-Ring RF Design . . . . .	366
422	9.4.1	Design Parameters . . . . .	366
423	9.4.2	Layout and RF powering . . . . .	367
424	9.4.3	Arc RF systems . . . . .	369
425	9.5	Crab crossing for the LHeC . . . . .	369
426	9.5.1	Luminosity Reduction . . . . .	371
427	9.5.2	Crossing Schemes . . . . .	371
428	9.5.3	RF Technology . . . . .	371
429	9.6	Ring Ring option power converters . . . . .	373
430	9.6.1	Overview . . . . .	373
431	9.6.2	Powering considerations . . . . .	373
432	9.6.3	Power converter topologies . . . . .	373
433	9.6.4	Main power converters . . . . .	374
434	9.6.5	Insertion and by-pass quadrupole power converters . . . . .	376
435	9.6.6	Power converter infrastructure . . . . .	377
436	9.7	Linac-Ring option power converters . . . . .	377
437	9.7.1	Overview . . . . .	377
438	9.7.2	Powering considerations . . . . .	377
439	9.7.3	Linac quadrupole and corrector power converters . . . . .	377
440	9.7.4	Recirculation main power converters . . . . .	379
441	9.7.5	Power converter infrastructure . . . . .	379
442	9.7.6	Conclusions on power converters . . . . .	380
443	9.8	Vacuum . . . . .	381
444	9.8.1	Vacuum requirements . . . . .	381
445	9.8.2	Synchrotron radiation . . . . .	382
446	9.8.3	Vacuum engineering issues . . . . .	384
447	9.9	Beam Pipe Design . . . . .	389

448	9.9.1	Requirements . . . . .	389
449	9.9.2	Choice of Materials for beampipes . . . . .	389
450	9.9.3	Beampipe Geometries . . . . .	389
451	9.9.4	Vacuum Instrumentation . . . . .	391
452	9.9.5	Synchrotron Radiation Masks . . . . .	392
453	9.9.6	Installation and Integration . . . . .	392
454	9.10	Cryogenics . . . . .	393
455	9.10.1	Ring-Ring Cryogenics Design . . . . .	393
456	9.10.2	Linac-Ring Cryogenics Design . . . . .	397
457	9.10.3	General Conclusions Cryogenics for LHeC . . . . .	399
458	9.11	Beam Dumps and Injection Regions . . . . .	401
459	9.11.1	Injection Region Design for Ring-Ring Option . . . . .	401
460	9.11.2	Injection transfer line for the Ring-Ring Option . . . . .	403
461	9.11.3	60 GeV internal dump for Ring-Ring Option . . . . .	406
462	9.11.4	Post collision line for 140 GeV Linac-Ring option . . . . .	408
463	9.11.5	Absorber for 140 GeV Linac-Ring option . . . . .	409
464	9.11.6	Energy deposition studies for the Linac-Ring option . . . . .	409
465	9.11.7	Beam line dump for ERL Linac-Ring option . . . . .	410
466	9.11.8	Absorber for ERL Linac-Ring option . . . . .	412
467	<b>10</b>	<b>Civil Engineering and Services</b>	<b>413</b>
468	10.1	Overview . . . . .	413
469	10.2	Location, Geology and Construction Methods . . . . .	413
470	10.2.1	Location . . . . .	413
471	10.2.2	Land Features . . . . .	415
472	10.2.3	Geology . . . . .	415
473	10.2.4	Site Development . . . . .	415
474	10.2.5	Construction Methods . . . . .	416
475	10.3	Civil Engineering Layouts for Ring-Ring . . . . .	416
476	10.4	Civil Engineering Layouts for Linac-Ring . . . . .	419
477	10.5	Summary . . . . .	419
478	<b>11</b>	<b>Project Planning</b>	<b>423</b>
479	<b>IV</b>	<b>Detector</b>	<b>429</b>
480	<b>12</b>	<b>Detector Requirements</b>	<b>430</b>
481	12.1	Requirements on the LHeC Detector . . . . .	430
482	12.1.1	Installation and Magnets . . . . .	430
483	12.1.2	Kinematic reconstruction . . . . .	432
484	12.1.3	Acceptance regions - scattered electron . . . . .	433
485	12.1.4	Acceptance regions - hadronic final state . . . . .	436
486	12.1.5	Acceptance at the High Energy LHC . . . . .	438
487	12.1.6	Energy Resolution and Calibration . . . . .	438
488	12.1.7	Tracking Requirements . . . . .	440
489	12.1.8	Particle Identification Requirements . . . . .	442
490	12.1.9	Summary of the Requirements on the LHeC Detector . . . . .	442

491	<b>13 Central Detector</b>	<b>444</b>
492	13.1 Basic Detector Description . . . . .	444
493	13.1.1 Baseline Detector Layout . . . . .	449
494	13.1.2 An Alternative Solenoid Placement - Option B . . . . .	451
495	13.2 Magnet Design . . . . .	454
496	13.2.1 Magnets configuration . . . . .	454
497	13.2.2 Detector Solenoid . . . . .	454
498	13.2.3 Detector integrated e-beam bending dipoles . . . . .	458
499	13.2.4 Cryogenics for magnets and calorimeter . . . . .	458
500	13.2.5 Twin Solenoid System . . . . .	461
501	13.3 Tracking Detector . . . . .	461
502	13.3.1 Tracking Detector - Baseline Layout . . . . .	461
503	13.3.2 Performance . . . . .	464
504	13.3.3 Tracking detector design criteria and possible solutions . . . . .	464
505	13.4 Calorimetry . . . . .	471
506	13.4.1 The Barrel Electromagnetic Calorimeter . . . . .	472
507	13.4.2 The Hadronic Barrel Calorimeter . . . . .	473
508	13.4.3 Endcap Calorimeters . . . . .	474
509	13.5 Calorimeter Simulation . . . . .	476
510	13.5.1 The Barrel LAr Calorimeter Simulation . . . . .	477
511	13.5.2 The Barrel Tile Calorimeter Simulation . . . . .	477
512	13.5.3 Combined Liquid Argon and Tile Calorimeter Simulation . . . . .	478
513	13.5.4 Lead-Scintillator Electromagnetic Option . . . . .	478
514	13.5.5 Forward and Backward Inserts Calorimeter Simulation . . . . .	483
515	13.6 Calorimeter Summary . . . . .	488
516	13.7 Muon Detector . . . . .	489
517	13.7.1 Muon detector design . . . . .	490
518	13.7.2 The LHeC muon detector options . . . . .	492
519	13.7.3 Forward Muon Extensions . . . . .	493
520	13.7.4 Muon Detector Summary . . . . .	494
521	13.8 Event and Detector Simulations . . . . .	494
522	13.8.1 Pythia6 . . . . .	496
523	13.8.2 1 MeV Neutron Equivalent . . . . .	497
524	13.8.3 Nearest Neighbor . . . . .	497
525	13.8.4 Cross Checking . . . . .	502
526	13.8.5 Future Goals . . . . .	503
527	<b>14 Forward and Backward Detectors</b>	<b>504</b>
528	14.1 Luminosity Measurement and Electron Tagging . . . . .	504
529	14.1.1 Options . . . . .	505
530	14.1.2 Use of the Main LHeC Detector . . . . .	505
531	14.1.3 Dedicated Luminosity Detectors in the tunnel . . . . .	506
532	14.1.4 Small angle Electron Tagger . . . . .	506
533	14.1.5 Summary and Open Questions . . . . .	509
534	14.2 Polarimeter . . . . .	510
535	14.2.1 Polarisation from the scattered photons . . . . .	511
536	14.2.2 Polarisation from the scattered electrons . . . . .	511
537	14.3 Zero Degree Calorimeter . . . . .	511
538	14.3.1 ZDC detector design . . . . .	512
539	14.3.2 Neutron Calorimeter . . . . .	512
540	14.3.3 Proton Calorimeter . . . . .	514
541	14.3.4 Calibration and monitoring . . . . .	514

542	14.4 Forward Proton Detection . . . . .	515
543	<b>V Summary</b>	<b>518</b>
544	<b>15 Appendix</b>	<b>550</b>
545	15.1 Scientific Advisory Committee . . . . .	550
546	15.2 Steering Committee . . . . .	551
547	15.3 Working Group Convenors . . . . .	552
548	15.4 CERN Referees . . . . .	553

549

## Part I

550

# Introduction



551 The present document is a detailed presentation of the physics, the accelerator options and a detector design  
552 comprising the LHeC project. It has been developed under the auspices and with support of CERN, ECFA  
553 and NuPECC, between 2008 and now. The paper is organised as follows:

554 In the introduction, **Chapter I**, cornerstones of deep inelastic scattering and the main considerations  
555 for the design of the LHeC are summarised. The emphasis is on adding a 60 GeV energy electron beam  
556 to the existing proton and ion beams of the LHC, in a manner which foresees the simultaneous *ep* and  
557 *pp* operation for the realisation of a luminous DIS programme while minimising the interference with the  
558 LHC. The introduction contains an executive summary of this report (which will be added before its final  
559 publication).

560 **Chapter II** presents major, selected subjects, with related simulation studies and theoretical consider-  
561 ations, in order to sketch the physics programme of the LHeC. These subjects are grouped in three areas:  
562 high precision QCD and electroweak physics, the potential for searches for phenomena beyond the standard  
563 model and its relation to the LHC, and finally the physics of high parton densities at low Bjorken  $x$  and in  
564 nuclei. It is clear that it has rarely been possible, fortunately, to accurately predict nor to fully simulate  
565 the physics of a new machine at much enlarged energies. The subjects here presented are neither supposed  
566 to cover the complete field as it is known today. For a new laboratory of particle physics as the LHeC  
567 represents, however, a broad view must be taken to what it comprises most likely.

568 **Chapter III** is devoted to the accelerator design studies presenting the ring-ring and linac-ring concepts,  
569 optics etc and in a third section the various technical systems which often are common to both accelerator  
570 options. The emphasis here is on an understanding of the main challenges and characteristics of both options  
571 and not on discussing their relative merits. The accelerator chapter is concluded with separate sections on  
572 the civil engineering and a tentative time schedule for the realisation of the LHeC within the next about ten  
573 years.

574 **Chapter IV** presents the design considerations for a detector with its challenging central part and further  
575 systems to tag forward nucleons and backward scattered electrons and photons, including a study for a high  
576 precision measurement of the lepton beam polarisation. The salient feature of the detector baseline design  
577 is its silicon tracker surrounded by an electromagnetic liquid argon calorimeter inside a superconducting coil  
578 which uses a tile hadron calorimeter for the flux return.

579 The present version of this document (as of July 2011) does not yet contain summary sections. These  
580 will be added in the fall when the referee process ended and corresponding updates of this document <sup>1</sup> are  
581 completed. One can not exclude today that this process, also in the light of the rapid increase in LHC  
582 luminosity, leads to revisions of not only details of the present draft report. The main characteristics of this  
583 *ep* collider, however, its high luminosity and its high cms energy, beyond a TeV, are on firm ground as they  
584 are achieved with the unique hadron beams of the LHC. The LHeC technologies require prototyping and  
585 preparations but essentially they are at hand which makes the LHeC a realistic opportunity.

586 This report has been organised jointly by a steering group and convenors for the various physics, accel-  
587 erator and detector parts of the design. It was accompanied by a scientific advisory committee. The present  
588 draft is handed to 24 referees nominated by the CERN directorate for a detailed evaluation of the design  
589 and its corresponding update. The composition of these groups is listed in the **Appendix** of the paper.  
590 Some members of the steering group, many of the covenors and various members of the advisory committee  
591 have made direct scientific contributions to the LHeC design as presented here. They therefore also appear  
592 among the authors of this study which are representing a group of about 150 physicists and engineers from  
593 50 institutes.

594 It is for the coming phase of the LHeC design to begin its technical development, beyond the initial  
595 prototyping of magnets, and to form the appropriate international collaborations, both for the accelerator  
596 and the detector.

---

<sup>1</sup>An estimate is underway of the cost of the detector and the accelerator options which will be made available to CERN when available. For a rough cost estimate, an order of magnitude guess, which will be sufficient for most of the purposes, it may suffice to state that the cost of the LHeC is expected to be comparable with the cost of LEP or the XFEL while the detector cost will be a fraction only of the cost of CMS or ATLAS.

# Chapter 1

## Lepton-Hadron Scattering

### 1.1 Development and Contributions

It is almost exactly 100 years since the birth of the scattering experiment as a means of revealing the structure of matter. Geiger and Marsden's experiment [25] and its interpretation by Rutherford [26] set the scene for a century of ever-deeper and more precise resolution of the constituents of the atom, the nucleus and the nucleon. Lepton-hadron scattering has played a crucial role in this exploration over the past 55 years. The finite radius of the proton of about 1 fm was first established through elastic electron-proton scattering experiments [27]. Later, through deep inelastic electron proton scattering at Stanford [19, 20], proton structure was understood in terms of quarks, still the smallest known constituents of matter. With the discovery of Bjorken scaling of the proton structure function  $F_2(x, Q^2)$ , its quark model interpretation, and the subsequent discovery of scaling violation in support of asymptotic freedom [28, 29], deep inelastic scattering (DIS) became a field of fundamental theoretical importance [30] to the understanding of the strong interaction. Precise measurements of the parton momentum distributions of the nucleon became a major testing ground for the selection and development of Quantum Chromodynamics (QCD) [31] as the appropriate theory of the strong interaction. Prior to these developments, the theory of strong interactions was of merely phenomenological nature, built around S matrix theory and general amplitude features and various concepts such as Regge, bootstrap or further models [32].

Quantum Chromodynamics is a Yang-Mills gauge theory, in which the interaction between confined quarks proceeds via coloured gluon exchange. With improved resolution, as provided by increased  $Q^2$ , quarks can be resolved as quarks radiating gluons, whilst gluons may split into quark-antiquark pairs or, due to the non-abelian nature of the underlying gauge field theory, into pairs of gluons [33, 35, 290]. The development of QCD calculations beyond leading order [36, 37] is one of the most remarkable recent achievements of particle physics theory supported by experiment. It leads to a consistent description of all perturbatively accessible hadron observables in DIS (and beyond), as has recently been established over the kinematic range accessible to HERA [38]. This includes the unexpected observation of deep inelastic diffractive scattering at HERA, according to which in a significant fraction of violent DIS interactions the proton remains intact, an exchange of vacuum quantum numbers which often is termed "Pomeron exchange".

Despite previous successes, many fundamental areas of QCD have not been verified experimentally, with instantons [39] as only one example. Even the classic areas related to quarks and gluons have not been exploited as required for limited precision, range and variation of initial conditions. Meanwhile the theory underlying DIS experiences further fundamental developments. Four-dimensional conformal field theory is seen to be related to superstring theory in the anti-de Sitter space in ten dimensions, which relates the  $N = 4$  supersymmetric pomeron to the graviton in this space [40]. The evolution of partons is expected to obey different laws than explored hitherto at HERA when at small  $x$  their interactions have to be damped for the restoration of unitarity, see [41] for a review.

Particle physics in the past could profit very much from the complementarity of hadron-hadron, DIS and

### The 10-100 GeV Energy Scale [1968-1986]

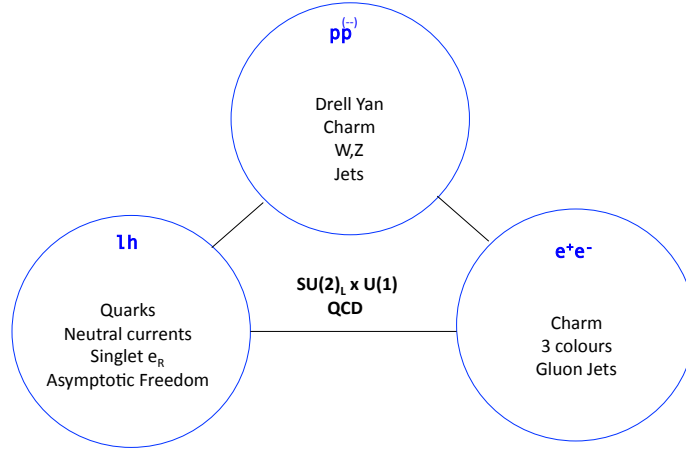


Figure 1.1: Key results of the exploration of the 10 – 100 GeV energy scale in hadron-hadron (top), deep inelastic (bottom left) and  $e^+e^-$  scattering (bottom right). These and further important results selected the  $SU(2)_L \times U(1)$  and QCD as the appropriate theories for the electroweak and the strong interaction, respectively, of leptons and quarks transmitted by the photon, the  $W^\pm$ ,  $Z$  bosons and gluons.

634  $e^+e^-$  experiments. Key observations were made in all three areas, and the overlap in physics coverage was  
 635 used to achieve confidence in new and precision results. This is sketched in Figure 1.1 for the experiments of  
 636 the seventies and eighties, which resulted in the birth of the Standard Model. Fig. 1.2 illustrates this for the  
 637 experiments of the nineties until now, when the Tevatron, HERA and the SLC/LEP machines determined  
 638 the progress in the exploration of particle physics at the energy frontier accessed with colliders. The present  
 639 report deals with the reasons and possibility to extend deep inelastic scattering experimentation into an  
 640 unexplored range of our knowledge for which the LHC at CERN provides the rare and single opportunity  
 641 for the next decades ahead. Simultaneous LHC and LHeC operation would put the  $ep$  part of the TeV scale  
 642 triangle, as shown in Figure 1.3, on a firm ground.

## 643 1.2 Open Questions

644 For a project as the LHeC one needs to understand which fundamental properties of nature it promises to  
 645 deal with and which possibly specific questions it is expected to answer.

646 The Standard Model of particle physics contains a remarkable, but unexplained, symmetry between  
 647 quarks and leptons [42], with three generations, in each of which two quarks and two leptons are embedded.  
 648 It was pointed out long ago [43] that it appears somewhat artificial that the basic building blocks of matter  
 649 share the electromagnetic and the weak interactions but differ in their sensitivity to the strong interaction.  
 650 Many theories which unify the quark and lepton sectors, such as models based on the E6 gauge group [44],  
 651  $R$ -parity violating supersymmetry and left-right symmetric extensions of the Standard Model [45], predict  
 652 new resonant states with both lepton and baryon numbers, usually referred to as leptoquarks (LQ). In the  
 653 technicolour theory, leptoquarks are bound states of technifermions [46, 47]. Although some of the specific  
 654 theories have not been supported by experiment, the search for leptoquarks has been a prime motivation for  
 655 high energy scattering, especially DIS experiments. The limits for leptoquark states as of the time of EPS11  
 656 from the LHC leave the possibility of new LQ states at around 1 TeV mass open while the absence of large

657 missing energy may be seen as being compliant with RPV SUSY states in which there is no LSP. An LHeC,  
 658 in combination with the existing LHC programme, can extend this search into a previously unexplored mass  
 659 region, with the prospect of deciphering the leptoquark quantum numbers.

660 No analytic proof yet exists that QCD should exhibit the property of colour confinement, though it  
 661 is reasonable to assume that it is a consequence of gluon dynamics, as reflected for example in popular  
 662 hadronisation models [48] and Monte Carlo simulations on the lattice. Studying the behaviour of gluons  
 663 under new extreme conditions and contrasting the conditions under which the proton stays intact with those  
 664 in which it is destroyed may help to shed light on the precise mechanism at work.

665 The search for the Higgs boson, which explains the masses of the electroweak bosons, and for the origin  
 666 of electroweak symmetry breaking is currently the central focus of particle physics and is expected to be  
 667 principally resolved within the near future by the ATLAS and CMS experiments. If there exists a Higgs  
 668 particle at masses around 130 GeV, the determination of its properties becomes an important issue. The  
 669 LHeC, due to its clean initial state and the absence of pile-up, has an interesting potential to accurately  
 670 determine the Higgs particle coupling to  $b\bar{b}$ , and to also investigate the quartic self-coupling of the scalar  
 671 doublet, from the HWW vertex, which provides direct insight into the nature of electroweak symmetry  
 672 breaking.

673 The question of hadronic mass deserves similar exploration. The mass of baryons is almost entirely due to  
 674 strong interaction field energy, generated through quark and gluon vacuum condensates the self-interaction  
 675 of gluons in a manner which is not yet well understood. It may be accessible through a more detailed  
 exploration of QCD dynamics.

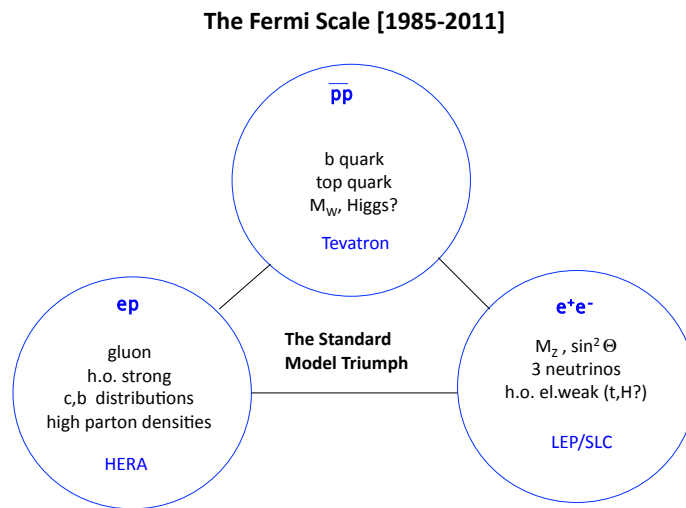


Figure 1.2: Key results of the exploration of the Fermi energy scale in  $p\bar{p}$  (top), deep inelastic (bottom left) and  $e^+e^-$  scattering (bottom right) with the energy frontier colliders, the Tevatron, HERA and the SLC/LEP, respectively. These and further important results established the Standard Model of particle physics with six types of quarks and leptons in three families, and the development of higher order precision calculations used for the prediction of the top quark and the Higgs mass, based mainly on  $e^+e^-$  scattering results, and for the understanding of the partonic contents of the proton to NNLO pQCD, based mainly on the results from HERA and previous DIS fixed target experiments.

676

677 The salient theme of physics with the LHeC is the mapping of the gluon field. This is achieved with  
 678 precision measurements of the evolution of structure functions over an unprecedented range of  $\ln Q^2$ . It

679 relates inclusive  $ep$  DIS with jets and heavy flavour, it concerns the unexplored role of the gluon in nuclei  
680 and in deeply virtual Compton scattering. The gluon field is central to QCD but not directly measurable. It  
681 may exhibit spots of maximum density (hot spots) and it may also disappear (cold spots) as it does towards  
682 low  $Q^2$  and  $x$ , and possibly at the scaling point near  $x \simeq 0.2$  [49]. Knowing the gluon means understanding  
683 the origin of baryonic matter, the production of the Higgs boson and of other new particles and not least  
684 important understanding Quantum Chromodynamics.

685 The study of deep inelastic  $ep$  scattering is important for the investigation of the nature of the Pomeron  
686 and Odderon, which are Regge singularities of the  $t$ -channel partial waves  $f_j(t)$  in the complex plane of the  
687 angular momentum  $j$ . The Pomeron is responsible for a growth of total cross sections with energy. The  
688 Odderon describes the behaviour of the difference of the cross sections for particle-particle and particle-  
689 antiparticle scattering which obey the Pommeranchuk theorem. In perturbative QCD, the Pomeron and  
690 Odderon are the simplest colorless reggeons (families of glueballs) constructed from two and three reggeized  
691 gluons, respectively. Their wave functions satisfy the generalized BFKL equation. In the next-to-leading  
692 approximation the solution of the BFKL equation contains an infinite number of Pomerons and to verify  
693 this prediction of QCD one needs to increase the energy of colliding particles. In the N=4 supersymmetric  
694 generalization of QCD, in the t'Hooft limit of large  $N_c$ , the BFKL Pomeron is equivalent to the reggeized  
695 graviton living in the 10-dimensional anti-de-Sitter space. Therefore, the Pomeron interaction describing  
696 the screening corrections to the BFKL predictions, at least in this model, should be based on a general  
697 covariant effective theory being a generalization of the Einstein-Hilbert action for general relativity. Thus,  
698 the investigation of high energy  $ep$  scattering could be interesting for the construction of a non-perturbative  
699 approach to QCD based on an effective string model in high dimensional spaces.

700 The strong coupling constant  $\alpha_s$  decreases as energy scales increase, in contrast to the energy dependence  
701 of the weak coupling and the fine structure constant. It appears possible in SUSY theories that the three  
702 constants approach a common value at energies of order  $10^{15}$  GeV. The distinctions we make between the  
703 electromagnetic, weak and strong interactions may merely be a consequence of the low energy scale at which  
704 we live. The possible grand unification of the known interactions has been one of the major goals of modern  
705 particle physics theory and experiment. Progress in this area requires that we know  $\alpha_s$ , by far the most  
706 poorly constrained of the fundamental couplings, much more accurately than is currently the case. The  
707 LHeC promises a factor of ten reduction in the uncertainty on  $\alpha_s$  based on a major renewal and extension  
708 of the experimental and the theoretical basis of the physics of deep inelastic scattering.

709 After quarks were discovered, a distinction was soon made between valence and sea quarks [50]. However,  
710 it was not until the high energy colliding beam configuration of HERA became available that the rich partonic  
711 structure of the proton was fully realised. Despite the resulting fast development of our knowledge of the  
712 parton distribution functions (PDFs) in the proton, there are still many outstanding important questions  
713 regarding the quark contents of the nucleon. These regard for example: i) the unresolved question of whether  
714 sea quarks and anti-quarks have the same momentum distributions; ii) the clarification of the role of heavy  
715 quarks in QCD, including the search for their intrinsic states [51], the precision measurement of the  $b$  quark  
716 density or, owing to the huge reach in  $Q^2$ , the novel exploration of top production in DIS and the transition  
717 of top from a heavy to a light quark, for  $Q^2 \gg m_t^2$ ; iii) the partonic structure of the neutron which is to be  
718 resolved over many orders of magnitude in  $1/x$ , as HERA had no deuteron data taken, and the assumption  
719 of isospin symmetry, which relates the neutron down-quark distribution to the proton up-quark distribution.  
720 Modern fits of PDFs use quite a number of symmetry assumptions and exploit parameterisations which are  
721 to be questioned and overcome by a new basis for the PDF determinations which the LHeC uniquely provides  
722 as it constrains all quark distributions,  $u_v, d_v, u, \bar{u}, d, \bar{d}, s, \bar{s}, c, b$  and likely  $t$  and  $\bar{t}$  over an unprecedented  
723 range of  $x$  and  $Q^2$ . The LHeC will put the whole PDF related physics on new, much firmer ground. That  
724 is crucial for searches for physics beyond the standard model. It also is necessary for high precision tests of  
725 the electroweak theory, as for the ultimate measurement of the mass of the  $W$  boson [52] as a test for the  
726 validity of the SM, especially the relation to the masses of the top quark and the Higgs boson.

727 The structure of the neutron at low  $x \leq 0.01$  in the DIS region is experimentally unknown. With  
728 no data on the scattering of leptons from heavy ions with colliding beam kinematics, the knowledge of the  
729 modifications to nucleon parton densities when they are bound inside nuclei, rather than free, is also restricted

730 to high  $x$  values. This is reflected in a lack of detailed understanding of shadowing phenomena, particularly  
731 for the gluon density and a corresponding lack of knowledge of the initial state of heavy ion collisions at LHC  
732 energies. The mechanism of shadowing at low  $x$  can be tested for the first time via Gribov's fundamental  
733 relation to diffraction and also via measurements with different light nuclei. Antishadowing at larger  $x$  [53]  
734 may possibly be non-universal and flavour specific. Nuclear corrections at large  $x$  may be dealt with in  $eD$   
735 scattering at the LHeC by tagging the spectator nucleon and reconstructing its momentum well enough to  
736 account for the so far disturbing effects of Fermi motion. This promises to overcome the uncertainty from  
737 nuclear corrections which has been an obstacle for decades in the understanding of nucleon structure and  
738 represents a formidable experimental task, see e.g. [53] for a recent study. Parton distributions in nuclei,  
739 for  $x \lesssim 0.01$ , presently are based in HERA's proton data convoluted with theoretical expectations. With  
740 the LHeC they will be determined down to almost  $10^{-6}$  and largely flavour separated. It is unknown what  
741 will be found from an experimental point of view, and it is critical for the understanding of the quark gluon  
742 plasma.

743 There are various fundamental properties predicted in QCD which have never been resolved or even tested  
744 so far and which will become accessible with the LHeC. While ordinary quark distributions correspond to  
745 an incoherent sum of squared amplitudes, a new approach has been developed, which uses quark amplitudes  
746 and Generalised Parton Distributions (GPDs) to understand proton structure in a new, three-dimensional  
747 way [54,55]. Our understanding of GPDs is limited by the relative paucity of experimental data on exclusive  
748 DIS channels. The emission of partons is assumed in PDF fits to be governed by the linear DGLAP evolution  
749 equations, an approximation to a full solution to QCD, in which parton cascades are ordered in transverse  
750 momentum. There are good reasons to believe that the DGLAP approximation is insufficient to describe  
751 the  $Q^2$  evolution of low  $x$  partons, even within the  $x$  range to which the LHC rapidity plateau corresponds.  
752 Inclusive DIS and jet data in an extended low  $x$  kinematic regime are required to resolve this situation.

753 The rapid rise of the proton gluon density as  $x$  decreases cannot continue indefinitely. At  $x$  values  
754 within the reach of LHeC  $ep$  and  $eA$  scattering, a transition takes place from the currently known DIS  
755 regime in which the proton behaves as a dilute system to a new low  $x$  domain in which parton densities  
756 saturate and the proton approaches a 'black disk' limit [56]. This latter region represents a fundamentally  
757 new regime of strong interaction dynamics, for which a rich phenomenology has developed, but where the  
758 detailed mechanisms and the full consequences are not yet known. Experimental data at sufficiently low  $x$   
759 with scales which are large enough to allow a partonic interpretation are required in order to test the models  
760 and fully understand the behaviour of partons at high densities. The so well known DGLAP evolution at low  
761  $x$  is to break and non-linear evolution equations will determine the parton distributions, for which various  
762 untested predictions exist.

763 The high precision and range of the LHeC DIS measurements provide many further opportunities for  
764 explorations of fundamental interest. With the  $ep$  initial state any new phenomenon singly produced can be  
765 investigated with particular sensitivity, as for example the possibility for excited leptons to exist. Variation  
766 of beam charge and polarisation lead to resolve quantum numbers of new, so-called contact interactions, of  
767 scale up to about 50 TeV, and to novel precision measurements of the scale dependence of the weak mixing  
768 angle around the  $Z$  pole.

769 Despite its huge success in describing existing high energy data, the Standard Model is known to be in-  
770 complete, not only due to the absence of an experimentally established mechanism for electroweak symmetry  
771 breaking. As the exploitation of the TeV energy regime and the high luminosities of the LHC era develop  
772 further, a full understanding requires to challenge the existing theory through new precision measurements,  
773 as broad in scope as possible, with initial states involving leptons as well as quarks and gluons. The LHeC  
774 will not just answer some of the currently outstanding questions but represents the opportunity to build a  
775 new laboratory for particle physics which owing to its specific configuration, its enlarged DIS energy range  
776 and unprecedented precision will accompany the LHC, and possibly built pure lepton machines, in exploring  
777 the next layer of the high energy frontier physics.

### The TeV Scale [2010-2035..]

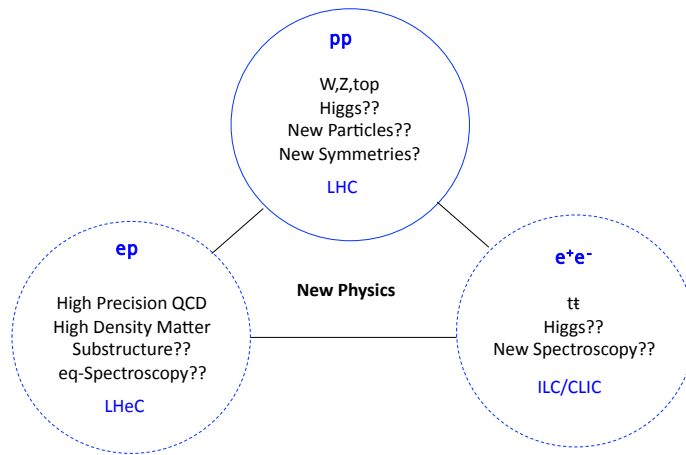


Figure 1.3: The exploration of the TeV energy scale has begun with the LHC. The present document describes one of its compliments, a new TeV scale  $ep$  and  $eA$  collider, while intense work is continuing on the development of concepts for new  $e^+e^-$  and possibly  $\mu^+\mu^-$  colliders. While each of the new machines has exciting standard model programmes to pursue with higher precision and range, physics beyond the SM has been elusive at the moment this report is released and  $1\text{ fb}^{-1}$  of 7 TeV cms LHC data have been analysed within a very short time for the EPS11 conference at Grenoble.

## Chapter 2

# Design Considerations

The following sections describe briefly which general considerations have determined the LHeC design as presented in this report. Major changes to the underlying assumptions would naturally require an appropriately changed variation of the design.

### 2.1 DIS and Particle Physics

Deep inelastic scattering experiments with charged leptons may be classified as low energy, medium and high energy experiments. The pioneering low energy DIS experiment, which discovered quarks, was performed at SLAC. Classic medium energy experiments were the BCDMS and the NMC experiments at CERN, while HERA, the first  $ep$  collider ever built, had pushed the DIS energy reach to the Fermi scale. This allowed the field of deep inelastic scattering to develop as part of the energy frontier particle physics, complementary to the Tevatron and LEP. In all three areas, the field of DIS is considering upgrade projects with the 12 GeV upgrade at Jlab, the medium energy colliders at Jlab and/or BNL, possibly fixed target further neutrino experiments and the LHeC.

The LHeC provides the only realistic possibility for an energy frontier  $ep$  programme in the coming probably three decades. Owing to the LHC, there is one opportunity to complement the TeV scale  $pp$  machine with a TeV energy  $ep$  collider, besides a pure lepton collider in this energy range. It took about 30 years for HERA, LEP and the Tevatron to be built, operated and analysed. The exploration of the TeV energy scale is subject to similar time horizons.

### 2.2 Synchronous $pp$ and $ep$ operation

The intense, energetic hadron beams of the LHC provide the unique possibility to realise a luminous experimental programme of deep inelastic scattering at TeV energies. The LHeC is therefore by its nature an upgrade to the LHC, which gives it its site and in a way determines its dimensions too. The first design consideration builds on the assumption that the LHC still runs in  $pp$  mode when an electron beam becomes operational. This has several implications:

- The construction of the LHeC has to be completed in the coming about 10 years.
- The design has to be adapted for synchronous  $pp$  and  $ep$  (and  $AA$  and  $eA$ ) operation, as with magnets in the IR to steer three beams and with civil engineering and detector modularity requirements to be compliant with the LHC operation and upgrade programme.
- The synchronous operation of  $pp$  and  $ep$  allows to collect a high integrated luminosity, with the goal of a total of order  $100 \text{ fb}^{-1}$ , and makes the most efficient use of both the proton beams and the electron beam installation too.



810 It can not realistically be assumed today, that the  $ep$  physics would commence only when the  $pp$  program  
 811 was finished because several key LHC components have a limited lifetime, which is nowadays estimated to  
 812 be about 20 years. Planning for an  $ep$  run after the  $pp$  program finishes therefore implies a significant risk  
 813 of additional cost for the project due to a substantial consolidation effort in the LHC.

814 The LHeC can be thought and it is designed to accompany the proton and the ion physics programme  
 815 of the LHC in its high luminosity phase, now assumed to begin in 2023.

## 816 2.3 Choice of Electron Beam Energy

817 The centre of mass energy squared of an  $ep$  collider is  $s = 4E_e E_p$ . It determines the maximum four-  
 818 momentum transfer squared,  $Q^2$ , between the electron and the proton because  $Q^2 = sxy$ , where  $x$  is the  
 819 fraction of four momentum of the proton carried by the struck parton while  $y$  is the inelasticity of the  
 820 scattering process which in the laboratory frame is the relative energy transfer, with  $0 < x, y \leq 1$ .

821 HERA has operated with a proton beam energy of  $E_p = 0.92$  TeV and an electron (and positron) beam  
 822 energy of  $E_e = 27.5$  GeV. With Sokolov-Ternov build-up times of about half an hour, the electron beam  
 823 became polarised and mean polarisations of up to 40% were achieved. HERA has not accelerated any  
 824 hadron beam other than protons. The LHeC has to surpass these parameters significantly for a unique and  
 825 exciting programme to be pursued.

826 The LHeC can use an up to 7 TeV energy proton beam. For this design study the electron beam energy  
 827 is set to 60 GeV. This implies that the gain in  $s$ , or  $Q^2$  at fixed  $(x, y)$ , as compared to HERA will be a  
 828 factor of 16.6, or about 4 in  $\sqrt{s}$ . The real gain in range of  $Q^2$  and  $x$  will even be larger as with the superior  
 829 luminosity even the highest  $Q^2$  values and  $x$  close to 1 become accessible. The kinematic range of the LHeC  
 830 as compared to HERA at low  $x$  and at high  $Q^2$  is illustrated in Fig. 2.1.

831 The choice of a default  $E_e = 60$  GeV for this design report is dictated by physics and by practical  
 832 considerations:

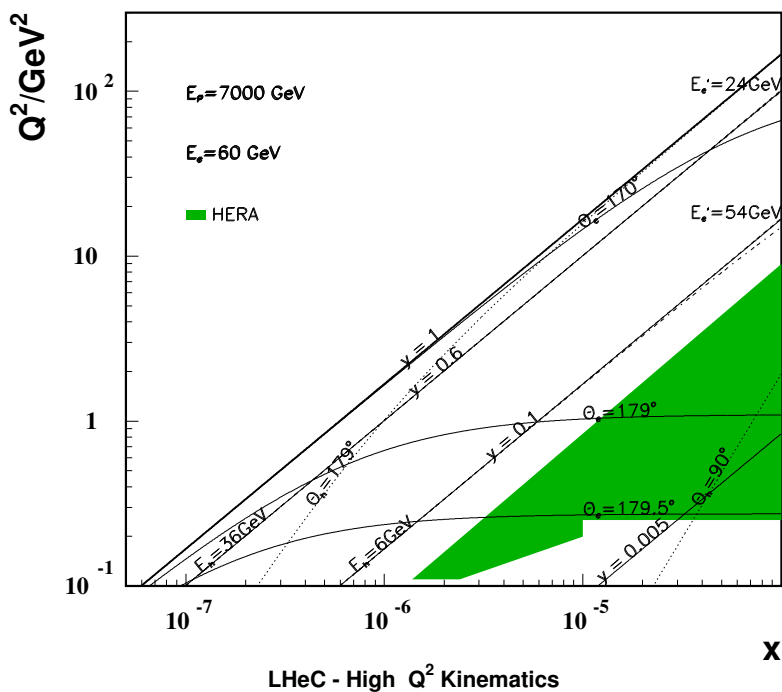
- 833 • New physics has been assumed to appear at the TeV energy scale. At the time of completion of this  
 834 report, the LHC has excluded much of the sub-TeV physics beyond the Standard Model (SM) but  
 835 leaves the possibility open of resonant lepton-parton states with masses of larger than about 500 GeV,  
 836 for which the LHeC would be a particularly suitable machine with a range of up to  $M \lesssim \sqrt{s}$ .
- 837 • High precision QCD and electroweak physics require a maximum range in  $\ln Q^2$  and highest  $Q^2$ ,  
 838 respectively. The unification of electromagnetic and weak forces takes place at  $Q^2 \simeq M_Z^2$  which is much  
 839 exceeded by the LHeC energies. Part of the electroweak physics requires lepton beam polarisation.
- 840 • The discovery of gluon saturation requires to measure at typical values of small  $x \simeq 10^{-5}$  with  $Q^2 \gg$   
 841  $M_p^2$ , where  $M_p$  is the mass of the proton. The choice of energies ensures this discovery at the LHeC in  
 842 the DIS region, both in  $ep$  and in  $eA$ .
- 843 • Energy losses by synchrotron radiation,  $\propto E_e^4$ , both in the ring and the return arcs for the linac, can be  
 844 kept at reasonable levels, in terms of the power,  $P$ , needed to achieve high luminosity and the radius  
 845 of the racetrack return arcs for the linac too.

846 It so appears that 60 GeV is an appropriate and affordable choice. It yet is well possible that the 60 GeV  
 847 may not be the final value of the electron beam energy, especially if the LHC would find non-SM physics  
 848 just above the now chosen energy range. The design therefore also considers a dedicated high energy beam  
 849 of 140 GeV as an option, which yet has not been worked out to any comparable detail <sup>1</sup>.

---

<sup>1</sup>Such a large  $E_e$  would also fit better to a future HE LHC, when about 16 TeV proton beam energy might become available in the yet much farther future, as that would keep the  $e - p$  beam energy asymmetry tolerable.

### LHeC - Low x Kinematics



### LHeC - High Q^2 Kinematics

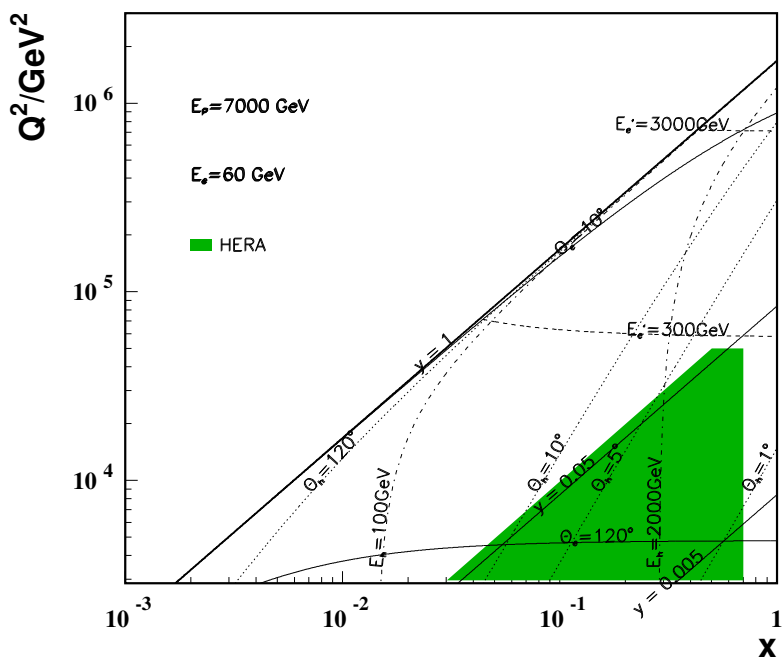


Figure 2.1: Kinematics of  $ep$  scattering at the LHeC at low  $x$  (top) and high  $Q^2$  (bottom). Solid (dotted) curves correspond to constant polar angles  $\theta_e$  ( $\theta_h$ ) of the scattered electron (hadronic final state). The polar angle is defined with respect to the proton beam direction. Dashed (dashed-dotted) curves correspond to constant energies  $E'_e$  ( $E_h$ ) of the scattered electron (hadronic final state). The shaded (green) area illustrates the region of kinematic coverage in neutral current scattering at HERA. The energy and angle isochrone lines are discussed in the detector design chapter in detail.

## 2.4 Detector Constraints

One easily recognises, in Fig. 2.1, that the asymmetry of the electron and proton beam energies poses severe constraints to the detector design: i) the “whole” low  $Q^2$  and low  $x$  physics requires to measure the electron, of energy  $E'_e \lesssim E_e$ , scattered in backward direction between about  $170^\circ$  and  $179^\circ$ , and ii) the forward scattered final state, of energy comparable to  $E_p$ , needs to be reconstructed down to very small angles in order to cover the high  $x$  region in a range of not too extreme  $Q^2$ .

The current detector design considers an option to have split data taking phases, like HERA I and II, with different interaction region configurations, a high acceptance phase, covering  $1^\circ - 179^\circ$ , at reduced luminosity and a high luminosity phase, of acceptance limited to  $8^\circ - 172^\circ$ . In the course of the study, however, an optics was found for the high acceptance configuration with only a factor of two reduced luminosity. It is likely, therefore, that the TDR will lead to a unification of these configurations and correspondingly weakened demands on the modularity of the inner detector region.

Synchronous  $ep$  and  $pp$  operation implies that at least one of the four IPs, currently occupied by experiments, will have to be free'd for an LHeC detector. It was decided to use for this report IP2 as an example site and to limit the study of bypasses, in the ring option, to IP1 and IP5. There has often been a discussion about the need for two detectors and ambitious detector push-pull concepts are discussed for the Linear Collider. For the LHeC this would imply a major overhead of cost and delay in construction time. The detector envisaged here will be challenging but also be based on known technology. Truly independent reconstruction, simulation and analysis software teams using one common facility may lead to sufficient confidence when it comes to crucial and most precise results.

## 2.5 Two Electron Beam Options

It was shown a few years ago [17] that an electron beam in the LHC tunnel would allow to achieve an outstanding luminosity of about  $10^{33} \text{ cm}^{-2} \text{ s}^{-1}$  in  $ep$  interactions for both electrons and positrons. It is obvious, however, that while such a ring may be built without any major technical obstacle, installing it on top of the LHC magnet ring would be a non-trivial engineering task. For this reason it was decided to consider besides this “ring-ring (RR)” option also a “linac-ring (LR)” configuration, with a linear electron accelerator tangential to the LHC. For the comparison of RR and LR options,  $E_e$  was kept the same 60 GeV. The ring may extend to somewhat higher energies, while only a Linac would allow to exceed 100 GeV  $E_e$  largely. The potential for higher energy is not the only, and possibly not the dominant reason for considering a linac-ring collider. Important other benefits include the potential for higher electron current than assumed in the LHeC baseline design and thus higher luminosity, and a construction time that can overlap with LHC running.

This report presents all major components and considerations for both the RR and the LR configuration. A choice between the two configurations is envisaged soon after the appearance of the CDR. It is important to consider that the RR configuration delivers high electron and positron luminosity, with difficulties for high polarisation, while the LR configuration has a high potential for polarised electrons, but difficulties to deliver an intense positron beam, yet offering also a photon beam option. The electrical power required for a ring-ring collider at constant beam current increases with the fourth power of energy, while for a linac-ring collider the increase is roughly linear as long as the synchrotron radiation in the return arcs remains a small fraction of the total. Also, for higher electron energies in the ring the polarization greatly decreases, whereas for the linac solution the polarization is independent of beam energy. A choice of one over the other option has primarily to be based on physics but as well technical, cost and further considerations, which is why considerable effort had been spent to develop both options to the required detail. No attempt is made in the report to favour one over the other configuration. In the period of this design study both options came into a very fruitful interaction and occasional competition which nicely boosted both designs.

## 2.6 Luminosity and Power

The relation of the luminosity, power and energy differs for the RR and the LR configurations. In the case of the ring accelerator, as for HERA, the luminosity for matched beams is determined by the number of protons per bunch ( $N_p$ ), the normalised proton beam emittance ( $\epsilon_p$ ), the  $x, y$  coordinates of the proton beam beta function values at the interaction point ( $\beta_{x,y}$ ) and the electron beam current ( $I_e$ ) as

$$L = \frac{N_p \cdot \gamma}{4\pi e \epsilon_p} \cdot \frac{I_e}{\sqrt{\beta_{px} \beta_{py}}}, \quad (2.1)$$

with  $\gamma = E_p/M_p$ . The design luminosity assumes the so-called ultimate proton beam parameters for  $E_p = 7$  TeV with  $1.7 \cdot 10^{11}$  protons per bunch and  $\epsilon_p = 3.8 \mu\text{m}$ . It is interesting to note that already the first year of operating the LHC has indicated that smaller emittance values are in reach and the bunch intensities have exceeded  $10^{11}$ , for 50 ns spacing. Eq. 2.1 then corresponds to

$$L = 8.2 \cdot 10^{32} \text{cm}^{-2} \text{s}^{-1} \cdot \frac{N_p 10^{11}}{1.7} \cdot \frac{m}{\sqrt{\beta_{px} \beta_{py}}} \cdot \frac{I_e}{50 \text{mA}}, \quad (2.2)$$

where the electron beam current is given by

$$I_e = 0.35 \text{mA} \cdot P_{\text{SR}}[\text{MW}] \cdot \left( \frac{100}{E_e[\text{GeV}]} \right)^4. \quad (2.3)$$

Consequently one needs to minimize the  $\beta$  functions and gains linearly with  $P$  and like  $E_e^4$  when decreasing the electron beam energy. With  $\beta_{x(y)} = 1.8(0.5)$  m, see the optics section, one obtains a typical value of  $10^{33} \text{cm}^{-2} \text{s}^{-1}$  luminosity for  $E_e = 60$  GeV with 30 MW of synchrotron-radiation power. The dependence of  $L(E, P)$  is shown in Fig. 2.2 (top) for the RR configuration. While with the matching requirement for each  $E_e$  an evaluation would have to be done of the  $\beta$  functions, one yet recognises that the RR option has a great potential to indeed achieve very high luminosities, even exceeding  $10^{33} \text{cm}^{-2} \text{s}^{-1}$  if  $E_e$  was a bit lowered and  $P$  somewhat enlarged.

For this design report on the LHeC the wall-plug power limit was set to 100 MW, about one fifth of what one is considering for CLIC, for example. With a 10 years running period at such a high luminosity and  $N_p$  probably enlarged, one can consider an integrated luminosity for the LHeC of  $O(100) \text{fb}^{-1}$  a realistic perspective in simultaneous operation with the LHC. This is two orders of magnitude more than HERA delivered. That is necessary for exploiting the high  $Q^2$  and large  $x$  boundaries. It means that the whole low  $Q^2$  physics program, with the exception of rare processes as DVCS and subject to trigger acceptance considerations, may yet be pursued in a rather short period of time.

A linear electron beam colliding with a storage ring proton beam was considered quite some time ago [13]. Its luminosity, for head-on collisions, can be obtained from the following relation [14], similar to Eq. 2.1

$$L = \frac{N_p \cdot \gamma}{4\pi e \epsilon_p} \cdot \frac{I_e}{\beta^*}, \quad (2.4)$$

which scales as

$$L = 8 \cdot 10^{31} \text{cm}^{-2} \text{s}^{-1} \cdot \frac{N_p 10^{11}}{1.7} \cdot \frac{0.2m}{\beta^*} \cdot \frac{I_e}{1 \text{mA}}, \quad (2.5)$$

where the electron beam current is given by

$$I_e = mA \cdot \frac{P_b[\text{MW}]}{(1 - \eta)E_e[\text{GeV}]}. \quad (2.6)$$

Here  $\eta$  denotes the efficiency of the energy recovery process, defined in terms of beam power at the collision point with and without recovery,  $P_{b,er}$  and  $B_{b,0}$ , respectively, for the same wall-plug power, as  $\eta \equiv 1/(1 - P_{b,0}/P_{b,er})$ . It is easy to see that a pulsed linac without recovery is short by an order of magnitude in the

926 luminosity to the RR configuration, even for an ambitious  $\beta^*$  value of 0.1 m, which is introduced in the LR  
927 section. With energy recovery, however, and an efficiency above 90 % as is expected to be realistic for the  
928 LHeC case, one obtains luminosities of similar value as in the RR case, see Fig. 2.2. The energy recovery  
929 linac (ERL) operates the cavities in CW mode at moderate gradients of typically 20 MV/m.

930 The recovery of energy requires a racetrack geometry of the linac with return arcs, or possibly two linacs  
931 of opposite orientation as was originally considered [57]. This introduces synchrotron radiation losses as a  
932 parameter of concern to the LR configuration also. With the design here proposed, the arcs have a bending  
933 radius of 764 m, which leads to a LR accelerator of about 9 km length, which is one third of the LHC  
934 circumference, and requires a small compensation stage for the energy losses in the arcs.

935 A straight high energy, pulsed linac is also considered, which at  $E_e = 140$  GeV, reaches a luminosity of  
936 about  $5 \cdot 10^{31}$ , the design value of the HERA upgrade phase. One can also contemplate about stages of ERL  
937 returns, which provide much higher luminosities in this case, as is briefly demonstrated in this report too.  
938 This machine would require a 40-MW beam dump, the design for which has been scaled from the 10-MW  
939 dump proposed for the ILC.

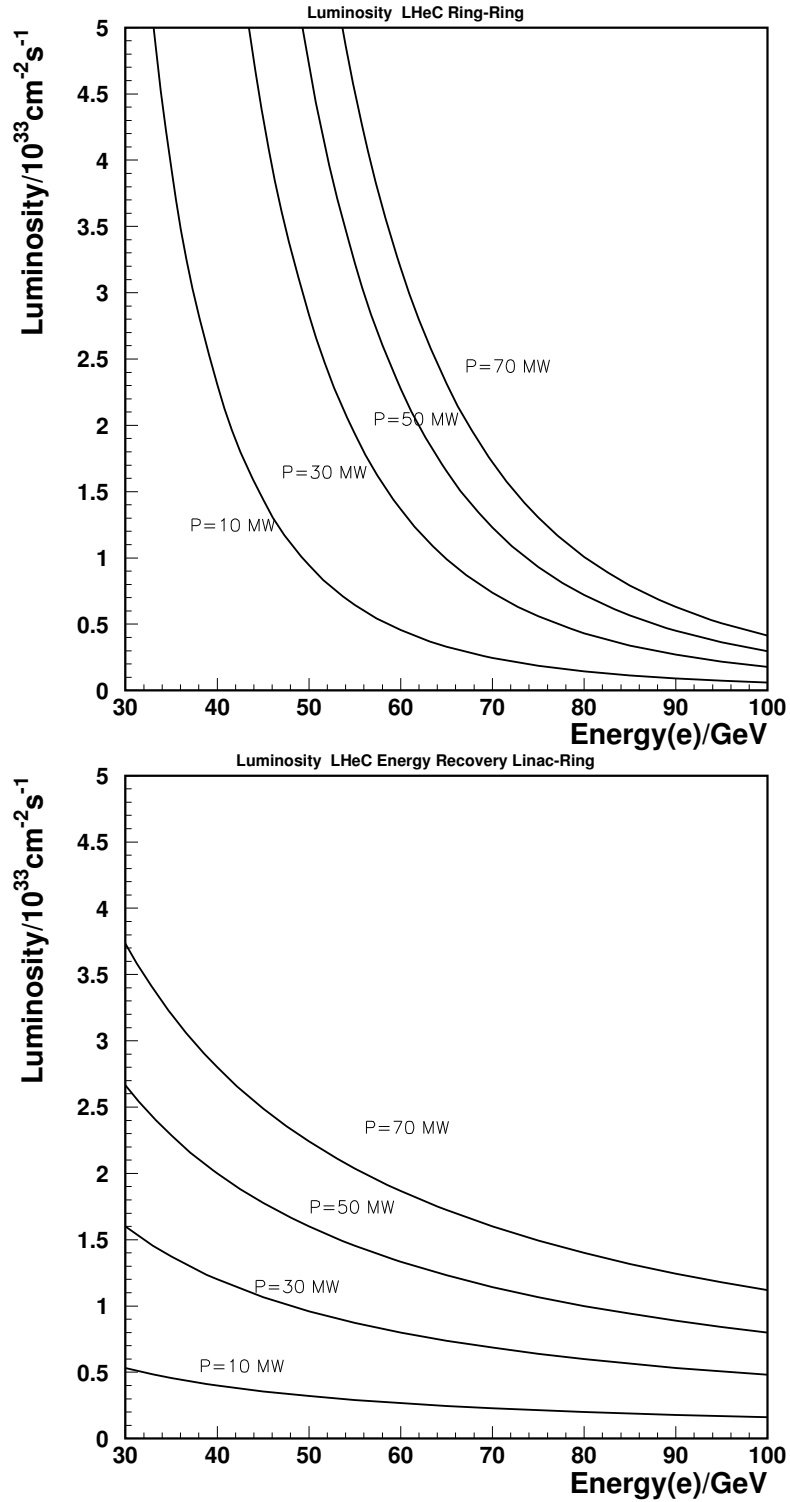


Figure 2.2: Estimated luminosity, in units of  $10^{33} \text{ cm}^{-2} \text{ s}^{-1}$ , for the RR configuration (top) and the LR energy recovery configuration (bottom), displayed as a function of the electron beam energy with the beam power as a parameter, see text.

## Chapter 3

# Executive Summary

The current version of the CDR, as of early August 2011, is for the referees as listed at the end of the draft to be evaluated. The authors are aware that various aspects of the project and the draft deserve a bit more attention prior to releasing the design report to the public. This concerns for example due consideration of the potential of the ring accelerator to reach higher than the here assumed 60 GeV beam energy, a further pass through physics and detector considerations and certainly various editorial finesses. The referee process will no doubt lead to further improvements and clarifications. The parameter table 3.1 given here may serve as a first overview for what the LHeC project as currently understood comprises. A genuine executive summary will be

For the linac technology. With the limit of present

electron beam	RR	LR	LR <sup>*)</sup>	proton beam	RR	LR
e- energy at IP[GeV]	60	60	140	bunch pop. [ $10^{11}$ ]	1.7	1.7
luminosity [ $10^{32}$ cm <sup>-2</sup> s <sup>-1</sup> ]	13	10	0.4	tr.emitt. $\gamma\epsilon_{x,y}$ [ $\mu$ m]	3.75	3.75
polarization [%]	40	90	90	spot size $\sigma_{x,y}$ [ $\mu$ m]	30, 16	7
bunch population [ $10^9$ ]	20	1.0	1.5	$\beta^*_{x,y}$ [m]	1.8,0.5	0.1
e- bunch length [mm]	10	0.3	0.3	bunch spacing [ns]	25	25
bunch interval [ns]	25	25	50			
transv. emit. $\gamma\epsilon_{x,y}$ [mm]	0.58, 0.29	0.05	0.1			
rms IP beam size $\sigma_{x,y}$ [ $\mu$ m]	30, 16	7	7			
e- IP beta funct. $\beta^*_{x,y}$ [m]	0.18, 0.10	0.12	0.14			
full crossing angle [mrad]	1	0	0			
geometric reduction $H_{hg}$	0.75	0.91	0.94			
repetition rate [Hz]	-	-	10			
beam pulse length [ms]	-	-	5			
ER efficiency	-	94%	-			
average current [mA]	131	6.4	0.27			
tot. wall plug power[MW]	100	100	100			



RR= Ring – Ring LR =Linac –Ring

Ring: with 1° as baseline : L/2  
Linac: clearing gap: L\*2/3

\*) pulsed, but high energy ERL not impossible

Figure 3.1: Parameters of the LHeC in the ring-ring and the linac-ring version as considered in the current report. The LHC proton beam parameters correspond to the “ultimate beam” configuration, to which even the current operation is already close, as with the emittance,  $\beta^*$ , the 50 ns bunch spacing and also the number of protons per bunch. The report has also parts for electron-deuteron and electron-ion scattering.

952

## Part II

953

# Physics



## Chapter 4

# Precision QCD and Electroweak Physics

This chapter elucidates the physics prospects which are related to high precision measurements with the LHeC to test and develop QCD and the electroweak theory. Section 4.1 presents inclusive deep inelastic scattering and consists of three parts: NC and CC cross sections and structure functions, the simulation of NC and CC data sets including estimates for the expected systematic uncertainties, and the simulation of LHeC precision measurements of the longitudinal structure function  $F_L$ . The LHeC is the first DIS experiment which is able to completely unfold the quark contents of the nucleon. Section 4.2 introduces assumptions for the QCD fit, used for illustrating the expected gain in precision at the LHeC as compared to HERA, BCDMS and precision  $W$  charge asymmetry data from the LHC. Results are then presented first for the determination of the valence quark and the strange quark distributions, which are also compared with the current information as contained in modern PDF determinations. A dedicated part is written for top quark physics at the LHeC as at very high  $Q^2$ ,  $t$  and  $\bar{t}$  production in DIS become a new subject of research. Sections 4.3 and 4.4 discuss in detail the expected precision measurements of the gluon distribution and of the strong coupling constant, respectively. Section 4.5 motivates the measurements with electron-deuteron scattering which extend current experimental knowledge on the structure of the neutron (and the deuteron) by nearly four orders of magnitude in  $Q^2$  and  $1/x$ . Section 4.6 introduces the measurements of the charm and beauty densities. Owing to the much extended range, higher energy (cross section) and dedicated Silicon tracking, high precision measurements of the  $c$  and  $b$  densities will be provided for the development of the QCD theory of heavy quarks and for the description of new phenomena which may be expected to be related especially to the  $b$  density, as the production of the Higgs particle in MSSM SUSY. Sections 4.7 illustrates the precision QCD tests that can be performed at the LHeC with jets in the final state, respectively. With the enlarged energy, new measurements of the total photoproduction cross sections can be performed as are discussed in Section 4.8. The Chapter is concluded with the electroweak physics Section 4.9 which focusses on the precision measurements of the light weak NC quark couplings and on the scale dependence of the electroweak mixing angle, as can be determined from polarisation asymmetries in NC and the NC/CC cross section ratio.

## 4.1 Inclusive Deep Inelastic Scattering

### 4.1.1 Cross Sections and Structure Functions

The scattering amplitude for electron-proton scattering is a product of lepton and hadron currents times the propagator characteristic of the exchanged particle, a photon or  $Z_0$  in neutral current scattering, a  $W^\pm$  in charged current scattering. The inclusive scattering cross section therefore is given by the product of two

987 tensors,

$$\frac{d^2\sigma}{dx dQ^2} = \frac{2\pi\alpha^2}{Q^4 x} \sum_j \eta_j L_j^{\mu\nu} W_j^{\mu\nu}, \quad (4.1)$$

988 where  $j$  denotes the summation over  $\gamma$ ,  $Z_0$  exchange and their interference for NC, and  $j = W^+$  or  $W^-$   
 989 for CC. The leptonic tensor  $L_j^{\mu\nu}$  is related to the coupling of the electron with the exchanged boson and  
 990 contains the electromagnetic or the weak couplings, such as the vector and axial-vector electron- $Z_0$  couplings,  
 991  $v_e$  and  $a_e$ , in the NC case. This leptonic part of the cross section can be calculated exactly in the standard  
 992 electroweak  $U_1 \times SU_2$  theory. The hadronic tensor, however, describing the interaction of the exchanged  
 993 boson with the proton, can only be reduced to a sum of structure functions,  $F_i(x, Q^2)$ , but not be fully  
 994 calculated. Conservation laws reduce the number of basic structure functions in unpolarised  $ep$  scattering to  
 995  $i = 1 - 3$ . In perturbative QCD the structure functions are related to parton distributions  $f$  *via* coefficient  
 996 functions  $C$

$$[F_{1,3}, F_2] = \sum_i \int_0^1 [1, z] \frac{dz}{z} C_{1,2,3}\left(\frac{x}{z}, \frac{Q^2}{\mu_r^2}, \frac{\mu_f^2}{\mu_r^2}, \alpha_s(\mu_r^2)\right) \cdot f_i(z, \mu_f^2, \mu_r^2), \quad (4.2)$$

997 where  $i$  sums the quark  $q$ , anti-quark  $\bar{q}$  and gluon  $g$  contributions and  $f_i(x)$  is the probability distribution of  
 998 the parton of type  $i$  to carry a fraction  $x$  of the proton's longitudinal momentum. The coefficient functions  
 999 are exactly calculable but depend on the factorisation and renormalisation scales  $\mu_f$  and  $\mu_r$ . The parton  
 1000 distributions are not calculable but have to be determined by experiment. Their  $Q^2$  dependence obeys  
 1001 evolution equations. A general factorisation theorem, however, has proven the parton distributions to be  
 1002 universal, i.e. to be independent of the type of hard scattering process. This makes deep inelastic lepton-  
 1003 nucleon scattering a most fundamental process: the parton distributions in the proton are measured best  
 1004 with a lepton probe and may be used to predict hard scattering cross sections at, for example, the LHC. The  
 1005 parton distributions are derived from measurements of the structure functions in NC and CC scattering, as  
 1006 is discussed below.

### 1007 4.1.2 Neutral Current

1008 The neutral current deep inelastic  $ep$  scattering cross section, at tree level, is given by a sum of generalised  
 1009 structure functions according to

$$\frac{d^2\sigma_{NC}}{dx dQ^2} = \frac{2\pi\alpha^2 Y_+}{Q^4 x} \cdot \sigma_{r,NC} \quad (4.3)$$

$$\sigma_{r,NC} = \mathbf{F}_2 + \frac{Y_-}{Y_+} \mathbf{xF}_3 - \frac{y^2}{Y_-} \mathbf{FL}, \quad (4.4)$$

1010 where the electromagnetic coupling constant  $\alpha$ , the photon propagator and a helicity factor are absorbed in  
 1011 the definition of a reduced cross section  $\sigma_r$ , and  $Y_{\pm} = 1 \pm (1-y)^2$ . The functions  $\mathbf{F}_2$  and  $\mathbf{xF}_3$  depend on  
 1012 the lepton beam charge and polarisation ( $P$ ) and on the electroweak parameters as [58]

$$\begin{aligned} \mathbf{F}_2^{\pm} &= F_2 + \kappa_Z (-v_e \mp P a_e) \cdot F_2^{\gamma Z} + \kappa_Z^2 (v_e^2 + a_e^2 \pm 2P v_e a_e) \cdot F_2^Z \\ \mathbf{xF}_3^{\pm} &= \kappa_Z (\pm a_e + P v_e) \cdot x F_3^{\gamma Z} + \kappa_Z^2 (\mp 2v_e a_e - P(v_e^2 + a_e^2)) \cdot x F_3^Z. \end{aligned} \quad (4.5)$$

1013 In the on-mass shell  $\overline{MS}$  scheme the propagator function  $\kappa_Z$  is given by the weak boson masses ( $M_Z$ ,  $M_W$ )

$$\kappa_Z(Q^2) = \frac{Q^2}{Q^2 + M_Z^2} \cdot \frac{1}{4 \sin^2 \Theta \cos^2 \Theta} \quad (4.6)$$

1014 with the weak mixing angle  $\sin^2 \Theta = 1 - M_W^2/M_Z^2$ . In the hadronic tensor decomposition [59] the structure  
 1015 functions are well defined quantities. In the Quark Parton Model (QPM) the longitudinal structure function

1016 is zero [60] and the two other functions are given by the sums and differences of quark ( $q$ ) and anti-quark  
 1017 ( $\bar{q}$ ) distributions as

$$\begin{aligned} (F_2, F_2^{\gamma Z}, F_2^Z) &= x \sum (e_q^2, 2e_q v_q, v_q^2 + a_q^2)(q + \bar{q}) \\ (xF_3^{\gamma Z}, xF_3^Z) &= 2x \sum (e_q a_q, v_q a_q)(q - \bar{q}), \end{aligned} \quad (4.7)$$

1018 where the sum extends over all up and down type quarks and  $e_q = e_u, e_d$  denotes the electric charge of up-  
 1019 or down-type quarks. The vector and axial-vector weak couplings of the fermions ( $f = e, u, d$ ) to the  $Z_0$   
 1020 boson in the standard electroweak model are given by

$$v_f = i_f - e_f 2 \sin^2 \Theta \quad a_f = i_f \quad (4.8)$$

1021 where  $e_f = -1, 2/3, -1/3$  and  $i_f = I(f)_{3,L} = -1/2, 1/2, -1/2$  denotes the left-handed weak isospin charges,  
 1022 respectively. Thus the vector coupling of the electron, for example, is very small,  $v_e = -1/2 + 2 \sin^2 \Theta \simeq 0$ ,  
 1023 since the weak mixing angle is roughly equal to  $1/4$ .

1024 At low  $Q^2$  and low  $y$  the reduced NC cross section, Eq. 4.3, to a very good approximation is given by  
 1025  $\sigma_r = F_2(x, Q^2)$ . At  $y > 0.5$ ,  $F_L$  makes a sizeable contribution to  $\sigma_{r,NC}$ . In the DGLAP approximation of  
 1026 perturbative QCD, to lowest order, the longitudinal structure function is given by [61]

$$F_L(x) = \frac{\alpha_s}{4\pi} x^2 \int_x^1 \frac{dz}{z^3} \cdot \left[ \frac{16}{3} F_2(z) + 8 \sum e_q^2 \left(1 - \frac{x}{z}\right) z g(z) \right], \quad (4.9)$$

1027 which at low  $x$  is dominated by the gluon contribution. A measurement of  $F_L$  requires a variation of the  
 1028 beam energy.

1029 Two further structure functions can be accessed with cross section asymmetry measurements, in which  
 1030 the charge and/or the polarisation of the lepton beam are varied. A charge asymmetry measurement, with  
 1031 polarisation values  $P_{\pm}$  of the  $e^{\pm}$  beam, determines the following structure function combination

$$\sigma_{r,NC}^+(P_+) - \sigma_{r,NC}^-(P_-) = -\kappa_Z a_e (P_+ + P_-) \cdot F_2^{\gamma Z} + \frac{Y_-}{Y_+} \kappa_Z a_e \cdot [2xF_3^{\gamma Z} + (P_+ - P_-) \kappa_Z a_e x F_3^Z] \quad (4.10)$$

1032 neglecting terms  $\propto v_e$  which can be easily obtained from Eq. 4.5. If data are taken with opposite polarisation  
 1033 and charge, the asymmetry represents a measurement of the difference of quark and anti-quark distributions  
 1034 in NC, see Eq. 4.7. In contrast to what is often stated, the charge asymmetry is a parity conserving quantity  
 1035  $\propto a_e a_q$ . Assuming symmetry between sea and antiquarks, it is a direct measure of the valence quarks,  
 1036  $xF_3^{\gamma Z} = 2u_v + d_v$  in  $ep$ . This function was measured for the first time in  $\mu^{\pm}$  Carbon scattering by the  
 1037 BCDMS Collaboration [62] at large  $x > 0.2$  and for  $Q^2$  of about  $50 \text{ GeV}^2$ . With the LHeC, for the first  
 1038 time, high precision measurements of  $xF_3$  in NC become possible as is demonstrated in Sect. 4.2.2. These  
 1039 will access the valence quarks at low  $x \lesssim 0.001$  for the first time in direct measurements.

1040 A genuine polarisation asymmetry measurement, keeping the beam charge fixed, according to eqs. 4.3  
 1041 and 4.5 determines a similar combination of  $F_2^{\gamma Z}$  and  $xF_3^{\gamma Z}$

$$\frac{\sigma_{r,NC}^{\pm}(P_L) - \sigma_{r,NC}^{\pm}(P_R)}{P_L - P_R} = \kappa_Z [\mp a_e F_2^{\gamma Z} + \frac{Y_-}{Y_+} v_e x F_3^{\gamma Z}] \simeq \mp \kappa_Z a_e F_2^{\gamma Z} \quad (4.11)$$

1042 neglecting again the term  $\propto v_e$ . The product  $a_e F_2^{\gamma Z}$  is proportional to combinations  $a_e v_q$  and thus a direct  
 1043 measure of parity violation at very small distances.

1044 The structure function  $F_2^{\gamma Z}$  accesses a new combination of quark distributions and is measurable for the  
 1045 first time, and with high precision, at the LHeC, see Fig. 4.1, in which the result is shown of its possible  
 1046 measurement. The remarkable precision on  $F_2^{\gamma Z}$  illustrates the huge potential in precision and range which  
 1047 the LHeC brings. For the study of electroweak effects one clearly desires to have the maximum beam energy  
 1048 and polarisation available as the comparison of the two results for different beam conditions but the same  
 1049 luminosity in Fig. 4.1 shows.

1050 The polarisation asymmetry also permits a high precision measurement of the weak mixing angle at  
 1051 different  $Q^2$  values, below and to much higher values than  $M_Z^2$ , at which  $\sin^2 \Theta$  was precisely measured at  
 1052 LEP and the SLC, see Sect. 4.9.3.

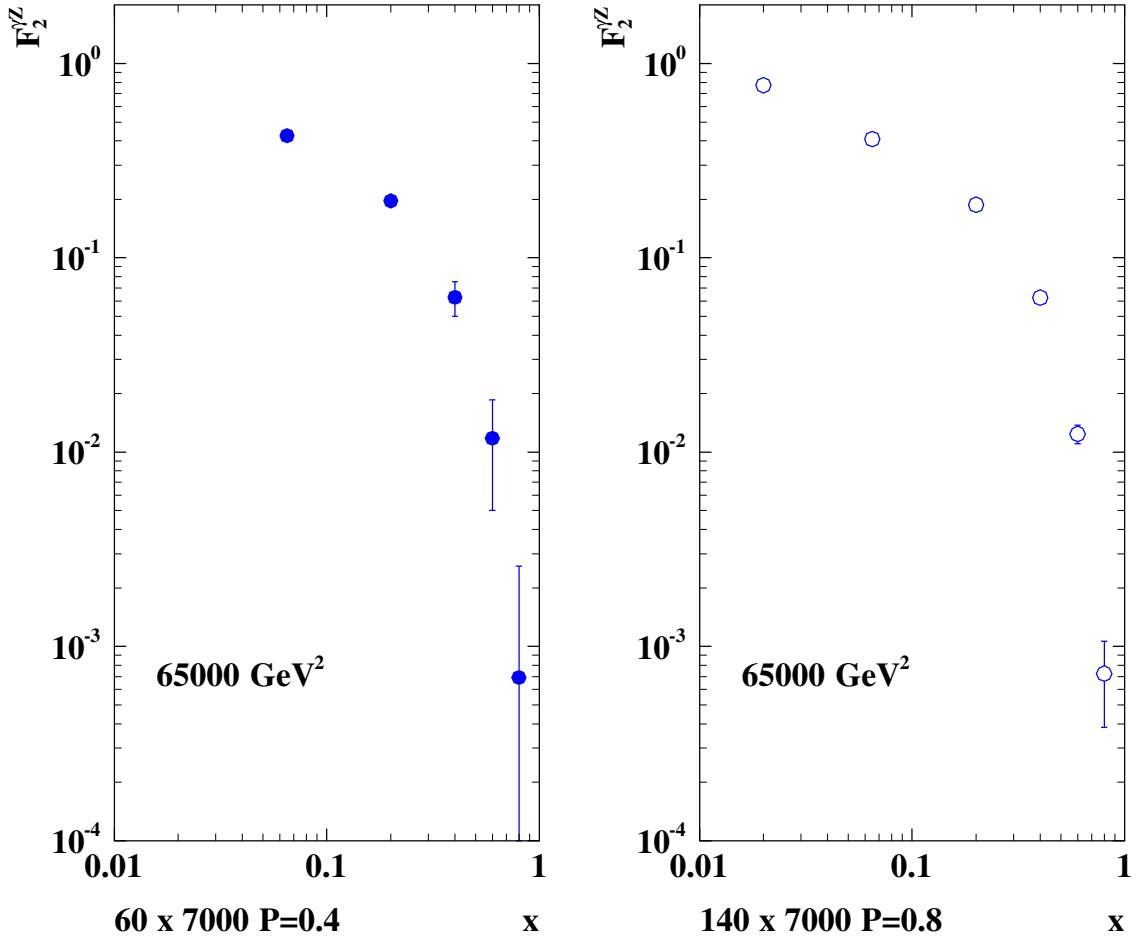


Figure 4.1: Simulation of the measurement of the  $\gamma Z$  interference structure function  $F_2^{\gamma Z}$ , shown as a function of  $x$  for a typical high  $Q^2$  value, for two LHeC configurations ( $E_e = 60$  GeV and  $P = \pm 0.4$ , left) and ( $E_e = 140$  GeV and  $P = \pm 0.9$ , right). The proton beam energy is 7 TeV and the luminosity assumed is  $10 \text{ fb}^{-1}$  per polarisation state. This function is a measure for parity violation and provides additional information on the quark distributions as it is proportional to  $e_q v_q$  to be compared with  $e_q^2$  in the lowest order function  $F_2$ . Shown are statistical uncertainties only. The systematic uncertainty can be expected to be small as in the asymmetry many effects cancel and because at the LHeC such asymmetries are large, and the polarisation possibly controlled at the per mille level, as is discussed in the technical part of the CDR.

### 1053 4.1.3 Charged Current

1054 The inclusive polarised charged current  $e^\pm p$  scattering cross section can be written as

$$\frac{d^2\sigma_{CC}^\pm}{dx dQ^2} = \frac{1 \pm P}{2} \cdot \frac{G_F^2}{2\pi x} \cdot \left[ \frac{M_W^2}{M_W^2 + Q^2} \right]^2 Y_+ \cdot \sigma_{r,CC}. \quad (4.12)$$

1055 The reduced charged current cross section, analogous to the NC case Eq. 4.3, is a sum of structure function  
1056 terms

$$\sigma_{r,CC}^\pm = W_2^\pm \mp \frac{Y_-}{Y_+} xW_3^\pm - \frac{y^2}{Y_+} W_L^\pm. \quad (4.13)$$

1057 In the on-mass shell scheme, the Fermi constant  $G_F$  is defined, see for example [63], using the weak boson  
1058 masses as

$$G_F = \frac{\pi\alpha}{\sqrt{2}M_W^2 \sin^2\theta(1 - \Delta r)} \quad (4.14)$$

1059 with  $\sin^2\theta = 1 - M_W^2/M_Z^2$  as above. The higher order correction term  $\Delta r$  can be approximated [64] as  
1060  $\Delta r = 1 - \alpha/\alpha(M_Z) - 0.0094(m_t/173\text{GeV})^2/\tan^2\theta$ , and thus introduces a dependence of the DIS cross section  
1061 on the mass of the top quark. The choice of  $G$  above allows the CC cross section, Eq. 4.12, to be rewritten  
1062 as

$$\frac{d^2\sigma_{CC}^\pm}{dx dQ^2} = \frac{1 \pm P}{2} \cdot \frac{2\pi\alpha^2 Y_+}{Q^4 x} \cdot \kappa_W^2 \cdot \sigma_{r,CC}, \quad (4.15)$$

1063 with

$$\kappa_W(Q^2) = \frac{Q^2}{Q^2 + M_W^2} \cdot \frac{1}{4\sin^2\theta}, \quad (4.16)$$

1064 which is convenient for the consideration of NC/CC cross section ratios.

1065 In the QPM (where  $W_L^\pm = 0$ ), the structure functions represent beam charge dependent sums and  
1066 differences of quark and anti-quark distributions and are given by

$$W_2^+ = x(\bar{U} + D), \quad xW_3^+ = x(D - \bar{U}), \quad W_2^- = x(U + \bar{D}), \quad xW_3^- = x(U - \bar{D}). \quad (4.17)$$

1067 Using these equations one finds

$$\sigma_{r,CC}^+ \sim x\bar{U} + (1-y)^2 xD, \quad (4.18)$$

$$\sigma_{r,CC}^- \sim xU + (1-y)^2 x\bar{D}. \quad (4.19)$$

1068 Combined with Equation 4.5, which approximately reduces to

$$\begin{aligned} \sigma_{r,NC}^\pm &\simeq [c_u(U + \bar{U}) + c_d(D + \bar{D})] + \kappa_Z[d_u(U - \bar{U}) + d_d(D - \bar{D})] \\ c_{u,d} &= e_{u,d}^2 + \kappa_Z(-v_e \mp Pa_e)e_{u,d}v_{u,d} \quad d_{u,d} = \pm a_e a_{u,d} e_{u,d}, \end{aligned} \quad (4.20)$$

1069 one finds that the NC and CC cross section measurements at the LHeC determine the complete set  $U, D, \bar{U}$   
1070 and  $\bar{D}$ , i.e. the sum of up-type, of down-type and of their anti-quark-type distributions. Below the  $b$  quark  
1071 mass threshold, these are related to the individual quark distributions as follows

$$U = u + c \quad \bar{U} = \bar{u} + \bar{c} \quad D = d + s \quad \bar{D} = \bar{d} + \bar{s}. \quad (4.21)$$

1072 Assuming symmetry between sea quarks and anti-quarks, the valence quark distributions result from

$$u_v = U - \bar{U} \quad d_v = D - \bar{D}. \quad (4.22)$$

#### 1073 4.1.4 Cross Section Simulation and Uncertainties

1074 The LHeC extends the kinematic range as compared to HERA in the negative momentum transfer squared  
 1075  $Q^2$  from a maximum of about 0.03 to 1 TeV<sup>2</sup> and towards low  $x$ , e.g. for  $Q^2 = 3 \text{ GeV}^2$ , from about  $4 \cdot 10^{-5}$   
 1076 to  $2 \cdot 10^{-6}$ . The projected increase of integrated luminosity by a factor of 100 allows to also extend the  
 1077 kinematic range at large  $x$ , in charged currents, from practically about 0.4 to 0.8. Due to the enlarged  
 1078 electron beam energy  $E_e$  the range of high inelasticity  $y \simeq 1 - E'_e/E_e$  should extend closer to 1. A reduced  
 1079 noise in the calorimeters may allow to reach lower values of  $y$  than at HERA, also because the hadronic  $y$   
 1080 is determined as the sum over  $E - p_z$  divided by twice the with the LHeC enhanced electron beam energy.  
 1081 Very recently it has been observed by H1 that the reconstruction of the hadronic final state with jets rather  
 1082 than the full sum of hadronic energy depositions allows to control better the region of low  $y$ , i.e. scattering  
 1083 close to the beam pipe. At the LHeC these jets are extremely energetic and one would expect, subject to  
 1084 detailed simulation studies at a later stage of the project, that kinematic reconstruction for values of  $y$  down  
 1085 to 0.001 or even below could be trusted.

1086 While the extensions of kinematic coverage and improvements of statistical precision are impressive,  
 1087 an estimate of the impact of LHeC NC and CC cross section measurements on derived quantities such as  
 1088 structure functions and parton distributions requires to also estimate the expected systematic measurement  
 1089 accuracy as may be achieved with the detector described in Chapter 13 below. In the following the assump-  
 1090 tions and simulation results are presented for the NC and the CC cross sections, which are subsequently  
 1091 used in QCD fit and other analyses throughout this report.

1092 The systematic uncertainties of the DIS cross sections have a number of sources, which at HERA have  
 1093 broadly been classified as uncorrelated and correlated across bin boundaries. For the NC case, the uncor-  
 1094 related sources, apart from data and Monte Carlo statistics, are a global efficiency uncertainty, due to for  
 1095 example tracking or electron identification errors, photoproduction background, calorimeter noise and radi-  
 1096 ative corrections. The correlated uncertainties result from imperfect energy scale and angle calibrations. In  
 1097 the classic kinematic reconstruction methods used here, and described in Sect. 12.1 one uses the scattered  
 1098 electron energy  $E'_e$  and polar angle  $\theta_e$  complemented by the energy of the hadronic final state  $E_h$ <sup>1</sup>. The  
 1099 correlated errors are due to scale uncertainties of the electron energy  $E'_e$  and of the hadronic final state  
 1100 energy  $E_h$ . There are also systematic errors due to an uncertainty of the measurement of the electron polar  
 1101 angle  $\theta_e$ . The assumptions used in the simulation of pseudodata are summarised in Table 4.1.

1102 In the absence of a detailed detector simulation at this stage, the systematic NC cross uncertainties due  
 1103 to  $E'_e$ ,  $\theta_e$  and  $E_h$  are calculated, following [65], from the derivatives of the NC cross section in the chosen bins  
 1104 taking into account the Jacobians where needed. The results have been compared, for the HERA kinematics,  
 1105 with the H1 MC simulation of systematic errors [66] and found to be in very good agreement for all three  
 1106 sources. The resulting error depends much on the kinematics. At low  $Q^2$ , for example, the systematic cross  
 1107 section error due to the uncertainty of  $\theta_e$  rises because of  $\delta Q^2/Q^2 = \delta E'_e/E'_e \oplus \tan(\theta_e/2) \cdot \delta\theta_e$  while at high  
 1108  $Q^2$  it is negligible. Low  $Q^2$  is the backward region, of large electron scattering angles with respect to the  
 1109 proton beam direction.

1110 A particular challenge is the measurement at large  $x$  because the cross section varies as  $(1-x)^c$ , with  
 1111  $c \simeq 3$ , and thus the relative error is amplified  $\propto 1/(1-x)$  as  $x$  approaches 1. At high  $x$  the hadronic final  
 1112 state is scattered into the forward detector region where the energy calibration becomes challenging. The  
 1113 calculated correlated NC cross section errors are illustrated in Figs. 4.2 and 4.3 for  $Q^2 = 2$  and 20000 GeV<sup>2</sup>,  
 1114 respectively. In the detector chapter these calculations have been taken to define approximate requirements  
 1115 on the scale calibrations in the different detector regions. An example for the resulting cross section  
 1116 measurement is displayed in Fig. 4.4 for low  $x$  and in Fig. 4.5 for large  $x$ .

---

<sup>1</sup>Basically one determines  $Q^2$  best with the electron kinematics and determines  $x$  from  $y = Q^2/sx$ . At large  $y$  the inelasticity is essentially measured with the electron energy  $y \simeq 1 - E'_e/E_e$ . At low  $y$  one has  $y = E_h \sin^2(\theta_h/2)/E_e$  with the hadronic final state energy  $E_h$  and angle  $\theta_h$  which results in  $\delta y/y \simeq \delta E_h/E_h$  to good approximation. There have been various refined methods proposed to determine the DIS kinematics, as the double angle method or the so-called sigma method. For the estimate of the cross section uncertainty behaviour as functions of  $Q^2$  and  $x$ , however, the simplest method using  $Q_e^2, y_e$  at large  $y$  and  $Q_e^2, y_h$  at low  $y$  is transparent and accurate enough within better than a factor of two. In much of the phase space, moreover, it is rather the uncorrelated efficiency or further specific errors than the kinematic correlations, which dominate the cross section measurement accuracy.

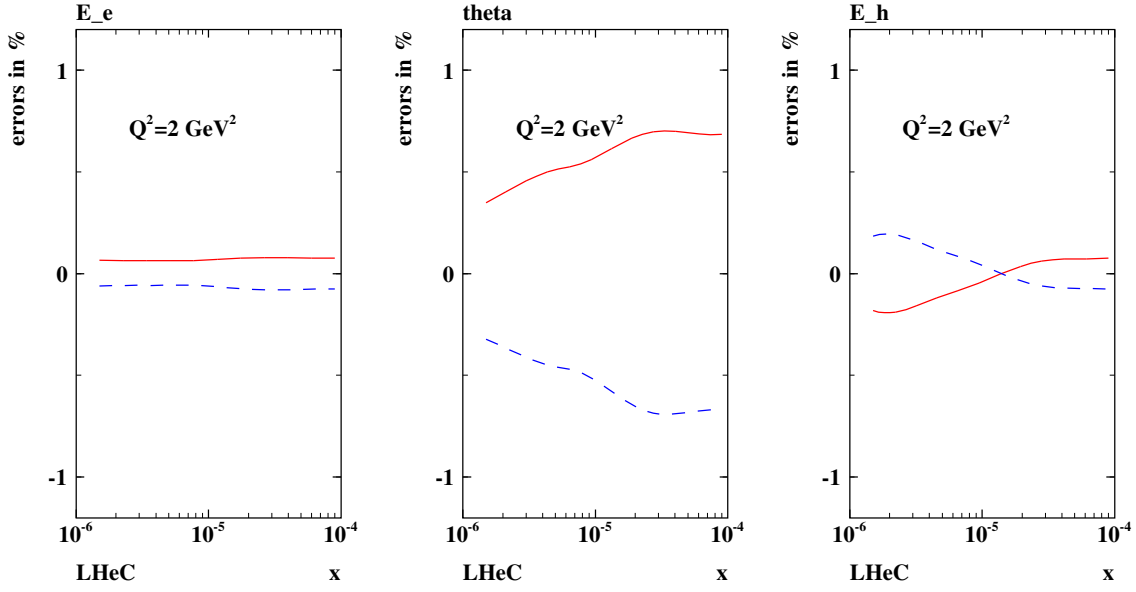


Figure 4.2: Neutral current cross section errors, calculated for  $60 \times 7000 \text{ GeV}^2$ , as result from scale uncertainties of the scattered electron energy  $\delta E'_e/E'_e = 0.1 \%$ , of its polar angle  $\delta\theta_e = 0.1 \text{ mrad}$  and the hadronic final state energy  $\delta E_h/E_h = 0.5 \%$ , at low  $Q^2 = 2 \text{ GeV}^2$  and correspondingly low  $x$ .

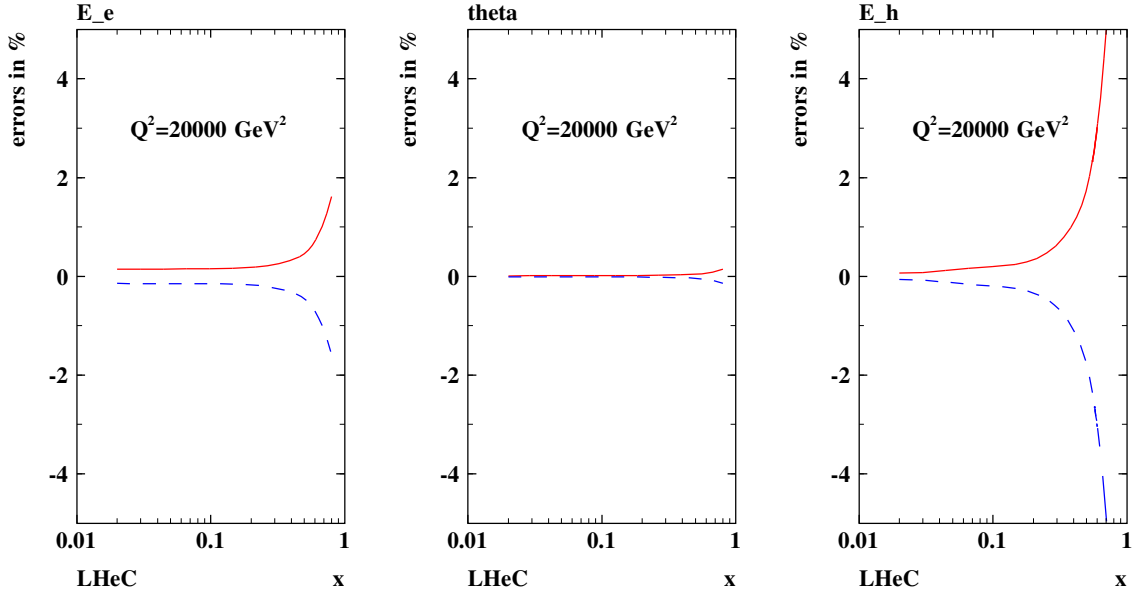


Figure 4.3: Neutral current cross section errors, calculated for  $60 \times 7000 \text{ GeV}^2$  unpolarised  $e^-p$  scattering, as result from scale uncertainties of the scattered electron energy  $\delta E'_e/E'_e = 0.1 \%$ , of its polar angle  $\delta\theta_e = 0.1 \text{ mrad}$  and the hadronic final state energy  $\delta E_h/E_h = 0.5 \%$ , at large  $Q^2 = 20000 \text{ GeV}^2$  and correspondingly large  $x$ . Note that the characteristic behaviour of the relative uncertainty at large  $x$ , i.e. to diverge  $\propto 1/(1-x)$ , is independent of  $Q^2$ , i.e. persistently observed at  $Q^2 = 200000 \text{ GeV}^2$  for example too.

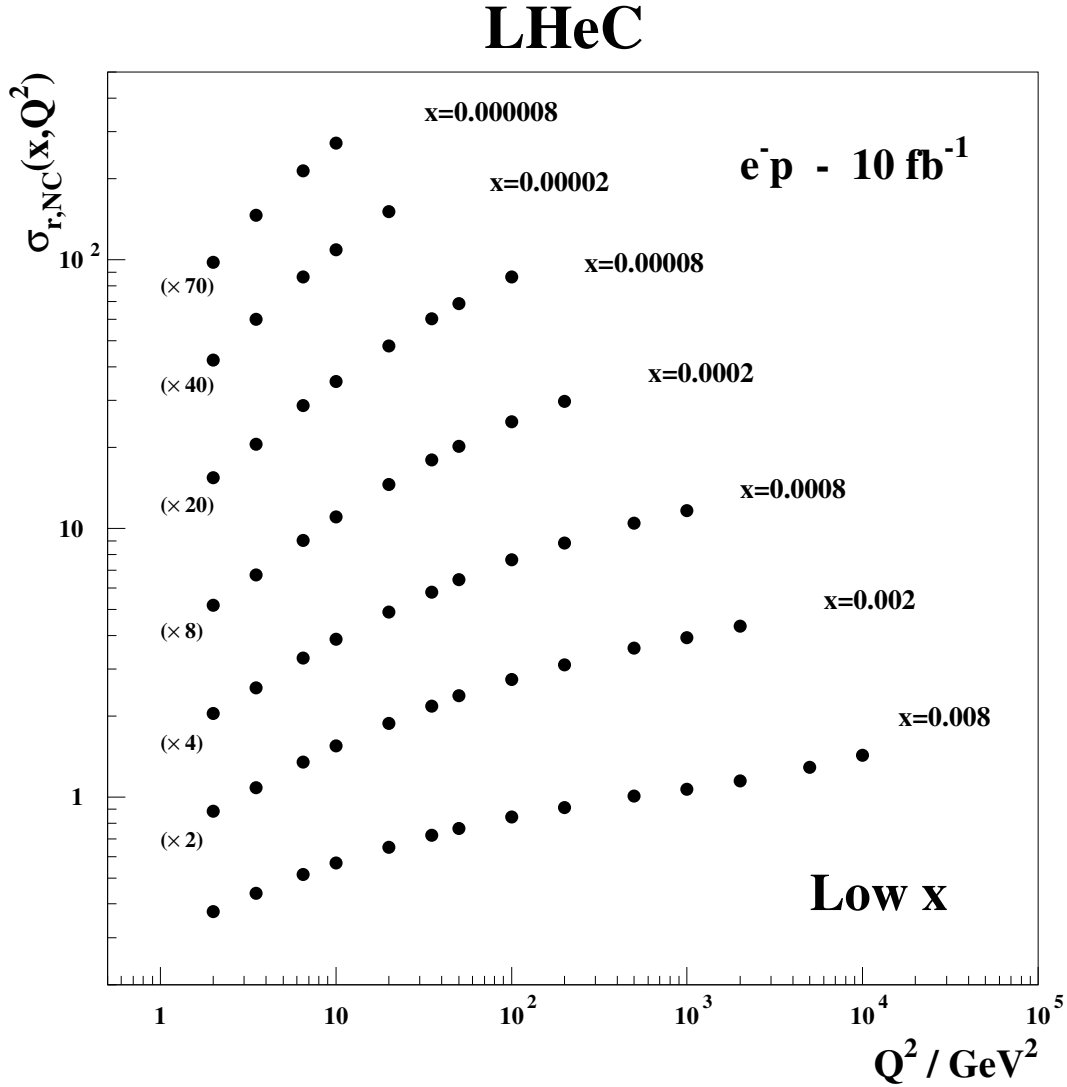


Figure 4.4: Simulated neutral current, inclusive reduced cross section measurement, for an integrated luminosity of  $10 \text{ fb}^{-1}$ , in unpolarised  $e^-p$  scattering at  $E_e = 60$  and  $E_p = 7000 \text{ GeV}$ . The DIS cross section is measurable at unprecedented precision and range. The uncertainty is about or below 1% and thus not visible on this plot. Departures from the strong rise of the reduced cross section,  $\sigma_r \simeq F_2$ , at very low  $x$  and  $Q^2$  are expected to appear due to non-linear gluon-gluon interaction effects in the so-called saturation region.



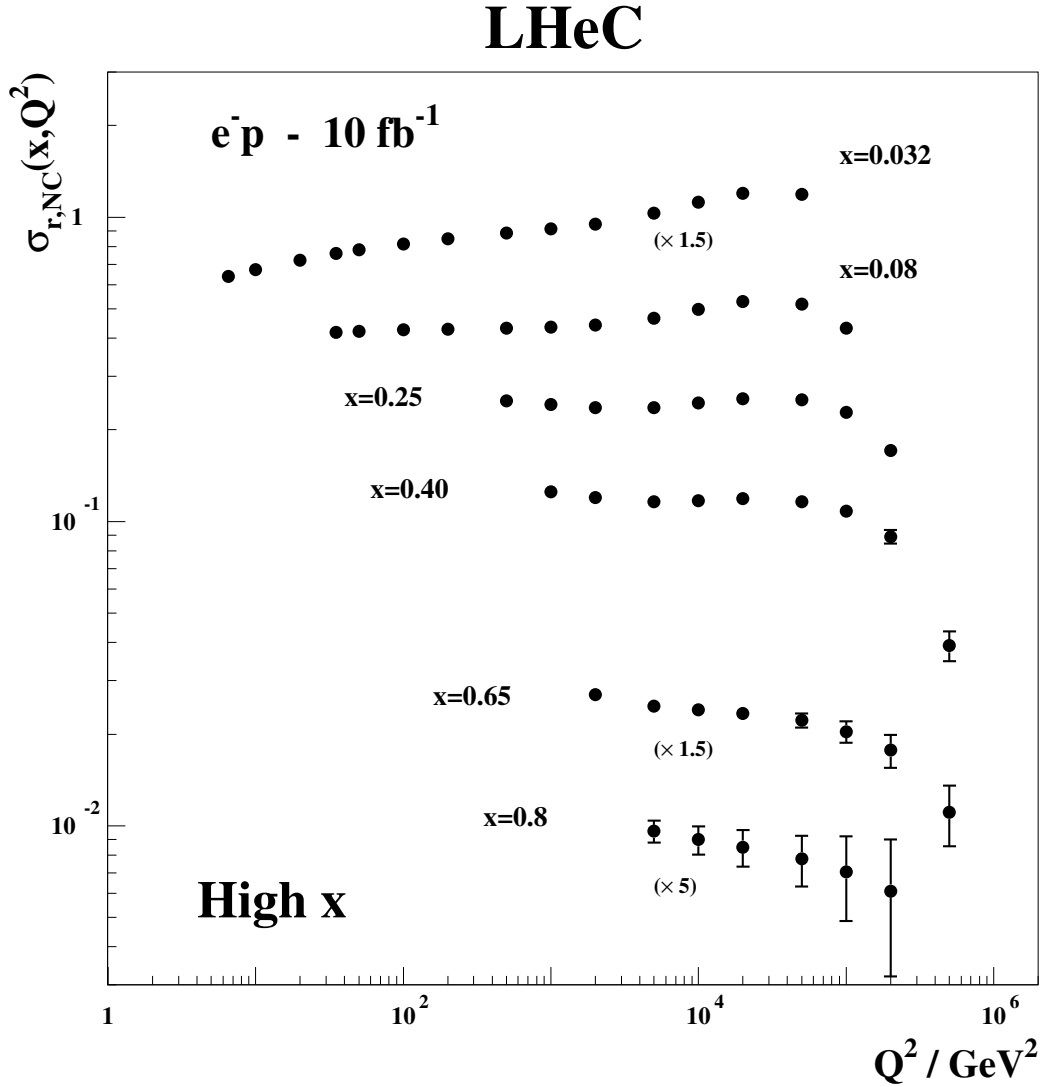


Figure 4.5: Simulated neutral current, inclusive reduced cross section measurement, for an integrated luminosity of  $10 \text{ fb}^{-1}$ , in unpolarised  $e^-p$  scattering at  $E_e = 60$  and  $E_p = 7000 \text{ GeV}$ . The DIS cross section is measurable at unprecedented precision and range. Plotted is the total uncertainty which, where visible at high  $x$  and  $Q^2$ , is dominated by the statistical error. Similar data sets are expected with different beam polarisations and charges, and in CC scattering, for  $Q^2 \geq 100 \text{ GeV}^2$ . The strong variations of  $\sigma_r$  with  $Q^2$ , as at  $x = 0.25$ , are due to the effects of  $Z$  exchange as is discussed and illustrated subsequently.

source of uncertainty	error on the source or cross section
scattered electron energy scale $\Delta E'_e/E'_e$	0.1 %
scattered electron polar angle	0.1 mrad
hadronic energy scale $\Delta E_h/E_h$	0.5 %
calorimeter noise (only $y < 0.01$ )	1-3 %
radiative corrections	0.5%
photoproduction background (only $y > 0.5$ )	1 %
global efficiency error	0.7 %

Table 4.1: Assumptions used in the simulation of the NC cross sections on the amount of uncertainties from various sources. These assumptions correspond to the typical or best of what was achieved in the H1 experiment. Note that in the cross section measurement the energy scale and angular uncertainties are relative to the Monte Carlo and not to be confused with resolution effects which determine the purity and stability of binned cross sections. The total cross section error due to these uncertainties, e.g. for  $Q^2 = 100 \text{ GeV}^2$ , is about 1.2, 0.7 and 2.0 % for  $y = 0.84, 0.1, 0.004$ .

1117 For the CC case, a similar simulation was done, albeit with less numeric effort. An illustration of the  
1118 high precision and large range of the inclusive CC cross section measurements is presented in Fig. 4.6. The  
1119 systematic cross section error, based on the H1 experience, was set to 2% and for larger  $x > 0.3$  a term  
1120 was added to allow the error to rise linearly to 10% at  $x = 0.9$ . For both NC and CC cross sections  
1121 the statistical error is given by the number of events but limited to 0.1% from below. With these error  
1122 assumptions a number of data sets was simulated, both for NC and CC, which is summarised in Table 4.2.  
1123 The energies of these sets had been chosen prior to the final baseline energy choice. For the simulation of  
1124 the  $F_L$  measurement, described below, a separate set of beam energies is considered.

#### 1125 4.1.5 Longitudinal Structure Function $F_L$

1126 The inclusive, deep inelastic electron-proton scattering cross section at low  $Q^2$ ,

$$\frac{d^2\sigma}{dx dQ^2} = \frac{2\pi\alpha^2 Y_+}{Q^4 x} [F_2(x, Q^2) - f(y) \cdot F_L(x, Q^2)], \quad (4.23)$$

1127 is defined by two proton structure functions,  $F_2$  and  $F_L$  with  $y = Q^2/sx$ ,  $Y_+ = 1 + (1-y)^2$  and  $f(y) = y^2/Y_+$ .  
1128 The two functions reflect the transverse and the longitudinal polarisation state of the virtual photon probing  
1129 the proton structure, i.e.  $F_T = F_2 - F_L$  and  $F_L$ , respectively. The positivity of the transverse and longitudinal  
1130 cross sections requires  $0 \leq F_L \leq F_2$ . Since for most of the kinematic range the  $y$  dependent factor  $f(y)$  is  
1131 very small, there follows that  $F_L$  causes in most of the kinematic range only a small correction to the reduced  
1132 cross section, which is governed by  $F_2$ , apart from the regio of maximum  $y$ . At small  $x$ , the inelasticity is  
1133 given as  $y \simeq 1 - E'_e/E_e$ . Therefore, in order to extract  $F_L$ , DIS has to be measured extremely accurately  
1134 at small scattered lepton energies, which is a question of how large  $E_e$  is, how to trigger and how to control  
1135 the background from particle production at low energies. A variation of the beam energies is required to  
1136 separate the two functions measured at the same  $x$  and  $Q^2$  by variation of  $y = Q^2/sx$ .

1137 A first measurement of  $F_L$  at low  $x$  at HERA has recently been performed by the ZEUS Collaboration [67]  
1138 and by the H1 Collaboration [68]. For the study of the gluon distribution at lowest  $x$ , the H1 data are crucial  
1139 as only H1 has measured  $F_L$  below  $Q^2$  of about  $10 \text{ GeV}^2$  owing to their backward detector constellation  
1140 upgraded in the nineties. The  $F_L$  measurement at HERA was performed towards the end of the accelerator  
1141 operation and could only extend over a period of three months with about  $10 \text{ pb}^{-1}$  of integrated luminosity  
1142 spent at two reduced proton beam energies, 450 and 565 GeV, besides the nominal 920 GeV. The H1 result is  
1143 consistent with pQCD predictions. The ratio  $R = F_L/(F_2 - F_L)$  has been found to be independent of  $x$  and  
1144  $Q^2$  at 20% accuracy, i.e.  $R = 0.26 \pm 0.05$  [68]. This interesting relation deserves a more precise investigation  
1145 and may break when the region of saturation is entered at lower  $x$  than HERA could access.

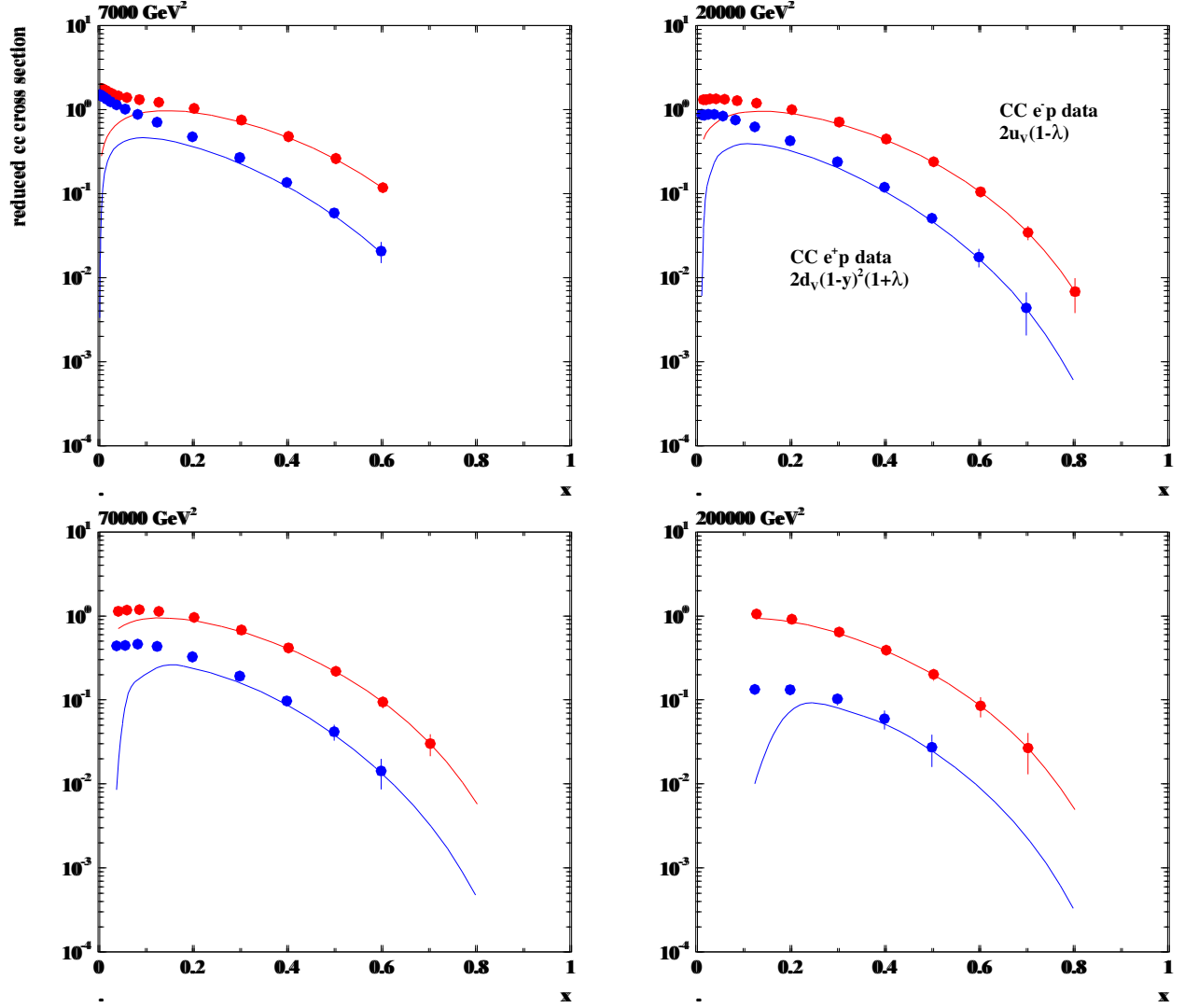


Figure 4.6: Reduced charged current cross sections with statistical uncertainties corresponding to  $1 \text{ fb}^{-1}$  electron (top data points, red) and positron (lower data points, blue) proton scattering at the LHeC, The curves are determined by the dominant valence quark distributions,  $u_v$  for  $e^-p$  and  $d_v$  for  $e^+p$ . In the simulation the lepton polarisation is taken to be zero. The valence-quark approximation of the reduced cross section is seen to hold at  $x \geq 0.3$ . A precise determination of the  $u/d$  ratio up to large  $x$  appears to be feasible at very high  $Q^2$ .

Set	$E_e/\text{GeV}$	$E_N/\text{TeV}$	N	$L^+/\text{fb}^{-1}$	$L^-/\text{fb}^{-1}$	Pol
A	20	7	7	1	1	0
B	50	7	7	50	50	0.4
C	50	7	7	1	1	0.4
D	100	7	7	5	10	0.9
E	150	7	7	3	6	0.9
F	50	3.5	7	1	1	0
G	50	2.7	7	0.1	0.1	0.4
H	50	1	7	-	1	0

Table 4.2: Conditions for simulated NC and CC data sets for studies on the LHeC physics. Here, A defines a low electron beam energy option which is of interest to reach lowest  $Q^2$  because  $Q_{min}^2$  decreases  $\propto E_e^{-2}$ ; B is the standard set, with a total luminosity split between different polarisation and charge states. C is a lower luminosity version which was considered in case there was a need for a dedicated low/large angle acceptance configuration, which according to more recent findings could be avoided since the luminosity in the restricted acceptance configuration is estimated, from the  $\beta$  functions obtained in the optics design, to be half of the luminosity in the full acceptance configuration; D is an intermediate energy linac-ring version, while E is the highest energy version considered, with the luminosities as given. It is likely that the assumptions for D and E on the positron luminosity are a bit optimistic. However, even with twenty times lower positron than electron luminosity one would have  $0.5 \text{ fb}^{-1}$ , i.e. the total HERA luminosity equivalent available in option D for example. F is the deuteron and G the lead option; finally H was simulated for a low proton beam energy configuration as is of interest to maximise the acceptance at large  $x$ .

1146 The LHeC will extend this initial measurement by using higher luminosities and dedicated detector  
1147 conditions into a much enlarged kinematic range. Since the LHeC is supposed to run synchronously with the  
1148 LHC, the simulation presented here has been made with reduced electron beam energies keeping the proton  
1149 beam energy untouched. The following set of energies and integrated luminosities: (60, 1), (30, 0.3), (20,  
1150 0.1) and (10, 0.05) ( $\text{GeV}, \text{fb}^{-1}$ ). Note that the  $F_L$  measurement requires to also have data with the opposite  
1151 beam charge in order to be able to reliably subtract the non DIS background which at high  $y$  is substantial.  
1152 This has not been simulated here.

1153 In the low  $x$  studies below a similar simulation was used for which the luminosity assumptions were  
1154 similar but a set of reduced proton beam energies was considered. The advantage of lowering  $E_p$  is that the  
1155 maximum  $y$  for all beam energy configurations can be high, e.g. 0.95 for  $E_e = 60 \text{ GeV}$ . When  $E_e$  is lowered  
1156 instead, one has to accept a lower  $y_{max}$  as below a few GeV of energy the background is too high for a  
1157 reliable measurement to be performed. The results of both  $F_L$  simulations, with reduced  $E_e$  or  $E_p$ , come  
1158 out to be very similar.

1159 The result of the simulation study is shown in Fig. 4.7. The technique applied is the conventional separa-  
1160 tion of  $F_2$  and  $F_L$  by fitting a straight line to the various reduced cross section data points at fixed  $Q^2$  and  
1161  $x$  with  $f(y)$  as the parameter and separating the uncorrelated from the correlated systematic uncertainties  
1162 which partially cancel in such an analysis. The expected accuracy on  $F_L$  is typically 4% at  $Q^2$  of  $3.5 \text{ GeV}^2$   
1163 or 7% at  $Q^2$  of  $25 \text{ GeV}^2$  at a number of points in  $x$ , with mainly similar contributions from the calculated  
1164 correlated and the assumed uncorrelated systematic uncertainties, and less due to statistics which yet starts  
1165 to become important for  $Q^2 \geq 100 \text{ GeV}^2$ . The LHeC thus will provide the first precision measurement of  
1166  $F_L(x, Q^2)$  ever, in a region where the behaviour of the gluon density ought to change significantly and new,  
1167 non-linear laws for parton evolution should emerge.

1168 A related measurement of prime interest is the determination of  $F_L$  in diffraction, as is discussed below.  
1169 A pioneering measurement of  $F_L^D$  has been performed by H1 (-cite when published in July-).

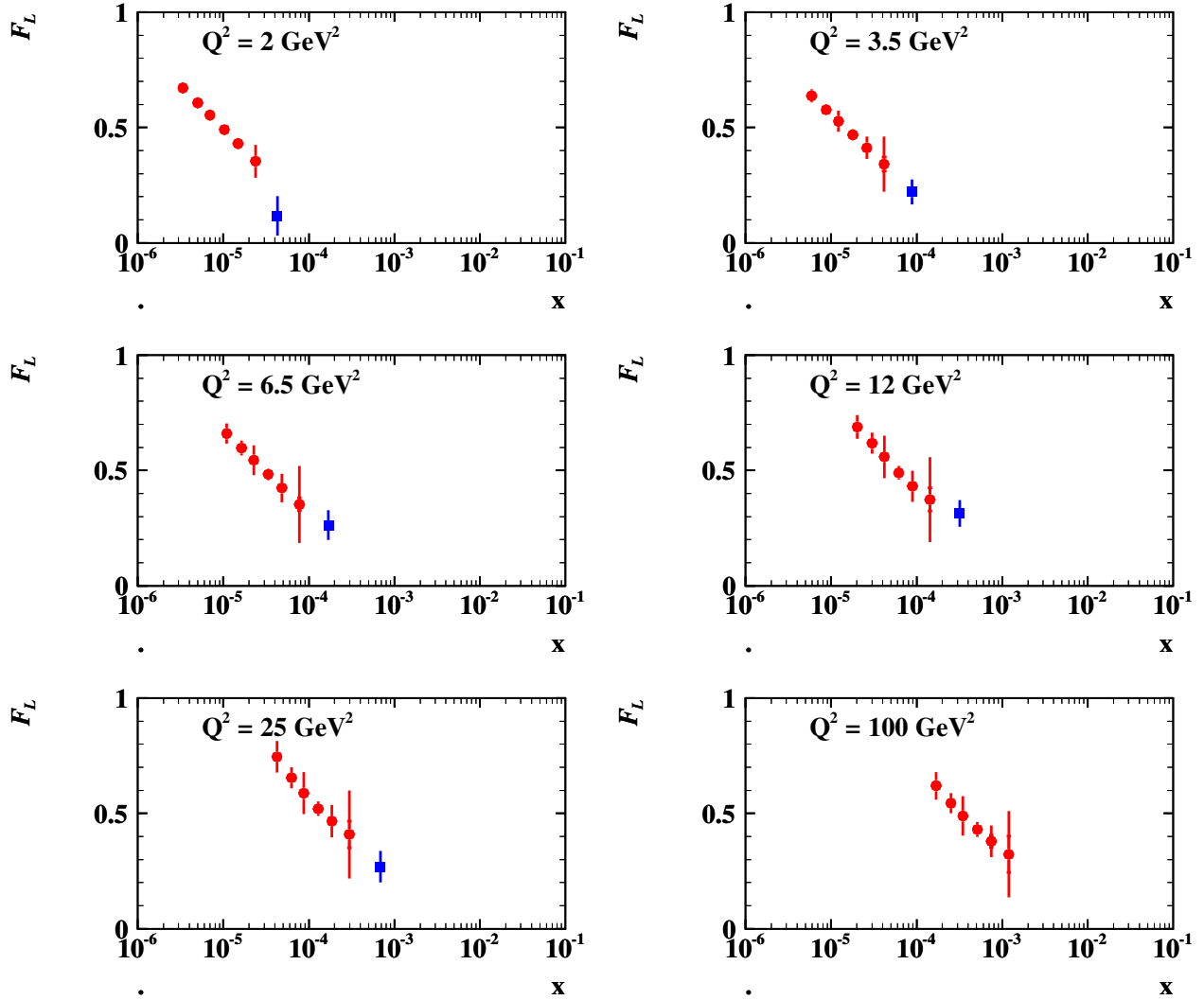


Figure 4.7: Simulated measurement of the longitudinal structure function  $F_L(x, Q^2)$  at the LHeC (red closed circles) from a series of runs with reduced electron beam energy, see text. The inner error bars denote the statistical uncertainty, the outer error bars are the total errors with the additional uncorrelated and correlated systematic uncertainties added in quadrature. The blue squares denote the recently published result of the H1 Collaboration, plotting only the  $x$  averaged results as the more accurate ones, see [68]. The LHeC extends the measurement towards low  $x$  and high  $Q^2$  (not fully illustrated here) with much improved precision.

## 4.2 Determination of Parton Distributions

Despite a series of deep inelastic scattering experiments with neutrinos, electrons and muons using stationary targets and with HERA, despite the addition of some Drell Yan data, the knowledge of the quark distributions in the proton is still limited. It often relies on pQCD analyses using various assumptions on the Bjorken  $x$  dependence of the PDFs and their symmetries. The LHeC has the potential to put the PDF knowledge on a qualitatively and quantitatively new and superior basis. This is due to the kinematic range, huge luminosity, availability of polarised electron and positron beams, as of proton and deuteron beams, and to the anticipated very high precision of the cross section measurements as has been discussed above.

The LHeC has the potential to provide crucial constraints and many determinations of parton distributions completely or rather independently of the conventional QCD fitting techniques. For example, the valence quarks can be measured up to high  $x$ , and all heavy quarks be determined from dedicated  $c$  and  $b$  tagging analyses with unprecedented precision. Therefore, the then evolving QCD fits based on real LHeC data will be set-up with a massively improved and better constrained input data base. Their eventual effect is thus not easy to simulate now, it yet may be illustrated based on the currently used procedures.

The striking potential of the determination of the quark and gluon distributions will be discussed and illustrated below. For the various PDFs, the current knowledge is illustrated with a series of plots based on the world's best PDF determinations available today. Simulations of essentially direct quark distribution measurements, as for the charm quark, will be shown. Moreover, a consistent set of standard QCD fits has been performed using the simulated LHeC and further data which is first described in what follows. This is used to illustrate the effect the inclusive NC and CC data from the LHeC are expected to have on the PDF uncertainties.

Currently extensive work is being performed to test and further constrain PDFs with Drell-Yan scattering data from the LHC. This naturally focusses on the  $Z$  and  $W^\pm$  production and decay. While such tests are undoubtedly of interest, they require an extremely high level of precision as at scales  $Q^2 \simeq M_{W,Z}^2$  any effect due to PDF differences at smaller scales is washed out by the overriding effect of quark-antiquark pair production from gluon emission, below the valence quark region. The present QCD fit results also use a set of simulated  $W^+ - W^-$  asymmetry data of ultimate precision in order to be able to estimate the effect the Drell-Yan data will have besides the LHeC in the determination of the PDF's.

### 4.2.1 QCD Fit Ansatz

NLO QCD fits are performed in order to study the effect of the (simulated) LHeC data on the PDF knowledge. Fits are done using the combined HERA data published and so available to date (HERA I), adding BCDMS proton data as the most accurate fixed target structure function set of importance at high  $x$ , simulated precision  $W^+ - W^-$  asymmetry LHC data, using the LHeC data alone and in combination. In the fits, for the central values of the LHeC data, the Standard Model expectation is used, smeared within the uncorrelated, Gaussian distributed uncertainties and taking into account the correlated uncertainties as well.

The procedure used here is adopted from the HERA QCD fit analysis [38]. The QCD fit analysis to extract the proton's PDFs is performed imposing a  $Q_{min}^2 = 3.5 \text{ GeV}^2$  to restrain to the region where perturbative QCD can be assumed to be valid. The fits are extended to lowest  $x$  for systematic uncertainty studies, even when at such low  $x$  values non-linear effects are expected to appear.

The fit procedure consists first in parametrising PDFs at a starting scale  $Q_0^2 = 1.9 \text{ GeV}^2$ , chosen to be below the charm mass threshold. The parametrised PDFs are the valence distributions  $xu_v$  and  $xd_v$ , the gluon distribution  $xg$ , and the  $x\bar{U}$  and  $x\bar{D}$  distributions, where  $x\bar{U} = x\bar{u}$ ,  $x\bar{D} = x\bar{d} + x\bar{s}$ . This ansatz is natural to the extent that the NC and CC inclusive cross sections determine the sums of up and down quark distributions, and their antiquark distributions, as the four independent sets of PDFs, which may be transformed to the ones chosen if one assumes  $u_v = U - \bar{U}$  and  $d_v = D - \bar{D}$ , i.e. the equality of anti- and sea quark distributions of given flavour.

The following standard functional form is used to parameterise them

$$xf(x) = Ax^B(1-x)^C(1+Dx+Ex^2), \quad (4.24)$$

1217 where the normalisation parameters ( $A_{uv}, A_{dv}, A_g$ ) are constrained by quark counting and momentum sum  
 1218 rules.

1219 The parameters  $B_{\bar{U}}$  and  $B_{\bar{D}}$  are set equal,  $B_{\bar{U}} = B_{\bar{D}}$ , such that there is a single  $B$  parameter for  
 1220 the sea distributions, an assumption the validity of which will be settled with the LHeC. The strange quark  
 1221 distribution at the starting scale is assumed to be a constant fraction of  $\bar{D}$ ,  $x\bar{s} = f_s x\bar{D}$ , chosen to be  $f_s = 0.31$ .  
 1222 In addition, to ensure that  $x\bar{u} \rightarrow x\bar{d}$  as  $x \rightarrow 0$ ,  $A_{\bar{U}} = A_{\bar{D}}(1 - f_s)$ . The  $D$  and  $E$  are introduced one by  
 1223 one until no further improvement in  $\chi^2$  is found. The best fit resulted in a total of 10 free parameters [38],  
 1224 while fits with a tested set of 14 parameters lead to very similar results. As discussed above this will change  
 1225 considerably when the LHeC data become available and more flexible parameterisations and methods can  
 1226 be tested. This has been studied to some extent in the simulation for  $\alpha_s$  presented below.

1227 The PDFs are then evolved using DGLAP evolution equations [69] at NLO in the  $\overline{MS}$  scheme with the  
 1228 renormalisation and factorisation scales set to  $Q^2$  using standard sets of parameters as for  $\alpha_s(M_Z)$ . These,  
 1229 as well as the exact treatment of the heavy quark thresholds, are of no significant influence for the estimates  
 1230 of the PDF uncertainties to which the subsequent analysis is only directed. The experimental uncertainties  
 1231 on the PDFs are determined using the  $\Delta\chi^2 = 1$  criterion.

## 1232 4.2.2 Valence Quarks

1233 The knowledge of the valence quark distributions, both at large and at low Bjorken  $x$ , as derived in the  
 1234 current world data QCD fit analyses is amazingly limited, as is illustrated in Fig. 4.8 from a comparison of  
 1235 the leading determinations of PDF sets. This has to do, at high  $x$ , with the limited luminosity, challenging  
 1236 systematics rising  $\propto 1/(1-x)$  and nuclear correction uncertainties, and, at low  $x$ , with the smallness of the  
 valence quark distributions as compared to the sea quarks. The impressive improvement expected from the

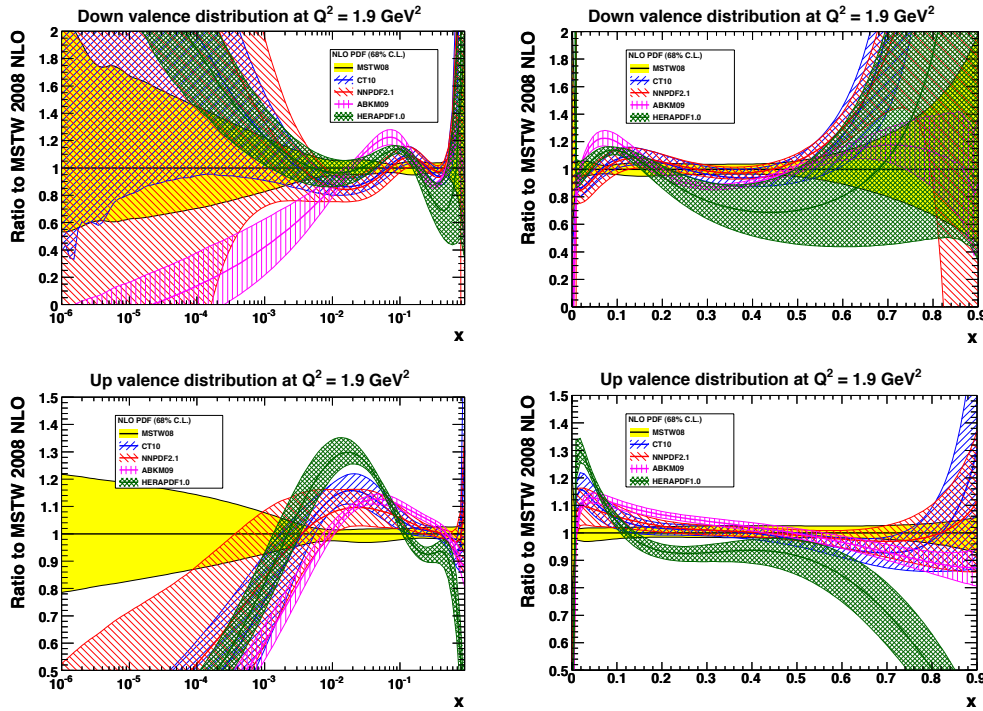


Figure 4.8: Ratios (to MSTW08) and uncertainty bands of valence quark distributions, at  $Q^2 = 1.9 \text{ GeV}^2$ , for most of the available recent PDF determinations. Top: up valence quark; down: down valence quark; left: logarithmic  $x$ , right: linear  $x$ .

1237

1238 LHeC is demonstrated in Fig. 4.9. As can be seen, the uncertainty of the down valence quark distribution at,

1239 for example,  $x = 0.7$  is reduced from a level of 50 – 100 % to about 5 %. The up valence quark distribution is  
 1240 better known than  $d_v$ , because it enters with a four-fold weight in  $F_2$ , due to the electric quark charge ratio  
 1241 squared, a big improvement yet is also visible. These huge improvement effects at large  $x$  are a consequence  
 1242 of the high precision measurements of the NC and the CC inclusive cross sections, which at high  $x$  tend to  
 1243  $4u_v + d_v$  and  $u_v$  ( $d_v$ ) for electron (positron) scattering, respectively. At HERA the luminosity and range had  
 1244 not been high enough to allow a similar measurement as will be possible for the first time with the LHeC.  
 1245 This is illustrated in Fig. 4.10 which compares recent results of the ZEUS Collaboration, on the CC cross  
 section with the LHeC simulation.

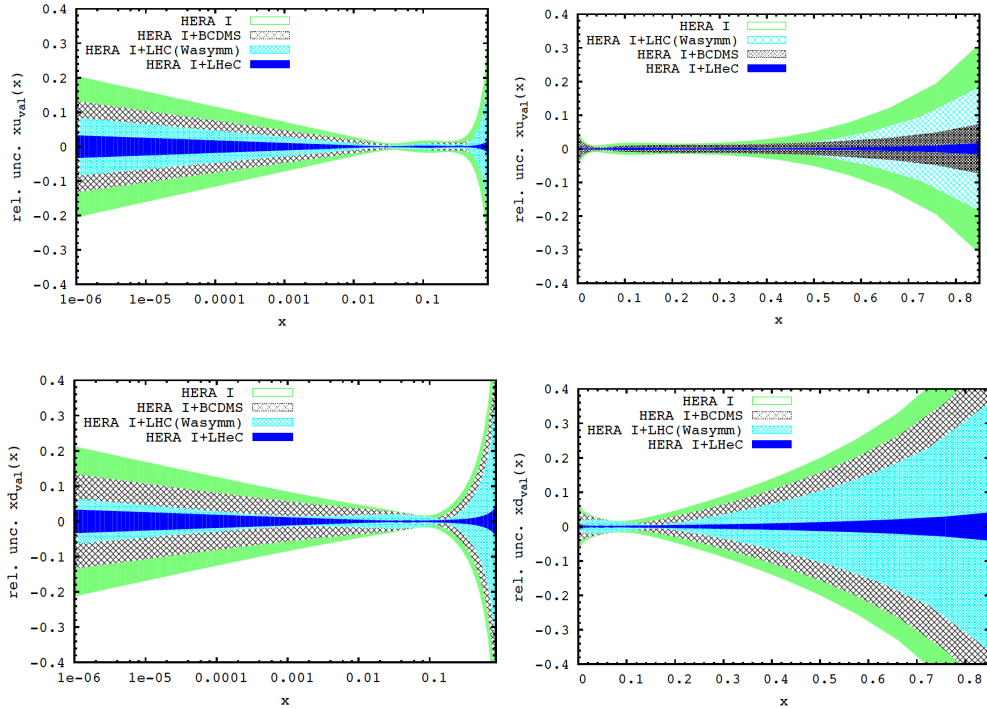


Figure 4.9: Uncertainty of valence quark distributions, at  $Q^2 = 1.9 \text{ GeV}^2$ , as resulting from an NLO QCD fit to HERA (I) alone (green, outer), HERA and BCDMS (crossed), HERA and LHC (light blue, crossed) and the LHeC added (blue, dark). Top: up valence quark; down: down valence quark; left: logarithmic  $x$ , right: linear  $x$ .

1246

1247 Access to valence quarks at low  $x$  can be obtained from the  $e^\pm p$  cross section difference as introduced  
 1248 above:

$$\sigma_{r,NC}^- - \sigma_{r,NC}^+ = 2 \frac{Y_-}{Y_+} (-a_e \cdot k x F_3^{\gamma Z} + 2v_e a_e \cdot k^2 x F_3^Z). \quad (4.25)$$

1249 Since the electron vector coupling,  $v_e$ , is small and  $k$  not much exceeding 1, to a very good approximation the  
 1250 cross section difference is equal to  $-2kY_- a_e x F_3^{\gamma Z} / Y_+$ . In leading order pQCD this “interference structure  
 1251 function” can be written as

$$x F_3^{\gamma Z} = 2x [e_u a_u (U - \bar{U}) + e_d a_d (D - \bar{D})], \quad (4.26)$$

1252 with  $U = u + c$  and  $D = d + s$  for four flavours. The  $x F_3^{\gamma Z}$  structure function thus provides information  
 1253 about the light-quark axial vector couplings ( $a_u$ ,  $a_d$ ) and the sign of the electric quark charges ( $e_u$ ,  $e_d$ ).  
 1254 Equivalently one can write

$$x F_3^{\gamma Z} = 2x [e_u a_u (u_v + \Delta_u) + e_d a_d (d_v + \Delta_d)]. \quad (4.27)$$



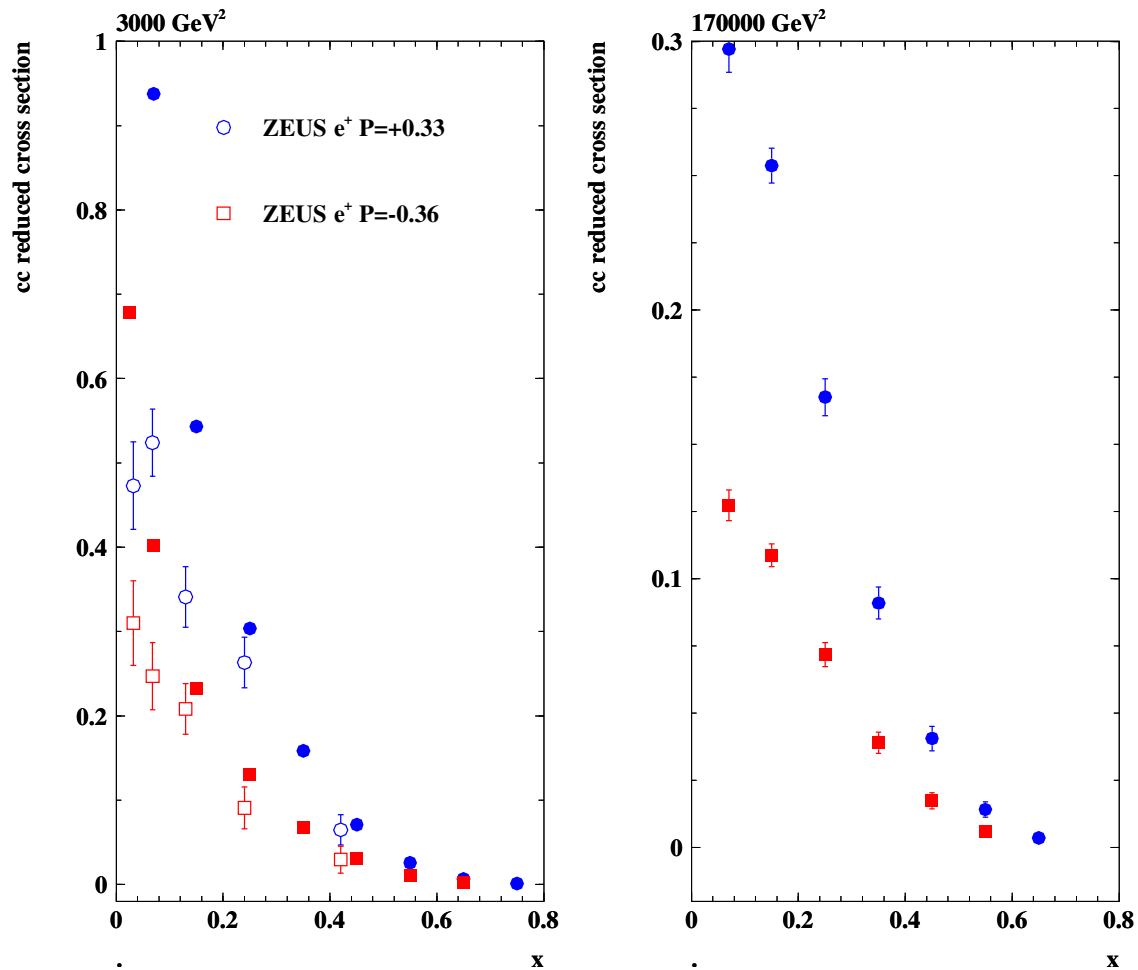


Figure 4.10: Reduced charged current  $e^+p$  scattering cross section versus Bjorken  $x$  for different polarisations  $\pm P$  and values of  $Q^2$ . Closed points: LHeC simulations for  $10 \text{ fb}^{-1}$ ; open points: ZEUS measurements based on the full HERA statistics of about  $0.15 \text{ fb}^{-1}$  per polarisation state. Note that the reduced CC cross section at fixed  $x$  and  $Q^2$  contains an explicit dependence on the beam energy via the ratio of inelasticity dependent factors  $Y_-/Y_+$ , which is at the origin of the simulated and measured cross section differences apparent at lower  $x$ .

1255 In the naive parton model as in conventional perturbative QCD, it is assumed that the differences  $\Delta_u =$   
 1256  $(u_{sea} - \bar{u} + c - \bar{c})$  and  $\Delta_d = (d_{sea} - \bar{d} + s - \bar{s})$  are zero <sup>2</sup>. Inserting the SM charge and axial coupling values  
 1257 one finds

$$xF_3^{\gamma Z} = \frac{x}{3}(2u_v + d_v + \Delta) \quad (4.28)$$

1258 with  $\Delta = 2\Delta_u + \Delta_d$ . Neglect of  $\Delta$  leads to a sum rule [70], which in leading order is

$$\int_0^1 xF_3^{\gamma Z} \frac{dx}{x} = \frac{1}{3} \int_0^1 (2u_v + d_v) dx = \frac{5}{3}. \quad (4.29)$$

1259 The  $xF_3^{\gamma Z}$  structure function thus is determined by the valence quark distributions and predicted to be only  
 1260 very weakly depending on  $Q^2$ . Fig. 4.11 shows a simulation of  $xF_3^{\gamma Z}$  and its comparison with the so far most  
 1261 accurate measurement from HERA. With such a high precision interesting tests are possible of the relation  
 1262 of  $xF_3^{\gamma Z}$  to  $xW_3$ , which should only differ by the weak couplings involved in NC and CC.

### 1263 4.2.3 Strange Quarks

1264 The strange quark distribution  $s(x, Q^2)$  has been very difficult to measure. In DIS some information is  
 1265 obtained from di-muon production in neutrino-nucleon scattering. Often  $s$  is linked to the behaviour of the  
 1266 sea quarks. Recently the HERMES Collaboration, from kaon multiplicities, derived an unusual behaviour of  
 1267 the strange quark density as compared to previous analyses [71]. Some hints for a difference between the  $s$   
 1268 and  $\bar{s}$  distributions have been discussed. The existing information on the sum of the strange and anti-strange  
 1269 quark distributions is plotted in Fig. 4.12. Obviously there is no real understanding of the strange quark  
 1270 distribution in the proton available. This will change with the LHeC. Here  $s$  and  $\bar{s}$  may be very well measured  
 1271 as a function of  $x$  and  $Q^2$  from the  $W^+s \rightarrow c$  and  $W^- \bar{s} \rightarrow \bar{c}$  processes, i.e. with charmed quark tagging  
 1272 in CC DIS using electron and positron beams, respectively. The precision for  $s$  which may be obtained is  
 1273 illustrated in Fig. 4.13. Accurate measurements may be obtained for the first time ever. The simulation of  
 1274  $\bar{s}$  obviously leads to the same picture such that over a wide kinematic range possible differences between  $s$   
 1275 and  $\bar{s}$  may be established.

### 1276 4.2.4 Top Quarks

1277 The top is the heaviest of the quarks. It decays before hadrons are formed. It has not been explored in  
 1278 DIS yet because the cross sections at HERA have been too small [72]. This is different at the LHeC where  
 1279 top in charged currents is produced with a cross section of order 5 pb as can easily be estimated from the  
 1280 LO calculation of  $Wb$  scattering. At the LHeC therefore, for the first time, one can study top quarks in  
 1281 deep inelastic scattering. Positron (electron) proton charged current scattering provides a clear distinction  
 1282 between top (anti-top) quark production in  $Wb$  to  $t$  fusion. The rates of this process are very high, as is  
 1283 illustrated as a function of  $Q^2$  in Fig. 4.14. Besides the rates and the charge tag it is notable that the  
 1284 absence of pile-up and underlying event effects, characteristic for LHC measurements, provide comfortable  
 1285 conditions for top quark physics at the LHeC.

1286 Due to its large mass, the top quark may very well play a role in the mechanism of electroweak symmetry  
 1287 breaking (EWSB) both in the Standard Model as well as BSM physics. In the Standard Model, a precise  
 1288 measurement of single top production in DIS (see for example [73]) is sensitive to the  $b$  quark content of  
 1289 the proton. In a BSM EWSB scenario, the top quark will couple to the new physics sector and give rise to  
 1290 anomalous production modes. The LHeC is expected to provide competitive sensitivity to flavor changing  
 1291 neutral currents (FCNC) especially anomalous  $tu\gamma$  and  $tuZ$  couplings.

1292 In the SM, top is produced dominantly in gluon-boson fusion at  $x \lesssim 0.1$ . In CC this leads to a top-beauty  
 1293 final state while in NC this gives rise to pair produced top-antitop quarks, with a cross section of order 10

---

<sup>2</sup>However, in non-perturbative QCD there may occur differences, for example between the strange and anti-strange quark distributions, for which there are some hints in DIS neutrino nucleon di-muon data and corresponding QCD fit analyses, see below.

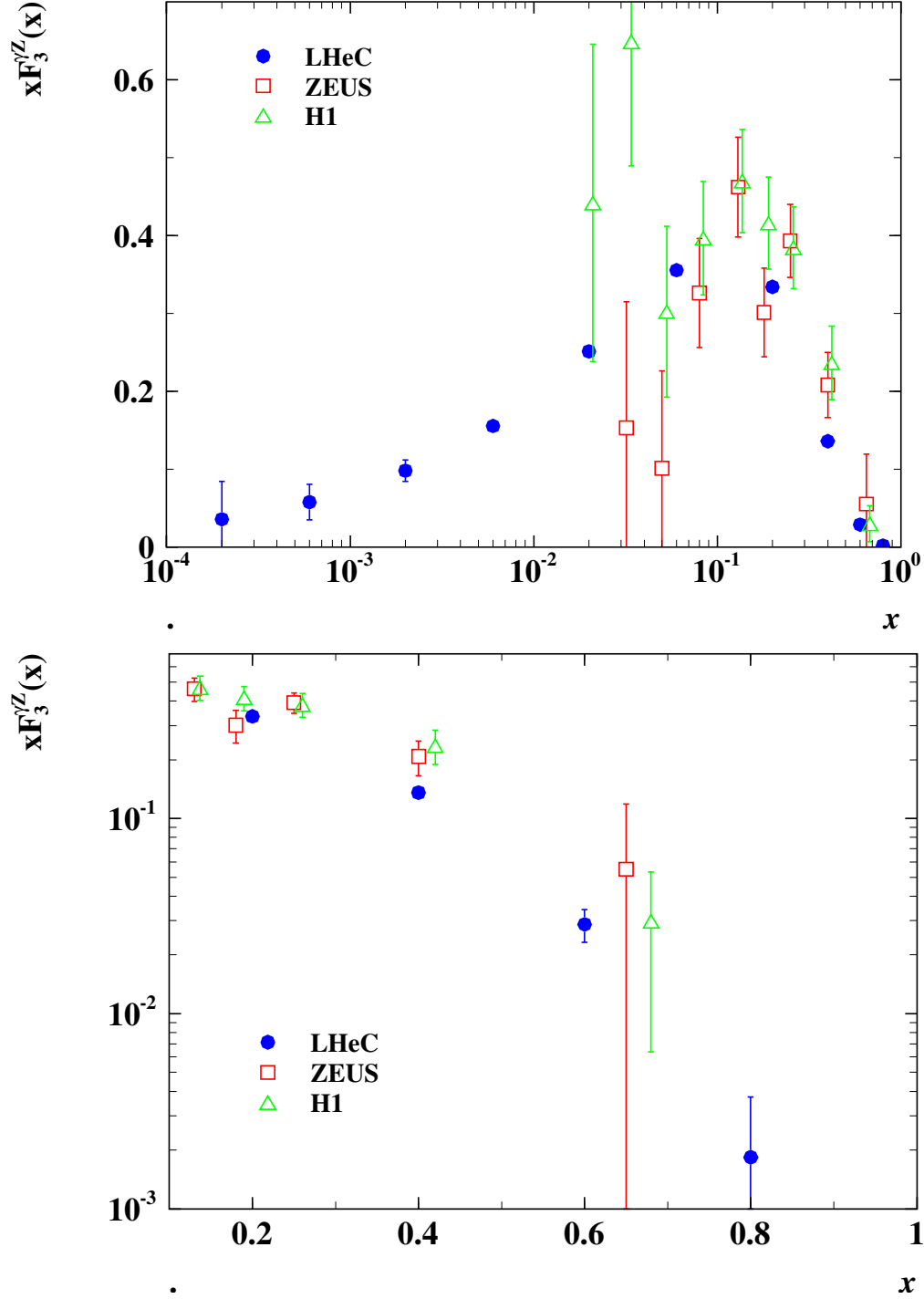


Figure 4.11: Simulation of the LHeC measurement of the interference structure function  $xF_3^{\gamma^Z}$  from unpolarised  $e^\pm p$  scattering with  $10\text{fb}^{-1}$  luminosity per beam (blue, closed points) compared with the HERA II data as obtained by H1 (preliminary, green triangles) and by ZEUS (red squares) with about  $0.15\text{fb}^{-1}$  luminosity per beam charge. The H1  $x$  values are enlarged by 10% of their given values for clarity. One should notice that any significant deviation of sea from anti-quarks, see Eq. 4.27, would cause  $xF_3^{\gamma^Z}$  at low  $x$  to not tend to zero. The top plot shows an average of  $xF_3^{\gamma^Z}$  over  $Q^2$  projected to a chosen  $Q^2$  value of  $1500\text{GeV}^2$  exploiting the fact that the valence quarks are approximately independent of  $Q^2$ . The lower plot is a zoom into the high  $x$  region.

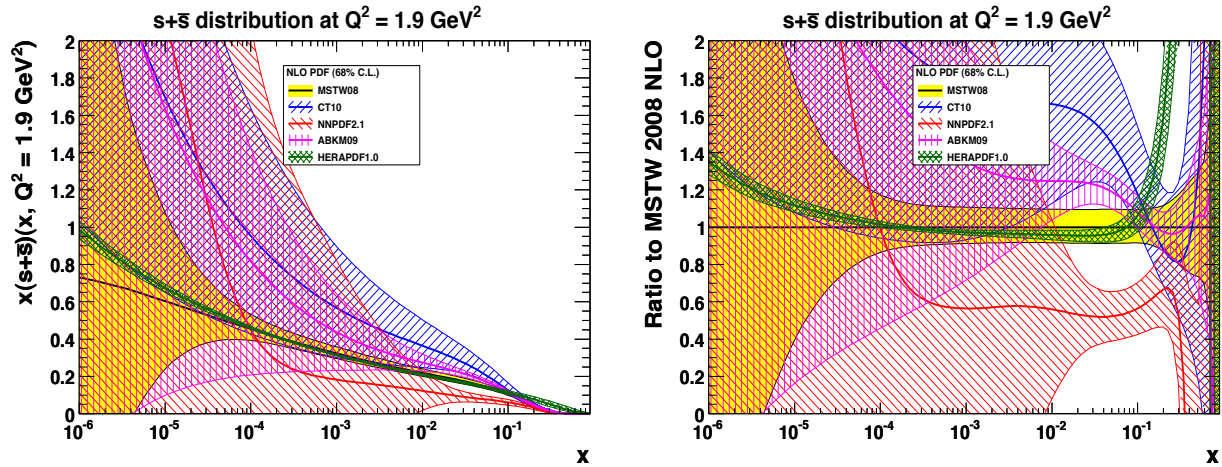


Figure 4.12: Sum of the strange and anti-strange quark distribution as embedded in the NLO QCD fit sets as noted in the legend. Left:  $s + \bar{s}$  versus Bjorken  $x$  at  $Q^2 = 1.9 \text{ GeV}^2$ ; right: ratio of  $s + \bar{s}$  of various PDF determinations to MSTW08. In the HERAPDF1.0 analysis (green) the strange quark distribution is assumed to be a fixed fraction of the down quark distribution which is conventionally assumed to have the same low  $x$  behaviour as the up quark distribution, which results in a small uncertainty of  $s + \bar{s}$ .

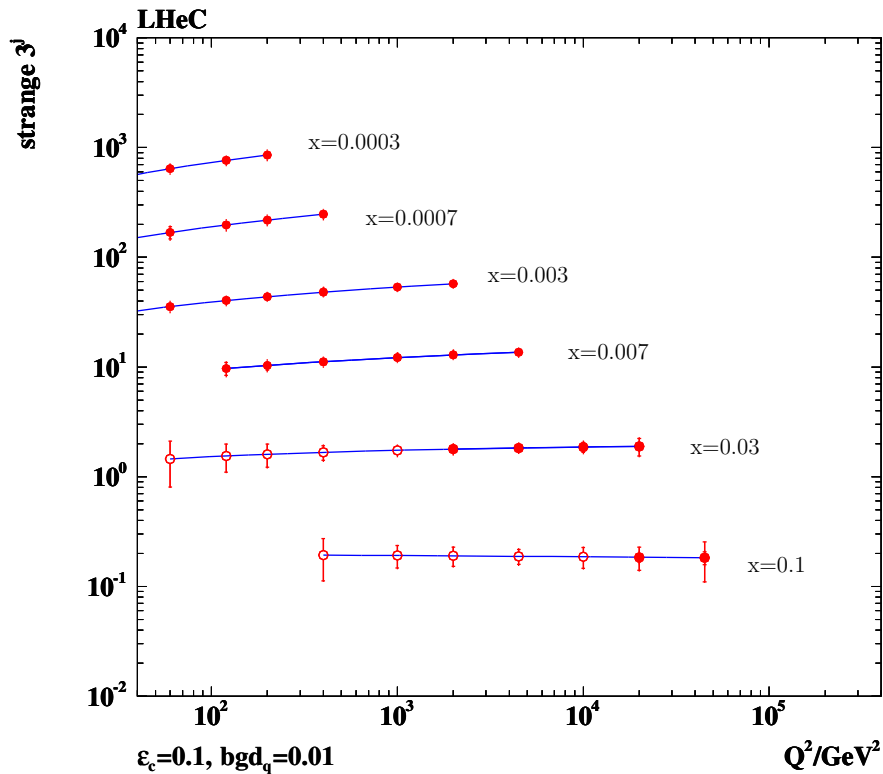


Figure 4.13: Simulated measurement of the strange quark density with the LHeC. Closed (open) points: tagging acceptance down to  $10^\circ$  ( $1^\circ$ ).

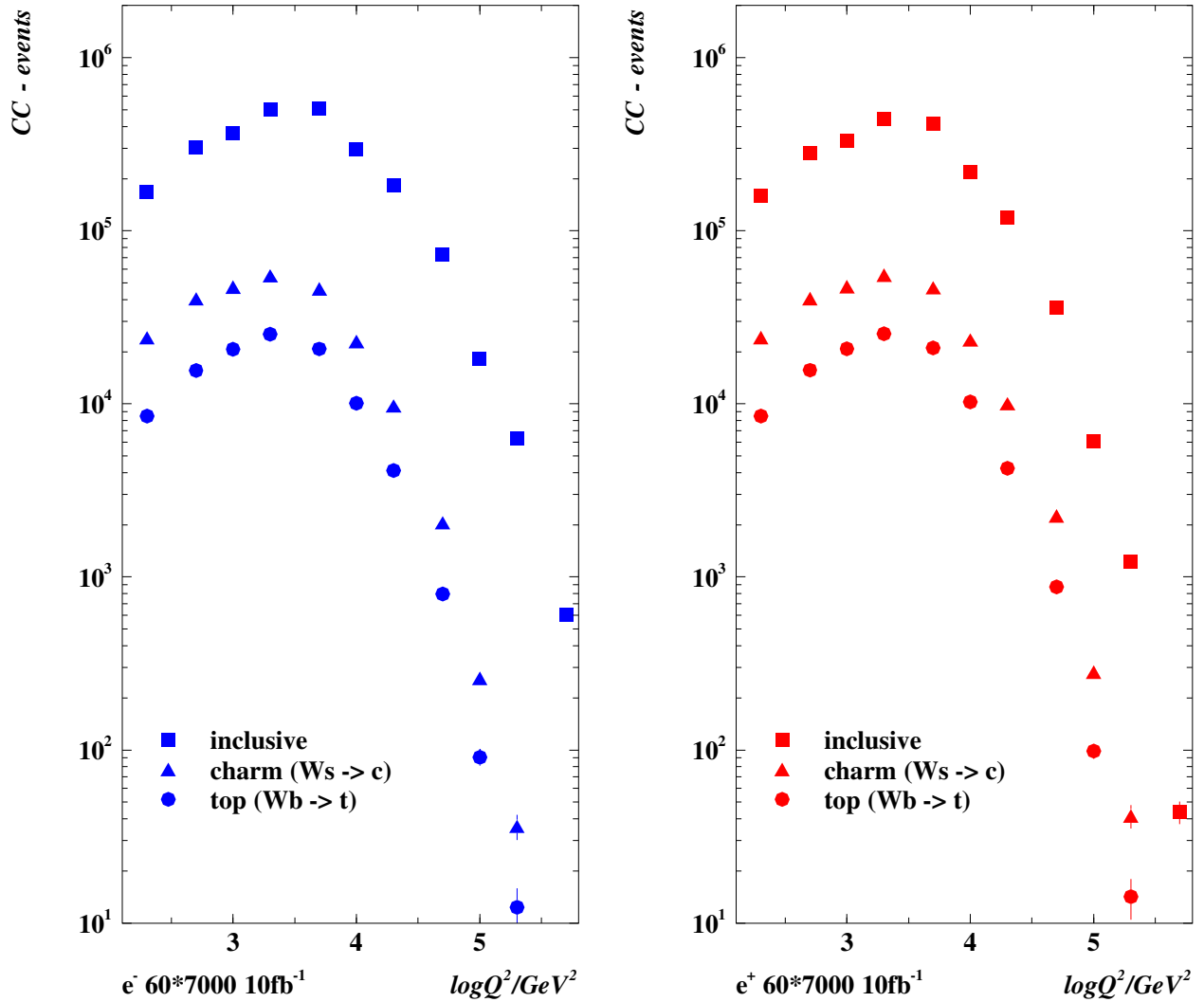


Figure 4.14: Charged current event rates for unpolarised  $e^-p$  (left) and  $e^+p$  (right) scattering in which  $\bar{t}$  and  $t$  is produced, respectively. Squares: inclusive CC rate vs.  $Q^2$ ; triangles: charm production from  $W_s$  fusion; closed circles: top production from  $W_b$  fusion, estimated in a massless heavy flavour treatment. The rates are calculated for the default beam energies for  $10\text{fb}^{-1}$  of integrated luminosity. The errors are only statistical.

1294 times lower than in CC [72]. The electron beam charge distinguishes top and anti-top quark production in  
 1295 CC. Thus a unique SM top physics program can be performed at the LHeC. This includes the consideration  
 1296 of a top-quark density which at very high scales may be considered “light”. Recently a six-flavour variable  
 1297 number scheme has been proposed [74], limited so far to leading order, in which it is predicted that the  
 1298 top contribution to proton structure has an on-set much below the threshold of its production in a massless  
 1299 scheme. This is illustrated in Fig. 4.15. Due to the very high  $Q^2$  and statistics, the LHeC opens top quark  
 PDF physics as a new field of research.

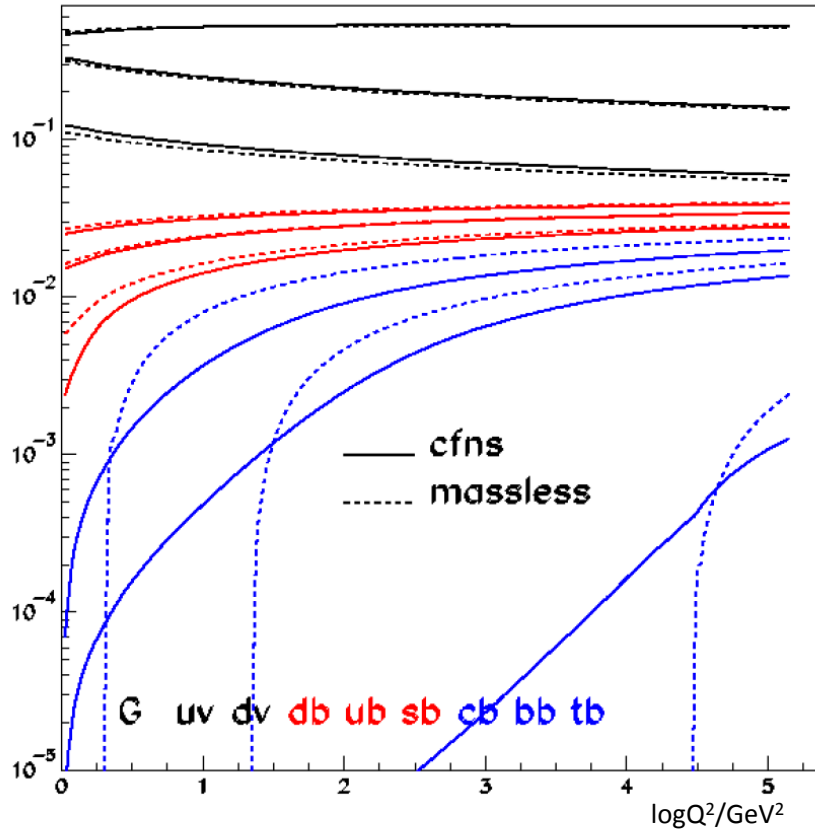


Figure 4.15: Parton momentum fractions as a function of  $Q^2$  in a novel six-flavour variable number scheme (CFNS), solid curves, and in the massless scheme, dashed curves. At HERA one has observed beauty and charm production already below the conventional threshold of  $\sqrt{Q^2} = m_Q$ . The scheme of [74] suggests that there is a very early onset of top with measurable rates already at  $Q^2$  values of only about one tenth of  $m_t^2 \simeq 3 \cdot 10^4 \text{ GeV}^2$ . With the LHeC the 'PDF' top physics is expected to commence.

1300

1301 Top, including anomalous couplings, has been considered for the CDR initially [75], based on some  
 1302 ANOTOP and PYTHIA studies at generation level. With a detector now simulated in GEANT4 and in  
 1303 the light of the first top results provided by the LHC experiments [76], as well as further prospects, the CC  
 1304 and NC top physics at the LHeC deserves a more detailed study. This shall include an analysis about the  
 1305 possible precision measurement of the top (and anti) top quark mass, which at the LHC may be determined  
 1306 with an accuracy of 1 GeV and possibly be better in *ep*. Independently of whether one soon finds the SM  
 1307 Higgs particle or it remains elusive, a high precision measurement of  $m_t$  is of prime importance.

### 4.3 Gluon Distribution

There are many fundamental reasons to understand the gluon distribution and the gluon interactions deeper than hitherto. Half of proton’s momentum is carried by gluons. Gluon self-interaction is responsible for the creation of baryonic mass. The Higgs particle, should it exist, is predominantly produced by gluon-gluon interactions. The rise of the gluon density towards low Bjorken  $x$  must be tamed for unitarity reasons: there is a new phase of hadronic matter to be discovered, in which gluons interact non-linearly while  $\alpha_s$  is smaller than 1.

The LHeC, with precision and range of the most appropriate process (DIS) to explore  $xg(x, Q^2)$ , will pin down the gluon distribution much more accurately than could be done before. This primarily comes from the extension of range and precision in the measurement of  $\partial F_2/\partial \ln Q^2$  which at small  $x$  is a measure of  $xg$ . The inclusive NC and CC measurements together provide a fully constrained data base for the determination of the quark distributions, which strongly constrains  $xg$ . The addition of precision measurements of  $F_L$ , discussed above and used in the small  $x$  chapter of this document, will unravel the saturating behaviour of  $xg$ . High precision measurements of boson-gluon fusion to heavy quark pairs will provide a complementary basis for understanding the gluon and its parton interactions.

The peculiarity of the gluon density is that it is defined and observable only in the context of a theory. Moreover, a crude data base and correspondingly rough fit ansatz can screen local deviations from an otherwise preferred smooth behaviour. It has yet not been settled whether there are gluonic “hot” spots in the proton or not. An example for possible surprises is provided by the analysis [49], in which Chebyshev polynomials have been used to parameterise the parton distributions in contrast to more conventional forms as in Eq. 4.24. Inspection of the gluon distribution obtained there reveals that it seems to be vanishing at  $x \simeq 0.2$ , i.e. at the point, in which scaling holds for  $F_2(x, Q^2)$ , which one might term a “cool” spot in the proton. Much more is still to be learned about the gluon, even when one is disregarding the yet to be explored role of the gluon in the theory of generalised and of unintegrated parton distributions.

The current knowledge of the gluon distribution in the proton is astonishingly limited as becomes clear from Fig. 4.16 showing the world determinations, and their uncertainties, of  $xg(x, Q^2)$  at a typical initial, low scale, and from Fig. 4.17 expressing this information with ratios to one of the PDF sets. At low  $x$  and  $Q^2$  most but not all of the PDF sets predict  $xg$  to be of valence like type with very large uncertainties for  $x$  below a few times  $10^{-4}$ . At large  $x$  inclusive DIS has difficulties to pin down  $xg$  because the evolution of valence quarks as non-singlet quantities in QCD is not directly coupled to the gluon and very weak. Yet, even the information from jets, used in some of the PDF sets, does not lead to a clear understanding of  $xg$  at large  $x$  as is illustrated too. In fact, there is a tendency of obtaining a smaller  $xg$  at large  $x$  from HERA (I) data alone, see Fig. 4.16, as compared to the other determinations, albeit with large uncertainties.

The determination of  $xg$  is predicted to be radically improved with the LHeC precision data which extend up to lowest  $x$  near to  $10^{-6}$  and large  $x \geq 0.7$ . The result of the QCD fit analysis for  $xg$  as described above in Sect. 4.2.1 is shown in Fig. 4.18. One observes a dramatic improvement at low  $x$ , as must be expected from the extension of the kinematic range, but also at high  $x$ , as is attributed to the high  $x$  precision measurements of the NC and CC cross sections. At  $x = 0.7$ , for example, the predicted experimental uncertainty of  $xg$  is 5%, which is about ten times more accurate than the results of MSTW08 or of the HERA fit indicate.

It is worth noting that the uncertainties considered here are restricted to those related to the genuine cross section measurement errors. There are further uncertainties, as discussed e.g. in [38], related to the difficulty of parameterising the PDFs and choosing the optimum solution in such a fit analysis. These will be also considerably reduced with the LHeC extended data base. Moreover, this analysis is not making use of the plethora of extra information on  $xg$ , which the LHeC will provide with  $F_L$ ,  $F_2^{c,b}$  and jet cross section measurements. The understanding of the gluon and its interactions is a primary task of the LHeC and undoubtedly a new horizon in strong interaction physics will be opened.

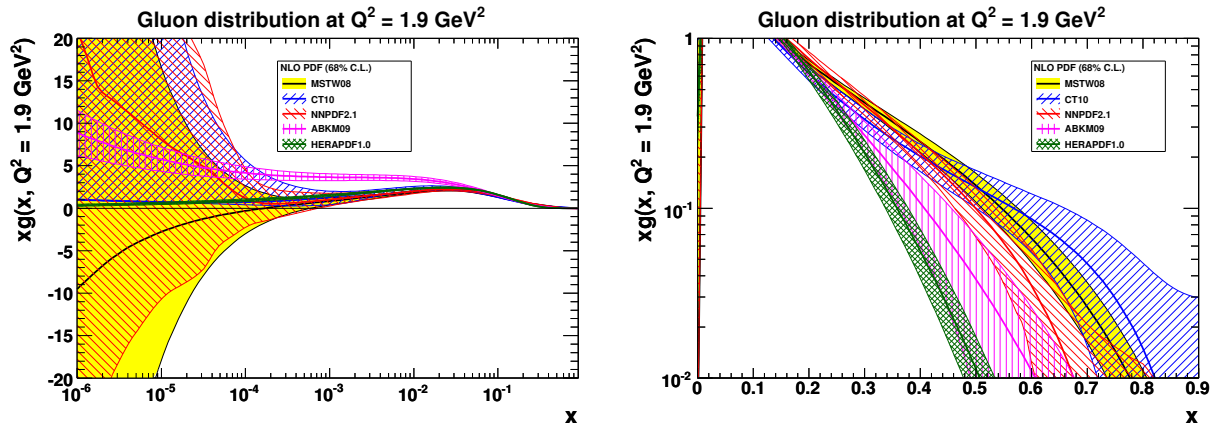


Figure 4.16: Gluon distribution and uncertainty bands, at  $Q^2 = 1.9 \text{ GeV}^2$ , for most of the available recent PDF determinations. Left: logarithmic  $x$ , right: linear  $x$ .

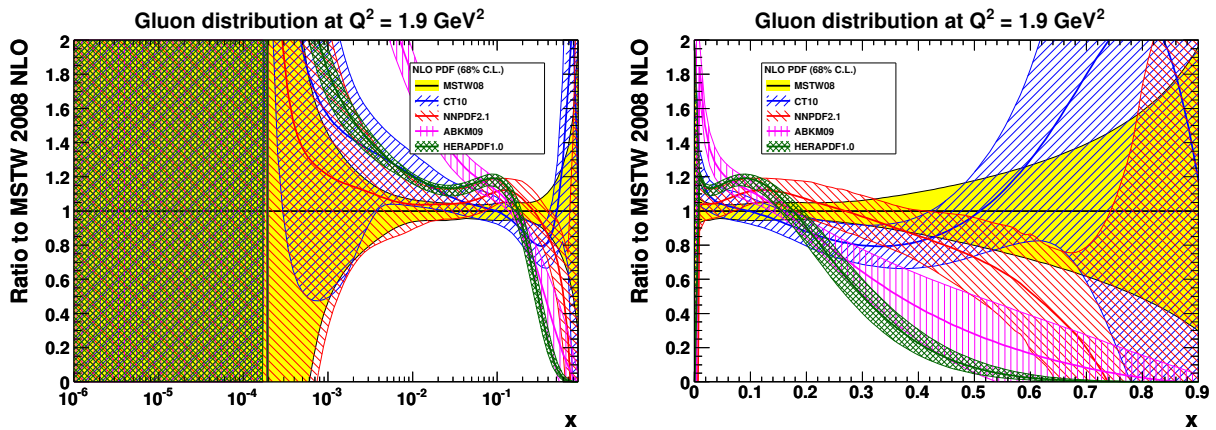


Figure 4.17: Ratios to MSTW08 of gluon distribution and uncertainty bands, at  $Q^2 = 1.9 \text{ GeV}^2$ , for most of the available recent PDF determinations. Left: logarithmic  $x$ , right: linear  $x$ .



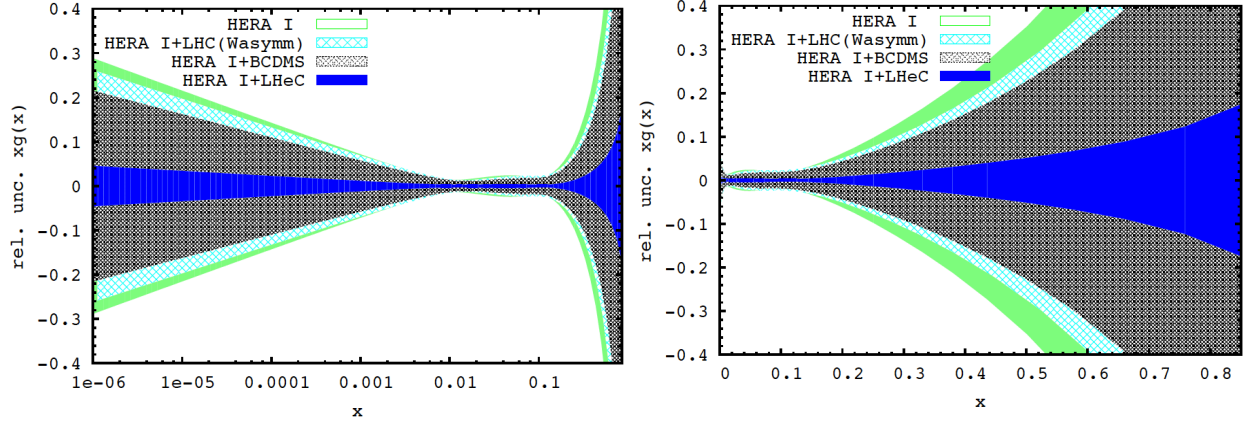


Figure 4.18: Relative uncertainty of the gluon distribution at  $Q^2 = 1.9 \text{ GeV}^2$ , as resulting from an NLO QCD fit to HERA (I) alone (green, outer), HERA and BCDMS (crossed), HERA and LHC (light blue, crossed) and the LHeC added (blue, dark). Left: logarithmic  $x$ , right: linear  $x$ .

## 1354 4.4 Prospects to Measure the Strong Coupling Constant

1355 The precise knowledge of  $\alpha_s(M_Z^2)$  is of instrumental importance for the correct prediction of the electro-  
 1356 weak gauge boson production cross sections and the Higgs boson cross section at Tevatron and the LHC  
 1357 [77]. Independently of such applications, the accurate determination of the coupling constants of the known  
 1358 fundamental forces is of importance in the search for their possible unification within a more fundamental  
 1359 theory. Among the coupling constants of the forces in the Standard Model, the strong coupling  $\alpha_s$  exhibits  
 1360 the largest uncertainty, which is currently of the size of  $\sim 1\%$ . Any future improvement of this accuracy, along  
 1361 with the consolidation of the genuine central value, is one of the central issues of contemporary elementary  
 1362 particle physics. It demands deep experimental and theoretical efforts to obtain the required precision and  
 1363 especially to handle all essential systematic effects.

1364 Experimentation at the LHeC will allow to measure the strong coupling constant  $\alpha_s(M_Z^2)$  at much higher  
 1365 precision than hitherto, both from the scaling violations of the deep inelastic structure functions, as will be  
 1366 demonstrated below, and using  $ep$  multiple jet cross sections. For the final inclusion of jet data in global  
 1367 pdf analyses, both from  $ep$  and from hadron colliders, their description at NNLO is required. At the LHeC,  
 1368 similar to HERA, the measurement of the  $ep$  jet cross sections will form important data samples <sup>3</sup> for the  
 1369 measurement of  $\alpha_s(M_Z^2)$ .

1370 Subsequently, a brief account will be given on the status and the complexity of determining  $\alpha_s$  in DIS,  
 1371 followed by a presentation of the study of the  $\alpha_s$  measurement uncertainty with the inclusive NC and CC  
 1372 data from the LHeC.

### 1373 4.4.1 Status of the DIS Measurements of $\alpha_s$

1374 During the last 35 years the strong coupling constant has been measured with increasing accuracy in lepton-  
 1375 nucleon scattering in various experiments at CERN, FERMILAB and DESY. The precision, which has  
 1376 been reached currently, requires the description of the deep-inelastic scattering structure functions at  $O(\alpha_s^3)$   
 1377 [36, 78, 79].

<sup>3</sup>These are presented below but have not been used in this document for a determination of the strong coupling constant. One knows of course that the use of jet data in DIS helps resolving the  $\alpha_s$ - $xg$  correlation, especially at large  $x$ , and consequently leads to a significant reduction of the uncertainty on the coupling constant. This, however, tends to also change the central value. The LHeC as will be shown below determines  $\alpha_s$  to permille precision already in inclusive scattering. Comparison with precise values from jets can be expected to shed light on the yet unresolved question as to whether there is a theoretical or systematic effect which leads to different values in inclusive DIS and jets or not.

	$\alpha_s(M_Z^2)$	
BBG	$0.1134^{+0.0019}_{-0.0021}$	valence analysis, NNLO [80]
GRS	0.112	valence analysis, NNLO [81]
ABKM	$0.1135 \pm 0.0014$	HQ: FFNS $N_f = 3$ [82]
ABKM	$0.1129 \pm 0.0014$	HQ: BSMN-approach [82]
JR	$0.1124 \pm 0.0020$	dynamical approach [83]
JR	$0.1158 \pm 0.0035$	standard fit [83]
MSTW	$0.1171 \pm 0.0014$	[84]
ABM	$0.1147 \pm 0.0012$	FFNS, incl. combined H1/ZEUS data [85]
BBG	$0.1141^{+0.0020}_{-0.0022}$	valence analysis, N <sup>3</sup> LO [80]
world average	$0.1184 \pm 0.0007$	[86]

Table 4.3: Recent NNLO and N<sup>3</sup>LO determinations of the strong coupling  $\alpha_s(M_Z)$  in DIS world data analyses.

As is well known [87], though also questioned [88], the fits at NLO exhibit scale uncertainties for both the renormalization and factorization scales of  $\Delta_{r,f}\alpha_s(M_Z^2) \sim 0.0050$ , which are too large to cope with the experimental accuracy of  $O(1\%)$ . Therefore, NNLO analyses are mandatory. In Table 1 recent NNLO results are summarised. NNLO non-singlet data analyses have been performed in [80,81]. The analysis [80] is based on an experimental combination of flavor non-singlet data referring to  $F_2^{p,d}(x, Q^2)$  for  $x < 0.35$  and using the respective valence approximations for  $x > 0.35$ . The  $\bar{d} - \bar{u}$  distributions and the  $O(\alpha_s^2)$  heavy flavor corrections were accounted for. The analysis could be extended to N<sup>3</sup>LO effectively due to the dominance of the Wilson coefficient in this order [78] if compared to the anomalous dimension, cf. [80,89]. This analysis led to an increase of  $\alpha_s(M_Z^2)$  by  $+0.0007$  if compared to the NNLO value.

A combined singlet and non-singlet NNLO analysis based on the DIS world data, including the Drell-Yan and di-muon data, needed for a correct description of the sea-quark densities, was performed in [82]. In the fixed flavor number scheme (FFNS) the value of  $\alpha_s(M_Z^2)$  is the same as in the non-singlet case [80]. The comparison between the FFNS and the BMSN scheme [90] for the description of the heavy flavor contributions induces a systematic uncertainty  $\Delta\alpha_s(M_Z^2) = 0.0006$ . One should note that also in the region of medium and lower values of  $x$  higher twist terms have to be accounted for within singlet analyses to cover data at lower values of  $Q^2$ . Moreover, systematic errors quoted by the different experiments usually cannot be combined in quadrature with the statistical errors, but require a separate treatment. The NNLO analyses [83] are statistically compatible with the results of [80–82], while those of [84] yield a higher value.

In [85] the combined H1 and ZEUS data were accounted for in an NNLO analysis for the first time, which led to a shift of  $+0.0012$ . However, running quark mass effects [91] and the account of recent  $F_L$  data reduce this value again to the NNLO value given in [82]. Other recent NNLO analyses of precision data, as the measurement of  $\alpha_s(M_Z^2)$  using thrust in high energy  $e^+e^-$  annihilation data [92,93], result in  $\alpha_s(M_Z^2) = 0.1153 \pm 0.0017 \pm 0.0023$ , resp.  $0.1135 \pm 0.0011 \pm 0.0006$ . Also the latter values are lower than the 2009 world average [86] based on NLO, NNLO and N<sup>3</sup>LO results.

#### 4.4.2 Simulation of $\alpha_s$ Determination

Since nearly twenty years, the  $\alpha_s$  determination in DIS is dominated by the most precise data from the BCDMS Collaboration, which hint to particularly low values of  $\alpha_s(M_Z) \simeq 0.113$  [94] and exhibit some peculiar systematic error effects, when compared to the SLAC data and in the pQCD analyses as are discussed in [95,96]. Recent analyses seem to indicate that the influence of the BCDMS data is limited, which, however, is possible only when jet and nuclear fixed target data, extending to very low  $Q^2$ , are used. Jet data sometimes tend to increase the value of  $\alpha_s$  and certainly introduce extra theoretical problems connected with hadronisation effects in non-inclusive measurements. The use of fixed target data poses problems due to the uncertainty of corrections from higher twists and from nuclear effects, because what is required is an extraordinary precision if indeed one wants to unambiguously determine the strong coupling

case	cut [ $Q^2$ in $\text{GeV}^2$ ]	$\alpha_s$	$\pm$ uncertainty	relative precision in %
HERA only (14p)	$Q^2 > 3.5$	0.11529	0.002238	1.94
HERA+jets (14p)	$Q^2 > 3.5$	0.12203	0.000995	0.82
LHeC only (14p)	$Q^2 > 3.5$	0.11680	0.000180	0.15
LHeC only (10p)	$Q^2 > 3.5$	0.11796	0.000199	0.17
LHeC only (14p)	$Q^2 > 20.$	0.11602	0.000292	0.25
LHeC+HERA (10p)	$Q^2 > 3.5$	0.11769	0.000132	0.11
LHeC+HERA (10p)	$Q^2 > 7.0$	0.11831	0.000238	0.20
LHeC+HERA (10p)	$Q^2 > 10.$	0.11839	0.000304	0.26

Table 4.4: Results of NLO QCD fits to HERA data (top, without and with jets) to the simulated LHeC data alone and to their combination. Here 10p or 14p denotes two different sets of parametrisations, one, with 10 parameters, the minimum parameter set used in [38] and the other one with four extra parameters added as has been done for the HERAPDF1.5 fit. The central values of the LHeC based results are obviously of no interest. The result quoted as relative accuracy includes all the statistical and the systematic error sources taking correlations as from the energy scale uncertainties into account.

constant in DIS. These problems have been discussed in detail above, and recently also in presentations by MSTW [97] and in a phenomenological study of the NNPDF group [98].

The question, of how large  $\alpha_s$  is, remains puzzling, as has been discussed at a recent workshop [99] and requires a qualitatively and quantitatively new level of experimental input if one wants to progress in DIS.

Following the description of the simulated LHeC data (Sec. 4.1.4) and the QCD fit technique (Sec. 4.2.1) a dedicated study has been performed to estimate the accuracy of an  $\alpha_s$  measurement with the LHeC. In the fits, for the central values of the LHeC data, the SM expectation is used smeared within the above uncertainties assuming their Gaussian distribution and taking into account correlated uncertainties as well.

The QCD fit results are summarised in Tab. 4.4. The first two lines give the result of a fit to the HERA I data. One observes that the inclusion of DIS jet data reduces the uncertainty, by a factor of two, but it also increases the central value by more than the uncertainty. The LHeC alone, in sole inclusive DIS, reaches values of better than 0.2% which when complemented with HERA data reaches a one per mille precision. From inspecting the results one finds that enlarging the  $Q^2$  minimum still leads to an impressive precision, as of two per mille in the LHeC plus HERA case, at values which safely are in the DIS region. A  $Q^2$  cut of for example  $10 \text{ GeV}^2$  excludes also the lowest  $x$  region in which non-linear gluon interaction effects may require to change the evolution equations.

It is obvious that the sole experimental uncertainty, while impressive and promising indeed, is not the only problem in such a complex analysis. That requires all relevant parameters to be correspondingly tuned and understood. For example, the charm mass has to be known at the 10 MeV level to allow an  $\alpha_s$  uncertainty of one per mille. The question of the uncertainty of the renormalisation and factorisation scales and their effect on  $\alpha_s$  will be posed newly and higher than NNLO approximations of pQCD appear to be necessary. However, as mentioned above there already exist first N<sup>3</sup>LO results.

From an experimental and phenomenological point of view it appears extremely exciting that with the LHeC the  $\alpha_s$  determination in DIS will be put on much more solid grounds, by the high precision and unprecedented kinematic range and but also by the resulting full constraints on the complete set of parton distributions, of light and heavy quarks, often by direct measurements, which hitherto had to be parameterised in an often crude way.

In view of the importance of this result, this analysis has been performed independently twice with separately generated NC and CC pseudodata under somewhat different assumption, albeit using the same simulation program, and using different versions of the QCD fit program. The results obtained before [100] are in good agreement with the numbers presented here.

1443 It is finally worth noting that there is an interest to measure  $\alpha_s$  also based on non-singlet quantities. The  
 1444 LHeC data provide high precision information both on the valence quarks and also on the proton-neutron  
 1445 structure function difference. The accuracy expected from such measurements has not been estimated.

## 1446 4.5 Electron-Deuteron Scattering

1447 The structure of the deuteron and of the neutron are experimental unknowns over most of the kinematic  
 1448 region of deep inelastic scattering. The last time lepton-deuteron scattering was measured occurred in the  
 1449 fixed target  $\mu D$  experiments at CERN [101–103], while it had only been considered at HERA [104–106].  
 1450 The LHeC so extends the range of these measurements by nearly four orders of magnitude in  $Q^2$  and  $1/x$ ,  
 1451 which gives rise to a most exciting programme in QCD and in experimental physics.

### 1452 DIS and Partons

1453 Electron-deuteron scattering complements  $ep$  scattering in that it makes possible accurate measurements of  
 1454 neutron structure in the new kinematic range accessed by the LHeC. In a collider configuration, in which  
 1455 the hadron “target” has momentum much larger than the lepton probe, the spectator proton can be tagged  
 1456 and its momentum measured with high resolution [104]. The resulting neutron structure function data are  
 1457 then free of nuclear corrections which have plagued the interpretation of deuteron data, especially at larger  
 1458  $x$ , until now [107]. At low  $x$ , for the first time, since diffraction is related to shadowing, one will be able to  
 1459 control the shadowing corrections<sup>4</sup> at the per cent level of accuracy as is also discussed below.

1460 Accurate  $en$  cross section measurements will resolve the quark flavour decomposition of the sea, i.e. via  
 1461 isospin symmetry, unfolding  $\bar{u}$  from  $\bar{d}$  contributions to the rise of  $F_2^p \propto x(4\bar{u} + \bar{d})$  towards low  $x$ , and, from  
 1462 the full set of  $e^\pm p$  and  $e^\pm n$  charged current cross section data, a full unfolding of the flavour content of the  
 1463 nucleon. For the study of the parton evolution with  $Q^2$ , the measurement of  $F_2^N = (F_2^p + F_2^n)/2$  is crucial  
 1464 since it disentangles the evolution of the non-singlet and the singlet contributions. Down to  $x$  of about  $10^{-3}$   
 1465 the  $W^+/W^-$  LHC data will also provide important information on the up-down quark distributions, albeit  
 1466 at high  $Q^2$ . With  $ep$ ,  $eD$  and  $W^+/W^-$  data, the low  $x$  sea will be resolved for the first time, as all the low  
 1467  $x$  light quark information from HERA has been restricted to  $F_2^p$  only.

1468 A special interest in high precision neutron data at high  $Q^2$  arises from the question of whether there  
 1469 holds charge symmetry at the parton level, as has been discussed recently [109]. It may be studied in the  
 1470 charged current  $ep$  and  $eD$  reactions, using both electrons and positrons, by measuring the asymmetry ratio

$$R^- = 2 \frac{W_2^{-D} - W_2^{+D}}{W_2^{-p} + W_2^{+p}}, \quad (4.30)$$

1471 which is directly sensitive to differences of up and down quark distributions in the proton and neutron,  
 1472 respectively, which conventionally are assumed to be equal. With the prospect of directly measuring the  
 1473 strange and anti-strange quark asymmetry in  $e^\pm p$  CC scattering and of tagging the spectator proton and  
 1474 thus eliminating the Fermi motion corrections in  $eD$ , such a measurement becomes feasible at the LHeC. It  
 1475 requires high luminosity of order  $1 \text{ fb}^{-1}$  in  $eD$  scattering.

### 1476 Hidden Colour

1477 In nuclear physics nuclei are simply the composites of nucleons. However, QCD provides a new perspec-  
 1478 tive [110, 111]. Six quarks in the fundamental  $3_C$  representation of  $SU(3)$  color can combine into five  
 1479 different color-singlet combinations, only one of which corresponds to a proton and neutron. The deuteron  
 1480 wavefunction is a proton-neutron bound state at large distances, but as the quark separation becomes

<sup>4</sup>For light nuclei, nuclear shadowing is dominated by the scattering off two nucleons. Since the probability of such double collisions is primarily determined by nuclear geometry, the  $A$ -dependence (though not the absolute value) of shadowing in light nuclei ( $A \leq 12$ ) is not sensitive to details of the dynamics. Consequently, one can extract the nuclear shadowing correction for electron-deuteron scattering with a small uncertainty (well below 1 the electron-carbon and electrondeuteron cross sections [108]).

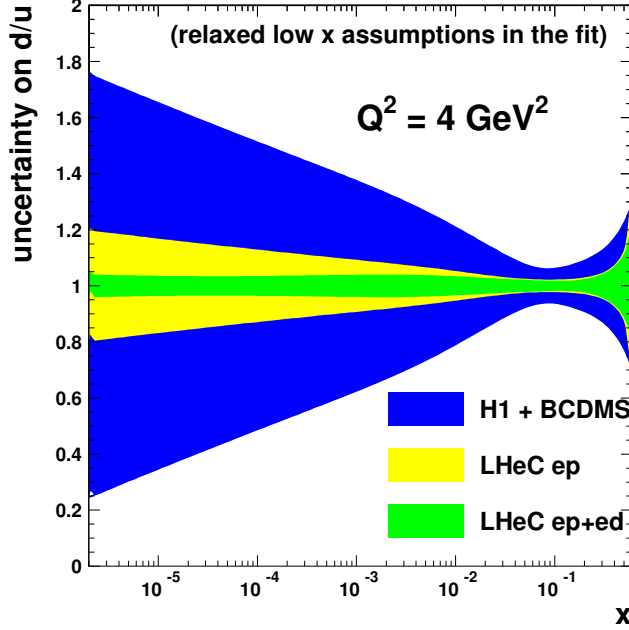


Figure 4.19: Uncertainty of the  $d/u$  ratio as a function of  $x$  from a QCD fit to H1 and BCDMS data (outer band, blue), to the LHeC proton data (middle band, yellow) and the combined simulated proton and deuteron data from the LHeC (inner band, green). In these fits the constraint of  $u$  and  $d$  to be the same at low  $x$  has been relaxed.

1481 smaller, QCD evolution due to gluon exchange introduces four other “hidden color” states into the deuteron  
 1482 wavefunction [112]. The normalization of the deuteron form factor observed at large  $Q^2$  [113], as well as  
 1483 the presence of two mass scales in the scaling behavior of the reduced deuteron form factor [110], sug-  
 1484 gest sizable hidden-color Fock state contributions in the deuteron wavefunction [114]. The hidden-color  
 1485 states of the deuteron can be materialized at the hadron level as  $\Delta^{++}(uuu)\Delta^{-}(ddd)$  and other novel quan-  
 1486 tum fluctuations of the deuteron. These dual hadronic components become important as one probes the  
 1487 deuteron at short distances, such as in exclusive reactions at large momentum transfer. For example, the  
 1488 ratio  $d\sigma/dt(\gamma d \rightarrow \Delta^{++}\Delta^{-})/d\sigma/dt(\gamma d \rightarrow np)$  is predicted to increase to a fixed ratio 2 : 5 with increasing  
 1489 transverse momentum  $p_T$ . Similarly, the Coulomb dissociation of the deuteron into various exclusive chan-  
 1490 nels  $ed \rightarrow e' + pn, pp\pi^{-}, \Delta\Delta, \dots$  will have a changing composition as the final-state hadrons are probed  
 1491 at high transverse momentum, reflecting the onset of hidden-color degrees of freedom. The hidden color  
 1492 of the deuteron can be probed at the LHeC in electron deuteron collisions by studying reactions such as  
 1493  $\gamma^*d \rightarrow npX$  where the proton and neutron emerge in the target fragmentation region at high and opposite  
 1494  $p_T$ . In principle, one can also study DIS reactions  $ed \rightarrow e'X$  at very high  $Q^2$  where  $x > 1$ . The production  
 1495 of high  $p_T$  anti-nuclei at the LHeC is also sensitive to hidden color-nuclear components.

## 1496 4.6 Charm and Beauty production

### 1497 4.6.1 Introduction and overview of expected highlights

1498 In this section it is shown that the measurements of charm and beauty production at LHeC provide high  
 1499 precision pQCD tests and are crucial to improve the knowledge of the proton structure. Historically the  
 1500 HERA charm and beauty studies extended by large amount results from previous fixed target experiments.  
 1501 This allowed a great advancement in the understanding of the dynamics of heavy quark production. The  
 1502 LHeC is the ideal machine for a further extension of similar historic importance because a higher centre

1503 of mass energy and a much larger integrated luminosity compared to HERA are available. On top of this  
 1504 the heavy flavour measurements will greatly benefit from the advanced detector design at LHeC with high  
 1505 precision (Silicon or similar) trackers all over the place. At HERA the tagging was restricted to central  
 1506 rapidities and effective efficiencies<sup>5</sup> of only 0.1% (1%) for charm (beauty) were reached. At LHeC efficiencies  
 1507 of 10% (50%) should be possible for charm (beauty) and a large rapidity range can be covered from the very  
 1508 backward to the very forward regions. Before further elucidating the great measurement prospects the next  
 1509 paragraph introduces the main heavy quark production processes, the relevant pQCD theoretical schemes  
 1510 and some related open questions.

1511 In leading order, heavy quarks are produced in  $ep$  collisions via the Boson Gluon Fusion (BGF) process  
 shown in Figure 4.20 on the left. This process provides direct access to the gluon density in the proton.

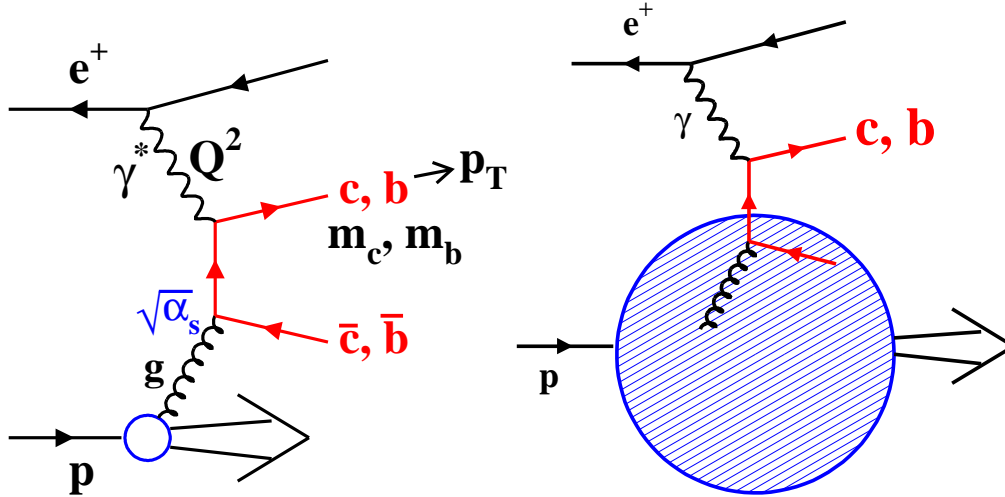


Figure 4.20: Left: Leading order Boson Gluon Fusion (BGF) diagram for charm and beauty production in  $ep$ -collisions. Right: Sketch of the leading order process in the massless approach where charm and beauty quarks are treated as massless sea quarks in the proton.

1512 BGF type processes dominate DIS scattering towards lower  $x$ , due to the large gluon density. In the high  $Q^2$   
 1513 limit, the events with charm and beauty quarks are expected to account for  $\sim 36\%$  and  $\sim 9\%$  of the BGF  
 1514 processes and hence contribute significantly to inclusive DIS. On the theoretical side, the description of heavy  
 1515 quark production in the framework of perturbative QCD is complicated due to the presence of several large  
 1516 scales like the heavy quark masses, the transverse momentum  $p_T$  of the produced quarks and the momentum  
 1517 transfer  $Q^2$ . Different calculation schemes have been developed to obtain predictions from pQCD. At low  
 1518 scales  $p_T$  (or  $Q^2$ ) the fixed-flavour number scheme (FFNS) [115–117] is expected to be most appropriate  
 1519 where the quark masses are fully accounted for. At very high scales the NLO FFNS scheme predictions  
 1520 are expected to break down since large logarithms  $\ln(p_T^2/m^2)$  are neglected that represent collinear gluon  
 1521 radiations from the heavy quark lines. These logarithms can be resummed to all orders in the alternative  
 1522 zero-mass variable flavour number (ZM-VFNS) [118–121] schemes. Here the charm and beauty quarks are  
 1523 treated above kinematic threshold as massless and appear also as active sea quarks in the proton, as depicted  
 1524 in figure 4.20 in the sketch on the right. Most widely used are nowadays the so-called generalised  
 1525 variable flavour number schemes (GM-VFNS) [122, 123]. These mixed schemes converge to the massive and  
 1526 massless schemes at low and high kinematical scales, respectively, and apply a suitable interpolation in the  
 1527 intermediate region. However, the exact modelling of the interpolation and in general the treatment of mass  
 1528 dependent terms in the perturbation series are still a highly controversial issue among the various theory  
 1529 groups. The different treatments have profound implications for global PDF fits and influence the fitted  
 1530

<sup>5</sup>The effective efficiency takes the background pollution into account. It is defined as the efficiency of an equivalent background free sample with the same signal precision as that obtained in the data.

densities of gluons and other quark flavours in the proton. This has direct consequences for many important cross section predictions at LHC, for instance for Z and W production. The value of the charm quark mass is also an important uncertainty in the calculations. Recently the running charm mass has been fitted [91] to fixed target and HERA charm data obtaining a value  $m_c(m_c) = 1.01 \pm 0.09(\text{exp}) \pm 0.03(\text{th})$  GeV.

The following main physics highlights are expected for heavy quark production measurements at LHeC:

- *Massive vs Massless scheme:* At HERA the charm and beauty production data were found to be well described by the NLO FFNS scheme calculations over the whole accessible phase space, up to the highest  $p_T$  and  $Q^2$  scales. An LHeC collider would allow to extend these studies to a much larger kinematical phase space and thus to map the expected transition to the massless regime. Further improvements in the determination of the charm quark mass and in the tuning of the GM-VFNS schemes are possible and will have strong impacts on global PDF fits.

- *Gluon density determination:* At HERA the recorded charm data provide already some interesting sensitivity to the gluon density in the proton. However due to the small tagging efficiencies the precisions are far below those obtained from the scaling violations of  $F_2$  or those from jet data. At LHeC this situation will highly improve and it will be possible to probe the gluon density via the BGF process down to proton momentum fractions  $x_g \leq 10^{-5}$ , where it is currently not well known.

At such low values of  $x_g$  a fixed-order perturbative computation becomes unreliable. It is then necessary to resum both evolution equations and hard matrix elements. In fact, heavy quark production is the first process for which all-order small  $x$  resummed terms were computed, and the high-energy factorization, on which the whole of perturbative small- $x$  resummation is based, was proven in this context [124,125]. Heavy quark production at the LHeC, with its high precision, energy and extended kinematic coverage, would thus provide an ideal setting for tests of high-energy factorization and small  $x$  resummation.

In this context it is also interesting to note that in the BGF process one can reach for charm production much smaller  $x_g$  values than with flavour inclusive jets since experimentally one can tag charm quarks with small transverse momenta. The studies of heavy flavour production sensitive to the gluon density can be done both in DIS and in the photoproduction kinematic regime.

- *Charm and beauty densities in the proton:* In general the measurements of the structure functions  $F_2^{cc}$  and  $F_2^{bb}$  are of highest interest for theoretical analyses of heavy flavour production in  $ep$  collisions. These structure functions are describing the parts of  $F_2$  which are due to events with charm or beauty quarks in the final state. At sufficiently high  $Q^2 \gg m_c^2, m_b^2$ , the two structure functions can be directly related to effective densities of charm and beauty quarks in the proton, This can be used for predictions of many interesting processes at LHC with charm or beauty quarks in the initial state. For instance, as discussed in [126], in the minimal supersymmetric extension of the standard model the production of the neutral Higgs boson  $A$  is driven by  $b\bar{b} \rightarrow A$  and for the calculation of this process the PDF uncertainties dominate over the theoretical uncertainties of the perturbative calculation. At HERA the measurements of  $F_2^{bb}$  barely reached the necessary high  $Q^2$  regime and only with modest precision. Huge phase space extensions and precision improvements will be possible at LHeC.

- *Intrinsic charm component:* Since long it has been suggested [51,127–129] that the proton wave function might contain an intrinsic charm component  $uudc\bar{c}$ . This would show up mainly at large  $x > 0.1$ . Unfortunately at HERA this large  $x$  region could not be studied mainly due to the limited detector acceptance in the forward region. Due to the even larger boost in the forward direction at LHeC the situation is also not easy there. However, with a forward tracking acceptance down to small polar angles there could be a chance to study this effect, in particular with the planned proton low energy runs.

- *Strange/antistrange densities:* Events with charm quarks in the final state can be also used as a tool for other purposes. The strange and antistrange quark densities in the proton can be analysed via the charge current process  $sW \rightarrow c$ , where the charm quark is tagged in the event. At HERA this was impossible due to the small cross sections, but at LHeC the cross sections for CC reactions are

1579 much higher and as noted before the other experimental conditions (luminosities, detector) will greatly  
 1580 improve. This leads to the first and precise measurement of both the strange and the anti-strange  
 1581 quark densities as is demonstrated in Sect. 4.2.

- 1582 • *Electroweak physics:* There are intriguing possibilities for LHeC electroweak physics studies with charm  
 1583 and beauty quarks in the final state. For example one should be able to do a lepton beam polarisation  
 1584 asymmetry measurement for neutral current events, where the scattered quark is tagged as a beauty  
 1585 quark. This will provide direct access to the axial and vector couplings of the beauty quark to the Z  
 1586 boson. Similar measurements are possible for charm.

1587 In summary the measurements of charm and beauty at an LHeC will be extremely useful for high precision  
 1588 pQCD tests, in particular for the understanding of the treatment of mass terms in pQCD, to improve the  
 1589 knowledge of the proton PDFs: directly for g, c, b, s,  $\bar{s}$  densities and indirectly also for u and d. Furthermore  
 1590 they provide a great potential for electroweak physics. At the time when the LHeC will be operated, the  
 1591 pQCD theory calculations are expected to have advanced considerably. In particular there is hope that full  
 1592 massive scheme NNLO calculations of order  $o(\alpha_s^3)$  will be available by then. These will allow theory to data  
 1593 comparisons for heavy flavour production in  $ep$  collisions with unprecedented precision.

1594 In the following subsections several dedicated simulation studies are presented which illustrate some of the  
 1595 expected highlights. First total cross sections are presented for various processes involving charm, beauty  
 1596 and also top quarks in the final state, showing that LHeC will be a genuine *multi heavy flavour factory*.  
 1597 Then the expected measurements of the structure functions  $F_2^{cc}$  and  $F_2^{bb}$  are discussed and compared to the  
 1598 existing HERA data. Next a study is presented of the possibility to measure intrinsic charm with dedicated  
 1599 low proton energy runs. Finally predictions for differential charm hadron production cross sections in the  
 1600 photoproduction kinematic regime are presented and compared to HERA, demonstrating the large phase  
 1601 space extension.

## 1602 4.6.2 Total production cross sections for charm, beauty and top quarks

1603 This section presents total cross sections for various heavy quark processes at LHeC (with 7 TeV proton  
 1604 beam energy) as a function of the lepton beam energy. Predictions are obtained for: charm and beauty  
 1605 production in photoproduction and DIS, the charged current processes  $sW \rightarrow c$  and  $bW \rightarrow t$  and top quark  
 1606 pair production in photoproduction and DIS. For comparison the flavour inclusive charged current total  
 1607 cross section is also shown. Table 4.5 lists the generated processes, the used Monte Carlo generators and the  
 1608 selected parton distribution functions. The resulting cross sections are shown in Figure 4.21. For comparison  
 1609 also the predicted cross sections for the HERA collider (with 920 GeV proton energy) are presented. The  
 1610 cross sections at LHeC are typically about one order of magnitude larger compared to HERA. Attached to  
 1611 the right of the plot are the number of events that are produced per  $10 \text{ fb}^{-1}$  of integrated luminosity. For  
 1612 instance for charm more than 10 billion events are expected in photoproduction and for beauty more than  
 1613 100 million events. In DIS the numbers are typically a factor of five smaller. The strange and antistrange  
 1614 densities can be probed with some hundred thousands of charged current events with charm in the final state.  
 1615 The top quark production is dominated by the single production in the charged current reaction with beauty  
 1616 in the initial state and about one hundred thousands tops and a similar number of antitops are expected.  
 1617 In summary the LHeC will be the first  $ep$  collider which provides access to all quark flavours and with high  
 1618 statistics.

## 1619 4.6.3 Charm and Beauty production in DIS

1620 This section presents predictions for charm and beauty production in neutral current DIS, for  $Q^2$  values  
 1621 of at least a few  $\text{GeV}^2$ . The predictions are given for the structure functions  $F_2^{c\bar{c}}$  and  $F_2^{b\bar{b}}$  which denote  
 1622 the contributions from charm and beauty events to  $F_2$ . As explained in section 4.6.1 the two structure  
 1623 functions are of large interest for theoretical analyses. Experimentally they are obtained by determining the  
 1624 total charm and beauty cross sections in two-dimensional bins of  $x$  and  $Q^2$ . The LHeC projections shown  
 1625 here were obtained with the Monte Carlo programme RAPGAP [132] which generates charm and beauty



Process	Monte Carlo	PDF
Charm $\gamma p$ Beauty $\gamma p$ tt $\gamma p$	PYTHIA6.4 [130]	CTEQ6L [131]
Charm DIS Beauty DIS tt DIS	RAPGAP3.1 [132]	CTEQ5L [133]
CC $e^+p$ CC $e^-p$ $sW \rightarrow c$ $\bar{s}W \rightarrow \bar{c}$ $bW \rightarrow t$ $\bar{b}W \rightarrow \bar{t}$	LEPTO6.5 [134]	CTEQ5L
tt DIS	RAPGAP 3.1	CTEQ5L

Table 4.5: Used generator programmes for the predictions of total cross sections at LHeC, shown in Figure 4.21. For all processes with top quarks the top mass was set to a value of 170 GeV. For both photoproduction (labelled as  $\gamma p$ ) and DIS only direct photon processes were generated and no reactions with resolved photons.

1626 production with massive leading order matrix elements supplemented by parton showers. The proton Parton  
1627 Distribution Function set CTEQ5L [133] were used and the heavy-quark masses were set to  $m_c = 1.5$  GeV  
1628 and  $m_b = 4.75$  GeV, respectively. In general at HERA the RAPGAP predictions are known to provide a  
1629 reasonable description of the measured charm and beauty DIS production data. The RAPGAP data were  
1630 generated for an LHeC collider scenario with 100 GeV electrons colliding with 7 TeV protons. The statistical  
1631 uncertainties have been evaluated such that they correspond to an integrated data luminosity of  $10 \text{ fb}^{-1}$ . All  
1632 studies were done at the parton level, hadronisation effects were not taken into account. Tagging efficiencies  
1633 of 10% for charm quarks and 50% for beauty quarks have been assumed, respectively. These efficiencies are  
1634 about a factor 100 larger compared to the effective efficiencies (including the dilution due to background  
1635 pollution) at HERA which may look surprisingly but is explainable. At HERA the charm quarks were tagged  
1636 either with full charm meson reconstruction or with inclusive secondary vertexing of charm hadron decays.  
1637 The first method suffered from very small branching ratios of suitable decay channels. The second technique  
1638 which was also used for the beauty tagging was affected by a large pollution from light quark background  
1639 events due to the limited detector capabilities to separate secondary from primary vertices. At LHeC one  
1640 can expect a much better secondary vertex identification and thus a very strong background reduction. It is  
1641 difficult to predict exactly how much background pollution will remain at LHeC, so for the purpose of this  
1642 simulation study it was completely neglected. Systematic uncertainties were also neglected for the studies  
1643 presented here. From the experiences at HERA the total systematic uncertainties for charm and beauty  
1644 cross sections in the visible ranges can be expected to be of similar size as the statistical ones.

1645 Figures 4.22 and 4.23 show the resulting RAPGAP predictions at LHeC for the structure functions  $F_2^{cc}$   
1646 and  $F_2^{bb}$ , respectively, compared to recent measurements [135] from HERA. The data are shown as a function  
1647 of  $x$  for various  $Q^2$  values. The  $Q^2$  values were chosen such that they cover a large fraction of the specific  
1648 values for which HERA results are available. Some further values demonstrate the phase space extensions  
1649 at LHeC. The projected LHeC data are presented as points with error bars which (where visible) indicate  
1650 the estimated statistical uncertainties. For the open points the detector acceptance is assumed to cover the  
1651 whole polar angle range. For the grey shaded and black points events are only accepted if at least one charm  
1652 quark is found with polar angles  $\theta_c > 2^0$  and  $\theta_c > 10^0$ , respectively. The selected results from HERA are  
1653 shown as triangles with error bars indicating the total uncertainty. The HERA  $F_2^{cc}$  results in Figure 4.22

## Total cross sections in ep collisions

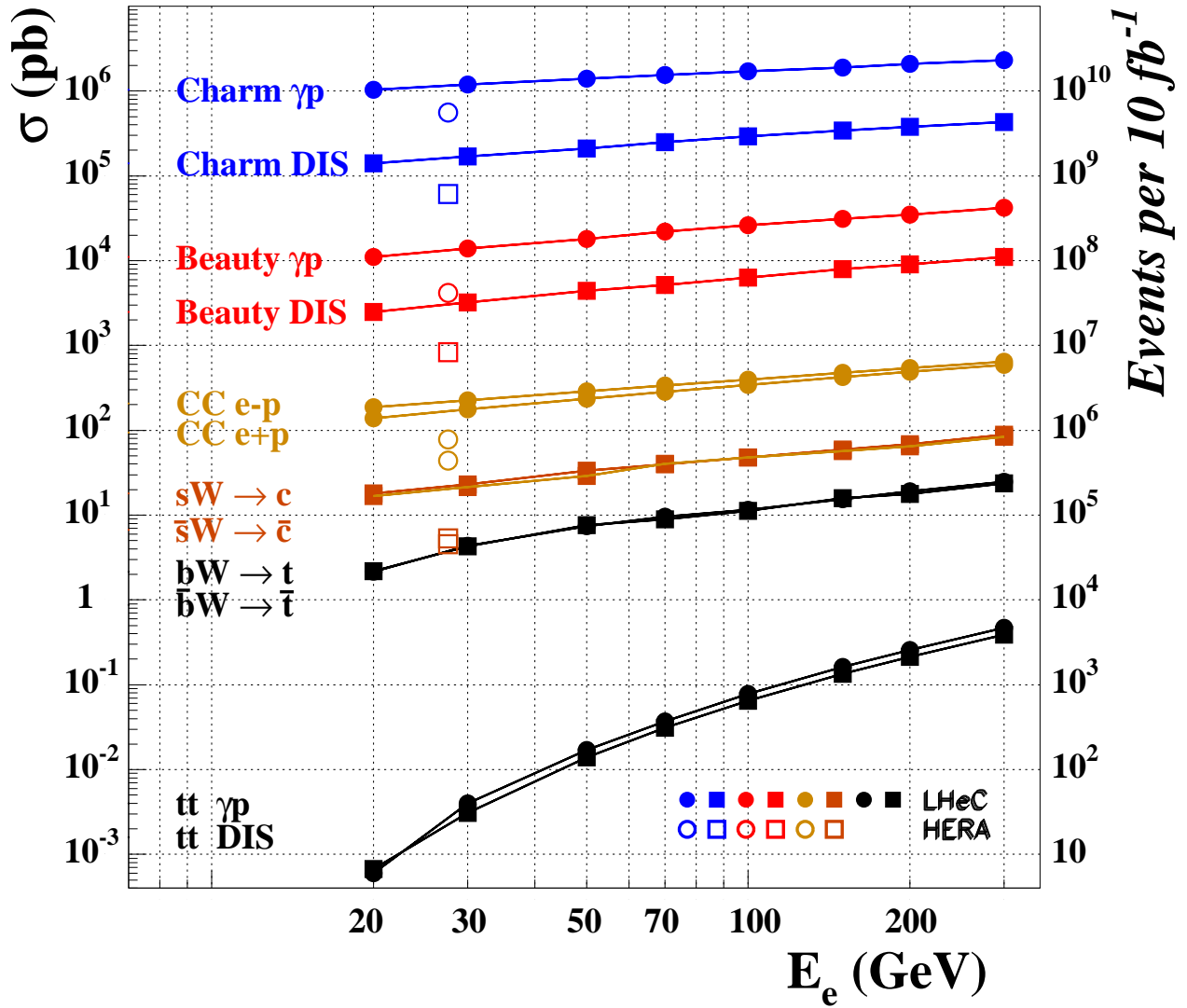


Figure 4.21: Total production cross section predictions for various heavy quark processes at the LHeC (with 7 TeV proton energy), as a function of the lepton beam energy. The following processes are covered: charm and beauty production in photoproduction and DIS, the charged current processes  $sW \rightarrow c$  and  $bW \rightarrow t$  and top pair production in photoproduction and DIS. The flavour inclusive charged current total cross section is also shown. All predictions are taken from Monte Carlo simulations, the details can be found in Table 4.5. For comparison also the predicted cross sections at HERA (with 920 GeV proton energy) are shown.

1654 are those of a recent weighted average [135] of almost all available measurements from H1 and ZEUS. In a  
 1655 large part of the covered phase space these results are already rather accurate, with precisions between 5%  
 1656 and 10%. The overlaid LHeC projections show a vast phase space increase to lower and larger  $x$  and also  
 1657 to much higher  $Q^2$  values. In the kinematic overlap region the expected statistical precisions at LHeC are  
 1658 typically a factor  $\sim 40$  better than at HERA which can be easily explained by the 20 times larger integrated  
 1659 luminosity and the  $\sim 100$  times better tagging efficiency. For the smaller  $x$  not covered by HERA the

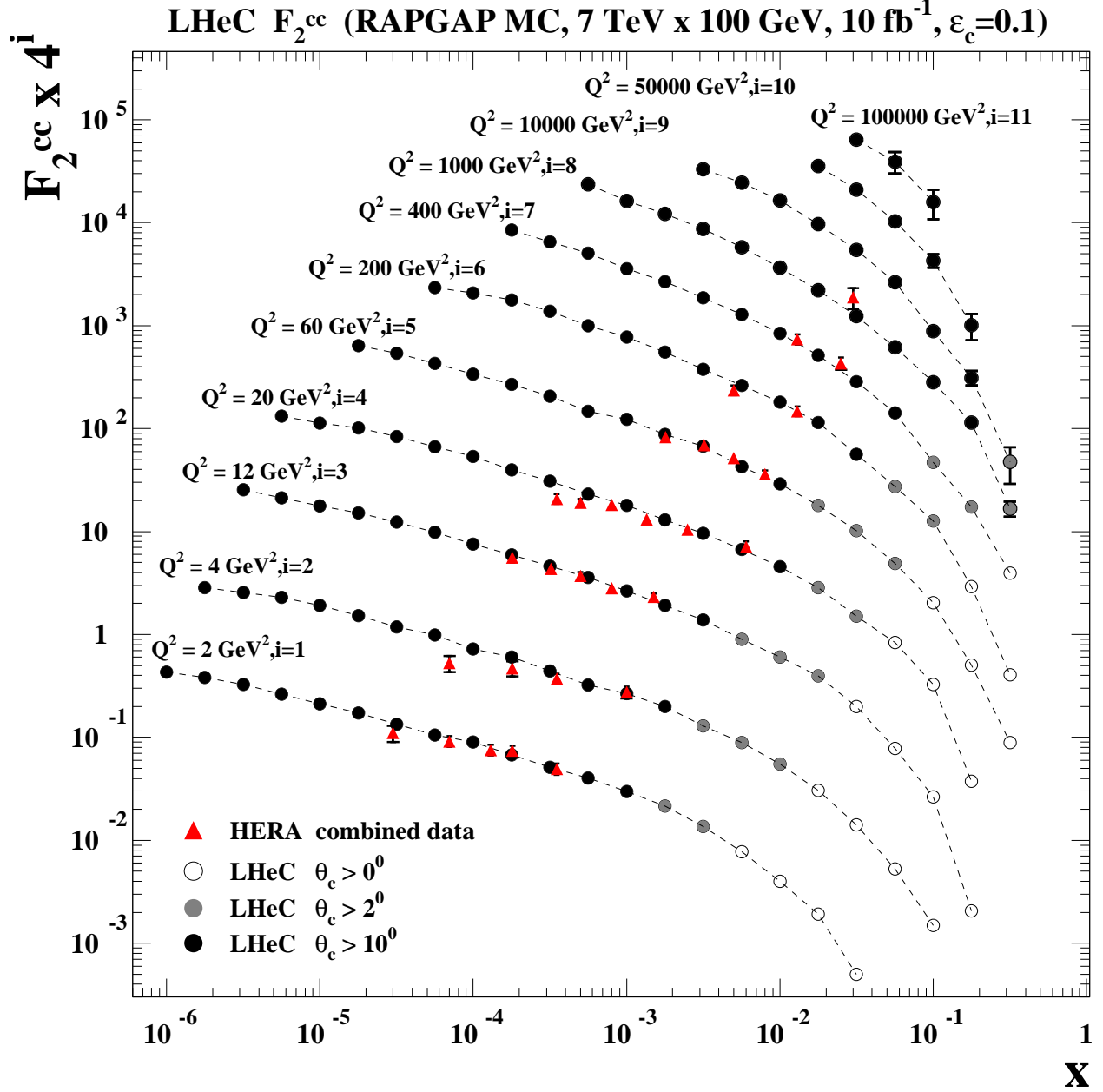


Figure 4.22:  $F_2^{cc}$  projections for LHeC compared to HERA data [135], shown as a function of  $x$  for various  $Q^2$  values. The expected LHeC results obtained with the RAPGAP MC simulation are shown as points with error bars representing the statistical uncertainties. The dashed lines are interpolating curves between the points. For the open points the detector acceptance is assumed to cover the whole polar angle range. For the grey shaded and black points events are only accepted if at least one charm quark is found with polar angles  $\theta_c > 2^0$  and  $\theta_c > 10^0$ , respectively. For further details of the LHeC simulation see the main text. The combined HERA results from H1 and ZEUS are shown as triangles with error bars representing their total uncertainty.

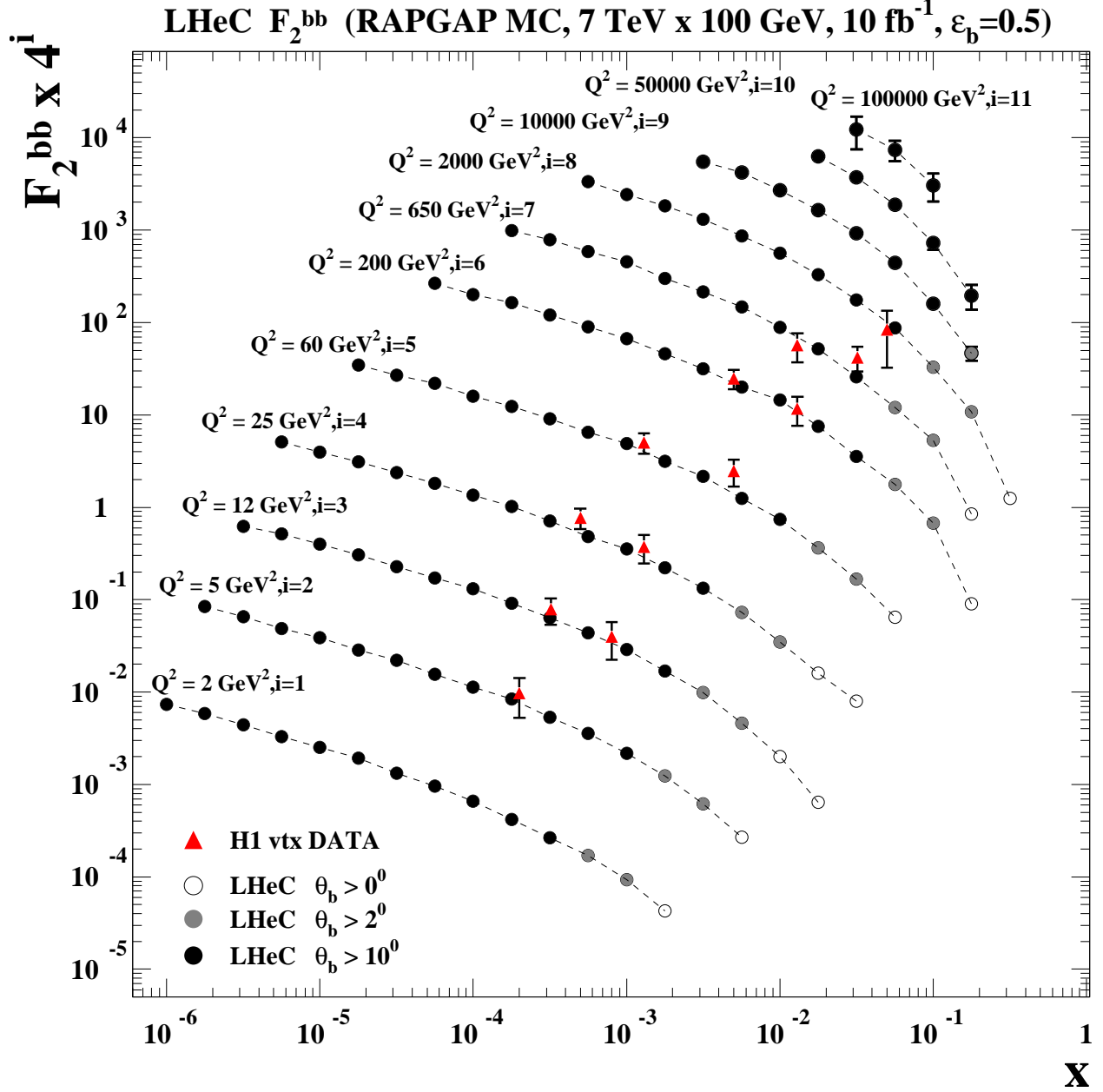


Figure 4.23:  $F_2^{bb}$  projections for LHeC compared to HERA data [136] from H1, shown as a function of  $x$  for various  $Q^2$  values. The expected LHeC results obtained with the RAPGAP MC simulation are shown as points with error bars representing the statistical uncertainties. The dashed lines are interpolating curves between the points. For the open points the detector acceptance is assumed to cover the whole polar angle range. For the grey shaded and black points events are only accepted if at least one beauty quark is found with polar angles  $\theta_b > 2^\circ$  and  $\theta_b > 10^\circ$ , respectively. For further details of the LHeC simulation see the main text. The HERA results from H1 are shown as triangles with error bars representing their total uncertainty.

1660 precision even improves at LHeC due to the growing cross sections driven by the rise of the gluon density.  
 1661 The best statistical precisions in the LHeC simulation are observed at smallest  $x$  values and small  $Q^2$  and

1662 reach down to 0.01%. As seen in the simulation (not shown here) the LHeC  $F_2^{cc}$  data provide access to the  
 1663 the gluon density in the BGF process down to proton momentum fractions  $x_g \sim 10^{-5}$ . The LHeC data can  
 1664 also provide an substantial extension to higher  $x$  compared to HERA where the measurements reached  $x$   
 1665 values of a few percent. As evident from the simulated points with different polar angle cuts this necessitates  
 1666 an excellent forward tagging of charm quarks. In any case values of  $x > 0.1$  should be accessible in the  
 1667 medium and large  $Q^2$  domain.

1668 Figure 4.23 show the RAPGAP predictions at LHeC for  $F_2^{bb}$ . Also shown are the results from the H1  
 1669 analysis [136] based on inclusive secondary vertex tagging. Clearly these results and similar ones (not shown)  
 1670 from ZEUS are not very precise, the typical total uncertainties are 20-50%. Again, the LHeC  $F_2^{bb}$  projections  
 1671 demonstrate a vast phase space increase, similar as for charm. The best statistical precisions obtained at  
 1672 LHeC for  $F_2^{bb}$  are seen in the simulation towards low  $x$  and small and medium  $Q^2$  and reach down to 1  
 1673 permille. The measurements at LHeC will enable a precision mapping of beauty production from kinematic  
 1674 threshold to large  $Q^2$ . In the context of the generalised variable flavour number schemes (GM-VFNS) this  
 1675 will allow to study in detail the onset of the beauty quark density in the proton and to compare it to the  
 1676 charm case. As mentioned in section 4.6.1, for high  $Q^2 \gg m_b^2$  the  $F_2^{bb}$  results can be directly interpreted  
 1677 in terms of an effective beauty density in the proton. The measurement of this density is of large interest  
 1678 because it can be used to predict beauty quark initiated processes at the LHC. As visible in the figure,  
 1679 HERA covers only a small phase space in this region and with moderate precision. However, at LHeC the  
 1680 prospects for measuring  $F_2^{bb}$  in this region are very good.

#### 1681 4.6.4 Intrinsic Heavy Flavour

1682 It is conventional to assume that the charm and bottom quarks in the proton structure function only arise  
 1683 from gluon splitting  $g \rightarrow Q\bar{Q}$ . In fact, the proton light-front wavefunction contains *ab initio* intrinsic  
 1684 heavy quark Fock state components such as  $|uudc\bar{c}\rangle$  [51, 127–129]. The intrinsic heavy quarks carry most  
 1685 of the proton's momentum since this minimizes the off-shellness of the state. The heavy quark pair  $Q\bar{Q}$   
 1686 in the intrinsic Fock state is primarily a color-octet, and the ratio of intrinsic charm to intrinsic bottom  
 1687 scales scales as  $m_c^2/m_b^2 \simeq 1/10$ , as can easily be seen from the operator product expansion in non-Abelian  
 1688 QCD [127, 129]. Intrinsic charm and bottom explain the origin of high  $x_F$  open-charm and open-bottom  
 1689 hadron production, as well as the single and double  $J/\psi$  hadroproduction cross sections observed at high  
 1690  $x_F$ . The factorization-breaking nuclear  $A^\alpha(x_F)$  dependence of hadronic  $J/\psi$  production cross sections is  
 1691 also explained.

1692 As emphasized recently [137], there are strong indications that the structure functions used to model  
 1693 charm and bottom quarks in the proton at large  $x$  have been underestimated, since they ignore intrinsic  
 1694 heavy quark fluctuations of hadron wavefunctions. Furthermore, the neglect of the intrinsic-heavy quark  
 1695 component in the proton structure function will lead to an incorrect assessment of the gluon distribution  
 1696 at larger  $x$  if it is assumed that sea quarks always arise from gluon splitting. The anomalous growth of the  
 1697  $p\bar{p} \rightarrow \gamma cX$  inclusive cross section observed by the D0 collaboration [138] at the Tevatron indicates that the  
 1698 charm distribution has been underestimated at  $x > 0.1$ .

1699 In [139] a novel mechanism for inclusive and diffractive Higgs production  $pp \rightarrow pHp$  is proposed, in which  
 1700 the Higgs boson carries a significant fraction of the projectile proton momentum. The production mechanism  
 1701 is based on the subprocess  $(Q\bar{Q})g \rightarrow H$  where the  $Q\bar{Q}$  in the  $|uudQ\bar{Q}\rangle$  intrinsic heavy quark Fock state  
 1702 of the colliding proton has approximately 80% of the projectile protons momentum. A similar mechanism  
 1703 could produce the Higgs at large  $x_F \sim 0.8$  in  $\gamma p \rightarrow HX$  at the LHeC based on the mechanism  $\gamma(Q\bar{Q}) \rightarrow H$   
 1704 since the heavy quarks typically each carry light-cone momentum fractions  $x \sim 0.4$  when they arise from the  
 1705 intrinsic heavy quark Fock states  $|uudQ\bar{Q}\rangle$  of the proton.

1706 The LHeC could establish the phenomenology of the charm and bottom structure functions at larger  
 1707  $x$ . In addition to DIS measurements, one can test the charm (and bottom) distributions at the LHeC by  
 1708 measuring reactions such as  $\gamma p \rightarrow cX$  where the charm jet is produced at high  $p_T$  in the reaction  $\gamma c \rightarrow cg$ .

1709 In order to access the charm and bottom distributions towards larger Bjorken  $x$ , it is required to tag  
 1710 heavy flavour production in the forward direction. As this is difficult in the asymmetric electron-proton  
 1711 beam energy configuration such a measurement can favourably be done with a reduced proton beam energy.

1712 Approximately, as may be derived from Eq. 12.8, the small hadronic scattering angle,  $\theta_h$ , is obtained from  
 1713 the relation,  $\theta_h^2 \simeq 2\sqrt{Q^2}/E_p x$ . Therefore a reduction by a factor of 7 of the proton beam energy  $E_p$  enhances  
 1714  $x$  by 7 at fixed  $Q^2$  and  $\theta_h$ . One also notices that large  $x$  is reached at fixed  $\theta_h$  and  $E_p$  only at high  $Q^2$ . The  
 1715 attempt to access maximum  $x$  thus requires to find an optimum of high luminosity, to reach high  $Q^2$ , and  
 1716 low proton beam energy, to access large  $x$ . Fig. 4.24 shows a simulated measurement of the charm structure  
 1717 function for  $E_p = 1$  TeV and a luminosity of  $1 \text{ fb}^{-1}$ . The two curves illustrate the difference between CTEQ66  
 PDF sets with and without an intrinsic charm component, based on [137]. The actual amount of intrinsic

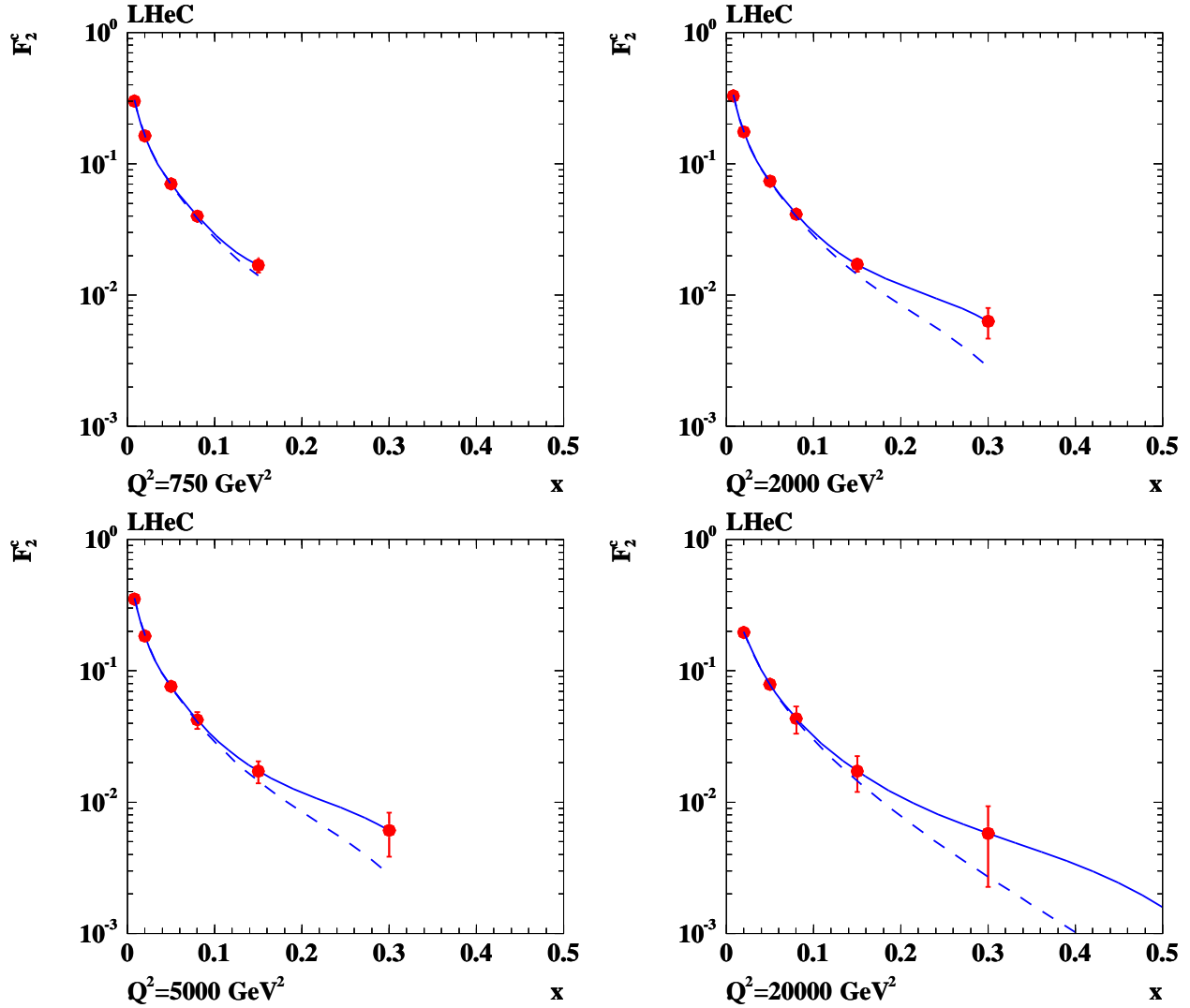


Figure 4.24: Simulation of measurement of the charm structure function at large  $x$ , see text. The errors are statistical, taking tagging and background efficiencies into account. The tagging efficiency for charm quarks was assumed to be 10% and the amount of background was estimated to be  $0.01 \cdot N_{ev}$ , where  $N_{ev}$  refers to the total number of expected NC events in the respective  $(Q^2, x)$  bin. Solide line: CTEQ66c predictions, including an intrinsic charm component, dashed line: ordinary CTEQ66m.

1718 charm may be larger than in the CTEQ attempt, it may also be smaller. One so finds that a reliable detection  
 1719 of an intrinsic heavy charm component at the LHeC may be possible, but will be a challenge for forward  
 1720 charm detection and requires high luminosity. The result yet may be rewarding as it would have quite some  
 1721

1722 theoretical consequences as sketched above. It would be obtained in a region of high enough  $Q^2$  to be able  
 1723 to safely neglect any higher twist effects which may mimic such an observation at low energy experiments.

#### 1724 4.6.5 $D^*$ meson photoproduction study

1725 A study is presented of  $D^*$  meson photoproduction at LHeC compared to HERA. It is based on NLO  
 1726 predictions in the so-called general-mass variable-flavour-number scheme (GM-VFNS) [122,123] for 1-particle  
 1727 inclusive heavy-meson production. Both direct and resolved photon contributions are taken into account.  
 1728 The cross section for direct photoproduction is a convolution of the proton PDFs, the cross section for the  
 1729 hard scattering process and the fragmentation functions FF for the transition of a parton to the observed  
 1730 heavy meson. For the resolved contribution, an additional convolution with the photon PDFs has to be  
 1731 performed. For the photoproduction predictions at the  $ep$ -colliders HERA and LHeC, the calculated photon  
 1732 proton cross sections are convoluted with the photon flux using the Weizsaecker-Williams approximation.

1733 In the GM-VFNS approach the large logarithms  $\ln(p_T^2/m^2)$ , which appear due to the collinear mass  
 1734 singularities in the initial and final state, are factorized into the PDFs and the FFs and summed by the  
 1735 well known DGLAP evolution equations. The factorization is performed following the usual  $\overline{\text{MS}}$  prescrip-  
 1736 tion which guarantees the universality of both PDFs and FFs. At the same time, mass-dependent power  
 1737 corrections are retained in the hard-scattering cross sections, as in the FFNS. For the photon PDF the  
 1738 parametrization of Ref. [140] with the standard set of parameter values is used and for the proton PDF the  
 1739 parametrization CTEQ6.5 [141] of the CTEQ group. For the FFs the set Belle/CLEO-GM of Ref. [142] is  
 chosen. Various combinations of beam energies are studied. To compare with the situation at HERA, as

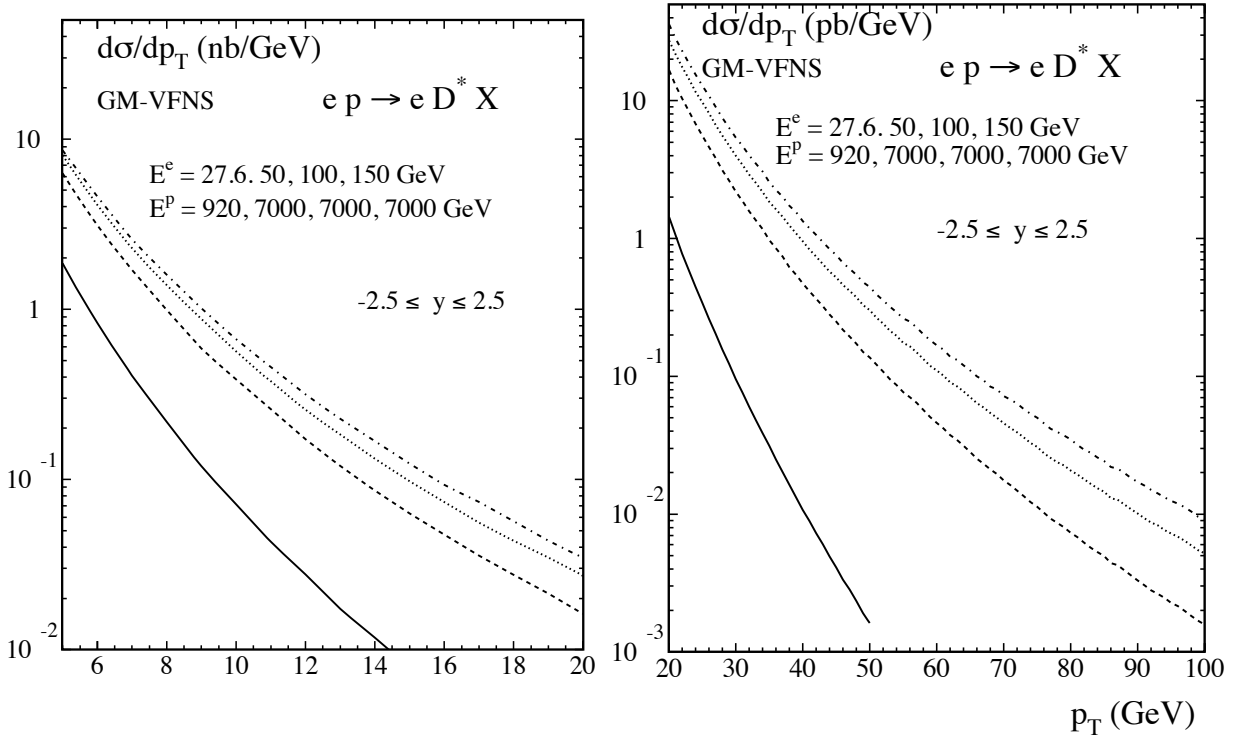


Figure 4.25: The  $p_T$ -differential cross section for the production of  $D^*$  mesons at LHeC for different beam energies integrated over rapidities  $|\eta| \leq 2.5$ , for the low- $p_T$  range  $5 \text{ GeV} \leq p_T \leq 20 \text{ GeV}$  (left) and for the high- $p_T$  range  $20 \text{ GeV} \leq p_T \leq 50 \text{ GeV}$  (right). The curves from bottom to top correspond to the combinations of beam energies as indicated in the figure.

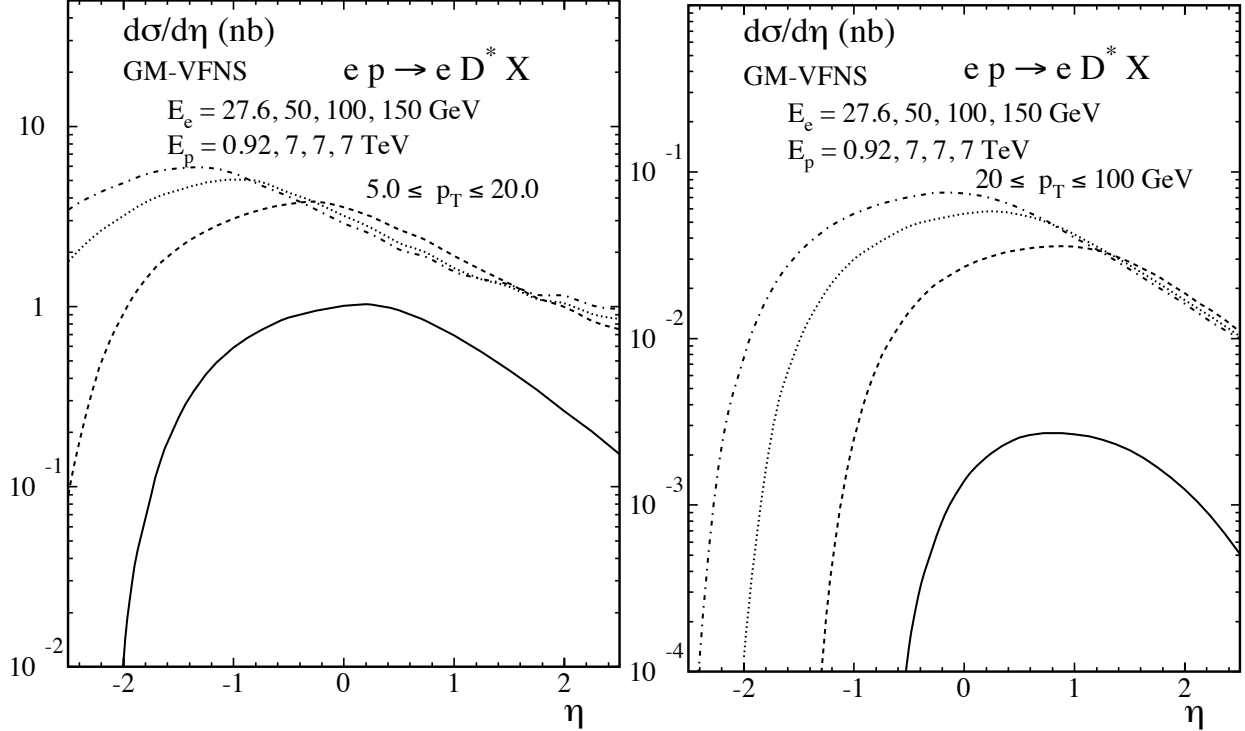


Figure 4.26: Rapidity distribution of the cross section for the production of  $D^*$  mesons at LHeC for different beam energies integrated over the low- $p_T$  range  $5 \text{ GeV} \leq p_T \leq 20 \text{ GeV}$  (left) and the high- $p_T$  range  $20 \text{ GeV} \leq p_T \leq 50 \text{ GeV}$  (right). The curves from bottom to top correspond to the combinations of beam energies as indicated in the figure.

1741 a reference, the values  $E^p = 920 \text{ GeV}$  and  $E^e = 27.5 \text{ GeV}$  for proton and electron energies, respectively,  
 1742 are also included. For the LHeC the proton energy is taken to be always  $E^p = 7 \text{ TeV}$  and the options  
 1743  $E^e = 50, 100$  and  $150 \text{ GeV}$  are considered. The exchanged photons are restricted to inelasticities  $y$  in the  
 1744 range  $0.1 < y < 0.9$ . The transverse momentum  $p_T$  and the rapidity  $\eta$  of the  $D^*$ -meson are varied in Fig. 4.25  
 1745 in the kinematic ranges  $5 < p_T < 20 \text{ GeV}$  or  $20 < p_T < 100$  and  $|\eta| < 2.5$ . Numerical results are shown in Fig. 4.25  
 1746 for the differential cross section  $d\sigma/dp_T$  integrated over the rapidity  $|\eta| \leq 2.5$  and in Fig. 4.26 for  $d\sigma/d\eta$ ,  
 1747 integrated over the  $p_T$ -ranges  $5 \leq p_T \leq 20 \text{ GeV}$  and  $20 \leq p_T \leq 100 \text{ GeV}$ .

1748 The higher centre-of-mass energies available at the LHeC lead to a considerable increase of the cross  
 1749 sections as compared to HERA. Obviously one can expect an increase in the precision of corresponding  
 1750 measurements and much higher values of  $p_T$ , as well as higher values of the rapidity  $\eta$ , will be accessible.  
 1751 Since theoretical predictions also become more reliable at higher  $p_T$ , measurements of heavy quark produc-  
 1752 tion constitute a promising testing ground for perturbative QCD. One may expect that the experimental  
 1753 information will contribute to an improved determination of the (extrinsic and intrinsic) charm content of  
 1754 the proton and the charm fragmentation functions.

## 1755 4.7 High $p_t$ jets

### 1756 4.7.1 Jets in $ep$

1757 The study of the jet final states in lepton-proton collisions allows the determination of aspects of the nucleon  
 1758 structure which are not accessible in inclusive scattering. Moreover, jet production allows for probing pre-



1759 ditions of QCD to a high accuracy. Depending on the virtuality of the exchanged photon, one distinguishes  
1760 processes in photoproduction (quasi-real photon) and deep inelastic scattering.

1761 The photoproduction cross section for di-jet final states can be studied in different kinematical regions,  
1762 thereby covering a wide spectrum of physical phenomena, and probing the structure of the proton and the  
1763 photon. Two-jet production in deep inelastic scattering is a particularly sensitive probe of the gluon distri-  
1764 bution in the proton and of the strong coupling constant  $\alpha_s$ . Both processes allow the study of potentially  
1765 large enhancement effects in di-jet and multi-jet production.

1766 Jet production in photoproduction proceeds via the direct processes, in which the quasi-real photon  
1767 interacts as a point-like particle with the partons from the proton, and the resolved processes, in which  
1768 the quasi-real photon interacts with the partons from the proton via its partonic constituents. The parton  
1769 distributions in the quasi-real photon are constrained mostly from the study of processes at  $e^+e^-$  colliders,  
1770 and are less well-determined than their counterparts in the proton. In both the direct and the resolved  
1771 process, there are two jets in the final state at lowest-order QCD. The jet production cross section is given in  
1772 QCD by the convolution of the flux of photons in the electron (usually estimated via the Weizacker-Williams  
1773 approximation), the parton densities in the photon, the parton densities in the proton and the partonic cross  
1774 section (calculable in pQCD). Therefore, the measurements of jet cross sections in photoproduction provide  
1775 tests of perturbative QCD and the structure of the photon and the proton.

1776 Owing to the large size of the cross section, photoproduction of di-jets can be used for precision physics  
1777 in QCD. A measurement at LHeC could improve upon previous HERA results and enter into a much larger  
1778 kinematical region. In measurements made by the ZEUS collaboration, the available photon-proton centre-of-  
1779 mass energy ranged from 142 to 293 GeV, and jets of a transverse energy of up to 90 GeV could be observed.  
1780 By comparing the measured cross section with the theoretical prediction in NLO pQCD, a value of  $\alpha_s(M_Z)$   
1781 was extracted with a total uncertainty of  $\pm 3\%$  and the running of  $\alpha_s$  was tested over a wide range of  $E_t^{\text{jet}}$  in  
1782 a single measurement. The limiting factors in this measurement were the theoretical uncertainty inherent  
1783 to the NLO prediction (which could be improved by computing NNLO corrections to jet photoproduction)  
1784 and the experimental systematic uncertainty in the detector energy calibration.

1785 Another motivation for making new photoproduction experiments is to improve the knowledge of the  
1786 parton content of the photon. At present, most information on the photon structure is inferred from the  
1787 collision of quasi-real photons with electrons at  $e^+e^-$  colliders, resulting in a decent determination of the  
1788 total (charge weighted) quark content of the quasi-real photon. Its gluonic content, and the quark flavour  
1789 decomposition are on the other hand only loosely constrained. Improvements to the photon structure are of  
1790 crucial importance to physics studies at a future linear  $e^+e^-$  collider like the ILC or CLIC. Such a collider,  
1791 operating far above the  $Z$ -boson resonance, will face a huge background from photon-photon collisions.  
1792 This background can be suppressed only to a certain extent by kinematical cuts. Consequently, accurate  
1793 predictions of it (which require an improved knowledge of the photon's parton content) are mandatory for  
1794 the reliable interpretation of hadronic final states at the ILC or CLIC. Several parametrizations of the parton  
1795 distributions in the photon are available. They differ especially in the gluon content of the photon. For the  
1796 studies presented here, the GRV-HO parametrization [143] is used as default.

1797 The photoproduction studies performed at LHeC were done for three different electron energy scenarios:  
1798  $E_e=50, 100$  and  $150$  GeV. In all cases, the proton energy was set to 7 TeV. PYTHIA MC samples of  
1799 resolved and direct processes were generated for these three scenarios. Jets were searched using the  $k_t$ -  
1800 cluster algorithm in the kinematic region of  $0.1 < y < 0.9$  and  $Q^2 < 1$  GeV<sup>2</sup>. Inclusive jet cross sections  
1801 were done for jets of  $E_t^{\text{jet}} > 15$  GeV and  $3 < \eta^{\text{jet}} < 3$ . Figure 4.27 shows the PYTHIA MC cross sections  
1802 as functions of  $y$  for the three scenarios plus the corresponding cross section for the HERA regime. It can  
1803 be seen that the LHeC cross sections are one to two orders of magnitude larger than the cross section at  
1804 HERA.

1805 The full study was complemented with fixed-order QCD calculations at order  $\alpha_s$  and  $\alpha_s^2$  using the  
1806 program by Klasen et al. [144] with the CTEQ6.1 sets for the proton PDFs, GRV-HO sets for the photon  
1807 PDFs,  $\alpha_s(M_Z) = 0.119$  and the renormalisation and factorisation scales were set to the transverse energy of  
1808 each jet.

1809 Figure 4.28 shows the inclusive jet cross sections at parton level as functions of  $E_t^{\text{jet}}$  for the three en-

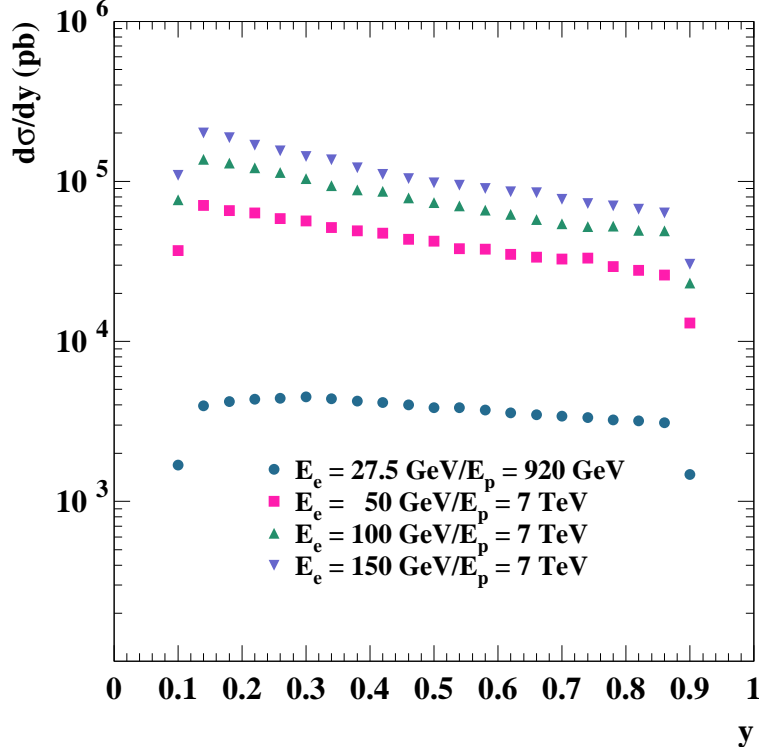


Figure 4.27: PYTHIA predictions for photoproduction cross section at HERA and for three LHeC scenarios.

1810 ergy scenarios for the PYTHIA res+dir (red dots), PYTHIA resolved (blue triangles) and PYTHIA direct  
 1811 (pink triangles) together with the predictions from the NLO (solid curves) and LO (dashed curves) QCD  
 1812 calculations. The calculations predict a sizeable rate for Etjet of at least up to 200 GeV. Resolved processes  
 1813 dominate at low  $E_t^{\text{jet}}$ , but the direct processes become increasingly more important as  $E_t^{\text{jet}}$  increases. The  
 1814 PYTHIA cross sections (which have been normalised to the NLO integrated cross section) agree well in shape  
 1815 with the NLO calculations. Investigating the  $\eta^{\text{jet}}$  distribution, we find that resolved processes dominate in  
 1816 the forward region, while direct processes produce more central jets.

1817 Figure 4.29 show the inclusive jet cross sections at parton level as functions of  $E_t^{\text{jet}}$  (on the left) and  
 1818  $\eta^{\text{jet}}$  (on the right) for the PYTHIA resolved+direct (symbols) and the predictions from the NLO (solid  
 1819 curves) and LO (dashed curves) QCD calculations together for the three energy scenarios. For comparison,  
 1820 the calculations for the HERA regime are also included. It is seen that the cross sections at fixed  $E_t^{\text{jet}}$   
 1821 increase and that the jets tend to go more backward as the collision energy increases. The much larger  
 1822 photon-proton centre-of-mass energies that could be available at LHeC provide a much wider reach in  $E_t^{\text{jet}}$   
 1823 and  $\eta^{\text{jet}}$  compared to HERA.

1824 Hadronisation corrections for the cross sections shown were investigated. The corrections are predicted  
 1825 to be quite small, below +5% for the chosen scenarios. Since the hadronisation corrections are very small,  
 1826 the features observed at parton level remain unchanged.

1827 Inclusive-jet and dijet measurements in deep-inelastic scattering (DIS) have since long been a tool to  
 1828 test concepts and predictions of perturbative QCD. Especially at HERA, jets in DIS have been thoroughly  
 1829 studied, and the results have provided deep insights, giving for example precise values for the strong coupling  
 1830 constant,  $\alpha_s$  and providing constraints for the proton PDFs.

1831 An especially interesting region for such studies has been the regime of large (for HERA)  $Q^2$  values of, for  
 1832 example,  $Q^2 > 125 \text{ GeV}^2$ . In this regime, the theoretical uncertainties, especially those due to the unknown

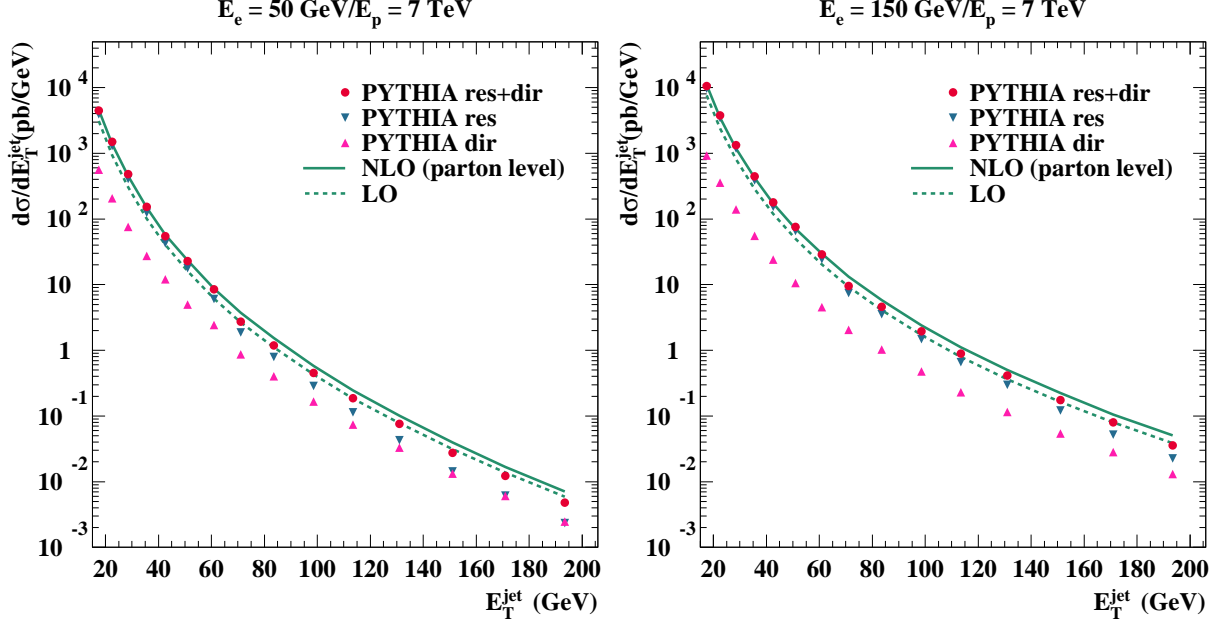


Figure 4.28: Parton level predictions for the inclusive transverse energy distribution in photoproduction.

1833 effects of missing higher orders in the perturbative expansion, are found to be small. Recently, both the H1  
 1834 and ZEUS collaborations have published measurements of inclusive-jet and dijet events in this kinematic  
 1835 regime.

1836 An extension of such measurements to the LHeC is interesting for two reasons: First, the provided high  
 1837 luminosity will allow measurements in already explored kinematic regions with still increased experimental  
 1838 precision. Second, the extension in centre-of-mass energy,  $\sqrt{s}$ , and thus in boson virtuality,  $Q^2$ , and in jet  
 1839 transverse energy,  $E_{T,jet}$ , will potentially allow to study pQCD at even higher scales, extending the scale  
 1840 reach for measurements of the strong coupling or the precision of the proton PDFs at large values of  $x$ .

1841 To explore the potential of such a measurement, we investigated DIS jet production for the following LHeC  
 1842 scenario: proton beam energy 7 TeV, electron beam energy 70 GeV and integrated luminosity  $10 \text{ fb}^{-1}$ . The  
 1843 study concentrates on the phase space of high boson virtualities  $Q^2$ , with event selection cuts  $100 < Q^2 < 500$   
 1844  $000 \text{ GeV}^2$  and  $0.1 < y < 0.7$ , where  $y$  is the inelasticity of the event. Jets are reconstructed using the  $k_T$   
 1845 clustering algorithm in the longitudinally invariant inclusive mode in the Breit reference frame. Jets were  
 1846 selected by requiring: a jet pseudorapidity in the laboratory of  $-2 < \eta_{lab} < 3$ , a jet transverse energy in the  
 1847 Breit frame of  $E_{T,jet}^{Breit} > 20 \text{ GeV}$  for the inclusive-jet measurement and jet transverse energies in the Breit  
 1848 frame of 25(20) GeV for the leading and the second-hardest jet in the case of the dijet selection.

1849 For inclusive-jet production we study cross sections in the indicated kinematic regime as functions of  
 1850  $Q^2$ ,  $x_{Bj}$ ,  $E_{T,jet}^{Breit}$  and  $\eta_{jet}^{lab}$ , the jet pseudorapidity in the laboratory frame. For dijet production, studies are  
 1851 presented as functions of  $Q^2$ , the logarithm of the proton momentum fraction  $\xi$ ,  $\log_{10} \xi$ , the invariant dijet  
 1852 mass  $M_{jj}$ , the average transverse energy of the two jets in the Breit frame,  $\overline{E_{T,jet}^{Breit}}$ , and of half of the absolute  
 1853 difference of the two jet pseudorapidities in the laboratory frame,  $\eta'$ .

1854 For the binning of the observables shown here, the statistical uncertainties for the indicated LHeC in-  
 1855 tegrated luminosity can mostly be neglected, even at the highest scales. The systematic uncertainties were  
 1856 assumed to be dominated by the uncertainty on the jet energy scale which was assumed to be known to 1%  
 1857 or 3% (both scenarios are indicated with different colours in the following plots), leading to typical effects on  
 1858 the jet cross sections between 1 and 15%. A further relevant uncertainty is the acceptance correction that is  
 1859 applied to the data which was assumed to be 3% for all observables.

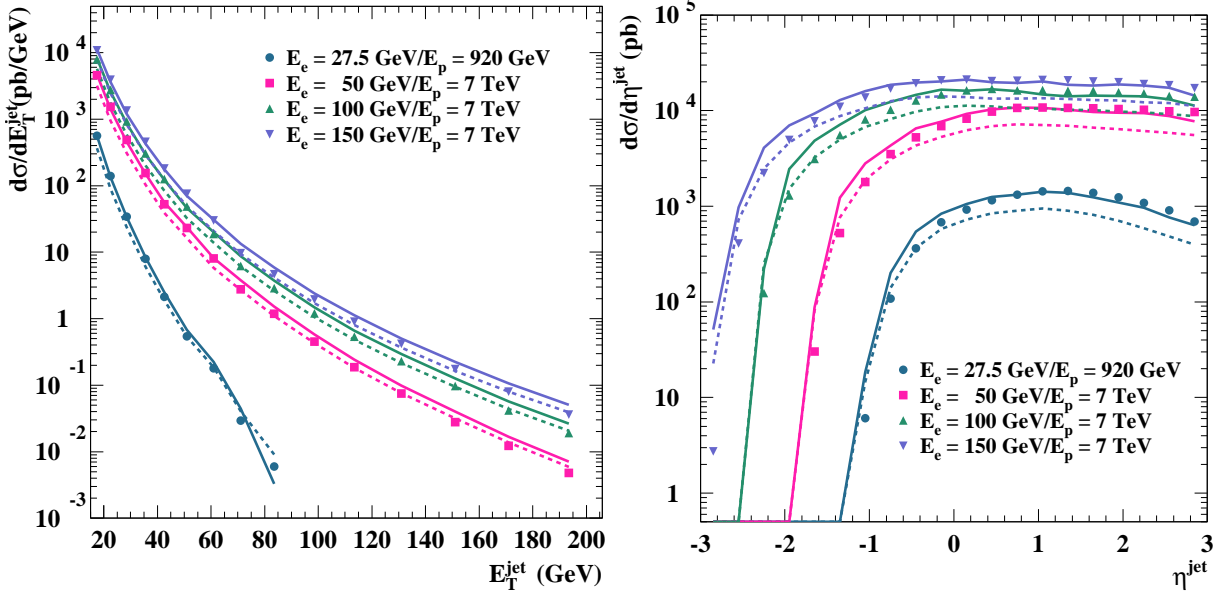


Figure 4.29: Dijet distributions in photoproduction as function of the jet transverse energy (left) and of the jet rapidity (right) for different LHeC energies compared to the HERA kinematic range.

1860 The theoretical calculations were performed with the DISINT program [145] using the CTEQ6.1 proton  
 1861 PDFs [131, 146]. The central default squared renormalisation and factorisation scales were set to  $Q^2$ . The  
 1862 theory calculations for the LHeC scenario were corrected for the effects of hadronisation and  $Z^0$  exchange  
 1863 using Monte Carlo data samples simulated with the LEPTO program [134].

1864 Theoretical uncertainties were assessed by varying the renormalization scale up and down by a factor  
 1865 2 (to estimate the potential effect of contributions beyond NLO QCD), by using the 40 error sets of the  
 1866 CTEQ6.1 parton distribution functions, and by varying  $\alpha_s$  using the CTEQ6AB PDF [147]. The dominant  
 1867 theory uncertainty turned out to be due to the scale variations, resulting in effects of a few to up to 20%  
 1868 or more, for example for low values of  $Q^2$  or, for the case of the dijet measurement, for low values of the  
 1869 invariant dijet mass,  $M_{jj}$ , or the logarithm of momentum fraction carried into the hard scattering,  $\log_{10} \xi$ .

1870 Note that for the inclusive-jet results also the predictions for a HERA scenario with almost the same  
 1871 selection are shown in order to indicate the increased reach of the LHeC with respect to HERA. The only  
 1872 change is a reduction in centre-of-mass energy to 318 GeV and a reduced  $Q^2$  reach,  $125 < Q^2 < 45\,000 \text{ GeV}^2$ .  
 1873 The HERA predictions shown were also corrected for hadronisation effects and the effects of  $Z^0$  exchange.

1874 Figure 4.30 shows the inclusive jet cross section as function of  $Q^2$  and of the jet transverse energy  
 1875 in the Breit frame, while Figure 4.31 shows the dijet cross section as function of  $Q^2$  and of  $\xi = x_{Bj}(1 +$   
 1876  $M_{jj}^2/Q^2)$ . The top parts of the figures show the predicted cross sections together with the expected statistical  
 1877 and (uncorrelated) experimental systematic uncertainties as error bars. The correlated jet energy scale  
 1878 uncertainty is indicated as a coloured band; the inner, yellow band assumes an uncertainty of 1%, the outer,  
 1879 blue band one of 3%. Also shown as a thin hashed area are the theoretical uncertainties; the width of the  
 1880 band indicates the size of the combined theoretical uncertainty. In case of inclusive-jet production, also the  
 1881 predictions for HERA are indicated as a thin line.

1882 The bottom parts of the figures show the relative uncertainties due to the jet energy scale (yellow band  
 1883 for 1%, blue band for 3%), the statistical and uncorrelated experimental systematic uncertainties as inner  
 1884 / outer error bars, and the combined theoretical uncertainties as hashed band. The inner part of this band  
 1885 indicates the uncertainty due to the variation of the renormalisation scale.

1886 The inclusive-jet cross section as function of  $Q^2$  shows a typical picture: In most region of the phase

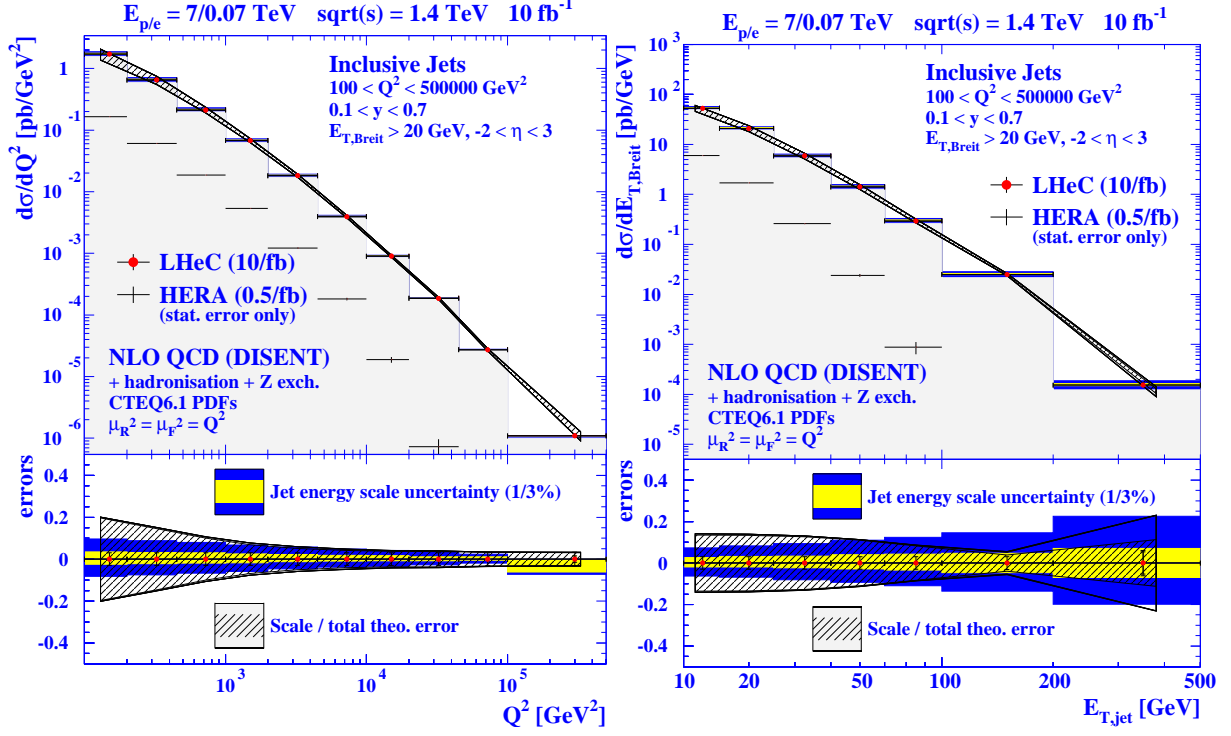


Figure 4.30: Predicted LHeC results for inclusive jet production as function of  $Q^2$  and of  $E_T$  in the Breit frame. Predictions for HERA results are also shown.

1887 space, the uncertainties are dominated by the theory uncertainties, and here mainly by the renormalisation  
 1888 scale uncertainty. The typical size of experimental uncertainties is of the order of 10%, with larger values  
 1889 in regions with low relevant scales — i.e. low invariant dijet masses, low jet transverse energies or low  $Q^2$   
 1890 values. The theoretical uncertainties are typically between 5 and 20%, with partially strong variations over  
 1891 the typical range of the observable in question.

1892 A comparison with the HERA predictions for inclusive-jet production shows that the LHeC cross sections  
 1893 is typically larger by 1 to 3 orders of magnitude. The dijet final state allows for a full reconstruction of the  
 1894 partonic kinematics, and can thus be used to probe the parton distribution functions in  $Q^2$  and  $\xi$ . It can  
 1895 be seen that a measurement at LHeC covers a large kinematical range ranging down to  $\xi \approx 10^{-3}$  and up to  
 1896  $Q^2 = 10^5$  GeV $^2$ . Potentially limiting factors in an extraction of parton distribution functions are especially  
 1897 the jet energy scale uncertainty on the experimental side and missing higher order (NNLO) corrections on the  
 1898 theory side. The jet energy scale uncertainty can be addressed by the detector design and by the experimental  
 1899 setup of the measurement. NNLO corrections to dijet production in deep inelastic scattering are already  
 1900 very much demanded by the precision of the HERA data, their calculation is currently in progress [148, 149].

1901 In summary, jet final states in photoproduction and deep inelastic scattering at the LHeC promise a wide  
 1902 spectrum of new results on the partonic structure of the photon and the proton. They allow for precision tests  
 1903 of QCD by independent determinations of the strong coupling constant over a kinematical range typically  
 1904 one to two orders of magnitude larger than what was accessible at HERA. The resulting parton distributions  
 1905 will have a direct impact for precision predictions at the LHC and a future linear collider.

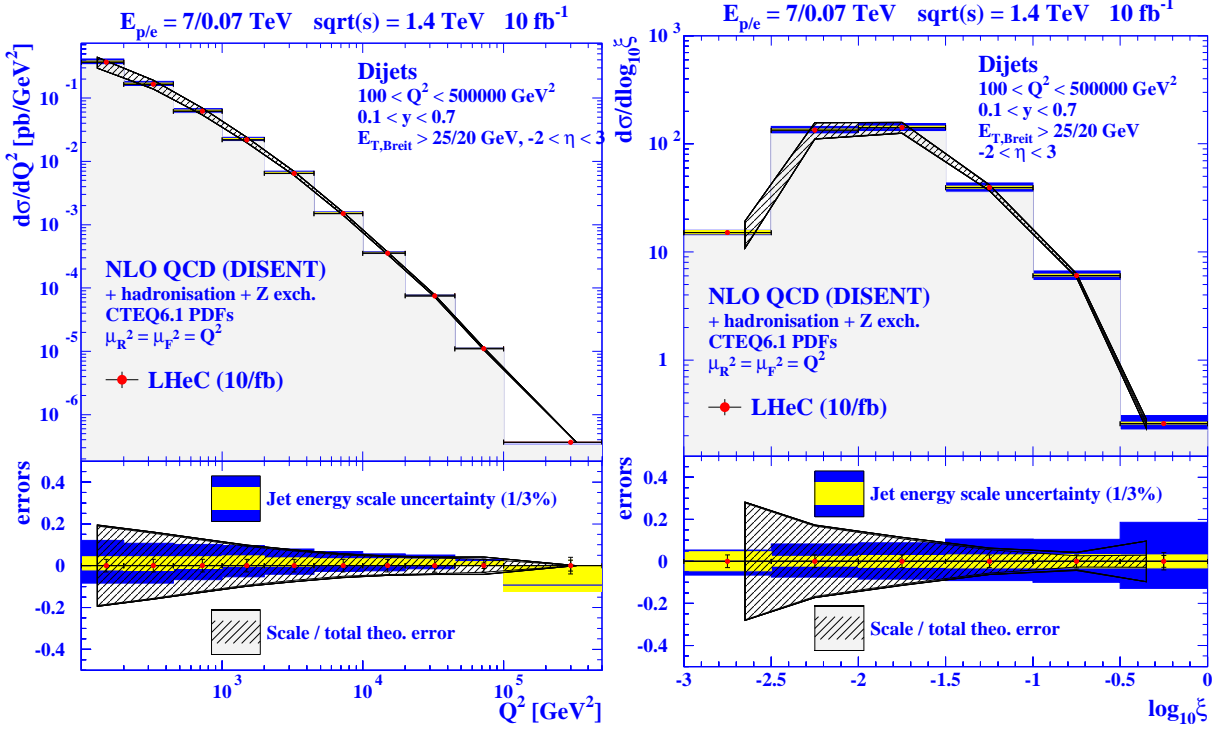


Figure 4.31: Predicted LHeC results for dijet production as function of  $Q^2$  and of  $\xi$ .

## 4.7.2 Jets in $\gamma A$

For photoproduction in  $eA$  collisions, jets provide an abundant yield of high-energy probes of the nuclear medium. The expected cross sections have been computed using the calculations in [150,151], for an electron beam of 50 GeV colliding with the LHC beams. For the nuclear case the same integrated luminosity ( $2 \text{ fb}^{-1}$ ) was assumed per nucleon as for  $ep$ . Only jets with  $E_{T,jet} > 20$  GeV are considered, and for the distribution in  $E_{T,jet}$  the pseudorapidity acceptance is  $|\eta_{jet}| < 3.1$ , corresponding to  $5^\circ < \theta_{jet} < 175^\circ$  in polar angle. The simulations use the Weizsäcker-Williams photon flux from the electron with the standard option in [150,151]. The chosen photon, proton and nuclear modified PDFs are taken from GRV-HO [152], CTEQ6.1M [146] and EPS09 [153], respectively - see Subsec. 5.1.4 for explanations on the nuclear modifications of PDFs. The renormalization and factorization scales are taken to be  $\mu_R = \mu_F = \sum_{jets} E_{T,jet}/2$  and the inclusive  $k_T$  jet algorithm [154] is used with  $D = 1$ . The statistical uncertainty in the computation (i.e. in the Monte Carlo integration) is smaller than 10 % for all results shown. This large statistical uncertainty is reached only for the largest  $E_{T,jet}$ , with much smaller uncertainties at lower values of  $E_T$ . No attempt has been made to estimate the uncertainties due to the choices of photons flux, photon or proton parton densities, scales or jet algorithms (see [155,156] for such considerations at HERA). The issues of background subtraction, experimental efficiencies in the jet reconstruction or energy calibration have also yet to be addressed. The only uncertainty studied thus far is that due to the nuclear parton densities, which is extracted in the EPS09 framework [153] using the Hessian method.

The results are shown in Fig. 4.32. One observes that yields of around  $10^3$  jets per GeV are expected with  $E_{T,jet} \sim 95$  (80) GeV in  $ep$  ( $ePb$ ), for  $|\eta_{jet}| < 3.1$  and the considered integrated luminosity of  $2 \text{ fb}^{-1}$  per nucleon. The effects of the nuclear modification of parton densities and their uncertainties are smaller than 10 %. The two-peak structure in the  $\eta_{jet}$ -plot results from the sum of the direct plus resolved contributions, each of which produce a single maximum, located in opposite hemispheres. Positive  $\eta_{jet}$  values are dominated by direct photon interactions, whereas negative  $\eta_{jet}$  values are dominated by contributions from resolved

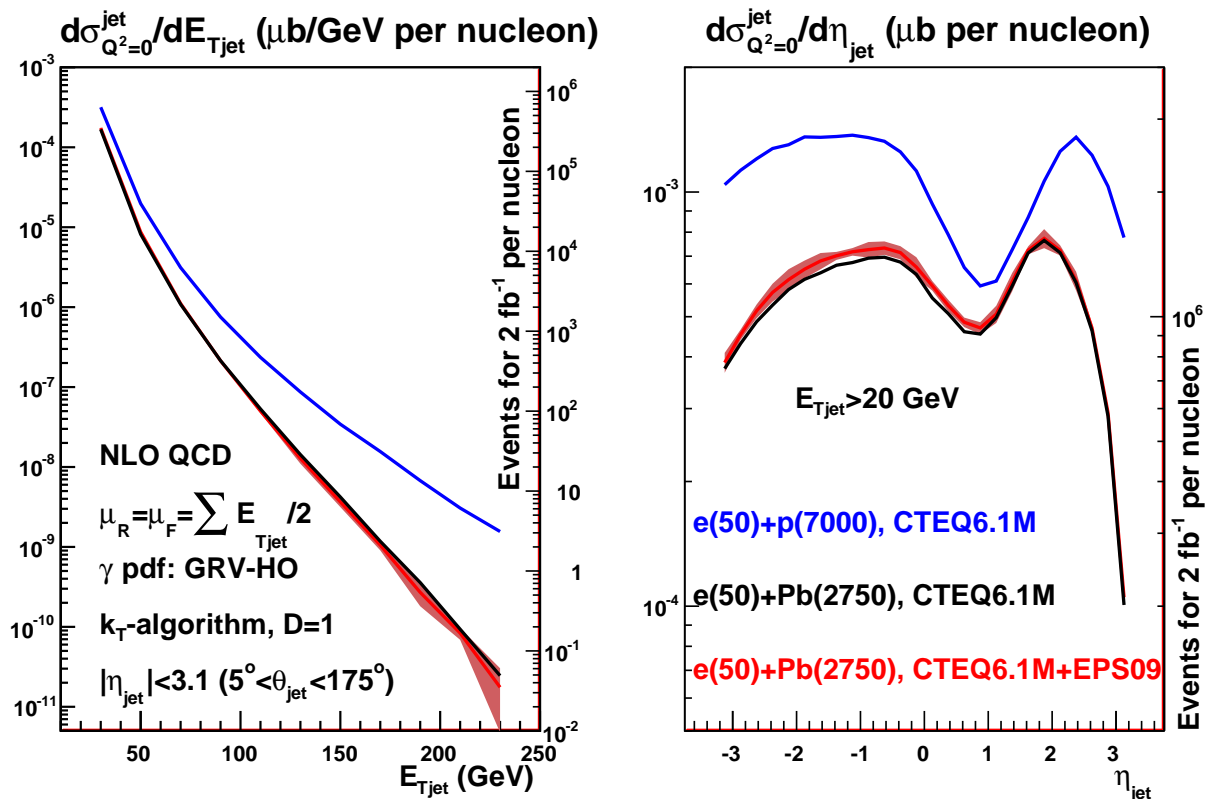


Figure 4.32: Predictions for the inclusive jet distribution in photoproduction, differential in  $E_{Tjet}$  (left) and  $\eta_{jet}$  (right) for  $e(50)+p(7000)$  (blue, top lines),  $e(50)+Pb(2750)$  without nuclear modification of the parton densities (black lines), and  $e(50)+Pb(2750)$  with EPS09 nuclear modification of the parton densities (red lines for the central value and bands for the uncertainty coming from the nuclear modification factors). See the text and the legends on the plots for further details of the calculations and kinematic cuts. In both plots, the axis on the left corresponds to the cross section in  $\mu\text{b}$ , while the axis on the right provides the number of jets expected for an integrated luminosity of  $2 \text{ fb}^{-1}$  per nucleon, per unit of  $E_{Tjet}$  ( $\eta_{jet}$ ) in the plot on the left (right).

1930 photons.

## 1931 4.8 Total photoproduction cross section

1932 Due to the  $1/Q^4$  propagator term, the LHeC  $ep$  cross section is dominated by very low  $Q^2$  quasi-real photons.  
 1933 With a knowledge of the effective photon flux [157], measurements in this kinematic region can be used to  
 1934 obtain real photoproduction ( $\gamma p$ ) cross sections. The real photon has a dual nature, sometimes interacting  
 1935 in a point-like manner and sometimes interacting through its effective partonic structure, resulting from  
 1936  $\gamma \rightarrow q\bar{q}$  and higher multiplicity splittings well in advance of the target [158, 159], the details of which are  
 1937 fundamental to the understanding of QCD evolution.

1938 The behaviour of the total photoproduction cross section at high energy is a topic of a major interest.  
 1939 It is now firmly established experimentally that all hadronic cross sections rise with centre of mass energy  
 1940 for large energies. The Froissart-Martin bound has been derived for hadronic probes. It therefore remains

1941 to be seen whether this bound is applicable to  $\gamma p$  scattering. For example in Refs. [160, 161] it has been  
 1942 argued that the bound for real photon-hadron interactions should be of a different functional form, namely  
 1943  $\ln^3 s$ . This would imply that the universality of the asymptotic behaviour of hadronic cross sections does  
 1944 not hold. Therefore the measurement of the total photoproduction cross section at high energies will bring  
 1945 an important insight into the problems of universality of hadronic cross sections, unitarity constraints, the  
 1946 role of diffraction and the interface between hard and soft physics.

1947 In Fig. 4.33, available data on the total cross section are shown [64, 162–164]<sup>6</sup>, together with a variety  
 1948 of models. More specifically, the dot-dashed black line labelled ‘FF model GRS’ is a minijet model [166],  
 1949 the yellow band labelled ‘Godbole et al.’ is an eikonized minijet model with soft gluon resummation [166]  
 1950 with the band defined by different choices of the parameters in the model, the red solid line labelled ‘Block  
 1951 & Halzen’ is based on a low energy parametrization of resonances joined with Finite Energy Sum Rules and  
 1952 asymptotic  $\ln^2 s$ -behaviour [167, 168], and the dashed blue line labelled ‘Aspen model’ is a QCD inspired  
 1953 model [169].

1954 The theoretical predictions diverge at energies beyond those constrained by HERA data, where cross  
 1955 sections were obtained by tagging and measuring the energies of electrons scattered through very small angles  
 1956 in dedicated calorimeters located well down the beampipe in the outgoing electron direction [162, 163]. As  
 1957 discussed in Chapter 14, the most promising location for similar small angle electron detectors at the LHeC  
 1958 is in the region around 62 m from the interaction point, which could be used to tag scattered electrons in  
 1959 events with  $Q^2 < 0.01 \text{ GeV}^2$  and  $y \sim 0.3$ . This naturally leads to measurements of the total photoproduction  
 1960 cross section at  $\gamma p$  center-of-mass energies  $W \sim 0.5\sqrt{s}$ . The measurements would be strongly limited by  
 1961 systematics. In the absence of a detailed simulation of an LHeC detector these uncertainties are hard to  
 1962 estimate. For the simulated data in Fig. 4.33, uncertainties of 7% have been assumed, matching the precision  
 1963 of the H1 and ZEUS data. This would clearly be more than adequate to distinguish between many of the  
 1964 available models. The HERA uncertainties were dominated by the invisible contributions from diffractive  
 1965 channels in which the diffractive masses were too small to leave visible traces in the main detector. If detector  
 1966 acceptances to  $1^\circ$  are achieved at the LHeC, better precision is expected to be possible.

## 1967 4.9 Electroweak physics

### 1968 4.9.1 The context

1969 Precision electroweak measurements at low energy have played a central role in establishing the Standard  
 1970 Model (SM) as the theory of fundamental interactions. More recently, measurements at LEP, SLD, and  
 1971 the Tevatron have confirmed the SM at the quantum level, verifying the existence of its higher-order loop  
 1972 contributions. The sensitivity of these contribution to virtual heavy particles has allowed for an estimate of  
 1973 the mass of the top quark prior to its actual discovery in 1995 by the CDF and DØ Collaborations. Now that  
 1974 the determination of the top mass at the Tevatron has become quite accurate, reaching the 1% level, and  
 1975  $M_W$  is known with an error of 23 MeV, electroweak precision measurements imply significant constraints on  
 1976 the mass of the last missing piece of the SM, the Higgs boson. The current situation has been analysed for  
 1977 instance in [170, 171] taking into account the results of direct searches for the Higgs boson at LEP-2 and the  
 1978 Tevatron, which currently exclude a SM Higgs boson with mass lower than 114 GeV or in a narrow window  
 1979 around 160 GeV. At 95% CL, if the SM is correct, the Higgs boson must soon be found with mass below  
 1980 155 GeV either at the Tevatron or at the LHC.

1981 Electroweak precision measurements are also very effective in constraining the possible extensions of  
 1982 the SM. In general, the observed good quality of the SM fit disfavors new physics at an energy scale of  
 1983  $O(100 \text{ GeV})$  that modifies the Higgs mechanism in a drastic way. On the other hand, the fit does present  
 1984 a few interesting deviations at the level of  $2\text{--}3\sigma$ . There is a significant tension between the FB asymmetry  
 1985 of  $Z \rightarrow b\bar{b}$  measured at LEP, which favors a heavy Higgs, and the LR asymmetry in  $Z \rightarrow \ell\bar{\ell}$  and the  $W$   
 1986 mass, which both favors a very light Higgs. Unfortunately, the present determination of  $M_H$  depends largely

<sup>6</sup>The recent results by ZEUS [165] refer only to the energy behavior of the cross section in the range  $194 < W < 296 \text{ GeV}$ , but do not provide absolute values.



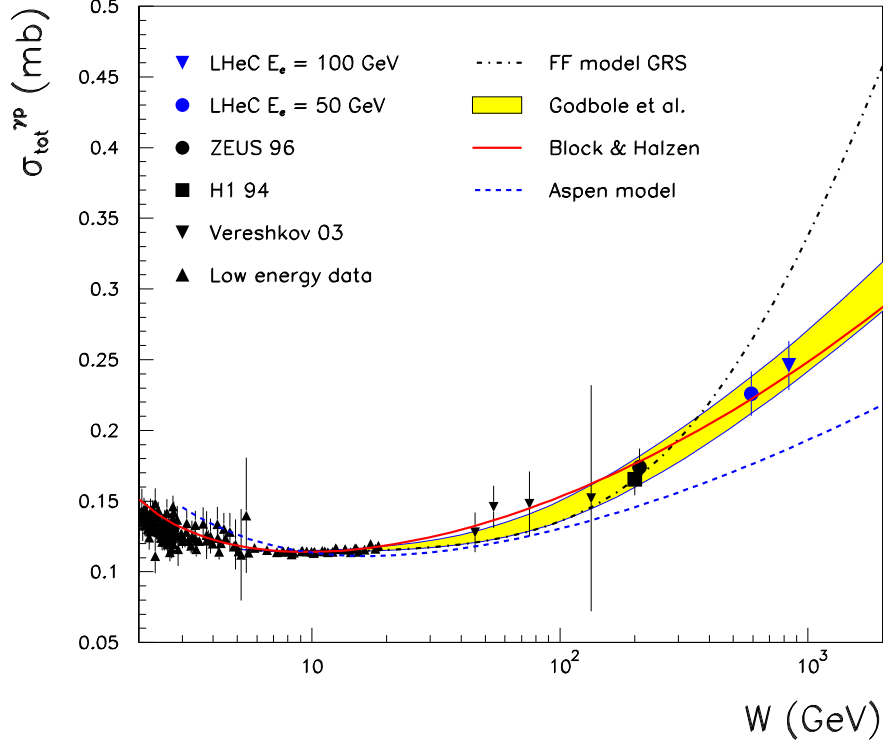


Figure 4.33: Simulated LHeC measurements of the total photoproduction cross section with  $E_e = 50$  GeV or  $E_e = 100$  GeV, compared with previous data and a variety of models (see text for details). This is derived from a similar figure in [166].

1987 on these conflicting information, whose origin could be either statistical or rooted in new physics around  
 1988 the corner [172]. Another plausible  $\sim 3\sigma$  hint of physics beyond the SM, without Higgs implications, is the  
 1989 discrepancy between the measured magnetic anomalous moment of the muon and its SM prediction [173].

1990 It is unlikely that operating experiments will change significantly the above picture of electroweak precision  
 1991 measurements. The Tevatron and LHC will marginally improve the current precision on the top mass  
 1992 and reach a combined 15 MeV uncertainty on  $M_W$ , while LHCb might be able to achieve an interesting accuracy  
 1993 in the measurement of  $\sin^2 \theta_W$  [174,175]. Two experiments at Jefferson Lab, Q-weak [176] and (later)  
 1994 MOLLER [177], will measure the weak mixing angle from parity violation in  $ep$  and  $e^-e^-$  scattering at low  
 1995 energy: these are interesting measurements complementary to the existing ones; MOLLER, in particular,  
 1996 may eventually reach an accuracy similar to that of LEP. It is widely expected that either the Higgs boson  
 1997 or further new physics will be discovered at the LHC, if not both. This is the context in which precision  
 1998 electroweak measurements at LHeC are set.

1999 The electroweak measurements possible at LHeC are of the kind performed at HERA (see [178,179] for  
 2000 an overview). However, they will greatly benefit from the higher energy and larger luminosity, as well as from  
 2001 highly polarized lepton beams, and therefore also include processes, as single standard model or anomalous  
 2002 top quark production, which were impossible to study in  $ep$  before.

2003 A first class of measurements involves polarized charged currents (CC) only. They include a verification  
 2004 of the left-handedness of CC from the polarization dependence of the CC cross-section. At HERA this has  
 2005 led to a bound on possible right-handed currents, expressed in terms of the mass of a right-handed  $W_R$  boson  
 2006 that couples to quarks with the same strength as the SM one. While the HERA result,  $M_{W_R} > 210$  GeV  
 2007 at 95% CL, can be significantly improved at the LHeC, low-energy flavour bounds and direct searches for  
 2008  $W$  type new bosons at the LHC are more sensitive. It yet is interesting to verify the universality of space-

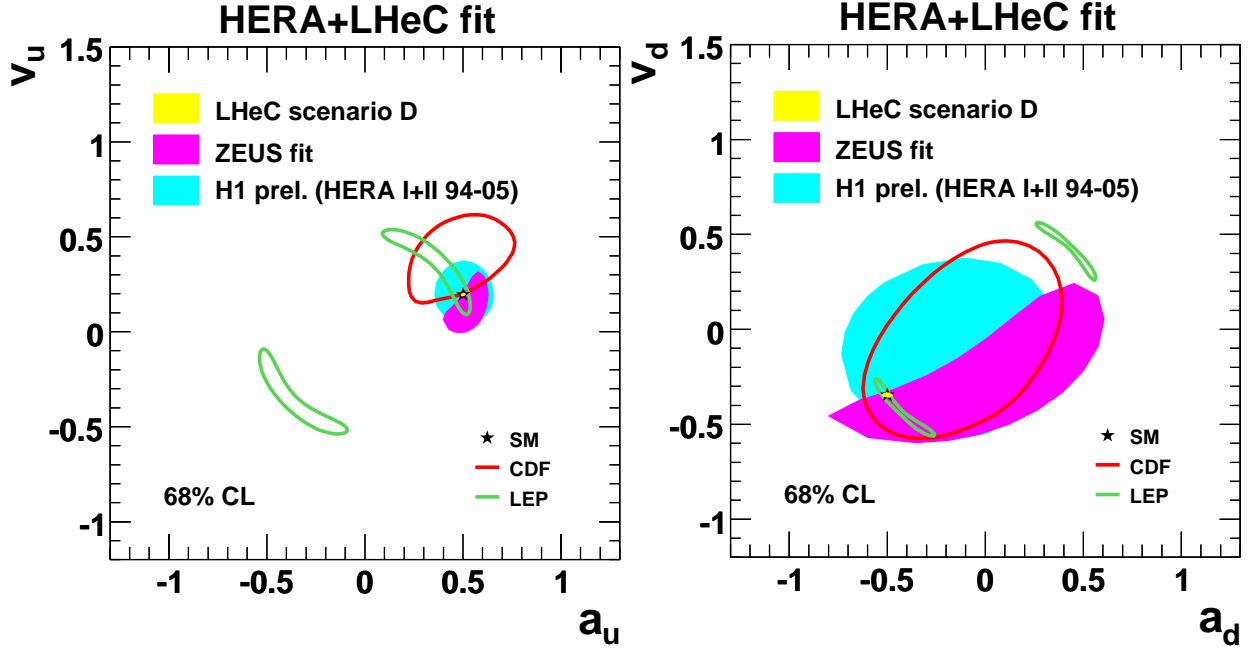


Figure 4.34: Determination of the vector and axial NC couplings of the light quarks at LEP, CDF, HERA and LHeC. - plot to be updated.

2009 and timelike interactions and thus to determine the propagator mass from the CC cross section through its  
 2010  $Q^2$  dependence,  $\propto (M_W^2/(M_W^2 + Q^2))^2 \phi(x, Q^2)$ . At the LHeC, the HERA  $W$  propagator mass uncertainty  
 2011 value may be improved by a factor of 10 to about 150 MeV.

#### 2012 4.9.2 Light Quark Weak Neutral Current Couplings

2013 The LHeC will be able to measure the neutral current couplings of the light quarks at unprecedented  
 2014 precision. As can be seen in Fig. 4.34, LEP has been able to constrain only an ambiguous combination of  
 2015 them as the couplings enter as squares in pure weak NC reactions.

2016 DIS experiments with polarized electron and positron beams can completely disentangle the vector and  
 2017 axial couplings of up and down type light quarks. As illustrated in Fig.4.34, the preliminary results by ZEUS  
 2018 and H1 have improved on the LEP determination in the case of the up quarks [179–181]. Very recent D0  
 2019 results, obtained from the  $Z/\gamma^*$  forward-backward asymmetry in the electron channel, somewhat improve on  
 2020 HERA constraints [182]. However, a simultaneous determination of the four light quark couplings, based on  
 2021 a luminosity of  $5 \text{ fb}^{-1}$  with D0, still gives uncertainties of order  $0.1 - 0.2$ , which are an order of magnitude  
 2022 less precise than the expected DIS result at the LHeC.

2023 The sensitivity of the LHeC to the light quark NC couplings has been studied with a QCD fit to the  
 2024 simulated data, in which the PDFs and the NC quark couplings are simultaneously determined. Here the  
 2025 electron couplings are fixed, as they are very precisely measured at LEP and SLD. The expected resolution  
 2026 for scenario D of LHeC is hardly visible on the scale of Fig. 4.34. A comparison among the various LHeC  
 2027 scenarios can be found in Fig. 4.35 The accuracy on the vector and axial vector couplings of the  $u$ ,  $d$  quarks  
 2028 ranges, in the best possible scenario, between 1 and 4%, with an improvement wrt HERA by a factor 10  
 2029 to 40. A better determination of the light quark NC couplings will particularly constrain New Physics  
 2030 models that modify significantly the light quark NC couplings, without affecting the well-measured lepton  
 2031 and heavy quark couplings. It is not easy to realize such an exotic scenario in a natural way, although  
 2032 family non-universal (leptophobic)  $Z'$  models (see for instance [183,184] and refs. therein), R-parity violating

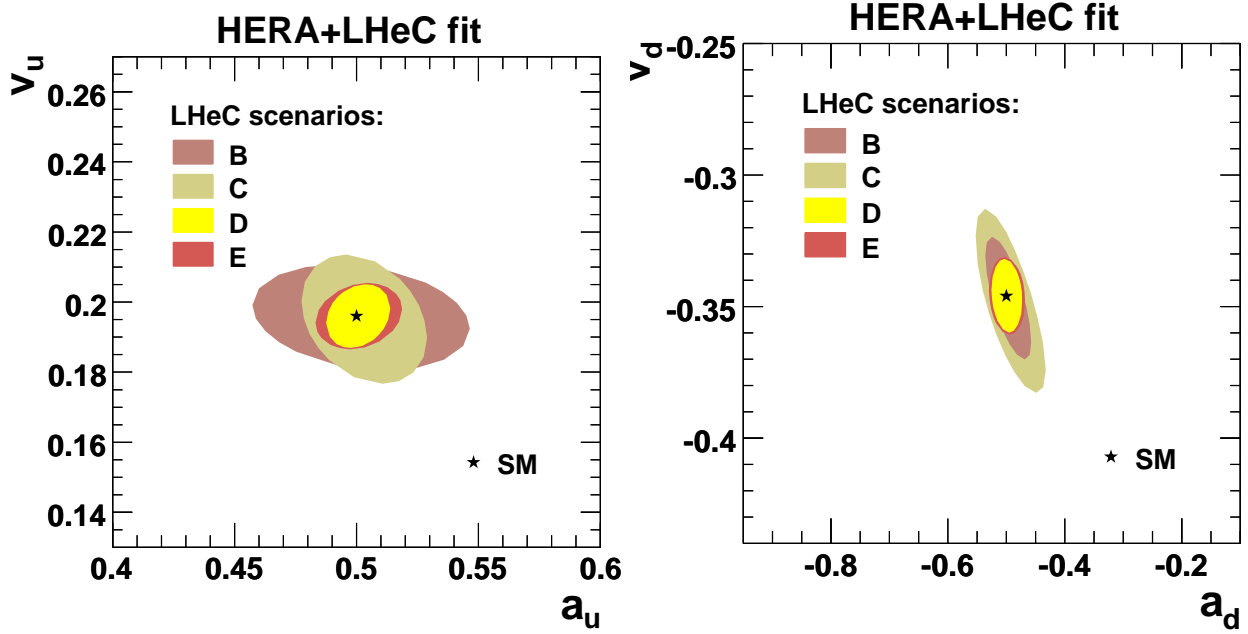


Figure 4.35: Determination of the vector and axial NC couplings of the light quarks at LHeC, comparison different scenarios.

2033 supersymmetry (see [185] for a review) and leptoquarks [186] can in principle succeed. LHeC could therefore  
 2034 accurately test a spectrum of interesting new physics models. A specific linear combination of the light quark  
 2035 NC vector couplings ( $v_u$  and  $v_d$ ) might be measured at the per cent level by the QWeak Collaboration [176].  
 2036 Their results, combined with existing precise measurements of Atomic Parity Violation and DIS, could  
 2037 provide a percent determination of  $v_u$  and  $v_d$  [187] and test the same kind of models, but it will not probe  
 2038 the axial quark couplings.

### 2039 4.9.3 Determination of the Weak Mixing Angle

#### 2040 Cross Section Asymmetries and Ratios

2041 The LHeC is a unique facility for electroweak physics because of the very high luminosity, high measurement  
 2042 precision and the extreme range of momentum transfer  $Q^2$ . Fig. 4.36 illustrates the reach and the size of  
 2043 the electroweak effects in NC scattering. Depending on the charge and polarisation of the electron beam,  
 2044 the contributions from  $\gamma Z$  interference and pure  $Z$  exchange become comparable to or even exceed the  
 2045 photon exchange contribution, i.e. of  $F_2$ , which has dominated hitherto all NC DIS measurements. With the  
 2046 availability of two charge and two polarisation states, of neutral and charged current measurements, proton  
 2047 and isoscalar targets, a unique menu becomes available for testing the electroweak theory. For example,  
 2048 one can very precisely measure light quark weak neutral current couplings, discussed above. One can also  
 2049 test the universality of  $\gamma - g$  and  $Z - g$  fusion by extracting the heavy quark ( $c$ ,  $b$ ) contributions from  $\gamma Z$   
 2050 interference. A remarkable measurement illustrated in the following regards the energy dependence of the  
 2051 weak mixing angle  $\sin^2 \Theta$ .

2052 Tests of the electroweak theory in DIS require to simultaneously control the parton distribution effects.  
 2053 With the outstanding data base from the LHeC, joint QCD and electroweak fits become possible to high  
 2054 orders perturbation theory. Cross section asymmetries and ratios can also be used to determine electroweak  
 2055 parameters. Particularly useful examples are polarisation and charge asymmetries and also NC to CC cross  
 2056 section ratios.

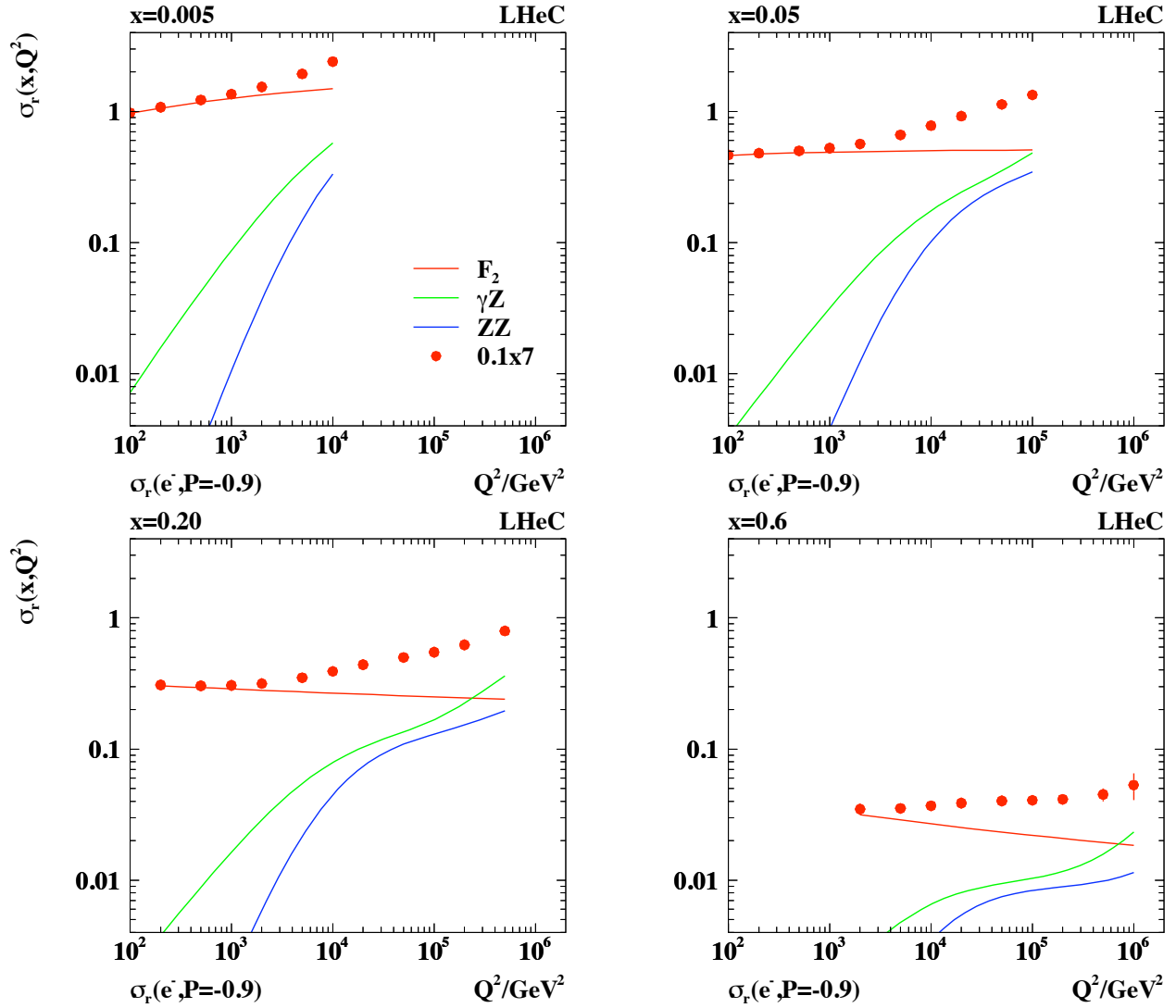


Figure 4.36: Simulated measurement of the neutral current DIS cross section (closed points) with statistical errors for  $10 \text{ fb}^{-1}$  shown as a function of  $Q^2$  for different values of Bjorken  $x$ . The different curves represent the contributions of pure photon exchange (red),  $\gamma Z$  interference (green) and pure  $Z$  exchange (blue) as prescribed in Eq. 4.5. Note the high precision of the reduced cross section measurement up to large  $x$  and  $Q^2$ .

2057

In NC scattering, the polarisation asymmetry

$$A^\pm = \frac{1}{P_R - P_L} \cdot \frac{\sigma_{NC}^\pm(P_R) - \sigma_{NC}^\pm(P_L)}{\sigma_{NC}^\pm(P_R) + \sigma_{NC}^\pm(P_L)} \quad (4.31)$$

2058

served for the decisive confirmation of the left handed weak neutral current doublet structure as was predicted by the GWS theory in 1979 [188]. The size of the electroweak asymmetries is given by the relative amount of  $Z$  to photon exchange  $O(10^{-4}Q^2/\text{GeV}^2)$ , i.e. it becomes of order 1 at high  $Q^2$  at the LHeC.

2060

To a good approximation the asymmetry measures the structure function ratio

$$A^\pm \simeq \mp \kappa_Z a_e \frac{F_2^{\gamma Z}}{(F_2 + \kappa_Z a_e Y_- x F_3^{\gamma Z} / Y_+)} \simeq \mp \kappa_Z a_e \frac{F_2^{\gamma Z}}{F_2}. \quad (4.32)$$

2062

Thus  $A^+$  is expected to be about equal to  $-A^-$  and to be only weakly dependent on the parton distributions. The product of the axial coupling of the electron and the vector coupling of the quarks, inherent in  $F_2^{\gamma Z}$ , determines the polarisation asymmetry to be parity violating. A measurement of  $A^\pm$  provides a unique and precise measurement of the scale dependence of the weak mixing angle, as is discussed below (Sect. 4.9.3). At large  $x$  the polarisation asymmetry provides an NC measurement of the  $d/u$  ratio of the valence quark distributions, according to

2063

2064

2065

2066

2067

$$A^\pm \simeq \pm \kappa \frac{1 + d_v/u_v}{4 + d_v/u_v}. \quad (4.33)$$

2068

Further asymmetries of NC cross sections have been discussed in [58].

2069

The neutral-to-charged current cross-section ratio

$$R^\pm = \frac{\sigma_{NC}^\pm}{\sigma_{CC}^\pm} = \frac{2}{(1 \pm P)\kappa_W^2} \cdot \frac{\sigma_{r,NC}^\pm}{\sigma_{r,CC}^\pm} \quad (4.34)$$

2070

is of interest for electroweak physics too as will be demonstrated below. At very high  $Q^2 \gg M_Z^2$  and neglecting terms in the NC part proportional to  $v_e$  it becomes approximately equal to

2071

$$R^\pm \simeq \frac{2a_e^2}{(1 \pm P)\cos^2\theta} \cdot \frac{Y_+ F_2^Z - Y_- P x F_3^Z}{Y_+ W_2^\pm + Y_- x W_3^\pm} \quad (4.35)$$

2072

which reveals the striking similarity of the neutral and charged weak interactions at high energies. One may further consider, for example, a quantity which is the  $eN$  analogon to the Paschos-Wolfenstein relation [189] in  $\nu N$  scattering

2073

2074

$$A_{NCC} = \frac{\sigma_{NC}^+ - \sigma_{NC}^-}{\sigma_{CC}^+ - \sigma_{CC}^-}. \quad (4.36)$$

2075

The very high luminosity and  $Q^2$  range of the LHeC as compared even to HERA will open a completely new era of electroweak physics in DIS.

2076

## 2077 Measurement of the Weak Mixing Angle

2078

Further tests of the SM at the quantum level and indirect searches for new physics require ultimate precision. Such corrections occur in the factor  $1 - \Delta r$ , see Eq. 4.14, which depends on the top mass, logarithmically on the Higgs mass and possibly on new, heavy particles. A measurement of the weak mixing angle,  $\sin^2\theta$ , to 0.01% precision should fix the Higgs mass to 5% accuracy. The so far most precise measurements of  $\sin^2\theta$  have been performed at the  $Z$  pole in  $e^+e^-$  scattering, using the very high statistics, at LEP, and in the case of the SLC, the large beam polarisation of 75% too. The LHeC has the potential to measure weak asymmetries and cross section ratios at, below and beyond the  $M_Z$  scale by precisely measuring their dependence on  $\sqrt{Q^2}$ .

2085

2086 The accuracy estimated for  $\sin^2 \theta$  depends on its definition. The electroweak theory has three independent  
 2087 parameters. For the subsequent study, as in a similar study of H1 [180], the values of  $\alpha$  and  $M_Z$  are fixed,  
 2088 which are best known,  $M_Z$  to 0.002 %. For the estimate of the sensitivity to electroweak effects as the third  
 2089 parameter here  $\sin^2 \theta$  is chosen, which is used, together with  $\alpha$  and  $M_Z$  to calculate  $G$  and  $M_W$  and also  
 2090 occurs in the weak neutral current couplings <sup>7</sup>. This way both the NC and the CC cross sections are sensitive  
 2091 to  $\sin^2 \theta$ . Equivalently one could have expressed all parameters using  $\alpha$ ,  $M_Z$  and  $M_W$ , and determine  $M_W$ .  
 2092 Due to the relation  $\sin^2 \theta = 1 - M_W^2/M_Z^2$ , the error of such an indirect measurement of  $M_W$  is

$$\Delta M_W = \frac{M_W \delta \sin^2 \theta}{2 \sin^2 \theta}, \quad (4.37)$$

2093 i.e. a one permille accuracy on  $\sin^2 \theta$  corresponds to  $\Delta M_W = 40$  MeV.

2094 A simulation is done of the NC and CC cross sections depending on the lepton beam charges and  
 2095 polarisations based on the formulae presented above. This allows to build a variety of asymmetries and  
 2096 cross section ratios and derive their sensitivity to the weak mixing angle. An example is illustrated in  
 2097 Fig. 4.37. Here the polarisation asymmetry (left) and the NC/CC ratio (right) are calculated for different  
 2098 values of  $\sin^2 \Theta$  using two recent sets of leading order parton distributions, CTEQ6LL and MSTW08. The  
 2099 measurement accuracy of  $\sin^2 \Theta$  has a statistical, a polarisation, a systematic and a pdf uncertainty. One  
 2100 derives that the statistical precision is about 0.1 % for the NC asymmetry  $A^-$  and even 0.05 % for the NC/CC  
 2101 ratio  $R^-$  for  $e^-p$  scattering with an assumed polarisation of  $-0.8$  and a luminosity of  $10 \text{ fb}^{-1}$  for default  
 2102 beam energies.

2103 At this early stage of consideration one may not present a full error study. However, a few first con-  
 2104 siderations are in order: The high luminosity and large  $Q^2$  range move the electroweak physics at this  $ep$   
 2105 machine to the level of highest accuracy demands. Most of the systematic errors cancel in asymmetry and  
 2106 ratio measurements. A 0.1 % electron energy scale uncertainty, as has been achieved with H1, for example,  
 2107 translates at the LHeC to a 0.15 % change of  $A^-$  and a negligible change of  $R^-$ . This measurement samples  
 2108 data in a region of very high cross section accuracy and can exclude the highest  $x$  region where uncertainties  
 2109 grow like  $1/(1-x)$ . The desired level of polarisation measurement is obviously about a permille, which seems  
 2110 to be possible as is discussed in the detector chapter.

2111 The requirements for  $A^-$  and  $R^-$  are different. The asymmetry  $A^-$  requires frequent changes of the  
 2112 polarisation to control the time dependence of the measurement. It measures essentially a ratio of the  
 2113 structure functions  $F_2^{\gamma Z}/F_2$  and therefore it is rather insensitive to uncertainties related to the parton  
 2114 distributions. In fact, one observes in Fig. 4.37 that the predictions of the two PDF sets considered differ  
 2115 by less than the statistical uncertainty for  $A^-$ . The NC/CC ratio  $R$  is less sensitive to time drifts as the  
 2116 NC and CC data are taken simultaneously. Its statistical power is highest, as had already been noticed for  
 2117 HERA [190]. It yet is sensitive to the PDFs. For the two sets of PDFs considered here, an about two per cent  
 2118 difference is calculated of the  $R^-$  ratios. This would spoil the extraction of  $\sin^2 \Theta$ . The high sensitivity of  $R$   
 2119 to the mixing angle can only be employed when the PDFs are much better known than so far. This, however,  
 2120 is one of the major goals of the LHeC physics programme and large improvements are to be expected as  
 2121 is discussed in Sec. 4.2. The potential of measuring  $\sin^2 \Theta$  from NC/CC ratios is observed to be particular  
 2122 striking. However, for the evaluation of the scale dependence of  $\sin^2 \Theta$  below, the results derived from  $A^-$   
 2123 are used due to its much smaller PDF sensitivity.

2124 The mixing angle, similar to  $\alpha_s$ , is predicted to vary strongly as a function of the scale  $\mu$ , which in DIS  
 2125 is precisely known and given as  $\sqrt{Q^2}$ . This dependence results from higher order loop effects as calculated  
 2126 in [191]. Precise measurements to per mille uncertainty were performed at the  $Z$  pole by SLC and LEP  
 2127 experiments. Recent low energy experiments have provided measurements of  $\sin^2 \Theta$  at very low  $Q^2$  as from  
 2128 the parity violation asymmetry due to polarisation conjugation in Moeller scattering at  $Q^2 = 0.026 \text{ GeV}^2$   
 2129 by the E158 experiment. At scale values of about  $5 \text{ GeV}$  the NuTeV Collaboration has determined the  
 2130 mixing angle which for some time created a substantial experimental and theoretical effort when it appeared

<sup>7</sup>An interesting test is also to fix  $\alpha$ ,  $M_Z$  and  $G$  and to determine derived electroweak parameters as  $M_W$  or  $\sin^2 \Theta$  for precision consistency checks in the search for deviations from the SM. Such a study has not been undertaken so far for the LHeC.

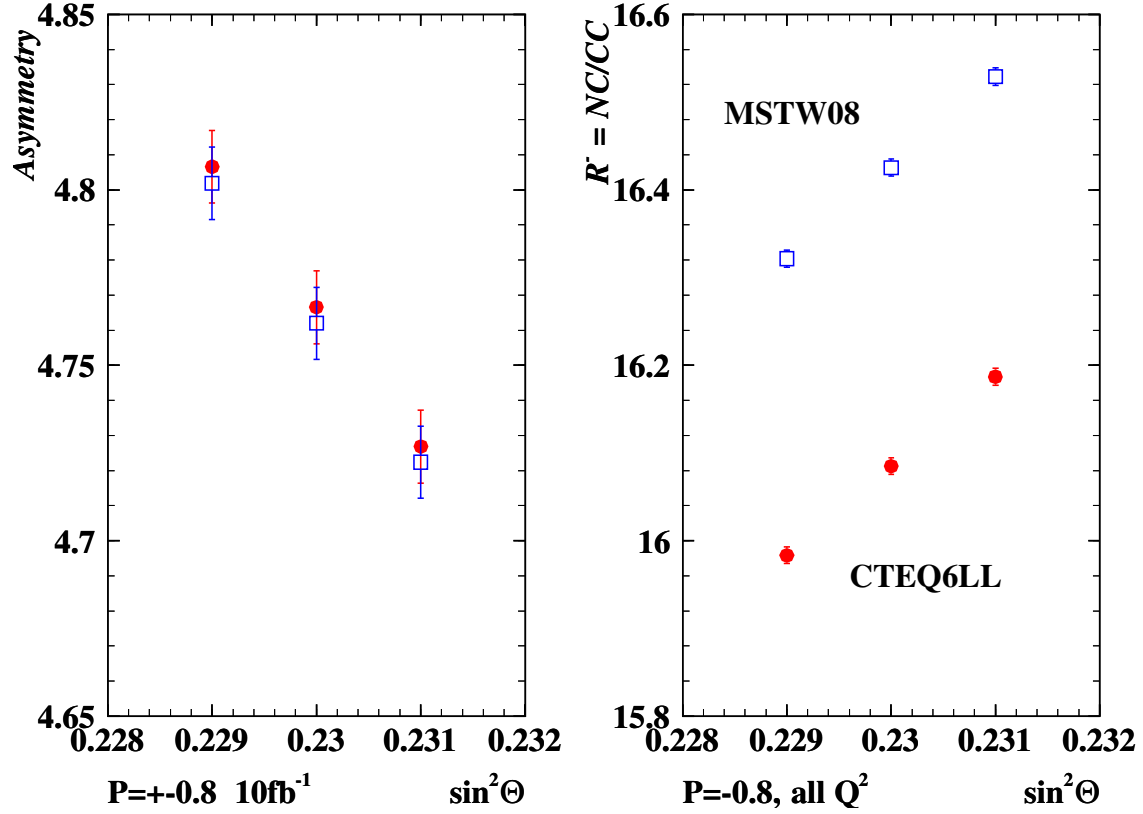


Figure 4.37: Simulated measurement of the polarisation NC cross section asymmetry  $A^-$  (left), in per cent for  $P = \pm 0.8$ , and the ratio of neutral-to-charged current cross sections,  $R = NC/CC$  (right), for  $P = -0.8$ , for different values of  $\sin^2 \theta$ . The errors are statistical for luminosities of  $10 \text{ fb}^{-1}$  per beam for polarised electron scattering for  $E_e = 60 \text{ GeV}$  and the nominal  $7 \text{ TeV}$  proton beam. The closed (open) symbols show the simulation for the CTEQ6LL (MSTW08) leading order parameterisations of the parton distributions. The average  $Q^2$  is  $1300 \text{ GeV}^2$  for the NC asymmetry  $A^-$ , while for the ratio  $R$  the average CC  $Q^2$  is about  $9500 \text{ GeV}^2$ . Consequently, the mean  $x$  in NC and CC differs by a factor of 6, which is at the origin of the large differences in  $R$  between the two PDF set predictions.

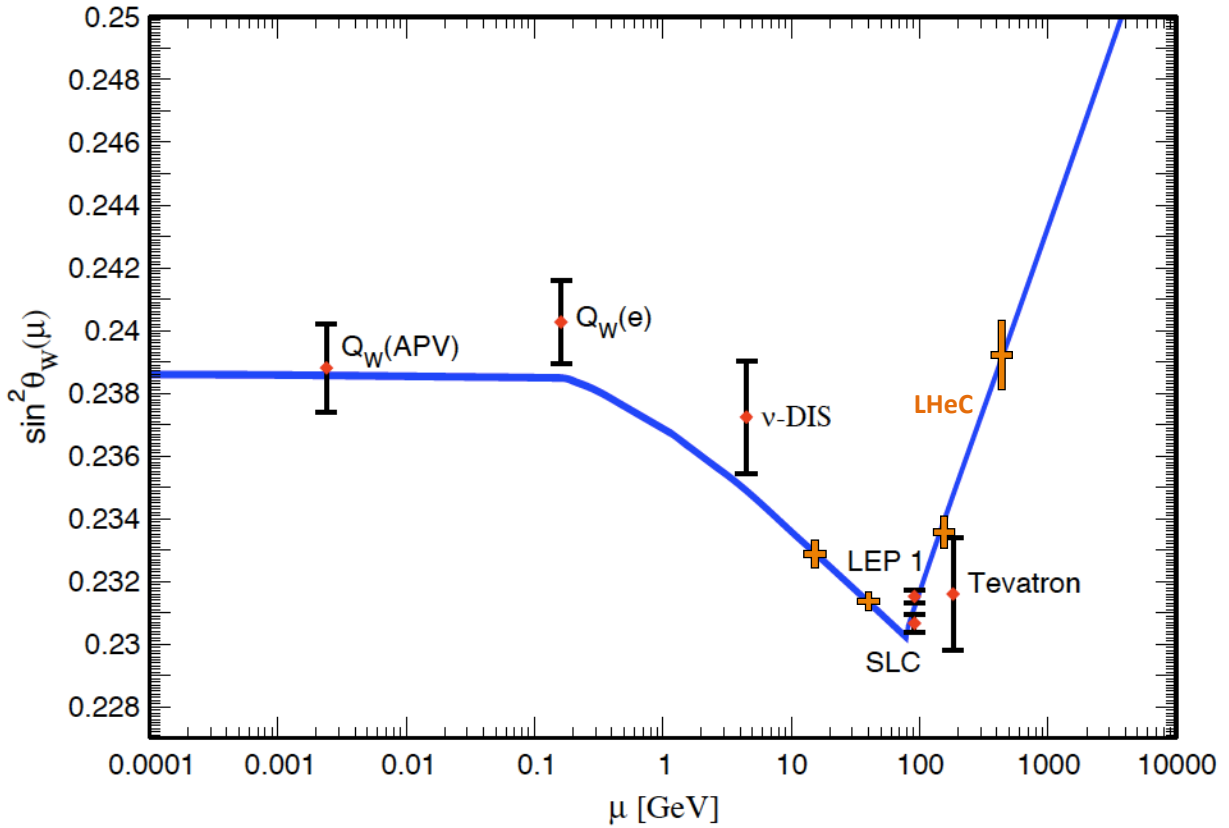


Figure 4.38: Dependence of the weak mixing angle on the energy scale  $\mu$ , taken from [64]. Four simulated points have been added based on the estimated measurement accuracy using the polarisation asymmetry  $A^-$  binned in intervals of  $\sqrt{Q^2}$ , see text.



Type	$Q_1$	$P_1$	$Q_2$	$P_2$	$\delta s(A_{12})$	$\delta s(R_1)$	$\delta s(R_2)$
$e^-$ Polarisation Conjugation	-1.	-0.8	-1.	0.8	0.00026	0.00009	0.00024
$e^+$ Polarisation Conjugation	+1.	-0.8	+1.	0.8	0.00027	0.00040	0.00015
$e^-$ Low P Conjugation	-1.	-0.4	-1.	0.4	0.00052	0.00010	0.00015
Charge Conjugation $P=0$	+1.	0.	-1.	0.	0.01600	0.00019	0.00012
Charge Conjugation $P=\mp 0.8$	+1.	-0.8	-1.	0.8	—	0.00040	0.00024
Charge Conjugation $P=\pm 0.8$	+1.	+0.8	-1.	-0.8	0.00790	0.00015	0.00009
$e^-$ PC Low $Q^2 \sim 300 \text{ GeV}^2$	-1.	-0.8	-1.	0.8	0.00068	0.00029	0.00083
$e^-$ PC Med $Q^2 \sim 1500 \text{ GeV}^2$	-1.	-0.8	-1.	0.8	0.00027	0.00012	0.00029
$e^-$ PC High $Q^2 \sim 22000 \text{ GeV}^2$	-1.	-0.8	-1.	0.8	0.00044	0.00071	0.00055
$e^-$ PC vHigh $Q^2 \sim 130000 \text{ GeV}^2$	-1.	-0.8	-1.	0.8	0.00170	0.00460	0.00200

Table 4.6: Estimated accuracies of the weak mixing angle,  $\delta \sin^2 \Theta$  from simulated measurements of the NC asymmetry and the NC/CC cross section ratio for different beam charge and polarisation conditions.

2131 to be above the theoretical expectation by a few standard deviations. Explanations of this “anomaly”  
2132 included variations of the strange quark density, effects from QED or nuclear corrections. An ultraprecise  
2133 measurement of  $\sin^2 \Theta$  is envisaged, yet still at  $\mu = M_Z$ , if a new  $Z_0$  factory was built.

2134 The current measurements are summarised in Fig.4.38. The plot also contains projected  $\sin^2 \Theta$  uncer-  
2135 tainty values from the LHeC, as listed in Table4.6, which result from simulations of the parity violation  
2136 asymmetry  $A^-$  in polarised  $e^-p$  scattering, for scales between about 10 and 400 GeV. Due to the high statis-  
2137 tics nature of the DIS NC process, the variation of  $\sin^2 \Theta$  as a function of  $\sqrt{Q^2}$  can be measured for a large  
2138 range of  $\sqrt{Q^2}$ . At low scales the range limited by the sensitivity to the  $Z$  exchange effects and at high scales  
2139 by the kinematic limit and luminosity. It may deserve a study to understand to how low values of  $Q^2$  the  
2140 asymmetry  $A^-$  can be determined in a meaningful measurement, which is related to time drifts, polarisation  
2141 flip times etc. and likely can only be answered with real data. It is to be noted that previous and planned  
2142 fixed target experiments measure this asymmetry at extremely small values of  $Q^2$  as compared to the range  
2143 of the LHeC.

2144 From the range considered here, with  $Q^2 > 300 \text{ GeV}^2$ , it can be concluded, see Fig.4.38, that the expected  
2145 measurement accuracy would lead to a decisive test of the scale dependence of  $\sin^2 \Theta$ .

## Chapter 5

# Physics at High Parton Densities

In Chapter 4, the opportunities offered by the LHeC to perform precision QCD studies were discussed in detail. Such studies have been done, until now, within the framework of standard, fixed-order perturbation theory and collinear factorization, which is valid when momentum scales are sufficiently hard and when the hadron can be described as a dilute set of partons. On the other hand, the parton densities extracted from HERA data exhibit a strong rise towards low  $x$  at fixed  $Q^2$ , indicating that the proton becomes increasingly densely packed. There are also compelling theoretical reasons to believe that collinear factorization should break down with increasing energies and sizes of the hadron. The low  $x$  regime of proton structure thus represents an exciting and largely unexplored territory whose dynamics are those of a densely packed partonic system. From very general considerations, it is clear that the increasing parton densities cannot continue undamped throughout the region of LHeC sensitivity. Non-linear evolution must eventually become relevant and the parton densities must ‘saturate’. The LHeC offers the unique possibility of observing these highly non-perturbative dynamics at sufficiently large  $Q^2$  values for weak coupling methods to be applied, suggesting the exciting possibility of a parton-level understanding of the collective properties of QCD. In this chapter we explore these possibilities in detail, addressing possible methods by which LHeC data might be used to establish the existence of this new high parton density regime of QCD and to explore its properties.

### 5.1 Physics at small $x$

#### 5.1.1 High energy and density regime of QCD

##### Introduction

Quantum Chromodynamics [31] is the fundamental theory of strong interactions that has been extensively tested in the last 39 years. Still, many open questions remain to be solved. One of them, which can be addressed at high energies, is the transition between the regimes in which the strong coupling constant is either large or small - the so-called *strong* and *weak coupling* regimes. In the former, standard perturbation theory techniques are not applicable and exact analytical results are not yet within the reach of current knowledge. Therefore various models, *effective* theories, whose parameters cannot yet be derived from QCD, or numerical lattice computations, have to be employed. One example of such an effective theory which has been used through the years and actually predates QCD, is the Regge-Gribov [286–288] theory.

The weak coupling regime has been well tested in high-energy experiments through a selected class of measurements - often referred to as *hard processes* - where weak and strong coupling effects can be cleanly separated. There exists a well-defined theoretical concept which has been derived from first principles and probed in the weak coupling regime, namely the collinear factorization theorem (for a comprehensive review see [289] and references therein). It allows a separation of the cross sections involving hadrons into: (i) parts that can be computed within perturbation theory, corresponding to the cross section for parton scattering, and (ii) pieces which cannot be calculated using weak coupling techniques, but whose evolution

with momentum scales is still perturbative. The latter are universal, process-independent distributions that either characterize the partonic content of the hadron - *parton densities* on which we will mainly focus the discussion - or the eventual projection of partons onto hadrons. Together with their corresponding (DGLAP) linear evolution equations [33,35,290], they have been used to describe experimental data to a high accuracy. Examples include total DIS cross sections, the production of jets with large transverse momenta and final states with heavy quarks, see the analysis and discussion in Chapter 4.

In recent years high-energy experiments have become sensitive to kinematic regions in which the coupling is small but the factorization assumption may no longer be valid. We will refer to this region as the high parton density domain, or simply the dense regime. As an example, several HERA DIS measurements at small longitudinal momentum fractions  $x$ , where parton densities are large, indicate deviations from the behavior expected within the standard collinear factorization. Similarly, hadronic or nuclear collisions involving partons with small values of  $x$  may also show such deviations. At the same time, cross sections grow rapidly with decreasing  $x$ , so contributions from these regions dominate hadronic cross sections in sufficiently high-energy scattering. Experiments sensitive to this kinematic region thus provide a way to test QCD in the new regime where the parton densities become very large and highly novel effects are expected. As has historically always been the case for the exploration of parton densities, the most promising approach is lepton-nucleon scattering, exploiting the point-like, non-strongly interacting nature of the lepton probe to take ‘snapshots’ of the hadronic structure with deeply sub-femtoscopic resolution.

From a theoretical viewpoint, this situation offers both opportunities and challenges. The fact that, at small- $x$ , there is no abrupt transition between the dilute and dense regimes, allows the use of techniques which, while still being weak coupling, go beyond those employed in the dilute limit. The usual parton multiplication processes have to be supplemented by processes in which partons recombine - thus adding non-linear terms to the evolution equations [291]. There are deep theoretical questions arising in this new dense partonic regime of QCD. At high energies the scattering amplitudes are close to the unitarity limit. Unitarity is violated when the linear regime is extrapolated to very high energies, so the dynamics of QCD beyond the linear dilute regime has to be such that unitarity is fulfilled. The generic expectations are that the dynamical mechanism responsible for the fulfillment of unitarity is that accountable for the taming of parton densities due to recombination effects - this phenomenon is generically referred to as parton *saturation*. Theoretical calculations [292–295] in the limit of high energies support these expectations. Furthermore, the experimental exploration of this transition region where the standard perturbative description based on collinear factorization and linear evolution equations requires large corrections, provides new possibilities of further understanding the strong coupling regime.

Deep inelastic lepton-hadron scattering has already been shown to address these questions in the most efficient manner. It provides the cleanest way of measuring the parton densities, including the small- $x$  region in which the transition between the dilute and dense regimes of QCD should occur within the weak coupling region where calculations can be done. Approaching this transition region from the dilute side by decreasing  $x$  or by increasing the number of nucleons in the target, one should observe features which cannot be understood within the framework of linear QCD evolution equations but, using more elaborate tools (non-linear evolution equations) can still be analyzed in terms of weak coupling techniques. Within the standard framework of the leading-twist linear QCD evolution equations (DGLAP) the parton densities are predicted to rise at small  $x$ , and this rise has been seen very clearly at HERA. This rise should eventually be tamed by the novel, nonlinear effects leading to parton saturation. In hadron-hadron scattering it is a unitarity bound that limits the growth of the total cross sections as a function of energy. As a result, according to Froissart and Martin [296, 297], total cross sections are bounded according to

$$\sigma_{\text{tot}} \leq \text{const.} \ln^2 s/s_0, \quad (5.1)$$

where  $s_0$  is a typical hadronic scale, and the dimensionful coefficient ‘const.’ is governed by the range of the strong interaction. This bound comes from two fundamental assumptions. The first is that the amplitude for the scattering at fixed value of impact parameter<sup>1</sup> is bounded by unity and the second is the finite range of the

---

<sup>1</sup>The impact parameter in a scattering process between two collinear particles is the perpendicular distance between the centres of the particles.

strong interaction. The bound on the amplitude has a simple physical interpretation in terms of a situation where the probability for the interaction becomes very high, so the target (or more precisely the interaction region) becomes completely absorptive. This situation is usually referred to as a *black disk* regime. The description of this regime is very challenging theoretically and it is expected that new phenomena will occur which are direct manifestations of a new state of QCD which is characterized by a high parton density [?, 56]. The LHeC will uniquely offer the possibility of exploring the transition towards this new state of dense QCD matter, as it can pursue a two-pronged approach: high center-of-mass energy, extending the kinematic range to lower  $x$ , and the possibility of deep inelastic scattering off heavy nuclei.

In the rest of this introductory section, we will present different approaches that are currently under discussion to describe the high-energy regime of QCD. We will recall the ideas that lead from linear evolution equations to non-linear ones. On the former, we will discuss both cases in which the evolution equations are computed within fixed-order perturbation theory (the DGLAP evolution equations) and where they include some kind of resummation - thus going beyond any fixed order in the perturbative expansion in the QCD coupling constant. The most famous example is the Balitsky-Fadin-Kuraev-Lipatov (BFKL) equation [298, 299]. Concerning the latter, non-linear evolution leads to the phenomenon of saturation of partonic densities in the hadron or nucleus. We will briefly review the realizations of saturation of parton densities both at strong coupling and, mainly, at weak coupling. We will end by discussing the importance of diffractive observables and of the use of nuclear targets for the investigation of the small- $x$  behavior of the hadron or nucleus wave function.

## Beyond DGLAP evolution

In DIS the structure function  $F_2(x, Q^2)$  is proportional to the total cross section  $\sigma_{\text{tot}}$  for the scattering of a virtual photon on a hadron  $h$ ,  $\gamma^* h \rightarrow X$ . The growth of  $F_2$  at small  $x$  translates into the rise of  $\sigma_{\text{tot}}$  as a function of the energy of the virtual photon-hadron system. Although the Froissart-Martin bound, derived for hadron-hadron scattering, cannot be applied to a process involving a virtual photon, direct calculations based on the evaluation of the QCD diagrams demonstrate unambiguously that, at small  $x$ , large corrections exist and need to be resummed. These corrections suppress the leading-twist results and there is no doubt that, for  $F_2$ , the rise with  $1/x$  predicted by DGLAP is modified by contributions which are not included in the framework of leading-twist linear evolution equations. The corrections which become numerically important in the small- $x$  limit are also important for the restoration of the unitarity bound, as mentioned previously. As a result of these modifications parton saturation is reached for sufficiently large energies or small values of Bjorken- $x$ .

In deep inelastic electron-proton scattering, the virtual photon emitted by the incoming electron interacts with partons inside the proton whose properties are specified by the kinematics of the photon. In particular, the effective transverse size of the partons is (roughly) inversely proportional to the square root of the virtuality of the photon,  $\langle r_T^2 \rangle \sim 1/Q^2$ . The deep inelastic cross section, parametrized through parton densities, thus *counts* the numbers of quarks and gluons per unit of phase space. For sufficiently large photon virtualities  $Q^2$  and not too small  $x$ , the improved QCD parton model works well because the partons forming the hadron, on the distance scale defined by the small photon, are in a dilute regime, and they interact only weakly. This is a direct consequence of the property of asymptotic freedom, which makes the strong coupling constant small. This diluteness condition is not satisfied if the density of partons increases. This happens if either the number of partons increases (large structure function) or the interaction between the partons becomes strong (large  $\alpha_s$ ). The former situation is realized at small  $x$ , the latter for small photon virtuality  $Q^2$  which sets the scale of the strong coupling  $\alpha_s(Q^2)$ . This simple qualitative argument shows that corrections to the standard QCD parton picture can be described in terms of quarks and gluons and their interactions as long as  $Q^2$  is not too small ( $\alpha_s(Q^2) \ll 1$ ) and the gluon density is large (small  $x$ ). Combining these two conditions one arrives at the picture shown in Fig. 5.1: there is an approximately diagonal line in the  $\ln Q^2 - \ln 1/x$  plane below which the parton distributions are dilute, and the standard QCD parton picture applies. In this regime linear evolution equations provide the correct description of parton dynamics. In the vicinity of the line, non-linear QCD corrections become important, and above the line partons are in a high-density state. The division between the two regimes is usually defined in terms of a

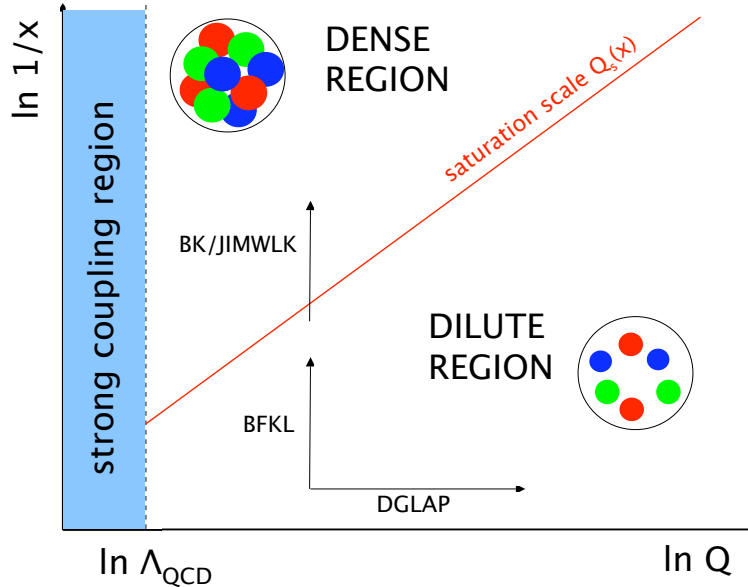


Figure 5.1: Schematic view of the different regions for the parton densities in the  $\ln Q^2 - \ln 1/x$  plane. See the text for comments.

2278 dynamically generated ‘saturation scale’, growing with decreasing  $x$  and, in the case of nuclei, with increasing  
 2279 mass number. Within this picture one easily understands which type of corrections can be expected. Once  
 2280 the density of gluons increases sufficiently, it becomes probable that, prior to their interaction with the  
 2281 photon, gluons undergo recombination processes.

## 2282 Resummation at low $x$

2283 As already mentioned in Sec. 4.6.1, the generic challenges that the small- $x$  region bears in QCD are inherently  
 2284 related to the divergence of the gluon number density with decreasing values of  $x$ . It is well known that the  
 2285 deep-inelastic partonic cross sections and parton splitting functions receive large corrections in the small- $x$   
 2286 limit due to the presence of powers of  $[\alpha_s \log x]$  to all orders in the perturbative expansion [33, 125, 298, 299,  
 2287 323]. It thus suggests dramatic effects from logarithmically enhanced corrections, so the success of fixed  
 2288 order NLO perturbation theory at HERA has been very hard to explain in regions where  $x$  becomes small.  
 2289 Recently, hints have been found that indeed the quality of the DGLAP fits tends to deteriorate systematically  
 2290 in the region of small  $x$  and  $Q^2$  [38, 324]. Direct calculations at next-to-leading logarithmic accuracy in the  
 2291 BFKL framework were performed [325, 326], and showed a slow convergence of the perturbative series in  
 2292 the high-energy, or small- $x$  regime. Therefore, generically one expects deviations from fixed-order DGLAP  
 2293 evolution in the small- $x$  and small- $Q$  regime which call for a resummation of higher orders in perturbation  
 2294 theory.

2295 Extensive analyses have been performed in the last few years [327–332], which indeed point to the  
 2296 importance of resummation to all orders. Resummation should embody important constraints like kinematic  
 2297 effects, momentum sum rules and running coupling effects.

2298 Several important questions arise here, such as the relation and interplay of the resummation and the  
 2299 non-linear effects, and possibly the role of resummation in the transition between the perturbative and non-  
 2300 perturbative regimes in QCD. Precise experimental measurements in extended kinematic regions are needed  
 2301 to explore the deviations from standard DGLAP evolution and to quantify the role of the resummation at  
 2302 small  $x$ .

2303 **Saturation in perturbative QCD**

2304 The original approach to implement unitarity and rescattering effects in high-energy hadron scattering was  
 2305 developed by Gribov [56, 287, 300]. The models based on this non-perturbative Regge-Gribov framework are  
 2306 quite successful in describing existing data on inclusive and diffractive ep and eA scattering (see e.g. [301, 302]  
 2307 and references therein). However, they lack solid theoretical foundations within QCD.

2308 On the other hand, attempts have been going on for the last 30 years to implement parton rescattering  
 2309 or recombination<sup>2</sup> in perturbative QCD in order to describe its high-energy behaviour. In the pioneering  
 2310 work in [291, 303], a non-linear evolution equation in  $\ln Q^2$  was proposed to provide the first correction to the  
 2311 linear equations. A non-linear term appeared, which was proportional to the local density of color charges  
 2312 seen by the probe (the virtual photon).

2313 An alternative, independent approach was developed in [304], where the amplitudes for diffractive pro-  
 2314 cesses in the triple Regge limit were calculated. This resulted in the extraction of the triple Pomeron vertex  
 2315 in QCD at small  $x$ , which is responsible for the non-linear term in the evolution equations.

2316 Later on these ideas were further developed to include all corrections enhanced by the local parton density,  
 2317 to constitute what is called the Color Glass Condensate (CGC) [292–295, 305–312] (see also the most recent  
 2318 developments in [313–316]). The CGC provides a non-perturbative, but weak-coupling, realization of parton  
 2319 saturation ideas within QCD. The linear limit of the basic CGC equation is the BFKL equation, which is  
 2320 the linear evolution equation derived in the high-energy limit. As illustrated in Fig. 5.1, the evolution in the  
 2321  $\ln Q^2 - \ln 1/x$  plane is driven by both linear equations: along  $\ln Q^2$  for DGLAP and along  $\ln 1/x$  for BFKL.

2322 The basic framework in which saturation ideas are discussed is illustrated in Fig. 5.2. One is considering  
 2323 the hadron wave function at high energy. Its partonic components can be separated into those partons with  
 2324 a large momentum fraction  $x$  and those with small  $x$ . The large- $x$  components form dilute systems and  
 2325 provide color sources for the corresponding small- $x$  components. Due to multiple splittings of the small- $x$   
 2326 gluons, a dense system is eventually formed. One can then construct within this formalism an evolution  
 2327 equation for the gluon correlators in the hadron wave function which is a renormalization group equation  
 2328 with respect to the rapidity separating large- and small- $x$  partons. This renormalization procedure assumes  
 2329 perturbative gluon emissions from the large- $x$  partons which imply a redefinition of the source at each step  
 2330 in rapidity.

2331 The mean field version of the CGC evolution equations, the Balitsky-Kovchegov (BK) equation [294, 295],  
 2332 provides a non-linear evolution equation for the so-called unintegrated gluon densities. These distributions,  
 2333 unlike the standard integrated densities, contain the information about the transverse momenta of the  
 2334 partons. They naturally appear in the theoretical formulations of small- $x$  physics. A detailed description of  
 2335 these distributions as well as the prospects of their precise determination at the LHeC through a variety of  
 2336 processes are discussed in Subsec. 5.2.5.

2337 It turns out that the BK approach results in a gluon density which, for a fixed resolution of the probe,  
 2338 is saturated for small longitudinal momentum fractions  $x$ , whereas at large values of  $x$ , the non-linear  
 2339 term is negligible. The separation between these two limits is given by a dynamically generated saturation  
 2340 momentum  $Q_s(x)$  which increases with decreasing  $x$  (c.f. Fig. 5.1), and therefore saturation is determined  
 2341 by the condition  $Q < Q_s(x)$ . Then, for large energies or small  $x$ , the system is in a dense regime of high  
 2342 gluon fields (thus non-perturbative) but the typical gluon momentum,  $\sim Q_s$ , is large (thus the coupling  
 2343 constant which determines gluon interactions is weak). The qualitative behavior of the saturation scale with  
 2344 energy and nuclear size can be argued as follows. The transition from a dilute to a dense regime occurs  
 2345 when the packing factor (in this case, the product of the density of gluons per unit transverse area times the  
 2346 gluon-gluon cross section) becomes of order unity i.e.

$$\frac{A \times xg(x, Q_s^2)}{\pi A^{2/3}} \times \frac{\alpha_s(Q_s^2)}{Q_s^2} \sim 1 \implies Q_s^2 \sim A^{1/3} Q_0^2 \left(\frac{1}{x}\right)^\lambda, \quad (5.2)$$

2347 where the growth of the gluon density at small  $x$  in the dilute system has been approximated by a power  
 2348 law,  $xg(x, Q^2) \sim x^{-\lambda}$ , logarithms are neglected and the nucleus is considered a simple superposition of

<sup>2</sup>Note that the rescattering and recombination concepts correspond to the same physical mechanism viewed in the rest frame and the infinite momentum frame of the hadron, respectively.

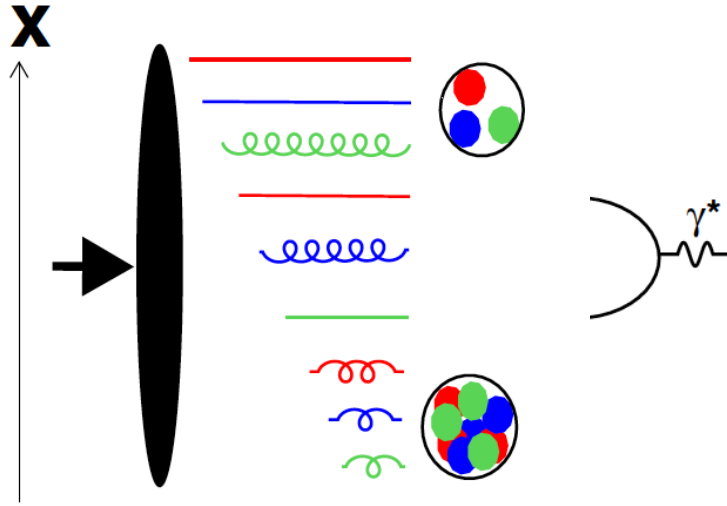


Figure 5.2: Illustration of saturation ideas. The hadron is moving very fast to the right, and its wave function contains many partonic components. Specifically, it includes partons with both large and small fractions of its longitudinal momentum  $x$ . The former are in a dilute regime and their lifetimes are very large, while the latter become densely packed due to multiple splitting and are short-lived (the length of the horizontal lines represents the extent of the lifetimes of the hadron fluctuations). Thus, the hard large  $x$  partons act as a frozen source for the dynamics of the soft ones. The photon with virtuality  $Q^2$  is moving to the left and it constitutes a probe of the hadron wave function with a spatial resolution proportional to  $1/Q$ .

2349 independent nucleons. The exponent  $\lambda \simeq 0.3$  can be derived from QCD and is broadly consistent with data  
 2350 from HERA. The scale  $Q_0^2$  can only be determined by experiment.

2351 The BK equation was derived under several simplifying assumptions such as the scattering of a dilute  
 2352 projectile on a dense target, a large number of QCD colours and the absence of correlations in the target.  
 2353 At present, the discussion is concentrated on how to overcome these difficulties [313, 317, 318]. Possible  
 2354 phenomenological implications [319–321] are being considered. Also, the proposed relation between high-  
 2355 energy QCD and Statistical Mechanics [317, 322] is under investigation.

2356 In the CGC formalism, the resummed terms are those enhanced by the energy and by the local density  
 2357 of partons, and the saturation scale depends on the matter (colour charge) density at the impact parameter  
 2358 probed by the virtual photon. For a nucleus, the nuclear size plays the role of an enhancement factor, see  
 2359 Eq. (5.2), in a manner which is analogous to impact parameter scanning. Therefore, it is expected that when  
 2360 scanning the impact parameter from the center to the periphery of the hadron at high energy, one should go  
 2361 from a non-linear to a linear regime. Analogously, non-linear effects will become more important for large  
 2362 nuclei than for smaller ones or for nucleons. Thus, a study of the variation of parton densities with impact  
 2363 parameter and with the nuclear size, will provide an exacting test of our ideas on parton saturation.

### 2364 The importance of diffraction

2365 It was observed at HERA that a substantial fraction, about 10%, of deep inelastic interactions are diffractive  
 2366 events of the type  $ep \rightarrow eXp$ . These are events in which the interacting proton stays intact, despite the  
 2367 inelasticity of the interaction. Moreover, the proton appears well separated from the rest of the hadronic  
 2368 final state  $X$  by a large rapidity gap. The events otherwise look similar to normal deep inelastic events.

2369 Diffraction has been extensively analyzed at HERA, with a variety of measurements as functions of  $x$ ,  $Q^2$   
 2370 and the fractional proton energy loss  $x_{\mathbb{P}}$ , as well as more differential analyses which include the dependence

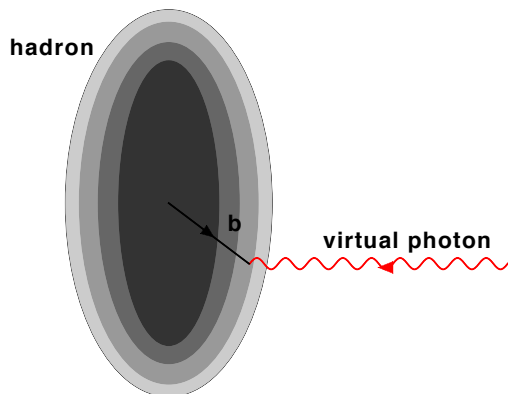


Figure 5.3: Illustration of the transverse profile of the hadron as explored by a virtual photon at impact parameter  $b$ .

2371 on the squared four-momentum transfer  $t$ . Physically, for the diffractive event to occur, there must be an  
 2372 exchange of a coherent, color neutral cluster of partons (a quasi-particle) which leaves the interacting proton  
 2373 intact. This color neutral cluster is often called the *pomeron*, and it can be characterised via a factorisation  
 2374 theorem [333] by a set of partonic densities analogous to those for the proton or nucleus. At lowest order,  
 2375 the QCD realisation of the pomeron is a pair of gluons [334, 335], which leads to enhanced sensitivity to  
 2376 saturation phenomena compared to the single gluon exchange in the bulk of non-diffractive processes.

2377 There are strong theoretical indications that diffraction is closely linked with the phenomenon of partonic  
 2378 saturation. From a wide range of calculations, mostly based on the so-called dipole model, see for example  
 2379 [336, 337], it is known that diffractive DIS events involve softer effective scales than non-diffractive events  
 2380 at the same  $Q^2$ . Thus, the exploration of diffractive phenomena offers a unique window to analyze both  
 2381 the relevance of non-linear effects and the transition between perturbative and non-perturbative dynamics  
 2382 in QCD.

2383 The LHeC will provide a widely extended kinematic coverage for diffractive events. In addition to the  
 2384 enhanced sensitivity to saturation effects through the basic 2-gluon exchange, their study at the LHeC will  
 2385 allow the extraction of diffractive parton densities for a larger range in  $Q^2$  than at HERA, and will thus  
 2386 provide crucial tests of parton dynamics and flavour decomposition in diffraction as well as of the factorization  
 2387 theorems. The high energy involved also enables the production of diffractive states with large masses which  
 2388 could include  $W$  and  $Z$  bosons as well as states with heavy flavours or even exotic states with quantum  
 2389 numbers  $1^-$ .

2390 Of particular importance is the exclusive diffractive production of vector mesons, for which differential  
 2391 measurements as a function of squared four-momentum transfer,  $t$ , are most easily performed. It has been  
 2392 demonstrated that in this case, information about the momentum transfer of the cross section can be trans-  
 2393 lated into the dependence of the scattering amplitude on impact parameter. As a result, a profile in impact  
 2394 parameter of the interaction region, illustrated in Fig. 5.3, can be extracted. The precise determination of  
 2395 the dynamics governing the high parton density regime requires a detailed picture of the spatial distribu-  
 2396 tion, in impact parameter space, of partons in the interaction region. By selecting small impact parameter  
 2397 values (large  $t$ ), it is possible to probe the regions of highest parton density, where the onset of saturation  
 2398 phenomena should most readily occur. One can then extract the value of the saturation scale as a function  
 2399 of energy and impact parameter.

2400 Even less differential measurements of the diffractive production of vector mesons can provide valuable  
 2401 information about parton dynamics and non-linear effects. For example, the measurement of the energy  
 2402 dependence of the diffractive cross section for the photoproduction of  $J/\psi$  mesons at the LHeC can distinguish  
 2403 between different scenarios for parton evolution and thus explore parton saturation to a greater accuracy  
 2404 than ever before.



## 2405 The importance of nuclei

2406 Studying lepton-nucleus collisions is an important ingredient of the LHeC low  $x$  programme for several  
2407 reasons. Most obviously, as discussed in sections 5.1.4 and 5.2.2, the nuclear structure functions and parton  
2408 densities are basically unknown at small  $x$ . This is an issue which is becoming increasingly problematic in  
2409 interpreting ultra-relativistic heavy ion collision data from RHIC and the LHC, as discussed in Subsec. 5.1.4.  
2410 The main reason for this lack of knowledge comes from the rather small area in the  $\ln Q^2 - \ln 1/x$  plane  
2411 covered by presently available experimental data, see Fig. 5.4. Current theoretical and phenomenological  
2412 analyses [338] point to the importance of non-linear dynamics in DIS off nuclei at small and moderate  $Q^2$  and  
2413 small  $x$ , which needs to be tested experimentally. In this respect, a relation exists, as reviewed in Sec. 5.2.4,  
2414 between diffraction in lepton-proton collisions and the small- $x$  behavior of nuclear structure functions. This  
2415 relation relies on only basic properties of Quantum Field Theory and its verification provides stringent tests  
2416 of our understanding of the strong interaction.

2417 Non-linear effects in parton evolution are enhanced by increasing the density of partons. Such an increase  
2418 can be achieved (see Fig. 5.5) either by increasing the energy of the collision (decreasing  $x$ ), or by increasing  
2419 the nuclear mass number  $A$ . The latter can be accomplished by either using the largest nuclei possible, or  
2420 by selecting subsets of collisions with small impact parameters  $b$  (i.e. more central collisions) between the  
2421 relatively light nuclei and the virtual photon, such that more nucleons are involved. The ideal situation  
2422 would be to map out the dependence of the saturation scale on  $x$ ,  $b$  and  $A$  as fully as possible (see Eq. (5.2)).  
2423 This is a key observable in formulations which resum multiple interactions and result in parton saturation.  
2424 As such it must be checked in experiment in order to clearly settle the mechanism underlying non-linear  
2425 parton dynamics.

2426 Beyond inclusive variables, measurements of diffractive observables in lepton scattering from nuclei have  
2427 never been obtained previously and the uncertainties in current theoretical predictions are very large. Inclu-  
2428 sive and exclusive diffraction measurements in lepton-nucleus collisions at the LHeC will offer a completely  
2429 new testing ground for our ideas on nuclear structure at small  $x$  and on parton saturation and non-linear  
2430 dynamics in QCD.

### 2431 5.1.2 Status following HERA data

2432 As discussed in the previous Section, in the low- $x$  region a high parton density can be achieved in DIS  
2433 and various novel phenomena are predicted. Ultimately, unitarity constraints become important and a  
2434 ‘black disk’ limit is approached [300], in which the cross section reaches the geometrical bound given by the  
2435 transverse proton or nucleus size. When  $\alpha_s$  is small enough for quarks and gluons to be the right degrees of  
2436 freedom, parton saturation effects are therefore expected to occur within the theoretically controllable weak  
2437 coupling regime. In this small- $x$  limit, many striking observable effects are predicted, such as  $Q^2$  dependences  
2438 of the cross sections which differ fundamentally from the usual logarithmic variations, and diffractive cross  
2439 sections approaching 50% of the total [339]. This fairly good phenomenological understanding of the onset of  
2440 unitarity effects is, unfortunately, not very quantitative. In particular, the precise location of the saturation  
2441 scale line in the DIS kinematic plane (see Fig. 5.1) is to be determined experimentally. The search for parton  
2442 saturation effects has therefore been a major issue throughout the lifetime of the HERA project.

2443 Although no conclusive saturation signals have been observed in parton density fits to existing HERA  
2444 data, various hints have been obtained, for example, by studying the change in fit quality as low- $x$  and  $Q^2$   
2445 data are progressively omitted, in the NNPDF [?, 324] and HERAPDF [38] analyses (see below).

2446 A more common approach is to fit the data to dipole models [336, 337, 340, 341], which are applicable at  
2447 very low  $Q^2$  values beyond the range in which quarks and gluons can be considered to be good degrees of  
2448 freedom. The typical conclusion [341] is that HERA data in the perturbative regime exhibit at best weak  
2449 evidence for saturation. However, when data in the  $Q^2 < 1 \text{ GeV}^2$  region are included, models which include  
2450 saturation effects are quite successful in the description of the wide variety of experimental data.

2451 The ‘geometric scaling’ [342] feature of the HERA data (Fig. 5.6left) reveals that, to a good approxima-  
2452 tion, the low- $x$  cross section is a function of a single combined variable  $\tau = Q^2/Q_s^2(x)$ , where  $Q_s^2 = Q_0^2 x^{-\lambda}$  is  
2453 the saturation scale, see Eq. (5.2). This parameterisation works well for scattering off both protons and ions,

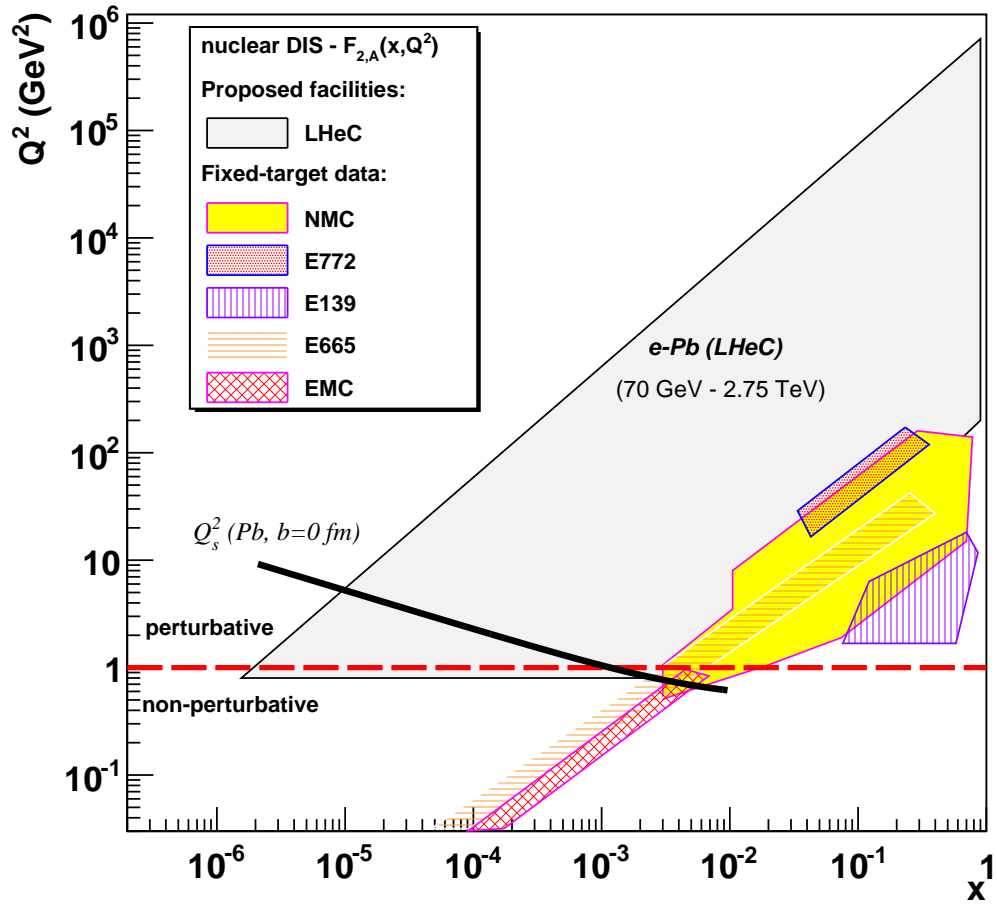


Figure 5.4: Kinematical coverage of the LHeC in the  $\ln Q^2 - \ln 1/x$  plane for nuclear beams, compared with existing nuclear DIS and Drell-Yan experiments.

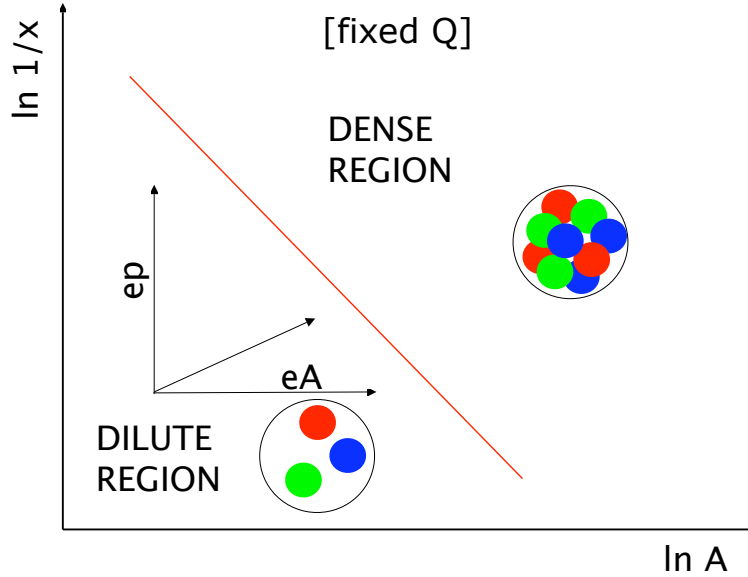


Figure 5.5: Schematic view of the different regions for the parton densities in the  $\ln 1/x - \ln A$  plane, for fixed  $Q^2$ . Lines of constant occupancy of the hadron are parallel to the diagonal line shown. See the text for further comments.

2454 as shown in Fig. 5.6right [342,343]. Geometric scaling is observed not only for the total  $\gamma^*p$  cross section,  
 2455 but also for other, more exclusive observables in  $\gamma^*p$  collisions [344,345] and even in hadron production in  
 2456 proton-proton collisions at the LHC [346] and nucleus-nucleus collisions at RHIC [343]. This feature supports  
 2457 the view (Subsec. 5.1.1) of the cross section as being invariant along lines of constant ‘gluon occupancy’.  
 2458 When viewed in detail (Fig. 5.6), there is a change in behaviour in the geometric scaling plot near  $\tau = 1$ ,  
 2459 which has been interpreted as a transition to the saturation region shown in Fig. 5.1. However, data with  
 2460  $\tau < 1$  exist only at very low, non-perturbative,  $Q^2$  values to date, precluding a partonic interpretation. Also,  
 2461 the fact that the scaling extends to large values of  $\tau$  which characterize the dilute regime, has prompted  
 2462 theoretical explanations of this phenomenon which do not invoke the physics of saturation [347].

### 2463 Dipole models

2464 As mentioned previously, one of the interesting observations at HERA is the success of the description of  
 2465 many aspects of the experimental data within the framework of the so-called dipole picture [292,348,349] with  
 2466 models that include unitarisation or saturation effects [350,351]. These models are based on the assumption  
 2467 that the relevant degrees of freedom at high energy are colour dipoles. Dipole models in DIS are closely  
 2468 related to the Good-Walker picture [352] previously developed for soft processes in hadron-hadron collisions.  
 2469 In DIS, dipoles are shown to be the eigenstates of high-energy scattering in QCD, and the photon wave  
 2470 function can be expanded onto the dipole basis.

2471 The dipole factorization for the inclusive cross section in DIS is illustrated in Fig. 5.7. It differs from  
 2472 the usual picture of the virtual photon probing the parton density of the target in that here the partonic  
 2473 structure of the probed hadron is not evident. Instead, one chooses a particular Lorentz frame where the  
 2474 photon fluctuates into a quark-antiquark pair with a transverse separation  $r$  and at impact parameter  $b$  with  
 2475 respect to the target. For sufficiently small  $x \ll (2m_N R_h)^{-1}$ , with  $m_N$  the nucleon mass and  $R_h$  the hadron  
 2476 or nuclear radius, the lifetime of the  $q\bar{q}$  fluctuation is much longer than the typical time for interaction with  
 2477 the target. The interaction of the  $q\bar{q}$  dipole with the hadron or nucleus is then described by a scattering  
 2478 matrix  $S(r, b; x)$  such that  $|S(r, b; x)| < 1$ . The unitarity constraints can be incorporated naturally in this  
 2479 picture [353] by the requirement that  $|S(r, b; x)| \geq 0$ , with  $S(r, b; x) = 0$  corresponding to the black disk

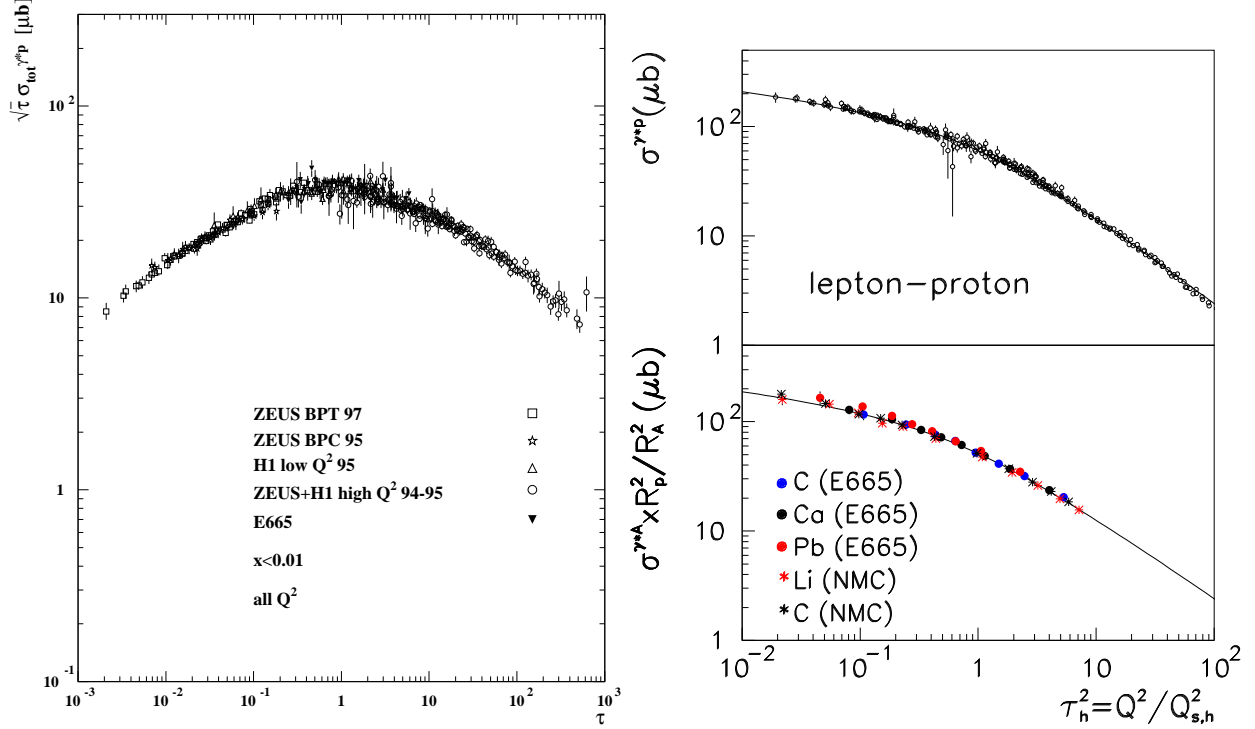


Figure 5.6: (left) Geometric scaling plot [342], in which low  $x$  data on the  $\gamma^*p$  cross section from HERA and E665 are plotted as a function of the dimensionless variable  $\tau$  (see text). The cross sections are scaled by  $\sqrt{\tau}$  for visibility. (right) Geometric scaling plot showing cross sections for electron scattering off nuclei as well as off protons [343].

2480 limit. Integrating  $1 - S(r, b; x)$  over the impact parameter  $b$  one obtains the dipole cross section  $\sigma^{q\bar{q}}(r, x)$ ,  
 2481 which depends on the dipole size and the energy (through the dependence on  $x = x_{Bj}$ ). The transverse size  
 2482 of the partons probed in this process is roughly proportional to the inverse of the virtuality of the photon  
 2483  $Q^2$ . This statement is most accurate in the case of a longitudinally polarized photon, while in the case of a  
 2484 transversely polarized one, the distribution of the probed transverse sizes of dipoles is broadened due to the  
 2485 so-called aligned jet configurations.

2486 At small values of the dipole size, such that  $r \ll 1/Q$ , the dipole cross section can be shown to be related  
 2487 to the integrated gluon distribution function

$$\sigma^{q\bar{q}}(r, x) \sim r^2 \alpha_s(C/r^2) xg(x, C/r^2), \quad (5.3)$$

2488 where  $C$  is a constant. In this regime, where  $r$  is small, the dipole cross section is small and consequently  
 2489 the amplitude is far from the unitarity limits. With increasing energy the dipole cross section grows and  
 2490 saturation corrections must be taken into account in order to guarantee the unitarity bound on  $S(r, b; x)$ .  
 2491 The transition region between the two limits is characterised by the saturation scale  $Q_s(x)$ . Several models  
 2492 [336, 340, 354] have been proposed which successfully describe the HERA data on the structure function  $F_2$ .

2493 Once the dipole cross section has been constrained by the data on the inclusive structure functions, it  
 2494 can be used to predict, with almost no additional parameters, the cross sections for diffractive production at  
 2495 small  $x$ . Inclusive diffraction has been computed within the dipole picture in [337], and exclusive diffraction  
 2496 of vector mesons in [355, 356]. One of the interesting aspects of these models is that they naturally lead  
 2497 to a constant ratio of the diffractive to total cross sections as a function of energy [337]. In models with  
 2498 saturation this is related to the fact that the saturation scale provides a natural  $x$ -dependent cut-off and

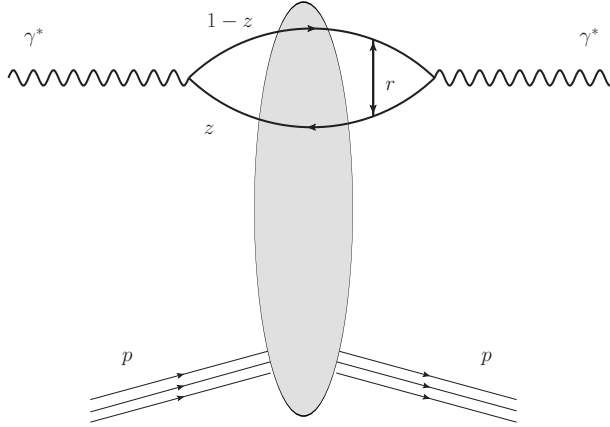


Figure 5.7: Schematic representation of dipole factorisation at small  $x$  in DIS. The virtual photon fluctuates into a quark-antiquark pair and subsequently interacts with the target. All the details of the dynamics of the interaction are encoded in the dipole scattering amplitude.

2499 gives the same leading-twist behavior for inclusive and diffractive cross sections. As a result the ratio of  
 2500 inclusive to diffractive cross sections is almost constant as a function of the energy.

2501 In spite of the fact that this approach has been able to successfully describe inclusive data and predict  
 2502 diffraction at small values of  $x$ , there is still important conceptual progress to be made. Certainly there  
 2503 are important hints from dipole models about the nature of the perturbative–non-perturbative transition in  
 2504 QCD. Nevertheless, dipole models should be rather regarded as effective phenomenological approaches. As  
 2505 such they only parametrize the essential dynamics at small  $x$ . For instance, the transverse impact parameter  
 2506 dependence of the dipole scattering amplitude  $S(r, b; x)$  is very poorly constrained. Indeed, it is possible  
 2507 simultaneously to describe  $F_2$  and  $F_2^D$  with a rather wide range of impact parameter dependences. On the  
 2508 theoretical side, it has not been possible so far to fully predict the realistic profile of the interaction region in  
 2509 transverse size. It is therefore of vital importance to measure accurately the  $t$ -dependencies of the diffractive  
 2510 cross sections in an extended kinematic range to pin down the impact parameter distribution of the proton  
 2511 at high energies.

### 2512 Hints of deviations from fixed-order linear DGLAP evolution in inclusive HERA data

2513 As discussed in previous sections, the experimental data on the inclusive structure functions  $F_2$  and  $F_L$   
 2514 measured at HERA have been successfully described - with  $\chi^2/d.o.f. \sim 1$  - by fits which use linear fixed-order  
 2515 DGLAP evolution, see e.g. [38, 68, 131, 133, 357–363]. The current status of the calculations is fixed order at  
 2516 next-to-next-to-leading accuracy. On the other hand, see Subsec. 5.1.1, there are several theoretical reasons  
 2517 to expect that at small  $x$  and/or at small  $Q^2$  the fixed-order DGLAP framework needs to be extended.  
 2518 Possible relevant phenomena predicted by perturbative QCD are linear small- $x$  resummation, non-linear  
 2519 evolution and parton saturation or other higher-twist effects. Although the exact kinematic regime in which  
 2520 these effects should become important remains unclear, it is evident that at some point they will lead to  
 2521 deviations from fixed-order DGLAP evolution. Therefore, an important question is whether these deviations  
 2522 are already present in HERA data. Several analyses have been performed which aimed to address this  
 2523 question.

2524 In one analysis [341], HERA  $F_2(x, Q^2)$  data are subjected to three fits in the framework of a dipole model.  
 2525 In one of the fits, the parameterisation of the dipole cross section does not contain saturation properties,  
 2526 whereas in the other two, saturation effects are included using two rather different models [340, 341]. All  
 2527 three dipole fits are able to describe the HERA data adequately in the perturbative region  $Q^2 \geq 2 \text{ GeV}^2$ .  
 2528 However, a clear preference for the models containing saturation effects becomes evident when data in the

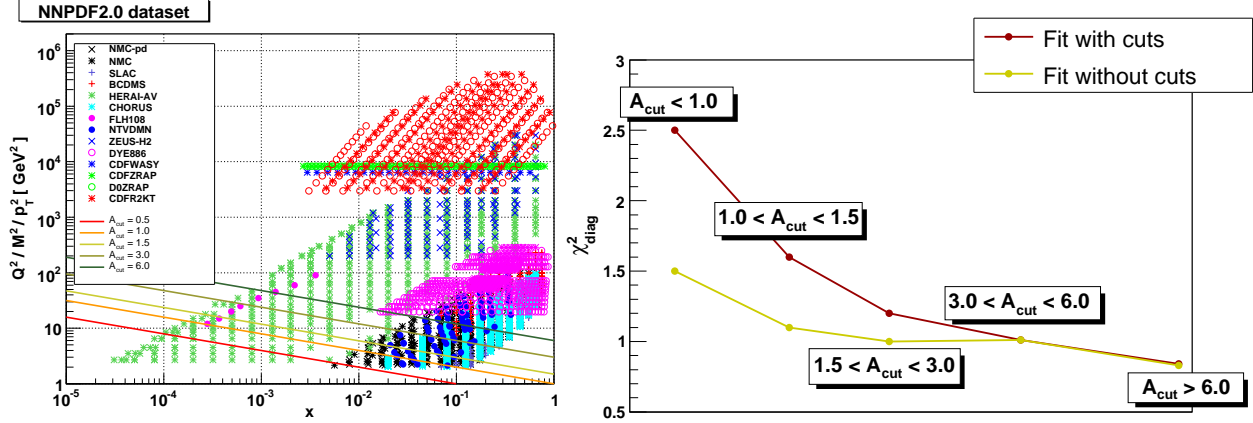


Figure 5.8: Left plot: the kinematic coverage of the data used in the NNPDF2.0 analysis, indicating the different choices of  $A_{\text{cut}}$  used to probe deviations from DGLAP. Right plot: the diagonal  $\chi^2_{\text{diag}}$  evaluated in kinematic slices corresponding to the different  $A_{\text{cut}}$  cuts, where  $\chi^2_{\text{diag}}$  has been computed using both the reference NNPDF2.0 fit without kinematic cuts (yellow line) and the NNPDF2.0 with the maximum  $A_{\text{cut}} = 1.5$  cut (red line).

range  $0.045 < Q^2 < 1 \text{ GeV}^2$  are added [341]. Similar conclusions are drawn when the same dipole cross section models are applied to various less inclusive observables at HERA [364]. These observations provide an intriguing hint that saturation effects may already be present in HERA data. However, due to the non-perturbative nature of the low  $Q^2$  kinematic region in which the effects appear, there is no clear interpretation in terms of perturbative QCD degrees of freedom and firm conclusions cannot be drawn on the existence and nature of parton recombination effects.

In another analysis [324], possible indications of deviations from linear DGLAP evolution were discussed. It was based on an unbiased PDF analysis of the inclusive HERA data. Here we present briefly an updated version of this study which uses the most precise inclusive DIS data to date, the combined HERA-I dataset [38] in the framework of the global NNPDF2.0 fitting framework. The key idea is to perform global fits only in the large- $x$ , large- $Q^2$  region, where NLO DGLAP is expected to be reliable. This way one can determine *safe* parton distributions which are not contaminated by possible non-DGLAP effects. These PDFs are then evolved backwards into the potentially *unsafe* low- $x$  and low- $Q^2$  kinematic region, and are used to compute physical observables, which are compared with data. A deviation between the predicted and observed behavior in this region can then provide a signal for effects beyond NLO DGLAP.

The PDFs were determined within the *safe* kinematic region in which  $Q^2 \geq A_{\text{cut}} \cdot x^{-\lambda}$ , where  $\lambda = 0.3$  and  $A_{\text{cut}}$  is a variable parameter (see the left plot in Fig. 5.8 and [324] for details on the procedure). The NNPDF2.0 analysis [363] was repeated for different choices of the kinematic cuts, one for each choice of  $A_{\text{cut}}$ , and the results were compared with experimental data. As shown in Fig. 5.9, at high  $Q^2 = 15 \text{ GeV}^2$  one does not see any significant deviation from NLO DGLAP. In this region all PDF sets agree with data and with one another, the only difference between them being that as  $A_{\text{cut}}$  increases the PDF uncertainty bands grow as expected due to the experimental information removed by the cuts. The situation is different at a lower  $Q^2 = 3.5 \text{ GeV}^2$ : the prediction obtained from the backwards evolution of the data above the cut exhibits a systematic downward trend, becoming more evident with increasing  $A_{\text{cut}}$ . These results are indicative of deficiencies in the description of HERA data at low- $x$  and low- $Q^2$  by NLO DGLAP evolution<sup>3</sup>. Specifically, the NLO DGLAP approach suggests a faster evolution with  $Q^2$  than is present in the data. To be sure that one is observing a genuine small- $x$  effect, one needs to check that it becomes less and less relevant as  $x$  and  $Q^2$  increase. To this aim the diagonal  $\chi^2_{\text{diag}}$  was computed, see the right plot in Fig. 5.8, in different kinematic slices, both from the fit without cuts and from that with the maximum cut  $A_{\text{cut}} = 1.5$ .

<sup>3</sup>This problem cannot be solved by NNLO corrections which work in the opposite direction, see in this respect [361]. Also, in the HERAPDF framework [38,68] the fit quality tends to worsen when low- $Q^2$  data are included. See [?] for a recent discussion and comparison with models containing non-linear dynamics.

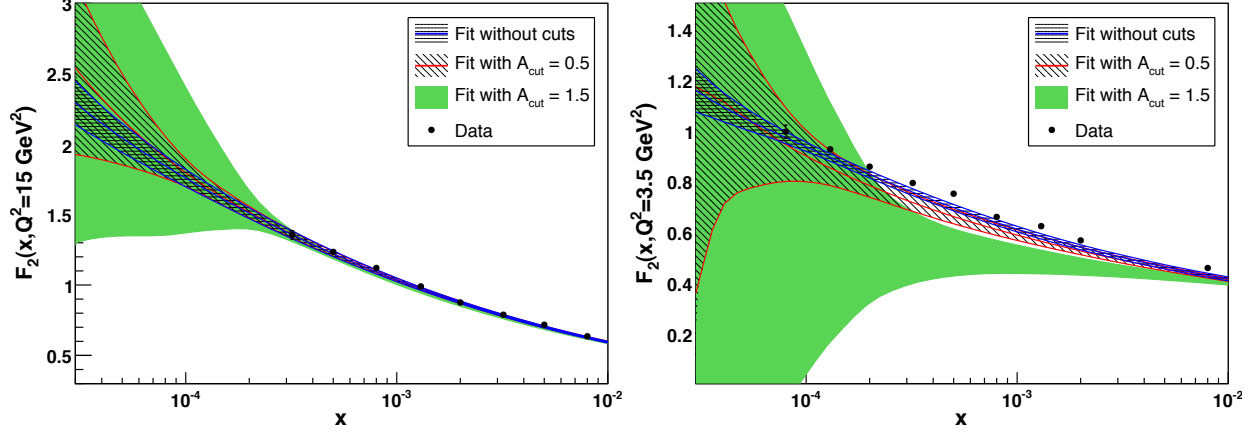


Figure 5.9: Left: the proton structure function  $F_2(x, Q^2 = 15 \text{ GeV}^2)$  at small- $x$ , computed from PDFs obtained from the NNPDF2.0 fits with different values of  $A_{\text{cut}}$ . Right: the same but at a lower  $Q^2 = 3.5 \text{ GeV}^2$  scale.

2558 The expectation is that at larger  $x$  and  $Q^2$  the difference between the two fits becomes smaller, as deviations  
 2559 from NLO DGLAP should become negligible. The data support this expectation: the contribution to the  
 2560  $\chi^2$  from the region with  $A_{\text{cut}} \geq 3$  is comparable for the fits with and without cuts, in contrast to the lower  $x$   
 2561 and  $Q^2$  region, where the  $\chi^2$  is substantially larger in the version of the fit with cuts applied. Nevertheless, it  
 2562 should be noted that there is no general consensus on the origins of these effects. e.g. in [365] it is suggested  
 2563 that their origin lies in bias due to the chosen initial conditions for DGLAP evolution

2564 In summary, there are hints that the low- $Q^2$ -low- $x$  region covered by HERA may exhibit deviations from  
 2565 fixed-order linear evolution. These hints are obtained from the success of dipole models with saturation  
 2566 features to describe the experimental data in this region, and from the fact that the quality of fixed-order  
 2567 DGLAP fits seems to deteriorate there. However, the region in which such effects may be present corresponds  
 2568 to rather small  $Q^2$ , preventing a clear interpretation in terms of perturbative QCD degrees of freedom. In  
 2569 addition, the overall quality of the fixed-order DGLAP fits to HERA data remains high. It is therefore  
 2570 premature to draw any firm conclusion on the failure of fixed-order linear evolution as the appropriate tool  
 2571 to describe all HERA data. In any case, it is clear that the methods discussed in this Subsection should be  
 2572 used to analyse LHeC inclusive structure function data, and would allow a detailed characterization of any  
 2573 new high-energy QCD dynamics unveiled by the LHeC. If the hints in the HERA data are correct, the novel  
 2574 phenomena should appear at the LHeC in a higher  $Q^2$  perturbative region where they can be established  
 2575 cleanly and understood in terms of parton dynamics.

## 2576 Linear resummation schemes

2577 The deviations from DGLAP evolution could be caused by higher order effects at small  $x$  and small  $Q$   
 2578 which need to be resummed to all orders of perturbation theory. As mentioned previously, the problem  
 2579 of resummation at small  $x$  has been extensively studied in recent years, see for example [327–332]. It has  
 2580 been demonstrated that the small- $x$  resummation framework accounts for running coupling effects, kinematic  
 2581 constraints, gluon exchange symmetry and other physical constraints. The results were shown to be very  
 2582 robust with respect to scale changes and different resummation schemes. As a result, the effect of the  
 2583 resummation of terms which are enhanced at small  $x$  is perceptible but moderate - comparable in size to  
 2584 typical NNLO fixed order corrections in the HERA region.

2585 A major development for high-energy resummation was presented in [329], where the full small- $x$  re-  
 2586 summation of deep-inelastic scattering (DIS) anomalous dimensions and coefficient functions was obtained  
 2587 including the quark contribution. This allowed for the first time a consistent small- $x$  resummation of DIS  
 2588 structure functions. These results are summarized in Fig. 5.10, taken from Ref. [329], where the  $K$ -factors

2589 for  $F_2$  and  $F_L$  for the resummed results are compared. As is evident from this figure, resummation is quite  
 2590 important in the region of low  $x$  for a wide range of  $Q^2$  values. One observes, for example, that the fixed order  
 2591 NNLO contribution leads to an enhancement of  $F_2$  with respect to NLO, whereas the resummed calculation  
 2592 leads to a suppression. This means that a truncation at any fixed order is very likely to be insufficient for  
 2593 the description of the LHeC data and therefore the fixed-order perturbative expansion becomes unreliable  
 2594 in the low- $x$  region, which calls for the resummation. Furthermore, the resummation of hard partonic cross  
 2595 sections has been performed for several LHC processes such as heavy quark production [366], Higgs pro-  
 2596 duction [367, 368], Drell-Yan [369, 370] and prompt photon production [371, 372]. The LHC is thus likely to  
 2597 provide a testing ground in the near future.

2598 We refer to the recent review in Ref. [373] as well as to the HERA-LHC workshop proceedings [374] for  
 2599 a more detailed summary of recent theoretical developments in high-energy resummation.

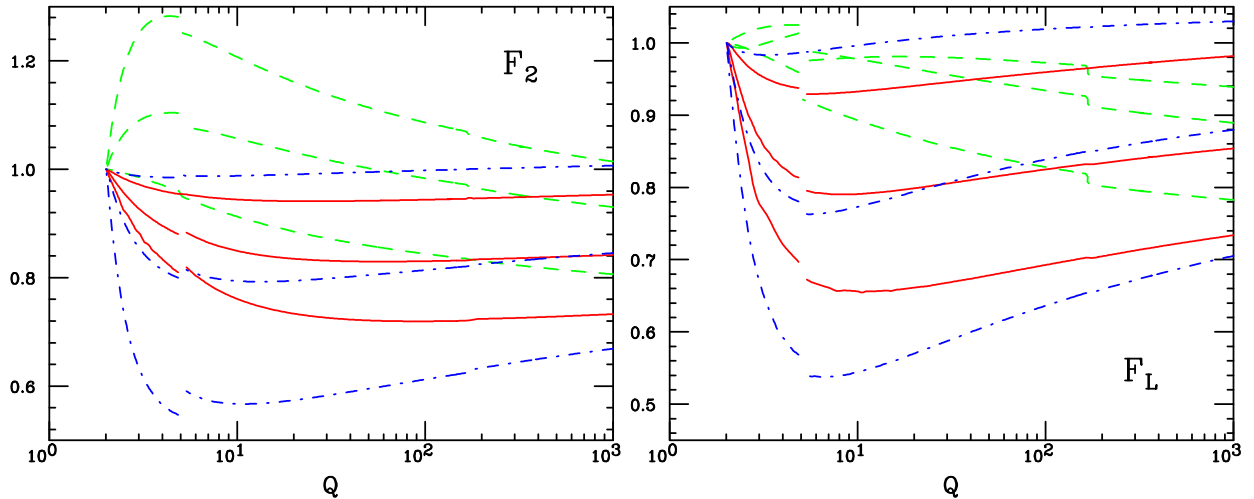


Figure 5.10: The  $K$ -factors, defined as the ratio of the fixed-order NNLO or resummed calculation to the NLO fixed-order results for the singlet  $F_2$  and  $F_L$  structure functions, with  $F_2$  and  $F_L$  kept fixed for all  $x$  at  $Q_0 = 2$  GeV. Results are shown at fixed  $x = 10^{-2}$ ,  $10^{-4}$  or  $10^{-6}$  as a function of  $Q$  in the range  $Q = 2 - 1000$  GeV with  $\alpha_s$  running and  $n_f$  varied in a zero-mass variable flavour number scheme. The breaks in the curves correspond to the  $b$  and  $t$  quark thresholds. The curves are: fixed order perturbation theory NNLO (green, dashed); resummed NLO in the  $Q_0\overline{\text{MS}}$  scheme (red, solid), resummed NLO in the  $\overline{\text{MS}}$  scheme (blue, dot-dashed). Curves with decreasing  $x$  correspond to those going from bottom to top for NNLO and from top to bottom in the resummed cases.

2600 To summarise, small- $x$  resummation is becoming a very important component for precision LHC physics,  
 2601 and will become a crucial ingredient of the LHeC small- $x$  physics program [375, 376]. The LHeC extended  
 2602 kinematic range will enhance the differences between the resummed predictions and fixed-order DGLAP  
 2603 calculations.

### 2604 5.1.3 Low- $x$ physics perspectives at the LHC

2605 The low- $x$  regime of QCD can also be analyzed in hadron and nucleus collisions at the LHC. The experimen-  
 2606 tally accessible values of  $x$  range from  $x \sim 10^{-3}$  to  $x \sim 10^{-6}$  for central and forward rapidities respectively.  
 2607 The estimates for the corresponding saturation scale at  $x \sim 10^{-3}$ , based on Eq. (5.2), result in  $Q_s^2 \approx 1$  GeV<sup>2</sup>  
 2608 for proton and  $Q_s^2 \approx 5$  GeV<sup>2</sup> for lead.

2609 The significant increase in the center-of-mass energy and the excellent rapidity coverage of the LHC  
 2610 detectors will extend the kinematic reach in the  $x$ - $Q^2$  plane by orders of magnitude compared to previous



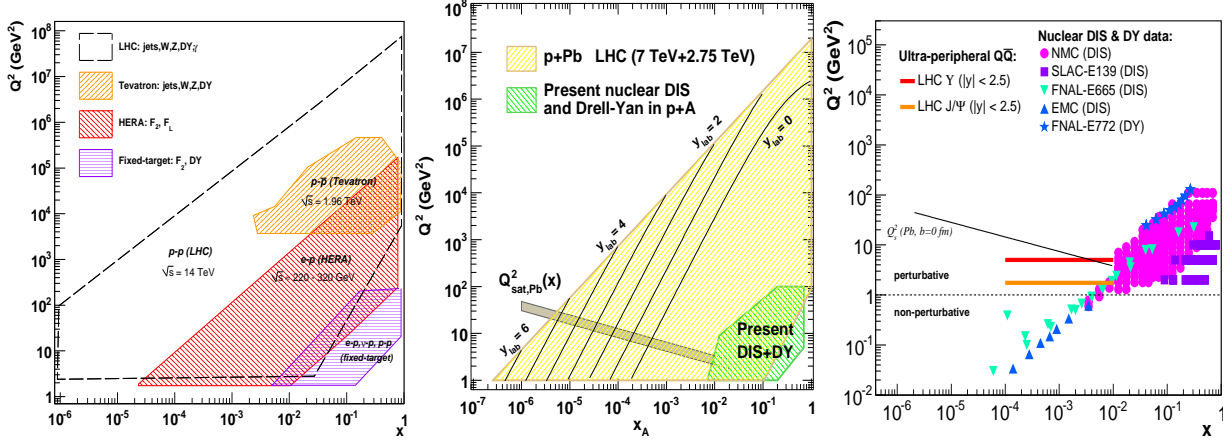


Figure 5.11: Kinematic reaches in the  $(x, Q^2)$  plane covered in proton-proton (left), proton-nucleus (center) [377] and ultraperipheral nucleus-nucleus (right) [378] collisions at the LHC. Also shown are the regions studied so far in collider and fixed-target experiments. Estimates of the saturation scale for lead are also shown.

2611 measurements at fixed-target and collider energies (see Fig. 5.11). Such measurements are particularly  
 2612 important in the nuclear case since, due to the scarcity of nuclear DIS data, the gluon PDF in the nucleus is  
 2613 virtually unknown at fractional momenta below  $x \approx 10^{-2}$  [153]. In addition, due to the dependence of the  
 2614 saturation scale on the hadron transverse size, non-linear QCD phenomena are expected to play a central role  
 2615 in the phenomenology of collisions involving nuclei. We succinctly review here the experimental possibilities  
 2616 to study saturation physics in  $pp$ ,  $pA$  and  $AA$  collisions at the LHC.

### 2617 Low- $x$ studies in proton-proton collisions

2618 The LHC experiments feature detection capabilities at forward rapidities ( $|\eta| \gtrsim 3$ ), which will allow mea-  
 2619 surements of various perturbative processes sensitive to the underlying parton structure and its dynamical  
 2620 evolution in the proton. The *minimum* parton momentum fractions probed in a  $2 \rightarrow 2$  process with a particle  
 2621 of momentum  $p_T$  produced at pseudo-rapidity  $\eta$  is

$$x_{min} = \frac{x_T e^{-\eta}}{2 - x_T e^{\eta}}, \quad \text{where } x_T = 2p_T/\sqrt{s}, \quad (5.4)$$

2622 i.e.  $x_{min}$  decreases by a factor  $\sim 10$  every 2 units of rapidity. The extra  $e^{\eta}$  lever-arm motivates the interest in  
 2623 *forward* particle production measurements to study the PDFs at small values of  $x$ . From Eq. (5.4) it follows  
 2624 that the measurement at the LHC of particles with transverse momentum  $p_T = 10$  GeV at rapidities  $\eta \approx 5$   
 2625 probes  $x$  values as low as  $x \approx 10^{-5}$  (Fig. 5.11, left). Various experimental measurements have been proposed  
 2626 at forward rapidities at the LHC to constrain the low- $x$  PDFs in the proton and to look for possible evidence  
 2627 for non-linear QCD effects. These include forward jets and Mueller-Navelet dijets in ATLAS and CMS [379];  
 2628 and forward isolated photons [380] and Drell-Yan (DY) [381] in LHCb.

### 2629 Low- $x$ studies in proton-nucleus collisions

2630 Until an electron-ion collider becomes available, proton-nucleus collisions will be the best available tool to  
 2631 study small- $x$  physics in a nuclear environment without the strong influence of the final-state medium as  
 2632 expected in the  $AA$  case. Though proton-nucleus collisions are not yet scheduled at the LHC, detailed feasi-  
 2633 bility studies exist [382] and strategies to define the accessible physics programme are being developed [377].  
 2634 The  $pA$  programme at the LHC serves a dual purpose [377]: to provide “cold QCD matter” benchmark

measurements for the physics measurements of the AA programme without significant final-state effects, and to study the nuclear wavefunction in the small- $x$  region. In Fig. 5.11 (center) we show how dramatically the LHC will extend the region of phase space in the  $(x, Q^2)$  plane<sup>4</sup> by orders of magnitude compared with those studied at present. The same figure also shows the scarcity of nuclear DIS and DY measurements and, correspondingly, the lack of knowledge of nuclear PDFs in the regions needed to constrain the initial state for the AA programme - there is almost no information at present in the region  $x \lesssim 10^{-2}$  [153].

Nuclear PDF constraints, checks of factorization (universality of PDFs) and searches for saturation of partonic densities will be performed in  $pA$  collisions at the LHC by studying different production cross sections for e.g. inclusive light hadrons [383], heavy flavour particles [384], isolated photons [385], electroweak bosons [386] and jets. Additional opportunities also appear in the so-called ultra-peripheral collisions in which the coherent electromagnetic field created by the proton or the large nucleus effectively acts as one of the colliding particles with photon-induced collisions at centre of mass energies higher than those reached in photoproduction at the HERA collider [387] (see next subsection).

At this point it is worth mentioning that particle production in the forward (proton) rapidity region in dAu collisions at RHIC shows features suggestive of saturation effects, although no consensus has been reached so far, see [?, 388–393] and references therein. The measurements at RHIC suffer from the limitation of working at the edge of the available phase space in order to study the small- $x$  region in the nuclear wave function. This limitation will be overcome by the much larger available phase space at the LHC.

#### Low- $x$ studies in nucleus-nucleus collisions

Heavy-ion ( $AA$ ) collisions at the LHC aim at the exploration of collective partonic behaviour both in the initial wavefunction of the nuclei as well as in the final produced matter, the latter being a hot and dense QCD medium (see the discussions in Subsection 5.1.4). The nuclear PDFs at small  $x$  define the number of parton scattering centers and thus the initial conditions of the system which then thermalises.

A possible means of obtaining direct information on the nuclear parton distribution functions is through the study of final state particles which do not interact strongly with the surrounding medium, such as photons [394] or electroweak bosons [386]. Beyond this, global properties of the collision such as the total multiplicities or the existence of long-range rapidity structures (seen in AuAu collisions at RHIC [395] and in  $pp$  and PbPb collisions at the LHC [?, 396]) are sensitive to the saturation momentum which at the LHC is expected to be well within the weak coupling regime [398],  $Q_{\text{sat,Pb}}^2 \approx 5 - 10 \text{ GeV}^2$ . CGC predictions for charged hadron multiplicities in central Pb-Pb collisions at 5.5 TeV per nucleon are  $dN_{ch}/d\eta|_{\eta=0} \approx 1500\text{--}2000$  [399]. (Note that the predictions done before the start of RHIC in 2000 were 3 times higher). Recent data from ALICE [400] give  $dN_{ch}/d\eta|_{\eta=0} \approx 1600$  in central Pb-Pb at 2.76 TeV per nucleon, in rough agreement with CGC expectations.

As already noted for the  $pA$  case, one of the cleanest ways to study the low- $x$  structure of the Pb nucleus at the LHC may be via ultra-peripheral collisions (UPCs) [387] in which the strong electromagnetic fields (the equivalent flux of quasi-real photons) generated by the colliding nuclei can be used for photoproduction studies at maximum energies  $\sqrt{s_{\gamma N}} \approx 1 \text{ TeV}$ , that is 3–4 times larger than at HERA. In particular, exclusive quarkonium photoproduction offers an attractive opportunity to constrain the low- $x$  gluon density at moderate virtualities, since in such processes the gluon couples *directly* to the  $c$  or  $b$  quarks and the cross section is proportional to the gluon density *squared*. The vector meson mass  $M_V$  introduces a relatively large scale, amenable to a perturbative QCD treatment. In  $\gamma A \rightarrow J/\psi (\Upsilon) A^{(*)}$  processes at the LHC, the gluon distribution can be probed at values as low as  $x = M_V^2/W_{\gamma A}^2 e^y \approx 10^{-4}$ , where  $W_{\gamma A}$  is the  $\gamma A$  centre of mass energy (Fig. 5.11 right). Full simulation studies [378, 401] of quarkonium photoproduction tagged with very-forward neutrons, show that ALICE and CMS can carry out detailed  $p_T, \eta$  measurements in the dielectron and dimuon decay channels.

In summary,  $pp$ ,  $pA$  and  $AA$  collisions at the LHC have access to the small- $x$  regime, and will certainly help to unravel the complex parton dynamics in this region. However, the excellent precision of a high

<sup>4</sup>Asymmetric colliding systems imply a rapidity shift in the two-in-one magnet design of the LHC. This shift has been taken into account in the figure: the quoted  $y$  values are those in the laboratory frame.

2683 energy electron-proton (ion) collider cannot be matched in hadronic collisions. The deep inelastic scattering  
 2684 process is much cleaner experimentally and under significantly better theoretical control. The description  
 2685 of hadron-hadron and heavy ion collisions in the regime of small  $x$  suffers from a variety of uncertainties,  
 2686 such as the question of the appropriate factorization, if any, and the large indeterminacy of fragmentation  
 2687 functions in the relevant kinematic region. Thus, the precise measurement of physical observables and parton  
 2688 densities and their interpretation in terms of QCD dynamics is only possible at an electron-hadron (ion)  
 2689 collider.

#### 2690 5.1.4 Nuclear targets

2691 As discussed in Subsection 5.1.1, the use of nuclei offers a means of modifying the parton density both  
 2692 through colliding different nuclear species and by varying the impact parameter of the collision. Therefore,  
 2693 the study of DIS on nuclear targets is of the utmost importance for our understanding of the dynamics  
 2694 which control the behaviour of hadron and nuclear wave functions at small  $x$ . On the other hand, the  
 2695 characterization of parton densities inside nuclei and the study of other aspects of lepton-nucleus collisions  
 2696 such as particle production, are of strong interest both fundamentally and because they are crucial for a  
 2697 correct interpretation of the experimental results from ultrarelativistic ion-ion collisions. In the rest of this  
 2698 section we focus on these last two aspects.

2699 Additionally, nuclear effects have to be better understood in order to improve the constraints on nucleon  
 2700 PDF in analyses which include DIS data with neutrino beams (e.g. [361, 363]). Due to the smallness of the  
 2701 cross section, such neutrino experiments use nuclear targets, so corrections for nuclear effects are a significant  
 2702 source of uncertainty in the extraction of parton densities even for the proton.

#### 2703 Comparing nuclear parton density functions

2704 The nuclear modification of structure functions has been extensively studied since the early 70's [402, 403].  
 2705 It is usually characterized through the so-called nuclear modification factor which, for a given structure  
 2706 function or parton density  $f$ , reads

$$R_f^A(x, Q^2) = \frac{f^A(x, Q^2)}{A \times f^N(x, Q^2)}. \quad (5.5)$$

2707 In this equation, the superscript  $A$  refers to a nucleus of mass number  $A$ , while  $N$  denotes the nucleon (either  
 2708 a proton or a neutron, or their average as obtained using deuterium). The absence of nuclear effects would  
 2709 result in  $R = 1$ .

2710 The nuclear modification factor for  $F_2$  shows a rich structure: an enhancement ( $R > 1$ ) at large  $x > 0.8$ ,  
 2711 a suppression ( $R < 1$ ) for  $0.3 < x < 0.8$ , an enhancement for  $0.1 < x < 0.3$ , and a suppression for  $x < 0.1$   
 2712 where isospin effects can be neglected. The latter effect is called shadowing [338], and is the dominant  
 2713 phenomenon at high energies (the kinematical region  $x < 0.1$  will determine particle production at the LHC,  
 2714 see Sec. 5.1.3 and [404]).

2715 The modifications in each region are believed to be of different dynamical origin. In the case of shadowing,  
 2716 the explanation is usually given in terms of a coherent interaction involving several nucleons, which reduces  
 2717 the nuclear cross section from the totally incoherent situation,  $R = 1$ , towards a region of total coherence.  
 2718 In the region of very small  $x$ , small-to-moderate  $Q^2$  and for large nuclei, the unitarity limit of the nuclear  
 2719 scattering amplitudes is expected to be approached and some mechanism of unitarisation such as multiple  
 2720 scattering should come into play. Therefore, in this region nuclear shadowing is closely related to the onset  
 2721 of the unitarity limit in QCD and the transition from coherent scattering of the probe off a single parton  
 2722 to coherent scattering off many partons. The different dynamical mechanisms proposed to deal with this  
 2723 problem should offer a quantitative explanation for shadowing, with the nuclear size playing the role of a  
 2724 density parameter in the way discussed in Subsection 5.1.1.

2725 At large enough  $Q^2$  the generic expectation is that the parton system becomes dilute and the usual  
 2726 leading-twist linear DGLAP evolution equations should be applicable to nuclear PDFs. In this framework,

global analyses of nuclear parton densities (in exact analogy to those of proton and neutron parton densities) have been developed up to NLO accuracy [?, 153, 405, 406]. In these global analyses, the initial conditions for DGLAP evolution are parametrized by flexible functional forms but they lack theoretical motivation in terms of e.g. the dynamical mechanisms for unitarization mentioned above. On the other hand, the relation between diffraction and nuclear shadowing [56, 300] can in principle be employed to constrain the initial conditions for DGLAP evolution, as has been explored previously at both LO [302] and NLO [407]<sup>5</sup> accuracy, see Subsec. 5.2.4. All nuclear PDF analyses [?, 153, 405, 406] include data from NC DIS and DY experiments, [?, 153] also use particle production data at mid-rapidity in deuterium-nucleus collisions at RHIC, and [?] CC DIS data from neutrino experiments. Error sets obtained through the Hessian method are provided in [?, 153]. Note that CC DIS data have been considered only recently [?, 53, 409]<sup>6</sup> in this context.

Results from different nuclear PDF analyses performed at NLO accuracy are shown in Fig. 5.12, with the band indicating the uncertainty obtained using the error sets in [153]. In addition to the discrepancies concerning the existence of an enhancement/suppression at large  $x$ , the different approaches lead to clear differences at small  $x$ , both in magnitude and in shape<sup>7</sup>, usually within the large uncertainty band shown. With nuclear effects vanishing logarithmically in the DGLAP analysis, the corresponding differences and uncertainties diminish, although they remain sizable until rather large  $Q^2$ .

These large uncertainties are due to the lack of experimental data on nuclear structure functions for  $Q^2 > 2 \text{ GeV}^2$  and  $x$  smaller than a few times  $10^{-2}$ . The constraints on the small- $x$  gluon are particularly poor. Particle production data at mid-rapidity coming from deuterium-nucleus collisions at RHIC offer an indirect constraint on the small- $x$  sea and glue [?, 153], but these data are bound to contain sizable uncertainties intrinsic to particle production in hadronic collisions at small and moderate scales. Therefore, only high-accuracy data on nuclear structure functions at smaller  $x$ , with a large lever arm in  $Q^2$ , as achievable at the LHeC, will be able to substantially reduce the uncertainties and clearly distinguish between the different approaches.

## Requirements for the ultra-relativistic heavy ion programs at RHIC and the LHC

The LHeC will offer extremely valuable information on several aspects of high-energy hadronic and nuclear collisions. On the one hand, it will characterize hard scattering processes in nuclei through a precise determination of initial state. On the other hand, it will provide quantitative constraints on theoretical descriptions of initial particle production in ultra-relativistic nucleus-nucleus collisions and the subsequent evolution into the quark-gluon plasma, the deconfined partonic state of matter whose production and study offers key information about confinement. Such knowledge will complement that coming from pA collisions and self-calibrating hard probes in nucleus-nucleus collisions (see [377, 394, 404, 410, 411]) regarding the correct interpretation of the findings of the heavy-ion programme at RHIC (see e.g. [412, 413] and refs. therein) and at the LHC. Beyond the qualitative interpretation of such findings, the LHeC will greatly improve the quantitative characterization of the properties of QCD extracted from such studies. The relevant information can be classified into three items:

### a. Parton densities inside nuclei:

The knowledge of parton densities inside nuclei is an essential piece of information for the analysis of the medium created in ultra-relativistic heavy-ion collisions using hard probes, i.e. those observables whose yield in nucleon-nucleon collisions can be predicted in pQCD (see [394, 404, 410, 411]). The comparison between the expectation from an incoherent superposition of nucleon-nucleon collisions and the measurement in nucleus-nucleus collisions characterises the nuclear effects. However, we need

<sup>5</sup>In the approach in [407] predictions are provided only for sea quarks and gluons, with the valence taken from the analysis in [408].

<sup>6</sup>The analyses in [?, 153, 409] show the compatibility of the nuclear corrections as extracted from NC DIS, DY and particle production in dAu at RHIC, with CC DIS data on nuclear targets, while in [53] some tension is found between NC and CC DIS data.

<sup>7</sup>The increasing shape of the gluon ratio with decreasing  $x$  at small  $x$  and  $Q^2$  in [?], is due to the fact that in this analysis the proton parton densities MSTW2008 [361], in which the gluon distribution becomes negative in that kinematical region, are used.

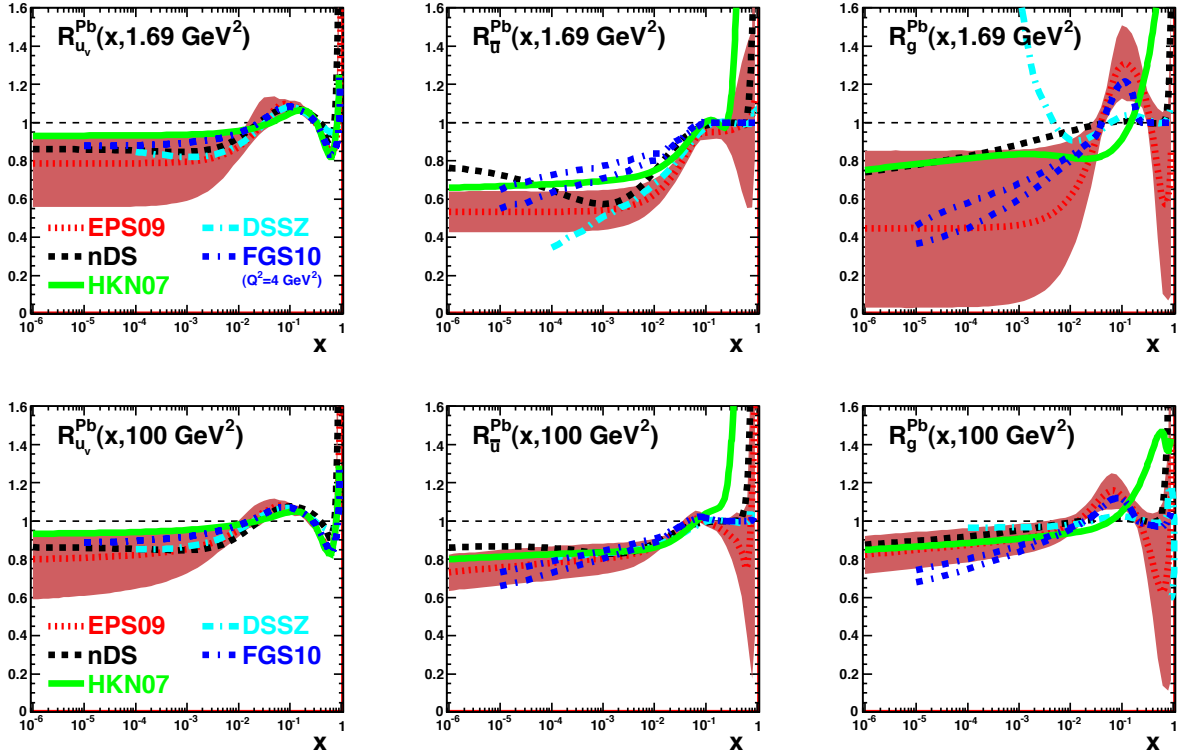


Figure 5.12: Ratio of parton densities in a bound proton in Pb to those in a free proton scaled by  $A = 207$ , for valence  $u$  (left),  $\bar{u}$  (middle) and  $g$  (right), at  $Q^2 = 1.69$  (top) and  $100$  (bottom)  $\text{GeV}^2$ . Results are shown from [405] (nDS, black dashed), [406] (HKN07, green solid), [153] (EPS09, red dotted), [407] (FGS10, blue dashed-dotted; in this case the lowest  $Q^2$  is  $4 \text{ GeV}^2$  and two lines are drawn reflecting the uncertainty in the predictions) and [?] (DSSZ, cyan dashed-dotted). The red bands indicate the uncertainties according to the EPS09 analysis [153].

2769 to disentangle those effects which originate from the creation of a hot medium in nucleus-nucleus  
2770 collisions, from effects arising only from differences in the partonic content between nucleons and  
2771 nuclei.

2772 Our present knowledge of parton densities inside nuclei is clearly insufficient in the kinematic regions of  
2773 interest for RHIC and, above all, for the LHC (see [404] and Subsection 5.1.3). Such ignorance reflects  
2774 in uncertainties larger than a factor 3–4 for the calculation of different cross sections in nucleus-nucleus  
2775 collisions at the LHC (see Fig. 5.12 and [383]), thus weakening strongly the possibility of extracting  
2776 quantitative characteristics of the produced hot medium. While the pA program at the LHC will offer  
2777 new constraints on the nuclear parton densities (e.g. [377,383]), measurements at the LHeC would be  
2778 far more constraining and would reduce the uncertainties in nucleus-nucleus cross sections to less than  
2779 a factor two.

2780 b. Parton production and initial conditions for a heavy-ion collision:

2781 The medium produced in ultra-relativistic heavy-ion collisions develops very early a collective behavior,  
2782 usually considered as that of a thermalized medium and describable by relativistic hydrodynamics. The  
2783 initial state of a heavy-ion collision for times prior to its eventual thermalization, and the thermalisation  
2784 or isotropisation mechanism, play a key role in the description of the collective behavior. Such an  
2785 initial condition for hydrodynamics or transport is presently modelled and fitted to data. But it  
2786 should eventually be determined by a theoretical formalism of particle production within a saturation  
2787 framework which embodies the both aspects: parton fluxes inside nuclei - discussed in the previous  
2788 item, and particle production and evolution, eventually leading to isotropization.

2789 The CGC offers a well-defined framework in which the initial condition and thermalization mechanism  
2790 can be computed from QCD, see Subsection 5.1.1 and e.g. [414] and refs. therein. Although our  
2791 theoretical knowledge is still incomplete, electron-nucleus collisions offer a setup, considerably less  
2792 complex than nucleus-nucleus collisions, in which these CGC-based calculations already exist and can  
2793 be tested. In this way, electron-ion collisions offer a testing ground for ideas on parton production in  
2794 a dense environment, which is required for a first principles calculation of the initial conditions for the  
2795 collective behavior in ultra-relativistic heavy-ion collisions. The LHeC offers the possibility of studying  
2796 particle production in the kinematic region relevant for experiments at RHIC and the LHC.

2797 c. Parton fragmentation and hadronization inside the nuclear medium:

2798 The mechanism through which a highly virtual parton evolves from an off-shell coloured state to a final  
2799 state consisting of colourless hadrons, is still subject to great uncertainties. Electron-ion experiments  
2800 offer a testing ground for our ideas and understanding of such phenomena, see [415] and refs. therein,  
2801 with the nucleus being a medium of controllable extent and density which modifies the radiation and  
2802 hadronization processes.

2803 The LHeC will have capabilities for particle identification and jet reconstruction for both nucleon and  
2804 nuclear targets. Its kinematic reach will allow the study of partons traveling through the nucleus  
2805 from low energies, for which hadronization is expected to occur inside the nucleus, to high energies  
2806 with hadronization outside the nucleus. Therefore the modification of the yields of energetic hadrons,  
2807 observed at RHIC<sup>8</sup> and usually attributed to in-medium energy loss - the so-called jet quenching  
2808 phenomenon - will be investigated. With jet quenching playing a key role in the present discussions  
2809 on the production and characterisation of the hot medium produced in ultra-relativistic heavy-ion  
2810 collisions, the LHeC will offer most valuable information on effects in cold nuclear matter of great  
2811 importance for clarifying and reducing the existing uncertainties.

---

<sup>8</sup>LHC experiments have already observed the jet quenching phenomenon both at the level of single-particle spectra [?, 416] and through the study of jets [?, 417, 418], which will play a central role in heavy-ion physics at these energies.

## 5.2 Prospects at the LHeC

### 5.2.1 Strategy: decreasing $x$ and increasing $A$

As discussed previously, in order to analyse the regime of high parton densities at small  $x$ , we propose a two-pronged approach which is illustrated in Fig. 5.5. To reach an interesting novel regime of QCD one can either decrease  $x$  by increasing the center-of-mass energy or increase the matter density by increasing the mass number  $A$  of the nucleus. In addition, we will see that diffraction, and especially exclusive diffraction, will play a special role in unravelling the new dense partonic regime of QCD.

The LHeC will offer a huge lever arm in  $x$  and also a possibility of changing the matter density at fixed values of  $x$ . This will allow us to pin down and compare the small  $x$  and saturation phenomena both in protons and nuclei and will offer an excellent testing ground for theoretical predictions. Thus, in the following, LHeC simulations of electron-proton collisions are paralleled by those in electron-lead wherever possible. For a complementary perspective on the opportunities for novel QCD studies offered by the LHeC, see [88].

### 5.2.2 Inclusive measurements

#### Predictions for the proton

The LHeC is expected to provide measurements of the structure functions of the proton with unprecedented precision, which will allow detailed studies of small- $x$  QCD dynamics. In particular, it will be highly sensitive to departures of the inclusive observables  $F_2$  and  $F_L$  from the fixed-order DGLAP framework, in the region of small  $x$  and  $Q^2$ . These deviations are expected by several theoretical arguments, as discussed in detail previously.

In Fig. 5.13 we show some predictions for the proton structure functions,  $F_2$  and  $F_L$ , in ep collisions at  $Q^2 = 10 \text{ GeV}^2$  and for  $10^{-6} \leq x \leq 0.01$  i.e.  $F_{2(L)}(x, Q^2 = 10 \text{ GeV}^2)$ . The different curves correspond to the extrapolation of models that reproduce correctly the available HERA data for the same observables in the small- $x$  region. They are classified into two categories: those based on linear evolution approaches and those that include non-linear small- $x$  dynamics. Among the linear approaches we include extrapolation from the NLO DGLAP fit as performed by the NNPDF collaboration [419] (solid yellow bands) and the results from a combined DGLAP/BFKL approach, which includes resummation of small- $x$  effects [420] (black-dotted-dotted lines). The non-linear calculations shown here are all formulated within the dipole model. We distinguish two categories: those based on the eikonalization of multiple scatterings together with DGLAP evolution of the gluon distributions [354,355] (blue dashed-dotted lines) and those relying in the Color Glass Condensate effective theory of high-energy QCD scattering (red dashed lines). The latter include calculations based on solutions of the running coupling Balitsky-Kovchegov equation [421] and other more phenomenological models of the dipole amplitude without [340], or with [356] impact parameter dependence. Finally, we also include a hybrid approach, where initial conditions based on Regge theory and including non-linearities are evolved in  $Q^2$  according to linear DGLAP evolution [301] (green dotted line). In all cases the error bands are generated by allowing variations of the free parameters in each subset of models. The green filled squares correspond to the subset of the simulated LHeC pseudodata at  $Q^2 = 10 \text{ GeV}^2$  (see Subsection 4.1.4).

Clearly, the accuracy of the data at the LHeC will offer huge possibilities for discriminating between different models and for constraining the dynamics underlying the small- $x$  region.

#### Constraining small- $x$ dynamics

The potential impact of the LHeC on low  $x$  parton densities within the framework of an NLO DGLAP analysis is assessed by adding the pseudodata introduced in subsection 4.1.4 into the NNPDF fitting analysis. The pseudodata are first generated at the extrapolated central values according to the existing NNPDF fits.

The extrapolated NNPDF1.2 gluon density and its uncertainty band are shown at the starting scale for QCD evolution,  $Q_0^2 = 2 \text{ GeV}^2$  in Fig. 5.14, where it can be seen that the lack of experimental constraints for  $x \lesssim 10^{-4}$  leads to an explosion in the uncertainties. When the LHeC  $F_2$  pseudodata are included in addition,

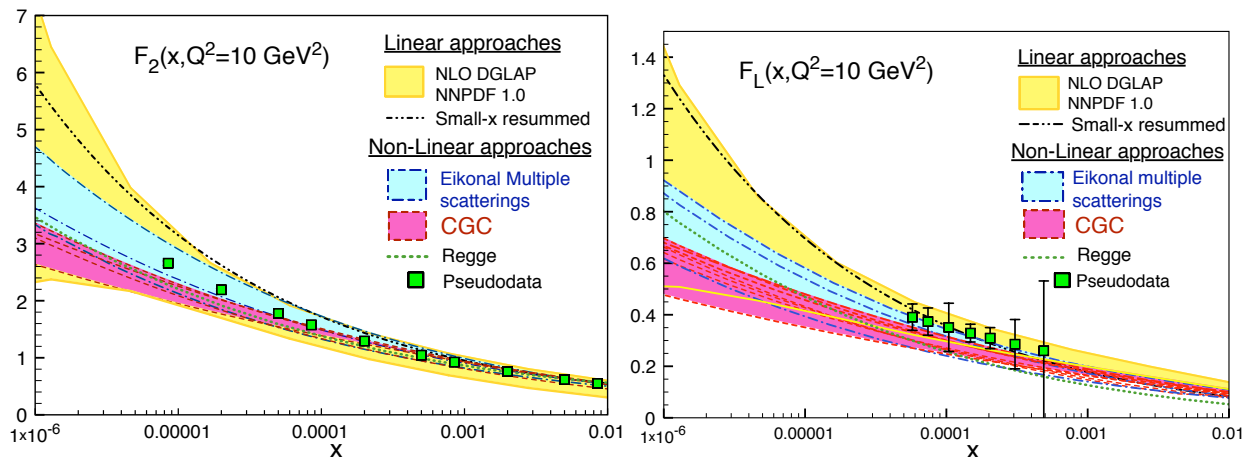


Figure 5.13: Predictions from different models for  $F_2(x, Q^2 = 10 \text{ GeV}^2)$  (plot on the left) and  $F_L(x, Q^2 = 10 \text{ GeV}^2)$  (plot on the right) versus  $x$ , together with the corresponding pseudodata. See the text for explanations.

the uncertainties improve considerably, but remain rather large at the lowest  $x$  values, due to the lack of a large lever-arm in  $Q^2$  to constrain the evolution. However, when the LHeC pseudodata on the longitudinal structure function  $F_L$  are included in addition, the additional constraints lead to a much more substantial improvement in the uncertainties on the gluon density.

As is well known from experience at HERA, the measurement of the longitudinal structure function presents many experimental challenges and involves possibly undesirable modifications to the beam energies. An alternative constraint on the gluon density from the charmed structure function  $F_2^c$  has therefore also been investigated. As discussed in detail in Subsec. 4.6.1, the LHeC will offer unique precision in the determination of the charm and beauty structure functions, extending to very small  $x$ .

In Fig. 5.15 the gluon distribution function is shown, as obtained from the NNPDF2.0 analysis. The green band corresponds to the standard analysis. The red band shows the modified analysis where additionally  $F_2^c$  pseudodata from the LHeC are included, using a novel technique based on Bayesian reweighting [422]. It is observed that the charmed structure function considerably improves the constraints on the gluon density at small values of  $x$ , especially between  $3 \times 10^{-5} - 10^{-2}$ , provided that the scattered electron acceptance extends to within around  $1^\circ$  of the beampipe. With a sufficiently good theoretical understanding, heavy flavour production data from the LHeC may thus offer an alternative to  $F_L$  for precision constraints on the gluon density at all but the lowest  $x$  values.

Given that for all models considered in Fig. 5.13 there are significant flexibilities in the initial parametrisations, it is conceivable that upon suitable changes of parameters it would be possible to obtain satisfactory fits of a wide range of models to the LHeC data. It is therefore essential to analyse in more detail the ability of the LHeC to distinguish unambiguously between different evolution dynamics. With this aim, a PDF analysis is performed including LHeC pseudodata which are generated using different scenarios for small- $x$  QCD dynamics. Pseudodata for  $F_2(x, Q^2)$  and  $F_L(x, Q^2)$  at small  $x$  are considered in a scenario in which the LHeC machine has electron energy  $E_e = 70 \text{ GeV}$  and electron acceptance for  $\theta_e \leq 179^\circ$ , for an integrated luminosity of  $1 \text{ fb}^{-1}$ . The study is carried out in the framework of the NNPDF1.0 analysis [423] and includes all HERA and fixed target data used in that analysis, in addition to LHeC pseudodata. The kinematics of the LHeC pseudodata included in the fit (together with other data included in the original NNPDF1.0 analysis) are shown in Fig. 5.16. In order to avoid correlations between low  $x$  and high  $x$  data e.g. through the momentum sum rule constraint, only LHeC pseudodata with  $x < 10^{-2}$  are considered. The average total uncertainty of the simulated  $F_2$  pseudodata is  $\sim 2\%$ , while that of  $F_L$  is  $\sim 8\%$ .

For the NNPDF fits, the input LHeC pseudodata are generated not within the DGLAP framework,



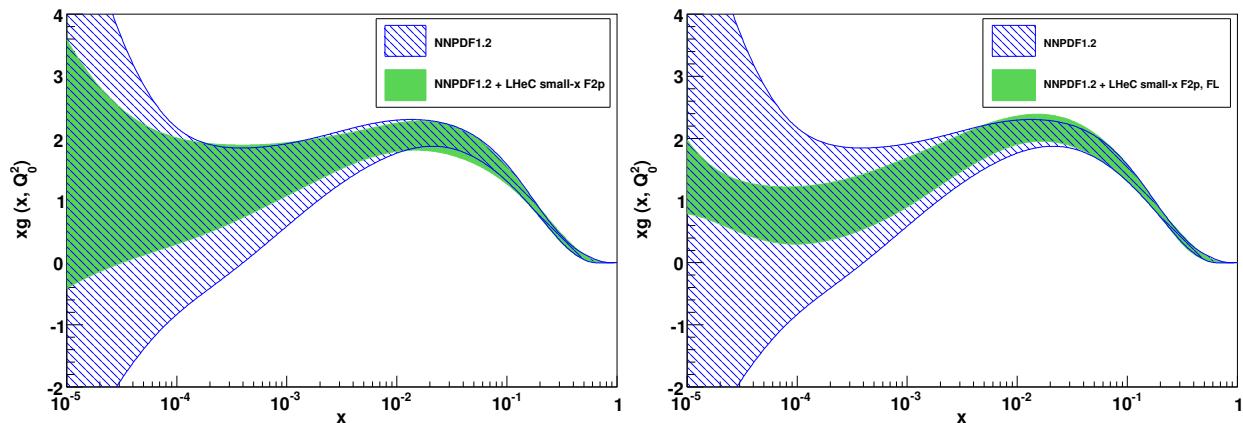


Figure 5.14: The results for the gluon distribution in the standard NNPDF1.2 DGLAP fit [419], together with the results when additionally including LHeC pseudodata for  $F_2$  (left) and for both  $F_2$  and  $F_L$  (right). The results are shown at the starting scale for DGLAP evolution,  $Q_0^2 = 2 \text{ GeV}^2$ .

2889 but rather using two different models which include saturation effects in the gluon density: the AAMS09  
 2890 model [421], which is based on non-linear Balitsky-Kovchegov evolution with a running coupling, and the  
 2891 FS04 dipole model [341]. Both of these models deviate significantly from linear DGLAP evolution in the  
 2892 LHeC regime.

2893 The global fit using the NNPDF1.0 framework with fixed-order DGLAP evolution is repeated, now  
 2894 including LHeC pseudodata generated using the scenarios including saturation effects. By assessing the quality  
 2895 of the fit with saturated LHeC pseudodata included, this study tests the sensitivity to parton dynamics be-  
 2896 yond fixed-order DGLAP. The conclusions are the same for both the AAMS09 and the FS04 models. The  
 2897 DGLAP analysis yields an acceptable fit when only the  $F_2(x, Q^2)$  LHeC pseudodata are included. This  
 2898 implies that although the underlying physical theories are different, the small- $x$  extrapolations of AAMS09  
 2899 and FS04 for  $F_2$  are sufficiently similar to DGLAP-based extrapolations for the differences to be absorbed as  
 2900 modifications to the shapes of the non-perturbative initial conditions for the PDFs at the starting scale  $Q_0^2$   
 2901 for DGLAP evolution. More sophisticated analyses, based for example on sequential kinematical cuts and  
 2902 backwards DGLAP evolution, as presented in Subsec. 5.1.2, could still be applied. However, it seems likely  
 2903 that it will not be possible unambiguously to establish non-linear effects using LHeC data on  $F_2$  alone.

2904 The situation is very different when data on the longitudinal structure function  $F_L(x, Q^2)$  are included  
 2905 in the NNPDF fit, provided the lever-arm in  $Q^2$  is large enough for the gluon sensitivity through the  $Q^2$   
 2906 evolution of  $F_2$  to conflict with that through  $F_L$ . The analysis based on linear DGLAP evolution fails to  
 2907 reproduce simultaneously  $F_2$  and  $F_L$  in all the  $Q^2$  bins, and thus the overall  $\chi^2$  is very large. The effect is  
 2908 illustrated in Fig. 5.17, where the best fits from the NNPDF DGLAP analysis are compared with the LHeC  
 2909  $F_L$  pseudodata generated from the AAMS09 model. This is a clear signal for a departure from fixed-order  
 2910 DGLAP of the simulated pseudodata. This analysis shows that the combined use of  $F_2$  and  $F_L$  data is  
 2911 a very sensitive probe of novel small- $x$  QCD dynamics, and that their measurement would be very likely  
 2912 to discriminate between different theoretical scenarios. Using  $F_2^c$  data in place of  $F_L$  may offer a similarly  
 2913 powerful means of establishing deviations from fixed-order linear DGLAP evolution at small  $x$ .

## 2914 Predictions for nuclei: impact on nuclear parton distribution functions

2915 The LHeC, as an electron-ion collider in the TeV regime, will have an enormous potential for measuring the  
 2916 nuclear parton distribution functions at small  $x$ . Let us start by a brief explanation of how the pseudodata  
 2917 for inclusive observables in  $e\text{Pb}$  collisions are obtained: To simulate an LHeC measurement of  $F_2$  in electron-  
 2918 nucleus collisions, the points  $(x, Q^2)$ , generated for  $e(50) + p(7000)$  collisions for a high acceptance, low

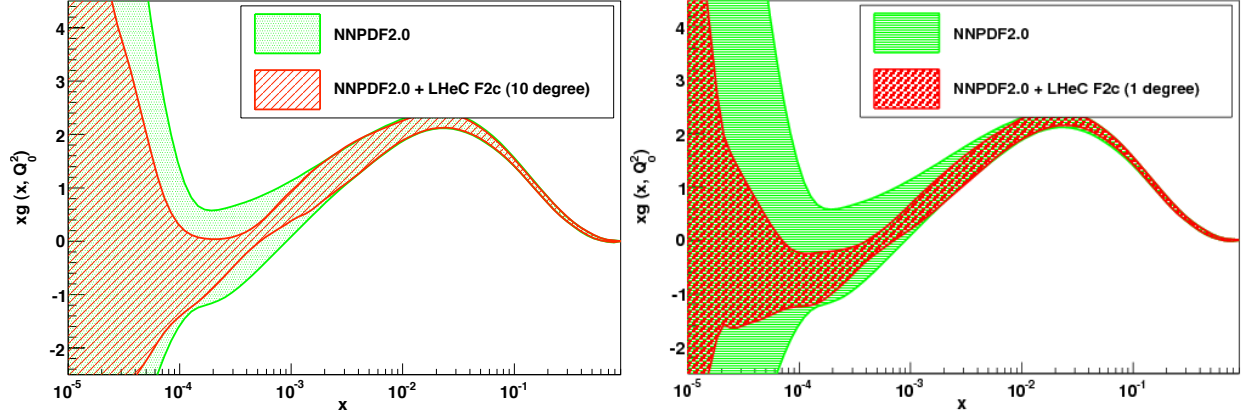


Figure 5.15: The effect on the extracted gluon distribution function of the inclusion of the LHeC pseudodata on the charmed structure function in the NNPDF global analysis. Left plot: scattered electron acceptance extending to within  $10^\circ$  of the beampipe. Right plot:  $1^\circ$  acceptance. The results are shown at the starting scale for DGLAP evolution,  $Q_0^2 = 2 \text{ GeV}^2$ .

2919 luminosity scenario, as explained in Subsection 4.1.4, are considered. Among them, we keep only those  
 2920 points at small  $x \leq 0.01$  and not too large  $Q^2 < 1000 \text{ GeV}^2$  with  $Q^2 \leq sx$ , for a Pb beam energy of  
 2921 2750 GeV per nucleon<sup>9</sup>. Under the assumption that the instantaneous luminosity per nucleon is the same  
 2922 in  $ep$  and  $eA$  [424], the number of events is scaled by a factor  $1/(5 \times 50 \times A)$ , with 50 coming from the  
 2923 transition from a high luminosity to a low luminosity scenario, and 5 being a crudely estimated reduction  
 2924 factor accounting for the shorter running time for ions than for proton.

2925 At each point of the grid,  $\sigma_r$  and  $F_2$  are generated using the dipole model of [336, 425] to get the  
 2926 central value. Then, for every point, the statistical error in  $ep$  is scaled by the previously mentioned factor  
 2927  $1/(5 \times 50 \times A)$ , and corrected for the difference in  $F_2$  or  $\sigma_r$  between the (Glauberized) 5-flavor GBW  
 2928 model [425] and the model used for the  $ep$  simulation. The fractional systematic errors are taken to be  
 2929 the same as for  $ep$  - as has been achieved in previous DIS experiments on nuclear targets<sup>10</sup>. An analogous  
 2930 procedure is applied when obtaining the nuclear pseudodata for  $F_2^c$  and  $F_2^b$ , considering the same tag and  
 2931 background rejection efficiencies as in the  $ep$  simulation.

2932 To generate LHeC  $F_L$  pseudodata for a heavy ion target, a dedicated simulation of  $e + p(2750)$  collisions  
 2933 has been performed, at three different energies: 10, 25 and 50 GeV for the electron, with assumed luminosities  
 2934 5, 10 and  $100 \text{ pb}^{-1}$  respectively, see Subsec. 4.1.5. Then, for each point in the simulated grid,  $F_L$  values  
 2935 for protons and nuclei are generated using the (Glauberized) 5-flavor GBW model [425]. The relative  
 2936 uncertainties are taken to be exactly the same as in the  $ep$  simulation, as explained above.

2937 In Fig. 5.18 we show several predictions for the nuclear suppression factor, Eq. (5.5), with respect to  
 2938 the proton, for the total and longitudinal structure functions,  $F_2$  and  $F_L$  respectively, in  $e\text{Pb}$  collisions at  
 2939 an example  $Q^2 = 5 \text{ GeV}^2$  and for  $10^{-5} < x < 0.1$ . Predictions based on global DGLAP analyses of existing  
 2940 data at NLO: nDS, HKN07, EPS09 and DSSZ [?, 153, 405, 406], plus those from models using the relation  
 2941 between diffraction and nuclear shadowing, AKST and FGS10 [302, 407], are shown together with the LHeC  
 2942 pseudodata. Brief explanations on the different models can be found in Subsec. 5.1.4. Clearly, the accuracy  
 2943 of the data at the LHeC will offer huge possibilities for discriminating between different models and for  
 2944 constraining the dynamics underlying nuclear shadowing at small  $x$ .

2945 In order to better quantify how the LHeC would improve the present situation concerning nuclear PDFs

<sup>9</sup>In this document we have restricted the discussion and results to Pb because it is the presently accelerated ion at the LHC. But simulations also exist for a Ca nucleus of 3500 GeV per nucleon, and they can be easily produced for other nuclei as Ar (3150 GeV per nucleon), whose acceleration at the LHC has been discussed as part of the AA program [382].

<sup>10</sup>A significant difference in the systematics may eventually come from the different size of the QED radiative corrections for protons and nuclei, an important point which remains to be addressed in future studies.

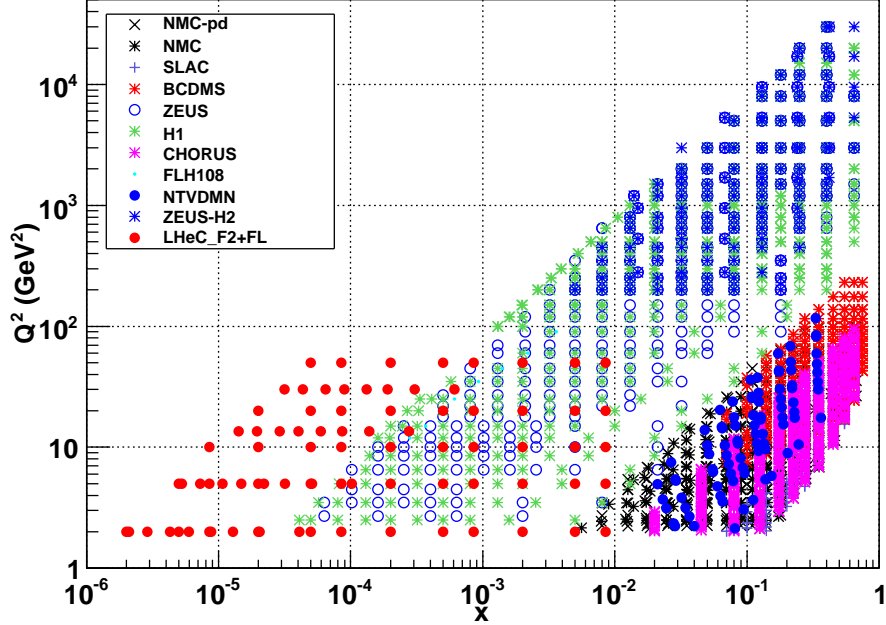


Figure 5.16: The kinematic coverage of the LHeC pseudodata used in the present studies, together with the data already included in the reference NNPDF1.0 dataset.

2946 in global DGLAP analyses (see the uncertainty band in Fig. 5.12), nuclear LHeC pseudodata have been  
 2947 included in the global EPS09 analysis [153]. The DGLAP evolution was carried out at NLO accuracy, in the  
 2948 variable-flavor-number scheme (SACOT prescription) with the CTEQ6.6 [359] set for free proton PDFs as a  
 2949 baseline. See [153] and references therein for further details. The only difference compared with the original  
 2950 EPS09 setup is that one additional gluon parameter,  $x_a$ , has been varied (this parameter was originally  
 2951 frozen in EPS09), and the only additionally weighted data set was the PHENIX data on  $\pi^0$  production at  
 2952 mid-rapidity [426] in dAu collisions at RHIC.

2953 Two different fits have been performed: the first one (Fit 1) includes pseudodata on the total reduced  
 2954 cross section. The results of the fit are shown in Fig. 5.19 in terms of the nuclear modification factors for  
 2955 the parton densities. A large improvement in the determination of sea quark and gluon densities at small  $x$   
 2956 is evident.

2957 The second fit (Fit 2) includes not only nuclear LHeC pseudodata on the total reduced cross section  
 2958 but also on its charm and beauty components. These data provide direct information on the nuclear effects  
 2959 on charm and beauty parton densities, which are generated mainly dynamically from the gluons through  
 2960 DGLAP evolution. Thus, the inclusion of such pseudodata further improves the determination of the nuclear  
 2961 effects on the gluon at small  $x$ , as illustrated in Fig. 5.20.

2962 In both Figs. 5.19 and 5.20 a sizable reduction of the uncertainties in the sea quark and gluon nuclear  
 2963 parton distributions at large  $x > 0.1$  can also be observed. This improvement is basically due to the  
 2964 constraints imposed by sum rules and to the fact that DGLAP evolution links large and small  $x$ . Although  
 2965 the study of parton distributions at large  $x$  is not the subject of this chapter, it is worth commenting  
 2966 that  $F_2$  could be measured in  $eA$  collisions at the LHeC with a statistical accuracy better than a few  
 2967 percent up to  $x \sim 0.6$  but for large  $Q^2 > 1000 \text{ GeV}^2$ . On the other hand, flavor decomposition will only  
 2968 be accessible for  $x < 0.1$ . Therefore, the LHeC will provide additional information on the antishadowing  
 2969 ( $R > 1$ ,  $0.1 < x < 0.3$ ) and - with less precision - on the EMC-effect ( $R < 1$ ,  $0.3 < x < 0.8$ ) regions. The  
 2970 latter is valence-dominated and there exist data from fixed target experiments, though at much smaller  $Q^2$ ,  
 2971 so at the LHeC the validity of leading-twist DGLAP evolution will be tested.

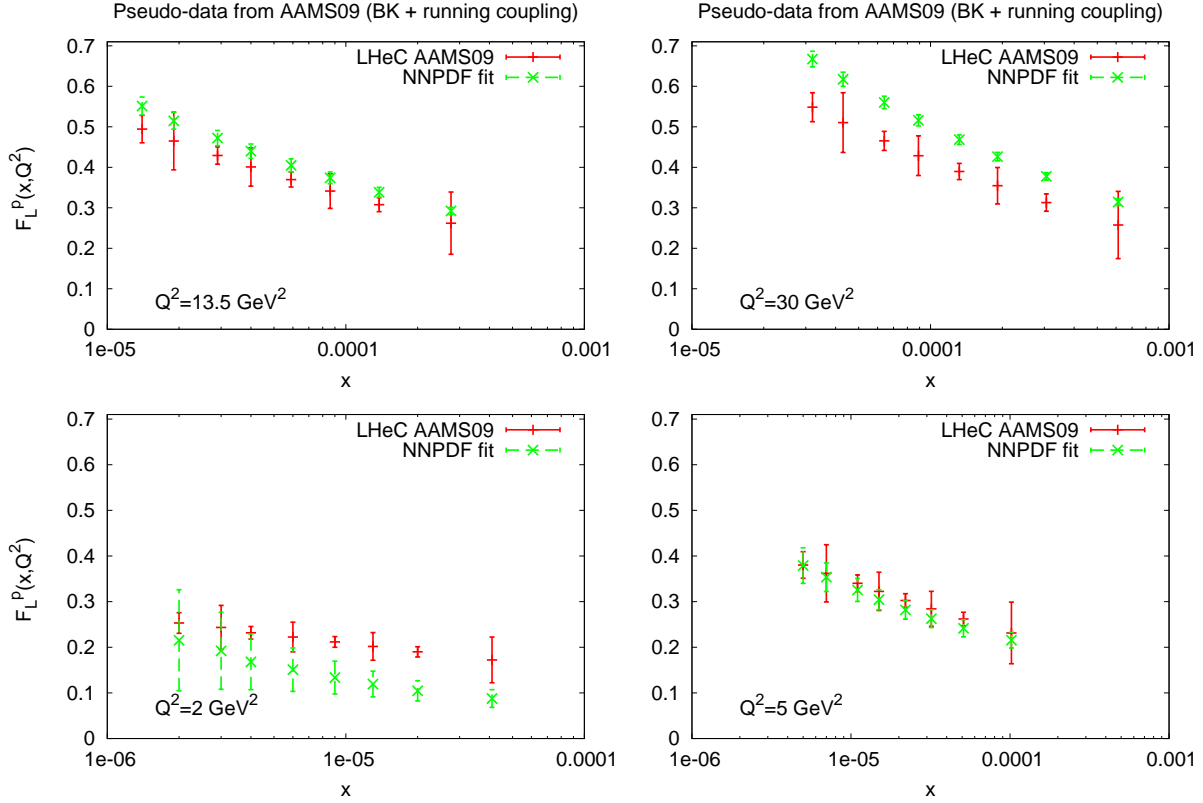


Figure 5.17: The results for  $F_L$  obtained from the best NLO DGLAP fit to the standard NNPDF1.2 data set, together with the LHeC pseudodata for  $F_2(x, Q^2)$  and  $F_L(x, Q^2)$  generated with the (saturating) AAMS09 model. The fit results are compared with the input AAMS09  $F_L$  pseudodata.

2972 Furthermore, the large lever-arm in  $Q^2$  opens the possibility of measuring CC events in electron scattering  
 2973 on nuclear targets, thus helping to improve the loose constraints on the flavour decomposition of the nuclear  
 2974 parton densities coming from existing DIS and DY data. In this respect (see the comments in Subsec.  
 2975 5.1.4) the LHeC may help to clarify the issue of the compatibility of the nuclear corrections extracted in  
 2976 neutrino-nucleus collisions with those coming from electron- or muon-nucleus collisions<sup>11</sup>.

2977 In conclusion, the precision and large lever-arm in  $x$  and  $Q^2$  of the nuclear data at the LHeC will offer huge  
 2978 possibilities for discriminating different models and for constraining the parton densities in global DGLAP  
 2979 analyses. Besides measurements of the reduced cross section, data on its charm and bottom components  
 2980 and on  $F_L$  will help to constrain the nuclear effects on PDFs, see e.g. the recent work in [428, 429].

### 2981 5.2.3 Exclusive Production

#### 2982 Introduction

2983 Exclusive processes such as the electroproduction of vector mesons and photons,  $\gamma^*N \rightarrow VN(V = \rho^0, \phi, \gamma)$ , or  
 2984 photoproduction of heavy quarkonia,  $\gamma N \rightarrow VN(V = J/\psi, \Upsilon)$  - see Fig. 5.21 - provide information on nucleon  
 2985 structure and small- $x$  dynamics which is complementary to that obtained in inclusive measurements [339].  
 2986 The exclusive production of  $J/\psi$  and  $\rho$  mesons in  $ep$  collisions and Deeply-Virtual Compton Scattering

<sup>11</sup>Note that the nuclear modifications of the structure function  $F_2$  in these two types of process are expected to differ due to the different coupling to quarks [427].

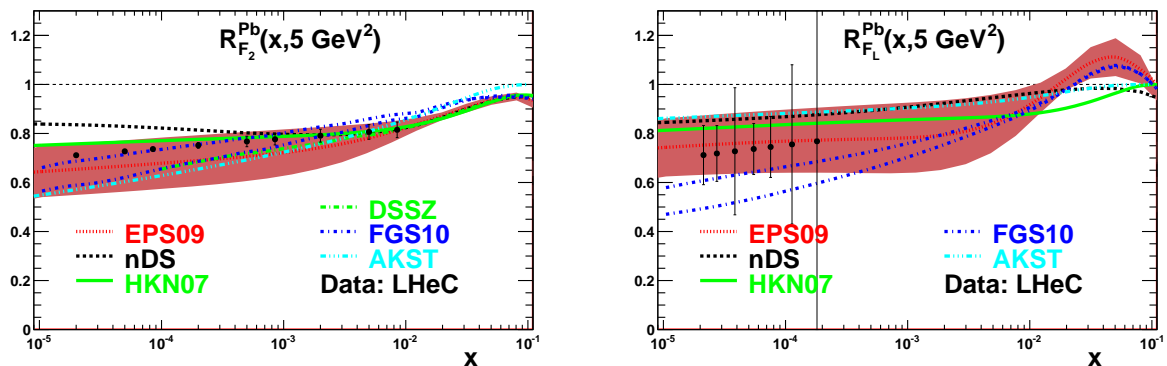


Figure 5.18: Predictions from different models for the nuclear modification factor, Eq. (5.5) for Pb with respect to the proton, for  $F_2(x, Q^2 = 5 \text{ GeV}^2)$  (plot on the left) and  $F_L(x, Q^2 = 5 \text{ GeV}^2)$  (plot on the right) versus  $x$ , together with the corresponding LHeC pseudodata. Dotted lines correspond to the nuclear PDF set EPS09 [153], dashed ones to nDS [405], solid ones to HKN07 [406], dashed-dotted ones to FGS10 [407], dashed-dotted-dotted ones to AKST [302] and long dashed-dotted ones to DSSZ [?] (only for  $F_2$ ). The band corresponds to the uncertainty in the Hessian analysis in EPS09 [153].

2987 (DVCS,  $ep \rightarrow e\gamma p$ ), have been particularly prominent in the development of our understanding of HERA  
 2988 physics [430].

2989 Diffractive channels such as these are favourable, since the underlying exchange crudely equates to a  
 2990 pair of gluons, making the process sensitive to the square of the gluon density [431], in place of the linear  
 2991 dependence for  $F_2$  or  $F_L$ . With a sufficiently good theoretical understanding of the exclusive production  
 2992 mechanism, this may enhance substantially the sensitivity to non-linear evolution and saturation phenomena.  
 2993 As already shown at HERA,  $J/\Psi$  production in particular is a potentially very clean probe of the gluonic  
 2994 structure of the hadron [356, 431]. The same exclusive processes can be measured in deep inelastic scattering  
 2995 off nuclei, where the gluon density is modified by nuclear effects [432]. In addition, exclusive processes  
 2996 give access to the spatial distribution of the gluon density, parametrized by the impact parameter [433]  
 2997 of the collision. The correlations between the gluons coupling to the proton contain information on the  
 2998 three-dimensional structure of the nucleon or nucleus, which is encoded in the Generalised Parton Densities  
 2999 (GPDs). The GPDs combine aspects of parton densities and elastic form factors and have emerged as a key  
 3000 concept for describing nucleon structure in QCD (see [55, 434, 435] for a review).

3001 Exclusive processes can be treated conveniently within the dipole picture described in Subsec. 5.1.2. In  
 3002 this framework, the cross section can be represented as a product of three factorisable terms: the splitting  
 3003 of an incoming photon into a  $q\bar{q}$  dipole; the ‘dipole’ cross section for the interaction of this  $q\bar{q}$  pair with the  
 3004 proton and, in the case of vector mesons, a wave function term for the projection of the dipole onto the  
 3005 meson. As discussed in Subsec. 5.1.2 the dipole formalism is particularly convenient since saturation effects  
 3006 can be easily incorporated.

### 3007 Generalised Parton Densities and Spatial Structure

3008 At sufficiently large  $Q^2$  the exclusively produced meson or photon is in a configuration of transverse size  
 3009 much smaller than the typical hadronic size,  $r_\perp \ll R_{\text{hadron}}$ . As a result its interaction with the target can  
 3010 be described using perturbative QCD [436]. A QCD factorisation theorem [437] states that the exclusive  
 3011 amplitudes in this regime can be factorised into a perturbative QCD scattering process and certain universal  
 3012 process-independent functions describing the emission and absorption of the active partons by the target,  
 3013 the generalized parton distributions (GPDs).

3014 Let us briefly review (see [55, 434, 435] for details) the definition of GPDs and their relation to the  
 3015 ordinary parton densities discussed in detail in Chapter 4. The parton distributions of the proton (or any

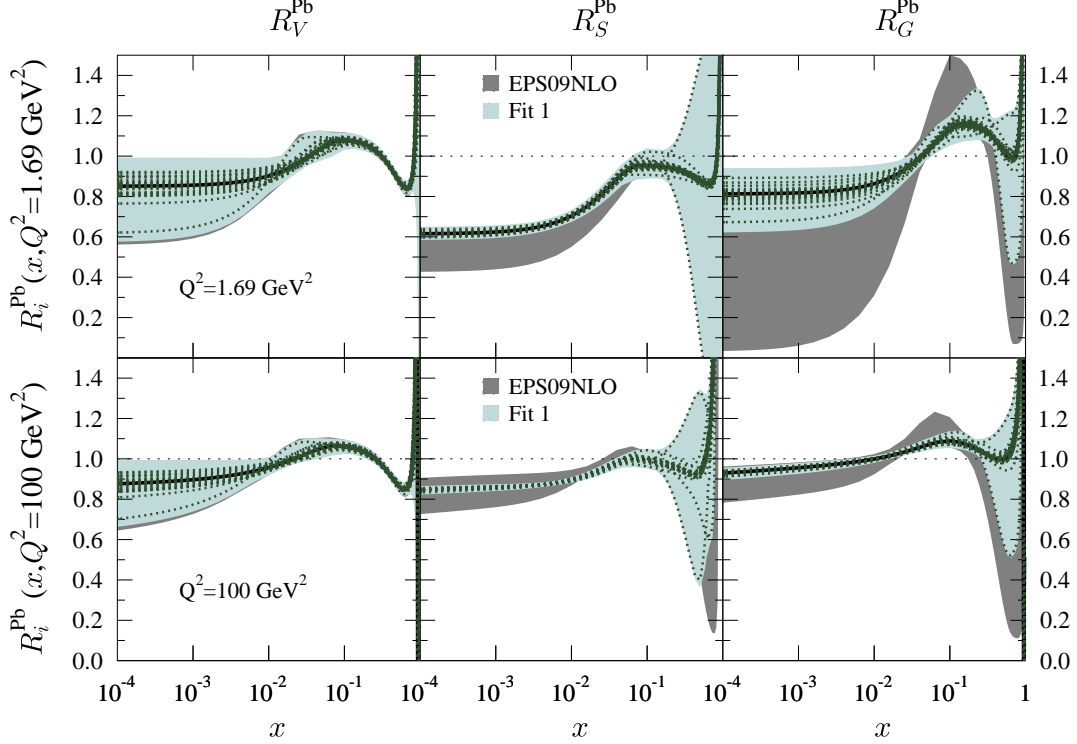


Figure 5.19: Ratio of parton densities for protons bound in Pb to those in a free proton, for valence  $u$  (left),  $\bar{u}$  (middle) and  $g$  (right), at  $Q^2 = 1.69$  (top) and  $100$  (bottom)  $\text{GeV}^2$ . The dark grey band corresponds to the uncertainty band using the Hessian method in the original EPS09 analysis [153], while the light blue band corresponds to the uncertainty obtained after including nuclear LHeC pseudodata on the total reduced cross sections (Fit 1). The dotted lines indicate the values corresponding to the different nPDF sets in the EPS09 analysis [153].

3016 other hadron) are given by the diagonal matrix elements  $\langle P, \lambda | \hat{O} | P, \lambda \rangle$ , where  $P$  and  $\lambda$  are the 4-momentum  
3017 and helicity of the proton, and  $\hat{O}$  is a twist-2 quark or gluon operator. However, there is new information in  
3018 the GPDs defined in terms of the off-diagonal matrix elements  $\langle P', \lambda' | \hat{O} | P, \lambda \rangle$ . Unlike the diagonal PDFs,  
3019 the GPDs cannot be regarded as parton densities, but are to be interpreted as probability amplitudes.

3020 The physical significance of GPDs is best seen using light-cone coordinates,  $z^\pm = (z^0 \pm z^3)/\sqrt{2}$ , and in  
3021 the light-cone gauge,  $A^+ = 0$ . It is conventional to define the generalised quark distributions in terms of  
3022 quark operators at light-like separation, resulting in

$$F_q(x, \xi, t) = \frac{1}{2\bar{P}^+} \left[ H_q((x, \xi, t) \bar{u}(P') \gamma^+ u(P) + E_q((x, \xi, t) \bar{u}(P') \frac{i\sigma^{+\alpha} \Delta_\alpha}{2m} u(P) \right] \quad (5.6)$$

3023 with  $\bar{P} = (P + P')/2$  and  $\Delta = P' - P$ , and where we have suppressed the helicity labels of the protons  
3024 and spinors. We now have two extra kinematic variables:  $t = \Delta^2$ ,  $\xi = -\Delta^+/(P + P')^+$ . We see that  
3025  $-1 \leq \xi \leq 1$ . Similarly, we may define GPDs  $\tilde{H}_q$  and  $\tilde{E}_q$  with an additional  $\gamma_5$  between the quark operators  
3026 in Eq. (5.6); and also an analogous set of gluon GPDs,  $H_g$ ,  $E_g$ ,  $\tilde{H}_g$  and  $\tilde{E}_g$ . These definitions correspond to  
3027 helicity-conserving GPDs. Analogous definitions exist for helicity-flip (transversity), chiral-odd GPDs  $H_T$ ,  
3028  $E_T$ ,  $\tilde{H}_T$ ,  $\tilde{E}_T$  [?].

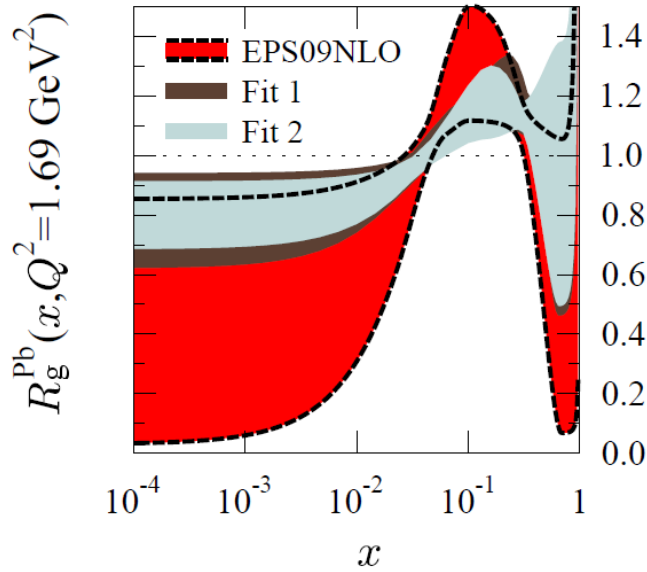


Figure 5.20: Ratio of the gluon density for protons bound in Pb to that of a free proton at  $Q^2 = 1.69 \text{ GeV}^2$ . The red band corresponds to the uncertainty using the Hessian method in the original EPS09 analysis [153], while the dark brown band corresponds to the uncertainty obtained after including nuclear LHeC pseudodata on the total reduced cross sections (Fit 1), and the light blue band shows the uncertainty obtained after further including pseudodata on charm and beauty reduced cross sections (Fit 2).

3029 For  $P' = P$ ,  $\lambda' = \lambda$  the matrix elements reduce to the ordinary PDFs:

$$\begin{aligned}
 H_q(x, 0, 0) &= q(x), & H_q(-x, 0, 0) &= -\bar{q}(x), & H_g(x, 0, 0) &= xg(x), \\
 \tilde{H}_q(x, 0, 0) &= \Delta q(x), & \tilde{H}_q(-x, 0, 0) &= \Delta \bar{q}(x), & \tilde{H}_g(x, 0, 0) &= x\Delta g(x), \\
 H_T(x, 0, 0) &= \Delta_T q(x), & & & & 
 \end{aligned}
 \tag{5.7}$$

3030 where  $\Delta q$  ( $\Delta_T q(x)$ ) is the difference between quark densities with opposite helicities (transversities). No  
 3031 corresponding relations exist for  $E$ ,  $\tilde{E}$ ,  $E_T$ ,  $\tilde{H}_T$ ,  $\tilde{E}_T$  as they decouple in the forward limit,  $\Delta = 0$ . For  
 3032 properties of all these distributions, see the reviews [55, 434, 435].

3033 For the evolution of the GPDs, there are two types of domain: (i) the time-like domain, with  $|x| < |\xi|$ ,  
 3034 where the GPDs describe the wave functions of a t-channel  $q\bar{q}$  (or gluon) pair and evolve according to modified  
 3035 ERBL equations [?, ?]; (ii) the space-like domain, with  $|x| > |\xi|$ , where the GPDs generalise the familiar  $q$ ,  
 3036  $\bar{q}$  (and gluon) PDFs and describe DVCS and exclusive vector meson production, and evolve according to  
 3037 modified DGLAP equations. The splitting functions for the evolutions of GPDs are known to NLO [?].

3038 The GPDs contain new information about proton structure and should be determined from experiment.  
 3039 We can parametrise them in terms of 'double distributions' [?, ?], which reduce to diagonal PDFs as  $\xi \rightarrow$   
 3040 0. With an additional physically reasonable 'Regge' assumption of no extra singularity at  $\xi = 0$ , GPDs  
 3041 at low  $\xi$  are uniquely given in terms of diagonal PDFs to  $\mathcal{O}(\xi)$  [?]. Alternatively, flexible  $SO(3)$ -based  
 3042 parametrisations have been used to determine GPDs from DVCS data [?].

3043 The Fourier transform of the GPDs with respect to the transverse momentum transferred to the nucleon  
 3044 describes the transverse spatial distribution of partons (illustrated in Fig. 5.3) with a given longitudinal

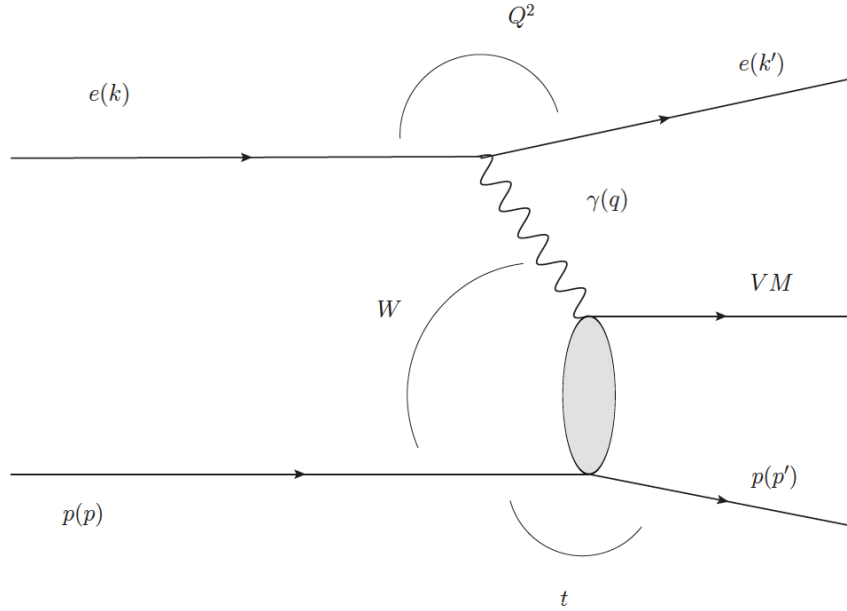


Figure 5.21: Schematic illustration of the exclusive vector meson production process and the kinematic variables used to describe it in photoproduction ( $Q^2 \rightarrow 0$ ) and DIS (large  $Q^2$ ). The outgoing particle labelled ‘VM’, may be either a vector meson with  $J^{PC} = 1^{--}$  or a photon.

3045 momentum fraction  $x$  [?, ?, 438]. The transverse spatial distributions of quarks and gluons are fundamental  
3046 characteristics of the nucleon, which reveal the size of the configurations in its partonic wave function and  
3047 allow the study of the non-perturbative dynamics governing their change with  $x$ , such as Gribov diffusion,  
3048 chiral dynamics, and other phenomena. The nucleon transverse gluonic size is also an essential input in  
3049 studies of saturation at small  $x$ . It determines the initial conditions of the non-linear QCD evolution equations  
3050 and thus directly influences the impact parameter dependence of the saturation scale for the nucleon [355,  
3051 439], which in turn predicates its nuclear enhancement [440]. Information on the nucleon transverse quark  
3052 and gluon distributions is further required in the phenomenology of high-energy  $pp$  collisions with hard  
3053 processes, including those with new particle production, where it determines the underlying event structure  
3054 (centrality dependence) in inclusive scattering [441] and the rapidity gap survival probability in hard single  
3055 diffraction [442] and central exclusive diffraction [443, 444]. In view of its considerable interest, the transverse  
3056 quark/gluon imaging of the nucleon with exclusive processes has been recognized as an important objective  
3057 of nucleon structure and small- $x$  physics.

3058 Mapping the transverse spatial distribution of quarks and gluons requires measurement of the  $t$ -dependence  
3059 of hard exclusive processes up to large values of  $|t|$ , of the order of  $1 \text{ GeV}^2$ . Studies of the  $Q^2$ -dependence  
3060 and comparisons between different channels provide crucial tests of the reaction mechanism and the uni-  
3061 versality of GPDs. Vector meson production at small  $x$  and heavy quarkonium photoproduction at high  
3062 energies probe the gluon GPD of the target, while real photon production (DVCS) involves the singlet quark  
3063 as well as the gluon GPDs. Measurements of exclusive  $J/\psi$  photo/electroproduction [445, 446] and  $\rho^0$  and  
3064  $\phi$  electroproduction at HERA have confirmed the applicability of the factorized QCD description through  
3065 several model-independent tests, and have provided basic information on the nucleon gluonic size in the  
3066 region  $10^{-4} < x < 10^{-2}$  and its change with  $x$  [339]. Measurements of DVCS at HERA [447, 448] hint that  
3067 the transverse distribution of singlet quarks may extend further than that of gluons. While these experi-  
3068 ments have given important insight into transverse nucleon structure, the interpretation of the HERA data  
3069 is limited by the low statistics which preclude a fully differential analysis. A major source of systematic  
3070 uncertainty at larger  $t$  arises from the lack of a complete separation between elastically scattered protons



3071 and proton excitations, illustrating the importance of good scattered proton detection at the LHeC.

3072 As discussed in the following, the LHeC would enable a comprehensive program of gluon and singlet  
 3073 quark transverse imaging through exclusive processes, with numerous applications to nucleon structure and  
 3074 small- $x$  physics. The high statistics would permit fully differential measurements of exclusive channels, as  
 3075 needed to understand the reaction mechanism. For example, measurements of the  $t$ -distributions for fixed  
 3076  $x$  differentially in  $Q^2$  are needed to confirm the dominance of small-size configurations. The LHeC would  
 3077 also push such measurements to the region  $Q^2 \sim \text{few} \times 10 \text{ GeV}^2$  where finite-size (higher-twist) effects are  
 3078 small and the effects of QCD evolution can be cleanly identified. Measurements of gluonic exclusive channels  
 3079 ( $J/\psi, \phi, \rho^0$ ) at the LHeC would provide gluonic transverse images of the nucleon down to  $x \sim 10^{-6}$  with  
 3080 unprecedented accuracy, testing theoretical ideas about diffusion dynamics in the wave function. Because  
 3081 exclusive cross sections are proportional to the square of the gluon GPD (i.e. the gluon density), such  
 3082 measurements would also offer new insight into non-linear effects in QCD evolution, and enable new tests of  
 3083 the approach to saturation by measuring the impact parameter dependence of the saturation scale. Along  
 3084 these lines, saturation effects in the exclusive vector meson production on protons and nuclei have been  
 3085 studied in [432, 449–451]. Furthermore, measurements of DVCS would provide additional information on  
 3086 the nucleon singlet quark size and its dependence on  $x$ . Besides its intrinsic interest for nucleon structure  
 3087 and small- $x$  physics, this information would greatly advance our theoretical understanding of the transverse  
 3088 geometry of high-energy  $pp$  collisions at the LHC. We note that these exclusive measurements at the LHeC  
 3089 would complement similar measurements at moderately small  $x$  ( $0.003 < x < 0.2$ ) with the COMPASS  
 3090 experiment at CERN and in the valence region  $x > 0.1$  with the JLab 12 GeV Upgrade, providing a  
 3091 comprehensive picture of the nucleon spatial structure.

3092 Further interesting information comes from hard exclusive measurements accompanied by the diffractive  
 3093 dissociation of the nucleon,  $\gamma^* N \rightarrow V + Y$  ( $Y = \text{low-mass proton dissociation state}$ ). The ratio of inelastic to  
 3094 elastic diffraction in these processes provides information on the quantum fluctuations of the gluon density,  
 3095 which reveals the quantum-mechanical nature of the non-perturbative colour fields in the nucleon and can  
 3096 be related to dynamical models of low-energy nucleon structure [452]. HERA results are in qualitative  
 3097 agreement with such model predictions but do not permit a quantitative analysis. These measurements of  
 3098 exclusive diffraction at the LHeC, and similar ones for  $eA$  collisions, would allow for detailed quantitative  
 3099 studies of all these new aspects of nucleon and nuclear structure.

### 3100 Exclusive Production Formalism in the Dipole Approach

3101 For the exclusive production of vector mesons, a QCD factorization theorem has been demonstrated (for  $\sigma_L$ )  
 3102 in [436]. The dipole model follows from this QCD factorization theorem in the LO approximation. Within  
 3103 the dipole model, see Subsec. 5.1.2, the amplitude for the exclusive diffractive production of a particle  $E$ ,  
 3104  $\gamma^* p \rightarrow Ep$ , shown in Fig. 5.22(a), can be expressed as

$$3105 \mathcal{A}_{T,L}^{\gamma^* p \rightarrow E+p}(x, Q, \Delta) = i \int d^2 \mathbf{r} \int_0^1 \frac{dz}{4\pi} \int d^2 \mathbf{b} (\Psi_E^* \Psi)_{T,L} e^{-i[\mathbf{b} - (1-z)\mathbf{r}] \cdot \Delta} \frac{d\sigma_{q\bar{q}}}{d^2 \mathbf{b}}. \quad (5.8)$$

3106 Here  $E = V$  for vector meson production, or  $E = \gamma$  for deeply virtual Compton scattering (DVCS). In Eq.  
 3107 (5.8),  $z$  is the fraction of the photon's light-cone momentum carried by the quark,  $r = |\mathbf{r}|$  is the transverse  
 3108 size of the  $q\bar{q}$  dipole, while  $\mathbf{b}$  is the impact parameter, that is,  $b = |\mathbf{b}|$  is the transverse distance from the centre  
 3109 of the proton to the centre-of-mass of the  $q\bar{q}$  dipole; see Fig. 5.22(a). The transverse momentum lost by the  
 3110 outgoing proton,  $\Delta$ , is the Fourier conjugate variable to the impact parameter  $\mathbf{b}$ , and  $t \equiv (p - p')^2 = -\Delta^2$ .  
 3111 The forward overlap function between the initial-state photon wave function and the final-state vector meson  
 3112 or photon wave function in Eq. (5.8) is denoted  $(\Psi_E^* \Psi)_{T,L}$ , while the factor  $\exp[i(1-z)\mathbf{r} \cdot \Delta]$  originates from  
 3113 the non-forward wave function [453]. The differential cross section for an exclusive diffractive process is  
 obtained from the amplitude, Eq. (5.8), by

$$\frac{d\sigma_{T,L}^{\gamma^* p \rightarrow E+p}}{dt} = \frac{1}{16\pi} \left| \mathcal{A}_{T,L}^{\gamma^* p \rightarrow E+p} \right|^2, \quad (5.9)$$

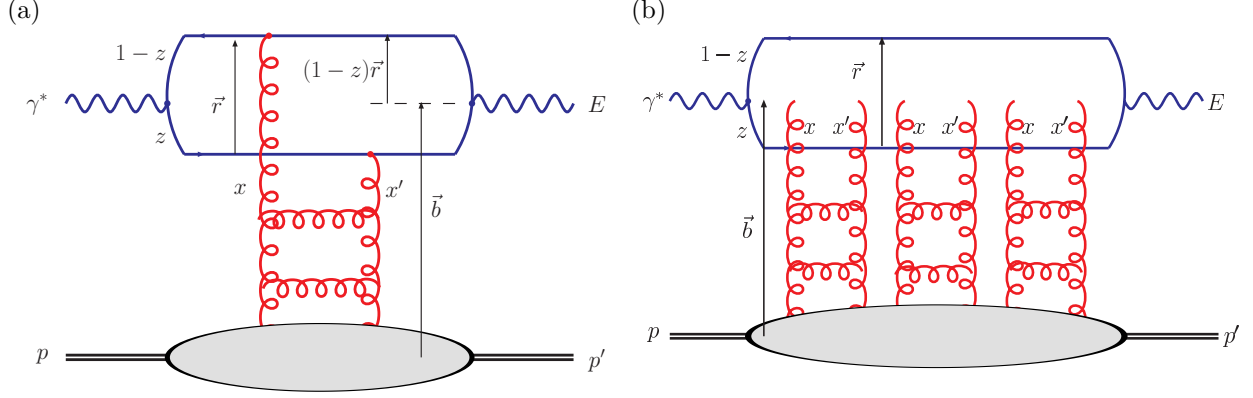


Figure 5.22: Parton level diagrams representing the  $\gamma^*p$  scattering amplitude proceeding via (a) single-Pomeron and (b) multi-Pomeron exchange, where the perturbative QCD Pomeron is represented by a gluon ladder. For exclusive diffractive processes, such as vector meson production ( $E = V$ ) or DVCS ( $E = \gamma$ ), we have  $x' \ll x \ll 1$  and  $t = (p - p')^2$ . These diagrams are related through the optical theorem to inclusive DIS, where  $E = \gamma^*$ ,  $x' = x \ll 1$  and  $p' = p$ .

3114 up to corrections from the real part of the amplitude and from skewedness ( $x' \ll x \ll 1$  for the variables  
3115 shown in figure 5.22a). Taking the imaginary part of the forward scattering amplitude immediately gives  
3116 the formula for the total  $\gamma^*p$  cross section (or equivalently, the proton structure function  $F_2 = F_T + F_L$ ) via  
3117 the optical theorem:

$$\sigma_{T,L}^{\gamma^*p}(x, Q) = \text{Im} \mathcal{A}_{T,L}^{\gamma^*p \rightarrow \gamma^*p}(x, Q, \Delta = 0) = \sum_f \int d^2\mathbf{r} \int_0^1 \frac{dz}{4\pi} (\Psi^* \Psi)_{T,L}^f \int d^2\mathbf{b} \frac{d\sigma_{q\bar{q}}}{d^2\mathbf{b}}. \quad (5.10)$$

3118 The dipole picture therefore provides a unified description of both exclusive diffractive processes and inclusive  
3119 DIS at small  $x$ .

3120 The unknown quantity common to Eqs. (5.8) and (5.10) is the  $b$ -dependent dipole–proton cross section,

$$\frac{d\sigma_{q\bar{q}}}{d^2\mathbf{b}} = 2 \mathcal{N}(x, r, b), \quad (5.11)$$

3121 where  $\mathcal{N}$  is the imaginary part of the dipole–proton scattering amplitude, which can vary between zero and  
3122 one, with  $\mathcal{N} = 1$  corresponding to the unitarity (“black disk”) limit. The scattering amplitude  $\mathcal{N}$  encodes  
3123 the information about the details of the strong interaction between the dipole and the target (proton or  
3124 nucleus). It is generally parameterised according to some theoretically-motivated functional form, with the  
3125 parameters fitted to data. Most dipole models assume a factorised  $b$  dependence,  $\mathcal{N}(x, r, b) = T(b)\mathcal{N}(x, r)$ ,  
3126 with  $\mathcal{N}(x, r) \in [0, 1]$  and, for example,  $T(b) = \Theta(R_p - b)$ , so that the  $b$ -integrated  $\sigma_{q\bar{q}} = (2\pi R_p^2)\mathcal{N}(x, r)$ .  
3127 However, the “saturation scale” is strongly dependent on impact parameter and the chosen of  $b$ -dependence  
3128 must be made consistent with the  $t$ -dependence of exclusive diffraction at HERA. This matching is compli-  
3129 cated by the non-zero effective “Pomeron slope”  $\alpha'_p$  measured at HERA, which implies a correlation between  
3130 the  $x$ - and  $b$ -dependences of  $\mathcal{N}(x, r, b)$ . Therefore, for accurate results,  $\mathcal{N}(x, r, b)$  should be determined from  
3131 the simultaneous description of inclusive DIS and exclusive diffractive processes.

3132 An impact-parameter-dependent saturation (“b-sat”) model [355, 356] has been shown to describe very  
3133 successfully a broad range of HERA data on exclusive diffractive vector meson ( $J/\psi$ ,  $\phi$ ,  $\rho$ ) production and  
3134 DVCS (see also the rather different approach in [454]), including almost all aspects of the  $Q^2$ ,  $W$  and  $t$   
3135 dependence with the exception of  $\alpha'_p$ , together with the inclusive structure functions  $F_2$ ,  $F_2^{c\bar{c}}$ ,  $F_2^{b\bar{b}}$  and  $F_L$ .  
3136 The “b-Sat” parameterisation is based on LO DGLAP evolution of an initial gluon density,  $xg(x, \mu_0^2) =$   
3137  $A_g x^{-\lambda_g} (1 - x)^{5.6}$ , with a Gaussian impact parameter dependence,  $T(b) \propto \exp(-b^2/2B_G)$ . The dipole

3138 scattering amplitude is parametrized as

$$\mathcal{N}(x, r, b) = 1 - \exp\left(-\frac{\pi^2}{2N_c} r^2 \alpha_S(\mu^2) xg(x, \mu^2) T(b)\right), \quad (5.12)$$

3139 where the scale  $\mu^2 = 4/r^2 + \mu_0^2$ ,  $B_G = 4 \text{ GeV}^{-2}$  was fixed from the  $t$ -slope of exclusive  $J/\psi$  photoproduction  
 3140 at HERA, and the other three parameters ( $\mu_0^2 = 1.17 \text{ GeV}^2$ ,  $A_g = 2.55$ ,  $\lambda_g = 0.020$ ) were fitted to ZEUS  
 3141  $F_2$  data with  $x_{\text{Bj}} \leq 0.01$  and  $Q^2 \in [0.25, 650] \text{ GeV}^2$  [356]. The eikonalised dipole scattering amplitude of  
 3142 Eq. (5.12) can be expanded as

$$\mathcal{N}(x, r, b) = \sum_{n=1}^{\infty} \frac{(-1)^{n+1}}{n!} \left[ \frac{\pi^2}{2N_c} r^2 \alpha_S(\mu^2) xg(x, \mu^2) T(b) \right]^n, \quad (5.13)$$

3143 where the  $n$ -th term in the expansion corresponds to  $n$ -Pomeron exchange; for example, the case  $n = 3$  is  
 3144 illustrated in Fig. 5.22(b). The terms with  $n > 1$  are necessary to ensure unitarity.

### 3145 Simulations of LHeC Elastic $J/\psi$ and $\Upsilon$ Production

3146 Due to the extremely clean final states produced, the relatively low effective  $x$ -values ( $x_{\text{eff}} \sim (Q^2 + m_V^2)/(Q^2 +$   
 3147  $W^2)$ ) and scales ( $Q_{\text{eff}}^2 \sim (Q^2 + m_V^2)/4$ ) accessed [431, 455], and the experimental possibility of varying both  
 3148  $W$  and  $t$  over wide ranges,  $J/\psi$  photoproduction ( $Q^2 \rightarrow 0$ ) may offer the cleanest available signature to study  
 3149 the transition between the dilute and dense regimes of small- $x$  partons. It should be possible to detect the  
 3150 muons from  $J/\psi$  or  $\Upsilon$  decays with acceptances extending to within  $1^\circ$  of the beampipe with dedicated muon  
 3151 chambers on the outside of the experiment. Depending on the electron beam energy, this makes invariant  
 3152 photon-proton masses  $W$  of well beyond 1 TeV accessible.

3153 For the analysis presented here we concentrate on the photoproduction limit, where the HERA data are  
 3154 most precise due to the large cross sections and where unitarity effects are most important. Studies have  
 3155 also been made at larger  $Q^2$  [456], where the extra hard scale additionally allows a perturbative treatment  
 3156 of exclusive light vector meson (e.g.  $\rho$ ,  $\omega$ ,  $\phi$ ) production. Again, perturbative unitarity effects are expected  
 3157 to be important for light vector meson production when  $Q^2 \gtrsim 1 \text{ GeV}^2$  is not too large.

3158 LHeC pseudodata for elastic  $J/\psi$  and  $\Upsilon$  photoproduction and electroproduction have been generated  
 3159 using the DIFFVM Monte Carlo generator [457] under the assumption of  $1^\circ$  acceptance and a variety  
 3160 of luminosity scenarios. The DIFFVM generator involves a simple Regge-based parameterization of the  
 3161 dynamics and a full treatment of decay angular distributions. Statistical uncertainties are estimated for  
 3162 each data point. Systematic uncertainties are hard to estimate without a detailed simulation of the muon  
 3163 identification and reconstruction capabilities of the detector, but are likely to be at least as good as the 10%  
 3164 measurements typically achieved for the elastic  $J/\psi$  at HERA.

3165 The plots in Fig. 5.23 show  $t$ -integrated predictions for exclusive  $J/\psi$  photoproduction ( $Q^2 = 0$ ) obtained  
 3166 from Eqs. (5.8) and (5.9), using the eikonalised “b-Sat” dipole scattering amplitude given in Eq. (5.12)  
 3167 together with a “boosted Gaussian” vector meson wave function [356, 458]. Also shown is the single-Pomeron  
 3168 exchange contribution obtained by keeping just the first ( $n = 1$ ) term in the expansion of Eq. (5.13), such  
 3169 that the scattering amplitude is linearly dependent on the gluon density, without refitting any of the input  
 3170 parameters.

3171 The difference between the “eikonalised” and “1-Pomeron” predictions therefore indicates the importance  
 3172 of unitarity corrections, which increase significantly with rising  $\gamma p$  centre-of-mass energy  $W$ . The maximum  
 3173 kinematic limit accessible at the LHeC,  $W = \sqrt{s}$ , is indicated with different options for electron beam  
 3174 energies ( $E_e$ ) and not accounting for the angular acceptance of the detector. The most precise HERA  
 3175 data [446, 459] are overlaid, together with sample LHeC pseudodata points, assuming  $1^\circ$  muon acceptance,  
 3176 with the errors (statistical only) given by an LHeC simulation with  $E_e = 150 \text{ GeV}$ . The central values of the  
 3177 LHeC pseudodata points were obtained from a Gaussian distribution with the mean given by extrapolating  
 3178 a power-law fit to the HERA data [446, 459] and the standard deviation given by the statistical errors  
 3179 from the LHeC simulation. The plots in Fig. 5.23 show that the errors on the LHeC pseudodata are much

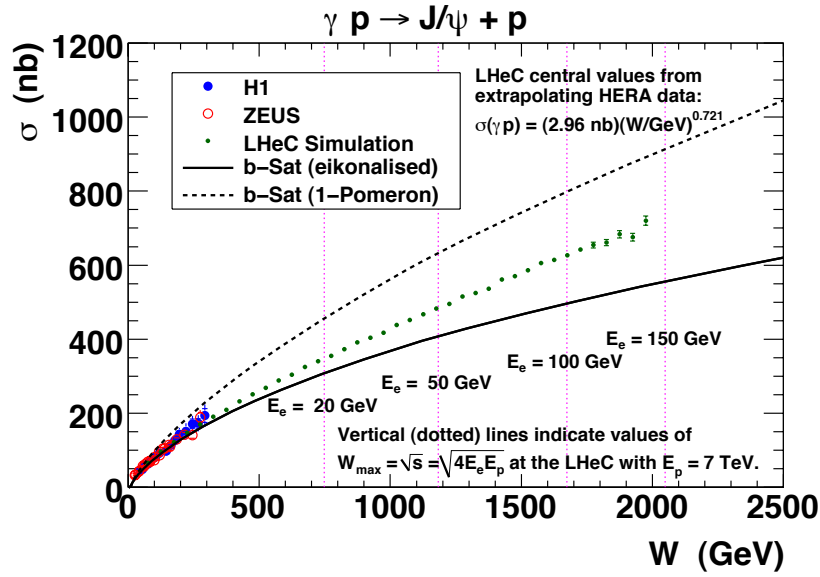
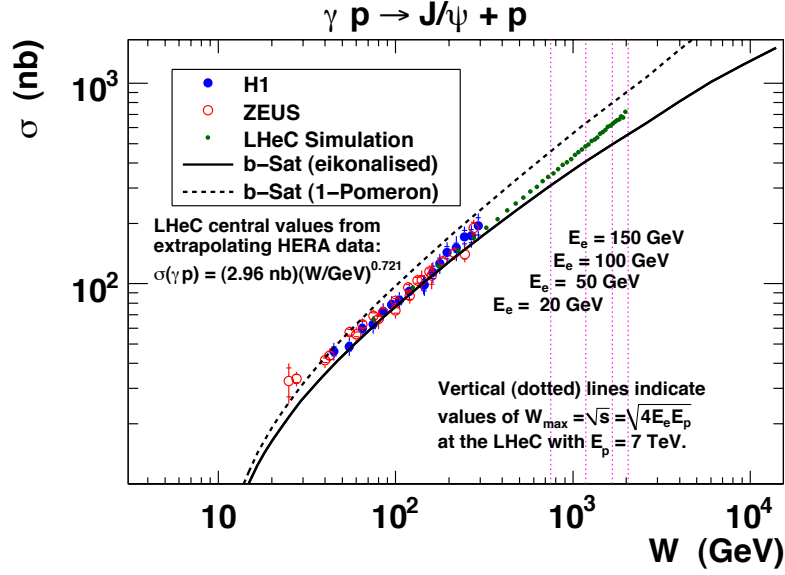


Figure 5.23: LHeC exclusive  $J/\psi$  photoproduction pseudodata, as a function of the  $\gamma p$  centre-of-mass energy  $W$ , plotted on a (top) log–log scale and (bottom) linear–linear scale. The difference between the solid and dashed curves indicates the size of unitarity corrections according to the b-Sat dipole model.

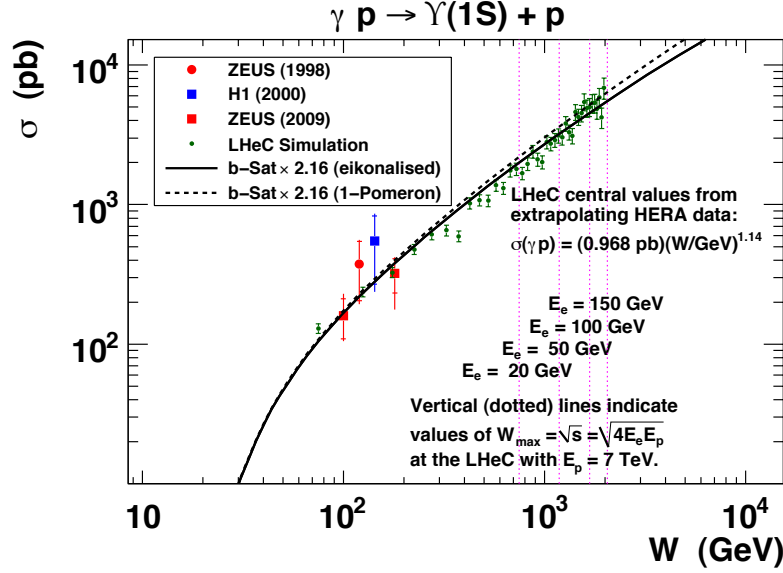


Figure 5.24: LHeC exclusive  $\Upsilon$  photoproduction pseudodata, as a function of the  $\gamma p$  centre-of-mass energy  $W$ , plotted on a log–log scale. The difference between the solid and dashed curves indicates the size of unitarity corrections according to the b-Sat model. The b-Sat theory predictions have been scaled by a factor 2.16 to best-fit the existing HERA data.

3180 smaller than the difference between the “eikonalised” and “1-Pomeron” predictions. Therefore, exclusive  
 3181  $J/\psi$  photoproduction at the LHeC may be an ideal observable for investigating unitarity corrections at a  
 3182 perturbative scale provided by the charm-quark mass.

3183 Similar plots for exclusive  $\Upsilon$  photoproduction are shown in Fig. 5.24. Here, the unitarity corrections are  
 3184 smaller than for  $J/\psi$  production due to the larger scale provided by the bottom-quark mass and therefore the  
 3185 smaller typical dipole sizes  $r$  being probed. The simulated LHeC pseudodata points also have larger statistical  
 3186 errors than for  $J/\psi$  production due to the much smaller cross sections. Nonetheless, the simulations indicate  
 3187 that a huge improvement in kinematic range and precision is possible compared with the very sparse  $\Upsilon$  data  
 3188 from HERA [460–462].

3189 In order to achieve a satisfactory description of the experimental data on exclusive  $\Upsilon$  photoproduction,  
 3190 an additional normalization factor of  $\sim 2$  has to be included in the dipole calculation (a similar factor is  
 3191 required for other calculations using the dipole model, see for example Ref. [463]). This normalization factor  
 3192 does not arise from any theoretical considerations. Therefore, the dipole model prediction for the  $\Upsilon$  in  
 3193 diffractive exclusive processes in DIS still poses significant theoretical questions which cannot be resolved  
 3194 without LHeC data.

3195 The cross sections shown in Figs. 5.23 and 5.24 are integrated over  $t \equiv (p - p')^2 = -\Delta^2$ , where  $\Delta$  is  
 3196 the Fourier conjugate variable to the impact parameter  $\mathbf{b}$ . One expects that at high center-of-mass energies  
 3197 (small  $x$ ), saturation effects are most important close to the centre of the proton (small  $b$ ), where the  
 3198 interaction region is densest. This is illustrated in Fig. 5.25(a) where the b-Sat model dipole scattering  
 3199 amplitude is shown as a function of  $b$  for various  $x$  values. By measuring exclusive diffraction in bins of  $|t|$   
 3200 one can extract the impact parameter profile of the interaction region. This is illustrated in Fig. 5.25(b)  
 3201 where the integrand of Eq. (5.8) is shown for different values of  $t$  as a function of impact parameter. Clearly  
 3202 for large values of  $|t|$ , small values of  $b$  are probed in the impact parameter profile, corresponding to the most  
 3203 densely populated region, where saturation effects should be most clearly visible. Indeed, the eikonalised  
 3204 dipole model of Eq. (5.12) leads to “diffractive dips” in the  $t$ -distribution of exclusive  $J/\psi$  photoproduction

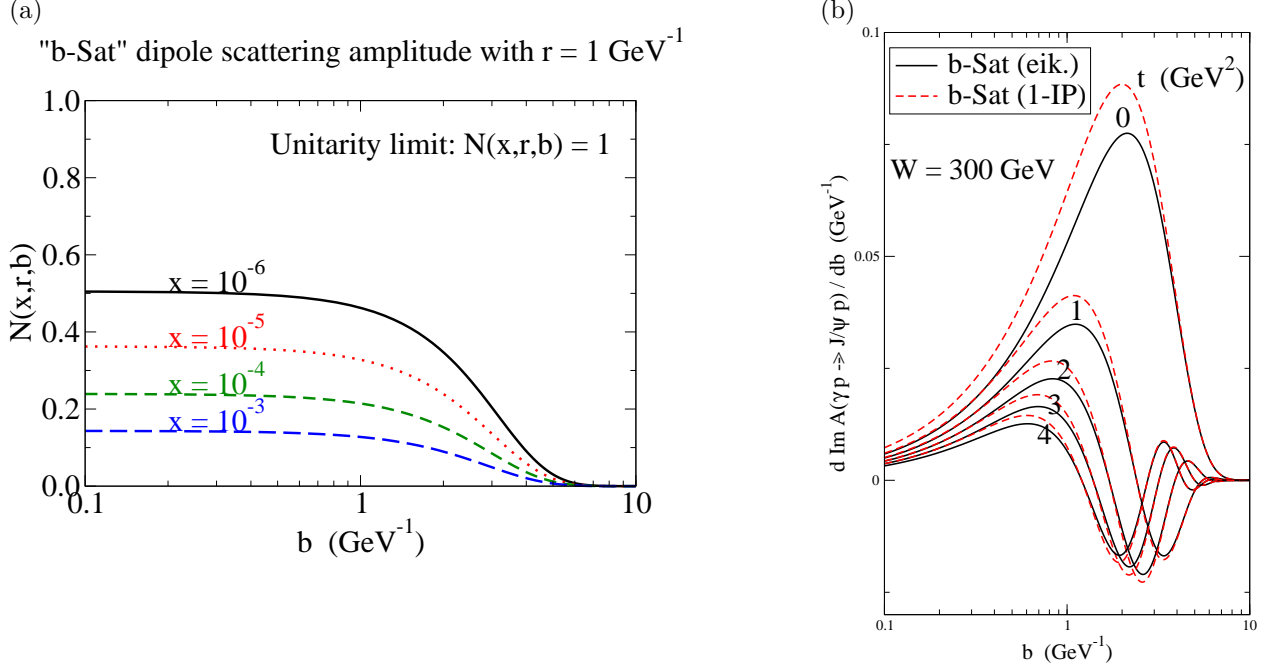


Figure 5.25: (a) The imaginary part of the dipole scattering amplitude,  $\mathcal{N}(x, r, b)$ , as a function of the impact parameter  $b$ , for fixed values of dipole size  $r = 1 \text{ GeV}^{-1}$  (typical for exclusive  $J/\psi$  photoproduction) and different  $x$  values. (b) The ( $r$ -integrated) amplitude - the integrand of Eq. (5.8) - for exclusive  $J/\psi$  photoproduction as a function of  $b$ , for  $W = 300 \text{ GeV}$  and  $|t| = 0, 1, 2, 3, 4 \text{ GeV}^2$ .

3205 at large  $|t|$  (reminiscent of the dips seen in the  $t$ -distribution of the proton-proton elastic cross section),  
 3206 departing from the exponential fall-off in the  $t$ -distribution seen with single-Pomeron exchange [355]. The  
 3207 HERA experiments have only been able to make precise measurements of exclusive  $J/\psi$  photoproduction at  
 3208 relatively small  $|t| \lesssim 1 \text{ GeV}^2$ , and no significant departure from the exponential fall-off,  $d\sigma/dt \sim \exp(-B_D|t|)$ ,  
 3209 has been observed.

3210 In Fig. 5.26, LHeC pseudodata on the differential cross section  $d\sigma/dt$  is shown as a function of the  
 3211 energy  $W$  in different bins of  $t$  for the case of exclusive  $J/\Psi$  production. Again two different b-Sat model  
 3212 scenarios are shown, with unitarisation effects and with single Pomeron exchange. Already for small values of  
 3213  $|t| \sim 0.2 \text{ GeV}^2$  and low values of electron energies there is a large discrepancy between the models. The LHeC  
 3214 simulated data still have very small errors in this regime, and can clearly distinguish between the different  
 3215 models. The differences are of course amplified for large  $t$  and large electron beam energies. However the  
 3216 precision of the data deteriorates at large  $t$ .

3217 Summarising, it is clear that the precise measurements of large- $|t|$  exclusive  $J/\psi$  photoproduction at the  
 3218 LHeC would have significant sensitivity to unitarity effects.

### 3219 Simulations of Deeply Virtual Compton Scattering at the LHeC

3220 Simulations of the DVCS measurement possibilities with the LHeC have been made using the Monte Carlo  
 3221 generator MILOU [464], in the 'FFS option', for which the DVCS cross section is estimated using the model  
 3222 of Frankfurt, Freund and Strikman [465]. A  $t$ -slope of  $B = 6 \text{ GeV}^{-2}$  is assumed.

3223 The  $ep \rightarrow e\gamma p$  DVCS cross section is estimated in various scenarios for the electron beam energy and  
 3224 the statistical precision of the measurement is estimated for different integrated luminosity and detector  
 3225 acceptance choices. Detector acceptance cuts at either  $1^\circ$  or  $10^\circ$  are placed on the polar angle of the final  
 3226 state electron and photon. Based on experience with controlling backgrounds in HERA DVCS measurements

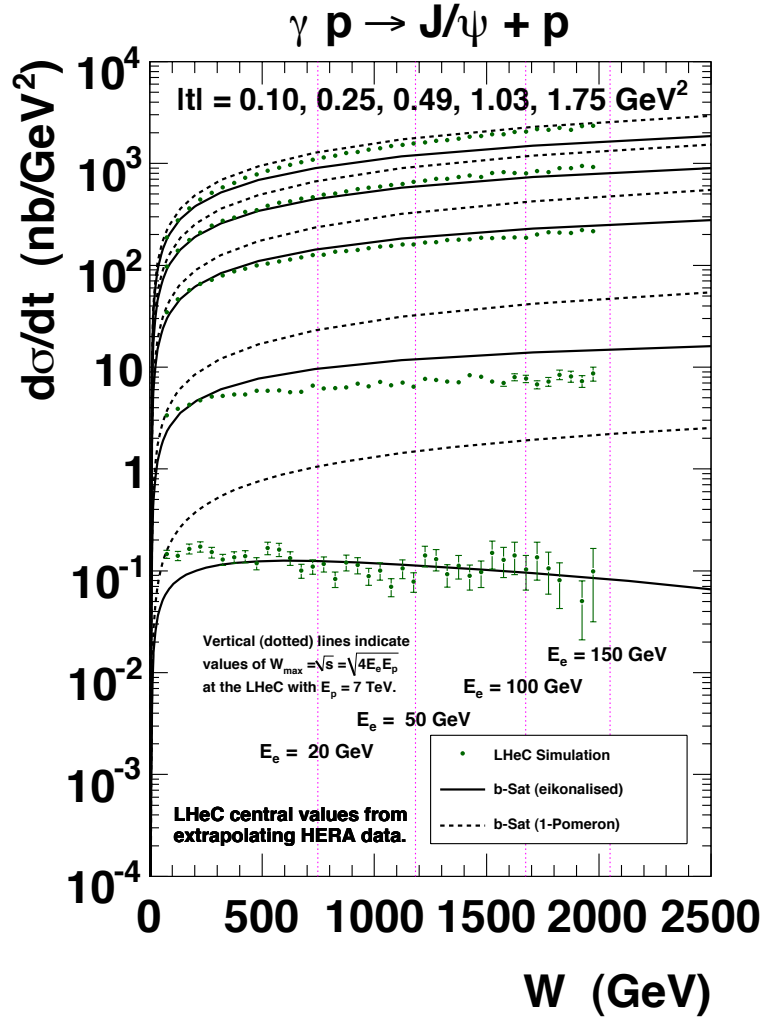


Figure 5.26: Simulated LHeC measurements of the  $W$ -dependence of exclusive  $J/\psi$  photoproduction at the LHeC, differentially in bins of  $|t| = 0.10, 0.20, 0.49, 1.03, 1.75$   $\text{GeV}^2$ . The difference between the solid and dashed curves indicates the size of unitarity corrections according to the b-Sat dipole model. The central values of the LHeC pseudodata points were obtained from a Gaussian distribution with the mean given by extrapolating a parameterization of HERA data and the standard deviation given by the statistical errors from the LHeC simulation with  $E_e = 150$  GeV. The  $t$ -integrated cross section ( $\sigma$ ) as a function of  $W$  for the HERA parameterization was obtained from a power-law fit to the data from both ZEUS [459] and H1 [446], then the  $t$ -distribution was assumed to behave as  $d\sigma/dt = \sigma \cdot B_D \exp(-B_D|t|)$ , with  $B_D = [4.400 + 4 \cdot 0.137 \log(W/90 \text{ GeV})]$   $\text{GeV}^{-2}$  obtained from a linear fit to the values of  $B_D$  versus  $W$  given by both ZEUS [459] and H1 [446].

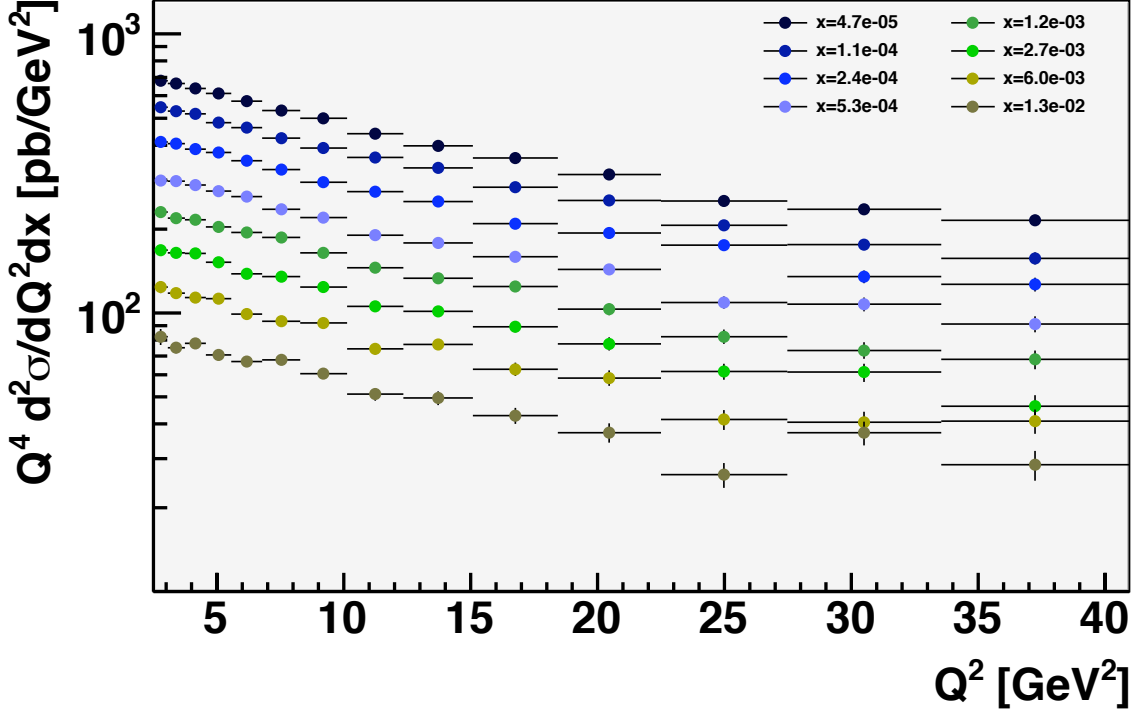


Figure 5.27: Simulated LHeC measurement of the DVCS cross section multiplied by  $Q^4$  for different  $x$  values for a luminosity of  $1 \text{ fb}^{-1}$ , with  $E_e = 50 \text{ GeV}$ , and electron and photon acceptance extending to within  $1^\circ$  of the beampipe with a cut at  $P_T^\gamma = 2 \text{ GeV}$ . Only statistical uncertainties are considered.

[447, 448, 466], an additional cut is placed on the transverse momentum  $P_T^\gamma$  of the final state photon.  
 The kinematic limitations due to the scattered electron acceptance follow the same patterns as for the inclusive cross section (see Subsec. 5.2.2). The photon  $P_T^\gamma$  cut is found to be a further important factor in the  $Q^2$  acceptance, with measurements at  $Q^2 < 20 \text{ GeV}^2$  almost completely impossible for a cut at  $P_T^\gamma > 5 \text{ GeV}$ , even in the scenario with detector acceptances reaching  $1^\circ$ . If this cut is relaxed to  $P_T^\gamma > 2 \text{ GeV}$ , it opens the available phase space towards the lowest  $Q^2$  and  $x$  values permitted by the electron acceptance.

A simulation of a possible LHeC DVCS measurement double differentially in  $x$  and  $Q^2$  is shown in Fig. 5.27 for a very modest luminosity scenario ( $1 \text{ fb}^{-1}$ ) in which the electron beam energy is  $50 \text{ GeV}$ , the detector acceptance extends to  $1^\circ$  and photon measurements are possible down to  $P_T^\gamma = 2 \text{ GeV}$ . High precision is possible throughout the region  $2.5 < Q^2 < 40 \text{ GeV}^2$  for  $x$  values extending down to  $\sim 5 \times 10^{-5}$ . The need to measure DVCS therefore places constraints on the detector performance for low transverse momentum photons, which in practice translates into the electromagnetic calorimetry noise conditions and response linearity at low energies.

If the detector acceptance extends to only  $10^\circ$ , the  $P_T^\gamma$  cut no longer plays such an important role. Although the low  $Q^2$  acceptance is lost in this scenario, the larger luminosity will allow precise measurements for  $Q^2 \gtrsim 50 \text{ GeV}^2$ , a region which is not well covered in the  $1^\circ$  acceptance scenario due to the small cross section. In the simulation shown in Fig. 5.28, a factor of 100 increase in luminosity is considered, resulting in precise measurements extending to  $Q^2 > 500 \text{ GeV}^2$ , well beyond the range explored for DVCS or other GPD-sensitive processes to date.

Maximising the lepton beam energy potentially gives access to the largest  $W$  and smallest  $x$  values, provided the low  $P_T^\gamma$  region can be accessed. However, the higher beam lepton energy boosts the final state photon in the scattered lepton direction, resulting in an additional acceptance limitation.



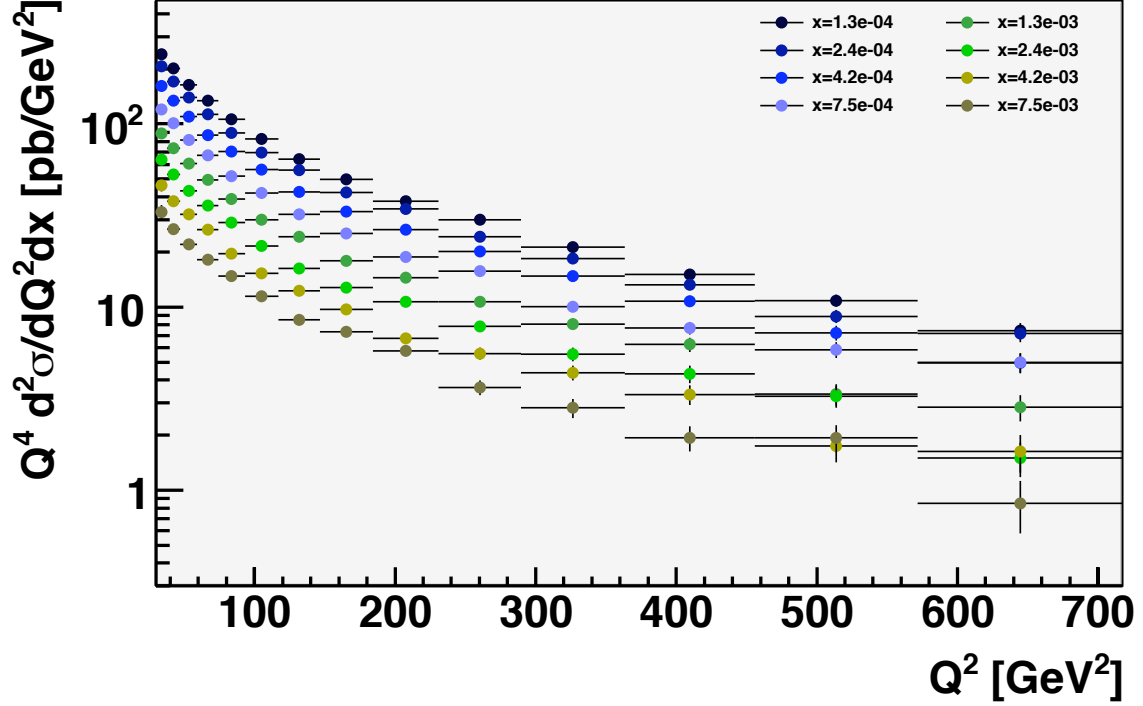


Figure 5.28: Simulated LHeC measurement of the DVCS cross section multiplied by  $Q^4$  for different  $x$  values for a luminosity of  $100 \text{ fb}^{-1}$ , with  $E_e = 50 \text{ GeV}$ , and electron and photon acceptance extending to within  $10^\circ$  of the beampipe with a cut at  $P_T^\gamma = 5 \text{ GeV}$ . Only statistical uncertainties are considered.

3249 Further studies of this process will require a better understanding of the detector in order to estimate  
 3250 systematic uncertainties. A particularly interesting extension would be to investigate possible beam charge  
 3251 [447, 466] and polarisation asymmetry measurements at lower  $x$  or larger  $Q^2$  than was possible at HERA.  
 3252 With the addition of such information, a full study of the potential of the LHeC to constrain GPDs could  
 3253 be performed.

#### 3254 Accessing chiral-odd transversity GPDs in diffractive processes

3255 Transversity quark distributions in the nucleon remain among the most unknown leading-twist hadronic  
 3256 observables. The four chiral-odd transversity GPDs [?], denoted  $H_T$ ,  $E_T$ ,  $\tilde{H}_T$ ,  $\tilde{E}_T$ , offer a new way to  
 3257 access the transversity-dependent quark content of the nucleon. The factorization properties of exclusive  
 3258 amplitudes apply in principle both to chiral-even and to chiral-odd sectors. However, one photon or one  
 3259 meson electroproduction leading-twist amplitudes are insensitive to the latter [?, ?]. At leading twist, they  
 3260 can be accessed experimentally through the quasi-forward exclusive electro- or photoproduction of a vector  
 3261 meson pair with a large invariant mass [?, ?]. In analogy with the virtual photon exchange occurring in the  
 3262 deep inelastic electroproduction of a meson, one considers the subprocess:

$$\mathcal{P}(q_P) p(p_2) \rightarrow \rho_T(p_\rho) N'(p_{2'}) , \quad (5.14)$$

3263 of almost forward scattering of a virtual Pomeron on a nucleon, the hard scale being the virtuality  $-q_P^2$   
 3264 of this Pomeron. The choice of a transversely polarized vector meson  $\rho_T(p_\rho)$  involves at leading twist a  
 3265 chiral-odd distribution amplitude (DA), which in turn selects the chiral-odd GPDs. Let us stress that the  
 3266 target needs not to be polarized for the amplitude to contain the transversity GPD. This subprocess is at

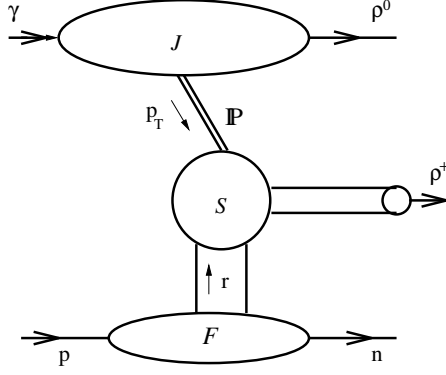


Figure 5.29: Factorization of the process  $\gamma^{(*)}p \rightarrow \rho\rho N'$  in the asymmetric kinematics discussed in the text.  $\mathcal{P}$  is the hard Pomeron modeled by two gluon exchange.

3267 work in the diffractive process

$$ep(p_2) \rightarrow e'\gamma_{L/T}^{(*)}(q) \quad p(p_2) \rightarrow e'\rho_{L,T}^0(q_\rho) \quad \rho_T(p_\rho) N'(p_{2'}), \quad (5.15)$$

3268 shown in Fig. 5.29. The final state may be either  $\rho^0\rho^0p$  or  $\rho^0\rho^+n$ . We consider the kinematics where the  
 3269 energy of the system ( $\rho_T(p_\rho) N'$ ) is smaller than the energy of the system ( $\rho_{L,T} \rho_T$ ) but still large enough  
 3270 to justify a factorized approach (in particular much larger than baryonic resonance masses). In this regime,  
 3271 the amplitude is calculable consistently within the collinear factorization method, as an integral (over the  
 3272 longitudinal momentum fractions of the quarks) of the product of two amplitudes: the first one (the *impact*  
 3273 *factor*  $J^{\gamma \rightarrow \rho^0}$ ) describes in the Born approximation the transition  $\gamma^{(*)} \rightarrow \rho_{L,T}^0$  via two gluon exchange and the  
 3274 second one describes the subprocess  $\mathcal{P} p \rightarrow \rho_T N'$ . The fact that this latter process is closely related to the  
 3275 electroproduction process  $\gamma^* p \rightarrow \rho N'$  allows to separate its long distance dynamics expressed through the  
 3276 GPDs from a perturbatively calculable coefficient function. The skewness parameter  $\xi$  is related in the usual  
 3277 way ( $\xi \approx x_B/(2-x_B)$ ) to the Bjorken variable defined by the Pomeron momentum  $x_B = -q_P^2/(2q_P \cdot p_2)$ .

3278 The resulting scattering amplitude  $\mathcal{M}^{\gamma^* p \rightarrow \rho^0 \rho_T p}$  then receives contributions from the four chiral-odd  
 3279 GPDs  $H_T, \tilde{H}_T, E_T$  and  $\tilde{E}_T$ , but only the first contribution does not vanish kinematically in the forward di-  
 3280 rection. Thus, assuming that the Mandelstam variable  $-t = -(p_2 - p_{2'})^2$  is sufficiently small, the transversity  
 3281 GPD  $H_T$  contribution dominates the amplitude which reads in the  $\rho^0\rho_T^+$  case:

$$\begin{aligned} \mathcal{M}^{\gamma p \rightarrow \rho^0 \rho_T^+ n} &= \sin\theta \, 16\pi^2 W^2 \alpha_s f_\rho^T \xi \sqrt{\frac{1-\xi}{1+\xi}} \frac{C_F}{N_c (p_T^2)^2} \\ &\times \int_0^1 \frac{du \phi_\perp(u)}{u^2 \bar{u}^2} J^{\gamma \rightarrow \rho^0}(u p_T, \bar{u} p_T) \frac{H_T^{ud}(\xi(2u-1), \xi, t)}{\sqrt{2}}, \end{aligned} \quad (5.16)$$

3282 with  $H_T^{ud} = H_T^u - H_T^d$ ,  $f_\rho$  the  $\rho$  decay constant,  $\phi_\perp(u)$  the DA of the  $\rho_T$  meson,  $W^2 = (q + p_2)^2$ ,  $\theta$   
 3283 the angle between the transverse polarization vector of the target  $\vec{n}$  and the polarization vector  $\vec{\epsilon}_T$  of the  
 3284 produced  $\rho_T$ -meson, and  $p_T$  the transverse momentum of the  $\rho^0$  meson (see [?, ?]). Note that the squared  
 3285 amplitude averaged over the nucleon polarizations does not cancel, enforcing the remarkable feature of  
 3286 exclusive unpolarized reactions to be sensitive to the transversity GPDs.

3287 To get an estimate of the differential cross section of this process, we use a simple meson pole model for the  
 3288 transversity GPD  $H_T^q(x, \xi, t)$  starting with the effective interaction Lagrangian  $\mathcal{L}_{\mathcal{A}NN} = \frac{g_{\mathcal{A}NN}}{2M} \bar{N} \sigma_{\mu\nu} \gamma_5 \partial^\nu A^\mu N$ .  
 3289 This yields, identifying the axial meson as  $A = b_1(1235)$ ,

$$H_T^{ud}(x, \xi, 0) = \frac{g_{b_1 NN} f_{b_1}^T \langle k_\perp^2 \rangle}{2\sqrt{2} M_N m_{b_1}^2} \frac{\phi_\perp^{b_1}\left(\frac{x+\xi}{2\xi}\right)}{2\xi}, \quad (5.17)$$

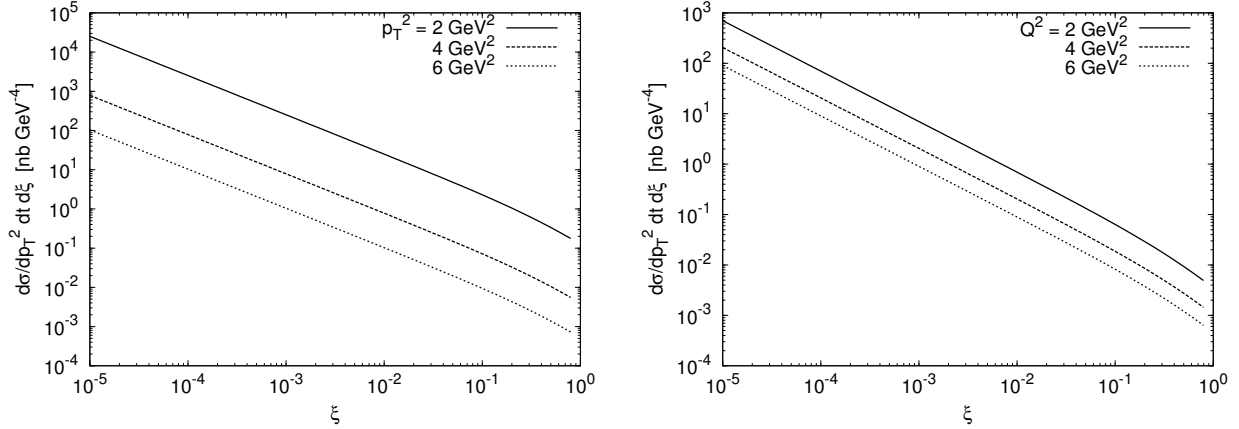


Figure 5.30: The differential cross section for the photoproduction (a) and electroproduction (b) of the meson pair  $\rho_T^0 \rho_T^+$  as a function of  $\xi$  for (a)  $p_T^2 = 2, 4$  and  $6 \text{ GeV}^2$  and for (b)  $p_T^2 = 2 \text{ GeV}^2$  and  $Q^2 = 2, 4$  and  $6 \text{ GeV}^2$ . The cross sections for the production of the meson pair  $\rho_T^0 \rho_T^0$  are two times smaller.

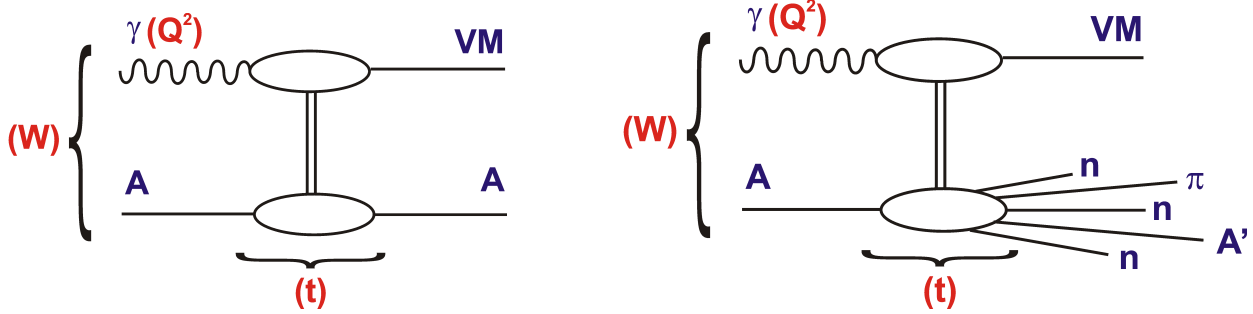


Figure 5.31: Diagrams illustrating the different types of exclusive diffraction in the nuclear case: coherent (plot on the left) and incoherent (plot on the right). While the diagrams have been drawn for the case of exclusive vector meson production, they equally apply to an arbitrary diffractively produced state.

3290 with the average of the intrinsic transverse momentum of the quarks  $\langle k_{\perp}^2 \rangle \approx 0.8 \text{ GeV}^2$ . The resulting cross  
 3291 sections estimated within the approximation where the Pomeron is modeled by a two gluon exchange do not  
 3292 depend on the variable  $W^2$ , but on the variable  $\xi$ . They are shown in Fig. 5.30 as a function of  $\xi$  for various  
 3293 values of  $p_T^2$  and  $Q^2$ . The rise at small  $\xi$  comes mostly from the phase space factor. NLO corrections for  
 3294 this amplitude are not known till now. The cross sections look reasonably large. The required studies on the  
 3295 possibilities for detection of the final states and of the accessible kinematic range are left for the future.

### 3296 **Diffractive Vector Meson Production off Nuclei**

3297 Exclusive diffractive processes are similarly promising as a source of information on the gluon density in  
 3298 the nucleus [432]. Quasi-elastic scattering of photons from nuclei at small  $x$  can be treated within the  
 3299 same dipole model framework as for  $ep$  scattering, making the comparisons with the proton case relatively  
 3300 straightforward. The interaction of the dipole with the nucleus can be viewed as a sum of dipole scatterings  
 3301 off the nucleons forming the nucleus. Nuclear effects can be incorporated into the dipole cross section by  
 3302 modifying the transverse gluon distribution and adding the corrections due to Glauber rescattering from  
 3303 multiple nucleons [355,432]. Previous experimental data on exclusive production from nuclei exist [467,468],  
 3304 but are limited in both kinematic range and precision.

3305 There is one aspect of diffraction which is specific to nuclei. The structure of incoherent diffraction with

3306 nuclear break-up ( $eA \rightarrow eXY$ ) is more complex than with a proton target, and it can also be more informative.  
 3307 In the case of a target nucleus, we expect the following qualitative changes in the  $t$ -dependence. First, the  
 3308 low- $|t|$  regime of coherent diffraction illustrated in Fig. 5.31 left, in which the nucleus scatters elastically and  
 3309 remains in its ground state, will be dominant up to a smaller value of  $|t|$  (about  $|t| = 0.05 \text{ GeV}^2$ ) than in  
 3310 the proton case, reflecting the larger size of the nucleus. The nuclear dissociation regime (incoherent case),  
 3311 see Fig. 5.31 right, will consist of two parts: an intermediate regime in momentum transfer up to perhaps  
 3312  $|t| = 0.7 \text{ GeV}^2$ , where the nucleus will predominantly break up into its constituent nucleons, and a large- $|t|$   
 3313 regime where the nucleons inside the nucleus will also break up, implying - for instance - pion production in  
 3314 the  $Y$  system. While these are only qualitative expectations, it is crucial to study this aspect of diffraction  
 3315 quantitatively in order to complete our understanding of the transverse structure of nuclei.

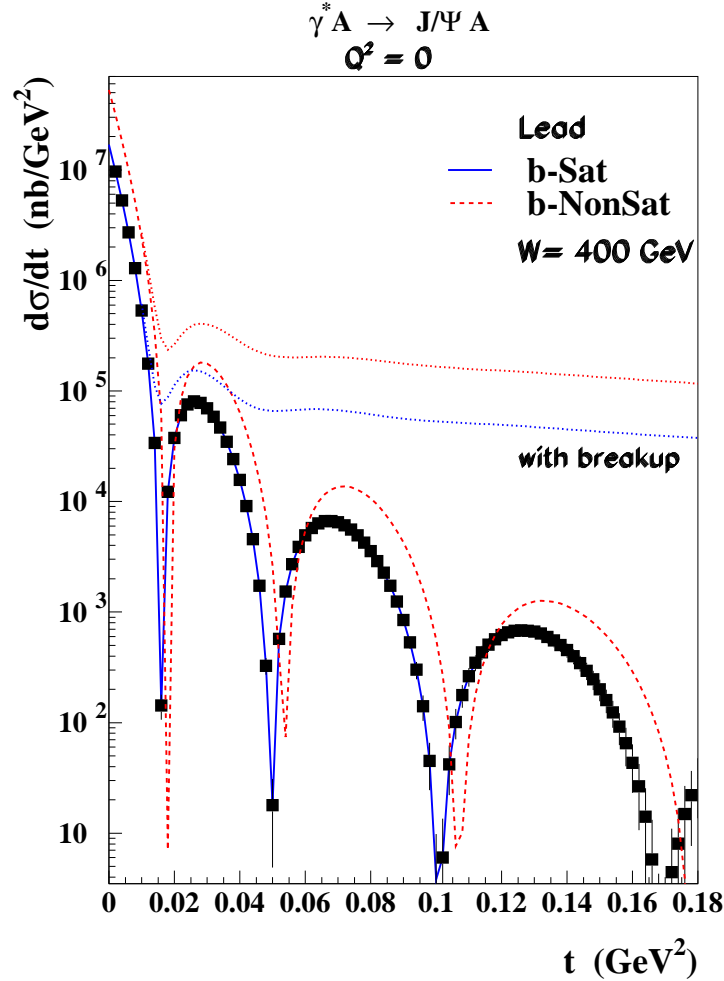


Figure 5.32: Differential cross section for the diffractive production of  $J/\Psi$  on a lead nucleus, as a function of the momentum transfer  $|t|$ . The dashed-red and solid-blue lines correspond to the b-Sat model predictions for coherent production without and with saturation effects, respectively. The dotted lines correspond to the predictions for the incoherent case. The pseudodata shown for the coherent case are explained in the text.

3316 Fig. 5.32 shows the diffractive cross sections for exclusive  $J/\Psi$  production off a lead nucleus with (b-Sat)  
 3317 and without (b-NonSat) saturation effects. The figure shows both the coherent and incoherent cross sections.  
 3318 According to both models shown, the cross section for  $t \sim 0$  is dominated by coherent production, whereas the  
 3319 nuclear break-up contribution becomes dominant for  $|t| \gtrsim 0.01 \text{ GeV}^2$ , leading to a relatively flat  $t$  distribution.

3320 The coherent cross section exhibits a characteristic multiple-dip structure at these relatively large  $t$  values,  
 3321 the details of which are sensitive to gluon saturation effects. Resolving these dips requires a clean separation  
 3322 between the coherent and nuclear break-up contributions, which may be possible with sufficient forward  
 3323 instrumentation. In particular, preliminary studies suggest that the detection of neutrons from the nuclear  
 3324 break-up in the Zero Degree Calorimeter (Subsec. 14.3) reduces the incoherent backgrounds dramatically.  
 3325 Assuming that it is possible to obtain a relatively clean sample of coherent nuclear diffraction, resolving  
 3326 the rich structure at large  $t$  should be possible based on the measurement of the transverse momentum of  
 3327 the elastically produced  $J/\psi$  according to  $t = -p_T^2(J/\psi)$ . The resolution on the  $t$  measurement is thus  
 3328 related to that on the  $J/\psi$  by  $\Delta t = 2\sqrt{-t} \Delta p_T(J/\psi)$ , amounting to  $\Delta t < 0.01 \text{ GeV}^2$  throughout the range  
 3329 shown in Fig. 5.32 assuming  $\Delta p_T(J/\psi) < 10 \text{ MeV}$ , as has been achieved at HERA. The pseudodata for  
 3330 the coherent process shown in the figure are consistent with this resolution and correspond to a modest  
 3331 integrated luminosity of order  $10 \text{ pb}^{-1}$ .

3332 Independently of the large  $|t|$  behaviour, important information can be obtained from the low  $|t|$  region  
 3333 alone. Coherent production for  $t \sim 0$  can easily be related to the properties of dipole-nucleon interactions,  
 3334 because all nuclear effects can be absorbed into the nuclear wave functions, such that only the average gluon  
 3335 density of the nucleus enters the calculation. For this forward cross section, the exact shape of the nuclear  
 3336 wave function is not important, in contrast to what happens at larger  $|t|$  where the distribution reflects the  
 3337 functional form of the nuclear density.

3338 Saturation effects can be studied in a very clean way using the  $t$ -averaged gluon density obtained in this  
 3339 way from the forward coherent cross section. Fig. 5.33 shows this cross section for  $J/\Psi$  production as a  
 3340 function of  $W$  for different nuclei. The cross section varies substantially as a function of the  $\gamma^*p$  centre of  
 3341 mass energy  $W$  and the nuclear mass number  $A$ . It is also very sensitive to shadowing or saturation effects  
 3342 due to the fact that the differential cross section at  $t = 0$  has a quadratic dependence on the gluon density  
 3343 and  $A$ . Due to this fact, the ratios of the cross sections for nuclei and protons are roughly proportional to the  
 3344 ratios of the gluon densities squared. This has been exploited in the calculation [469] presented in Fig. 5.34,  
 3345 where the nuclear modification factor  $R$  for the square of the gluon density is shown. The predictions are  
 3346 consistent with those obtained from the b-Sat model (Fig. 5.33). Therefore, a precise measurement of the  
 3347  $J/\psi$  cross section around  $t = 0$  is an invaluable source of information on the gluon density and in particular  
 3348 on non-linear effects.

3349 Another region of interest is the measurement at larger  $|t|$ ,  $|t| \gtrsim 0.15 \text{ GeV}^2$ . Here the reaction is fully  
 3350 dominated by the incoherent processes in which the nucleus breaks up. The shadowing or saturation effects  
 3351 should be stronger in this region than in the coherent case [440] and the shape of the diffractive cross  
 3352 section should be only weakly sensitive to nuclear effects [432]. Finally, the intermediate region between  
 3353  $|t| \sim 0.01 \text{ GeV}^2$  and  $|t| \sim 0.1 \text{ GeV}^2$  is also very interesting because here the barely known gluonic nuclear  
 3354 effects can be studied.

### 3355 Searching for the Odderon

3356 Exclusive processes in photoproduction and DIS offer unique sensitivity to rare exchanges in QCD. One  
 3357 prominent example is that of exclusive pseudoscalar meson production, which could proceed via the exchange  
 3358 of the Odderon. The Odderon is the postulated Reggeon which is the C-odd partner of the Pomeron. The  
 3359 exchange of an Odderon should contribute with different signs to particle-particle and particle-antiparticle  
 3360 scattering. Therefore, in the case of hadron-hadron collisions it could lead, via the optical theorem, to a  
 3361 difference between proton-proton and proton-antiproton total cross sections at high energies, provided the  
 3362 intercept of the Odderon is close to unity. Despite many searches, no evidence for Odderon exchange has  
 3363 been found so far, see for example [470]. Nevertheless, the existence of the Odderon is a firm prediction of  
 3364 high-energy QCD, for a comprehensive review see [471]. At lowest order in perturbation theory it can be  
 3365 described as a system of three non-interacting gluons. In the leading logarithmic approximation in  $x$  its  
 3366 evolution is governed by the Bartels-Kwieciński-Praszałowicz (BKP) equations [472–474]. Up to now, two  
 3367 solutions to the BKP equations are known, one with intercept slightly below one [475] and the other with  
 3368 intercept exactly equal to one [476].

3369 Several channels involving Odderon exchange are possible at the LHeC, leading to the exclusive production

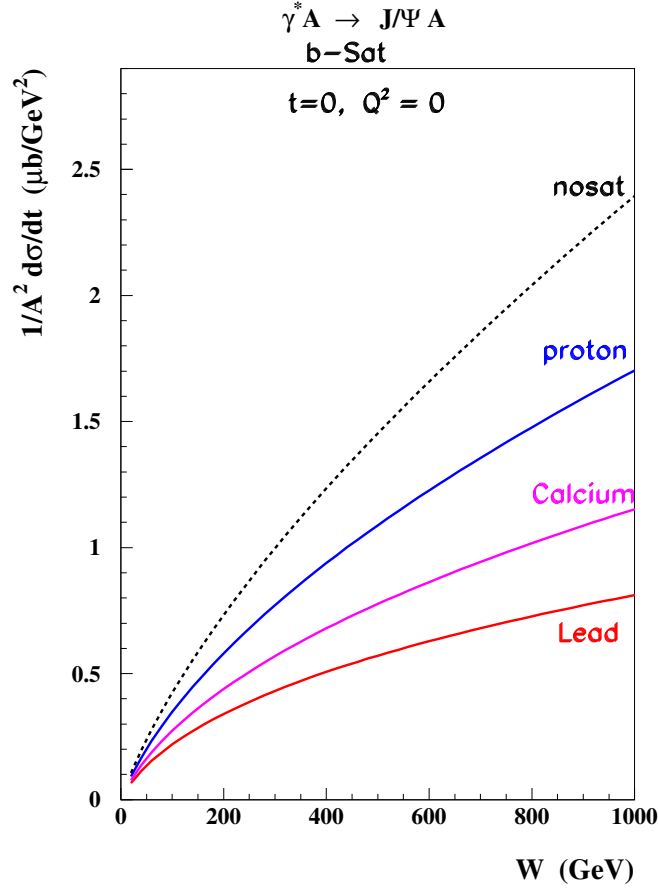


Figure 5.33: Energy dependence of the coherent photoproduction of the  $J/\Psi$  on a proton and different nuclei in the forward case  $t = 0$  according to the b-Sat model. The cross sections are normalized by a factor  $1/A^2$ , corresponding to the dependence on the gluon density squared if no nuclear effects are present.

3370 of pseudoscalar mesons,  $\gamma^{(*)}p \rightarrow Cp$ , where  $C = \pi^0, \eta, \eta', \eta_c \dots$ . Searches for the Odderon in the reaction  
3371  $ep \rightarrow e\pi^0 N^*$  were performed by the H1 collaboration at HERA [477] at an average  $\gamma p$  c.m.s energy  $\langle W \rangle =$   
3372  $215$  GeV. No signal was found and an upper limit on the cross section was derived,  $\sigma(ep \rightarrow e\pi^0 N^*, 0.02 <$   
3373  $|t| < 0.3 \text{ GeV}^2) < 49$  nb at the 95 % confidence level. Although the predicted cross sections for processes  
3374 governed by Odderon exchange are rather small, they are not suppressed with increasing centre-of-mass  
3375 energy and the large luminosities offered by the LHeC may be exactly what is required for a discovery. In  
3376 addition to  $\pi^0$  production, Odderon searches at the LHeC could be based on other exclusive channels, for  
3377 example with heavier mesons  $\eta_c, \eta_b$  [478].

3378 It has been advocated [479] that one could devise more sensitive tests of the existence of the Odderon  
3379 exchange by searching for interference effects between Pomeron and Odderon exchange amplitudes. Such an  
3380 observable is the measurement of the difference between charm and anti-charm angular or energy distributions  
3381 in  $\gamma^* p \rightarrow c\bar{c}N^*$ . Another channel is the exclusive photo or electroproduction of two pions [?, ?, ?]. Indeed  
3382 a  $\pi^+\pi^-$  pair may be produced both as a charge symmetric  $C^+$  and a charge antisymmetric  $C^-$  state. The  
3383 Pomeron exchange amplitude will contribute to the  $C^- \pi^+\pi^-$  state, the Odderon exchange amplitude will  
3384 contribute to the  $C^+ \pi^+\pi^-$  state. A (mesonic) charge antisymmetric observable will select the interference  
3385 of these two amplitudes. In the hard electroproduction case, one may estimate the effect through a lowest

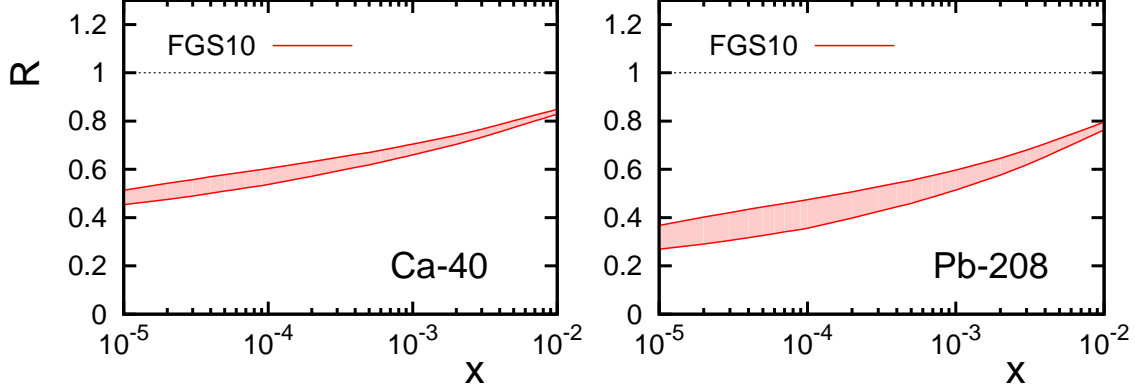


Figure 5.34: The  $x$  dependence of the nuclear modification ratio for the gluon density squared, from nuclei to protons (rescaled by  $A^2$ ), for the scale corresponding to the exclusive production of the  $J/\Psi$ . The results have been obtained from the model described in [469].

3386 order calculation where Pomeron (Odderon) exchange is calculated through the exchange of two (three)  
 3387 non-interacting gluons in a colour singlet state in the  $t$ -channel, as shown in Fig. 5.35.

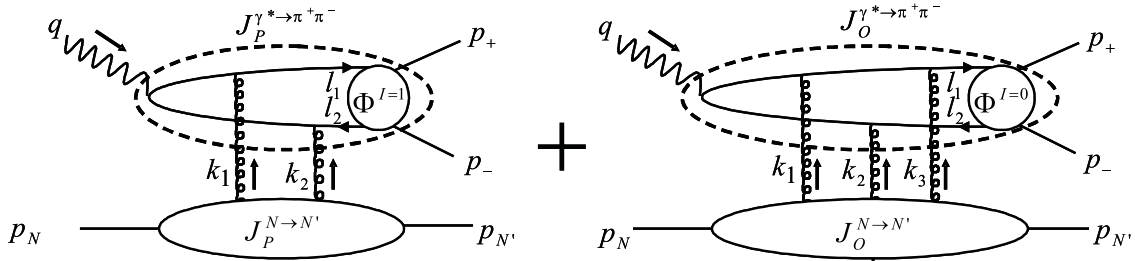


Figure 5.35: Feynman diagrams describing  $\pi^+\pi^-$  electroproduction in the Born approximation.

3388 The impact representation of the amplitude has the form of an integral over the 2-dimensional transverse  
 3389 momenta  $k_i$  of the  $t$ -channel gluons:

$$\mathcal{M}_P = -i W^2 \int \frac{d^2 k_1 d^2 k_2 \delta^{(2)}(k_1 + k_2 - p_{2\pi})}{(2\pi)^2 k_1^2 k_2^2} J_P^{\gamma^* \rightarrow \pi^+ \pi^-}(k_1, k_2) \cdot J_P^{N \rightarrow N'}(k_1, k_2), \quad (5.18)$$

$$\mathcal{M}_O = -\frac{8\pi^2 W^2}{3!} \int \frac{d^2 k_1 d^2 k_2 d^2 k_3 \delta^{(2)}(k_1 + k_2 + k_3 - p_{2\pi})}{(2\pi)^6 k_1^2 k_2^2 k_3^2} J_O^{\gamma^* \rightarrow \pi^+ \pi^-}(k_1, k_2, k_3) \cdot J_O^{N \rightarrow N'}(k_1, k_2, k_3),$$

3390 where  $J_{P/O}^{\gamma^* \rightarrow \pi^+ \pi^-}$  is the impact factor for the transition  $\gamma^* \rightarrow \pi^+ \pi^-$  and  $J_{P/O}^{N \rightarrow N'}$  is the impact factor for the  
 3391 transition of the nucleon in the initial state  $N$  into the nucleon in the final state  $N'$ .

3392 The impact factors are calculated by standard methods. An important feature of the  $J_{P/O}^{\gamma^* \rightarrow \pi^+ \pi^-}$  impact  
 3393 factors is the presence of the appropriate two-pion generalized distribution amplitude (GDA) [?, ?, ?]:

$$J_P^{\gamma^* \rightarrow \pi^+ \pi^-}(k_1, k_2) = -\frac{i e g^2 \delta^{ab} Q}{2 N_C} \int_0^1 dz z \bar{z} P_P(k_1, k_2) \Phi^{I=1}(z, \zeta, m_{2\pi}^2), \quad (5.19)$$

$$J_O^{\gamma^* \rightarrow \pi^+ \pi^-}(k_1, k_2, k_3) = -\frac{i e g^3 d^{abc} Q}{4 N_C} \int_0^1 dz z \bar{z} P_O(k_1, k_2, k_3) \frac{1}{3} \Phi^{I=0}(z, \zeta, m_{2\pi}^2), \quad (5.20)$$

3395 where  $P_P$  and  $P_O$  are known perturbatively calculated functions.  $\zeta$  is the light-cone momentum fraction of  
 3396 the  $\pi^+$  in the two pion system of invariant mass  $m_{2\pi}$ , which is related to the polar decay angle  $\theta$  of the  $\pi^+$

3397 in the rest frame of the two pion system. The GDAs  $\Phi^I(z, \zeta, m_{2\pi}^2)$  are non-perturbative matrix elements  
 3398 containing the full strong interactions between the two pions. They are universal quantities much related to  
 3399 GPDs in the meson. One must distinguish the GDA  $\Phi^{I=0}$  where the pion pair is in an isosinglet state from  
 3400 the GDA  $\Phi^{I=1}$  where it is in an isovector state. The charge conjugation parity of the exchanged particle  
 3401 selects the charge parity, hence the isospin of the emerging two-pion state: the Pomeron (Odderon) exchange  
 3402 process involves the production of a pion pair in the  $C$ -odd (even) channel which corresponds to odd(even)  
 3403 isospin. In the numerical studies we use a simple ansatz [?] for the generalized distribution amplitudes  
 3404  $\Phi^I(z, \zeta, m_{2\pi}^2)$ . A crucial point is the choice of the parametrization of the phases in the GDA's since, through  
 3405 interference effects, the rapid variation of a phase shift leads to a characteristic  $m_{2\pi}$ -dependence of the  
 3406 asymmetry. We show on Fig. 5.36 the resulting estimate for the charge asymmetry defined as

$$A(Q^2, t, m_{2\pi}^2) = \frac{\int \cos \theta d\sigma(W^2, Q^2, t, m_{2\pi}^2, \theta)}{\int d\sigma(W^2, Q^2, t, m_{2\pi}^2, \theta)} = \frac{\int_{-1}^1 \cos \theta d \cos \theta 2 \operatorname{Re} [\mathcal{M}_P^{\gamma_L^*} (\mathcal{M}_O^{\gamma_L^*})^*]}{\int_{-1}^1 d \cos \theta [|\mathcal{M}_P^{\gamma_L^*}|^2 + |\mathcal{M}_O^{\gamma_L^*}|^2]}, \quad (5.21)$$

3407 where  $\theta$  is the polar decay angle of the  $\pi^+$  in the rest frame of the two pion system. In order to visualize  
 3408 a rather large uncertainty in our modeling we present our results with an error band dominated by the  
 3409 value of the soft coupling constant  $\alpha_{soft}$  which we vary in the interval of  $\alpha_{soft} = 0.3 - 0.7$  (see Ref. [?] for  
 3410 details). While detailed studies on the possibilities for detection of the final states are left for the future,  
 3411 this estimate demonstrates that the presence of the perturbative Odderon may be discovered in two pion  
 electroproduction at high energy (note that the asymmetry (5.21) is independent of  $W^2$ ).

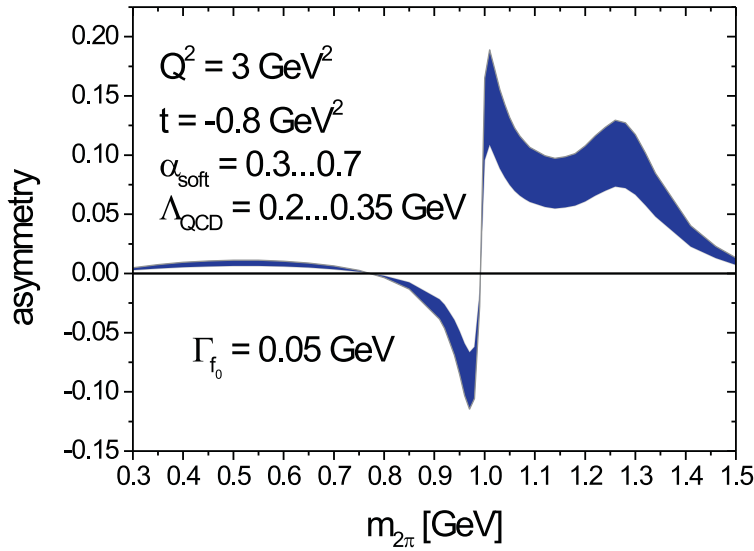


Figure 5.36: The charge asymmetry defined in Eq. (5.21) as a function of the  $\pi^+\pi^-$  invariant mass  $m_{2\pi}$ .

3412

## 3413 5.2.4 Inclusive diffraction

### 3414 Introduction to Diffractive Deep Inelastic Scattering

3415 Approximately 10% of low- $x$  DIS events are of the diffractive type,  $ep \rightarrow eXp$ , with the proton surviving the  
 3416 collision intact despite the large momentum transfer from the electron (Fig. 5.37). This process is usually  
 3417 interpreted as the diffractive dissociation of the exchanged virtual photon to produce any hadronic final state  
 3418 system  $X$  with mass much smaller than  $W$  and the same net quantum numbers as the exchanged photon  
 3419 ( $J^{PC} = 1^{--}$ ). Due to the lack of colour flow, diffractive DIS events are characterised by a large gap in the  
 3420 rapidity distribution of final state hadrons between the scattered proton and the diffractive final state  $X$ .



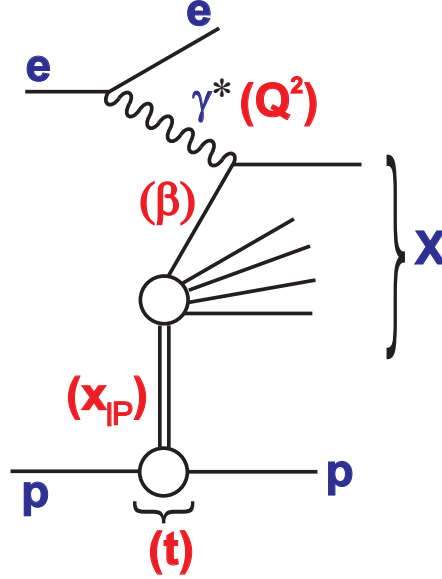


Figure 5.37: Illustration of the kinematic variables used to describe the inclusive diffractive DIS process  $ep \rightarrow eXp$ .

3421 As discussed in Subsection 5.2.3, similar processes exist in electron-ion scattering, where they can be  
 3422 sub-divided into fully coherent diffraction, where the nucleus stays intact ( $eA \rightarrow eXA$ ) and incoherent  
 3423 diffraction, where the nucleons within the nucleus are resolved and the nucleus breaks up ( $eA \rightarrow eXY$ ,  $Y$   
 3424 being a system produced via nuclear or nucleon excitation, with the same quantum numbers as  $A$ ).

3425 Theoretically, rapidity gap production is usually described in terms of the exchange of a net colourless  
 3426 object in the  $t$ -channel, which is often referred to as a pomeron [480,481]. In the simplest models [482,483],  
 3427 this pomeron has a universal structure and its vertex couplings factorise, such that it is applicable for  
 3428 example to proton-(anti)proton scattering as well as DIS. One of the main achievements at HERA has been  
 3429 the development of an understanding of diffractive DIS in terms of parton dynamics and QCD [484]. Events  
 3430 are selected using the experimental signatures of either a leading proton [485–487] or the presence of a large  
 3431 rapidity gap [486,488]. The factorisable pomeron picture has proved remarkably successful for the description  
 3432 of most of these data.

3433 The kinematic variables used to describe diffractive DIS are illustrated in Fig. 5.37. In addition to  $x$ ,  $Q^2$   
 3434 and the squared four-momentum transfer  $t$ , the mass  $M_X$  of the diffractively produced final state provides  
 3435 a further degree of freedom. In practice, the variable  $M_X$  is often replaced by

$$\beta = \frac{Q^2}{Q^2 + M_X^2 - t}. \quad (5.22)$$

3436 Small values of  $\beta$  refer to events with diffractive masses much bigger than the photon virtuality, while values  
 3437 of  $\beta$  close to unity are associated with small  $M_X$  values. In models based on a factorisable pomeron,  $\beta$  may  
 3438 be interpreted as the fraction of the pomeron longitudinal momentum which is carried by the struck parton.  
 3439 The variable

$$x_{\mathbb{P}} = \frac{x}{\beta} = \frac{Q^2 + M_X^2 - t}{Q^2 + W^2 - M^2}, \quad (5.23)$$

3440 with  $M$  the nucleon mass, is then interpreted as the longitudinal momentum fraction of the Pomeron with  
 3441 respect to the incoming proton or ion. It also characterises the size of the rapidity gap as  $\Delta\eta \simeq \ln(1/x_{\mathbb{P}})$ .

## Measuring Diffractive Deep Inelastic Scattering at the LHeC

Diffractive DIS (DDIS) can be studied in a substantially increased kinematic range at the LHeC, which will allow a whole new level of investigations of the factorisation properties of inclusive diffraction, will lead to new insights into low- $x$  dynamics and will provide a subset of final states with known quantum numbers for use in searches for new physics and elsewhere.

As shown in [333], collinear QCD factorisation holds in the leading-twist approximation in diffractive DIS and can be used to define diffractive parton distribution functions for the proton or ion. That is, within the collinear framework, the diffractive structure functions [489] can be expressed as convolutions of the appropriate coefficient functions with diffractive quark and gluon distribution functions, which in general depend on all of  $\beta$ ,  $Q^2$ ,  $x_{\mathbb{P}}$  and  $t$ . The diffractive parton distribution functions (DPDFs) are physically interpreted as probabilities for finding a parton with a small fraction of the proton momentum  $x = \beta x_{\mathbb{P}}$ , under the condition that the proton stays intact with a final state four-momentum which is specified up to an azimuthal angle by  $x_{\mathbb{P}}$  and  $t$ . The DPDFs may then be evolved in  $Q^2$  with the DGLAP evolution equations, with  $\beta$  playing the role of the Bjorken- $x$  variable. The other two variables  $x_{\mathbb{P}}$  and  $t$  play the role of external parameters to the DGLAP evolution.

In various extractions using HERA DDIS data [488,490–492] the DPDFs have been found to be dominated by gluons. Proton vertex factorisation holds to good approximation, such that the DPDFs vary only in normalisation with the four-momentum of the final state proton, the normalisation being well modelled using Regge phenomenology [481].

The LHeC will offer the opportunity to study diffractive DIS in an unprecedented kinematic range. The diffractive kinematic plane is illustrated in Fig. 5.38 for two different values of the Pomeron momentum fraction,  $x_{\mathbb{P}} = 0.01$  and  $x_{\mathbb{P}} = 0.0001$ . In each plot, accessible kinematic ranges are shown for three different electron energies in collision with the 7 TeV proton beam. Figure 5.38a corresponds to the coverage that will be possible based on leading proton detection (see Chapter 14). Figure 5.38b is more representative of the possibilities using the large rapidity gap technique (see the following). It is clear that the LHeC will have a much increased reach compared with HERA towards low values of  $x_{\mathbb{P}}$ , where the interpretation of diffractive events is not complicated by the presence of sub-leading meson exchanges, rapidity gaps are large and diffractive event selection systematics are correspondingly small. The range in the fractional struck quark momentum  $\beta$  extends by a factor of around 20 below that accessible at HERA.

Figure 5.39 further illustrates the achievable kinematic range of diffractive DIS measurements at the LHeC for the example of a 150 GeV electron beam combining large rapidity gap and proton tagging acceptance, compared with an estimation of the final HERA performance. For ease of illustration, a binning scheme is chosen in which the  $\beta$  dependence is emphasized and very large bins in  $x_{\mathbb{P}}$  and  $Q^2$  are taken. There is a large difference between the kinematically accessible ranges with backward acceptance cuts of  $1^\circ$  and  $10^\circ$ . Statistical uncertainties are typically much smaller than 1% for a luminosity of  $2 \text{ fb}^{-1}$ , so a much finer binning is possible, as required. The data points are plotted according to the H1 Fit B DPDF predictions [488], which amounts to a crude extrapolation based on dependences in the HERA range.

Systematic uncertainties are difficult to estimate without a detailed knowledge of the forward detectors and their acceptances. At HERA, sub-5% systematics have been achieved in the bulk of the phase space and it is likely that the LHeC could do at least as well.

The limitations in the kinematic range accessible with the large rapidity gap technique are investigated in Fig. 5.40. This shows the correlation between  $x_{\mathbb{P}}$  and the pseudorapidity  $\eta_{\text{max}}$  of the most forward particle in the hadronic final state system  $X$ , in simulated samples with LHeC and HERA beam energies, according to the RAPGAP event generator [132]. This correlation depends only on the proton beam energy and is thus the same for all LHeC running scenarios. At HERA, a cut at  $\eta_{\text{max}} \sim 3.2$  has been used to select diffractive events. Assuming LHeC forward instrumentation extending to around  $\theta = 1^\circ$ , a cut at  $\eta_{\text{max}} = 5$  may be possible, which would allow measurements to be made comfortably up to  $x_{\mathbb{P}} \sim 0.001$ , with some limited sensitivity at larger  $x_{\mathbb{P}}$ , a region where the proton tagging acceptance takes over (see Chapter 14). The two methods are thus complementary, and offer some common acceptance in an overlap region of  $x_{\mathbb{P}}$ . This redundancy could be used for cross-calibration of the two methods and their systematics, as has been done at HERA.

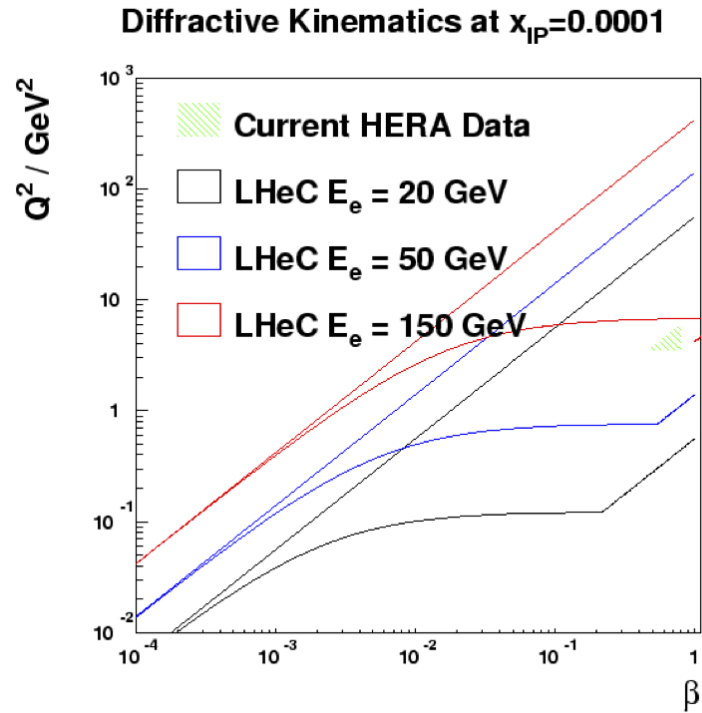
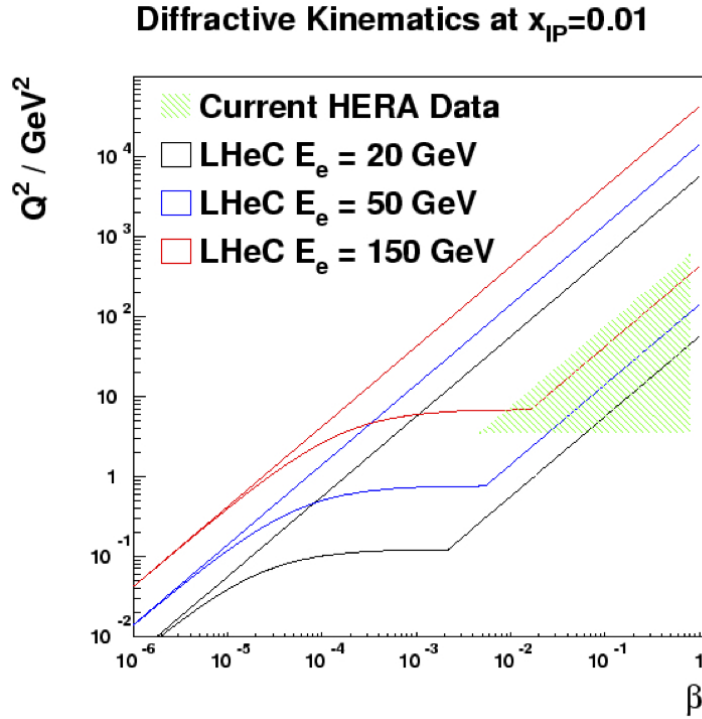


Figure 5.38: Diffractive DIS kinematic ranges in  $Q^2$  and  $\beta$  of HERA and of the LHeC for different electron energies  $E_e = 20, 50, 150 \text{ GeV}$  at  $x_{\text{P}} = 0.01$  (upper plot), and  $x_{\text{P}} = 0.0001$  (lower plot). In both cases,  $1^\circ$  acceptance is assumed for the scattered electron and the typical experimental restriction  $y > 0.01$  is imposed. No rapidity gap restrictions are applied.

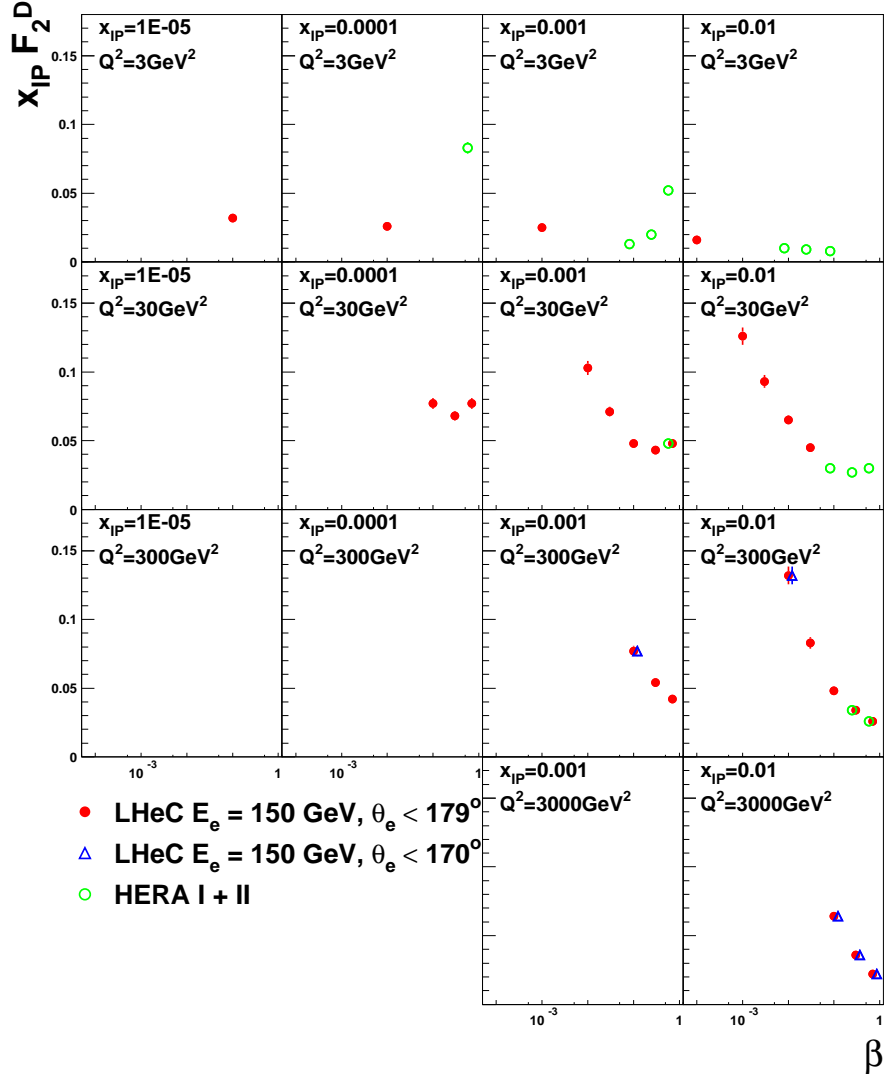


Figure 5.39: Simulation of a possible LHeC measurement of the diffractive structure function,  $F_2^D$  using a  $2 \text{ fb}^{-1}$  sample, compared with an estimate of the optimum results achievable at HERA using the full luminosity for a single experiment ( $500 \text{ pb}^{-1}$ ). The loss of kinematic region if the LHeC scattered electron acceptance extends to within  $10^\circ$  of the beam-pipe, rather than  $1^\circ$  is also illustrated.

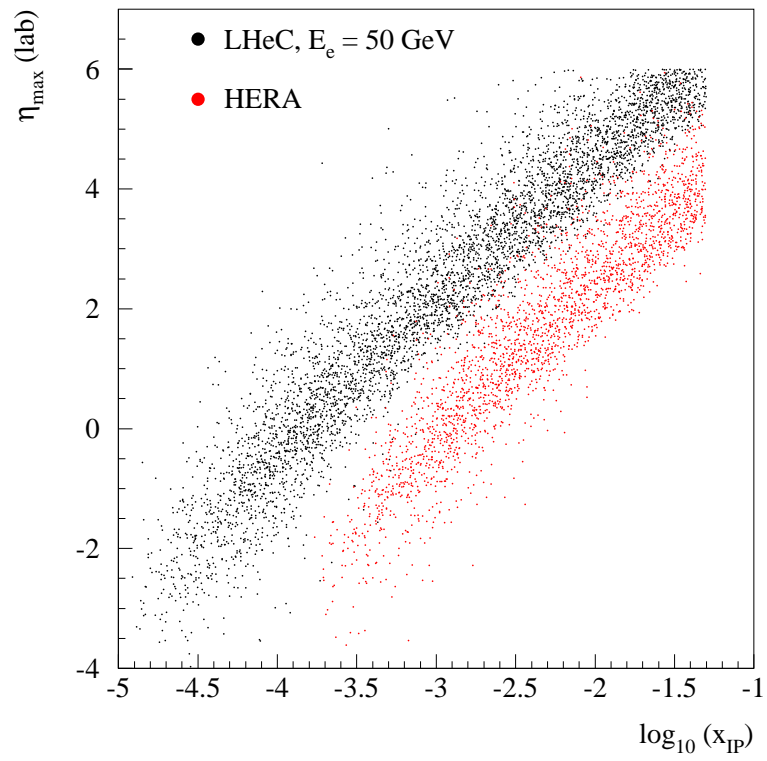


Figure 5.40: Comparison of the correlation between the rapidity gap selection variable,  $\eta_{\max}$  and  $x_{\text{P}}$  at HERA and at the LHeC, using events simulated with the RAPGAP Monte Carlo generator.

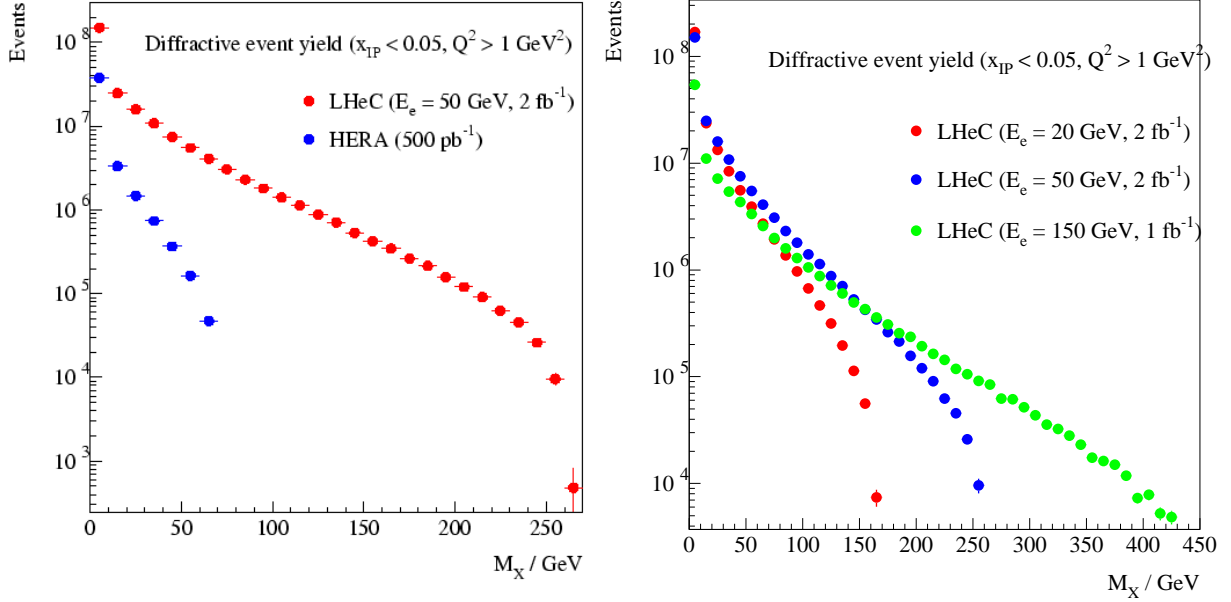


Figure 5.41: Simulated distributions in the invariant mass  $M_X$  according to the RAPGAP Monte Carlo model for samples of events obtainable with  $x_{\mathbb{P}} < 0.05$ . Left: one year of high acceptance LHeC running at  $E_e = 50$  GeV compared with HERA (full luminosity for a single experiment). Right: comparison between three different high acceptance LHeC luminosity and  $E_e$  scenarios.

### 3493 Diffractive Parton Densities and Final States

3494 The previously unexplored diffractive DIS region of very low  $\beta$  is of particular interest. Here, diffractively  
 3495 produced systems will be created with unprecedented invariant masses. Figure 5.41 left shows a comparison  
 3496 between HERA and the LHeC in terms of the  $M_X$  distribution which could be produced in diffractive  
 3497 processes with  $x_{\mathbb{P}} < 0.05$  (using the RAPGAP Monte Carlo model [132]). Figure 5.41 right compares the  
 3498 expected  $M_X$  distributions for one year of running at three LHeC electron beam energy choices. Diffractive  
 3499 masses up to several hundred GeV are accessible with reasonable rates, such that diffractive final states  
 3500 involving beauty quarks and  $W$  and  $Z$  bosons, or even exotic states with  $1^-$  quantum numbers, could be  
 3501 produced.

3502 Large improvements in DPDFs are likely to be possible from NLO DGLAP fits to LHeC diffractive  
 3503 structure function data. In addition to the extended phase space in  $\beta$ , the extension of the kinematic range  
 3504 towards larger  $Q^2$  increases the lever-arm for extracting the diffractive gluon density and opens the possibility  
 3505 of significant weak gauge boson exchange, which would allow a quark flavour decomposition for the first time.

3506 Proton vertex factorisation can be tested precisely by comparing the  $\beta$  and  $Q^2$  dependences at the LHeC  
 3507 at different small  $x_{\mathbb{P}}$  values in their considerable regions of overlap. The production of dijets or heavy quarks  
 3508 as components of the diffractive system  $X$  will allow precise testing of QCD collinear factorisation. These  
 3509 processes are driven by boson-gluon fusion ( $\gamma^*g \rightarrow q\bar{q}$ ) and thus provide complementary sensitivity to the  
 3510 diffractive gluon density to be compared with that from the scaling violations of the inclusive diffractive  
 3511 cross section.

3512 Diffractive final states containing charm signatures or relatively high transverse momentum dijets have  
 3513 been analyzed in detail at HERA. In the DIS regime, the cross sections for these processes are reproduced  
 3514 within uncertainties by calculations based on NLO DPDFs extracted from inclusive diffractive data for both  
 3515 the dijet [?, ?, 490, 493] and charm [?, 494] cases. By far the limiting factor in the precision of these tests  
 3516 is the large scale uncertainty on the theoretical predictions, due to the strong kinematic limitations on the

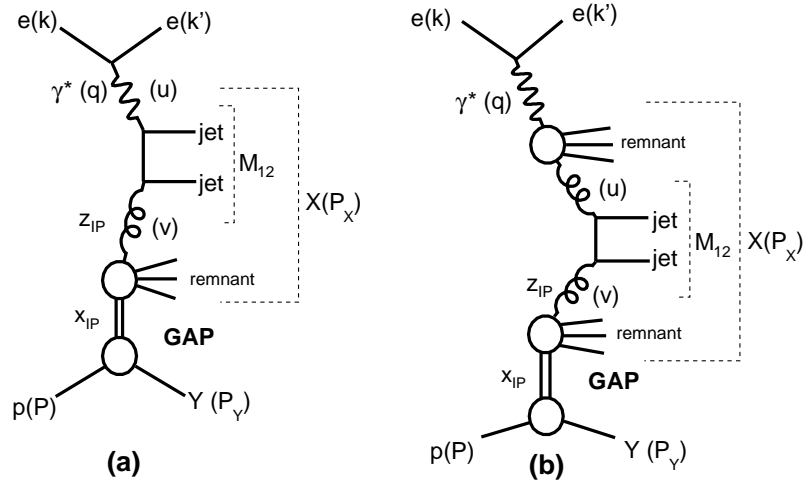


Figure 5.42: Leading order diagrams for diffractive dijet photoproduction. Diagrams (a) and (b) are examples of direct and resolved photon interactions, respectively.

3517 accessible jet transverse energies in diffraction at HERA. The situation from HERA photoproduction data is  
3518 more complex and is usually divided into direct and resolved photon contributions (figures 5.42a and 5.42b,  
3519 respectively). In the direct photon case, where the highly virtual photon has a point-like coupling, the pro-  
3520 cess is driven by photon-gluon fusion and at the current level of precision, cross sections are well predicted  
3521 using DPDFs extracted in fits to inclusive diffractive data [?, 442, 493]. In contrast, the resolved photon case  
3522 introduces sensitivity to the rich partonic structure of the quasi-real photon. It is these partons which par-  
3523 ticipate in the hard scattering sub-process producing the dijets, in a manner which resembles the situation  
3524 in hadron-hadron scattering. In this case, the possibility of additional rescatterings between the hadronic  
3525 remnants leads to a non-unit ‘survival probability’ for the rapidity gap [?, ?, ?] and a breakdown of factori-  
3526 sation. Factorisation tests have been carried out on several occasions in diffractive dijet photoproduction at  
3527 HERA, resulting in a somewhat confused situation on the size of the gap destruction effects [?, 442] and the  
3528 roles of resolved and direct contributions. Data in which the parton entering the hard scattering carries a  
3529 lower fraction  $x_\gamma$  of the photon momentum are required to clarify the situation, both experimentally and  
3530 theoretically.

3531 At the LHeC, much larger diffractive jet transverse momenta are measurable ( $p_T \lesssim M_X/2$ ) in both  
3532 photoproduction and DIS. An example study is shown in Fig. 5.43, where the diffractive DIS dijet cross  
3533 section is simulated for the LHeC kinematics and acceptance, using NLOJET++ [?], with the H1 2006 Fit B  
3534 DPDFs [488]. Kinematic cuts of  $x_P < 0.01$ ,  $Q^2 > 2 \text{ GeV}^2$ ,  $0.1 < y < 0.7$  and  $\theta_e > 1^\circ$ , matching the expected  
3535 LHeC detector geometry and ensuring good containment for the jets and the scattered electron. Jets were  
3536 reconstructed using the  $k_T$  algorithm with  $R = 1$  and an integrated luminosity of  $100 \text{ fb}^{-1}$  is assumed. The  
3537 statistical precision remains excellent up to jet  $p_T$  values of around 40 GeV, with measurements possible up  
3538 to around 50 GeV. Theory scale variations in the range of  $(0.25\mu^2, 4\mu^2)$  lead to much smaller uncertainties  
3539 than is the case in the HERA data.

3540 Diffractive dijet photoproduction at the LHeC is expected to be dominated by the resolved photon  
3541 contribution. A range of transverse momenta similar to the DIS case is accessible in photoproduction,  
3542 assuming tagging of electrons scattered through small angles as described in section 4.8. Fractional DPDF  
3543 momenta  $z_P$ , and in the resolved photoproduction case,  $x_\gamma$  values, between one and two orders of magnitude  
3544 smaller than at HERA are typically accessible. All of these improvements will lead to a new level of precision  
3545 in tests of factorization and constraints on the diffractive gluon density in new kinematic regions from  
3546 diffractive jet production at the LHeC [495].

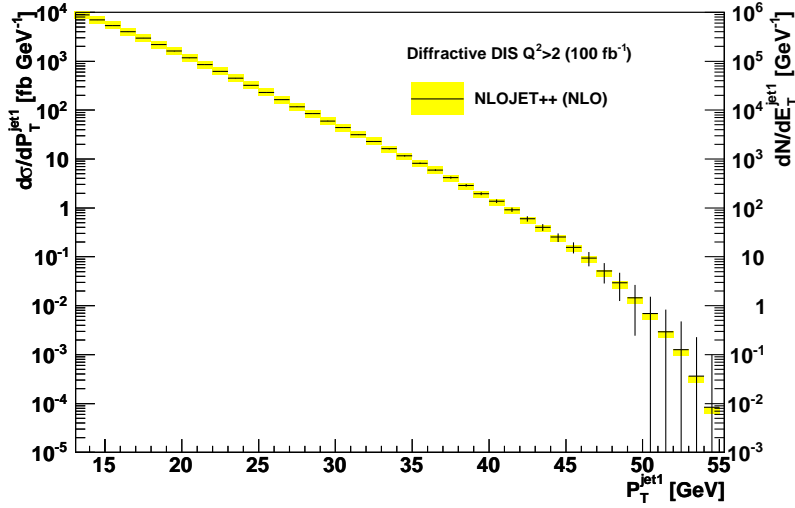


Figure 5.43: Simulated transverse momentum distribution of the jets in diffractive dijet production in DIS ( $Q^2 > 2 \text{ GeV}^2$ ). The simulation was performed using NLOJET++, assuming integrated luminosity of  $100 \text{ fb}^{-1}$  and high acceptance for the scattered electron ( $1^\circ$ ). Scale uncertainties are illustrated by varying the factorization scale in the range  $(0.25\mu^2, 4\mu^2)$ .

3547 The simulated measurement of the longitudinal proton structure function,  $F_L$  described in subsec-  
 3548 tion 4.1.5, could also be extended to extract the diffractive analogue,  $F_L^D$ . At small  $\beta$ , where the cross  
 3549 section for longitudinally polarised photons is expected to be dominated by a leading twist contribution,  
 3550 an  $F_L^D$  measurement provides further complementary constraints on the role of gluons in the diffractive  
 3551 PDFs. As  $\beta \rightarrow 1$ , a higher twist contribution from longitudinally polarised photons, closely related to that  
 3552 driving vector meson electroproduction, dominates the diffractive cross section in many models [496] and a  
 3553 measurement to even modest precision would give considerable insight. A first measurement of this quantity  
 3554 has recently been reported by the H1 Collaboration [?], though the precision is strongly limited by statistical  
 3555 uncertainties. The LHeC provides the opportunity to explore it in much finer detail.

3556 In contrast to leading proton production, the production of leading neutrons in DIS ( $ep \rightarrow eXn$ ) requires  
 3557 the exchange of a net isovector system. Data from HERA have supported the view that this process is  
 3558 driven dominantly by charged pion exchange over a wide range of neutron energies [498]. With the planned  
 3559 emphasis on zero degree calorimetry for leading neutron measurements (see Chapter 14), LHeC data will  
 3560 thus constrain the structure of the pion at much lower  $x$  and larger  $Q^2$  values than has been possible hitherto.  
 3561 Note also that the combination of rapidity gap detection and zero degree calorimetry offers the possibility  
 3562 of disentangling coherent from incoherent nuclear diffraction.

### 3563 Diffractive DIS, Dipole Models and Sensitivity to Non-linear Effects

3564 Diffractive DIS at the LHeC will provide an opportunity to test the predictions of collinear factorisation  
 3565 and the possible onset of non-linear or higher-twist effects in the evolution. Of particular importance is the  
 3566 semi-hard regime  $Q^2 < 10 \text{ GeV}^2$  and  $x$  as small as possible. It is possible that the non-linear saturation  
 3567 regime will be easier to reach with diffractive than with inclusive measurements, since diffractive processes  
 3568 are mostly sensitive to quantum fluctuations in the proton wave function that have a virtuality of order of  
 3569 the saturation scale  $Q_s^2$ , instead of  $Q^2$ . As a result, power corrections (not the generic  $\Lambda_{QCD}^2/Q^2$  corrections,  
 3570 but rather the sub-class of them of order  $Q_s^2/Q^2$ ) are expected to come into play starting from a higher  
 3571 value of  $Q^2$  in diffractive than in inclusive DIS. Indeed, there is already a hint of this at HERA: collinear



3572 factorization starts to fail below about  $3 \text{ GeV}^2$  in the case of  $F_2$  [38], while it breaks down already around  
 3573  $8 \text{ GeV}^2$  in the case of  $F_2^D$  [488]. This fact can alternatively be observed in the feature that models which  
 3574 in principle should only work for small  $Q^2$ , can in practice be used up to larger  $Q^2$  for diffractive than for  
 3575 inclusive observables (see e.g. [301]).

3576 With the sort of measurement precision for  $F_2^D$  achievable at the LHeC, it ought to be possible to  
 3577 distinguish between different models, as illustrated in Fig. 5.44. For the simulated data shown here, a  
 3578 conservative situation is assumed, in which the electron beam energy is  $50 \text{ GeV}$  and only the rapidity gap  
 3579 selection method is used, such that the highest  $x_{\mathbb{P}}$  bin is at  $0.001$ . H1 Fit B [488] extrapolations (as in  
 3580 Fig. 5.39) are compared with the “b-sat” [355, 356] and bCGC [499] dipole models. As has been found  
 3581 to be necessary to describe HERA data, photon fluctuations to  $q\bar{q}g$  states are included in addition to the  
 3582 usual  $q\bar{q}$  dipoles used to describe inclusive and vector meson cross sections. Both dipole models differ  
 3583 substantially from the H1 Fit B extrapolation. The LHeC simulated precision and kinematic range are  
 3584 sufficient to distinguish between a range of models with and without saturation effects, and also between  
 3585 different models which incorporate saturation.

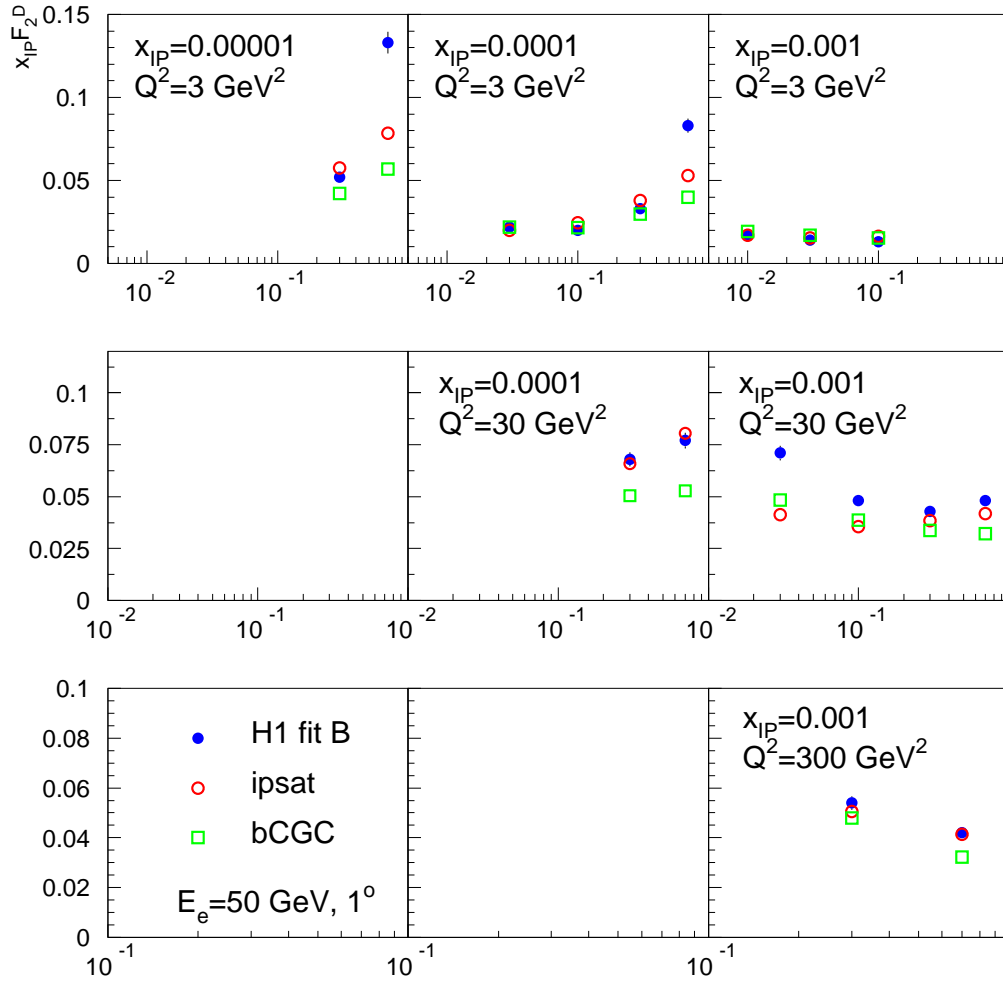


Figure 5.44: Simulated  $F_2^D$  measurements in selected  $x_{\mathbb{P}}$ ,  $\beta$  and  $Q^2$  bins. An extrapolation of the H1 Fit B DPDF fit to HERA data is compared with two different implementations of the dipole model, both of which contain saturation effects and include  $q\bar{q}g$  photon fluctuations in addition to  $q\bar{q}$  ones.

## Predicting nuclear shadowing from inclusive diffraction in ep

The connection between nuclear shadowing and diffraction was established a long time ago by Gribov [300]. Its key approximation is that the nucleus can be described as a dilute system of nucleons in the nucleus rest frame. The accuracy of this approximation for hadron-nucleus interactions is on the level of a few %, which reflects the small admixture of non-nucleonic degrees of freedom in nuclei and the small off-shellness of the nucleons in nuclei as compared to the soft strong interaction scale. Gribov's result can be derived using the AGK cutting rules [500] and hence it is a manifestation of unitarity [501, 502]. The formalism can be used to calculate directly cross sections of  $\gamma(\gamma^*)$ -nucleus scattering for the interaction with  $N = 2$  nucleons, but has to be supplemented by additional considerations to account for the contribution of the interactions with  $N \geq 3$  nucleons.

In this context, nuclear PDFs at small  $x$  can be calculated [501, 502] combining unitarity relations for different cuts of the shadowing diagrams corresponding to diffractive and inelastic final states, with the QCD factorisation theorem for hard diffraction [333]. A *model-independent* expression for the nuclear PDF at fixed impact parameter  $b$ , valid for the case  $N = 2$  [501], reads:

$$\begin{aligned} \Delta [xf_{j/A}(x, Q^2, b)] &= xf_{j/N}(x, Q^2, b) - xf_{j/A}(x, Q^2, b) \\ &= 8\pi A(A-1)\Re e \left[ \frac{(1-i\eta)^2}{1+\eta^2} \int_x^{0.1} dx_{\mathbb{P}} \beta f_j^{D(4)}(\beta, Q^2, x_{\mathbb{P}}, t_{\min}) \right. \\ &\quad \left. \times \int_{-\infty}^{\infty} dz_1 \int_{z_1}^{\infty} dz_2 \rho_A(\vec{b}, z_1) \rho_A(\vec{b}, z_2) e^{i(z_1-z_2)x_{\mathbb{P}}m_N} \right], \end{aligned} \quad (5.24)$$

where  $f_{j/A}(x, Q^2)$ ,  $f_{j/N}(x, Q^2)$  are nuclear and nucleon PDFs respectively,  $f_j^{D(4)}(\beta, Q^2, x_{\mathbb{P}}, t_{\min})$  are diffractive nucleon PDFs,  $\eta = \Re e A^{diff}/\Im m A^{diff} \approx 0.17$ ,  $\rho_A(r)$  is the nuclear matter density, and  $t_{\min} = -m_N^2 x_{\mathbb{P}}^2$  with  $m_N$  the nucleon mass. Eq. (5.24) satisfies the QCD evolution equations to all orders in  $\alpha_s$ . Numerical studies indicate that the dominant contribution to the shadowing probed by present experiments - corresponding to not very small  $x$  - comes from the region of relatively large  $\beta$ , for which small- $x$  approximations which involve resummation of  $\ln x$  terms are not important.

In Eq. (5.24), the interaction of different configurations of the hard probe (e.g.  $q\bar{q}$ ,  $q\bar{q}g$ , vector meson resonances, ...) are encoded in  $f_j^{D(4)}(\beta, Q^2, x_{\mathbb{P}}, t_{\min})$ . For the case of more than  $N = 2$  nucleons, there are two or more intermediate nucleon diffractive states which may be different and thus result in a different interaction between the the virtual photon and the nucleus. Therefore the interaction of the hard probe with  $N \geq 3$  nucleons is sensitive to finer details of the diffractive dynamics, namely the interplay between the interactions of the hard probe with  $N$  nucleons with different cross sections. This (colour) fluctuation effect is analogous to the inelastic shadowing phenomenon for the scattering of hadrons from nuclei, with the important difference that the dispersion of the interaction cross sections for the configurations in the projectile is much smaller in the hadronic case than in DIS.

In order to estimate this effect, one should note that, experimentally, the energy dependence of hard diffraction is close to that observed for soft Pomeron dynamics (the soft Pomeron intercept  $\alpha_{\mathbb{P}} \approx 1.11$ ) with the hard Pomeron contribution ( $\alpha_{\mathbb{P}} \approx 1.25$ ) being a small correction. This fact indicates that hadron-like (aligned jet) configurations [503], evolved via DGLAP evolution to large  $Q^2$ , dominate hard diffraction in DIS, while point-like configurations give an important, and increasing with  $Q^2$ , contribution to small- $x$  PDFs. This reduces the uncertainties in the treatment of  $N \geq 3$  contributions [407, 469]. Calculations show that the difference between two extreme scenarios of colour fluctuations is  $\leq 20\%$  for  $A \sim 200$  and much smaller for lighter nuclei, see the two FGS10 curves in Figs. 5.12 and 5.18. Besides, fluctuations tend to reduce the shadowing somewhat compared with the approximations neglecting them [302, 501, 504, 505] (compare the FGS10 results in Fig. 5.18 left with those labelled AKST). The gluon density is more sensitive to the magnitude of fluctuations than  $F_2$ , as can be inferred from Figs. 5.12 and 5.18 right.

Finally, the AGK technique also allows the calculation of the nuclear diffractive PDFs, see below, and fluctuations of multiplicity in non-diffractive DIS [469, 501, 506]. Both observables turn out to be sensitive to the pattern of colour fluctuations.

## Predictions for inclusive diffraction on nuclear targets

Inclusive diffraction was first measured in DIS events in  $ep$  collisions at the HERA collider. LHeC would be the first electron-ion collider machine, and therefore DDIS off nuclei at this machine will be a completely unexplored territory throughout the whole kinematic domain accessed. This implies a huge discovery potential in this field.

Despite this lack of experimental information on DDIS off nuclei, we have expectations, based on our current understanding of QCD, of how it should look. For instance, the theory of nuclear shadowing allows us to construct nuclear diffractive PDFs for large  $Q^2$  (see the previous item) while, within the Color Glass Condensate framework, nuclear diffractive structure functions can be predicted at small  $x$ . Depending on kinematics and the heavy ion species, different patterns of nuclear shadowing or antishadowing are expected as a function of  $\beta$  and  $x_{\mathbb{P}}$ . This is just one of many examples of what should be checked with an  $eA$  collider. Others are the impact parameter dependence introduced in the models, or the relation between nuclear shadowing and diffraction in  $ep$  which relies on what we know on DDIS from HERA. Therefore, in the larger kinematic domain accessible at the LHeC there are many things to discover about the structure of nuclei with diffractive measurements.

One of the main issues which needs to be established is whether the collinear, leading twist, factorization of inclusive diffraction, proved for protons, is applicable for scattering off nuclei, and the region of its applicability. An important question arises as to where the factorization would break down, i.e. for which values of  $Q^2$  and  $W$ , and whether it depends on the mass number, which would provide most important information on the role of the higher twists in different nuclei. A related issue is whether the factorization of the hadron vertex which is used in the proton case also holds in the nuclear case. In the analysis of the diffractive structure functions, the Regge-type factorization is usually assumed. This factorization states that the diffractive structure function is written as a product of the two factors: one of them is the Pomeron structure function that depends on  $\beta$  and  $Q^2$ , and the other is the Pomeron flux factor that is a function of  $t$  and  $x_{\mathbb{P}}$ . The latter one is usually parametrized using a Regge form with a Pomeron intercept being close to, albeit slightly higher than, the value obtained from soft interactions. It is currently unclear whether such factorization would still hold in the nuclear case, and this is one of the issues that can be tested at the LHeC. Also the range of possible parameters, like the Pomeron intercept, extracted from such analysis, would provide important details on the nuclear dynamics.

Predictions from a variety of models for nuclear coherent diffraction (see comments on the different types of diffractive processes on nuclei in subsection 5.2.3), are shown in Figs. 5.45 and 5.46. The chosen models here are FGS10 [469] and KLMV [507, 508]. Both plots show selected LHeC pseudodata for  $x_{\mathbb{P}}F_2^D$  as a function of  $\beta$  in bins of  $Q^2$  and  $x_{\mathbb{P}}$ . Statistical and systematic errors are added in quadrature, with systematic errors estimated to be at the level of 5%. The models give very different predictions both in absolute value and in their detailed dependence on  $x_{\mathbb{P}}$  and  $Q^2$ , which cannot be resolved without LHeC data.

Also shown in Fig. 5.47 are predicted diffractive-to-total ratios of the structure function  $F_2$  as a function of  $W$ . It was demonstrated in [337] that the constancy with  $W$  of this ratio for the proton - approximately shown by HERA data - can be naturally explained in models which include saturation effects, because in the black disk regime the ratio of diffractive-to-total cross sections tends to a constant value. It has been predicted that in the black disk regime this ratio (for coherent diffraction) may grow as large as 50% [?]. In reality, it could be smaller due to the density distribution in impact parameter. Within the given energy range the models shown in Fig. 5.47 predict a slight variation with energy. Note however the rather substantial difference between predictions coming from the different models as well as the fact that the plot shows the ratio of structure functions for given  $\beta$  and  $x_{\mathbb{P}}$  and not integrated cross sections. The uncertainty in modeling the impact parameter is one of the main sources of the discrepancies between the models. Precise LHeC data are required for clarifying these aspects.

Finally we note that, if the scattering on a nucleus at small  $x$  is dominated almost entirely by the so-called black disk regime, then in principle dramatic effects are expected that can be revealed by studying the final states in diffractive events [160]. As demonstrated in [56], the total virtual photon-nucleus cross section in the black disk limit reads simply

$$\sigma_{\gamma^*A} = 2\pi R_A^2 (1 - Z_3), \quad (5.25)$$

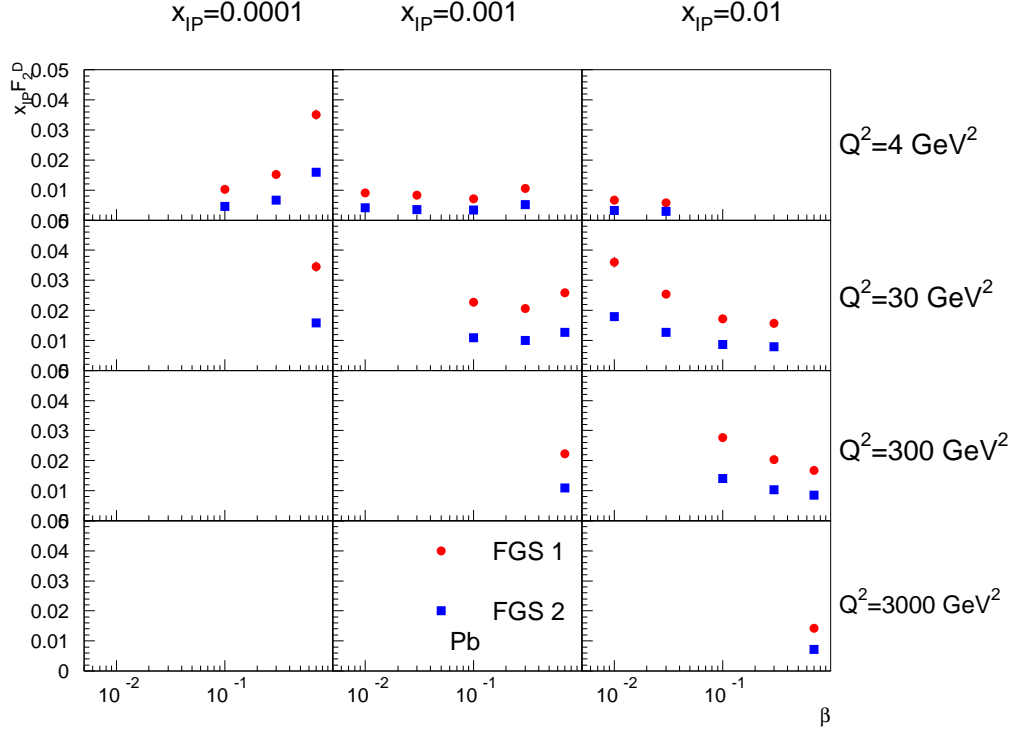


Figure 5.45: Diffractive structure function  $x_{\mathbb{P}}F_2^D$  for Pb in bins of  $Q^2$  and  $x_{\mathbb{P}}$  as a function of  $\beta$ . Model calculations are taken from [469].

3679 where  $R_A$  is the nuclear radius and  $Z_3$  the charge renormalization constant due to hadrons. The coefficient  
3680  $1 - Z_3$  can be computed in terms of the hadronic components of the photon wave function and related to  
3681 the cross section for the annihilation of electron-positron pairs into hadrons. Since the elastic part (i.e. that  
3682 due to diffraction) is half the total cross section in this regime, one can obtain from eq. (5.25) a spectrum  
3683 of the diffractive masses [160] that, in the center-of-mass of the diffractively produced system, should be the  
3684 same as in  $e^+e^-$  annihilation. A similar analysis for exclusive processes in this limit shows that the exclusive  
3685 diffractive production cross sections on nuclei (see subsection 5.2.3) would exhibit a  $1/Q^2$  behavior instead  
3686 of the  $1/Q^6$  behaviour expected from pQCD. This is due to the fact that a factor  $1/Q^4$  which comes from  
3687 the square of the cross section of the interaction of a small dipole with the target disappears in the black  
3688 disk limit.

## 3689 5.2.5 Jet and multi-jet observables, parton dynamics and fragmentation

### 3690 Introduction

3691 Inclusive measurements provide essential information about the integrated distributions of partons in a  
3692 proton. However, as was discussed in previous sections, more exclusive measurements are needed to pin  
3693 down the essential details of the small- $x$  dynamics. For example, a central prediction of the BFKL framework  
3694 at small  $x$  is the diffusion of the transverse momenta of the emitted partons between the photon and the  
3695 proton. In the standard collinear approach with integrated parton densities the information about the  
3696 transverse momentum is not accessible. However, it can be recovered within a different framework which  
3697 utilizes unintegrated parton distribution functions, dependent on parton transverse momentum as well as  $x$   
3698 and  $Q^2$ . Unintegrated PDFs are natural in the BFKL approach to small- $x$  physics. A general, fundamental  
3699 expectation is that as  $x$  decreases, the distribution in transverse momentum of the emitted partons broadens,  
3700 resulting in diffusion.

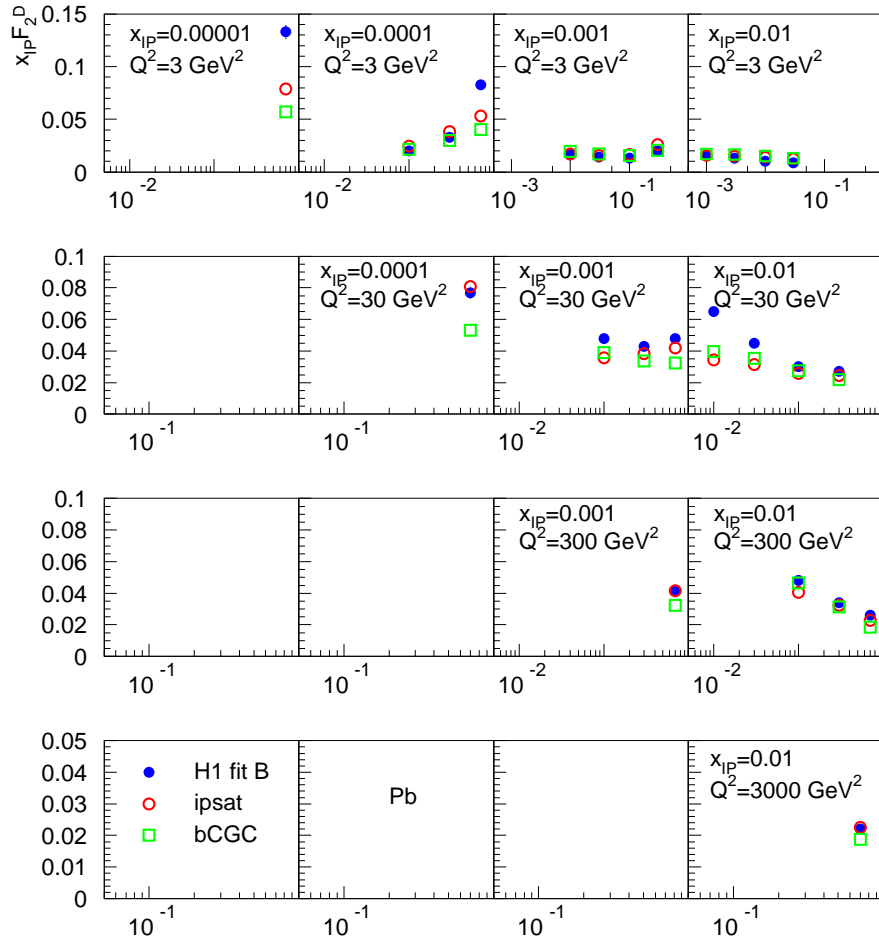


Figure 5.46: Diffractive structure function  $x_P F_2^D$  for Pb in bins of  $Q^2$  and  $x_P$  as a function of  $\beta$ . Model calculations are based on the dipole framework [507, 508].

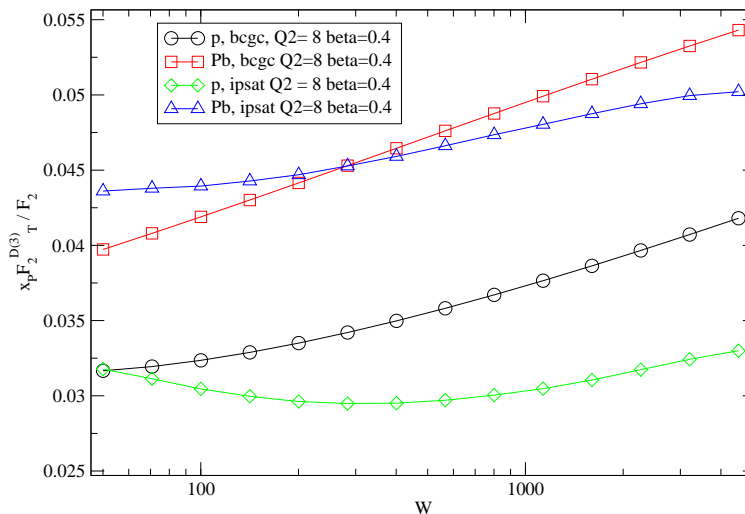


Figure 5.47: Ratio of the transversely polarised photon contribution to the diffractive structure function  $x_p F_2^{D(3)}$  to the inclusive structure function  $F_2$  in  $p$  and  $Pb$  for fixed values of  $Q^2$  and  $\beta$  as a function of the energy  $W$ . Model calculations are based on the dipole framework [507, 508].

3701 The specific parton dynamics can be tested by a number of exclusive measurements. These in turn can  
 3702 provide valuable information about the distribution of transverse momentum in the proton. As discussed  
 3703 in [509], for many inclusive observables the collinear approximation with integrated PDFs is completely  
 3704 insufficient, and even just including parton transverse momentum effects by hand may not be sufficient to  
 3705 describe many observables. In DIS, for example, processes needing unintegrated distributions include the  
 3706 transverse momentum distribution of heavy quarks. Similar problems are encountered in hadron collisions  
 3707 when studying heavy quark and Higgs production. The natural framework using unintegrated PDFs gives a  
 3708 much more reliable description. Furthermore, lowest-order calculations in the framework with unintegrated  
 3709 PDFs provide a much more realistic description of cross sections concerning kinematics. This may well lead  
 3710 to NLO and higher corrections being much smaller numerically than they typically are at present in standard  
 3711 collinear factorization, since the LO description is better.

3712 This approach, however, calls for precise measurements of a variety of relatively exclusive processes in  
 3713 a wide kinematic range. As discussed below, measurements of dijets, forward jets and particles, as well as  
 3714 transverse energy flow, are required to constrain the unintegrated PDFs and will give valuable information  
 3715 about parton dynamics at small  $x$ . While we will discuss the case of DIS on a proton, all conclusions can be  
 3716 paralleled for DIS on nuclei.

### 3717 Unintegrated PDFs

3718 The standard integrated parton densities are functions of the longitudinal momentum fraction of a parton  
 3719 relative to its parent hadron, with an integral over the parton transverse momentum. In contrast, uninte-  
 3720 grated, or transverse-momentum-dependent (TMD), parton densities depend on both parton longitudinal  
 3721 momentum fraction and parton transverse momentum. Processes for which unintegrated densities are natural  
 3722 include the Drell-Yan process (and its generalization to Higgs production), and semi-inclusive DIS (SIDIS).  
 3723 In SIDIS, we need TMD fragmentation functions as well as TMD parton densities.

3724 In the literature there are several apparently different approaches to TMD parton densities, with varying  
 3725 degrees of explicitness in the definitions and derivations.

- 3726 • The CSS approach [510–513] and some further developments [514].
- 3727 • The CCFM approach [515–518] for small  $x$ .

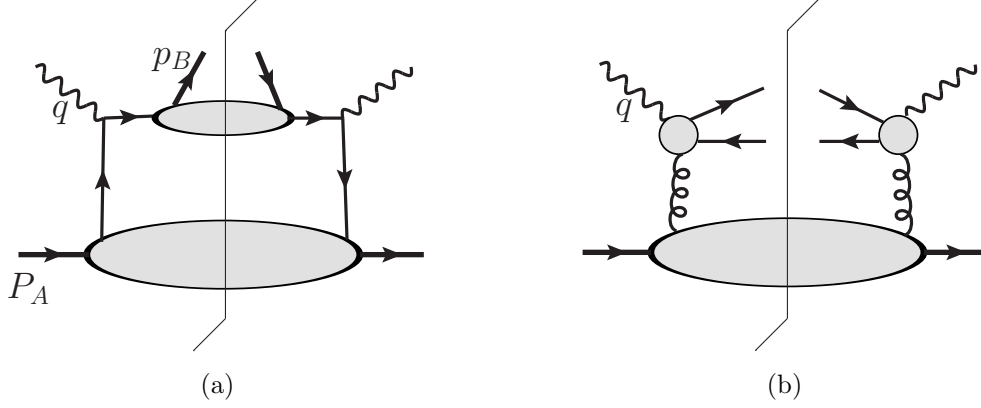


Figure 5.48: (a) Parton model factorisation for a SIDIS cross section. (b) Factorization for high-energy  $q\bar{q}$  photoproduction.

- Related BFKL associated works [316, 519].

Central to this subject is the concrete definition of TMD densities, and complications arise because QCD is a gauge theory. A natural initial definition uses light-front quantization: the unintegrated density of parton  $j$  in hadron  $h$  would be

$$f_{j/h}(x, \mathbf{k}_\perp) \stackrel{?}{=} \frac{1}{2x(2\pi)^3} \sum_\lambda \frac{\langle P, h | b_{k, \lambda, j}^\dagger b_{k, \lambda, j} | P, h \rangle_c}{\langle P, h | P, h \rangle}, \quad (5.26)$$

where  $b_{k, \lambda, j}$  and  $b_{k, \lambda, j}^\dagger$  are light-front annihilation and creation operators,  $j$  and  $\lambda$  label parton flavor and helicity, while  $k = (k^+, \mathbf{k}_\perp)$  is its momentum, and only connected graphs ‘c’ are considered. The ‘?’ over the equality sign warns that the formula does not apply literally in QCD. Expressing  $b_{k, \lambda, j}$  and  $b_{k, \lambda, j}^\dagger$  in terms of fields gives the TMD density as the Fourier transform of a light-front parton correlator. For example, for a quark

$$f_j(x, \mathbf{k}_\perp) \stackrel{?}{=} \int \frac{dw^- d^2\mathbf{w}_\perp}{(2\pi)^3} e^{-ixP^+ w^- + i\mathbf{k}_\perp \cdot \mathbf{w}_\perp} \langle P | \bar{\psi}_j(0, w^-, \mathbf{w}_\perp) \frac{\gamma^+}{2} \psi_j(0) | P \rangle_c. \quad (5.27)$$

One can similarly define a TMD fragmentation function [511]  $d_{h/j}(z, \mathbf{p}_\perp)$ , for the probability density of final-state hadron  $h$  in an outgoing parton  $j$ .

The corresponding factorization formula for SIDIS  $e + A(P_A) \rightarrow e + B(p_B) + X$  is [514]

$$\frac{d\sigma}{dx dQ^2 dz d^2\mathbf{P}_{B\perp}} = \sum_j \int d^2\mathbf{k}_\perp H_j f_{j/A}(x, \mathbf{k}_\perp) d_{B/j}(z, \mathbf{p}_{B\perp} + z\mathbf{k}_\perp), \quad (5.28)$$

where  $z$  and  $\mathbf{P}_{B\perp}$  are the fractional longitudinal momentum and the transverse momentum of the detected hadron relative to the simplest parton-model calculation of the outgoing jet, while  $H_j$  is the hard-scattering factor for electron-quark elastic scattering; see Fig. 5.48(a). In the fragmentation function  $d_{B/j}$  in Eq. (5.28), the use of  $z\mathbf{k}_\perp$  with its factor of  $z$  is because the transverse-momentum argument of the fragmentation function is a transverse momentum of the outgoing hadron relative to the parton initiating the jet, whereas  $\mathbf{k}_\perp$  is the transverse momentum of a parton relative to a hadron.

The most obvious way of applying (5.27) in QCD is to define the operators in light-cone gauge  $A^+ = 0$ , or, equivalently, to attach Wilson lines to the quark fields with a light-like direction for the Wilson lines. One minor problem in QCD is that, because the wave function is infinite (see below), the exact probability interpretation of parton densities cannot be maintained.

A much harder problem occurs because QCD is a gauge theory. Evaluating TMD densities defined by (5.27) in light-cone gauge gives divergences where internal gluons have infinite negative rapidity [510]. These

cancel only in the integrated density. The physical problem is that any coloured parton entering (or leaving) the hard scattering is accompanied by a cloud of soft gluons, and the soft gluons of a given transverse momentum are distributed uniformly in rapidity. A parton density defined in light-cone gauge corresponds to the asymptotic situation of infinite available rapidity.

A quark in a realisable hard scattering can be considered as having a transverse recoil against the soft gluons, but with a physically restricted range of rapidity. So a proper definition of a TMD density must implement a rapidity cut-off in the gluon momenta. Evolution equations must take into account the rapidity cut-off. The CSS formalism [510] has an explicit form of the rapidity cut-off and an equation for the dependence of TMD functions on the cut-off. But in any alternative formalism the need in the definitions for a cut-off to avoid rapidity divergences is non-negotiable.

Parton densities and fragmentation functions are only useful because they appear in factorisation theorems, so a useful definition must allow useful factorisation theorems to be formulated and derived. An improved definition involving Wilson line operators has recently been given in [520]; see also [521].

A second train of argument leads to a related kind of factorisation (the so-called  $k_{\perp}$ -factorisation) for processes at small  $x$  [125]. A classic process is photo- or electro-production of charm pairs  $\gamma(p_1) + h(p_2) \rightarrow Q(p_3) + \bar{Q}(p_4) + X$ , for which  $k_{\perp}$ -factorisation has the form

$$4M^2\sigma_{\gamma g}(\rho, M^2/Q_0^2) = \int d^2\mathbf{k}_{\perp} \int_0^1 \frac{dz}{z} \hat{\sigma}(\rho/z, \mathbf{k}_{\perp}^2/M^2) f_{g/h}(x, \mathbf{k}_{\perp}), \quad (5.29)$$

see Fig. 5.48(b). Here  $\rho = M^2/(p_1 + p_2)^2 \ll 1$ , and  $M$  is the mass of the heavy quark. The corresponding definition of the TMD gluon density [515] is said to use light-cone gauge, but there is in fact a hidden rapidity cut-off resulting from the use of the BFKL formalism.

Although both (5.28) and (5.29) use  $k_{\perp}$ -dependent parton densities, there are important differences. In (5.29), the hard scattering cross section  $\hat{\sigma}$  has the incoming gluon *off*-shell, whereas in (5.28), the hard scattering  $H_j$  uses on-shell partons. This is associated with a substantial difference in the kinematics. In (5.28) for SIDIS, the transverse momenta of the partons relative to their hadrons are less than  $Q$ , which allows the neglect of parton virtuality in the hard scattering. This approximation fails at large partonic transverse momentum,  $\mathbf{k}_{\perp} \sim Q$ , but ordinary collinear factorisation is valid in that region. So the factorisation formula is readily corrected, by adding a suitable matching term [510].

In contrast, in the small- $x$  formula (5.29), the gluon transverse momentum is comparable with the hard scale  $M$ . So it is not appropriate to neglect  $\mathbf{k}_{\perp}$  with respect to  $M$ , and the hard scattering is computed with an off-shell gluon. Factorisation is actually obtained from BFKL physics, where the gluons in Fig. 5.48(b) couple the charm quark subgraph to a subgraph where the lines have much larger rapidity.

The evolution equation of the CS-style TMD functions used in (5.28) gives the dependence of the TMD functions on the rapidity difference between the hadron and the virtual photon momenta. The results for TMD functions and for the cross sections can finally be obtained [514] in terms of (a) ordinary integrated parton densities and fragmentation functions, (b) perturbatively calculable quantities, and (c) a restricted set of non-perturbative quantities. The most important of these non-perturbative quantities is the distribution in recoil transverse momentum per unit rapidity against the emission of the soft interacting gluons, which is exponentiated after evolution. Importantly, it is independent of  $x$  and  $z$ , and it is universal between processes [522], and different only between gluons (color octet) and quarks (color triplet). There is also what can be characterised as a non-perturbative intrinsic transverse momentum distribution in both parton densities and fragmentation functions. In the quark sector, all but the fragmentation function are well measured in Drell-Yan processes [523].

On the other hand, evolution for the small- $x$  formalism in (5.29) is given by the BFKL method.

The avenues for further improvement on this subject are both theoretical and experimental. On the theory side, these concern the relation between different formalisms for evolution [316, 510, 514, 519, 524], the extension of factorisation theorems to a larger number of particles in the final state, and the matching to Monte Carlo generators. On the experimental side, the sensitivity to TMD functions is linked to a sensitivity to parton transverse momentum. This is the case of SIDIS at low transverse momentum. Another interesting process which would enable the TMD gluon functions to be probed is  $ep \rightarrow e\pi\pi X$ , with the pions being in



3800 different directions (different jets), but such that they are close to back-to-back in the  $(q, p_i)$  (the so-called  
 3801 brick wall) frame.

3802 Finally, measuring SIDIS and dijet production off protons or nuclei at the LHeC will allow detailed  
 3803 investigations of non-linear parton evolution in QCD. In this respect, the SIDIS cross section [525] and  
 3804 dihadron production [526] have been studied in the CGC framework. It turns out that, for small  $x$ , one is  
 3805 sensitive to the saturation regime of the target (proton or nucleus) wave function if the transverse momentum  
 3806 of the produced hadron is of the order of the saturation momentum.

### 3807 Dijet production and angular decorrelation

3808 Dijet production in high energy deep inelastic electron-proton scattering is a very valuable process for the  
 3809 study of the small- $x$  behavior in QCD. The dominant process is illustrated in Fig. 5.49, which is that of the  
 3810  $\gamma^* g \rightarrow q\bar{q} \rightarrow$  dijet production. The incoming gluon can have sizeable transverse momentum accumulated  
 3811 from diffusion in  $k_T$  along the gluon chain. As Bjorken- $x$  becomes smaller, and therefore the longitudinal  
 3812 momentum of the gluon also decreases, larger values of the transverse momentum  $k_T$  can be sampled. This  
 3813 will lead to an azimuthal decorrelation between the jets which increases with decreasing  $x$ . The definition of  
 3814  $\Delta\phi$  is indicated in Fig. 5.49. That is, the jets are no longer back-to-back since they must balance the sizable  
 3815 transverse momentum  $k_T$  of the incoming virtual gluon.

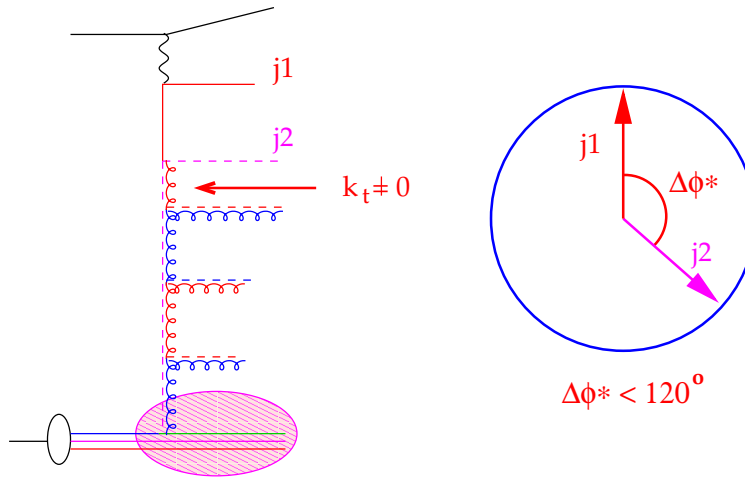


Figure 5.49: Schematic representation of the production of a system of two jets in the process of virtual photon-gluon fusion. The incoming gluon has non-vanishing transverse momentum  $k_T \neq 0$  which leads to the decorrelation of the jets.  $\Delta\phi$  is the angle between two jets.

3816 This picture of dijet production is to be contrasted with the conventional picture which uses integrated  
 3817 parton distributions, and typically leads to a narrow distribution about the back-to-back jet configuration.  
 3818 Higher orders usually broaden the distribution. However, as shown by direct measurements of DIS dijet  
 3819 data [527], NLO DGLAP calculations are not able to accommodate the pronounced effect of the decorrelation.

3820 Explicit calculations for HERA kinematics show that the models which include the resummation of  
 3821 powers of  $\log 1/x$  compare favourably with the experimental data [528–532]. The proposal and calculations  
 3822 to extend such studies to diffractive DIS also exist [533, 534].

3823 In Fig. 5.50 we show the differential cross section as a function of  $\Delta\phi$  for jets in the region  $-1 < \eta_{jet} <$   
 3824  $2.5$  with  $E_{T,jet1} > 7$  GeV and  $E_{T,jet2} > 5$  GeV found with the  $k_t$  jet algorithm in the kinematic range  
 3825  $Q^2 > 5$  GeV,  $0.1 < y < 0.6$  for different regions in  $x$ . The ‘MEPS’ prediction comes from a Monte Carlo  
 3826 generator [132] using  $\mathcal{O}(\alpha_s)$  matrix elements with a DGLAP-type parton shower. The ‘CDM’ prediction  
 3827 uses the same generator [132], but with higher order parton radiation simulated with the Colour Dipole

3828 Model [535], thus effectively including some  $k_t$  diffusion. Finally, the CASCADE Monte Carlo prediction  
 3829 [536], uses off-shell matrix elements convoluted with an unintegrated gluon distribution (CCFM set A), with  
 3830 subsequent parton showering according to the CCFM evolution equation.

3831 At large  $x$  all predictions agree reasonably well, in both shape and normalisation. At smaller  $x$  the  
 3832  $\Delta\phi$ -distribution becomes flatter for CDM and CASCADE, indicating higher order effects leading to a larger  
 3833 decorrelation of the produced jets. Whereas a decorrelation is observed, its size depends on the details of the  
 3834 parton evolution and thus a measurement of the  $\Delta\phi$  cross section provides a direct measurement of higher  
 order effects which need to be taken into account at small  $x$ .

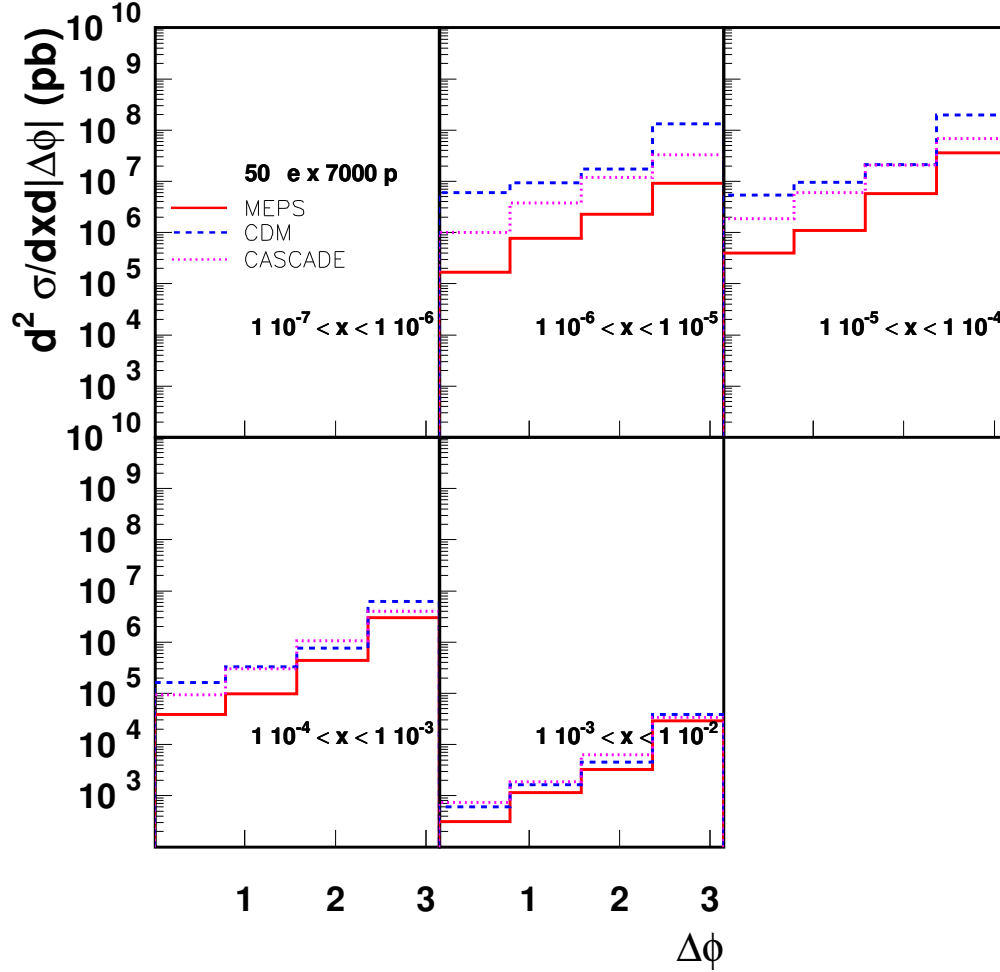


Figure 5.50: Differential cross section for dijet production as a function of the azimuthal separation  $\Delta\phi$  for dijets with  $E_{T,\text{jet}1} > 7$  GeV and  $E_{T,\text{jet}2} > 5$  GeV.

3835

3836 Thus, in principle, a measurement of the azimuthal dijet distribution offers a direct determination of  
 3837 the  $k_T$ -dependence of the unintegrated gluon distribution. When additionally supplemented by inclusive  
 3838 measurements, it can serve as an important constraint for the precise determination of the fully unintegrated  
 3839 parton distribution, with the transverse momentum dynamics in the proton completely unfolded.

## 3840 Dihadron correlations

3841 Another interesting observable which is directly sensitive to the transverse momentum dependence of the  
 3842 parton distribution in the proton or nucleus is the process of two hadron production<sup>12</sup>. Instead of two jets,  
 3843 one observes semi-inclusively two hadrons with certain transverse momentum. One can define the function  
 3844 which describes the angular correlation of the two produced hadrons in the following way:

$$C(\phi_{12}) = \frac{1}{\frac{d\sigma(\gamma^*N \rightarrow h_1 X)}{dz_{h_1}}} \frac{d\sigma^{\gamma^*N \rightarrow h_1 h_2 + X}}{dz_{h_1} dz_{h_2} d\phi_{12}}. \quad (5.30)$$

3845 In the above formula  $z_{h_1}, z_{h_2}$  are the longitudinal momentum fractions of the two produced hadrons w.r.t.  
 3846 the photon momentum and  $\phi_{12}$  is the azimuthal angle between them. The quantity  $\frac{d\sigma(\gamma^*N \rightarrow h_1 X)}{dz_{h_1}}$  is the single  
 3847 inclusive cross section. In Fig. 5.51 we show the results of the calculation using the formalism presented  
 3848 in [525]. The gluon density was evaluated using the GBW model [336] for the proton and a modified version  
 3849 of the same model for the nucleus. The electron energy is assumed to be  $E_e = 50$  GeV, the proton energy is  
 3850 7 TeV and the nucleus energy is 2.75 TeV. Also for the direct comparison with the nuclear case the curve  
 3851 with proton energy of 2.75 TeV is shown. The transverse momenta of the produced pions are integrated  
 3852 over, it is assumed that the leading particle has a minimum transverse momentum of  $p_T = 3$  GeV and the  
 3853 associated particle  $p_T = 2$  GeV. The photon virtuality is  $Q^2 = 4$  GeV<sup>2</sup>,  $y = 0.7$  and the fractions of the  
 3854 longitudinal momenta of the produced pions are fixed to be equal to  $z_{1h} = z_{2h} = 0.3$ . One clearly sees that  
 3855 the correlation function is wider for a larger target (nucleus) than for the proton. This suppression of the  
 3856 peak in the correlation function can be interpreted in this model as the effect of the stronger saturation in the  
 3857 gluon density for the nucleus than for the proton. We also see that the correlation function varies mildly with  
 3858 the available energy for the same target (i.e. proton). One observes stronger de-correlation of the produced  
 3859 hadrons with a higher energy or at smaller values of  $x$  which is indicative of the importance of the  $\ln 1/x$   
 3860 effects for this observable. Therefore the measurement of the dihadron correlation provides another way of  
 3861 constraining the unintegrated gluon distribution. In particular, measuring the dihadron correlations in DIS  
 3862 provides with a unique opportunity [?,526] to directly study the so-called Weizsäcker-Williams unintegrated  
 3863 gluon distribution.

## 3864 Forward observables

3865 It was proposed some time ago [537,538] that a process which would be very sensitive to the parton dynamics  
 3866 and the transverse momentum distribution was the production of forward jets in DIS. According to [537,538],  
 3867 DIS events containing identified forward jets provide a particularly clean window on small- $x$  dynamics. The  
 3868 schematic view of the process is illustrated in Fig. 5.52. The forward jet transverse momentum provides  
 3869 the second hard scale  $p_T$ . Hence one has a process with two hard scales: the photon virtuality  $Q$  and  
 3870 the transverse momentum of the forward jet  $p_T$ . As a result the collinear (DGLAP) configurations (with  
 3871 no diffusion and strongly ordered transverse momenta) can be eliminated by choosing the scales to be  
 3872 of comparable size,  $Q^2 \simeq p_T^2$ . Additionally, the jet is required to be produced in the forward direction by  
 3873 demanding that  $x_J$ , the longitudinal momentum fraction of the produced jet, is as large as possible, and  $x/x_J$   
 3874 is as small as possible. This requirement selects events with a large sub-energy between the jet and the virtual  
 3875 photon, such that the BFKL framework should be applicable. There have been dedicated measurements of  
 3876 forward jets at HERA [539–544], which demonstrated that DGLAP dynamics at NLO are indeed incompatible  
 3877 with the experimental measurements. On the other hand, calculations based on resummations of powers of  
 3878  $\log 1/x$  (BFKL and others) [545–551] are consistent with the data. The azimuthal dependence of forward  
 3879 jet production has also been studied [552,553] as a sensitive probe of the small- $x$  dynamics.

3880 Another observable that provides a valuable insight into the features of small- $x$  physics is the transverse  
 3881 energy ( $E_T$ -flow) accompanying DIS events at small  $x$ . The diffusion of the transverse momenta in this

<sup>12</sup>This observable is currently discussed in the forward (proton) rapidity region in dAu collisions at RHIC and it shows features suggestive of physics beyond standard collinear factorization, although no consensus has been reached so far, see [?, 390–393] and references therein.

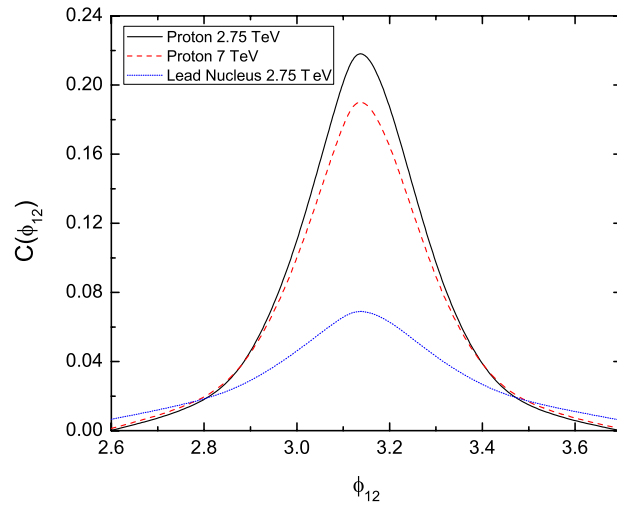


Figure 5.51: Di-hadron correlation function for the case of the scattering off the proton (red-dashed and black-solid lines) compared to the  $eA$  case (blue-dotted line). The energy of the electron is assumed to be equal  $E_e = 50$  GeV. The observed hadrons are pions.

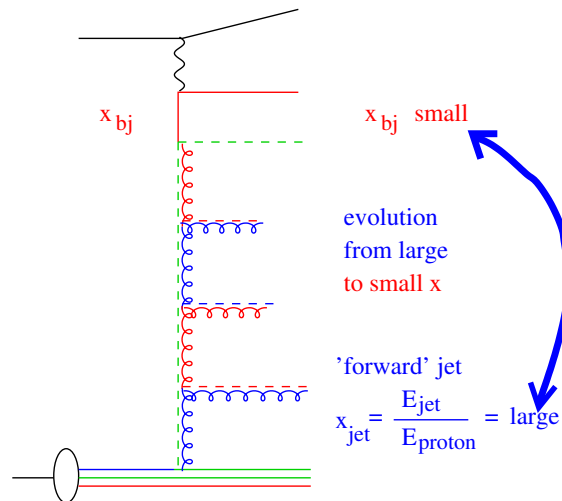


Figure 5.52: Schematic representation of the production of a high transverse momentum forward jet in DIS.

3882 region leads to a strongly enhanced distribution of  $E_T$  at small  $x$ . As shown in [554,555], small- $x$  evolution  
 3883 results in a broad Gaussian  $E_T$ -distribution as a function of rapidity. This should be contrasted with the  
 3884 much smaller  $E_T$ -flow obtained assuming strong  $k_T$ -ordering as in DGLAP-based approaches, which give an  
 3885  $E_T$ -distribution that narrows with decreasing  $x$ , for fixed  $Q^2$ .

3886 The first experimental measurements of the  $E_T$ -flow in small- $x$  DIS events indicate that there is signifi-  
 3887 cantly more  $E_T$  than is given by conventional QCD cascade models based on DGLAP evolution. Instead we  
 3888 find that they are in much better agreement with estimates which incorporate dynamics beyond fixed-order  
 3889 DGLAP [535,550,556] such as BFKL evolution. The latter dynamics are characterized by an increase of the  
 3890  $E_T$ -flow in the central region with decreasing  $x$ .

3891 However, the experimental data from HERA do not enable a detailed analysis due to their constrained  
 3892 kinematics. At the LHeC one could perform measurements with large separations in rapidity and for different  
 3893 selections of the scales  $(Q, p_T)$ . In particular, there is a possibility of varying scales to test systematically  
 3894 the parton dynamics from the collinear (strongly ordered) regime  $Q^2 \gg p_T^2$  to the BFKL (equal scale, Regge  
 3895 kinematics) regime  $Q^2 \simeq p_T^2$ . Measurements of the energy flow in different  $x$ -intervals, in the small- $x$  regime,  
 3896 should therefore allow a definitive check of the applicability of BFKL dynamics and of the eventual presence  
 3897 of more involved, non-linear effects.

3898 A simulation of forward jet production at the LHeC is shown in Figs. 5.53 and 5.54. The jets are required  
 3899 to have  $E_T > 10$  GeV with a polar angle  $\Theta_{jet} > 1^\circ$  or  $3^\circ$  in the laboratory frame. Jets are found with the  
 3900 SIScone jet-algorithm [557]. The DIS phase space is defined by  $Q^2 > 5$  GeV,  $0.05 < y < 0.85$ .

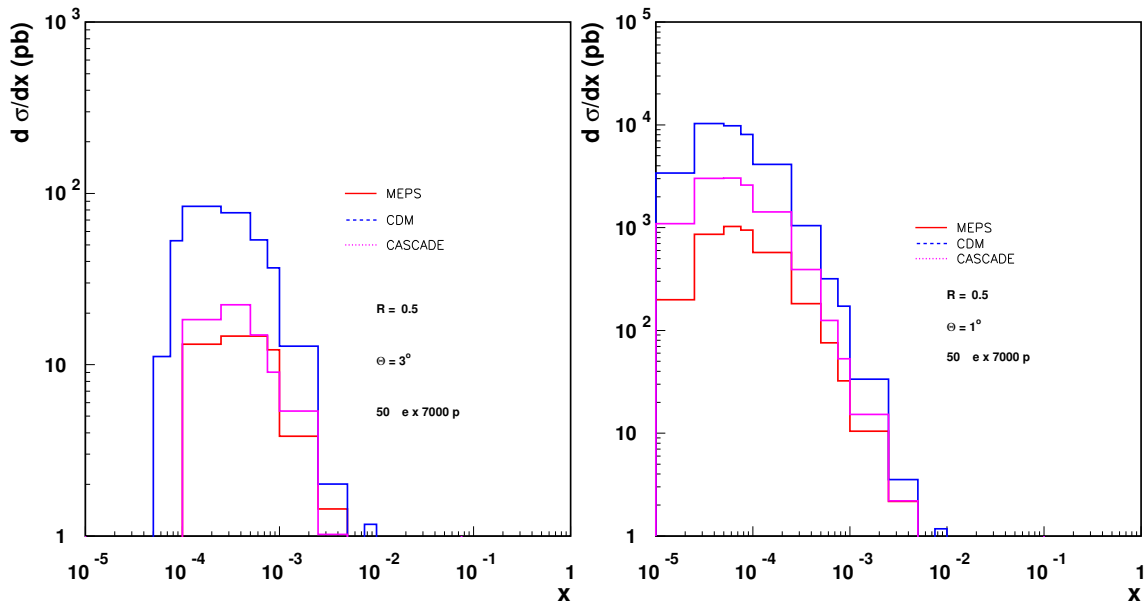


Figure 5.53: Cross section for forward jets with  $\Theta_{jet} > 3^\circ$  (left) and  $\Theta_{jet} > 1^\circ$  (right). Predictions from MEPS, CDM and CASCADE are shown. Jets are found with the SIScone algorithm using  $R = 0.5$ .

3901 In Fig. 5.53 the differential cross section is shown as a function of Bjorken  $x$  for an electron energy of  
 3902  $E_e = 50$  GeV. The calculations are obtained from the MEPS [132], CDM [535] and CASCADE [550] Monte  
 3903 Carlo models, as described in the previous section. Predictions for  $\Theta_{jet} > 3^\circ$  and  $\Theta_{jet} > 1^\circ$  are shown. One  
 3904 can clearly see that the small- $x$  range is explored in detail with the small angle scenario. In Fig. 5.54 the  
 3905 forward jet cross section is shown when using  $R = 1$  instead of  $R = 0.5$  (Fig. 5.53). It is important to note  
 3906 that good forward acceptance of the detector is crucial for the measurement of forward jets. The dependence  
 3907 of the cross section on the acceptance angle is very strong as is evident from comparisons between the cross  
 3908 sections for different  $\Theta_{jet}$  cuts in Figs. 5.53 and 5.54.

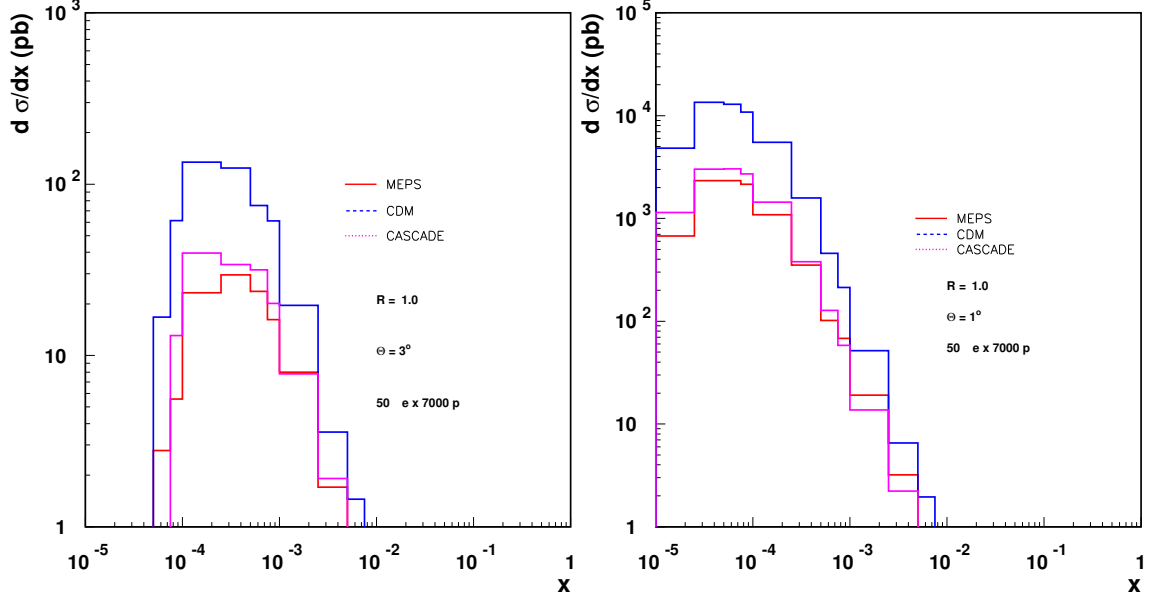


Figure 5.54: Cross section for forward jets with  $\Theta_{jet} > 3^\circ$  (left) and  $\Theta_{jet} > 1^\circ$  (right). Predictions from MEPS, CDM and CASCADE are shown. Jets are found with the SIScone algorithm using  $R = 1.0$ .

3909 A complementary reaction to that of forward jets is the production of forward  $\pi^0$  mesons in DIS. Despite  
 3910 having a lower rate, this process offers some advantages over forward jet production. By looking onto  
 3911 single particle production the dependencies on the jet finding algorithms can be eliminated. Also, the  
 3912 non-perturbative hadronisation effects can be effectively encompassed into fragmentation functions [546].

### 3913 Perturbative and non-perturbative aspects of final state radiation and hadronization

3914 The mechanism through which a highly virtual parton produced in a hard scattering gets rid of its virtuality  
 3915 and colour and finally projects onto an observable final state hadron, is unknown to a great extent (see [415]  
 3916 and references therein). The different postulated stages of the process are illustrated in Fig. 5.55. The  
 3917 coloured parton undergoes QCD radiation before forming first a coloured excited bound state (pre-hadron),  
 3918 then a colourless pre-hadron and ultimately a final state hadron. These sub-processes are characterised by  
 3919 different time scales. While the first stage can be described in perturbative QCD [558], subsequent ones  
 3920 require models (e.g. the QCD dipole model for the pre-hadron stages) and non-perturbative information.

3921 The LHeC offers great opportunities to study these aspects and improve our understanding of all of  
 3922 them. The energy of the parton which is struck by the virtual photon implies a Lorentz dilation of the  
 3923 time scales for each stage of the radiation and hadronisation processes. All of them are influenced by the  
 3924 fact that they do not take place in the vacuum, but within the QCD field created by the other components  
 3925 of the hadron or nucleus. While at fixed target SIDIS or DY experiments, the lever arm in energy is  
 3926 relatively small (energy transfer to the struck parton in its rest frame  $\nu < 100$  GeV), at the LHeC this lever  
 3927 arm will be huge ( $\nu < 10^5$  GeV; see also in Subsec. 4.7.2 the abundant yield of expected high transverse  
 3928 momentum jets in photoproduction), implying that the different stages can be considered to happen in or  
 3929 out of the hadron field depending on the parton energy. Furthermore, the fact that we can introduce a piece  
 3930 of coloured matter of known length and density - a nucleus - by doing ePb collisions at different centralities,  
 3931 allows a controllable variation of the contribution of the different processes. The induced differences in  
 3932 the final distributions of hadrons, both in terms of their momenta and of their relative abundance, will  
 3933 provide important information about the time scales and the detailed physical mechanisms at work in each  
 3934 stage. Dramatic effects are predicted in some models [160], with a significant suppression of the forward

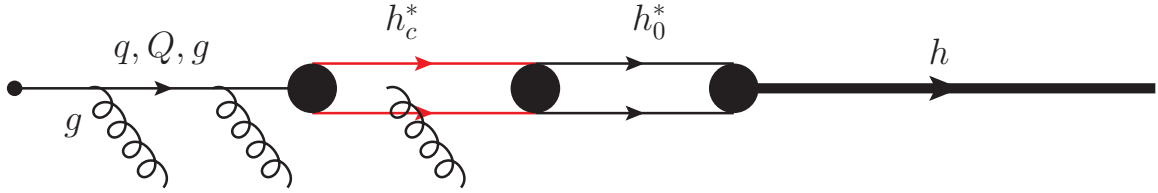


Figure 5.55: Sketch of the different postulated stages in the hadronisation of a highly virtual parton. From left to right: radiating parton; radiating coloured pre-hadron, colourless pre-hadron and final state hadron.

3935 hadron spectra due to the existence of a dense partonic system. Note that SIDIS experiments already  
 3936 provide information for the determination of standard fragmentation functions (see [559, 560] for a recent  
 3937 analysis). The other pieces of information, coming mainly from  $e^+e^-$  experiments, will not be improved  
 3938 until next-generation linear colliders become available.

3939 Furthermore, these studies will shed light on two aspects already discussed in Subsec. 5.1.4, related  
 3940 to the study of ultrarelativistic heavy-ion collisions: the characterization of the medium created in such  
 3941 collisions through hard probes, and the details of particle production in a dense situation which will define  
 3942 the initial conditions for the collective behavior of this medium. Concerning the latter, our theoretical tools  
 3943 for computing particle production in  $eA$  collisions are more advanced e.g. within the CGC framework, and  
 3944 on a safer ground than in nucleus-nucleus collisions (see Subsec. 5.1.1 and e.g. [414] and refs. therein). The  
 3945 possibility of disentangling the different mechanisms through which the factorisation that is used in dilute  
 3946 systems - collinear factorisation [289] - becomes broken by density effects (e.g. initial and final state energy  
 3947 loss or final state absorption) will be possible at the LHeC and will complement existing studies done at  
 3948 much smaller energies in fixed target SIDIS and DY experiments [415].

3949 In order to quantify the possibilities for SIDIS studies, we first show the expected cross sections for  $\pi^0$   
 3950 production in  $ep$  and  $ePb$  collisions at the LHeC for  $E_e = 60$  GeV, see Fig. 5.56. There the calculations are  
 3951 done at NLO [?], using as nucleon PDFs those from [361] and, in order to illustrate their effect, different  
 3952 nuclear PDFs [153, 405] and both ordinary [559, 560] and modified [?]<sup>13</sup> fragmentation functions. Cuts have  
 3953 been applied as in the H1 study [?]<sup>14</sup> whose data are well reproduced by the NLO calculation: angle of  
 3954 the  $\pi^0$  from the proton in the laboratory  $\theta_\pi \in [5^\circ, 25^\circ]$ , pion energy fraction  $x_\pi = E_\pi/E_p > 0.01$  and pion  
 3955 transverse momentum  $2.5 < p_T < 15$  GeV/c. All scales in the calculation have been fixed to  $(Q^2 + p_T^2)/2$   
 3956 ( $K$ -factors and the scale dependence of the results are discussed in [?]). From the plots in the figure, it  
 3957 becomes clear that even for these very restrictive cuts and for a modest integrated luminosity of  $1 \text{ fb}^{-1}$ , a  
 3958 large number of pions will be produced with relatively large transverse momentum. The nuclear effects on  
 3959 PDFs and on fragmentation require measurements with good statistic and systematic precision in order to  
 3960 be disentangled.

3961 The results with looser cuts:  $\theta_\pi \in [1^\circ, 25^\circ]$ ,  $x_\pi = E_\pi/E_p > 0.005$  that could be achieved at the LHeC,  
 3962 have also been studied. Their effect is an increase of the cross section by a factor  $\sim 3$  with respect to the  
 3963 results with the more restrictive H1 cuts.

3964 SIDIS also offers the possibility to measure the nuclear effects on fragmentation functions through the  
 3965 double ratio for nucleus  $A$  and particle  $k$ :

$$R_A^k(\nu, z, Q^2) = \frac{1}{N_A^e} \frac{dN_A^k}{d\nu dz} \bigg/ \frac{1}{N_p^e} \frac{dN_p^k}{d\nu dz}, \quad (5.31)$$

3966 with  $N^e$  the number of scattered electrons at a given  $\nu$  and  $Q^2$  i.e. the DIS cross section. At LO and for a  
 3967 single quark flavour, this double ratio becomes the ratio of fragmentation functions in  $eA$  over  $ep$ , see [415].

<sup>13</sup>In this reference, fragmentation functions in nuclear matter are extracted in a DGLAP analysis at LO and NLO.

<sup>14</sup>Studies with looser cuts - a more realistic situation at the LHeC, and of the achievable resolution in  $x$  and  $p_T$ , are left for the future.

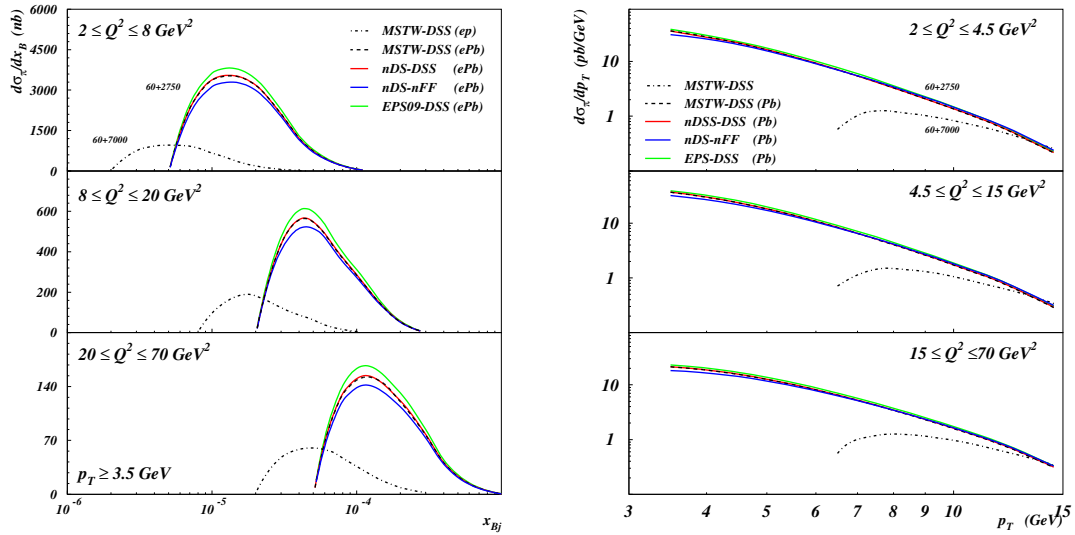


Figure 5.56: Cross section for inclusive  $\pi^0$  production versus Bjorken  $x_{Bj}$  for  $p_T > 3.5$  GeV/c (left) and versus  $p_T$  (right), computed in NLO QCD [?]. Dashed-dotted black lines refer to  $ep$  collisions. All other line types refer to  $ePb$  collisions: dashed black ones to standard nucleon PDFs [361] and fragmentation functions [559,560], solid red (green) ones to nuclear PDFs [405] ([153]) and nucleon fragmentations functions, and solid blue ones to nuclear PDFs [405] and nuclear fragmentation functions [?]. All cross sections are given per nucleon i.e. divided by 208 for Pb. Cuts:  $\theta_\pi \in [5^\circ, 25^\circ]$ ,  $x_\pi = E_\pi/E_p > 0.01$ , have been applied. See the text for further explanations.

Usually, the energy of the lepton-hadron/nucleus collisions are the same in numerator and denominator, and the collisions in the denominator are  $eD$  in order to suppress isospin effects as much as possible.

In order to estimate the nuclear modifications of fragmentation functions for the case of the LHeC, we compute this double ratio. For the numerator, we consider  $ePb$  collisions at 60+2750 GeV while for the denominator we take  $ep$  collisions at 60+7000 GeV. We follow the model in [?] which considers the energy loss of the parent parton through radiative processes<sup>15</sup> plus formation time arguments which make the effective length of traversed nuclear matter  $L$  smaller at small  $\nu$  than the geometrical one  $L_{max}$ . We use the LO nucleon PDFs in [361] and the nucleon fragmentation functions in [559,560], and also considered the nuclear modification of PDFs in [153]. We employ a value of the transport coefficient characterizing the strength of the interaction of a quark with nuclear matter  $\hat{q} = 0.7$  GeV<sup>2</sup>/fm<sup>16</sup>.

The results for  $\pi^0$  production are shown in Fig. 5.57. Several conclusions can be drawn. First, the effect of the difference in energy between numerator and denominator, and of isospin, are very small. Second, nuclear effects on fragmentation are larger for smaller  $\nu$ , as expected in a model in which the energy loss becomes energy-independent [?,?]. Third, the nuclear suppression is larger for larger  $z$  and it decreases with increasing  $Q^2$ , both effects due to the steepness of the fragmentation function and its evolution with  $Q^2$ . Finally, formation time limitations are only sizable for small  $\nu$ , as naively expected due to the possibility of hadron formation inside the nucleus in this kinematical region, see [?].

From these results we conclude that the study of SIDIS at the LHeC looks very promising. Still, extensive analyses at detector level are required in order to establish the accesible kinematical regions and to further explore the possibilities for particle identification.

<sup>15</sup>For this, we use the quenching weights in [?] instead of the simplified expressions employed in [?].

<sup>16</sup>This value is larger than the one used in [?]. We have checked that the model reproduces fixed target data on the  $\nu$  dependence of the ratio (5.31) for pion production on Kr over D in [?] using this value of  $\hat{q}$  without formation time considerations.



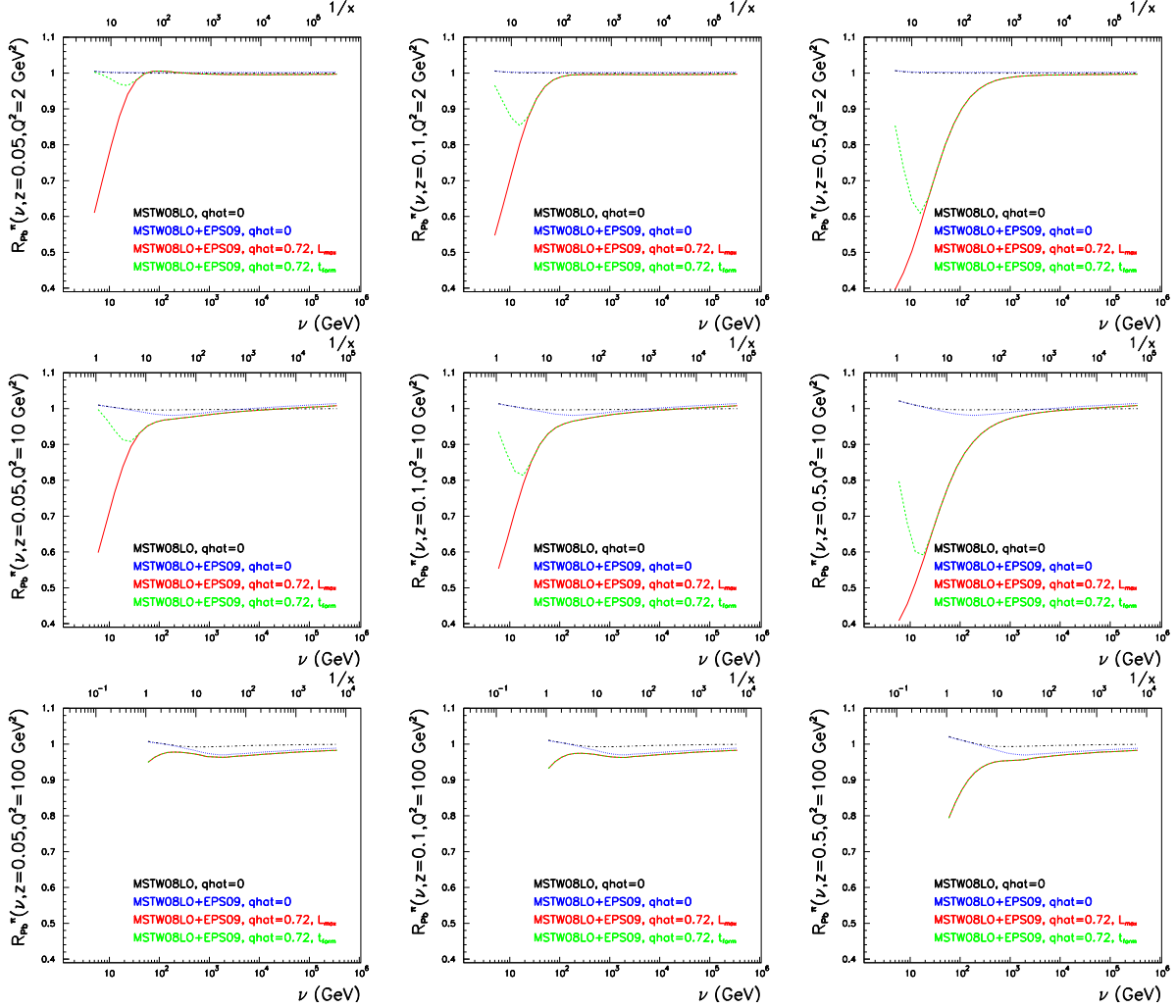


Figure 5.57: Ratio  $R_{\text{Pb}}^{\pi^0}(\nu, z, Q^2)$ , Eq. (5.31), versus  $\nu$  (lower horizontal axes) or  $1/x$  (upper horizontal axes) in ePb over  $ep$  at the LHeC, for  $z = 0.05, 0.1$  and  $0.5$  (from left to right) and  $Q^2 = 2, 10$  and  $100 \text{ GeV}^2$  (from top to bottom). Dashed-dotted black lines show the results without any nuclear effect but isospin, dotted blue ones further include the nuclear modification of PDFs [153], solid red ones the effect of parton energy loss with a geometrical length, and dashed green include formation time considerations. See the text and [?] for details of the calculation.

3988

## 5.2.6 Implications for ultra-high energy neutrino interactions and detection

The stringent constraints of the parton distributions at very small  $x$  from a future LHeC will have important implications for neutrino astronomy. Ultra-high energy neutrinos can provide important information about distant astronomical objects and the origin of the Universe. They have attracted a lot of attention during recent years, see the reviews [561,562]. Neutrino astronomy has many advantages over conventional photon astronomy. This is due to the fact that neutrinos, unlike photons, interact only weakly, so they can travel long distances being practically undisturbed. The typical interaction lengths for neutrinos and photons at energy  $E \sim 1 \text{ TeV}$  are about

$$\mathcal{L}_{\text{int}}^{\nu} \sim 250 \times 10^9 \text{ g/cm}^2, \quad \mathcal{L}_{\text{int}}^{\gamma} \sim 100 \text{ g/cm}^2.$$

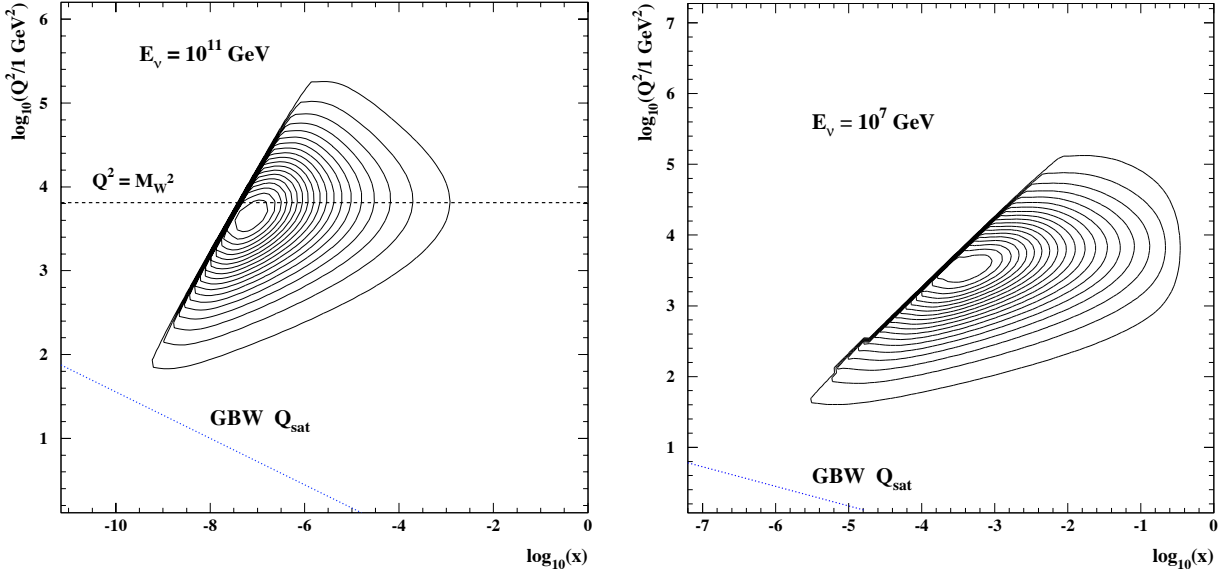


Figure 5.58: Contour plot showing the  $x, Q^2$  domain of the dominant contribution to the differential cross section  $d\sigma/d\ln(1/x)d\log Q^2$  for the total  $\nu$ -nucleon interaction at neutrino laboratory energies of  $E_\nu = 10^{11}$  GeV (left plot) and  $E_\nu = 10^7$  GeV (right plot). The 20 contours enclose contributions of 5, 10, 15  $\dots$  100 % of the cross section. The saturation scale according to the model in [336] is shown as a dashed line. See the text for further explanation.

3989 Thus, very energetic photons with energy bigger than  $\sim 10$  TeV cannot reach the Earth from the very distant  
 3990 corners of our Universe without being rescattered. In contrast, neutrinos can travel very long distances  
 3991 without interacting. They are also not deflected by galactic magnetic fields, and therefore at ultra-high  
 3992 energies the angular distortion of the neutrino trajectory is very small. As a result, highly energetic neutrinos  
 3993 reliably point back to their sources. The interest in the neutrinos at these high energies has led to the  
 3994 development of several neutrino observatories, see [562] and references therein.

3995 For reliable observations based on neutrino detection, precise knowledge about their production rates  
 3996 and interactions is essential to estimate the background, the expected fluxes and the detection probabilities.  
 3997 Even though neutrinos interact only weakly with other particles, strong interactions play an essential role  
 3998 in the calculations of their production rates and interaction cross sections. This is due to the fact that  
 3999 neutrinos are produced in the decays of various mesons such as  $\pi, K, D$  and even  $B$ , which are produced  
 4000 in high-energy proton-proton (or proton-nucleus or nucleus-nucleus) collisions. These hadronic processes  
 4001 occur mainly in the atmosphere though possibly also in the accretion discs of remote Active Galactic Nuclei.  
 4002 Further, the interactions of highly energetic neutrinos with matter are dominated by the deep inelastic cross  
 4003 section with nucleons or nuclei. Hence, low- $x$  information from high-energy collider experiments such as  
 4004 HERA, Tevatron, LHC and, most importantly, the future LHeC, is invaluable.

4005 One of the main uncertainties (if not the dominant one) in the current limits on high-energy neutrino  
 4006 production is due to the neutrino-nucleon (nucleus) cross section. In fact, event rates are proportional to  
 4007 the neutrino cross section in many experiments. This cross section involves the gluon distribution probed  
 4008 at very small values of Bjorken  $x$ , down to even  $\sim 10^{-9}$ , which corresponds to a very high centre of mass  
 4009 energy.

4010 To visualize the kinematic regime probed in ultra-high energy neutrino-nucleon interactions, contour  
 4011 plots of the differential cross section  $\frac{d^2\sigma}{d\ln 1/x d\ln Q^2/\Lambda^2}$  in the  $(x, Q^2)$  plane are shown in Fig. 5.58. The  
 4012 contours enclose regions with different contributions to the total cross section  $\sigma(E_\nu)$ . For very high energy  
 4013  $E_\nu = 10^{11}$  GeV the dominant contribution comes from the domain  $Q^2 \simeq M_W^2$  and  $x_{\min} \simeq M_W^2/(2M_N E) \sim$   
 4014  $10^{-8} - 10^{-7}$  where  $M_N$  is the nucleon mass, inaccessible to any current or proposed accelerators. However,

4015 at lower neutrino energy  $E_\nu = 10^7$  GeV the relevant domain of  $(x, Q^2)$  could be very well covered by the  
 4016 LHeC, thus providing important new constraints on the neutrino-nucleon cross section.

4017 On the other hand, another process that has been proposed for neutrino detection comes from the  
 4018 discovery of neutrino flavor oscillations, which makes it possible that high rates of  $\tau$  neutrinos reach the Earth  
 4019 despite being heavily suppressed in most postulated production mechanisms. The possibility to search for  
 4020  $\nu_\tau$ 's by looking for  $\tau$  leptons that exit the Earth, Earth-skimming neutrinos, has been shown to be particularly  
 4021 advantageous to detect neutrinos of energies in the EeV ( $10^{18}$  eV) range [563]. The short lifetime of a  $\tau$   
 4022 lepton originating a neutrino charged current interaction allows the  $\tau$  to decay in flight while still close to  
 4023 the Earth's surface, producing an outgoing air shower, detectable in principle by various techniques. This  
 4024 channel suffers from negligible contamination for other neutrino flavors. The sensitivity to  $\nu_\tau$ 's through the  
 4025 Earth-skimming channel directly depends both on the neutrino charged current cross section and on the  $\tau$   
 4026 range (the energy loss) which is determined by the amount of matter with which the neutrino has to interact  
 4027 to produce an emerging  $\tau$ . It turns out that the  $\tau$  energy loss is also determined by the behavior of the  
 4028 proton and nucleus structure functions at very small values of  $x$ , see e.g. [564]. The average energy loss per  
 4029 unit depth,  $X$ , is conveniently represented by:

$$-\left\langle \frac{dE}{dX} \right\rangle = a(E) + b(E)E, \quad b(E) = \frac{N_A}{A} \int dy y \int dQ^2 \frac{d\sigma^{lA}}{dQ^2 dy}, \quad (5.32)$$

4030 where the  $a(E)$  term is due to ionization,  $b(E)$  is the sum of fractional losses due to  $e^+e^-$  pair production,  
 4031 bremsstrahlung and photonuclear interactions,  $N_A$  is Avogadro's number and  $A$  is the mass number. The  
 4032 parameter  $a(E)$  is nearly constant and the term  $b(E)E$  dominates the energy loss above a critical energy  
 4033 that for  $\tau$  leptons is a few TeV, with the photonuclear interaction being dominant for  $\tau$  energies exceeding  
 4034  $E = 10^7$  GeV (as already assumed in Eq. (5.32)). In Fig. 5.59 the relative contribution to  $b(E)$  of different  
 4035  $x$  and  $Q^2$  regions is shown. It can be observed that the energy loss is dominated by very small  $x$  and, in  
 contrast to the case of the neutrino cross section, by small and moderate  $Q^2 \lesssim m_\tau^2$ .

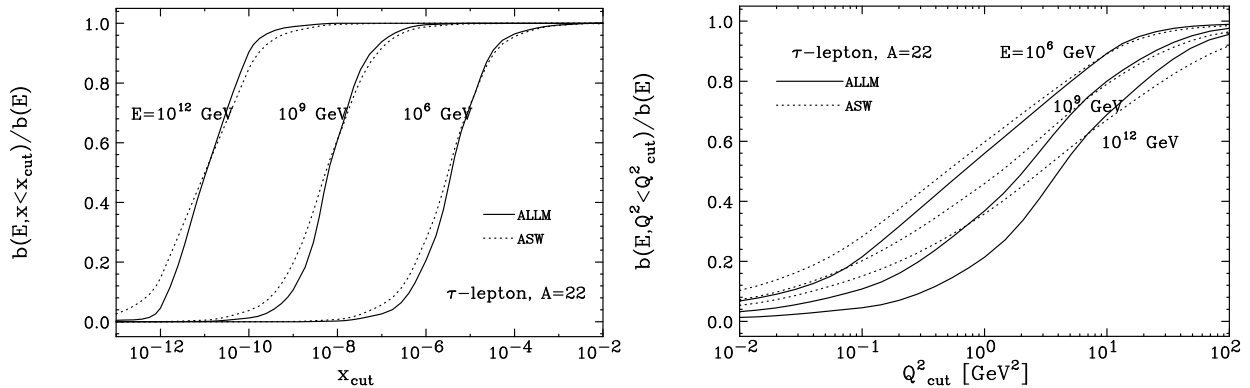


Figure 5.59: The relative contribution of  $x < x_{cut}$  (plot on the left) and of  $Q^2 < Q_{cut}^2$  (plot on the right) to the photonuclear energy loss rate,  $b(E)$ , for different neutrino energies  $E = 10^6, 10^9$  and  $10^{12}$  GeV, in two different models for the extrapolation of structure functions to very small  $x$ . See the text and [564] - from which these plots were taken - for explanations.

4036 As the LHeC will be able to explore a new regime of low  $x$  and moderate-to-high  $Q^2$ , and constrain the  
 4037 parton distributions, the measurements performed at this collider will be invaluable for the precise evaluation  
 4038 of the neutrino-nucleon (or nucleus) scattering cross sections and  $\tau$  energy loss necessary for ultra-high energy  
 4039 neutrino astronomy.  
 4040

## Chapter 6

# New Physics at Large Scales

Although the LHC is expected to be the discovery machine for physics beyond the Standard Model at the TeV scale, it will not always be possible to measure with precision the parameters of the new physics. In this section, it is shown that in many cases the LHeC can probe in detail deviations from the expected electroweak interactions shared by leptons and quarks, thus adding essential information on the new physics. Previous studies [2, 192–194] of the potential of high-energy  $e-p$  colliders for the discovery of exotic phenomena have considered a number of processes, most of which are reviewed here.

In some cases, Standard Model processes can also be better measured at the LHeC. Here, the charged and neutral current processes of SM Higgs production by vector boson fusion are investigated with the goal of measuring the  $H-b-b$  coupling.

### 6.1 New Physics in inclusive DIS at high $Q^2$

The LHeC collider would enable the study of deep inelastic neutral current scattering at very high squared momentum transfers  $Q^2$ , thus probing the structure of  $eq$  interactions at very short distances. At large scales new phenomena not directly detectable may become observable as deviations from the Standard Model predictions. A convenient tool to assess the experimental sensitivity beyond the maximal available center of mass energy and to parameterise indirect signatures of new physics is the concept of an effective four-fermion contact interaction. If the contact terms originate from a model where fermions have a substructure, a compositeness scale can be related to the size of the composite object. If they are due to the exchange of a new heavy particle, such as a leptoquark, the effective scale is related to the mass and coupling of the exchanged boson. Contact interaction phenomena are best observed as a modification of the expected  $Q^2$  dependence and all information is essentially contained in the differential cross section  $d\sigma/dQ^2$ . An alternative way to parameterize the effects of fermion substructure makes use of form factors, which would also lead to deviations of  $d\sigma/dQ^2$  with respect to the SM prediction. As a last example, low scale quantum gravity effects, which may be mediated via gravitons coupling to SM particles and propagating into large extra spatial dimensions, could also be observed as a modification of  $d\sigma/dQ^2$  at highest  $Q^2$ . These possible manifestations of new physics in inclusive DIS are addressed in this section.

#### 6.1.1 Quark substructure

The remarkable similarities in the electromagnetic and weak interactions of leptons and quarks in the Standard Model, and their anomaly cancellations in the family structure, strongly suggest a fundamental connection. It would therefore be natural to conjecture that they could be composed of more fundamental constituents, or that they form a representation of a larger gauge symmetry group than that of the Standard Model, in a Grand Unified Theory.

4074  
4075  
4076  
4077  
4078

A possible method to investigate fermion substructures is to assign a finite size of radius  $R$  to the electroweak charges of leptons and/or quarks while treating the gauge bosons  $\gamma$  and  $Z$  still as pointlike particles [195]. A convenient parametrisation is to introduce ‘classical’ form factors  $f(Q^2)$  at the gauge boson–fermion vertices, which are expected to diminish the Standard Model cross section at high momentum transfer

$$f(Q^2) = 1 - \frac{1}{6} \langle r^2 \rangle Q^2, \tag{6.1}$$

$$\frac{d\sigma}{dQ^2} = \frac{d\sigma^{SM}}{dQ^2} f_e^2(Q^2) f_q^2(Q^2). \tag{6.2}$$

4079  
4080  
4081  
4082

The square root of the mean-square radius of the electroweak charge distribution,  $R = \sqrt{\langle r^2 \rangle}$ , is taken as a measure of the particle size. Since the pointlike nature of the electron/positron is already established down to extremely low distances in  $e^+ e^-$  and  $(g - 2)_e$  experiments, only the quarks are allowed to be extended objects i.e. the form factor  $f_e$  can be set to unity in the above equation.

4083  
4084

Figure.6.1 shows the sensitivity that an LHeC collider could reach on the “quark radius” [196]. Two configurations have been studied ( $E_e = 70$  GeV and  $E_e = 140$  GeV), and two values of the integrated luminosity, per charge, have been assumed in each case. A sensitivity to quark radius below  $10^{-19}$  m could

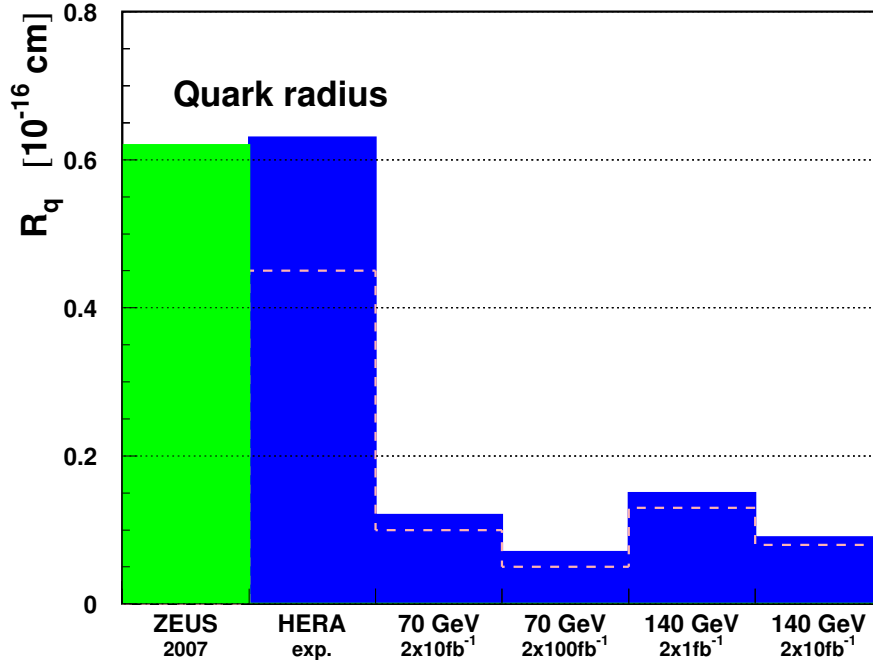


Figure 6.1: Sensitivity (95% confidence level limits) of an LHeC collider to the effective quark radius.

4085  
4086  
4087

be reached, which is one order of magnitude better than the current constraints, and comparable to the sensitivity that the LHC is expected to reach.

### 4088 6.1.2 Contact Interactions

4089  
4090  
4091

New currents or heavy bosons may produce indirect effects through the exchange of a virtual particle interfering with the  $\gamma$  and  $Z$  fields of the Standard Model. For particle masses and scales well above the available energy,  $\Lambda \gg \sqrt{s}$ , such indirect signatures may be investigated by searching for a four-fermion pointlike

4092  $(\bar{e}e)(\bar{q}q)$  contact interaction. The most general chiral invariant Lagrangian for neutral current vector-like  
 4093 contact interactions can be written in the form [197–199]

$$\mathcal{L}_V = \sum_{q=u,d} \{ \eta_{LL}^q (\bar{e}_L \gamma_\mu e_L) (\bar{q}_L \gamma^\mu q_L) + \eta_{LR}^q (\bar{e}_L \gamma_\mu e_L) (\bar{q}_R \gamma^\mu q_R) + \eta_{RL}^q (\bar{e}_R \gamma_\mu e_R) (\bar{q}_L \gamma^\mu q_L) + \eta_{RR}^q (\bar{e}_R \gamma_\mu e_R) (\bar{q}_R \gamma^\mu q_R) \}, \quad (6.3)$$

4094 where the indices  $L$  and  $R$  denote the left-handed and right-handed fermion helicities and the sum extends  
 4095 over  $up$ -type and  $down$ -type quarks and antiquarks  $q$ . In deep inelastic scattering at high  $Q^2$  the contributions  
 4096 from the first generation  $u$  and  $d$  quarks completely dominate and contact terms arising from sea quarks  $s$ ,  
 4097  $c$  and  $b$  are strongly suppressed. Thus, there are eight independent effective coupling coefficients, four for  
 4098 each quark flavour

$$\eta_{ab}^q \equiv \epsilon \frac{g^2}{\Lambda_{ab}^q{}^2}, \quad (6.4)$$

4099 where  $a$  and  $b$  indicate the  $L$ ,  $R$  helicities,  $g$  is the overall coupling strength,  $\Lambda_{ab}^q$  is a scale parameter and  $\epsilon$   
 4100 is a prefactor, often set to  $\epsilon = \pm 1$ , which determines the interference sign with the Standard Model currents.  
 4101 The ansatz eq. (6.3) can be easily applied to any new phenomenon, *e.g.* ( $eq$ ) compositeness, leptoquarks  
 4102 or new gauge bosons, by an appropriate choice of the coefficients  $\eta_{ab}$ . Scalar and tensor interactions of  
 4103 dimension 6 operators involving helicity flip couplings are strongly suppressed at HERA [199] and therefore  
 4104 not considered.

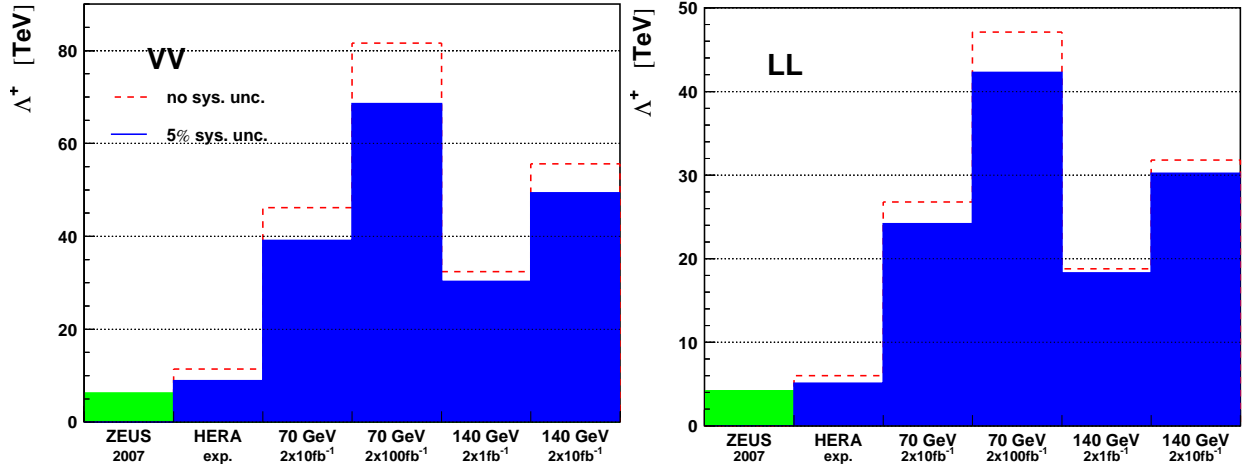


Figure 6.2: Sensitivity (95% confidence level limits) on the scale  $\Lambda$  for two example contact interactions.

4105 Figure 6.2 shows the sensitivity that an LHeC could reach on the scale  $\Lambda$ , for two example cases of contact  
 4106 interactions [196]. In general, with  $10 \text{ fb}^{-1}$  of data, LHeC would probe scales between 25 TeV and 45 TeV,  
 4107 depending on the model. The sensitivity of LHC to such  $eeqq$  interactions, which would affect the di-electron  
 4108 Drell-Yan (DY) spectrum at high masses, is similar.

4109 Figure 6.3 shows how the DY cross-section at LHC would deviate from the SM value, for three examples  
 4110 of  $eeqq$  contact interactions. In the “LL” model considered here, the sum in eq. (6.3) only involves left-  
 4111 handed fermions and all amplitudes have the same phase  $\epsilon$ . With only  $pp$  data, it will be difficult to  
 4112 determine simultaneously the size of the contact interaction scale  $\Lambda$  and the sign of the interference of the  
 4113 new amplitudes with respect to the SM ones: for example, for  $\Lambda = 20 \text{ TeV}$  and  $\epsilon = -1$ , the decrease of the  
 4114 cross-section with respect to the SM prediction for di-electron masses below  $\sim 3 \text{ TeV}$ , which is characteristic

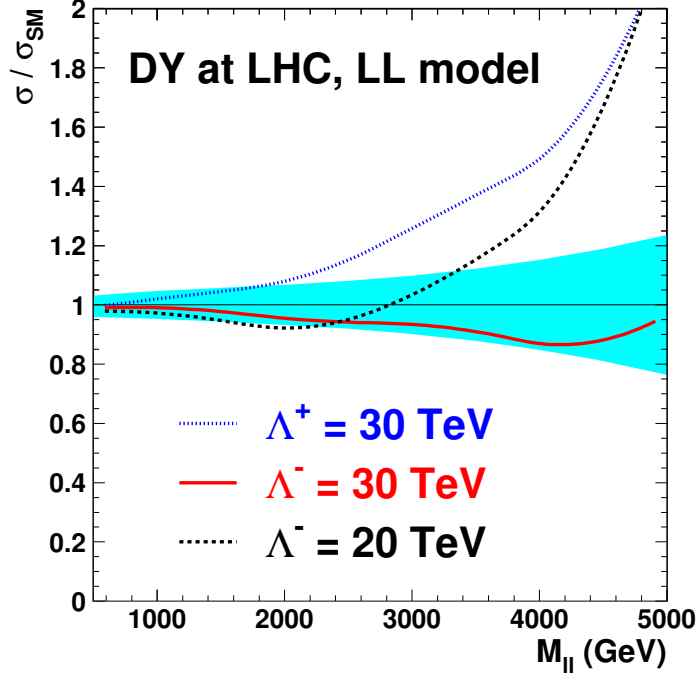


Figure 6.3: Example deviations, from its SM value, of the Drell-Yan cross-section at LHC as a function of the dilepton mass, in the presence of an  $eeqq$  contact interaction. The blue band shows the relative uncertainty of the predicted SM cross-sections due to the current uncertainties of the parton distribution functions, as obtained from the CTEQ 6.1 sets.

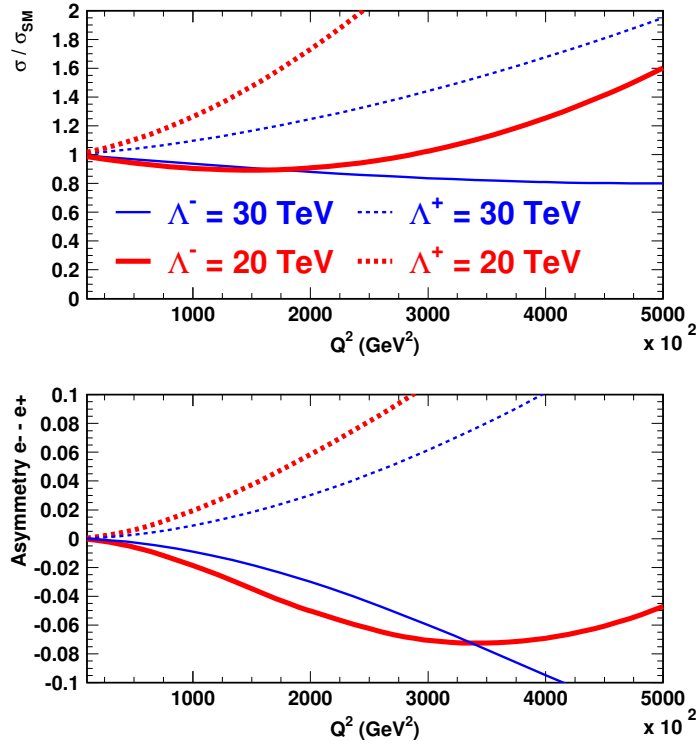


Figure 6.4: (top) Example deviations of the  $e^-p$  DIS cross-section at LHeC, in the presence of an  $eeqq$  CI. The ratio of the “measured” to the SM cross-sections,  $r = \sigma/\sigma_{SM}$ , is shown. (bottom) Asymmetry  $\frac{r(e^+) - r(e^-)}{r(e^+) + r(e^-)}$  between  $e^+p$  and  $e^-p$  measurements of  $\sigma/\sigma_{SM}$ .

4115 of a negative interference, is too small to be firmly established when uncertainties due to parton distribution  
4116 functions are taken into account.

4117 For the same “LL” model, the sign of this interference can be unambiguously determined at LHeC from  
4118 the asymmetry of  $\sigma/\sigma_{SM}$  in  $e^+p$  and  $e^-p$  data, as shown in Fig. 6.4.

4119  
4120 Moreover, with a polarised lepton beam,  $ep$  collisions would help determine the chiral structure of the  
4121 new interaction. More generally, it is very likely that both  $pp$  and  $ep$  data would be necessary to underpin the  
4122 structure of new physics which would manifest itself as an  $eeqq$  contact interaction. Such a complementarity  
4123 of  $pp$ ,  $ep$  (and also  $ee$ ) data was studied in [200] in the context of the Tevatron, HERA and LEP colliders.

### 4124 6.1.3 Kaluza-Klein gravitons in extra-dimensions

4125 In some models with  $n$  large extra dimensions, the SM particles reside on a four-dimensional “brane”, while  
4126 the spin 2 graviton propagates into the extra spatial dimensions and appears in the four-dimensional world  
4127 as a tower of massive Kaluza-Klein (KK) states. The summation over the enormous number of Kaluza-Klein  
4128 states up to the ultraviolet cut-off scale, taken as the Planck scale  $M_S$  in the  $4 + n$  space, leads to effective  
4129 contact-type interactions  $ff'f'$  between two fermion lines, with a coupling  $\eta = O(1)/M_S^4$ . In  $ep$  scattering,  
4130 the exchange of such a tower of Kaluza-Klein gravitons would affect the  $Q^2$  dependence of the DIS cross-  
4131 section  $d\sigma/dQ^2$ . At LHeC, such effects could be observed as long as the scale  $M_S$  is below 4 – 5 TeV. While  
4132 at the LHC, virtual graviton exchange may be observed for scales up to  $\sim 10$  TeV, and the direct production  
4133 of  $KK$  gravitons, for scales up to 5 – 7 TeV depending on  $n$ , would allow this phenomenon to be studied  
4134 further, LHeC data may determine that the new interaction is universal by establishing that the effect in  
4135 the  $eq \rightarrow eq$  cross-section is independent of the lepton charge and polarization, and, to some extent, of the  
4136 quark flavor.

## 4137 6.2 Leptoquarks and leptogluons

4138 The high energy of the LHeC extends the kinematic range of DIS physics to much higher values of electron-  
4139 quark mass  $M = \sqrt{sx}$ , beyond those of present  $ep$  colliders. By providing both baryonic and leptonic  
4140 quantum numbers in the initial state, it is ideally suited to a study of the properties of new bosons possessing  
4141 couplings to an electron-quark pair in this new mass range. Such particles can be squarks in supersymmetric  
4142 models with  $R$ -parity violation ( $\tilde{R}_p$ ), or first-generation leptoquark (LQ) bosons which appear naturally in  
4143 various unifying theories beyond the Standard Model (SM) such as:  $E_6$  [44], where new fields can mediate  
4144 interactions between leptons and quarks; extended technicolor [47,201], where leptoquarks result from bound  
4145 states of technifermions; the Pati-Salam model [45], where the leptonic quantum number is a fourth color of  
4146 the quarks or in lepton-quark compositeness models. They are produced as single  $s$ -channel resonances via  
4147 the fusion of incoming electrons with quarks in the proton. They are generically referred to as “leptoquarks”  
4148 in what follows. The case of “leptogluons”, which could be produced in  $ep$  collisions as a fusion between the  
4149 electron and a gluon, is also addressed at the end of this section.

### 4150 6.2.1 Phenomenology of leptoquarks in $ep$ collisions

4151 In  $ep$  collisions, LQs may be produced resonantly up to the kinematic limit of  $\sqrt{s_{ep}}$  via the fusion of  
4152 the incident lepton with a quark or antiquark coming from the proton, or exchanged in the  $u$ -channel, as  
4153 illustrated in Fig. 6.5. The coupling  $\lambda$  at the  $LQ - e - q$  vertex is an unknown parameter of the model.

4154 In the narrow-width approximation, the resonant production cross-section is proportional to  $\lambda^2 q(x)$  where  
4155  $q(x)$  is the density of the struck parton in the incoming proton.

4156 The resonant production or  $t$ -channel exchange of a leptoquark gives  $e + q$  or  $\nu + q'$  final states leading to  
4157 individual events indistinguishable from SM NC and CC DIS respectively. For the process  $eq \rightarrow LQ \rightarrow eq$ ,  
4158 the distribution of the transverse energy  $E_{T,e}$  of the final state lepton shows a Jacobian peak at  $M_{LQ}/2$ ,  
4159  $M_{LQ}$  being the LQ mass. Hence the strategy to search for a LQ signal in  $ep$  collisions is to look, among



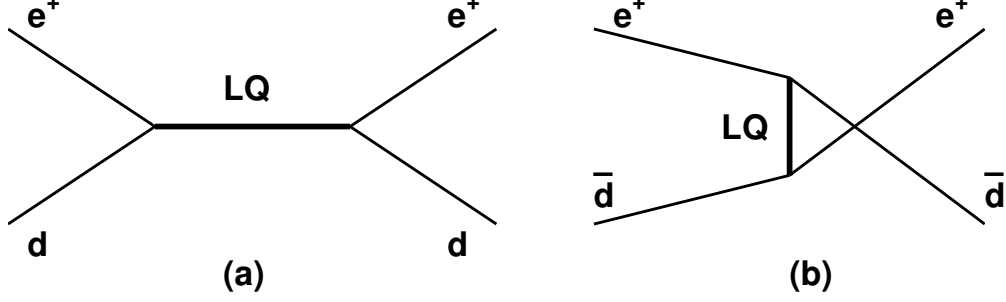


Figure 6.5: Example diagrams for resonant production in the  $s$ -channel (a) and exchange in the  $u$ -channel (b) of a LQ with fermion number  $F = 0$ . The corresponding diagrams for  $|F| = 2$  LQs are obtained from those depicted by exchanging the quark and antiquark.

4160 high  $Q^2$  (i.e. high  $E_{T,e}$ ) DIS event candidates, for a peak in the invariant mass  $M$  of the final  $e - q$  pair.  
 4161 Moreover, the significance of the LQ signal over the SM DIS background can be enhanced by exploiting the  
 4162 specific angular distribution of the LQ decay products (see spin determination, below).

## 4163 6.2.2 The Buchmüller-Rückl-Wyler Model

4164 A reasonable phenomenological framework to study first generation LQs is provided by the BRW model [202].  
 4165 This model is based on the most general Lagrangian that is invariant under  $SU(3) \times SU(2) \times U(1)$ , respects  
 4166 lepton and baryon number conservation, and incorporates dimensionless family diagonal couplings of LQs  
 4167 to left- and/or right-handed fermions. Under these assumptions LQs can be classified according to their  
 4168 quantum numbers into 10 different LQ isospin multiplets (5 scalar and 5 vector), half of which carry a  
 4169 vanishing fermion number  $F = 3B + L$  ( $B$  and  $L$  denoting the baryon and lepton number respectively) and  
 couple to  $e^+ + q$  while the other half carry  $|F| = 2$  and couple to  $e^+ + \bar{q}$ . These are listed in Table 6.1.

$F = -2$	Prod./Decay	$\beta_e$	$F = 0$	Prod./Decay	$\beta_e$
Scalar Leptoquarks					
$^{1/3}S_0$	$e_R^+ \bar{u}_R \rightarrow e^+ \bar{u}$	1/2	$^{5/3}S_{1/2}$	$e_R^+ u_R \rightarrow e^+ u$	1
	$e_L^+ \bar{u}_L \rightarrow e^+ \bar{u}$	1		$e_L^+ u_L \rightarrow e^+ u$	1
$^{4/3}\tilde{S}_0$	$e_L^+ \bar{d}_L \rightarrow e^+ \bar{d}$	1	$^{2/3}S_{1/2}$	$e_L^+ d_L \rightarrow e^+ d$	1
$^{4/3}S_1$	$e_R^+ \bar{d}_R \rightarrow e^+ \bar{d}$	1	$^{2/3}\tilde{S}_{1/2}$	$e_R^+ d_R \rightarrow e^+ d$	1
$^{1/3}S_1$	$e_R^+ \bar{u}_R \rightarrow e^+ \bar{u}$	1/2			
Vector Leptoquarks					
$^{4/3}V_{1/2}$	$e_L^+ \bar{d}_R \rightarrow e^+ \bar{d}$	1	$^{2/3}V_0$	$e_L^+ d_R \rightarrow e^+ d$	1
	$e_R^+ \bar{d}_L \rightarrow e^+ \bar{d}$	1		$e_R^+ d_L \rightarrow e^+ d$	1/2
$^{1/3}V_{1/2}$	$e_L^+ \bar{u}_R \rightarrow e^+ \bar{u}$	1	$^{5/3}\tilde{V}_0$	$e_L^+ u_R \rightarrow e^+ u$	1
$^{1/3}\tilde{V}_{1/2}$	$e_R^+ \bar{u}_L \rightarrow e^+ \bar{u}$	1	$^{5/3}V_1$	$e_R^+ u_L \rightarrow e^+ u$	1
			$^{2/3}V_1$	$e_R^+ d_L \rightarrow e^+ d$	1/2

Table 6.1: Leptoquark isospin families in the Buchmüller-Rückl-Wyler model. For each leptoquark, the superscript corresponds to its electric charge, while the subscript denotes its weak isospin.  $\beta_e$  denotes the branching ratio of the LQ into  $e + q$ .

4170  
 4171

We use the nomenclature of [203] to label the different LQ states. In addition to the underlying hypotheses

4172 of BRW, we restrict LQs couplings to only one chirality state of the lepton, given that deviations from lepton  
 4173 universality in helicity suppressed pseudoscalar meson decays have not been observed [204, 205].

4174 In the BRW model, LQs decay exclusively into  $eq$  and/or  $\nu q$  and the branching ratio  $\beta_e = \beta(LQ \rightarrow eq)$   
 4175 is fixed by gauge invariance to 0.5 or 1 depending on the LQ type.

### 4176 6.2.3 Phenomenology of leptoquarks in $pp$ collisions

4177 **Pair production** In  $pp$  collisions leptoquarks would be mainly pair-produced via  $gg$  or  $qq$  interactions. As  
 4178 long as the coupling  $\lambda$  is not too strong (e.g.  $\lambda \sim 0.3$  or below, corresponding to a strength similar to or lower  
 4179 than that of the electromagnetic coupling,  $\sqrt{4\pi\alpha_{em}}$ ), the production cross-section is essentially independent  
 4180 of  $\lambda$ . At the LHC, LQ masses up to about 1.5 to 2 TeV will be probed [206], independently of the coupling  $\lambda$ .  
 4181 However, the determination of the quantum numbers of a first generation LQ in the pair-production mode  
 4182 is not possible (e.g. for the fermion number) or ambiguous and model-dependent (e.g. for the spin). Single  
 4183 LQ production is much better suited for such studies.

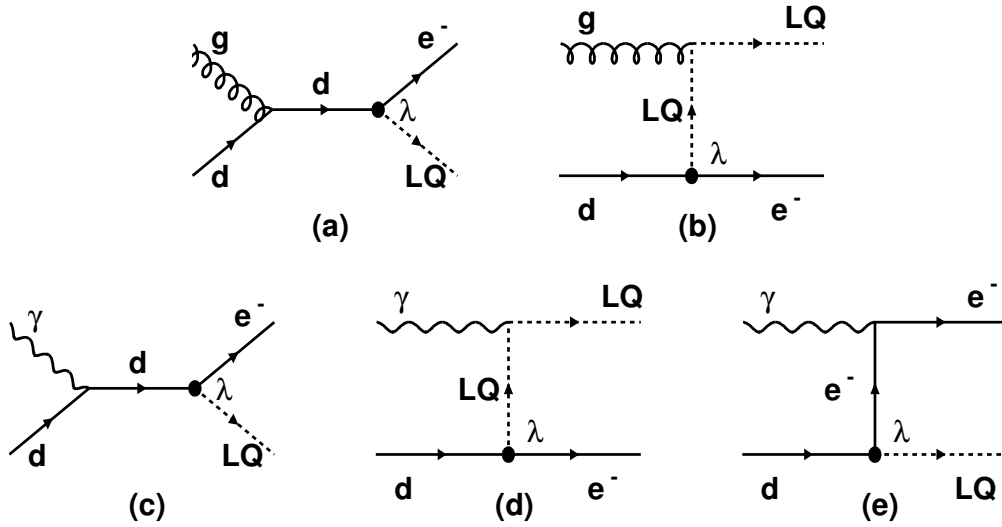


Figure 6.6: Diagrams for single LQ production in  $pp$  collisions, shown for the example case of the  $\tilde{S}_{1/2}^L$  scalar leptoquark. The production may occur via  $qq$  interactions (a and b), or via  $q\gamma$  interactions (c, d and e). In the latter case, the photon can be emitted by the proton (elastic regime) or by a quark coming from the proton (inelastic regime).

4184 **Single production** Single LQ production at the LHC is also possible. So far, only the production mode  
 4185  $gq \rightarrow e + LQ$  (see example diagrams in Fig. 6.6a and b) has been considered in the literature (see e.g. [206]).  
 4186 In the context of this study, the additional production mode  $\gamma q \rightarrow e + LQ$  has been considered as well (see  
 4187 example diagrams in Fig. 6.6c, d and e). This cross-section has been calculated by taking into account:

- 4188 • the inelastic regime, where the photon virtuality  $q^2$  is large enough and the proton breaks up in a  
 4189 hadronic system with a mass well above the proton mass. In that case, the photon is emitted by a  
 4190 parton in the proton, and the process  $qq' \rightarrow q + e + LQ$  is calculated.
- 4191 • the elastic regime, in which the proton emitting the photon remains intact. This calculation involves  
 4192 the elastic form factors of the proton.

4193 As the resonant LQ production in  $ep$  collisions, the cross-section of single  $LQ$  production in  $pp$  collisions  
 4194 approximately scales with the square of the coupling,  $\sigma \propto \lambda^2$ . Figure 6.7 (left) shows the cross-section for  
 4195 single  $LQ$  production at the LHC as a function of the LQ mass, assuming a coupling  $\lambda = 0.1$ . While the  
 4196 inelastic part of the  $\gamma q$  cross-section can be neglected, the elastic production plays an important role at high  
 4197 masses; its cross-section is larger than that of LQ production via  $gq$  interactions for masses above  $\sim 1$  TeV.  
 4198 However, the cross-section for single LQ production at LHC is much lower than that at LHeC, in  $e^+p$  or  $e^-p$   
 4199 collisions, as shown in Fig.6.7 (right).

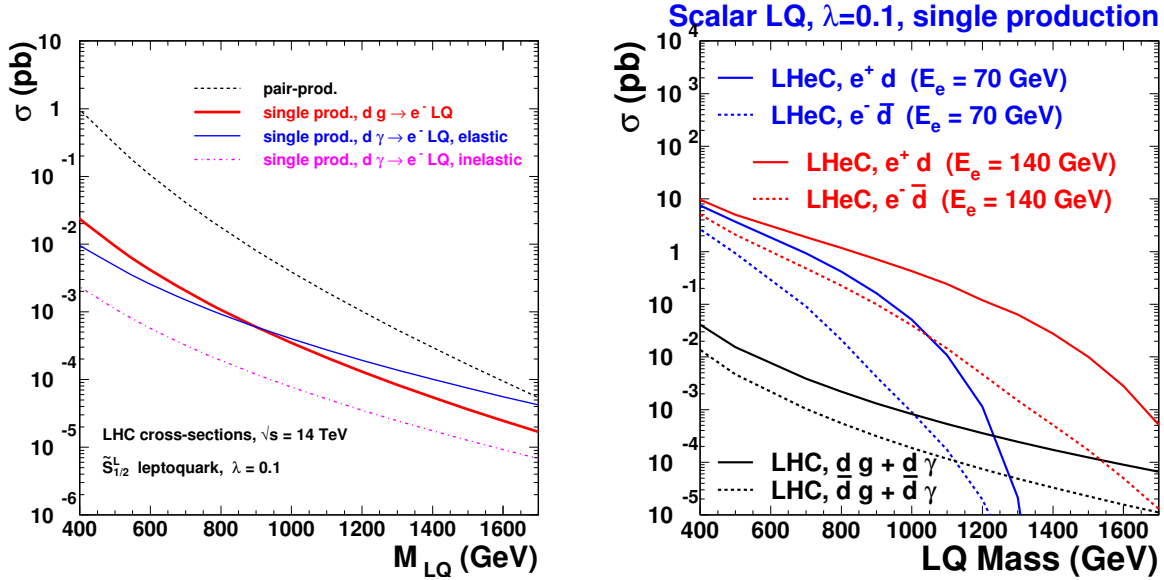


Figure 6.7: left: Single LQ production cross-section at the LHC. right: comparison of the cross-section for single LQ production, at LHC and at LHeC.

4200 **The Contact Term Approach** For LQ masses far above the kinematic limit, the contraction of the  
 4201 propagator in the  $eq \rightarrow eq$  and  $qq \rightarrow ee$  amplitudes leads to a four-fermion interaction. Such interactions are  
 4202 studied in the context of general contact terms, which can be used to parameterize any new physics process  
 4203 with a characteristic energy scale far above the kinematic limit.

4204 In  $ep$  collisions, Contact Interactions (CI) would interfere with NC DIS processes and lead to a distortion  
 4205 of the  $Q^2$  spectrum of NC DIS candidate events. The results presented in section 6.1 can be re-interpreted  
 4206 into expected sensitivities on high mass leptoquarks.

## 4207 6.2.4 Current status of leptoquark searches

4208 The H1 and ZEUS experiments at the HERA  $ep$  collider have constrained the coupling  $\lambda$  to be smaller than  
 4209 the electromagnetic coupling ( $\lambda < \sqrt{4\pi\alpha_{em}} \sim 0.3$ ) for first generation LQs lighter than 300 GeV. The D0 and  
 4210 CDF experiments at the Tevatron  $pp$  collider set constraints on first-generation LQs that are independent of  
 4211 the coupling  $\lambda$ , by looking for pair-produced LQs that decay into  $eq$  ( $\nu q$ ) with a branching ratio  $\beta$  ( $1 - \beta$ ).  
 4212 For a branching fraction  $\beta = 1$ , masses below 299 GeV are excluded by the D0 experiment [207]. The CMS  
 4213 and ATLAS experiments have recently set tighter constraints [208, 209]. Fig. 6.8 shows the bounds obtained  
 4214 by the CMS experiment with  $\sim 32 \text{ pb}^{-1}$  collected in 2010, in the  $\beta$  versus  $M_{LQ}$  plane. For  $\beta = 1$  ( $\beta = 0.5$ ),  
 4215 masses below 384 GeV (340 GeV) are ruled out.

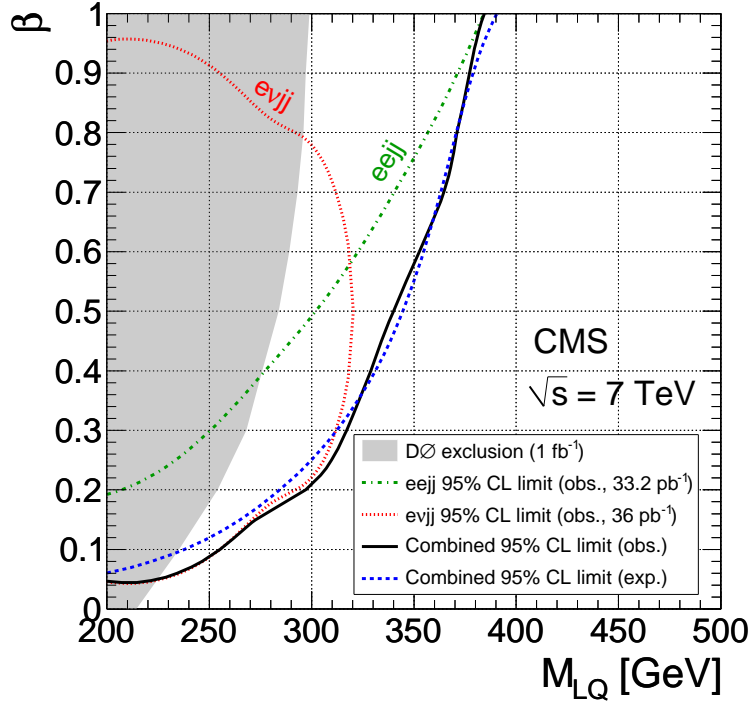


Figure 6.8: Constraints on first generation leptoquarks obtained by the CMS experiment.

### 4216 6.2.5 Sensitivity on leptoquarks at LHC and at LHeC

4217 **Mass - coupling reach** Fig. 6.9 shows the expected sensitivity [196] of the LHC and LHeC colliders for  
 4218 scalar leptoquark production. The single LQ production cross section depends on the unknown coupling  $\lambda$   
 4219 of the LQ to the electron-quark pair. For a coupling  $\lambda$  of  $\mathcal{O}(0.1)$ , LQ masses up to about 1 TeV could be  
 4220 probed at the LHeC. In  $pp$  interactions at the LHC, such leptoquarks would be mainly produced via pair  
 4221 production, or singly produced with a much reduced cross section.

### 4222 6.2.6 Determination of LQ properties

4223 In  $ep$  collisions LQ production can be probed in detail, taking advantage of the formation and decay of sys-  
 4224 tems which can be observed directly as a combination of jet and lepton invariant mass in the final state. It will  
 4225 thereby be possible at the LHeC to probe directly and with high precision the perhaps complex structures  
 4226 which will result in the lepton-jet system and to determine the quantum numbers of new states. Exam-  
 4227 ples of the sensitivity of high energy  $ep$  collisions to the properties of LQ production follow. In particular,  
 4228 a quantitative comparison of the potential of LHC and LHeC to measure the fermion number of a LQ is given.  
 4229

**Fermion number ( $F$ )** Since the parton densities for  $u$  and  $d$  at high  $x$  are much larger than those for  $\bar{u}$   
 and  $\bar{d}$ , the production cross section at LHeC of an  $F = 0$  ( $F = 2$ ) LQ is much larger in  $e^+p$  ( $e^-p$ ) than in  
 $e^-p$  ( $e^+p$ ) collisions. A measurement of the asymmetry between the  $e^+p$  and  $e^-p$  LQ cross sections,

$$\mathcal{A}_{ep} = \frac{\sigma_{prod}(e^+p) - \sigma_{prod}(e^-p)}{\sigma_{prod}(e^+p) + \sigma_{prod}(e^-p)}$$

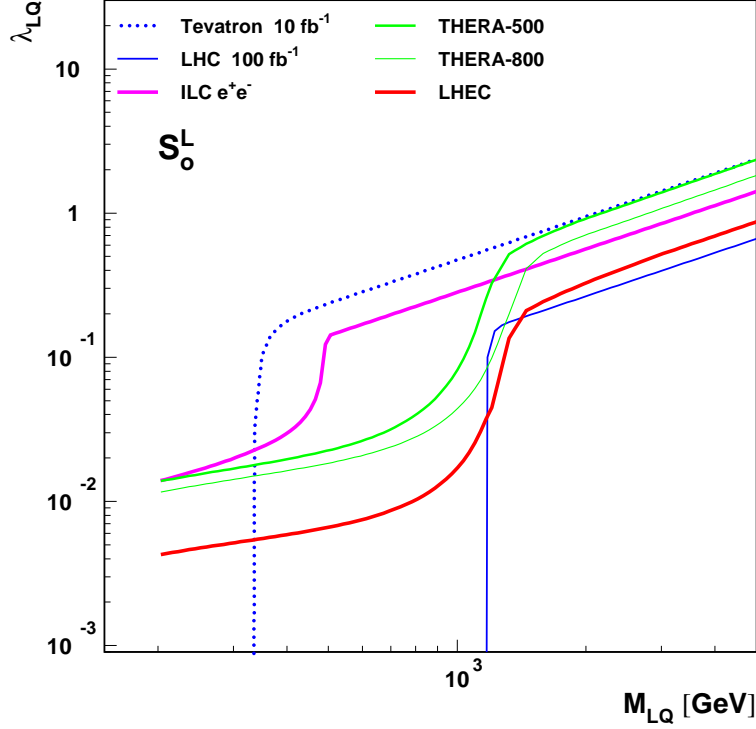


Figure 6.9: Mass-dependent upper bounds on the LQ coupling  $\lambda$  as expected at LHeC for a luminosity of  $10 \text{ fb}^{-1}$  (full red curve) and at the LHC for  $100 \text{ fb}^{-1}$  (full blue curve). These are shown for an example scalar LQ coupling to  $e^-u$ .

thus determines, via its sign, the fermion number of the produced leptoquark. Pair production of first generation LQs at the LHC will not allow this determination. Single LQ production at the LHC, followed by the LQ decay into  $e^\pm$  and  $q$  or  $\bar{q}$ , could determine  $F$  by comparing the signal cross sections with an  $e^+$  and an  $e^-$  coming from the resonant state. Indeed, for a  $F = 0$  leptoquark, the signal observed when the resonance is made by a positron and a jet corresponds to diagrams involving a *quark* in the initial state (see Fig.6.10a). Hence the corresponding cross-section,  $\sigma(e_{out}^+j)$  is larger than that of the signal observed when the resonance is made by an electron and a jet,  $\sigma(e_{out}^-j)$ , since a high  $x$  antiquark is involved in that latter case (see Fig.6.10b). In contrast, for a  $F = 2$  LQ,  $\sigma(e_{out}^+j)$  is smaller than  $\sigma(e_{out}^-j)$ . The measurement of (the sign of) the asymmetry

$$\mathcal{A}_{pp} = \frac{\sigma(e_{out}^+j) - \sigma(e_{out}^-j)}{\sigma(e_{out}^+j) + \sigma(e_{out}^-j)}$$

4230 should thus provide a determination of the LQ fermion number. However, the single LQ production cross  
 4231 section at the LHC is two orders of magnitude lower than at the LHeC (Fig. 6.7), so that the asymmetry  $\mathcal{A}_{pp}$   
 4232 measured at the LHC may suffer from statistics in a large part of the parameter space. For a LQ coupling  
 4233 to  $ed$  and  $\lambda = 0.1$ , no information on  $F$  can be extracted from  $300 \text{ pb}^{-1}$  of LHC data for a LQ mass above  
 4234  $\sim 1 \text{ TeV}$ , while the LHeC can determine  $F$  for LQ masses up to  $1.5 \text{ TeV}$  (Fig. 6.11 and Fig. 6.12). Details  
 4235 of the determination of  $\mathcal{A}_{pp}$  at the LHC are given in the next paragraph.

4236

4237

4238

4239

4240

An estimate of the precision with which the fermion number determination of a leptoquark can be determined at the LHC was obtained from a Monte Carlo simulation. First, using the model [210] implemented in CalcHep [211], samples were generated for the processes  $g u \rightarrow e^+e^-u$  and  $g \bar{u} \rightarrow e^+e^-\bar{u}$ , keeping only diagrams involving the exchange of a scalar LQ exchange of charge  $1/3$ , isospin 0 and fermion number 2.

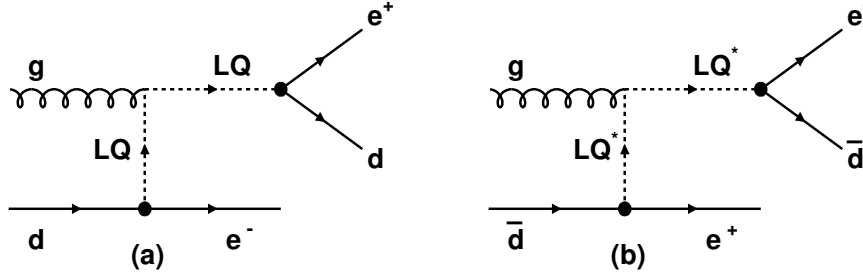


Figure 6.10: Single production of a  $F = 0$  leptoquark decaying (a) into a positron and a jet and (b) into an electron and a jet. In (a) (resp. (b)), the jet comes from a quark (an antiquark); conservation of the baryon number implies that the parton involved in the initial state is a quark (an antiquark).

4241 This leptoquark ( $^{1/3}S_0$  in the notation of Table 6.1) couples to  $e_R^- u_R$ . Assuming that it is chiral, only right-  
 4242 handed coupling was allowed. The  $^{1/3}S_0$  leptoquark was also assumed to couple only to the first generation.  
 4243 Masses of 500 GeV, 750 GeV and 1 TeV were considered. The renormalization and factorization scales were  
 4244 set at  $Q^2 = m_{LQ}^2$  and the coupling parameter  $\lambda = 0.1$ . A center of mass energy of 14 TeV was assumed at  
 4245 the LHC.

4246 High statistics background samples, corresponding to  $150 \text{ fb}^{-1}$  were also produced by generating the  
 4247 same processes  $pp \rightarrow e^+e^- + \text{jet}$ , including all diagrams except those involving the exchange of leptoquarks.  
 4248 Kinematic preconditions were applied at the generation level to both signals and background: (i)  $p_T(\text{jet}) >$   
 4249  $50 \text{ GeV}$ , (ii)  $p_T(e^\pm) > 20 \text{ GeV}$ , (iii) invariant mass of jet- $e^+ - e^-$  system  $> 200 \text{ GeV}$ . The cross sections for  
 4250 the signals and backgrounds under these conditions are: 19.7 fb, 3.4 fb and 0.87 fb for LQ's of mass 500 GeV,  
 4251 750 GeV and 1 TeV respectively, and 1780 fb for the background. These events were subsequently passed to  
 4252 Pythia [130] to perform parton showering and hadronization, then processed through Delphes [212] for a fast  
 4253 simulation of the ATLAS detector. Finally, considering events with two reconstructed electrons of opposite  
 4254 sign and, assuming that the leptoquark has already been discovered (at the LHC), the combination of the  
 4255 highest  $p_T$  jet with the reconstructed  $e^-$  or  $e^+$  with a mass closest to the known leptoquark mass is chosen  
 4256 as the LQ candidate. The following cuts for  $m_{LQ} = 500, 750$  and  $1000 \text{ GeV}$ , respectively, are applied:

- 4257 • dilepton invariant mass  $m_{ll} > 150, 200, 250 \text{ GeV}$ . This cut rejects very efficiently the  $Z + \text{jets}$  back-  
 4258 ground.
- 4259 •  $p_T(e_1) > 150, 200, 250 \text{ GeV}$  and  $p_T(e_2) > 75, 100, 100 \text{ GeV}$ , where  $e_1$  is the reconstructed  $e^\pm$  with  
 4260 higher  $p_T$  and  $e_2$  the lower  $p_T$  electron.
- 4261 •  $p_T(j_1) > 100, 250, 400 \text{ GeV}$ , where  $j_1$  is the reconstructed jet with highest  $p_T$ , used for the reconstruction  
 4262 of the LQ.

4263 Table 6.2 summarizes the results of the simulation for an integrated luminosity of  $300 \text{ fb}^{-1}$ . The expected  
 4264 number of signal events shown in the table is then simply the number of events due to the leptoquark  
 4265 production and decay, falling in the resonance peak within a mass window of width (60, 100, 160 GeV) for  
 4266 the three cases studied, respectively. Although this simple analysis can be improved by considering other  
 4267 less dominant backgrounds and by using optimized selection criteria, it should give a good estimate of the  
 4268 precision with which the asymmetry can be measured. This precision falls rapidly with increasing mass and,  
 4269 above  $\sim 1 \text{ TeV}$ , it becomes impossible to observe simultaneously single production of both  $^{1/3}S_0$  and  $^{1/3}\bar{S}_0$ .  
 4270 It must be noted that the asymmetry at the LHC will be further diluted by the abundant leptoquark pair  
 4271 production, not taken into account here.

4272 **Flavour structure of the LQ coupling** More generally, using the same charge asymmetry observable,  
 4273 the LHeC will be sensitive to the flavour structure of the leptoquark, through the dependence on the parton

LQ mass (GeV)	$^{1/3}S_1 \rightarrow e^+\bar{u}$		$^{1/3}\bar{S}_1 \rightarrow e^-u$		Charge Asymmetry
	Signal	Background	Signal	Background	
500	121	431	771	478	$0.73 \pm 0.05$
750	18.3	137	132	102	$0.76^{+0.16}_{-0.14}$
1000	4.9	57	44	42	$0.77^{+0.23}_{-0.24}$

Table 6.2: Estimated number of events of signal and background, and the charge asymmetry measurement with  $300 \text{ fb}^{-1}$  at the LHC, for  $\lambda = 0.1$ .

distribution functions of the interacting quark in the proton. Fig. 6.13 shows the calculated asymmetry for scalar LQs. Provided that the coupling  $\lambda$  is not too small, the accuracy of the measurement of  $\mathcal{A}_{ep}$  at LHeC (see Fig. 6.11) would allow the various LQ types to be disentangled, as different LQs lead to values of  $\mathcal{A}_{ep}$  that differ by typically 20–30%. A similar measurement at the LHC would be possible only in a very limited part of the phase space (low masses and large couplings), where the statistics would be large enough to yield an accuracy of about 20% on the measured asymmetry  $\mathcal{A}_{pp}$ .

**Spin** At the LHeC, the angular distribution of the LQ decay products is unambiguously related to its spin. Indeed, scalar LQs produced in the  $s$ -channel decay isotropically in their rest frame leading to a flat  $d\sigma/dy$  spectrum where  $y = \frac{1}{2}(1 + \cos\theta^*)$  is the Bjorken scattering variable in DIS and  $\theta^*$  is the decay polar angle of the lepton relative to the incident proton in the LQ centre of mass frame. In contrast, events resulting from the production and decay of vector LQs would be distributed according to  $d\sigma/dy \propto (1-y)^2$ . These  $y$  spectra from scalar or vector LQ production are markedly different from the  $d\sigma/dy \propto y^{-2}$  distribution expected at fixed  $M$  for the dominant  $t$ -channel photon exchange in neutral current DIS events<sup>1</sup>. Hence, a LQ signal in the NC-like channel will be statistically most prominent at high  $y$ .

The spin determination will be much more complicated, even possibly ambiguous, if only the LHC leptoquark pair production data are available. Angular distributions for vector LQs depend strongly on the structure of the  $gLQ\bar{LQ}$  coupling, i.e. on possible anomalous couplings. For a structure similar to that of the  $\gamma WW$  vertex, vector LQs produced via  $q\bar{q}$  fusion are unpolarised and, because both LQs are produced with the same helicity, the distribution of the LQ production angle will be similar to that of a scalar LQ. The study of LQ spin via single LQ production at the LHC will suffer from the relatively low rates and more complicated backgrounds.

**Neutrino decay modes** At the LHeC, there is similar sensitivity for LQ decay into both  $eq$  and  $\nu q$ . At the LHC, in  $pp$  collisions, LQ decay into neutrino-quark final states is plagued by huge QCD background. At the LHeC, production through  $eq$  fusion with subsequent  $\nu q$  decay is thus very important if the complete pattern of LQ decay couplings is to be determined.

**Coupling  $\lambda$**  In the narrow-width approximation, the production cross-section of a LQ in  $ep$  collisions can be written as, depending on the LQ spin :

$$\sigma_{prod} = \frac{\lambda^2}{16\pi} q(x = M^2/s_{ep}) \quad (J = 0) \quad \text{or} \quad \sigma_{prod} = \frac{\lambda^2}{8\pi} q(x = M^2/s_{ep}) \quad (J = 1).$$

At LHeC, the determination of:

- the  $LQ$  spin, via the analysis of the angular distribution of its decay products;
- the flavor of the quark  $q$  involved in the  $e-q-LQ$  vertex, via the charge asymmetry described above;

<sup>1</sup>At high momentum transfer,  $Z^0$  exchange is no longer negligible and contributes to less pronounced differences in the  $y$  spectra between LQ signal and DIS background.

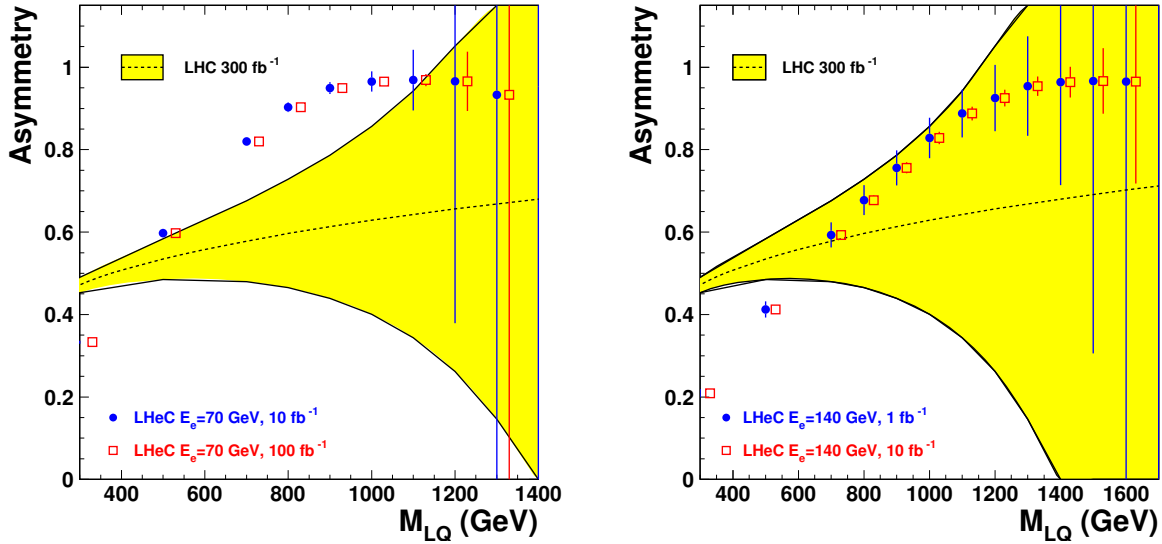


Figure 6.11: *Asymmetries which would determine the fermion number of a LQ, the sign of the asymmetry being the relevant quantity. The dashed curve shows the asymmetry that could be measured at the LHC; the yellow band shows the statistical uncertainty of this quantity, assuming an integrated luminosity of  $300 \text{ fb}^{-1}$ . The red and blue symbols, together with their error bars, show the asymmetry that would be measured at LHeC, assuming  $E_e = 70 \text{ GeV}$  (left) or  $E_e = 140 \text{ GeV}$  (right). Two values of the integrated luminosity have been assumed. These determinations correspond to the  $\hat{S}_{1/2}^L$  (scalar LQ coupling to  $e^+ + d$ ), with a coupling of  $\lambda = 0.1$ .*

4302 • the production cross-section, via the cross-sections measured in the  $eq$  and  $\nu q$  decay modes

4303 allows the value of the coupling  $\lambda$  to be determined, from the above formula.

4304 **Chiral structure of the LQ coupling** Chirality is central to the SM Lagrangian. Polarised electron and  
 4305 positron beams<sup>2</sup> at the LHeC will shed light on the chiral structure of the LQ-e-q couplings. Measurements  
 4306 of a similar nature at LHC are impossible.

4307

4308 In summary, would a first generation leptoquark exist in the TeV mass range with a coupling  $\lambda$  of  $\mathcal{O}(0.1)$ ,  
 4309 the LHeC would allow a rich program of “spectroscopy” to be carried out, resulting in the determination of  
 4310 most of the LQ properties.

### 4311 6.2.7 Leptogluons

4312 While leptoquarks and excited fermions are widely discussed in the literature, leptogluons have not received  
 4313 the same attention. However, they are predicted in all models with colored preons [213–218]. For example,  
 4314 in the framework of fermion-scalar models, leptons would be bound states of a fermionic preon and a scalar  
 4315 anti-preon  $l = (F\bar{S}) = 1 \oplus 8$  (both F and S are color triplets), and each SM lepton would have its own colour  
 4316 octet partner [218].

<sup>2</sup>Whether it is possible to achieve longitudinal polarisation in a 70 GeV  $e^\pm$  beam in the LHC tunnel remains to be clarified.



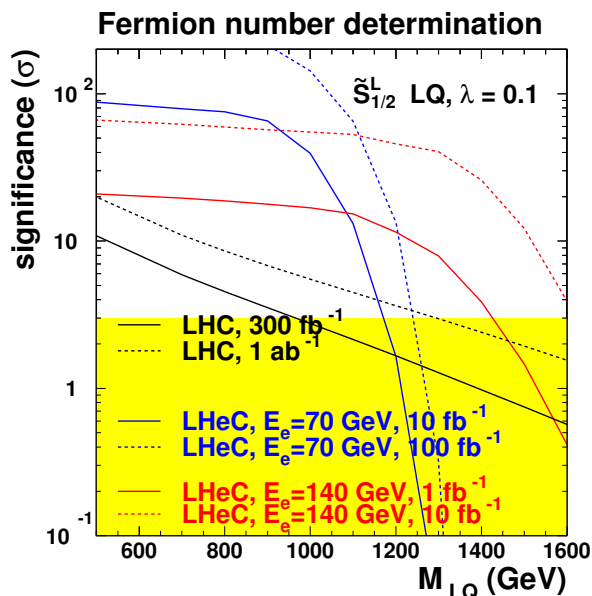


Figure 6.12: Significance of the determination of the fermion number of a LQ, at the LHC (black curve) and at the LHeC (blue and red curves). This corresponds to a  $\tilde{S}_{1/2}^L$  leptoquark, assuming a coupling of  $\lambda = 0.1$ .

4317 A study of leptogluons production at LHeC is presented in [219]. It is based on the following Lagrangian:

$$L = \frac{1}{2\Lambda} \sum_l \{ \bar{l}_8^\alpha g_s G_{\mu\nu}^\alpha \sigma^{\mu\nu} (\eta_L l_L + \eta_R l_R) + h.c. \} \quad (6.5)$$

4318 where  $G_{\mu\nu}^\alpha$  is the field strength tensor for gluon, index  $\alpha = 1, 2, \dots, 8$  denotes the color,  $g_s$  is gauge coupling,  
 4319  $\eta_L$  and  $\eta_R$  are the chirality factors,  $l_L$  and  $l_R$  denote left and right spinor components of lepton,  $\sigma^{\mu\nu}$  is the  
 4320 anti-symmetric tensor and  $\Lambda$  is the compositeness scale. The leptonic chiral invariance implies  $\eta_L \eta_R = 0$ .

4321 The phenomenology of leptogluons at LHC and LHeC is very similar to that of leptoquarks, despite  
 4322 their different spin (leptogluons are fermions while leptoquarks are bosons) and their different interactions.  
 4323 Figure 6.14 shows typical cross-sections for single leptogluon production at the LHeC, assuming  $\Lambda$  is equal  
 4324 to the leptogluon mass. It is estimated that, for example, a sensitivity of to a compositeness scale of 200  
 4325 TeV, at  $3\sigma$  level can be achieved with LHeC having  $E_e = 70$  GeV and with  $1 \text{ fb}^{-1}$ . The mass reach for  $M_{e8}$   
 4326 is 1.1 TeV for  $\Lambda = 10$  TeV.

4327 As for leptoquarks, would leptogluons be discovered at the LHC, LHeC data would be of highest value  
 4328 for the determination of the properties of this new particle.

### 4329 6.3 Excited leptons and other new heavy leptons

4330 The three-family structure and mass hierarchy of the known fermions is one of the most puzzling charac-  
 4331 teristics of the Standard Model (SM) of particle physics. Attractive explanations are provided by models  
 4332 assuming composite quarks and leptons [220]. The existence of excited states of fermions ( $F^*$ ) is a natural  
 4333 consequence of compositeness models. More generally, various models predict the existence of fundamental  
 4334 new heavy leptons, which can have similar experimental characteristics as excited leptons. They could, for  
 4335 example, be part of a fourth Standard model family. They arise also in Grand Unified Theories, and appear  
 4336 as colorless fermions in technicolor models.

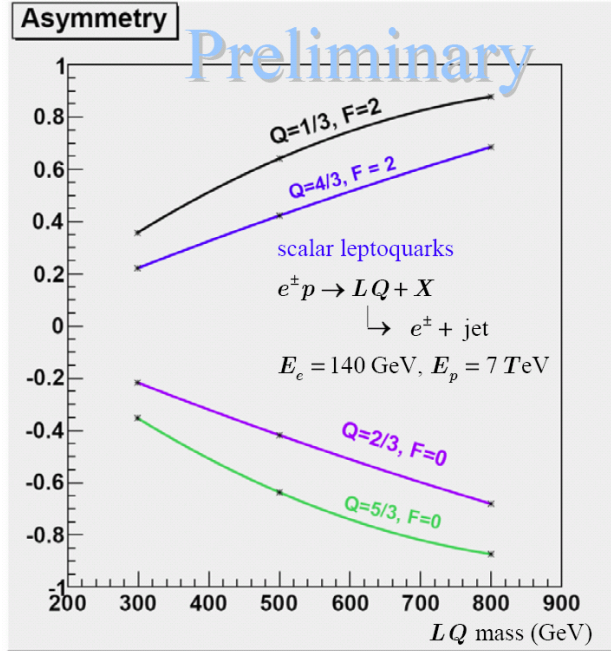


Figure 6.13: Charge asymmetry vs LQ mass for different types of scalar LQ's.

4337 New heavy leptons could be pair-produced at the LHC up to masses of  $\mathcal{O}(300)$  GeV. As for the case  
 4338 of leptoquarks,  $pp$  data from pair-production of new leptons may not allow for a detailed study of their  
 4339 properties and couplings. Single production of new leptons is also possible at the LHC, but is expected to  
 4340 have a larger cross-section at LHeC, via  $e\gamma$  or  $eW$  interactions. The case of excited electrons is considered  
 4341 in the following, with more details being given in [221].

4342 Single production of excited leptons at the LHC ( $\sqrt{s}$  up to 14 TeV) may happen via the reactions  
 4343  $pp \rightarrow e^\pm e^* \rightarrow e^+ e^- V$  and  $pp \rightarrow \nu e^* + \nu^* e^\pm \rightarrow e^\pm \nu V$ . The LHC should be able to tighten considerably the current  
 4344 constraints on these possible new states and to probe excited lepton masses of up to 1 TeV [222]. A sensitivity  
 4345 similar to the LHC could be reached at the ILC [223], with different  $e^+e^-$ ,  $e\gamma$  and  $\gamma\gamma$  collisions modes and  
 4346 a centre of mass energy of  $\sqrt{s} \geq 500$  GeV.

4347 Recent results of searches for excited fermions [224–226] at HERA using all data collected by the H1  
 4348 detector have demonstrated that  $ep$  colliders are very competitive to  $pp$  or  $e^+e^-$  colliders. Indeed limits  
 4349 set by HERA extend at high mass beyond the kinematic reach of LEP searches [227, 228] and to higher  
 4350 compositeness scales than those obtained at the Tevatron [229] using  $1 \text{ fb}^{-1}$  of data. Therefore a future  
 4351 LHeC machine, with a centre of mass energy of 1 – 2 TeV, much higher than at the HERA  $ep$  collider,  
 4352 would be ideal to search for and study excited fermions. This has motivated us to examine excited electron  
 4353 production at a future LHeC collider and compare it to the potential of other types of colliders at the TeV  
 4354 scale, the LHC and the ILC.  
 4355

### 4356 6.3.1 Excited Fermion Models

4357 Compositeness models attempt to explain the hierarchy of masses in the SM by the existence of a substructure  
 4358 within the fermions. Several of these models [230–232] predict excited states of the known fermions, in which  
 4359 excited fermions are assumed to have spin 1/2 and isospin 1/2 in order to limit the number of parameters  
 4360 of the phenomenological study. They are expected to be grouped into both left- and right-handed weak  
 4361 isodoublets with vector couplings. The existence of the right-handed doublets is required to protect the

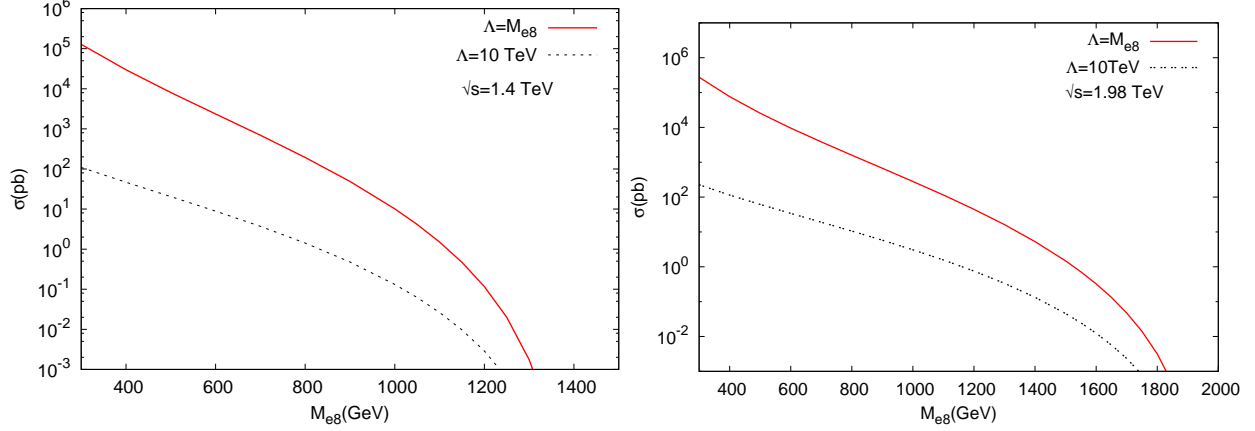


Figure 6.14: Resonant  $e_8$  production at the LHeC, for two values of the center-of-mass energy.

ordinary light fermions from radiatively acquiring a large anomalous magnetic moment via  $F^*FV$  interaction (where  $V$  is a  $\gamma, Z$  or  $W$ ).

Interactions between excited and ordinary fermions may be mediated by gauge bosons, as described by the effective Lagrangian:

$$\mathcal{L}_{GM} = \frac{1}{2\Lambda} \bar{F}_R^* \sigma^{\mu\nu} \left[ g f \frac{\vec{\tau}}{2} \vec{W}_{\mu\nu} + g' f' \frac{Y}{2} B_{\mu\nu} + g_s f_s \frac{\vec{\lambda}}{2} \vec{G}_{\mu\nu} \right] F_L + h.c., \quad (6.6)$$

where  $Y$  is the weak hypercharge,  $g_s$ ,  $g = \frac{e}{\sin \theta_W}$  and  $g' = \frac{e}{\cos \theta_W}$  are the strong and electroweak gauge couplings, where  $e$  is the electric charge and  $\theta_W$  is the weak mixing angle;  $\vec{\lambda}$  and  $\vec{\tau}$  are the Gell-Mann matrices and the Pauli matrices, respectively.  $G_{\mu\nu}$ ,  $W_{\mu\nu}$  and  $B_{\mu\nu}$  are the field strength tensors describing the gluon, the  $SU(2)$ , and the  $U(1)$  gauge fields.  $f_s$ ,  $f$  and  $f'$  are the coupling constants associated to each gauge field. They depend on the composite dynamics. The parameter  $\Lambda$  has units of energy and can be regarded as the compositeness scale which reflects the range of the new confinement force.

In addition to gauge mediated (GM) interactions, novel composite dynamics may be visible as contact interactions (CI) between excited fermions and ordinary fermions. Such interactions can be described by an effective four-fermion Lagrangian [232]:

$$\mathcal{L}_{CI} = \frac{4\pi}{2\Lambda^2} j^\mu j_\mu, \quad (6.7)$$

where  $\Lambda$  is here assumed to be the same parameter as in the gauge interaction Lagrangian (6.6) and  $j_\mu$  is the fermion current

$$j_\mu = \eta_L \bar{F}_L \gamma_\mu F_L + \eta'_L \bar{F}_L^* \gamma_\mu F_L^* + \eta''_L \bar{F}_L^* \gamma_\mu F_L + h.c. + (L \rightarrow R). \quad (6.8)$$

By convention, the  $\eta$  factors of left-handed currents are set to  $\pm 1$ , while the factors of right-handed currents are considered to be zero.

### 6.3.2 Simulation and Results

In the following study, excited electron ( $e^*$ ) production and decays via both GM and CI are considered. For GM interactions, the  $e^*$  production cross section under the assumption  $f = -f'$  becomes much smaller than for  $f = +f'$  and therefore only the case  $f = +f'$  is studied.

4384 Considering pure gauge interactions, excited electrons could be produced in  $ep$  collisions at the LHeC  
 4385 via a  $t$ -channel  $\gamma$  or  $Z$  bosons exchange. The Monte Carlo (MC) event generator COMPOS [233] is used for  
 4386 the calculation of the  $e^*$  production cross section and the simulation of signal events. The production cross  
 4387 sections of excited neutrinos at the LHeC is also shown in figure 6.15. These results are obtained with the  
 4388 assumption  $f = +f'$  and  $M_{e^*} = \Lambda$  and are compared to production cross section at HERA and also at the  
 4389 LHC [222]. In the mass range accessible by the LHeC, the  $e^*$  production cross section is clearly much higher  
 4390 than at the LHC.

4391 Considering gauge and contact interactions together, formulae for the  $e^*$  production cross section via  
 4392 CI and of the interference term between contact and gauge interactions have been incorporated into COM-  
 4393 POS [224, 234]. For simplicity, the relative strength of gauge and contact interactions are fixed by setting  
 4394 the parameters  $f$  and  $f'$  of the gauge interaction to one. Comparisons of the  $e^*$  production cross section  
 4395 via only gauge interactions and via GM and CI together, as a function of the  $e^*$  mass, are presented in  
 4396 figure 6.16(a) for  $M_{e^*} = \Lambda$  and figure 6.16(b) for  $\Lambda = 10$  TeV, respectively. These results for the LHeC  
 4397 at  $\sqrt{s} = 1.4$  TeV are compared to the cross section at an LHC operating at  $\sqrt{s} = 14$  TeV. These plots  
 4398 demonstrate that at the LHeC the ratio of the contact and gauge cross sections (proportional to  $\hat{s}/\Lambda^4$  and  
 4399  $1/\Lambda^2$  respectively) decreases as  $\Lambda$  and  $M_{e^*}$  increase differently than for the LHC where contact interactions  
 4400 may be an important source of production of excited electrons. In the mass range accessed at the LHeC,  $e^*$   
 4401 decays are dominated by gauge decays, provided that  $\Lambda$  is large enough. Therefore, only gauge decays are  
 4402 looked for in the present study.

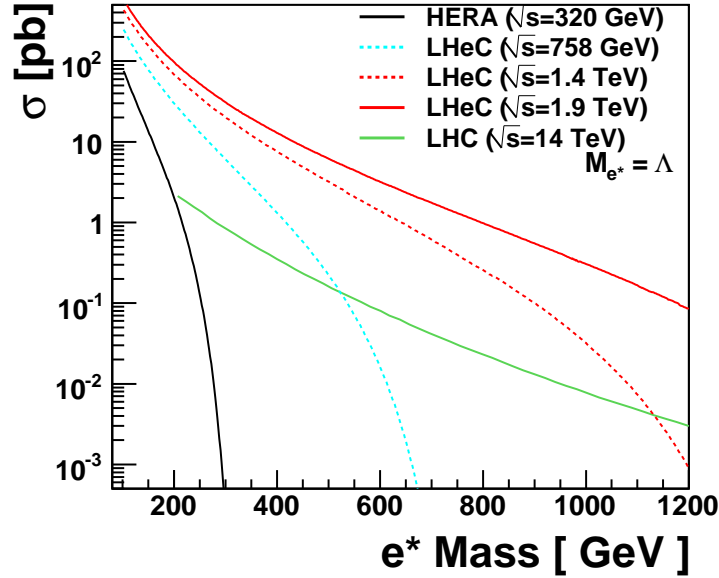


Figure 6.15: The  $e^*$  production cross section for different design scenarios of the LHeC electron-proton collider, compared to the cross sections at HERA and at the LHC.

4403 In order to estimate the sensitivity of excited electron searches at the LHeC, the  $e^*$  production followed  
 4404 by its decay in the channel  $e^* \rightarrow e\gamma$  is considered. This is the key channel for excited electron searches in  $ep$   
 4405 collisions as it provides a very clear signature and has a large branching ratio. Only the main sources of  
 4406 backgrounds from SM processes are considered here, namely neutral currents (NC DIS) and QED-Compton  
 4407 ( $e\gamma$ ) events. Other possible SM backgrounds are negligible. The MC event generator WABGEN [235] is used  
 4408 to generate these background events. Figure 6.17 compares the  $e^*$  production cross section to the total cross  
 4409 section of SM backgrounds. Background events dominate in the low  $e^*$  mass region. Hence to enhance the  
 4410 signal, candidate events are selected with two isolated electromagnetic clusters with a polar angle between

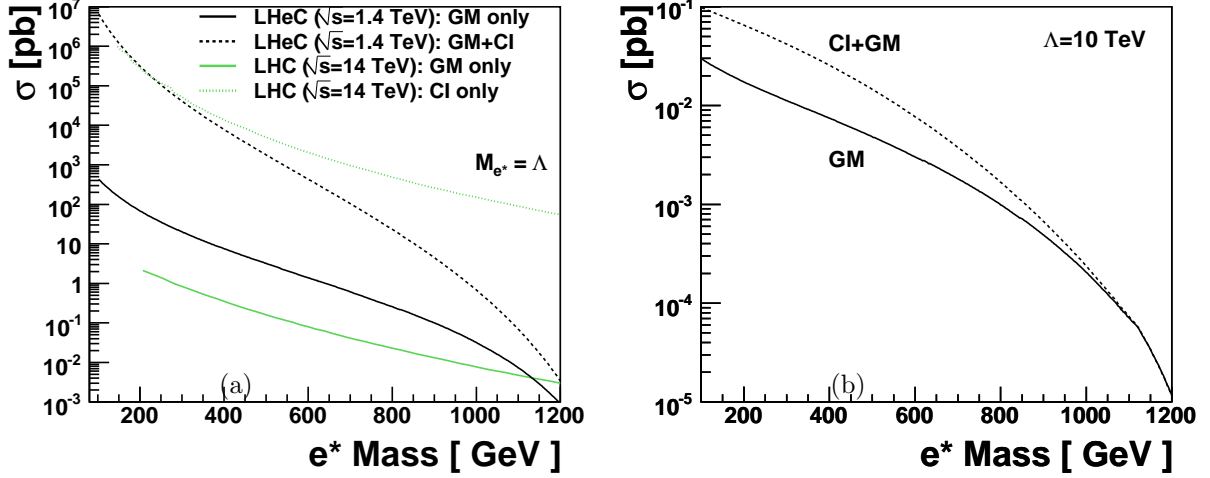


Figure 6.16: Comparison of the  $e^*$  production cross section via gauge and contact interactions. In figure (a), the results for the LHeC ( $\sqrt{s} = 1.4$  TeV) and for the LHC ( $\sqrt{s} = 14$  TeV) are compared. Production cross sections for a fixed  $\Lambda$  value of 10 TeV are shown in figure (b) for the LHeC.

4411  $5^\circ$  and  $145^\circ$  and transverse energies greater than 15 GeV and 10 GeV, respectively.

4412 To translate the results into exclusion limits, expected upper limits on the coupling  $f/\Lambda$  are derived at  
4413 95% Confidence Level (CL) as a function of excited electron masses.

4414 In case of gauge interaction, the attainable limits at the LHeC on the ratio  $f/\Lambda$  are shown in figure 6.18  
4415 for excited electrons, for the hypothesis  $f = +f'$  and different integrated luminosities  $L = 10 \text{ fb}^{-1}$  for  
4416  $\sqrt{s}$  up to 1.4 TeV and  $L = 1 \text{ fb}^{-1}$  for  $\sqrt{s}$  up to 2 TeV. They are compared to the upper limits obtained  
4417 at LEP [227, 228], HERA [224] and also to the expected sensitivity of the LHC [222]. Considering the  
4418 assumption  $f/\Lambda = 1/M_{e^*}$  and  $f = +f'$ , excited electrons with masses up to 1.2(1.5) TeV, corresponding  
4419 to centre of mass energies of  $\sqrt{s} = 1.4(1.9)$  TeV of the LHeC, are excluded. Under the same assumptions,  
4420 LHC ( $\sqrt{s} = 14$  TeV) could exclude  $e^*$  masses up to 1.2 TeV for an integrated luminosity of  $100 \text{ fb}^{-1}$ . In  
4421 the accessible mass range of LHeC, the LHeC would be able to probe smaller values of the coupling  $f/\Lambda$   
4422 than the LHC. Similarly to leptoquarks (see section 6.2), if an excited electron is observed at the LHC with  
4423 a mass of  $\mathcal{O}(1 \text{ TeV})$ , the LHeC would be better suited to study the properties of this particle, thanks to the  
4424 larger single production cross-section (see Fig. 6.15).

### 4425 6.3.3 New leptons from a fourth generation

4426 New leptons from a fourth generation ( $l_4, \nu_4$ ) may have anomalous couplings to the standard leptons, as  
4427 given by the following effective Lagrangian:

$$\begin{aligned}
\mathcal{L}_{nc} &= \left( \frac{\kappa_\gamma^{\ell_4 l_i}}{\Lambda} \right) e_\ell g_e \bar{\ell}_4 \sigma_{\mu\nu} \ell_i F^{\mu\nu} \\
&+ \left( \frac{\kappa_Z^{\ell_4 l_i}}{2\Lambda} \right) g_Z \bar{\ell}_4 \sigma_{\mu\nu} \ell_i Z^{\mu\nu} + \left( \frac{g_Z}{2} \right) \bar{\nu}_i \frac{i}{2\Lambda} \kappa_Z^{\nu_4 \nu_i} \sigma_{\mu\nu} q^\nu P_L \nu_4 Z^\mu + h.c. \\
\mathcal{L}_{cc} &= \left( \frac{g_W}{\sqrt{2}} \right) \bar{l}_i \left[ \frac{i}{2\Lambda} \kappa_W^{\nu_4 l_i} \sigma_{\mu\nu} q^\nu \right] P_L \nu_4 W^\mu + h.c.
\end{aligned}$$

4428 In that case, the single production of  $l_4$  and  $\nu_4$  would be similar to that of excited electrons and neutrinos. For  
4429 a study of the properties and couplings of such a new lepton, an  $ep$  machine would offer the same advantages

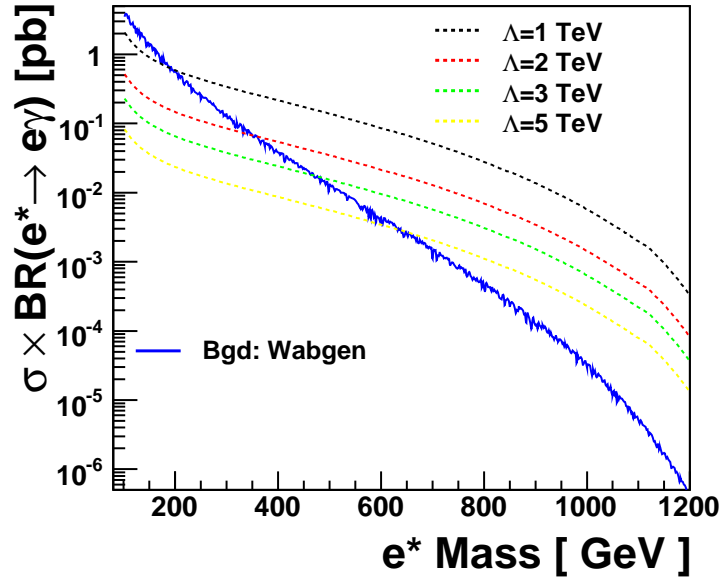


Figure 6.17: Electromagnetic production cross section for  $e^*$  ( $e^* \rightarrow e\gamma$ ) for different values of  $\Lambda$ .

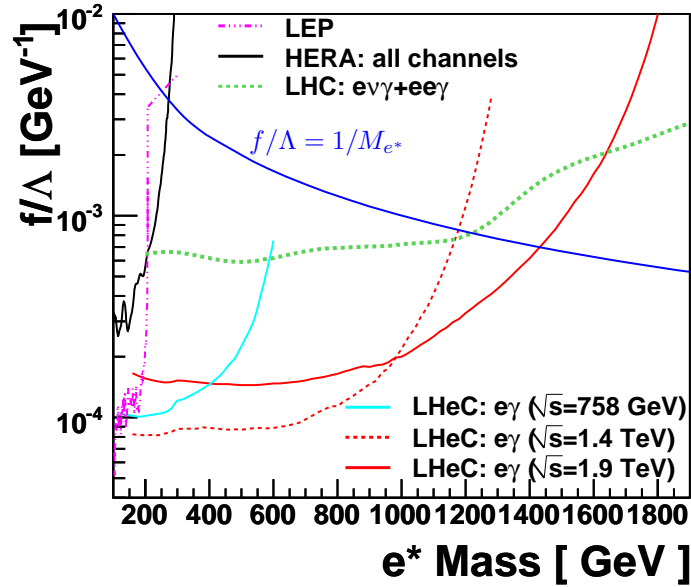


Figure 6.18: Sensitivity to excited electron searches for different design scenarios of the LHeC electron-proton collider, compared to the expected sensitivity of the LHC ( $\sqrt{s} = 14$  TeV,  $L = 100$  fb $^{-1}$ ). Different integrated luminosities at the LHeC ( $L = 10$  fb $^{-1}$  for  $\sqrt{s}$  up to 1.4 TeV and  $L = 1$  fb $^{-1}$  for  $\sqrt{s}$  up to 2 TeV) are assumed. The curves present the expected exclusion limits on the coupling  $f/\Lambda$  at 95% CL as a function of the mass of the excited electron with the assumption  $f = +f'$ . Areas above the curves are excluded. Present experimental limits obtained at LEP and HERA are also represented.

4430 as presented above in the case of excited electrons. A study of the processes  $ep \rightarrow l_4 X \rightarrow Ze(\gamma\mu)X$   
 4431 and  $ep \rightarrow \nu_4 X \rightarrow W(e, \mu)X$  at the LHeC is presented in [236]. For example, for an anomalous coupling  
 4432  $\kappa/\Lambda = 1 \text{ TeV}^{-1}$ , LHeC would be able to cover  $l_4$  masses up to  $\sim 900 \text{ GeV}$ .

## 4433 6.4 New physics in boson-quark interactions

4434 Several extensions of the Standard Model predict new phenomena that would be directly observable in boson-  
 4435 quark interactions. For example, the top quark may have anomalous couplings to gauge bosons, leading to  
 4436 Flavour Changing Neutral Current (FCNC) vertices  $tq\gamma$ , where  $q$  is a light quark. Similarly, excited quarks  
 4437 ( $q^*$ ) or quarks from a fourth generation ( $Q$ ) could be produced via  $\gamma q \rightarrow q^*$  or  $\gamma q \rightarrow Q$ . The transitions  
 4438  $\gamma q \rightarrow t, q^*, Q$  can be studied in  $ep$  collisions at the LHeC, but a much larger cross-section would be achieved  
 4439 at a  $\gamma p$  collider, due to the much larger  $\gamma p$  centre-of-mass energy. The single production of  $q^*$ ,  $Q$  or of a top  
 4440 quark via anomalous couplings is also possible at the LHC, but it involves an anomalous coupling together  
 4441 with an electroweak coupling and the main background processes involve the strong interaction. The signal  
 4442 to background ratio will thus be much more challenging at the LHC, and any constraints on anomalous  
 4443 couplings would therefore be obtained from the decay channels of these quarks. The example of anomalous  
 4444 single top production is detailed in the following.

### 4445 6.4.1 An LHeC-based $\gamma p$ collider

4446 The possibility to operate the LHeC as a  $\gamma p$  collider is described in 8.1.6. If the electron beam is accelerated  
 4447 by a linac, it can be converted into a beam of high energy real photons, by backscattering off a laser pulse.  
 4448 The energy of these photons would be about 80% of the energy of the initial electrons.

### 4449 6.4.2 Anomalous Single Top Production at the LHeC Based $\gamma p$ Collider

4450 The top quark is expected to be most sensitive to physics beyond the Standard Model (BSM) because  
 4451 it is the heaviest available particle of the Standard Model (SM). A precise measurement of the couplings  
 4452 between SM bosons and fermions provides a powerful tool for the search of BSM physics allowing a possible  
 4453 detection of deviations from SM predictions [237]. Anomalous  $tqV$  ( $V = g, \gamma, Z$  and  $q = u, c$ ) couplings can  
 4454 be generated through dynamical mass generation [73], sensitive to the mechanism of dynamical symmetry  
 4455 breaking. They have a similar chiral structure as the mass terms, and the presence of these couplings would  
 4456 be interpreted as signals of new interactions. This motivates the study of top quark flavour changing neutral  
 4457 current (FCNC) couplings at present and future colliders.

4458 Current experimental constraints at 95% C.L. on the anomalous top quark couplings are [238]:  $BR(t \rightarrow$   
 4459  $\gamma u) < 0.0132$  and  $BR(t \rightarrow \gamma u) < 0.0059$  from HERA;  $BR(t \rightarrow \gamma q) < 0.041$  from LEP and  $BR(t \rightarrow \gamma q) <$   
 4460  $0.032$  from CDF. The HERA has much higher sensitivity to  $u\gamma t$  than  $c\gamma t$  due to more favorable parton  
 4461 density: the best limit is obtained from the ZEUS experiment.

4462 The top quarks will be produced in large numbers at the Large Hadron Collider (LHC), allowing great  
 4463 precision measurement of the coupling. For a luminosity of  $1 \text{ fb}^{-1}$  ( $100 \text{ fb}^{-1}$ ) the expected ATLAS sensitivity  
 4464 to the top quark FCNC decay is  $BR(t \rightarrow q\gamma) \sim 10^{-3}(10^{-4})$  [239, 240]. The production of top quarks by  
 4465 FCNC interactions at hadron colliders has been studied in [241–253],  $e^+e^-$  colliders in [73, 254–257] and  
 4466 lepton-hadron collider in [73, 258–260]. LHC will give an opportunity to probe  $BR(t \rightarrow ug)$  down to  
 4467  $5 \times 10^{-3}$  [261]; ILC/CLIC has the potential to probe  $BR(t \rightarrow q\gamma)$  down to  $10^{-5}$  [262].

4468 A linac-ring type collider presents the sole realistic way to TeV scale in  $\gamma p$  collisions [263–268]. Recently  
 4469 this opportunity has been widely discussed in the framework of the LHeC project [17]. Two stages of the  
 4470 LHeC were considered: QCD Explorer ( $E_e = 50 - 100 \text{ GeV}$ ) and Energy Frontier ( $E_e > 250 \text{ GeV}$ ). The po-  
 4471 tential of the LHeC as a  $\gamma p$  collider to search for anomalous top quark interactions has been investigated [269].  
 4472 The effective Lagrangian involving anomalous  $t\gamma q$  ( $q = u, c$ ) interactions is given by [261].

$$L = -g_e \sum_{q=u,c} Q_q \frac{\kappa_q}{\Lambda} \bar{t} \sigma^{\mu\nu} (f_q + h_q \gamma_5) q A_{\mu\nu} + h.c. \quad (6.9)$$

4473 where  $A_{\mu\nu}$  is the usual photon field tensor,  $\sigma_{\mu\nu} = \frac{i}{2}(\gamma_\mu \gamma_\nu - \gamma_\nu \gamma_\mu)$ ,  $Q_q$  is the quark charge, in general  $f_q$  and  
 4474  $h_q$  are complex numbers,  $g_e$  is the electromagnetic coupling constant,  $\kappa_q$  is a real and positive anomalous  
 4475 FCNC coupling constant and  $\Lambda$  is the new physics scale. The neutral current magnitudes in the Lagrangian  
 4476 satisfy  $|(f_q)^2 + (h_q)^2| = 1$  for each term. The anomalous decay width can be calculated as

$$\Gamma(t \rightarrow q\gamma) = \left(\frac{\kappa_q}{\Lambda}\right)^2 \frac{2}{9} \alpha_{em} m_t^3 \quad (6.10)$$

4477 Taking  $m_t = 173$  GeV and  $\alpha_{em} = 0.0079$ , the anomalous decay width  $\approx 9$  MeV for  $\kappa_q/\Lambda = 1$  TeV<sup>-1</sup>  
 4478 while the SM decay width is about 1.5 GeV.

4479 For numerical calculations anomalous interaction vertices are implemented into the CalcHEP pack-  
 4480 age [211] using the CTEQ6M [131] parton distribution functions. The Feynman diagrams for the subprocess  
 4481  $\gamma q \rightarrow W^+ b$ , where  $q = u, c$  are shown in Fig. 6.19. The first three diagrams correspond to irreducible back-  
 4482 grounds and the last one to the signal. The main background comes from associated production of  $W$  boson  
 4483 and the light jets.

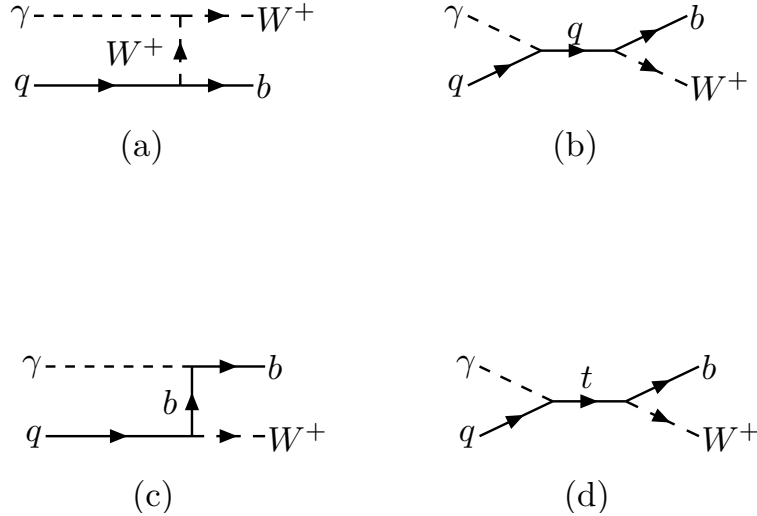


Figure 6.19: Feynman diagrams for  $\gamma q \rightarrow W^+ b$ , where  $q = u, c$ .

4484 The differential cross sections for the final state jets are given in Fig. 6.20 ( $\kappa/\Lambda = 0.04$  TeV<sup>-1</sup>) for  
 4485  $E_e = 70$  GeV and  $E_p = 7000$  GeV assuming  $\kappa_u = \kappa_c = \kappa$ . It is seen that the transverse momentum  
 4486 distribution of the signal has a peak around 70 GeV.

4487 Here, b-tagging efficiency is assumed to be 60% and the mistagging factors for light ( $u, d, s$ ) and  $c$  quarks  
 4488 are taken as 0.01 and 0.1, respectively. A  $p_T$  cut reduce the signal (by  $\sim 30\%$  for  $p_T > 50$  GeV), whereas  
 4489 the background is essentially suppressed (by a factor 4-6). In order to improve the signal to background  
 4490 ratio further, one can apply a cut on the invariant mass of  $W + jet$  around top mass. In Table 6.3, the cross  
 4491 sections for signal and background processes are given after having applied both a  $p_T$  and an invariant mass  
 4492 cuts ( $M_{Wb} = 150 - 200$  GeV).

4493 In order to calculate the statistical significance ( $SS$ ) we use following formula [270] :

$$SS = \sqrt{2 \left[ (S + B) \ln\left(1 + \frac{S}{B}\right) - S \right]} \quad (6.11)$$



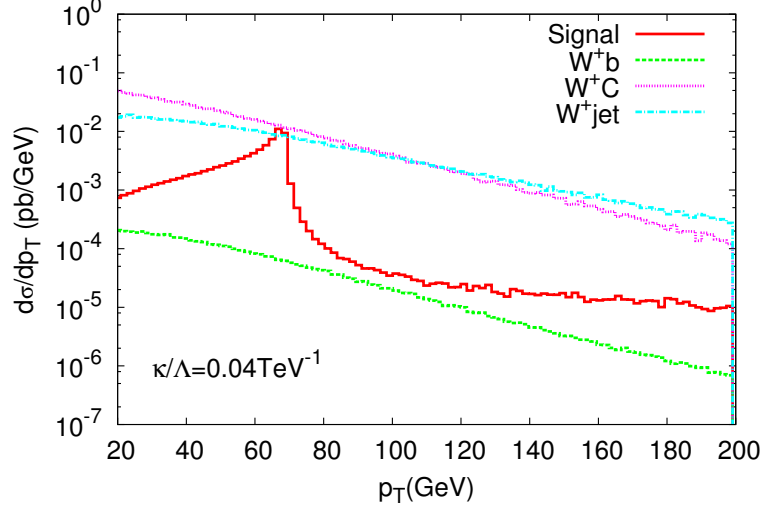


Figure 6.20: The transverse momentum distribution of the final state jet for the signal and background processes. The differential cross section includes the  $b$ -tagging efficiency and the rejection factors for the light jets. The center of mass energy  $\sqrt{s_{ep}} = 1.4$  TeV and  $\kappa/\Lambda = 0.04$  TeV $^{-1}$ .

$\kappa/\Lambda = 0.01$ TeV $^{-1}$	$p_T > 20$ GeV	$p_T > 40$ GeV	$p_T > 50$ GeV
Signal	$8.86 \times 10^{-3}$	$7.54 \times 10^{-3}$	$6.39 \times 10^{-3}$
Background: $W^+b$	$1.73 \times 10^{-3}$	$1.12 \times 10^{-3}$	$7.69 \times 10^{-4}$
Background: $W^+c$	$3.48 \times 10^{-1}$	$2.30 \times 10^{-1}$	$1.63 \times 10^{-1}$
Background: $W^+jet$	$1.39 \times 10^{-1}$	$9.11 \times 10^{-2}$	$6.38 \times 10^{-2}$

Table 6.3: The cross sections (in pb) according to the  $p_T$  cut and invariant mass interval ( $M_{Wb} = 150 - 200$  GeV) for the signal and background at  $\gamma p$  collider based on the LHeC with  $E_e = 70$  GeV and  $E_p = 7000$  GeV.

4494 where  $S$  and  $B$  are the numbers of signal and background events, respectively. Results are presented in Table  
4495 6.4 for different  $\kappa/\Lambda$  and luminosity values. It is seen that even with  $2$  fb $^{-1}$  the LHeC based  $\gamma p$  collider will  
4496 provide  $5\sigma$  discovery for  $\kappa/\Lambda = 0.02$  TeV $^{-1}$ .

4497 Up to now, we have assumed  $\kappa_u = \kappa_c = \kappa$ . However, it would be interesting to analyze the case  
4498  $\kappa_u \neq \kappa_c$ . Indeed, at HERA, valence  $u$ -quarks dominate whereas at LHeC energies the  $c$ -quark and  $u$ -quark  
4499 contributions become comparable. Therefore, the sensitivity to  $\kappa_c$  will be enhanced at LHeC comparing to  
4500 HERA. In Fig. 6.21 contour plots for anomalous couplings in  $\kappa_u - \kappa_c$  plane are presented. For this purpose,  
4501 a  $\chi^2$  analysis was performed with

$$\chi^2 = \sum_{i=1}^N \left( \frac{\sigma_{S+B}^i - \sigma_B^i}{\Delta\sigma_B^i} \right)^2 \quad (6.12)$$

4502 where  $\sigma_B^i$  is the cross-section for the SM background in the  $i^{th}$  bin, including both  $b$ -jet and light-jet  
4503 contributions with their corresponding efficiency factors. In the  $\sigma_{S+B}$  calculations, we take into account the  
4504 different values for  $\kappa_u$  and  $\kappa_c$  as well as the signal-background interference. Figs. 6.20-6.21 show that the  
4505 sensitivity is enhanced by a factor of 1.5 when the luminosity changes from  $2$  fb $^{-1}$  to  $10$  fb $^{-1}$ . Concerning the  
4506 energy upgrade, increasing electron energy from  $70$  GeV to  $140$  GeV results in 20% improvement for  $\kappa_c$  [269].  
4507 Increasing the electron energy further (energy frontier  $ep$  collider) does not give an essential improvement in

$SS$	$L = 2 \text{ fb}^{-1}$	$L = 10 \text{ fb}^{-1}$
$\kappa/\Lambda = 0.01 \text{ TeV}^{-1}$	2.58 (2.88)	5.79 (6.47)
$\kappa/\Lambda = 0.02 \text{ TeV}^{-1}$	5.26 (5.92)	11.78 (13.25)

Table 6.4: The signal significance ( $SS$ ) for different values of  $\kappa/\Lambda$  and integral luminosity for  $E_e = 70 \text{ GeV}$  and  $E_p = 7000 \text{ GeV}$  (the numbers in parenthesis correspond to  $E_e = 140 \text{ GeV}$ ).

4508 the sensitivity to anomalous couplings [271].

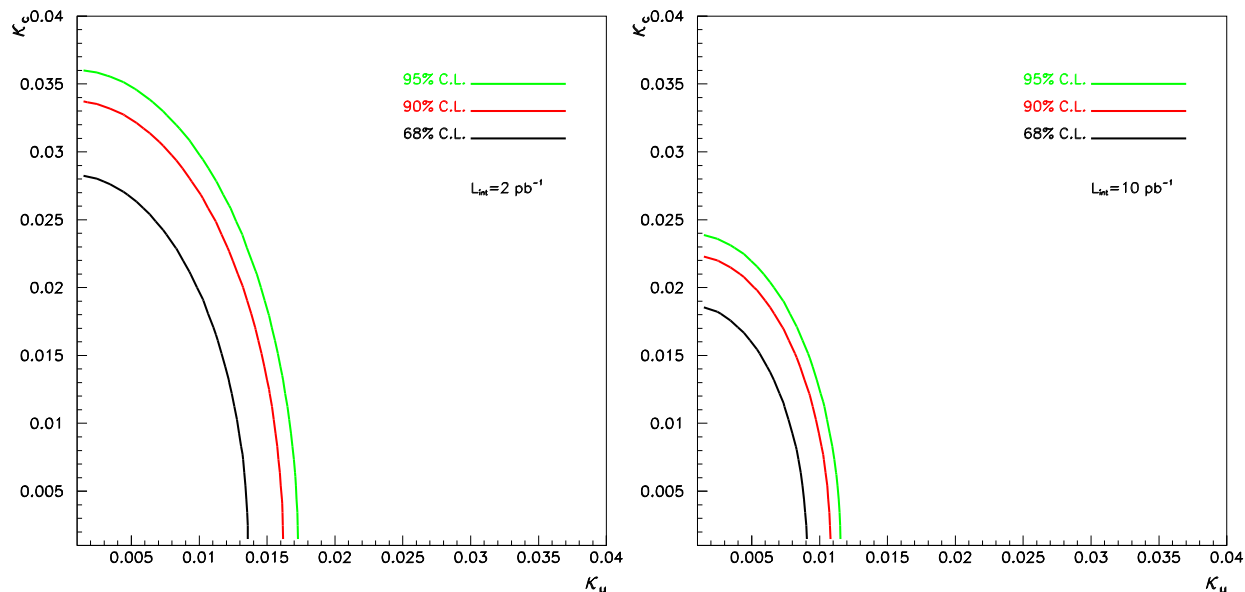


Figure 6.21: Contour plot for the anomalous couplings reachable at the LHeC based  $\gamma p$  collider with the center of mass energy  $\sqrt{s_{ep}} = 1.4 \text{ TeV}$  and integrated luminosity of  $L_{int} = 2 \text{ fb}^{-1}$  (left) or  $L_{int} = 10 \text{ fb}^{-1}$  (right)

4509 Table 6.4 shows that a sensitivity to anomalous coupling  $\kappa/\Lambda$  down to  $0.01 \text{ TeV}^{-1}$  could be reached.  
 4510 Noting that the value of  $\kappa/\Lambda = 0.01 \text{ TeV}^{-1}$  corresponds to  $BR(t \rightarrow \gamma u) \approx 2 \times 10^{-6}$  which is two orders  
 4511 smaller than the LHC reach with  $100 \text{ fb}^{-1}$ , it is obvious that even an upgraded LHC will not be competitive  
 4512 with LHeC based  $\gamma p$  collider in the search for anomalous  $t\gamma q$  interactions. Different extensions of the SM  
 4513 (SUSY, technicolor, little Higgs, extra dimensions etc.) predict branching ratio  $BR(t \rightarrow \gamma q) = O(10^{-5})$ , hence  
 4514 the LHeC will provide an opportunity to probe these models. The top quark could provide very important  
 4515 information for the Standard Model extensions due to its large mass close to the electroweak symmetry  
 4516 breaking scale.

### 4517 6.4.3 Excited quarks in $\gamma p$ collisions at LHeC

4518 Excited quarks will have vertices with SM quark and gauge bosons (photon, gluon, Z or W bosons). They  
 4519 can be produced at  $ep$  and  $\gamma p$  colliders via quark photon fusion. Interactions involving excited quark are  
 4520 described by the Lagrangian of eq. 6.6 (where  $F$  is now a quark  $q$ )

4521 A sizeable  $f_s$  coupling would allow for resonant  $q^*$  production at the LHC via quark-gluon fusion. In that  
 4522 case, the LHC would offer a large discovery potential for excited quarks and would be well suited to study  
 4523 the properties and couplings of these new quarks. However, if the coupling of excited quarks to  $gq$  happens

4524 to be suppressed, the LHC would mainly produce  $q^*$  via pair-production and would have little sensitivity to  
 4525 couplings  $f/\Lambda$  or  $f'/\Lambda$ . Such couplings would be better studied, or probed down to much lower values, via  
 4526 single-production of  $q^*$  at the LHeC. A study of the LHeC potential for excited quarks is presented in [272].  
 4527 An example of the  $3\sigma$  discovery reach, assuming  $f = f' = f_s$  and setting  $\Lambda$  to be equal to the  $q^*$  mass, is  
 given in Fig. 6.22. Both decays  $q^* \rightarrow q\gamma$  and  $q^* \rightarrow qg$  have been considered here.

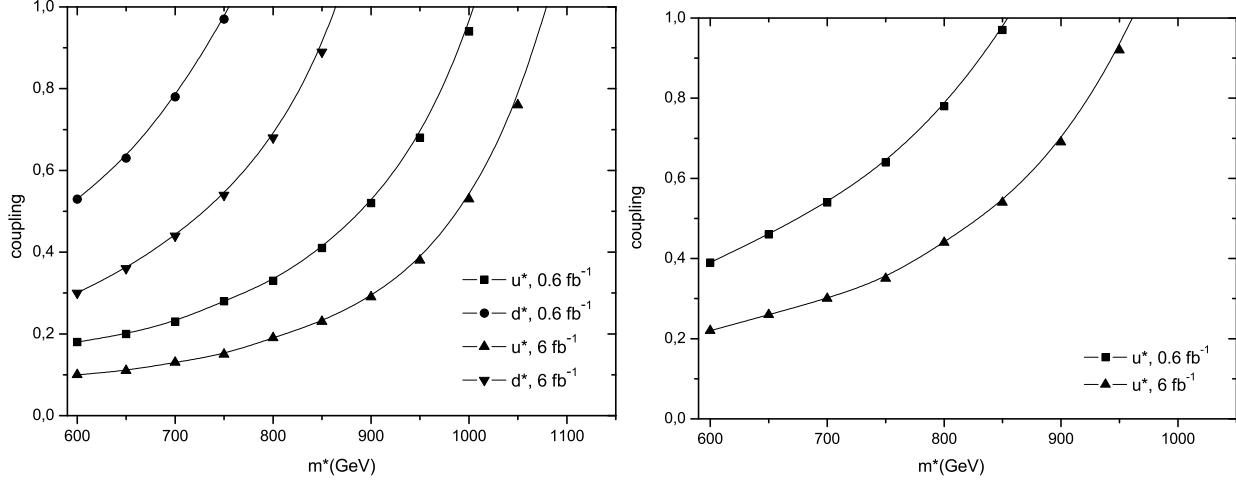


Figure 6.22: Observation reach at  $3\sigma$  for coupling and excited quark mass at a  $\gamma p$  collider with  $\sqrt{s} = 1.27$  TeV from an analysis of (left) the  $jj$  channel and (right) the  $\gamma j$  channel.

4528

#### 4529 6.4.4 Quarks from a fourth generation at LHeC

4530 The case of fourth generation quarks with magnetic FCNC interactions to gauge bosons and standard quarks,

$$\mathcal{L} = \left( \frac{\kappa_{\gamma}^{q_4 q_i}}{\Lambda} \right) e_q g_e \bar{q}_4 \sigma_{\mu\nu} q_i F^{\mu\nu} + \left( \frac{\kappa_Z^{q_4 q_i}}{2\Lambda} \right) g_Z \bar{q}_4 \sigma_{\mu\nu} q_i Z^{\mu\nu} + \left( \frac{\kappa_g^{q_4 q_i}}{\Lambda} \right) g_s \bar{q}_4 \sigma_{\mu\nu} T^a q_i G_a^{\mu\nu} + h.c. \quad (6.13)$$

4531 is very similar to that of excited quarks. A  $\gamma p$  collider based on LHeC would have a better sensitivity than  
 4532 LHC to anomalous couplings  $\kappa_{\gamma}$  and  $\kappa_Z$ . A detailed study is presented in [236] and example results are  
 4533 shown in Fig. 6.23. These figures also show the clear advantage of a  $\gamma p$  collider compared to an  $ep$  collider,  
 4534 for the study of new physics in  $\gamma q$  interactions.

#### 4535 6.4.5 Diquarks at LHeC

4536 The case of diquark production at LHeC has been studied in [273]. The production cross-section can be  
 4537 sizeable at a high energy  $ep$  machine, especially when operated as a  $\gamma p$  collider. The measurement of the  
 4538  $\gamma p \rightarrow DQ + X$  cross-section, for a diquark  $DQ$  of known mass and known coupling to the diquark pair<sup>3</sup>  
 4539 would provide a measurement of the electric charge of the diquark. It would thus be complementary to  
 4540 the  $pp$  data, which offer no simple way to access the  $DQ$  electric charge. However, the diquark masses and  
 4541 couplings that could be accessible at LHeC appear to be already excluded by the recent search for dijet  
 4542 resonances at the LHC [274].

<sup>3</sup>The LHC would observe diquark as di-jet resonances, and could easily determine its mass, width and coupling to the quark pair.

### 6.4.6 Quarks from a fourth generation in $Wq$ interactions

In case fourth generation quarks do not have anomalous interactions as in Eq. 6.13, they (or vector-like quarks coupling to light generations [275, 276]) could be produced in  $ep$  collisions by  $Wq$  interactions provided that the  $V_{Qq}$  elements of the extended CKM matrix are not too small, via the usual vector  $WqQ$  interactions. An example of the sensitivity that could be reached at LHeC is presented in [277], assuming some values for the  $V_{Qq}$  parameters. Measurements of single  $Q$  production at LHeC would provide complementary information to the LHC data, that could help in determining the extended CKM matrix.

## 6.5 Sensitivity to a Higgs boson

Understanding the mechanism of electroweak symmetry breaking is a key goal of the LHC physics programme. In the SM, the symmetry breaking is realized via a scalar field (the Higgs field) which, at the minimum of the potential, develops a non-zero vacuum expectation value. The breaking of the  $SU(2)_L \times U(1)_Y$  symmetry gives mass to the electroweak gauge bosons via the Higgs mechanism while the fermions obtain their mass via Yukawa couplings with the Higgs field. The LHC experiments should be able to discover a Higgs boson within the full allowable mass range, with an integrated luminosity of less than  $10 \text{ fb}^{-1}$ . Following its discovery, it will be crucial to measure the couplings of this Higgs boson to the SM particles, in particular to the fermions, in order to:

- establish that the Higgs field is indeed accounting for the fermion masses, via Yukawa couplings  $y_f H \bar{f} f$ ;
- disentangle between the SM and (some of) its extensions. For example, despite the richer content of the Higgs sector in the Minimal Supersymmetric Standard Model, only the light SUSY Higgs boson  $h$  would be observable at the LHC in certain regions of parameter space. Its properties are very similar to those of the SM Higgs  $H$ , and precise measurements of ratios  $BR(\Phi \rightarrow VV)/BR(\Phi \rightarrow ff)$  will be essential in determining whether or not the observed boson,  $\Phi$ , is the SM Higgs scalar.

Electroweak precision measurements strongly suggest that the SM Higgs boson should be light, in which case it would decay into a  $b\bar{b}$  pair with a branching ratio of  $\sim 70\%$ , but a measurement of the  $Hb\bar{b}$  coupling will be very challenging at the LHC [239, 270, 278]. Indeed, the observation of  $H \rightarrow b\bar{b}$  in the inclusive production mode is made very difficult by the huge QCD background, although a possible search channel would be associated  $WH$  and  $ZH$  production, with highly boosted Higgs, leading to a high mass jet with substructure [279]. The observability of the signal in the  $t\bar{t}H$  production mode also suffers from a large background, including background of combinatorics origin, and from experimental systematic uncertainties.

The signal  $H \rightarrow b\bar{b}$  may be observed in the exclusive production mode, thanks to the much cleaner environment in a diffractive process. However, the production cross-section in this mode suffers from large theoretical uncertainties, such that this measurement, if feasible at all, would not translate into a precise measurement of the  $Hb\bar{b}$  coupling.

At the LHeC, a light Higgs boson could be produced via  $WW$  or  $ZZ$  fusion with a sizeable cross-section. This section focusses on the observability of the signal  $ep \rightarrow H + X \rightarrow b\bar{b} + X$  at LHeC, which may be the first observation of the  $H \rightarrow b\bar{b}$  decay. A recent similar study can be found in [280].

### 6.5.1 Higgs production at LHeC

In  $ep$  collisions, the Higgs boson could be produced in neutral current (NC) interactions via the  $ZZH$  coupling, and in charged current (CC) interactions via the  $WWH$  coupling. The corresponding diagrams are shown in Fig. 6.24, and the production cross-sections, as a function of the Higgs mass, is displayed in Fig. 6.25. The  $WWH$  production largely dominates the total cross-section. As is the case for the inclusive CC DIS interactions, the cross-section is much larger in  $e^-p$  collisions than in  $e^+p$  collisions, due to the more favorable density of the valence quark that is involved ( $u$  in  $e^-p$ ,  $d$  in  $e^+p$ ), and to the more favorable helicity factors. Table 6.5 shows the Higgs production cross-section (at leading order) via CC interactions in  $e^-p$  collisions, for various values of the Higgs mass and three example values of the electron

4588 beam energy. The scale dependency of these leading order estimate is of  $\mathcal{O}(10\%)$ . Next-to-leading order  
 4589 corrections were calculated in [281, 282]. They are small, but can affect within  $\mathcal{O}(20\%)$  the shape of some  
 4590 kinematic distributions.

$M_H$ in GeV :	100	120	160	200	240	280
$E_e = 50$ GeV	102	81	50	32	20	12
$E_e = 100$ GeV	201	165	113	79	55	39
$E_e = 150$ GeV	286	239	170	123	90	67

Table 6.5: Production cross-section in fb of a SM Higgs boson via charged current interactions in  $e^-p$  collisions, for three example values of the electron beam energy.

## 4591 6.5.2 Observability of the signal

4592 The dominating source of background at large missing transverse energy is coming from multi-jet production  
 4593 in CC DIS interactions. In particular, a good rejection of the background coming from single top production  
 4594 ( $e^-b \rightarrow \nu t$ ), where the top decays hadronically, puts severe constraints on the acceptance and the resolution  
 4595 of the detector, as will be seen below. The background due to multijet production in NC interactions is also  
 4596 considered.

4597 MadGraph [283] has been used to generate SM Higgs production, CC and NC DIS background events.  
 4598 Calculations of cross-sections and generation of final states of outgoing particles are performed by MadGraph,  
 4599 given the beam parameters, considering all possible tree-level Feynman diagrams in the SM. In the case of  
 4600 NC, since the cross section is very high, diverging at low scattering angle, only processes producing two or  
 4601 more b quarks were generated in order to have sufficient MC statistics. By artificially increasing the mistag  
 4602 probability, it was possible to verify that, after the selection, essentially all the remaining NC background is  
 4603 indeed due to events with two truly b-quark jets in the final state. Fragmentation and hadronization processes  
 4604 were simulated by PYTHIA [130] with custom modifications to apply for  $ep$  collisions. Finally, particles were  
 4605 passed through a generic detector using the PGS [284] fast detector simulation tool. We assumed tracking  
 4606 coverage of  $|\eta| < 3$  and calorimeter coverage of  $|\eta| < 5$  with electromagnetic calorimeter resolution of  
 4607  $5\%/\sqrt{E(\text{GeV})}$  (plus 1% of constant term) and hadronic calorimeter resolution of  $60\%/\sqrt{E(\text{GeV})}$ . Jets  
 4608 were reconstructed by a cone algorithm with a cone size of  $\Delta R = 0.7$ . The efficiency of b-flavor tagging was  
 4609 assumed to be 60% and flat within the calorimeter coverage, whereas mistagging probabilities of 10% and  
 4610 1% for charm-quark jets and for light-quark jets, respectively, were taken into account.

4611 We set 150 GeV of electron beam energy with 7 TeV of proton beam energy as the reference beam  
 4612 configuration and assumed 120 GeV of SM Higgs boson mass in the MC simulation study. The results were  
 4613 compared with those with a different beam energy and Higgs mass.

4614 The following selection criteria were applied, based on observable variables generated by the PGS detector  
 4615 simulation, to distinguish  $H \rightarrow b\bar{b}$  from the CC and NC DIS backgrounds.

### 4616 • cut (1): Primary cuts

- 4617 – Exclude electron-tagged events
- 4618 –  $E_{T,miss} > 20$  GeV
- 4619 –  $N_{jet}(P_{T,jet} > 20 \text{ GeV}) \geq 3$
- 4620 –  $E_{T,total} > 100$  GeV
- 4621 –  $y_{JB} < 0.9$ , where  $y_{JB} = \Sigma(E - p_z)/2E_e$
- 4622 –  $Q_{JB}^2 > 400$  GeV, where  $Q_{JB}^2 = E_{T,miss}^2/(1 - y_{JB})$

### 4623 • cut (2): b-tag requirement

–  $N_{b\text{-jet}}(P_{T,\text{jet}} > 20 \text{ GeV}) \geq 2$ , where b-jet means a b-tagged jet

• **cut (3): Higgs invariant mass cut**

–  $90 < M_H < 120 \text{ GeV}$ ; due to the energy carried by the neutrino from  $b$  decays, the mass peaks are slightly lower than the true Higgs mass

Fig. 6.26 shows the missing  $E_T$  and number of b-tagged jets for  $H \rightarrow b\bar{b}$  events together with the CC and NC DIS background. The NC background is strongly suppressed by the missing  $E_T$  cut and electron-tag requirement. We required at least two b-tagged jets, and reconstructed the Higgs invariant mass using the two b-tagged jets with lowest and second lowest  $\eta$ . After cuts (1) + (2) + (3) were applied, 44.4% of the remaining CC background was due to single top production. The following cuts were further applied.

• **cut (4): rejection of single top production** Single top events result in a final state with two b-jets and a W decaying into two light-quark jets. The following cuts were found to be efficient in suppressing this background.

–  $M_{jjj,top} > 250 \text{ GeV}$ , where the three-jet invariant mass ( $M_{jjj,top}$ ) was reconstructed from two b-jets with the lowest  $\eta$  and any third jet with the lowest  $\eta$  regardless of b-tag

–  $M_{jj,W} > 130 \text{ GeV}$ , where di-jet invariant mass ( $M_{jj,W}$ ) was reconstructed from one b-jet with the lowest  $\eta$  and any second jet with the lowest  $\eta$  regardless of b-tag but excluding the second lowest  $\eta$  b-jet

• **cut (5): forward jet tagging**

–  $\eta_{jet} > 2$  for the lowest- $\eta$  jet excluding the two  $b$ -jets

Fig. 6.27 shows the reconstructed three-jet ( $M_{jjj,top}$ ) and di-jet ( $M_{jj,W}$ ) invariant masses after cuts (1) and (2) are applied. It is seen that, for CC background, the former peaks at the top mass and the latter peaks at the  $W$  mass. The last cut is motivated by the fact that the jet from light quark participating in the CC reaction for the signal is kinematically boosted to forward rapidity (in the proton beam direction), as shown in Fig. 6.28.

Fig. 6.29 shows the reconstructed Higgs mass distribution for an integrated luminosity of  $10 \text{ fb}^{-1}$ , after all selection criteria except for the Higgs mass cut have been applied. The results are summarized in Table 6.6. After the selection, 85  $H \rightarrow b\bar{b}$  events are expected for  $10 \text{ fb}^{-1}$  luminosity with a 150 GeV electron beam. The signal to background ratio is 1.79 and the significance of the signal  $S/\sqrt{N} = 12.3$ . For a higher Higgs mass,  $m_H=150 \text{ GeV}$ , the production cross section decreases and the  $b\bar{b}$  branching ratio also decreases. The expected number of signal events becomes 25 and  $S/N$  and  $S/\sqrt{N}$  are 0.52 and 3.60, respectively. On the other hand, with 60 GeV electron beam and five times larger luminosity ( $50 \text{ fb}^{-1}$ ), for 120 GeV Higgs, 124  $H \rightarrow b\bar{b}$  events are expected after the same cuts have been applied. Considering the CC and NC DIS background,  $S/N$  and  $S/\sqrt{N}$  are 1.05 and 11.4, respectively.

	Higgs production	CC DIS	NC $b\bar{b}j$	$S/N$	$S/\sqrt{N}$
cut (1)	816	123000	4630	$6.38 \times 10^{-3}$	2.28
cut (1) + (2) + (3)	178	1620	179	$9.92 \times 10^{-2}$	4.21
All cuts	84.6	29.1	18.3	1.79	12.3

Table 6.6: Expected  $H \rightarrow b\bar{b}$  signal and background events with 150 GeV electron beam for an integrated luminosity of  $10 \text{ fb}^{-1}$ . Contents of the cuts are listed in text.

The results shown here are subject to large uncertainties. First, as mentioned above, the very large NC background cross section at forward scattering angles makes it impossible to simulate a sufficient number

4659 of events to limit the Monte Carlo statistical uncertainty. It is estimated that the background evaluation,  
4660 with the above method where only events with at least two b quarks were simulated, has an uncertainty of  
4661 about a factor 3. With a full simulation, it can be expected to be negligible when the true measurement  
4662 is realized. Neglecting, therefore, this source of uncertainty, the systematic errors which will dominate are  
4663 expected to be the theoretical estimates of signals and backgrounds and instrumental effects: efficiency and  
4664 acceptance of lepton and jet reconstruction, b-tagging and mistagging probabilities. They are difficult to  
4665 estimate without real data and a real detector. The statistical uncertainty on the cross section can, however,  
4666 be estimated: 15% for the reference case of 150 GeV  $\times$  7 TeV beams and a Higgs of mass 120 GeV. This  
4667 represents a direct measure of the statistical uncertainty on the product of the squares of couplings  $Hbb$  and  
4668  $HWW$ .

### 4669 6.5.3 Probing Anomalous HWW Couplings at the LHeC

4670 The  $HWW$  vertex is an excellent handle on the quartic self-coupling of the scalar doublet. Its measurement  
4671 provides a direct insight into the nature of electroweak symmetry-breaking. Parametrising the  $H(k) -$   
4672  $W_\mu^+(p) - W_\nu^-(q)$  vertex in the form  $i\Gamma^{\mu\nu}(p, q) \epsilon_\mu(p) \epsilon_\nu^*(q)$ , any deviations from the simple SM formula  
4673  $\Gamma_{(\text{SM})}^{\mu\nu}(p, q) = gM_W \lambda^{\mu\nu}$  at a level incompatible with SM loop corrections would immediately indicate the  
4674 presence of new physics. Following Ref. [285], we can parametrize these deviations using two dimension-5  
4675 operators

$$\Gamma_{\mu\nu}^{(\text{BSM})}(p, q) = \frac{-g}{M_W} [\lambda(p \cdot q \lambda_{\mu\nu} - p_\nu q_\mu) + i \lambda' \epsilon_{\mu\nu\rho\sigma} p^\rho q^\sigma] \quad (6.14)$$

4676 where  $\lambda$  and  $\lambda'$  are, respectively, effective coupling strengths for the  $CP$ -conserving and the  $CP$ -violating  
4677 parts.

4678 An  $ep$  collider has a unique advantage in the fact that the  $HWW$  vertex gives rise to the process  
4679  $e + p \rightarrow \nu_e + X + H(bb)$  though the single Feynman diagram shown in Figure 6.24(left). The final state  
4680 has, therefore, missing transverse energy (MET) and three jets  $J_1, J_2$  and  $J_3$ , of which two (say  $J_2$  and  $J_3$ )  
4681 are tagged as  $b$ -jets. It can be shown [285] that in the limit when there is practically no energy transfer  
4682 to the  $W$  bosons and the final states are very forward, the  $CP$ -conserving ( $CP$ -violating) coupling  $\lambda$  ( $\lambda'$ )  
4683 contributes to the matrix element for this process a term of the form which goes through zero when the  
4684 missing transverse momentum is perpendicular to the  $p_T$  of the jet:

$$\mathcal{M} \sim +\lambda \vec{p}_T \cdot \vec{p}_T^{J_1} \quad \widetilde{\mathcal{M}} \sim -\lambda' \vec{p}_T \cdot \vec{p}_T^{J_1} . \quad (6.15)$$

4685 This explains the general trend illustrated in Figure 6.30, for an exact calculation of the  $2 \rightarrow 3$  process  
4686  $eq \rightarrow \nu_e q' H$  at the parton level, with parton density functions from the CTEQ-6L1 set [131]. In the case  
4687 considered, 140 GeV electrons collide with 7 TeV protons and the Higgs boson mass is set to 120 GeV.

4688 A detailed simulation of the charged current process was discussed above in Sect. 6.5.2. Here, the analysis  
4689 is based on the kinematic cuts and efficiencies adopted in Ref. [280]. The azimuthal distribution has been  
4690 simulated in 10 bins, each of width  $\pi/5$ , and the signal and SM backgrounds have been calculated in each  
4691 bin using the same formulae used to create Figure 6.30, followed by a detailed simulation of fragmentation,  
4692 jet identification and detector effects. Assuming statistical errors dependent on the integrated luminosity  
4693  $L$ , we then determine the sensitivity, for a given  $L$ , of the experiment to  $\lambda, \lambda'$  by making a log-likelihood  
4694 analysis. Our results are exhibited in Figure 6.31, where we present 95% exclusion plots for the  $\lambda$  and  $\lambda'$   
4695 couplings as a function of  $L$ . It is clear from this figure that by the time the LHeC has collected 10 fb $^{-1}$   
4696 of data, we will be able to exclude the anomalous couplings to the level of 0.3 or lower. The experimental  
4697 set-up is somewhat more sensitive to the  $CP$ -even coupling, as evidenced by the narrower inaccessible region  
4698 indicated on the left panel.

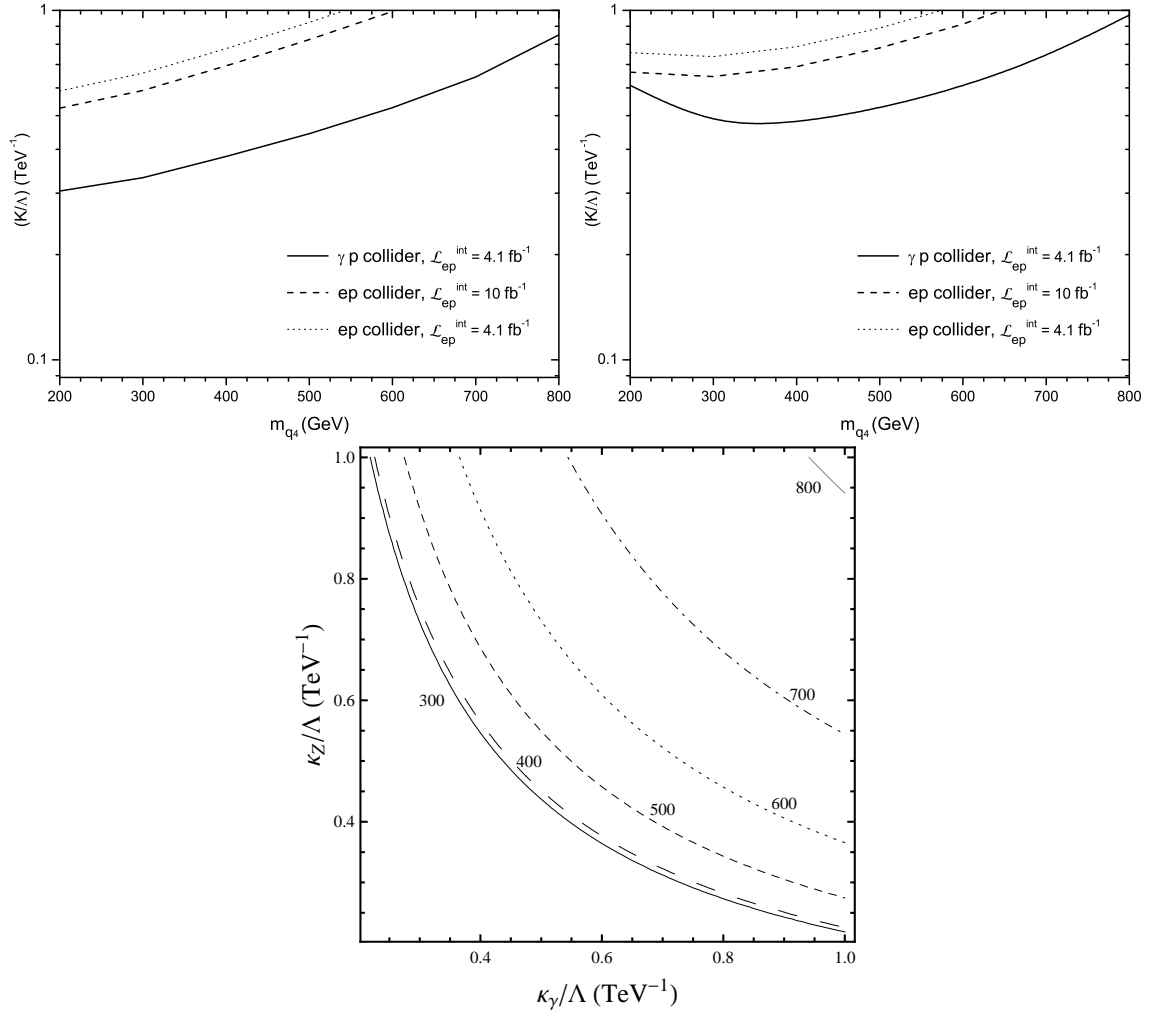


Figure 6.23: The achievable values of the anomalous coupling strength at  $ep$  and  $\gamma p$  colliders for a)  $q_4 \rightarrow \gamma q$  anomalous process and (b)  $q_4 \rightarrow Zq$  anomalous process as a function of the  $q_4$  mass; (c) the reachable values of anomalous photon and Z couplings with  $L_{int} = 4.1 \text{ fb}^{-1}$ .



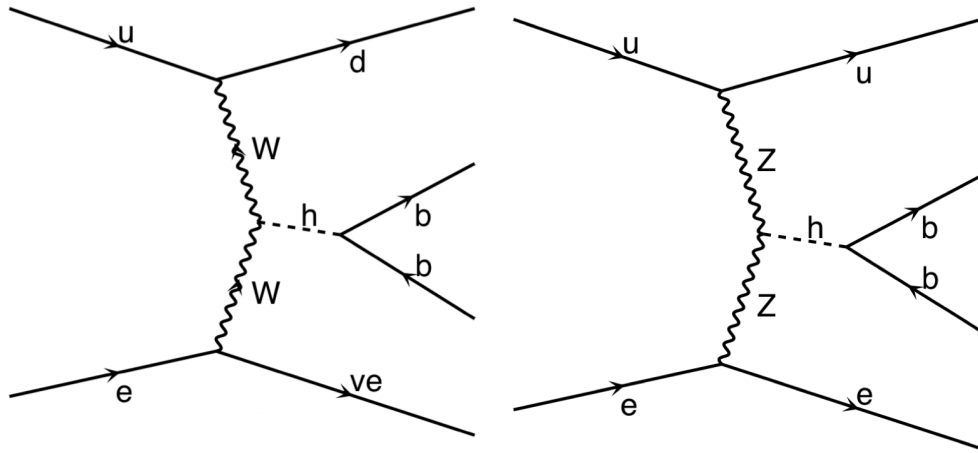


Figure 6.24: Feynman diagrams for CC(left) and NC(right) Higgs production at the LHeC.

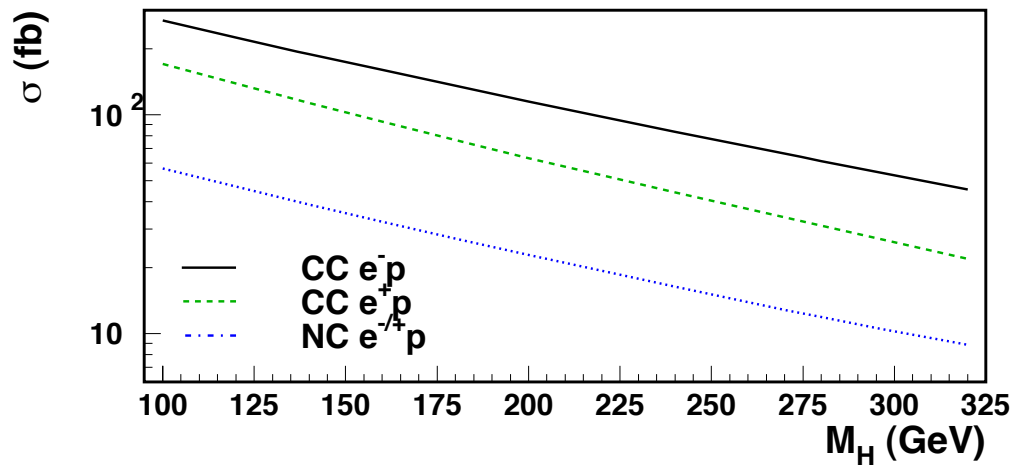


Figure 6.25: Production cross-section of a SM Higgs boson in  $ep$  collision with  $E_e=150$  GeV and  $E_p=7$  TeV, as a function of the Higgs mass.

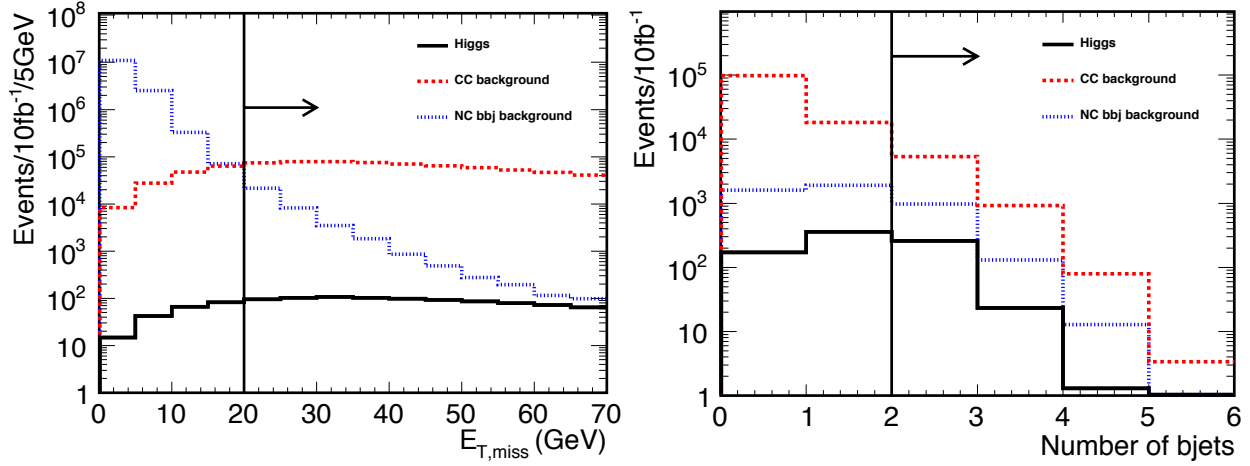


Figure 6.26: Missing  $E_T$  (left) and number of b-tagged jets (right). Solid (black), dashed (red) and dotted (blue) histograms show  $H \rightarrow b\bar{b}$ , CC and NC DIS background, respectively. The right plot is for events passing cut (1) in the text.

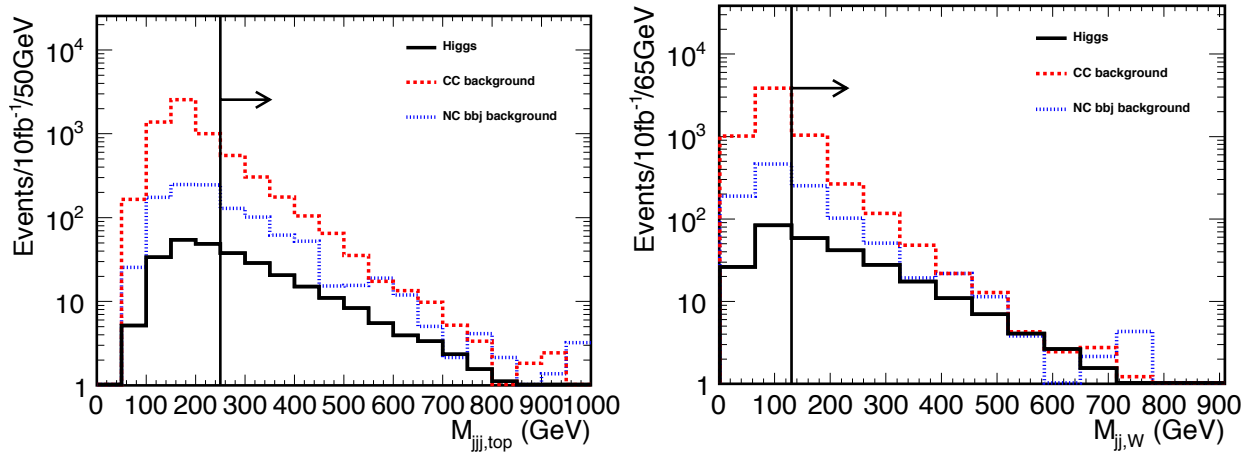


Figure 6.27: Three-jet (left) and di-jet (right) invariant masses. Solid (black), dashed (red) and dotted (blue) histograms show  $H \rightarrow b\bar{b}$ , CC and NC DIS background, respectively.

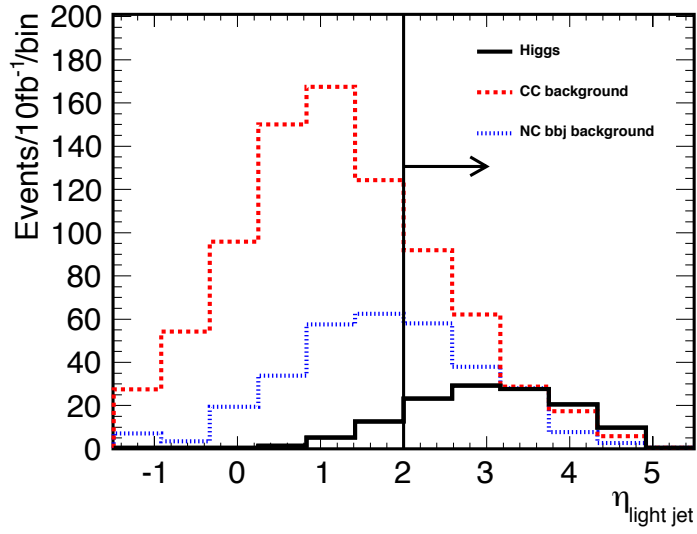


Figure 6.28:  $\eta_{jet}$  distribution for the lowest- $\eta$  jet excluding the two  $b$ -tagged jets. Solid (black), dashed (red) and dotted (blue) histograms show  $H \rightarrow b\bar{b}$ , CC and NC DIS background, respectively.

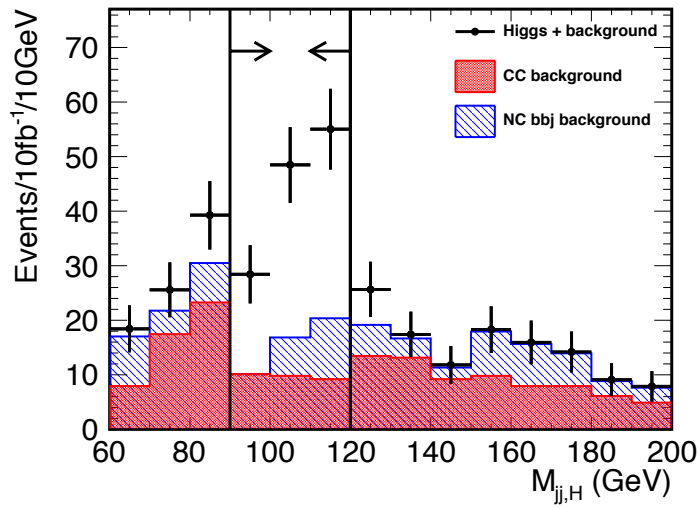


Figure 6.29: Reconstructed invariant Higgs mass after all selection criteria, except for the Higgs mass cut, have been applied. Points with error bars (black) show the  $H \rightarrow b\bar{b}$  signal added to the CC (red histogram) and NC (hatched blue histogram) DIS background for an integrated luminosity of  $10 \text{ fb}^{-1}$ .

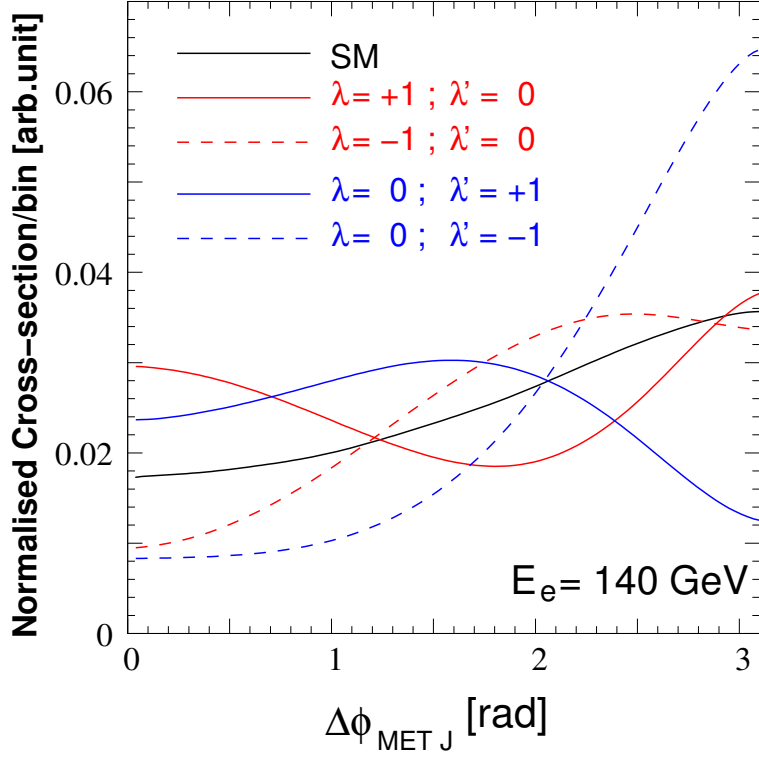


Figure 6.30: Illustrating the SM distribution in azimuthal angle and deviations therefrom which are due to anomalous  $HWW$  couplings.

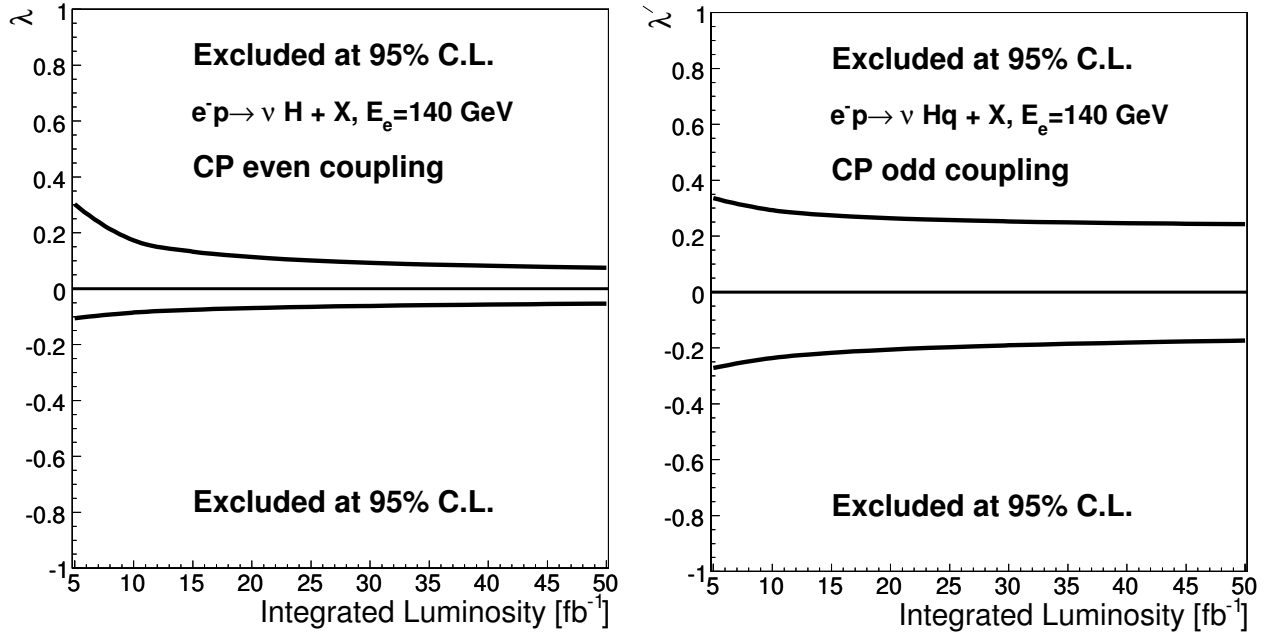


Figure 6.31: Exclusion plots obtainable by a study of the azimuthal angle distributions at the LHeC for the  $CP$ -even coupling  $\lambda$  and the  $CP$ -odd coupling  $\lambda'$ . Note that this study is for  $M_H = 120$  GeV.

## Part III

# Accelerator

4699

4700

## Chapter 7

# Ring-Ring Collider

### 7.1 Baseline Parameters and Configuration

Intense electron-proton beam interactions in the LHC tunnel can be realised with an electron storage ring and the LHC, as has been discussed already at the Lausanne workshop back in 1984. This solution was revived [17] when it had been seen that a hundred fold higher luminosity can be achieved than with HERA, owing to the intense proton beams available with the LHC. With an electron beam energy set between about 50 and 100 GeV and the 7 TeV proton beam energy one can realise a new  $ep$  collider of cms energy,  $\sqrt{s} = 2\sqrt{E_e E_p}$  beyond 1 TeV. The advantages of a ring-ring (RR) configuration are that one uses known technology, with much experience from HERA and LEP, and that intense beams of both lepton charges are readily available.

For the present design study the electron beam energy has been set to 60 GeV as is discussed above, Sect. 2.3. With extra efforts and higher investments one may double that energy, as had been achieved for LEP [565], should there be strong physics requirements. One yet has to see that power losses vary  $\propto E_e^{-4}$  and much higher synchrotron radiation occurs, which causes the operation and technical conditions to be increasingly demanding as  $E_e$  increases. A 60 GeV  $e^\pm$  beam may be polarised while, following the calculations presented below, that becomes questionable when  $E_e$  increases.

Due to the smallness of the  $ep$  tuneshift, synchronous  $pp$  and  $ep$  interactions can be realised with the LHC and the LHeC. This requires to bypass the active  $pp$  experiments with separate tunnels which, in adjacent caverns, can house the RF. Excavation of such tunnels may proceed in parallel to LHC operation, like the CMS cavern was excavated while LEP ran. Due to machine hardware or unfortunate geological conditions, none of the 4 machine points (3,4 and 6,7) could house the LHeC interaction region. For the present study IP2 was chosen as the  $ep$  IR, currently housing ALICE, and bypasses were considered for ATLAS and CMS.

Maximum luminosity can be achieved with focussing magnets placed close to the interaction point. This limits, however, the polar angle acceptance. Two principal interaction optics solutions have been developed, the high luminosity optics, with acceptance down to about  $8^\circ$ , and the large acceptance optics, covering polar angles down to  $1^\circ$ . As is shown below, there is only a factor of 4 difference in the product of the  $\beta$  functions. It then is likely that one further develops the large acceptance solution only, but both are fully described here.

A complete lattice has been designed for the new ring. This takes into account some peculiarities due to the LHC. In particular, an asymmetric FODO cell, of half the LHC FODO cell length, had to be designed to account for LHC service modules and the DFBS. Similarly, a non-standard solution for the dispersion matching had to be developed, using 8 individually powered quadrupoles instead of regulating the position of dipoles which is too constrained by the LHC.

A further baseline parameter is the injection energy. The LHeC electron storage ring differs from LEP in its bunch structure. The LHeC has a maximum of about  $2 \cdot 10^{10}$  electrons per bunch in a much higher repetition rate than LEP, which had a bunch intensity of  $4 \cdot 10^{11}$ . The smaller intensity allows to inject at

4738 lower energy than LEP. For the current design a new injector is considered, using linac technology with high  
4739 frequency cavities, of energy of 10 GeV. This poses constraints on the quality of the main dipole magnets,  
4740 which have to ensure a magnetic field reproducibility of about  $10^{-4}$ .  $C$ - (and  $H$ ) shape prototype magnets  
4741 have been developed, built and successfully tested at BINP Novosibirsk. Alternative magnets have been built  
4742 and are being tested also at CERN. Besides the magnetic field properties, attention was given to small outer  
4743 dimensions (of about  $35\text{ cm}^2$  compared to  $50\text{ cm}^2$  at LEP) and to a reduction of the weight (from  $800\text{ kg/m}$   
4744 at LEP to  $250\text{ kg/m}$  for the LHeC) in order to facilitate the installation. The total number of magnets is  
4745 less than 4000. Such an amount is large, but it may be obtained within a few years production, following  
4746 1 : 1 prototyping within the technical design phase.

4747 The key question for the storage ring is its possible installation in the LHC tunnel without posing too  
4748 harsh constraints on the LHC operation schedule. A first inspection has been made of the various elements  
4749 of concern, as described below, with the conclusion that installation of the LHeC was possible but very  
4750 demanding. For a TDR of the ring-ring solution, a detailed 3D CAD integration study of both accelerators  
4751 is mandatory.

4752 The subsequent chapter describes the studies dedicated to characterize the RR option. It is followed by a  
4753 similar chapter on the LR option. Much of the system hardware is common or similar and thus it is contained  
4754 in a following chapter. From today's perspective both options may be realised within the coming ten years,  
4755 albeit the differences which distinguish them. It is part of the referee process to understand the relative  
4756 merits in terms of physics, technics, operation, infrastructure and future developments, which is expected  
4757 to lead to a sufficiently deep consideration and comparison of the storage ring versus the linac options, such  
4758 that the TDR can be developed for just one of them. Since, however, the cavities, for the ring injector and  
4759 for the linac, the dipole magnets, for the ring and for the linac return arcs, and the 3 beam superconducting  
4760 triplet of magnets near the interaction point, all have very similar constraints, a next phase of prototyping  
4761 and design has been possible to already prepare.

## 4762 7.2 Baseline Parameters and Configuration

### 4763 7.3 Geometry

4764 All lattice descriptions in this chapter are based on the LHeC lattice Version 1.1.

#### 4765 7.3.1 General Layout

4766 The general layout of the LHeC consists of eight arcs, six straight sections and two bypasses around the  
4767 experiments in Point 1 and Point 5. The e-p collision experiment is assumed to be located in Point 2, the  
4768 only interaction point of the beams. All straight sections except those in the bypasses have the same length  
4769 as the LHC straight sections:  $538.8\text{ m}$  at even points and  $537.8\text{ m}$  at odd points.

4770 The insertions shared with the LHC are already used for the experiments or for LHC equipment.  
4771 Therefore the RF for the electron ring is installed in the straight sections of the bypasses [?]. For the same  
4772 reason the beam is injected in the bypass around Point 1. Point 1 is preferred over Point 5 for geological  
4773 and infrastructural reasons. The overall layout of the LHeC is shown in Fig. 7.1.

#### 4774 7.3.2 Electron Ring Circumference and e-p Synchronization

4775 The LHeC electron beam collides only in one point (Point 2) with the protons of the LHC. This leaves the  
4776 options to either exactly match the circumferences of the proton and electron rings or to allow a difference of  
4777 a multiple of the LHC bunch spacing. In the case of different circumferences the proton beam could become  
4778 unstable due to beam-beam interactions with the electrons [566], [?]. To avoid this possible effect in the  
4779 LHeC, the electron ring circumference is matched exactly to the proton ring circumference.

4780 The circumference can be adjusted in two ways:

1. Different bypass designs, e.g. inner and outer bypass, which compensate each other in length.
2. Radial displacement of the electron ring to the inside or outside of the LHC in the places where the two rings share the same tunnel to compensate for the path length difference caused by the bypasses.

The various design possibilities for the bypasses are discussed in Sec. 7.3.4. Considering their characteristics, the best choice seems to be outer bypasses around both experiments.

In general asynchronization between the e- and p-beam could arise from small differences in the circumferences of the central orbits. Both beams could be synchronized by adjusting the RF frequency of the electron or proton beam accordingly [?]. The feasibility of this method was demonstrated with proton lead in the LHC [?] and also for electrons and protons in Hera [?].

### 7.3.3 Idealized Ring

In the following the average between LHC beam 1 and beam 2 is taken as reference geometry for the LHC.

#### General Layout

To compensate the path length differences from the bypasses, the electron ring is placed on average 61 cm to the inside of the LHC in the sections where both rings share the tunnel. For this a complete ring with an ideally constant radial offset of 61 cm to the LHC was designed. In the following we refer to this ring as the *Idealised Ring*.

In addition to the horizontal displacement, the electron ring is set 1 m above the LHC in order to minimize the interference with the LHC elements. The main remaining conflict in the arc are then the service modules as shown in Fig. 7.16.1 and the DFBs in the insertions [?]. A representative cross section of the LHC tunnel is shown in Fig. 7.2.

In the main arcs the service modules have a length of 6.62 m and are installed at the beginning of each LHC arc cell. The insertions host a different number of DFBs with a varying placement and length. The idealised ring lattice is designed to avoid overlaps of magnet elements with all service modules in the main arcs. In order to show that it is possible to design an optics with no e-ring elements at any DFB positions in the insertions, the dispersion suppressors of the even and odd insertions were adapted to the DFB positions and lengths in IR2 and IR3 respectively. For simplicity all straight sections are filled with a regular FODO cell structure.

#### Geometry

To adjust the beam optics to the regular reappearance of the service modules at the beginning of each LHC arc cell it was suggested to use a multiple  $n$  or submultiple  $1/n$  ( $n \in \mathbb{N}$ ) of the LHC arc cell length as LHeC FODO cell length. Beside the integration constraints, the cell has to provide the right emittance. Taking half the LHC arc cell length as LHeC FODO cell length already fulfils this second criterion (Sec. 7.4.1).

As the LHC arc cell is symmetric, the best geometrical alignment with the LHC main arc would be achieved, if the LHeC cell also had a symmetrical layout. Because of the service modules, no elements can be placed in the first 6.9 m of two consecutive cells. If all cells had the same layout, another 6.9 m would be lost in the second FODO cell. This would result in additional unwanted synchrotron radiation losses as the energy loss in a dipole magnet is proportional to the inverse length of the dipole

$$U_{\text{dipole}} = \frac{C_\gamma}{2\pi} E_0^4 \frac{\theta^2}{l}, \quad C_\gamma = \frac{4\pi}{3} \frac{r_e}{(m_e c^2)^3} \quad (7.1)$$

where  $\theta$  is the bending angle,  $l$  the length of the dipole and  $E_0$  the beam energy. In order to avoid this, the LHeC arc cell is a double FODO cell, symmetric in the positioning of the quadrupoles but asymmetric in the placement of the dipoles (Fig. 7.3).

The bending angle in the arc cells and also in the DS is determined by the LHC geometry. In the following we refer to the LHC DS as the section from the end of the arc to the beginning of the LSS. With



4823 this definition the LHC DS consists of two cells. Keeping the same conversion rule as in the arc (one LHC  
 4824 FODO cell corresponds to two LHeC FODO cells), the LHeC DS would then ideally consist of 4 equal cells.  
 4825 For consistency the ratio between the LHeC DS and arc cell lengths is the same as between the LHC DS  
 4826 and arc cell. For the LHC this ratio is 2/3. This leaves the following choices for the number of dipoles in  
 4827 the arc and DS cell:

$$N_{\text{Dipole, arc cell}} = \frac{3}{2} N_{\text{Dipole, DS cell}} = 3, 6, 9, 12, 15 \dots \quad (7.2)$$

4828 A good compromise between a reasonable dipole length and optimal use of the available space for the bending  
 4829 is 15 dipoles per arc cell. The dipoles are then split up in packages of 3 + 4 + 4 + 4 in one arc cell and 2 + 3  
 4830 in one DS cell.

4831 Beside the bending angle, the module length of the electron ring has to be matched to the LHC geometry.  
 4832 As the electron ring is radially displaced to the inside of the proton ring, all e-ring modules are slightly shorter  
 4833 than their proton ring equivalents (Table 7.1).

	Proton Ring	Electron Ring
Arc Cell Length	106.9 m	106.881 m
DSL Length (even points)	172.80 m	172.78 m
DSR Length (even points)	161.60 m	161.57 m
DSL Length (odd points)	173.74 m	173.72 m
DSR Length (odd points)	162.54 m	162.51 m

Table 7.1: Proton and Electron-Ring Module Lengths. DSL=Dispersion Suppressor Left side, DSR=Dispersion Suppressor Right side

4834 The above considerations already fix the bending angle of the dipoles, which leaves only position and  
 4835 length as free parameters. Ideally the dipole length would be chosen as long as possible, but because of the  
 4836 asymmetry of the arc cell, the dipoles have to be shortened and moved to the right in order to fit the LHC  
 4837 geometry.

4838 The LHeC DS layout would ideally be similar to the LHC DS layout (Fig. 7.4), but has to be modified in  
 4839 order to leave space for the DFBS in the DS region. In the final design the dipoles are placed as symmetrically  
 4840 as possible between the regular arrangement of the quadrupoles (Fig. 7.5, 7.6). The difference between the  
 4841 LHC proton ring and the idealised LHeC electron ring is shown in Fig. 7.7 and 7.8.

### 4842 7.3.4 Bypass Options

4843 In the design of the e-ring geometry, it is foreseen to bypass the LHC experiments at Point 1 and Point  
 4844 5. The main requirements for both bypasses are that all integration constraints are respected, synchrotron  
 4845 radiation losses are not significantly increased and that the change in circumference can be compensated by  
 4846 increasing or decreasing the radius of the ring.

4847 Three different options are considered as basic bypass designs:

4848 **Vertical Bypass:** A vertical bypass would have to be a vertically upward bypass as downward would  
 4849 imply crossing the LHC magnets and other elements. For this a separation of about 20 to 25 m is  
 4850 required [567]. This can only be achieved by strong additional vertical bending. In general a vertical  
 4851 bypass would therefore be rather long, increase the synchrotron radiation due to the additional vertical  
 4852 bends and decrease the polarization compared to a horizontal bypass. A vertical bypasses is therefore  
 4853 only considered as an option if horizontal bypasses are not possible.

4854 **Horizontal Inner Bypass:** A horizontal inner bypass can be constructed by simply decreasing the bending  
 4855 radius of the main bends. Consequently the synchrotron radiation losses for an inner bypass are larger  
 4856 than for a comparable outer bypass. The advantage of an inner bypass is, if used in combination with

4857 an outer one, that it reduces the circumference and the two bypasses could compensate each other's  
 4858 path length differences.

4859 **Horizontal Outer Bypass:** A horizontal outer bypass uses the existing curvature of the ring instead of  
 4860 additional or stronger dipoles and consequently does not increase the synchrotron radiation losses. In  
 4861 general this is the preferred option.

### 4862 7.3.5 Bypass Point 1

4863 The cavern in Point 1 reaches far to the outside of the LHC, so that a separation of about 100 m would be  
 4864 necessary in order to fully bypass the experimental hall. For a bypass on the inside, a smaller separation of  
 4865 about 39 m would be required. For an inner bypass with minimal separation, the bending strength in three  
 4866 normal arc cells would have to be doubled resulting in a bypass of more than 2 km length. A sketch of such  
 4867 an inner bypass is shown in Fig. 7.9.

4868 Instead of a long inner bypass, an outer bypasses using the existing survey gallery is chosen as final  
 4869 design. With this design the separation is brought down to 16.25 m. The RF is installed in the straight  
 4870 section next to the straight section of the proton ring. The electron beam is injected into the arc on the  
 4871 right side of the bypass. The design is shown in Fig. 7.10.

### 4872 7.3.6 Bypasses Point 5

4873 Due to the compact design of the cavern in Point 5 a separation of only about 20 m is needed to completely  
 4874 bypass the experiment on the outside (Fig. 7.11). The separation in the case of an inner horizontal bypass  
 4875 or a vertical bypass would be the same or larger and therefore, as in the case of Point 1, the horizontal outer  
 4876 bypass is preferred over an inner or vertical one. The RF is installed in the centre straight section parallel  
 4877 to the proton ring.

### 4878 7.3.7 Matching Proton and Electron Ring Circumference

4879 Both bypasses in Point 1 and Point 5 require approximately the same separation and a similar design was  
 4880 chosen for both. To obtain the necessary separation  $\Delta_{BP}$  a straight section of length  $s_{BP}$  is inserted into the  
 4881 lattice of the idealised ring (Sec. 7.3.3) in front of the last two arc cells. The separation  $\Delta_{BP}$ , the remaining  
 4882 angle  $\theta_{BP}$  and the inserted straight section  $s_{BP}$  are related by (Fig. 7.12):

$$\Delta_{BP} = s_{BP} \sin \theta_{BP} \quad (7.3)$$

4883 As indicated in Fig. 7.12 the separation could be increased by inserting a S-shaped chicane including negative  
 4884 bends. The advantage of additional bends would be the faster separation of the electron and proton ring.  
 4885 On the other hand the additional bends would need to be placed in the LHC tunnel, the straight sections of  
 4886 the bypass would be reduced and the synchrotron radiation losses increased. Hence this is not the preferred  
 4887 solution.

4888 In the following, estimates for the current bypass design, which does not include any extra bends, are  
 4889 presented. Given the separation, angle and length of the inserted straight section, the induced change in  
 4890 circumference is then:

$$\Delta s_{BP} = s_{BP} - x_{BP} = 2\Delta_{BP} \tan\left(\frac{\theta_{BP}}{2}\right) \quad (7.4)$$

4891 This change can be compensated by a change in radius of the idealised ring by:

$$\Delta s_{BP} = 2\pi\Delta R \quad (7.5)$$

4892 Taking the change in radius into account, the separation  $\Delta_{BP}$  has to be substituted by  $\Delta_{BP,tot} :=$   
 4893  $\Delta_{BP} + \Delta R$ . The radius change and the total separation are then related by:

$$\Delta R = \frac{\Delta_{BP}}{\pi \cot\left(\frac{\theta_{BP}}{2}\right) - 2}, \quad \text{with } \Delta_{BP} = \Delta_{BP1} + \Delta_{BP5} \quad (7.6)$$

4894 As the bypass in Point 1 passes through the existing survey gallery, the geometry and with it the separation  
 4895 in Point 1, cannot be changed. The bypass in Point 5, on the other hand, is fully decoupled from the existing  
 4896 LHC cavern and tunnel and is therefore used for the fine adjustment of the circumference. The design values  
 of both bypasses are summarized in Table 7.2.

	Point 1	Point 5
Total bypass length	1303.3 m	1303.7 m
Separation	16.25 m	20.56 m
Dispersion free straight section	172 m	297 m
Ideal radius change of the idealised ring	61 cm	

Table 7.2: Lengths characterising the bypasses.

4897

## 4898 7.4 Layout and Optics

4899 Throughout the whole electron ring lattice, the choice of the optics is strongly influenced by the geometrical  
 4900 constraints and shortage of space in the LHC tunnel. The main interference with the LHC beside Point 1  
 4901 and Point 5, which have to be bypassed, are the service modules and DFBs in the tunnel, where no electron  
 4902 ring elements can be placed.

### 4903 7.4.1 Arc Cell Layout and Optics

4904 The LHC service modules are placed at the beginning of each LHC main arc cell. In order to obtain a periodic  
 4905 solution of the lattice, the electron ring arc cell length can only be a multiple or  $1/n$ th,  $n \in \mathbb{N}$ , of the LHC  
 4906 FODO cell length. Given the same phase advance and bending radius, the emittance increases with increasing  
 4907 cell length  $L$  of a FODO cell. In the case of the LHeC electron ring a FODO cell length corresponding to  
 4908 half the LHC FODO cell length delivers an emittance close to the design value of  $\epsilon_{\text{rms},x/y} = 5.0/2.5$  nm.  
 4909 The emittance of a cell with the full LHC FODO cell length is about a factor of 4 too large.

4910 Choosing half the LHC FODO cell length divides the arc into 23 equal double FODO cells with a  
 4911 symmetric configuration of the quadrupoles and an asymmetric distribution of the dipoles, precisely 8 dipoles  
 4912 in the first FODO cell and 7 in the second. The dipole configuration is asymmetric in order to use all  
 4913 available space for the bending of the e-beam and consequently minimize the synchrotron radiation losses.  
 4914 With a phase advance of  $180^\circ$  horizontally and  $120^\circ$  vertically over the complete double FODO cell, which  
 4915 corresponds to a phase advance of  $90^\circ/60^\circ$  per FODO cell, the horizontal emittance lies with 3.96 nm well  
 4916 below the design value of 5 nm. The optics of one arc cell is shown in Fig. 7.3 and the parameters are listed  
 4917 in Table 7.3.

### 4918 7.4.2 Insertion Layout and Optics

4919 For simplicity all even and all odd insertions of the electron ring have the same layout as described in Sec.  
 4920 7.3.1. Each insertion is divided in three parts: the dispersion suppressor on the left side (DSL), the straight  
 4921 section and the dispersion suppressor on the right side (DSR).

#### 4922 Dispersion Suppressor

4923 Various well known standard DS designs like the missing bend or half bend scheme exist, but they are all  
 4924 based on specific placement of the dipoles. In the case of the LHeC the position of the dipoles is strongly  
 4925 determined by the LHC geometry and does not match any of the standard schemes. Therefore the dispersion  
 4926 matching is achieved by 8 individually powered quadrupoles and not with the positioning of the dipoles. The  
 4927 DS on the left side is split into two DS sections, reaching from the first DFB to the second and from the

Beam Energy	60 GeV
Phase Advance per Cell	180°/120°
Cell length	106.881 m
Dipole Fill factor	0.75
Damping Partition $J_x/J_y/J_e$	1.5/1/1.5
Coupling constant $\kappa$	0.5
Horizontal Emittance (no coupling)	3.96 nm
Horizontal Emittance ( $\kappa = 0.5$ )	2.97 nm
Vertical Emittance ( $\kappa = 0.5$ )	1.49 nm

Table 7.3: Optics Parameters of one LHeC arc cell with a phase advance of 90°/60° per half cell.

second to the beginning of the straight section. In the DSL the quadrupoles are distributed equally in each section. In the DSR they are placed with equal distances from each other throughout the complete DS. This layout turned out to be better for the right side due to the different arrangement of the DFBS. The DSs of the even and odd points differ slightly in their length but have the same general layout. The lengths of the DSs are listed in Table 7.1. The DS optics are shown in Fig. 7.5 and 7.6.

### 4933 Straight Section

4934 For simplicity the straight sections consist of a regular FODO lattice with a phase advance of 90°/60° except  
4935 the straight section at Point 3 and Point 7 where the phase advance of the FODO cells is used for the  
4936 adjustment of the working point. In a later stage the lattice and optics of the straight sections will have to  
4937 be adjusted to the various insertions.

### 4938 7.4.3 Bypass Layout and Optics

4939 The general layout and nomenclature of the bypasses is illustrated in Fig. 7.13. The straight sections LSSL,  
4940 LSSR and IR are dispersion free sections reserved for the installation of RF, wiggler(s), injection etc. Two  
4941 normal arc cells (4 FODO cells) with 8 individual quadrupoles are used as dispersion suppressor before the  
4942 first straight section LSSL and after the last straight section LSSR. In the sections TLIR and TRIR the  
4943 same configuration of dipoles is kept as in the idealised lattice for geometric reasons. Among this fixed  
4944 arrangement of dipoles 14 matching quadrupoles per side are placed as equally as possible.

4945 The straight sections consist of a regular FODO lattice with a phase advance of 90°/60°.

4946 The complete bypass optics in Point 1 and Point 5 are shown in Fig. 7.14 and 7.15.

### 4947 7.4.4 Chromaticity Correction

4948 The phase advance of one LHeC FODO cell of 90°/60° suggests a chromaticity correction with in total 5  
4949 interleaved sextupole families, 2 horizontal and 3 vertical. In order to reduce the chromatic stopband and the  
4950 off momentum beta beating each arc contains an equal number of sextupoles per family, so  $n \cdot 2$  horizontal  
4951 and  $m \cdot 3$  in the vertical. Further to reduce the sextupole strength and therefore the excitation of resonances,  
4952 the families are completed by placing sextupoles also in the dispersion suppressors. This yields a sextupole  
4953 scheme as illustrated in Fig. 7.16. A large part of the total natural chromaticity usually comes from the  
4954 experiments due to their large  $\beta$ -functions and magnet strength in the final focus quadrupoles. This is only  
4955 true for the vertical plane of the 1 Degree optics. In the case of the 10 Degree option and the horizonat  
4956 plane of the 1 Degree optics, all insertions including the experimental insertion in Point 2 contribute more  
4957 or less equally to the chromaticity. This suggest a global correction of the chromaticity with 2 sextupoles  
4958 for the horizontal and 3 for the vertical plane for the 10 Degree option. For the 1 Degree option a local

4959 correction of the off-momentum beta-beating with the two arcs adjacent to IP2 could be considered instead  
 4960 of a simple global correction [?]. The contribution of the different insertions to the total chromaticity is  
 4961 listed in Table 7.4 and Table 7.5.

	$-dQ_{x/y}$	$-(dQ_{x/y}/dQ_{x/y,tot}) \cdot 100$
full sequence	142.1/115.6	100/100
IR 1	9.6/8.2	6.8/7.1
IR 2	4.6/3.8	3.2/3.3
IR 3/7	4.5/3.6	3.2/3.1
IR 4/6/8	4.6/3.8	3.2/3.3
IR 5	10.0/7.8	7.0/6.7

Table 7.4: Contribution of the insertions to the natural chromaticity for the 10 Degree Option

	$-dQ_{x/y}$	$-(dQ_{x/y}/dQ_{x/y,tot}) \cdot 100$
full sequence	144.1/136.2	100/100
IR 1	9.9/7.5	6.7/5.5
IR 2	7.5/25.0	5.2/18.3
IR 3/7	4.7/3.7	3.2/2.7
IR 4/6/8	4.6/3.7	3.2/2.7
IR 5	10.2/7.8	7.0/5.7

Table 7.5: Contribution of the insertions to the natural chromaticity for the 1 Degree Option

4962 In general the chromaticity correction is expected to be rather unchallenging.

### 4963 7.4.5 Working Point

4964 Because of the bypasses and the single interaction region, the LHeC lattice has no reflection or rotation  
 4965 symmetry. As 50% emittance ratio is required, betatron coupling resonances may be excited and must  
 4966 be taken into account for the choice of the working point. In addition the beam will suffer a maximum  
 4967 beam-beam tune shift of 0.087 in both planes in the case of the 1° option and 0.085 in the horizontal and  
 4968 0.090 in the vertical plane in the case of the 10° option. Besides the systematic resonances also the first  
 4969 synchrotron sidebands of at least the integer resonances have to be avoided. Taking the beam-beam tune  
 4970 shift and the detuning with amplitude from head-on interactions into account a possible working point could  
 4971 be  $Q_x = 123.155/Q_y = 83.123$  for the 1° as well as for the 10° option. The working point diagrams for both  
 4972 cases are shown in Figs. 7.17 and 7.18.

### 4973 7.4.6 Aperture

4974 The current LHeC e-ring magnet apertures [?] are based on the experience from LEP [?] applied on the  
 4975 LHeC arc cells. They correspond to minimum 36.2  $\sigma$  hor./39.9  $\sigma$  ver. in the arc dipoles, 32.9  $\sigma$  hor./59  
 4976  $\sigma$  ver. in the arc quadrupoles, 14.7  $\sigma$  hor./35.9  $\sigma$  ver. in the insertion dipoles and 14.6  $\sigma$  hor./51.6  $\sigma$  ver.  
 4977 in the insertion quadrupoles. In the estimate all insertions were included wherat for the IP (Point 2) the  
 4978 values were only calculated for the 1 Degree option. All values are summarized in Table 7.6, 7.7, 7.8, 7.9.  
 4979 The hor. aperture in the insertion dipoles and quadrupoles is slightly too tight, but as the gradients are  
 4980 small, it can be easily increased by around 5 to 7 mm without changing considerably the magnet design.

4981 In all calculations a gaussian profile in all three dimensions was assumed and the maximum beam size is  
 4982 consequently given by:

$$\sigma_{x,y} = \sqrt{\beta_{x,y}\epsilon_{x,y} + D_{x,y}^2\sigma_E^2} \quad (7.7)$$

4983 where  $\epsilon_{x,y}$  are the design emittances of 5 respectively 2.5 nm.

Hor. Half Apert. Dip.	30 mm
Ver. Half Apert. Dip.	20 mm
Max. Hor. Beam Size	0.82 mm
Max. Ver. Beam Size	0.50 mm
Hor. Apert./Max. Beam Size	36.2
Ver. Apert./Max. Beam Size	39.9

Table 7.6: Aperture and beam sizes for the arc dipoles

Hor. Half Aperture Dipole	30 mm
Ver. Half Aperture Dipole	20 mm
Max. Hor. Beam Size	2.04 mm
Max. Ver. Beam Size	0.56 mm
Hor. Aperture/Max. Beam Size	14.7
Ver. Aperture/Max. Beam Size	35.9

Table 7.7: Aperture and beam sizes for the insertion dipoles including Point 2 (1° Option)

Apert. Radius Arc Quad.	30 mm
Max. Hor. Beam Size	0.91 mm
Max. Ver. Beam Size	0.51 mm
Hor. Apert./Max. Beam Size	32.9
Ver. Apert./Max. Beam Size	59.0

Table 7.8: Aperture and beam sizes for the arc quadrupoles

Apert. Radius Quad.	30 mm
Max. Hor. Beam Size	2.06 mm
Max. Ver. Beam Size	0.58 mm
Hor. Apert./Max. Beam Size	14.6
Ver. Apert./Max. Beam Size	51.6

Table 7.9: Aperture and beam sizes for the insertion quadrupoles including Point 2 (1° Option)

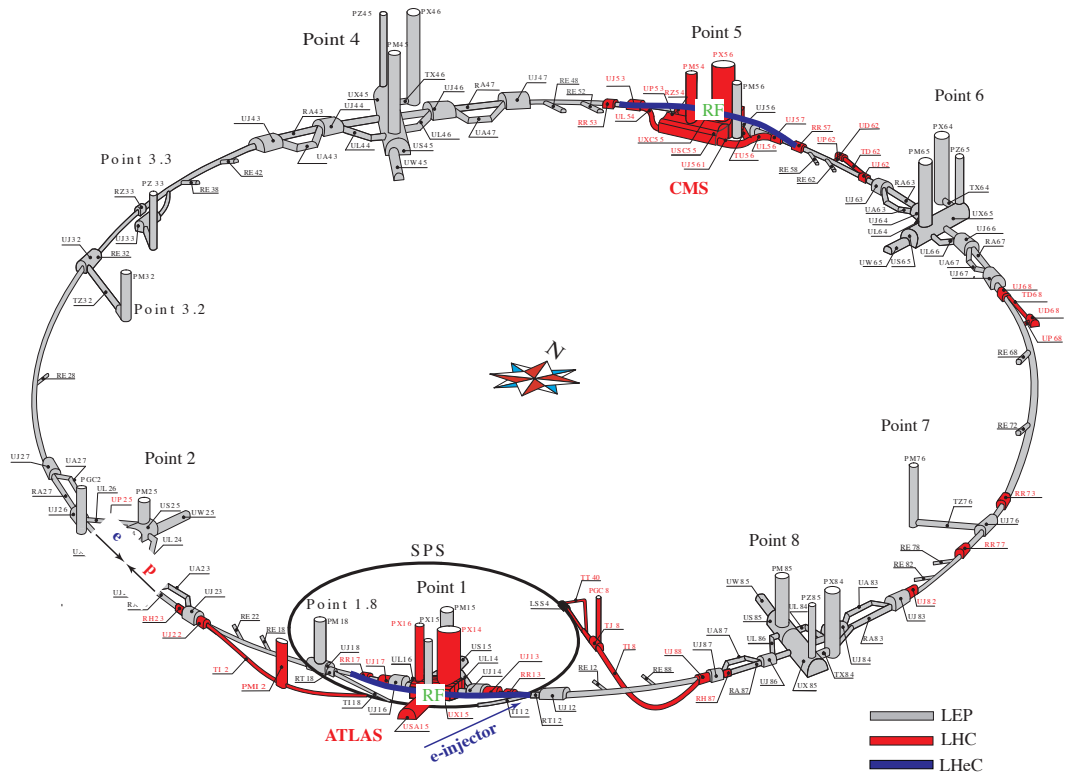


Figure 7.1: Schematic Layout of the LHeC: In grey the LEP tunnel now used for the LHC, in red the LHC extensions. The two LHeC bypasses are shown in blue. The RF is installed in the central straight section of the two bypasses. The bypass around Point 1 hosts in addition the injection.

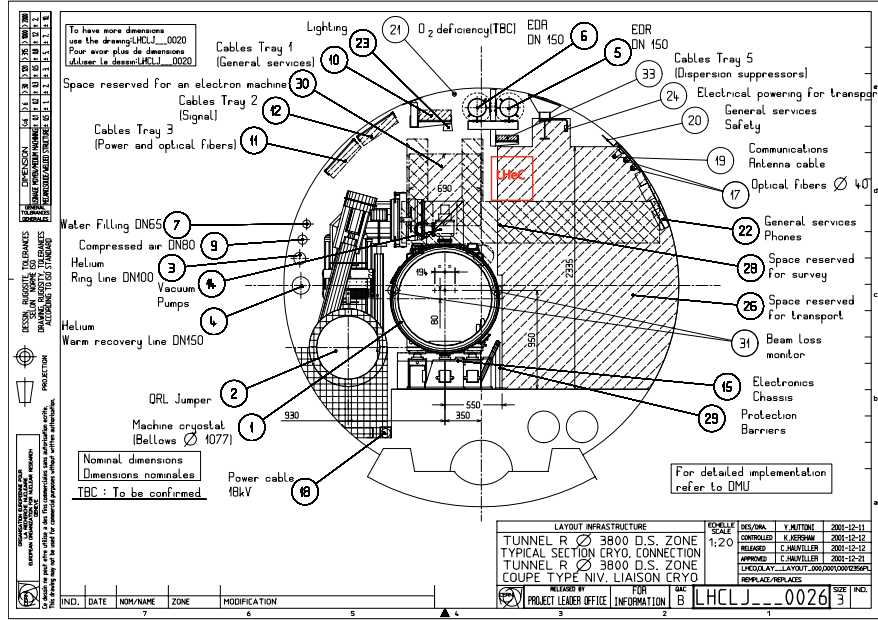


Figure 7.2: Representative cross section of the LHC tunnel. The location of the electron ring is indicated in red.

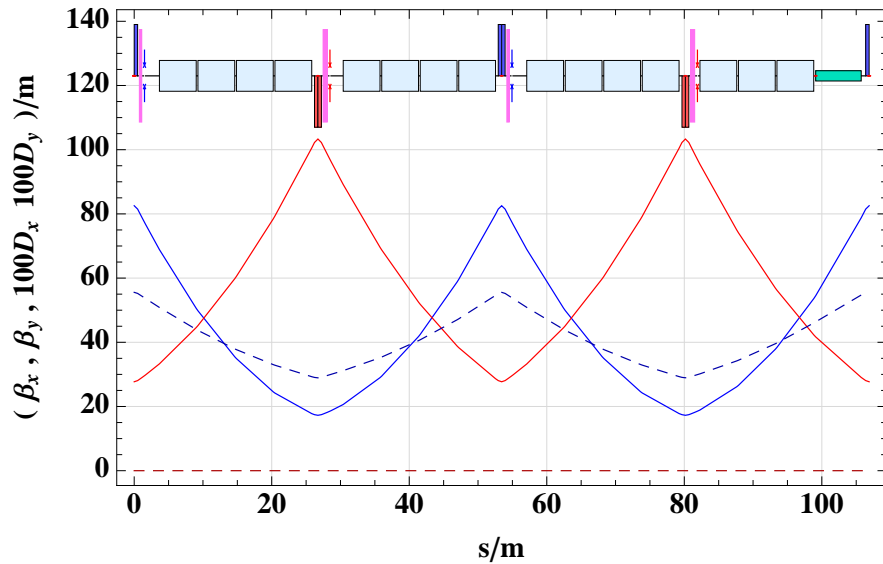


Figure 7.3: Electron ring arc cell optics. One arc cell consists of two FODO cells symmetric in the placement of the quadrupoles and asymmetric for the dipoles.



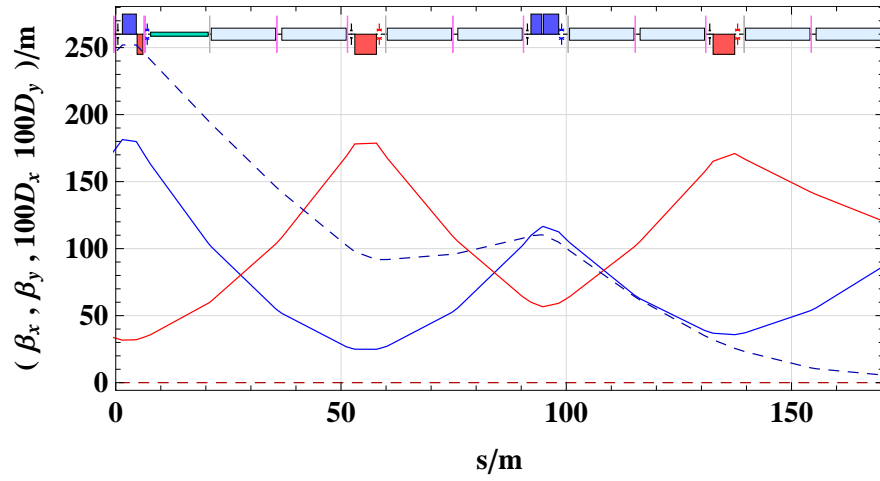


Figure 7.4: LHC DS on the left side of IP2.

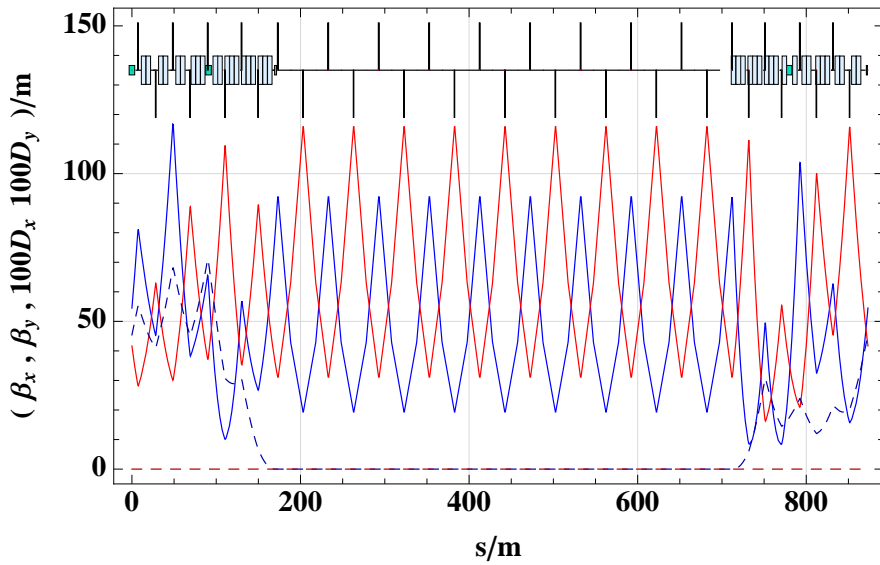


Figure 7.5: LHeC IR for even IRs, based on the DFB configuration in Point 2.

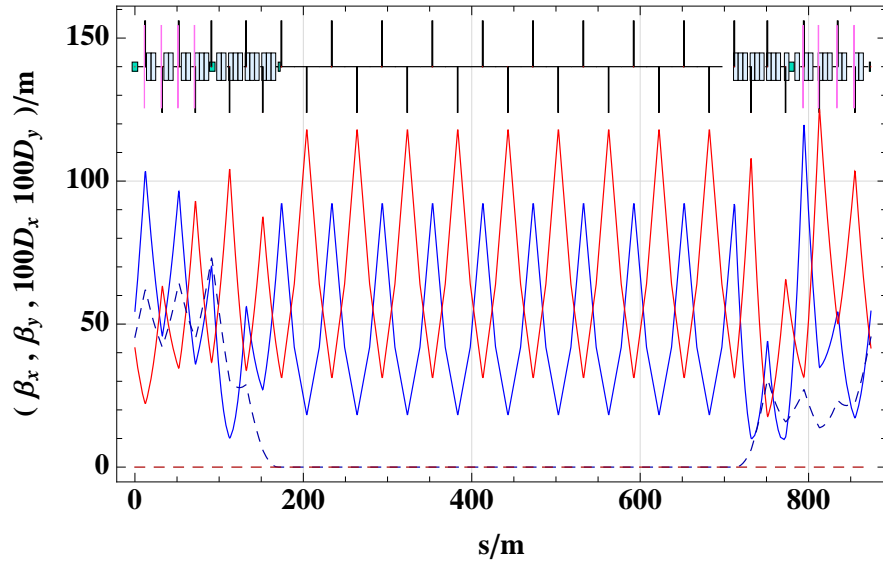


Figure 7.6: LHeC IR for odd IRs, based on the DFB configuration in Point 3.

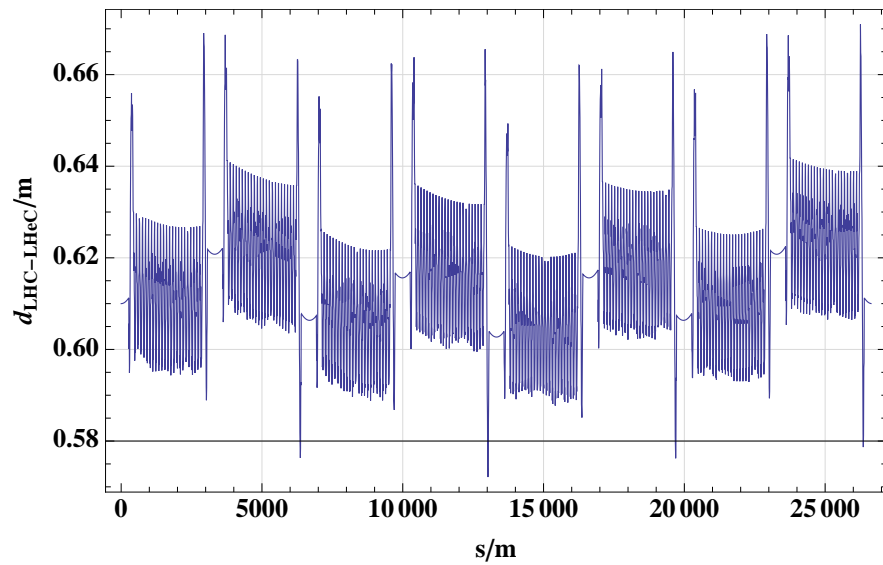


Figure 7.7: Radial distance between the idealised electron ring and the proton ring

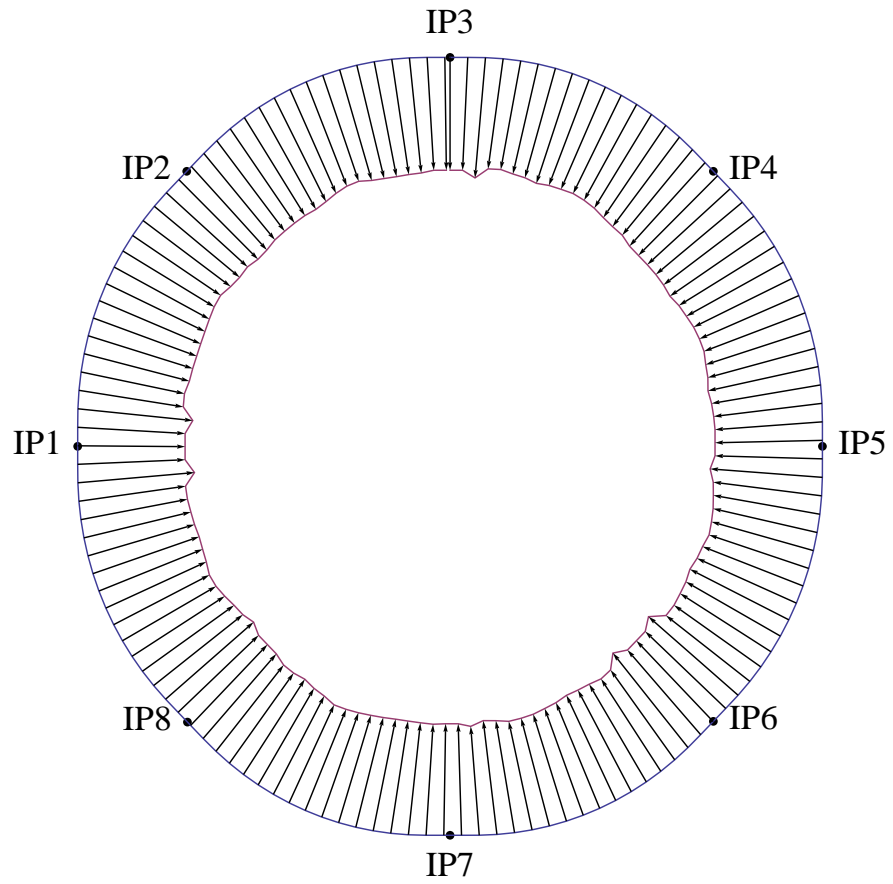


Figure 7.8: LHC and LHeC. The distance between the two rings is exaggerated by a factor 2000.

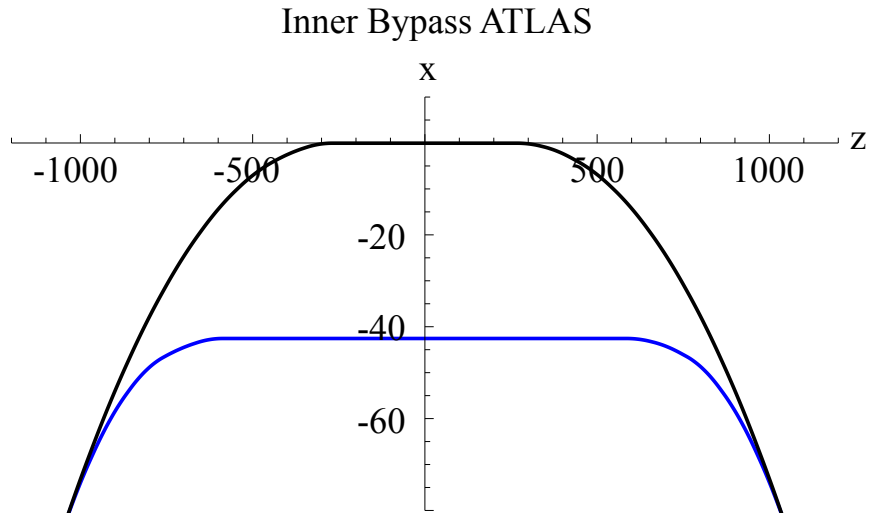


Figure 7.9: Example of an inner Bypass around Point 1. The Bypass is shown in blue, The LHC proton ring in black.

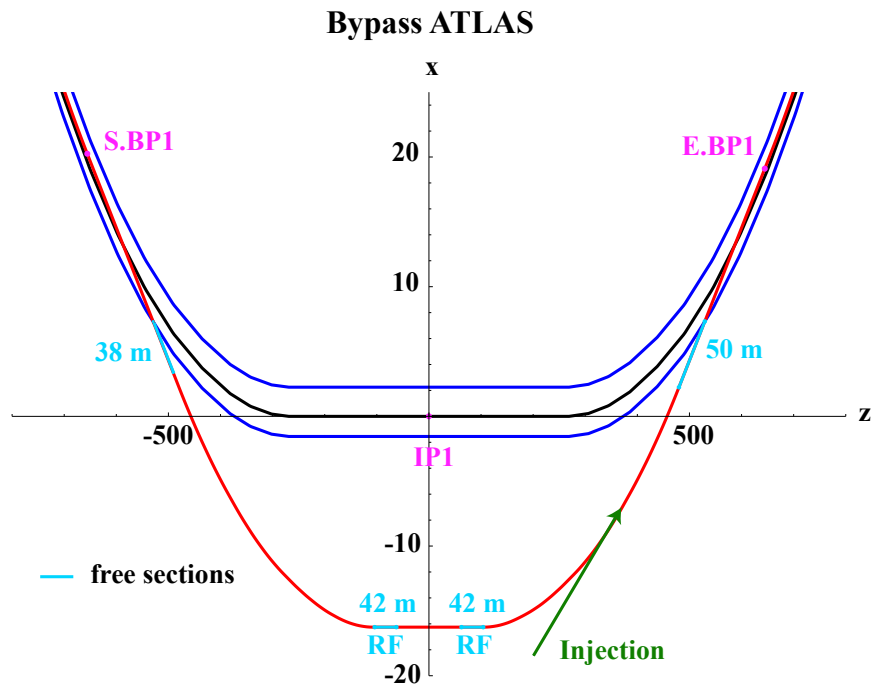


Figure 7.10: Final bypass design using the survey gallery in Point 1. The LHC proton ring is shown in black, the electron ring in red and the tunnel walls in blue. Dispersion free sections reserved for the installation of RF, wiggler(s), injection and other equipment are marked in light blue. The injection is marked in green and is located in the right arc of the bypass. Beginning and end of the bypass are marked with S.BP1 and E.BP1

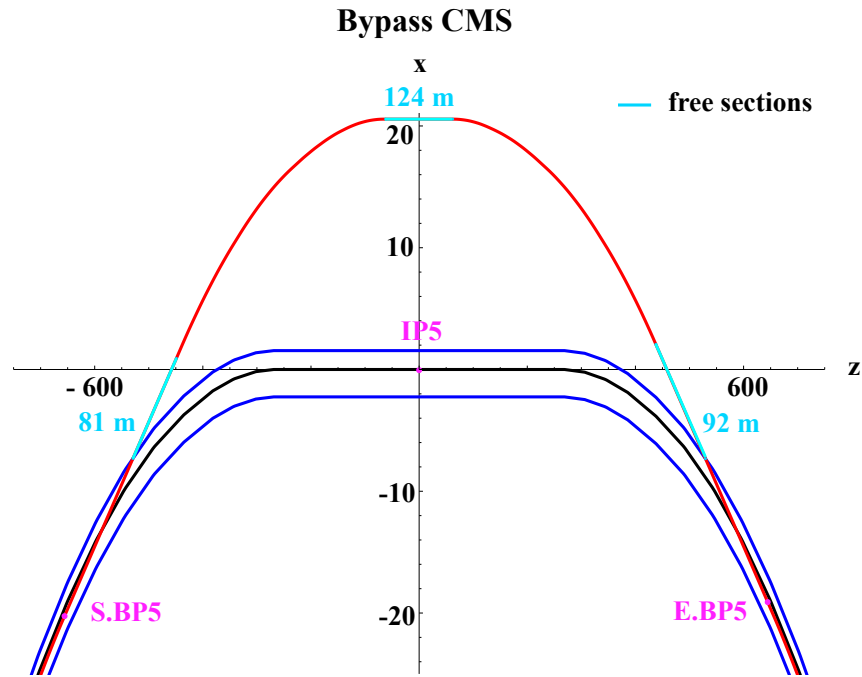


Figure 7.11: Horizontal outer bypass in Point 5. The LHC proton ring is shown in black, the electron ring in red and the tunnel walls in blue. Dispersion free sections reserved for the installation of RF, wiggler(s), injection and other equipment are marked in light blue. Beginning and end of the bypass are marked with S.BP5 and E.BP5

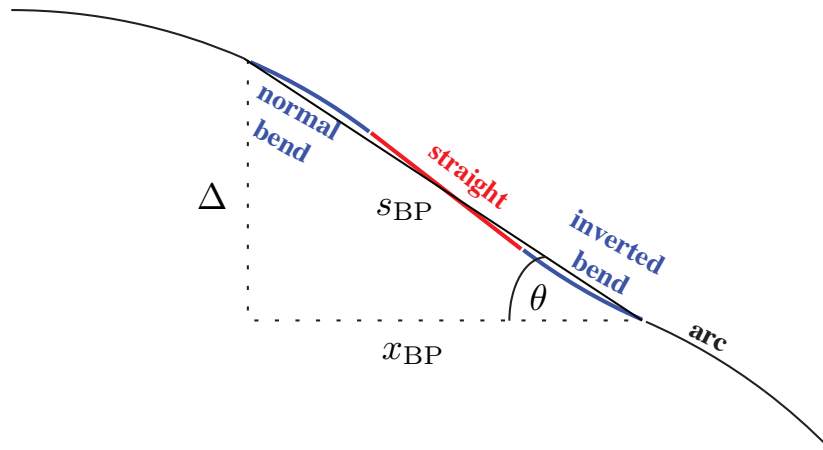


Figure 7.12: Outer bypass: a straight section is inserted to obtain the required separation. A larger separation could be achieved by inserting inverted bends.

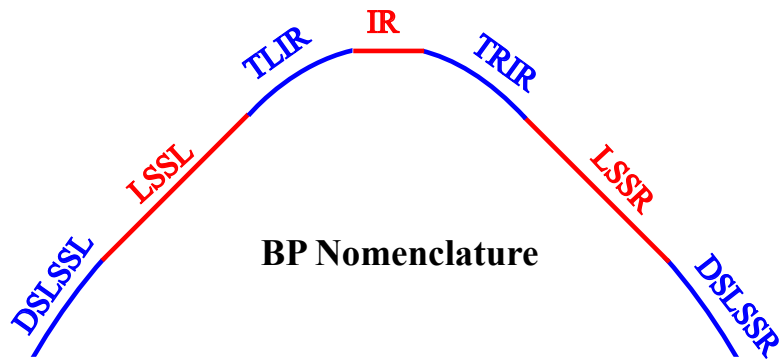


Figure 7.13: Bypass layout and nomenclature.

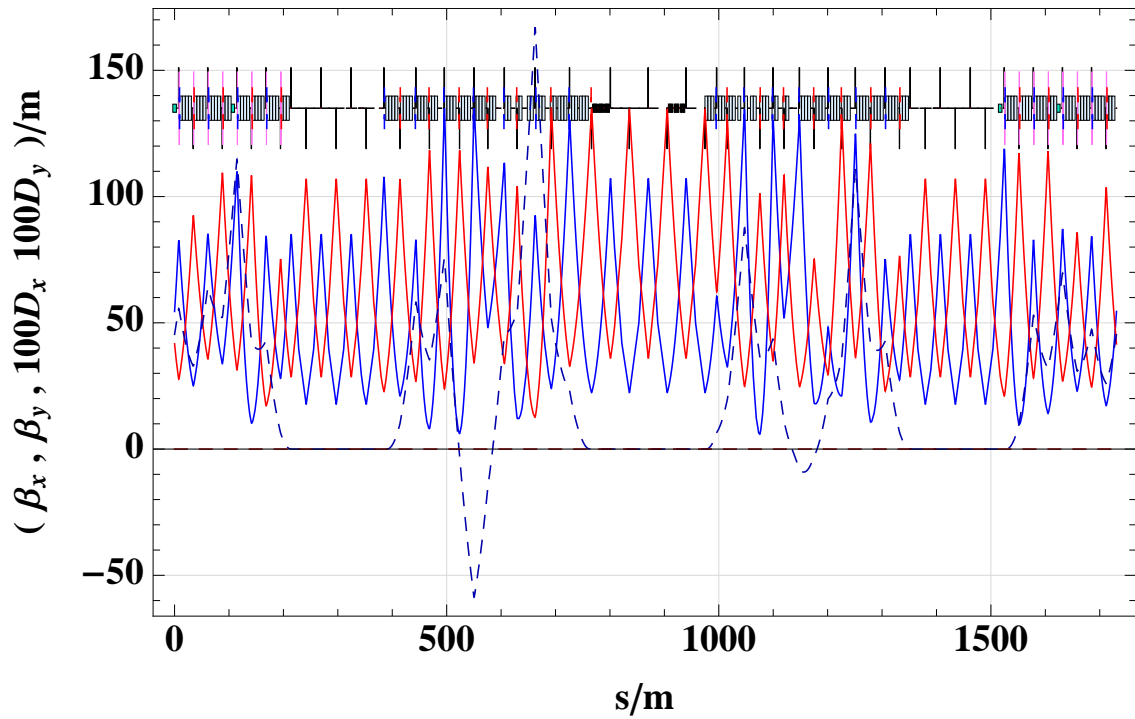


Figure 7.14: Bypass optics Point 1.

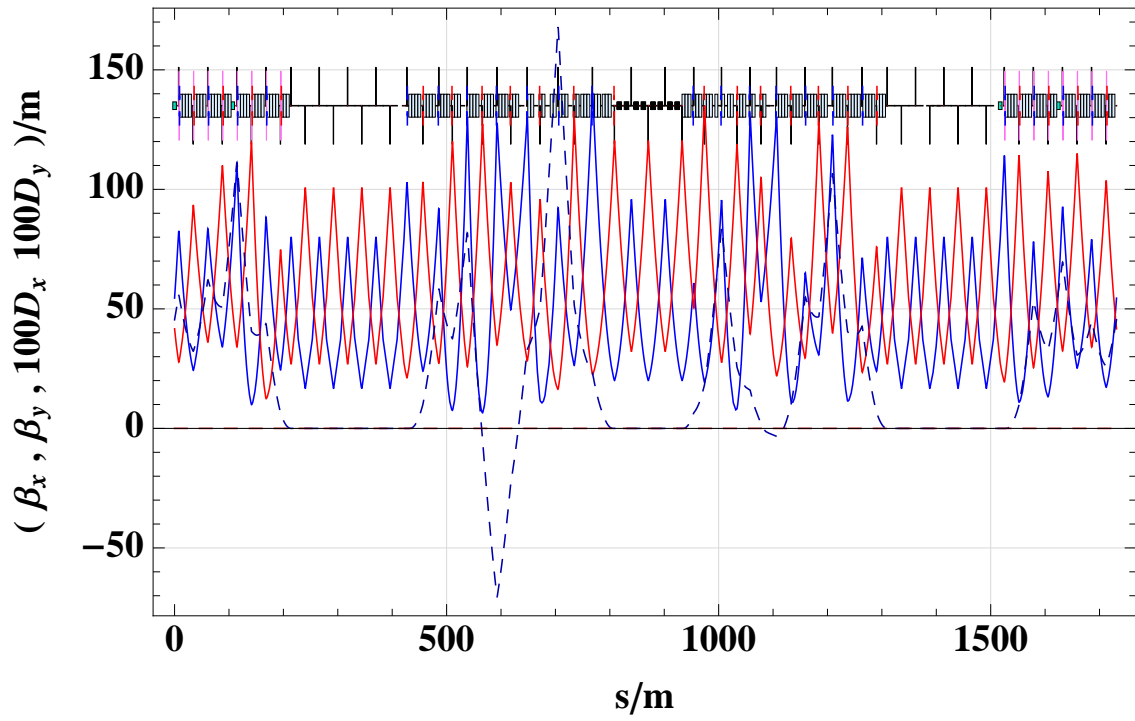


Figure 7.15: Bypass Optics Point 5.

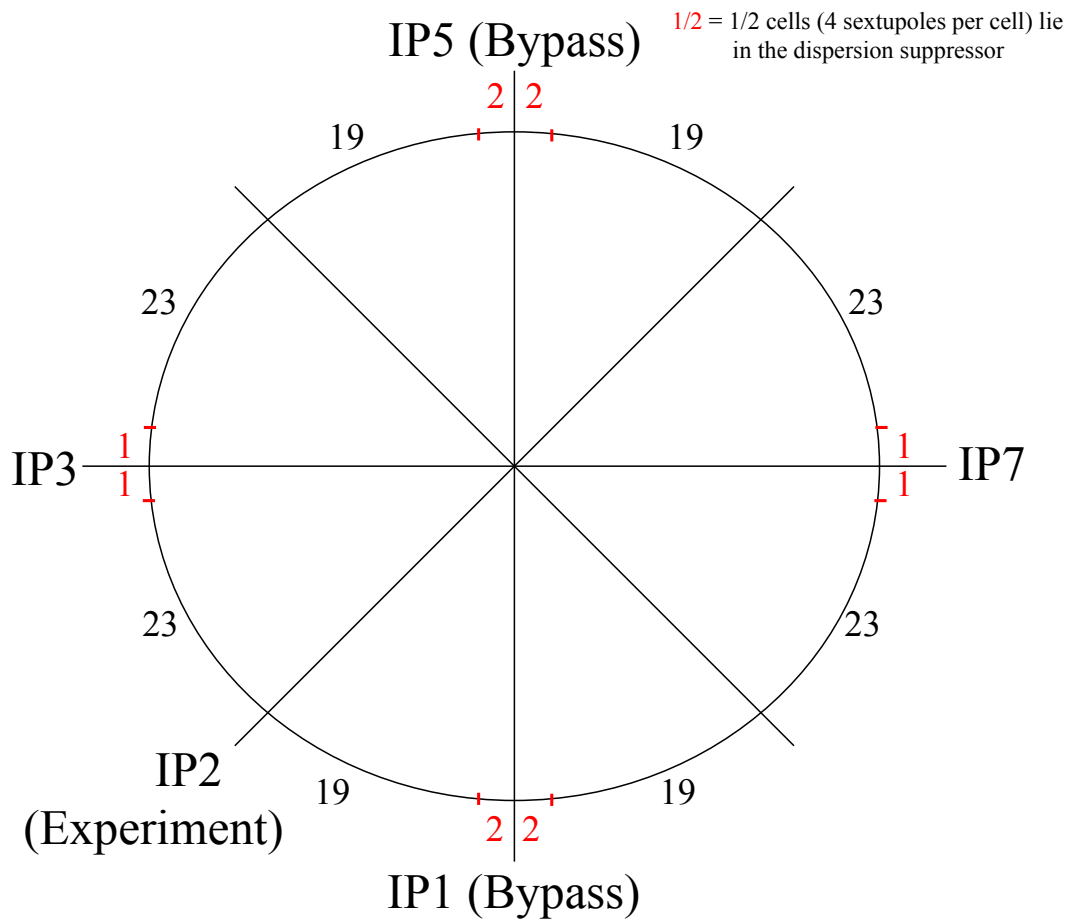


Figure 7.16: LHeC Sextupole Scheme for a phase advance of  $90^\circ/60^\circ$  with sextupoles also placed in the dispersion suppressor.



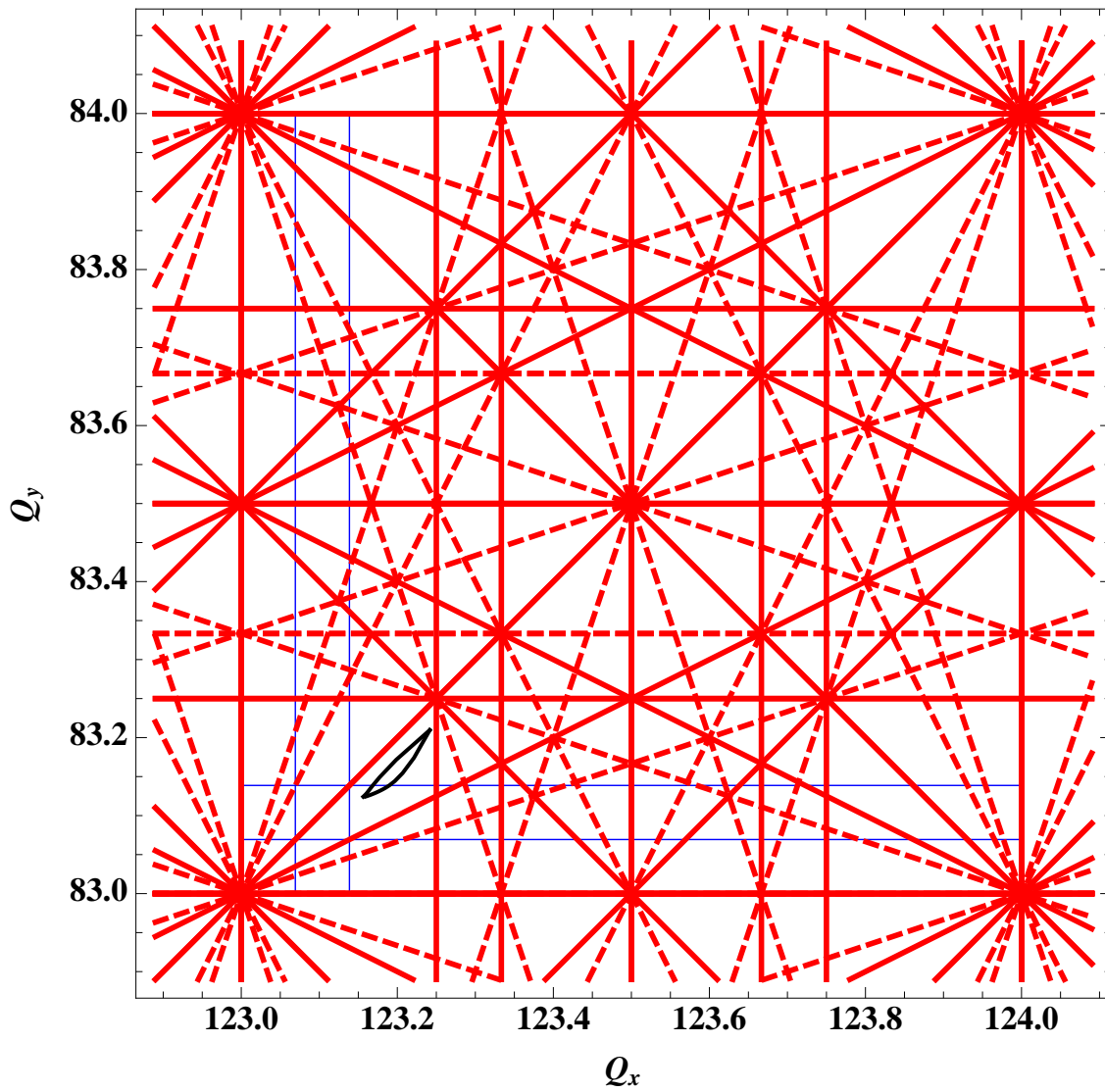


Figure 7.17: Working Point for the 1° optics. The dashed lines are the coupling resonances up to 4th order, the solid lines the constructive resonances up to 4th order. The black dot indicates the working point without beam-beam tune shift and the blue one with beam-beam tune shift.

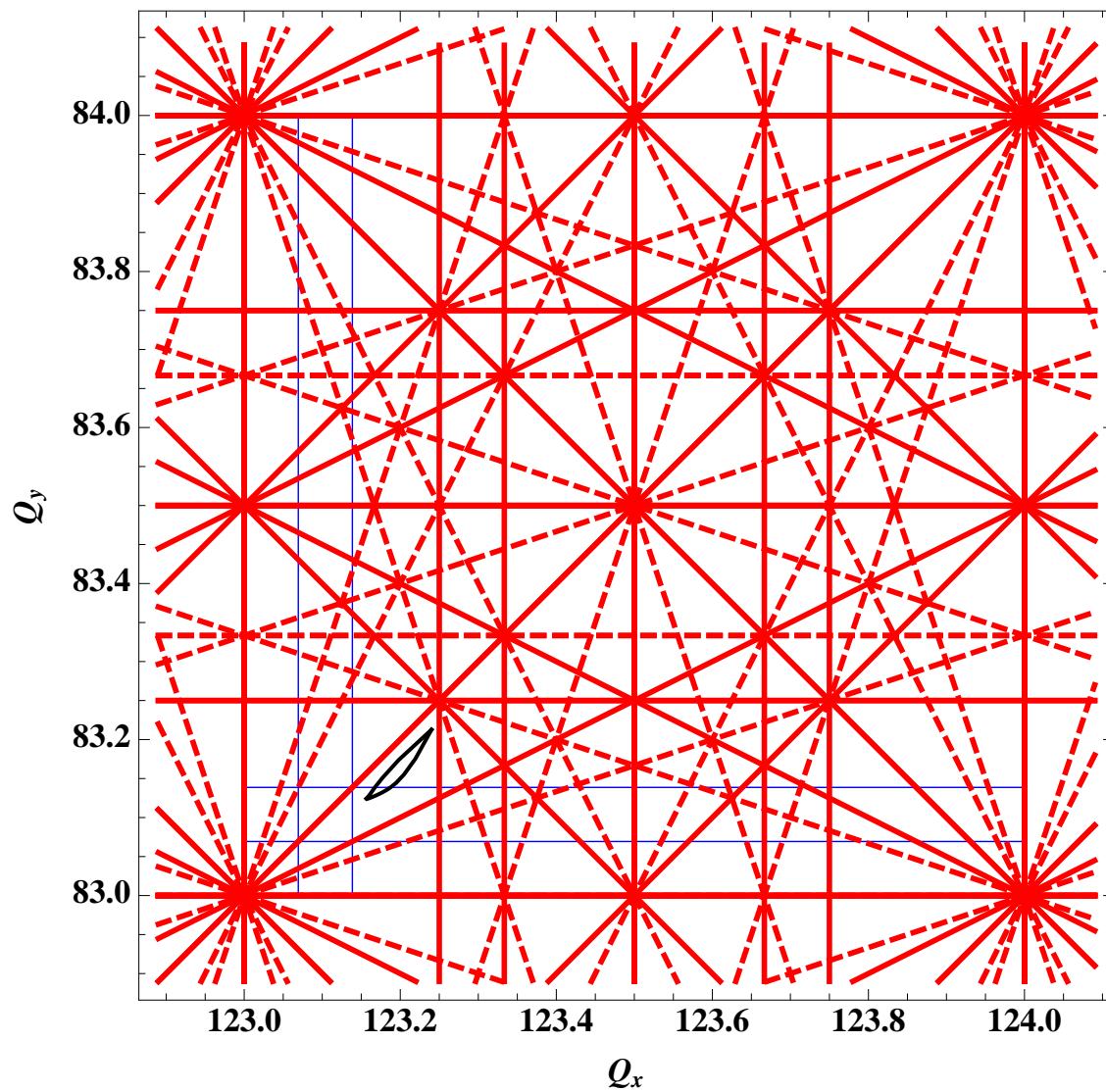


Figure 7.18: Working Point for the  $10^\circ$  optics. The dashed lines are the coupling resonances up to 4th order, the solid lines the constructive resonances up to 4th order. The black dot indicates the working point without beam-beam tune shift and the blue one with beam-beam tune shift.

## 7.5 Layout

The design of the Interaction Region (IR) of the LHeC is particularly challenging as it has to consider boundary conditions from

- The lattice design and beam optics of the electron and proton beam
- The geometry of the LHC experimental cavern and the tunnel
- The beam separation scheme which is determined by the bunch pattern of the LHC standard proton operation and related to this the optimisation of the synchrotron light emission and collimation
- The technical feasibility of the hardware.

Therefore the IR has to be optimised with respect to a well matched beam optics that adapts the optical parameters from the new electron-proton interaction point to the standard LHC proton beam optics in the arc and to the newly established beam optics of the electron ring. At the same time the two colliding beams as well as the non-colliding proton beam of LHC have to be separated efficiently and guided into their corresponding magnet lattices. As a general rule that has been established in the context of this study any modification in the standard LHC lattice and any impact on the LHC proton beam parameters had to be chosen moderately to avoid detrimental effects on the performance of the LHC proton-proton operation.

The layout and parameters of the new e/p interaction point are defined by the particle physics requirements. At present the physics programme that has been proposed for the LHeC [568] follows two themes - a high luminosity, high  $Q^2$  programme requiring a forward and backward detector acceptance of around  $10^\circ$  and a low x, low  $Q^2$  programme, which requires an increased detector acceptance in forward and backward direction of at least  $1^\circ$  and could proceed with reduced luminosity. Accordingly two machine scenarios have been studied for the interaction region design. Firstly, a design that has been optimised for high luminosity with an acceptance of  $10^\circ$  and secondly, a high acceptance design that allows for a smaller opening angle of the detector. In both cases the goal for the machine luminosity is in the range of  $10^{33} \text{ cm}^{-2} \text{ s}^{-1}$  but the layouts differs in the magnet lattice, the achievable absolute luminosity and mainly the synchrotron radiation that is emitted during the beam separation process. Both options will be presented here in detail and the corresponding design luminosity, the technical requirements and the synchrotron radiation load will be compared. In both cases however, a well matched spot size of the electron and proton beam had to be established at the collision point: Experience in SPS and HERA [569], [570] showed that matched beam cross sections have to be established between the two colliding beams to guarantee stable beam conditions. Considering the different nature of the beams, namely the emittances of the electron beam in the two transverse planes, the interaction region design has to consider this boundary condition and the beam optics has to be established to achieve equal beam sizes  $\sigma_x(p) = \sigma_x(e)$ ,  $\sigma_y(p) = \sigma_y(e)$  at the IP.

The basic beam parameters however like energy, particle intensity and beam emittances are identical for both designs, determined by the electron and proton ring lattices and the pre-accelerators. They are summarised in Table 7.10.

Colliding two beams of different characteristics, the luminosity obtained is given by the equation

$$L = \sum_{i=1}^{n_b} (I_e * I_p) \frac{1}{e^2 f_0 2\pi \sqrt{\sigma_{xp}^2 + \sigma_{xe}^2} \sqrt{\sigma_{yp}^2 + \sigma_{ye}^2}}, \quad (7.8)$$

where  $\sigma_{x,y}$  denotes the beam size of the electron and proton beam in the horizontal and vertical plane and  $I_e, I_p$  the electron and proton single bunch currents. In all IR layouts the electron beam size at the IP is matched to the proton beam size in order to optimise the delivered luminosity and minimise detrimental beam beam effects.

The main difference of the IR design for the electron proton collisions with respect to the existing LHC interaction regions is the fact that the two beams of LHeC cannot be focussed and / or guided at the same time: The different nature of the two beams, the fact that the electrons emit synchrotron radiation

Table 7.10: Main parameters for e/p collisions.

Quantity	unit	e	p
Beam energy	GeV	60	7000
Total beam current	mA	100	860
Number of bunches		2808	2808
Particles/bunch $N_b$	$10^{10}$	2.0	17
Horiz. emittance	nm	5.0	0.5
Vert. emittance	nm	2.5	0.5
Bunch distance	ns	25	

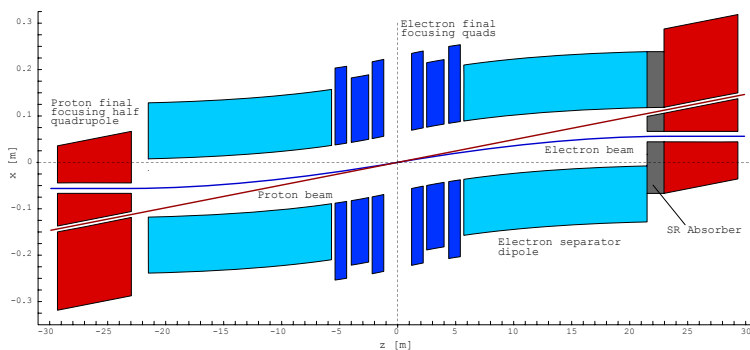


Figure 7.19: Schematic layout of the LHeC 10 degree interaction region

5027 and mainly the large difference in the particle momentum make a simultaneous focusing of the two beams  
 5028 impossible. The strong gradients of the proton quadrupoles in the LHC triplet structure cannot be tolerated  
 5029 nor compensated for the electron lattice and a stable optical solution for the electrons is not achievable under  
 5030 the influence of the proton magnet fields. The electron beam therefore has to be separated from the proton  
 5031 beam after the collision point before any strong “7 TeV like” magnet field is applied.

5032 In order to obtain still a compact design and to optimize the achievable luminosity of the new e/p interaction  
 5033 region, the beam separation scheme has to be combined with the electron mini-beta focusing structure.

5034 Figure 7.19 shows a schematic layout of the interaction region. It refers to the 10 degree option and  
 5035 shows a compact triplet structure that is used for early focusing of the electron beam. The electron mini  
 5036 beta quadrupoles are embedded into the detector opening angle and in order to obtain the required separation  
 5037 effect they are shifted in the horizontal plane and act effectively as combined function magnets: Thus focusing  
 5038 and separation of the electron beam are combined in a very compact lattice structure, which is the prerequisite  
 5039 to achieve luminosity values in the range of  $10^{33} \text{ cm}^{-2} \text{ s}^{-1}$ .

### 5040 7.5.1 Beam Separation Scheme

5041 The separation scheme of the two beams has to be optimised with respect to an efficient (i.e. fast) beam  
 5042 separation and a synchrotron radiation power and critical energy of the emitted photons that can be tolerated  
 5043 by the absorber design. Two main issues have to be accomplished: a sufficient horizontal distance between  
 5044 the beams has to be generated at the position of the first proton (half) quadrupole, located at a distance of  $s$   
 5045  $= 23\text{m}$  from the interaction point (the nominal value of the LHC proton lattice). In addition to that, harmful  
 5046 beam beam effects have to be avoided at the first parasitic bunch encounters which will take place at  $s =$   
 5047  $3.75\text{m}$ , as the nominal bunch distance in LHC corresponds to  $\Delta t = 25\text{ns}$ . These so-called parasitic bunch  
 5048 crossings have to be avoided as they would lead to intolerable beam-beam effects in the colliding beams. As

Ring-ring option half-quadrupole, 4900 A, Gradient 137 T/m,  
+ 2.5 T dipole field from feeddown

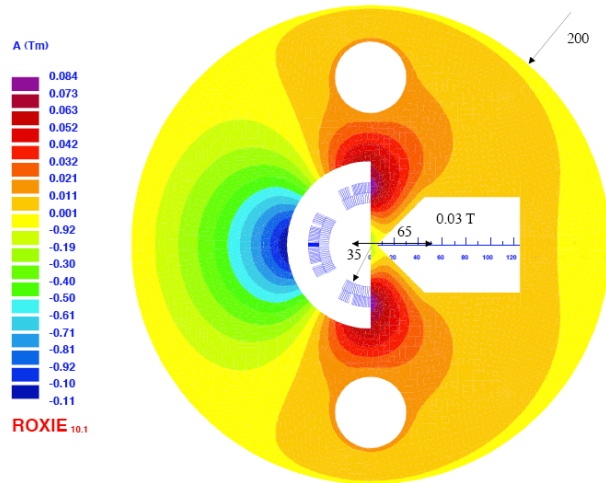


Figure 7.20: Super conducting half quadrupole in the proton lattice: The electron beam will pass on the right hand side of the mirror plate in a quasi field free region (see section 9.1).

5049 a consequence the separation scheme has to deliver a sufficiently large horizontal distance between the two  
5050 counter rotating bunches at these locations.

5051 To achieve the first requirement a separation effect is created inside the mini beta quadrupoles of the  
5052 electron beam: The large momentum difference of the two colliding beams provides a very elegant way to  
5053 separate the lepton and the hadron beams: Shifting the mini-beta quadrupoles of the electron beam and  
5054 installing a 15.8m long, but weak separator dipole magnet close to the IP provides the gentle separation that  
5055 is needed to keep the synchrotron radiation level in the IR within reasonable limits.

5056 The nearest proton quadrupole to the IP is designed as a half-quadrupole to ease the extraction of the  
5057 outgoing electron beam. At this location (at  $s=23$  m) a minimum separation of  $\Delta x = 55\text{mm}$  is needed to  
5058 guide the electron beam along the mirror plate of a sc. proton half quadrupole (see section 9.1). A first  
5059 layout of this magnet is sketched in figure 7.20

5060 The horizontal offsets of the mini beta lenses are chosen individually in such a way that the resulting  
5061 bending strength in the complete separation scheme (quadrupole triplet / doublet and separator dipole) is  
5062 constant. In this way a moderate separation strength is created with a constant bending radius of  $\rho = 6757m$   
5063 for the 10 degree option. In the case of the 1 degree option the quadrupole lenses of the electron lattice  
5064 cannot be included inside the detector design as the opening angle of the detector does not provide enough  
5065 space for the hardware of the electron ring lattice. Therefore a much larger distance between the IP and the  
5066 location of the first electron lens had to be chosen ( $\Delta s = 6.2\text{m}$  instead of  $\Delta s = 1.2\text{m}$ ). As a consequence  
5067 - in order to achieve the same overall beam separation - stronger magnetic separation fields have to be  
5068 applied resulting in a bending radius of  $\rho = 4057m$  in this case. In both cases the position of the electron  
5069 quadrupoles is following the design orbit of the electron beam to avoid local strong bending fields and keep  
5070 the synchrotron radiation power to a minimum. This technique has already been succesfully applied at the  
5071 layout of the HERA electron-proton collider [571].

5072  
5073 Still the separation at the location of the first proton magnet is small and a half quadrupole design for  
5074 this super conducting magnet has been chosen at this point. The resulting beam parameters - including the  
5075 expected luminosity for this ring ring option - are summarised in Table 2.

5076 It has to be pointed out in this context that the arrangement of the off centre quadrupoles as well as  
5077 the strength of the separator dipole depend on the beam optics of the electron beam. The beam size at the

Table 7.11: Parameters of the mini beta optics for the 1° and 10° options of the LHeC Interaction Region.

Detector Option Quantity	unit	1°		10°	
		electrons	protons	electrons	protons
Number of bunches		2808			
Particles/bunch $N_b$	$10^{10}$	1.96	17	1.96	17
Horiz. beta-function	m	0.4	4.0	0.18	1.8
Vert. beta-function	m	0.2	1.0	0.1	0.5
Horiz. emittance	nm	5.0	0.5	5.0	0.5
Vert. emittance	nm	2.5	0.5	2.5	0.5
Distance to IP	m	6.2	22	1.2	22
Crossing angle	mrad	1.0		1.0	
Synch. Rad. in IR	kW	51		33	
absolute Luminosity	$m^{-2} s^{-1}$	$8.54 * 10^{32}$		$1.8 * 10^{33}$	
Loss-Factor S		0.86		0.75	
effective Luminosity	$m^{-2} s^{-1}$	$7.33 * 10^{32}$		$1.34 * 10^{33}$	

5078 parasitic crossings and at the proton quadrupole will determine the required horizontal distance between the  
 5079 electron and proton bunches. The strength and position of these magnets however will determine the optical  
 5080 parameters, including the dispersion function that is created during the separation process itself. Therefore  
 5081 a self-consistent layout concerning optics, beam separation and geometry of the synchrotron light absorbers  
 5082 has to be found.

5083 It is obvious that these boundary conditions have to be fulfilled not only during luminosity operation of  
 5084 the e/p rings. During injection and the complete acceleration procedure of the electron ring the influence  
 5085 of the electron quadrupoles on the proton beam has to be compensated with respect to the proton beam  
 5086 orbit (as a result of the separation fields) as well as to the proton beam optics: The changing deflecting  
 5087 fields and gradients of the electron magnets will require correction procedures in the proton lattice that will  
 5088 compensate this influence at any moment.

## 5089 7.5.2 Crossing Angle

5090 A central aspect of the LHeC IR design is the beam-beam interaction of the colliding electron and proton  
 5091 bunches. The bunch structure of the electron beam will match the pattern of the LHC proton filling scheme  
 5092 for maximal luminosity, giving equal bunch spacings of 25 ns to both beams. The IR design therefore  
 5093 is required to separate the bunches as quickly as possible to avoid additional bunch interactions at these  
 5094 positions and limit the beam-beam effect to the desired interactions at the IP. The design bunch distance  
 5095 in the LHC proton bunch chain corresponds to  $\Delta t = 25$  ns or  $\Delta s = 7.5$  m. The counter rotating bunches  
 5096 therefore meet after the crossing at the interaction point at additional, parasitic collision points in a distance  
 5097  $s = 3.75$  m from the IP. To avoid detrimental effects from these parasitic crossings the above mentioned  
 5098 separation scheme has to be supported by a crossing angle that will deliver a sufficiently large horizontal  
 5099 distance between the bunches at the first parasitic bunch crossings. This technique is used in all LHC  
 5100 interaction points. In the case of the LHeC however, the crossing angle is determined by the emittance of  
 5101 the electron beam and the resulting beam size which is considerably larger than the usual proton beam size  
 5102 in the storage ring. In the case of the LHeC IR a crossing angle of  $\theta = 1$  mrad is considered as sufficient  
 5103 in the 1° as well as in the 10° option to avoid beam-beam effects from this parasitic crossings. Figure 7.21  
 5104 shows the position of the first possible parasitic encounters and the effect of the crossing angle to deliver a  
 5105 sufficient separation at these places.

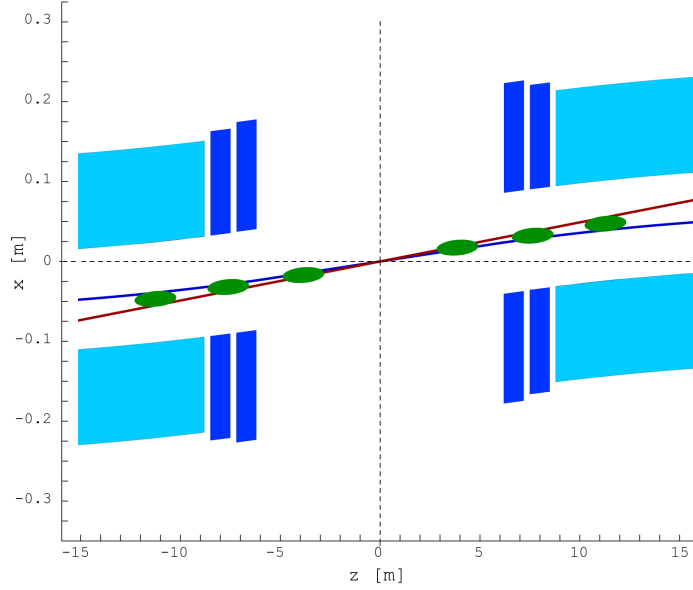


Figure 7.21: LHeC interaction region including the location of the first parasitic bunch encounters where a sufficient beam separation is achieved by a crossing angle of 1 mrad. The location of the parasitic encounters is indicated by green ovals.

5106 The detailed impact of one beam on another is evaluated by a dedicated beam-beam interaction study  
 5107 which is included in this report, based on a minimum separation of  $5\sigma_e + 5\sigma_p$  at every parasitic crossing node.  
 5108 Due to the larger electron emittance the separation is mainly dominated by the electron beam parameters,  
 5109 and as a general rule it can be stated that the rapid growth of the  $\beta$ -function in the drift around the IP,

$$\beta(s) = \beta^* + \frac{s^2}{\beta^*}, \quad (7.9)$$

5110 makes it harder to separate the beams if small  $\beta^*$  and a large drift space  $s$  is required in the optical design.

5111 In any design for the LHeC study, a crossing angle is used to establish an early beam separation, reduce  
 5112 the required strength in the separation magnets and minimise the synchrotron radiation power that is created  
 5113 inside the interaction region.

5114 As a draw back however the luminosity is reduced due to the fact that the bunches will not collide  
 5115 anymore head on. This reduction is expressed in a geometric luminosity reduction factor “S”, that depends  
 5116 on the crossing angle  $\theta$ , the length of the electron and proton bunches  $\sigma_{ze}$  and  $\sigma_{zp}$  and the transverse beam  
 5117 size in the plane of the bunch crossing  $\sigma_x^*$ :

$$S(\theta) = \left[ 1 + \left( \frac{\sigma_{sp}^2 + \sigma_{se}^2}{2\sigma_x^{*2}} \right) \tan^2 \frac{\theta}{2} \right]^{-\frac{1}{2}}. \quad (7.10)$$

5118

5119

5120

Accordingly, the effective luminosity that can be expected for a given IR layout is obtained by

$$L = S(\theta) * L_0 \quad (7.11)$$

5121

5122

5123

5124

For the two beam optics that have been chosen for this design study (the  $1^\circ$  and the  $10^\circ$  option) and a crossing angle of  $\theta = 1\text{mrad}$  the loss factor amounts to  $S = 86\%$  and  $S = 75\%$  respectively.

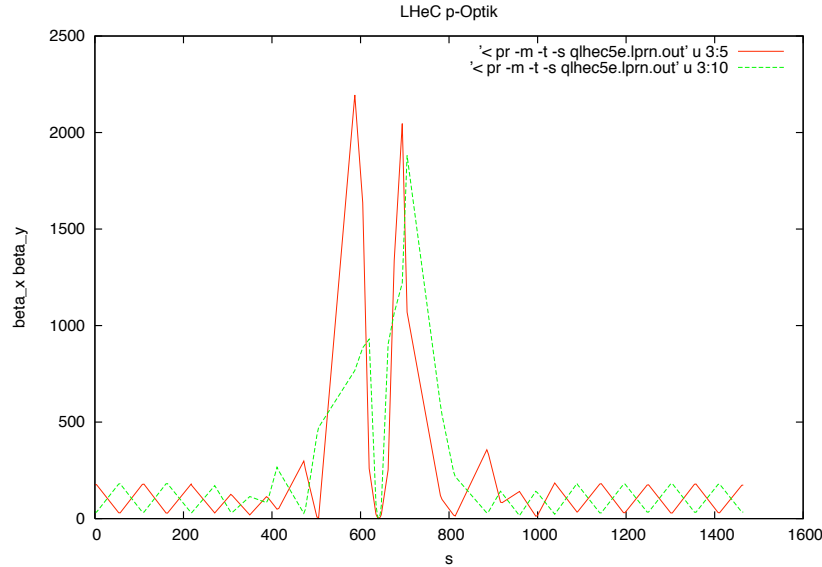


Figure 7.22: Proton optics for the LHeC interaction region. The gradients of the antisymmetric triplet lattice in the standard LHC have been modified to adopt for the requirements of the LHeC flat beam parameters.

### 7.5.3 Beam Optics and Luminosity

A special boundary condition had to be observed in the design of the proton beam optics of the LHeC: For the layout of the four present proton-proton interaction regions in the LHC machine an anti-symmetric option had been chosen: A solution that is appropriate for a round beam optics ( $\sigma_x^* = \sigma_y^*$ ). An optimised design for collisions with the flat  $e^\pm$  beams however requires unequal  $\beta$ -functions for the hadron beam at the IP and the existing LHC optics can no longer be maintained. Therefore the optical layout of the existing triplet structure in the LHC had to be modified to match the required beta functions ( $\beta_x = 1.8\text{m}$ ,  $\beta_y = 0.5\text{m}$ ) at the IP to the regular optics of the FODO structure in the arc (Figure 7.22).

In the case of the electron beam optics, two different layouts of the interaction region are considered: One optical concept for highest achievable luminosity and a solution for maximum detector acceptance. In the first case an opening angle of  $10^\circ$  is available inside the detector geometry and allows to install an embedded magnet structure where the first electron quadrupole lenses can be placed as close as  $s = 1.2\text{m}$  from the IP. This early focusing scheme leads to moderate values of the  $\beta$  function inside the mini beta quadrupoles and therefore allows for a smaller spot size at the IP and larger luminosity values can be achieved. Still however the quadrupoles require a compact design: While the gradients required by the optical solution are small (for a super conducting magnet design) the outer radius of the first electron quadrupole has been limited to  $r_{max} = 210\text{mm}$ .

In the case of the  $1^\circ$  option the detector design is optimised for largest detector acceptance. Accordingly the opening angle of the detector hardware is too small to deliver space for accelerator magnets. The mini beta quadrupoles therefore have to be located outside the detector, and a distance  $s = 6.2\text{m}$  from the IP had to be chosen in this case. Even if the magnet dimensions are not limited by the detector design in this case, the achievable luminosity is about a factor of two smaller than in the  $10^\circ$  case.

The two beam optics that are based on these considerations are discussed in detail in the next chapter of this report. In the case of the  $10^\circ$  option a triplet structure has been chosen to allow for moderate values of the beta functions inside the mini beta quadrupoles. As a special feature of the optics that is shown in Figure 7.23 the focusing effect of the first quadrupole magnet is moderate: Its gradient has been limited as it has to deliver mainly the first beam separation. Table 7.11 includes as well the overall synchrotron radiation power that is produced inside the IR. Due to the larger bending radius (i.e. smaller bending forces) in the case of the  $10^\circ$  option the produced synchrotron radiation power is limited to about 30 kW, while the



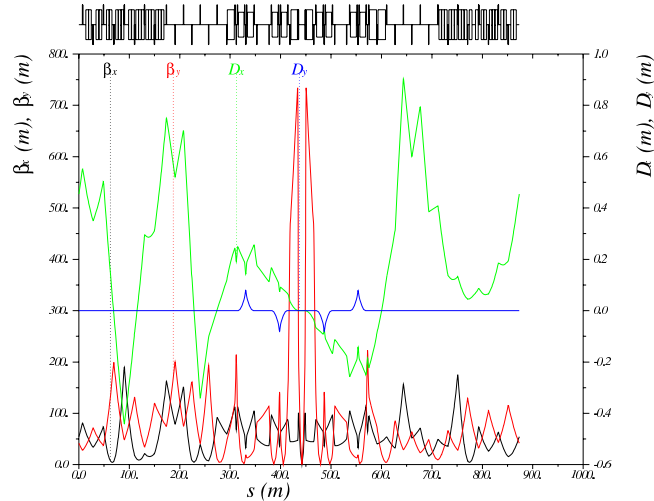


Figure 7.23: Electron optics for the LHeC interaction region. The plot corresponds to the 1 degree option where a doublet structure combined with a separation dipole has been chosen to separate the two beams.

5154 alternative - high acceptance - option has to handle 50kW of synchrotron light.  
 5155 The details of the synchrotron light characteristics are covered in the next chapters of this report for both  
 5156 cases, including the critical energies and the design of the required absorbers.  
 5157 For the 1° option the mini beta focusing is based on a quadrupole doublet as the space limitations in  
 5158 the transverse plane are much more relaxed compared to the alternative option and the main issue here  
 5159 was to find a compact design in the longitudinal coordinate: Due to the larger distance of the focusing  
 5160 and separating magnets from the IP the magnet structure has to be more compact and the separating  
 5161 field stronger to obtain the required horizontal beam distance at the location  $s=23\text{m}$  of the first proton  
 5162 quadrupole. The corresponding beam optics for both options are explained in full detail below.

## 5163 7.6 Design Requirements

### 5164 7.6.1 Detector Coverage and Acceptance

5165 Acceptance describes the amount of angular obstruction of the detector due to the presence of machine  
 5166 elements, as shown in figure 7.24. For example, an acceptance of  $10^\circ$  implies a protrusion of machine ele-  
 5167 ments into the detector such that a cone of  $10^\circ$  half-angle along the beam axis is blocked. The detector is  
 5168 thus unable to see particles emitted at less than this angle, and event data is lost at high pseudo-rapidities.  
 5169 Accordingly larger detector opening angles denote lower acceptance but allows to position machine elements  
 5170 at a smaller distance to the IP

5171 Since  $\beta$  grows quadratically with distance, a smaller  $l^*$  generally allows stronger focusing of a beam and  
 5172 thus higher luminosity. While there is no direct relationship between  $l^*$  and luminosity, a balance must be  
 5173 found to optimise both luminosity and acceptance. Two IR designs are proposed as solutions to the balance  
 5174 between luminosity and acceptance. Both designs aim to achieve a luminosity in the range of  $\sim 10^{33} \text{ cm}^{-2}\text{s}^{-1}$ .  
 5175

#### 5176 1. High Luminosity Layout (HL)

- 5177 •  $10^\circ$  acceptance

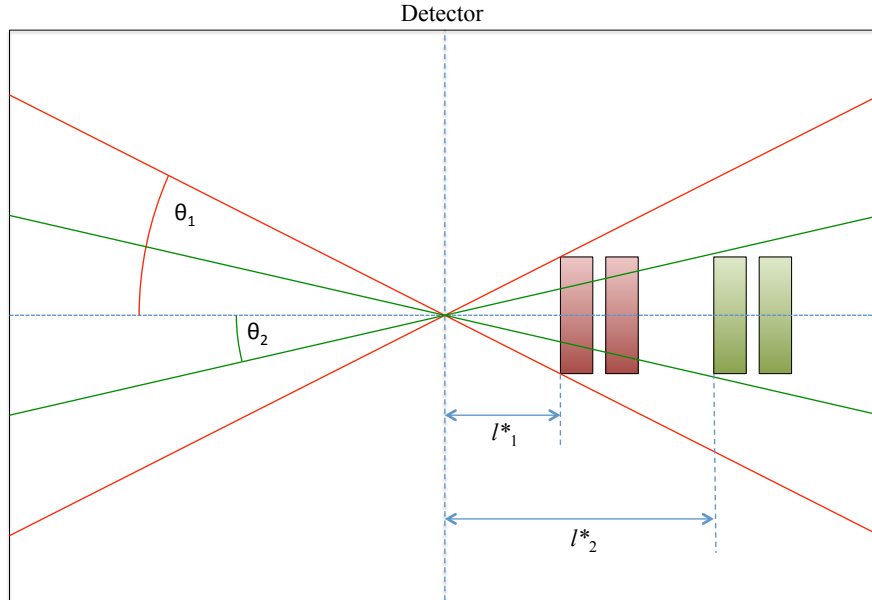


Figure 7.24: Graphical representation of acceptance.  $\theta_1$  shows a lower acceptance cone, while  $\theta_2$  shows a higher acceptance cone. For machine elements of constant diameter, higher acceptance increases  $l^*$ .

- 5178 • Higher luminosity

## 5179 2. High Acceptance Layout (HA)

- 5180 •  $1^\circ$  acceptance
- 5181 • Lower luminosity

5182 In concert with these designs, two plans are proposed for running LHeC. One option is to run with the HL  
 5183 layout, then switch to the HA layout during a shutdown. The second option is to optimise the HA layout  
 5184 for sufficient luminosity to replace the HL layout entirely.

### 5185 7.6.2 Lattice Matching and IR Geometry

5186 The principle layout and requirements of the beam separation scheme have been described above. A  
 5187 minimum separation of  $5\sigma_e + 5\sigma_p$  is specified at each parasitic node. In addition an overall distance between  
 5188 the proton and electron beam of 55 mm at the location of the first proton magnet,  $s = 23$  m, has been  
 5189 chosen as an attainable target from optical, radiation [ref:SR section] and magnet design [ref: Magnets  
 5190 section] standpoints.

5191 Once the beams are separated into independent beam pipes, the electron beam must be transported into  
 5192 the ring lattice. Quadrupoles are used in the long straight section (LSS) of the electron machine to transport  
 5193 the beam from the IP to the dispersion suppressor and match the twiss parameters at either end. Space  
 5194 must be available to insert dipoles and further quadrupoles to allow the orbit of the beam to be designed  
 5195 with regard to the physical layout of the ring and the IR.

5196

5197 The IR and LSS geometries must be designed around a number of further constraints. In addition to  
5198 the beam separation required to avoid parasitic bunch encounters, the electron beam must be steered from  
5199 the electron ring into the IR and back out again. The colliding proton beam must be largely undisturbed  
5200 by the electron beam. The non-colliding proton beam must be guided through the IR without interacting  
5201 with either of the other beams.

## 5202 7.7 High Luminosity IR Layout

### 5203 7.7.1 Parameters

5204 Table 7.12 details the interaction point parameters and other parameters for this design. To optimise for  
5205 luminosity, a small  $l^*$  is desired. An acceptance angle of  $10^\circ$  is therefore chosen, which gives an  $l^*$  of 1.2m  
5206 for final focusing quadrupoles of reasonable size.

$L(0)$	$1.8 \times 10^{33}$
$\theta$	$1 \times 10^{-3}$
$S(\theta)$	0.746
$L(\theta)$	$1.34 \times 10^{33}$
$\beta_x^*$	0.18 m
$\beta_y^*$	0.1 m
$\sigma_x^*$	$3.00 \times 10^{-5}$ m
$\sigma_y^*$	$1.58 \times 10^{-5}$ m
SR Power	33 kW
$E_c$	126 keV

Table 7.12: Parameters for the HL IR. Note that the geometric luminosity reduction factor, S, is calculated using the LHC ultimate bunch length of  $7.5 \times 10^{-2}$ .

5207 SR calculations are detailed in section [ref: SR section]. The total power emitted in the IR is similar to that  
5208 in the HERA-2 IR [?] and as such appears to be reasonable, given enough space for absorbers.

### 5209 7.7.2 Layout of the Electron Lattice

5210 A symmetric final quadrupole triplet layout followed by a long weak dipole magnet has been chosen for this  
5211 design, due to the relatively round beam spot aspect ratio of 1.8:1. Figure 7.25 and table 7.13 detail the  
5212 layout.  
5213

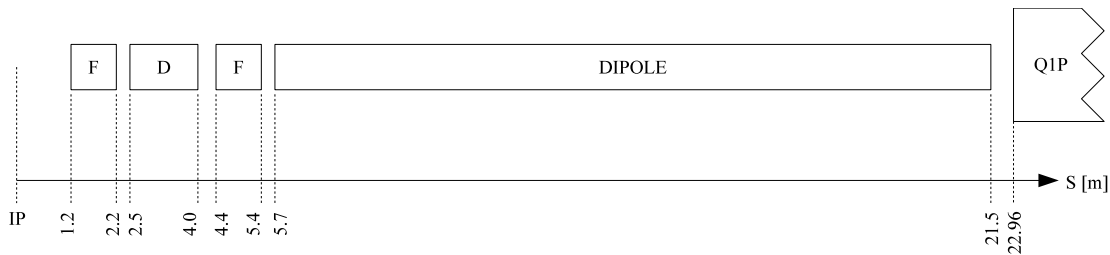


Figure 7.25: Layout of machine elements in the HL IR. Note that the left side of the IR is symmetric.

Element	$S_{entry}$ [m]	L [m]	Gradient [T/m]	Dipole Field [T]	Offset [m]
BS.L	-21.5	15.8	-	-0.0296	-
Q3E.L	-5.4	1.0	89.09229	-0.0296	$-3.32240 \times 10^{-4}$
Q2E.L	-4	1.5	-102.2013	-0.0296	$2.89624 \times 10^{-4}$
Q1E.L	-2.2	1.0	54.34071	-0.0296	$-5.44711 \times 10^{-4}$
IP	0.0	-	-	-	-
Q1E.R	1.2	1.0	54.34071	0.0296	$5.44711 \times 10^{-4}$
Q2E.R	2.5	1.5	-102.2013	0.0296	$-2.89624 \times 10^{-4}$
Q3E.R	4.4	1.0	89.09229	0.0296	$3.32240 \times 10^{-4}$
BS.R	5.7	15.8	-	-0.0296	-

Table 7.13: Machine elements for the HL IR.  $S_{entry}$  gives the leftmost point of the idealised magnetic field of an element. Note that S is relative to the IP.

5214 The distance of the first electron magnet from the IP,  $l^*$  of 1.2 m, allows both strong focusing of the beam,  
5215 and constant bending of the beam from  $s = 1.2$  m to 21.5 m. This is achieved with offset quadrupoles and  
5216 a separation dipole.

5217

5218 Figure 7.26 shows the  $\beta$  functions of the beam in both planes from the IP to the face of the final pro-  
5219 ton quadrupole at  $s = 23$  m.

### 5220 7.7.3 Separation Scheme

5221 The electron triplet is powered in FDF mode generating a large peak in  $\beta_x$ , but is designed such that the  
5222 peak is between parasitic crossings. The first F quadrupole reduces  $\beta_x$  at  $s = 3.75$  m compared to an initial  
5223 D quadrupole. The third F quadrupole then reduces  $\beta_x$  sufficiently to avoid large beam-beam interactions  
5224 at the second parasitic crossing,  $s = 7.5$  m.

5225

5226 This is aided by the bending provided by the offset quadrupoles, and also the IP crossing angle of 1 mrad.  
5227 These elements ensure that the separation between the beams, normalised to the beam size, increases at each  
5228 parasitic crossing. Note that 1 mrad is not a minimum crossing angle required by beam-beam interaction  
5229 separation criteria but is a chosen balance between luminosity loss and minimising bend strength. In theory,  
5230 this layout could support an IP with no crossing angle; however the bend strength required to achieve this  
5231 would generate an undesirable level of SR power.

## 5232 7.8 High Acceptance IR Layout

### 5233 7.8.1 Parameters

5234 Table 7.14 details the main parameters for this design. The chosen acceptance for this layout is  $1^\circ$ . For final  
5235 electron focusing magnets of reasonable strength this places all elements outside the limits of the detector,  
5236 at  $s = \pm 6.2m$ . Due to the small crossing angle the first electron magnets have to be placed beyond this  
5237 distance. As such, the actual acceptance of the layout is limited by the beam pipe diameter rather than the  
5238 size of machine elements. This also gives further flexibility in the strengths and designs of the final focusing  
5239 quadrupoles.

5240

5241 SR calculations are detailed in section [ref: SR section]. Again, the total power emitted in the IR is similar to  
5242 that in the HERA-2 IR [?] and as such appears to be reasonable, given enough space for absorbers. However  
5243 it is significantly higher than that in the HL layout. As discussed in section [ref: SR section], an option

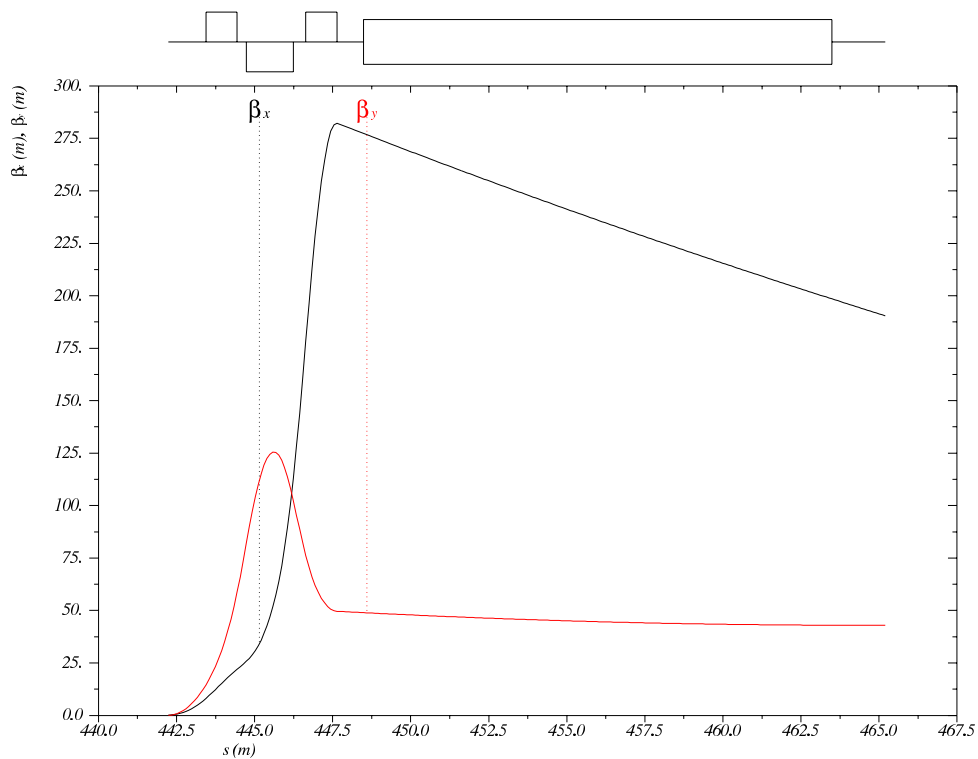


Figure 7.26:  $\beta$  functions in both planes for the HL IR layout, from the IP to the face of the final proton quadrupole at  $s = 23$  m. Note that  $s$  is relative to the ring, which begins at the left side of the left dispersion suppressor of IP2.

$L(0)$	$8.54 \times 10^{32}$
$\theta$	$1 \times 10^{-3}$
$S(\theta)$	0.858
$L(\theta)$	$7.33 \times 10^{32}$
$\beta_x^*$	0.4 m
$\beta_y^*$	0.2 m
$\sigma_x^*$	$4.47 \times 10^{-5}$ m
$\sigma_y^*$	$2.24 \times 10^{-5}$ m
SR Power	51 kW
$E_c$	163 keV

Table 7.14: Parameters for the HA IR. Note that the geometric luminosity reduction factor,  $S$ , is calculated using the LHC ultimate bunch length of  $7.5 \times 10^{-2}$ .

5244 exists to reduce the total SR power by including a dipole field in the detector, thus mitigating the limitation  
 5245 imposed on dipole length by the larger  $l^*$ .

## 5246 7.8.2 Layout

5247 A symmetric final quadrupole doublet layout has been chosen for the electron lattice in this design. The  
 5248 beam spot aspect ratio of 2:1 is marginally flatter than the HL layout, and as such a triplet is less suitable.  
 5249 Figure 7.27 and table 7.15 summarise the details of the layout.  
 5250

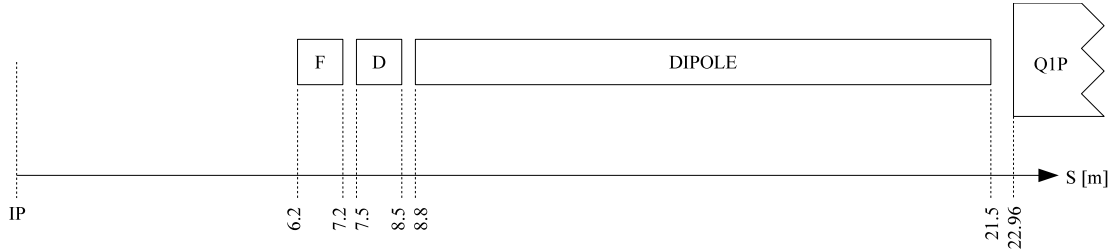


Figure 7.27: Layout of machine elements in the HA IR. Note that the left side of the IR is symmetric.

Element	$S_{entry}$ [m]	L [m]	Gradient [T/m]	Dipole Field [T]	Offset [m]
BS.L	-21.5	12.7	-	-0.0493	-
Q2E.L	-8.5	1.0	-77.30906	-0.0493	$6.37700 \times 10^{-4}$
Q1E.L	-7.2	1.0	90.38473	-0.0493	$-5.45446 \times 10^{-4}$
IP	0.0	-	-	-	-
Q1E.R	6.2	1.0	90.38473	0.0493	$5.45446 \times 10^{-4}$
Q2E.R	7.5	1.0	-77.30906	0.0493	$-6.37700 \times 10^{-4}$
BS.R	8.8	12.7	-	0.0493	-

Table 7.15: Machine elements for the HA IR.  $S_{entry}$  gives the leftmost point of the idealised magnetic field of an element. Note that S is relative to the IP.

5251 The  $l^*$  of 6.2m imposes limitations on focusing and bending in this case. Focusing is limited by quadratic  $\beta$   
 5252 growth through a drift space, which is increased for smaller  $\beta^*$ . As such, the achievable luminosity is smaller  
 5253 than in the HL design lattice.

5254  
 5255 Again offset quadrupoles are used to separate the beams. However this layout has less total dipole length  
 5256 available. Additionally, the first parasitic crossing occurs before the location of the first electron quadrupole.  
 5257 This further limits final focusing as the beam cannot be permitted to grow too large by this time. Due to  
 5258 the reduced effective length for focusing and beam separation, stronger bending must be applied to obtain  
 5259 the overall separation of 55 mm at the place of the first proton quadrupole. Accordingly higher synchrotron  
 5260 radiation power is generated in this design.

5261  
 5262 Figure 7.28 shows the  $\beta$  functions of the beam in both planes from the IP to the face of the final proton  
 5263 quadrupole at  $s = 23$  m.

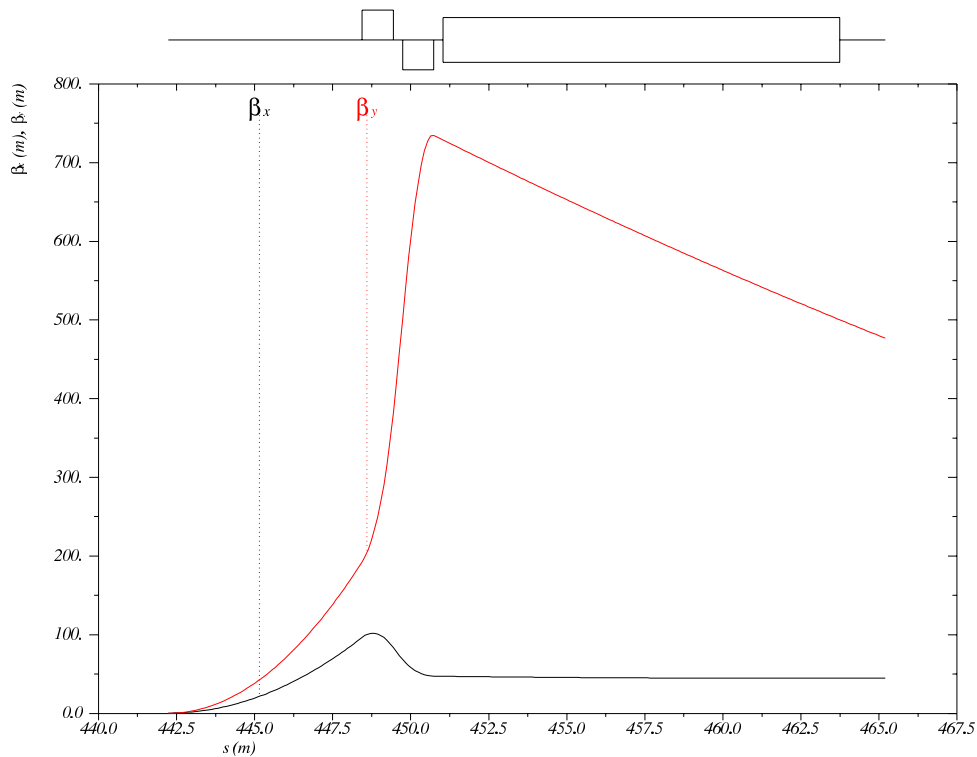


Figure 7.28:  $\beta$  functions in both planes for the HA IR layout, from the IP to the face of the final proton quadrupole at  $s = 23$  m. Note that  $s$  is relative to the ring, which begins at the left side of the left dispersion suppressor of IP2.

### 7.8.3 Separation Scheme

The final electron doublet is optimised to limit the peak in  $\beta_x$  on the cost of higher  $\beta_y$ . Unlike the HL layout, the first parasitic crossing is reached before focusing begins. As such a minimum crossing angle of roughly 0.7 mrad is required, which is dependent solely upon  $\beta$  growth in the drift space. As a balance between luminosity loss and SR power generation, and aiding comparison with the HL layout, a crossing angle of 1 mrad has been chosen.

## 7.9 Comparison of the two Layouts

Table 7.16 shows a direct comparison of various parameters of the two layouts.

The difference in luminosity after considering losses due to the crossing angle is a factor of 1.8. However it should be noted that this design strives for technical feasibility and both layouts could potentially be squeezed further to decrease  $\beta^*$  in both planes. The HL layout could likely be squeezed further than the HA layout due to the large difference in  $l^*$ , as shown in figure 7.29 which compares the two IR layouts. At

Parameter	HL	HA
$L(0)$	$1.8 \times 10^{33}$	$8.54 \times 10^{32}$
$\theta$	$1 \times 10^{-3}$	$1 \times 10^{-3}$
$S(\theta)$	0.746	0.858
$L(\theta)$	$1.34 \times 10^{33}$	$7.33 \times 10^{32}$
$\beta_x^*$	0.18 m	0.4 m
$\beta_y^*$	0.1 m	0.2 m
$\sigma_x^*$	$3.00 \times 10^{-5}$ m	$4.47 \times 10^{-5}$ m
$\sigma_y^*$	$1.58 \times 10^{-5}$ m	$2.24 \times 10^{-5}$ m
SR Power	33 kW	51 kW
$E_c$	126 keV	163 keV

Table 7.16: Parameter comparison for the HL and HA layouts.

5277 this stage both designs deliver their required IP parameters of luminosity and acceptance and appear feasible.  
5278  
5279 The HA design on the other side generates more SR power. This appears to be within reasonable lim-  
5280 its and is discussed in section [ref: SR section]. Furthermore, an option is discussed to install a dipole  
5281 magnet in the detector. This early separation would reduce the required strength of the dipole fields in the  
5282 IR, significantly reducing total SR power.

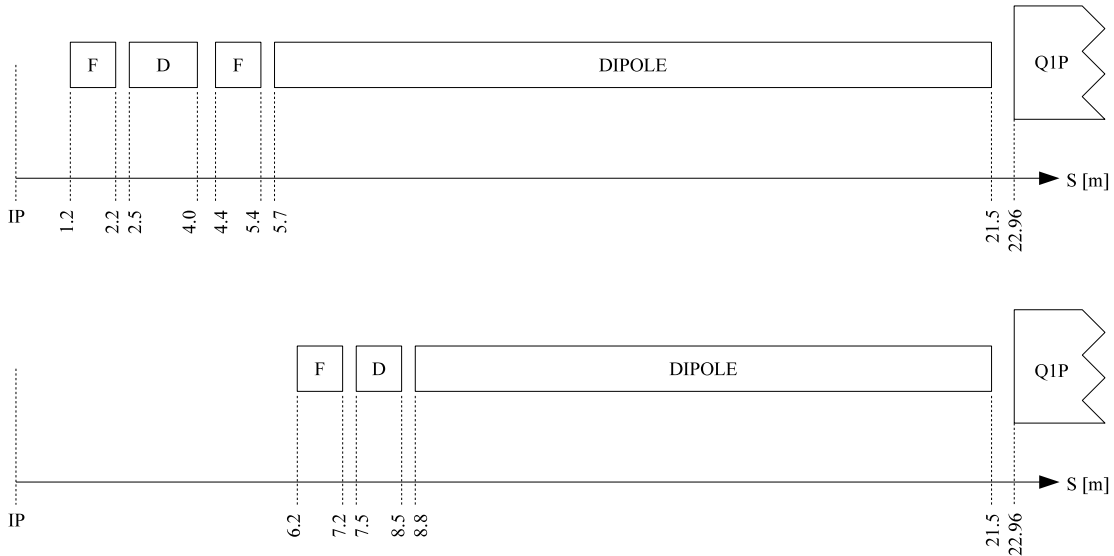


Figure 7.29: Scale comparison of the layouts for the HL and HA designs. Note the large difference in  $l^*$ .

### 5283 7.9.1 Crab Cavities

5284 Both IR designs incorporate a crossing angle of 1mrad to facilitate fast beam separation. As discussed this  
5285 introduces a luminosity loss factor  $S$ . The crossing angle is optimised to balance separation, SR power and  
5286 luminosity. The loss factor is greater for the HL layout (0.746) than the HA (0.858) due to the smaller beam  
5287 spot. However both are moderate, and as such a need for crab cavities is not foreseen.



5288

5289 Crab cavities rotate the bunch locally to the IP to counteract the effect of the crossing angle. They present  
5290 a significant technical challenge, although feasibility has been demonstrated at KEKB [?]. It is preferred  
5291 to avoid their necessity. However, their use remains a possibility if needs arise. For example, if designs for  
5292 the proton half-quadrupoles prove to require larger beam separation than expected, increasing the crossing  
5293 angle is likely the best option, as increased bending would quickly generate unfeasible levels of SR power.  
5294 In this case, crab cavities would need to be considered to recover luminosity.

## 5295 **7.10 Long Straight Section**

5296 The Long Straight Section (LSS) geometrically and optically matches the IR to the rest of the LHeC ring  
5297 lattice. For the purposes of this report, the LSS is defined from the start of the left dispersion suppressor  
5298 (DS) to the end of the right DS. This is due to the need to alter the DS's optically and geometrically from  
5299 the nominal design to obtain a valuable solution.

5300

5301 The LSS geometry for the electron ring uses a complex bending scheme in the horizontal and vertical  
5302 planes to satisfy the various constraints. These include the 0.6 m radial offset of the LHeC ring as mentioned  
5303 in section [ref: Ring lattice section], the 1 m vertical offset, and the IR separation geometry. The resulting  
5304 small path length difference must be compensated elsewhere in the ring, nominally in the bypasses.

5305

5306 It has to be noted that in the current LSS design there are some conflicts between placements of the mag-  
5307 nets for the LSS layout of the LHeC and standard LHC rings. The aim has been to design a self-consistent  
5308 LHeC solution, and then iterate upon this to eliminate these conflicts. Future plans are discussed later in  
5309 this section. It should also be noted that the solution presented is only matched for the HA IR layout.  
5310 However generating a similar solution for the HL layout presents no additional challenges.

### 5311 **7.10.1 Dispersion**

5312 A key constraint coupled to optics and geometry is dispersion. Since dispersion is an optical quantity  
5313 generated by the deflecting fields, this becomes a challenge for the complex LSS bending scheme. The LHeC  
5314 DSs are designed to match horizontal dispersion from the LSS to the arc. There is no equivalent scheme to  
5315 deal with large vertical dispersion. Therefore an achromatic vertical separation scheme is proposed. Two  
5316 vertical double bend achromat (DBA) sections on either side of the IR form doglegs while generating no  
5317 vertical dispersion outside this region. Figures 7.30 and 7.31 detail the geometry and optics of the DBA  
5318 sections used in the LSS.

### 5319 **7.10.2 Geometry**

5320 Figure 7.32 shows the geometry of the LSS solution on a larger scale. Note that the vertical doglegs are  
5321 placed between the two horizontal dipole sets. To maximise use of space, schemes were explored with inter-  
5322 leaved horizontal and vertical bends, as shown in figure 7.33. This allows increased bend length and distance  
5323 between the bending magnets to reduce the SR power. However this coupled bending generates rotation of  
5324 the beam around the s axis, effectively causing all subsequent quadrupoles to have a skew component.

5325

5326 Note that the left DS has nominal bend strength, while the right DS dipoles are weakened to accommodate the  
5327 1.2 m horizontal separation. Note also that future iterations of the LSS will include changes to accommodate  
5328 the solution for the non-colliding proton beam detailed in section 7.11. In practise this simply manifests as  
5329 a rotation of the IR section, and no complex changes are required.

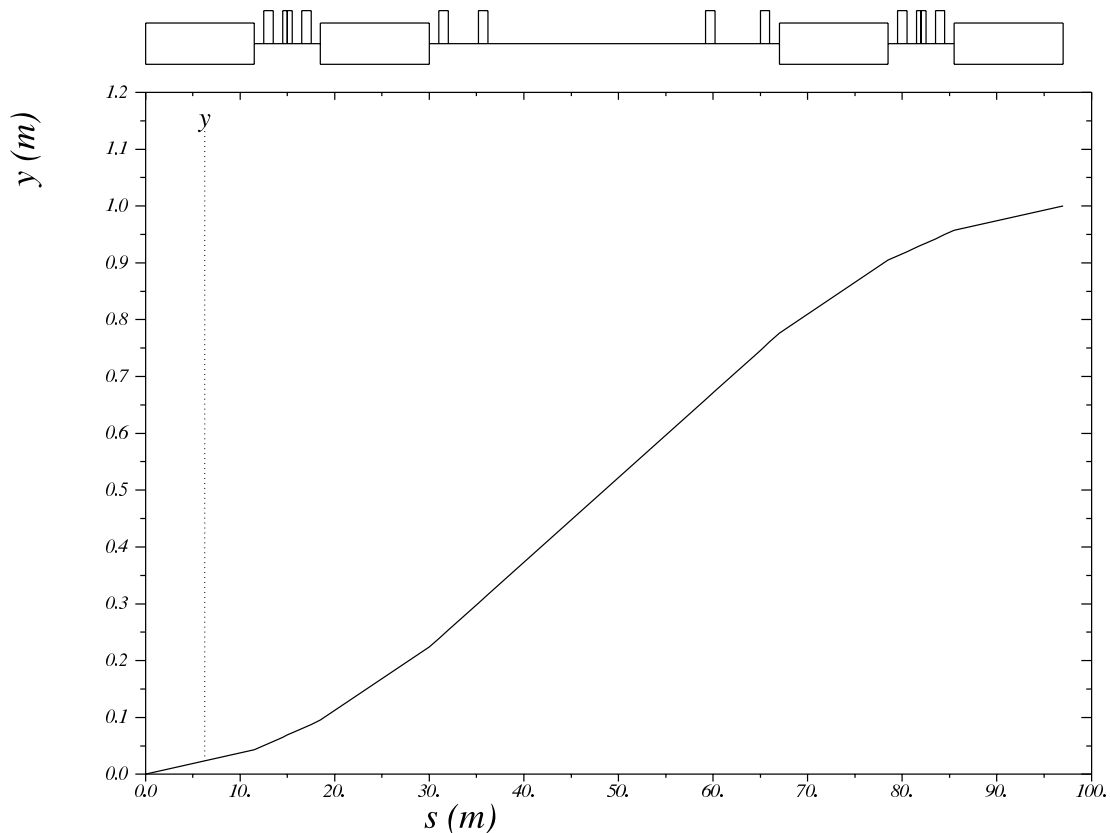


Figure 7.30: Geometry plot for a DBA dogleg pair in the HA LSS design.

### 5330 7.10.3 Electron Optics in the LSS

5331 Placement of quadrupole elements is constrained by LSS geometry requirements, and by the LHC lattice,  
 5332 although this constraint is ignored for this iteration. While the LSS horizontal dipoles alone do not signif-  
 5333 icantly constrain space, the combination of these and the vertical DBA scheme takes up large amounts of  
 5334 space.

5335

5336 To gain sufficient matching flexibility, quadrupole triplets are used in the centre of the DBAs. The triplet  
 5337 DBA generates a characteristic beta function shape, resulting in peaks and waists which make matching  
 5338 more challenging but feasible. Figure 7.34 shows the beta and dispersion functions of the LSS optics.

### 5339 7.10.4 Synchrotron Radiation

5340 While detailed simulations have not yet been run, a simple analytical calculation of SR generated by the  
 5341 dipoles in the LSS has been performed, giving an initial estimate of  $\sim 1.4$  MW. Note that this includes the  
 5342 left and right DS sections. This is manageable considering the  $\sim 50$  MW estimate for the rest of the ring.

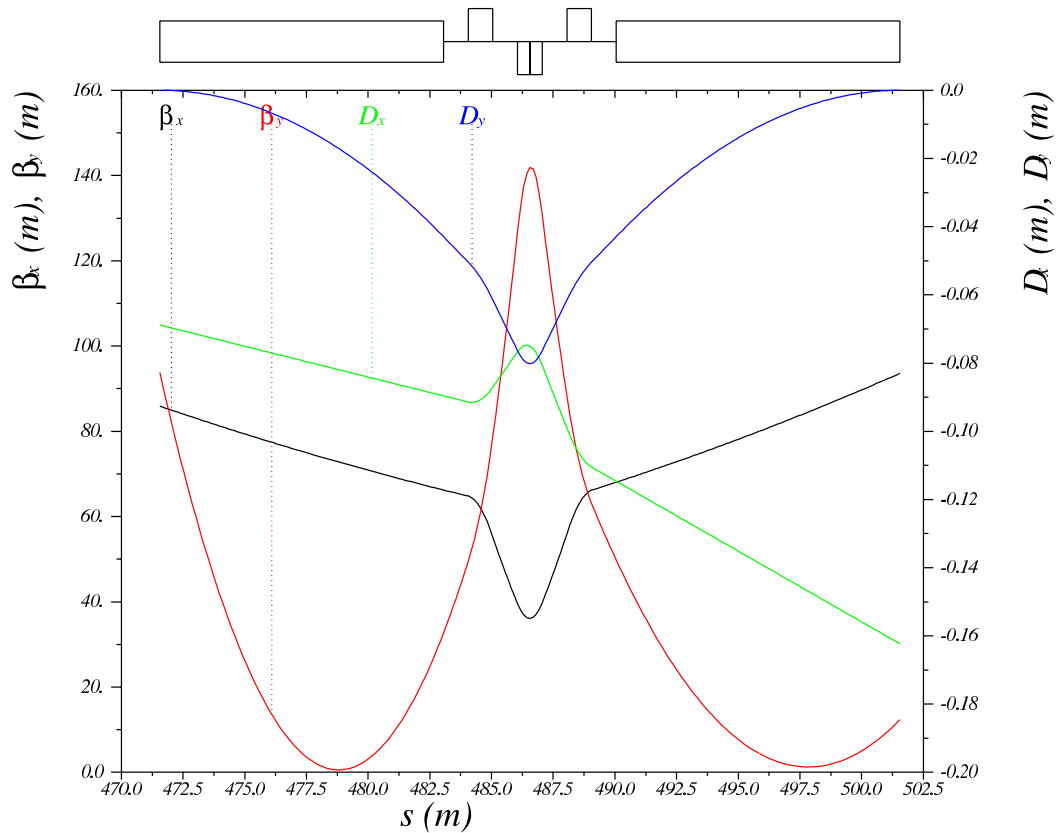


Figure 7.31: Optics plot for a single DBA module in the HA LSS design. Note waists and peaks in  $\beta_y$ .

### 5343 7.10.5 LHC Integration

5344 Currently, the DBA modules and quadrupoles near the IP conflict with the LHC proton triplet. After suffi-  
 5345 cient horizontal and/or vertical separation electron elements may be placed arbitrarily. Work is in progress  
 5346 on an updated design which moves vertical separation outward from the IP, after horizontal separation. In  
 5347 this case, no quadrupoles are required until  $\sim 75$  m from the IP, leaving space for the proton triplet. This  
 5348 geometry also successfully incorporates the solution for the non-colliding proton beam. However at the time  
 5349 of writing, optical matching is not yet finalised.

5350

5351 This "late vertical separation" scheme changes optical constraints. In the current "early" vertical sepa-  
 5352 ration scheme, limited space between the IR and the DBA decreases matching flexibility. In the "late"  
 5353 design, flexibility between the IR and DBA increases, but decreases correspondingly between the DBA and  
 5354 the DS.

5355

5356 Note that it is to some degree possible to reduce a bending scheme's space requirements arbitrarily, at  
 5357 the cost of more SR power.

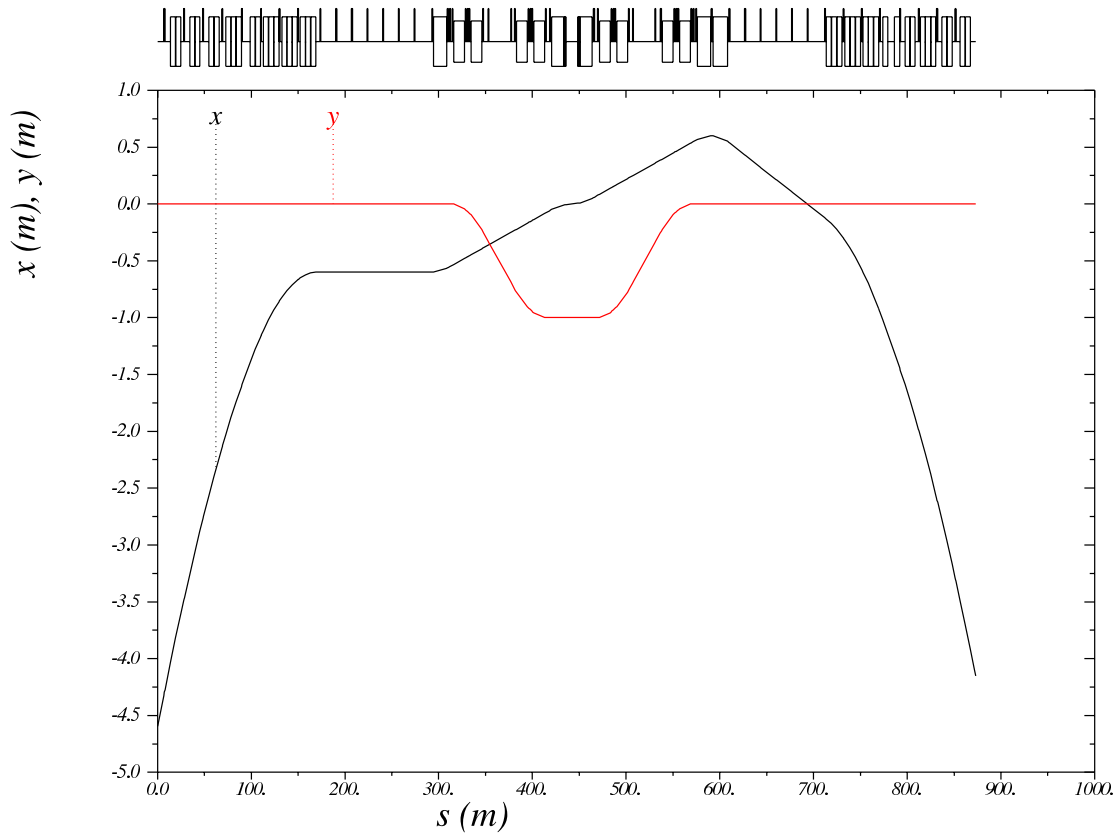


Figure 7.32: Geometry of the LSS design. Due to small angles involved, the  $s$  axis approximates the  $z$  axis well, and is used to allow MADX to display lattice elements.

## 5358 7.11 The Non-Colliding Proton Beam

5359 In both IRs, a solution must be found for dealing with the second proton beam. The second beam must not  
 5360 collide with either of the other two beams, or generate significant beam-beam effects. Also, detector designs  
 5361 strongly prefer for the second beam to occupy the same central beam pipe as the other two beams, rather  
 5362 than allowing space through the detector for a second pipe.

### 5363 7.11.1 Design Elements

5364 To avoid collisions and beam-beam effects, the bunches of the non-colliding (NC) beam will be shifted in  
 5365 time by half a bunch distance. This prevents proton-proton collisions at the IP, and allows the NC beam to  
 5366 overlap with the co-rotating electron beam.

5367  
 5368 Proton-proton interactions at the parasitic encounters however and accordingly beam-beam effects can still  
 5369 occur. To minimise these, the NC beam is left unsqueezed, and a proton-proton crossing angle is imple-  
 5370 mented which generates sufficient separation at these locations. For the unsqueezed optics, the so-called  
 5371 LHC alignment optics [CDR v1.0 reference 664] is modified for use on the NC beam only. The same scenario

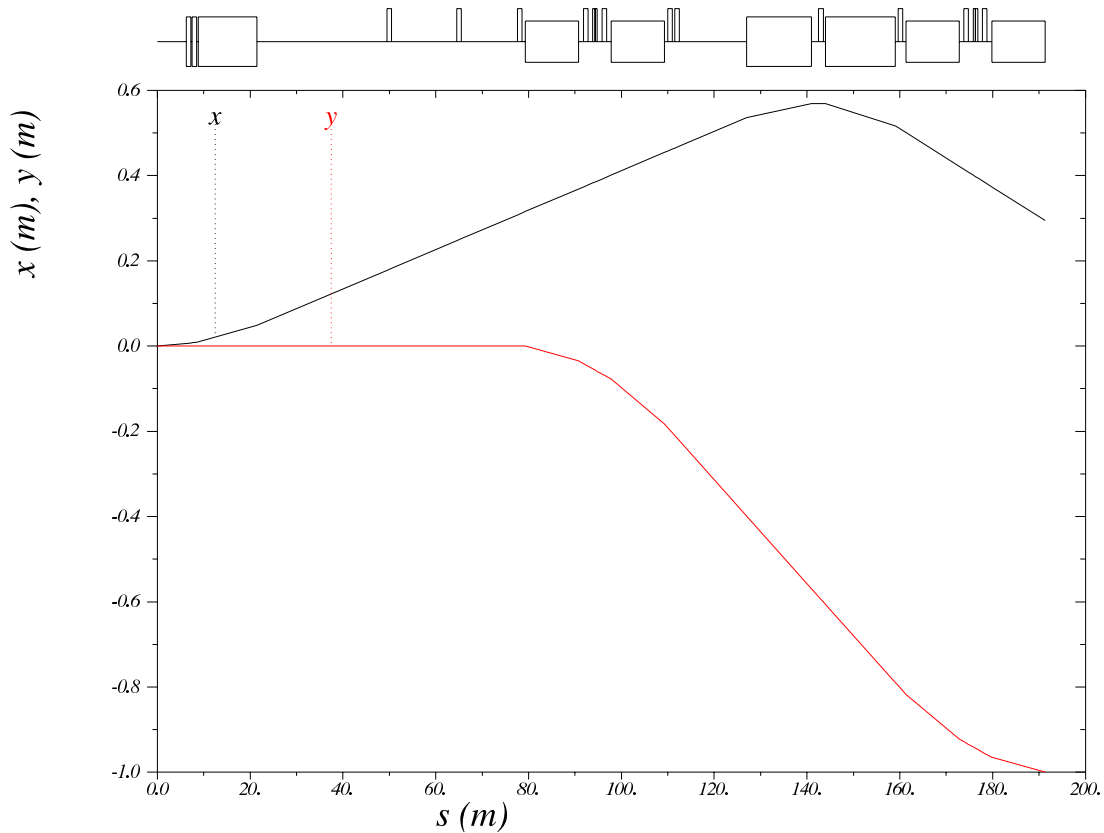


Figure 7.33: Example of geometry of a design with coupled horizontal and vertical bends. Interleaving bends in this way generates roll around  $s$  axis. The IP is at zero in both axes.

5372 is proposed in the linac-ring design in section [LR IR].

5373

5374 The required crossing angle for the second proton beam is generated by changing the LHC separator dipoles  
 5375 D1 and D2. Figure 7.35 shows the trajectories of the three beams for the HA design. The proton final triplet  
 5376 is rotated in the horizontal plane and moved to match the new trajectory of the colliding beam while its  
 5377 position in  $s$  stays constant.

5378

5379 Note that the electron trajectory is rotated as well to match the colliding proton beam, such that the  
 5380 electron-proton crossing angle of 1 mrad is kept constant. This requires a change to the LSS geometry and  
 5381 optics solution which has not yet been implemented. This will be included in the next iteration of the LSS  
 5382 design. No new issues are likely to be introduced. Note also that the electron IR itself is unchanged in both  
 5383 the HL and HA designs, so SR calculations and detector designs do not require updates.

### 5384 7.11.2 Solution

5385 For the unsqueezed optics of the second proton beam, zero triplet strength is required. The triplet quadrupoles  
 5386 each have a single proton aperture and as such the proton beams cannot be focused differently if both pass

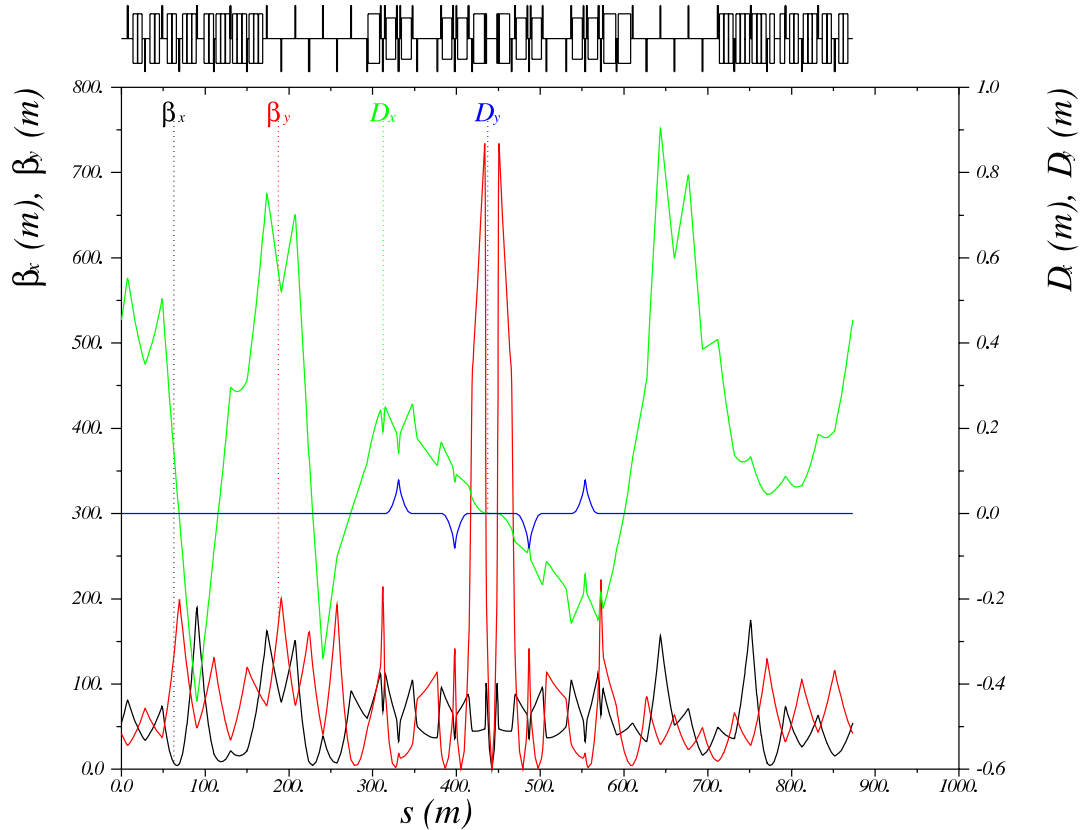


Figure 7.34: Optics plot for the HA LSS design.

5387 through the main aperture. Therefore the NC beam is guided through the same aperture as the electron  
 5388 beam, and experiences effectively no focusing. The proton LSS matching quadrupoles, which are separately  
 5389 powered for each beam, are then used to implement the NC beam optics.

5390

5391 As shown in section [ref: Magnets section], Q1 will be a half-quadrupole. A large field-free aperture accom-  
 5392 modates the electron beam and the NC proton beam. Q2 and Q3 have standard designs which incorporate  
 5393 low-field pockets which will be used for the shared electron and NC proton apertures.

5394

5395 Aperture calculations are based on  $15\sigma$  proton envelopes and  $20\sigma$  electron envelopes. In both cases, the  
 5396 aperture need is driven by horizontal requirements, since the horizontal envelopes and horizontal separation  
 5397 dominate over the vertical electron envelope. Note that the Q2 and Q3 apertures are circular; aperture  
 5398 radius is thus determined by the larger dimension.

### 5399 High Luminosity

5400 The proton-proton crossing angle is optimised to 3 mrad to minimise aperture requirements, by making  
 5401 the NC beam follow the electron beam closely. The electron trajectory is determined by the IR separation  
 5402 scheme.

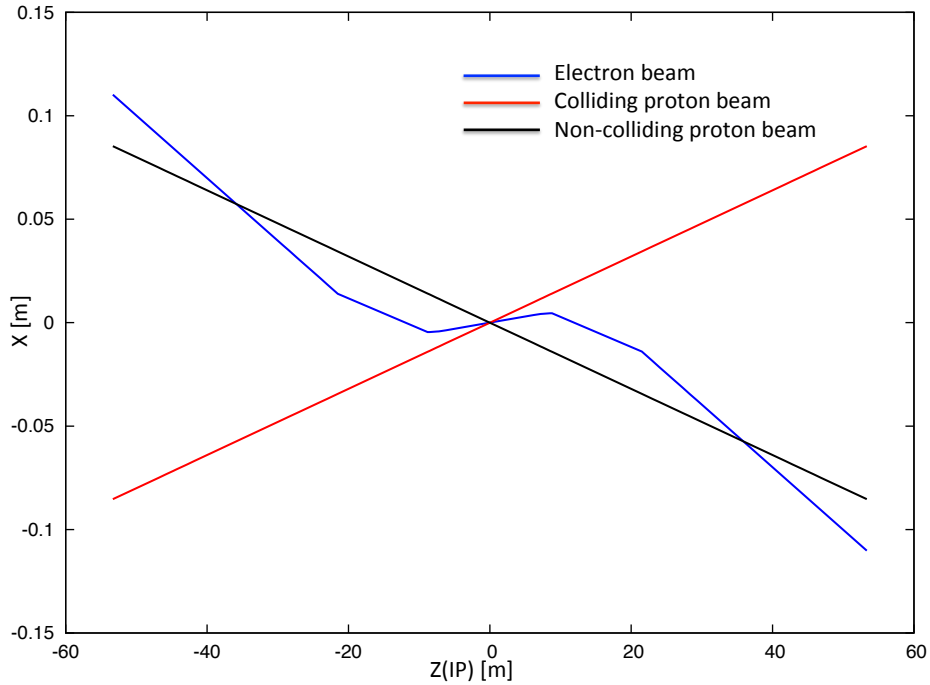


Figure 7.35: Trajectories of the three beams in the HA interaction region design. Note that in this plot the beams are reversed compared to the LSS plots.

Element	Ap Radius	Ap Centre
Q1	0.0311	-0.0666
Q2A	0.0274	-0.1001
Q2B	0.0259	-0.1251
Q3	0.0257	-0.1592

Table 7.17: Proton triplet aperture requirements of the non-colliding proton beam for the HL layout.

### 5403 High Acceptance

5404 In this case the proton-proton crossing angle is optimised to 3.4 mrad to minimise aperture requirements.  
 5405 Again the NC proton beam will follow closely the electron beam trajectory, which is determined by the  
 5406 IR separation scheme. The electron beam, having larger emittance, dominates aperture requirements. The  
 5407 separation between the electron beam and the NC proton beam is larger in the HA layout than in the HL  
 5408 layout, due to the later bending in the HA separation scheme. Table 7.18 and figure 7.37 show the required  
 5409 apertures.

### 5410 7.11.3 Summary

5411 Aperture requirements for the HL layout are somewhat less demanding than for the HA layout, but both  
 5412 sets of requirements are feasible and do not present difficulties in magnet design using existing technology.  
 5413 The existing Q1 design is easily sufficient. Q2A and Q2B would ideally be two copies of the same yoke,  
 5414 requiring a larger hole in each. Q3 requires a larger yoke than the existing 200 mm radius design, but the  
 5415 tooling limit of 270 mm should be sufficient.

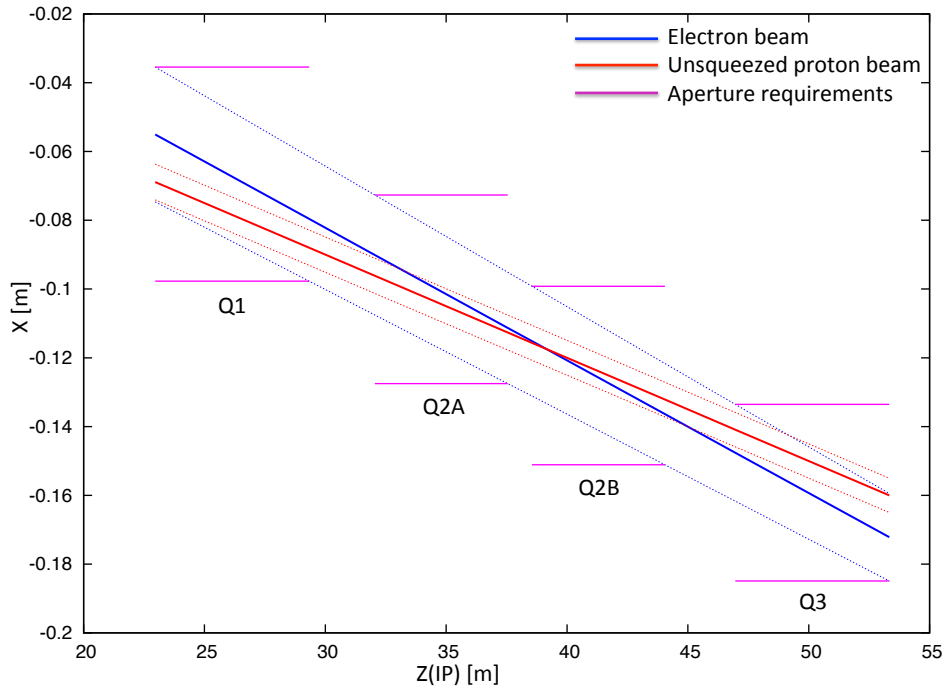


Figure 7.36: Proton triplet aperture requirements with trajectories and envelopes of the electron beam and NC proton beam for the HL layout. Note that in this plot the beams are reversed compared to the LSS plots.

Element	Aperture Radius	Aperture Centre
Q1	0.0296	-0.0752
Q2A	0.0227	-0.1100
Q2B	0.0233	-0.1402
Q3	0.0264	-0.1811

Table 7.18: Proton triplet aperture requirements of the non-colliding proton beam for the HA layout.

5416

5417 In both designs, the crossing angle may be increased if desired for beam-beam reasons. The existing Q1  
 5418 design supports a crossing angle up to 4 mrad, but this would require significantly larger apertures in the  
 5419 other magnets.

## 5420 7.12 Synchrotron radiation and absorbers

### 5421 7.12.1 Introduction

5422 The synchrotron radiation (SR) in the interaction region has been analyzed in three ways. The SR was  
 5423 simulated in depth using a program made with the Geant4 (G4) toolkit. In addition a cross check of the  
 5424 total power and average critical energy was done in IRSYN, a Monte Carlo simulation package written by



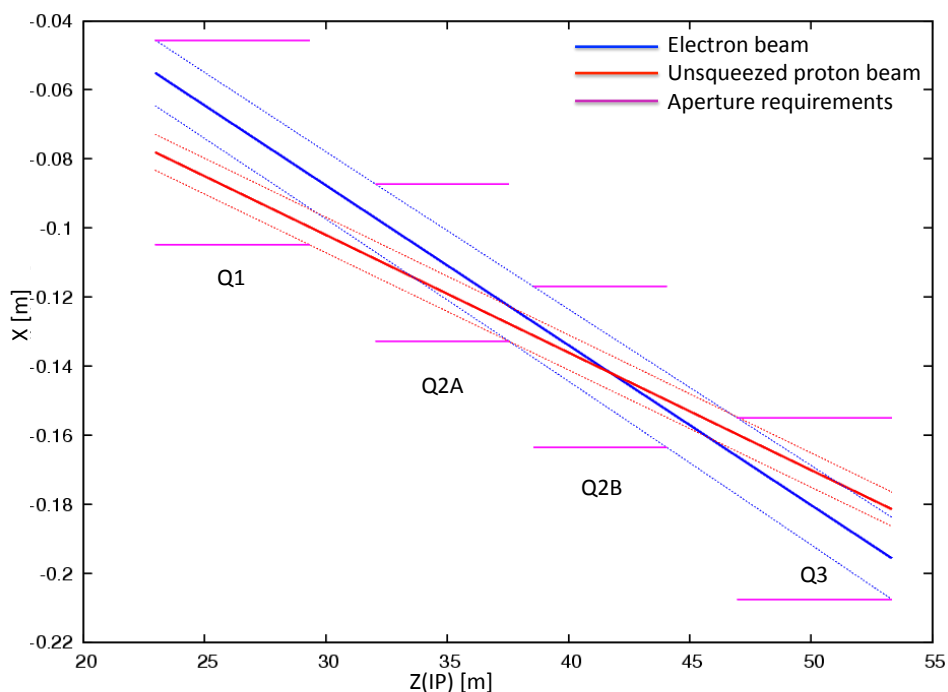


Figure 7.37: Proton triplet aperture requirements with trajectories and envelopes of the electron beam and NC proton beam for the HA layout. Note that in this plot the beams are reversed compared to the LSS plots.

5425 R. Appleby. [572] A final cross check has been made for the radiated power per element using an analytic  
 5426 method. These other methods confirmed the results seen using G4. The G4 program uses Monte Carlo  
 5427 methods to create gaussian spatial and angular distributions for the electron beam. The electron beam is  
 5428 then guided through vacuum volumes that contain the magnetic fields for the separator dipoles and electron  
 5429 final focusing quadrupoles.

5430 The SR is generated in these volumes using the appropriate G4 process classes. The G4 SR class was  
 5431 written for a uniform magnetic field, and therefore the quadrupole volumes were divided such that the  
 5432 field remained approximately constant in each volume. This created agreement between upstream and  
 5433 downstream quadrupoles since for a downstream quadrupole the beta function at the entrance and exit are  
 5434 reversed from its upstream counterpart. This agreement confirms that the field was approximately constant  
 5435 in each volume.

5436 The position, direction, and energy of each photon created is written as ntuples at user defined Z values.  
 5437 These ntuples are then used to analyze the SR fan as it evolves in Z. The analysis was done primarily  
 5438 through the use of MATLAB scripts. It was necessary to make two versions of this program. One for the  
 5439 high luminosity design and one for the high detector acceptance design.

5440 Before going further I will explain some conventions used for this section. I will refer to the electron  
 5441 beam as *the beam* and the proton beams will be referred to as either the interacting or non interacting  
 5442 proton beams. The beam propagates in the -Z direction and the interacting proton beam propagates in the  
 5443 +Z direction, I will use a right handed coordinate system where the X axis is horizontal and the Y axis is  
 5444 vertical. The beam centroid always remains in the  $Y = 0$  plane. The *angle of the beam* will be used to refer  
 5445 to the angle between the beam centroid's velocity vector and the Z axis, in the  $Y = 0$  plane. This angle is

5446 set such that the beam propagates in the -X direction as it traverses Z.

5447 The SR fans extension in the horizontal direction is driven by the angle of the beam at the entrance  
 5448 of the upstream separator dipole. Because the direction of emitted photons is parallel to the direction of  
 5449 the electron that emitted it, the angle of the beam and the distance to the absorber are both greatest at  
 5450 the entrance of the upstream separator dipole and therefore this defines one of the edges of the synchrotron  
 5451 fan on the absorber. The other edge is defined by the crossing angle and the distance from the IP to the  
 5452 absorber. The S shaped trajectory of the beam means that the smallest angle of the beam will be reached  
 5453 at the IP. Therefore the photons emitted at this point will have the lowest angle and for this given angle the  
 5454 smallest distance to the absorber. This defines the other edge of the fan in the horizontal direction.

5455 The SR fans extension in the vertical direction is driven by the beta function and angular spread of the  
 5456 beam. The beta function along with the emittance defines the r.m.s. spot size of the beam. The vertical  
 5457 spot size defines the Y position at which photons are emitted. On top of this the vertical angular spread  
 5458 defines the angle between the velocity vector of these photons and the Z axis. Both of these values produce  
 5459 complicated effects as they are functions of Z. These effects also affect the horizontal extension of the fan  
 5460 however are of second order when compared to the angle of the beam. Since the beam moves in the Y = 0  
 5461 plane these effects dominate the vertical extension of the beam.

5462 The number density distribution of the fan is a complicated issue. The number density at the absorber  
 5463 is highest between the interacting beams. The reason for this is that although the separator dipoles create  
 5464 significantly more photons the number of photons generated per unit length in Z is much lower for the dipoles  
 5465 as opposed to the quadrupoles due to the high fields experienced in the quadrupoles. The position of the  
 5466 quadrupole magnets then causes the light radiated from them to hit the absorber in the area between the  
 5467 two interacting beams.

## 5468 7.12.2 High Luminosity

### 5469 Parameters

5470 The parameters for the high luminosity option are listed in Table 7.19. The separation refers to the dis-  
 5471 placement between the two interacting beams at the face of the proton triplet.

Characteristic	Value
Electron Energy [GeV]	60
Electron Current [mA]	100
Crossing Angle [mrad]	1
Absorber Position [m]	-21.5
Dipole Field [T]	0.0296
Separation [mm]	55
$\gamma/s$	$5.39 \times 10^{18}$

Table 7.19: High Luminosity: Parameters

5472 The energy, current, and crossing angle ( $\theta_c$ ) are common values used in all RR calculations. The dipole  
 5473 field value refers to the constant dipole field created throughout all dipole elements in the IR. The direction  
 5474 of this field is opposite on either side of the IP. The quadrupole elements have an effective dipole field created  
 5475 by placing the quadrupole off axis, which is the same as this constant dipole field. The field is chosen such  
 5476 that 55 mm of separation is reached by the face of the proton triplet. This separation was chosen based on  
 5477 S. Russenschuck's SC quadrupole design for the proton final focusing triplet. [573] The separation between  
 5478 the interacting beams can be increased by raising the constant dipole field. However, for a dipole magnet  
 5479  $P_{SR} \propto |B^2|$ , [574] therefore an optimization of the design will need to be discussed. The chosen parameters  
 5480 give a flux of  $5.39 \times 10^{18}$  photons per second at Z = -21.5 m.

5481 **Power and Critical Energy**

5482 Table 7.20 shows the power of the SR produced by each element along with the average critical energy  
 5483 produced per element. This is followed by the total power produced in the IR and the average critical  
 5484 energy. Since the G4 simulations utilize Monte Carlo, multiple runs should be made with various seeds to  
 5485 get an estimate for the standard error.

Element	Power [kW]	Critical Energy [keV]
DL	6.4	71
QL3	5.3	308
QL2	4.3	218
QL1	0.6	95
QR1	0.6	95
QR2	4.4	220
QR3	5.2	310
DR	6.4	71
Total/Avg	33.2	126

Table 7.20: High Luminosity: Power and Critical Energies as calculated with Geant4.

5486 The power from the dipoles is greater than any one quadrupole however the critical energies of the  
 5487 quadrupoles are significantly higher than in the dipoles. It is expected that the dipole and quadrupole  
 5488 elements can create power on the same order however have very different critical energies. This is because  
 5489 the dipole is an order of magnitude longer than the quadrupole elements. Since the SR power created for  
 5490 both the quadrupole and dipoles are linearly dependent on length [574] one needs to have a much higher  
 5491 average critical energy to create comparable amounts of power.

5492 **Comparison**

5493 The IRSYN cross check of the power and critical energies is shown in Table 7.21. This comparison was done  
 5494 for the total power and the average critical energy.

	Power [kW]		Critical Energy [keV]	
	Geant4	IRSYN	Geant4	IRSYN
Total/Avg	33.2	33.7	126	126

Table 7.21: High Luminosity: Geant4 and IRSYN comparison

5495 A third cross check to the G4 simulations was made for the power as shown in Table 7.22. This was done  
 5496 using an analytic method for calculating power in dipole and quadrupole magnets. [574] This was done for  
 5497 every element which provides confidence in the distribution of this power throughout the IR.

5498 **Number Density and Envelopes**

5499 The number density of photons as a function of  $Z$  is shown in Figure 7.38. Each graph displays the density  
 5500 of photons in the  $Z = Z_o$  plane for various values of  $Z_o$ . The first three figures give the growth of the SR  
 5501 fan inside the detector area. This is crucial for determining the dimensions of the beam pipe. Since the  
 5502 fan grows asymmetrically in the  $-Z$  direction an asymmetric elliptical cone geometry will minimize these  
 5503 dimensions, allowing the tracking to be placed as close to the beam as possible. The horizontal extension of  
 5504 the fan in the high luminosity case is the minimum for the two Ring Ring options as well as the Linac Ring

Element	Power [kW]	
	Geant4	Analytic
DL	6.4	6.3
QL3	5.3	5.4
QL2	4.3	4.6
QL1	0.6	0.6
QR1	0.6	0.6
QR2	4.4	4.6
QR3	5.2	5.4
DR	6.4	6.3
Total/Avg	33.2	33.8

Table 7.22: High Luminosity: Geant4 and Analytic method comparison

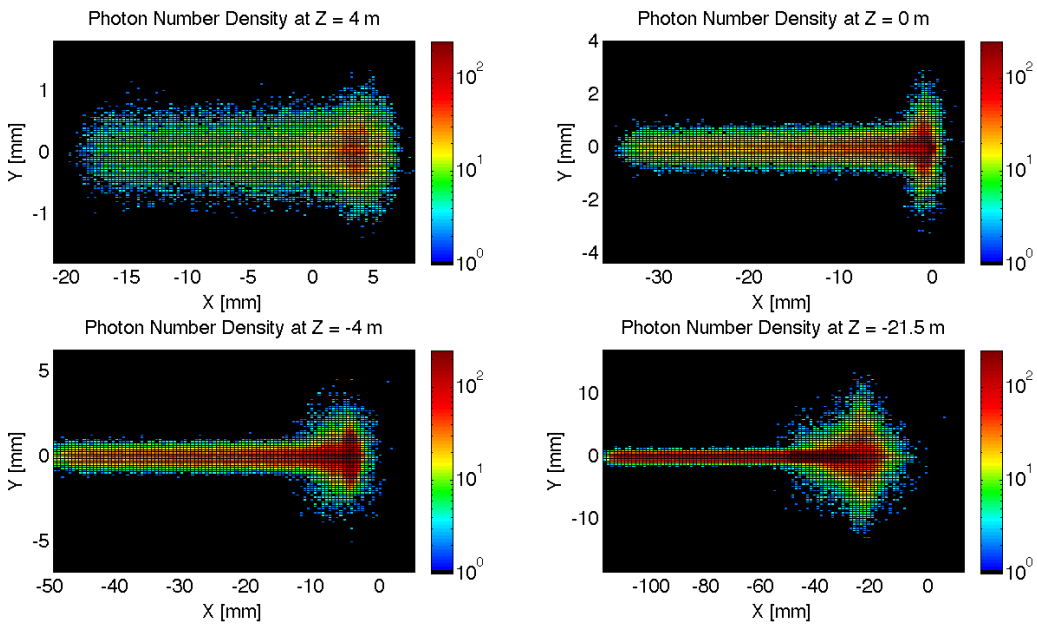


Figure 7.38: High Luminosity: Number Density Growth in Z

option, which is most important inside the detector region. This is due to the lower value of  $l^*$ . Because the quadrupoles are closer to the IP and contain effective dipole fields the angle of the beam at the entrance of the upstream dipole can be lower as the angle of the beam doesn't need to equal the crossing angle until  $Z = l^*$ . The number density of this fan appears as expected. There exists the highest density between the two beams at the absorber.

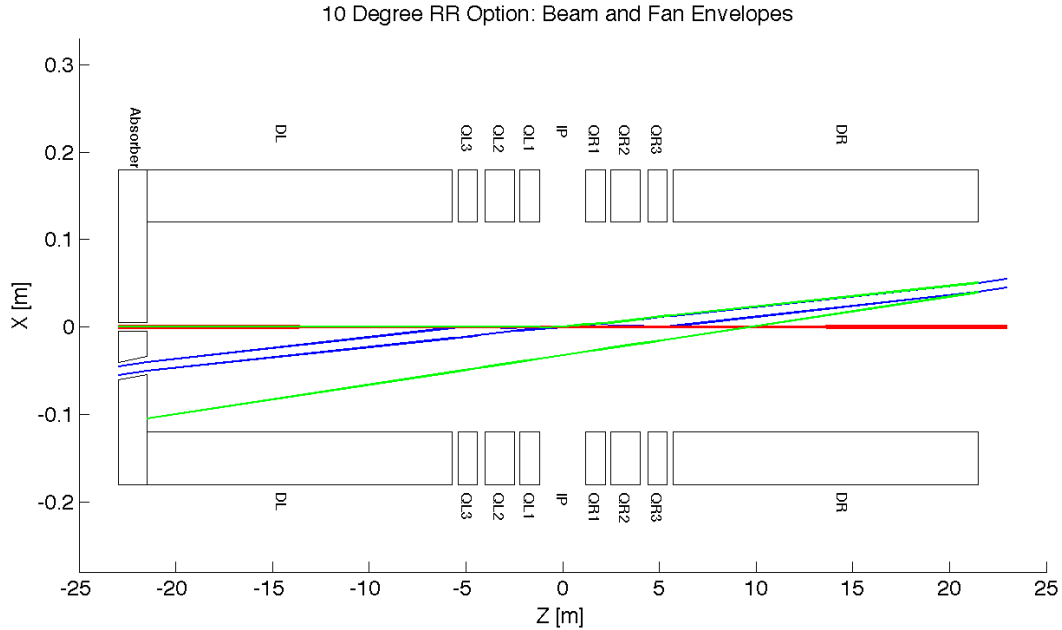


Figure 7.39: High Luminosity: Beam Envelopes in Z

In Figure 7.38 the distribution was given at various Z values however a continuous envelope distribution is also important to see everything at once. This can be seen in Figure 7.39, where the beam and fan envelopes are shown in the  $Y = 0$  plane. This makes it clear that the fan is antisymmetric which comes from the S shape of the electron beam as previously mentioned.

### Critical Energy Distribution

The Critical Energy is dependent upon the element in which the SR is generated, and for the quadrupole magnets it is also dependent upon Z. This is a result of the fact that the critical energy is proportional to the magnetic field component that is perpendicular to the particle direction. i.e.  $E_c \propto B_{\perp}$ . [575] Since the magnitude of the magnetic field is dependent upon x and y, then for a gaussian beam in position particles will experience different magnetic fields and therefore have a spectrum of critical energies. In a dipole the field is constant and therefore regardless of the position of the particles as long as they are in the uniform field area of the magnet they have a constant critical energy. Since the magnetic field is dependent upon x and y it is clear that as the r.m.s. spot size of the beam decreases there will be a decrease in critical energies. The opposite will occur for an increasing spot size. This is evident from Figure 7.40.

### Absorber

The Photon distribution on the absorber surface is crucial. The distribution decides how the absorber must be shaped. The shape of the absorber in addition to the distribution on the surface then decides how much SR is backscattered into the detector region. In HERA backscattered SR was a significant source of background that required careful attention. [576] Looking at Figure 7.41 it is shown that for the high luminosity option

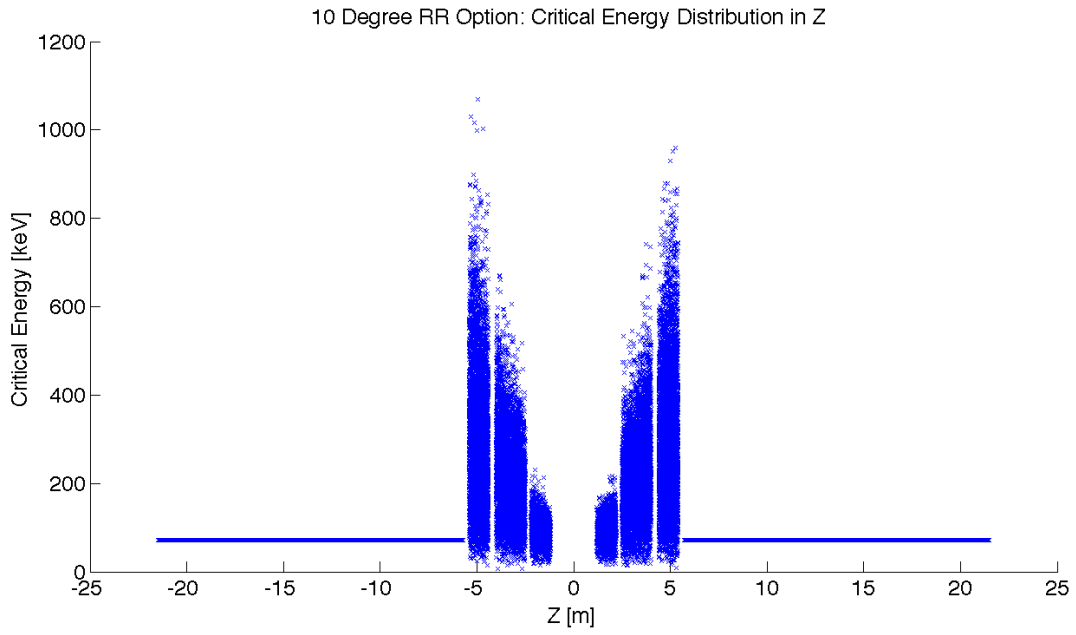


Figure 7.40: High Luminosity: Critical Energy Distribution in Z

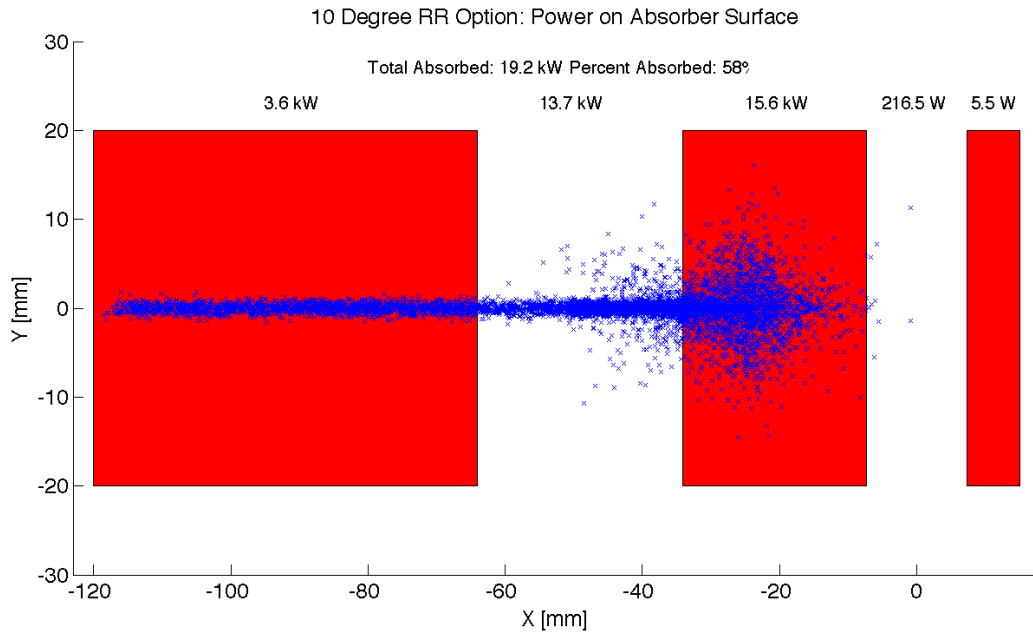


Figure 7.41: High Luminosity: Photon distribution on Absorber Surface

5529 19.2 kW of power from the SR light will fall on the face of the absorber which is 58% of the total power.  
5530 This gives a general idea of the amount of power that will be absorbed. However, backscattering and IR  
5531 photons will lower the percent that is actually absorbed.

## 5532 **Proton Triplet**

5533 The super conducting final focusing triplet for the protons needs to be protected from radiation by the  
5534 absorber. Some of the radiation produced upstream of the absorber however will either pass through the  
5535 absorber or pass through the apertures for the two interacting beams. This is most concerning for the  
5536 interacting proton beam aperture which will have the superconducting coils. A rough upper bound for  
5537 the amount of power the coils can absorb before quenching is 100W [577]. There is approximately 217 W  
5538 entering into the interacting proton beam aperture as is shown in Figure 7.41. This doesn't mean that all  
5539 this power will hit the coils but simulations need to be made to determine how much of this will hit the  
5540 coils. The amount of power that will pass through the absorber can be disregarded as it is not enough to  
5541 cause any effects. The main source of power moving downstream of the absorber will be the photons passing  
5542 through the beams aperture. This was approximately 13.7 kW as can be seen from Figure 7.41. Most of  
5543 this radiation can be absorbed in a secondary absorber placed after the first downstream proton quadrupole.  
5544 Overall protecting the proton triplet is important and although the absorber will minimize the radiation  
5545 continuing downstream this needs to be studied in depth.

## 5546 **Backscattering**

5547 Another Geant4 program was written to simulate the backscattering of photons into the detector region.  
5548 The ntuple with the photon information written at the absorber surface is used as the input for this program.  
5549 An absorber geometry made of copper is described, and general physics processes are set up. A detector  
5550 volume is then described and set to record the information of all the photons which enter in an ntuple. The  
5551 first step in minimizing the backscattering was to optimize the absorber shape. Although the simulation  
5552 didnt include a beam pipe the backscattering for different absorber geometries was compared against one  
5553 another to find a minimum. The most basic shape was a block of copper that had cylinders removed for the  
5554 interacting beams. This was used as a benchmark to see the maximum possible backscattering. In HERA a  
5555 wedge shape was used for heat dissipation and minimizing backscattering [576]. The profile of two possible  
5556 wedge shapes in the YZ plane is shown in Figure 7.42. It was found that this is the optimum shape for  
5557 the absorber. The reason for this is that a backscattered electron would have to have its velocity vector be  
5558 almost parallel to the wedge surface to escape from the wedge and therefore it works as a trap. As can be  
5559 seen from Table 7.23 utilizing the wedge shaped absorber did not reduce the power by much. This appears  
5560 to be a statistical limitation. This needs to be redone with higher statistics to get a better opinion on the  
5561 difference between the two geometries.

5562 After the absorber was optimized it was possible to set up a beam pipe geometry. An asymmetric  
5563 elliptical cone beam pipe geometry made of beryllium was used since it would minimize the necessary size  
5564 of the beam pipe as previously mentioned. The next step was to place the lead shield and masks inside this  
5565 beam pipe. To determine placement a simulation was run with just the beam pipe. Then it was recorded  
5566 where each backscattered photon would hit the beam pipe in Z. A histogram of this data was made. This  
5567 determined that the shield should be placed in the Z region ranging from -20 m until the absorber (-21.5  
5568 m). The shields were then placed at -21.2 m and -20.5 m. This decreased the backscattered power to zero as  
5569 can be seen from Table 7.23. Although this is promising this number should be checked again with higher  
5570 statistics to judge its accuracy. Overall there is still more optimization that can occur with this placement.

5571 Cross sections of the beam pipe in the  $Y = 0$  and  $X = 0$  planes with the shields and masks included can  
5572 be seen in Figure 7.43.

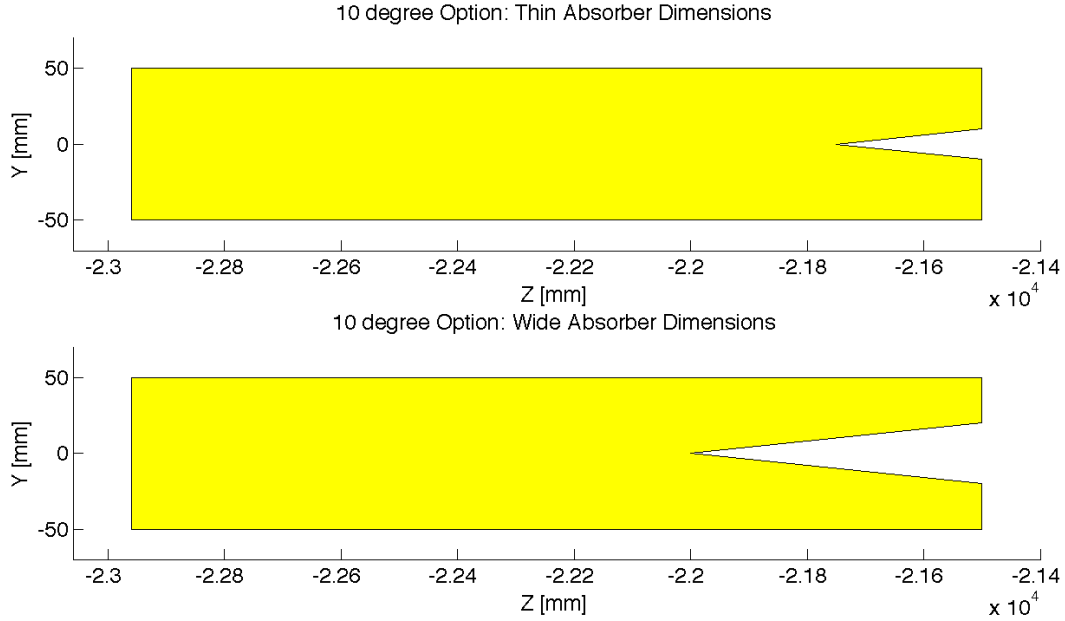


Figure 7.42: 10 deg: Absorber Dimensions

Absorber Type	Power [W]
Flat	22
Wedge	18.5
Wedge & Mask/Shield	0

Table 7.23: High Luminosity: Backscattering/Mask

### 7.12.3 High Detector Acceptance

#### Parameters

For the Ring Ring high acceptance option the basic parameters are listed in Table 7.24. The separation refers to the displacement between the two interacting beams at the face of the proton triplet.

Characteristic	Value
Electron Energy [GeV]	60
Electron Current [mA]	100
Crossing Angle [mrad]	1
Absorber Position [m]	-21.5
Dipole Field [T]	0.0493
Separation [mm]	55.16
$\gamma/s$	$6.41 \times 10^{18}$

Table 7.24: High Acceptance: Parameters

The energy, current, and crossing angle ( $\theta_c$ ) are common values used in all RR calculations. The dipole



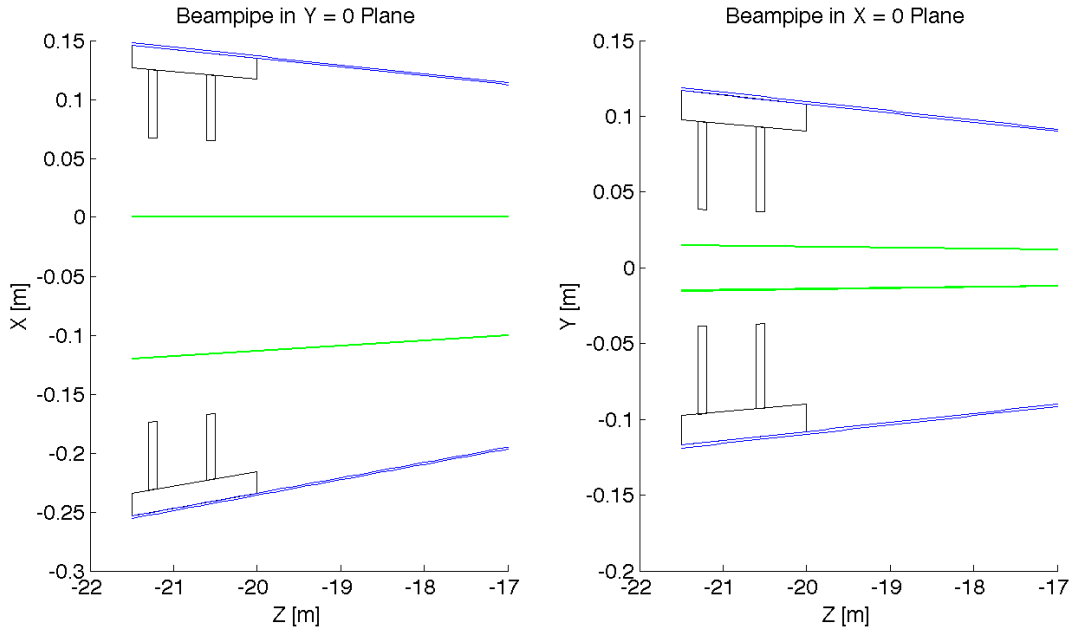


Figure 7.43: High Luminosity: Beampipe Cross Sections

5578 field value refers to the constant dipole field created throughout all dipole elements in the IR. The separation  
 5579 is the same as in the high luminosity case and can be altered for the same reasons with the same ramifica-  
 5580 tions. The chosen parameters give a flux of  $6.41 \times 10^{18}$  photons per second at  $Z = -21.5$  m, which is slightly  
 5581 higher than in the high luminosity case. This is expected as the fields experienced in the high acceptance  
 5582 case are higher.

### 5583 Power and Critical Energy

5584 Table 7.25 shows the power of the SR produced by each element along with the average critical energy  
 5585 produced per element. This is followed by the total power produced in the IR and the average critical  
 5586 energy. Since the G4 simulations utilize Monte Carlo, multiple runs should be made with various seeds to  
 5587 get an estimate for the standard error.

Element	Power [kW]	Critical Energy [keV]
DL	13.9	118
QL2	6.2	318
QL1	5.4	294
QR1	5.4	293
QR2	6.3	318
DR	13.9	118
Total/Avg	51.1	163

Table 7.25: High Acceptance: Power and Critical Energies [Geant4]

5588 The distribution of power and critical energy over the IR elements is similar to that of the high acceptance  
 5589 option with the exception of the upstream and downstream separator dipole magnets. The power and

critical energies are significantly higher than before. This is due to the higher dipole field and the quadratic dependence of power on magnetic field and linear dependence of critical energy on magnetic field. [575]

**Comparison**

The IRSYN cross check of the power and critical energies is shown in Table 7.26. This comparison was done for the total power and the critical energy.

	Power [kW]		Critical Energy [keV]	
	Geant4	IRSYN	Geant4	IRSYN
Total/Avg	51.1	51.3	163	162

Table 7.26: High Acceptance: Geant4 and IRSYN comparison

A third cross check to the G4 simulations was also made for the power as shown in Table 7.27. This was done using an analytic method for calculating power in dipole and quadrupole magnets. [574] This comparison provides confidence in the distribution of the power throughout the IR.

Element	Power [kW]	
	Geant4	Analytic
DL	13.9	14
QL2	6.2	6.2
QL1	5.4	5.3
QR1	5.4	5.3
QR2	6.3	6.2
DR	13.9	14
Total	51.1	51

Table 7.27: High Acceptance: Geant4 and Analytic method comparison

**Number Density and Envelopes**

The number density of photons as a function of Z is shown in Figure 7.44. The horizontal extension of the fan in the high acceptance case is larger than in the high luminosity case however still lower than in the LR option. Since the beam stays at a constant angle for the first 6.2 m after the IP it requires larger fields to bend in order to reach the desired separation. This means that an overall larger angle is reached near the absorber, and since the S shaped trajectory is symmetric in Z the angle of the beam at the entrance of the upstream quadrupoles is also larger and therefore the fan extends further in X.

The envelope of the SR fan can be seen in Figure 7.45, where the XZ plane is shown at the value Y = 0. Once again the fan is antisymmetric due to the S shape of the electron beam.

**Critical Energy Distribution**

The critical energy distribution in Z is similar to that of the high luminosity case. This is due to the focusing of the beam in the IR. This is evident from Figure 7.46.

**Absorber**

Looking at Figure 7.47 it is shown that for the high acceptance option 38.5 kW of power from the SR light will fall on the face of the absorber which is 75% of the total power. This gives a general idea of the amount of

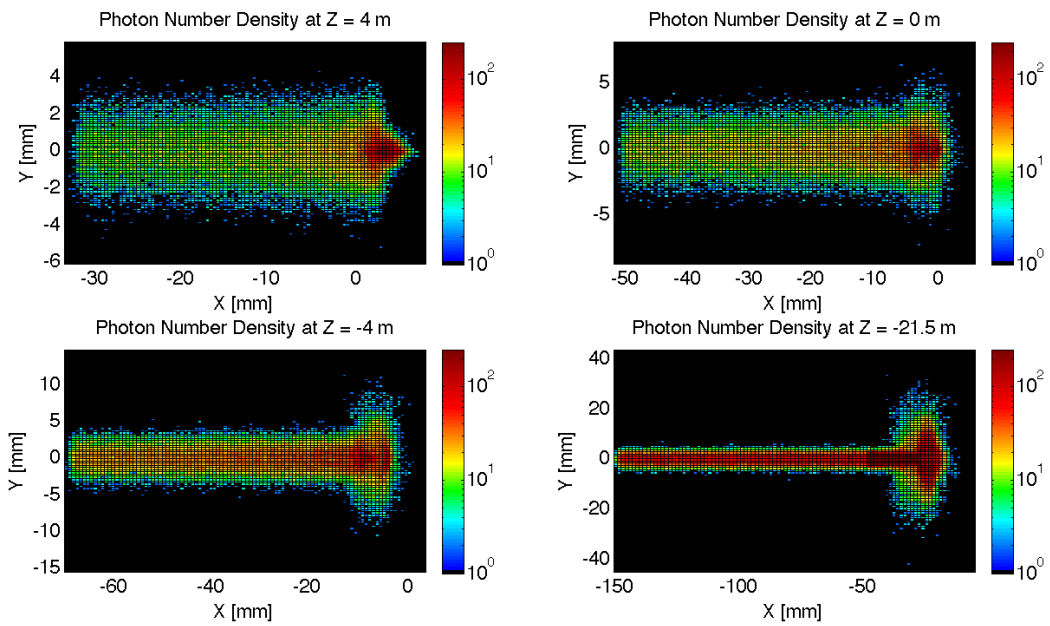


Figure 7.44: High Acceptance: Number Density Growth in Z

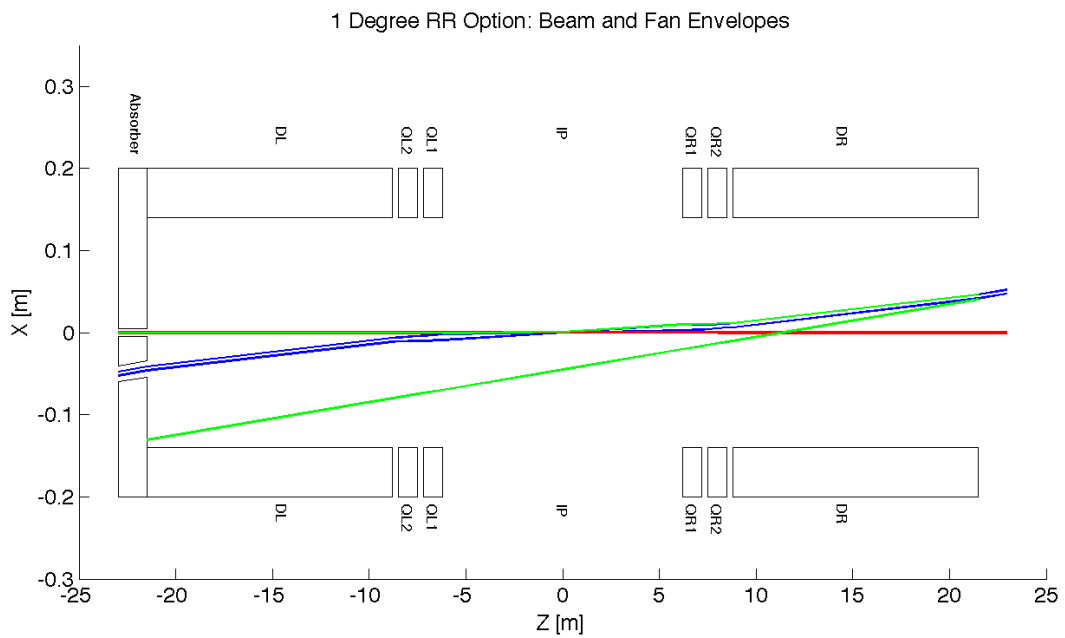


Figure 7.45: High Acceptance: Beam Envelopes in Z

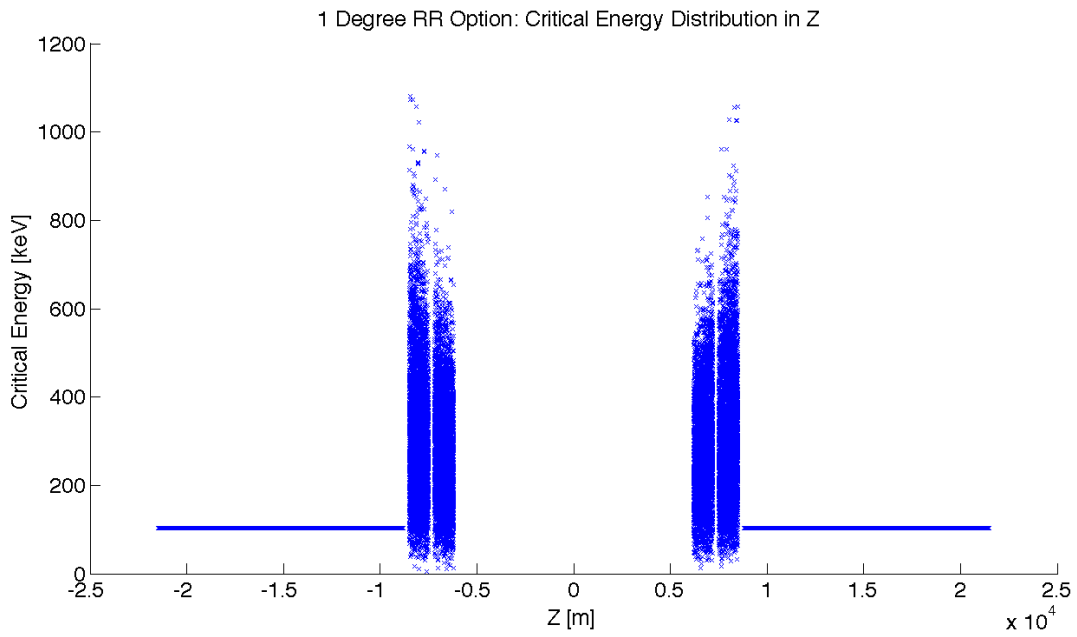


Figure 7.46: High Acceptance: Critical Energy Distribution in Z

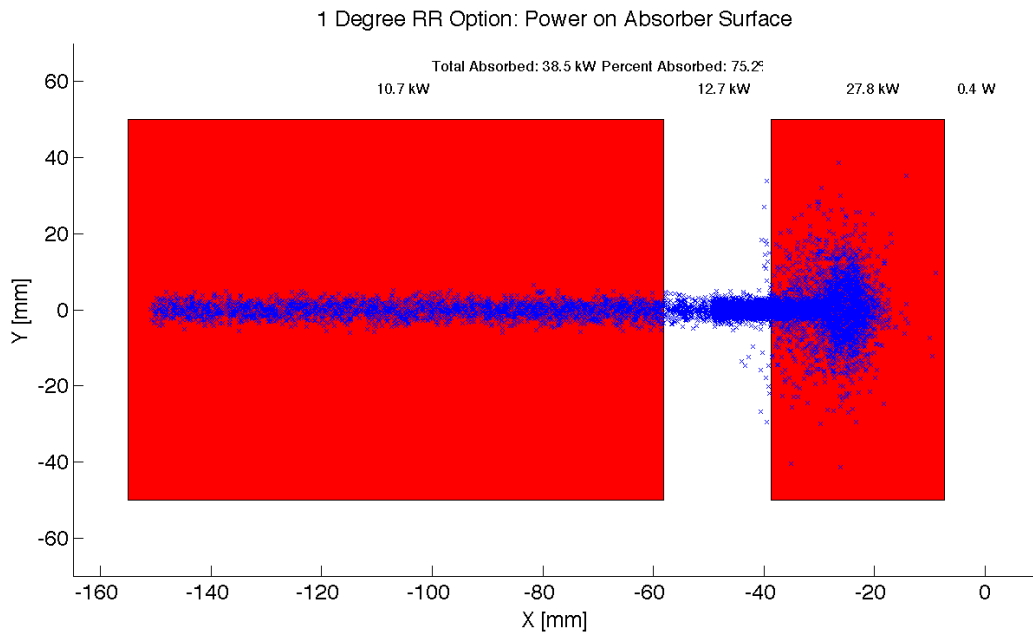


Figure 7.47: High Acceptance: Photon distribution on Absorber Surface

5613 power that will be absorbed. However, backscattering and IR photons will lower the percent that is actually  
5614 absorbed.

### 5615 Proton Triplet

5616 The super conducting final focusing triplet for the protons needs to be protected from radiation by the  
5617 absorber. Some of the radiation produced upstream of the absorber however will either pass through the  
5618 absorber or pass through the apertures for the two interacting beams. This is most concerning for the  
5619 interacting proton beam aperture which will have the superconducting coils. A rough upper bound for  
5620 the amount of power the coils can absorb before quenching is 100 W. [577] In the high acceptance option  
5621 there is approximately 0.4 W entering into the interacting proton beam aperture as is shown in Figure 7.47.  
5622 Therefore for the high acceptance option this is not an issue. The amount of power that will pass through  
5623 the absorber can be disregarded as it is not enough to cause any significant effects. The main source of  
5624 power moving downstream of the absorber will be the photons passing through the beams aperture. This  
5625 was approximately 12.7 kW as can be seen from Figure 7.47. Most of this radiation can be absorbed in  
5626 a secondary absorber placed after the first downstream proton quadrupole. Overall protecting the proton  
5627 triplet is important and although the absorber will minimize the radiation continuing downstream this needs  
5628 to be studied in depth.

### 5629 Backscattering

5630 Another Geant4 program was written to simulate the backscattering of photons into the detector region.  
5631 The ntuple with the photon information written at the absorber surface is used as the input for this program.  
5632 An absorber geometry made of copper is described, and general physics processes are set up. A detector  
5633 volume is then described and set to record the information of all the photons which enter in an ntuple. The  
5634 first step in minimizing the backscattering was to optimize the absorber shape. Although the simulation  
5635 didnt include a beam pipe the backscattering for different absorber geometries was compared against one  
5636 another to find a minimum. The most basic shape was a block of copper that had cylinders removed for the  
5637 interacting beams. This was used as a benchmark to see the maximum possible backscattering. In HERA a  
5638 wedge shape was used for heat dissipation and minimizing backscattering. [576] The profile of two possible  
5639 wedge shapes in the YZ plane is shown in Figure 7.48. It was found that this is the optimum shape for  
5640 the absorber. The reason for this is that a backscattered electron would have to have its velocity vector be  
5641 almost parallel to the wedge surface to escape from the wedge and therefore it works as a trap. As can be  
5642 seen from Table 7.28 utilizing the wedge shaped absorber decreased the backscattered power by a factor of  
5643 9.

5644 After the absorber was optimized it was possible to set up a beam pipe geometry. An asymmetric  
5645 elliptical cone beam pipe geometry made of beryllium was used since it would minimize the necessary size  
5646 of the beam pipe as previously mentioned. The next step was to place the lead shield and masks inside this  
5647 beam pipe. To determine placement a simulation was run with just the beam pipe. Then it was recorded  
5648 where each backscattered photon would hit the beam pipe in Z. This determined that the shield should be  
5649 placed in the Z region ranging from -20 m until the absorber (-21.5 m). The shields were then placed at -21.2  
5650 m and -20.6 m. This decreased the backscattered power to zero as can be seen from Table 7.28. Although  
5651 this is promising this number should be checked again with higher statistics to judge its accuracy. Overall  
5652 there is still more optimization that can occur with this placement.

Absorber Type	Power [W]
Flat	91.1
Wedge	10
Wedge & Mask/Shield	0

Table 7.28: High Acceptance: Backscattering/Mask

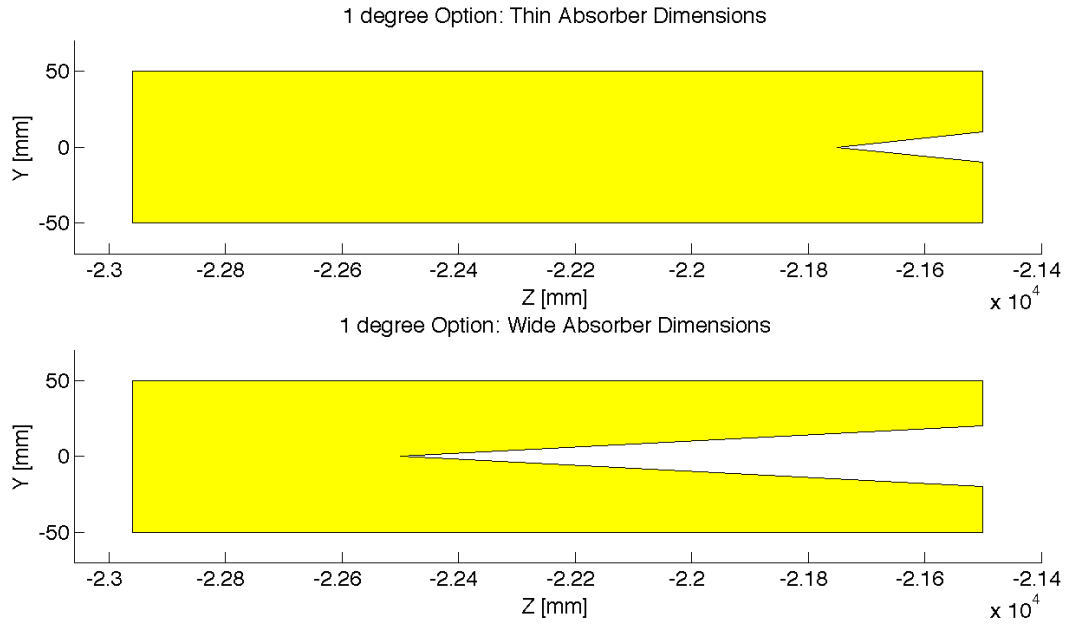


Figure 7.48: 1 deg: Absorber Dimensions

5653 Cross sections of the beam pipe in the  $Y = 0$  and  $X = 0$  planes with the shields and masks included can  
 5654 be seen in Figure 7.49.

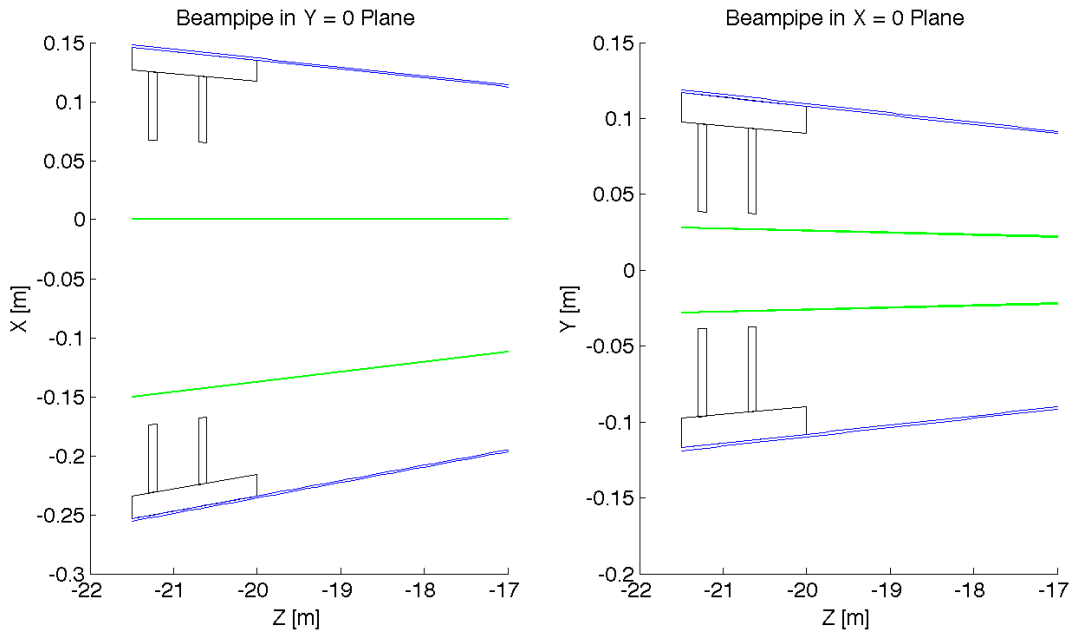


Figure 7.49: High Acceptance: Beampipe Cross Sections

## 7.13 Beam-beam effects in the LHeC

In the framework of the Large Hadron electron Collider a ring-ring option is considered where protons of one beam collide with the protons of the second proton beam as well as with leptons from a separate ring. To deduce possible limitations the present knowledge of the LHC beam-beam effects from proton-proton collisions are fundamental to define parameters of an interaction point with electron-proton collisions. From past experience it is known that the maximum achievable luminosity in a collider is limited by beam-beam effects. These are often quantified by the maximum beam-beam tune shifts in each of the two beams. An important aspect in electron-proton collisions is that the proton beam, more sensitive to transverse noise, could be perturbed by a higher level of noise in the electron beam. In this section we will assess some limits to the possible tune shift achievable in collision based on experience from past colliders as CESR [578] and LEP [579] and more recent ones like the LHC [580].

### 7.13.1 Head-on beam-beam effects

A first important performance issue in beam-beam interaction comes from the restricted choice of the  $\beta$ -function at the interaction point to keep the transverse beam sizes equal for the two beams since proton and electron emittances are different. The choice of beta functions at the interaction point has to be different for the two beams in order to keep  $\sigma_x^e = \sigma_x^p$  and  $\sigma_y^e = \sigma_y^p$  for the reasons explained in detail in [581]. In a mismatched collision the larger bunch may suffer more because a large part of the particle distribution will experience the non-linear beam-beam force of the other bunch. With this in mind it is preferable to keep the electron beam slightly larger than the proton beam since the electron beam may be less sensitive due to strong radiation damping. This matching implies that the electron emittances must be controlled during operation and kept as constant as possible (i.e. H/V coupling). For the proton beam the beam-beam effects from the electron beam will be different for the two planes. Optical matching of the beam sizes at the IP is the first constraint for any interaction region layout proposed.

Another important issue is the achievable tune shift and how this relates to the linear beam-beam parameter which is normally the parameter used to evaluate the strength of the beam-beam interaction.

The linear beam-beam parameter is defined as  $\xi_{bb}$  and is expressed for the case of round beams like in proton-proton collision at the LHC as:

$$\xi_{bb} = \frac{Nr_p\beta^*}{4\pi\gamma\sigma^2} \quad (7.12)$$

where  $r_p$  is the classical proton radius,  $\beta^*$  is the optical amplitude function ( $\beta$ -function) at the interaction point,  $\sigma = \sigma_{x,y}$  is the transverse beam size in meters at the interaction point,  $N_p$  is the bunch intensity and  $\gamma$  is the relativistic factor. For proton-proton collisions where  $\xi_{bb}$  does not reach too large values and the operational tune is far enough away from linear resonances, this parameter is about equal to the linear tune shift  $\Delta Q$  expected from the head-on beam-beam interaction. This is the case for the LHC proton-proton collisions at IP1 and IP5 where the linear tune shift per IP is of the order of 0.0034/0.0037 for nominal beam parameters as summarized in Table 7.29 and corresponds to the linear beam-beam parameter  $\xi_{bb}$ . This is in general not true for lepton colliders where the operational scenario differs from hadron colliders and other effects become dominant and have to be taken into account.

In the case of electron beams the transverse shape of the beams is normally elliptical with  $\sigma_x > \sigma_y$ . In this configuration one can generalize the linear beam-beam parameter calculation with the following formula [582]:

$$\xi_{x,y} = \frac{Nr_e\beta_{x,y}^*}{2\pi\gamma\sigma_{x,y}(\sigma_x + \sigma_y)} \quad (7.13)$$

with  $r_e$  is the electron classical radius.

In the case of electron-proton collisions one has to also take into account the different species during collision and the beam-beam parameters become:

Parameter	LEP	LHC (nominal)
Beam sizes	180 $\mu\text{m}$ $\cdot$ 7 $\mu\text{m}$	16.6 $\mu\text{m}$ $\cdot$ 16.6 $\mu\text{m}$
Intensity N	4.0 $\cdot$ 10 <sup>11</sup> /bunch	1.15 $\cdot$ 10 <sup>11</sup> /bunch
Energy	100 GeV	7000 GeV
$\beta_x^* \cdot \beta_y^*$	1.25 m $\cdot$ 0.05 m	0.55 m $\cdot$ 0.55 m
Crossing angle	0.0	0/285 $\mu\text{rad}$
Beam-beam tune shift( $\Delta Q$ )	0.0400	0.0037/0.0034

Table 7.29: Comparison of parameters for the LEP collider and the LHC.

$$\xi_{(x,y),b_1} = \frac{N_{b_2} r_{b_1} \beta_{(x,y),b_1}^*}{2\pi \gamma_{b_1} \sigma_{(x,y),b_2} (\sigma_{x,b_2} + \sigma_{y,b_2})} \quad (7.14)$$

5698 Here  $b_1$  and  $b_2$  refer to Beam1 and Beam2 respectively. The linear beam-beam parameter  $\xi$  is often used  
5699 to quantify the strength of the beam-beam interaction, however it does not reflect the non-linear nature of  
5700 the electromagnetic interaction. Nevertheless, it can be used for comparison and as a scaling parameter.  
5701 Since a general beam-beam limit cannot be found and will be different from one collider to the next, the  
5702 interpretation should be conservative.

5703 In Table 7.29 we compare LEP and LHC beam parameters and achieved linear beam-beam parameters.  
5704 Some of the differences are striking: while the beams in the LHC are round at the interaction point, they are  
5705 very flat in LEP. This is due to the excitation of the beam in the horizontal plane by the strong synchrotron  
5706 radiation and damping in the vertical plane. Another observation is the much larger beam-beam parameter  
5707 in LEP.

5708 One reason for the larger achievable beam-beam parameter in lepton colliders is due to a significant  
5709 dynamic beta effect when operating at a working point close to integer tune. This is considered more  
5710 difficult with proton beams. In Equation 7.15 the perturbed  $\beta^*$  is expressed as a function of the beam-beam  
5711 parameter  $\xi$  and the phase advance between two interaction points  $2\pi Q^i$ . The tune shift  $\Delta Q$  becomes a  
5712 function of the tune which can be chosen to keep the actual shift small.

$$\beta^*(Q, \xi) = \frac{\beta}{\sqrt{1 + 4\pi\xi(\cot(2\pi Q^i)) - 4\pi^2\xi^2}} \quad (7.15)$$

5713 From experience it is known that electrons have a bigger range for the linear head-on beam-beam param-  
5714 eter: LEP II has proved an unperturbed beam-beam parameter of 0.07 per interaction point corresponding  
5715 to a measured  $\Delta Q$  of 0.03 - 0.04 as also confirmed in other lepton colliders. The large difference between the  
5716 beam-beam parameter and the achieved tune shift was due to the strong dynamic  $\beta$  effect in LEP. CESR  
5717 demonstrated the possibility to achieve tune shifts of the order of 0.09. A second and most important reason  
5718 for a higher acceptable tune shift in lepton colliders is the synchrotron radiation damping. Furthermore,  
5719 while for lepton colliders a clear indication for a "beam-beam limit" exists, not such criteria can be easily de-  
5720 fined for hadron machines [580]. From these considerations we have to assume that the choice of beam-beam  
5721 parameters  $\xi_{bb}$  of the proton beam is restricted.

5722 The LHC as a proton-proton collider has confirmed previous experience from  $Spp\bar{p}S$  and Tevatron that  
5723 a total linear tune shift of 0.018 (0.006 per IP) is tolerable with neither important losses nor reduction of  
5724 beam lifetime during normal operation. It is generally admitted that  $\xi_{bb}$  could reach a value of 0.01 per  
5725 interaction point. Recent experiments at the LHC with very high intensity beams beyond ultimate and  
5726 reduced transverse beam sizes demonstrated the possibility to reach head-on tune shifts well beyond the  
5727 nominal values [580]. At the LHC tune shifts per IP close to 0.02 have been achieved. Total tune shifts  
5728 exceeding 0.034 have also been achieved with stable beams for two symmetric crossings at IP1 and IP5. These  
5729 latest experiments demonstrate the possibility to operate with larger than nominal beam-beam parameters.



IR Option	1 degree		10 degree	
	Electrons	Protons	Electrons	Protons
Beams	Electrons	Protons	Electrons	Protons
Energy	60 GeV	7 TeV	60 GeV	7 TeV
Intensity	$2 \cdot 10^{10}$	$1.7 \cdot 10^{11}$	$2 \cdot 10^{10}$	$1.7 \cdot 10^{11}$
$\beta_x^*$	0.4 m	4.05 m	0.18 m	1.8 m
$\beta_y^*$	0.2 m	0.97 m	0.1 m	0.5 m
$\epsilon_x$	5 nm	0.5 nm	5 nm	0.5 nm
$\epsilon_y$	2.5 nm	0.5 nm	2.5 nm	0.5 nm
$\sigma_x$	45 $\mu\text{m}$		30 $\mu\text{m}$	
$\sigma_y$	22 $\mu\text{m}$		15.8 $\mu\text{m}$	
Crossing angle	1 mrad		1 mrad	
$\xi_{bb,x}$	0.086	0.0008	0.085	0.0008
$\xi_{bb,y}$	0.088	0.0004	0.090	0.0004
Luminosity	$7.33 \cdot 10^{32}$	$\text{cm}^{-2}\text{s}^{-1}$	$1.34 \cdot 10^{33}$	$\text{cm}^{-2}\text{s}^{-1}$

Table 7.30: Beam parameters for the interaction region options and the linear beam-beam parameters  $\xi$ .

	Nominal		Upgrade	
	Electrons	Protons	Electrons	Protons
$\xi_{bb,x}$	0.016	0.0013	0.027	0.0017
$\xi_{bb,y}$	0.018	0.0012	0.041	0.0005

Table 7.31: Linear beam-beam parameters for HERA, nominal machine and upgrade parameters.

5730 The calculated beam-beam parameters for the electron and proton beams due to an electron-proton  
5731 collision in the LHeC are summarized in Table 7.30 for the two interaction region options (1 Degree Option  
5732 and 10 Degree Option).

5733 The two proposed interaction region options will give for the proton beam a maximum beam-beam  
5734 parameter in the horizontal plane of about  $8 \cdot 10^{-4}$ . This effect is in the shadow of the proton-proton  
5735 collision at IP1 and IP5 which will give a beam-beam parameter of  $5.5 \cdot 10^{-3}$  per IP for nominal beam  
5736 emittances and assuming intensities of  $1.7 \cdot 10^{11}$  protons/bunch, which was already exceeded during 2010  
5737 operation at the LHC with reduced emittances and nominal beam intensities. One should not expect  
5738 detrimental effects of the head-on interactions with the electron beam apart from a potential coupling of  
5739 noise from the electron into the proton beam.

5740 For the electron beam, on the contrary, the beam-beam parameter of  $8.6 \cdot 10^{-2}$  is large and represents a  
5741 value at the limit of what has been achieved so far in other lepton machines (LEP at 90 GeV energy achieved  
5742 an unperturbed beam-beam parameter of 0.07, (with a maximum tune shift of 0.04) while KEK and HERA  
5743 achieved a maximum  $\xi_{bb} = 0.04$  during operation, CESR achieved a beam-beam parameter of 0.09 for single  
5744 IP but with lower luminosity). The beam-beam tune shifts achieved at HERA for the nominal and upgrade  
5745 version are summarized in Table 7.31 for comparison. The foreseen beam-beam parameter of  $8.6 \cdot 10^{-2}$  is  
5746 optimistic and a significant reduction due to dynamic beta and the small number of interaction points could  
5747 make it feasible.

IR Option	1 degree		10 degree	
Beams	Electrons	Protons	Electrons	Protons
$\beta_x^*$	0.4 m	4.05 m	0.18 m	1.8 m
$\beta_y^*$	0.2 m	0.97 m	0.1 m	0.5 m
$\epsilon_x$	5 nm	0.5 nm	5 nm	0.5 nm
$\epsilon_y$	2.5 nm	0.5 nm	2.5 nm	0.5 nm
Crossing angle	1 mrad		1 mrad	
$d_x$	$90 \sigma_p$	$8.94 \sigma_e$	$60 \sigma_p$	$6.0 \sigma_e$

Table 7.32: Normalized beam separation  $d_x$  at beam-beam long range encounters for the two interaction region options.

### 7.13.2 Long range beam-beam effects

So far we have discussed head-on beam-beam interactions but an important issue are the long range interactions which will occur at the electron-proton collision and their interplay with the proton-proton crossings at IP1 and IP5. The two interaction points IP1 and IP5 will give up to 60 proton-proton long-range interactions which should be added to the two interaction region options which will give two additional parasitic encounters. The beam separation at this encounters should be as large as possible to reduce any non-linear perturbation. The parasitic encounters occur every 3.75 m from the interaction point for a bunch spacing of 25 ns. The proposed optics will then lead to parasitic beam-beam interactions which will occur at a transverse separation  $d$  as:

$$d(s)_{x,y} = \alpha \frac{s}{\sqrt{\epsilon_{x,y} \beta(s)_{x,y}}} \quad (7.16)$$

with  $\epsilon_{x,y}$  are the beam emittance in the separation plane and  $\beta(s)$  is the betatron function at a distance  $s$  from the interaction point.

In Table 7.32 the distances of the parasitic encounters in units of the transverse beam sizes are shown for both interaction region layouts.

The 1 degree option gives long range interactions at larger separation with respect to the 10 degree option which results in small separations of  $\approx 6 \sigma$  for the proton beam. Particles in the tail of the proton beam particles will experience the non linearity of the electron beam electromagnetic force. The presence of two long range at  $6 \sigma$  separation may be acceptable since it is shown experimentally that few encounters also at smaller separation do not affect the beams dramatically [583]. However, the interplay of these two encounters with the long-range interactions from IP1 and IP5 should be studied in detail with numerical simulation to highlight possible limitations. In this framework future experiments at the LHC will help defining a possible beam parameters space for the control of the long-range effects from proton-proton collisions. If encounters at  $6 \sigma$  present a limitation to the collider performance then a possible cure to increase the long-range separation could be a further increase of the crossing angle and using crab cavities can recover the increased geometric luminosity reduction factor. In this case a study of the crab cavities effects on the proton beam would be essential to define the effects of transverse noise on colliding beams.

For any reliable study of the LHeC project one has to address other possible beam-beam issues with extensive numerical simulations of the operational scenario of the LHeC. This is fundamental since there is no other possible simplification which can be adopted in evaluating the non-linear parts of the beam-beam forces. For this reason a detailed and full interaction layout with crossing schemes matched in thin lens version is needed. With the complete optic layout beam-beam effects which still need further studies by means of numerical simulation campaign are the following:

- Long-range tune shifts and orbit effects.
- Self-consistent study of the proton-proton and electron-proton beam dynamics interplay.

- 5781 • Dynamic aperture tracking studies.
- 5782 • Multi-bunch effects.
- 5783 • Noise coupling from the electron to the proton beam.

5784 The evaluation of the non-linear effects of the beam-beam interactions with self-consistent calculations will  
 5785 define a set of parameters for operation [584].

## 5786 7.14 Performance as an electron-ion collider

### 5787 7.14.1 Heavy nuclei, e-Pb collisions

5788 With the first collisions of lead nuclei ( $^{208}\text{Pb}^{82+}$ ) in 2010 [382, 585], the LHC has already demonstrated  
 5789 its capability as a heavy-ion collider and this naturally opens up the possibility of electron-nucleus (e-A)  
 5790 collisions in the LHeC.

5791 In order to avoid interference with the high luminosity proton-proton operation, this mode of operation  
 5792 would naturally be included in the annually-scheduled ion operation period of the LHC. In principle, the  
 5793 CERN complex could provide A-A (or even p-A) collisions to the LHC experiments while the LHeC operates  
 5794 with e-A collisions. The lifetime of the nuclear beam would depend mainly on whether it was exposed to  
 5795 the losses from A-A luminosity in the LHC (in this case it would be at least a few hours).

5796 In the first decade or so of LHC operation, the ion injector chain is expected to provide mainly  $^{208}\text{Pb}^{82+}$ ,  
 5797 but also other species such as  $^{40}\text{Ar}^{18+}$  or  $^{129}\text{Xe}^{54+}$ , either to the LHC or from the SPS to fixed target  
 5798 experiments in the North Area. These beams could also be collided with electrons in the LHeC but solid  
 5799 intensity estimates are not yet available for the lighter ions. For simplicity, we shall estimate LHeC perfor-  
 5800 mance in e-Pb collisions with the design performance values of the ion injector chain as described in [586]  
 5801 and the assumption of a single nuclear beam in one ring of the LHC with parameters as recalled from [587]  
 5802 in Table 7.33. It is assumed that present uncertainties about the Pb intensity limits at full energy in the  
 5803 LHC will have been resolved, if necessary, by installation of new collimators in the dispersion suppressors of  
 5804 the collimation insertions in the LHC. This simplifies the discussion because the design emittances of Pb and  
 5805 proton beams in the LHC are such that both species have the same geometric beam sizes and considerations  
 5806 of optics and aperture can be taken over directly. The “Ultimate Pb” value of the Pb single bunch intensity  
 5807 was already attained in 2010 [585] using a simplified injection scheme but not yet with the nominal filling  
 5808 scheme for 592 bunches; it can be considered an optimistic goal. At present, there are no prospects for  
 5809 increasing the number of bunches significantly. Lower Pb emittances may be possible but would not increase  
 5810 e-Pb luminosity unless matched with smaller optical functions or emittances for the electron beam.

		Design Pb	Ultimate Pb
Energy	$E_{\text{Pb}}$	574. TeV	
Energy per nucleon	$E_N$	2.76 TeV	
No. of bunches	$n_b$	592	
Ions per bunch	$N_{\text{Pb}}$	$7. \times 10^7$	$1.2 \times 10^8$
Normalised emittance	$\varepsilon_n$	$1.5 \mu\text{m}$	

Table 7.33: Parameters for the  $^{208}\text{Pb}^{82+}$  beam according to Chapter 21 of [587].

5811 Assume that the injection system can create an electron bunch train matching the 592-bunch train of Pb  
 5812 nuclei in the LHC so that every Pb bunch finds a collision partner in the electron beam. Assuming further  
 5813 that the hadron optics can be adjusted to match the sizes of the electron and Pb beams, the luminosity  
 5814 can be expressed in terms of the interaction point optical functions and emittances of the electron beam.

5815 Since the e-A physics is focused on low- $x$  these are taken from Table 7.14 describing the Ring-Ring High  
 5816 Acceptance optics, which reduces the luminosity by a factor 2 as compared with the High-Luminosity optics.

5817 In e-p mode, the intensity of the 2808 electron bunches,  $N_e$  is limited for the Ring-Ring version of the  
 5818 LHeC by the total RF power available to compensate the synchrotron radiation loss. For the same power  
 5819 (some 44 MW for  $N_e = 2 \times 10^{10}$  of Table ??), the intensity of the  $n_b = 592$  bunches required to collide  
 5820 with the Pb nuclei can be increased by a factor 2808/592 to  $N_e = 9.5 \times 10^{10}$ . Electron beam parameters  
 5821 for the LHeC Ring-Ring option other than the single bunch intensity can be taken from Table ?. Present  
 5822 experience with beam-beam effects in the LHC suggests that the additional electron intensity would not  
 5823 present any problem for the proton beam. The single-bunch intensity is still well below that achieved in  
 5824 LEP although the feasibility of these values should be confirmed by further analysis of the ring impedance  
 5825 and collective effects.

5826 Neglecting the geometric reduction factor due to the crossing angle and the hourglass effect, the *electron-*  
 5827 *nucleon* luminosity,  $L_{eN} = AL_{eA}$ , is then given by

$$L_{eN} = \frac{n_b f_0 N_e (AN_{\text{Pb}})}{4\pi \sqrt{\beta_{xe}^*} \varepsilon_x \sqrt{\beta_{ye}^*} \varepsilon_y} = \begin{cases} 2.6 \times 10^{31} \text{ cm}^{-2}\text{s}^{-1} & \text{(Nominal Pb)} \\ 4.5 \times 10^{31} \text{ cm}^{-2}\text{s}^{-1} & \text{(Ultimate Pb)} \end{cases} \quad (7.17)$$

5828 This gives an indication of the range of peak luminosities that can be expected. A factor of 2 could be gained  
 5829 by switching to the high-luminosity interaction region optics.

5830 By the time the LHeC comes into operation, it is not unreasonable to hope that ways to increase the  
 5831 number of Pb bunches and perhaps to reduce their emittance (by cooling) may be implemented. Therefore,  
 5832 on an optimistic view, the luminosity could be even higher than the value quoted here.

5833 Finally, we note that the dependence of luminosity on electron beam energy ( $\propto E_e^{-6}$ ) is very strong at  
 5834 the power limit so that a trade-off between energy and luminosity may be of interest.

## 5835 7.14.2 Electron-deuteron collisions

5836 As discussed in [377], deuteron beams are not presently available in the CERN complex. Meanwhile it has  
 5837 been clearly demonstrated [588] that it would not be feasible to set up a  $D^-$  source and accelerate them  
 5838 via Linac4. The present proton Linac2 is due to be shut down so the only way to accelerate them would  
 5839 be via the heavy ion Linac3. However this would require a new source, RFQ and switch-yard at the input  
 5840 to Linac3. The study of practical feasibility, space limitations, design and potential performance of these  
 5841 modifications to the injector complex will start only in late 2011 with a view to supplying D and other light  
 5842 ions to fixed target experiments and the LHC in several years' time.

5843 Assuming that a practical design can be implemented, the intensity of bunches in the LHC ring can be  
 5844 estimated as follows.

5845 The present GTS-LHC source delivers  $^{208}\text{Pb}^{29+}$  ions with a charge-to-mass ratio  $Q/A = 1/7.2$ . A  
 5846 safe estimate of the space-charge limit at the entrance of Linac3 is  $200 \mu\text{A}$ . To accelerate deuterons with  
 5847  $Q/A = 1/2$ , all magnetic and electric fields would have to be reduced by a factor 3.6, leading to a space-charge  
 5848 limited current of  $55 \mu\text{A}$ .

5849 However there is then a very comfortable margin in the electric and magnetic fields and deuterons are  
 5850 not subject to the loss factors associated with the subsequent stripping stages for Pb. If enough deuteron  
 5851 current is available from the source (say 5 mA), and one accepts losses in the linac and a somewhat degraded  
 5852 beam quality at the end, then a current in the range of 200-500  $\mu\text{A}$  would probably be available at the end  
 5853 of the linac.

5854 As a caveat, early measurements of poor transmission of helium ions in Linac3 [589] should be mentioned.  
 5855 However the explanation is unclear due to the lack of appropriate diagnostics.

5856 The bunch number and filling pattern in the LHC would be similar to that of the Pb beam. A naive  
 5857 transposition of the scaling of the ratios of Linac3 output current ( $50 \mu\text{A}$ ) to LHC bunch intensity ( $7 \times 10^7$ )  
 5858 from Pb to deuterons would suggest that the deuteron single-bunch intensity in the LHC could be  $N_D \approx$   
 5859  $1.5 \times 10^{10}$ .

5860 However this does not consider the differences in performance of the remainder of the injector chain (the  
5861 LEIR cooling ring, PS and SPS synchrotrons). A proper evaluation of these requires a more detailed study.  
5862 To be safe, we can apply a factor 5 reduction to this value.

5863 Then, assuming that we collide such a beam with the electron beam described in the preceding sub-  
5864 section, we see that *electron-nucleon* luminosities of order  $L_{eN} \gtrsim 10^{31} \text{ cm}^{-2}\text{s}^{-1}$  could be accessible in e-D  
5865 collisions at the LHeC.

## 5866 7.15 Spin polarisation – an overview

5867 Before describing concepts for attaining electron and positron spin polarisation for the ring-ring option of  
5868 the LHeC we present a brief overview of the theory and phenomenology. We can then draw on this later as  
5869 required. This overview is necessarily brief but more details can be found in [590,591].

### 5870 7.15.1 Self polarisation

5871 The spin polarisation of an ensemble of spin-1/2 fermions with the same energies travelling in the same  
5872 direction is defined as

$$\vec{P} = \left\langle \frac{2}{\hbar} \vec{\sigma} \right\rangle \quad (7.18)$$

5873 where  $\vec{\sigma}$  is the spin operator in the rest frame and  $\langle \rangle$  denotes the expectation value for the mixed spin  
5874 state. We denote the single-particle rest-frame expectation value of  $\frac{2}{\hbar} \vec{\sigma}$  by  $\vec{S}$  and we call this the “spin”.  
5875 The polarisation is then the average of  $\vec{S}$  over an ensemble of particles such as that of a bunch of particles.

5876 Electrons and positrons circulating in the (vertical) guide field of a storage ring emit synchrotron radiation  
5877 and a tiny fraction of the photons can cause spin flip from up to down and vice versa. However, the up-  
5878 to-down and down-to-up rates differ, with the result that in ideal circumstances the electron (positron)  
5879 beam can become spin polarised anti-parallel (parallel) to the field, reaching a maximum polarisation,  $P_{\text{st}}$ ,  
5880 of  $\frac{8}{5\sqrt{3}} = 92.4\%$ . This, the Sokolov-Ternov (S-T) polarising process, is very slow on the time scale of other  
5881 dynamical phenomena occurring in storage rings, and the inverse time constant for the exponential build up  
5882 is [592]:

$$\tau_{\text{st}}^{-1} = \frac{5\sqrt{3}}{8} \frac{r_e \gamma^5 \hbar}{m_e |\rho|^3} \quad (7.19)$$

5883 where  $r_e$  is the classical electron radius,  $\gamma$  is the Lorentz factor,  $\rho$  is the radius of curvature in the magnets  
5884 and the other symbols have their usual meanings. The time constant is usually in the range of a few minutes  
5885 to a few hours.

5886 However, even without radiative spin flip, the spins are not stationary but precess in the external fields.  
5887 In particular, the motion of  $\vec{S}$  for a charged particle travelling in electric and magnetic fields is governed by  
5888 the Thomas-BMT equation  $d\vec{S}/ds = \vec{\Omega} \times \vec{S}$  where  $s$  is the distance around the ring [591,593]. The vector  $\vec{\Omega}$   
5889 depends on the electric ( $\vec{E}$ ) and magnetic ( $\vec{B}$ ) fields, the energy and the velocity ( $\vec{v}$ ) which evolves according  
5890 to the Lorentz equation:

$$\vec{\Omega} = \frac{e}{m_e c} \left[ - \left( \frac{1}{\gamma} + a \right) \vec{B} + \frac{a\gamma}{1+\gamma} \frac{1}{c^2} (\vec{v} \cdot \vec{B}) \vec{v} + \frac{1}{c^2} \left( a + \frac{1}{1+\gamma} \right) (\vec{v} \times \vec{E}) \right] \quad (7.20)$$

$$= \frac{e}{m_e c} \left[ - \left( \frac{1}{\gamma} + a \right) \vec{B}_{\perp} - \frac{g}{2\gamma} \vec{B}_{\parallel} + \frac{1}{c^2} \left( a + \frac{1}{1+\gamma} \right) (\vec{v} \times \vec{E}) \right]. \quad (7.21)$$

5891 Thus  $\vec{\Omega}$  depends on  $s$  and on the position of the particle  $u \equiv (x, p_x, y, p_y, l, \delta)$  in the 6-D phase space of  
5892 the motion. The coordinate  $\delta$  is the fractional deviation of the energy from the energy of a synchronous  
5893 particle (“the beam energy”) and  $l$  is the distance from the centre of the bunch. The coordinates  $x$  and  $y$  are

5894 the horizontal and vertical positions of the particle relative to the reference trajectory and  $p_x = x', p_y = y'$   
5895 (except in solenoids) are their conjugate momenta. The quantity  $g$  is the appropriate gyromagnetic factor  
5896 and  $a = (g - 2)/2$  is the gyromagnetic anomaly. For  $e^\pm$ ,  $a \approx 0.0011596$ .  $\vec{B}_\parallel$  and  $\vec{B}_\perp$  are the magnetic fields  
5897 parallel and perpendicular to the velocity.

5898 In a simplified picture, the majority of the photons in the synchrotron radiation do not cause spin flip but  
5899 tend instead to randomise the  $e^\pm$  orbital motion in the (inhomogeneous) magnetic fields. Then, if the ring is  
5900 insufficiently-well geometrically aligned and/or if it contains special magnet systems like the “spin rotators”  
5901 needed to produce longitudinal polarisation at a detector (see below), the spin-orbit coupling embodied in  
5902 the Thomas-BMT equation can cause spin diffusion, i.e. depolarisation. Compared to the S-T polarising  
5903 effect the depolarisation tends to rise very strongly with beam energy. The equilibrium polarisation is then  
5904 less than 92.4% and will depend on the relative strengths of the polarisation and depolarisation processes. As  
5905 we shall see later, even without depolarisation certain dipole layouts can reduce the equilibrium polarisation  
5906 to below 92.4%.

5907 Analytical estimates of the attainable equilibrium polarisation are best based on the Derbenev-Kondratenko  
5908 (D-K) formalism [594, 595]. This implicitly asserts that the value of the equilibrium polarisation in an  $e^\pm$   
5909 storage ring is the same at all points in phase space and is given by

$$P_{\text{dk}} = \mp \frac{8}{5\sqrt{3}} \frac{\oint ds \left\langle \frac{1}{|\rho(s)|^3} \hat{b} \cdot (\hat{n} - \frac{\partial \hat{n}}{\partial \delta}) \right\rangle_s}{\oint ds \left\langle \frac{1}{|\rho(s)|^3} \left(1 - \frac{2}{9} (\hat{n} \cdot \hat{s})^2 + \frac{11}{18} \left| \frac{\partial \hat{n}}{\partial \delta} \right|^2 \right) \right\rangle_s} \quad (7.22)$$

5910 where  $\langle \rangle_s$  denotes an average over phase space at azimuth  $s$ ,  $\hat{s}$  is the direction of motion and  $\hat{b} = (\hat{s} \times \dot{\hat{s}})/|\dot{\hat{s}}|$ .  
5911  $\hat{b}$  is the magnetic field direction if the electric field vanishes and the motion is perpendicular to the magnetic  
5912 field.  $\hat{n}(u; s)$  is a unit 3-vector field over the phase space satisfying the Thomas-BMT equation along particle  
5913 trajectories  $u(s)$  (which are assumed to be integrable), and it is 1-turn periodic:  $\hat{n}(u; s + C) = \hat{n}(u; s)$  where  
5914  $C$  is the circumference of the ring.

5915 The field  $\hat{n}(u; s)$  is a key object for systematising spin dynamics in storage rings. It provides a reference  
5916 direction for spin at each point in phase space and it is now called the “invariant spin field” [591, 596, 597].  
5917 At zero orbital amplitude, i.e. on the periodic (“closed”) orbit, the  $\hat{n}(0; s)$  is written as  $\hat{n}_0(s)$ . For  $e^\pm$  rings  
5918 and away from spin-orbit resonances (see below),  $\hat{n}$  is normally at most a few milliradians away from  $\hat{n}_0$ .

5919 A central ingredient of the D-K formalism is the implicit assumption that the  $e^\pm$  polarisation at each  
5920 point in phase space is parallel to  $\hat{n}$  at that point. In the approximation that the particles have the same  
5921 energies and are travelling in the same direction, the polarisation of a bunch measured in a polarimeter at  
5922  $s$  is then the ensemble average

$$\vec{P}_{\text{ens,dk}}(s) = P_{\text{dk}} \langle \hat{n} \rangle_s . \quad (7.23)$$

5923 In conventional situations in  $e^\pm$  rings,  $\langle \hat{n} \rangle_s$  is very nearly aligned along  $\hat{n}_0(s)$ . The *value* of the ensemble  
5924 average,  $P_{\text{ens,dk}}(s)$ , is essentially independent of  $s$ .

5925 Equation 7.22 can be viewed as having three components. The piece

$$P_{\text{bk}} = \mp \frac{8}{5\sqrt{3}} \frac{\oint ds \left\langle \frac{1}{|\rho(s)|^3} \hat{b} \cdot \hat{n} \right\rangle_s}{\oint ds \left\langle \frac{1}{|\rho(s)|^3} \left(1 - \frac{2}{9} (\hat{n} \cdot \hat{s})^2 \right) \right\rangle_s} \approx \mp \frac{8}{5\sqrt{3}} \frac{\oint ds \frac{1}{|\rho(s)|^3} \hat{b} \cdot \hat{n}_0}{\oint ds \frac{1}{|\rho(s)|^3} \left(1 - \frac{2}{9} n_{0s}^2 \right)} . \quad (7.24)$$

5926 gives the equilibrium polarisation due to radiative spin flip. The quantity  $n_{0s}$  is the component of  $\hat{n}_0$  along the  
5927 closed orbit. The subscript “bk” is used here instead of “st” to reflect the fact that this is the generalisation  
5928 by Baier and Katkov [598, 599] of the original S-T expression to cover the case of piecewise homogeneous  
5929 fields. Depolarisation is then accounted for by including the term with  $\frac{11}{18} \left| \frac{\partial \hat{n}}{\partial \delta} \right|^2$  in the denominator. Finally,  
5930 the term with  $\frac{\partial \hat{n}}{\partial \delta}$  in the numerator is the so-called kinetic polarisation term. This results from the dependence  
5931 of the radiation power on the initial spin direction and is not associated with spin flip. It can normally be  
5932 neglected but is still of interest in rings with special layouts.

5933 In the presence of radiative depolarisation the rate in Eq. 7.19 must be replaced by

$$\tau_{\text{dk}}^{-1} = \frac{5\sqrt{3} r_e \gamma^5 \hbar}{8 m_e C} \oint ds \left\langle \frac{1 - \frac{2}{9} (\hat{n} \cdot \hat{s})^2 + \frac{11}{18} \left| \frac{\partial \hat{n}}{\partial \delta} \right|^2}{|\rho(s)|^3} \right\rangle_s. \quad (7.25)$$

5934 This can be written in terms of the spin-flip polarisation rate,  $\tau_{\text{bk}}^{-1}$ , and the depolarisation rate,  $\tau_{\text{dep}}^{-1}$ , as:

$$\frac{1}{\tau_{\text{dk}}} = \frac{1}{\tau_{\text{bk}}} + \frac{1}{\tau_{\text{dep}}}, \quad (7.26)$$

5935 where

$$\tau_{\text{dep}}^{-1} = \frac{5\sqrt{3} r_e \gamma^5 \hbar}{8 m_e C} \oint ds \left\langle \frac{\frac{11}{18} \left| \frac{\partial \hat{n}}{\partial \delta} \right|^2}{|\rho(s)|^3} \right\rangle_s \quad (7.27)$$

5936 and

$$\tau_{\text{bk}}^{-1} = \frac{5\sqrt{3} r_e \gamma^5 \hbar}{8 m_e C} \oint ds \left\langle \frac{1 - \frac{2}{9} (\hat{n} \cdot \hat{s})^2}{|\rho(s)|^3} \right\rangle_s. \quad (7.28)$$

5937 The time dependence for build-up from an initial polarisation  $P_0$  to equilibrium is

$$P(t) = P_{\text{ens,dk}} \left[ 1 - e^{-t/\tau_{\text{dk}}} \right] + P_0 e^{-t/\tau_{\text{dk}}}. \quad (7.29)$$

5938 In perfectly aligned  $e^\pm$  storage rings containing just horizontal bends, quadrupoles and accelerating  
 5939 cavities, there is no vertical betatron motion and  $\hat{n}_0(s)$  is vertical. Since the spins do not “see” radial  
 5940 quadrupole fields and since the electric fields in the cavities are essentially parallel to the particle motion,  
 5941  $\hat{n}$  is vertical, parallel to the guide fields and to  $\hat{n}_0(s)$  at all  $u$  and  $s$ . Then the derivative  $\frac{\partial \hat{n}}{\partial \delta}$  vanishes and  
 5942 there is no depolarisation. However, real rings have misalignments. Then there is vertical betatron motion  
 5943 so that the spins also see radial fields which tilt them from the vertical. Moreover,  $\hat{n}_0(s)$  is also tilted and  
 5944 the spins can couple to vertical quadrupole fields too. As a result  $\hat{n}$  becomes dependent on  $u$  and “fans out”  
 5945 away from  $\hat{n}_0(s)$  by an amount which usually increases with the orbit amplitudes. Then in general  $\frac{\partial \hat{n}}{\partial \delta}$  no  
 5946 longer vanishes in the dipoles (where  $1/|\rho(s)|^3$  is large) and depolarisation occurs. In the presence of skew  
 5947 quadrupoles and solenoids and, in particular, in the presence of spin rotators,  $\frac{\partial \hat{n}}{\partial \delta}$  can be non-zero in dipoles  
 5948 even with perfect alignment. The deviation of  $\hat{n}$  from  $\hat{n}_0(s)$ , and the depolarisation, tend to be particularly  
 5949 large near to the spin-orbit resonance condition

$$\nu_0 = k_0 + k_I Q_I + k_{II} Q_{II} + k_{III} Q_{III}. \quad (7.30)$$

5950 Here  $k_0, k_I, k_{II}, k_{III}$  are integers,  $Q_I, Q_{II}, Q_{III}$  are the three tunes of the synchrotron motion and  $\nu_0$  is  
 5951 the spin tune on the closed orbit, i.e. the number of precessions around  $\hat{n}_0(s)$  per turn, made by a spin on  
 5952 the closed orbit<sup>1</sup>. In the special case, or in the approximation, of no synchrotron coupling one can make  
 5953 the associations:  $I \rightarrow x$ ,  $II \rightarrow y$  and  $III \rightarrow s$ , where, here, the subscript  $s$  labels the synchrotron mode.  
 5954 In a simple flat ring with no closed-orbit distortion,  $\nu_0 = a\gamma$  where  $\gamma$  is the Lorentz factor for the nominal  
 5955 beam energy. For  $e^\pm$ ,  $a\gamma$  increments by 1 for every 441 MeV increase in beam energy. In the presence of  
 5956 misalignments and special elements like rotators,  $\nu_0$  is usually still approximately proportional to the beam  
 5957 energy. Thus an energy scan will show peaks in  $\tau_{\text{dep}}^{-1}$  and dips in  $P_{\text{ens,dk}}(s)$ , namely at around the resonances.  
 5958 Examples can be seen in figures 7.50 and 7.51 below. The resonance condition expresses the fact that the  
 5959 disturbance to spins is greatest when the  $|\tilde{\Omega}(u; s) - \tilde{\Omega}(0; s)|$  along a trajectory is coherent (“in step”) with  
 5960 the natural spin precession. The quantity  $(|k_I| + |k_{II}| + |k_{III}|)$  is called the order of the resonance. Usually,  
 5961 the strongest resonances are those for which  $|k_I| + |k_{II}| + |k_{III}| = 1$ , i.e., the first-order resonances. The next

<sup>1</sup>In fact the resonance condition should be more precisely expressed in terms of the so-called amplitude dependent spin tune [591, 596, 597]. But for typical  $e^\pm$  rings, the amplitude dependent spin tune differs only insignificantly from  $\nu_0$ .

5962 strongest are usually the so-called “*synchrotron sideband resonances*” of parent first-order resonances, i.e.  
 5963 resonances for which  $\nu_0 = k_0 \pm Q_{I,II,III} + \tilde{k}_{III} Q_{III}$  where  $\tilde{k}_{III}$  is an integer and mode *III* is associated with  
 5964 synchrotron motion. All resonances are due to the non-commutation of successive spin rotations in 3-D and  
 5965 they therefore occur even with purely linear orbital motion.

5966 We now list some keys points.

- 5967 • The approximation on the r.h.s. of Eq. 7.24 makes it clear that if there are dipole magnets with fields  
 5968 not parallel to  $\hat{n}_0$ , as is the case, for example, when spin rotators are used, then  $P_{\text{bk}}$  can be lower than  
 5969 the 92.4% attainable in the case of a simple ring with no solenoids and where all dipole fields and  $\hat{n}_0(s)$   
 5970 are vertical.
- 5971 • If, as is usual, the kinetic polarisation term makes just a small contribution, the above formulae can  
 5972 be combined to give

$$P_{\text{ens,dk}} \approx P_{\text{bk}} \frac{\tau_{\text{dk}}}{\tau_{\text{bk}}} . \quad (7.31)$$

5973 From Eq. 7.26 it is clear that  $\tau_{\text{dk}} \leq \tau_{\text{bk}}$ .

- 5974 • The underlying rate of polarisation due to the S-T effect,  $\tau_{\text{bk}}^{-1}$ , increases with the fifth power of the  
 5975 energy and decreases with the third power of the bending radii.
- 5976 • It can be shown that as a general rule the “normalised” strength of the depolarisation,  $\tau_{\text{dep}}^{-1}/\tau_{\text{bk}}^{-1}$ ,  
 5977 increases with beam energy according to a tune-dependent polynomial in even powers of the beam  
 5978 energy. So we expect that the attainable equilibrium polarisation decreases as the energy increases.  
 5979 This was confirmed LEP, where with the tools available, little polarisation could be obtained at 60  
 5980 GeV [600].

## 5981 7.15.2 Suppression of depolarisation – spin matching

5982 Although the S-T effect offers a convenient way to obtain stored high energy  $e^\pm$  beams, it is only useful in  
 5983 practice if there is not too much depolarisation. Depolarisation can be significant if the ring is misaligned,  
 5984 if it contains spin rotators or if it contains uncompensated solenoids or skew quadrupoles. Then if  $P_{\text{ens,dk}}$   
 5985 and/or  $\tau_{\text{dk}}$  are too small, the layout and the optic must be adjusted so that  $(|\frac{\partial \hat{n}}{\partial \delta}|)^2$  is small where  $1/|\rho(s)|^3$   
 5986 is large. So far it is only possible to do this within the linear approximation for spin motion. This technique  
 5987 is called “*linear spin matching*” and when successful, as for example at HERA [601], it immediately reduces  
 5988 the strengths of the first-order spin-orbit resonances. Spin matching requires two steps: “*strong synchrobeta*  
 5989 *spin matching*” is applied to the optics and layout of the perfectly aligned ring and then “*harmonic closed-*  
 5990 *orbit spin matching*” is applied to soften the effects of misalignments. This latter technique aims to adjust  
 5991 the closed orbit so as to reduce the tilt of  $\hat{n}_0$  from the vertical in the arcs. Since the misalignments can  
 5992 vary in time and are usually not sufficiently well known, the adjustments are applied empirically while the  
 5993 polarisation is being measured.

5994 Spin matching must be approached on a case-by-case basis. An overview can be found in [590].

## 5995 7.15.3 Higher order resonances

5996 Even if the beam energy is chosen so that first-order resonances are avoided and in linear approximation  
 5997  $P_{\text{ens,dk}}$  and/or  $\tau_{\text{dk}}$  are expected to be large, it can happen that that beam energy corresponds to a higher  
 5998 order resonance. As mentioned above, in practice the most intrusive higher order resonances are those for  
 5999 which  $\nu_0 = k_0 \pm Q_k + \tilde{k}_s Q_s$  ( $k \equiv I, II$  or *III*). These synchrotron sideband resonances of the first-order  
 6000 parent resonances are due to modulation by energy oscillations of the instantaneous rate of spin precession  
 6001 around  $\hat{n}_0$ . The depolarisation rates associated with sidebands of isolated parent resonances ( $\nu_0 = k_0 \pm Q_k$ )



6002 are related to the depolarisation rates for the parent resonances. For example, if the beam energy is such  
 6003 that the system is near to a dominant  $Q_y$  resonance we can approximate  $\tau_{\text{dep}}^{-1}$  in the form

$$\tau_{\text{dep}}^{-1} \propto \frac{A_y}{(\nu_0 - k_0 \pm Q_y)^2}. \quad (7.32)$$

6004 This becomes

$$\tau_{\text{dep}}^{-1} \propto \sum_{\tilde{k}_s=-\infty}^{\infty} \frac{A_y B_y(\zeta; \tilde{k}_s)}{(\nu_0 - k_0 \pm Q_y \pm \tilde{k}_s Q_s)^2}$$

6005 if the synchrotron sidebands are included. The quantity  $A_y$  depends on the beam energy and the optics and  
 6006 is reduced by spin matching. The proportionality constants  $B_y(\zeta; \tilde{k}_s)$  are called *enhancement factors*, and  
 6007 they contain modified Bessel functions  $I_{|\tilde{k}_s|}(\zeta)$  and  $I_{|\tilde{k}_s|+1}(\zeta)$  which depend on  $Q_s$  and the energy spread  $\sigma_\delta$   
 6008 through the *modulation index*  $\zeta = (a\gamma \sigma_\delta / Q_s)^2$ . More formulae can be found in [602, 603].

6009 Thus the effects of synchrotron sideband resonances can be reduced by doing the spin matches described  
 6010 above. Note that these formulae are just meant as a guide since they are approximate and explicitly neglect  
 6011 interference between the first-order parent resonances. To get a complete impression, the Monte-Carlo  
 6012 simulation mentioned later must be used. The sideband strengths generally increase with the energy spread  
 6013 and the beam energy and the sidebands are a major contributor to the increase of  $\tau_{\text{dep}}^{-1}/\tau_{\text{bk}}^{-1}$  with energy.

#### 6014 7.15.4 Calculations of the $e^\pm$ polarisation in the LHeC

6015 As a first step towards assessing the attainable polarisation we have considered an early version of the LHeC  
 6016 lattice: a flat ring with no rotators, no interaction point and no bypasses. The tunes are  $Q_x = 123.83$   
 6017 and  $Q_y = 85.62$ . The horizontal emittance is 8 nm. The ring is therefore typical of the designs under  
 6018 consideration. With perfect alignment,  $\hat{n}_0$  is vertical everywhere and there is no vertical dispersion. The  
 6019 polarisation will then reach 92.4%. At  $\approx 60$  GeV,  $\tau_{\text{bk}} \approx 60$  minutes.

6020 For the simple flat ring these values can be obtained by hand from Eq. 7.24 and Eq. 7.28. However, in  
 6021 general, e.g., in the presence of misalignments or rotators, the calculation of polarisation requires special  
 6022 software and for this study, the thick-lens code SLICKTRACK was used [604]. This essentially consists of  
 6023 four sections which carry out the following tasks:

- 6024 (1) Simulation of misalignments followed by orbit correction with correction coils.
- 6025 (2) Calculation of the optical properties of the beam and the beam sizes.
- 6026 (3) Calculation of  $\partial\hat{n}/\partial\delta$  for linearised spin motion with the thick-lens version (SLICK [605]) of the SLIM  
 6027 algorithm [590].

6028 The equilibrium polarisation is then obtained from Eq. 7.22. This provides a first impression and only  
 6029 exhibits the first order resonances.

- 6030 (4) Calculation of the rate of depolarisation beyond the linear approximation of item 3.

6031 In general, the numerical calculation of the integrand in Eq. 7.27 beyond first order represents a difficult  
 6032 computational problem. Therefore a pragmatic approach is adopted, whereby the rate of depolarisation  
 6033 is obtained with a Monte-Carlo spin-orbit tracking algorithm which includes radiation emission. The  
 6034 algorithm employs full 3-D spin motion in order to see the effect of the higher order resonances. The  
 6035 Monte-Carlo algorithm can also handle the effect on the particles and on the spins of the non-linear  
 6036 beam-beam forces. An estimate of the equilibrium polarisation is then obtained from Eq. 7.31.

6037 Some basic features of the polarisation for the misaligned flat ring are shown in figures 7.50 and 7.51  
 6038 where polarisations are plotted against  $a\gamma$  around 60 GeV. In both cases the r.m.s. vertical closed-orbit  
 6039 deviation is about  $75\mu\text{m}$ . This is obtained after giving the quadrupoles r.m.s. vertical misalignments of

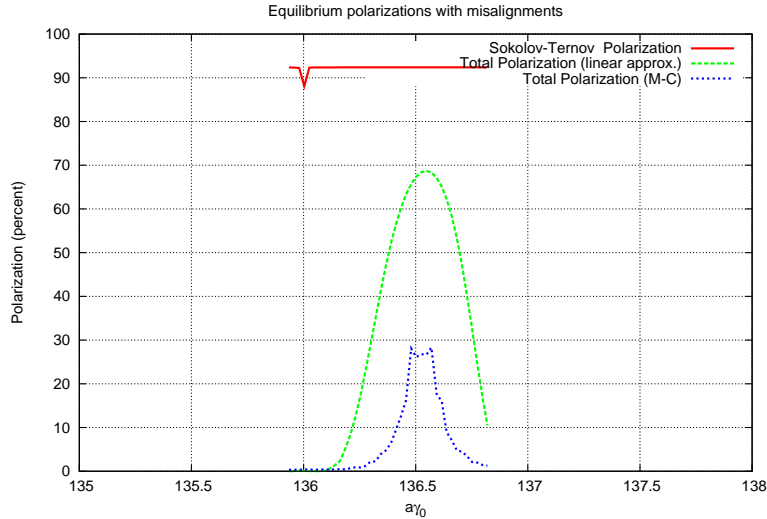


Figure 7.50: Estimated polarisation for the LHeC without spin rotators,  $Q_s = 0.06$ .

6040  $150\mu\text{m}$  and assigning a correction coil to every quadrupole. The vector  $\hat{n}_0$  has an r.m.s. tilt of about 4  
 6041 milliradians from the vertical near  $a\gamma = 136.5$ . For figure 7.50 the synchrotron tune,  $Q_s$ , is 0.06 so that  
 6042  $\xi \approx 5$ . For figure 7.51,  $Q_s = 0.1$  so that  $\xi \approx 1.9$ .

6043 The red curves depict the polarisation due to the Sokolov-Ternov effect alone. The dip to below 92.4%  
 6044 at  $a\gamma = 136$  is due to the characteristic very large tilt of  $\hat{n}_0$  from the vertical at an integer value of  $a\gamma$ .  
 6045 See [590].

6046 The green curves depict the equilibrium polarisation after taking into account the depolarisation associ-  
 6047 ated with the misalignments and the consequent tilt of  $\hat{n}_0$ . The polarisation is calculated with the linearised  
 6048 spin motion as in item 3 above. In these examples the polarisation reaches about 68 %. The strong fall off  
 6049 on each side of the peak is mainly due to first-order “synchrotron” resonances  $\nu_0 = k_0 \pm Q_s$ . Since  $Q_s$  is  
 6050 small these curves are similar for the two values of  $Q_s$ .

6051 The blue curves show the polarisation obtained as in item 4 above. Now, by going beyond the linearisa-  
 6052 tion of the spin motion, the peak polarisation is about 27 %. The fall from 68 % is mainly due to synchrotron  
 6053 sideband resonances. With  $Q_s = 0.06$  (Fig. 7.50) the resonances are overlapping. With  $Q_s = 0.1$ , (Fig. 7.51)  
 6054 the sidebands begin to separate. In any case these curves demonstrate the extreme sensitivity of the attain-  
 6055 able polarisation to small tilts of  $\hat{n}_0$  at high energy. Simulations for  $Q_s = 0.1$  with a series of differently  
 6056 misaligned rings, all with r.m.s. vertical closed-orbit distortions of about  $75\mu\text{m}$ , exhibit peak equilibrium  
 6057 polarisations ranging from about about 10 % to about 40 %. Experience at HERA suggests that harmonic  
 6058 closed-orbit spin matching can eliminate the cases of very low polarisation.

6059 Figure 7.52 shows a typical energy dependence of the peak equilibrium polarisation for a fixed RF voltage  
 6060 and for one of the misaligned rings. The synchrotron tune varies from  $Q_s = 0.093$  at 40 GeV to  $Q_s = 0.053$   
 6061 at 65 GeV due to the change in energy loss per turn. As expected the attainable polarisation falls steeply  
 6062 as the energy increases. However, although with this good alignment, a high polarisation is predicted at 45  
 6063 GeV,  $\tau_{\text{bk}}$  would be about 5 hours as at LEP. A small  $\tau_{\text{bk}}$  is not only essential for a programme of particle  
 6064 physics, but essential for the application of empirical harmonic closed-orbit spin matching.

6065 As mentioned above, it was difficult to get polarisation at 60 GeV at LEP. However, these calculations  
 6066 suggest that by adopting the levels of alignment that are now standard for synchrotron-radiation sources  
 6067 and by applying harmonic closed-orbit spin matching, there is reason to hope that high polarisation in a flat  
 6068 ring can still be obtained.

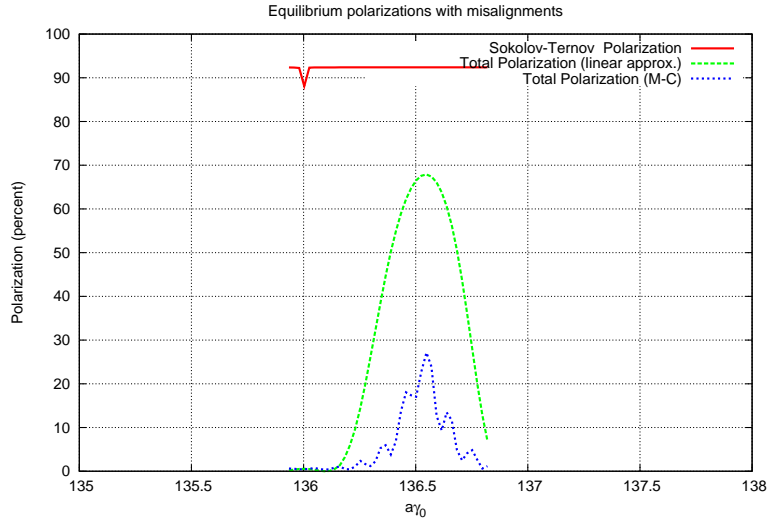


Figure 7.51: Estimated polarisation for the LHeC without spin rotators,  $Q_s = 0.1$ .

### 7.15.5 Spin rotator concepts for the LHeC

The LHeC, like all analogous projects involving spin, needs longitudinal polarisation at the interaction point. However, if the S-T effect is to be the means of producing and maintaining the polarisation, then as is clear from Eq. 7.24,  $\hat{n}_0$  must be close to vertical in most of the dipoles. We have seen at Eq. 7.23 that the polarisation is essentially parallel to  $\hat{n}_0$ . So to get longitudinal polarisation at a detector, it must be arranged that  $\hat{n}_0$  is longitudinal at the detector but vertical in the rest of the ring. This can be achieved with magnet systems called spin rotators which rotate  $\hat{n}_0$  from vertical to longitudinal on one side of the detector and back to vertical again on the other side.

Spin rotators use sequences of magnets which generate large spin rotations around different axes and exploit the non-commutation of successive large rotations around different axes. According to the T-BMT equation, the rate of spin precession in longitudinal fields is inversely proportional to the energy. However, for motion perpendicular to a magnetic field spins precess at a rate essentially proportional to the energy:  $\delta\theta_{\text{spin}} = (a\gamma + 1)\delta\theta_{\text{orb}}$  in obvious notation. Thus for the high-energy ring considered here, spin rotators should be based on dipoles as in HERA [601]. In that case the rotators consisted of interleaved horizontal and vertical bending magnets set up so as to generate interleaved, closed, horizontal and vertical bumps in the design orbit. The individual orbit deflections were small but the spin rotations were of the order of a radian. The success in obtaining high longitudinal polarisation at HERA attests to the efficacy of such rotators.

Eq. 7.24 shows that  $P_{\text{bk}}$  essentially scales with the cosine of the angle of tilt of  $\hat{n}_0$  from the vertical in the arc dipoles. Thus a rotation error resulting in a tilt of  $\hat{n}_0$  of even a few degrees would not reduce  $P_{\text{bk}}$  by too much. However, as was mentioned above, a tilt of  $\hat{n}_0$  in the arcs can lead to depolarisation. In fact the calculations below show that at 60 GeV, tilts of more than a few milliradians cause significant depolarisation. Thus well-tuned rotators are essential for maintaining polarisation.

Dipole rotators require a significant amount of space in the ring. To minimise the power density as well as to preserve the polarisation, the amount of synchrotron radiation from the rotators needs to be kept to a minimum, in direct conflict with the desire to keep the dipole magnets as short as possible. In addition, longer dipole magnets lead to larger orbit excursions. A numerical example for HERA-type spin rotators in the LHeC with a bending radius of each dipole equal to that of the arc dipoles yields a length of each spin rotator of about 150 m. The net space appears to be available; the challenge being the integration of the string of dipoles and the vertical magnet movers in an already crowded area of the LHC tunnel. Note that

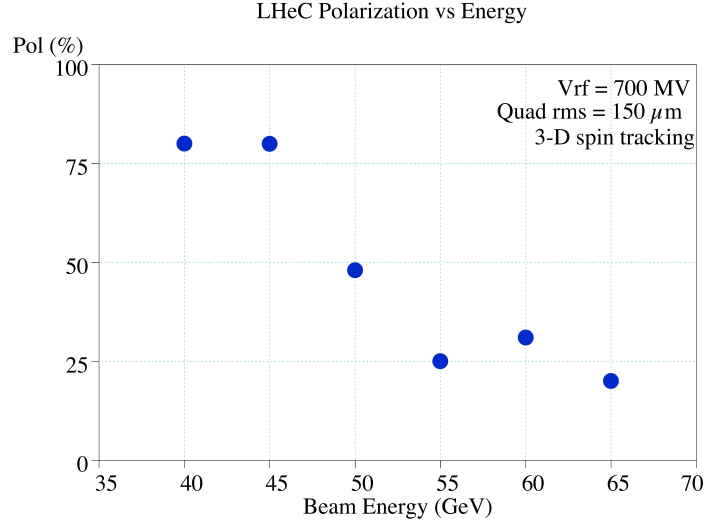


Figure 7.52: Equilibrium polarisation *vs* ring energy, full 3-D spin tracking results

6099 the rotator incorporates a certain amount of bending angle. The excursion away from the nominal orbit is  
 6100 about 0.3 m.

6101 A scheme using two Siberian Snakes has been considered by Derbenev and Grote [606] (see below) that  
 6102 would integrate the IR rotators with the vertical dogleg required to bring the beams into collision. For this  
 6103 the horizontal bends are all of the same polarity and contribute to the overall 360° bend so that the added  
 6104 dipole strength in the IR is minimised.

6105 Table 7.34 gives an indication of possible parameters for LHeC spin rotators. These are subject to change  
 6106 as the specific geometry in the IR is being further refined. Note that the effect of these rotators on the degree  
 6107 of polarisation remains to be evaluated (but see below for further comments on the Derbenev-Grote scheme).

Table 7.34: Possible Parameters for LHeC Spin Rotators

Parameter	Unit	HERA-type	Derbenev-Grote (IP only)
No. of vertical dipole magnets		12	10
No. of horizontal dipole magnets		12	10
Bending angle/magnet	°	0.110	0.132
Length of magnet	m	5.45	5.45
Total length of rotator	m	170	80
Net bending angle	°	0.66	1.32
Vertical offset	m	0	1.25

### 6108 7.15.6 Further work

6109 We now list the next steps towards obtaining longitudinal polarisation at the interaction point.

- 6110 (1) A harmonic closed-orbit spin matching algorithm must be implemented for the LHeC to try to correct  
 6111 the remaining tilt of  $\hat{n}_0$  and thereby increase the equilibrium polarisation.

6112 (2) Practical spin rotators must be designed and appropriate strong synchro-beta spin matching must be  
6113 implemented. The design of the rotators and spin matching are closely linked. Some preliminary  
6114 numerical investigations (below) show, as expected, that without this spin matching, little polarisation  
6115 will be obtained.

6116 (3) If synchrotron sideband resonances are still overwhelming after items 1 and 2 are implemented, a  
6117 scheme involving Siberian Snakes could be tried. Siberian Snakes are arrangements of magnets which  
6118 manipulate spin on the design orbit so that the closed-orbit spin tune is independent of beam energy.  
6119 Normally the spin tune is then  $1/2$  and heuristic arguments suggest that the sidebands should be  
6120 suppressed. However, the two standard schemes [607] either cause  $\hat{n}_0$  to lie in the machine plane (just  
6121 one snake) or ensure that it is vertically up in one half of the ring and vertically down in the other  
6122 half (two snakes). In both cases Eq. 7.24 shows that  $P_{bk}$  vanishes. In principle, this problem can be  
6123 overcome for two snakes by again appealing to Eq. 7.24 and having short strong dipoles in the half of  
6124 the ring where  $\hat{n}_0$  points vertically up and long weaker dipoles in the half of the ring where  $\hat{n}_0$  points  
6125 vertically down (or vice versa). Of course, the dipoles must be chosen so that the total bend angle is  
6126  $\pi$  in each half of the ring. Moreover, Eq. 7.24 shows that the pure Sokolov-Ternov polarisation would  
6127 be much less than 92.4%. One version of this concept [606] uses a pair of rotators which together form  
6128 a snake while a complementary snake is inserted diametrically opposite to the interaction point. Each  
6129 rotator comprises interleaved strings of vertical and horizontal bends which not only rotate the spins  
6130 from vertical to horizontal, but also bring the  $e^\pm$  beams down to the level of the proton beam and then  
6131 up again. However, the use of short dipoles in the arcs increases the radiation losses.

6132 Note that because of the energy dependence of spin rotations in the dipoles,  $\hat{n}_0$  is vertical in the  
6133 arcs at just one energy. This concept has been tested with SLICKTRACK but in the absence of a  
6134 strong synchro-beta spin match, the equilibrium polarisation is very small as expected. Nevertheless  
6135 the effects of misalignments and of the tilt of  $\hat{n}_0$  away from design energy, have been isolated by  
6136 imposing an artificial spin match using standard facilities in SLICKTRACK. The snake in the arc has  
6137 been represented as a thin element that has no influence on the orbital motion. Then it looks as if  
6138 the synchrotron sidebands are indeed suppressed in the depolarisation associated with tilts of  $\hat{n}_0$ . In  
6139 contrast to the rotators in HERA, this kind of rotator allows only one helicity for electrons and one  
6140 for positrons.

6141 (4) If a scheme can be found which delivers sufficient longitudinal polarisation, the effect of non-linear  
6142 orbital motion, the effect of beam-beam forces and the effect of the magnetic fields of the detector  
6143 must then be studied.

### 6144 7.15.7 Summary

6145 We have investigated the possibility of polarisation in the LHeC electron ring. At this stage of the work it  
6146 appears that a polarisation of between 25 and 40% at 60 GeV can be reasonably aimed for, assuming the  
6147 efficacy of harmonic closed-orbit spin matching. Attaining this degree of polarisation will require precision  
6148 alignment of the magnets to better than  $150\mu\text{m}$  rms, a challenging but achievable goal. The spin rotators  
6149 necessary at the IP need to be properly spin matched to avoid additional depolarisation and this work is  
6150 in progress. An interesting alternative involving the use of Siberian Snakes to try to avoid the depolarising  
6151 synchrotron sideband resonances is being investigated. At present, this appears to potentially yield a similar  
6152 degree of polarisation, at the expense of increased energy dissipation in the arcs arising from the required  
6153 differences of the bending radii in the two halves of the machine.

## 7.16 Integration and machine protection issues

### 7.16.1 Space requirements

The integration of an additional electron accelerator into the LHC is a difficult task. Firstly, the LEP tunnel was designed for LEP and not for the LHC, which is now using up almost all space in the tunnel. It is not evident, how to place another accelerator into the limited space. Secondly, the LHC will run for several years, before the installation of a second machine can start. Meanwhile the tunnel will be irradiated and all installation work must proceed as fast as possible to limit the collective and individual doses. The activation after the planned high-luminosity-run of the LHC and after one month of cool-down is expected to be around  $0.5...1\mu Sv/h$  [608] on the proton magnets and many times more at exposed positions. Moreover the time windows for installation will be short and other work for the LHC will be going on, maybe with higher priority. Nevertheless, with careful preparation and advanced installation schemes an electron accelerator can be fitted in.

For the installation of the LHC machine proper, all heavy equipment had to pass the UJ2, while entering the tunnel. There the equipment had to be moved from TI2, which comes in from the outside, to the transport zone of LHC, which is on the inner side of the ring. Clearly, applying this procedure to the installation of the LHeC everything above the cold dipoles has to be removed. The new access shafts and the smaller size of the equipment for the electron ring may render this operation unnecessary.

**General** The new electron accelerator will be partially in the existing tunnel and partially in specially excavated tunnel sections and behind the experiments in existing underground areas. The excavation work will need special access shafts in the neighborhood of the experiments from where the stub-tunnels can be driven. The connection to the existing LEP tunnels will be very difficult. The new tunnel enters with a very small grazing angle, which means over a considerable length. Very likely the proton installation will have to be removed while the last meters of the new tunnel is bored.

Figure 7.53 shows a typical cross section of the LHC tunnel, where the two machines are together. The LHC dipole dominates the picture. The transport zone is indicated at the right (inside of the ring). The cryogenic installations (QRL) and various pipes and cable trays are on the left. The dipole cross section shows two concentric circles. The larger circle corresponds to the largest extension at the re-enforcement rings and marks a very localized space restriction on a very long object. The inner circle is relevant for items shorter than about 10 m longitudinally. A hatched square above the dipole labeled 30 indicates the area, which was kept free in the beginning for an electron machine. Unfortunately, the center of this space is right above the proton beam. Any additional machine will, however, have to avoid the interaction points 1 and 5. In doing so additional length will be necessary, which can only be compensated for by shifting the electron machine in the arc about 60 cm to the inside (right), as indicated by the red square in Figure 7.53. The limited space for compensation puts a constraint on the extra length created by the bypasses. The transport zone will, however, be affected. This requires an unconventional way to mount the electron machine. Nevertheless, there is clearly space to place an electron ring into the LHC, for most of the arc. Figure 7.54 gives the impression that the tunnel for most of its length is not too occupied.

**In the arc** In Fig. 7.54 one sees the chain of superconducting magnets and in the far distances the *QRL Service Module* with its jumper, the cryogenic connection between the superconducting machine and the cryogenic distribution line. The service modules come always at the position of every second quadrupole and have a substantial length. The optics of the LHeC foresees no e-ring magnet at these positions. A photo of service modules in the workshop is shown in figure 7.55 (courtesy CERN) illustrating that the QRL extends substantially in the vertical direction above the LHC arc cryostat and cryo line. The picture 7.54, taken in sector 3, shows also the critical tunnel condition in this part of the machine. Clearly, heavy loads cannot be suspended from the tunnel ceiling. The limit is set to 100 kg per meter along the tunnel. The e-ring components have to rest on stands from the floor wherever possible. Normally there is enough space between the LHC dipoles and the QRL to place a vertical 10 cm quadratic or rectangular support. Alternatively a

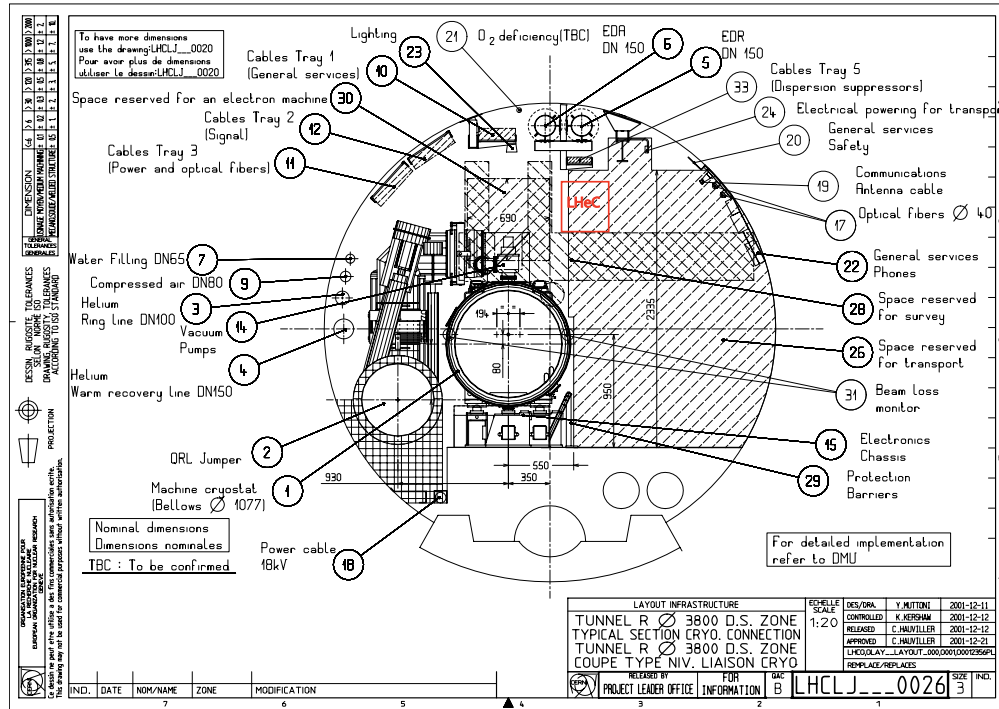


Figure 7.53: Cross-section of the LHC tunnel with the original space holder for the electron beam installation directly above the LHC cryostat and the shifted new required space due to the additional bypass in IR1 and IR5 and the need to keep the overall circumference of the electron ring identical to that of the proton beams.

6201 steel arch bolted to the tunnel walls and resting on the floor can support the components from above. This  
 6202 construction is required wherever the space for a stand is not available.

6203 The electron machine, though partially in the transport zone, will be high up in the tunnel. The transport  
 6204 of cryogenic equipment may need the full height. Transports of that kind will only happen, when part of the  
 6205 LHC are warmed up. This gives enough time to shift the electron ring to the outside by 30 cm, if the stands  
 6206 are prepared for this operation. The outside movement causes also a small elongation of the inter-magnet  
 6207 connections. This effect is locally so small that the expansion joints, required anyway, can accommodate it.  
 6208 One could even think of moving large sections of the e-machine outwards in a semi-automatic way. Thus the  
 6209 time to clear the transport path can be kept in the shadow of the warm-up and cool-down times.

6210 **Dump area** The most important space constraints for the electron machine are in the proton dump area,  
 6211 the proton RF cavities, point 3, and in particular the collimator sections.

6212 Figure 7.56 [609] shows the situation at the dump kicker. The same area is also shown in a photo in Figure  
 6213 7.57, while Figure 7.58 shows one of the outgoing dump-lines. The installation of the e-machine requires  
 6214 the proper rerouting of cables (which might be damaged by radiation and in need of exchange anyhow),  
 6215 eventually turning of pumps by 90 degrees or straight sections in the electron optics to bridge particularly  
 6216 difficult stretches with a beam pipe only.

6217 **Point 4, proton RF** The Figures 7.59 [610] and 7.60 illustrate the situation at the point 4, where the  
 6218 LHC RF is installed. Fortunately, the area is not very long. A short straight section could be created for  
 6219 the electron ring. This would allow to pass the area with just a shielded beam pipe.



Figure 7.54: View of sector 4 showing the chain of superconducting magnets in the arc.



Figure 7.55: Sideview of a QRL service module with the jumper that extends vertically above the LHC cryostat and the cryogenic distribution line.



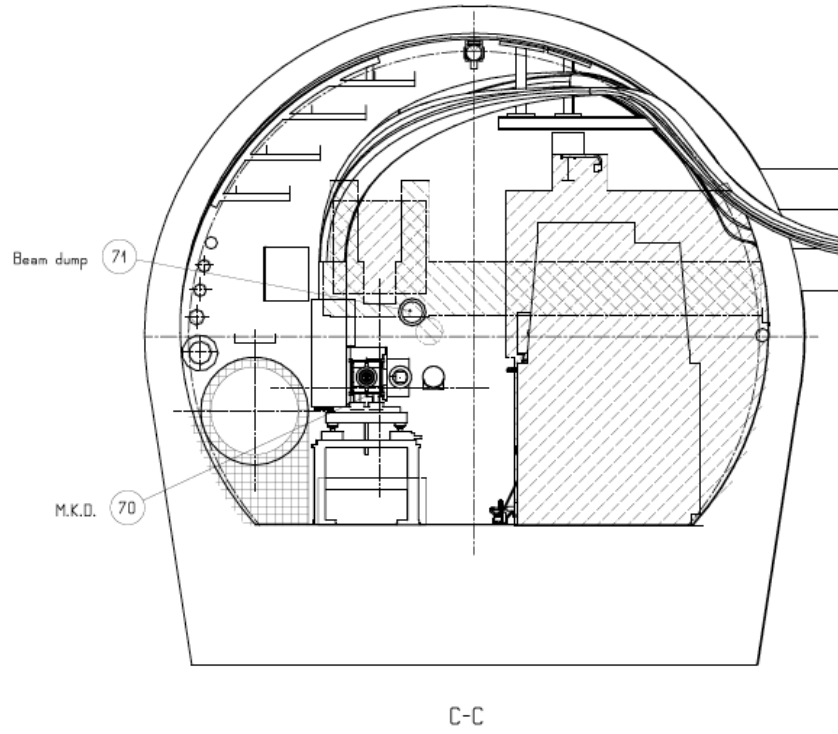


Figure 7.56: Dump kicker [609]

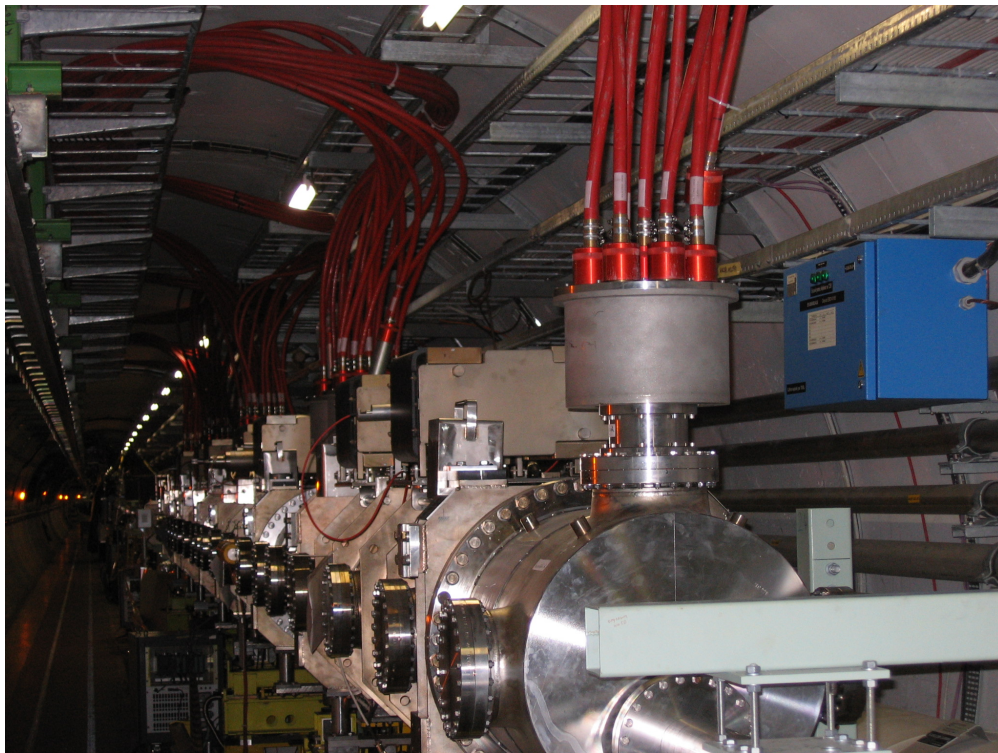


Figure 7.57: Dump kicker installation in IR6 for one of the two LHC proton rings.

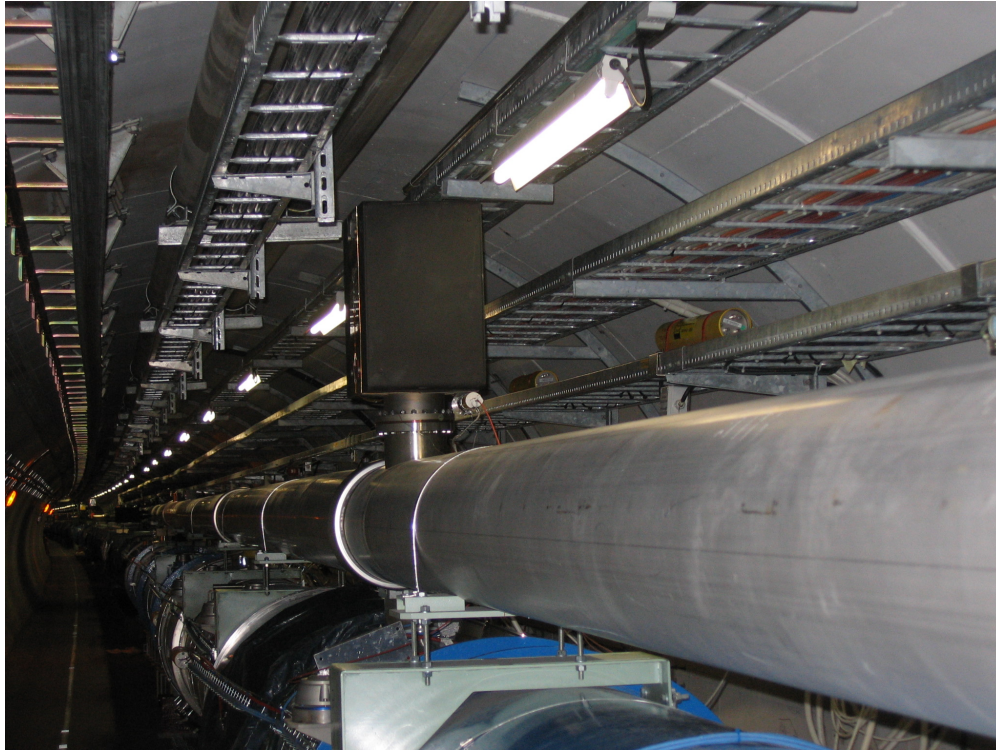
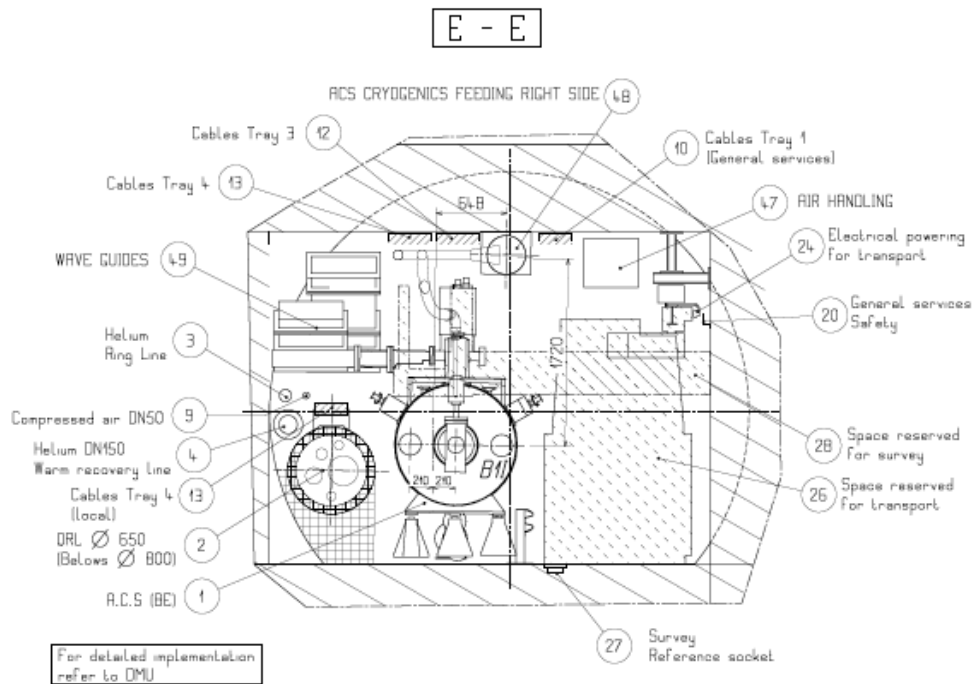


Figure 7.58: Dump line of one of the LHC proton rings.



h

Figure 7.59: Schematic tunnel cross section with the LHC Proton Proton RF in point 4 [610].

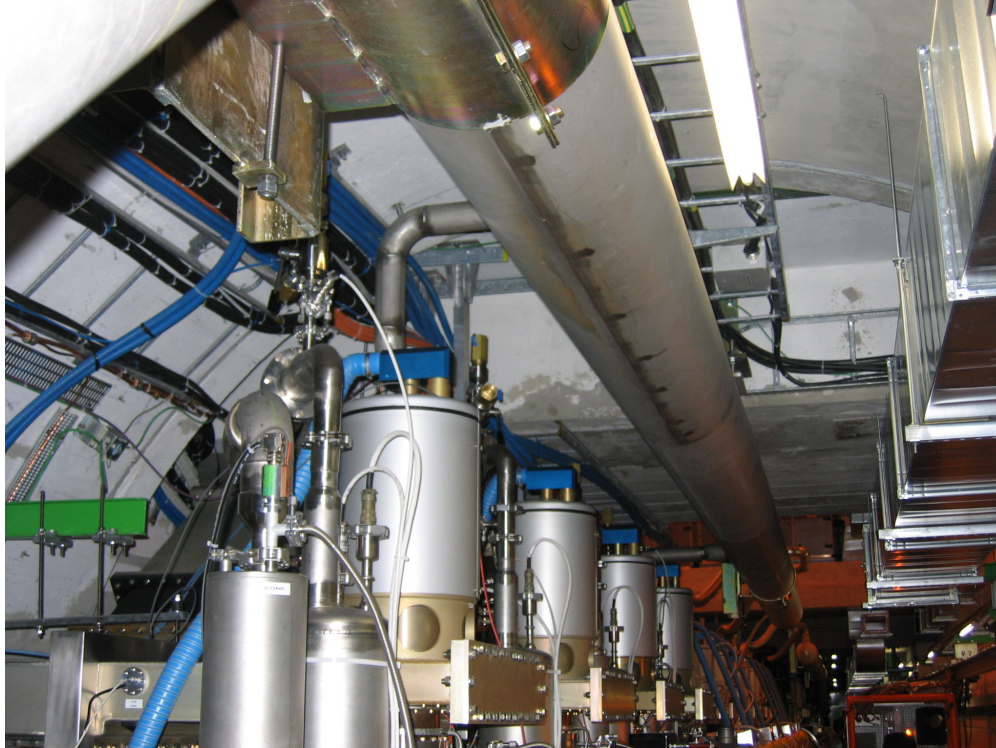


Figure 7.60: Tight space restriction in Point 4 due to the LHC proton RF installation.

6220 **Cryolink in point 3** The geography around point 3 did not permit to place there a cryoplant. The  
 6221 cryogenic cooling for the feedboxes is provided by a cryolink, as is shown in the figures 7.61 and 7.62. In  
 6222 particular above the Q6 proton quadrupole changes have to be made. There are other interferences with the  
 6223 cryogenics, as for example at the DFBA's (main feedboxes). An example is shown in figure 7.63. Eventually  
 6224 the electron optics has to be adapted to allow the beampipe to pass the cables, which may have to be moved  
 6225 a bit.

6226 **Long straight section 7** An extra air duct is mounted in the long straight section 7 (LSS7) as is indicated  
 6227 in Fig. 7.64 (labelled Plenum de ventilation) avoiding the air pollution of the area above point 7. The duct  
 6228 occupies the space planned for the electron machine. The air duct has to be replaced by a slightly different  
 6229 construction mounted further outside (to the right in the figure). There are also air ducts at points 1 and 5,  
 6230 but they are not an issue. The electron ring is passing behind the experiments in these points

6231 **Proton collimation** The areas around Point 3 (-62...+177m) and Point 7 (-149...+205m) [611] are heavily  
 6232 used for the collimation of the proton beam. The high dose rate in the neighborhood of a collimator  
 6233 makes special precautions for the installation of new components or the exchange of a collimator necessary.  
 6234 Moreover, the collimator installation needs the full height of the tunnel. Hence, the electron ring installation  
 6235 has to be suspended from the re-enforced tunnel roof. The electron machine components must be removable  
 6236 and installable, easy and fast. The re-alignment must be well prepared and fast, possibly in a remote fashion.  
 6237 It is uncommon to identify fast mounting and demounting as a major issue. However, with sufficient emphasis  
 6238 during the R&D phase of the project, this problem can be solved.

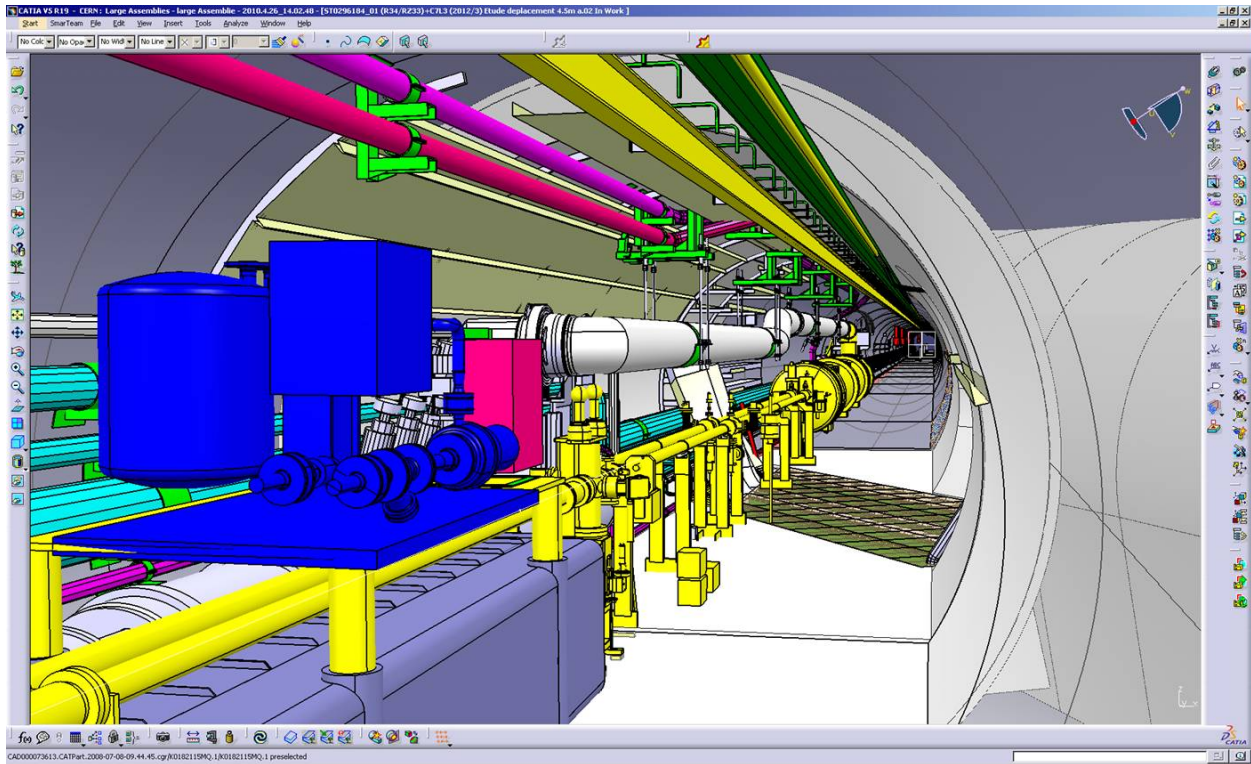


Figure 7.61: The cryogenic connection in point 3

### 7.16.2 Impact of the synchrotron radiation on tunnel electronics

It is assumed that the main power converters of the LHC will have been moved out of the RRs because of the single event upsets, caused by proton losses.

The synchrotron radiation has to be intercepted at the source, as in all other electron accelerators. A few millimeter of lead are sufficient for the relatively low (critical) energies around 100 to 200 keV. The K-edge of lead is at 88 keV, the absorption coefficient is above 80/cm at this energy [612]. One centimeter of lead is sufficient to suppress 300 keV photons by a factor of 100. Detailed calculations of the optics will determine the amount of lead needed in the various places. The primary shielding needs an effective water cooling to avoid partial melting of the lead.

The electronics is placed below the proton magnets. Only backscattered photons with correspondingly lower energy will reach the electronics. If necessary, a few millimeter of extra shielding could be added here.

The risk for additional single event upsets due to synchrotron radiation is negligible.

### 7.16.3 Compatibility with the proton beam loss system

The proton beam loss monitoring system works very satisfactory. It has been designed to detect proton losses by observing secondaries at the outside of the LHC magnets. The sensors are ionization chambers. Excessive synchrotron radiation (SR) background will presumably trigger the system and dump the proton beam. The SR background at the monitors has to be reduced by careful shielding of either the monitors or the electron ring. Alternatively, the impact of the photon background can be reduced by using a new loss monitoring system which is based on coincidences (as was done elsewhere [613]).

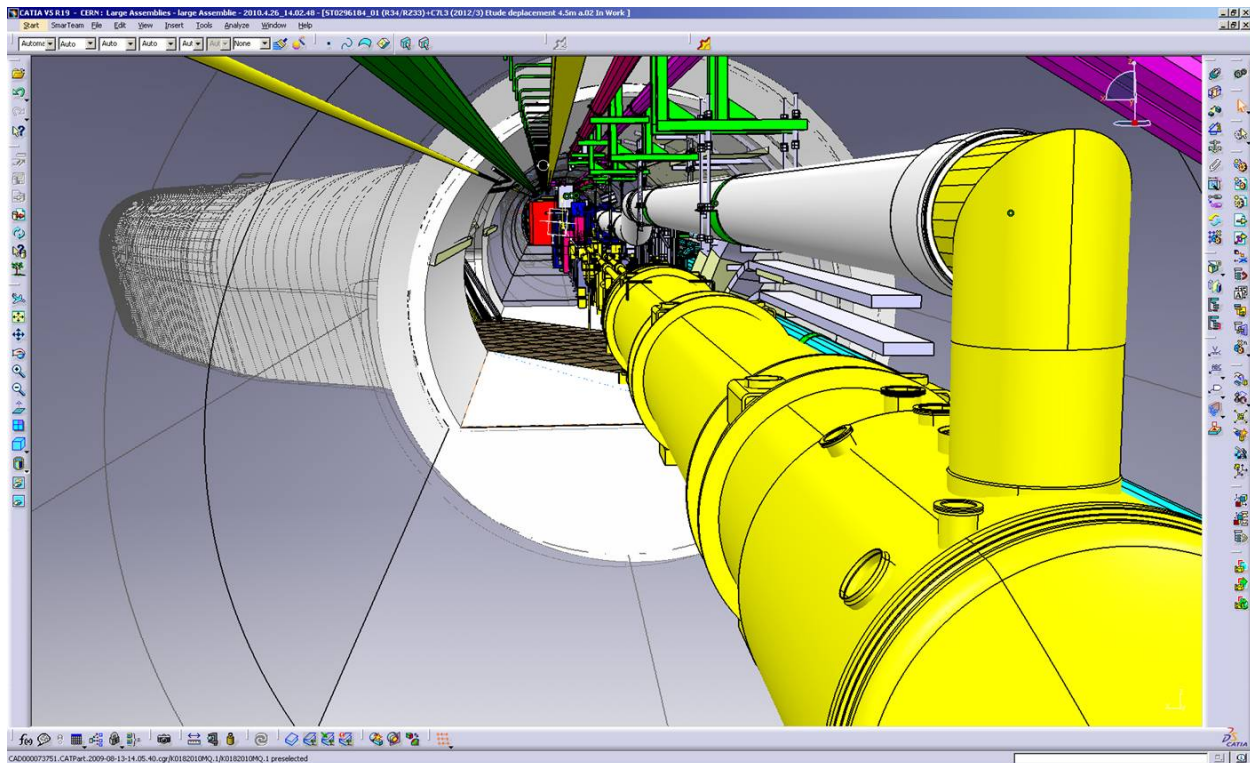


Figure 7.62: The cryogenic connection in point 3 (grey tube passing above the two LHC proton beam vacuum tubes [yellow]).

#### 6258 **7.16.4 Space requirements for the electron dump**

6259 The electron beam of the LHeC installation requires a dedicated dump section. Potential interference of  
 6260 the losses during or after an electron beam dump with equipment of the LHC proton rings still needs to be  
 6261 studied and a suitable space still needs to be found in the LHC tunnel.

#### 6262 **7.16.5 Protection of the p-machine against heavy electron losses**

6263 The existing proton loss detectors are placed, as mentioned above, at the LHC magnets. The trigger threshold  
 6264 requires certain number of detectors to be hit by a certain number of particles. The assumption is that the  
 6265 particles come from the inside of the magnets and the particle density there is much higher. Electron losses,  
 6266 creating a similar pattern in the proton loss detectors will result in a much lower particle density in the  
 6267 superconducting coils. Hence, still tolerable electron losses will unnecessarily trigger the proton loss system  
 6268 and dump the proton beam. The proton losses are kept at a low level by installing an advanced system  
 6269 of collimators and masks. Fast changes of magnet currents, which will result in a beam loss, are detected.  
 6270 A similar system is required for the electrons. An electron loss detection system, like the one mentioned  
 6271 in Ref. [613], combined with the proton loss system can be used to identify the source of the observed loss  
 6272 pattern and to minimize the electron losses by improved operation. It seems very optimistic to think of a  
 6273 hardware discrimination system, which determines very fast the source of the loss and acts correspondingly.  
 6274 Such a system could be envisaged only after several years of running.

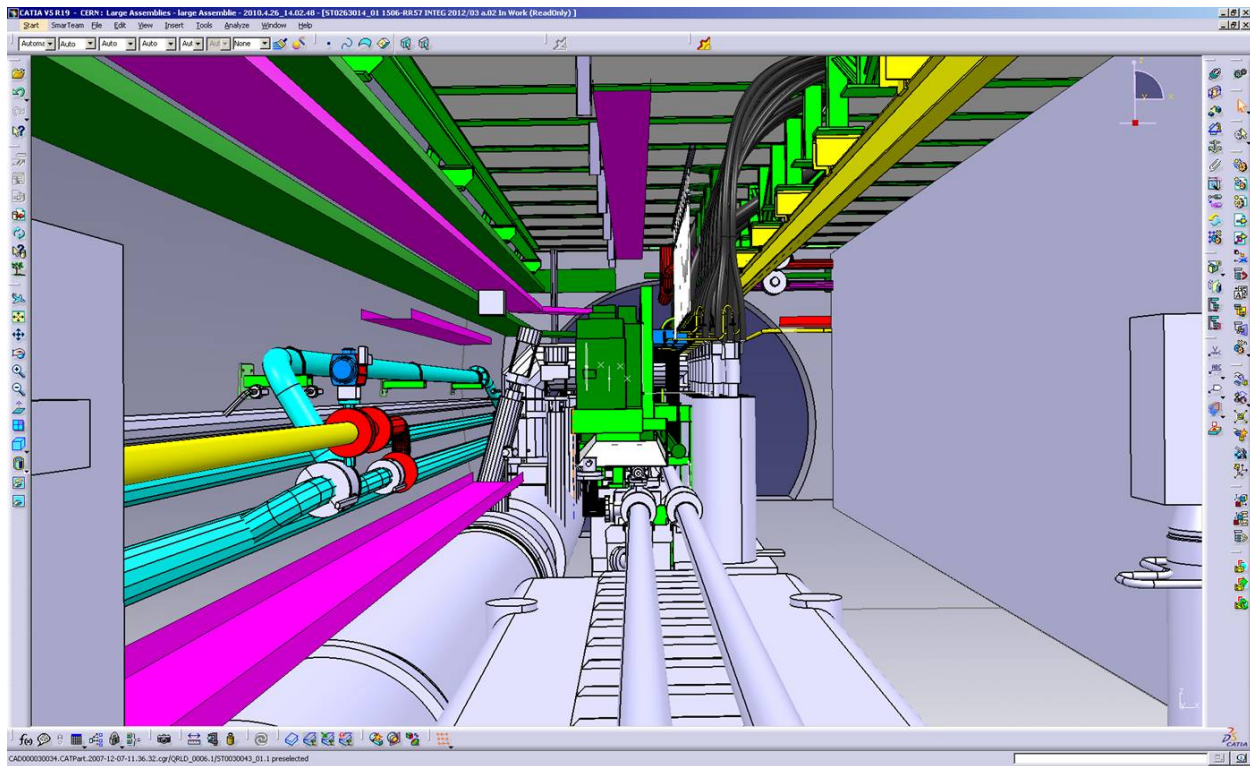


Figure 7.63: A typical big current feed-box (DFBA) on top of (green) and next to (grey shafts with black power lines) the two proton beam pipes.

### 6275 7.16.6 How to combine the Machine Protection of both rings?

6276 The existing machine-protection system combines many different subsystems. The proton loss system, the  
 6277 quench detection system, cryogenics, vacuum, access, and many other subsystems may signal a dangerous  
 6278 situation. This requirement lead to a very modular architecture, which could be expanded to include the  
 6279 electron accelerator.

## 6280 7.17 LHeC Injector for the Ring-Ring option

### 6281 7.17.1 Injector

6282 The LEP pre-injectors have been dismantled and the infrastructure re-used for the CLIC test facility CTF3.  
 6283 The RF cavities that accelerated leptons in the SPS have been removed to reduce its impedance. Re-  
 6284 installation of an injector chain similar to LEP's through the PS and SPS would be costly and potentially  
 6285 limit the proton performance.

6286 The LHeC e-ring therefore requires new lepton injectors.

6287 In the 30 years from the design of the LEP injectors, there has been substantial progress in accelerator  
 6288 technology. This is particularly true in the field of superconducting radio frequency technology which was  
 6289 very successfully used for LEP2 on a large scale and which has been further developed for TESLA and the  
 6290 ILC. It makes it feasible to design a very compact and efficient 10 GeV injector based on the principle of a  
 6291 recirculating LINAC and to take advantage of the studies for ELFE at CERN [614].

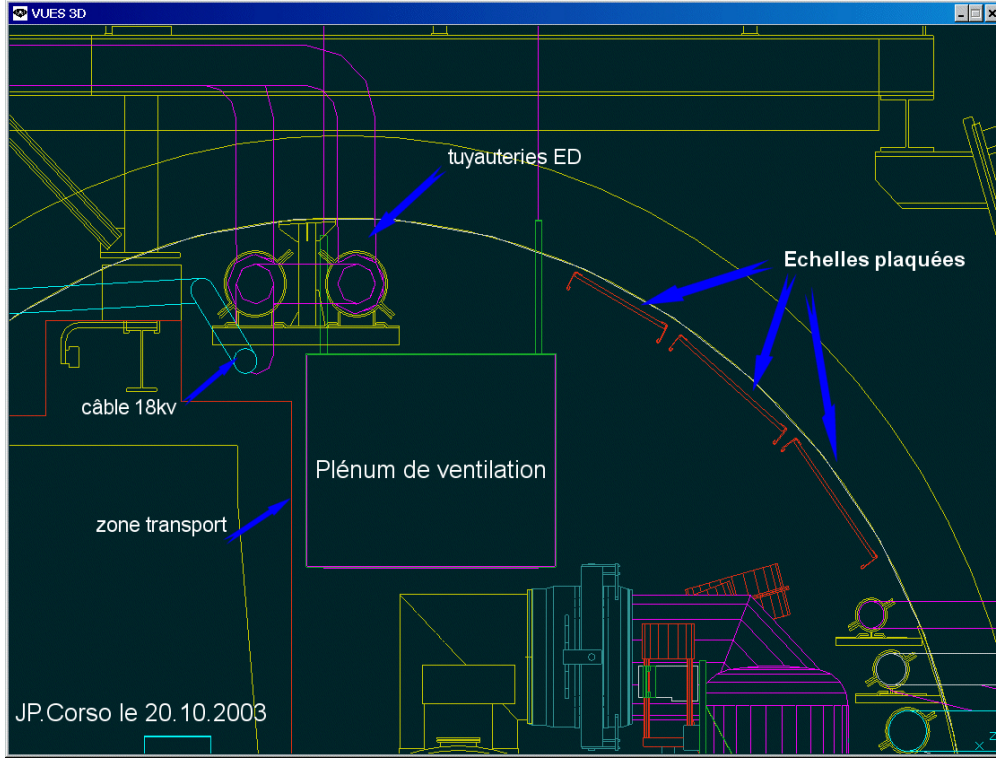


Figure 7.64: Air-duct in LSS7 indicated by the box labelled 'Plenum de ventilation' [610].

6292 **7.17.2 Required performance**

6293 The main requirements for the LHeC ring-ring electron and positron injectors are summarized in Table 7.35.

Table 7.35: Main parameters for the LHeC RR injector

particle types	$e^+, e^-$
polarized	no
injection energy	$E_b = 10 \text{ GeV}$
bunch intensity	$2 \times 10^{10} e = 3.2 \text{ nC}$
pulse frequency	$\geq 5/\text{s}$

6294 Polarization is not required from the ring injectors. It would be very difficult to maintain the polarization  
 6295 during the acceleration in the main ring. Instead, polarization can be built up at top energy from synchrotron  
 6296 radiation.

6297 The electron bunch intensity for nominal LHeC performance is  $1.4 \times 10^{10}$ . The target intensity for the  
 6298 injector is taken as  $2 \times 10^{10}$  which includes a safety factor and allows for losses at injection and during the  
 6299 ramp. Higher single-bunch intensities may be useful, with a smaller number of bunches, for the e-A mode of  
 6300 operation. LEP was operated with much higher bunch intensities up to  $4 \times 10^{11}$  limited by the transverse  
 6301 mode coupling instability (TMCI). The TMCI threshold current can be estimated from [615]

$$I_{th} = \frac{\omega_s E}{e \sum \beta k_{\perp}(\sigma_s)} \quad (7.33)$$

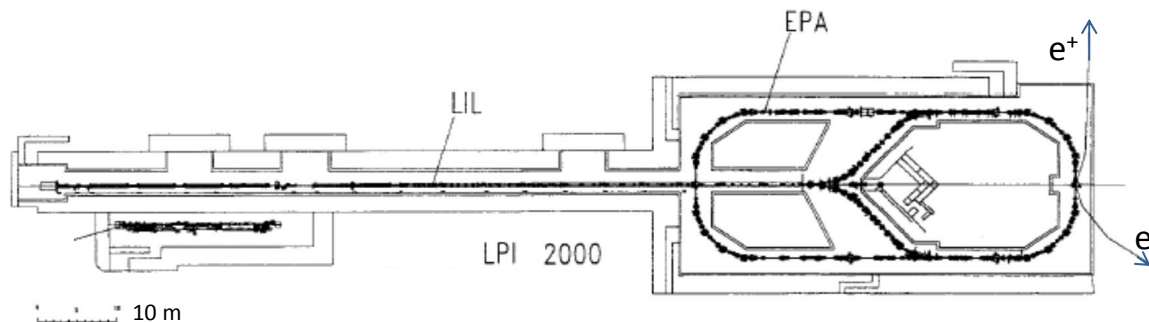


Figure 7.65: Layout of the LPI in 2000.

6302 where  $\omega_s = 2\pi Q_s f_{\text{rev}}$  is the synchrotron frequency,  $e$  the elementary charge,  $E$  is the beam energy,  $\beta$  the  
 6303 beta function value at the location of the impedance and  $k_{\perp}$  the loss factor which accounts for the transverse  
 6304 impedance of the machine. LEP had a design injection energy of 20 GeV. It was raised to 22 GeV to increase  
 6305 the TMCI threshold.

6306 The relatively low bunch intensity required for the LHeC allows for direct injection without accumulation  
 6307 and for a lower injection energy compared to LEP. The LHeC transverse impedance will be similar to LEP,  
 6308 with a smaller contribution from the reduced number of cavities and an increased impedance contribution  
 6309 from the more compact beam-pipe cross-section. Lowering the beam energy results in weak bending fields  
 6310 and loss of synchrotron radiation damping. A beam energy of a few GeV may still be tolerable for transverse  
 6311 mode coupling but would not be practical for magnet stability and require strong wigglers to get a significant  
 6312 radiation damping (otherwise this requires a minimum beam energy of the order of 10 GeV).

6313 A pulse frequency of on average 5 Hz is required, to fill the LHeC electron ring with 2808 bunches in  
 6314 10 minutes.

6315 The injector requirements summarized in Table 7.35 are within the reach of proven technology and con-  
 6316 cepts. An example is the FACET facility at SLAC which provides  $2 \times 10^{10}$  electrons of 23 GeV energy at  
 6317 30 Hz repetition frequency [616].

6318 The intensities and repetition frequency required here match well with the performance of the LIL, the  
 6319 first part of the LEP pre-injectors, which we reconsider here for the source, positron accumulation and pre-  
 6320 acceleration to 0.6 GeV. For the acceleration to 10 GeV we propose a new, superconducting recirculating  
 6321 LINAC.

### 6322 7.17.3 Source, accumulator and acceleration to 0.6 GeV

6323 Figure 7.65 shows the layout of the LPI (LEP Pre-Injector) as it was working in 2000. The LPI was composed  
 6324 of the LIL (LEP Injector Linac) and the EPA (Electron Positron Accumulator).

6325 Table 7.36 gives the beam characteristics at the end of LIL.

Beam energy	200 to 700 MeV
Charge	$5 \times 10^8$ to $2 \times 10^{10} e^-$ / pulse
Pulse length	10 to 40 ns (FWHM)
Repetition frequency	1 to 100 Hz
Beam sizes (rms)	3 mm

Table 7.36: LIL beam parameters.



6326

Table 7.37 gives the electron and positron beam parameters at the exit of EPA.

Energy	200 to 600 MeV
Charge	up to $4.5 \times 10^{11} e^\pm$
Intensity	up to 0.172 A
Number of bunches	1 to 8
Emittance	0.1 mm.mrad
Tune	$Q_x = 4.537, Q_y = 4.298$

Table 7.37: The electron and positron beam parameters at the exit of EPA.

6327

6328

6329

6330

6331

With 8 bunches in the EPA for a 1.14 s cycle, the 2808 bunches required for the LHeC could be filled in 6.7 min which is perfectly adequate. According to the original LEP injector design report [617–619] Vol.I, the cycle length for positrons is 11.22 s which would allow the 2808 bunches to be filled in 66 minutes. We conclude that the LIL+EPA performance is fully adequate for the LHeC. A reduction of the cycle length for positrons would be useful to reduce the filling time.

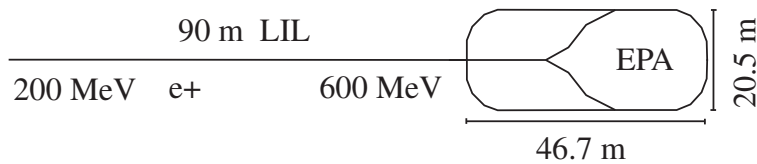


Figure 7.66: LIL and EPA

6332

### Timing considerations

6333

6334

6335

6336

6337

6338

6339

6340

EPA was planned for 1 to 8 bunches compatible with the LEP RF-frequency. The EPA circumference of 125.665 m corresponds to  $t_{\text{rev}} = 419.173$  ns, which is  $16.75 \times 25$  ns and would in theory allow for 16 bunches spaced by 25 ns as relevant for the LHeC. Injection in batches of 72 bunches as possible for protons into the LHC would require a five times larger damping ring which would be rather expensive.

EPA had an RF-frequency  $f_{\text{RF}} = 19.0852$  MHz. It will be increased to 40 MHz to allow for a bunch spacing of 25 ns. For the injection into the LHC we propose a fast kicker system with a kicker rise-time below 25 ns. This conserves the dimensions of EPA and gives full flexibility to place the bunches into the LHeC electron ring as required to collide with the proton or ion bunches [586, 587].

6341

### 7.17.4 10 GeV injector

6342

6343

For the acceleration to 10 GeV we propose a re-circulating LINAC, designed as a downscaled, low energy version of the 25 GeV ELFE at CERN design [614] using modern ILC-type RF-technology.

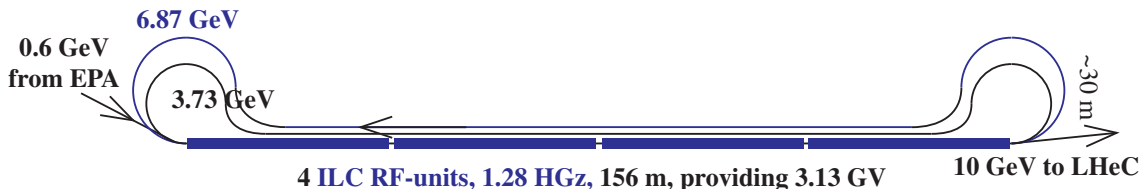


Figure 7.67: Recirculator using 4 ILC modules.

6344

6345

A sketch of the proposed machine is shown in Fig. 7.67. The acceleration is provided by 4 RF-units of the ILC type, providing together 3.13 GV acceleration.

6346 The acceleration from 0.6 GeV to 10 GeV is achieved in three passages through the LINAC. This requires  
 6347 only two re-circulation arcs which can be constructed in the horizontal plane. The maximum energy in the  
 6348 last re-circulation arc is  $10 - 3.13 = 6.87$  GeV.

6349 For a beam energy  $E$  and bending radius  $\rho$ , the energy loss  $U_0$  by synchrotron radiation in the single  
 6350 passage through a re-circulation arc is

$$U_0 = C_\gamma \frac{E^4}{\rho} \quad (7.34)$$

6351 where

$$C_\gamma = \frac{e^2}{3\epsilon_0} \frac{1}{(mc^2)^4} = 8.846 \times 10^{-5} \text{ m GeV}^{-3} .$$

6352 where  $e$  is the elementary charge and  $m$  the electron mass. The relative energy spread is increased by the  
 6353 synchrotron radiation in a single passage by

$$\sigma_e = r_e c_f \frac{\gamma^{5/2}}{\rho} \quad (7.35)$$

6354 where  $r_e$  is the classical electron radius and

$$c_f = \frac{3}{2} \sqrt{\frac{55\pi}{27\sqrt{3}\alpha}} = 33.75 . \quad (7.36)$$

6355 A bending radius of  $\rho = 2$  m at  $E = 6.87$  GeV would result in an energy loss by recirculation of  $U_0 = 98$  MeV  
 6356 and an energy spread of  $10^{-3}$ . This would both be tolerable, but require very strong superconducting 11 tesla  
 6357 magnets for the 6.87 GeV recirculation.

6358 At this stage, we propose the use of warm 2 tesla magnets, resulting in a bending radius of  $\rho = 11.5$  m  
 6359 for the 6.87 GeV recirculation and  $\rho = 6.2$  m for the 3.73 GeV recirculation. The values for the energy loss  
 6360 and spread are listed in Table 7.38.

Table 7.38: Energy, bending field and radius, energy loss and energy spread in the recirculator magnets.

$E$ GeV	$B$ tesla	$\rho$ m	$U_0$ MeV	$\sigma_e$
6.87	2	11.45	17.1	$1.7 \times 10^{-4}$
3.73	2	6.23	2.8	$7 \times 10^{-5}$

6361 To save space and allow for a single LINAC tunnel, we propose a dogbone-like shape for the recirculators  
 6362 as shown in Fig. 7.67.

## Chapter 8

# Linac-Ring Collider

## 8.1 Basic Parameters and Configurations

### 8.1.1 General Considerations

A high-energy electron-proton collider can be realized by accelerating electrons (or positrons) in a linear accelerator (linac) to 60–140 GeV and colliding them with the 7-TeV protons circulating in the LHC. Except for the collision point and the surrounding interaction region, the tunnel and the infrastructure for such a linac are separate and fully decoupled from the LHC operation, from the LHC maintenance work, and from other LHC upgrades (e.g., HL-LHC and HE-LHC).

The technical developments required for this type of collider can both benefit from and be used for many future projects. In particular, to deliver a long or continuous beam pulse, as required for high luminosity, the linac must be based on superconducting (SC) radio frequency (RF) technology. The development and industrial production of its components can exploit synergies with numerous other advancing SC-RF projects around the world, such as the European XFEL at DESY, eRHIC, ESS, ILC, CEBAF upgrade, CESR-ERL, JLAMP, and the CERN HP-SPL.

For high luminosity operation at a beam energy of 50–70 GeV the linac should be operated in continuous wave (CW) mode, which restricts the maximum RF gradient through the associated cryogenics power, to a value of about 20 MV/m or less. In order to limit the active length of such a linac and to keep its construction and operating costs low, the linac should, and can, be recirculating. For the sake of energy efficiency and to limit the overall site power, while boosting the luminosity, the SC recirculating CW linac can be operated in energy-recovery (ER) mode.

Electron-beam energies higher than 70 GeV, e.g. 140 GeV, can be achieved by a pulsed SC linac, similar to the XFEL, ILC or SPL. In this case the accelerating gradient can be larger than for CW operation, i.e. above 30 MV/m, which minimizes the total length, but recirculation is no longer possible at this beam energy due to prohibitively high synchrotron-radiation energy losses in any return arc of reasonable dimension. As a consequence the standard energy recovery scheme using recirculation cannot be implemented and the luminosity of such a higher-energy lepton-hadron collider would be more than an order of magnitude lower than the one of the lower-energy CW ERL machine, at the same wall-plug power.

For a linac it is straightforward to deliver a 80–90% polarized electron beam.

The production of a sufficient number of positrons to deliver positron-proton collisions at a similar luminosity as for electron-proton collisions is challenging for a linac-ring collider<sup>1</sup> A conceivable path towards decent proton-positron luminosities would include a recycling of the spent positrons, together with the recovery of their energy.

The development of a CW SC recirculating energy-recovery linac (ERL) for LHeC would prepare the ground, the technology and the infrastructure for many possible future projects, e.g., for an International

---

<sup>1</sup>A review of linac-ring type collider proposals can be found in Ref. [?].

6398 Linear Collider, for a Muon Collider<sup>2</sup>, for a neutrino factory, or for a proton-driven plasma wake field  
6399 accelerator. A ring-linac LHeC would, therefore, promote any conceivable future high-energy physics project,  
6400 while pursuing an attractive forefront high-energy physics programme in its own right.

### 6401 8.1.2 ERL Performance and Layout

6402 Particle physics imposes the following performance requirements. The lepton beam energy should be 60  
6403 GeV or higher and the electron-proton luminosity of order  $10^{33} \text{ cm}^{-2}\text{s}^{-1}$ . Positron-proton collisions are  
6404 also required, with at least a few percent of the electron-proton luminosity. Since the LHeC should operate  
6405 simultaneously with LHC  $pp$  physics, it should not degrade the  $pp$  luminosity. Both electron and positron  
6406 beams should be polarized. Lastly, the detector acceptance should extend down to  $1^\circ$  or less. In addition,  
6407 the total electrical power for the lepton branch of the LHeC collider should stay below 100 MW.

6408 For round-beam collisions, the luminosity of the linac-ring collider [13] is written as

$$L = \frac{1}{4\pi e} \frac{N_{b,p}}{\epsilon_p} \frac{1}{\beta_p^*} I_e H_{hg} H_D, \quad (8.1)$$

6409 where  $e$  denotes the electron charge,  $N_{b,p}$  the proton bunch population,  $\beta_p^*$  the proton IP beta function,  $I_e$  the  
6410 average electron beam current,  $H_{hg}$  the geometric loss factor arising from crossing angle and hourglass effect,  
6411 and  $H_D$  the disruption enhancement factor due to the electron pinch in collision, or luminosity reduction  
6412 factor from the anti-pinch in the case of positrons. In the above formula, it is assumed that the electron  
6413 bunch spacing is a multiple of the proton beam bunch spacing. The latter could be equal to 25, 50 or 75 ns,  
6414 without changing the luminosity value.

6415 The ratio  $N_{b,p}/\epsilon_p$  is also called the proton beam brightness. Among other constraints, the LHC beam  
6416 brightness is limited by the proton-proton beam-beam limit. For the LHeC design we assume the brightness  
6417 value obtained for the ultimate bunch intensity,  $N_{p,p} = 1.7 \times 10^{11}$ , and the nominal proton beam emittance,  
6418  $\epsilon_p = 0.5 \text{ nm}$  ( $\gamma\epsilon_p = 3.75 \mu\text{m}$ ). This corresponds to a total  $pp$  beam-beam tune shift of 0.01. More than two  
6419 times higher values have already been demonstrated, with good  $pp$  luminosity lifetime, during initial LHC  
6420 beam commissioning, indicating a potential for higher  $ep$  luminosity.

6421 To maximize the luminosity the proton IP beta function is chosen as 0.1 m. This is considerably smaller  
6422 than the 0.55 m for the  $pp$  collisions of the nominal LHC. The reduced beta function can be achieved by  
6423 reducing the free length between the IP and the first proton quadrupole (10 m instead of 23 m), and by  
6424 squeezing only one of the two proton beams, namely the one colliding with the leptons, which increases the  
6425 aperture available for this beam in the last quadrupoles. In addition, we assume that the final quadrupoles  
6426 could be based on Nb<sub>3</sub>Sn superconductor technology instead of Nb-Ti. The critical field for Nb<sub>3</sub>Sn is almost  
6427 two times higher than for Nb-Ti, at the same temperature and current density, allowing for correspondingly  
6428 larger aperture and higher quadrupole gradient. Nb<sub>3</sub>Sn quadrupoles are presently under development for  
6429 the High-Luminosity LHC upgrade (HL-LHC).

6430 The geometric loss factor  $H_{hg}$  needs to be optimized as well. For round beams with  $\sigma_{z,p} \gg \sigma_{z,e}$  (well  
6431 fulfilled for  $\sigma_{z,p} \approx 7.55 \text{ cm}$ ,  $\sigma_{z,e} \approx 300 \mu\text{m}$ ) and  $\theta_c \ll 1$ , it can be expressed as<sup>3</sup>

$$H_{hg} = \frac{\sqrt{\pi} z e^{z^2} \text{erfc}(z)}{S}, \quad (8.2)$$

6432 where

$$z \equiv 2 \frac{(\beta_e^*/\sigma_{z,p})(\epsilon_e/\epsilon_p)}{\sqrt{1 + (\epsilon_e/\epsilon_p)^2}} S$$

<sup>2</sup>The proposed Muon Collider heavily relies on SC recirculating linacs for muon acceleration as well as on a SC-linac proton driver.

<sup>3</sup>The derivation of this formula is similar to the one for the LHC in Ref. [621], with the difference that here the two beams have different emittances and IP beta functions, and the electron bunch length is neglected. Curves obtained with formula (8.2) were first reported in [622].

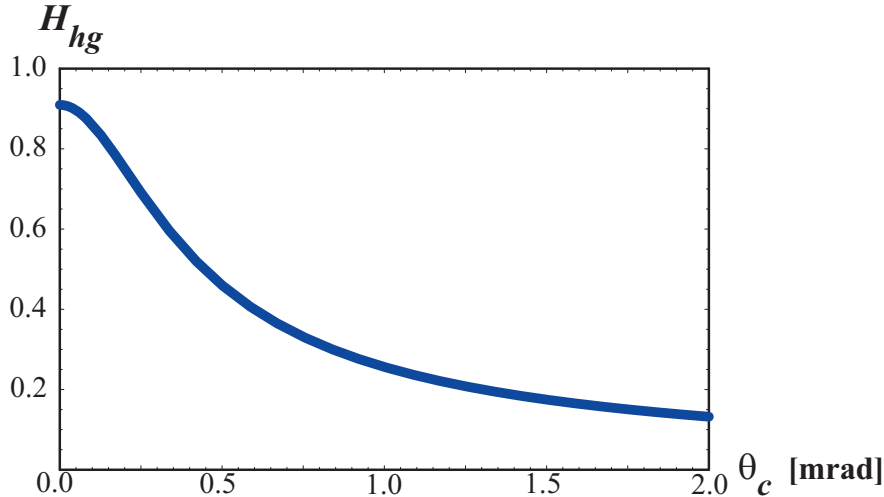


Figure 8.1: Geometric luminosity loss factor  $H_{hg}$ , (8.2), as a function of the total crossing angle

6433 and

$$S \equiv \sqrt{1 + \frac{\sigma_{x,p}^2 \theta_c^2}{8\sigma_p^{*2}}}.$$

6434 Luminosity loss from a crossing angle is avoided by head-on collisions. The luminosity loss from the hourglass  
 6435 effect, due to the long proton bunches and potentially small electron beta functions, is kept small, thanks  
 6436 to a “small” linac electron beam emittance of 0.43 nm ( $\gamma\epsilon_e = 50 \mu\text{m}$ ). We note that the assumed electron-  
 6437 beam emittance, though small when compared with a storage ring of comparable energy, is still very large  
 6438 by linear-collider standards.

6439 The disruption enhancement factor for electron-proton collisions is about  $H_D \approx 1.35$ , according to  
 6440 Guinea-Pig simulations [623] and a simple estimate based on the fact that the average rms size of the  
 6441 electron beam during the collision approaches a value equal to  $1/\sqrt{2}$  of the proton beam size. This additional  
 6442 luminosity increase from disruption is not taken into account in the numbers given below. On the other  
 6443 hand, for positron-proton collisions the disruption of the positrons leads to a significant luminosity reduction,  
 6444 by roughly a factor  $H_D \approx 0.3$ , similar to the case of electron-electron collisions [624].

6445 The final parameter determining the luminosity is the average electron (or positron) beam current  $I_e$ . It  
 6446 is closely tied to the total electrical power available (taken to be 100 MW).

### 6447 Crossing Angle and IR Layout

6448 The colliding electron and proton beams need to be separated by 7 cm at a distance of 10 m from the  
 6449 IP in order to enter through separate holes in the first proton quadrupole magnet. This separation could  
 6450 be achieved with a crossing angle of 7 mrad and crab cavities. The required crab voltage would, however,  
 6451 need to be of order 200 MV, which is 20–30 times the voltage needed for  $pp$  crab crossing at the HL-LHC.  
 6452 Therefore, crab crossing is not considered an option for the L-R LHeC. Without crab cavities, any crossing  
 6453 angle should be smaller than 0.3 mrad, as is illustrated in Fig. 8.1. Such small a crossing angle is not useful,  
 6454 compared with the 7 mrad angle required for the separation. The R-L interaction region (IR), therefore, uses  
 6455 detector-integrated dipole fields around the collision point, to provide head-on  $ep$  collisions ( $\theta_c = 0$  mrad)  
 6456 and to separate the beams by the required amount. A dipole field of about 0.3 T over a length of  $\pm 9$  m  
 6457 accomplishes these goals.

6458 The IR layout with separation dipoles and crossing angle is sketched in Fig. 8.2. Significant synchrotron  
 6459 radiation, with 48 kW average power, and a critical photon energy of 0.7 MeV, is emitted in the dipole

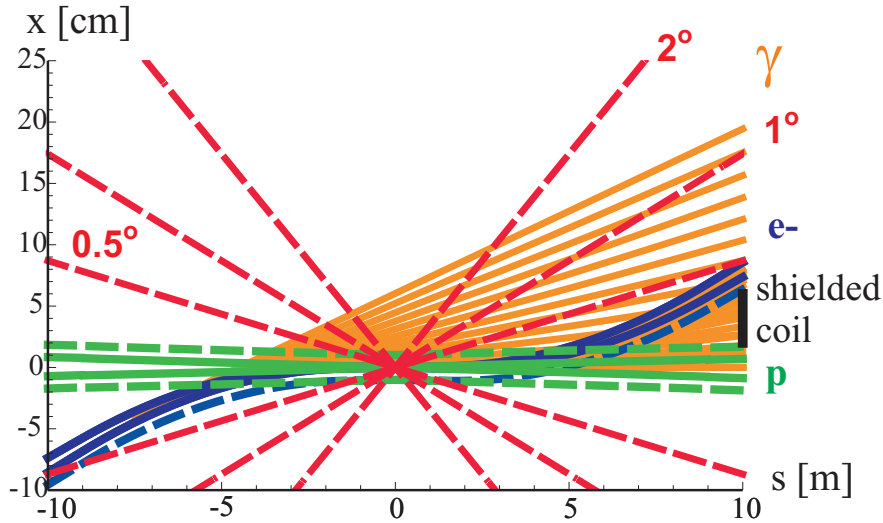


Figure 8.2: Linac-ring interaction-region layout. Shown are the beam envelopes of  $10\sigma$  (electrons) [solid blue] or  $11\sigma$  (protons) [solid green], the same envelopes with an additional constant margin of 10 mm [dashed], the synchrotron-radiation fan [orange], the approximate location of the magnet coil between incoming protons and outgoing electron beam [black], and a “1 degree” line.

6460 fields. A large portion of this radiation is extracted through the electron and proton beam pipes. The SC  
 6461 proton magnets can be protected against the radiation heat load by an absorber placed in front of the first  
 6462 quadrupole and by a liner inside the beam pipe. Backscattering of synchrotron radiation into the detector  
 6463 is minimized by shaping the surface of absorbers and by additional masking.

6464 The separation dipole fields modify, and enhance, the geometric acceptance of the detector. Figure 8.3  
 6465 illustrates that scattered electrons with energies of 10–50 GeV might be detected at scattering angles down  
 6466 to zero degrees.

### 6467 **Electron Beam and the Case for Energy Recovery**

6468 The electron-beam emittance and the electron IP beta function are not critical, since the proton beam size is  
 6469 large by electron-beam standards (namely about  $7\ \mu\text{m}$  rms compared with nm beam-sizes for linear colliders).  
 6470 The most important parameter for high luminosity is the average beam current,  $I_e$ , which linearly enters  
 6471 into the luminosity formula (8.1). In addition to the electron beam current, also the bunch spacing (which  
 6472 should be a multiple of the LHC 25-ns proton spacing) and polarization (80–90% for the electrons) need  
 6473 to be considered. Having pushed all other parameters in (8.1), Fig. 8.4 illustrates that an average electron  
 6474 current of about 6.4 mA is required to reach the target luminosity of  $10^{33}\ \text{cm}^{-2}\text{s}^{-1}$ .

6475 For comparison, the CLIC main beam has a design average current of 0.01 mA [625], so that it falls  
 6476 short by a factor 600 from the LHeC requirement. For other applications it has been proposed to raise the  
 6477 CLIC beam power by lowering the accelerating gradient, raising the bunch charge by a factor of two, and  
 6478 increasing the repetition rate up to three times, which raises the average beam current by a factor 6 to about  
 6479 0.06 mA (this type of CLIC upgrade is described in [268]). This ultimate CLIC main beam current is still  
 6480 a factor 100 below the LHeC target. On the other hand, the CLIC drive beam would have a sufficiently  
 6481 high current, namely 30 mA, but at the low energy 2.37 GeV, which would not be useful for high-energy  $ep$   
 6482 physics. Due to this low energy, also the drive beam power is still a factor of 5 smaller than the one required  
 6483 by LHeC. Finally, the ILC design current is about 0.04 mA [626], which also falls more than a factor 100  
 6484 short of the goal.

6485 Fortunately, SC linacs can provide higher average current, e.g. by increasing the linac duty factor 10–100  
 6486 times, or even running in continuous wave (CW) mode, at lower accelerating gradient. Example average

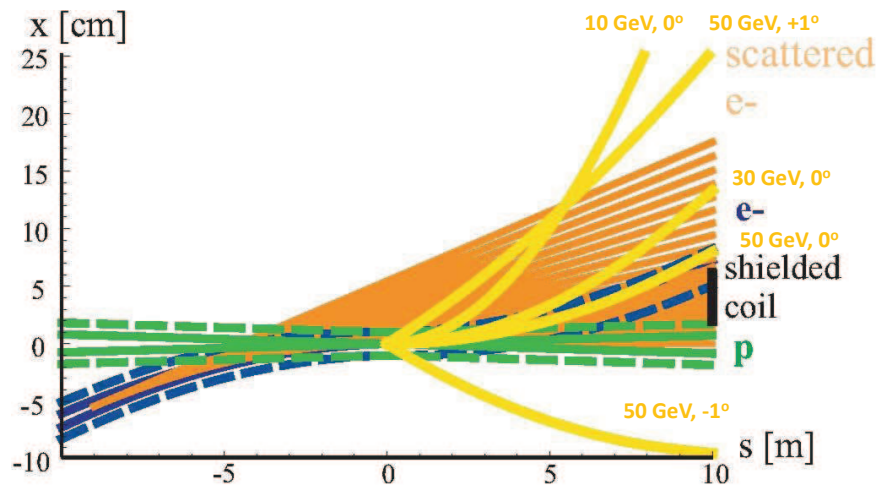


Figure 8.3: Example trajectories in the detector dipole fields for electrons of different energies and scattering angles, demonstrating an enhancement of the detector acceptance by the dipoles.

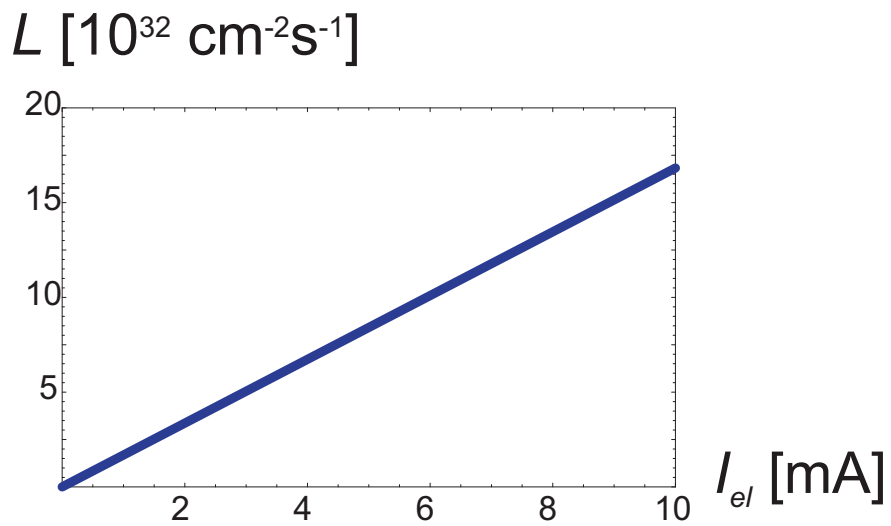


Figure 8.4: Linac-ring luminosity versus average electron beam current, according to (8.1).

6487 currents for a few proposed designs illustrate this point: The CERN High-Power Superconducting Proton  
 6488 Linac aims at about 1.5 mA average current (with 50 Hz pulse rate) [627], the Cornell ERL design at 100  
 6489 mA (cw) [628], and the eRHIC ERL at about 50 mA average current at 20 GeV beam energy (cw) [629].  
 6490 All these designs are close to, or exceed, the LHeC requirements for average beam current and average beam  
 6491 power (6.4 mA at 60 GeV). It is worth noting that the JLAB UV/IR 4th Generation Light Source FEL is  
 6492 routinely operating with 10 mA average current (135 pC pulses at 75 MHz) [630]. The 10-mA current limit  
 6493 in the JLAB FEL arises from well understood beam break up [?] and significantly larger currents would be  
 6494 possible with suitably designed cavities. It is, therefore, believed that more than 6.4 mA for the LHeC ERL  
 6495 would be feasible.

6496 The target LHeC IP electron-beam power is 384 MW. With a standard wall-plug-power to RF conversion  
 6497 efficiency around 50%, this would imply about 800 MW electrical power, far more than available. This  
 6498 highlights the need for energy recovery where the energy of the spent beam, after collision, is recuperated  
 6499 by returning the beam 180° out of phase through the same RF structure that had earlier been used for its  
 6500 acceleration, again with several recirculations. An energy recovery efficiency  $\eta_{ER}$  reduces the electrical power  
 6501 required for RF power generation at a given beam current by a factor  $(1 - \eta_{ER})$ . We need an efficiency  $\eta_{ER}$   
 6502 above 90% or higher to reach the beam-current goal of 6.4 mA with less than 100 MW total electrical power.

6503 The above arguments have given birth to the LHeC Energy Recovery Linac high-luminosity baseline  
 6504 design, which is being presented in this chapter.

### 6505 Choice of RF Frequency

6506 Two candidate RF frequencies exist for the SC linac. One possibility is operating at the ILC and XFEL RF  
 6507 frequency around 1.3 GHz, the other choosing a frequency of about 720 MHz, close to the RF frequencies of  
 6508 the CERN High-Power SPL, eRHIC, and the European Spallation Source (ESS).

6509 The ILC frequency would have the advantage of synergy with the XFEL infrastructure, of profiting from  
 6510 the high gradients reached with ILC accelerating cavities, and of smaller structure size, which could reduce  
 6511 the amount of high-purity niobium needed by a factor 2 to 4.

6512 Despite these advantages, the present LHeC baseline frequency is 720 MHz, or, more precisely, 721 MHz  
 6513 to be compatible with the LHC bunch spacing. The arguments in favor of this lower frequency are the  
 6514 following:

- 6515 • A frequency of 721 MHz requires less cryo-power (about two times less than at 1.3 GHz according to  
 6516 BCS theory; the exact difference will depend on the residual resistance [631]).
- 6517 • The lower frequency will facilitate the design and operation of high-power couplers [632], though the  
 6518 couplers might not be critical [633].
- 6519 • The smaller number of cells per module (of similar length) at lower RF frequency is preferred with  
 6520 regard to trapped modes [634].
- 6521 • The lower-frequency structures reduce beam-loading effects and transverse wake fields.
- 6522 • The project can benefit from synergy with SPL, eRHIC and ESS.
- 6523 • Other projects, e.g. low-emittance ERL light sources, can reduce the bunch charge by choosing a higher  
 6524 RF frequency. This is not the case for the LHeC, where the bunch distance is not determined by the  
 6525 RF frequency, but by the distance between proton bunches.

6526 In case the cavity material costs at 721 MHz would turn out to be a major concern, they could be reduced  
 6527 by applying niobium as a thin film on a copper substrate, rather than using bulk niobium. Establishing  
 6528 the necessary cavity performance with thin-film coating will require further R&D. It is expected that the  
 6529 thin-film technology may also enhance the intrinsic cavity properties, e.g. increase the  $Q_0$  value.

6530 Linac RF parameters for both 720 MHz and 1.3 GHz in CW mode as well as for a pulsed 1.3-GHz  
 6531 option are compared in Table 8.1. The 721 MHz parameters are derived from eRHIC [635]. Pulsed-linac  
 6532 applications for LHeC are discussed in subsections 8.1.4 and 8.1.6.



	ERL 721 MHz	ERL 1.3 GHz	Pulsed
RF duty factor	CW	CW	0.05
RF frequency [GHz]	0.72	1.3	1.3
cavity length [m]	1	~1	~1
energy gain / cavity [MeV]	18	18	31.5
R/Q [ $1\Omega$ in Linac def.]	450	1200	1200
$Q_0$ [ $10^{10}$ ]	4.0	1	1
power loss stat. [W/cav.]	5	< 0.5	< 0.5
power loss RF [W/cav.]	18	27	< 10
“W per W” (1.8 K to RT)	700	700	700
power loss / GeV at RT [MW]	0.51–1.44	0.6–1.1	0.24
length / GeV [m] (filling=0.57)	97	97	56

Table 8.1: Linac RF parameters for two different RF frequencies and two modes of operation. The row “W to W” refers to the power needed at room temperature (RT) to cool a heat unit at 1.8 K. The numbers quoted for 721 MHz reflect the (measured) parameters of eRHIC prototype cavity BNL-I and an extrapolation to the improved cavity BNL-III [636]. The heat-load values at 18 MV/m indicated for 1.3 GHz have been extrapolated from [626]. The additional static heat loss depends on the cryomodule design and can be made small compared with the dynamic loss.

### 6533 ERL Electrical Site Power

6534 The cryopower for two 10-GeV accelerating SC linacs is 28.9 MW, assuming 23 W/m heat load at 1.8 K and  
6535 18 MV/m cavity gradient and 700 “W per W” cryo efficiency as for the ILC. The RF power needed to control  
6536 microphonics for the accelerating RF is estimated at 22.2 MW, considering that 10 kW/m RF power may  
6537 be required, as for eRHIC, with 50% RF generation efficiency. The electrical power for the additional RF  
6538 compensating the synchrotron-radiation energy loss is 24.1 MW, with an RF generation efficiency of 50%.  
6539 The cryo power for the compensating RF is 2.1 MW, provided in additional 1.44 GeV linac sections, and  
6540 the microphonics control for the compensating RF requires another 1.6 MW. In addition, with an injection  
6541 energy of 50 MeV, 6.4 mA beam current, and as usual 50% efficiency, the electron injector consumes about  
6542 6.4 MW. A further 3 MW is budgeted for the recirculation-arc magnets [637]. Together this gives a grand  
6543 total of 88.3 MW electrical power, some 25% below the 100 MW limit. The LHeC ERL power budget is  
6544 summarized in Table 8.2.

Item	Electrical Power [MW]
Main linac cryopower	18.0
Microphonics control	22.2
Extra RF to compensate SR losses	24.1 MW
Extra-RF cryopower	1.6
Electron injector	6.4
Arc magnets	3.0
Total	75.3

Table 8.2: ERL power budget.

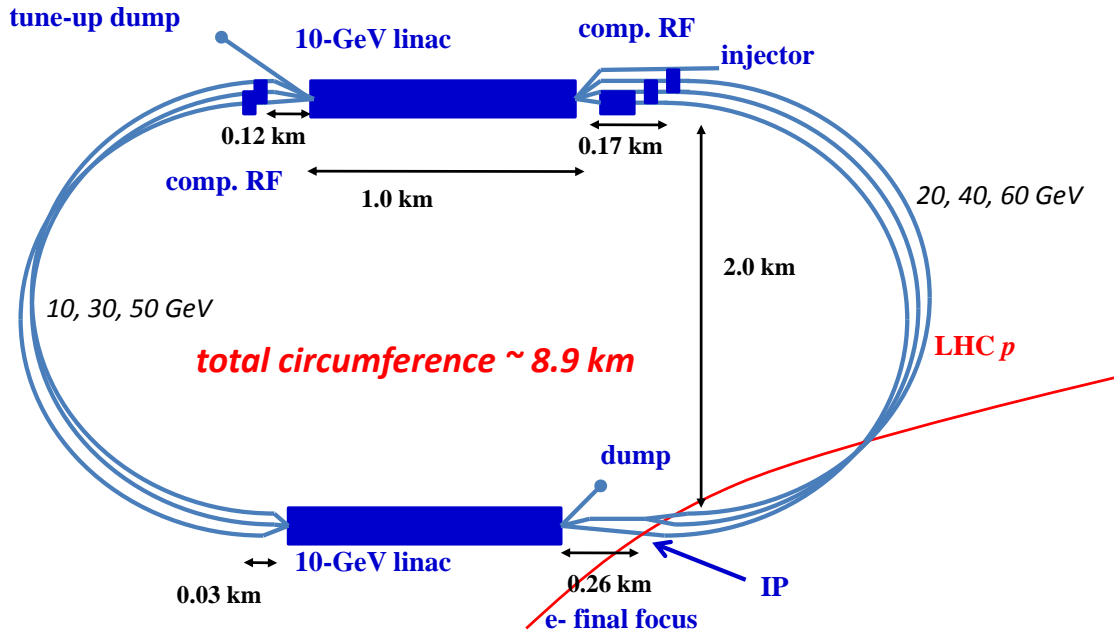


Figure 8.5: LHeC ERL layout including dimensions.

## ERL Configuration

The ERL configuration is depicted in Fig. 8.5. The shape, arc radius and number of passes have been optimized with respect to construction cost and with respect to synchrotron-radiation effects [638].

The ERL is of racetrack shape. A 500-MeV electron bunch coming from the injector is accelerated in each of the two 10-GeV SC linacs during three revolutions, after which it has obtained an energy of 60 GeV. The 60-GeV beam is focused and collided with the proton beam. It is then bent by  $180^\circ$  in the highest-energy arc beam line before it is sent back through the first linac, at a decelerating RF phase. After three revolutions with deceleration, re-converting the energy stored in the beam to RF energy, the beam energy is back at its original value of 500 MeV, and the beam is now disposed in a low-power 3.2-MW beam dump. A second, smaller (tune-up) dump could be installed behind the first linac.

Strictly speaking, with an injection energy into the first linac of 0.5 GeV, the energy gain in the two accelerating linacs need not be 10 GeV each, but about 9.92 GeV, in order to reach 60 GeV after three passages through each linac. Considering a rough value of 10 GeV means that we overestimate the electrical power required by about 1%.

Each arc contains three separate beam lines at energies of 10, 30 and 50 GeV on one side, and 20, 40 and 60 GeV on the other. Except for the highest energy level of 60 GeV, at which there is only one beam, in each of the other arc beam lines there always co-exist a decelerating and an accelerating beam. The effective arc radius of curvature is 1 km, with a dipole bending radius of 764 m [639].

The two straight sections accommodate the 1-km long SC accelerating linacs. In addition to the 1km linac section, there is an additional space of 290 m in each straight section of the racetrack. In one straight of the racetrack 260 m of this additional length is allocated for the electron final focus (plus matching and splitting), the residual 30 m on the other side of the same straight allows for combining the beam and matching the optics into the arc. In the second straight section of the racetrack the additional length of the straight sections houses the additional linacs for compensating the 1.88 GeV energy loss in the return arcs [640]. For the highest energy, 60 GeV, there is a single beam and the compensating RF (750 MV) can have the same frequency, 721 MHz, as in the main linac [640]. For the other energies, a higher harmonic RF

6571 system, e.g. at 1.442 GHz, can compensate the energy loss for both decelerating and accelerating beams,  
 6572 which are  $180^\circ$  out of phase at 721 MHz. On one side of the second straight one must compensate a total  
 6573 energy loss of about 907 MeV per particle ( $=750+148+9$  MeV, corresponding to the energy loss at 60, 40  
 6574 and 20 GeV, respectively), which should easily fit within a length of 170 m. On the other side one has to  
 6575 compensate 409 MeV ( $=362+47$  MeV), corresponding to SR energy losses at 50 and 30 GeV), for which a  
 6576 length of 120 m is available.

6577 The total circumference of the ERL racetrack is chosen as 8.9 km, equal to one third of the LHC  
 6578 circumference. This choice has the advantage that one could introduce ion-clearing gaps in the electron  
 6579 beam which would match each other on successive revolutions (e.g. for efficient ion clearing in the linacs  
 6580 that are shared by six different parts of the beam) and which would also always coincide with the same proton  
 6581 bunch locations in the LHC, so that in the latter a given proton beam would either always collide or never  
 6582 collide with the electrons [641]. Ion clearing may be necessary to suppress ion-driven beam instabilities. The  
 6583 proposed implementation scheme would remove ions while minimizing the proton emittance growth which  
 6584 could otherwise arise when encountering collisions only on some of the turns. In addition, this arrangement  
 6585 can be useful for comparing the emittance growth of proton bunches which are colliding with the electrons  
 6586 and those which are not.

6587 The length of individual components is as follows. The exact length of the 10-GeV linac is 1008 m. The  
 6588 individual cavity length is taken to be 1 m. The optics consists of 56-m long FODO cells with 32 cavities.  
 6589 The number of cavities per linac is 576. The linac cavity filling factor is 57.1%. The effective arc bending  
 6590 radius is set to be 1000 m. The bending radius of the dipole magnets is 764 m, corresponding to a dipole  
 6591 filling factor of 76.4% in the arcs. The longest SR compensation linac has a length of 84 m (replacing the  
 6592 energy lost by SR at 60 GeV). Combiners and splitters between straights and arcs require about 20–30 m  
 6593 space each. The electron final focus may have a length of 200–230 m.

## 6594 IP Parameters and Beam-Beam Effects

6595 Table 8.3 presents interaction-point (IP) parameters for the electron and proton beams.

	protons	electrons
beam energy [GeV]	7000	60
Lorentz factor $\gamma$	7460	117400
normalized emittance $\gamma\epsilon_{x,y}$ [ $\mu\text{m}$ ]	3.75	50
geometric emittance $\epsilon_{x,y}$ [nm]	0.40	0.43
a IP beta function $\beta_{x,y}^*$ [m]	0.10	0.12
rms IP beam size $\sigma_{x,y}^*$ [ $\mu\text{m}$ ]	7	7
initial rms IP beam divergence $\sigma_{x',y'}^*$ [ $\mu\text{rad}$ ]	70	58
beam current [mA]	$\geq 430$	6.4
bunch spacing [ns]	25 or 50	(25 or) 50
bunch population [ns]	$1.7 \times 10^{11}$	(1 or) $2 \times 10^9$

Table 8.3: IP beam parameters

6596 Due to the low charge of the electron bunch, the proton head-on beam-beam tune shift is tiny, namely  
 6597  $\Delta Q_p = +0.0001$ , which amounts to only about 1% of the LHC  $pp$  design tune shift (and is of opposite  
 6598 sign). Therefore, the proton-beam tune spread induced by the  $ep$  collisions is negligible. In fact, the electron  
 6599 beam acts like an electron lens and could conceivably increase the  $pp$  tune shift and luminosity, but only  
 6600 by about 1%. Long-range beam-beam effects are equally insignificant for both electrons and protons, since  
 6601 the detector-integrated dipoles separate the electron and proton bunches by about  $36\sigma_p$  at the first parasitic  
 6602 encounter, 3.75 m away from the IP.

6603 One further item to be looked at is the proton beam emittance growth. Past attempts at directly  
6604 simulating the emittance growth from  $ep$  collisions were dominated by numerical noise from the finite number  
6605 of macroparticles and could only set an upper bound [642], nevertheless indicating that the proton emittance  
6606 growth due to the pinching electron beam might be acceptable for centered collisions. Proton emittance  
6607 growth due to electron-beam position jitter and simultaneous  $pp$  collisions is another potential concern. For  
6608 a  $1\sigma$  offset between the electron and proton orbit at the IP, the proton bunch receives a deflection of about  
6609 10 nrad (approximately  $10^{-4}\sigma_{x',y'}^*$ ). Beam-beam simulations for LHC  $pp$  collisions have determined the  
6610 acceptable level for random white-noise dipole excitation as  $\Delta x/\sigma_x \leq 0.1\%$  [643]. This translates into a very  
6611 relaxed electron-beam random orbit jitter tolerance of more than  $1\sigma$ . The tolerance on the orbit jitter will  
6612 then not be set by beam-beam effects, but by the luminosity loss resulting from off-center collisions, which,  
6613 without disruption, scales as  $\exp(-(\Delta x)^2/(4\sigma_{x,y}^*)^2)$ . The random orbit jitter observed at the SLAC SLC had  
6614 been of order  $0.3\text{--}0.5\sigma$  [644, 645]. A  $0.1\sigma$  offset at LHeC would reduce the luminosity by at most  $0.3\%$ , a  
6615  $0.3\sigma$  offset by  $2.2\%$ . Disruption further relaxes the tolerance.

6616 The strongest beam-beam effect is encountered by the electron beam, which is heavily disrupted. The  
6617 electron disruption parameter is  $D_{x,y} \equiv N_{b,p}r_e\sigma_{z,p}/(\gamma_e\sigma^{*2}) \approx 6$ , and the “nominal disruption angle”  $\theta_0 \equiv$   
6618  $D\sigma^*/\sigma_{z,p} = N_{b,p}r_e/(\gamma_e\sigma^*)$  [646] is about  $600\ \mu\text{rad}$  (roughly  $10\sigma_{x',y'}^*$ ), which is huge. Simulations show that  
6619 the actual maximum angle of the disrupted electrons is less than half  $\theta_0$ .

6620 Figure 8.6 illustrates the emittance growth and optics-parameter change for the electron beam due to  
6621 head-on collision with a “strong” proton bunch. The intrinsic emittance grows by only  $15\%$ , but there is a  
6622  $180\%$  growth in the mismatch parameter “ $B_{\text{mag}}$ ” (defined as  $B_{\text{mag}} = (\beta\gamma_0 - 2\alpha\alpha_0 + \beta_0\gamma)/2$ , where quantities  
6623 with and without subindex “0” refer to the optics without and with collision, respectively. Without adjusting  
6624 the extraction line optics to the parameters of the mismatched beam the emittance growth will be about  
6625  $200\%$ . This would be acceptable since the arc and linac physical apertures have been determined assuming  
6626 up to  $300\%$  emittance growth for the decelerating beam [639]. However, if the optics of the extraction line  
6627 is rematched for the colliding electron beam (corresponding to an effective  $\beta^*$  of about  $3\ \text{cm}$  rather than the  
6628 nominal  $12\ \text{cm}$ ; see Fig.8.6 bottom left), the net emittance growth can be much reduced, to only about  $20\%$ .  
6629 The various optics parameters shown in Fig. 8.6 vary by no more than  $10\text{--}20\%$  for beam-beam orbit offsets  
6630 up to  $1\sigma$ .

6631 Figure 8.7 presents the average electron deflection angle as a function of the beam-beam offset. The  
6632 extraction channel for the electron beam must have sufficient aperture to accommodate both the larger  
6633 emittance due to disruption and the average trajectory change due to off-center collisions.

### 6634 8.1.3 Polarization

6635 The electron beam can be produced from a polarized DC gun with about  $90\%$  polarization, and with,  
6636 conservatively,  $10\text{--}50\ \mu\text{m}$  normalized emittance [647]. Spin-manipulation tools and measures for preserving  
6637 polarization, like Wien filter and/or spin rotators, and polarimeters should be included in the optics design  
6638 of the injector, the final focus, and the extraction line.

6639 As for the positrons, up to about  $60\%$  polarization can be achieved either with an undulator [648] or  
6640 with a Compton-based  $e^+$  source [649, 650]<sup>4</sup>.

### 6641 8.1.4 Pulsed Linacs

6642 For beam energies above about  $140\ \text{GeV}$ , due to the growing impact of synchrotron radiation, the construction  
6643 of a single straight linac is cheaper than that of a recirculating linac [638]. Figure 8.8 shows the schematic of  
6644 an LHeC collider based on a pulsed straight  $140\text{-GeV}$  linac, including injector, final focus, and beam dump.  
6645 The linac could be either of ILC type ( $1.3\ \text{GHz}$  RF frequency) or operate at  $721\ \text{MHz}$  as the preferred ERL  
6646 version. In both cases, ILC values are assumed for the cavity gradient ( $31.5\ \text{MV/m}$ ) and for the cavity  
6647 unloaded  $Q$  value ( $Q_0 = 10^{10}$ ). This type of linac would be extendable to ever higher beam energies and  
6648 could conceivably later become part of a linear collider. In its basic, simplest and conventional version no

<sup>4</sup>The primary challenge for positrons is to produce them in sufficient number and with a small enough emittance.

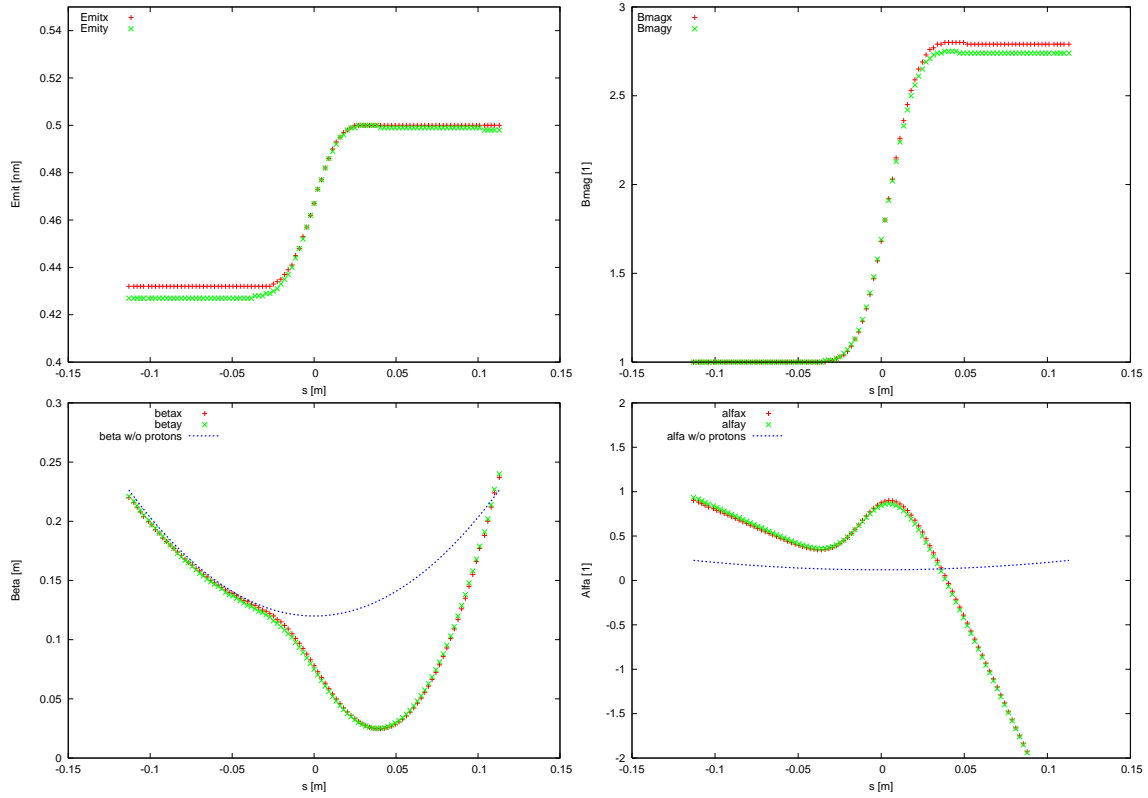


Figure 8.6: Simulated evolution of the electron beam emittance (top left), mismatch factor  $B_{\text{mag}}$  (top right) beta function (bottom left) and alpha function (bottom right) during the collision with a proton bunch, as a function of distance from the IP.

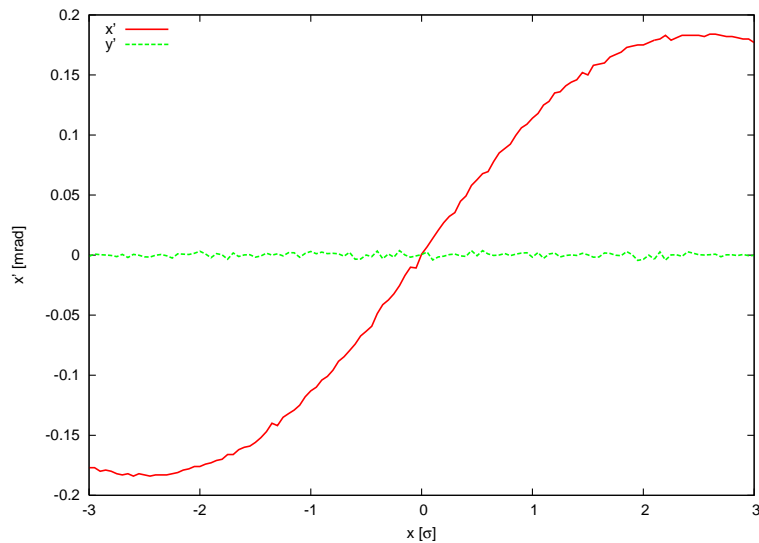


Figure 8.7: Simulated electron horizontal center-of-mass deflection angle as a function of the horizontal beam-beam offset.



Figure 8.8: Pulsed single straight 140-GeV linac for higher-energy ep collisions.

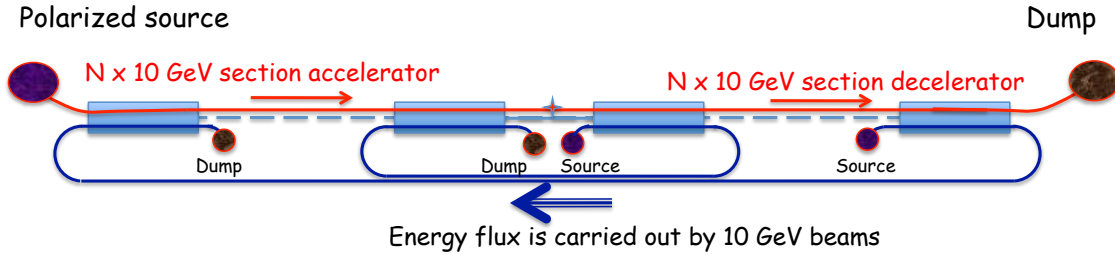


Figure 8.9: Highest-energy high-luminosity ERL option based on two straight linacs and multiple 10-GeV energy-transfer beams [651].

6649 energy recovery is possible for this configuration, since it is impossible to bend the 140-GeV beam around.  
 6650 The lack of energy recovery leads to significantly lower luminosity. For example, with 10 Hz repetition rate,  
 6651 5 ms pulse length (longer than ILC), a geometric reduction factor  $H_g = 0.94$  and  $N_{b,e} = 1.5 \times 10^9$  per bunch,  
 6652 the average electron current would be 0.27 mA and the luminosity  $4 \times 10^{31} \text{ cm}^{-2}\text{s}^{-1}$ .

6653 The construction of the 140-GeV pulsed straight linac could be staged, e.g. so as to first feature a pulsed  
 6654 linac at 60 GeV, which could also be used for  $\gamma$ - $p/A$  collisions (see subsection 8.1.6). The linac length  
 6655 decreases directly in proportion to the beam energy. For example, at 140-GeV the pulsed linac measures 7.9  
 6656 km, while at 60 GeV its length would be 3.4 km. For a given constant wall-plug power, of 100 MW, both  
 6657 the average electron current and the luminosity scale roughly inversely with the beam energy. At 60 GeV  
 6658 the average electron current becomes 0.63 mA and the pulsed-linac luminosity, without any energy recovery,  
 6659 would be more than  $9 \times 10^{31} \text{ cm}^{-2}\text{s}^{-1}$ .

### 6660 8.1.5 Higher-Energy LHeC ERL Option

6661 The simple straight linac layout of Fig. 8.8 can be expanded as shown in Fig. 8.9 [651]. The main electron  
 6662 beam propagates from the left to the right. In the first linac it gains about 150 GeV, then collides with  
 6663 the hadron beam, and is then decelerated in the second linac. By transferring the RF energy back to the  
 6664 first accelerating linac, with the help of multiple, e.g. 15, 10-GeV “energy-transfer beams,” a novel type  
 6665 of energy recovery is realized without bending the spent beam. With two straight linacs facing each other  
 6666 this configuration could easily be converted into a linear collider, or vice versa, pending on geometrical and  
 6667 geographical constraints of the LHC site. As there are negligible synchrotron-radiation losses the energy  
 6668 recovery could be more efficient than in the case of the 60-GeV recirculating linac. Such novel form of ERL  
 6669 could push the LHeC luminosity to the  $10^{35} \text{ cm}^{-2}\text{s}^{-1}$  level. In addition, it offers ample synergy with the  
 6670 CLIC two-beam technology.

### 6671 8.1.6 $\gamma$ - $p/A$ Option

6672 In case of a (pulsed) linac without energy recovery the electron beam can be converted into a high-energy  
 6673 photon beam, by backscattering off a laser pulse, as is illustrated in Fig. 8.10. The rms laser spot size at the  
 6674 conversion point should be similar to the size of the electron beam at this location, that is  $\sigma_\gamma \approx 10 \mu\text{m}$ .

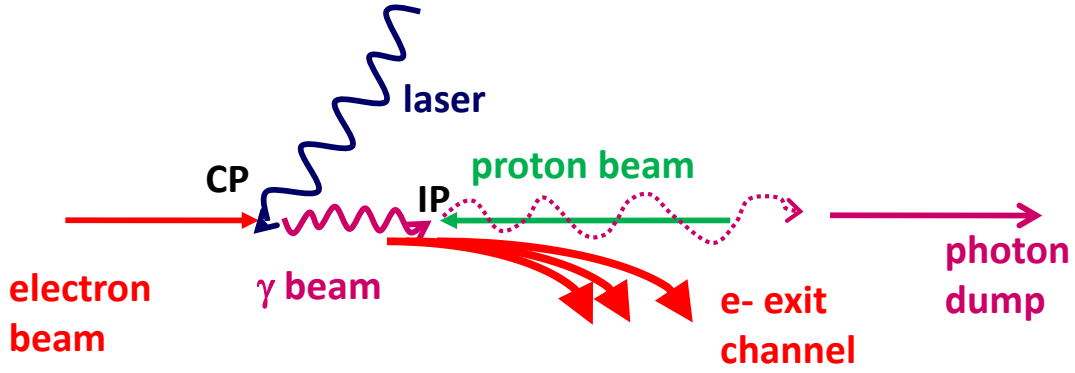


Figure 8.10: Schematic of  $\gamma$ - $p/A$  collision; prior to the photon-hadron interaction point (IP), the electron beam is scattered off a several-J laser pulse at the conversion point (CP).

6675 With a laser wavelength around  $\lambda_\gamma \approx 250$  nm ( $E_{\gamma,0} \approx 5$  eV), obtained e.g. from a Nd:YAG laser with  
 6676 frequency quadrupling, the Compton-scattering parameter  $x$  [652, 653],

$$x \approx 15.3 \left[ \frac{E_{e,0}}{\text{TeV}} \right] \left[ \frac{E_{\gamma,0}}{\text{eV}} \right], \quad (8.3)$$

6677 is close to the optimum value 4.8 for an electron energy of 60 GeV (for  $x > 4.8$  high-energy photons get  
 6678 lost due to the creation of  $e^+e^-$  pairs). The maximum energy of the Compton scattered photons is given by  
 6679  $E_{\gamma,\text{max}} = x/(x+1)E_0$ , which is larger than 80% of the initial electron-beam energy  $E_{e,0}$ , for our parameters.  
 6680 The cross section and photon spectra depend on the longitudinal electron polarization  $\lambda_e$  and on the circular  
 6681 laser polarization  $P_c$ . With proper orientation ( $2\lambda_e P_c = -1$ ) the photon spectrum is concentrated near the  
 6682 highest energy  $E_{\gamma,\text{max}}$ .

6683 The probability of scattering per individual electron is [654]

$$n_\gamma = 1 - \exp(-q) \quad (8.4)$$

6684 with

$$q = \frac{\sigma_c A}{E_{\gamma,0} 2\pi\sigma_\gamma^2}, \quad (8.5)$$

6685 where  $\sigma_c$  denotes the (polarized) Compton cross section and  $A$  the laser pulse energy. Using the formulae  
 6686 in [655], the Compton cross section for  $x = 4.8$  and  $2\lambda_e P_c = -1$  is computed to be  $\sigma_c = 3.28 \times 10^{-25}$  cm<sup>2</sup>. The  
 6687 pulse energy corresponding to  $q = 1$ , i.e. to a conversion efficiency of 65%, is estimated as  $A \approx E_{\gamma,0} 2\pi\sigma_\gamma^2 / \sigma_c \approx$   
 6688 16 J. To set this into perspective, for a  $\gamma\gamma$  collider at the ILC, Ref. [656] considered a pulse energy of 9 J at  
 6689 a four times longer wavelength of  $\lambda \approx 1$   $\mu$ m.

6690 The energies of the leftover electrons after conversion extend from about 10 to 60 GeV. This spent  
 6691 electron beam, with its enormous energy spread, must be safely extracted from the interaction region. The  
 6692 detector-integrated dipole magnets will assist in this process. They will also move the scattered electrons  
 6693 away from the interaction point. A beam dump for the high-energy photons should also be installed, behind  
 6694 the downstream quadrupole channel.

6695 Figure 8.11 presents the photon energy spectrum after the conversion and the luminosity spectrum [657],  
 6696 obtained from a simulation with the Monte-Carlo code CAIN [658].

6697 The much larger interaction-point spot size and the lower electron beam energy at the LHeC compared  
 6698 with  $\gamma\gamma$  collisions at a linear collider allow placing the conversion point at a much greater distance  $\Delta s \approx$   
 6699  $\beta^* \sim 0.1$  m from the interaction point, which could simplify the integration in the detector, and is also

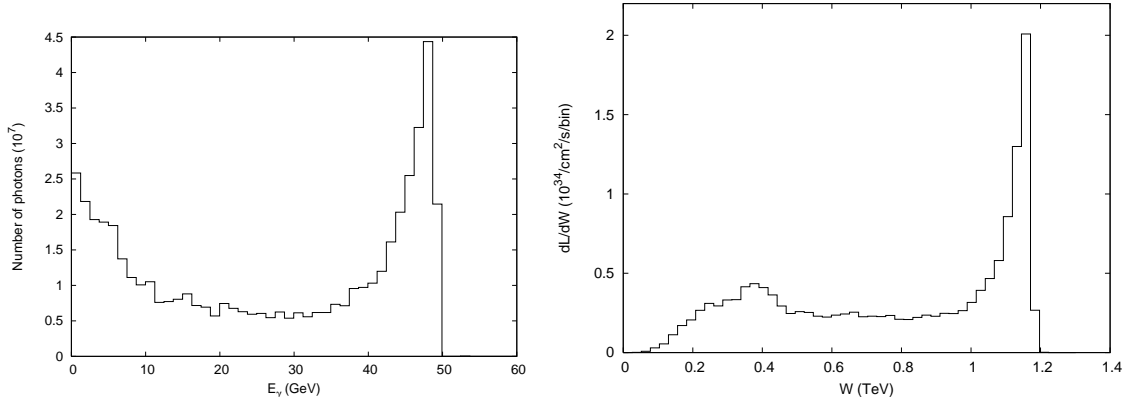


Figure 8.11: Simulated example photon spectrum after the conversion point (left) and  $\gamma$ - $p$  luminosity spectrum [657].

6700 necessary as otherwise, with e.g. a mm-distance between CP and IP, the conversion would take place inside  
 6701 the proton bunch.

6702 To achieve the required laser pulse energy, external pulses can be stacked in a recirculating optical cavity.  
 6703 For an electron bunch spacing of e.g. 200 ns, the path length of the recirculation could be 60m. A schematic  
 6704 of a possible mirror system is sketched in Fig. 8.12 (adapted from [656]).

### 6705 8.1.7 Summary of Basic Parameters and Configurations

6706 The baseline 60-GeV ERL option presented here can provide a  $ep$  luminosity of  $10^{33} \text{ cm}^{-2}\text{s}^{-1}$ , at less than  
 6707 100 MW total electrical power for the electron branch of the collider, and with less than 9 km circumference.  
 6708 The 21 GV of SC-RF installation represents its main hardware component.

6709 A pulsed 140-GeV linac, without energy recovery, could achieve a luminosity of  $1.4 \times 10^{31} \text{ cm}^{-2}\text{s}^{-1}$ , at  
 6710 higher c.m. energy, again with less than 100 MW electrical power, and shorter than 9 km in length. The  
 6711 pulsed linac can accommodate a  $\gamma$ - $p/A$  option. An advanced, novel type of energy recovery, proposed for  
 6712 the single straight high-energy linac case, includes a second decelerating linac, and multiple 10-GeV “energy-  
 6713 transfer beams”. This type of collider could potentially reach luminosities of  $10^{35} \text{ cm}^{-2}\text{s}^{-1}$ .

6714 High polarization is possible for all linac-ring options. Beam-beam effects are benign, especially for the  
 6715 proton beam, which should not be affected by the presence of the electron beam.

6716 Producing the required number of positrons needed for high-luminosity proton-positron collisions is the  
 6717 main open challenge for a linac-ring LHeC. Recovery of the positrons together with their energy, as well as  
 6718 fast transverse cooling schemes, are likely to be essential ingredients for any linac-based high-luminosity  $ep$   
 6719 collider involving positrons. L

## 6720 8.2 Interaction region

6721 This section presents a first conceptual design of the LHeC linac-ring Interaction Region (IR). The merits of  
 6722 the IR are a very low  $\beta^*$  of 0.1m with proton triplets as close as possible to the IP to minimize chromaticity.  
 6723 Head-on proton-electron collisions are achieved by means of dipoles around the Interaction Point (IP). The  
 6724 Nb<sub>3</sub>Sn superconductor has been chosen for the proton triplets since it provides the largest gradient. If this  
 6725 technology proves not feasible in the timescale of the LHeC a new design of the IR can be pursued using  
 6726 standard technology.

6727 The main goal of this first design is to evaluate potential obstacles, decide on the needs of special  
 6728 approaches for chromaticity correction and evaluate the impact of the IR synchrotron radiation.



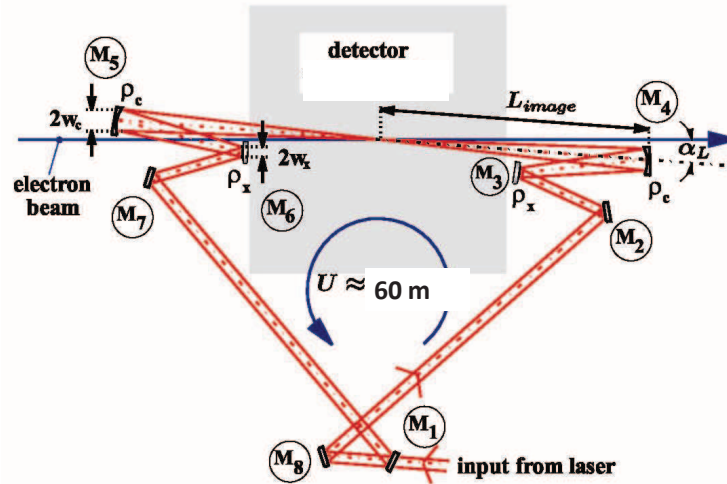


Figure 8.12: Recirculating mirror arrangement providing a laser-pulse path length of 60 m for pulse stacking synchronously with the arriving electron bunches (adapted from [656]).

### 8.2.1 Layout

A crossing angle of 6.8 mrad between the non-colliding proton beams allows enough separation to place the proton triplets. Only the proton beam colliding with the electrons is focused. A possible configuration in IR2 could be to inject the electrons parallel to the LHC Beam 1 and collide them head-on with Beam 2, see Fig. 8.13. The signs of the separation and recombination dipoles (D1 and D2) have to be changed to allow for the large crossing angle at the IP. The new D1 has one aperture per beam and is 4.5 times stronger than the LHC design D1. The new D2 is 1.5 times stronger than the LHC design D2. Both dipoles feature about a 6 T field. The lengths of the nominal LHC D1 and D2 dipoles have been left unchanged, 23 m and 9 m, respectively. However the final IR design will need to incorporate an escape line for the neutral particles coming from the IP, probably requiring to split D1 into two parts separated by tens of meters.

Bending dipoles around the IP are used to make the electrons collide head-on with Beam2 and to safely extract the disrupted electron beam. The required field of these dipoles is determined by the  $L^*$  and the minimum separation of the electron and the focused beam at the first quadrupole (Q1). A 0.3 T field extending over 9 m allows for a beams separation of 0.07 m at the entry of Q1. This separation distance is compatible with mirror quadrupole designs using Nb<sub>3</sub>Sn technology; see Section 9.1. The electron beam radiates 48 kW in the IR dipoles. A sketch of the 3 beams, the synchrotron radiation fan and the proton triplets is shown in Fig. 8.14.

### 8.2.2 Optics

#### Colliding proton optics

The colliding beam triplet starts at  $L^*=10\text{m}$  from the IP. It consists of 3 quadrupoles with main parameters given in Table 8.4. The quadrupole aperture is computed as  $11\max(\sigma_x, \sigma_y)+5$  mm. The 5 mm split into 1.5 mm for the beam pipe, 1.5 mm for mechanical tolerances and 2 mm for the closed orbit. The magnet parameters for the first two quadrupoles correspond to Nb<sub>3</sub>Sn design described in Section 9.1. The total chromaticity from the two IP sides amounts to 960 units. The optics functions for the colliding beam are shown in Fig. 8.15

It was initially hoped that a compact Nb<sub>3</sub>Sn triplet with  $L^*=10\text{m}$  would allow for a normal chromaticity correction using the arc sextupoles. However after matching this triplet to the LHC and correcting linear

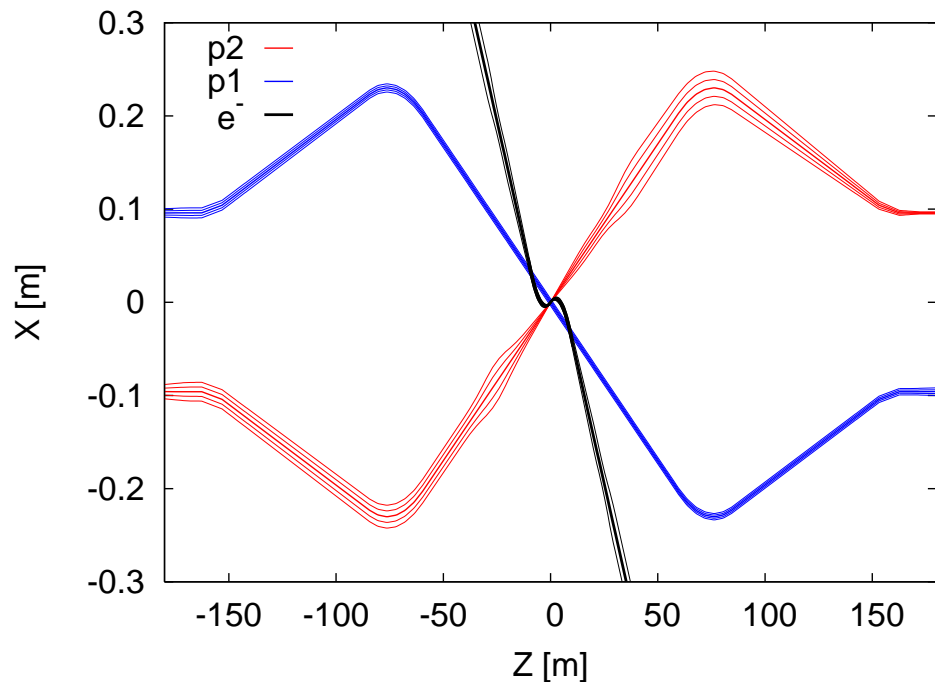


Figure 8.13: LHeC interaction region displaying the two proton beams and the electron beam trajectories with  $5\sigma$  and  $10\sigma$  envelopes.

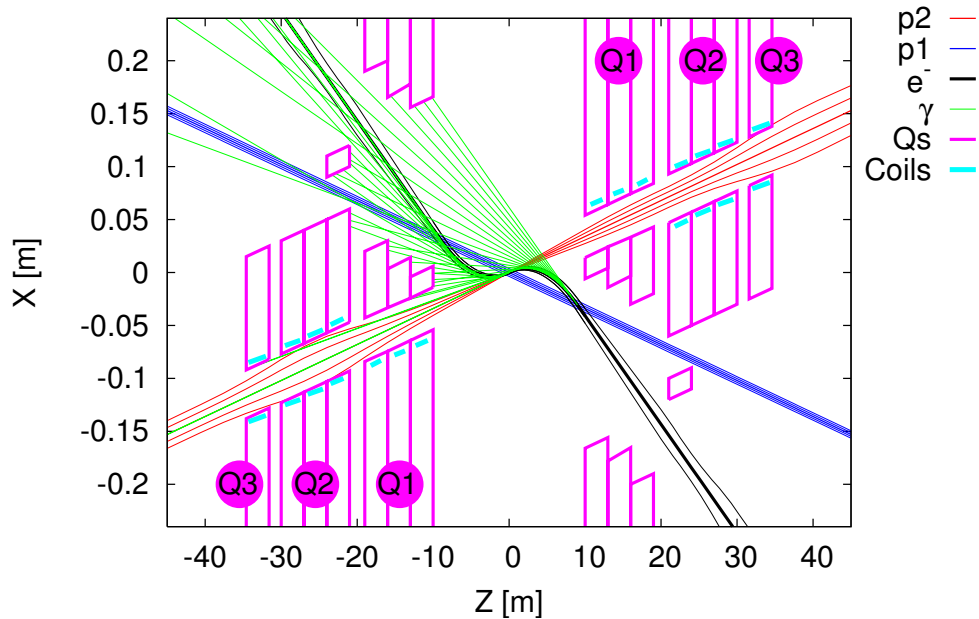


Figure 8.14: LHeC interaction region with a schematic view of synchrotron radiation. Beam trajectories with  $5\sigma$  and  $10\sigma$  envelopes are shown. The parameters of the Q1 and Q2 quadrupole segments correspond to the Nb<sub>3</sub>Sn half-aperture and single-aperture (with holes) quadrupole of Fig. 9.5.

Name	Gradient [T/m]	Length [m]	Radius [mm]	p1-p2 Sep. [mm]	“Radius” of Field-Free Hole [mm]
Q1	187	9	22	63	40
Q2	308	9	30	87	26
Q3	185	9	32	–	–

Table 8.4: Parameters of the proton triplet quadrupoles. The radius is computed as  $11\max(\sigma_x, \sigma_y) + 5$  mm. For Q2 the hole “radius” describes the distance from the closest aperture. “p1-p2 Sep.” refers to the distance between the two proton beams at the entrance of the quadrupole.

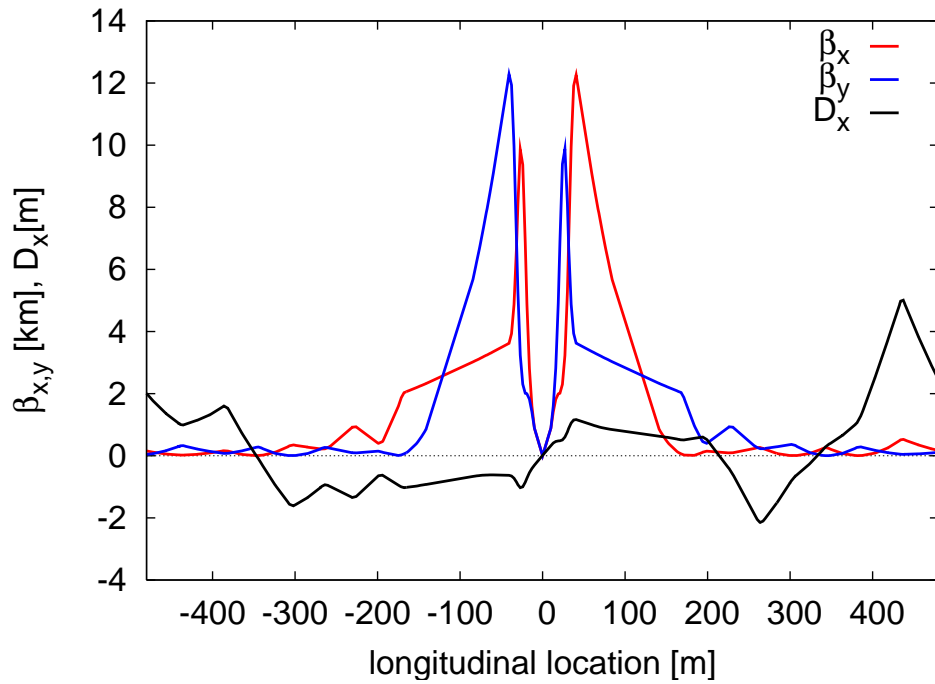


Figure 8.15: Optics functions for main proton beam.

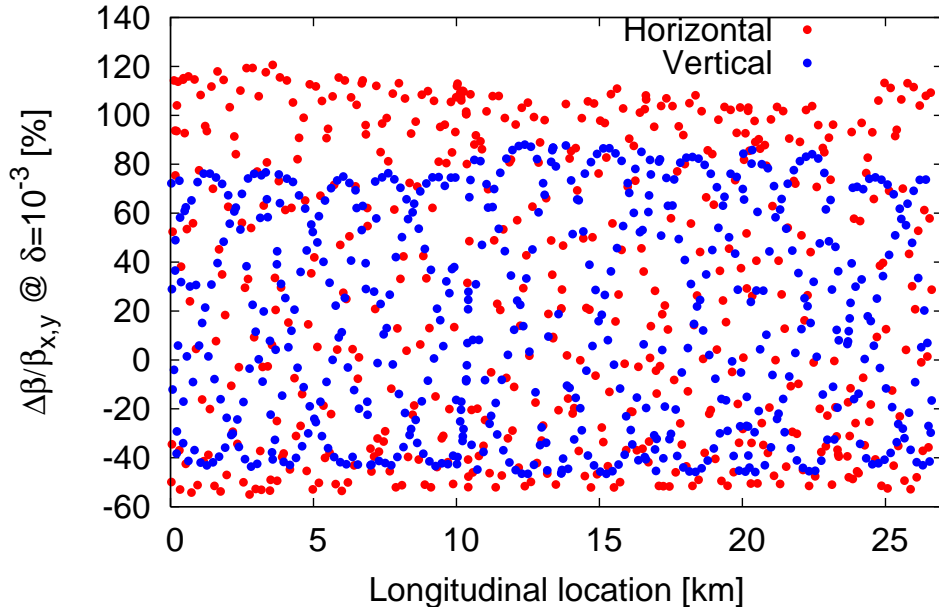


Figure 8.16: Chromatic beta-beating at  $dp/p=0.001$ .

6756 chromaticity the chromatic  $\beta$ -beating at  $dp/p=0.001$  is about 100% (see Fig. 8.16). This is intolerable  
 6757 regarding collimation and machine protection issues. Therefore a dedicated chromaticity correction scheme  
 6758 has to be adopted. A large collection of studies exist showing the feasibility of correcting even larger  
 6759 chromaticities in the LHC [659–661]. Other local chromatic correction approaches as [?], where quadrupole  
 6760 doublets are used to provide the strong focusing, could also be considered for the LHeC.

6761 Since LHeC anyhow requires a new dedicated chromaticity correction scheme, current NbTi technology  
 6762 could be pursued instead of Nb<sub>3</sub>Sn and the  $L^*$  could also be slightly increased. The same conceptual three-  
 6763 beam crossing scheme as in Fig. 8.13 could be kept.

6764 To achieve  $L^*$  below 23 m requires a cantilever supported on a large mass as proposed for the CLIC  
 6765 QD0 [663] to provide sub-nanometer stability at the IP. The LHeC vibration tolerances are much more  
 6766 relaxed, being on the sub-micrometer level.

### 6767 Non-colliding proton optics

6768 The non-colliding beam has no triplet quadrupoles since it does not need to be focused. The LHC “alignment  
 6769 optics” [664] was used as a starting point. Figure 8.17 shows the optics functions around the IP. The LHeC  
 6770 IP longitudinal location can be chosen so as to completely avoid unwanted proton-proton collisions.

6771 The non-colliding proton beam travels through dedicated holes in the proton triplet quadrupoles, in Q1  
 6772 together with the electron beam. The Q1 hole dimensions are determined by the electron beam, see below.  
 6773 By contrast, the non-colliding proton beam travels alone through the first module of the Q2, requiring about  
 6774 30 mm full aperture. No fields are assumed in these apertures but the possible residual fields could easily  
 6775 be taken into account for the proton optics.

### 6776 Electron optics

6777 About 200 m are available between the exit of the linac and the IP, of which at least 40 m should be allocated  
 6778 for matching, collimation and beam diagnostics. On the IP side, a free length  $L^*$  of 30 m is chosen to allow  
 6779 for enough separation between the proton and the electron final focusing quadrupoles. Respecting these  
 6780 length constraints two final-focus optics for the electron beam have been developed.

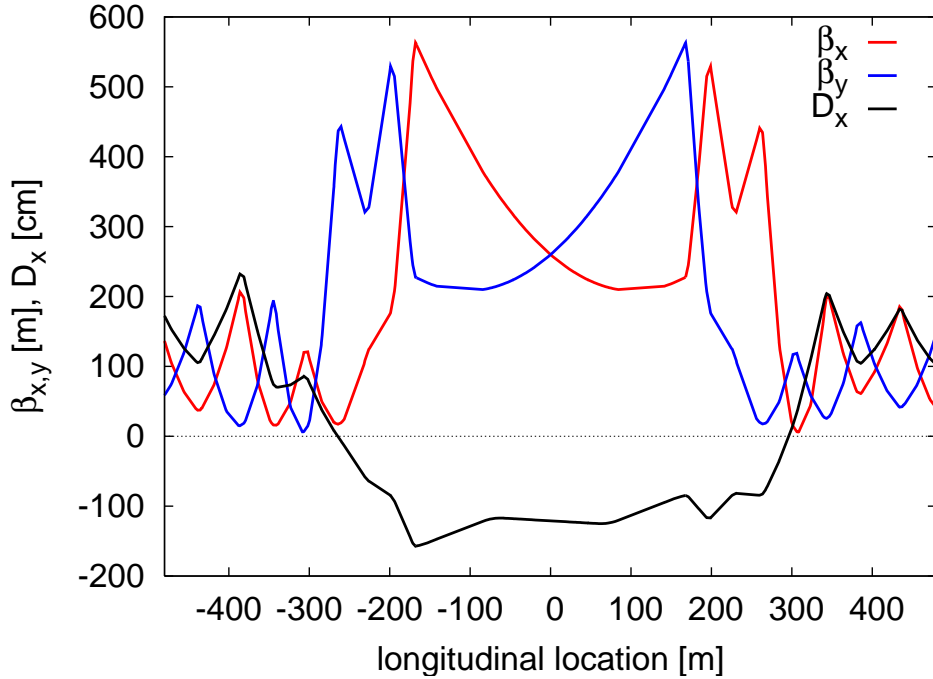


Figure 8.17: Optics functions for the non-colliding proton beam without triplets.

6781 The first optics is a round-beam electron optics with  $\beta_{e;x,y}^* = 0.1$  m realized by a plain triplet without any  
 6782 sextupoles. Upstream bending magnets complement the separation dipole so as to match the dispersion at  
 6783 the IP. The total length is 90 m. The SR power is small, about 25 kW on the incoming side of the IP, coming  
 6784 almost entirely from the separation dipole before the collision point. Without any chromatic correction the  
 6785 IP beam size increase for an rms relative momentum spread of  $3 \times 10^{-4}$  is about 10% horizontally and 21%  
 6786 vertically.

6787 The second optics [?] employs a final quadrupole doublet with local chromatic correction using 4 sex-  
 6788 tupoles arranged according to the “compact final-focus” scheme proposed for future linear colliders [?]. It  
 6789 is optimized for unequal IP beta functions  $\beta_{e;x}^* = 0.2$  m and  $\beta_{e;y}^* = 0.05$ , which are more suitable for a  
 6790 final doublet. In order to correct the chromaticity without generating unacceptable residual geometric  
 6791 aberrations a sufficiently large dispersion is needed across the final quadrupoles. Achieving this without  
 6792 introducing too much synchrotron radiation requires a longer system. The actual triplet optics has a length  
 6793 of 150 m. The SR power is 84 kW for the entire final focus on the incoming side of the IP, of which only one  
 6794 third, about 24 kW, is due to last separation dipole, with (at least) the same 24 kW again on the outgoing  
 6795 side. With this optics the IP beam size increase for an rms relative momentum spread of  $3 \times 10^{-4}$  is about  
 6796 2.5% horizontally and 3.8% vertically. This increase is a factor 4–5 smaller than for the triplet solution.

6797 The optics of both systems are shown in Fig. 8.18, already matched to the exit of the linac. The electron  
 6798 focusing quadrupoles feature moderately low gradients as shown in Table 8.5.

6799 The higher-order aberrations for both optics were analyzed and minimized by applying a combination of  
 6800 the codes MAD-X/PTC and MAPCLASS [?] with and without the effect of synchrotron radiation. Table  
 6801 8.6 summarizes the relative beam-size increase for the two alternative optics.

6802 The linear momentum bandwidths for both optics are compared in Fig. 8.19. The bandwidth was  
 6803 computed by MAD-X for a mono-chromatic beam with zero energy spread and varying offset from the  
 6804 design beam energy. More accurately, Fig. 8.20 presents the IP beam size as a function of the relative  
 6805 rms energy spread assuming a finite Gaussian energy distribution. The beam size was obtained both by  
 6806 tracking 50,000 particles and analytically by means of the MAPCLASS code. According to the left picture,

Name	triplet			doublet		
	Gradient [T/m]	Length [m]	Radius [mm]	Gradient [T/m]	Length [m]	Radius [mm]
Q1	19.7	1.34	20	-19.1	1.1	36
Q2	-38.8	1.18	32	17.7	1.1	37
Q3	-3.46	1.18	20	-14.7	1.1	41
Q4	22.3	1.34	22	11.8	1.1	41

Table 8.5: Final electron quadrupole parameters for the triplet and doublet optics. The radius is computed as  $11 \max(\sigma_x, \sigma_y) + 5$  mm. In the doublet solution the third and fourth quadrupole, Q3 and Q4, are located further upstream.

Table 8.6: Relative IP electron beam-size increase with respect to the linear spot size  $\sigma_{0,x(y)} = \sqrt{\epsilon_{x(y)} \beta_{x(y)}^*}$  considering a Gaussian momentum distribution of  $\delta_{\text{rms}} = 3 \times 10^{-4}$ .

	triplet	doublet
$\Delta\sigma_x/\sigma_{x,0}$ , no SR	10%	1.5%
$\Delta\sigma_y/\sigma_{y,0}$ , no SR	21%	2.6%
$\Delta\sigma_x/\sigma_{x,0}$ , with SR	10%	2.5%
$\Delta\sigma_y/\sigma_{y,0}$ , with SR	21%	3.8%

6807 the performance of the plain triplet without chromatic correction is adequate only for a relative rms energy  
6808 spread below  $3 \times 10^{-4}$ .

6809 The electrons shares a hole with the non-colliding proton beam in the first half-quadrupole, Q1, and  
6810 then travels through a dedicated hole in the cryostat of Q2. The common hole in the proton Q1 must  
6811 have about 160 mm full horizontal aperture to allow for the varying separation between the electron and  
6812 non-colliding proton orbit (120 mm) with the usual electron-beam aperture assumptions ( $\pm 20$  mm). First  
6813 design of mirror magnets for Q1 feature a field of 0.5 T in the electron beam pipe. This value is considered  
6814 too large when compared to the IR dipole of 0.3 T, but new designs with active isolation or dedicated coils  
6815 could considerably reduce this field. Migrating to NbTi technology would reduce this field too.

### 6816 Spent electron beam

6817 The proton electromagnetic field provides extra focusing to the electron beam. This increases the divergence  
6818 of the electron. Figure 8.21 shows the horizontal distribution of the electrons at 10 m from the IP (entry of  
6819 Q1) as computed by Guineapig [665]. The contribution of dispersion and energy spread to the transverse size  
6820 of the exiting collided beam can be neglected. Therefore, it is possible to linearly scale the sigmas at 10 m to  
6821 estimate both the horizontal and vertical sigmas at any other longitudinal location. The simulation used  $10^5$   
6822 particles. No particles are observed beyond 4.5 mm from the beam centroid at 10 m from the IP and beyond  
6823 9 mm at 20 m. A radial aperture of 10 mm has been reserved for the beam size at the incoming electron Q1  
6824 hole. The same value of 10 mm seem to be enough to also host the spent electron beams, although it might  
6825 be worth to allocate more aperture margin in the last block of Q1.

### 6826 8.2.3 Modifications for $\gamma p$ or $\gamma$ -A

6827 The electron beam can be converted into photons by Compton scattering off a high-power laser pulse, as  
6828 discussed Section 8.1.6. For this option a laser path and high-finesse optical cavities must be integrated into

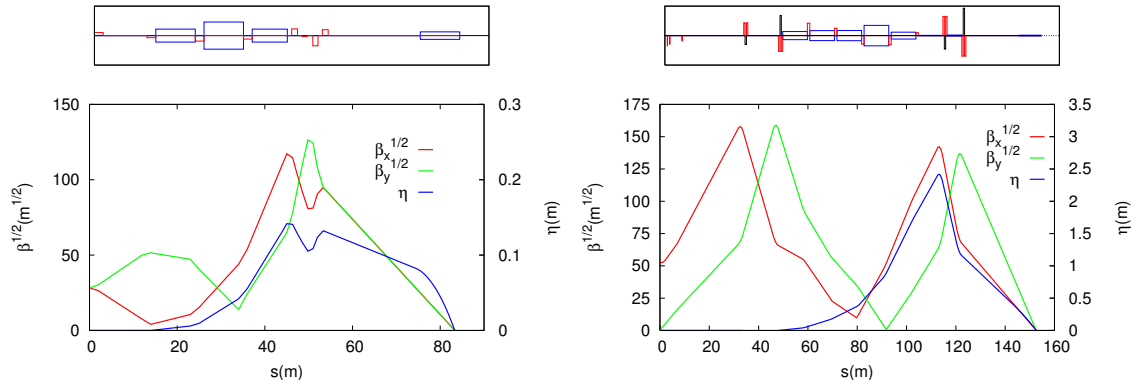


Figure 8.18: Plain triplet optics (left) and doublet optics with local chromatic correction (right) for the electron final focus.

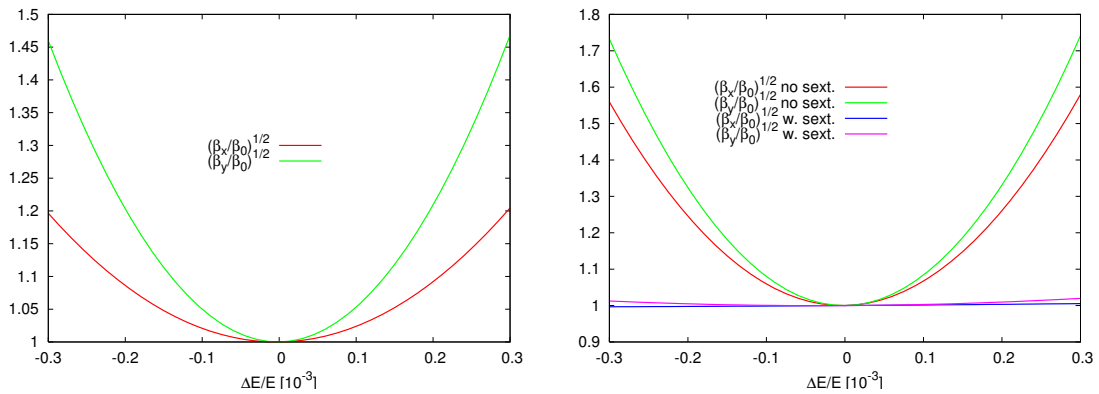


Figure 8.19: Relative increase in the linear beam size ( $\sqrt{\beta}$ ) as a function of beam energy error, as computed by MAD-X.

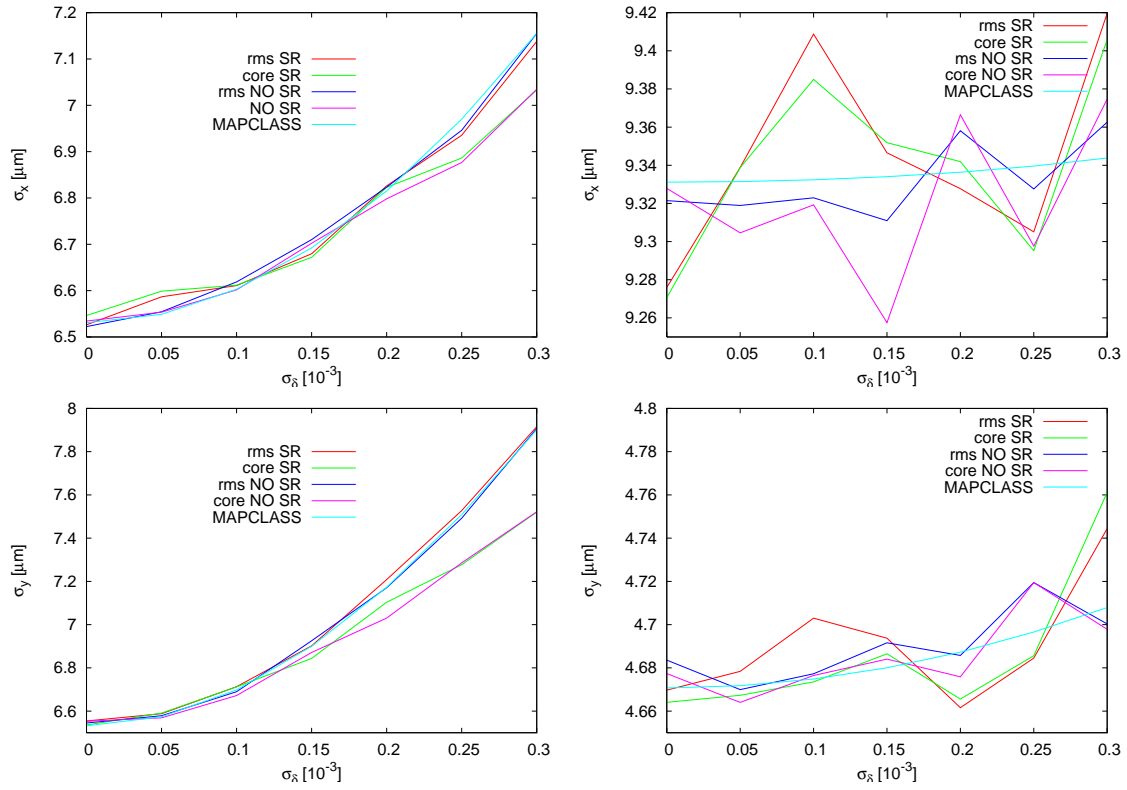


Figure 8.20: IP electron horizontal (top) and vertical beam size (bottom) versus rms relative momentum spread for the triplet (left) and doublet optics (right). The beam-size increase was computed both analytically with the MAPCLASS tool (only without SR) and also through particle tracking by MAD-X/PTC.



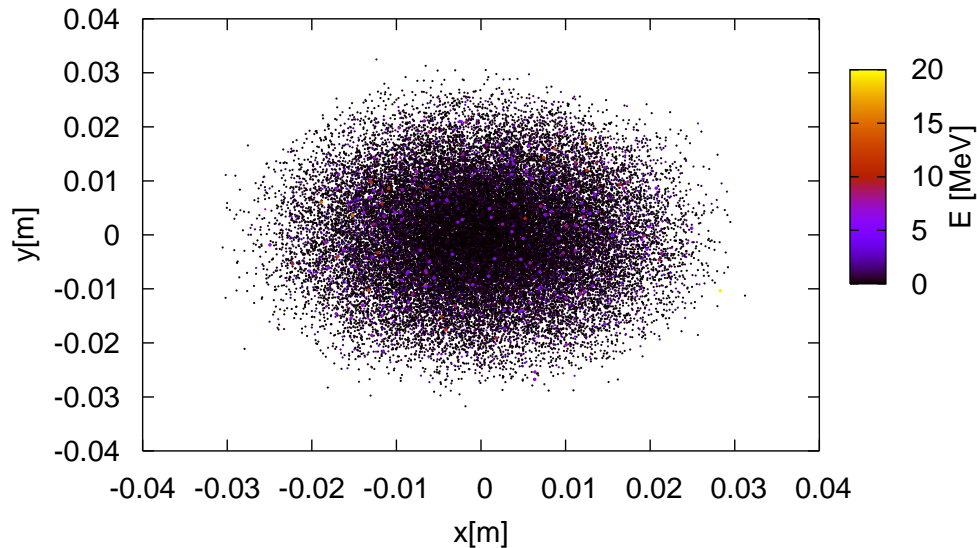


Figure 8.21: Distribution of the spent electron beam at 10 m from the IP. The Gaussian and rms sigmas are shown on the plot.

6829 the interaction region. A multiple mirror arrangement has been sketched in Fig. 8.12. The 0.3-T dipole field  
 6830 after the (now)  $\gamma$ -p interaction point will help to separate the Compton-scattered spent electron beam from  
 6831 the high-energy photons. The high-energy photons propagate straight into the direction of the incoming  
 6832 proton beam through the main openings of Q1 and Q2, while the spent electrons will be extracted through  
 6833 the low-field exit holes shared with the non-colliding proton beam, as for electron-proton collisions.

## 6834 8.2.4 Synchrotron radiation and absorbers

### 6835 Introduction

6836 The synchrotron radiation (SR) in the linac-ring interaction region has been analyzed by three different  
 6837 approaches. The SR was simulated using a program made with the Geant4 (G4) toolkit. In addition, a cross  
 6838 check of the total power and average critical energy was done in IRSYN, a Monte Carlo simulation package  
 6839 written by R. Appleby [572]. A final cross check of the radiated power has been performed using an analytic  
 6840 method. The latter two checks confirmed the results obtained from G4. The G4 program uses Monte Carlo  
 6841 methods to create the desired Gaussian spatial and angular distributions of an electron beam. This electron  
 6842 beam distribution is then transported through a “vacuum system,” including the magnetic fields for the  
 6843 separator dipoles. In a non-zero magnetic field SR is generated using the appropriate G4 process classes.  
 6844 The position, direction, and energy of each photon emitted is written as ntuples at user defined longitudinal  
 6845 positions ( $Z$  values). These ntuples are then used to analyze the SR fan as it evolves in  $Z$ . The latter  
 6846 analysis was done primarily through MATLAB scripts.

6847 This section uses the following conventions. The electron beam is being referred to as *the beam* and the  
 6848 proton beams will be called either the interacting or non interacting proton beams. The (electron) beam  
 6849 propagates in the  $-Z$  direction and the interacting proton beam propagates in the  $+Z$  direction. At the  
 6850 collision point both beams propagate up the straight  $Z$  (or  $-Z$ ) direction. A right-handed coordinate system

6851 is used where the  $X$  axis is horizontal and the  $Y$  axis vertical. The beam centroid always remains in the  
6852  $Y = 0$  plane. The *angle of the beam* will be used to refer to the angle between the beam centroid's direction  
6853 and the  $Z$  axis, in the  $Y = 0$  plane. This angle is defined such that the beam propagates in the  $-X$  direction  
6854 when it passes through the dipole field as it moves along  $Z$ .

6855 The SR fans extension in the horizontal direction is determined by the angle of the beam at the entrance  
6856 of the upstream separator dipole. Because the direction of the photons is parallel to the direction of the  
6857 electron from which it is emitted, the angle of the beam and the  $X$ -distance to the interacting proton beam  
6858 at the  $Z$  location of the last proton quadrupole are both greatest for photons generated at the entrance of  
6859 the upstream separator dipole and, therefore, this angle defines one of the edges of the synchrotron fan on  
6860 the absorber in front of the proton quadrupole. The other edge is defined by the crossing angle, which is  
6861 zero for the linac-ring option. The S shaped trajectory of the beam means that the smallest angle of the  
6862 beam will be reached at the IP. Therefore, the photons emitted at this point will move exactly along the  $Z$   
6863 axis. This defines the other edge of the fan in the horizontal direction.

6864 The SR fans extent in the vertical direction is determined by the beta function and angular spread of  
6865 the beam. The beta function along with the emittance defines the local rms beam size. The vertical rms  
6866 beam size characterizes the range of  $Y$  positions at which photons are emitted. Possibly more importantly,  
6867 the vertical angular spread defines the angle between the velocity vector of these photons and the  $Z$  axis.  
6868 Both of these dependencies are functions of  $Z$ . Similar effects also affect the horizontal extension of the SR  
6869 fan, however, in the horizontal plane they are of second order when compared to the horizontal deflection  
6870 angle in the strong dipole field.

6871 The number density distribution of the SR fan is inferred from the simulations. The number density at  
6872 the location of the absorber is highest in the region between the two interacting beams. This is due to the  
6873 S shaped trajectory of the beam.

## 6874 Parameters

6875 The parameters for the Linac Ring option are listed in Table 8.7. The separation refers to the displacement  
6876 between the two interacting beams at the face of the proton triplet.

Characteristic	Value
Electron Energy [GeV]	60
Electron Current [mA]	6.6
Crossing Angle [mrad]	0
Absorber Position [m]	-9
Dipole Field [T]	0.3
Separation [mm]	75
$\gamma/s$	$1.37 \times 10^{18}$

Table 8.7: LR: Parameters

6877 The energy, current, and crossing angle ( $\theta_c$ ) are the common values used in all LR calculations. The  $B$   
6878 value refers to the constant dipole field created throughout the two dipole magnets in the IR. The direction  
6879 of this field is opposite on either side of the IP. The field is chosen such that 75 mm of separation is reached  
6880 by the face of the proton triplet. This separation was chosen based on S. Russenschuck's SC quadrupole  
6881 design. [573] The separation between the interacting beams can be increased by raising the constant dipole  
6882 field however for a dipole magnet  $P_{SR} \propto |B^2|$ , [574] therefore an optimization of the design will need to be  
6883 discussed. The chosen parameters give a flux of  $1.37 \times 10^{18}$  photons per second at  $Z = -9$  m.

6884 **Power and Critical Energy**

6885 Table 8.8 shows the power of the SR produced in the IR along with the critical energy. This is followed by  
 6886 the total power produced in the IR and the critical energy. Since the G4 simulations utilize Monte Carlo,  
 6887 multiple runs were used to provide a standard error. This only caused fluctuations in the power since the  
 6888 critical energy is static for a constant field and constant energy.

Element	Power [kW]	Critical Energy [keV]
DL	24.4 +/- 0.1	718
DR	24.4 +/- 0.1	718
Total	48.8 +/- 0.1	718

Table 8.8: LR: Power and Critical Energies as calculated with Geant4.

6889 These magnets have strong fields and therefore produce high critical energies and a substantial amount  
 6890 of power. Although the power is similar to that of the RR design the critical energy is much larger. This  
 6891 comes from the linear dependence of critical energy on magnetic field (*i.e.*  $E_c \propto B$ ) [575]. With the dipole  
 6892 field in the LR case being an order of magnitude larger than the dipole fields in the RR case the critical  
 6893 energies from the dipole magnets are also an order of magnitude larger in the LR case.

6894 **Comparison**

6895 The IRSYN cross check of the power and critical energies is shown in Table 8.9. This comparison was done  
 6896 for the total power and the critical energy.

	Power [kW]		Critical Energy [keV]	
	Geant4	IRSYN	Geant4	IRSYN
Total	48.8 +/- 0.1	48.8	718	718

Table 8.9: LR: Geant4 and IRSYN comparison.

6897 A third cross check to the Geant4 simulations was made for the power as shown in Table 8.10. This was  
 6898 done using an analytic method for calculating power in dipole magnets [574].

	Power [kW]	
Element	Geant4	Analytic
DL	24.4 +/- 0.1	24.4
DR	24.4 +/- 0.1	24.4
Total/Avg	48.8 +/- 0.1	48.8

Table 8.10: LR: Geant4 and Analytic method comparison.

6899 **Number Density and Envelopes**

6900 The number density of photons at different Z values is shown in Figure 8.22. Each graph displays the density  
 6901 of photons in the  $Z = Z_o$  plane for various values of  $Z_o$ . The first three graphs give the growth of the SR fan  
 6902 inside the detector area. This is crucial for determining the dimensions of the beam pipe inside the detector  
 6903 area. Since the fan grows asymmetrically in the -Z direction an asymmetric elliptical cone shaped beam  
 6904 pipe will minimize these dimensions, allowing the tracking to be placed as close to the beam as possible.

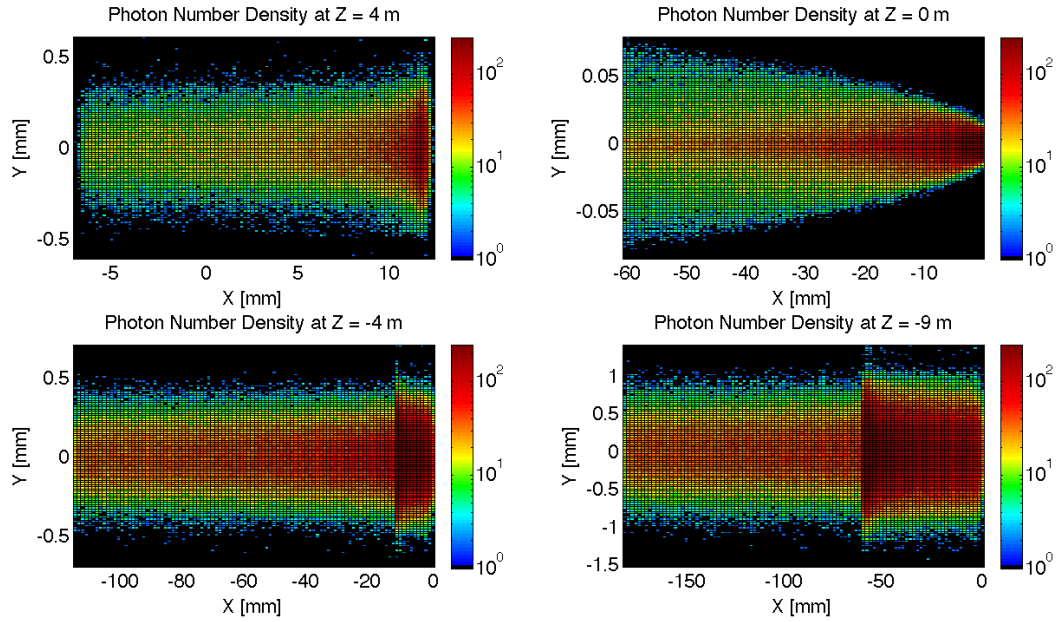


Figure 8.22: LR: Number Density of photons Growth in Z direction.

6905 The horizontal extension of the fan in the LR option is larger than in the RR case. This is due to the large  
 6906 angle of the beam at the entrance of the upstream separator dipole. As mentioned in the introduction this  
 6907 angle defines the fans extension, and in the LR case this angle is the largest, hence the largest fan. The  
 6908 number density of this fan appears as expected. There exists the highest density between the two beams  
 6909 at the absorber.

6910 In Figure 8.22 the distribution was given at various Z values however a continuous envelope distribution is  
 6911 also important to see everything at once. This can be seen in Figure 8.23, where the beam and fan envelopes  
 6912 are shown in the  $Y = 0$  plane. This makes it clear that the fan is antisymmetric which comes from the S  
 6913 shape of the electron beam as previously mentioned.

#### 6914 Absorber

6915 The Photon distribution on the absorber surface is crucial. The distribution decides how the absorber must  
 6916 be shaped. The shape of the absorber in addition to the distribution on the surface then decides how  
 6917 much SR is backscattered into the detector region. In HERA backscattered SR was a significant source of  
 6918 background that required careful attention [576]. Looking at Figure 8.24 it is shown that for the LR option  
 6919 35.15 kW of power from the SR light will fall on the face of the absorber which is 73% of the total power.  
 6920 This gives a general idea of the amount of power that will be absorbed. However, backscattering and IR  
 6921 photons will lower the percent that is actually absorbed.

6922 **Proton Triplet:** The super conducting final focusing triplet for the protons needs to be protected from  
 6923 radiation by the absorber. Some of the radiation produced upstream of the absorber however will either pass  
 6924 through the absorber or pass through the apertures for the two interacting beams. This is most concerning  
 6925 for the interacting proton beam aperture which will have the superconducting coils. A rough upper bound  
 6926 for the amount of power the coils can absorb before quenching is 100 W. [577] There is approximately 2 kW  
 6927 entering into the interacting proton beam aperture as is shown in Figure 8.24. This doesnt mean that all  
 6928 this power will hit the coils but simulations need to be made to determine how much of this will hit the coils.  
 6929 The amount of power that will pass through the absorber (0.25 W) can be disregarded as it is not enough

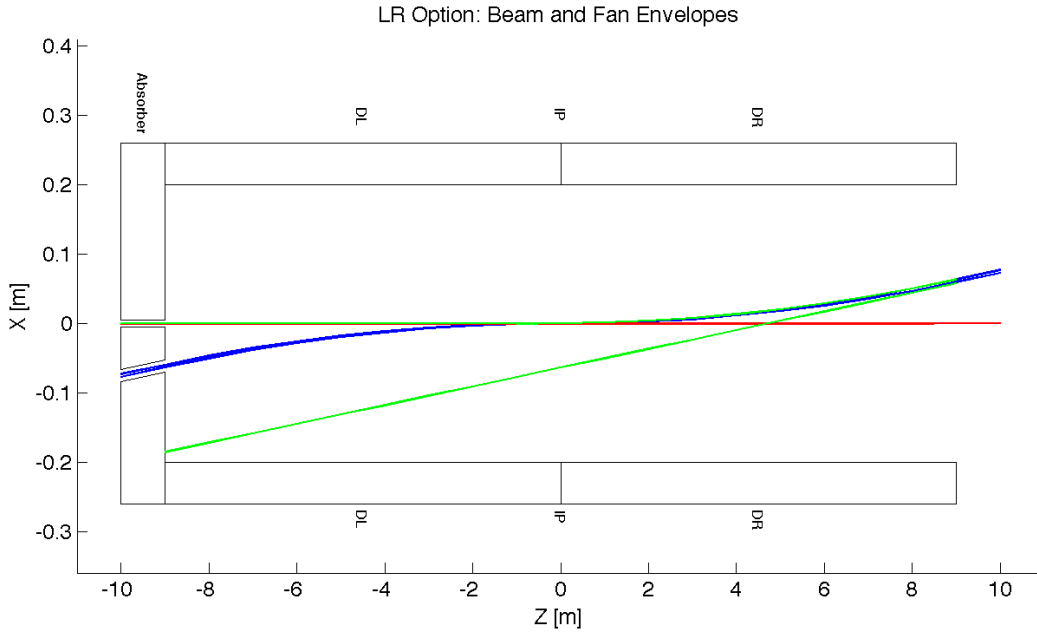


Figure 8.23: LR: Beam Envelopes in Z direction.

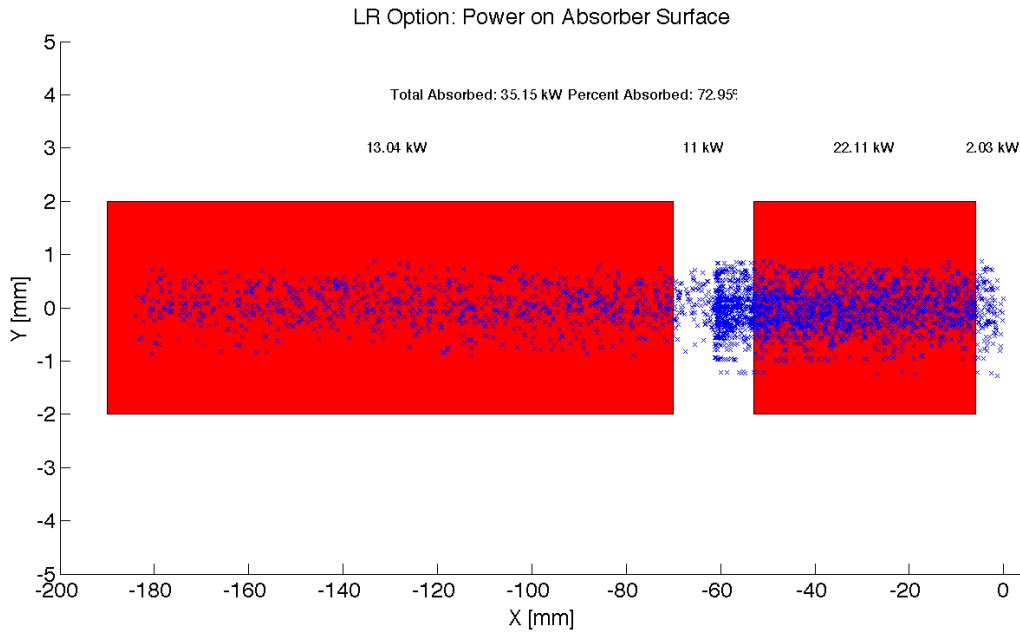


Figure 8.24: LR: Photon distribution on the Absorber Surface.

6930 to cause any significant effects. The main source of power moving downstream of the absorber will be the  
 6931 photons passing through the beams aperture. This was approximately 11 kW as can be seen from Figure  
 6932 8.24. Most of this radiation can be absorbed in a secondary absorber placed after the first downstream proton  
 6933 quadrupole. Overall protecting the proton triplet is important and although the absorber will minimize the

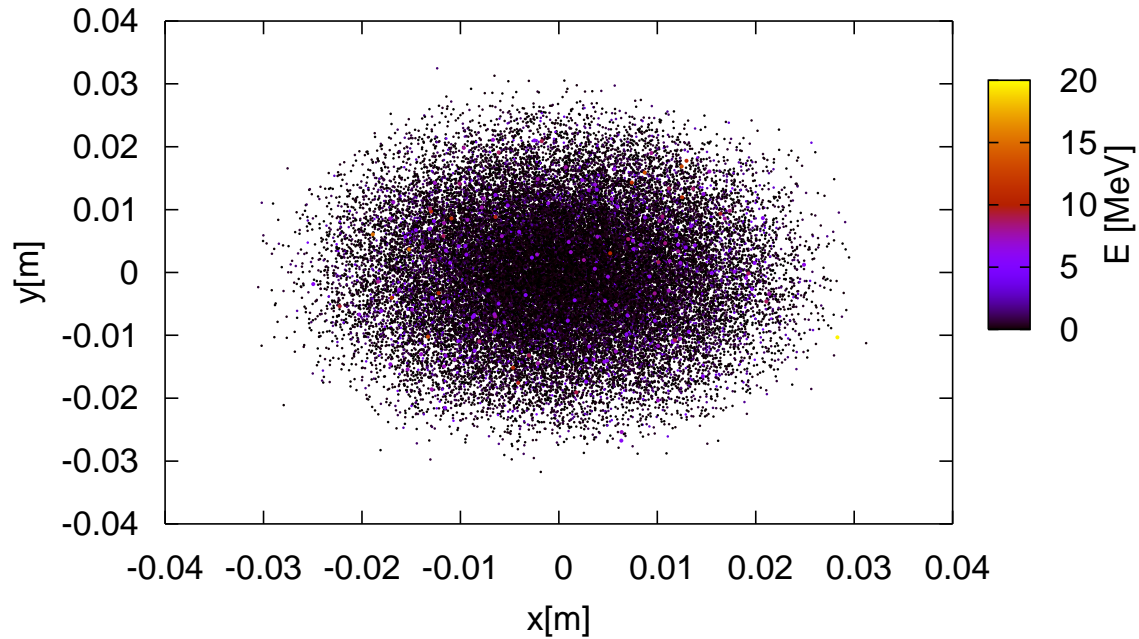


Figure 8.25: Beamstrahlung photons at the entrance of D1.

6934 radiation continuing downstream this needs to be studied in depth.

6935 **Beamstrahlung** The beamstrahlung photons travel parallel to the proton beam until the entrance of D1  
 6936 without impacting the triplets. Figure 8.25 shows the transverse and energy distributions of the beamstrahlung  
 6937 photons at the entry of D1 as computed with Guineapig [665]. The maximum photon energy is about 20 MeV  
 6938 the average photon energy is 0.4 MeV. The beamstrahlung power is 980 W. D1 has to be designed to properly  
 6939 dispose the neutral debris from the IP. Splitting D1 into two parts could allow an escape line for the neutral  
 6940 particles.

6941 **Backscattering** Another G4 program was written to simulate the backscattering of photons into the  
 6942 detector region. The ntuple with the photon information written at the absorber surface is used as the  
 6943 input for this program. An absorber geometry made of copper is described, and general physics processes  
 6944 are set up. A detector volume is then described and set to record the information of all the photons which  
 6945 enter in an ntuple. The first step in minimizing the backscattering was to optimize the absorber shape.  
 6946 Although the simulation didnt include a beam pipe the backscattering for different absorber geometries was  
 6947 compared against one another to find a minimum. The most basic shape was a block of copper that had  
 6948 cylinders removed for the interacting beams. This was used as a benchmark to see the maximum possible  
 6949 backscattering. In HERA a wedge shape was used for heat dissipation and minimizing backscattering [576].  
 6950 The profile of this geometry in the YZ plane is shown in Figure 8.26. It was found that this is the optimum  
 6951 shape for the absorber. The reason for this is that a backscattered electron would have to have its  
 6952 velocity vector be almost parallel to the wedge surface to escape from the wedge and therefore it works as  
 6953 a trap. One can be seen from Table 8.11 utilizing the wedge shaped absorber decreased the backscattered  
 6954 power by a factor of 4. The energy distribution for the backscattered photons can be seen in Figure 8.27.

6955 After the absorber was optimized it was possible to set up a beam pipe geometry. An asymmetric elliptical  
 6956 cone beam pipe geometry made of beryllium was used since it would minimize the necessary size of the beam  
 6957 pipe as previously mentioned. The next step was to place the lead shield and masks inside this beam pipe.  
 6958 To determine placement a simulation was run with just the beam pipe. Then it was recorded where each  
 6959 backscattered photon would hit the beam pipe in Z. A histogram of this data was made as shown in Figure

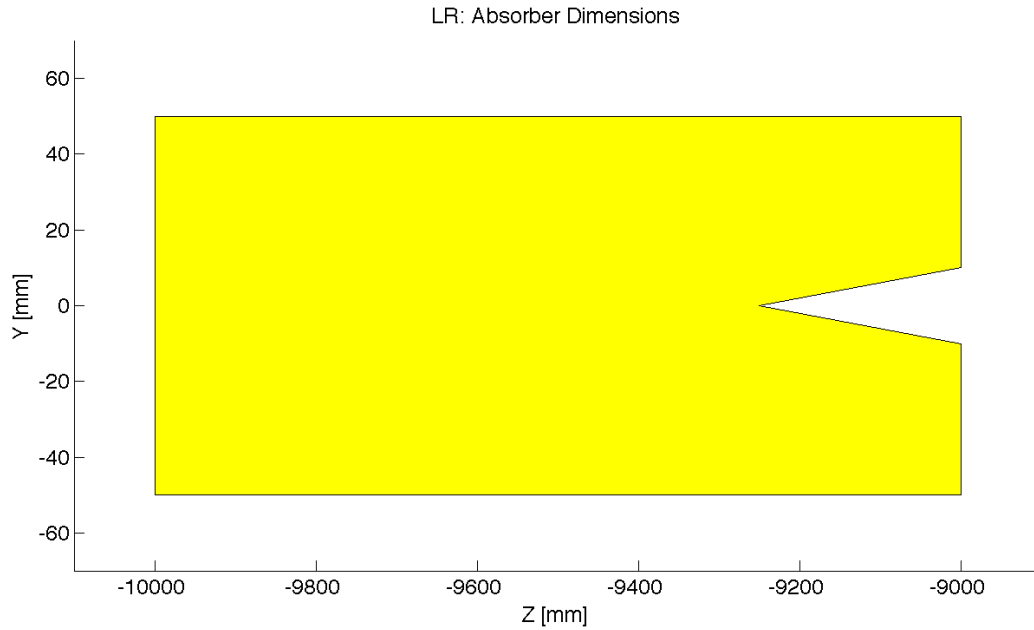


Figure 8.26: LR: Absorber Dimensions.

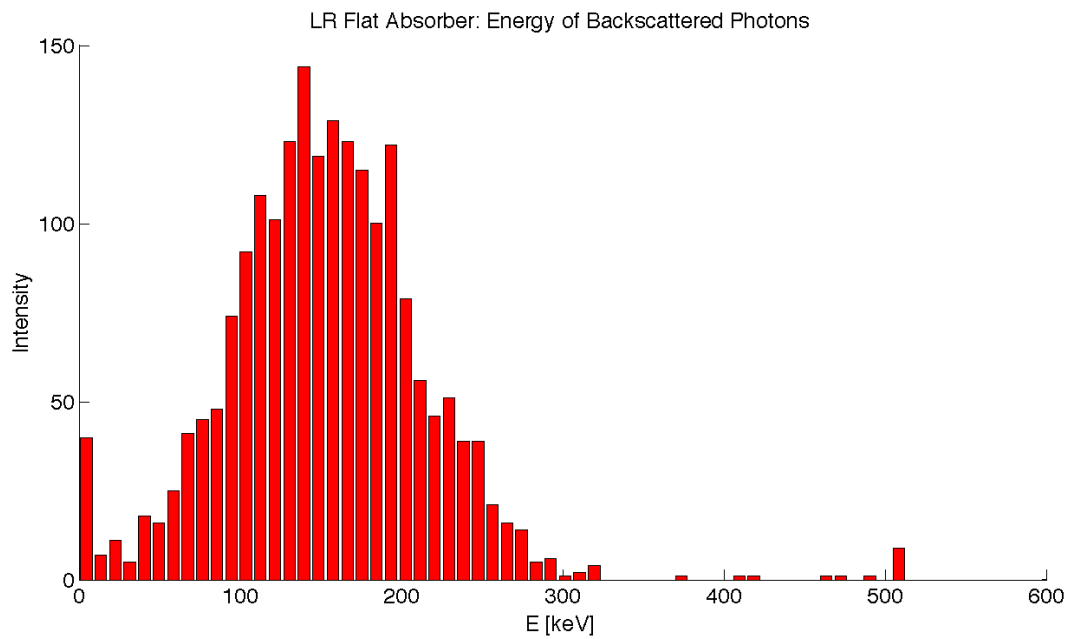


Figure 8.27: LR: Backscattered Energy Distribution.

6960 8.28. This determined that the shield should be placed in the Z region ranging from -8 m until the absorber  
 6961 (-9 m). The masks were then placed at -8.9 m and -8.3 m. This decreased the backscattered power by a  
 6962 factor of 40 as can be seen from Table 8.11. Overall there is still more optimization that can occur with this  
 6963 placement.

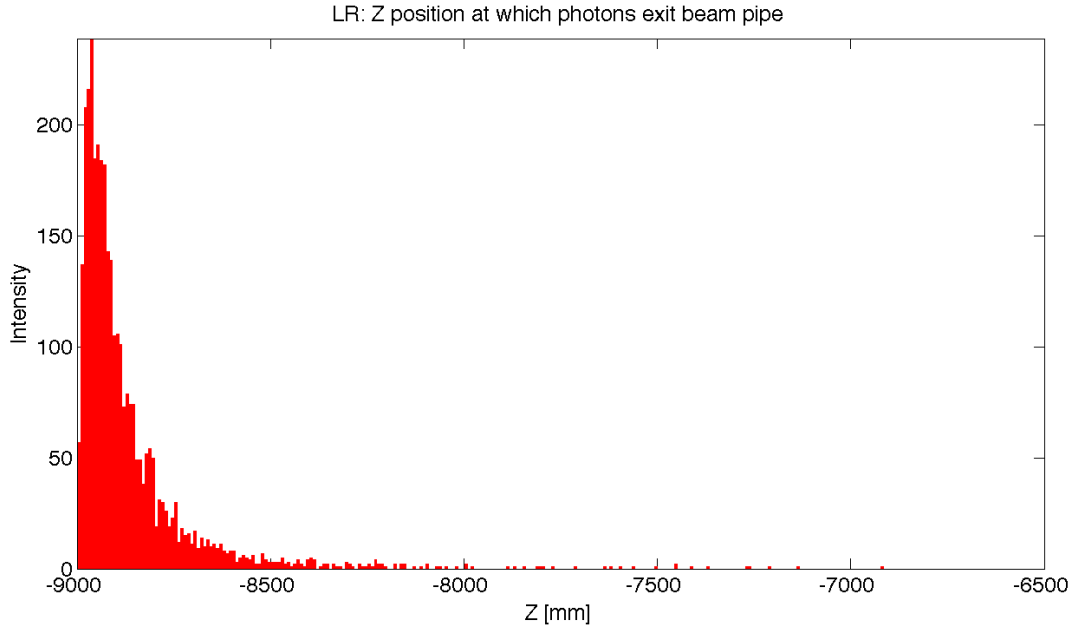


Figure 8.28: LR: Backscattered Photons Exiting the Beam Pipe.

Absorber Type	Power [W]
Flat	645.9
Wedge	159.1
Wedge & Mask/Shield	4.3

Table 8.11: LR: Power deposition due to Backscattered photons.

6964 Cross sections of the beam pipe in the  $Y = 0$  and  $X = 0$  planes with the shields and masks included can  
 6965 be seen in Figure 8.29.

## 6966 8.3 Linac Lattice and Impedance

### 6967 8.3.1 Overall Layout

6968 The proposed layout of the recirculating linear accelerator complex (RLA) is illustrated schematically in  
 6969 Fig. 8.30. It consists of the following components:

- 6970 • A 0.5 GeV injector with an injection chicane.
- 6971 • A pair of 721.44MHz SCRF linacs. Each linac is one kilometer long with an energy gain 10GeV per  
 6972 pass.
- 6973 • Six  $180^\circ$  arcs. Each arc has a radius of one kilometer.
- 6974 • For each arc one re-accelerating station that compensates the synchrotron radiation emitted in this  
 6975 arc.
- 6976 • A switching station at the beginning and end of each linac to combine the beams from different arcs  
 6977 and to distribute them over different arcs.



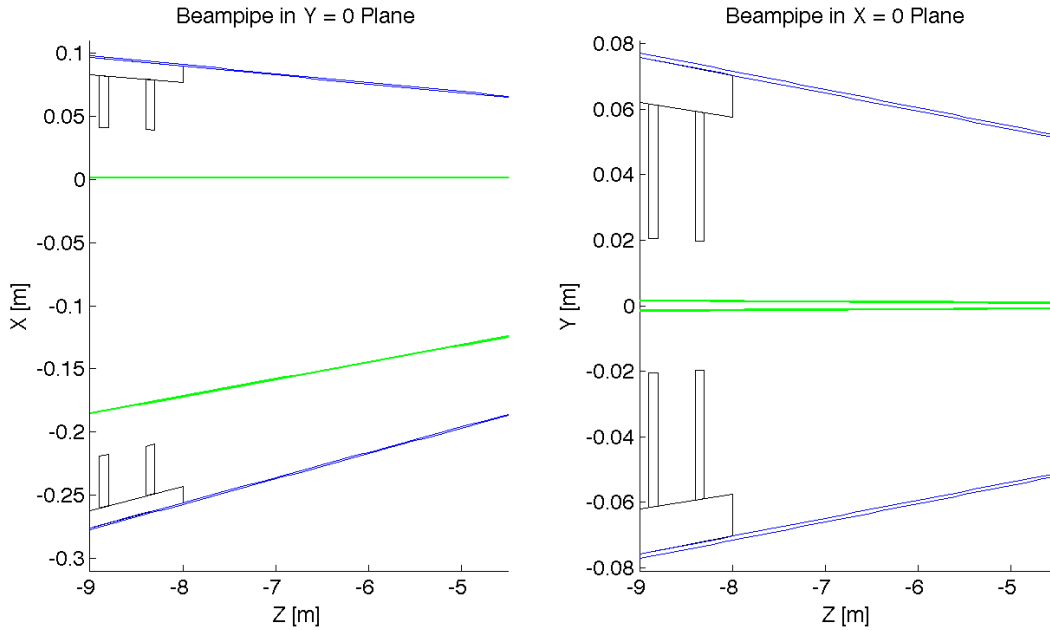


Figure 8.29: LR: Beampipe Cross Sections.

Figure 8.30: The schematic layout of the recirculating linear accelerator complex.

- 6978 • An extraction dump at 0.5 GeV.

6979 After injection, the beam makes three passes through the linacs before it collides with the LHC beam.  
 6980 The beam will then perform three additional turns in which the beam energy is almost completely extracted.  
 6981 The size of the complex is chosen such that each turn has the same length and that three turns correspond  
 6982 to the LHC circumference. This choice is motivated by the following considerations:

- 6983 • To avoid the build-up of a significant ion density in the accelerator complex, clearing gaps may be  
 6984 required in the beam.
- 6985 • The longitudinal position of these gaps must coincide for each of the six turns that a beam performs.  
 6986 This requires that the turns have the same length.
- 6987 • Due to the gaps some LHC bunches will collide with an electron bunch but some will not. It is  
 6988 advantageous to have each LHC bunch either always collide with an electron bunch or to never collide.  
 6989 The choice of length for one turn in the RLA allows to achieve this.

6990 Some key beam parameters are given in table 8.12.

### 6991 8.3.2 Linac Layout and Lattice

6992 The key element of the transverse beam dynamics in a multi-pass recirculating linac is an appropriate choice  
 6993 of multi-pass linac optics. The focusing strength of the quadrupoles along the linac needs to be set such  
 6994 that one can transport the beam at each pass. Obviously, one would like to optimize the focusing profile to  
 6995 accommodate a large number of passes through the RLA. In addition, the requirement of energy recovery  
 6996 puts a constraint on the exit/entrance Twiss functions for the two linacs. As a baseline we have chosen a  
 6997 FODO lattice with a phase advance of  $130^\circ$  for the beam that passes with the lowest energy and a quadrupole

Parameter	Symbol	Value
Particles per bunch	$N$	$2 \cdot 10^9$
Initial normalised transverse emittance	$\epsilon_x, \epsilon_y$	$30\mu\text{m}$
Normalised transverse emittance at IP	$\epsilon_x, \epsilon_y$	$50\mu\text{m}$
Bunch length	$\sigma_z$	$600\mu\text{m}$

Table 8.12: Key beam parameters. It should be noted that normalised emittances are used throughout.

Figure 8.31: Beta-functions in the first linac. On the top, the beta-functions of the six different beam passages in the first linac are shown. On the bottom, the beta-function as seen by the beam during its stay in the linacs are shown.

spacing of 28m [666]. Alternative choices are possible. An example is an optics that avoids any quadrupole in the linacs [667].

### Linac Module Layout

The linac consists of a series of units, each consisting of two cryomodules and one quadrupole pack. We consider one possible configuration for the 10-GeV linac, containing  $36 \times 2$  cryomodules with an RF gradient of 18 MV/m. This design is slightly different from the one described in the RF section later, which uses fewer cavities per linac at a higher gradient; in this case also the modules are longer. However, the conclusions on the beam stability do not change with these small differences. In the simulations, each cryomodule is 12.8 m and contains eight 1m-long accelerating cavities, which allows 1.6 m per cavity unit, which leaves little extra space for interconnects between cavities, with implications on the cavity design. The interconnect between two adjacent cryomodules is 0.8 m long. The quadrupole pack is 1.6m long, including the interconnects to the adjacent cryomodules. The whole unit is 28m long.

Each quadrupole pack contains a quadrupole, a beam position monitor and a vertical and horizontal dipole corrector, see section 2.9.

### Linac Optics

The linac consists of 36 units with a total length of 1008 m. In the first linac, the strength of the quadrupoles has been chosen to provide a phase advance per cell of  $130^\circ$  for the beam in its first turn. In the second linac, the strength has been set to provide a phase advance of  $130^\circ$  for the last turn of the beam. The initial Twiss parameters of the beam and the return arcs are optimised to minimise the beta-functions of the beams in the following passages. The criterion used has been to minimise the integral

$$\int_0^L \frac{\beta}{E} ds \quad (8.6)$$

Single bunch transverse wakefield effects and multi-bunch effects between bunches that have been injected shortly after each other are proportional to this integral [668]. The final solution is shown in Fig. 8.31. A significant beta-beating can be observed due to the weak focusing for the higher energy beams.

### Return Arc Optics

At the ends of each linac the beams need to be directed into the appropriate energy-dependent arcs for recirculation. Each bunch will pass each arc twice, once when it is accelerated before the collision and once when it is decelerated after the collision. The only exception is the arc at highest energy that is passed

Figure 8.32: The optics of the lowest (top) and the highest (bottom) energy return arcs.

turn no	$E$ [GeV]	$\Delta E$ [MeV]	$\sigma_E/E$ [%]
1	10.4	0.7	0.00036
2	20.3	9.9	0.0019
3	30.3	48.5	0.0053
4	40.2	151	0.011
5	50.1	365	0.020
6	60.5	751	0.033
7	50.1	365	0.044
8	40.2	151	0.056
9	30.3	48.5	0.074
10	20.3	9.9	0.11
11	10.4	0.7	0.216
dump	0.5	0.0	4.53

Table 8.13: Energy loss due to synchrotron radiation in the arcs as a function of the arc number. The integrated energy spread induced by synchrotron radiation is also shown.

7025 only once. For practical reasons, horizontal rather than vertical beam separation was chosen. Rather than  
 7026 suppressing the horizontal dispersion created by the spreader, the horizontal dispersion can be smoothly  
 7027 matched to that of the arc, which results in a very compact, single dipole, spreader/recombiner system.

7028 The initial choice of large arc radius (1 km) was dictated by limiting energy loss due to synchrotron  
 7029 radiation at top energy (60.5 GeV) to less than 1%. However other adverse effects of synchrotron radiation  
 7030 on beam phase-space such as cumulative emittance and momentum growth due to quantum excitations  
 7031 are of paramount importance for a high luminosity collider that requires normalized emittance of 50 mm  
 7032 mrad. Energy losses from resistive wall and cfrom oherent synchrotron radiation have both been shown to  
 7033 be negligible compared with the energy loss due to incoherent synchrotron radiation [667].

7034 Three different arc designs have been developed [666]. In the design for the lowest energy turns, the beta-  
 7035 functions are kept small in order to limit the required vacuum chamber size and consequently the magnet  
 7036 aperture. At the highest energy, the lattice is optimised to keep the emittance growth limited, while the  
 7037 beta-functions are allowed to be larger. A cell of the lowest and one of the highest energy arc is shown in  
 7038 Fig. 8.32 All turns have a bending radius of 764m. The beam pipe diameter is 25mm, which corresponds to  
 7039 more than  $12\sigma$  aperture.

7040 An interesting alternative optics, which pushes towards a smaller beam pipe, has also been devel-  
 7041 oped [667].

#### 7042 Synchrotron Radiation in Return Arcs

7043 Synchrotron radiation in the arcs leads to a significant beam energy loss. This loss is compensated by the  
 7044 small linacs that are incorporated before or after each arc when the beams are already or still separated  
 7045 according to their energy, see Fig. 8.30. The energy loss at the 60GeV turn-round can be compensated by  
 7046 a linac with an RF frequency of 721.44MHz. The compensation at the other arcs is performed with an RF  
 7047 frequency of 1442.88MHz. In this way the bunches that are on their way to the collision point and the ones  
 7048 that already collided can both be accelerated. This ensures that the energy of these bunches are the same  
 7049 on the way to and from the interaction point, which simplifies the optics design. If the energy loss were not  
 7050 compensated the beams would have a different energy at each turn, so that the number of return arcs would

turn no	$E$ [GeV]	$\Delta\epsilon_{arc}$ [ $\mu\text{m}$ ]	$\Delta\epsilon_t$ [ $\mu\text{m}$ ]
1	10.4	0.0025	0.0025
2	20.3	0.140	0.143
3	30.3	0.380	0.522
4	40.2	2.082	2.604
5	50.1	4.268	6.872
6	60	12.618	19.490
5	50.1	4.268	23.758
4	40.2	2.082	25.840
3	30.3	0.380	26.220
2	20.3	0.140	26.360
1	10.4	0.0025	26.362

Table 8.14: The emittance growth due to synchrotron radiation in the arcs.  $\Delta\epsilon_{arc}$  is the growth in each individual arc,  $\Delta\epsilon_t$  is the integrated growth including all previous arcs. The collision with the proton beam will take place at the beginning of the arc 6, so one finds  $\Delta\epsilon_t \approx 4.3 \mu\text{m}$ .

7051 need to be doubled.

7052 The synchrotron radiation is also generating an energy spread of the beam. In Tab. 8.13 the relative  
7053 energy spread is shown as a function of the arc number that the beam has seen. At the interaction point,  
7054 the synchrotron radiation induced RMS energy spread is only  $2 \times 10^{-4}$ , which adds to the energy spread of  
7055 the wakefields. At the final arc the energy spread reaches about 0.22%, while at the beam dump it grows to  
7056 a full 4.5%.

7057 The growth of the normalised emittance is given by

$$\Delta\epsilon = \frac{55}{48\sqrt{3}} \frac{\hbar c}{mc^2} r_e \gamma^6 I_5 \quad (8.7)$$

7058 Here,  $r_e$  is the classical electron radius, and  $I_5$  is given by

$$I_5 = \int_0^L \frac{H}{|\rho|^3} ds = \frac{\langle H \rangle \theta}{\rho^2} \quad H = \gamma D^2 + 2\alpha DD' + \beta D'^2 \quad (8.8)$$

7059 For a return arc with a total bend angle  $\theta = 180^\circ$  one finds

$$\Delta\epsilon = \frac{55}{48\sqrt{3}} \frac{\hbar c}{mc^2} r_e \gamma^6 \pi \frac{\langle H \rangle \theta}{\rho^2} \quad (8.9)$$

7060 The synchrotron radiation induced emittance growth is shown in table 8.14. Before the interaction point  
7061 a total growth of about  $7 \mu\text{m}$  is accumulated. The final value is  $26 \mu\text{m}$ . While this growth is significant  
7062 compared to the target emittance of  $50 \mu\text{m}$  at the collision point, it seems acceptable.

### 7063 Matching Sections and Energy Compensation

7064 Currently we do not have a design of the matching sections. However, we expect these sections to be  
7065 straightforward. For the case of the linac optics without quadrupoles and the alternative return arc lattice  
7066 design matching sections designs exist and exhibit no issues [667]. Also the sections that compensate the  
7067 energy loss in the arcs have not been designed. But this again should be straightforward.

Figure 8.33: The RMS energy spread due to single bunch wakefields along the linacs. The bunch has been cut longitudinally at  $\pm 3\sigma_z$  and at  $\pm 3\sigma_E$  in the initial uncorrelated energy spread.

Figure 8.34: The single-bunch emittance growth along the LHeC linacs for a bunch with an initial offset of  $\Delta x = \sigma_x$ . The arcs have been represented by a simple transfer matrix.

### 8.3.3 Beam Break-Up

#### Single-Bunch Wakefield Effect

In order to evaluate the single bunch wakefield effects we used PLACET [669]. The full linac lattice has been implemented for all turns but the arcs have each been replaced by a simple transfer matrix, since the matching sections have not been available.

Single bunch wakefields were not available for the SPL cavities. We therefore used the wakefields in the ILC/TESLA cavities [670]. In order to adjust the wakefields to the lower frequency and larger iris radius (70mm vs. 39mm for the central irises) we used the following scaling

$$W_{\perp}(s) \approx \frac{1}{(70/39)^3} W_{\perp,ILC}(s/(70/39)) \quad W_L(s) \approx \frac{1}{(70/39)^2} W_{L,ILC}(s/(70/39)) \quad (8.10)$$

First, the RMS energy spread along the linacs is determined. An initial uncorrelated RMS energy spread of 0.1% is assumed. Three different bunch lengths were studied, i.e.  $300\mu\text{m}$ ,  $600\mu\text{m}$  and  $900\mu\text{m}$ . This longest value yields the smallest final energy spread. The energy spread along during the beam life-time can be seen in Fig. 8.33. The wakefield induced energy spread is between  $1 \times 10^{-4}$  and  $2 \times 10^{-4}$  at the interaction point,  $1-2 \times 10^{-3}$  at the final arc and 3.5–4.5% at the beam dump.

Second, the single bunch beam-break-up is studied by tracking a bunch with an initial offset of  $\Delta x = \sigma_x$ . The resulting emittance growth of the bunch is very small, see Fig. 8.34.

#### Multi-Bunch Transverse Wakefield Effects

For a single pass through a linac the multi-bunch effects can easily be estimated analytically [668]. Another approach exists in case of two passes through one cavity [671]. It is less straightforward to find an analytic solution for multiple turns in linacs with wakefields that vary from one cavity to the next. In this case the also phase advance from one passage through a cavity to the next passage depends on the position of the cavity within the linac. We therefore addressed the issue by simulation.

Two multi-bunch beam break-up studies have been performed independently. The first study is based on a new code that we developed to simulate the multi-bunch effect in the case of recirculation and energy recovery [672]. It assumes point-like bunches and takes a number of dipole wake field modes into account. A cavity-to-cavity frequency spread of the wakefield modes can also be modeled. The arcs are replaced with simple transfer matrices. In the simulation, we offset a single bunch of a long train by one unit and determine the final position in phase space of all other bunches.

We evaluated the beam stability using the wakefield modes that have been calculated for the SPL cavity design [673]. The level of the  $Q$ -values of the transverse modes is not yet known. We assume  $Q = 10^5$  for all modes, which is comparable to the larger of the  $Q$ -values found in the TESLA cavities. A random variation of the transverse mode frequencies of 0.1% has been assumed, which corresponds to the target for ILC [670]. The results in Fig. 8.35 indicate that the beam remains stable in our baseline design. Even in the alternative lattice with no focusing in the linacs, the beam would remain stable but with significantly less margin. An independent beam-breakup analysis for linacs without focusing, based on measurements and simulations for

$f$ [GHz]	$k$ [V/pCm <sup>2</sup> ]	$f$ [GHz]	$k$ [V/pCm <sup>2</sup> ]
0.9151	9.323	1.675	4.160
0.9398	19.095	2.101	1.447
0.9664	8.201	2.220	1.427
1.003	5.799	2.267	1.377
1.014	13.426	2.331	2.212
1.020	4.659	2.338	11.918
1.378	1.111	2.345	5.621
1.393	20.346	2.526	1.886
1.408	1.477	2.592	1.045
1.409	23.274	2.592	1.069
1.607	8.186	2.693	1.256
1.666	1.393	2.696	1.347
1.670	1.261	2.838	4.350

Table 8.15: The considered dipole modes of the SPL cavity design.

Figure 8.35: Multi-bunch beam break-up assuming the SPL cavity wakefields. One bunch has been offset at the beginning of the machine and the normalised amplitudes of the bunch oscillations are shown along the train at the end of the last turn. The upper plot shows a small number of bunches before and after the one that has been offset (i.e. bunch 3000). The lower plot shows the amplitudes along the full simulated train for the baseline lattice and the alternative design with no quadrupole focusing. One can see the fast decay of the amplitudes.

Figure 8.36: Multi-bunch beam break-up for the SPL cavities. In one case only damping, in the other case only cavity-to-cavity mode detuning is present.

Figure 8.37: Quality factor of BNL3 cavity per “High Current SRF Cavity Design for SPL and eRHIC”, S. Belomestnykh et al., Proceedings of 2011 Particle Accelerator Conference, New York, NY, USA.

Figure 8.38: Large scale TDBBU simulation results for various beam currents: 4 (top left), 5 (top right) and 6 mA.

7102 the BNL 5-cell cavity, demonstrated as well that for all practical scenarios with a HOM frequency spread  
7103 above 0.2% the instability threshold current is well above the design beam current [667].

7104 We also performed simulations, assuming that either only damping or detuning were present, see Fig. 8.36.  
7105 The beam is unstable in both cases. Similarly, increasing the  $Q$  value to  $10^6$  will make the beam unstable  
7106 Based on our results we conclude

7107 • One has to ensure that transverse higher order cavity modes are detuned from one cavity to the next.  
7108 While this detuning can naturally occur due to production tolerances, one has to find a method to  
7109 ensure its presence. This problem exists similarly for the ILC.

7110 • Damping of the transverse modes is required with a  $Q$  value below  $10^5$ .

7111 If these requirements are met, the beam will remain stable in the cavities at 720 MHz. Further studies can  
7112 give more precise limits on the maximum required  $Q$  and minimum mode detuning.

7113 A further study used the code TDBBU [?]. The optics model of the machine is the same as for the first  
7114 study. The wakefield model has been based on the BNL3 5-cell cavities, even if their fundamental mode  
7115 frequency is 703.79 MHz. The summary of measured HOMs is illustrated in Figure 8.37.

7116 One can notice that all the  $Q$  values are less than  $1 \cdot 10^6$  and most of them are smaller than  $1 \cdot 10^4$ . For  
7117 our BBU simulation, we consider the worst case of  $Q_l = 1 \cdot 10^6$ . Out of all HOMs collected in Figure 8.37, we  
7118 selected three most offending HOMs with relatively high  $R/Q$  values. They are summarized in table 8.16.

Frequency[MHz]	$Q_l$	R/Q[Ohm]
1003	$1 \cdot 10^6$	32
1337	$1 \cdot 10^6$	32
1820	$1 \cdot 10^6$	32

Table 8.16: The most offending HOMs selected into BBU simulation.

7119 In the simulation, for each cavity along the linac, the three offending HOM frequencies are randomly  
7120 distributed with the full width of 2 MHz. In practice, the HOM frequencies are generated using random  
7121 numbers in that range and these are distributed at each cavity. Twenty samples for different HOM frequency  
7122 distributions are generated. The plots below show the beam behavior near the threshold. The horizontal  
7123 axis corresponds to a bunch number and can be considered as an axis of time (if the bunch numbers are  
7124 divided by frequencies). The vertical axis represents the transverse beam position at the end of the second  
7125 linac. We plot the transverse positions of every 1117th particles. The number 1117 is somehow arbitrary;  
7126 however it is a large prime number chosen to avoid an unexpected sub-harmonic redundancy in the data  
7127 sampling. The simulation results for various beam currents: 4, 5 and 6 mA are illustrated in Figure 8.38.

7128 As illustrated in Figure 8.38, the beam is stable at 4 mA. At 5 mA the transverse position is increasing,  
7129 which indicate onset of the instability. Finally, at 6 mA one explicitly observes an exponential increase  
7130 in transverse beam position - a vivid case of beam instability. Therefore, we could infer that the BBU  
7131 threshold current is somewhere around 5 mA. One needs to keep in mind, our study assumed the worst case  
7132 interpretation of HOM’s measurement for a cavity with limited HOM suppression, only one pair of HOM

Figure 8.39: The oscillation frequency  $f_c$  of ions of different mass number  $A$  in the linacs using the average focusing strength of the bunches at different energy. The frequency is normalised to the limit frequency  $f_{limit}$  above which the ions would not be trapped any more.

7133 dampers per cavity, positioned at 120 degrees to each other. This suggests more extended HOM damping will  
 7134 bring the stability threshold above 6.5 mA. Further BBU study with more realistic HOM selection extracted  
 7135 from the same measurement, summarized in Figure 8.37, is under way.

7136 From this study we conclude that the  $Q$  values of the transverse modes have to remain below  $10^5$ .

### 7137 Fast Beam-Ion Instability

7138 Collision of beam particles with the residual gas in the beam pipe will lead to the production of positive  
 7139 ions. These ions can be trapped in the beam. Their presence modifies the betatron function of the beam  
 7140 since the ions focus the beam. They can also lead to beam break-up, since bunches with an offset will induce  
 7141 a coherent motion in the ions. This can in turn lead to a kick of the ions on following bunches.

7142 **Trapping Condition in the beam pulse** In order to estimate whether ions are trapped or not, one can  
 7143 replace each beam with a thin focusing lens, with the strength determined by the charge and transverse  
 7144 dimension of the beam. In this case the force is assumed to be linear with the ion offset, which is a good  
 7145 approximation for small offsets.

7146 The coherent frequency  $f_i$  of the ions in the field of a beam of with bunches of similar size is given  
 7147 by [674]:

$$f_i = \frac{c}{\pi} \sqrt{\frac{Q_i N r_e \frac{m_e}{A m_p}}{3 \sigma_y (\sigma_x + \sigma_y) \Delta L}} \quad (8.11)$$

7148 Here,  $N$  is the number of electrons per bunch,  $\Delta L$  the bunch spacing,  $r_e$  the classical electron radius,  $m_e$   
 7149 the electron mass,  $Q_i$  the charge of the ions in units of  $e$  and  $A$  is their mass number and  $m_p$  the proton  
 7150 mass. The beam transverse beam size is given by  $\sigma_x$  and  $\sigma_y$ . The ions will be trapped in the beam if

$$f_i \leq f_{limit} = \frac{c}{4 \Delta L} \quad (8.12)$$

7151 In the following we will use  $\Delta L \approx 2.5\text{m}$ , i.e. assume that the bunches from the different turns are almost  
 7152 evenly spaced longitudinally.

7153 In the linacs, the transverse size of the beam changes from one passage to the next while in each of  
 7154 the return arcs the beams have (approximately) the same size at both passages. But the variation from  
 7155 one turn to the next is not huge, so we use the average focusing strength of the six turns. The calculation  
 7156 shows that ions will be trapped for a continuous beam in the linacs. Since we are far from the limit of the  
 7157 trapping condition, the simplification in our model should not matter. As can be seen in Fig. 8.39  $\text{CO}_2^+$   
 7158 ions are trapped all along the linacs. Even hydrogen ions  $H_2^+$  would be trapped everywhere. If one places  
 7159 the bunches from the six turns very close to each other longitudinally, the limit frequency  $f_{limit}$  is reduced.  
 7160 However, the ratio  $f_c/f_{limit}$  is not increased by more than a factor 6, which is not fully sufficient to remove  
 7161 the  $H_2^+$ .

7162 **Impact and Mitigation of Ion Effects** Without any methods to remove ions, a continuous beam would  
 7163 collect ions until they neutralise the beam current. This will render the beam unstable. Hence one needs to  
 7164 find methods to remove the ions. We will first quickly describe the mitigation techniques and then give a  
 7165 rough estimate of the expected ion effect.

7166 A number of techniques can be used to reduce the fast beam-ion instability:



Figure 8.40: The trace of the transfer matrix for  $H_2^+$ ,  $CH_4^+$  and  $CO_2^+$  ions in presence of a clearing gap. Values above 2 or below  $-2$  indicate that the ions will not be trapped.

- 7167 • An excellent vacuum quality will slow down the build-up of a significant ion density.
- 7168 • Clearing gaps can be incorporated in the electron beam. During these gaps the ions can drift away  
7169 from the beam orbit.
- 7170 • Clearing electrodes can be used to extract the ions. They would apply a bias voltage that lets the ions  
7171 slowly drift out of the beam.

7172 **Clearing Gaps** In order to provide the gap for ion cleaning, the beam has to consist at injection of short  
7173 trains of bunches with duration  $\tau_{beam}$  separated by gaps  $\tau_{gap}$ . If each turn of the beam in the machine takes  
7174  $\tau_{cycle}$ , the beam parameters have to be adjusted such that  $n(\tau_{beam} + \tau_{gap}) = \tau_{cycle}$ . In this case the gaps of  
7175 the different turns fall into the same location of the machine. This scheme will avoid beam loading during  
7176 the gap and ensure that the gaps are fully empty. By choosing the time for one round trip in the electron  
7177 machine to be an integer fraction of the LHC roundtrip time  $\tau_{LHC} = m\tau_{cycle}$ , one ensures that each bunch  
7178 in the LHC will either always collide with an electron bunch or never. We chose to use  $\tau_{cycle} = 1/3\tau_{LHC}$   
7179 and to use a single gap with  $\tau_{gap} = 1/3\tau_{cycle} \approx 10 \mu s$ .

7180 In order to evaluate the impact of a clearing gap in the beam, we model the beam as a thick focusing lens  
7181 and the gap as a drift. The treatment follows [675], except that we use a thick lens approach and correct a  
7182 factor two in the force. The focusing strength of the lens can be calculated as

$$k = \frac{2Nr_e m_e}{A_{ion} m_p \sigma_y (\sigma_x + \sigma_y) \Delta L} \quad (8.13)$$

7183 The ions will not be collected if the following equation is fulfilled

$$\left| 2 \cos(\sqrt{k}(L_{erl} - L_g)) - \sqrt{k} L_g \sin(\sqrt{k}(L_{erl} - L_g)) \right| \geq 2 \quad (8.14)$$

7184 Since the beam size will vary as a function of the number of turns that the beam has performed, we replace  
7185 the above defined  $k$  with the average value over the six turns using the average bunch spacing  $\Delta L$ ,

$$k = \frac{1}{n} \sum_{i=1}^n \frac{2Nr_e m_e}{A_{ion} m_p \sigma_{y,i} (\sigma_{x,i} + \sigma_{y,i}) \Delta L}. \quad (8.15)$$

7186 The results of the calculation can be found in Fig. 8.40. As can be seen, in most locations the ions are not  
7187 trapped. But small regions exist where ions will accumulate. More study is needed to understand which ion  
7188 density is reached in these areas. Longitudinal motion of the ions will slowly move them into other regions  
7189 where they are no longer trapped.

7190 **Ion Instability** While the gap ensures that ions will be lost in the long run, they will still be trapped  
7191 at least during the full train length of  $20 \mu s$ . We therefore evaluate the impact of ions on the beam during  
7192 this time. This optimistically ignores that ions will not be completely removed from one turn to the next.  
7193 However, the stability criteria we employ will be pessimistic. Clearly detailed simulations will be needed in  
7194 the future to improve the predictive power of the estimates.

7195 Different theoretical models exist for the rise time of a beam instability in the presence of ions. A  
7196 pessimistic estimate is used in the following. The typical rise time of the beam-ion instability for the  $n$ th

Figure 8.41: The instability length of the beam-ion instability assuming a very conservative partial pressure of  $10^{-11}$ hPa for each gas.

7197 bunch can be estimated to be [674]

$$\tau_c = \frac{\sqrt{27}}{4} \left( \frac{\sigma_y(\sigma_x + \sigma_y)}{Nr_e} \right)^{\frac{3}{2}} \sqrt{\frac{A_{ion} m_p}{m} \frac{kT}{p \sigma_{ion}} \frac{\gamma}{\beta_y c n^2 \sqrt{L_{sep}}}} \quad (8.16)$$

7198 This estimate does not take into account that the ion frequency varies with transverse position within the  
7200 bunch and along the beam line.

7201 We calculate the local instability rise length  $c\tau_c$  for a pressure of  $p = 10^{-11}$ hPa at the position of the  
7202 beam. As can be seen in Fig. 8.41 this instability rise length ranges from a few kilometers to several hundred.  
7203 One can estimate the overall rise time of the ion instability by averaging over the local ion instability rates:

$$\left\langle \frac{1}{\tau_c} \right\rangle = \frac{\int \frac{1}{\tau_c(s)} ds}{\int ds} \quad (8.17)$$

7203 For the worst case in the figure, i.e.  $CH_4^+$ , one finds  $c\tau_c \approx 14$  km and for  $H_2^+$   $c\tau_c \approx 25$ km. The beam  
7204 will travel a total of 12km during the six passes through each of the two linacs. So the typical time scale  
7205 of the rise of the instability is longer than the life time of the beam and we expect no issue. This estimate  
7206 is conservative since it does not take into account that ion frequency varies within the beam and along the  
7207 machine. Both effects will stabilise the beam. Hence we conclude that a partial pressure below  $10^{-11}$  hPa is  
7208 required for the LHeC linacs.

7209 In the cold part of LEP a vacuum level of  $0.5 \times 10^{-9}$ hPa has been measured at room temperature, which  
7210 corresponds to  $0.6 \times 10^{-10}$ hPa in the cold [676]. This is higher than required but this value “represents  
7211 more the outgassing of warm adjacent parts of the vacuum system” [676] and can be considered a pessimistic  
7212 upper limit. Measurements in the cold at HERA showed vacuum levels of  $10^{-11}$ hPa [677], which would be  
7213 sufficient but potentially marginal. Recent measurements at LHC show a hydrogen pressure of  $5 \times 10^{-12}$ hPa  
7214 measured at room temperature, which corresponds to about  $5 \times 10^{-13}$ hPa in the cold [678]. For all other  
7215 gasses a pressure of less than  $10^{-13}$ hPa is expected measured in the warm [678], corresponding to  $10^{-14}$ hPa  
7216 in the cold. These levels are significantly better than the requirements. The shortest instability rise length  
7217 would be due to hydrogen. With a length of  $c\tau_c \approx 500$ km which is longer than 40 turns. Hence we do not  
7218 expect a problem with the fast beam-ion instability in the linacs provided the vacuum system is designed  
7219 accordingly.

7220 The effect of the fast beam-ion instability in the arcs has been calculated in a similar way, taking into  
7221 account the reduced beam current and the baseline lattice for each arc. Even  $H_2^+$  will be trapped in the  
7222 arcs. We calculate the instability rise length  $c\tau_c$  for a partial pressure of  $10^{-9}$  hPa for each ion mass and find  
7223  $c\tau_c \approx 70$ km for  $H_2^+$ ,  $c\tau_c \approx 50$ km for  $N_2^+$  and  $CO^+$  and  $c\tau_c \approx 60$ km for  $CO_2^+$ . The total distance the beam  
7224 travels in the arcs is 15km. Hence we conclude that a partial pressure below  $10^{-9}$  hPa should be sufficient  
7225 for the arcs. More detailed work will be needed in the future to fully assess the ion effects in LHeC but we  
7226 remain confident that they can be handled.

**Ion Induced Phase Advance Error** The relative phase advance error along a beam line can be calculated using [675] for a round beam:

$$\frac{\Delta\phi}{\phi} = \frac{1}{2} \frac{Nr_e}{\Delta L \epsilon_y} \frac{\theta}{\langle \beta_y^{-1} \rangle}$$

7227 Here  $\theta$  is the neutralisation of the beam by the ions. We use the maximum beta-function in the linac to  
7228 make a conservative approximation  $\langle \beta_y^{-1} \rangle = 1/700$ m. At the end of the train we find  $\rho \approx 3.3 \times 10^{-5}$  for  
7229  $p = 10^{-11}$ hPa in the cold and  $p = 10^{-9}$ hPa in the warm parts of the machine. This yields  $\Delta\Phi/\Phi \approx 7 \times 10^{-4}$ .  
7230 Hence the phase advance error can be neglected.

7231 **Impact of the Gap on Beam Loading** It should be noted that the gaps may create some beam-loading  
 7232 variation in the injector complex. We can estimate the associated gradient variation assuming that the same  
 7233 cavities and gradients are used in the injector as in the linacs. We use

$$\frac{\Delta G}{G} \approx \frac{1}{2} \frac{R}{Q} \omega \frac{\tau_{gap} \tau_{beam} I}{\tau_{gap} + \tau_{beam}} \frac{1}{G} \quad (8.18)$$

7234 In this case the 10 $\mu$ s gaps in the bunch train correspond to a gradient variation of about 0.6%. This seems  
 7235 very acceptable.

### 7236 8.3.4 Imperfections

7237 Static imperfections can lead to emittance growth in the LHeC linacs and arcs. However, one can afford an  
 7238 emittance budget that is significantly larger than the one for the ILC, i.e. 10 $\mu$ m vs. 20nm. If the LHeC  
 7239 components are aligned with the accuracy of the ILC components, one would not expect emittance growth  
 7240 to be a serious issue. In particular in the linacs dispersion free steering can be used and should be very  
 7241 effective, since the energies of the different probe beams are much larger than they would be in ILC.

### 7242 Gradient Jitter and Cavity Tilt

Since the cavities have tilts with respect to the beam line axis, dynamic variations of the gradient will lead to transverse beam deflections. This effect can be easily calculated using the following expression:

$$\frac{\langle y^2 \rangle}{\sigma_y^2} = \frac{\langle (y')^2 \rangle}{\sigma_{y'}^2} = \frac{1}{2} \frac{1}{\epsilon} \int \frac{\beta}{E} ds \frac{L_{cav} \langle \Delta G^2 \rangle \langle (y'_{cav})^2 \rangle}{mc^2}$$

For an RMS cavity tilt of 300 $\mu$ radian, an RMS gradient jitter of 1% and an emittance of 50 $\mu$ m we find

$$\frac{\langle y^2 \rangle}{\sigma_y^2} = \frac{\langle (y')^2 \rangle}{\sigma_{y'}^2} \approx 0.0125$$

7243 i.e. an RMS beam jitter of  $\approx 0.07\sigma_y$ . At the interaction point the beam jitter would be  $\approx 0.05\sigma_{y'}$ .

### 7244 8.3.5 Touschek Scattering

7245 In recirculating energy recovery linacs, intrabeam scattering and Touschek scattering give rise to beam  
 7246 halo and to some unavoidable amount of beam losses, in particular, for high brightness beams and after  
 7247 deceleration [?]. In the LHeC ERL a few dedicated collimators should be foreseen to localize and control  
 7248 these losses [?]. For round beams the Touschek loss rate can be approximated as [?] (corrected by a factor  
 7249 of two [?])

$$\frac{\Delta N_b}{\Delta s} = - \frac{N_b^2 r_e^2}{8\sqrt{\pi} \gamma^2 \sigma_z \epsilon_x \epsilon_y} \frac{1}{\eta(s)} D \left( \frac{\delta q(s)}{\eta(s)} \right), \quad (8.19)$$

7250 where  $\delta q(s) = \gamma \sigma_x(s) / \beta_x(s)$ ,

$$D(\epsilon) = \sqrt{\epsilon} \int_{\epsilon}^{\infty} \frac{e^{-u}}{u^{3/2}} \left( \frac{1}{\epsilon} - 1 - \frac{1}{2} \ln \frac{u}{\epsilon} \right) du, \quad (8.20)$$

7251 and  $\eta_{acc}$  denotes the relative momentum acceptance, which varies along the beamline and is a function of the  
 7252 downstream beam energy, RF voltage, optics and aperture. Equation (8.19) describes the number of bunch  
 7253 particles which are Touschek scattered per unit length at location  $s$  and lost at a later location. No detailed  
 7254 analysis of Touschek scattering has yet been performed for the LHeC, but with normalized emittances  $\epsilon_{x(y)}$   
 7255 much larger than envisioned for other projects, e.g. CESR-ERL, with less beam current, and higher beam  
 7256 energy, the effect is expected to be comparatively benign.

## 8.4 Performance as a Linac-Ring electron-ion collider

The performance as an e-A collider can be evaluated on a basis similar to the Ring-Ring version of the LHeC discussed in Section 7.14. Again, this relies on the fact that the nominal emittances for Pb beams in the LHC imply equal geometric beam sizes, at the IP in particular.

### 8.4.1 Heavy nuclei, e-Pb collisions

The Pb beam is specified in Table 7.33. Assuming that the 60 GeV electron beam specified in Table 8.7 can be adapted to the irregular 100 ns spacing of the Pb beam, the luminosity follows from Eq. 8.1 (including the additional factor of  $A = 208$  to obtain the electron-nucleon luminosity):

$$L_{eN} = \begin{cases} 9 \times 10^{31} \text{ cm}^{-2}\text{s}^{-1} & \text{(Nominal Pb)} \\ 1.6 \times 10^{32} \text{ cm}^{-2}\text{s}^{-1} & \text{(Ultimate Pb)} \end{cases} \quad (8.21)$$

where we assume  $H_{hg} = H_D = 1$  for the additional factors in Eq. 8.1.

### 8.4.2 Electron-deuteron collisions

An estimate of the parameters for deuteron beams in the LHC is also given in Section 7.14. Proceeding in the same manner as above, we find that *electron-nucleon* luminosities of order  $L_{eN} \gtrsim 3 \times 10^{31} \text{ cm}^{-2}\text{s}^{-1}$  could be accessible in e-D collisions in a Linac-Ring LHeC.

## 8.5 Polarized-Electron Injector for the Linac-Ring LHeC

We present the injector for the polarized electron beam. The issue of producing a sufficient number of polarized or unpolarized positrons is discussed in section 8.7.

The Linac-Ring option is based on an ERL machine where the beam pattern, at IP, is shown in Figure 8.42.

With this bunch spacing, one needs  $20 \times 10^9$  bunches/second and with the requested bunch charge, the average beam current is  $20 \times 10^9 \text{ b/s} \times 0.33 \text{ nC/b} = 6.6 \text{ mA}$ .

Figure 8.43 shows a possible layout for the injector complex, as source of polarized electron beam.

The injector is composed of a DC gun where a photocathode is illuminated by a laser beam. Then a linac accelerates electron beam up to the requested energy before injection into the ERL. Downstream a bunch compressor system allows to compress the beam to 1 ps and finally a spin rotator, brings the spin in the vertical plane.

Assuming 90% of transport efficiency between the source and the IP, the bunch charge at the photocathode should  $2.2 \times 10^9 \text{ e-/b}$ . According to the laser and photocathode performance, the laser pulse width, corresponding to the electron bunch length, will be between 10 and 100 ps.

Table 8.17 summarises the electron beam parameters at the exit of the DC gun.

The challenges to produce the 7 mA beam current are the following:

- a very good vacuum ( $< 10^{-12}$  mbar) is required in order to get a good lifetime.
- the issues related to the space charge limit and the surface charge limit should be considered. A peak current of 10 A with 4 ns pulse length has been demonstrated. Assuming a similar value for the DC gun, a laser pulse length of 35 ps would be sufficient to produce the requested LHeC charge.
- the high voltage (100 kV to 500 kV) of the DC gun could induce important field emissions.
- the design of the cathode/anode geometry is crucial for a beam transport close to 100%.
- the quantum efficiency should be as high as possible for the photocathode ( $\sim 1\%$  or more).

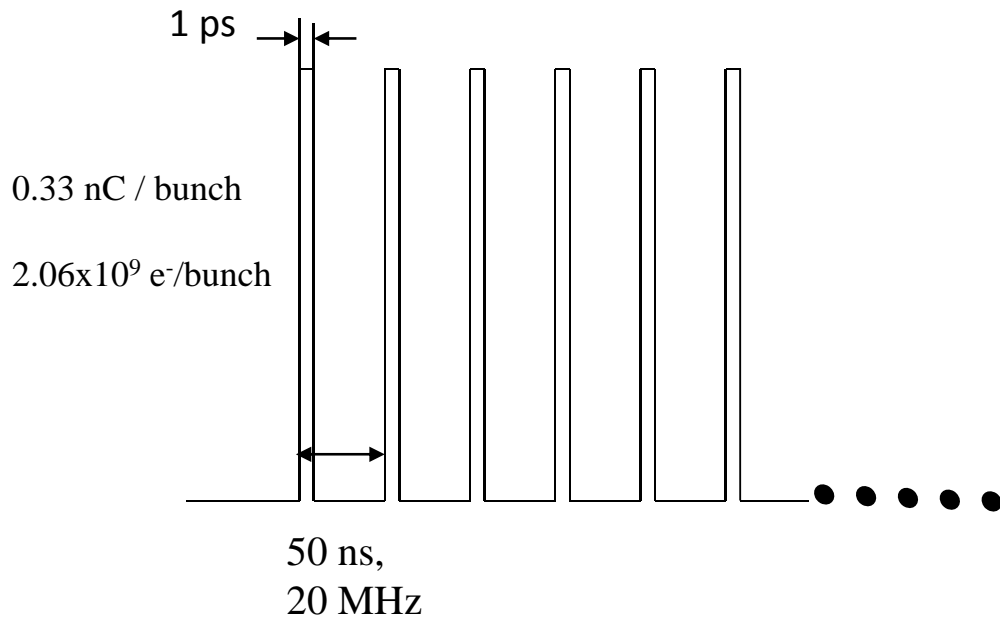


Figure 8.42: Beam pattern at IP

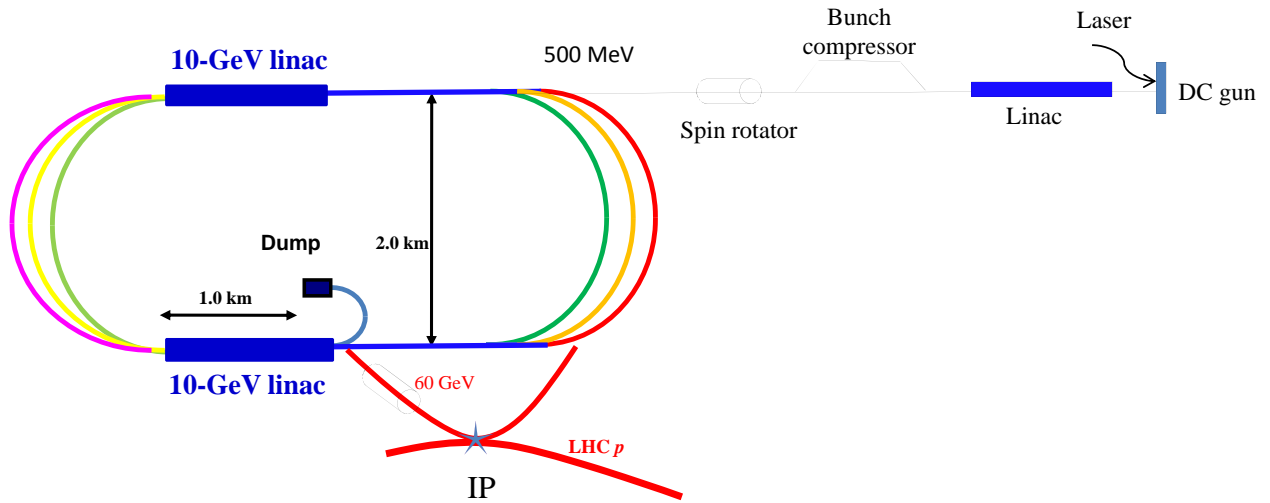


Figure 8.43: Layout of the injector (not to scale).

Parameters	60 GeV ERL
Electrons /bunch	$2.2 \times 10^9$
Charge /bunch	0.35 nC
Number bunches / s	$20 \times 10^9$
Bunch length	10 – 100 ps
Bunch spacing	50 ns
Pulse repetition rate	CW
Average current	7 mA
Peak current of the bunch	3.5 – 350 A
Current density (1 cm)	1.1 – 110 A/cm <sup>2</sup>
Polarization	> 90%

Table 8.17: Beam parameters at the source.

- 7294 • the laser parameters (300 nJ/pulse on the photocathode, 20 MHz repetition rate) will need some R&D  
7295 according to what is existing today on the market.
- 7296 • the space charge could increase the transverse beam emittances.

7297 In conclusion, a tradeoff between the photocathode, the gun and the laser seems reachable to get accept-  
7298 able parameters at the gun exit. A classical Pre-Injector Linac accelerates electron beam to the requested  
7299 ERL energy. Different stages of bunch compressor are used to compensate the initial laser pulse and the  
7300 space charge effects inducing bunch lengthening. A classical spin rotator system rotates the spin before  
7301 injection into the ERL.

## 7302 8.6 Spin Rotator

7303 The LHeC physics requires polarized electrons with spin aligned longitudinally at the collision point [679].  
7304 In the electron accelerator of LHeC, consisting of two 10-GeV superconducting linear accelerators linked  
7305 with six 180° arc paths, the depolarization due to the arcs is negligible if the spin is aligned vertically in the  
7306 arcs.

7307 The motion of the spin vector  $\vec{S}$  is governed by Thomas-BMT equation [680] shown in Eq. 8.22

$$\frac{d\vec{S}}{dt} = \frac{e}{m\gamma} \vec{S} \times [(1 + G\gamma)\vec{B}_\perp + (1 + G)\vec{B}_\parallel] \quad (8.22)$$

7308 where  $e$ ,  $m$  and  $\gamma$  are the electric charge, mass and Lorentz factor of the particle.  $G$  is the anomalous  
7309 g-factor. For protons,  $G = 1.7928474$  and for electrons,  $G = 0.00115$ .  $\vec{B}_\perp$  and  $\vec{B}_\parallel$  are the magnetic field  
7310 perpendicular and parallel to the particle velocity direction, respectively. In Eq. 8.22, magnetic field is in the  
7311 laboratory frame while the spin vector  $\vec{S}$  is in the particle's rest frame. In a bending dipole, a spin vector  
7312 precesses  $G\gamma$  times of the particle's orbital rotation in the particle's moving frame. It is also evident that  
7313 solenoid field is less effective to manipulate spin motion at high energies.

7314 For the LHeC physics program, the polarization of 60 GeV electron beam needs to be aligned longitu-  
7315 dinally at the collision point which is after the last arc and the acceleration. The most economical way to  
7316 control the spin direction at the collision point is to control the spin direction of the low energy electron  
7317 beam at the early stage of injector using a Wien Filter, a traditional low energy spin rotator. Since spin  
7318 vector rotates  $G\gamma\pi$  each time it passes through a 180° arc, the goal of the Wien Filter is to put the spin  
7319 vector in the horizontal plane with an angle to the direction of the particle's velocity to compensate the  
7320 amount of spin rotations before collision.

7321

For the layout of LHeC, i.e. two linear accelerators linked with two arcs, spin vector rotates

$$\phi_{arc} = G\pi[\gamma_i(2n - 1) + \Delta\gamma n(2n - 1)] \tag{8.23}$$

7322  
7323  
7324  
7325  
7326  
7327

after its  $n$ th path. Here,  $\gamma_i$  is the initial Lorentz factor of the beam and  $\Delta\gamma$  is the energy gain of each linear accelerator. In addition, LHeC also employs two horizontal bending dipoles on either side of the collision point to separate the electrons from the protons. Each of this bending dipole is 0.3 T and spans 9 m from the collision point. For 60 GeV electron beam, it rotates the spin vector by  $\phi_{IP} = 104.4^\circ$ . For initial energy of 10 GeV and each linear accelerator energy gain of 10 GeV, Table 8.18 lists the amount of spin rotation through the arcs and the amount of spin rotation through the final bending dipole at the collision point for 20 GeV, 40 GeV and 60 GeV beam, respectively. Here, the amount of spin rotation is the net

beam energy [GeV]	# of path n	$\phi_{arc}$ [degrees]	$\phi_{IP}$ [degrees]
20	1	8101.8	34.8
40	2	36457.9	69.6
60	3	81017.6	104.4

Table 8.18: total spin rotation from arcs and final bending dipole at collision point

7328  
7329  
7330  
7331  
7332  
7333  
7334  
7335

spin rotations in the range of  $2\pi$ . Since the spin rotation is proportional to beam energy, for a beam of particles with non-zero momentum spread, different amount of spin rotation then generates a spread of spin vector directions. This results in an effective polarization loss due to the spread of the spin vector. Fig. 8.44 shows the angle spread of the spin vector for an off-momentum particle at 20GeV, 40GeV and 60GeV. The calculation assumes the initial energy before the electron beam enters the arc is 10 GeV and energy gain of each linear accelerator is 10 GeV. It shows that for 60 GeV electron beam, a momentum spread of  $3 \times 10^{-4}$  can cause about 10% polarization loss effectively due to the spread of the spin vectors. This may not be able to satisfy the requirement on high polarization.

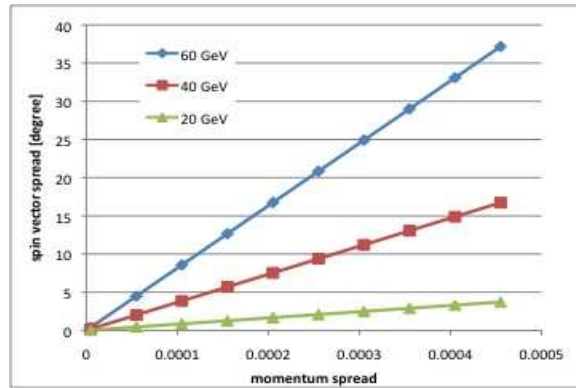


Figure 8.44: Calculated spin vector spread as function of momentum spread. The effective polarization loss is the cosine of spin vector spread angle, i.e. for an angle of 30 degrees, the effective polarization is 86% of initial beam polarization

7336  
7337  
7338  
7339  
7340  
7341

In order to provide the desirable polarization direction without sacrificing polarization, one can take the traditional approach of high energy polarized beams at HERA and RHIC, i.e. to rotate the spin vector to vertical direction before it gets accelerated to high energy. Since the spin vector aligns with the main bending magnetic fields' direction, this prevents the spread of the spin vector due to the momentum spread. After the last arc and acceleration, at 60 GeV beam energy, the spin vector must be rotated back so as

7342 to be longitudinally aligned at the collision point. To this end, for the current compact LHeC design, we  
 7343 propose to use a RHIC type spin rotator [681, 682] at the LHeC. Besides saving space of being compact,  
 7344 this approach also provides the advantage of independent control of the spin vector orientation, as well as  
 7345 nearly energy independent spin rotation for the same magnetic field. The four helical dipoles are arranged  
 7346 in a similar fashion as the RHIC spin rotator, i.e. with alternating helicity. Fig. 8.45 shows the schematic  
 7347 layout. Each helical dipole is 3.3 m long and the helicity alternates between right hand to left hand between  
 7348 each helical dipole. The two inner helical dipoles have the same magnetic field but opposite helicity. Same  
 applies to the two outer helical dipoles.

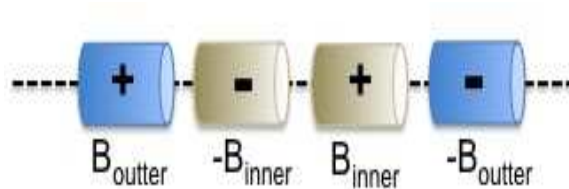


Figure 8.45: Schematic layout of LHeC spin rotator. A total of four helical dipoles with alternating helicity marked as + and -. The polarity of two outer helical dipole fields are also opposite. And so is the polarity of the two inner helical dipoles.

7349 For each helical dipole, the magnetic field is given by  
 7350

$$B_x = B \cos kz; B_y = B \sin kz; B_z = 0.0 \quad (8.24)$$

7351 where,  $B_{x,y,z}$  are the horizontal, vertical and longitudinal component of the magnetic field, respectively.  $Z$   
 7352 is the longitudinal distance along the helical dipole axis.  $|k| = \frac{2\pi}{\lambda}$  and  $\lambda$  are wave number and wave length  
 7353 of the helical field, respectively.

7354 For spin roator, all helical dipoles are chosen to be one period, i.e.  $\lambda = L$ , where  $L$  is the length of each  
 7355 helical dipole. Depending on the direction of the helicity,  $\frac{k}{|k|} = \pm 1$ . Fig. 8.46 shows the correlation of the  
 7356 magnetic field for the inner and outer helical magnets of a spin rotator which brings the spin vector from  
 7357 vertical direction to be in the horizontal plane. Fig. 8.47 shows the calculated angle of the spin vector for  
 7358 each outer helical magnet field. Both plots show that this design provides a flexible choice of the direction  
 7359 of spin vector by adjusting the outer and inner helical magnetic fields respectively.

7360 This rotator will be placed in the straight section of between LINAC and final focusing section (FFS).  
 7361 This is upstream of the final bending dipole at the collision point as well as three bends right upstream  
 7362 of the triplet. The 0.3 T final bending dipole rotates spin vector by 104.4 degrees for 60 GeV electron  
 7363 beam, while the other three bends rotates spin vector by -1.8 degrees. In order to bring the spin vector  
 7364 of polarized electron along longitudinal direction, it requires that spin rotator to put the spin vector from  
 7365 vertical direction to the horizontal plane with an angle of 102.6 degrees away from longitudinal direction.  
 7366 This requirement then yields the magnetic field of the inner pair and outer pair to be 1.92 T and 0.93 T,  
 7367 respectively. The maximum orbital excursion is 17 mm in horizontal and 8.5mm in vertical. The fine tuning  
 7368 of the direction of spin vector can be achieved by empirically adjusting the helical dipole magnetic field  
 7369 strength based on the measurements of the polarimeters before and after the collision point.

7370 Detailed calculations including helical dipole design, orbital and spin tracking of spin rotator are in  
 7371 working progress.

## 7372 8.7 Positron Options for the Linac-Ring LHeC

### 7373 8.7.1 Motivation

7374 It is known that the generation of an intense positron beam with a linac configuration is a particular  
 7375 challenge. This raises the question as to how crucial the availability of positron-proton scattering to the



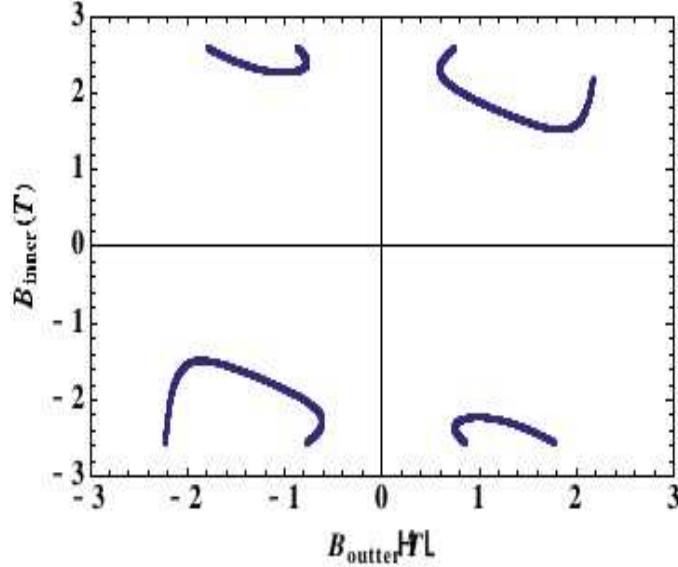


Figure 8.46: correlation of the outer and inner helical dipole magnetic field strength for a spin rotator which is designed to bring a vertically aligned spin vector to the horizontal plane.

LHeC is. Reasons for the importance of  $e^+p$  scattering are given in the physics chapters and have been summarized in an introduction to a topical meeting [683] in May 2011 at CERN, the technical results of which are summarized below. For the physics program, the following topics may serve as important example processes which require very high statistics positron (and electron) data:

- If there exist so far unknown resonant states of leptons and partons, quarks or/and gluons, the asymmetry between the  $e^+p$  and  $e^-p$  cross sections determines the fermion number of the produced leptoquark to be  $F = 2$ , as for an  $e_L u$  state of charge  $-1/3$ , or  $F = 0$  for an  $e_L \bar{u}$  state of charge  $-5/3$ .
- If there appears a new contact interaction, its nature may be disentangled by considering its charge dependence. If there was an excited electron observed, one surely would like to check whether the positron has the same structure.
- It has been a long standing question whether the strange quark and anti-quark distributions are different, for which neutrino-nucleon data provide certain hints. With electron and positron charged current data, this can be resolved and both  $s$  and  $\bar{s}$  can be measured. Similarly one will be able to measure single top and single anti-top quark distributions for the first time.
- Access to valence quarks at low  $x$  is possible with the precision measurement of the  $x F_3^{\gamma Z}$  structure function, which can be accessed only with high statistics NC cross section asymmetry data.
- High statistics beam charge asymmetry data are essential to access generalized parton distributions at low  $Q^2$

An example for the importance of  $e^+p$  scattering with high but perhaps not maximum luminosity is the precision measurement of the longitudinal structure function  $F_L$ , in which the charge symmetric background at low scattered electron energies has to be experimentally determined and subtracted in order to safely reach the region of highest sensitivity to  $F_L$ . One would finally like to note that if the positron-proton luminosity was significantly lower than the electron-proton luminosity, there would always be a tendency to preferentially run with electrons in order to collect a maximum integrated luminosity for those processes

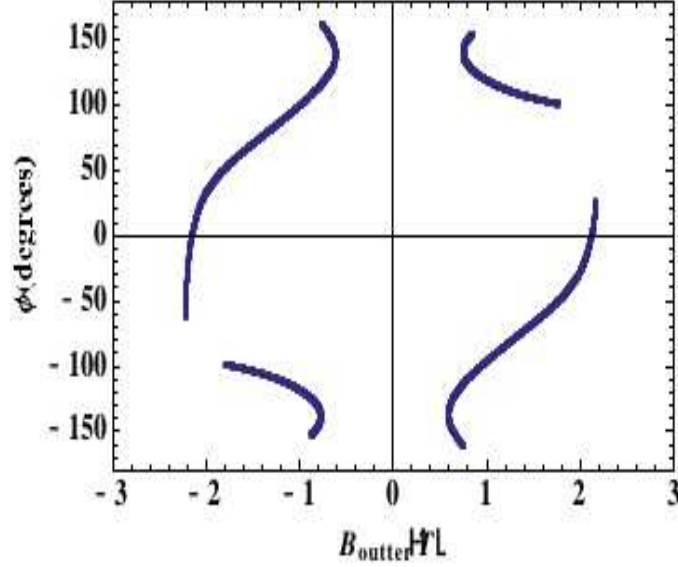


Figure 8.47: spin vector direction in the horizontal plane as function of outer helical magnet field strength

7400 and topics which are less or not dependent on the availability of both beam charge configurations. Examples  
 7401 here are the precision measurement in polarized  $e^-p$  scattering of the weak mixing angle, the physics at low  
 7402  $x$  or the precision measurement of  $\alpha_s$ . It is the physics beyond the standard model, and the searches for  
 7403 it, which has the highest demands on the  $e^+p$  luminosity. One concludes that the physics demands for the  
 7404 availability of intense  $e^+p$  scattering are very strong. A further aspect regards the importance of positron  
 7405 beam polarization which may deserve further consideration.

### 7406 8.7.2 LHeC Linac-Ring $e^+$ Requirements

7407 Table 8.19 compares the  $e^+$  beam flux foreseen for LHeC with those obtained at the SLC, and targeted for  
 7408 CLIC and the ILC.

	SLC	CLIC (3 TeV)	ILC (500 GeV)	LHeC (p= 140)	LHeC (ERL)
Energy (GeV)	1.19	2.86	4	140	60
$e^+$ /bunch at IP ( $\times 10^9$ )	40	3.72	20	1.6	2
Norm. emittance (mm.mrad)	30 (H) 2 (V)	0.66 (H) 0.02 (V)	10 (H) 0.04 (V)	100	50
Longit. rms emittance (eV-m)	7000	5000	60000	10000	5000
$e^+$ /bunch after capture ( $\times 10^9$ )	50	7.6	30	1.8	2.2
Bunches / macropulse	1	312	2625	$10^5$	NA
Macropulse repetition rate	120	50	5	10	CW
Bunches / second	120	15600	13125	$10^6$	$20 \times 10^6$
$e^+$ / second ( $\times 10^{14}$ )	0.06	1.1	3.9	18	440

Table 8.19: Comparison of the  $e^+$  flux.

7409 The SLC (Stanford Linear Collider) was the only linear-collider type machine which has produced  $e^+$  for  
7410 a high-energy particle physics experiment. The flux for the CLIC project (a factor 20 compared to SLC)  
7411 is already considered challenging and possible options with hybrid targets are under investigation on paper.  
7412 Even more positrons would be required for the ILC. The requested LHeC flux for pulsed operation at 140  
7413 GeV (a factor 300 compared to SLC) could be obtained, in a first approximation, with 10  $e^+$  target stations  
7414 working in parallel. Several more advanced solutions are proposed to meet the requested LHeC flux for the  
7415 CW option (a factor 7300 compared to SLC).

### 7416 8.7.3 Mitigation Schemes

7417 Two main approaches can be considered to reduce the rate of positrons that needs to be produced at the  
7418 source, namely

- 7419 • Recycling the positrons after the collision, with implied considerations on  $e^+$  emittance after collision,  
7420 emittance growth in the 60-GeV return arc due to synchrotron radiation, and the possible introduction  
7421 of a cooling scheme, e.g. laser cooling at lower beam energy, introducing a tri-ring recovery scheme  
7422 with fast laser cooling in central ring (see below), or using a large damping ring. If 90% of the positrons  
7423 are recycled the requirement for the source drops by an order of magnitude.
- 7424 • Repeated collisions on multiple turns, e.g. using a (pulsed) phase-shift chicane in order to recover 60  
7425 GeV when reaching the collision point again on the following turn.

### 7426 Reuse and Cooling of Positrons

7427 One of the most challenging problems associated with the continuous production of positrons is cooling  
7428 (damping) of the positron beam emerging from a source or recycled after the collision. The cooling process  
7429 in a storage ring requires many synchrotron and betatron oscillation periods as well as the emission of many  
7430 photons. The direct connection of the ERL's output and input aiming at a reuse of the positron beam does  
7431 not solve the problem of beam cooling, since the electron suffers from noticeable disruption.

7432 Beam cooling, that is at least an  $e$ -fold reduction of energy spread and transverse emittances, usually  
7433 requires at least thousand turns of beam in a damping ring. The employment of a novel idea of fast  
7434 cooling [684] may reduce this period, down to 200...500 turns. Even further reduction of the cooling period  
7435 might be attained by designing a damping ring with multiple,  $S$ , superperiods, each of which of the double  
7436 chicane scheme (to provide about  $S/2$  synchrotron oscillations per full turn). In this latter case, the number  
7437 of turns needed for cooling would be reduced by another factor of  $S$ .

7438 The next section presents considerations on the pushed performance of a conventional damping ring, and it  
7439 estimates the damping that could be obtained in a ring with the size of the SPS. An elegant complementary or  
7440 alternative solution to relax the damping requirements — the tri-ring scheme — is described in the following  
7441 section.

### 7442 Damping-Ring Considerations

7443 The main parameter driving the circumference choice of a positron damping ring for the LHeC complex is  
7444 the train length (for the pulsed option) and the structure. For  $10^5$  bunches with separation of 25 ns the  
7445 damping ring has to be unreasonably long (around 750 km). The bunch train has thus to be compressed  
7446 in the damping ring and uncompressed by extracting individual bunches every 25 ns using a fast extraction  
7447 kicker or RF deflector. The minimum bunch spacing in the ring is determined by the fastest achievable rise  
7448 time of the extraction systems. A fast kicker can probably pulse with rise/fall times of around 2.5 ns and an  
7449 RF deflector may be reduced even further (0.5 ns). Both systems have to present a stability of the order of  
7450 a few  $10^{-4}$ . Given the larger emittance the kicker stability requirement may be relaxed compared with the  
7451 damping rings of CLIC and ILC. Considering a 2.5-ns bunch spacing, the ring circumference can be reduced  
7452 by a factor of 10 but remains still very large. A further order-of-magnitude reduction can be obtained by  
7453 considering either ten times less bunches (with correspondingly higher charge) or an order of magnitude

increase of the repetition rate, i.e. 100 Hz instead of 10 Hz. Indeed, with a 100-Hz repetition rate, the ring becomes 7.5 km, which is very close to the circumference of the SPS of  $C = 2200\pi = 6911.5$  m.

In this respect, a parameter set can be deduced by taking as base a damping ring in the SPS tunnel<sup>5</sup>, where a train of 9221 bunches with 2.5 ns can fit. The high repetition rate option demands that the bunches are damped and then extracted within 10 ms. Considering that at least 5 damping times are needed to reach equilibrium, the transverse damping time should be less than 2 ms. This number is assumed in the following. We note, however, that a damping time of 10 or 20 ms, with much relaxed constraints on the ring, may already be sufficient for recycling spent positrons and recovering their original emittance.

The transverse damping time is given by

$$\tau_{x,y} = \frac{2EC}{cJ_{x,y}U} , \quad (8.25)$$

with  $E$  the energy,  $J_{x,y} \approx 1$  the damping partition numbers,  $c$  the speed of light and  $U$  the energy loss per turn:

$$U = \frac{C\gamma E^4}{\rho}(1 + F_w) , \quad (8.26)$$

with  $\rho = E/(eB)$  the bending radius and  $F_w$  the wiggler damping factor:

$$F_w = \frac{L_w B_w^2}{4\pi B^2 \rho} , \quad (8.27)$$

with  $L_w$  and  $B_w$  the wiggler length and field respectively. The transverse damping time can be rewritten as

$$\tau = \frac{8\pi C}{ceC_\gamma E(eB_w^2 L_w + 4\pi B E)} , \quad (8.28)$$

connecting it directly with the ring energy and radiating magnet characteristics. Considering a maximum bending field of 1.8 T and wiggler field of 1.9 T, there is a parametric interdependence between beam energy, the total wiggler length and the damping time. Figure 8.48 shows the dependence of the damping ring energy on the total wiggler length for a damping time of 2 ms (red curve). Without wigglers, the ring has to run at 22 GeV, whereas for around 10 GeV, wigglers with a total length of 800 m are needed. The blue curve represents the same dependence when the low repetition rate is considered which indeed increases the damping time by an order of magnitude. In that case, the ring energy without any wigglers can be reduced to 7 GeV and it can be dropped to less than 4 GeV for a total wiggler length of 200 m.

A tentative parameter list for the low and high repetition rate option can be found in table 8.20. This example considers for both cases, 234 bending magnets of 0.5m-long dipoles with 1.8T bending field. The wiggler field of 1.9 T and a period of 5 cm is within the reach of modern hybrid wiggler technology. A big challenge is the longitudinal parameters driven from the high energy loss per-turn, especially in the high repetition rate case, where around 300 MV of total RF voltage is needed to restore the high-energy loss/turn. In addition, the bunch has to be kept short (around 5 mm) in order to achieve the longitudinal emittance target of 10 keV-m, which necessitates a quasi-isochronous ring, with momentum compaction factor, close to  $10^{-6}$ . This may be a challenge for lattice design as low momentum compaction factors are achieved for strong focusing conditions, which increase chromaticity, and necessitate strong sextupoles with detrimental effects for the dynamic aperture of the ring. The average beam power of 25 MW indicates that the wall-plug power would be quite high and may necessitate the use of super-conducting RF system to increase efficiency. In the low repetition case, the RF voltage and power are an order of magnitude more relaxed.

### Tri-Ring Scheme

A possible solution to cool down a continuous positron beam, both the recycled beam and/or a new beam from a source, is the tri-ring scheme illustrated in Fig. 8.49.

The operation cycle of the system is as follows:

<sup>5</sup>A damping ring in the SPS tunnel has already been considered as early as 1988 by L. Evans and R. Schmidt, in CLIC Note 58, although their parameter set has been far away from present LHeC and CLIC requirements.

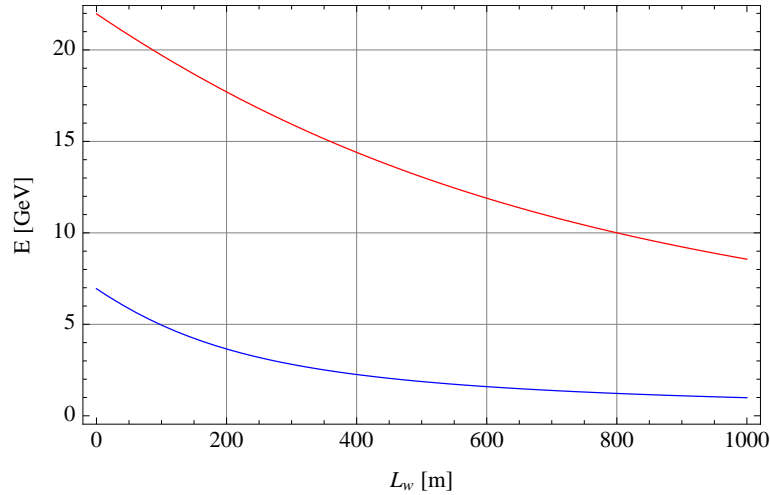


Figure 8.48: Dependence of the damping ring energy on the total wiggler length for a transverse damping time of 2 ms (red curve) and 20 ms (blue curve).

- 7491 • The basic cycle lasts  $N$  turns
- 7492 –  $N$ -turn injection from ERL into the accumulating ring (bottom)

Parameter [unit]	High Rep-rate	Low Rep-rate
Energy [GeV]	10	7
Bunch population [ $10^9$ ]	1.6	1.6
Bunch spacing [ns]	2.5	2.5
Number of bunches/train	9221	9221
Repetition rate [Hz]	100	10
Damping times trans./long. [ms]	2/1	20/10
Energy loss/turn [MeV]	230	16
Horizontal norm. emittance [ $\mu\text{m}$ ]	20	100
Optics detuning factor	80	80
Dipole field [T]	1.8	1.8
Dipole length [m]	0.5	0.5
Wiggler field [T]	1.9	-
Wiggler period [cm]	5	-
Total wiggler length [m]	800	-
Dipole length [m]	0.5	0.5
Longitudinal norm. emittances [keV.m]	10	10
Momentum compaction factor	$10^{-6}$	$10^{-6}$
RF voltage [MV]	300	35
rms energy spread [%]	0.20	0.17
rms bunch length [mm]	5.2	8.8
average power [MW]	23.6	3.6

Table 8.20: Tentative parameter list for a damping ring in the SPS tunnel considering high and low repetition-rate options.

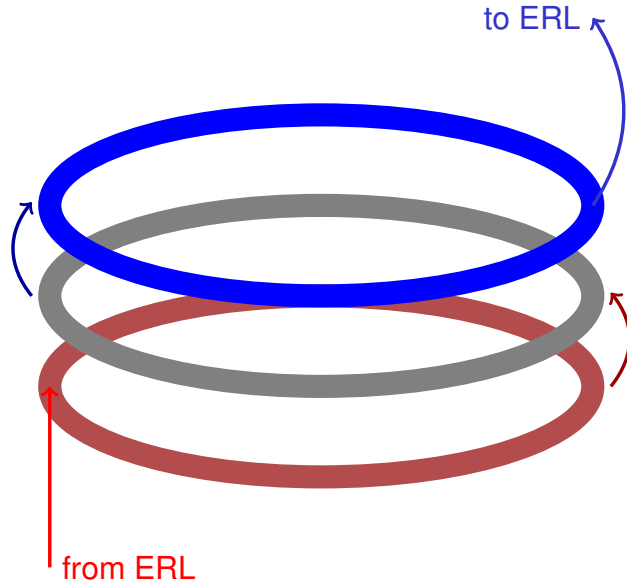


Figure 8.49: Tri-ring scheme

- 7493           –  $N$ -turn cooling in the cooling ring (middle); fast laser cooling may be employed here
- 7494           –  $N$ -turn slow extraction from the extracting ring (top) into the ERL
- 7495           • One-turn transfer from the cooling ring into the extracting ring
- 7496           • One-turn transfer from the accumulating ring into the cooling ring

7497 The average current in the cooling ring is  $N \times$  average ERL current. The number of turns of the main cycle  
 7498 is limited by the efficiency of multi-turn injection and the maximum current which can be stored (and cooled)  
 7499 in the cooling ring.

7500 Laser cooling may generate a new low-emittance positron beam to compensate for losses and emittance  
 7501 growth of the recycled beam.

7502 Reusing and/or cooling of positrons relaxes the requirements for all types of positron sources discussed in  
 7503 the following. The cooling period is limited by the maximal stored current in the ring and by the multi-turn  
 7504 injection. Fast laser cooling may be employed for compensating positron emittance growth when reusing  
 7505 positrons or to compensate losses (without a dedicated high-current positron source). A slow extraction  
 7506 process would be capable of further reducing the energy spread (chromatic extraction) or, alternatively, the  
 7507 transverse emittance (using resonant extraction).

#### 7508 8.7.4 Positron Production Schemes

7509 Positrons can be produced by pair creation when high-energy electrons or photons hit a target. Conventional  
 7510 sources, as used at the SLC, send a high-energy electron beam on a conversion target. Alternatively, a high-  
 7511 energy electron beam can first be used to create high-energy photons, which are then sent onto a target.  
 7512 The prior conversion into photons reduces the heat load of the target for a given output intensity and it may  
 7513 also improve the emittance of the generated positrons.

7514 There exist a number of schemes that can accomplish the conversion of electrons into photons. Several  
 7515 of them employ Compton scattering off a high-power laser pulse stacked in an optical cavity. According to  
 7516 the electron-beam accelerator employed, one distinguishes Compton rings, Compton linacs, and Compton

ERLs. An alternative scheme uses the photons emitted by an electron beam of very high energy (of order 100 GeV) when passing through a short-period undulator.

Finally, there even exists a simpler scheme where a high-power laser pulse itself serves as the target for (coherent) pair creation.

Applications of the various possible schemes to the LHeC are discussed in the following sections.

### 8.7.5 Targets

For the positron flux considered for the LHeC the heating and possible destruction of the target are important concerns. Different target schemes and types can address these challenges:

- Multiple targets operating in parallel (Section 8.7.6).
- He-cooled granular W-sphere targets (Section 8.7.6).
- Rotating-wheel targets (Section 8.7.6).
- Sliced-rod W tungsten conversion targets (Section 8.7.7);
- Liquid mercury targets (Section 8.7.7).
- Running tape with annealing process (Section 8.7.7).

### 8.7.6 Conventional Scheme based on $e^-$ Beam Hitting Target

The LHeC ERL option requires a positron current of 6 mA or  $4 \times 10^{16} e^+/s$ , with normalized emittance of  $\leq 50 \mu\text{m}$  and longitudinal emittance  $\leq 5 \text{ MeV}\cdot\text{mm}$ .

For a conversion target with optimized length the power of the primary beam is converted as follows  $P_{\text{primary}}(100\%) = P_{\text{thermal}}(30\%) + P_{\gamma}(50\%) + P_{e^-}(12\%) + P_{e^+}(8\%)$ . The average kinetic energy of the newly generated positrons is  $\langle T_{e^+} \rangle \approx 5 \text{ MeV}$ , which allows estimating the total power incident on the target as  $P_{\text{target}} = 5 \text{ MV} \times 6 \text{ mA} / 0.08 = 375 \text{ kW}$ . Assuming an electron linac efficiency of  $\eta_{\text{acc}} \approx 20\%$  we find  $P_{\text{wall}} = P_{\text{target}}/0.2 = 1.9 \text{ MW}$ . This wall-plug power level looks feasible and affordable.

Figure 8.50 illustrates a possible option, which alone would already meet the requirements for the 140-GeV single-linac case, where the repetition rate is 10 Hz. The idea is to use 10  $e^+$  target stations in parallel. This implies installing 2 RF deflectors upstream and the same downstream. Experience exists for RF deflectors at 3 GHz and with operating 2 lines in parallel. Assuming that this configuration is acceptable from the beam-optics point-of-view, it would be necessary to implement a fast damping scheme because the bare emittances from the target will be too high for the injection into the ERL.

Table 8.21 shows the beam characteristics at the end of the 10 GeV Primary beam Linac for electrons, before splitting the beam.

Primary beam energy ( $e^-$ )	10 GeV
Number $e^-$ / bunch	$1.2 \times 10^9$
Number of bunches / pulse	100000
Number $e^-$ / pulse	$1.2 \times 10^{14}$
Pulse length	5 ms
Beam power	1900 kW
Bunch length	1 ps

Table 8.21: Electron beam parameters before splitting.

Table 8.22 shows the beam parameters at each  $e^+$  target. Energy of 5.6 kW is deposited in each target and the Peak Energy Deposition Density (PEDD) is around 30 J/g. This value has been chosen, in order

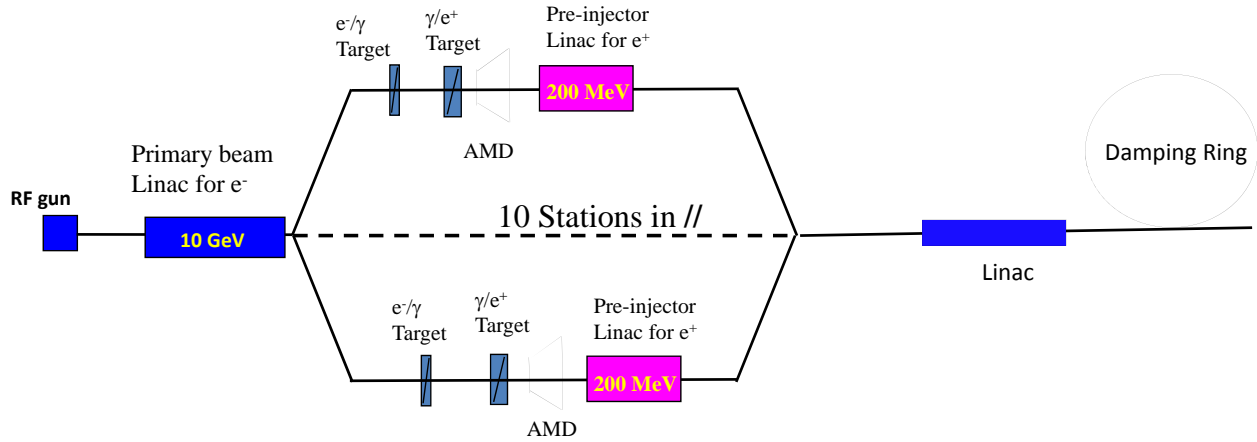


Figure 8.50: Possible layout with unpolarised  $e^+$  for the LHeC injector (p-140 GeV).

7549 to be below the breakdown limit for tungsten (W) target. It is based on recent simulations [685] with  
 7550 conventional W targets. A new study has been done [686], assuming a target made out of an assembly of  
 7551 densely packed W spheres (density about 75% of solid tungsten) with diameters of 1–2 mm. The cooling is  
 7552 provided by blowing He-gas through the voids between the spheres. Such He-cooled granular targets have  
 7553 been considered for neutrino factories and recently for the European Spallation Source ESSS.

Yield ( $e^+/e^-$ )	1.5
Beam power (for $e^-$ )	190 kW
Deposited power / target	5.6 kW
PEDD	30 J/g
Number $e^+$ / bunch	$1.8 \times 10^9$
Number bunches / pulse	10,000
Number $e^+$ / pulse	$1.8 \times 10^{13}$

Table 8.22: Beam parameters at each  $e^+$  target.

7554 To achieve the required cooling and the corresponding mass flow of the cooling fluid, we consider pres-  
 7555 surized He at 10 bar entering the target volume at a velocity of 10 m/s, i.e. a mass flow 1.8 g/s is required  
 7556 for each target. From this a convection coefficient of about  $\alpha = 1 \text{ W/cm}^2/\text{K}$  can be expected and a cooling  
 7557 time constant  $\tau$  (exponential decay time after an adiabatic temperature rise of a sphere) of 185 ms will  
 7558 result. Clearly, not much cooling during a pulse of 5 ms duration will occur, but cooling will set in during  
 7559 the off-beam time of 95 ms between the pulses. The peak temperature after each pulse will stabilize at about  
 7560 500 K above that of the cooling fluid. An average exit temperature of the He-gas of about 600 °C will have  
 7561 still to be added, which drives the maximum temperature of the spheres up to about 1100 °C. Although  
 7562 compatible with W in an inert atmosphere, it should be attempted to reach lower temperatures. This could  
 7563 be achieved by increasing the He-pressure to 20 bar and the velocity of He to 20 m/s which might reduce  
 7564 the maximum temperature in a sphere to 500 °C. Thus, a He-cooled granular 10-W-target system could be  
 7565 a viable solution.

7566 Another approach has been considered. To achieve, as in the previous case, a reduction of the energy  
 7567 deposition density by a factor of 10, a fast rotating wheel could be designed. The beam pulse of 5 ms duration  
 7568 is spread over the rim of the rotating wheel and a linear velocity of the rotating rim of 20 m/s would be  
 7569 required. This would lead to a repetition rate of about 1000 rpm, assuming a wheel diameter of 0.4 m. Such



7570 a solution is actually under investigation for the ILC with a rotation speed of 1800 rpm.

7571 Here tungsten spheres, again, are contained in a structure, similar to a care tyre, as is illustrated in  
7572 Fig. 8.51. The container is possibly made of light Ti-alloy where the sides, facing the beam entrance and  
7573 exit should be made of Beryllium, compatible with the beam heating. The helium for the cooling is injected  
7574 from the rotating axle through spokes into the actual target ring and is recuperated in the same way.

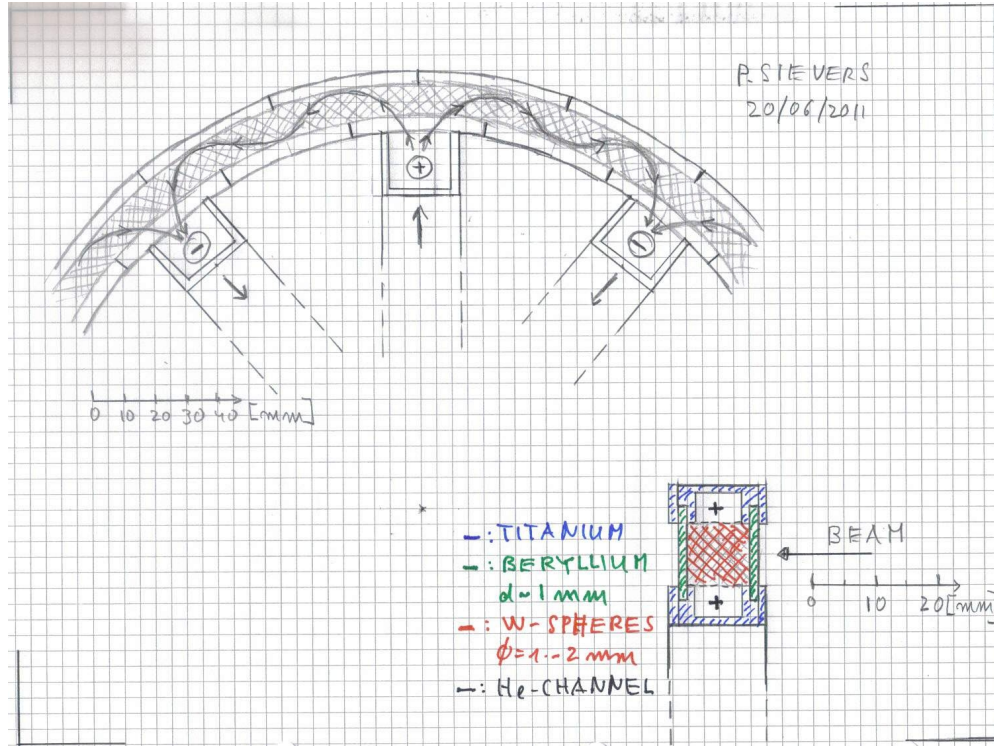


Figure 8.51: Sketch of rotating wheel containing W spheres with He cooling.

7575 If the beam pulse duration is extended by a factor 10, i.e. 50 ms duration, maintaining of course the  
7576 same average power, then the rotation time could be reduced. The velocity of the wheel is such that over  
7577 the duration of 5 ms the rim is displaced by one beam width, i.e. 1 cm. This leads to much reduced rotation  
7578 speeds of 2 m/s, which can readily be achieved in a wheel with a diameter of 16 cm, rotating at 240 rpm.

7579 By choosing appropriately the rotation velocity, the average time between two hits of the same spot on  
7580 the rim of the wheel, is about 0.5 s. With the aforementioned cooling time constant for the He-circuit of  
7581 185 ms, the adiabatic temperature rise during one hit over 5 ms of 211 K will have dropped close to zero  
7582 before the next hit. Since we assume to simultaneously cool the whole rim of the wheel, a He-flow of 90 g/s  
7583 must be provided. Taking into account the temperature increase in the cooling fluid, a maximum tungsten  
7584 temperature in the W-spheres of about 350°C can be expected, which is rather comfortable.

7585 Using a continuous D.C.-beam with no gaps will further alleviate the structure and performance of the  
7586 target wheel.

7587 The interference of the rotating wheel with the downstream flux concentrator will have to be assessed. One  
7588 may, however, expect considerably less forces than presently considered for the ILC, due to the much lower  
7589 velocity of the wheel. Moreover, proper choice of materials with high electrical resistivity and laminating  
7590 the structure may be considered.

7591 Clearly, the W-granules must be contained inside the beam vacuum within a structure which is He-leak  
7592 tight at the selected He-pressure. As material for the upstream and downstream beam windows, Beryllium  
7593 must be considered which, due to its large radiation length (34 cm as compared to W with 0.34 cm), should

7594 resist to the thermal loads. This, however, has to be verified.

7595 Also, radiation damage and life time issues will still have to be assessed.

7596 It is believed that rotating “Air to Vacuum” seals at 240 rpm are commercially available or can be  
7597 adapted to the radiation environment. Rotating “High Pressure He to Air” seals may have to be developed,  
7598 where small He-leaks can be tolerated.

7599 This last approach is focused on  $e^+$  targets. Presently with conventional targets, the transverse normal-  
7600 ized rms beam emittances, in both planes, are in the range of 6000 to 10 000 mm.mrad. With the new type  
7601 of target, we do not know yet by how much the transverse emittances will be changed. In any case, a strong  
7602 reduction of emittances is mandatory for the requested LHeC performance.

7603 Assuming that large or small emittances could be recombined, Table 8.23 shows a possible  $e^+$  flux after  
7604 recombination.

7605 Finally, if a solution is found for the emittances, it will be necessary to design and implement a linac  
7606 accelerating the positron beam up to 500 MeV, the energy for the ERL injection.

Secondary beam energy ( $e^+$ )	200 MeV
Number $e^+$ bunch	$1.8 \times 10^9$
Number of bunches / pulse	100000
Number of $e^+$ / pulse	$1.8 \times 10^{14}$
Bunch spacing	50 ns
Repetition rate	10 Hz

Table 8.23: Positron beam parameters after recombination.

### 7607 8.7.7 Compton Sources

7608 In Compton sources, (polarized) positrons are produced as a result of the following processes:

- 7609 1. Electron beam (current  $I_{e^-}$ ) scatters off polarized laser photons (energy in pulse  $W$ ).
- 7610 2. Gamma flux,  $\sim I_{e^-} \times W$ , is first collimated and then impinging on a conversion target.
- 7611 3. Produced positrons lose a fraction of energy while traversing the target.
- 7612 4. Postselection: low-energy positrons are discarded to attain the required polarization.

7613 Three principal factors limit the performance of polarized positron sources based on Compton scattering.  
7614 They are:

- 7615 1. Limited average current of electrons scattering off laser photons (world record  $I_{e^-} = 5$  A – PEP ring).
- 7616 2. Limited energy of pulses stored in optical resonators (fast progress, an array of resonators may be  
7617 employed, 1...5 J assumed maximal accepted: higher energy of pulses violates electron dynamics).
- 7618 3. Limited power density of gammas, to which the conversion target is tolerable (sliced-rod convertor  
7619 reduces positron losses and increases the current).

7620 The polarization degree of positrons is determined by the cut-off energy of positrons exiting from the target:  
7621 the higher the polarization required the higher the energy threshold for discarding low-energy positrons (and  
7622 the lower the yield). The optimal target thickness that maximizes the yield also decreases with the increase  
7623 of the polarization requested, along with a decrease in the yield of positrons (but with an improved quality  
7624 of the positron beam: a smaller energy spread, and a smaller transverse emittance).

7625 For a CLIC source of polarized positrons [687] (1 GeV electron energy, 1  $\mu$ m YAG laser system, and,  
7626 correspondingly, 20 MeV maximal energy of the Compton spectrum) “envelopes” describing the limiting  
7627 number of positrons from the conversion target per scattered gamma and the associated polarization are  
7628 presented in Fig. 8.52.

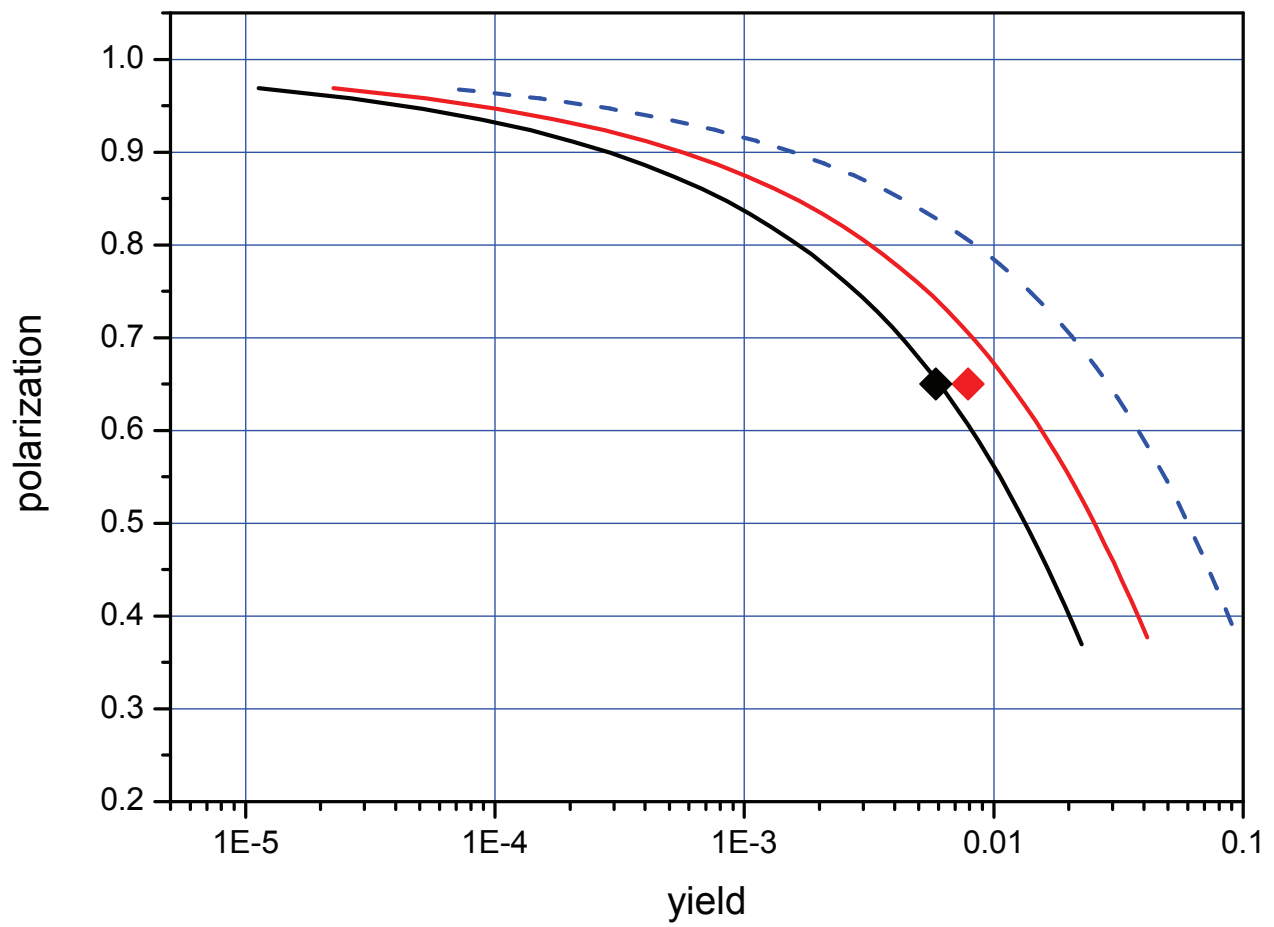


Figure 8.52: Limits for Ti (black) and W (red) conversion targets. Diamonds: simulations (A.Schalicke, S.Riemann). Blue Dashed curve: a sliced-rod conversion target.

	unit	SLC	CLIC (3TeV)	LHeC p-140	LHeC ERL
$I_{e^+}$ at IP	$\mu\text{A}$	0.96	18	290	7050
typical $I_{e^-}$	A	1.4E-2	0.26	4.3	105.7
$I_{e^-}$ with 5 J	A	1.5E-3	2.8E-2	0.46	11.2
$I_{e^-}$ with 5 J+1 m rod	A	2.2E-4	4.0E-3	6.5E-2	1.6

Table 8.24: IP positron current and the implied minimum electron beam current in a Compton Ring

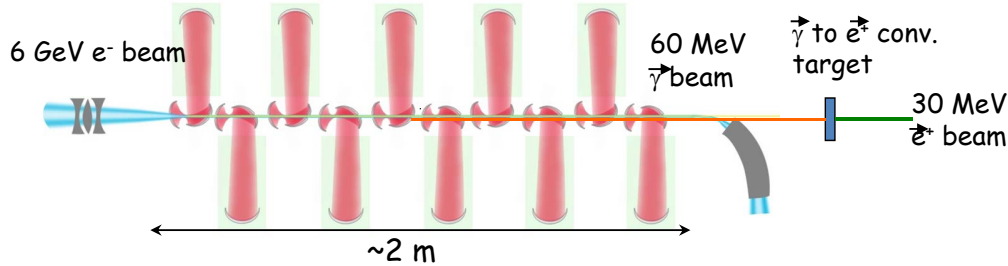


Figure 8.53: Layout based on Compton Linac.

## 7629 Compton Ring

7630 A typical Compton-ring gamma source (the CLIC ring) with the parameters listed in [687], and modified  
 7631 to accommodate an entire array of optical resonators, namely 10 units with 50 mJ of laser energy stored in  
 7632 each, installed in the dispersive section, is capable of producing 0.01 gammas per electron-turn. This scheme  
 7633 can be enhanced by increasing the laser energy by a factor of 10, up to 5 J, and by halving the collision  
 7634 angle, to 4 degrees, which increases the yield by an order of magnitude, up to 0.1 gammas per electron-turn.

7635 A typical tungsten converter optimized for Compton gammas with a maximal energy of 20 MeV can  
 7636 deliver 0.01 positrons with 60% polarization per incident scattered gamma. The converter can be enhanced  
 7637 as well: a sliced-rod converter target produces 0.07/0.13 positrons per gamma for a 1 m or 3 m long rod,  
 7638 respectively [688].

7639 Including a 50% overhead, for either the standard scheme and with the two types of enhancements,  
 7640 various projects require the minimal circulating currents in Compton rings listed in Table 8.24.

7641 Table 8.24 illustrates that a Compton-ring source equipped with an array of optical resonators yielding  
 7642 a total laser-pulse energy of 5 Joule, together with a sliced-rod conversion target, will produce the desired  
 7643 flux of polarized positrons even for the LHeC ERL option.

7644 In conclusion, according to the present understanding and simulations, a Compton positron source may  
 7645 produce sufficient average positron beam current for all LHeC options. The conversion of gammas to positrons  
 7646 is a bottleneck, which requires a study and optimization of effective converter targets such as the sliced-rod  
 7647 converter.

## 7648 Compton Linac

7649 Positrons, even polarized, can be generated by the Compton scattering process of high-power laser pulses  
 7650 stacked in optical cavities with a high-energy electron beam from a linac. Figure 8.53 presents a possible  
 7651 layout for such configuration.

7652 At BNL, a ratio photon/electron close to 1 has been demonstrated. Assuming that a ratio positron/photon  
 7653 close to 2% is achievable, then 50 photons are required to produce 1  $e^+$ . For LHeC, one needs 0.35 nC/bunch  
 7654 (for the  $e^+$  to be produced). Based on above estimations, it implies  $\sim 18$  nC/bunch (for the  $e^-$  beam). Then  
 7655 with 10 optical cavities, the requested  $e^-$  charge is about 1.8 nC / bunch which is a reasonable value.

## Power Analysis for Compton Schemes and Compton ERL

A number of pertinent technologies have been investigated, but are not yet established:

1. 1.3 Ampere ERL (R&D at BNL)
2. Mercury target or annealing target (Muon collider collaboration)
3. High finesse optical stacking cavities with factor 1000 enhancement, 1 kW pump (France, KEK, ...)

This section considers different Compton-based options for an LHeC positron source including power considerations. The following source requirements were taken into account:

- 6mA average current or  $4 \times 10^{16}$  e<sup>+</sup>/sec.
- $2 \times 10^7$  bunches with  $2 \times 10^9$  e<sup>+</sup>/bunch.
- Normalized rms emittance of 50 microns.
- Longitudinal emittance 5 MeV-mm or 10 mm normalized.

The **power analysis** for the different schemes can be done backwards:

1. Power of the captured positron beam.
2. → Power of the gamma beam entering the conversion target and generating electron positron pairs.
3. → Electron drive beam generating the gamma beam.
4. → Klystron accelerating the electron drive beam.
5. → Wall plug power.

Scattering of the multi MeV gammas on the target produces the electrons and positrons. The optimal gamma beam energy range of 30-60 MeV is selected as a compromise between conversion efficiency and capture efficiency as well as longitudinal emittance. Beam power of the captured positron beam is estimated at 6 mA × 30 MeV or 180 kW.

The conversion efficiency of gamma beam into captured positrons ranges from 0.3 to 2% for different schemes of the ILC positron source. This (optimistically) sets a requirement for the gamma beam entering the target at 9 MW. A 2–6 GeV electron beam is used in different schemes to generate a gamma beam by Compton scattering of the powerful laser beam. The efficiency of electron beam power conversion is at most 10%, for the scheme with a CO<sub>2</sub> laser. This puts a lower limit on the drive beam power at 90 MW. A CLIC type driver can optimistically generate the drive beam at approximately 50 percent efficiency and, therefore, an overall power requirement to generate a 6 mA positron beam with pulsed linac (CLIC type) and the CO<sub>2</sub> laser can be estimated at 180 MW.

To summarize:

- 6 mA × 30 MeV → 180 kW e<sup>+</sup> beam (Output of conversion target).
- $\gamma \rightarrow e^+$  efficiency about 2% → 9 MW  $\gamma$  beam (conversion efficiency).
- $e^- \rightarrow \gamma$  about 10%, 90 MW e<sup>-</sup> beam
- Wall → e<sup>-</sup> about 50% or 180 MW wall power.

The wall plug power for the electron beam alone exceeds the limit of 100 MW set for the entire project. On the other hand, the energy spread of the circulating beam would be prohibitive in a Compton ring scheme subjected to the requirement to generate 9 MW from a 30-MeV gamma beam. Both issues can be handled by exploring the energy recovery linac option. A 3-GeV 1.3-Ampere ERL with 2 micron laser enhancement cavities has the potential of generating the required positron beam with only 50 MW of wall plug power, as follows:

- 7696 • 6 mA x 30MeV → 180kW e+ beam (Output of conversion target).
- 7697 •  $\gamma \rightarrow e^+$  about 1% → 18 MW  $\gamma$  beam (Conversion efficiency).
- 7698 •  $e^- \rightarrow \gamma$  about 0.5% 4 GW  $e^-$  beam (99.9% efficient ERL).
- 7699 • Wall →  $e^-$  about 50% of  $0.001 \times 4$  GW + 18 MW.
- 7700 • Total  $\approx 50$  MW wall power.

7701 The major challenge of a pulsed linac scheme is in the cost of driving the linac. A high wall power require-  
 7702 ment combined with long pulse format make the CO2 laser/pulse linac combination an unlikely solution.  
 7703 The challenge of the ERL scheme lies in the development of the recirculating cavities and target/capture  
 7704 system that would be able to perform the CW mode of operation.

7705 **Emittances:** The upper estimate on the transverse and longitudinal emittances in the case of the 3 GeV  
 7706 ERL for the captured positron beams can be estimated as follows:

- 7707 • Normalized positron beam emittance, expressed through its energy, RMS beam size and angular di-  
 7708 vergence at the target exit:  $\epsilon_N \approx \gamma_{e^+} \sigma \sigma'$ .
- Acquired angular spread in the length target (typically selected at 0.4 radiation length) can be estimated  
 as

$$\sigma_{e^+} \approx \frac{1}{\sqrt{2}} \frac{14\text{MeV}}{E_{e^+}} \sqrt{\frac{L_{\text{target}}}{X_0}} \approx \frac{10}{\gamma_{e^+}} .$$

- 7709 • Three components contribute to the beam size:

1. Scattering in the target:

$$\sigma_{e^+,sc} \approx \frac{\sqrt{2}}{3} \sigma'_{e^+} L_{\text{target}} \approx \frac{\sqrt{2}}{3} 0.3 \cdot 1.2 \text{ mm} \approx 150 \mu\text{m} .$$

2. Beam size due to gamma beam divergence:

$$\sigma_{\gamma,div} \approx \frac{1}{2\gamma_{e^-}} \frac{L_{IR}}{\sqrt{2}} \approx \frac{1}{2 \times 4000} \frac{0.1 \text{ m}}{\sqrt{2}} \approx 15 \mu\text{m} .$$

3. and e- beam size on target:

$$\sigma_{\gamma e^-} \approx \sqrt{\frac{\epsilon_{Ne^-}}{\gamma_{e^-}} \beta_{e^-}} \approx \sqrt{\frac{10 \mu\text{m}}{4000}} 1 \text{ m} \approx 50 \mu\text{m} .$$

This results in the normalized transverse emittance of 1.5 mm. The strong magnetic field in which the target would likely be immersed will lower this estimate. The estimate for the longitudinal emittance is:

$$\epsilon_{||,N} \approx \Delta \gamma_{e^+} \sigma_{\tau e^-} \approx \frac{60 - 30}{4} 60 \mu\text{m} \approx 450 \mu\text{m} .$$

7710 **Compton-ERL Target:** Charged particle beams exiting the conversion target generate most of the  
 7711 heat. The deposited power can be estimated (roughly) as 6 mA × 5 MeV × 2 × 2, or 120 kW. 5 MeV is  
 7712 estimated for the energy loss and factors of 2 are attributed to equal parts of captured and non-captured low  
 7713 energy positrons, and to the equal number of electrons and positrons. This suggests that a liquid mercury  
 7714 target may be an important candidate.

7715 **Compton ERL Summary:** High current ERL seems the most promising approach, e.g. a 3-GeV 1.3-A  
 7716 ERL with 2-micron wavelength optical enhancement cavities.

7717 Target is going to be a very difficult consideration (candidates would be a liquid mercury target or running  
 7718 tape with annealing process). The desired emittances are not reached from any Compton scheme source,  
 7719 even if the target is immersed in a strong magnetic field. Therefore, cooling or scraping would be required.

## 7720 Laser Pulses and Optical Cavities

7721 Different experimental programs presently underway aim at achieving a very important photon pulse intensity  
7722 by direct production in a laser system and stacking in a passive optical resonator. This laser-stacking scheme  
7723 allows increasing the available average power in the optical cavity without requiring impossible performances  
7724 to the drive laser system. As far as Compton-source developments are concerned, depending on the purpose  
7725 of the application, the stored pulse length ranges from a few hundreds of femtoseconds to a few picoseconds,  
7726 the repetition frequency (which determines the cavity length) from 20 to 200 MHz, and the wavelength from  
7727 0.5 to 1.1  $\mu\text{m}$ .

7728 When trying to achieve storing a very high power in a Fabry-Perot optical resonator the state of the  
7729 art of the present technology has to be taken into account. As far as the laser is concerned, in the last  
7730 years an impressive increase in the available average power has been provided by the development of the  
7731 fiber amplifiers. The best performances have been obtained by combining the development of large core  
7732 single mode photonic crystal fibers with the chirped-pulse amplification (CPA) technique. For example, a  
7733 200-fs, 1048-nm wavelength, 78-MHz oscillator pulse after a first stretching to 800 ps, has been amplified  
7734 in a system composed of a two-stage double-clad photonic crystal fiber preamplifier (30  $\mu\text{m}$  mode field and  
7735 170  $\mu\text{m}$  pump cladding diameter) pumped at 976-nm wavelength, and a main-amplifier double-clad water  
7736 cooled fibre (27- $\mu\text{m}$  mode field and 500  $\mu\text{m}$  air clad). After this phase a recompression of the pulse to 640  
7737 fs has yielded an “incredible” average power of 830 W and about 10  $\mu\text{J}$  per puls [689].

7738 To stack many short laser pulses in a Fabry Perot resonator, and obtain an important pulse enhancement,  
7739 it is necessary to lock the cavity characteristic comb with the laser one. This implies to act on two degrees  
7740 of freedom given by the repetition frequency and by the carrier to phase envelope ( $\Phi_{ce}$ ). In this context the  
7741 Pound Driver Hall locking techniques is employed in the LAL cavity [690]. This technique has attained the  
7742 best performances in gain, as far as pulses of few ps are concerned. A gain of about 10000 was achieved,  
7743 storing a laser pulse of close to 20 kW in a confocal two mirror cavity. However, the best result, as far as the  
7744 stored power is concerned, has been achieved by the MPQ laboratory using the Hansch-Couillaud locking  
7745 technique [691]. With a pulse length of 200 fs an average power of 18 kW was obtained in a 78-MHz tie bow  
7746 cavity with an enhancement factor of 1800. After this achievement, thermal problems were noticed due to  
7747 the very high-power density of the pulse. Stretching the pulse to 2 ps the stacking process was efficient up  
7748 to 72 kW with an estimated gain of 1400. In the cavity waist this corresponded to a  $10^{14}$  W/cm<sup>2</sup> power  
7749 density. At this power level the coupling between the laser power and the cavity was near 50%.

7750 In the framework of the Compton facilities another important experimental effort is carried out jointly  
7751 by LAL Orsay (France) and KEK Tsukuba (Japan) [692]. In fact, to validate the use of optical passive  
7752 cavities, different tests have to be performed also taking into account the reliability and the compatibility  
7753 of a given optical cavity with the accelerator environment. A 176 MHz, a four-mirror vacuum-compatible  
7754 optical cavity has been designed, realized and installed in the KEK-ATF ring. A four-mirror configuration  
7755 was chosen instead of a two-mirror one, because with the former it is possible to achieve very small laser-  
7756 waists without losing in mechanical stability. An estimated stored power of 2 kW has been achieved during  
7757 the commissioning of the system at the end of 2010. A future program to explore the 100kW range is  
7758 envisaged. At the ATF beam energy, Compton collision will produce gamma rays near 20 MeV resulting in  
7759 the world's first beam-driven gamma factory.

### 7760 8.7.8 Undulator Source

7761 Another positron production option would be an undulator process, based on the main high-energy electron  
7762 (or positron) beam. The LHeC undulator scheme can benefit from the pertinent development work done  
7763 for the ILC. The beam energy at LHeC would be lower, e.g. 60 GeV, which might possibly be compensated  
7764 by more ambitious undulator magnets, e.g. ones based on Nb<sub>3</sub>Sn or HTS. However, the requested photon  
7765 flux calls for a careful investigation. The undulator parameters needed for 60 GeV, the expected positron  
7766 production rate, and technical feasibility all require further study.

### 8.7.9 Source based on Coherent Pair Creation

The normalized transverse emittance of all positrons from a target is of order  $\epsilon_N \approx 1 - 10$  mm, to be compared with a requested emittance of  $\epsilon_N = 0.05$  mm. Therefore, a factor 100 emittance reduction is required.

Solution 1 would be to simply cut the phase space. However, this would give rise to an unrealistic increase of the primary beam power.

Solution 2 would be to collect all positrons, accelerate them to 1 GeV and damp them for  $\text{Log}(100) \sim 5$  damping times, with an implied RF power of  $P_{RF} = 1 \text{ GeV} \times 5 \text{ mA} \times 5/0.6 = 60 \text{ MW}$ , where an RF efficiency of 50% was assumed.

Solution 3 would be to produce positrons in a smaller phase space volume. Indeed the inherent transverse emittance from pair production is small. The large phase space volume only comes from multiple scattering in the production target.

Pair production from relativistic electrons in a strong laser field would not need any solid target, since the laser itself serves as the target, and it would not suffer from multiple scattering. This process has been studied in the 1960's and 1990's [693–695]. It should be reconsidered with 2011 state of the art TiSa lasers and X-ray FELs [696].

### 8.7.10 Conclusions

The challenging requirements for the LHeC Linac-Ring positron source are relaxed if positrons can be collided several times before deceleration, if they can be reused over several acceleration/deceleration cycles, and/or if they can be cooled. The compact tri-ring scheme is an attractive proposal for recooling the spent and recycled positrons. A conventional damping ring in the SPS tunnel would be an alternative.

Assuming some of the aforementioned measures are taken to reduce the required positron intensity, which needs to be generated, by at least an order of magnitude, and also assuming that an advanced target, e.g. W-granules, rotating wheel, sliced-rod converter, liquid metal jet, or running tape, can be used, several of the proposed source and cooling concepts could provide the intensity and the beam quality required by the LHeC ERL.

For example, the Compton-ring source and the Compton ERL are viable candidates for the Linac-Ring LHeC positron source. Coherent pair production and an advanced undulator represent other possible schemes, still to be explored for LHeC in greater detail. The coherent pair production would have the appealing feature of generating positrons with an inherently small emittance.

In conclusion, it does seem technically possible to meet the very demanding requirements for the LHeC positron source by a combination of approaches. A serious and concerted R&D effort will be required to determine the optimum linac-ring positron configuration.



## Chapter 9

# System Design

### 9.1 Magnets for the Interaction Region

#### 9.1.1 Introduction

The technical requirements for the ring-ring options are easily achieved with superconducting magnets of proven technology. It is possible to make use of the wire and cable development for the LHC inner triplet magnets. We have studied all-together seven variants of which two are selected for this CDR. Although these magnets will require engineering design efforts, there are no challenges because the mechanical design will be very similar to the MQXA [697] magnet built for the LHC [587].

The requirements in terms of aperture and field gradient are much more difficult to obtain for the linac-ring option. We reverse the arguments and present the limitations for the field gradient and septum size, that is, the minimum distance between the proton and electron beams, for both Nb-Ti and Nb<sub>3</sub>Sn superconducting technology. Here we limit ourselves to the two most promising conceptual designs.

#### 9.1.2 Magnets for the ring-ring option

The interaction region requires a number of focussing magnets with apertures for the two proton beams and field-free regions to pass the electron beam after the collision point. The lattice design was presented in Sections 7.3 and 8.45; the schematic layout is shown in Fig. 7.19.

The field requirements for the ring-ring option (gradient of 127 T/m, beam stay clear of 13 mm (12  $\sigma$ ), aperture radius of 21 mm for the proton beam, 30 mm for the electron beam) allow a number of different magnet designs using the well proven Nb-Ti superconductor technology and making use of the cable development for the LHC. In the simulations presented here, we have used the parameters (geometrical, critical surface, superconductor magnetization) of the cables used in the insertion quadrupole MQY of the LHC.

Fig. 9.1 shows a superferric magnet as built for the KEKb facility [698]. This design comes to its limits due to the saturation of the iron poles. Indeed, the fringe field in the aperture of the electron beam exceeds the limit tolerable for the electron beam optics, and the field quality required for proton beam stability, on the order of one unit in  $10^{-4}$  at a reference radius of 2/3 the aperture, is difficult to achieve.

The magnetic flux density in the low-field region of the design shown in Fig. 9.1 (right) is about 0.3 T. We therefore disregard this design as well. Moreover, the engineering design work required for the mechanical structure of this magnet would be higher than for the proven designs shown in Fig. 9.2.

Fig. 9.2 shows the three alternatives based on LHC magnet technology. In the case of the double aperture version the aperture for the proton beams is 21 mm in radius, in the single aperture version the beam pipe radius is 26 mm. In all cases the 127 T/m field gradient can be achieved with a comfortable safety margin to quench (exceeding 30%) and using the cable(s) of the MQY magnet of the LHC. The operation temperature is supposed to be 1.8 K, employing superfluid helium technology. The cable characteristic data are given in

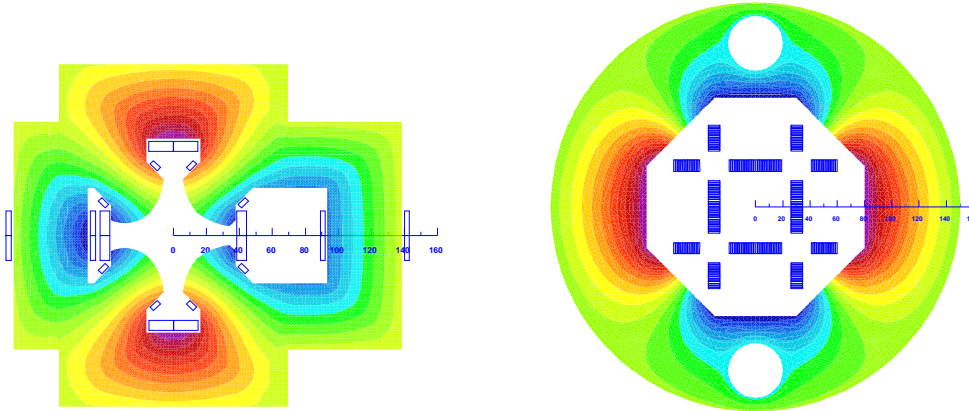


Figure 9.1: Cross-sections of insertion quadrupole magnets with iso-surfaces of the magnetic vector potential (field-lines). Left: Super-ferric, similar to the design presented in [698]. Right: Superconducting block-coil magnet as proposed in [699] for a coil-test facility.

7835 Table 9.1. The outer radii of the magnet coldmasses do not exceed the size of the triplet magnets installed  
 7836 in the LHC (diameter of 495 mm). The fringe field in the aperture of the electron beam is in all cases below  
 7837 0.05 T.

7838 Fig. 9.3 shows half-aperture quadrupoles (single and double-aperture versions for the proton beams) in a  
 7839 similar design as proposed in [17]. The reduced aperture requirement in the double-aperture version makes  
 7840 it possible to use a single layer coil and thus to reduce the beam-separation distance between the proton and  
 7841 the electron beams. The field-free regions is large enough to also accommodate the counter rotating proton  
 7842 beam. The version shown in Fig. 9.3 (left) employs a double-layer coil. In all cases the outer diameter of  
 7843 the coldmasses do not exceed the size of the triplet magnets currently installed in the LHC tunnel.

7844 For this CDR we retain only the single aperture version for the Q2 (shown in Fig. 9.2, left) and the  
 7845 half-aperture quadrupole for the Q1 (shown in Fig. 9.3, top left). The separation distance between the  
 7846 electron and proton beams in Q1 requires the half-aperture quadrupole design to limit the overall synchrotron  
 7847 radiation power emitted by bending of the 60 GeV electron beam. The single aperture version for Q2 is  
 7848 retained in the present layout, because the counter rotating proton beam can be guided outside the Q2  
 7849 triplet magnet. The design of Q3 follows closely that of Q2, except for the size of the septum between the  
 7850 proton and the electron beams.

7851 The coils in all three triplet magnets are made from two layers, using both Nb-Ti composite cables as  
 7852 specified in Table 9.1. The layers are individually optimized for field quality. This reduces the sensitivity  
 7853 to manufacturing tolerances and the effect of superconductor magnetization [700]. The mechanical design  
 7854 will be similar to the MQXA magnet where two kinds of interleaved yoke laminations are assembled under  
 7855 a hydraulic press and locked with keys in order to obtain the required pre-stress of the coil/collar structure.  
 7856 The main parameters of the magnets are given in Table 9.2.

### 7857 9.1.3 Magnets for the linac-ring option

7858 The requirements in terms of aperture and field gradient are more difficult to obtain for the linac-ring option.  
 7859 Consequently we present the limitations for the field gradient and septum size achievable with both Nb-Ti  
 7860 and Nb<sub>3</sub>Sn superconducting technologies. We limit ourselves to the two conceptual designs already chosen  
 7861 for the ring-ring option. For the half quadrupole, shown in Fig. 9.5 (right), the working points on the  
 7862 load-line are given for both superconducting technologies in Fig. 9.4.

7863 However, the conductor size must be increased and in case of the half quadrupole, a four layer coil must

Table 9.1: Characteristic data for the superconducting cables and strands. OL = outer layer, IL = inner layer

Magnet	MQY (OL)	MQY (IL)
Diameter of strands (mm)	0.48	0.735
Copper to SC area ratio	1.75	1.25
Filament diameter ( $\mu$ m)	6	6
$B_{\text{ref}}$ (T) @ $T_{\text{ref}}$ (K)	8 @ 1.9	5 @ 4.5
$J_c(B_{\text{ref}}, T_{\text{ref}})$ ( $\text{A mm}^{-2}$ )	2872	2810
$-dJ_c/dB$ ( $\text{A mm}^{-2} \text{T}$ )	600	606
$\rho(293 \text{ K})/\rho(4.2 \text{ K})$ of Cu	80	80
Cable width (mm)	8.3	8.3
Cable thickness, thin edge (mm)	0.78	1.15
Cable thickness, thick edge (mm)	0.91	1.40
Keystone angle (degree)	0.89	1.72
Insulation thicken. narrow side (mm)	0.08	0.08
Insulation thicken. broad side (mm)	0.08	0.08
Cable transposition pitch length (mm)	66	66
Number of strands	34	22
Cross section of Cu ( $\text{mm}^2$ )	3.9	5.2
Cross section of SC ( $\text{mm}^2$ )	2.2	4.1

7864 be used; see Fig. 9.5. The thickness of the coil is limited by the flexural rigidity of the cable, which will  
7865 make the coil-end design difficult. Moreover, a thicker coil will also increase the beam separation between  
7866 the proton and the electron beams. The results of the field computation are given in Table 9.2, column 3  
7867 and 4. Because of the higher iron saturation, the fringe fields in the electron beam channel are considerably  
7868 higher than in the magnets for the ring-ring option.

7869 For the  $\text{Nb}_3\text{Sn}$  option we assume composite wire produced with the internal Sn process (Nb rod extru-  
7870 sions), [701]. The non-Cu critical current density is  $2900 \text{ A/mm}^2$  at 12 T and 4.2 K. The filament size of 46  
7871  $\mu\text{m}$  in  $\text{Nb}_3\text{Sn}$  strands give rise to higher persistent current effects in the magnet. The choice of  $\text{Nb}_3\text{Sn}$  would  
7872 impose a considerable R&D and engineering design effort, which is however, not more challenging than other  
7873 accelerator magnet projects employing this technology [702].

7874 Fig. 9.6 shows the conceptual design of the mechanical structure of these magnets. The necessary  
7875 prestress in the coil-collar structure, which must be high enough to avoid unloading at full excitation, cannot  
7876 be exerted with the stainless-steel collars alone. For the single aperture magnet as shown in Fig. 9.6 left,  
7877 two interleaved sets of yoke laminations (a large one comprising the area of the yoke keys and a smaller,  
7878 floating lamination with no structural function) provide the necessary mechanical stability of the magnet  
7879 during cooldown and excitation. Preassembled yoke packs are mounted around the collars and put under  
7880 a hydraulic press, so that the keys can be inserted. The sizing of these keys and the amount of prestress  
7881 before the cooldown will have to be calculated using mechanical FEM programs. This also depends on the  
7882 elastic modulus of the coil, which has to be measured with a short-model equipped with pressure gauges.  
7883 Special care must be taken to avoid nonallowed multipole harmonics because the four-fold symmetry of the  
7884 quadrupole will not entirely be maintained.

7885 The mechanical structure of the half-quadrupole magnet is somewhat similar, however, because of the  
7886 left/right asymmetry four different yoke laminations must be produced. The minimum thickness of the  
7887 septum will also have to be calculated with structural FEM programs.

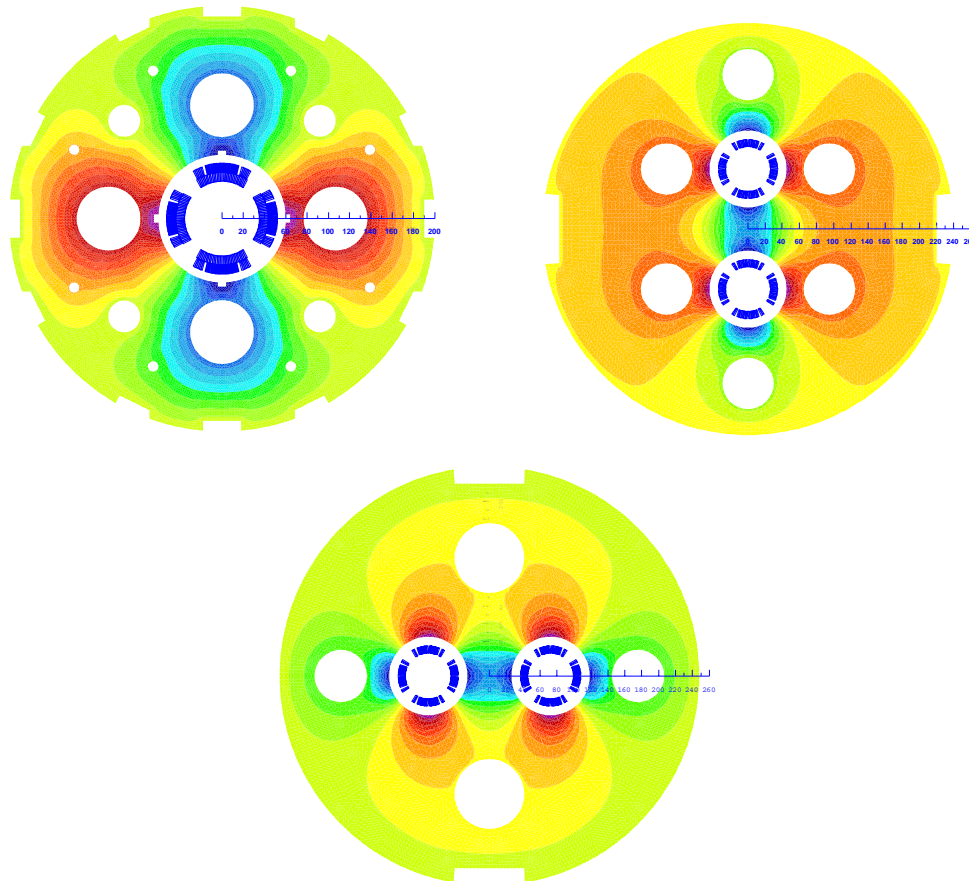


Figure 9.2: Cross-sections with field-lines of insertion quadrupole magnets. Classical designs similar to the LHC magnet technology. Top left: Single aperture with a double layer coil employing both cables listed in Table 9.1. Design chosen for Q2. Top right: Double aperture vertical. Bottom: Double aperture horizontal. The double-aperture magnets can be built with a single layer coil using only the MQY inner layer cable; see the right column of Table 9.1.

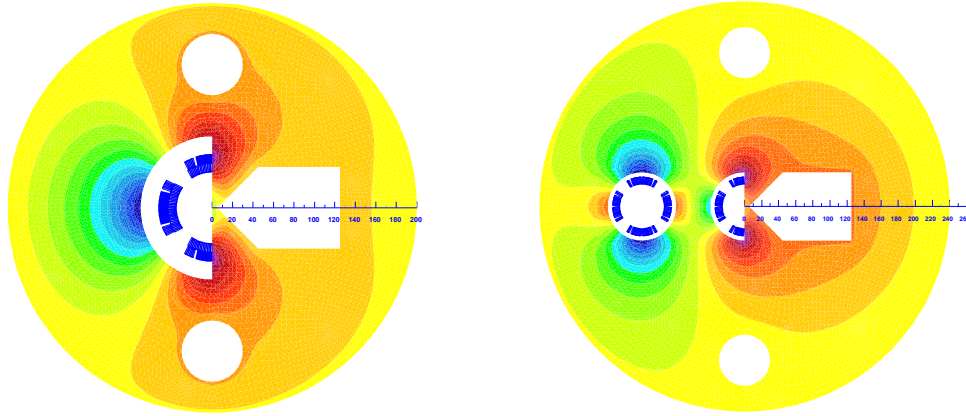


Figure 9.3: Cross-sections of insertion quadrupole magnets with field-lines. Left: Single half-aperture quadrupole with field-free domain [17]; design selected for Q1. Right: Double-aperture magnet composed of a quadrupole and half quadrupole.

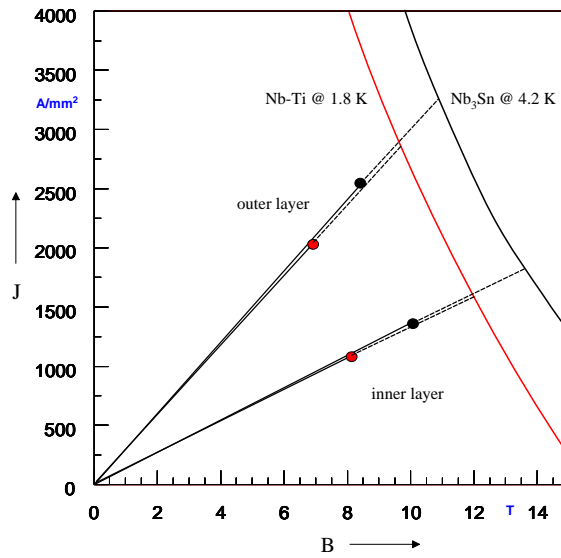


Figure 9.4: Working points on the load-line for both Nb-Ti and Nb<sub>3</sub>Sn variants of the half quadrupole for Q1.

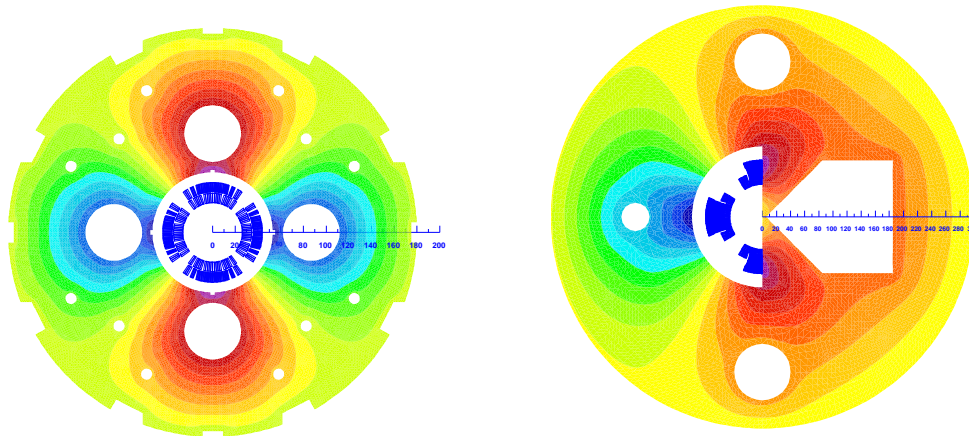


Figure 9.5: Cross-sections of the insertion quadrupole magnets for the linac-ring option. Left: Single aperture quadrupole. Right: Half quadrupole with field-free region.

Table 9.2: SC = type of superconductor,  $g$  = field gradient,  $R$  = radius of the aperture (without coldbore and beam-screen), LL = operation percentage on the load line of the superconductor material,  $I_{\text{nom}}$  = operational current,  $B_0$  = main dipole field,  $S_{\text{beam}}$  = beam separation distance,  $B_{\text{fringe}}$  = fringe field in the aperture for the electron beam,  $g_{\text{fringe}}$  = gradient field in the aperture for the electron beam.

Type		Ring-ring single aperture	Ring-ring half-quad	Linac-ring single aperture	Linac-ring half-quad
Function		Q2	Q1	Q2	Q1
SC		Nb-Ti at 1.8 K			
R	mm	36	35	23	46
$I_{\text{nom}}$	A	4600	4900	6700	4500
$g$	T/m	137	137	248	145
$B_0$	T	-	2.5	-	3.6
LL	%	73	77	88	87
$S_{\text{beam}}$	mm	107	65	87	63
$B_{\text{fringe}}$	T	0.016	0.03	0.03	0.37
$g_{\text{fringe}}$	T/m	0.5	0.8	3.5	18
SC		Nb <sub>3</sub> Sn at 4.2 K			
$I_{\text{nom}}$	A			6700	4500
$g$	T/m			311	175
$B_0$	T			-	4.7
LL	%			83	82
$B_{\text{fringe}}$	T			0.09	0.5
$g_{\text{fringe}}$	T/m			9	25

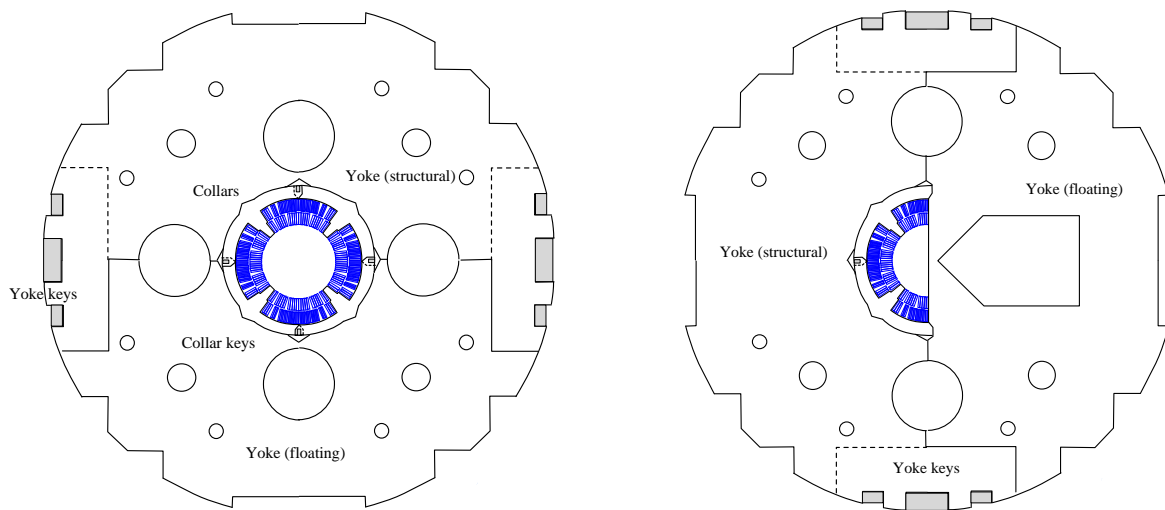


Figure 9.6: Sketch of the mechanical structure. Left: Single aperture magnet. Right: Half quadrupole with field-free region.

## 9.2 Accelerator Magnets

In this section the main magnets needed for the accelerator are considered. The analysis focuses separately on the ring-ring (RR) and linac-ring (LR) layouts. The requirements are listed and an initial design is proposed. The RR dipoles prompted an experimental activity, involving the manufacturing and magnetic characterization of short models, whose results are briefly reported here.

We gratefully acknowledge the fruitful discussion with Neil Marks about the design of these electromagnets. We thank Miriam Fitterer and Alex Bogacz for help in checking the requirements of the magnets according to the lattice, for the RR and LR option, respectively.

### 9.2.1 RR option, dipole magnets

A total of 3080 bending magnets, 5.35 m long, are needed in the LHC tunnel for the RR layout, of which 3040 for in the arcs and the remaining 40 for the insertion and by-pass regions. The nominal strength is 0.0127 T at 10 GeV and 0.0763 T at 60 GeV. As a comparison, the LEP collider contained 3280 main dipole magnets, with a nominal flux density at injection (20 GeV) of 0.0215 T, and at collision energy (100 GeV) of 0.1100 T [?].

The main points to consider in the design of these magnets are:

- the low working flux density, in particular at injection, that constitutes a challenge for cycle-to-cycle reproducibility and for good field quality throughout the ramp;
- the need for compactness, to fit in the present tunnel with the installed LHC systems;
- the required compatibility with the emitted synchrotron radiation power.

Different designs have been proposed at BINP and CERN to respond to these demands. In particular, the first point (low injection field) has prompted an experimental activity, with several short models manufactured and measured. This experience is briefly summarized next.

#### BINP model

Two different types of models have been manufactured at BINP, see Fig. 9.7. The aim was to demonstrate that a cycle-to-cycle reproducibility at injection better than  $0.1 \cdot 10^{-4}$  T can be achieved. Both models have shown a field reproducibility at injection current within  $\pm 0.075 \cdot 10^{-4}$  T, when cycled between injection and maximum field. To achieve such results the iron laminations were made of 3408 type grain oriented silicon steel 0.35 mm thick. Their coercive force in the direction of the grain orientation is  $H_{c\parallel} \approx 6$  A/m, while in the direction perpendicular to the grain orientation it remains relatively low,  $H_{c\perp} \approx 22$  A/m. The C-type model has been assembled in two variants, with the central iron part with the grains oriented vertically and horizontally (both blocks are as shown in the picture). The magnetic measurements did not show relevant differences between the two versions.

#### CERN model

As a complementary study to the one made by BINP, the CERN model has explored the manufacture of lighter magnets, with the yoke consisting of interleaved steel and plastic laminations. A thickness ratio between plastic and steel of 2:1 has been chosen. As the flux produced in the magnet aperture is concentrated in the high permeability regions only, the magnetic field in the iron pole is about 3 times that in the gap. In addition to a lighter assembly, this solution has the advantage of increasing the magnetic working point of the iron at injection field. This makes the design less sensitive to the characteristics of the iron and in particular to the coercive force. A similar strategy had been adopted for the LEP dipoles, where 1.5 mm thick low-carbon steel laminations were spaced by 4 mm and embedded in a cement mortar.

The proposed design is a compact C type dipole, see Fig. fig:CERN-Model. The aperture is on the external side of the ring, so that the magnet does not intercept the emitted synchrotron radiation, and



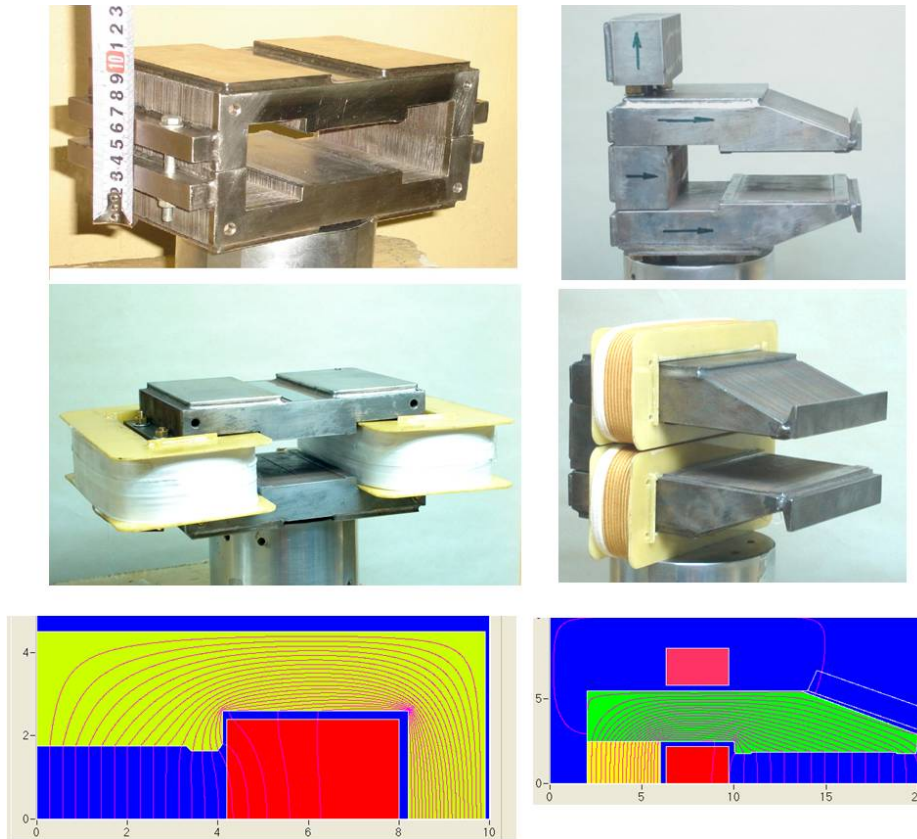


Figure 9.7: H and C type model magnets made by BINP at Novosibirsk.

7931 possibly room is left for a vacuum pre-chamber. The geometry involves a rather unusual shape for the poles.  
 7932 The objective was to design a cross-section able to minimize the difference of flux lines length over the  
 7933 horizontal aperture. This makes the field quality (in particular, the quadrupole component) less dependent  
 7934 on variations of iron characteristics, both at injection and collision energies.

7935 For the coils, a 1-turn solution (per pole) has been adopted, with solid copper bars which after insulation  
 7936 are individually slid inside the magnet.

7937 To explore the potential of the proposed design, in particular in terms of magnetic field reproducibility  
 7938 at injection energy, three models have been built using three different materials:

- 7939 • model 1: a rather noble Supra 36 NiFe steel, 1.0 mm thick laminations, with a measured coercive field  
 7940 (after heat treatment for 4 hours at 1050 °C under hydrogen), equal to  $H_c \approx 6$  A/m;
- 7941 • model 2: a conventional low carbon steel with low silicon content, 1.0 mm thick laminations, 0.5% Si,  
 7942  $H_c \approx 70$  A/m;
- 7943 • model 3: a 35M6 grain oriented steel, 0.35 mm thick laminations, 3.1% silicon, with  $H_{c\parallel} \approx 7$  A/m and  
 7944  $H_{c\perp} \approx 25$  A/m.

7945 In all cases 2 mm thick phenolic sheets have been used as spacers, stacked and glued with an epoxy  
 7946 resin together with the steel sheets. For the last model, to compensate for the thinner laminations, three of  
 7947 them were stacked together, in order to keep a similar magnetic field distribution as in the stacks with the  
 7948 isotropic steels.

7949 Magnetic measurements have been performed to assess the field reproducibility at injection. A cycle from  
 7950 10 GeV to 60 GeV, requiring a dipole field of 0.0127 T to 0.0763 T, corresponds to currents from 210 A to



Figure 9.8: One of the 400 mm long model magnets made at CERN with interleaved laminations.

7951 1340 A. Unfortunately the available power converter could provide a sufficiently good stability only over a  
 7952 smaller range, namely between 260 A and 1300 A, with measured stabilities of  $4 \cdot 10^{-5}$  at 260 A and  $2 \cdot 10^{-5}$   
 7953 at 1300 A. Each of the models was submitted to 5 conditioning cycles and thereafter to 8 cycles between  
 7954 these currents at a ramp rate of 400 A/s. The reproducibility of the magnetic field in the gap was measured  
 7955 with an integral coil coupled with a digital integrator, providing the results summarized in Tables 9.3 and  
 7956 9.4.

7957 The performance is in all cases very satisfactory. There might be an indication that models 1 and 3,  
 7958 as expected, perform better than model 2; however, the values are close to the measurement errors. In  
 7959 practice these results show that within this range of field levels the value of the coercive field does not seem  
 7960 to play a major role in the reproducibility of the magnetic field from cycle to cycle. More details about the  
 7961 manufacturing of these models and the magnetic measurements can be found in [?].

Model	Low field	High field
Model 1 (NiFe steel)	$5 \cdot 10^{-5}$	$4 \cdot 10^{-5}$
Model 2 (Low carbon steel)	$6 \cdot 10^{-5}$	$6 \cdot 10^{-5}$
Model 3 (Grain oriented 3.5% Si steel)	$4 \cdot 10^{-5}$	$6 \cdot 10^{-5}$

Table 9.3: Reproducibility of magnetic field over 8 cycles, maximum deviation from average.

Model	Low field	High field
Model 1 (NiFe steel)	$3 \cdot 10^{-5}$	$3 \cdot 10^{-5}$
Model 2 (Low carbon steel)	$4 \cdot 10^{-5}$	$5 \cdot 10^{-5}$
Model 3 (Grain oriented 3.5% Si steel)	$2 \cdot 10^{-5}$	$4 \cdot 10^{-5}$

Table 9.4: Reproducibility of magnetic field over 8 cycles, standard deviation from average.

7962 The conclusion of this analysis is that all three models meet the LHeC specifications. However, the

7963 similarity that can be achieved in a series production of 3080 units has to be further investigated. The low  
7964 value of injection field amplifies the problem, as in that region the variation in magnetic parameters is larger.  
7965 This problem is already partially taken care of in the design of the cross-section, that is meant to be less  
7966 sensitive to the iron characteristics, and in the low stacking factor. Furthermore, the usual procedure of  
7967 “shuffling” (or “sorting”) the laminations during the production has to be envisaged, with results that might  
7968 depend on the statistical distribution of coercive forces and permeabilities (at low field) in the steel, as well  
7969 as on the shuffling technique.

### 7970 **Proposal for dipole magnets, RR option**

7971 The proposed cross-section for the dipoles of the ring-ring option is shown in Fig. 9.9. The main parameters  
7972 are summarized in Table 9.5.

7973 The idea of assembling the yoke with steel laminations interleaved by plastic spacers is retained, as in  
7974 the CERN models. This has the mechanical advantage of a lower weight of the assembly, and the magnetic  
7975 advantage of magnifying the field in the steel by a factor of about 3. This is of particular interest at injection  
7976 energy.

7977 The conductor can be in aluminium (like in LEP) or in copper depending on economical reasons coming  
7978 from a correct balance between investment and operation costs. The present design is based on an aluminium  
7979 conductor. With respect to copper, this has the advantage of making the magnet lighter (about 200 kg of  
7980 coil instead of about 625 kg). Using copper, however, would imply a power consumption, per magnet, at  
7981 60 GeV around 190 W instead of around 300 W. Notwithstanding the material, the choice of having 1-turn  
7982 coils, i.e., solid straight bars, has several technical and economical consequences:

- 7983 • the coil manufacturing is simpler and hence cheaper;
- 7984 • the high current (1300 A) involves large terminals and connections between the magnets;
- 7985 • the power supply is rated at high current, but with rather low voltage and impedance;
- 7986 • the resistive losses in the interconnections, terminals and in the power cables are significantly higher  
7987 than those for a multi-turn magnet working at lower current;
- 7988 • it is possible to envisage to use the conductor as bus-bar to connect the string of magnets in series,  
7989 thus reducing the number of interconnections.

7990 The solution proposed here for the conductor is similar to the one that had been adopted for LEP. However,  
7991 these aspects need to be further investigated in the TDR on a wider perspective.

7992 The conductor size is sufficiently large so that the current density is around 0.4 A/mm<sup>2</sup>. The dissipated  
7993 resistive power (of the order of 50 W per meter of length of the magnet, considering aluminium as conductor)  
7994 is reduced to levels which can be possibly dealt with by the ventilation in the LHC tunnel: this is a  
7995 considerable advantage in terms of simplicity of magnet manufacture, connections, reliability and of course  
7996 it avoids the installation of a water cooling circuit dedicated to the dipoles in the arcs.

### 7997 **9.2.2 RR option, quadrupole magnets**

7998 The quadrupole magnets needed for the ring-ring option can be considered undemanding and well within  
7999 the compass of standard design.

#### 8000 **Quadrupoles in the arcs**

8001 In the arcs, 336 focusing quadrupoles (QF) providing 10.28 T integrated strength, and 336 defocusing  
8002 quadrupoles (QD) each providing 8.40 T integrated strength are needed. These are to be installed in the  
8003 LHC tunnel.

8004 Considering that the integrated strengths of the QD and QF are not much different, it is proposed here to  
8005 have the same type of magnets. The relevant parameters are summarized in Table 9.6 and the cross-section  
8006 is illustrated in Fig. 9.10.

8007 **Quadrupoles in the insertion and by-pass**

8008 In total 148 QF and 148 QD magnets are needed in the insertion and by-pass regions. The required integrated  
8009 strength is 18 T for the QF and 13 T for the QD. In this case, it is proposed to keep the same magnet cross-  
8010 section but to have two different lengths for the quadrupoles, namely, 1.0 m for the QF and 0.7 m for the  
8011 QD. The relevant parameters are summarized in Table 9.7 and the cross-section is illustrated in Fig. 9.11.  
8012 A value of 19 T/m is taken as design gradient.

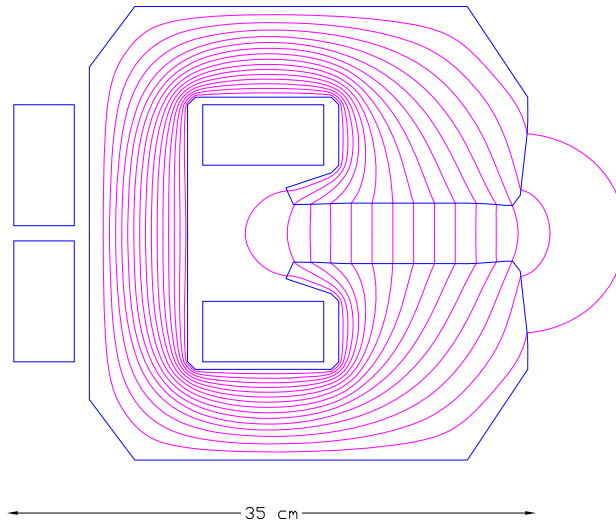


Figure 9.9: Bending magnets for the RR option (scale 1:5).

Beam energy	10 to 60	GeV
Magnetic field	0.0127 to 0.0763	T
Magnetic length	5.35	m
Vertical aperture	40	mm
Pole width	150	mm
Mass	1400	kg
Number of magnets	3080	
Current @ 0.0763 T	1300	A
Number of turns per pole	1	
Current density @ 0.0763 T	0.4	A/mm <sup>2</sup>
Conductor material	aluminium	
Magnet inductance	0.13	mH
Magnet resistance	0.18	mΩ
Power @ 60 GeV	300	W
Total power consumption @ 60 GeV	0.92	MW
Cooling	air	

Table 9.5: Main parameters of bending magnets for the RR option.

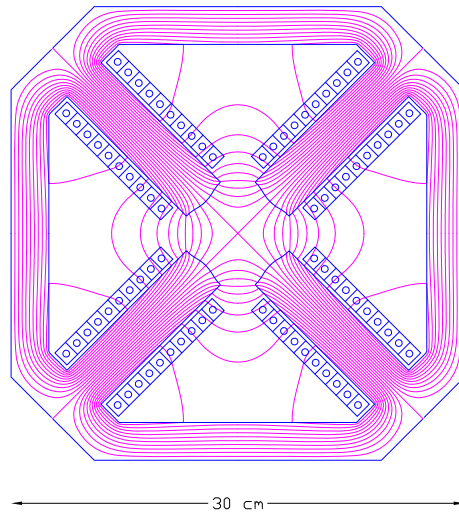


Figure 9.10: Arc quadrupoles for the RR option (scale 1:5).

Beam energy	10 to 60	GeV
Field gradient @ 60 GeV (QF/QD)	10.28 / -8.40	T/m
Magnetic length	1.0	m
Aperture radius	30	mm
Mass	400	kg
Number of magnets (QF/QD)	336 / 336	
Current @ 60 GeV (QF/QD)	380 / 310	A
Number of turns per pole	10	
Current density @ 60 GeV (QF/QD)	4.0 / 3.3	A/mm <sup>2</sup>
Conductor material	copper	
Magnet inductance	4	mH
Magnet resistance	16	mΩ
Power @ 60 GeV (QF/QD)	2.3 / 1.5	kW
Total power consumption @ 60 GeV (QF/QD)	0.77 / 0.52	MW
Cooling	water	

Table 9.6: Main parameters of arc quadrupoles for the RR option.

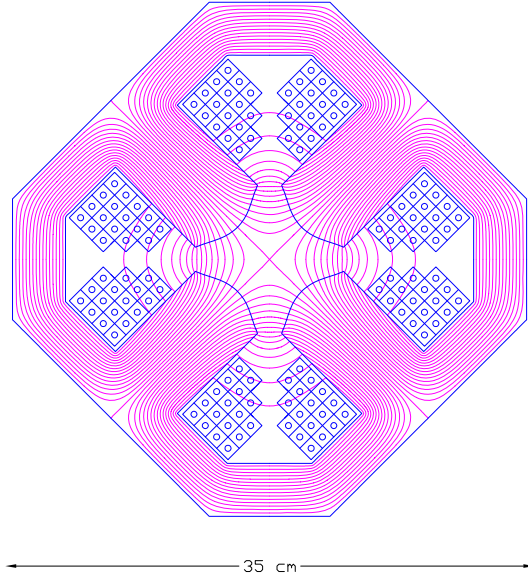


Figure 9.11: Insertion and by-pass quadrupole magnets for the RR Option (scale 1:5).

Beam energy	10 to 60	GeV
Field gradient @ 60 GeV	19	T/m
Magnetic length (QD/QF)	1.0 / 0.7	m
Aperture radius	30	mm
Mass (QD/QF)	560 / 390	kg
Number of magnets (QD/QF)	148 / 148	
Current @ 19 T/m	420	A
Number of turns per pole	17	
Current density @ 19 T/m	4.6	A/mm <sup>2</sup>
Conductor material	copper	
Magnet inductance (QD/QF)	15 / 10	mH
Magnet resistance (QD/QF)	30 / 23	mΩ
Power @ 60 GeV (QD/QF)	5.3 / 3.9	kW
Total power consumption @ 60 GeV (QD/QF)	0.78 / 0.58	MW
Cooling	water	

Table 9.7: Main parameters of insertion and by-pass quadrupoles for the RR option.

### 8013 **9.2.3 LR option, dipole magnets**

8014 The bending magnets for the LR option are used in the arcs of the recirculator. Each of the six arcs needs  
8015  $58 \times 10 = 580$  dipoles for the standard arc cells, plus  $2 \times 2 = 4$  for the dispersion suppression regions at the  
8016 two ends. This results in a total of 584 units. These magnets are 4 m long and they provide a magnetic field  
8017 ranging from 0.046 T to 0.264 T depending on the arc energy, from 10.5 GeV to 60.5 GeV. Additionally, a  
8018 few bending magnets (4 at each end of an arc) are needed for the switch-yards regions. These magnets –  
8019 providing vertical bends – are in a separate category and are not considered at the moment.

8020 Considering the relatively low field strength required even for the highest energy arc, and the small  
8021 required physical aperture of 25 mm only, it is proposed here to adopt the same cross-section for all the  
8022 magnets, possibly using smaller conductors for the ones at the lowest energies. This allows the design of very  
8023 compact and relatively cheap magnets, running at low current densities to minimize the power consumption.

8024 The choice of having 1-turn coils prompts the same comments as for the dipoles of the RR option. In  
8025 this case, though, the maximum current is considerably higher (2700 A vs. 1300 A), although the overall  
8026 dissipated power is lower.

8027 Table 9.8 summarizes the main parameters of the proposed magnet design, which is illustrated in Fig. 9.12.

8028 The proposed design is based on classical resistive electromagnets. The use of units embedding permanent  
8029 magnets could be envisaged, given the (almost stationary) requirements on the field. The capital cost would  
8030 be significantly higher, but savings would occur on the side of power supplies and interconnections, besides  
8031 clearly on the electric bill.

### 8032 **9.2.4 LR option, quadrupole magnets**

#### 8033 **Quadrupoles for the recirculator arcs**

8034 In each of the six recirculator arcs, four different types of quadrupoles are needed, each type in 60 units,  
8035 adding up to 240 quadrupoles per arc. The Q0, Q1 and Q3 magnets provide each about 35 T integrated  
8036 strength, whereas the Q2 ones provide each about 50 T integrated strength. The required integrated gradients  
8037 can be met with one type of quadrupole manufactured in two different length, 900 mm (for Q0, Q1 and  
8038 Q3) and 1200 mm (for Q2). A few additional quadrupoles (of the order of 14 per arc) are needed for the  
8039 switch-yard regions; these units are not included in the total count here.

8040 As for the dipoles, also the quadrupoles in the different arcs may or may not have the same conductor,  
8041 that is, it is possible to use a smaller conductor (or less turns) in the low energy arcs, or to use the same  
8042 conductor everywhere and simply operating the first ones at a lower power. The relevant parameters are  
8043 summarized in Table 9.9 and the cross-section is illustrated in Figure 9.13.

8044 Also for the quadrupoles, it could be envisaged to use a hybrid configuration, with most of the excitation  
8045 given by permanent magnets. The gradient strength could be varied by trim coils and/or by mechanical  
8046 methods (see, for example, [?]).

#### 8047 **Quadrupoles for the two 10 GeV linacs**

8048 In the two 10 GeV linacs,  $37 + 37$  quadrupoles each providing 2.5 T integrated strength are required. The  
8049 present design solution considers 70 mm aperture radius magnets to be compatible with any possible aperture  
8050 requirement. The relevant parameters are summarized in Table 9.10 and the cross-section is illustrated in  
8051 Figure 9.14.

8052 The magnet could be more compact, but a bit longer to compensate for the lower gradient. Alternatively,  
8053 one could consider superconducting magnets that could be hosted in the linac cryostats.

8054 It could also be convenient to have in the two linacs, or at different positions along the acceleration,  
8055 several families of quadrupoles with different apertures. Here a cross-section for the more demanding ones  
8056 is reported.



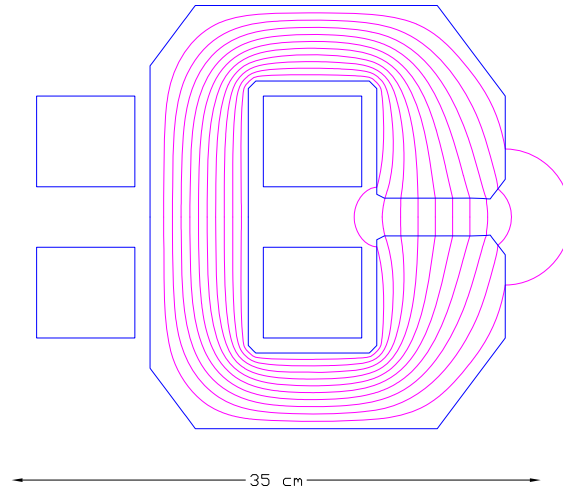


Figure 9.12: Bending magnets for the LR recirculator (scale 1:5).

Beam energy	10.5 to 60.5	GeV
Magnetic field	0.046 to 0.264	T
Magnetic length	4.0	m
Vertical aperture	25	mm
Pole width	80	mm
Mass	2000	kg
Number of magnets	$6 \times 584 = 3504$	
Current @ 60.5 GeV	2700	A
Number of turns per pole	1	
Current density @ 0.264 T	0.7	A/mm <sup>2</sup>
Conductor material	copper	
Magnet inductance	0.08	mH
Magnet resistance	0.08	mΩ
Power @ 10.5 GeV	20	W
Power @ 20.5 GeV	65	W
Power @ 30.5 GeV	150	W
Power @ 40.5 GeV	260	W
Power @ 50.5 GeV	405	W
Power @ 60.5 GeV	585	W
Total power consumption six arcs	0.87	MW
Cooling	air	

Table 9.8: Main parameters of bending magnets for the LR recirculator. Resistance and powers refer to the same conductor size across the six arcs.

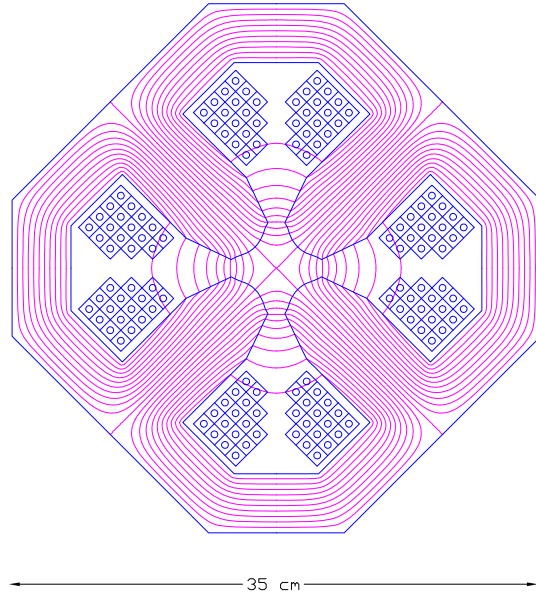


Figure 9.13: Quadrupoles for the recirculators of the LR option (scale 1:5).

Beam energy	10.5 to 60.5	GeV
Field gradient	41	T/m
Magnetic length (short/long)	0.9 / 1.2	m
Aperture radius	20	mm
Mass (short/long)	750 / 980	kg
Number of magnets (Q0+Q1+Q2+Q3)	$6 \times 240 = 1440$	
Current @ 41 T/m	400	A
Number of turns per pole	17	
Current density @ 41 T/m	4.8	A/mm <sup>2</sup>
Conductor material	copper	
Magnet inductance (short/long)	17 / 22	mH
Magnet resistance (short/long)	30 / 40	mΩ
Power @ 10.5 GeV (short/long)	0.15 / 0.20	kW
Power @ 20.5 GeV (short/long)	0.55 / 0.74	kW
Power @ 30.5 GeV (short/long)	1.22 / 1.63	kW
Power @ 40.5 GeV (short/long)	2.15 / 2.87	kW
Power @ 50.5 GeV (short/long)	3.35 / 4.46	kW
Power @ 60.5 GeV (short/long)	4.80 / 6.40	kW
Total power consumption six arcs	3.17	MW
Cooling	water	

Table 9.9: Main parameters of quadrupoles for the recirculators of the LR option. Resistance and powers refer to the same conductor size across the six arcs.

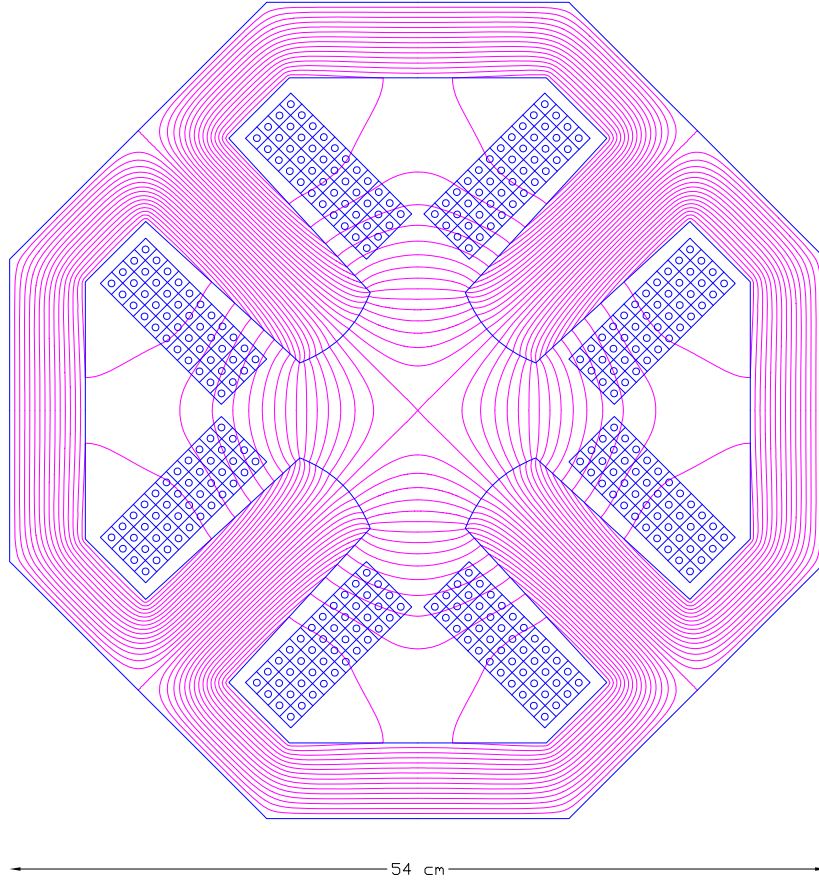


Figure 9.14: Quadrupoles for the 10 GeV linacs of the LR option (scale 1:5).

Field gradient	10	T/m
Magnetic length	0.250	m
Aperture radius	70	mm
Mass (QD/QF)	440	kg
Number of magnets	37 + 37	
Current @ 10 T/m	460	A
Number of turns per pole	44	
Current density @ 10 T/m	5.0	A/mm <sup>2</sup>
Conductor material	copper	
Magnet inductance	24	mH
Magnet resistance	25	mΩ
Power @ 10 T/m	5.3	kW
Cooling	water	

Table 9.10: Main parameters of quadrupoles for the 10 GeV linacs of the LR option.

8057 **9.2.5 LR option, corrector magnets for the two 10 GeV linacs**

8058 In the two 10 GeV linacs, 37 + 37 dipole (vertical / horizontal) correctors are needed. These combined  
 8059 function correctors shall provide an integrated field of 10 mTm in an aperture of 140 mm. The relevant  
 8060 parameters are summarized in Table 9.11 and the cross-section is illustrated in Figure 9.15.

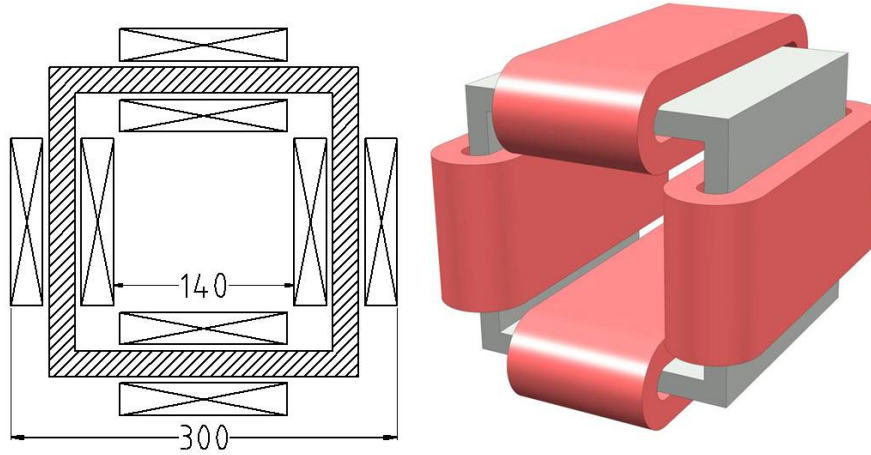


Figure 9.15: Combined function corrector magnets for the LR option.

Magnetic field	25	mT
Magnetic length	0.400	m
Yoke length	0.250	m
Total length	0.350	m
Free aperture	140 × 140	mm × mm
Mass	100	kg
Number of magnets (QD+QF)	37 + 37	
Current	40	A
Number of turns per circuit	2 × 100	
Current density	1.5	A/mm <sup>2</sup>
Conductor material	copper	
Magnet inductance per circuit	10	mH
Magnet resistance per circuit	0.1	Ω
Power per circuit	160	W
Cooling	air	

Table 9.11: Main parameters of combined function corrector magnets for the LR option.

## 8061 **9.3 Ring-Ring RF Design**

### 8062 **9.3.1 Design Parameters**

8063 The RF system parameters for the e-ring are listed in Table 9.12. For a beam energy of 60 GeV the  
8064 synchrotron losses are 437 MeV/turn. With a nominal beam current of 100 mA the rather significant  
8065 amount power of 47.3 MW is lost due to synchrotron radiation. For the voltages needed superconducting  
8066 RF is the only choice.

### 8067 **9.3.2 Cavities and klystrons**

#### 8068 **Cavity design**

8069 The most important issue determining the RF design is not so much in achieving high accelerating gradient  
8070 but rather the need to handle large powers through the power coupler. The choice of RF frequency is based  
8071 on relatively compact cavities which are able to handle the relatively high beam intensities and allowing  
8072 fitting of power couplers of sufficient dimensions to handle the RF power. A frequency in the range 600 to  
8073 800 MHz is the most appropriate. Cavities of frequency of 704 MHz are currently being developed at CERN  
8074 in the context of the study of a Superconducting Proton Linac (SPL) [703] [704] [705]. The same frequency  
8075 is also used at BNL for ERL cavities for the RHIC upgrade project [706]. Both cavities are 5-cell and can  
8076 achieve gradients greater than 20 MV/m. For the present study we take an RF frequency of 721.42 MHz,  
8077 which is compatible with the minimum 25 ns bunch spacing in the LHC. An RF voltage of 500 MV gives a  
8078 quantum lifetime of 50 hours; this is taken as the minimum operating voltage. An RF voltage of 560 MV  
8079 gives infinite quantum lifetime and a margin of 60 MV which permits feedback system voltage excursions  
8080 and provides tolerance to temporary failure of part of the RF system without beam loss.

8081 5-cell cavities would require too much RF power transferred through the power coupler, therefore we use  
8082 2-cell cavities here in keeping the cell shape. Then with a total of 112 cavities, the power per cavity supplied  
8083 to the beam to compensate the synchrotron radiation losses is 390 kW. This level of power handling is only  
8084 just reached for the power couplers of the larger 400 MHz cavities of the LHC. It is therefore proposed to use  
8085 two power couplers per cavity and split the power. In terms of voltage, only 5 MV per cavity is required to  
8086 make 560 MV, hence it is sufficient to use cavities with two cells instead of five. The resulting cavity active  
8087 length is 0.42 m and the gradient is 11.9 MV/m. Under these conditions the matched loaded Q is  $2.8 \cdot 10^5$ .  
8088 Over-coupling by 50 % to  $1.9 \cdot 10^5$  provides a stability margin and incurs relatively small power overhead.  
8089 Under this condition the average forward power through the coupler is just under 200 kW. This nevertheless  
8090 remains challenging for the design of power coupler.

#### 8091 **Cryomodule layout**

8092 With 8 cavities per cryomodule there are a total of 14 cryomodules. The estimated cryomodule length, scaled  
8093 from the 8 5-cell cavity of SPL to two cells per cavity is 10 m. There are 8 double cell cavities in 14 10m  
8094 cryomodules, the total RF cryomodule length is therefore 140 m, but space must be allowed for quadrupoles,  
8095 vacuum equipment and beam instrumentation. A total of 208 m is available in the by-passes: 124 m at CMS  
8096 and 2 x 42m at ATLAS. Eight cryomodules can therefore be installed in the CMS bypass and six, three on  
8097 each side, in the ATLAS by-passes. The distance between the modules can be taken as 3 m to allow space  
8098 for the other equipment. The positioning of the RF tunnels in the CMS and ATLAS bypasses is shown in  
8099 Figure 9.16.

#### 8100 **RF Power System**

8101 The configuration for powering the eight cavities within one cryomodule is shown in figure 9.17. Each  
8102 klystron feeds two cavities with power being split near the cavity to its two couplers. Taking two cavities  
8103 per klystron with an estimated 7 % losses in the waveguide system gives a mean required klystron output  
8104 power of 870 kW. A 15 % margin for the feedbacks gives a klystron rated power of 1 MW. The total number

Energy	GeV	60
Beam current	mA	100
Synchrotron losses	MeV/turn	437
Power loss to synchrotron radiation	MW	43.70
Bunch frequency (25 ns spacing)	MHz	40.08
Multiplying factor		18
RF frequency	MHz	721.42
Harmonic number		64152
RF Voltage for 50 hour quantum lifetime	MV	500.00
Nominal RF voltage (MV)	MV	560.00
Synchronous phase angle	degrees	129
Quantum lifetime at nominal RF voltage	hrs	infinite
Number of cavities		112
Number of 8-cavity cryomodules		14
Power couplers per cavity		2
Average RF power to beam per power coupler	kW	195
Voltage per cavity at nominal voltage	MV	5.00
Cells per cavity		2
Cavity active length	m	0.42
Cavity R/Q		114
Cavity Gradient	MV/m	11.90
Cavity loaded Q (Matched)		$2.8 \cdot 10^5$
Cavity forward power (nom. current, nom. voltage) for matched condition	kW	390
Nominal cavity loaded Q (matched for 50 % more beam)		$1.9 \cdot 10^5$
Cavity forward power (nominal current, voltage & loaded Q)	kW	406
Forward power per coupler	kW	203
Number of cavities per klystron		2
Waveguide losses	%	7
Klystron output power	kW	870
Feedbacks & detuning power margins	%	15
Klystron rated power	kW	1000
Total number of klystrons		56
Total average operating klystron RF power	MW	49
DC power to klystrons assuming 65% klystron efficiency	%	75
Grid power for RF, assuming 95% efficiency of power converters	MW	79

Table 9.12: RF system parameters for the electron ring.

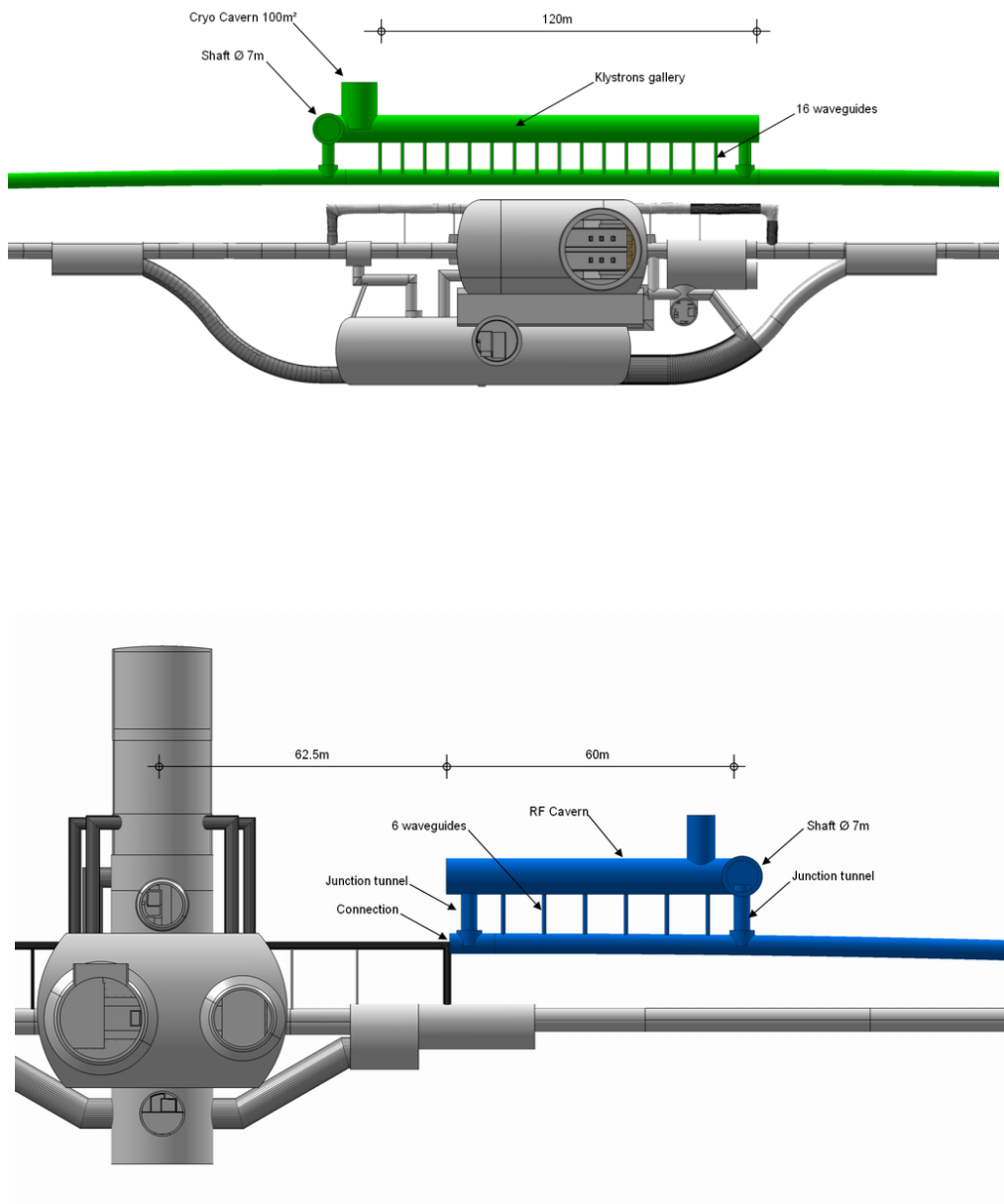


Figure 9.16: RF tunnel Layouts at CMS and ATLAS bypasses. Note only the right hand side at ATLAS shown.

8105 of klystrons is 56, delivering an average total RF power of 49 MW. Taking 65 % klystron efficiency and 95 %  
 8106 efficiency in the power converters gives roughly 79 MW grid power needed for the RF power system.

8107 **RF Power System Layout**

8108 The klystrons are installed in the additional tunnels parallel to the by-passes. An estimated surface area of  
 8109  $100\text{ m}^2$  is needed for the two klystrons, circulators, HV equipment and Low Level RF and controls racks for  
 8110 each 8 cavity module in adjacent RF gallery. This defines the tunnel width over the 13 m module interval  
 8111 (length + spacing) to be 8 m. Waveguide ducts are needed between the by-passes and the RF tunnels. With  
 8112 one waveguide per klystron into the tunnel, and two waveguides per duct, there are 16 ducts in the CMS  
 8113 tunnels, spaced roughly 6.5 m apart. At ATLAS there would be six ducts on either side with the same  
 8114 spacing. The required diameter of the duct tunnel is 90cm.

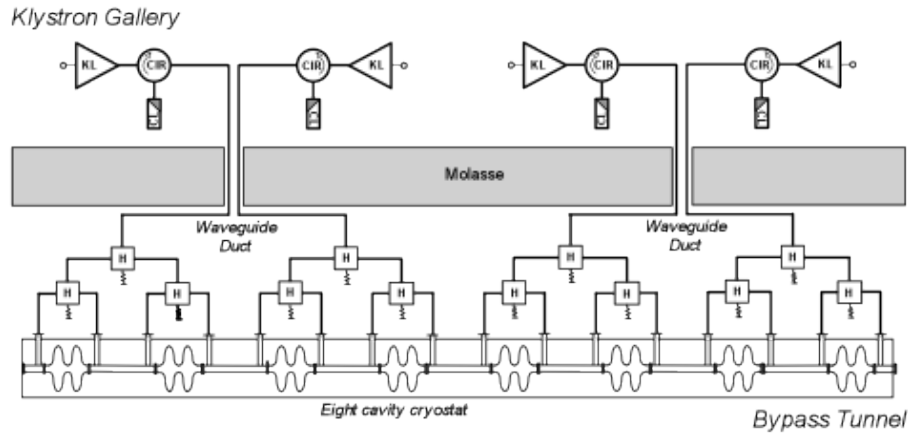


Figure 9.17: Layouts of RF power equipment in bypass and in RF gallery for one cryomodule.

8115 **Surface Installations**

8116 One HV Power Converter rated at 6 MVA is needed per 4 klystrons. These are housed in surface buildings:  
 8117 eight converters at CMS, and six at ATLAS.

8118 **Conclusions**

8119 721.4 MHz RF systems can be just fitted in the two bypasses nearest ATLAS and CMS. Detailed studies need  
 8120 to be done on the optimization of the cavity geometry for the high beam current and ensuring acceptable  
 8121 transverse impedance. The RF power system is large. Further work is needed on integration to exactly  
 8122 define tunnel and cavity cavern layouts and quantify the space requirements. Phased installation with  
 8123 gradual energy build-up, as was done for LEP, is an interesting possibility. The power needed for RF is  
 8124 79 MW. To this must be added power for RF controls, cryogenics and all other machine equipment.

8125 **9.4 Linac-Ring RF Design**

8126 **9.4.1 Design Parameters**

8127 The ERL design [707] [708] [709] is based on two 10 GeV linacs, with a 0.3 GeV injection energy and 6 linac  
 8128 passes to reach 60 GeV. This is shown in Figure 8.5.



Arc	Arc energy [GeV]	Energy loss per arc passage [MeV]	Number of passages	Beam current in arc [mA]	Total energy loss per arc [MeV]
6	60	751.3	1	6.6	751.3
5	50	362.3	2	13.2	724.6
4	40	148.4	2	13.2	296.8
3	30	47.0	2	13.2	94.0
2	20	9.3	2	13.2	18.6
1	10	0.6	2	13.2	1.2
		1319.9			1886.5

Table 9.13: Energy losses in the arcs on a half circle of 764 m radius

8129 The overall parameters are given in Table 8.1. With a beam current of 6.6 mA produced, there are  
8130 currents of nearly 20 mA in both directions in the linacs. Significant power, greater than the injection  
8131 energy, is lost in the passages though the arcs due to synchrotron radiation as shown in Table 9.13.

8132 The energy loss in the arcs can be compensated by independent RF systems operating at twice the normal  
8133 RF frequency. As proposed by [667, 710] it could be envisaged to let the main linacs replace the energy lost  
8134 to synchrotron radiation, i.e. the linacs had to supply about 0.75 GeV and 0.36 GeV, respectively, more  
8135 voltage (maximum energy loss per turn for arc 6 and 5, table 9.13). However, this scheme significantly  
8136 restricts operational freedom and is not tested yet. Therefore we keep it only as one possible option. For  
8137 the present report only the case for additional RF systems in the arcs compensating synchrotron radiation  
8138 losses is shown.

### 8139 Linac design

8140 High accelerating gradient is needed. First tests on cavities at similar frequency at BNL have already reached  
8141 20 MV at  $Q_0$  of  $2.5 \cdot 10^{10}$ . Improved cavity design and careful cavity processing should allow meeting the  
8142 specifications. The optimum number of cavities and the gradient is an overall compromise taking into account  
8143 cost, cryogenics consumption and operational reliability. The RF power system needs to compensate energy  
8144 loss and non-ideal energy recovery due to beam losses, phasing errors, transients, ponderomotive effects and  
8145 noise. It also needs to allow testing and processing of the cavities at full gradient without circulating beam.  
8146 The main RF parameters are given in Table 9.14, for the two cases described above.

8147 The linac RF design is based on 5-cell cavities operating at 721.42 MHz, this frequency being compatible  
8148 with 25 ns bunch spacing in LHC, as for the electron ring option. A gradient of 20 MV/m can be taken.  
8149 This is a conservative estimate based on SPL type cavities presently being developed, with a design aim of  
8150 25 MV/m. The unloaded Q ( $Q_0$ ) is taken as  $2.5 \cdot 10^{10}$ . This is presently a challenging figure, but recent  
8151 tests on cavities at this frequency for e-RHIC have been very encouraging. With an active cavity length of  
8152 1.04 m the voltage is 20.8 MV per cavity. This requires 960 cavities in total, or 480 cavities per linac. The  
8153 cavity external Q ( $Q_{ext}$ ) is derived from optimum coupling to the required beam power to compensate the 4  
8154 energy losses. It should be noted that the 300 MeV injection linac, with nearly 2 MW beam power will also  
8155 take grid power of between 3 and 4 MW.

## 8156 9.4.2 Layout and RF powering

### 8157 Cryomodule and RF power system layout

8158 With eight cavities in a cryomodule, there are 60. cryomodules per linac with a total linac length of 990 m.  
8159 This is summarized in table 9.15.

Parameter	Unit	Main RF system
Beam energy	GeV	60.0
Injection energy	GeV	0.3
Average beam current out	mA	6.6
Av. accelerated beam current in linacs	mA	19.8
Required total voltage in both linacs	GV	20.0
Energy recovery efficiency	%	96
Total power needed to compensate recovery losses	MW	15.8
RF frequency	MHz	721.42
Gradient	MV/m	20
Cells per cavity		5
Active cavity length	m	1.04
Cavity voltage	MV	20.8
Number of cavities		960
Energy gain per cycle	GeV	20
Power to compensate recovery losses per cavity	kW	16.5
Cavity R/Q	circuit $\Omega$	285
Cavity unloaded Q [ $Q_o$ ]	$10^{10}$	2.5
Loaded Q [ $Q_{ext}$ ]	$10^6$	46
Cavity forward power	kW	16.5
Cavity forward power - no beam	kW	4.1
Number of cavities per solid state amp.		1
Transmission losses	%	7
Amplifier output power per cavity	kW	17.6
Feedbacks power margin	%	15
Amplifier rated power	kW	21
Total number of amplifiers		960
Total average amplifier output power	MW	16.9
Assumed overall conversion efficiency grid to amplifier RF output	%	70
Grid power for linacs RF (without cryogenics power)	MW	24

Table 9.14: Linac RF parameters.

Parameter	Unit	Value
Number of cryomodules		60
Cavities per cryomodule		8
Number of cavities		480
Module length incl. bellows, vac. pumps, cold-warm transitions, BPM, $\frac{1}{2}$ quad	m	15.5
Linac length	m	990

Table 9.15: ERL cryomodule numbers and length.

## 8160 RF power system

8161 Assuming optimum coupling the forward power per cavity is approximately 16.5 kW. The available power  
8162 per cavity must be somewhat higher to allow margin for operation of RF the feedback systems; i.e. 21 kW.  
8163 These levels can certainly be achieved with solid state amplifiers, avoiding the need for high voltage power  
8164 supplies and associated protection equipment. The grid to RF conversion efficiency is also somewhat higher;  
8165 70 % can be taken. The total supplied average RF power is 17 MW and the grid power required for powering  
8166 of the linacs is 24 MW.

## 8167 RF Power system layout

8168 The RF amplifiers and RF feedback and controls racks are housed in a separate parallel powering gallery.  
8169 There is one RF amplifier per cavity, the power being fed by WR1150 standard waveguides, each 11.5 inches  
8170 by 5.75 inches (30 cm by 15 cm). The number of holes between the powering and linac tunnels can be limited  
8171 to one per four cavities, i.e. two per cryomodule, spaced 8 m apart giving 118 holes per linac. The diameter  
8172 is 90cm. The diameters could be reduced if half height waveguides or coax lines are used.

## 8173 9.4.3 Arc RF systems

8174 Table 9.13 shows the synchrotron radiation losses in the arcs; they are negligible in the 10 GeV arc. In the  
8175 20, 30, 40 and 50 GeV arc both the accelerated and decelerated beams pass the same arc RF system with  
8176  $180^\circ$  phase shift at the basic frequency of 721.42 MHz; hence to accelerate both beams, the arc RF system  
8177 is operated at twice the frequency, i.e. at 1442.82 MHz. The 60 GeV arc carries only the decelerated beam  
8178 and there one can use the linac RF cavities at 721.42 MHz. However, since here the required power per  
8179 cavity is much larger the solid state amplifiers of the main linac cannot be used but a klystron or IOT must  
8180 be applied. Overall parameters for these RF systems are given in Table 9.16.

8181 The arc systems provide very different voltages. Parameters for the individual systems are given in  
8182 table 9.17. Use of cavities and cryostats scaled to those in the linacs is assumed; however short cryostats  
8183 containing four cavities could be used in the 20 and 40 GeV arc systems. Powering would be by klystrons,  
8184 at 1442 MHz a total of 31 rated at a maximum of 360 kW with one klystron supplying two cavities and at  
8185 721 MHz 10 klystrons of 680 kW with one klystron supplying four cavities.

## 8186 9.5 Crab crossing for the LHeC

8187 Due to the very high electron beam energies in the LHeC and the associated interaction region design, the  
8188 emitted synchrotron radiation and the required RF power are challenging. The IR layout for the RR option  
8189 consists of a crossing angle to mitigate parasitic interactions and allows for a simple scheme to accommodate  
8190 the synchrotron radiation fan. A crab crossing scheme for the proton beam is highly desirable to recover the  
8191 geometric luminosity loss due to this crossing angle. Some issues associated with the complexity of the IR

Parameter	Unit	Value
Total energy loss in 20-60GeV arcs	MeV	1885.3
Power loss in 20-60GeV arcs	MW	12.4
Arc RF frequency	MHz	1442/721
Number of cavities	-	58/38
Number of klystrons	-	31/10
Total average supplied klystron RF power	MW	10.5
Assumed overall conversion efficiency - grid to klystrons RF out	%	60
Grid power for arc RF systems	MW	23

Table 9.16: Arc RF systems overall parameters.

Parameter	Unit	Arc 2	Arc 3	Arc 4	Arc 5	Arc 6	Totals
Arc energy	GeV	20	30	40	50	60	
Energy lost per arc passage	MeV	9.3	47.0	148.4	362.3	751.3	
Number of passes		2	2	2	2	1	
Total beam current in arc	mA	13.2	13.2	13.2	13.2	6.6	
Power loss in arc	MW	0.1	0.6	2.0	4.8	5.0	12.4
RF frequency 1442 MHz	MHz	x	x	x	x		
RF frequency 721 MHz	MHz					x	
Max. acc. gradient	MV/m	20.0	20.0	20.0	20.0	20.0	
Max. acc. voltage	MV	10.4	10.4	10.4	10.4	20.8	
Cavities at 1442 MHz		1	5	156	37		38
Cavities at 721 MHz						40	41
Required voltage/cavity	MV	9.6	8.1	9.6	9.6	19.0	
RF Power/cavity	kW	123	124	131	129	130	
Nominal RF power/cavity	kW	128	129	136	135	136	
Klystron output power per cavity	kW	137	138	146	144	145	
Kl. rated power/cavity	kW	160	160	170	170	170	
Cavities/klystron		2	2	2	2	4	
Klystron rated power	kW	320	320	340	340	780	
Klystrons at 1442 MHz		1	3	8	19	-	31
Klystrons at 721 MHz	-	-	-	-	-	10	10
Total average supplied klystron RF power	MW	0.1	0.5	1.7	4.0	4.2	10.5
Assumed overall conversion efficiency grid to klystrons total RF power	%	60	60	60	60	60	
Grid power arc RF systems	MW	0.2	1.2	3.6	8.9	9.2	23

Table 9.17: Parameters of the individual arc RF systems.

8192 design and the associated synchrotron radiation can be relaxed with the implementation of crab crossing near  
8193 the IR. A crab crossing scheme would also provide a natural knob for regulating the beam-beam parameter  
8194 if required. Although the linac-ring option plans to employ separation dipoles and mirrors for synchrotron  
8195 radiation, crab crossing can prove to be a simpler option if the technology is viable.

### 8196 9.5.1 Luminosity Reduction

8197 In the nominal LHC with proton-proton collision, the two beams share a common vacuum chamber for  
8198 approximately a 100m from the IP. Therefore, a crossing angle is required in the IRs to avoid parasitic inter-  
8199 actions. Consequently, the luminosity is reduced by a geometrical reduction factor which can be expressed  
8200 as

$$R = \frac{1}{\sqrt{1 - \Phi^2}} \quad (9.1)$$

8201 where  $\Phi = \sqrt{\theta\sigma_z/2\sigma_x}$  is the Piwinski parameter, which is proportional to ratio of the longitudinal and  
8202 transverse beam sizes in the plane of the crossing.

8203 Reducing  $\beta^*$  at a constant beam-to-beam separation in the IRs ( $\sim 10\sigma$ ), the luminosity reduction factor  
8204 can become quite significant. To compensate for this reduction from the crossing angle, a crab crossing  
8205 scheme is proposed and R&D is moving rapidly to realize the technology [711, 712].

8206 For the electron-proton collisions, the Piwinski parameter can be redefined as

$$\Phi_p = \frac{\theta_c}{2\sqrt{2}\sigma_x^*} \sqrt{\sigma_{z,p}^2 + \sigma_{z,e}^2} \quad (9.2)$$

8207 where  $\sigma_{z,p}$  and  $\sigma_{z,e}$  are the proton and electron bunch lengths. Table 9.18 lists the relevant parameters of  
the crossing schemes in the LHeC as compared to some other machines.

	KEK-B	LHC		LHeC		eRHIC
		Nominal	Upgrade	RR	LR	
$\theta_c$ [mrad]	22.0	0.285	0.4-0.6	1.0	0.0 (4.0)	0.0 (5.0)
$\sigma_z$ [cm]	0.7	7.55		7.55 (0.7 $\dagger$ )		20/1.2 $\dagger$
$\sigma_x^*$ [ $\mu\text{m}$ ]	103	16.6	11.2	30 (15.8*)	-	32
$\Phi$	0.75	0.64	1-1.4	0.9 (1.6*)	0.0	0.0 (11.0)

Table 9.18: Relevant parameters of the crossing schemes in the LHeC compared to LHC, KEK-B and eRHIC. Note  $\dagger$  corresponds to electrons and \* corresponds vertical plane.

8208

### 8209 9.5.2 Crossing Schemes

8210 Since the bunch length of the electrons are significantly smaller (at least factor 10) than that of the protons,  
8211 the geometrical overlap due to crossing angle is mainly dominated by the angle of the proton bunches. Four  
8212 different cases (see Fig. 9.18) were simulated to determine the luminosity gain in the different cases with  
8213 crab cavities and comparing it to the nominal case (see Table 9.19).

8214 The luminosity gains strongly depend on the choice of RF frequency as the reduction factor due to the  
8215 RF curvature at frequencies of interest (0.4-0.8 GHz) is non-negligible.

### 8216 9.5.3 RF Technology

8217 The required cavity voltage can be calculated using

$$V_{crab} = \frac{2cE_0 \tan(\theta_c/2) \sin(\mu_x/2)}{\omega_{RF} \sqrt{\beta_{crab}} \beta^* \cos(\psi_{cc \rightarrow ip}^x - \mu_x/2)} \quad (9.3)$$

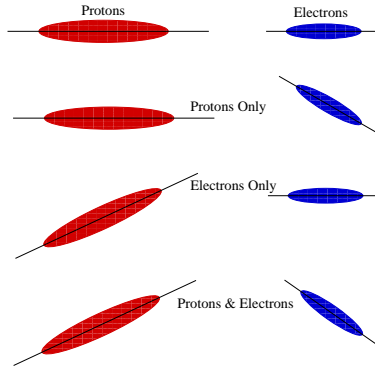


Figure 9.18: Schematic of different crossing schemes using crab cavities on either proton or electron beams as compared to the head-on collision. Top: Crabbing of both beams; Second from top: crabbing of the proton beam only; Third from top: crabbing of electron beam only; Bottom: no crabbing at all.

Scenario	L/L <sub>0</sub>	
	400 MHz	800 MHz
X-Angle (1 mrad)	1.0	
Uncross both $e^-$ and $p^+$	1.88%	1.48
Uncross only $e^-$	1.007	
Uncross only $p^+$	1.88	1.48

Table 9.19: Luminosity gains computed for different crossing schemes with crab cavities and a crossing angle of 1 mrad.

8218 where  $E_0$  is the beam energy,  $\omega_{RF}$  is the RF frequency of the cavity,  $\beta_{crab}$  and  $\beta^*$  are the beta-functions  
8219 at the cavity and the IP respectively,  $\psi_{cc \rightarrow ip}^x$  is the phase advance from the cavity to the IP and  $\mu_x$  is the  
8220 betatron tune. The nominal scenarios for both proton-proton and electron-proton IRs are anticipated to  
8221 have local crab crossing with two cavities per beam to create a local crab-bump within the IR. Since the  
8222  $\beta$ -functions are typically large in the location of the crab cavities, a voltage of approximately 20 MV should  
8223 suffice for crossing angles of approximately 1-2 mrad. The exact voltage will depend on the final interaction  
8224 region optics of both the proton and the electron beams.

8225 To accommodate the crab cavities within the IR region, deflecting structures with a compact footprint are  
8226 required. Conventional pill-box type elliptical cavities at frequencies of 400 MHz are too large to fit within  
8227 the LHC interaction region constraints. The effort to compress the cavity footprint recently resulted in  
8228 several TEM type deflecting mode geometries [712]. Apart from being significantly smaller than its elliptical  
8229 counterpart, the deflecting mode is the primary mode of the TEM type cavity, paving the way to a new class  
8230 of cavities at lower frequencies (400 MHz) which is preferred from the RF curvature point of view.

8231 Demonstration of a robust operation of such novel RF concepts with high deflecting gradients within the  
8232 LHC constraints is the prerequisite for exploiting the crab crossing concept for the LHeC IR design. R&D  
8233 on these novel concepts is already underway for the LHC upgrade. The issues of impedance, collimation and  
8234 machine protection are similar to that of the implementation of the proton-proton IRs.

## 9.6 Ring Ring option power converters

### 9.6.1 Overview

The LHeC Ring-Ring Collider option at 60 GeV with normal conducting magnets could be compared to LEP phase 1 (60 GeV) in particular for the main magnet (MB and MQs) circuits. The emergence of IGBT (new power semiconductors) in the 1990s has permitted the development of new power converter topologies and today the SCR power converters are replaced by switch mode power converters. Here, the possible topologies of power converters and the powering strategies for the main magnet circuits (MB and MQ) are presented. The last paragraph concerns infrastructure needs for LHeC Ring-Ring Collider power converters.

### 9.6.2 Powering considerations

The characteristics of power converters depend mainly on the electrical parameters of magnet circuits (e.g. R, L or current) and on operating mode of the accelerator (eg Einj/Ecoll or time need to reach collision energy): The LHeC Ring-Ring Collider option could be compared to LEP Phase 1 and the main parameters to define the power converters are similar:

1. Time constants of the magnet circuits are low ( $< 1$  s).
2. Time to reach collision energy is relatively long ( $> 1$  min) with the consequence that the inductive voltages of the circuits ( $L \cdot di/dt$ ) are low ( $< 10\%$  resistive voltage).
3. Currents in the circuits are below 1 kA and the voltages below 500 V, except for main magnet (MB and MQ) circuits.

### 9.6.3 Power converter topologies

Based on the assumptions mentioned in the preceding paragraph, the needs for the LHeC could be covered by three power converter families.

1. 1 quadrant ( $I > 0$  and  $V > 0$ ) high power ( $> 0.5$  MW) switch mode power converters for the main magnet circuits. Voltages and currents needed are achieved by putting sub-converters with maximum ratings of 800 A and 600 V in parallel and/or in series (see figure 9.19).

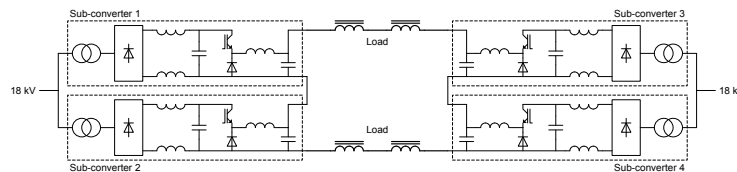


Figure 9.19: Possible topology for main magnet power converters To reduce harmonic currents sent to the CERN electrical network, the input diode rectifier could be replaced by active front-end rectifier.

2. 4 quadrant ( $I$  and  $V$  bidirectional) medium power ( $< 0.5$  MW) switch mode power converters for corrector circuits and insertion quadrupole circuits (see figure 9.20).
3. 4 quadrant low power ( $< 2$  kW) switch mode power converters for COD (see figure 9.21).

The advantages of switch mode power converters are mainly the following:

1. Better robustness against network disturbances.
2. No reactive power sent to the network.

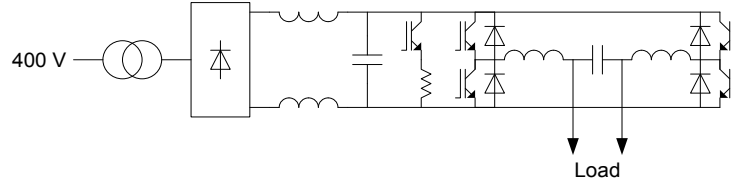


Figure 9.20: Possible topology for corrector power converters.

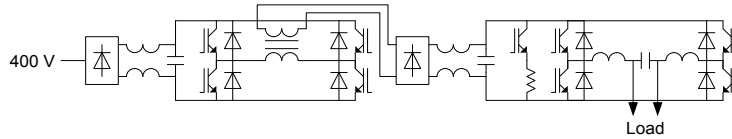


Figure 9.21: Possible topology for COD power converters.

8265 3. Small power converters.

8266 But the disadvantages are:

- 8267 1. EMI (Electro-Magnetic Interference) constraints are more significant, but experience with LHC power  
8268 converters has shown that solutions exist and can be easily implemented (shielding, earth connexions,  
8269 etc...).
- 8270 2. Lower MTBF (Mean Time Between Failures), but the loss of MTBF could be compensated by redun-  
8271 dancy strategies using additional sub-converters.

## 8272 9.6.4 Main power converters

### 8273 Main dipole power converters

8274 The Ring-Ring Collider option needs 3080 MB magnets and the characteristics of the circuit are given in  
8275 table 9.20.

Current [A]	1300
Number of magnets	3080
Total magnet inductance [H]	0.462
Total magnet resistance [ $\Omega$ ]	0.493
Total magnet voltage [V]	640
Total magnet consumption [MW]	0.832
Total magnet length [m]	16478
Total circuit length [m]	54000

Table 9.20: Electrical characteristics of MB circuit.

8276 If the coils of the MB magnets could be used to interconnect the magnet (see figure 9.22), 30 km of  
8277 DC cable can be saved and the output power of the MB converter can be reduced. For example, 54 km of  
8278 1500mm<sup>2</sup> DC cable (reasonable cable size for 1300 A) is about 0.6 $\Omega$  and would need the same power and  
8279 voltage as the magnets.

8280 Different strategies are possible to power the MB magnets: 1 or several independent circuits, as illustrated  
8281 in figure 9.23.





Figure 9.22: Different possibilities to connect the MB magnets.

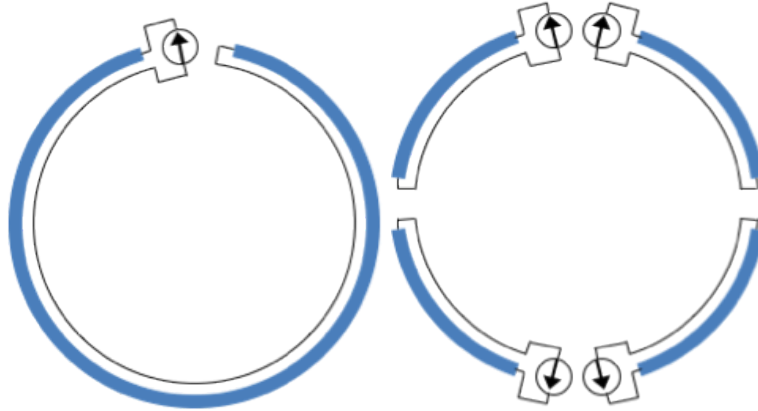


Figure 9.23: Different possibilities to power the MB magnets.

8282 In the case of a single main dipole circuit, to avoid a dipole moment, it is not possible to close the circuit  
 8283 directly by doing a single loop. The circuit must be closed by return path close to the magnets path. 4  
 8284 independent circuits solution seems to be the optimal solution:

- 8285 1. The total power is the same as that for the 1 circuit solution
- 8286 2. The voltage constraints for magnets are lower
- 8287 3. This solution allows different currents between sectors to compensate the SR energy losses.
- 8288 4. The LHC has shown that the current tracking between the different MB circuits is not an issue.

8289 To allow  $e^-$  and  $e^+$  physics, mechanical or semiconductor polarity switches will be needed at the output  
 8290 of the main dipole power converters (also for the MQ power converters).

### 8291 Main quadrupole power converters

8292 The Ring-Ring Collider option needs  $2 \times 368$  magnets for the MQD et MQF circuits and the characteristics  
 8293 of these circuits are given in table 9.21.

Current [A]	390
Number of magnets	$2 \times 368$
Total magnet inductance [H]	$2 \times 1.104$
Total magnet resistance [ $\Omega$ ]	$2 \times 5.888$
Total magnet voltage [V]	$2 \times 2300$
Total magnet consumption [MW]	$2 \times 0.900$
Total magnet length [m]	$2 \times 441.6$
Total circuit length [m]	$2 \times 27000$

Table 9.21: Electrical characteristics of MQ circuits.

8294 The length of the MQ circuits is mainly dominated by the DC cable length and in this case it is important  
8295 to optimise the MQ circuits to reduce power and voltage requested to supply the two MQ circuits (magnets  
8296 and DC cables). The actual MQ magnet design optimises the DC cable part of the circuits with low current,  
8297 but not the magnet part with high resistance magnets. High current in the MQ circuits is disadvantageous  
8298 for the magnet part but not for the DC cable part of the circuits. An optimum must be sought with a current  
8299 between 0.5 kA and 1.5 kA to reduce power and voltage needed to supply the circuits and also to reduce  
8300 the global cost, material and electricity. Two options are possible for supplying the MQ magnets, shown in  
8301 figure 9.24. Two independent circuits or several circuits with trim power converters. The advantages and  
8302 disadvantages of each option must be studied in detail before taking a final decision, but in both cases the  
8303 total power and cost of the powering system will be similar.

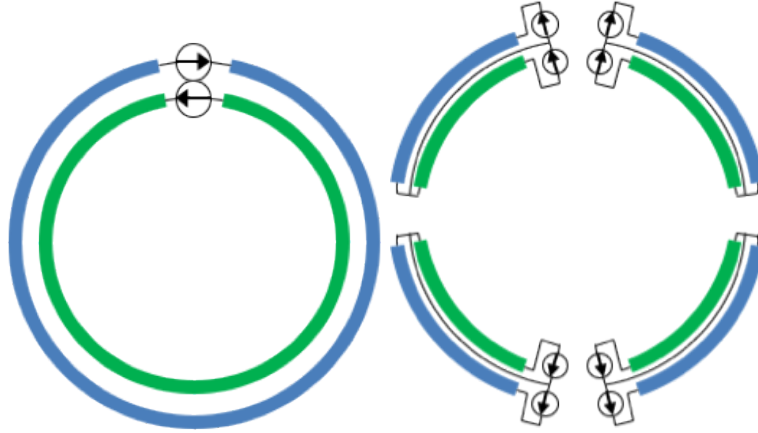


Figure 9.24: Different possibilities to power the MQ magnets.

### 8304 9.6.5 Insertion and by-pass quadrupole power converters

8305 The Ring-Ring option requires 97 QF magnets and 97 QD magnets in insertion and bypass regions. To  
8306 obtain flexibility for the beam setting, these magnets could be powered individually. In this case the main  
8307 characteristics of these circuits are given in table 9.22.

Current [A]	385
Number of magnets per circuit	1
Number of circuits	97 + 97
Magnet inductance (QD/QF) [H]	0.012/0.009
Magnet resistance (QD/QF) [ $\Omega$ ]	0.04/0.03
Magnet voltage [V]	15.4/11.55
PC output voltage [V]	30
PC power [kW]	15

Table 9.22: Electrical characteristics of IPQ circuits.

8308 To allow  $e^-$  and  $e^+$  physics, the insertion and bypass quadrupole power converters must be 4 quadrants  
8309 (second family of converter) to reverse the magnet currents when the physic type is changed. The use of  
8310 polarity switches to reverse the magnet currents would be too complex and too expensive for the 194 IPQ  
8311 (Individually Powered Quadrupole) circuits.

### 8312 **9.6.6 Power converter infrastructure**

8313 The magnets being resistive, there are no real advantages to install the power converters in the underground  
8314 facilities. In this case, it is better to install them at the surface. This solution simplifies power converter  
8315 operation and avoids possible issues with radiation. LEP infrastructure (buildings, shafts and AC network,  
8316 etc...) can be reused for LHeC. However, this solution must be confirmed by a detailed integration study. If  
8317 new infrastructure is needed for the power converters, it should be installed on the current CERN sites.

## 8318 **9.7 Linac-Ring option power converters**

### 8319 **9.7.1 Overview**

8320 The second option for the LHeC is a Linac-Ring accelerator with two 10 GeV Linacs and six recirculation  
8321 arcs allowing several passes of the beam in the two linacs to reach the final beam energy of 60 GeV. As for  
8322 the Ring-ring option, the needs for the Linac-Ring option could be covered by three IGBT power converter  
8323 families: 1 quadrant high power converters, 4 quadrant medium power converters and 4 quadrants low  
8324 power converters. Here, the different power converters of the linacs and recirculation arc main magnets are  
8325 described. The last paragraph concerns infrastructure needs for Linac-Ring LHeC power converters.

### 8326 **9.7.2 Powering considerations**

8327 The power converter study for the Linac-Ring option is based on the assumption that the power converters  
8328 are operated in DC. In this case the inductive voltage needed to ramp the current in the circuit can be  
8329 ignored to define the characteristics of power converters. As for the Ring-Ring option, the power converters  
8330 for the Linac-Ring option will be based on three IGBT power converter families:

- 8331 1. Family 1: 1 quadrant high power switch mode power converters for the main dipole and quadrupole  
8332 magnets of recirculation arcs. To reverse the current in the circuit for  $e^-$  or  $e^+$  physics, mechanical or  
8333 semiconductor polarity switches will be installed at the output of the power converters.
- 8334 2. Family 2: 4 quadrant medium power switch mode power converters for corrector circuits and individ-  
8335 ually powered dipole (IPD) and quadrupole (IPQ) circuits.
- 8336 3. Family 3: 4 quadrant low power switch mode power converters mainly for orbit corrector circuits.

### 8337 **9.7.3 Linac quadrupole and corrector power converters**

8338 Each linac is about 1.3 km long and contains 37 quadrupoles and 37 associated correctors.

#### 8339 **Linac quadrupole power converters**

8340 For the design of linac main quadrupole power converters (Family 2), the assumption is that the magnet  
8341 currents are similar (less than 10% of difference). In this case, two solutions are possible to power the  
8342 magnets:

- 8343 1. Power each quadrupole magnet independently.
- 8344 2. Power the quadrupole magnets in clusters of 4 magnets with TRIM power converters to allow different  
8345 currents in the magnets.

8346 The two powering options are shown in figure 9.25.

8347 Tables 9.23 and 9.24 give the main characteristics of the linac quadrupole circuits and power converters  
8348 for the both solutions.

8349 The second solution, with clusters of four magnets, saves a factor of two in the cost of power converters and  
8350 DC cables without a significant increase of the circuit complexity. In addition, the TRIM power converters  
8351 can be similar to those used for linac orbit corrector circuits.

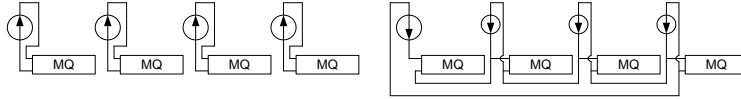


Figure 9.25: Different possibilities to power the linac quadrupoles magnets.

Circuit current [A]	500
Number of magnets per circuit	1
Number of circuits	37 + 37
Magnet inductance [H]	0.012
Magnet resistance [ $\Omega$ ]	0.024
DC cable section [mm <sup>2</sup> ]	500
Max. DC cable length [m]	1200
Max. DC cable resistance [ $\Omega$ ]	0.045
PC output voltage [V]	35
PC power [kW]	18

Table 9.23: Electrical characteristics of circuits for IPQ option.

Circuit Current [A]	500
Max. Nb. of magnets per circuit	4
Number of circuits	10 + 10
Magnet inductance [H]	0.012
Magnet resistance [ $\Omega$ ]	0.024
Main DC cable section [mm <sup>2</sup> ]	500
Trim DC cables section [mm <sup>2</sup> ]	50
Max. DC cable length [m]	1200
Max. main DC cable resistance [ $\Omega$ ]	0.045
Max. TRIM DC cable resistance [ $\Omega$ ]	0.45
Main PC output voltage [V]	75
Main PC output current [A]	500
Main PC output power [kW]	38
Trim PC output voltage [V]	40
Trim PC output current [A]	50
Trim PC output power [kW]	2

Table 9.24: Electrical characteristics of circuit for cluster option.

### 8352 Linac corrector power converters

8353 Each orbit corrector magnet of the linacs will be powered individually. The characteristics of the circuits  
8354 and power converters (family 3) are given in table 9.25.

Current [A]	40
Number of magnets per circuit	1
Number of circuits	37 + 37
Magnet inductance [H]	0.010
Magnet resistance [ $\Omega$ ]	0.1
DC cable section [mm <sup>2</sup> ]	50
Max. DC cable length [m]	1200
Max. DC cable resistance [ $\Omega$ ]	0.45
PC output voltage [V]	40
PC output current	50
PC power [kW]	2

Table 9.25: Electrical characteristics of linac COD.

### 8355 **9.7.4 Recirculation main power converters**

8356 6 recirculation arcs connect the two linacs together and allow several passes of the beam in the linacs to  
8357 reach the final energy of 60 GeV. Each recirculation arc has one main dipole circuit (MB) and four main  
8358 quadrupole circuits (MQ0, MQ1, MQ2 and MQ3).

#### 8359 **Main dipole power converters**

8360 All the main dipole magnets of the same recirculation arc are powered in series. The main characteristics of  
8361 the 6 main dipole power converters are described in table 9.26.

8362 To reduce the number of different types of power converter and simplify the LHeC operation, a modular  
8363 approach will be chosen with two types of sub converters: [400 A/100 V] for the first three power converters  
8364 and [750 A/200 V] for the last three converters. Desired PC output current is achieved by putting sub  
8365 converters in parallel.

#### 8366 **Main quadrupole power converters**

8367 Each recirculation arc has four MQ circuits with 60 magnets connected in series for each circuit, as shown  
8368 in table 9.27.

8369 As for the MB circuits, the MQ power converters will be composed of sub converters connected in series  
8370 to achieve the desired output voltage. For the first three recirculation arcs (10.5, 20.5 and 30.5 GeV), the  
8371 MQ power converters will be composed of [210 A/170 V] sub converters. For the other three recirculation  
8372 arcs, the sub converter ratings will be [420 A/680 V].

### 8373 **9.7.5 Power converter infrastructure**

8374 4 shafts are planned in the LHeC Linac-Ring option (see figure 9.26): Two at each end of the “TI2” linac  
8375 (points 3 and 4) and two at each third of ”outside” linac (point 1 and 2).

8376 For the power converter installation, a solution with 4 surface buildings is proposed:

- 8377 • Two small buildings in points 1 and 2 for the “outside” linac power converters.
- 8378 • Two large buildings in points 3 and 4 for the “TI2” linac power converters and the recirculation arcs.

8379 Concerning the two small buildings, the area required for the power converter installation is estimated  
8380 at 400 m<sup>2</sup> per building. The global AC consumption of the power converters is estimated at 0.5 MVA per  
8381 building. Each building must be equipped with a 100 kW air-conditioning system to extract the power

Number of MB circuits	6
Number of magnets per MB circuit	600
Total magnet inductance per MB circuit [H]	0.060
Total magnet resistance per MB circuit [ $\Omega$ ]	0.060
DC cable section [mm <sup>2</sup> ]	1000
DC cable length [m]	1600
DC cable resistance [ $\Omega$ ]	0.030
PC output current @10.5 GeV [A]	367
PC output voltage @10.5 GeV [V]	33
PC output current @20.5 GeV [A]	734
PC output voltage @20.5 GeV [V]	66
PC output current @30.5 GeV [A]	1100
PC output voltage @30.5 GeV [V]	99
PC output current @40.5 GeV [A]	1467
PC output voltage @40.5 GeV [V]	132
PC output current @50.5 GeV [A]	1834
PC output voltage @50.5 GeV [V]	165
PC output current @60.5 GeV [A]	2200
PC output voltage @60.5 GeV [V]	198

Table 9.26: Electrical characteristics of recirculation arc MB circuits.

8382 converter losses. Concerning the two large buildings, the area required for power converter installation is  
8383 estimated at 800 m<sup>2</sup> per building. In point 4 of LHeC (point 2 of LHC), a large part of SR2 is available for  
8384 LHeC power converters. Per building, the electric power requirements are estimated at 1 MVA and cooling  
8385 requirements at 200 kW.

### 8386 9.7.6 Conclusions on power converters

8387 From the power converter point of view, the two options of LHeC are similar. The power converter topologies  
8388 will be based on diode input rectifiers with IGBT legs. The converters can be classified into three main  
8389 families:

- 8390 • Family 1: 1 quadrant ( $I > 0$  and  $V > 0$ ) high power switch mode power converters for the main dipole  
8391 and quadrupole circuits.
- 8392 • Family 2: 4 quadrant ( $I$  and  $V > 0$  and  $< 0$ ) medium power switch mode power converters for the  
8393 correctors circuits and individual power dipole and quadrupole magnets.
- 8394 • Family 3: 4 quadrant and low power switch mode power converters mainly for the orbit corrector  
8395 magnets.

8396 When the option has been chosen for the LHeC (Ring-Ring or Linac-Ring) the next studies should focus  
8397 on the circuit definition and optimisation.

Number of MQ circuits	$6 \times 4$
Number of magnets per MQ circuit	60
Total magnet inductance per MQ circuit [H]	0.9/1.2
Total magnet resistance per MQ circuit [ $\Omega$ ]	1.8/2.4
DC cable section [mm <sup>2</sup> ]	500
DC cable length [m]	6000
DC cable resistance [ $\Omega$ ]	0.2
PC output current @10.5 GeV [A]	69
PC output voltage @10.5 GeV [V]	140/170
PC output current @20.5 GeV [A]	138
PC output voltage @20.5 GeV [V]	280/340
PC output current @30.5 GeV [A]	207
PC output voltage @30.5 GeV [V]	420/510
PC output current @40.5 GeV [A]	276
PC output voltage @40.5 GeV [V]	560/680
PC output current @50.5 GeV [A]	345
PC output voltage @50.5 GeV [V]	700/850
PC output current @60.5 GeV [A]	414
PC output voltage @60.5 GeV [V]	840/1020

Table 9.27: Electrical characteristics of recirculation arc MQ circuits.

## 9.8 Vacuum

### 9.8.1 Vacuum requirements

In particle accelerators, beams are traveling under vacuum to reduce beam-gas interactions i.e. the scattering of beam particles on the molecules of the residual gas. The beam-gas interaction is dominated by the bremsstrahlung on the nuclei of gas molecules and therefore depends on the partial pressure, the weight and the radiation length [g/cm<sup>2</sup>] of the gas species. In presence of a photon-stimulated desorption, the residual gas is dominated by hydrogen (75%) followed by CO/CO<sub>2</sub> (24%) and 1% CH<sub>4</sub>. Argon normally represents less than 1% of the residual gas if welding best practice for UHV applications is applied. It is to be noted that Argon is 67 times more harmful than hydrogen (H<sub>2</sub>); CO<sub>2</sub>, CO and N<sub>2</sub> are about 30 times worst than hydrogen and Methane is 10 times worst than hydrogen.

The beam-gas interactions are responsible for machine performance limitations such as reduction of beam lifetime (nuclear scattering), machine luminosity (multiple coulomb scattering), intensity limitation by pressure instabilities (ionization) and for positive beams only, electron (ionization) induced instabilities (beam blow up). The heat load induced by scattered protons and ions can also be an issue for the cryomagnets since local heat loads can lead to a magnet quench i.e. a transition from the superconducting to the normal state. The heavy gases are the most dangerous because of their higher ionization cross-sections. In the case of the LHeC, this limitation exists only in the experimental areas where the two beams travel in the same beam pipe. The beam-gas interactions can also increase the background to the detectors in the experimental areas (non-captured particles or nuclear cascade generated by the lost particles upstream the detectors) and the radiation dose rates in the accelerator tunnels. Thus, leading to material activation, dose rates to intervention crews, premature degradation of tunnel infrastructures like cables and electronics and finally higher probability of electronic single events induced by neutrons which can destroy the electronics in the tunnel but also in the service galleries.

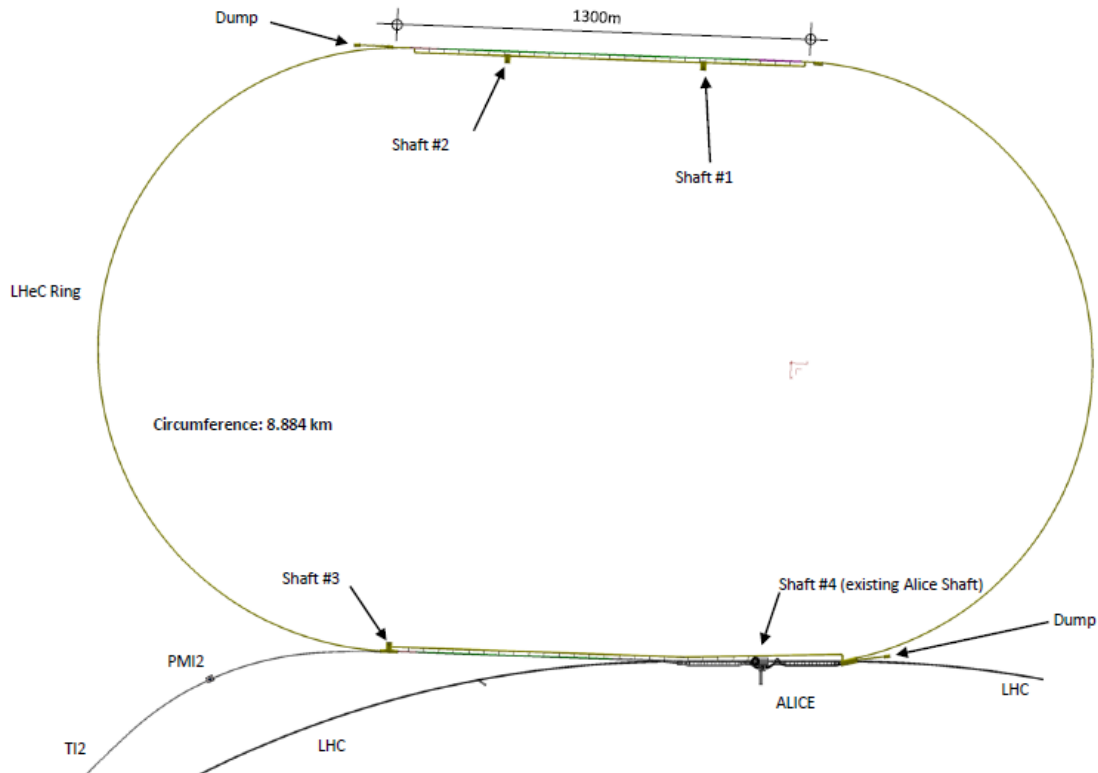


Figure 9.26: LHeC Linac Ring civil engineering.

8421 The design of the vacuum system is also driven by severe additional constraints which have to be consid-  
 8422 ered at the design stage since retrofitting mitigation solutions is often impossible or very expensive. Among  
 8423 them, the vacuum system has to be designed to minimise beam impedance and higher order modes (HOM)  
 8424 generation while optimising beam aperture in particular in the magnets. It has to provide also enough ports  
 8425 for the pumps and vacuum diagnostics. For accelerators with cryogenic magnets, the beampipe has to be  
 8426 designed to intercept heat loads induced by synchrotron radiation, energy loss by nuclear scattering, image  
 8427 currents, energy dissipated during the development of electron clouds, the later building up only in presence  
 8428 of positively charged beams.

8429 The integration of all these constraints often lead to a compromise in performances and in the case of  
 8430 the LHeC, the compromise will differ between the Linac-Ring and the Ring-Ring options.

## 8431 9.8.2 Synchrotron radiation

8432 The presence of a strong synchrotron radiation has two major implications for the vacuum system: it has  
 8433 to be designed to operate under the strong photon-induced stimulated desorption while being compatible  
 8434 with the significant heat loads onto the beampipes. In the common beampipe, the photo-electrons generated  
 8435 by the synchrotron radiation will dramatically enhance the electron cloud build-up and mitigation solutions  
 8436 shall be included at the design stage. Furthermore, experience with LEP has shown that the Compton  
 8437 scattering of the beam on photons coming from Blackbody radiation can have a significant effect on the  
 8438 beam lifetime [713] [714]. In the following analysis, we have neglected this effect, assuming that a technical  
 8439 solution can be found for keeping the beam vacuum chamber at sufficiently low temperatures. While this  
 8440 does not impose a principle problem to the vacuum system design, it still requires a detailed technical study  
 8441 for identifying a suitable solution for cooling the vacuum system in the presence of ca. 3 kW/m synchrotron



8442 radiation power.

### 8443 Synchrotron radiation power

8444 The synchrotron radiation power is an issue for the heat load deposited on the beam pipes and for its  
8445 evacuation and will be the driving factor for the mechanical engineering of the beam pipes. Indeed, the  
8446 heated surfaces will have a higher outgassing rates, the increase being exponentially dependent with the  
8447 surface temperature (factor 10 for a  $\Delta T = 50^\circ\text{C}$  increase). The synchrotron radiation power can be calculated  
8448 with equation 9.4. Since scaling linearly with the beam intensity,  $I$ , with the power of 4 for energy,  $E$ , and  
8449 inversely to power of 2 of the bending radius, the synchrotron radiation power in the Ring-Ring option is  
8450 expected to be 45 times higher than LEP and locally at the by-passes, the power can be about 180 times  
8451 higher. To be compared with the factor 10 expected in the bending and injection sections of the Linac-Ring  
8452 option.

$$P[\text{W/m}] = 1.24 \times 10^3 \frac{E^4 I}{\rho^2} \quad (9.4)$$

### 8453 Photon-induced desorption

8454 The desorption rate depends on critical energy of the synchrotron light,  $\epsilon_c$ , the energy which divides in two  
8455 the emitted power. For most materials, the desorption rates vary quasi linearly with the critical energy  
8456 (equation 9.5).

$$\epsilon_c(\text{eV}) = \frac{3 \cdot 10^{-7}}{R} \left( \frac{E_B}{E_0} \right)^3 \quad (9.5)$$

8457  $E_0 = 5.10^{-4}$  GeV for electrons,  $E_B$  is the energy of the beam and  $R$  the bending radius.

8458 For the LHeC, the beam energies will be equivalent to the LEP at start. Then, a similar value of the  
8459 critical energy can be assumed allowing the comparison with LEP pressure observations. Figure 9.27 shows  
8460 typical photo-desorption yields measured on copper and stainless steel samples. But the beam intensities  
8461 being by far larger, the linear photon flux which scales linearly (equation 3) with energy and intensity and  
8462 inversely with bending radius will increase significantly.

$$\Gamma[\text{photons/s/m}] = 7 \times 10^{19} \frac{EI}{\rho} \quad (9.6)$$

8463 For the Ring-Ring option (bending sections and by-passes), the linear photon flux is expected to be 45  
8464 times larger than in LEP, to be compared to the factor 5 expected for the Linac-Ring option.

8465 The photon stimulated pressure rise,  $\Delta P$ , depends linearly on the critical energy, on the beam energy and  
8466 beam intensity as shown by equation 9.7. The temperature affecting the dependence of the desorption yield  
8467 (equation 9.8 and 9.9),  $\eta$ , to the critical energy,  $\epsilon_c$  the pressure rises will differ between surfaces at ambient  
8468 temperature (equation 9.8) and at cryogenic temperature (equation 9.9).

$$\Delta P \propto \eta(\epsilon_c) EI \quad (9.7)$$

$$\text{at room temperature : } \eta \propto \epsilon_c \text{ and } \epsilon_c \propto E^3 \text{ such that } \Delta P \propto E^4 I \quad (9.8)$$

$$\text{at cryogenic temperature : } \eta \propto \epsilon_c^{2/3} \text{ and } \epsilon_c \propto E^3 \text{ such that } \Delta P \propto E^3 I \quad (9.9)$$

8469 Therefore, the photon stimulated pressure rise is expected to be 45 times higher than LEP for the Ring-  
8470 Ring option, to be compared with the factor 30 for the Linac-Ring option.

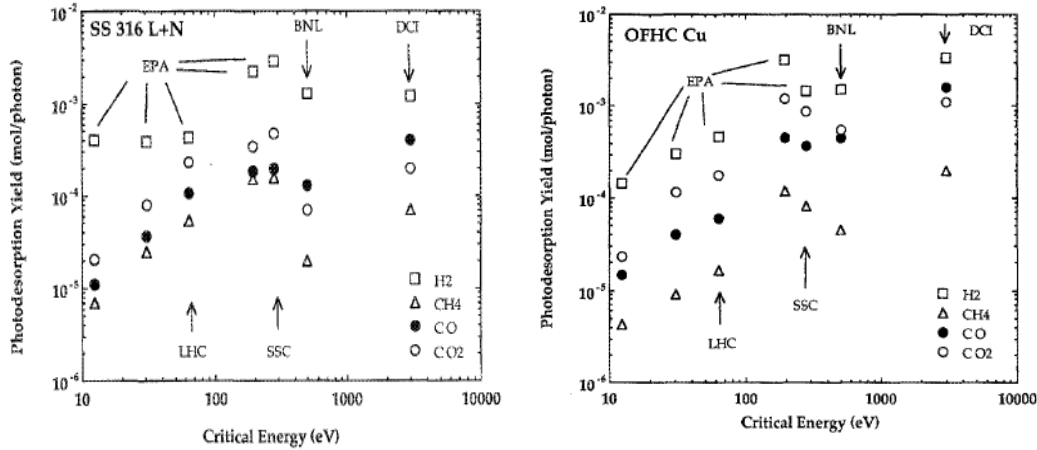


Figure 9.27: Photodesorption yields measured on copper and stainless steel surfaces. To be noted that the desorption yields of methane,  $\eta_{CH_4}$ , is 50 times lower than  $\eta_{H_2}$ .

### 8471 Vacuum cleaning and beam scrubbing

8472 The dynamic pressure i.e. the pressure while operating the accelerator with beams will be dominated by the  
 8473 beam-induced dynamic effects like stimulated desorption due to beam losses or synchrotron radiations or by  
 8474 electron stimulated desorption in case an electron cloud is building-up.

8475 In presence of synchrotron radiation, the vacuum cleaning process which characterises the reduction of  
 8476 the desorption yields ( $\eta$ ) of a surface resulting from the bombardment of the surface by electrons, photons  
 8477 or ions, significantly decreases the induced gas loads (3 – 4 orders of magnitude observed in LEP) improving  
 8478 the dynamic pressure at constant pumping speed. This results in a progressive increase of the beam lifetime.

8479 In presence of an electron cloud, the beam scrubbing which characterises the reduction of the secondary  
 8480 electron yield (SEY,  $\delta$ ) of a surface resulting from the bombardment of the surface by electrons, photons or  
 8481 ions, significantly decreases the induced gas loads (2 – 3 orders of magnitude observed in SPS) improving  
 8482 the dynamic pressure at constant pumping speed. Similarly to what happens with the vacuum cleaning, this  
 8483 results also in a progressive increase of the beam lifetime.

8484 By default and mainly driven by costs and integration issues, the vacuum system of an accelerator  
 8485 dominated by beam-induced dynamic effects is never designed to provide the nominal performances as from  
 8486 “day 1”. Indeed, vacuum cleaning and beam scrubbing are assumed to improve the beampipe surface  
 8487 characteristics while the beam intensity and beam energy are progressively increased during the first years  
 8488 of operation.

8489 This implies accepting a shorter beam lifetime or reduced beam current during the initial phase; about  
 8490 500 h of operation with beams were required for LEP to achieve the nominal performances. New technical  
 8491 developments such as Non-Evaporable Coatings (NEG) shall be considered since significantly decreasing the  
 8492 time required to achieve the nominal performances (Figures 9.28 and 9.29).

### 8493 9.8.3 Vacuum engineering issues

8494 The engineering of the vacuum system has to be integrated right from the beginning of the project. This  
 8495 becomes imperative for the Ring-Ring option since it has to take into account the constraints of the LHC and  
 8496 allow for future consolidations and upgrades. For the Linac-Ring option, the tangential injection and dump  
 8497 lines will be in common with the LHC beam vacuum over long distances. The experience has shown that  
 8498 the vacuum engineering shall proceed in parallel on the following topics: expertise provided to beam-related  
 8499 components (magnets, beam instrumentation, radio-frequency systems, etc.), engineering of vacuum related

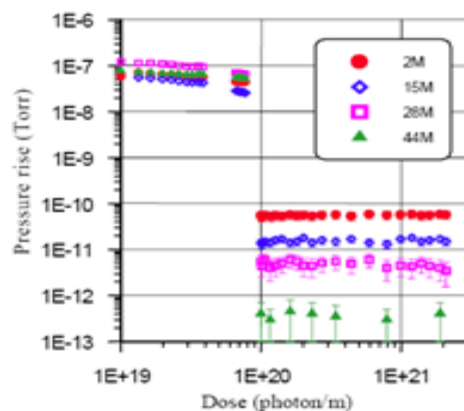
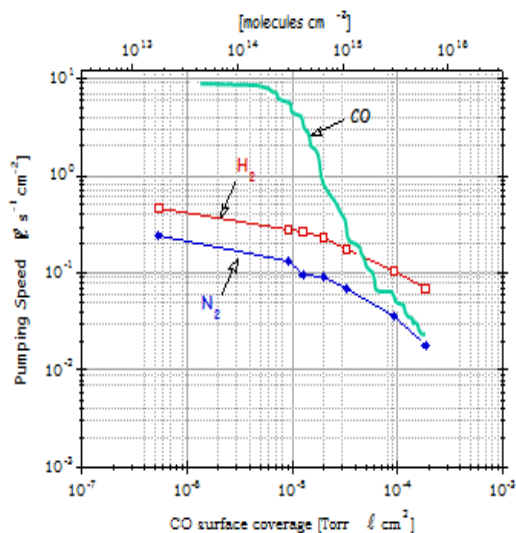
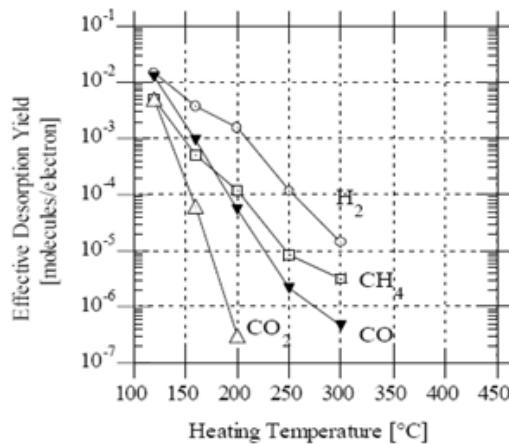


Figure 2: Pressure rise measured in the centre of the TiZrV coated test chamber before activation ( $<1 \cdot 10^{20}$  photons/m) and after activation ( $>1 \cdot 10^{20}$  photons/m).

Figure 9.28: NEG pumping speed for different gas species and pressure rises measured in presence of a photon flux before and after NEG activation.

Table 2: Summary of results from the activated test chamber

Gas	Sticking probability	Photodesorption yield (molecules/photon)
H <sub>2</sub>	~0.007	$\sim 1.5 \cdot 10^{-5}$
CH <sub>4</sub>	0	$2 \cdot 10^{-7}$
CO (28)	0.5	$< 1 \cdot 10^{-5}$
C <sub>x</sub> H <sub>y</sub> (28)	0	$< 3 \cdot 10^{-8}$
CO <sub>2</sub>	0.5	$< 2 \cdot 10^{-6}$



•C. Benvenuti et al. J.Vac Sci Technol A 16(1) 1998

Figure 9.29: Photon (left) and Electron (right) desorption yields.

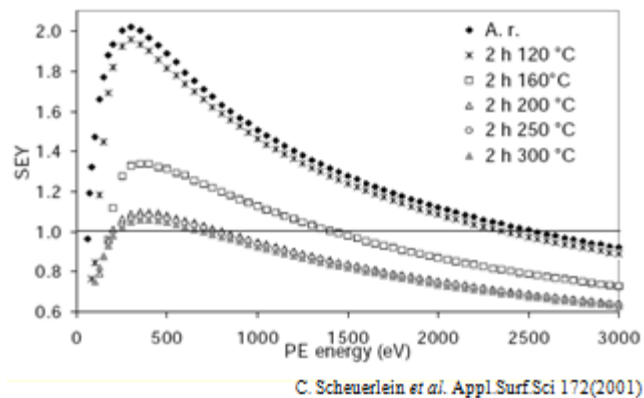


Figure 9.30: Reduction of the secondary electron yield (SEY,  $\delta$ ) by Photons a) and Electron b) desorption yields.

8500 components (beampipes, bellows, pumping ports, etc.) and machine integration including the cabling and  
 8501 the integration of the services.

8502 Basically, the vacuum system is designed to interconnect the beam related equipments installed on the  
 8503 beam line (magnets, kickers, RF cavities, beam absorbers, beam instrumentation, etc.) and to provide  
 8504 the adequate pumping speed and vacuum instrumentation. The vacuum components are often composed  
 8505 by vacuum pipes, interconnection bellows, diagnostics, pumping ports and sector valves. The number of  
 8506 pumps, vacuum diagnostics, bellows and ports will differ significantly between the two options discussed in  
 8507 this CDR and also between vacuum sectors of the same accelerator.

### 8508 Vacuum pumping

8509 The vacuum system of the LHeC will be mainly operated at ambient temperature. These systems rely more  
 8510 and more on NEG coatings since they provide a distributed pumping and huge pumping speed (Fig.2) and  
 8511 capacity and reduce the outgassing and desorption yields (Fig.3-4). These coatings are compatible with  
 8512 copper, aluminium and stainless steel beampipes. An alternative could be to use the LEP configuration  
 8513 with NEG strips. This alternative solution has only the advantage of avoiding the bake out constraints for  
 8514 the activation of the NEG coatings. A configuration of a distributed ion pumps is not considered since less  
 8515 performing and only applicable in dipole magnets i.e. bending sections. In any case, ion pumps are required  
 8516 as a complement of the NEG coatings to pump the noble gasses and methane to avoid the ion beam-induced  
 8517 instability. Sublimation pumps are not excluded in case of local huge outgassing rates, NEG cartridges being  
 8518 an interesting alternative since recent developments made by manufacturers include an ion pump and a NEG  
 8519 cartridge in the same body.

8520 The roughing from atmosphere down to the UHV range will be obtained using mobile turbo-molecular  
 8521 pumping stations. These pumps are dismantled prior to beam circulations.

8522 The part of the vacuum system operated at cryogenic temperature, if any, could rely on gas condensation if  
 8523 the operating temperatures are below 2 K. Additional cryosorbing material could be required if an important  
 8524 hydrogen gas load is expected. This issue still needs to be addressed. As made for the LHC, the parts at  
 8525 cryogenic temperature must be isolated from the NEG coated part by sector valves when not at their  
 8526 operating temperature to avoid the premature saturation of the NEG coatings.

8527 The pumping layout will be simpler for the Ring-Ring option since more space is available around the  
 8528 beam pipes. The tighter tolerances for the Linac-Ring option make the integration and pumping layout  
 8529 more delicate. However, the vacuum stability will be easier to ensure in the Linac-Ring option since only  
 8530 the bending sections are exposed to the synchrotron radiation.

## 8531 Vacuum Diagnostics

8532 For both options, the radiation level expected will be too high to use pressure sensors with onboard electron-  
8533 ics. Therefore, passive gauges shall be used, inducing additional cabling costs and need for gauge controllers.

## 8534 Vacuum Sectorisation

8535 The sectorisation of the beam vacuum system results from the integration of various constraints, the major  
8536 being: venting and bake-out requirements, conditioning requirements (RF and HV devices), protection  
8537 of fragile and complex systems (experimental areas and ceramic chambers), decoupling of vacuum parts at  
8538 room temperature from upstream and downstream parts at cryogenic temperature thus non-baked, radiation  
8539 issues, etc.

8540 For UHV beam vacuum systems, all-metal gate valves shall be preferred in order to allow for bake-out at  
8541 temperature above 250°C. VITON-sealed valves even though the VITON has been submitted to a special  
8542 treatment are not recommended nearby NEG coatings or NEG pumps since minor outgassing of Fluor will  
8543 degrade the pump characteristics.

8544 In the injection and extraction regions, the installation of the sector valves will lead to integration issues  
8545 since the space left between the beampipes with a tangential injection/extraction and the circulating beams  
8546 is often limited. This could result in a long common beam vacuum which implies that the LHC beam vacuum  
8547 requirements will apply to the LHeC part shared with LHC.

## 8548 Vacuum protection

8549 The distribution of the vacuum sector valves will be made in order to provide the maximum protection to  
8550 the beam vacuum in case of failure (leak provoked or not). Interlocking the sector valves is not an obvious  
8551 task. Indeed, increasing the number of sensors will provide more pressure indications but often results in  
8552 a degradation of the overall reliability. The protection at closure (pressure rise, leaks) is treated differently  
8553 from the protection while recovering from a technical stop with parts of the accelerator beampipe vented or  
8554 being pumped down.

8555 The vacuum protections of the common beampipes between LHeC and LHC shall fulfill the strong LHC  
8556 requirements. Indeed, any failure in the LHeC propagating to the LHC could lead to long machine downtime  
8557 (several months) in case of an accidental venting of an LHC beam vacuum sector.

## 8558 HOM and Impedance implications

8559 The generation and trapping of higher order mode (HOM) resulting from the changes in beampipe cross-  
8560 sections are severe issues for high intensity electron machines. Thus, the engineering design of LHeC must  
8561 be inspired on new generation of synchrotron radiation light sources instead of the simple LEP design. All  
8562 bellows and gaps shall be equipped with optimised RF fingers, designed to avoid sparking resulting from bad  
8563 electrical continuity. Indeed, these effects could induce pressure rises and machine performance limitations.

## 8564 Bake-out of vacuum system

8565 An operating pressure in the UHV range ( $10^{-10}$  Pa) will be required for both options. This implies the use  
8566 of a fully baked-out beam vacuum system. Two options are possible: permanent and dismountable bake out.  
8567 The permanent solution could be an option for the Linac-Ring but has to be excluded for the Ring-Ring  
8568 option for cost reasons. As done for the dipole chambers (bending sections) of LEP, hot pressurised water can  
8569 be used but the limit at 150°C is a constraint for the activation of NEG coatings. Developments are being  
8570 carried on at CERN to lower the activation temperature from 180°C down to 150°C but this technology is  
8571 not yet available.

8572 **Shielding issues**

8573 The synchrotron radiation power is an engineering challenge for the beam pipes. Indeed, 50% of the radiation  
8574 power hitting the vacuum chamber is absorbed in the beam pipe chamber (case of LEP aluminum chamber).  
8575 The remainder 50%, mainly the high-energy part of the spectrum, escapes into the tunnel and creates severe  
8576 problems like degradation of organic material and electronics due to high dose rates and formation of ozone  
8577 and nitric acid could lead to severe corrosion problems in particular with aluminum and copper materials.

8578 In this respect, the Ring-Ring option is less favorable since the synchrotron radiation will be localized at  
8579 the plane of the existing LHC cable trays and electrical distribution boxes in the tunnel. Similar constraints  
8580 exist also for the Linac-Ring option but these zones are localized at the bending sections of the LHeC.

8581 Detailed calculations are still to be carried on but based on LEP design, a lead shielding of 3 to 8 mm  
8582 soldered directly on the vacuum chamber would be required for 70 GeV beams. Higher energies could require  
8583 more thickness. The evacuation of the synchrotron radiation induced heat load on the beam pipe wall and  
8584 on lead shielding is a critical issue which needs to be studied. In case of insufficient heat propagation and  
8585 cooling, the lead will get melted as observed in LEP in the injection areas. The material fatigue shall also  
8586 be investigated since running at much higher beam current as compared to LEP, will increase the induced  
8587 stress to the material and welds of the beampipes.

8588 As made in LEP, the best compromise to fulfill the above mentioned constraints is the use of aluminum  
8589 beam pipes, covered by a lead shielding layer. The complex beam pipe cross-section required to optimize  
8590 the water cooling of the beam pipe and shielding is feasible by extrusion of aluminum billets and the costs  
8591 are acceptable for large productions. The large heat conductivity helps also the heat exchange. However,  
8592 extruded aluminum beam pipes induce limitations for the maximum bake out temperature and therefore  
8593 for the NEG coatings activation. Special grades of aluminum shall be used. The reliability of vacuum  
8594 interconnections based on aluminum flanges is a concern at high temperature ( $>150^{\circ}\text{C}$ ) and corrosion issues  
8595 shall be addressed. The stainless steel beam pipes do not have these limitations but they have poorer heat  
8596 conductivity and they are more difficult and costly to machine and shape.

8597 The LEP 110 GeV operation has shown the criticality of unexpected synchrotron radiations heating  
8598 vacuum components and in particular the vacuum connections between pipes or equipments. Indeed, the  
8599 flanges, by “offering” a thick path, are behaving as photon absorbers and heat up very quickly. Hence, at  
8600 cool down and due to the differential dilatation, leaks are opening. In LEP, these unexpected SR induced  
8601 heat loads resulted from orbit displacement in quadrupoles during the ramp in energy and of the use of the  
8602 wigglers also during the ramp. In LHeC, resulting from the much higher beam current, these issues shall be  
8603 carefully studied.

8604 **Corrosion issues**

8605 In vacuum systems, feedthroughs and bellows are particularly exposed to corrosion. The feedthroughs,  
8606 particularly those of the ion pumps where high voltage is permanently present, are critical parts. A demon-  
8607 strated and cheap solution to prevent the risk of corrosion consists in heating directly the protective cover  
8608 to reduce the relative humidity around the feedthrough.

8609 The bellows are critical due to their thickness, often between 0.1 – 0.15 mm. PVC material must be  
8610 prohibited in the tunnel. Indeed, in presence of radiations, it can generate hydrochloric acid (HCl) which  
8611 corrodes stainless steel materials. This corrosion has the particularity to be strongly penetrating, once seen  
8612 at the surface, it is often too late to mitigate the effects. Aluminum bellows are exposed to corrosion by  
8613 nitric acid ( $\text{HNO}_3$ ) which is generated by the combination of  $\text{O}_3$  and  $\text{NO}$ .

8614 Humidity is the driving factor and shall be kept 50%. However, in the long term, accidental spillage can  
8615 compromise locally the conditions and therefore, corrosion-resistant design are strongly recommended.

## 9.9 Beam Pipe Design

### 9.9.1 Requirements

The vacuum system inside the experimental sector has a number of different and sometimes conflicting requirements. Firstly, it must allow normal operation of the LHC with two circulating beams in the chamber. This implies conformity with aperture, impedance, RF, machine protection as well as dynamic vacuum requirements. The addition of the incoming electron beam adds constraints in terms of geometry for the associated synchrotron radiation (SR) fan and the addition of SR masks in the vacuum. Finally, optimization of the surrounding detector for high acceptance running means that all materials for chambers, instrumentation and supports must be optimized for transparency to particles and the central chamber must be as small and well aligned as possible to allow detectors to approach the beam aperture limit at the interaction point.

### 9.9.2 Choice of Materials for beampipes

LHC machine requirements imply an inner beam pipe wall that has low impedance (good electrical conductivity) along with low desorption yields for beam stimulated emissions and resistance to radiation damage.

Ideal materials for transparency to particles have low radiation length ( $Z$ ) and hence low atomic mass. These materials either have poor (i.e. high) desorption yields (eg. aluminum, beryllium) or are not vacuum and impedance compatible (eg. carbon). Solutions to this problem typically include thin film coatings to improve desorption yields and composite structures to combine good mechanical properties with vacuum and electrical properties.

The LHC experimental vacuum systems, along with most other colliders currently use metallic beryllium vacuum chambers around the interaction points due to a very favourable combination of  $Z$ , electrical conductivity, vacuum tightness, radiation resistance, plus mechanical stiffness and strength. High desorption yields are suppressed by a thin film TiNiV non-evaporable getter (NEG) coating. This coating also gives a high distributed vacuum pumping speed, allowing long, small aperture vacuum chambers to be used that would otherwise be conductance-limited. Activation of this coating requires periodic heating of the chamber to  $180-220^\circ\text{C}$  under vacuum for a few hours. This means that the chamber and environment must be designed for these temperatures. This activation is scheduled in annual LHC shutdowns. Long-term development is in progress for low desorption yield coatings that do not require high temperature activation [715]. These may have applications for LHeC.

Production technology developed for the LHC uses beryllium sections machined from hot-pressed blocks and electron beam welded to produce chambers. This has the advantage that a wide range of vacuum chamber forms can be manufactured. Cylindrical and conical chamber sections are installed in the LHC experiments.

Disadvantages of beryllium include high cost, fragility and toxicity in the powder form, as well as limited availability. For this reason, long-term development of other technologies for experimental beam pipes is under way at CERN which may yield applications for LHeC.

Composite beam pipe structures made from carbon and other low- $Z$  materials have been developed for colliders. These typically use a thin inner membrane to comply with vacuum and impedance requirements. Composite structure pipes were eventually rejected for LHC application for reasons of temperature and radiation resistance and the risk of de-lamination due to mismatch of thermal expansion coefficients. Lower luminosity in LHeC experiments combined with new low temperature coatings may allow these materials to be re-evaluated.

### 9.9.3 Beampipe Geometries

The proposed geometry has a cross section composed of a half-circle intersecting with a half-ellipse. Cylindrical cross-sections under external pressure fail by elastic instability (buckling) whereas elliptical sections can (depending on the geometry) fail by plastic collapse (yielding).

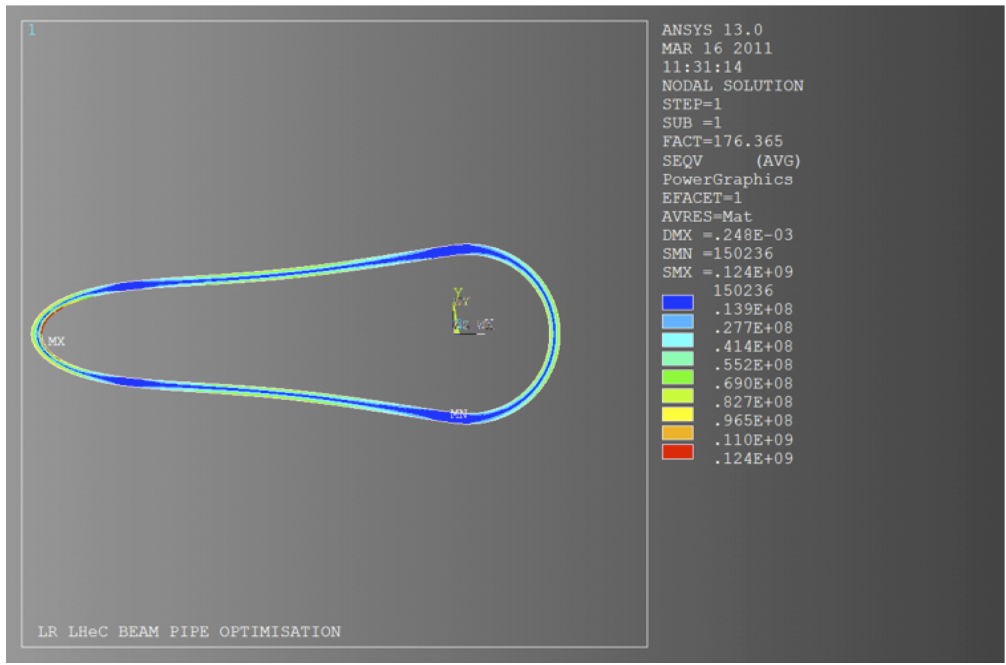


Figure 9.31: Section through the LR geometry showing contours of Von Mises equivalent stress (Pa).

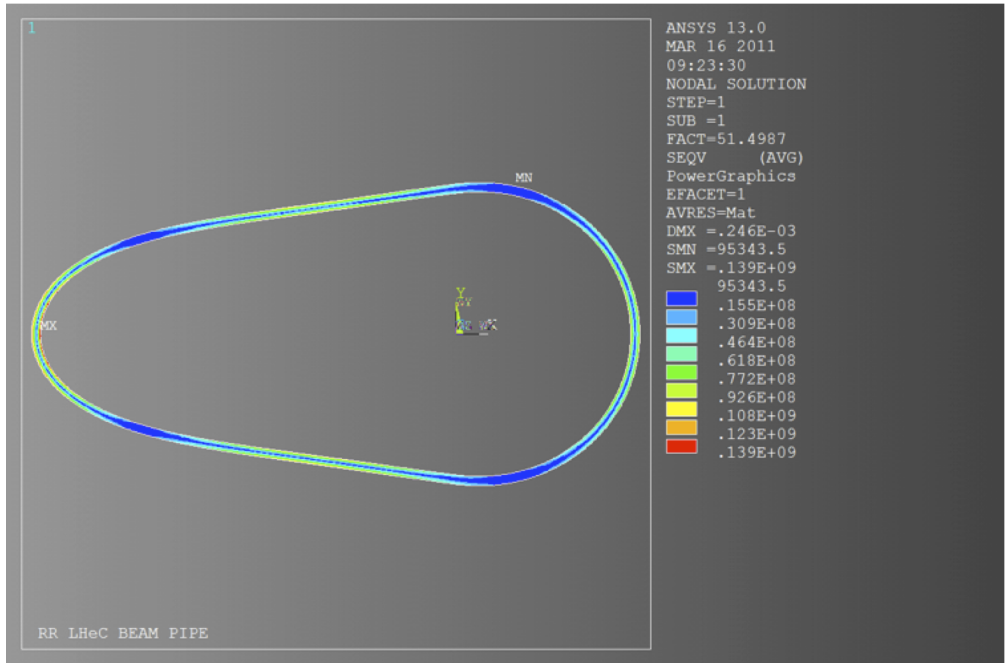


Figure 9.32: Section through the RR geometry showing contours of Von Mises equivalent stress (Pa).



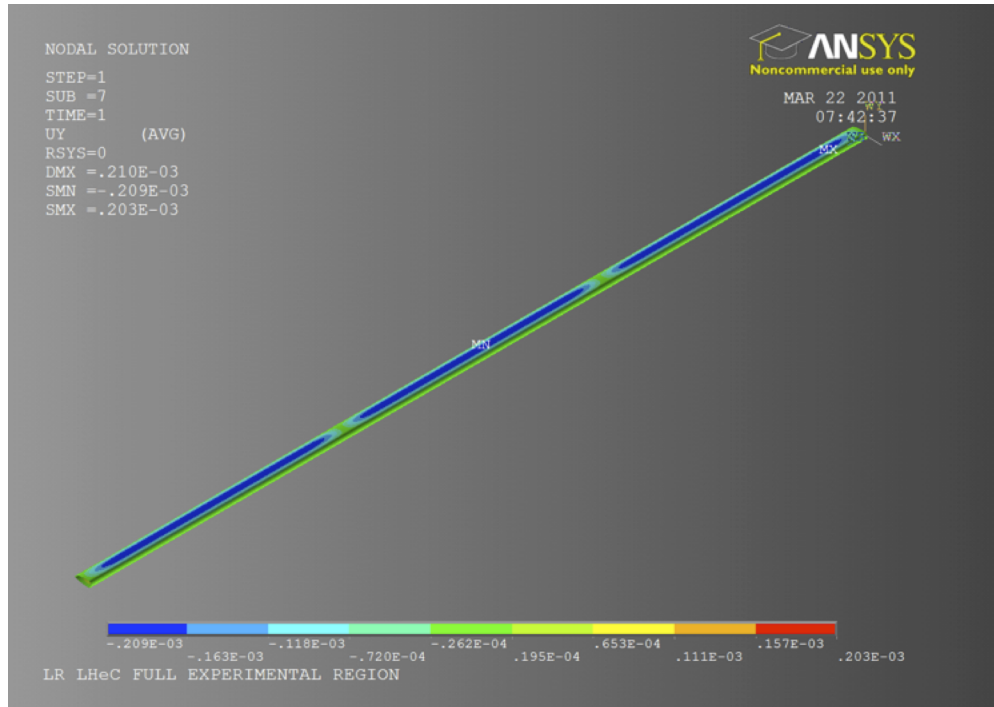


Figure 9.33: 3-D view of the LR geometry showing contours of bending displacement [m].

8662 Figure 9.31 and 9.32 show optimizations of the proposed geometries for the LINAC-Ring (LR) and Ring-  
 8663 Ring (RR) beam pipes assuming a long chamber of constant cross section made from beryllium metal.  
 8664 Preliminary analyses have been performed using the ANSYS finite element code. The wall thickness was  
 8665 minimized for the criteria of yield strength and buckling load multiplier. The LR geometry considered has  
 8666 a circular section radius of 22 mm and elliptical major radius of 100 mm. The RR geometry has a circular  
 8667 section radius of 22 mm and elliptical major radius of 55 mm. This preliminary analysis suggests that a  
 8668 constant wall thickness of 2.5 – 3 mm for the LR and 1.3 to 1.5 mm for the RR would be sufficient to resist  
 8669 the external pressure. Failure for both of these sections would be expected to occur by plastic collapse.

8670 At this stage of the project, these geometries represent the most optimized forms that fulfill the LHC  
 8671 machine requirements. However, for 1 degree tracks this corresponds to  $X/X_0 \approx 21\text{-}25\%$  for the LR and  
 8672  $\approx 41\text{-}49\%$  for the RR designs. This suggests that additional effort must be put into beam pipe geometries  
 8673 optimized for low angles. Composite beam pipe concepts suggested for machines such as the LEP [716]  
 8674 should be re-considered in the light of advances in lightweight materials and production techniques.

8675 The optimized section of the experimental chamber is 6.1 m in length. This length will require a number of  
 8676 optimized supports. These supports function to reduce bending deflection and stresses to within acceptable  
 8677 limits and to control the natural frequency of chamber vibration. The non-symmetric geometry will lead to  
 8678 a torsional stress component between supports which must be considered in their design. Figure 9.33 shows  
 8679 a preliminary analysis of bending displacement for the LR chamber geometry. With 2 intermediate supports  
 8680 the maximum calculated displacement (without bakeout equipment) is 0.21 mm.

#### 8681 9.9.4 Vacuum Instrumentation

8682 If, as assumed, this chamber is coated with a NEG film on the inner surfaces, then a high pumping speed of  
 8683 chemically active gasses will be available. Additional lumped pumps will be required for non-gettered gasses  
 8684 such as  $CH_4$  and noble gasses; however, outgassing rates for these gasses are typically very low.

8685 The vacuum sector containing the experiment will be delimited from the adjacent machine by sector  
8686 valves. These will be used to allow independent commissioning of machine and experiment vacuum. The  
8687 experimental vacuum sector will require pressure gauges covering the whole range from atmospheric to UHV,  
8688 these are used both for monitoring the pressure in the experimental chamber and as interlocks for the machine  
8689 control system.

### 8690 **9.9.5 Synchrotron Radiation Masks**

8691 LHeC experimental sector will require a moveable SR mask upstream of the interaction. From the vacuum  
8692 perspective, this implies a system for motion separated from atmosphere by UHV bellows. The SR flux on  
8693 the mask will generate a gas load that should be removed by a local pumping system dedicated to the mask.  
8694 As the load due to thermally stimulated desorption increases exponentially with the temperature, cooling  
8695 may be required. However, cooling the mask would significantly complicate the vacuum system design. The  
8696 generation of photo-electrons must also be avoided since these photo-electrons can interact with the proton  
8697 beam and lead to an electron cloud build-up.

### 8698 **9.9.6 Installation and Integration**

8699 The installation of the vacuum system is closely linked to the detector closure sequence. Therefore, the  
8700 design has to be validated in advance to prevent integration issues which would lead to significant delay  
8701 and increase of costs. Temporary supports and protections are required at each stage of the installation.  
8702 Indeed, as compared to the size of the detectors, the beam pipe are small, fragile and need to be permanently  
8703 supported and protected while moving the detector components. Leak tightness and bake-out testing are  
8704 compulsory at each step of the installation since all vacuum systems are subsequently enclosed in the detector,  
8705 preventing any access or repair. Their reliability is therefore critical. Precise survey procedures must also  
8706 be developed and incorporated in the beam pipe design to minimize the mechanical component of the beam  
8707 aperture requirement. Engineering solutions for bake out also has to be studied in details since the equipment  
8708 (heaters, probes and cables) must fit within the limited space available between beam pipes and the detector  
8709 components.

## 9.10 Cryogenics

### 9.10.1 Ring-Ring Cryogenics Design

#### Introduction

The Ring-Ring version foresees the 60 GeV accelerator to be installed in the existing LHC tunnel. Acceleration of the particles is done with 0.42 m long 5 MV superconducting (SC) cavities housed in fourteen 10 m long cryomodules. They will be placed at two opposite locations in by-passes of point 1 (ATLAS) and, point 5 (CMS). While at CMS a continuous straight by-pass can be built, at ATLAS two straight sections are conceived on each side of the detector cavern (“left” and “right”) with a connecting beam pipe crossing the detector hall. Lay-outs and detailed RF description see Chapter 9.3. The three separate cryomodules locations require three dedicated 2 K cryo-systems. Injection to the Ring at 10 GeV is done with a 1.3 GHz pulsed three-pass re-circulating high field injector. A dedicated cryoplant provides 2 K cooling of its SC cavities. In total four independent cryoplants with their respective distribution systems are needed for the Ring-Ring version. For the LHeC detector the high gradient focusing insertion magnets will be SC and housed in LHC dipole type cryostats. The cooling principle is the same as for LHC dipoles and, the existing cryogenic infrastructure can be used with comparatively small adaptations of the feed boxes. More detailed engineering studies are beyond the scope of this report. This chapter describes the cryosystems of the e-Ring accelerator and the related injector.

#### Ring-Ring cryogenics

The cavities operate at 2 K superfluid helium temperatures and dissipate an estimated 4 W per cavity at 5 MV. The 8-cavity cryomodule has three temperature levels; a 2 K saturated bath containing the cavities, a 5 – 8 K combined thermal shield and heat intercept for couplers and other equipment and, a 40 – 80 K thermal shield. The thermal loss estimates are listed in Table 9.28 . With efficiencies of modern state of the art cryoplants reaching 1/COP values of 1000 W/W at 2 K, 250 W/W at 5 K and 20 W/W at 40 – 80 K the minimum plant powers are calculated. To the equivalent cooling power at 4.5 K we add a 50% contingency for the distribution system with transfer lines running parallel to the cryomodules. In Table 9.29 the equivalent cooling powers of the three cryoplants are given.

Temperature (K)	2	5 – 8	40 – 80
One cryomodule			
Static loss (W)	5	15	100
Dynamic loss (W)	32	15	80
Sum (W)	37	30	180
8 modules (CMS site) (W)	296	240	1440(2160)
3 modules (ATLAS left) (W)	111	90	720(1080)
3 modules (ATLAS right) (W)	111	90	720(1080)

Table 9.28: Thermal loss estimate of cryomodules. In brackets the values with ultimate thermal losses (50% contingency) which are taken into account for the cryoplant sizing.

At CMS site a dedicated 3 kW @ 4.2 K cryoplant is needed. Except for some general infrastructure equipment like e.g. gas tanks it will be separated from the existing CMS cryoplant used to cool the solenoid magnet. Comparatively modest cooling powers suggest the use of a single compact refrigerator cold box, in contrast to split versions as proposed in this CDR for the Linac-Ring version described below. (The split version is based on LHC technology with a combined surface and underground cold box.) The cold box will be installed directly in the underground cavern at proximity to the cryomodule string. Ambient temperature high and low pressure lines make the link to the compressor stations on surface. For the 2 K

Site	Plant power @ 4.2 K (kW)
CMS site	3.0
ATLAS left	1.2
ATLAS right	1.2

Table 9.29: Cryoplant equivalent cooling powers.

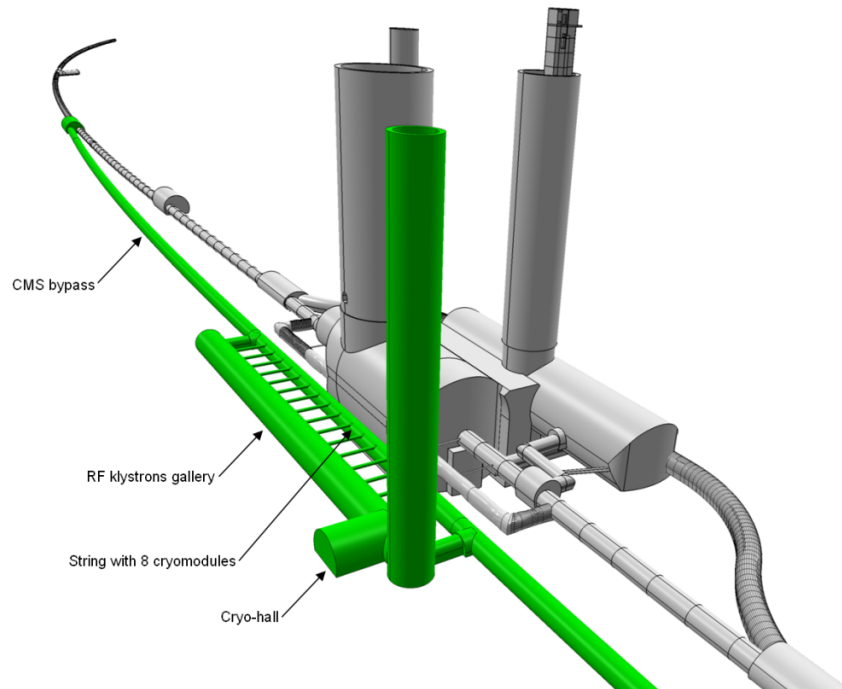


Figure 9.34: Lay-out of the CMS by-pass with location of the cryomodules and the 3 kW @ 4.5 K cryoplant.

8743 temperature level two cold compressors with a total compression ratio of 10 are proposed followed by warm  
8744 compressors to compress the gas to ambient pressure. Figure 9.34 shows the lay-out of the CMS by-pass  
8745 region. At the two ATLAS sites (left, right) with three cryomodules each, two options are conceivable. The  
8746 first consists of connecting to the LHC QRL transfer lines and their terminal feedboxes at vicinity for a  
8747 “parasitic” use of excessive cooling power of the LHC cryoplants. For this two additional 10 – 15 m long  
8748 perpendicular tunnels to connect the LHC tunnel with the LHeC by-pass would have to be constructed. The  
8749 feasibility of this option and potential (negative) impacts have to be studied in more detail in a subsequent  
8750 report. The second option is to use two dedicated cryoplants as proposed for the CMS site, however, with  
8751 reduced capacity. Also in this case the cold box will be installed at proximity to the cryomodule strings in  
8752 the cryo-hall. The two refrigerators are of the same design principle as for CMS, except for their size and  
8753 capacity which is smaller. Their location will be on ATLAS terrain which allows to potentially use already  
8754 existing cryogenic infrastructure of the large cryo-system for the cooling of the ATLAS toroidal and solenoid  
8755 magnets. Among these are the gas storage tanks, the compressor hall and control rooms. Figure 9.35 shows  
8756 the lay-out of the ATLAS by-pass region.

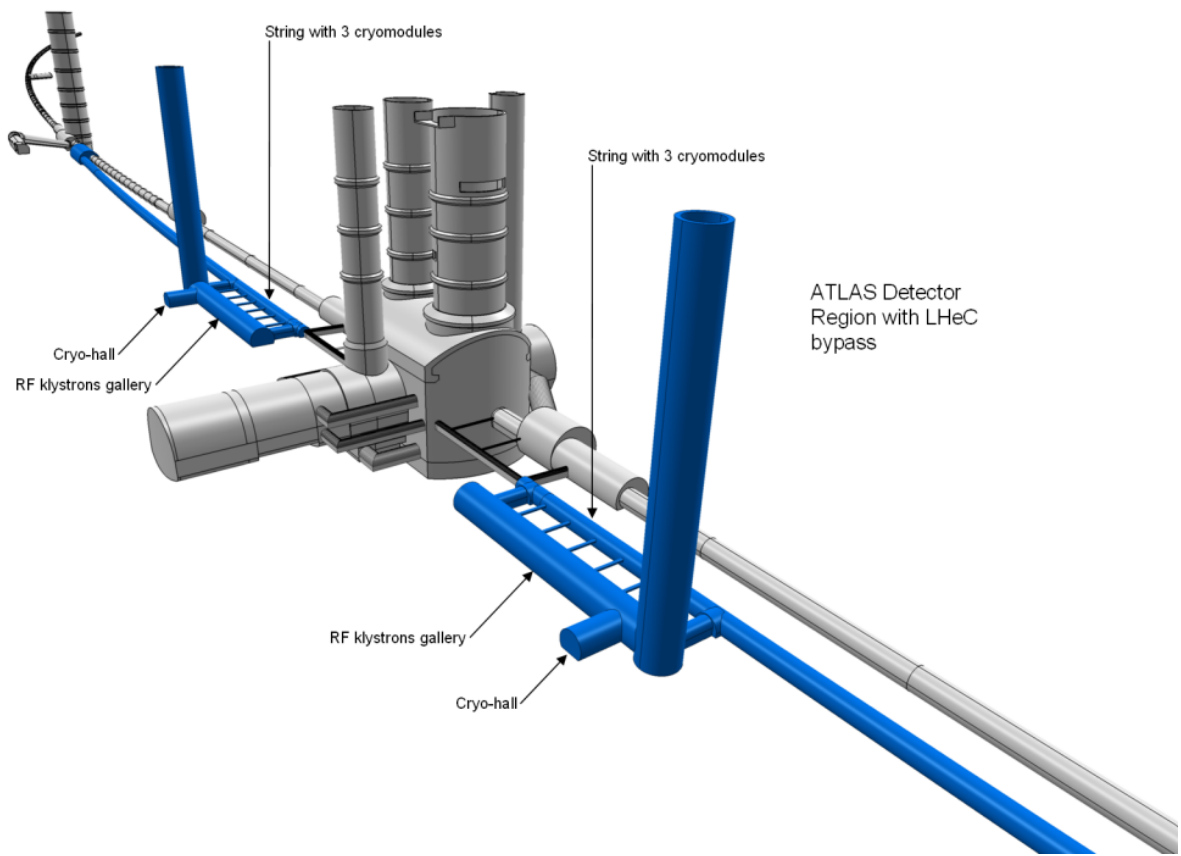


Figure 9.35: Lay-out of the ATLAS by-pass with locations of the cryomodules and the two 1.2 kW @ 4.5 K cryoplants.

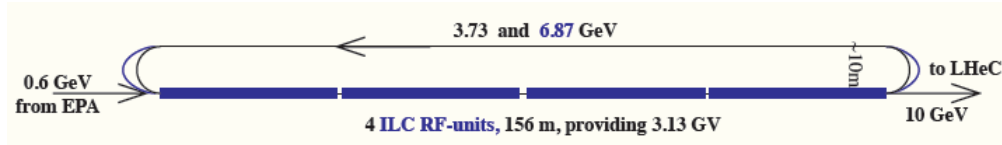


Figure 9.36: Principle of the 10 GeV re-circulating Injector with high gradient pulsed SC cavities (23 MV/m) and 12 cryomodules of the ILC/XFEL type operating at 2 K.

### 8757 Cryogenics for the 10 GeV Injector

8758 The injector is a three-pass recirculating pulsed 10 Hz machine providing leptons at injection energies of 10  
 8759 GeV to the LHeC Ring machine. Figure 9.36 shows its basic principle. Cryomodules of the XFEL (ILC)  
 8760 type with 1.3 GHz superconducting cavities are proposed which allow the application of already existing  
 8761 technology requiring little adaptation effort for LHeC. A 146 m long string will be composed of in total  
 8762 12 cryomodules each 12.2 m long. Cryogen distribution is done within the volume of the cryostats. Bath  
 8763 cooling is at 2 K saturated superfluid helium. Adopted from XFEL the common pump line of 300 mm  
 8764 runs within the cryomodules envelope to collect vapor of all individual cavity baths. Therefore no external  
 8765 transfer line is required which simplifies the overall design. The suction pressure of 30 mbar is provided by  
 8766 cold compressors in the cold box and subsequent ambient temperature compressors. Two more temperature  
 8767 levels of 5–8 K and 40–80 K are used for intercepts and thermal shielding. The operation of the injector at  
 8768 LHeC is in part comparable to XFEL, this during the injection and loading phase of leptons into the LHeC  
 8769 ring. During all other operation phases of a complete LHeC cycle (ramping to final particle energies in the  
 8770 LHC/LHeC tunnel and subsequent physics runs) the injector machine is “idle”. Only static heat losses of  
 8771 the cryomodules and the cryogenic infrastructure have to be intercepted during this time period. Principly a  
 8772 reduced power cryogenic system operating with an “economizer” could be conceived, i.e. a large liquid helium  
 8773 storage is filled during low demands which in turn boosts the cryomodules during the injection phases. A  
 8774 simpler approach, however, is the design for constant (maximum) cooling power when active and, during idle  
 8775 periods, internal electric heaters in the 2 K bath are switched on to keep the load constant. This principle  
 8776 is adopted for these initial studies. A compact single refrigerator cold box providing temperatures from 300  
 8777 K to 2 K will be installed in a protected area at vicinity to the extraction region of the cryomodule string  
 8778 while the compressor set is at surface. For the estimation of power consumption and cooling performances  
 8779 we shall use the experience gained at DESY during testing of XFEL cryomodules. With a final energy of  
 8780 10 GeV and three pass operation the acceleration field required is 23 MV/m. At DESY power consumption  
 8781 measurements have been made with cryomodules for a similar acceleration field of 23.8 MV/m and 10 Hz  
 8782 operation. Our estimates as shown in the Table 9.30 are based on these recent data. With 1/COP values  
 8783 as used in above chapter and a 50% margin for additional thermal losses we estimate the required cooling  
 8784 power of the plant to 2 kW @ 4.5 K.

Temperature (K)	2	5 – 8	40 – 80
Static loss (W)	5	15	100
Dynamic loss (W)	8	3	40
Sum (W)	11	18	140
Sum 12 modules (W)	132(198)	216(324)	1680(2520)

Table 9.30: Thermal loss estimate of the 146 m long string built of 12 XFEL type cryo-modules. In brackets values with 50% contingency. Cryoplant equivalent cooling power; 2 kW @ 4.5 K.

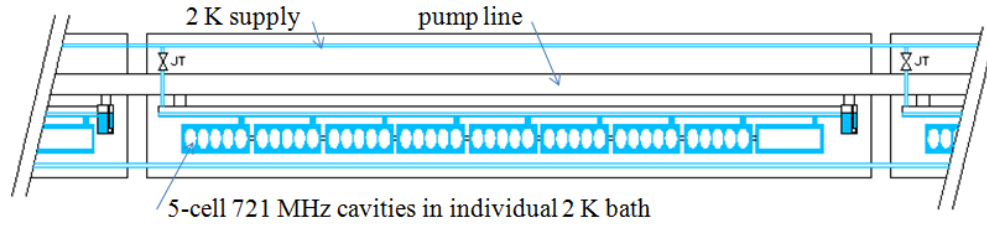


Figure 9.37: Schematic proposal of the 14 m long cryomodules with eight 5-cell 721 MHz cavities operating at 2 K. Supply pipes and the 30 mbar pump line are within cryostat envelope. For the case with inclination right part is lower (only 2 K circuits are shown).

## 9.10.2 Linac-Ring Cryogenics Design

### Location and basic lay-out

The ERL (Energy Recovery Linac) is of racetrack shape with two 1 km long straight SC acceleration sections and, two arcs of 1 km radius with normal conducting magnets. Location and lay-out studies made are described in chapter 10. The currently favored position is within the LHC perimeter (see Figure 10.9) versus the external version being largely under St. Genis community. For the “inside” version more of the newly required surface areas could be located on existing CERN grounds comprising SM18, North Area and, Point 2. Next steps following this CDR will require more detailed combined studies of civil engineering, RF, cryogenics and other services to try optimize the lay-out also, and in particular, for the cryogenic equipment having impact on its own complexity and costs. As base in this study we propose a symmetric lay-out with a sub-division of the respective 1 km long straight sections in four equally spaced sections each housing four 250 m long cryomodule strings. As indicated in chapter 10, the ERL will be inclined towards the Lake of Geneva by 1.4%, however, due to its orientation the tilt in longitudinal direction relevant to the cryogenics is smaller.

### Cryomodules

Eight 721 MHz SC 5-cell cavities of length 1.04 m long will be housed in 14 m long cryomodules. Bath cooling of the cavities is done with slightly subcooled saturated superfluid helium at 2 K. Each cryostat is equipped with a J.T. valve located upstream to expand the 2 K supply helium to the 30 mbar bath pressure and the liquid is brought gravity assist to the downstream individual 8 cavity bath volumes via an interconnecting header pipe. This principle is similar to the SPL preliminary design which has to cope with a tilt of 1.7% [717]. Heat intercept and thermal shielding is at 5-8 K and 40-80 K. The final LHeC L-R cryomodule design can be based on extensive previous work and studies of both existing SC linear accelerators and, such being under construction or planned ones. Among these are CEBAF, ILC, XFEL, SPL, e-RHIC. For this study adapted TESLA/XFEL type cryomodules are proposed. Figure 9.37 shows a design proposal of a module with the eight cavities and the cold correction magnets in their individual bath. All cryogen distribution is done within the cryostat module which interconnects to the adjacent ones with the pipe runs throughout a 250 m long cryomodule string. Also the pump line is proposed to be within the cryostat envelope. The expected mass flow rate of 180 g/s at 2 K of a 250 m long section with 15 cryomodules (see calculations next chapter) is approximately comparable to XFEL for its entire machine for which the corresponding pump line diameter has been designed and tested [718]. The parameters of the LHeC SC cavities and cooling requirements are listed in Table 9.31.

Parameter	Value
Two linacs	length 1 km
5-cell cavities	length 1.04 m
Number	944
Cavities/ cryomodule	8
Number cryomodules	118
Length cryomodule	14 m
Voltage per cavity	21.2 MV
R/Q	285 $\Omega$
Cavity $Q_0$	$2.5 \cdot 10^{10}$
Operation	CW
Bath cooling	2 K
Cooling power/cav.	32 W @ 2 K
Total cooling power (2 linacs)	30 kW @ 2 K

Table 9.31: Parameters and cooling requirements of the ERL (Linac-Ring version).

## 8816 Cryogenic System

8817 The estimated thermal loads per cavity are based on a voltage of 21.2 MV, an R/Q of 285 $\Omega$  and a  $Q_0$   
8818 of  $2.5 \cdot 10^{10}$ . With CW operation the dissipated heat per cavity will be 32 W, respectively 256 W per  
8819 cryomodule. This consists of a very high load. The 1 km long straight sections are sub-divided in four 250 m  
8820 long sub-sections each with 15 interconnecting cryomodules forming a string which are individually supplied  
8821 by a respective refrigerator through local distribution boxes. Eight dedicated refrigerators supply the eight  
8822 strings. Figure 9.38 gives a basic lay-out of the cryo-system with its sectorisation. The refrigerator cold boxes  
8823 will be of the so-called “split” type with a surface cold box and a connecting underground cold box as explored  
8824 and implemented first for LEP2 and later at a larger scale for LHC. The surface cold box will be installed  
8825 close to the compressor set and produce temperature levels between 300 K and 4.5 K. The underground  
8826 cold box will be installed at proximity to the respective cryomodule string in a protected area and produce  
8827 the 2 K with cold compressors. Figure 9.39 gives a principle lay-out of the refrigerator configuration. The  
8828 final location of the ERL will dictate civil engineering constraints and the “ideal” symmetric configuration  
8829 of placement of the refrigerators as done here will have to be reviewed accordingly and, hence, partially  
8830 deviate from this proposal. Also in case only one access shaft per linac can be conceived the four surface  
8831 cold boxes may be installed in form of clusters around the pit while the four related 2 K underground cold  
8832 boxes will be installed remotely close to the respective cryomodule string to be supplied as described above  
8833 and shown in Figure 9.38. The total dynamic cooling power of the ERL with 944 cavities amounts to 30 kW  
8834 @ 2 K. For the calculation of the cooling performances of the refrigerators in this document only the largely  
8835 dominating dynamic thermal loads of the cavities are taken into account dwarfing all other thermal losses  
8836 of the cryomodules which become negligible in a first order approach. Recent developments and industrial  
8837 design of large scale refrigerator systems as for LHC [719] indicate the feasibility of a 1/COP of 700 W/W  
8838 for 2 K large scale cryoplants. Hence, with this figure the total electric grid power amounts to 21 MW. The  
8839 total equivalent refrigerator power at 4.5 K is estimated to 80 kW. This corresponds to about half of the  
8840 installed cooling power at LHC. In case contingencies are taken into account in the engineering design the  
8841 cooling capacity could approach LHC. For this preliminary study contingencies are omitted, this also in view  
8842 of expected future improved cavity performances. Eight cryoplants with 10 kW @ 4.5 K each are proposed  
8843 for the ERL. The technology to design and construct such units as well as the overall systems engineering is  
8844 largely available today and can be based on experience from LHC, CEBAF, XFEL. Nevertheless it consists  
8845 of an engineering challenge due to its sheer size and the large performance capacities required. Development  
8846 work will have to be done for the cold compressors units together with detailed combined CERN/industrial



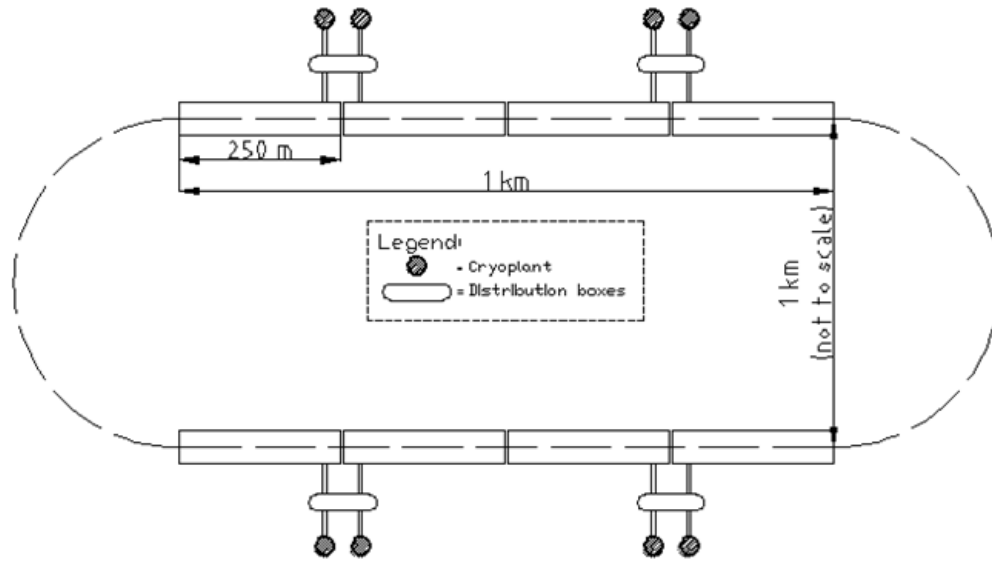


Figure 9.38: Basic lay-out of the 6 pass ERL. Two 1 km long SC acceleration sections with a 10 GeV linac each. Eight 10 kW @ 2 K cryoplants. Configuration such that each plant supplies a cryomodule string of 250 m length (figure not to scale).

8847 engineering design of the refrigerator cold boxes. Implementation and operation of such large systems will  
 8848 consist of a complex task. Further cavities and cryomodules will require a limited R&D program. From this  
 8849 we expect improved quality factors with respect to today's state of the art. The cryogenics of the L-R version  
 8850 consists of a formidable engineering challenge, however, it is feasible and, CERN disposes of the respective  
 8851 know-how.

Parameter	Value
Number of Refrigerators	8
1/COP @ 2 K	700
Minimum cooling capacity/refrigerator	10 kW @ 4.5 K
Contingency	none
Minimum total cooling power	80 kW @ 4.5 K
Grid power consumption	21 MW

Table 9.32: Refrigerator cooling capacity and power consumption (minimum cooling power).

### 8852 9.10.3 General Conclusions Cryogenics for LHeC

8853 These conclusions reference to the complete cryogenic contributions, i.e. for the detector cryogenics, the R-R  
 8854 and the L-R version;

8855 The striking advantage of an extension from LHC to a LHeC lies, apart from the new physics, in the  
 8856 comparatively small investment cost, the possibility of quasi undisturbed continuation of LHC hadron physics  
 8857 and the fact that the technologies are largely already at hand today. This applies also to the cryogenic part.  
 8858 No so-called "show-stoppers" could be detected during these studies. For the detector SC magnet and

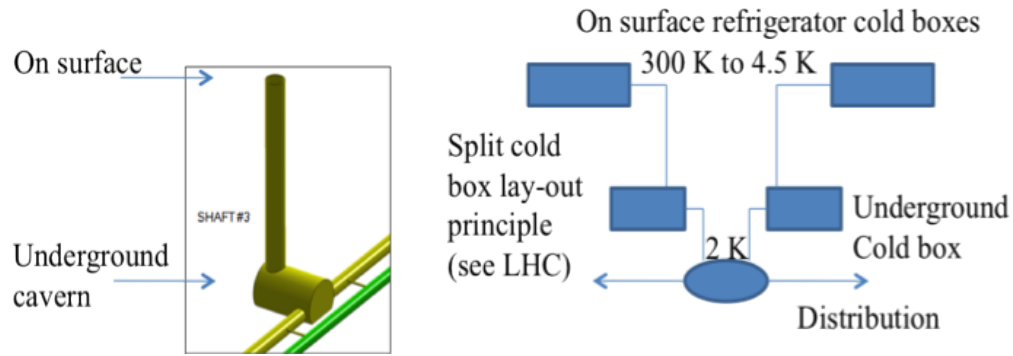


Figure 9.39: Basic principle of a Split Cold Box lay-out (comparable to LHC accelerator cryogenics).

8859 LArgon cryogenics technologies developed and implemented at the ATLAS experiment can be used in a  
 8860 “down-scaled” way. For the accelerator cryogenics the two options Ring-Ring and Linac-Ring differ strongly  
 8861 in principle and investment. While for the R-R only four small to medium sized 2 K refrigerators are  
 8862 required, for the cryomodules of the injector and the three LHC tunnel bypasses, the L-R option with two  
 8863 1 km long CW operated 2 K SC cavities is extremely demanding. The total installed cryogenic power will  
 8864 likely exceed 100 kW @ 4.5 K equivalent, approaching values of the LHC. However, these estimates are only  
 8865 based on currently proved data of the cavity  $Q_0$ . The development of high Q SC cavities is being pursued  
 8866 in several laboratories and new encouraging results are on the horizon indicating improvement of quality  
 8867 having positive and direct impact for cryogenic requirements and respective plant sizes.

## 9.11 Beam Dumps and Injection Regions

### 9.11.1 Injection Region Design for Ring-Ring Option

A 10 GeV recirculating Linac will be used to inject the electrons in the LHeC. This will be built on the surface or underground and a transfer line will connect the linac to the LHeC injection region. At this stage a purely horizontal injection is considered, since this will be easier to integrate into the accelerator. The electron beam will be injected in the bypass around ATLAS, with the baseline being injection into a dispersion free region (at the right side of ATLAS). Bunch-to-bucket injection is planned, as the individual bunch intensities are easily reachable in the injector and accumulation is not foreseen. Two options are considered: a simple septum plus kicker system where single bunches or short trains are injected directly onto the closed orbit; and a mismatched injection, where the bunches are injected with either a betatron or dispersion offset.

#### Injection onto the closed orbit

The baseline option is injection onto the orbit, where a kicker and a septum would be installed in the dispersion free region at the right side of ATLAS bypass (see Fig. 9.40). Injecting the beam onto the closed orbit has the advantage that the extra aperture requirements around the rest of the machine from injection oscillations or mismatch are minimised. The kicker and septum can be installed around a Defocusing

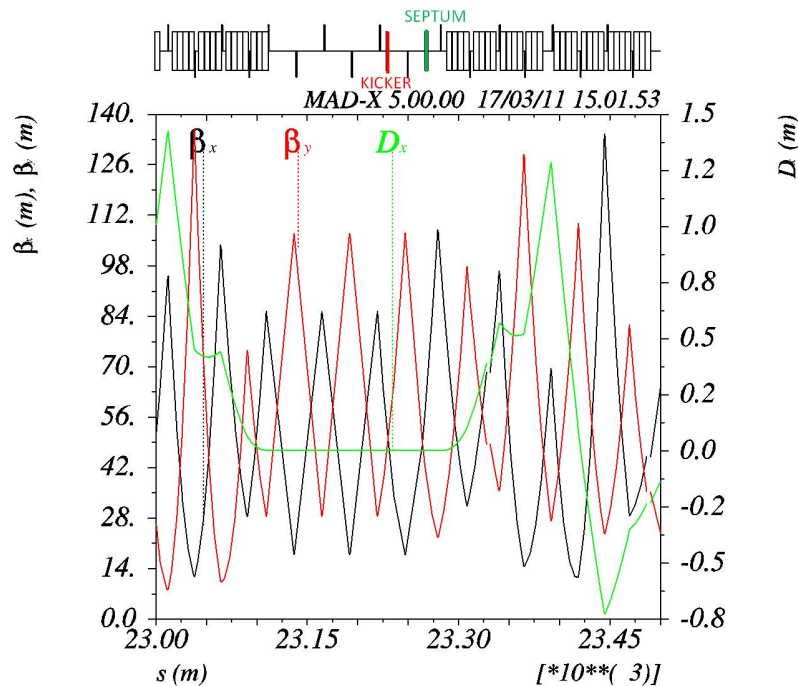


Figure 9.40: Injection optics is shown. The sequence starts ( $s=0$ ) at the beginning of the dispersion suppressor at the left side of IP2 and proceeds clockwise, while the electron beam rotates counterclockwise (from right to left in the figure). The injection kicker and septum are installed in the dispersion free region of the bypass at the right side of ATLAS.

quadrupole to minimise the kicker strength required. The kicker-septum phase advance is  $75^\circ$ .

Some assumptions made to define the required element apertures are made in Table 9.33.

For the septum, an opening between injected and circulating beam of 47 mm is required, taking into account some pessimistic assumptions on orbit, tolerances and with a 4 mm thick septum. This determines

8888 the kicker strength of about 1 mrad.

Orbit variation	$\pm 4$ mm
Injection precision	$\pm 3$ mm
Mechanical/alignment tolerance	$\pm 1$ mm
Horizontal normalised emittance $\varepsilon_{n,x}$	0.58 mm
Vertical normalised emittance $\varepsilon_{n,y}$	0.29 mm
Injection mismatch (on emittance)	100 %
$\beta_x, \beta_y$ @ Kicker	61.3 m, 39.7 m
$\beta_x, \beta_y$ @ Septum	57.3 m, 42.3 m
$\sigma_x, \sigma_y$ @ Kicker and Septum	0.8 mm, 0.4 mm

Table 9.33: Assumptions for beam parameters used to define the septum and kicker apertures

8889 The septum strength should be about 33 mrad to provide enough clearance for the injected beam at the  
 8890 upstream lattice quadrupole, the yoke of which is assumed to have a full width of 0.6 m. This requires about  
 8891 1.1 T m, and a 3.0 m long magnet at about 0.37 T is reasonable, of single turn coil construction with a  
 8892 vertical gap of 40 mm and a current of 12 kA.

8893 The RF frequency of the linac is 1.3 GHz and a bunch spacing of 25 ns is considered, as the LHeC electron  
 8894 beam bunch structure is assumed to match with the LHC proton beam structure. Optimally a train of 72  
 8895 bunches would be injected, which would require a 1.8  $\mu$ s flattop for the kickers and a very relaxed 0.9  $\mu$ s  
 8896 rise time (as for the LHC injection kickers [720]). However, this train length is too long for the recirculating  
 8897 linac to produce, and so the kicker rise time and fall time requirements are therefore assumed to be about  
 8898 23 ns, to allow for the bunch length and some jitter.

8899 For a rise time  $t_m = 23$  ns, a system impedance  $Z$  of 25  $\Omega$  is assumed, and a rather conservative system  
 8900 voltage  $U$  of 60 kV.

8901 Assuming a full vertical opening  $h$  of 40 mm, and a full horizontal opening  $w$  of 60 mm (which allow  $\pm 6$   
 8902  $\sigma$  beam envelopes with pessimistic assumptions on various tolerances and orbit), the magnetic length  $l_m$  of  
 8903 the individual magnets is:

$$l_m = ht_m Z / \mu_0 w = 0.31 \text{ m}$$

8904 For a terminated system the gap field  $B$  is simply:

$$B = \frac{\mu_0 U}{2hZ} = 0.037 \text{ T}$$

8905 As 0.03 Tm are required, the magnetic length should be 0.8 m, which requires 3 magnets. Assuming each  
 8906 magnet is 0.5 m long, including flanges and transitions the total installed kicker length is therefore about  
 8907 1.5 m.

### 8908 Mismatched injection

8909 A mismatched injection is also possible, Figure 9.41 with a closed orbit bump used to bring the circulating  
 8910 beam orbit close to the septum, and then switched off before the next circulating bunch arrives.

8911 The injected beam then performs damped betatron or synchrotron oscillations, depending on the type of  
 8912 mismatch used. In LHeC the damping time is about 3 seconds, so that to achieve the suggested 0.2 s period  
 8913 between injections, a damping wiggler would certainly be needed - the design of such a wiggler needs to be  
 8914 investigated.

8915 Three kickers (KICKER 1, KICKER 2 and KICKER 3 in Fig. 9.41) are used to generate a closed orbit  
 8916 bump of 20 mm at the injection point. The kicker parameters are summarized in table 9.34. In case of

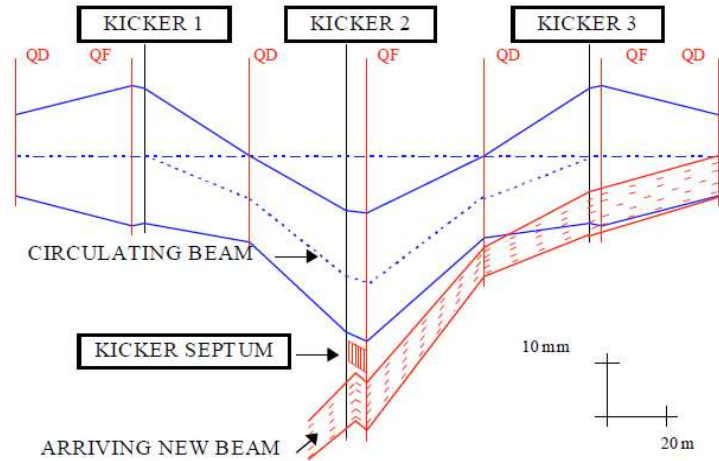


Figure 9.41: layout of mismatched injection system. To minimise kicker strengths the magnets are located near focusing quadrupoles.

Magnet	$\theta_x$ [mrad]	B dl [Tm]
KICKER1	1.35	0.04
KICKER2	2.37	0.08
KICKER3	0.55	0.02

Table 9.34: Kickers strength and integrated magnetic field needed to generate an orbit bump of 20 mm at the injection point.

8917 betatron mismatch, the bumpers can be installed in the dispersion free region considered for the injection  
 8918 onto the closed orbit case discussed in the previous section (see Fig. 9.42). The installed magnet lengths of  
 8919 the kickers should be 2 m, 3.5 m and 1 m respectively, for the kickers size,  $Z$  and  $U$  parameters given above.  
 8920 Overall the kicker system is not very different to the system needed to inject onto the orbit.

8921 To allow for the possibility of synchrotron injection, the injection kicker-septum would need to be located  
 8922 where the horizontal dispersion  $D_x$  is large. The beam is then injected with a position offset  $x$  and a  
 8923 momentum offset  $\delta p$ , such that:

$$x = D_x \delta p$$

8924 The beam then performs damped synchrotron oscillations around the ring, which can have an advantage  
 8925 in terms of faster damping time and also smaller orbit excursions in the long straight sections, particularly  
 8926 experimental ones, where the dispersion functions are small.

8927 As an alternative to the fast (23 ns rise time) kicker for both types of mismatched injection, the kicker  
 8928 rise- and fall-time could be increased to almost a full turn, so that the bump is off when the mismatched  
 8929 bunch arrives back at the septum. This relaxes considerably the requirements on the injection kicker in  
 8930 terms of fall time. However, this does introduce extra complexity in terms of synchronizing the individual  
 8931 kicker pulse lengths and waveform shapes, since for the faster kicker once the synchronization is reasonably  
 8932 well corrected only the strengths need to be adjusted to close the injection bump for the single bunch.

### 8933 9.11.2 Injection transfer line for the Ring-Ring Option

8934 The injection transfer line from the 10 GeV injection recirculating linac is expected to be straightforward.  
 8935 A transfer line of about 900 m, constituted by 15 FODO cells, has been considered. The phase advance of

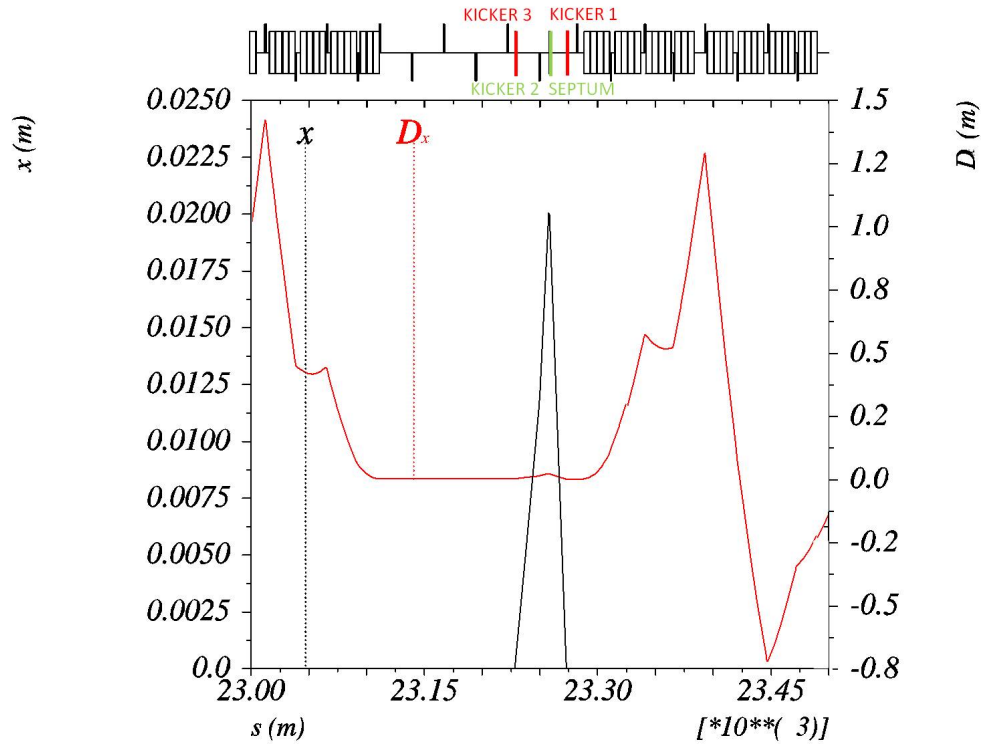


Figure 9.42: A closed orbit bump of 20 mm is generated by three kickers installed in the dispersion free region located at the right side of the bypass around ATLAS (electron beam moves from right to left in the Figure).

8936 each cell corresponds to about  $100^\circ$ .

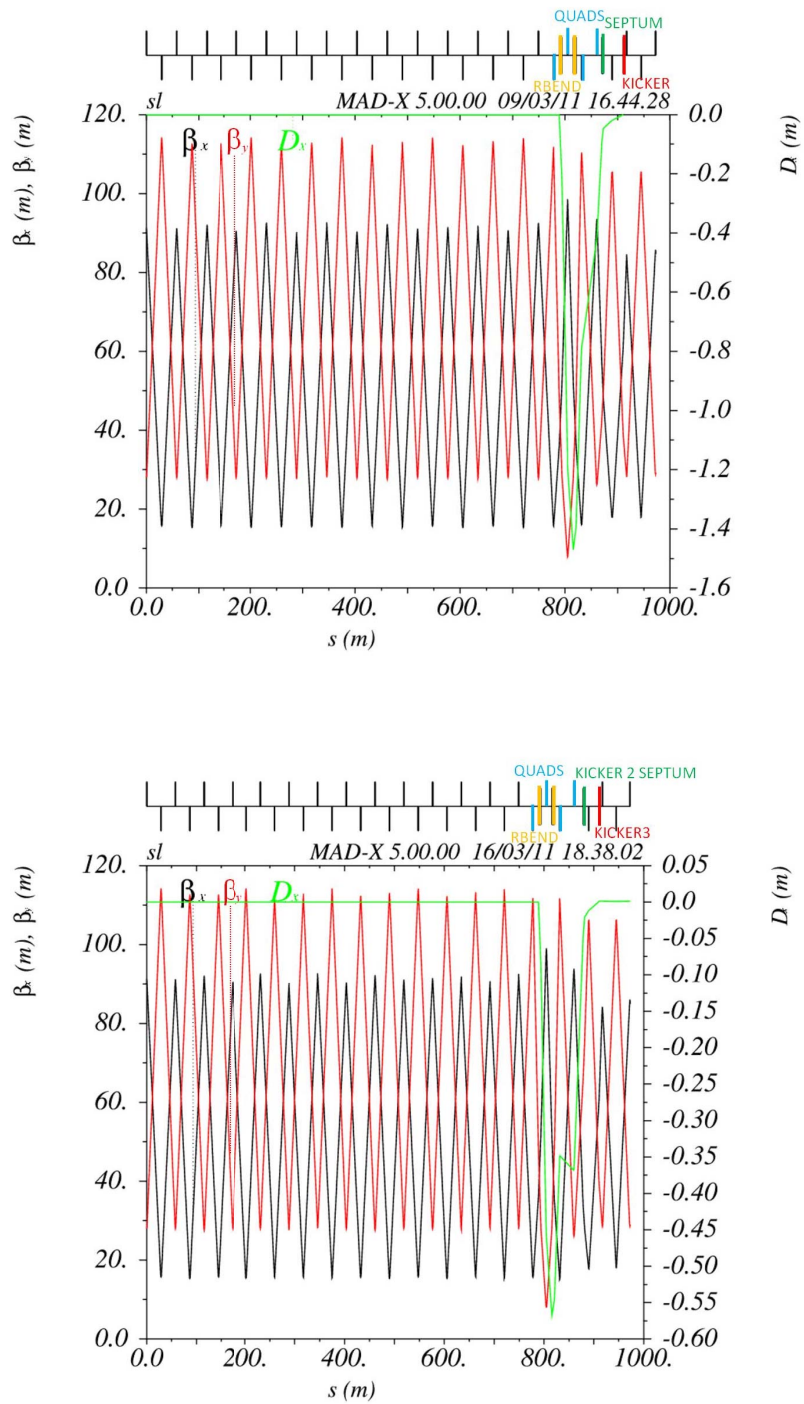


Figure 9.43: Transfer line optics for the injection onto orbit case (top) and mismatched injection case (bottom).

8937 The last two cells are used for optics matching. In particular, four quadrupoles, 1 m long each, are used  
 8938 for  $\beta_x$  and  $\beta_y$  matching, while two rectangular bending magnets, 5 m long each, are used for matching the  
 8939 horizontal dispersion  $D_x$  to 0 (maximum  $D_x = -1.48$  m for the injection onto closed orbit case and maximum  
 8940  $D_x = -0.57$  m for the mismatched injection case). The “good field region” for a  $6\sigma$  beam envelope requires  
 8941 a minimum half-aperture, in the matching insertion, of 15 mm and 10 mm for the focusing and defocusing  
 8942 quadrupoles respectively, corresponding to a pole tip field of about 0.02 T. The maximum strength of the  
 8943 bending magnets, which are used for dispersion matching, corresponds to about 39 mrad. This requires  
 8944 1.3 T m and a maximum field of 0.3 T. A single turn coil of 9.5 kA with a vertical gap of 40 mm could be  
 8945 used.

### 8946 9.11.3 60 GeV internal dump for Ring-Ring Option

8947 An internal dump will be needed for electron beam abort. The design for LEP [721] consisted of a boron  
 8948 carbide spoiler and an Aluminum alloy (6% copper, low magnesium) absorbing block (0.4 m  $\times$  0.4 m  $\times$  2.1 m  
 8949 long). A fast kicker was used to sweep eight bunches, of  $8.3 \times 10^{11}$  electrons at 100 GeV, onto the absorber.  
 8950 The first bunch was deflected by 65 mm and the last by 45 mm, inducing a temperature increase  $\Delta T$  of  
 8951  $165^\circ$ .

8952 The bunch intensity for the LHeC is about a factor of 20 lower than for LEP and beam size is double ( $\sigma$   
 8953  $= 0.5$  mm in LEP and  $\sigma = 1$  mm in LHeC).

8954 The lower energy (60 GeV) and energy density permit to dump 160 bunches in 20 mm to obtain the  
 8955 same  $\Delta T$  as for LEP. However, in total LHeC will be filled with 2808 bunches, which means that significant  
 8956 additional dilution will be required. A combination of a horizontal and a vertical kicker magnet can be  
 8957 used, as an active dilution system, to paint the beam on the absorber block and increase the effective sweep  
 8958 length. The kickers and the dump can be located in the bypass around CMS, in a dispersion free region (see  
 8959 fig. 9.44).

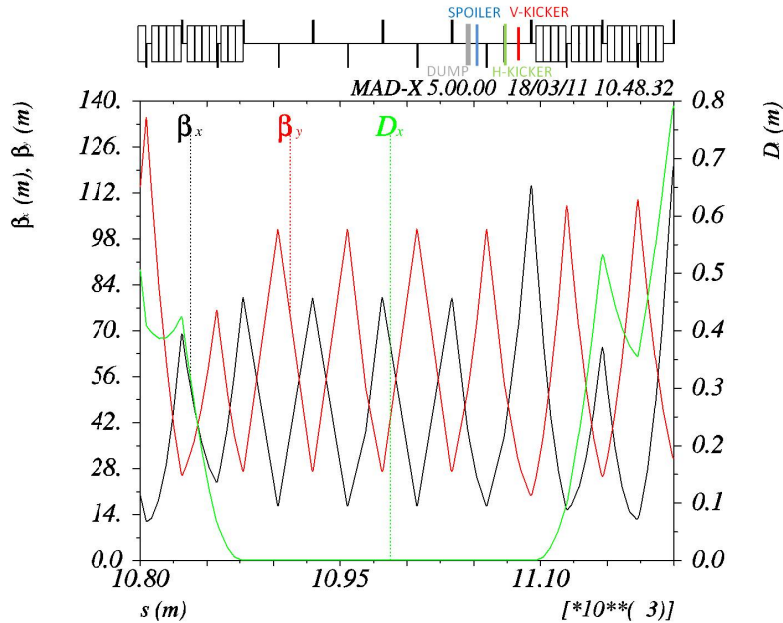


Figure 9.44: The optics in the region of the CMS bypass where the beam dump system could be installed is shown. The system consists of two kickers, one spoiler and a Carbon-composite absorber which are installed in the dispersion free region of the bypass at the right side of CMS (beam proceeds from right to left in the Figure).



8960 It is envisaged to use Carbon-composite for the absorber block, since this has much better thermal and  
 8961 mechanical properties than aluminum. The required sweep length is then assumed to be about 100 mm,  
 8962 from scaling of the LEP design. The minimum sweep speed in this case is about 0.6 mm per  $\mu\text{s}$ , which  
 8963 means about 54 bunches per mm. Taking into account the energy and the beam size, this represents less  
 8964 than a factor 2 higher energy density on the dump block, compared to the average determined by the simple  
 8965 scaling, that should be feasible using carbon. More detailed studies are required to optimise the diluter and  
 8966 block designs. Vacuum containment, shielding and a water cooling system has to be incorporated. A beam  
 8967 profile monitor can be implemented in front of each absorber to observe the correct functioning of the beam  
 8968 dump system.

8969 The vertical kicker would provide a nominal deflection of about 55 mm (see fig.9.45), modulated by  
 8970  $\pm 13\%$  for three periods during the 100  $\mu\text{s}$  abort (see fig.9.46), while the horizontal kicker strength would  
 8971 increase linearly from zero to give a maximum deflection at the dump of about 55 mm (see Fig.9.45 and  
 8972 Fig.9.46). This corresponds to system kicks of 2.7 and 1.6 mrad respectively.

8973 Parameters characterizing the kicker magnets are presented in Table 9.35.

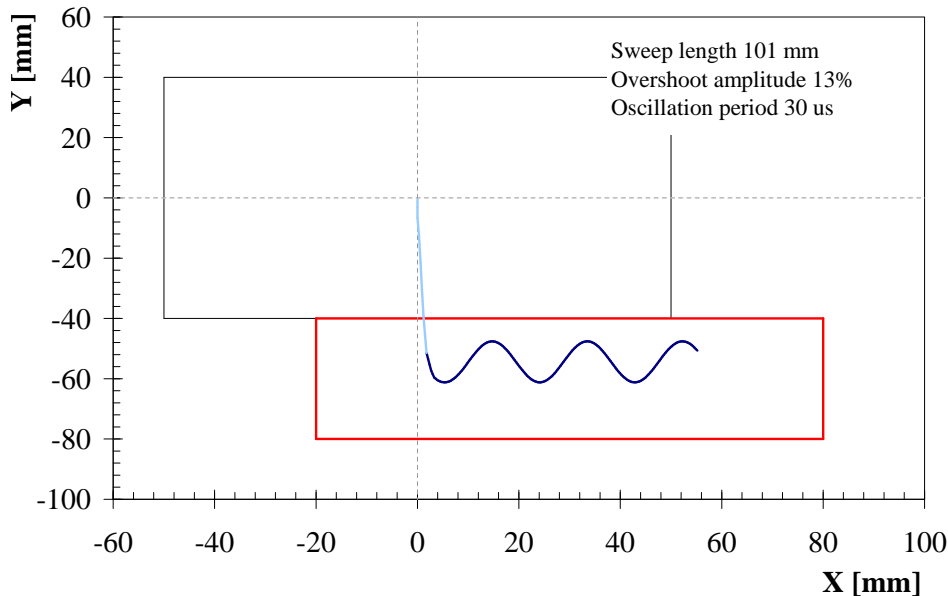


Figure 9.45: A vertical and a horizontal kicker are used to dilute the beam on the dump absorbing block.

8974 In the present lattice the dump is placed  $\sim 30$  m downstream of the kickers, corresponding to a phase  
 8975 advance of about  $63^\circ$  in the horizontal plane and  $35^\circ$  in the vertical plane. The minimum horizontal and  
 8976 vertical aperture at the dump are 26 mm and 22 mm respectively (at the dump:  $\beta_x = 37$  m and  $\beta_y = 55$  m,  
 8977 using the same beam and machine parameter assumptions, as presented in Table 9.33). The kicker system  
 8978 field rise time is assumed to be at most 3  $\mu\text{s}$  (abort gap) and the kicker field flat-top at least 90  $\mu\text{s}$  as for the  
 8979 LHC proton beam. Same design as for the LHC dump kicker magnets MKD can be used: a steel yoke with  
 8980 a one-turn HV winding. These magnets can provide a magnetic field in the gap of 0.34 T. For a magnetic  
 8981 length of 0.31 m ( $Z = 25 \Omega$  and  $U = 60$  kV), a total installed kicker length of 1.5 m for the horizontal system  
 8982 and 2.5 m for the vertical system has to be considered.

8983 A spoiler (one-side single graphite block: 0.3 m  $\times$  0.10 m  $\times$  0.5 m long) can be installed 5 m upstream  
 8984 of the dump at the extraction side to provide further dilution.

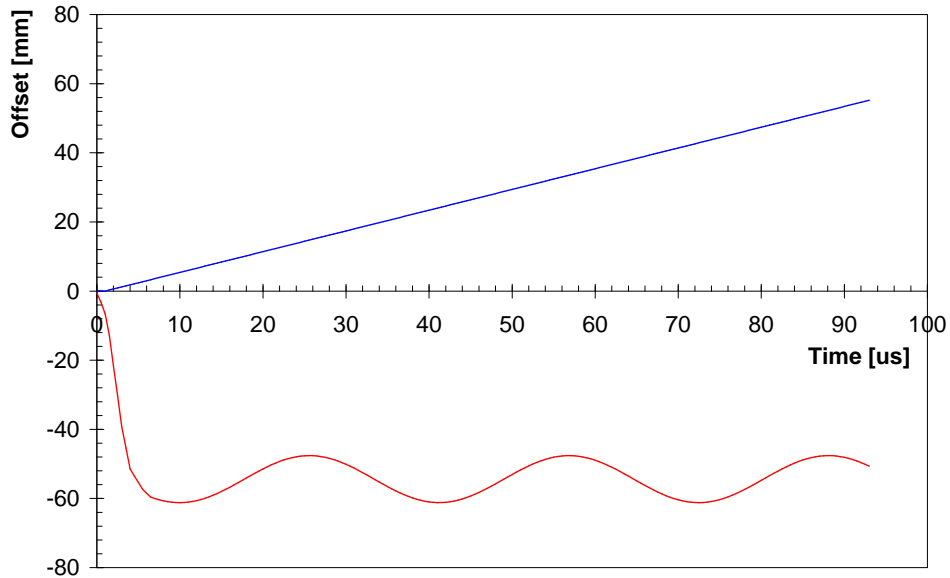


Figure 9.46: The strength of the vertical kicker oscillates in time by  $\pm 13\%$  around its nominal value. The deflection provided by the horizontal kicker increases almost linearly in time.

	MKDV	MKDH
Length [m]	2.5	1.5
Maximum angle [mrad]	2.7	1.6
Maximum field [T]	0.34	0.34
Rise/Fall time [ns]	800	800
Flat top length [ $\mu$ s]	90	90

Table 9.35: Parameters characterising vertical and horizontal kicker magnets of the extraction system.

#### 9.11.4 Post collision line for 140 GeV Linac-Ring option

The post collision line for the 140 GeV Linac option has to be designed taking care of minimizing beam losses and irradiation. The production of Beamstrahlung photons and  $e^-e^+$  pairs is negligible and the energy spread limited to  $2 \times 10^{-4}$ . A standard optics with FODO cells and a long field-free region allowing the beam to naturally grow before reaching the dump can be foreseen. The aperture of the post collision line is defined by the size of the spent beam and, in particular, by its largest horizontal and vertical angular divergence (to be calculated). A system of collimators could be used to keep losses below an acceptable level. Strong quadrupoles and/or kickers should be installed at the end of the line to dilute the beam in order to reduce the energy deposition at the dump window. Extraction line requirements:

- Acceptable radiation level in the tunnel.
- Reasonably big transverse beam size at the dump window and energy dilution.
- Beam line aperture big enough to host the beam: beta function and energy spread must be taken into account.
- Elements of the beam line must have enough clearance.

### 9.11.5 Absorber for 140 GeV Linac-Ring option

Nominal operation with the 140 GeV Linac foresees to dump a 50 MW beam. This power corresponds to the average energy consumption of 69000 Europeans. An *Eco Dump* could be used to recover that energy; detailed studies are needed and are not presented here. Another option is to start from the concept of the ILC water dump and scale it linearly to the LHeC requirements. The ILC design is based on a water dump with a vortex-like flow pattern and is rated for 18 MW beam of electrons and positrons [722]. Cold pressurized water (18 m<sup>3</sup> at 10 bar) flows transversely with respect to the direction of the beam. The beam always encounters fresh water and dissipates the energy into it. The heat is then transmitted through heat exchangers. Solid material plates (Cu or W) are placed beyond the water vessel to absorb the tail of the beam energy spectrum and reduce the total length of the dump. This layer is followed by a stage of solid material, cooled by air natural convection and thermal radiation to ambient, plus several meters of shielding. The size of the LHeC dump, including the shielding, should be 36 m longitudinally and 21 m transversely and it should contain 36 m<sup>3</sup> of water. The water is separated from the vacuum of the extraction line by a thin Titanium Alloy (Ti-6Al-4V) window which has high temperature strength properties, low modulus of elasticity and low coefficient of thermal expansion. The window is primarily cooled by forced convection to water in order to reduce temperature rise and thermal stress during the passage of the beam. The window must be thin enough to minimise the energy absorption and the beam spot size of the undisturbed beam must be sufficiently large to prevent window damage. A combination of active dilution and optical means, like strong quadrupoles or increased length of the transfer line, can be use on this purpose. Further studies and challenges related to the dump design are:

- Pressure wave formation and propagation into the water vessel.
- Remotely operable window exchange.
- Handling of tritium gas and tritiated water.

### 9.11.6 Energy deposition studies for the Linac-Ring option

Preliminary estimates, of the maximum temperature increase in the water and at the dump window, have been defined according to FLUKA simulation results performed for the ILC dump [723]. A 50 MW steady state power should induce a maximum temperature increase  $\Delta T$  of 90° corresponding to a peak temperature of 215°. The water in the vessel should be kept at a pressure of about 35 bar in order to insure a 25° margin from the water boiling point.

FLUKA studies have been carried out for a 1 mm thick Ti window with a hemispherical shape. The beam size at the ILC window is  $\sigma_x = 2.42$  mm and  $\sigma_y = 0.27$  mm; an extraction line with 170 m drift and 6 cm sweep radius for beam dilution have been considered. A beam power of 25 W with a maximum heat source of 21 W/cm<sup>3</sup> deposited on the window have been calculated. This corresponds to a maximum temperature of 77° for the minimum ionisation particle ( $dE/dx = 2$  MeV  $\times$  cm<sup>2</sup>/g), no shower is produced because the thickness of the window is significantly smaller than the radiation length. A maximum temperature lower than 100° would require a minimum beam size of  $\sigma_{x,y} = 1.8$  mm. A minimum  $\beta$  function of 8877 m would be needed being the beam emittance  $\varepsilon_{x,y} = 0.37$  nm for the undisturbed beam. The radius of the dump window depends on the size of the disrupted beam. The emittance of the disrupted beam is  $\varepsilon_{x,y} = 0.74$  nm corresponding to a beam size  $\sigma_{x,y}$  of 2.56 mm (for  $\beta = 8877$  m); a radius  $R = 5$  cm could then fit a  $10\sigma$  envelope. The yield strength of the Ti alloy used for the window is  $\sigma_{Ti} = 830$  MPa, this, according to the formula:

$$\sigma_{Ti} = 0.49 \times \Delta P \frac{R^2}{d^2} \quad (9.10)$$

where  $\Delta P = 3.5$  MPa, imposes that the thickness of the window  $d$  is bigger than 2.3 mm.

Length of the transfer line drift space and possible dilution have to be estimated together with possible cooling.

9043 **9.11.7 Beam line dump for ERL Linac-Ring option**

9044 The main dump for the ERL Linac-ring option will be located downstream of the interaction point. Splitting  
 9045 magnets and switches have to be installed in the extraction region and the extracted beam has to be tilted  
 9046 away from the circulating beam by 0.03 rad to provide enough clearance for the first bending dipole of the  
 9047 LHeC arc (see Fig. 9.47). A 90 m transfer line, containing two recombination magnets and dilution kickers,  
 is considered to be installed between the LHeC and the LHC arcs(see Fig. 9.48). The beam dump will be

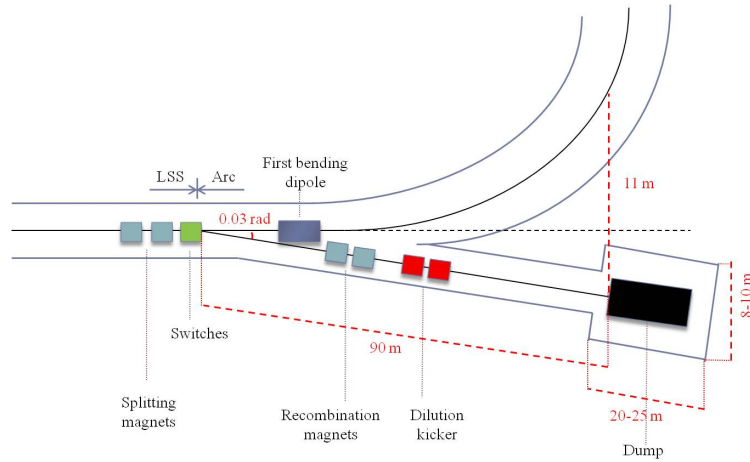


Figure 9.47: Scheme of the transfer line from end of long straight section of the linac and beam dump.

9048 housed in a UD62/UD68 like cavern at the end of the TL and the option of having service caverns for water  
 9049 treatment and heat exchange is explored. An additional dump, and its extraction line, could be installed at  
 9050 the end of the first linac(see Fig. 9.48) for beam setup purposes at intermediate energy. The same design as  
 9051 for the nominal dump and extraction line would be applied.  
 9052

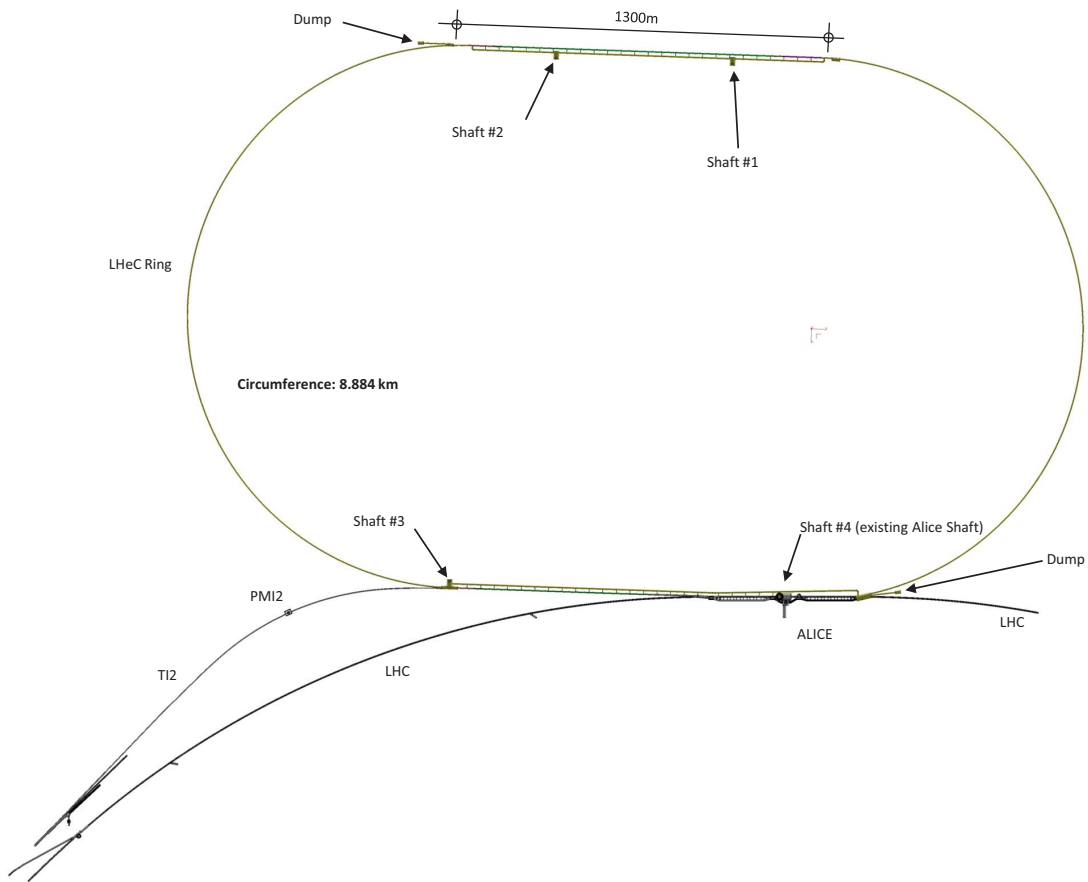


Figure 9.48: Two beam dumps are installed 90 m downstream the end of the long straight section of each linac for nominal operation and beam setup. Note that this drawing is only indicative for the beam dump positions: the currently preferred location of the Linac is 'mirrored' such that it is inside the LHC.

### 9053 **9.11.8 Absorber for ERL Linac-Ring option**

9054 During nominal operation a 0.5 GeV beam has to be dumped with a current of 6.6 mA. The setup beam  
9055 will have a maximum current of 0.05 mA and an energy varying from 10 GeV to 60 GeV (10 GeV step size).  
9056 Globally, a maximum beam power of 3 MW has to be dumped. The same design as for the 140 GeV option  
9057 can be used by scaling linearly. In this case, a 3 m<sup>3</sup> water dump (0.5 m diameter and 8 m length) with a  
9058 3 m × 3 m × 10 m long shielding has to be implemented. No show stopper has been identified for the 18  
9059 MW ILC dump, same considerations are valid in this less critical case.

## Chapter 10

# Civil Engineering and Services

### 10.1 Overview

Infrastructure costs for projects such as LHeC, typically represent approximately one third of the overall budget. For this reason, particular emphasis has been placed on Civil Engineering and Services studies, to ensure a cost efficient conceptual design. This chapter provides an overview of the designs adopted for the key infrastructure cost driver, namely, civil engineering. The costs for the other infrastructure items such as cooling & ventilation, electrical supply, transport & installation will be pro-rated for the CDR and studied in further detail during the next phase of the project. For the purposes of this conceptual design report, the Civil Engineering (CE) studies have assumed that the Interaction Region (IR) for LHeC will be at LHC Point 2, which currently houses the ALICE detector. As far as possible, any surface facilities have been situated on existing CERN land. Both the Ring-Ring and Linac-Ring underground works will be discussed in this Chapter. Surface buildings/structures have not been considered for the CDR.

### 10.2 Location, Geology and Construction Methods

This section describes the general situation and geology that can be expected for both the Ring-Ring and Linac Ring options.

#### 10.2.1 Location

The proposed siting for the LHeC project is in the North-Western part of the Geneva region at the existing CERN laboratory. The proposed Interaction Region is fully located within existing CERN land at LHC Point 2, close to the village of St.Genis, in France. The CERN area is extremely well suited to housing such a large project, with the very stable and well understood ground conditions having several particle accelerators in the region for over 50 years. The civil engineering works for the most recent machine, the LHC were completed in 2005, so excellent geological records exist and have been utilised for this study to minimise the costs and risk to the project. Any new underground structures will be constructed in the stable Molasse rock at a depth of 100-150m in an area with little seismic activity. CERN and the Geneva region have all the necessary infrastructure at their disposal to accommodate such a project. Due to the fact that Geneva is the home of many international organizations excellent transport and communication networks already exist. Geneva Airport is only 5km from the CERN site, with direct links and a newly constructed tramway, shown in Figure 10.1, gives direct access from the Meyrin Site to the city centre.

The governments of France and Switzerland have long standing agreements concerning the support of particle accelerators in the Geneva region, which make it very likely that the land could be made available free of charge, as it was for previous CERN projects.



Figure 10.1: Tram stop outside CERN Meyrin Site.



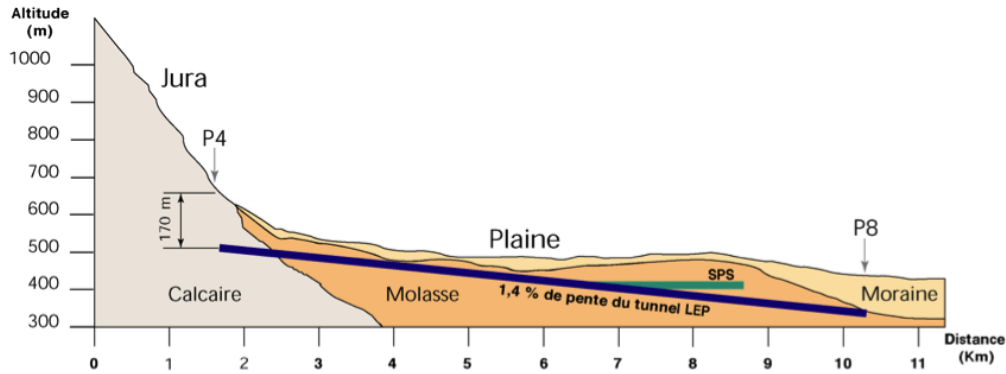


Figure 10.2: Simplified cross section of the LHC housed mostly in Molasse Rock

## 10.2.2 Land Features

The proposed location for the accelerator is situated within the Swiss midlands embedded between the high mountain chains of the Alps and the lower mountain chain of the Jura. CERN is situated at the feet of the Jura mountain chain in a plain slightly inclined towards the lake of Geneva. The surface terrain was shaped by the Rhone glacier which once extended from the Alps to the valley of the Rhone. The water of the area flows to the Mediterranean Sea. The absolute altitude of the surface ranges from 430 to 500m with respect to sea level. The physical positioning for the project has been developed based on the assumption that the maximum underground volume possible should be housed within the Molasse Rock and should avoid as much as possible any known geological faults or environmentally sensitive areas. The shafts leading to any on-surface facilities have been positioned in the least populated areas, however, as no real discussions have taken place with the local authorities, the presented layouts can only be regarded as indicative, for costing purposes only.

## 10.2.3 Geology

The LHeC project is within the Geneva Basin, a sub-basin of the large North Alpine Foreland (or Molasse) Basin. This is a large basin which extends along the entire Alpine Front from South-Eastern France to Bavaria, and is infilled by Molasse deposits of Oligocene and Miocene age. The basin is underlain by crystalline basement rocks and formations of Triassic, Jurassic and Cretaceous age. The Molasse, comprising an alternating sequence of marls and sandstones (and formations of intermediate compositions) is overlain by Quaternary glacial moraines related to the Würmian and Rissian glaciations. Figure 10.2 shows a simplified layout of the LHC.

## 10.2.4 Site Development

As most of the new works are on a close to existing facilities, it is assumed for the CDR that the existing facilities such as restaurant, main access, road network etc are sufficient and have not been costed. However, for the parts located outside the existing fence line, but within CERN property, the following items will have to be included in the costs:

- Roads and car parks.
- Drainage networks.
- Landscaping and planting.
- Spoil dumps.



Figure 10.3: TBM Gripper type machine used for Neutrino tunnel at CERN (left) and roadheader type machine (right).

9121 All temporary facilities needed for the construction works have also been included in the cost estimate.

### 9122 10.2.5 Construction Methods

9123 It is envisaged that Tunnel Boring Machines (TBMs) will be utilised for the main tunnel excavation greater  
 9124 than approximately 2km in length. In the Molasse rock, a shielded TBM will be utilised, with single pass pre-  
 9125 cast segmental lining, followed by injection grouting behind the lining. For planning and costing exercises,  
 9126 an average TBM advancement of 25m per day, or 150m per week is predicted.

9127 The second phase excavation will be executed using a roadheader type machine. Both machine types are  
 9128 shown in Figure 10.3. Any new shafts that have to pass through substantial layers of water bearing moraines  
 9129 (for example at CMS) will have to utilize the ground freezing technique. This involves freezing the ground  
 9130 with a primary cooling circuit using ammonia and a secondary circuit using brine at -23C, circulating in  
 9131 vertical tubes in pre-drilled holes at 1.5 metre intervals. This frozen wall allows excavation of the shafts in  
 9132 dry ground conditions and also acts as a retaining wall. Figure 10.4 shows this method being utilized for  
 9133 LHC shaft excavation at CMS.

## 9134 10.3 Civil Engineering Layouts for Ring-Ring

9135 The Ring-Ring solution will require new bypass tunnels at both Point 5 (currently housing the CMS detector)  
 9136 and Point 1 (ATLAS). Both of the bypass tunnels are on the outside of the LHC ring.

9137 The Bypass around CMS Point 5 is 1km long with an internal tunnel diameter of 4.5m. Only one new  
 9138 shaft is required for excavation works. A roadheader type machine will be used for excavation, with the new  
 9139 tunnel position as close as possible to the LHC tunnel as not to induce movements or create operational  
 9140 problems to the existing facilities. Figure 10.5 shows the new bypass tunnel and service cavern required  
 9141 around CMS.

9142 Figure 10.6 shows the bypass tunnel in blue needed around Point 1. This tunnel is 730 m long and has  
 9143 an internal diameter of 4.5 m. Two new 7 m diameter shafts are required to allow access to construct the  
 9144 underground areas with minimum disruption to LHC operations. Underground areas are made available for  
 9145 RF/Cryogenic and general services. Two junction caverns will be excavated to create a liaison with the LHC  
 9146 tunnel.

9147 Waveguides ducts (0.9 m diameter) will connect the LHeC Bypass tunnel to the RF cavern, as shown in  
 9148 Figure 10.7. In order to position the bypass as close as possible to the LHC ring, it has been assumed that

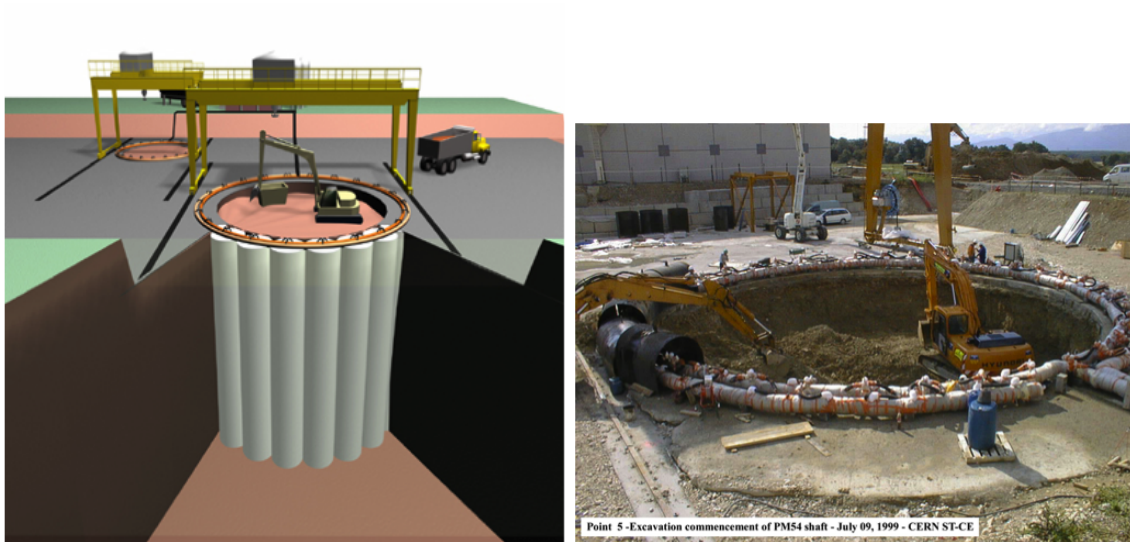


Figure 10.4: LHC Shaft PM54, linking up cylinders of ice to construct a temporary wall.

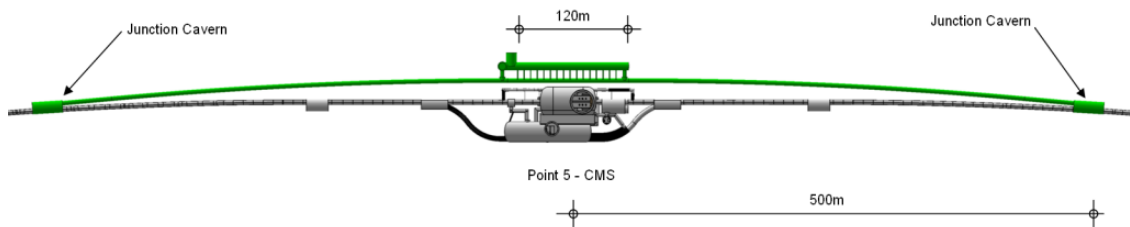


Figure 10.5: Ring-Ring Bypass around CMS Point 5.

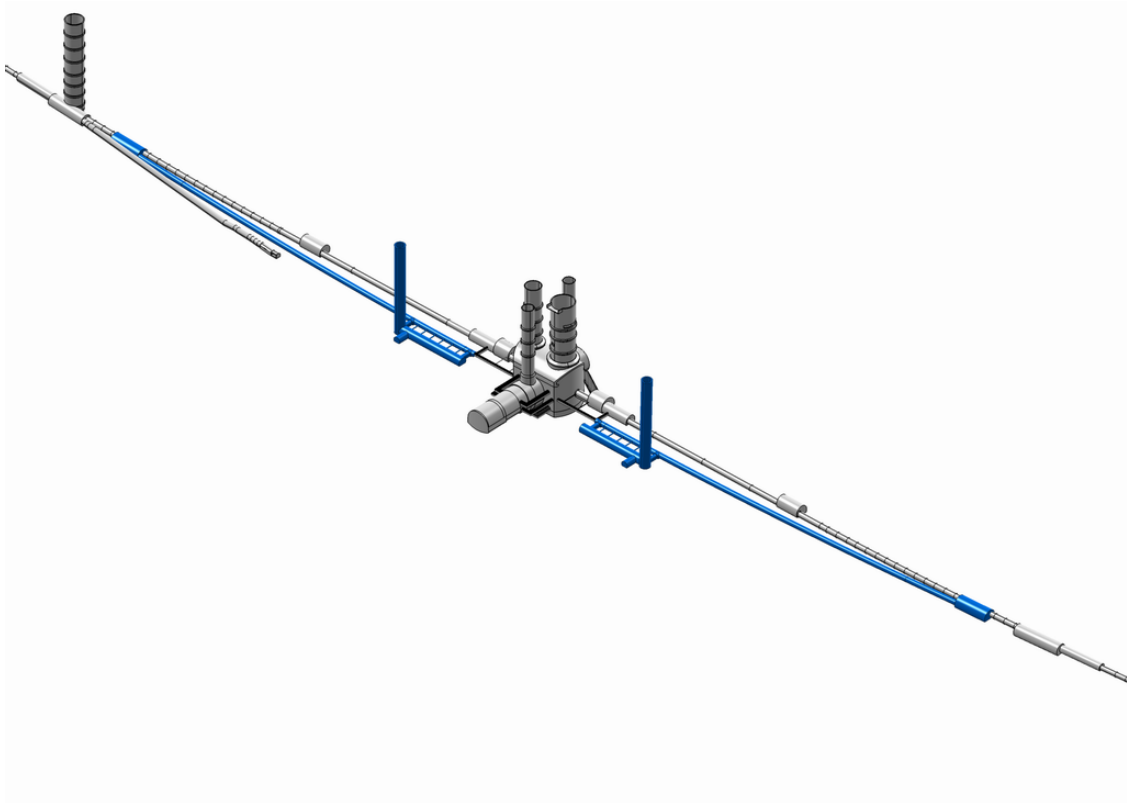


Figure 10.6: Ring-Ring Bypass around ATLAS Point 1.

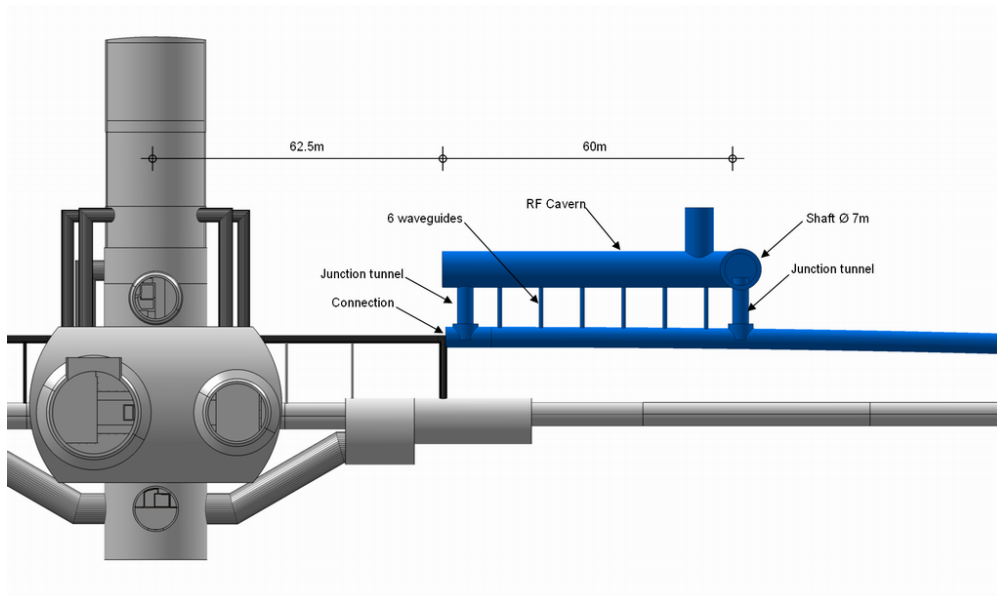


Figure 10.7: Cryo and RF Cavern (one side only) at Point 1.

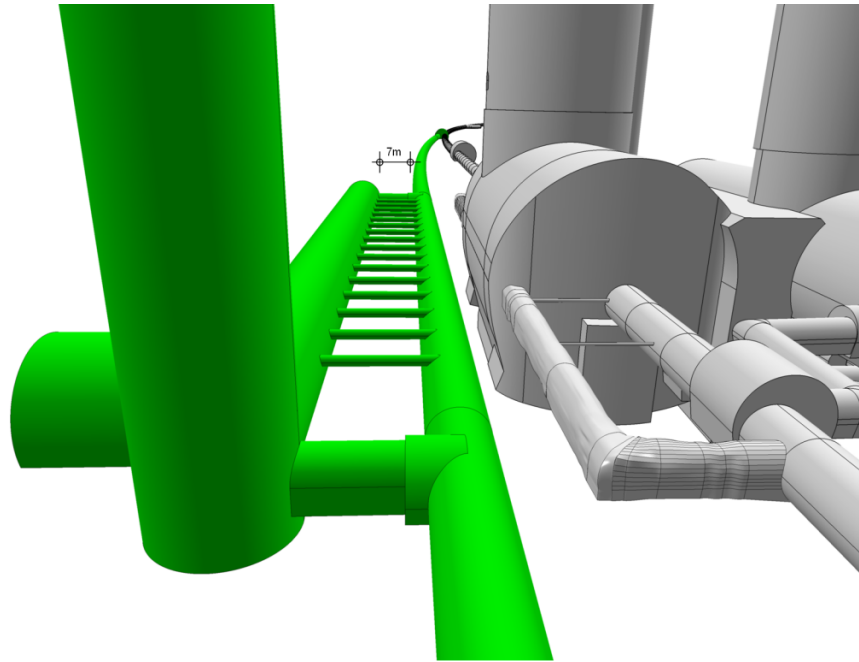


Figure 10.8: 3d model of Ring-Ring Bypass around CMS Point 5.

9149 the LHeC beampipe can be accommodated within the existing survey gallery, and pass through the ATLAS  
 9150 experimental hall.

9151 Figure 10.8 shows a 3d model of the bypass around the CMS Point 5. The new excavations will have a  
 9152 minimum of 7m of Molasse rock separating the new works from existing LHC structures. This is to avoid  
 9153 any unwanted deformation or vibration problems on the existing LHC structures.

9154 The civil engineering for the electron beam injection complex for the Ring-Ring option has not been  
 9155 studied for the CDR.

## 9156 10.4 Civil Engineering Layouts for Linac-Ring

9157 For the CDR it has been assumed that the 60 GeV Energy Recovery Linac (ERL) will be located around  
 9158 the St.Genis area of France, injecting directly into the LHC ALICE Cavern at Point 2. Approximately  
 9159 10 km of new tunnels (5 m and 6 m diameter), 2 shafts and 9 caverns will be required. The majority of civil  
 9160 engineering works can be completed while LHC is operational. Figure 10.9 highlights the area on the LHC  
 9161 where the new ERL will be situated.

9162 The ERL will be positioned inside the LHC Ring, in order to ensure that new surface facilities are  
 9163 located, as much as possible, on existing CERN land. Secondary tunnels running alongside the long straight  
 9164 sections will house RF, Cryogenic and Services for the machine. One of the long straight sections is shown  
 9165 in Figure 10.10. The entire ERL, illustrated in Figure 10.11, will be tilted in order to follow a suitable layer  
 9166 of Molasse rock. On average the ERL will be tilted approximately 1.4%, dipping towards Lake Geneva, as  
 9167 per LHC.

## 9168 10.5 Summary

9169 From a civil engineering point of view, both the Ring-Ring and Linac-Ring options are feasible. The Ring-  
 9170 Ring option will provide a cheaper solution, however, with a marginally increased risk to LHC activity, due

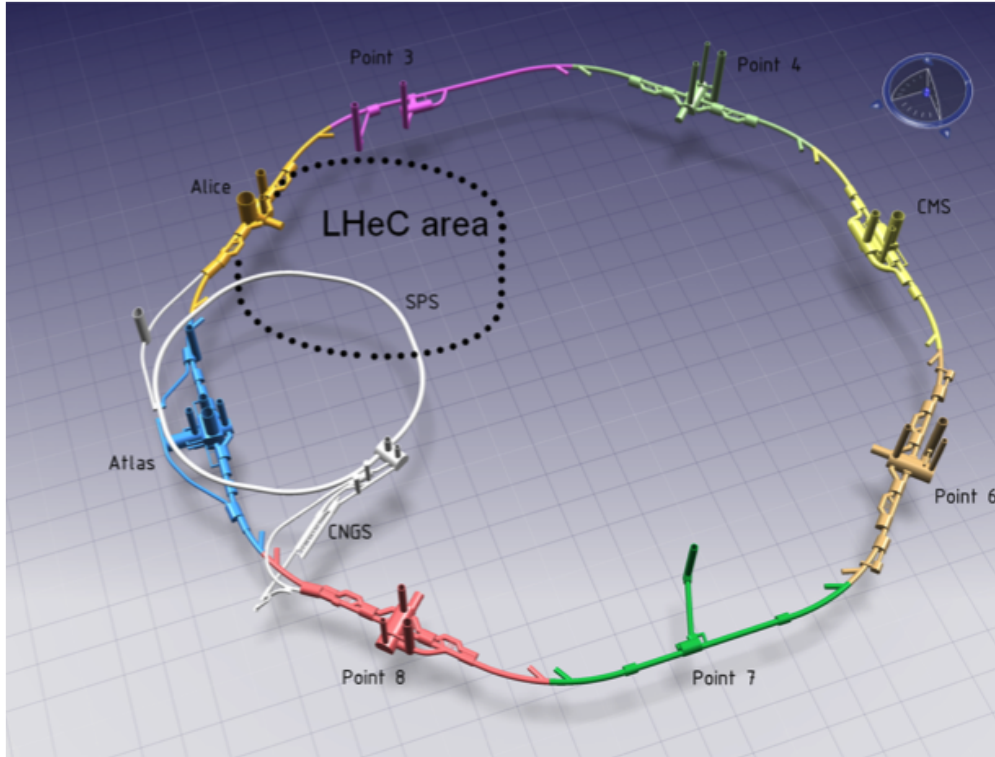


Figure 10.9: Schematic model of ERL position injecting into IP2.

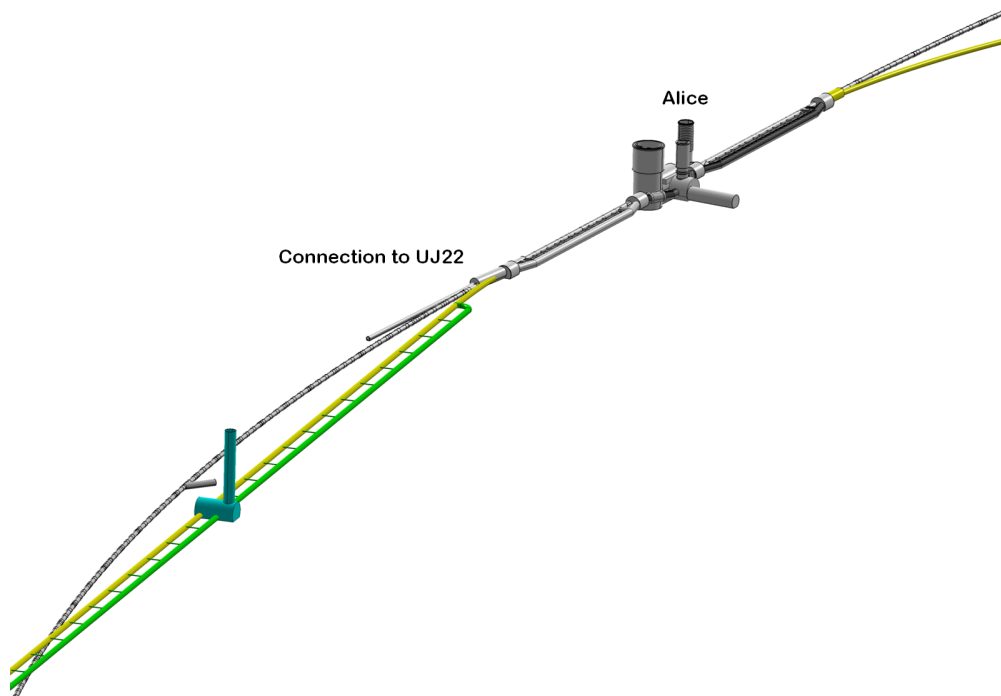


Figure 10.10: ERL Injection area into IP2 and RF/Cryo/Services Cavern (yellow & green).

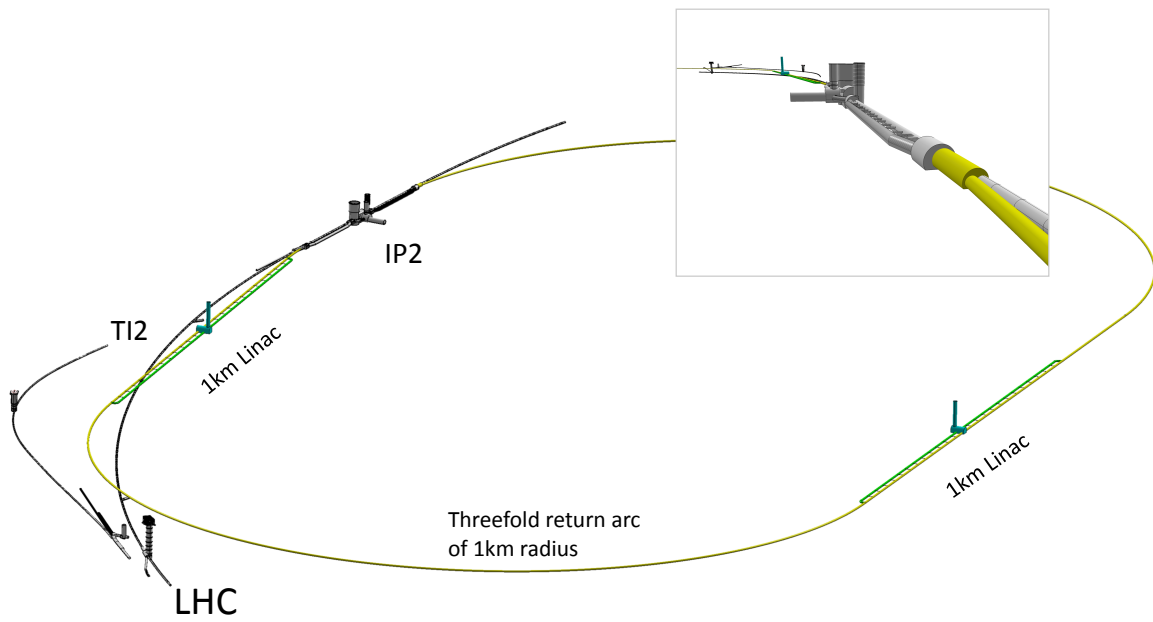


Figure 10.11: View on the ERL placed inside the LHC ring and tangential to IP2. TI2 is the injection line into the LHC. The insert shows the view towards IP2, which currently houses the ALICE experiment, from the direction of the protons colliding with the electron beam incoming from behind.

<sup>9171</sup> to the fact that most of the excavation works being in close proximity to the existing installations. The  
<sup>9172</sup> Linac-Ring option is the cleaner solution from a civil engineering point of view, with much less risk to LHC,  
<sup>9173</sup> but with substantial extra cost and greater time needed for environmental and building permit procedures.



# Chapter 11

## Project Planning

We base the planning of the LHeC project on the assumption that the LHC machine will reach the end of its lifetime when the High Luminosity LHC project reaches its design goal of  $3000fb^{-1}$ . Figure 11.1 shows the current status of the CERN planning for the LHC related upgrade projects. The current planning foresees three long shutdowns:

- Long Shutdown 1 (LS1) for repairing the faulty splice connections in the LHC and allowing operations at nominal energy of 7 TeV.
- Long Shutdown 2 (LS2) for consolidating the LHC for operation above nominal beam intensities
- Long Shutdown 3 (LS3) for implementing the HL-LHC upgrade installations.

Figure 11.2 shows the resulting evolution of the integrated luminosity per experiment over time assuming the LHC performance stabilizes at nominal luminosity after LS1. Figure 11.3 shows a similar evolution of the integrated luminosity assuming the LHC performance stabilizes at ultimate luminosity after LS1.

In both scenarios, the LHC reaches a total integrated luminosity of ca.  $200fb^{-1}$  before LS3 and the installation of the HL-LHC upgrade. The HL-LHC project aims at a generation of  $200fb^{-1}$  to  $300fb^{-1}$  per year [725] and one can assume that the HL-LHC design goal can be reached by between 9 and 13 years after the LS3. Assuming a one year long shutdown for LS3, this implies the accumulation of  $3000fb^{-1}$  by ca. 2030 to 2035. Aiming for the LHeC at an exploitation time of 10 years the LHeC operation should therefore start together with the HL-LHC operation after the LS3 in 2022.

We base our estimates for the project time line on the experience of other projects, such as (LEP, LHC and LINAC4 at CERN and the European XFEL at DESY and the PSI XFEL). In the following we will analyze separately the required time line for the project construction for the RF system development, the production of the magnet system, the required civil engineering and the installation of the accelerator components in the tunnel.

The superconducting RF development for LEP and LHC both required approximately 2 to 3 years for the cavity prototyping and testing and approximately 5 to 6 years of test stand operation of the superconducting RF cavity modules adding up to a total time of approximately 6 to 8 years from first prototype to final installation. The first LHC cavity prototypes were constructed in 2000 with a final installation of the 4 cryo modules in the LHC tunnel in 2006. The first LEP superconducting RF cavity was tested in LEP in 1991. LEP2 operation started in 1996 but still required 2 years of progressively commissioning all cryo modules in building B180 before their final installation in the LEP tunnel. The last cryo module of the 73 4-cell LEP cryo modules was installed in the LEP tunnel in 1999. Both RF installations featured extensive test stand operations. The LEP RF system had cavity test stands in building SM18 and a separate power test in building B180 which were operated from 1994 until 1999. The LHC RF system had both, the cavity and the power test stands, in SM18. The LHC test stands were operated from 2002 until 2006 (the test stand operation was slowed down at the end due to difficulties with the RF coupler design). In both cases, LEP

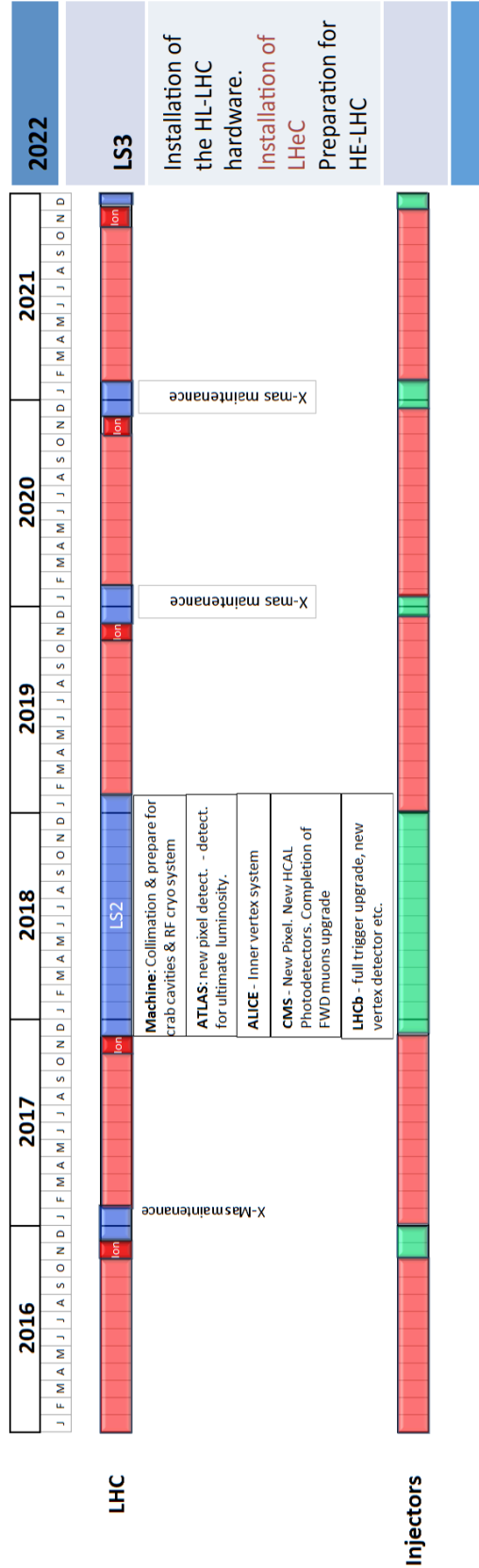
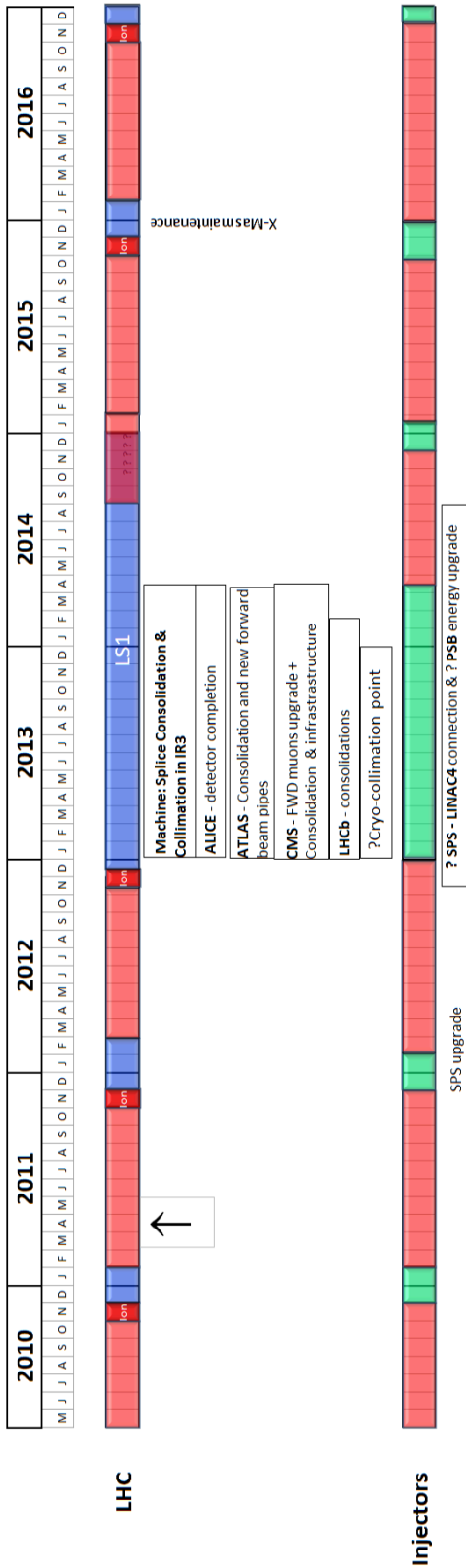


Figure 11.1: CERN medium term plan (MTP), draft as of July 2011, from [724].

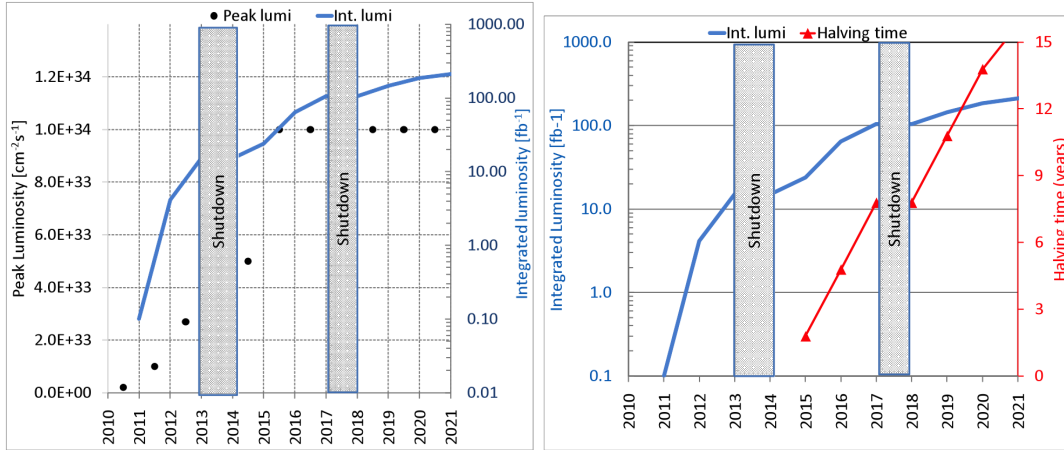


Figure 11.2: Left: Projected luminosity evolution for the LHC assuming the LHC reaches nominal performance levels after the first long shutdown (LS1) and then remains at nominal performance after 2016. Right: The resulting evolution of the integrated luminosity for the LHC experiments. [725].

9210 and LHC, the RF system installation was therefore accompanied by a 5 to 6 year test stand operation which  
 9211 overlapped with the actual installation period in the tunnel [726].

9212 The LHeC linac-ring RF system requires 118 cryomodules of eight 721 MHz 5-cell superconducting RF  
 9213 structures, amounting to a total of approximately 950 structures or thirteen times the number of LEP RF  
 9214 structures. It seems therefore reasonable to assume for the LHeC linac-ring RF system a total time of  
 9215 10 years from first prototype construction to final installation in the tunnel with a dedicated test stand  
 9216 operation for approximately 8 years. <sup>1</sup> The LHeC ring-ring RF system corresponds approximately to the  
 9217 LEPII RF system in terms of total power and overall length of the RF installation and it seems reasonable  
 9218 to assume for the LHeC ring-ring RF system a slightly shorter time scale. Here we assume the same time  
 9219 scale as for LEPII: a total time of 8 years from first prototype construction to final installation in the tunnel  
 9220 with a dedicated test stand operation for approximately 6 years.

9221 For the magnet system we base a first order estimate of the required timescale for the magnet production  
 9222 and installation on the experience with LHC transfer lines. The LHC transfer lines have a total length of 6 km  
 9223 and feature a total of ca. 350 normal conducting magnets. The magnet production extended over 3 years  
 9224 with a production rate of ca. 10 magnets per month [728]. It is, however, important to underline that the  
 9225 production rate was not limited by production capacity but rather, was following the project requirements  
 9226 and the CERN ability for magnet testing after reception at CERN. Both LHeC options feature a relatively  
 9227 large number of magnets, approximately 4000 magnets. Compared to the LHC transfer line magnets, these  
 9228 magnets are much more compact and one can assume that the magnet production rate can be significantly  
 9229 larger than that for the LHC transfer lines. The LHeC magnet production requires therefore industrial  
 9230 production rates featuring several contractors and production lines. The price to pay for such an industrial  
 9231 production scheme will be the requirement for a pre-series production and a thorough quality assurance

<sup>1</sup>Faster production rates could be possible by using several manufacturers in parallel as it is, for example, planned for the ILC. The ILC project requires approximately 15000 cavities and aims at a 10 to 15 times faster production rate as compared to the XFEL cavity production. But such an approach requires long preparation studies for the industrialization (the ILC assumes more than 3 years for such studies [727]), dedicated production test facilities (the ILC has production test facilities at three different laboratories: DESY, KEK and FNAL), an extensive pre-series production and test bench operation for verifying the cavity and cryomodule design before launching the mass production (the ILC project has more than 20 years experience of pre-series production and test bench operation in form of the TTF, FLASH and XFEL installations) and a large production volume so that it is lucrative for several manufacturers to split the overall production while still undertaking significant investments for the production lines. Such an approach may not apply to a 'small' project like the LHeC and may therefore not lead to a much faster production time line.

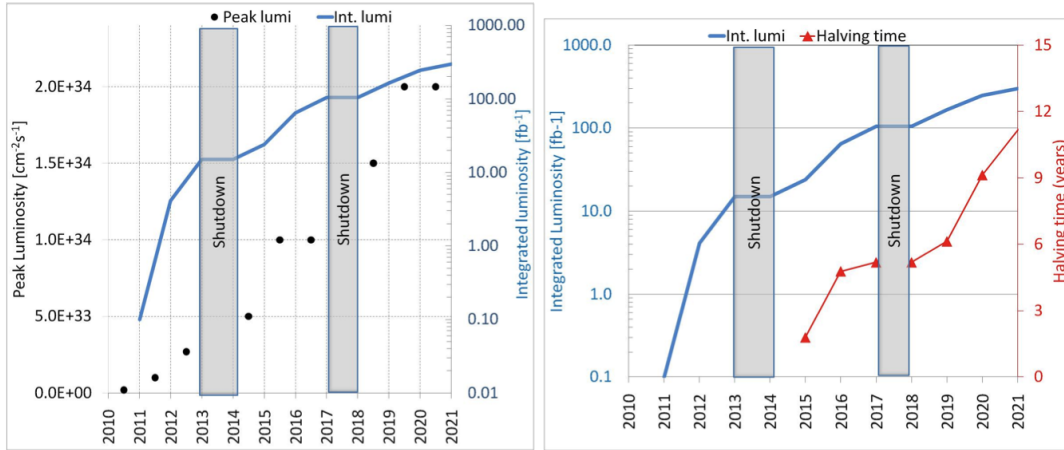


Figure 11.3: Left: Optimistic projection of the luminosity evolution for the LHC assuming the LHC reaches ultimate performance levels after the first long shutdown (LS2). Right: The resulting evolution of the integrated luminosity for the LHC experiments. [725].

9232 over the whole production process. All LHeC magnets will require furthermore a detailed geometry and  
 9233 field quality measurement program after reception at CERN. In the following we assume 1-2 years for the  
 9234 pre-series production and first testing followed by potential design modifications and a peak production rate  
 9235 of ca. 60 dipoles and 20 quadrupoles per month (ca. ten times the production rate of the LHC transfer  
 9236 lines). These assumptions lead to a total construction time of ca. 4 to 6 years and a total of 6 to 8 years  
 9237 from magnet design to final installation in the tunnel.

9238 For the civil engineering we base our first order estimate for the time line on the estimates for the CLIC  
 9239 500 GeV option which features a total length that is comparable to the 60 GeV linac-ring option. The  
 9240 civil engineering work requires for the LHeC linac-ring option the construction of ca. 10 km underground  
 9241 installations which is estimated to take approximately 4 years construction time (the required underground  
 9242 construction for the ring-ring solution is smaller but will occur in the direct vicinity of the main LHC tunnel).  
 9243 The installation of the technical infrastructure (water, electricity etc.) will take approximately 2 years and  
 9244 the final installation of the machine elements in the tunnel another 2 years. All three activities can partially  
 9245 overlap, leading to an estimate of the total construction time of ca. 6 years [729].

9246 For all other components (cryogenics, injector complex, detector etc.) we assume for the moment that  
 9247 their development and installation can be done in the shadow of the three components mentioned above.

9248 In summary, we estimate:

- 9249 • Between 8 and 10 years for the production of the RF system (time from prototype to final installation  
 9250 in the tunnel) with dedicated test stand operation over 6 to 8 years.
- 9251 • Between 6 and 8 years for the production of the magnet system (time from prototype to final installation  
 9252 in the tunnel) with several production lines and test facilities for the quality assurance during the  
 9253 magnet production.
- 9254 • Approximately 6 years for the civil engineering work and actual installation in the tunnel.
- 9255 • All other components such as injector complex, cryogenics installation, detector construction etc, are  
 9256 assumed to lie in the shadow of the above components.

9257 The above time estimates appear as reasonable estimates compared to the planning of other projects like  
 9258 the European XFEL at DESY, the European Spallation Source (ESS) in Sweden, LINAC4 at CERN and  
 9259 the PSI XFEL facilities:

9260  
9261  
9262  
9263  
9264  
9265  
9266  
  
9267  
9268  
  
9269  
9270  
9271  
9272  
9273  
9274  
9275  
  
9276  
9277  
9278  
9279  
  
9280  
9281  
9282  
9283  
9284  
9285  
9286  
9287  
9288  
9289  
9290  
9291  
9292  
9293  
9294  
9295  
9296  
9297  
9298  
9299  
9300  
9301  
9302

- The European XFEL project features a 3 km long superconducting linear accelerator (comparable in size to the linac section of the LHeC linac-ring option) started the civil engineering in January 2009 and plans for completing the civil engineering work in end 2012 (→ 4 years of bare civil engineering work) [730]. The project had in form of the FLASH (TTF) installation a pre-series production of 150 1.3 GHz 9-cell cavity modules that went from 1993 to 2005 (12 years) and an extended test stand operation. The XFEL project plans for an industrial production of more than 600 1.3 GHz 9-cell cavity module from 2010 until 2014 (4 to 5 year production time) [731].
- The ESS facility features ca. 300 m superconducting RF sections and plans for a construction phase of 9 years (2009 until 2017) with first operation in 2018 and full performance reach in 2025 [732].
- The LINAC4 project is a ca. 200 m long normal conducting linac installation which has a ca. 3 year long civil engineering construction period, followed by one year of infrastructure installation and 1.5 years of waveguide and accelerator component installation, amounting to a total construction period of ca. 5.5 years (start of civil engineering in beginning 2008 and end of the accelerator installation by mid 2013) which seems rather long compared to the civil engineering estimates for the LHeC (installation length of ca. 10 km and ca. 100 m underground; ca. 50 times the LINAC4 installation length which is mainly above surface) [733].
- The PSI XFEL project features an approximately 1 km long normal conducting linac and plans for 2 years for the generation of a TDR, a 5 year test stand operation, a 4 year construction period and an installation period of 3 years leading to a total project time line of 6 years from start of the test facilities to the start of the actual project [734].

Except for the European XFEL project, which has a longer superconducting RF section than both LHeC versions, all of the above reference facilities are smaller in scale than the LHeC project and plan between 6 and 9 years from beginning of construction (civil engineering) until the start of operation. All facilities with superconducting cavities plan for an RF production time of ca. 5 years for their key components and a substantial period of test bench operation and pre-series production for critical elements (5 years or more).

Figure 11.4 summarizes the above considerations in form of a schematic outline of the project planning. The planning in Fig. 11.4 addresses only aspects related to the accelerator complex and does not address additional constraints coming from the detector installation in the cavern. Furthermore, it does not include additional constraints arising from the LHC operation, logistics constraints and resource limitations due to the planning for the long shutdowns of the LHC and does therefore certainly not attempt to be an accurate project projection. Rather than presenting an accurate timeline for the LHeC installation, the presented planning aims at illustrating that a start of the LHeC operation in 2023 requires the start of first prototype development and testing already by 2012. Meeting the milestone of an LHeC operation start in 2023 requires a rather swift project launch starting with the generation of a proper TDR and the launch of first RF R&D activities by 2012. This ambitious goal can only be achieved if the project receives adequate resource allocations in 2012. Potential first activities for the prototype development and testing could focus around the development of superconducting RF cavities, where synergies with ESS and SPL studies exist, with the goal of setting up an ERL test facility. It could also include the development of electron and positron sources where synergies with the CLIC and ILC projects exist. Because of their synergies with the ESS, SPL and the linear collider projects, a start of R&D activities for the LHeC by 2012 appears to be quite timely. In case the Ring-Ring installation turns out to be the better option for the LHeC, a ERL test facility could in the end also serve as an injector complex for the Ring-Ring option of the LHeC. It represents therefore a reasonable investment into the LHeC project independent of a the final implementation choice.

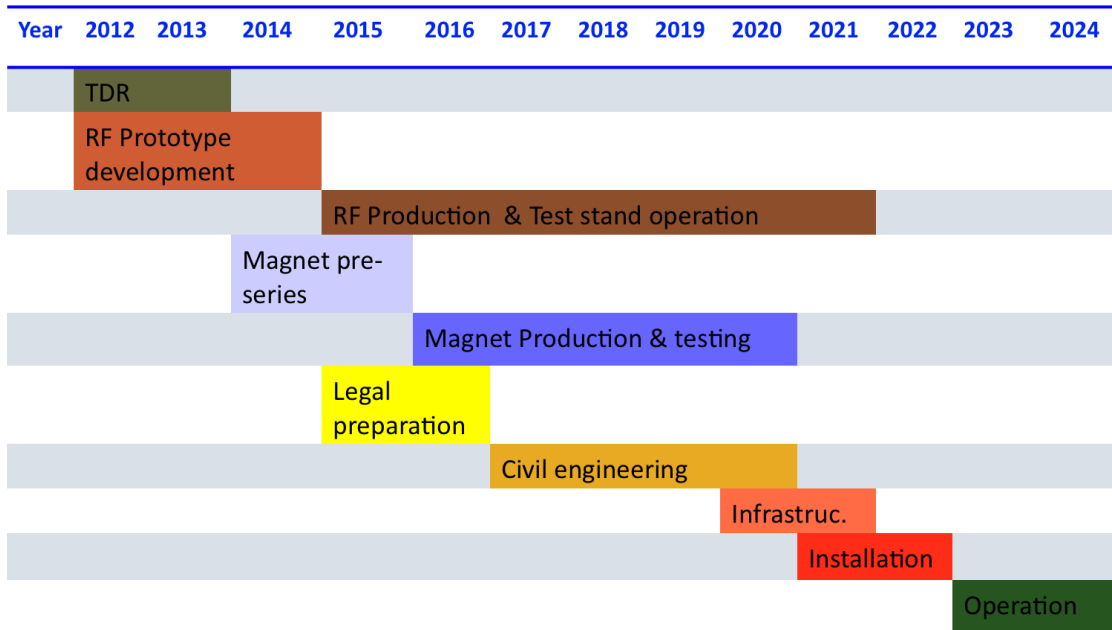


Figure 11.4: Planning considerations for the LHeC, where we assumed a partial overlap of the time lines for the various LHeC project steps (for example a partial overlap of the civil engineering for the tunnel construction and the installation of the technical infrastructure and accelerator components). The overall planning goal of completion by the LS3 seems quite ambitious even with such a partial overlap of individual activities and requires first prototype development as soon as by 2012. The presented planning discusses only aspects related to the accelerator complex and does not address additional constraints coming from the detector installation in the cavern.

## Part IV

# Detector

9303

9304

## Chapter 12

# Detector Requirements

In this chapter the core aspects of the main detector design for the LHeC are discussed. The physics requirements are illustrated along with the boundary conditions from the accelerator options and the interaction region design. These considerations converge in chapter 13 where a first picture of the main detector is presented along with a discussion on the choice for the detector elements and the overall detector assembly. Aspects involving the design of the interaction region, the beam pipe, the particle backgrounds, the magnets and the simulation environment are discussed in the later sections. Finally the single detector components are presented starting from the innermost ones, tracking, calorimetry and muon detectors. Detector components not located in the proximity of the interaction region are described in chapter 14.

### 12.1 Requirements on the LHeC Detector

The new  $ep/A$  detector at the LHeC has to basically be a precision instrument of maximum acceptance. The physics program depends on a high level of precision, as for the measurement of  $\alpha_s$ , and in the reconstruction of complex final states, like the charged current single top production and decay or the precision measurement of the  $b$ -quark density. The acceptance has to extend as close as possible to the beam axis because of the interest in the physics at low and at large Bjorken  $x$ . The dimensions of the detector are constrained by the radial extension of the beam pipe in combination with maximum polar angle coverage<sup>1</sup>, desirably down to about  $1^\circ$  and  $179^\circ$  for forward going final state particles and backward scattered electrons at low  $Q^2$ , respectively. A further general demand is a high modularity enabling much of the detector construction to be performed above ground for keeping the installation time at a minimum, and to be able to access inner detector parts within reasonable shut down times.

The time schedule of the project demands to have a detector ready within about ten years. This prevents any significant R&D program to be performed. The choice of components fortunately can rely on the vast experience obtained at HERA, the LHC, including its detector upgrades to come, and on ILC detector development studies. The next few sections outline the acceptance and measurement requirements on the detector in detail. Then follow more detailed technical considerations, including alternative solutions, which taken together illustrate the feasibility of experimentation at the LHeC.

#### 12.1.1 Installation and Magnets

The LHeC project represents an upgrade of the LHC. The experiment would be the fifth large experiment, and the detector the third multi-purpose  $4\pi$  acceptance detector. It requires a cavern, which for the purpose

---

<sup>1</sup>This CDR adopts the HERA convention of the coordinate system, which has been defined with the  $z$  axis given by the proton beam direction. This implies that Rutherford "backscattering" of the electron is viewed as scattering into small angles. When the partons are essentially at rest, at very small  $x$ , the electrons are scattered "forward" as in fixed target forward spectrometers. The somewhat unfortunate HERA convention calls this backwards. The  $x$  and  $y$  coordinates are defined such that there is a right handed coordinate system formed with  $y$  pointing upwards and  $x$  to the center of the proton ring.



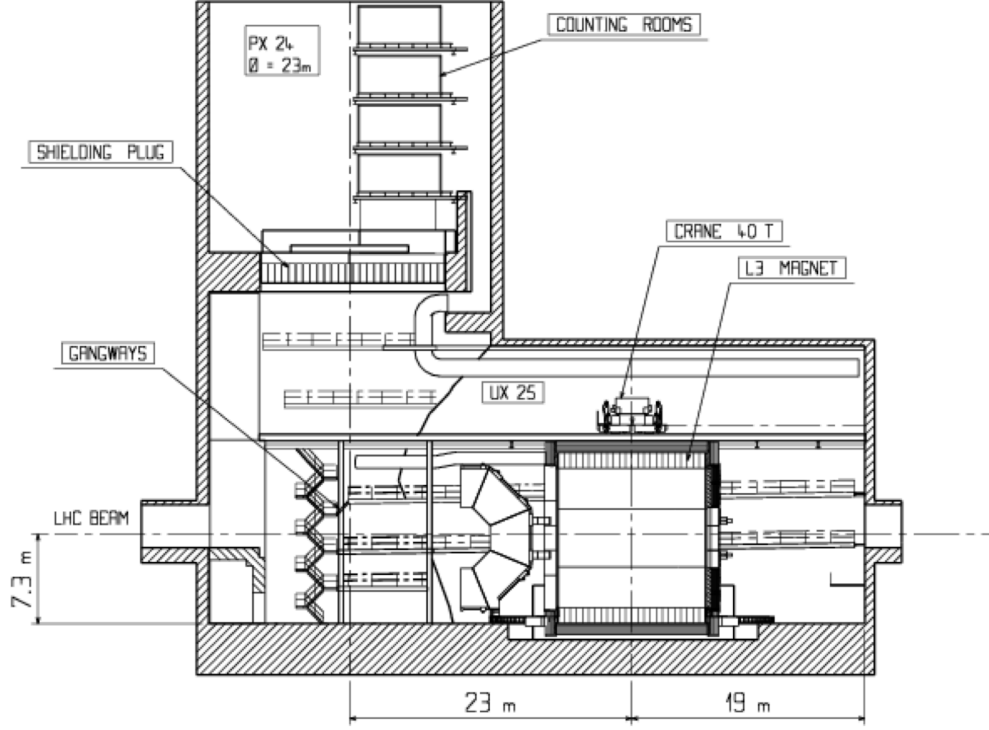


Figure 12.1: Cross section of the IP2 cavern with the ALICE detector inside the L3 magnet. Round access shaft of 23m diameter, cavern about 50m along the beam-line.

9335 of the design study has been considered to be the ALICE cavern in IP2, see Fig. 12.1. The installation of the  
 9336 detector has to proceed as fast as possible in order not to introduce large extra delays to the LHC program.  
 9337 High modularity and pre-assembly above ground are therefore inevitable demands for the design.

9338 The cost has to be limited in order for the project to be fundable in parallel to when the large upgrade  
 9339 investments are presumably made for the ATLAS and CMS detectors in the high luminosity phase of the  
 9340 LHC. The cost is related to technology choices, the detector granularity and its size. Crucial parameters of  
 9341 the detector are the beam pipe dimensions, when combined with the small angle acceptance constraint, see  
 9342 below this section, and the parameters of the solenoid. The cost  $C$  of a solenoid can be represented as a  
 9343 function of the energy density,  $\rho_E$ ,  $C \simeq 0.5(\rho_E/MJ)^{0.66}$  [64], which is determined as

$$\rho_E = \frac{1}{2\mu_0} \cdot \int B^2 dV \simeq \frac{1}{2\mu_0} \cdot \pi r^2 \cdot l \cdot B^2. \quad (12.1)$$

9344 From these relations one derives roughly that the solenoid cost scales linearly with the radius  $r$  and field  
 9345 strength  $B$  and with the length  $l$  to the power 0.66. The solenoid radius influences the track length in the  
 9346 transverse plane, which determines  $\propto r^{-2}$  the transverse momentum resolution whereas field strength enters  
 9347 linearly  $\propto B^{-1}$ .

9348 The Linac-Ring version of the LHeC requires to put an extended dipole field of 0.3T into the detector  
 9349 for ensuring head-on  $ep$  collisions and for separating the beams.

9350 A balance between a strong magnetic field for optimal tracking resolution and an affordable sized magnet  
 9351 has to be found, knowing that the magnets themselves represent one source of inactive material and that  
 9352 the energy stored in the magnets and their return flux require an outer shielding proportional to the field  
 9353 and to the square of the solenoid radius.

9354 In the current design the solenoid is placed in between the electromagnetic and the hadron calorime-

9355 ter<sup>2</sup> at a radius of about 1 m. The magnetic field is set to 3.5 T in order to compensate the small radial  
 9356 extension of the tracker, the focus of which in the LHeC environment is on the forward direction. The cho-  
 9357 sen design position with dipoles and solenoid placed outside the electromagnetic calorimeter ensures good  
 9358 electromagnetic calorimetry and high dipole field quality near to the beam line. Fig. 12.2 shows such the  
 magnet arrangement inside the detector volume schematically. The total material budget of the solenoid

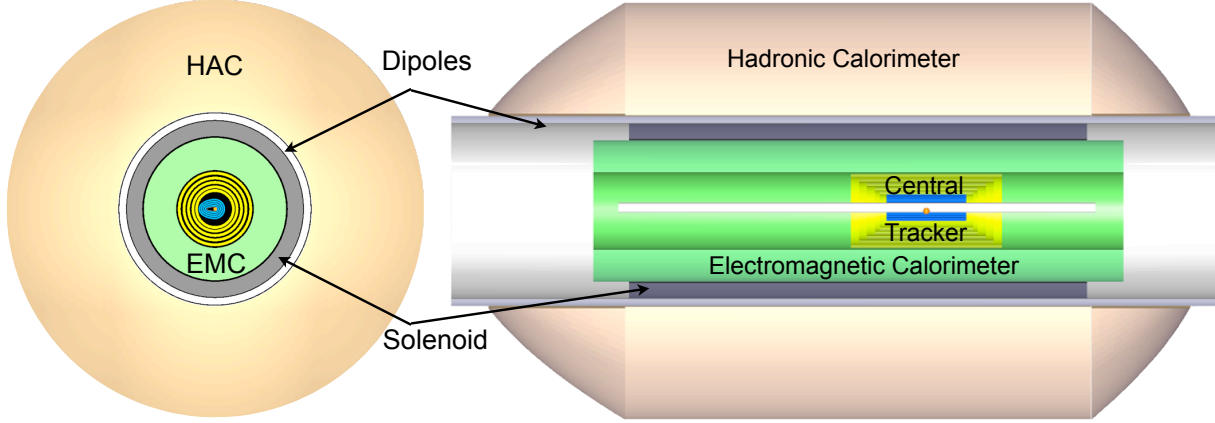


Figure 12.2: Schematic  $xy$  and  $rz$  views of the magnets and barrel calorimeter arrangement for the baseline layout.

9359 and the dipole, at perpendicular crossing, may be represented by about 16 cm of Aluminum, corresponding  
 9360 to about one quarter of an interaction length ( $\lambda_I$ ) and about 1 radiation length ( $X_0$ ). This further supports  
 9361 the choice of the magnets located outside of the electromagnetic calorimeter, yet placed before the hadronic  
 9362 calorimeter in order to limit the radial dimensions. More details on the design study of the detector magnets  
 9363 are addressed in Sect.13.2.  
 9364

### 9365 12.1.2 Kinematic reconstruction

9366 The inclusive  $ep$  DIS kinematics are defined by the negative four-momentum transfer squared,  $Q^2$ , and  
 9367 Bjorken  $x$ . Both are related to the cms energy squared  $s$  via the inelasticity  $y$  through the relation  $Q^2 = sxy$ ,  
 9368 which implies  $Q^2 \leq s$ . The energy squared  $s$  is determined by the product of the beam energies,  $s = 4E_p E_e$ ,  
 9369 for head-on collisions and large energies compared to the proton mass.

9370 The kinematics are determined from the scattered electron with energy  $E'_e$  and polar angle  $\theta_e$  and from  
 9371 the hadronic final state of energy  $E_h$  and scattering angle  $\theta_h$ . The variables  $Q^2$  and  $y$  can be calculated from  
 9372 the scattered electron kinematics as

$$\begin{aligned}
 Q_e^2 &= 4E_e E'_e \cos^2\left(\frac{\theta_e}{2}\right) \\
 y_e &= 1 - \frac{E'_e}{E_e} \sin^2\left(\frac{\theta_e}{2}\right)
 \end{aligned}
 \tag{12.2}$$

9373 and from the hadronic final state kinematics as

$$\begin{aligned}
 Q_h^2 &= \frac{1}{1 - y_h} \cdot E_h^2 \sin^2(\theta_h) \\
 y_h &= \frac{E_h}{E_e} \sin^2\left(\frac{\theta_h}{2}\right)
 \end{aligned}
 \tag{12.3}$$

<sup>2</sup>An option is also considered of placing the solenoid outside the calorimeters, at about 2.5 m radius, combined with a second, bigger solenoid for the flux return, with the muon detector in between. A two-solenoid solution was considered already in the fourth detector concept for the ILD [735].

9374 and  $x$  is given as  $Q^2/sy$ . The kinematic reconstruction in neutral current scattering therefore is redundant,  
 9375 which is one reason why DIS experiments at  $ep$  colliders are precise. An important example is the calibration  
 9376 of the electromagnetic energy scale from the measurements of the electron and the hadron scattering angles.  
 9377 At HERA, this led to energy calibration accuracies for  $E'_e$  at the per mil level. In a large part of the phase  
 9378 space, around  $x = E_e/E_p$ , the scattered electron energy is approximately equal to the beam energy,  $E'_e \simeq E_e$ ,  
 9379 which causes a large “kinematic peak” in the scattered electron energy distribution. The hadronic energy  
 9380 scale can be obtained from the transverse momentum balance in neutral current scattering,  $p_t^e \simeq p_t^h$ . It is  
 9381 determined to about 1% at HERA.

9382 Following Eq.12.3, the kinematics in charged current scattering is reconstructed from the transverse and  
 9383 longitudinal momenta and energy of the final state particles according to

$$\begin{aligned} Q_h^2 &= \frac{1}{1-y_h} \sum p_t^2 \\ y_h &= \frac{1}{2E_e} \sum (E - p_z). \end{aligned} \quad (12.4)$$

9384 There have been many refinements used in the reconstruction of the kinematics, as discussed e.g. in [736],  
 9385 which for the principle design considerations, however, are of less importance.

### 9386 12.1.3 Acceptance regions - scattered electron

9387 The positions of isolines of constant energy and angle of the scattered electron in the  $(Q^2, x)$  plane are given  
 9388 by the relations:

$$\begin{aligned} Q^2(x, E'_e) &= sx \cdot \frac{E_e - E'_e}{E_e - xE_p} \\ Q^2(x, \theta_e) &= sx \cdot \frac{E_e}{E_e + xE_p \tan^2(\theta_e/2)}. \end{aligned} \quad (12.5)$$

9389 Following these relations, an acceptance limitation of the scattered electron angle, as due to the beam pipe  
 9390 or focussing magnets, to a maximum value  $\theta_e^{max}$  defines a constant minimum  $Q^2$  which independently of  $E_p$   
 9391 is given as

$$Q_{min}^2(x, \theta_e^{max}) \simeq [2E_e \cot(\theta_e^{max}/2)]^2. \quad (12.6)$$

9392 apart from the smallest  $x$ . This is illustrated in Fig.12.3. There follows that a  $179^\circ(170^\circ)$  angular cut  
 9393 corresponds to a minimum  $Q^2$  of about 1(100)  $\text{GeV}^2$  at nominal electron beam energy. One easily recognizes  
 9394 in Fig.12.3 that the physics at low  $x$  and  $Q^2$  requires to measure electrons scattered backwards from about  
 9395  $135^\circ$  up to  $179^\circ$ . Their energy in this  $\theta_e$  region does not exceed  $E_e$  significantly. At lower  $x$  to very good  
 9396 approximation  $y = E'_e/E_e$  (as can be seen from the lines  $y = 0.5$  and  $E'_e = 30 \text{ GeV}$  in Fig.12.3).

9397 Following Eq.12.6,  $Q_{min}^2$  varies  $\propto E_e^2$ . It thus is as small as  $0.03 \text{ GeV}^2$  for  $E_e = 10 \text{ GeV}$ , the injection  
 9398 energy of the ring accelerator but increases to  $6.0 \text{ GeV}^2$  for  $E_e = 140 \text{ GeV}$ , the maximum electron beam  
 9399 energy considered in this design report, apart from smallest  $x$ , if  $\theta_e^{max} = 179^\circ$ . While  $Q_{min}^2$  decreases  $\propto E_e^2$ ,  
 9400 the acceptance loss towards small  $x$  is only  $\propto E_e$ . The measurement of the transition region from hadronic  
 9401 to partonic behavior, from  $0.1$  to  $10 \text{ GeV}^2$ , therefore requires to take data at lower electron beam energies<sup>3</sup>.  
 9402 These variations are illustrated in Fig.12.4 for an electron beam energy of  $10 \text{ GeV}$ , the injection energy for  
 9403 the ring and a one-pass linac energy, and for the highest  $E_e$  of  $140 \text{ GeV}$  considered in this report.

<sup>3</sup>The requirement of acceptance up to  $179^\circ$  determines the length of the backward detector. It could be tempting to utilize this  $E_e$  dependence in the design: if one limited the backward electron acceptance to for example  $178^\circ$  instead of  $179^\circ$  this would reduce the backward detector extension in  $-z$ . With data taken at reduced  $E_e$  one would come back to lower  $Q^2$ . From Eq.12.6 one derives that  $E_e = 30 \text{ GeV}$  and  $178^\circ$  is leading to the same  $Q_{min}^2$  of about  $1.1 \text{ GeV}^2$ , at not extremely small  $x$ , as is  $E_e = 60 \text{ GeV}$  and  $179^\circ$ . However, one would loose in acceptance to the lowest  $x$ , linearly with  $E_e$ . Moreover, for the present design the (inner) beam pipe radius in vertical direction is  $2.2 \text{ cm}$ . This results in an extension of about  $1.5 \text{ m}$  for the first tracker plane to register an electron scattered at  $179^\circ$ . If one adds about  $1 \text{ m}$  for the tracker length, and  $1 \text{ m}$  for the backward calorimeter following the tracker, one arrives at about  $3.5 \text{ m}$  backward detector length. Obviously for  $178^\circ$  one could reduce

### LHeC - electron kinematics

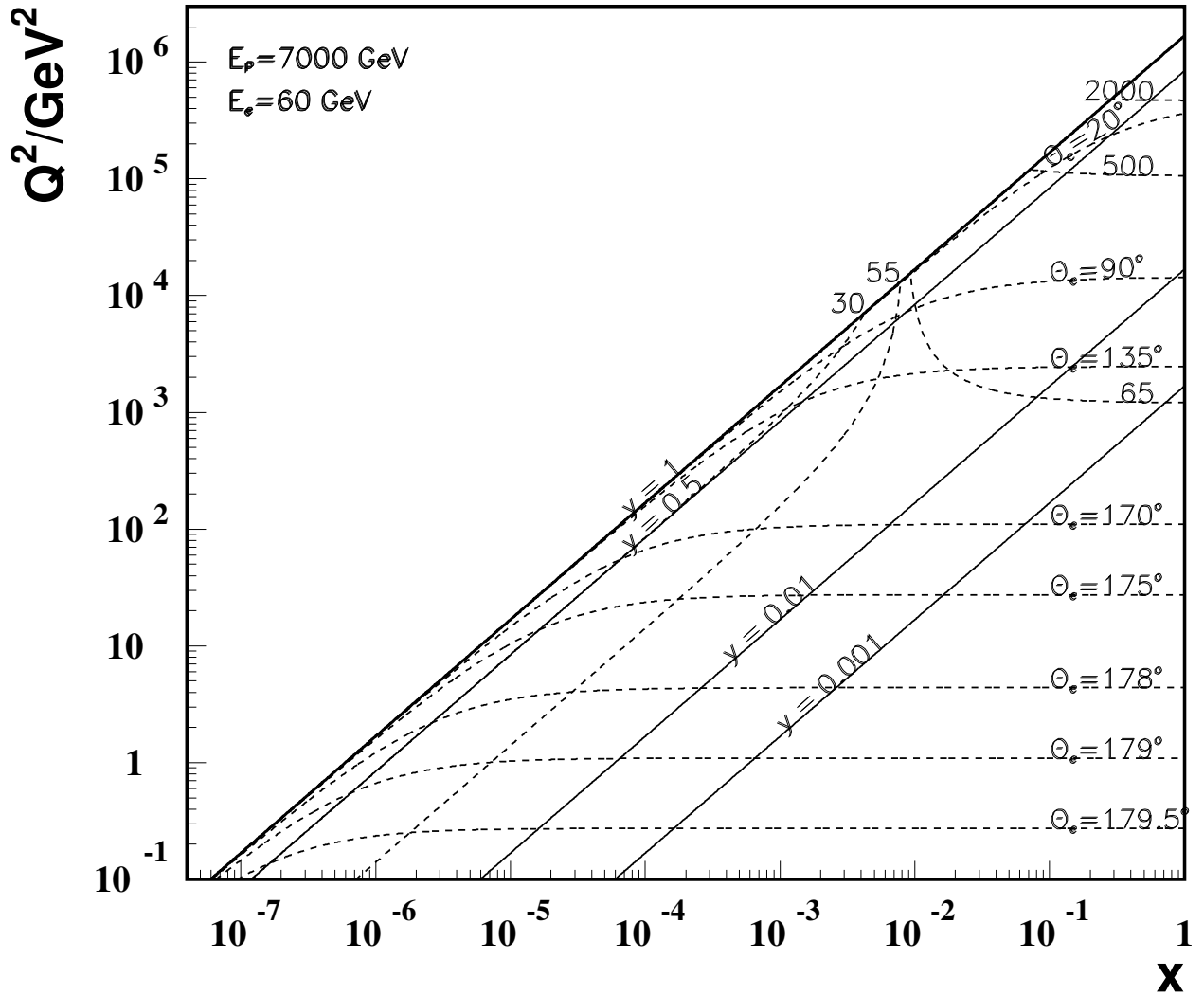


Figure 12.3: Kinematics of electron detection at the LHeC. Lines of constant scattering angle  $\theta_e$  and energy, in GeV, are drawn. The region of low  $Q^2 \lesssim 10^2 \text{ GeV}^2$ , comprising the lowest  $x$  region, requires to measure electrons scattered backwards with energies not exceeding  $E_e$ . At small energies, for  $y \lesssim 0.5$  a good  $e/h$  separation is important to suppress hadronic background, as from photoproduction. The barrel calorimeter part, of about  $90 \pm 45^\circ$ , measures scattered electrons of energy not exceeding a few hundreds of GeV, while the forward calorimeter has to reconstruct electron energies of a few TeV. Both the barrel and the forward calorimeters measure the high  $x$  part, which requires very good scale calibration as the uncertainties diverge  $\propto 1/(1-x)$  towards large  $x$ .

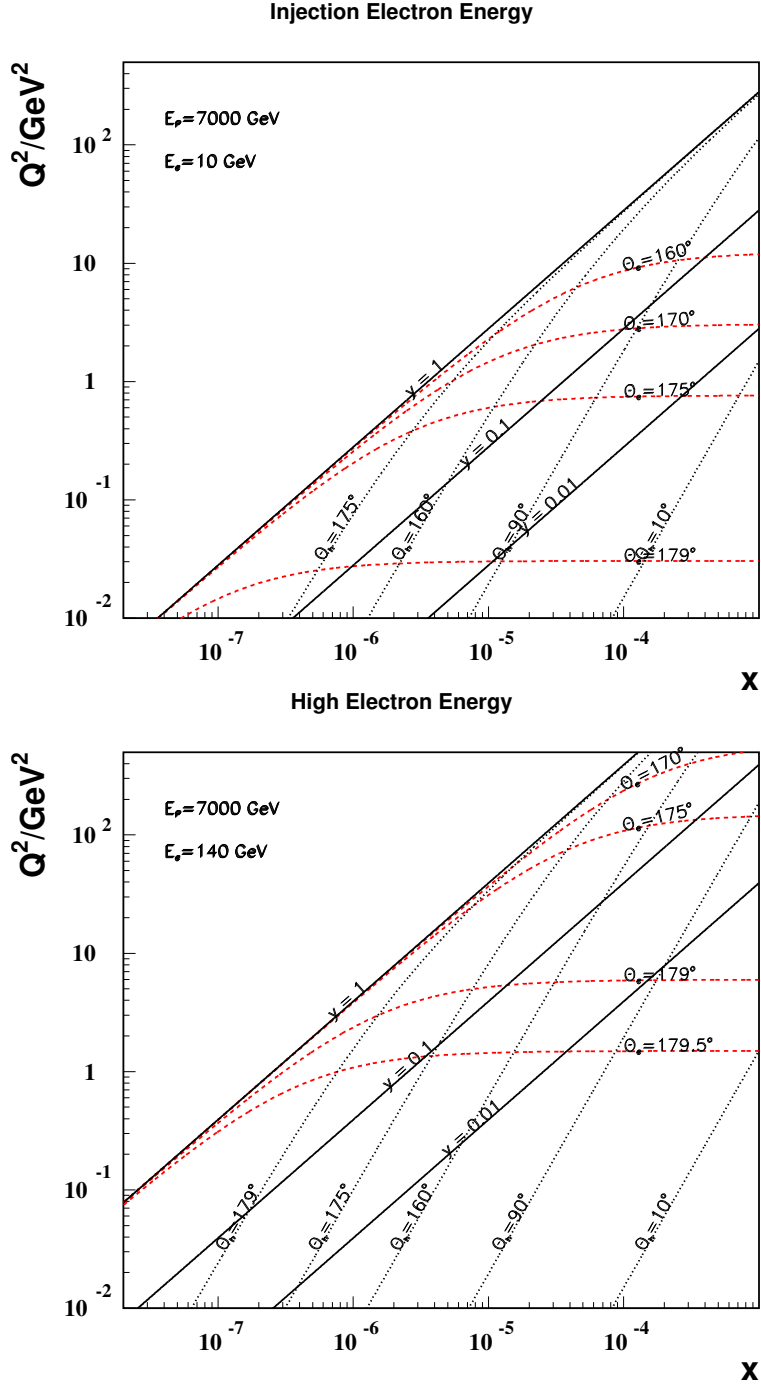


Figure 12.4: Kinematics at low  $x$  and  $Q^2$  of electron and hadronic final state detection at the LHeC with an electron beam energy of 10 GeV (top) as compared to 140 GeV (bottom). At larger  $x$ , the iso- $\theta_e$  lines are at about constant  $Q^2 \propto E_e^2$ . At low  $x$ , the scattered energies, not drawn here, are approximately at  $E'_e \simeq (1 - y) \cdot E_e$ , and at lower  $Q^2$  and  $x$  one has  $E_h \simeq E_e - E'_e \simeq y \cdot E_e$ . At very high  $E_e$  part of the very low  $Q^2$  region may be accessible with the electron tagged along the  $e$  beam direction, outside the central detector, and the kinematics measured with the hadronic final state.

9404 Electrons scattered forward correspond to scattering at large  $Q^2 \geq 10^4 \text{ GeV}^2$ , as is illustrated in the  
 9405 zoomed kinematic region plot Fig. 12.5. The energies in the very forward region,  $\theta_e \lesssim 10^\circ$ , exceed 1000 GeV.  
 9406 For large  $E_e$  and  $x$ , Eq. 12.5 simplifies to  $Q^2 \simeq 4E_e E'_e$ , i.e. a linear relation of  $Q^2$  and  $E'_e$  which is independent  
 of  $x$  and of  $E_p$ , apart from the fact that  $Q_{max}^2 = s$ .

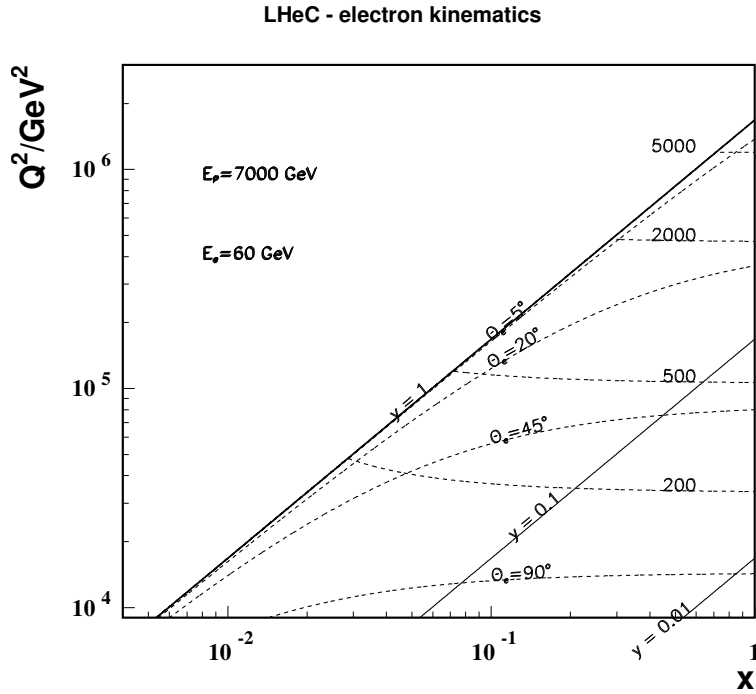


Figure 12.5: Kinematics of electron detection in the forward detector region corresponding to large  $Q^2 \geq 10^4 \text{ GeV}^2$ . The energy values are given in GeV. At very high  $Q^2$  the iso- $E'_e$  lines are rather independent of  $x$ , i.e.  $Q^2(x, E'_e) \simeq 4E_e E'_e$ .

9407

#### 9408 12.1.4 Acceptance regions - hadronic final state

9409 The positions of isolines in the  $(Q^2, x)$  plane of constant energy and angle of the hadronic final state,  
 9410 approximated here by the current jet or struck quark direction, are given by the relations:

$$\begin{aligned}
 Q^2(x, E_h) &= sx \cdot \frac{x E_p - E_h}{x E_p - E_e} \\
 Q^2(x, \theta_h) &= sx \cdot \frac{x E_p}{x E_p + E_e \cot^2(\theta_h/2)}
 \end{aligned}
 \tag{12.7}$$

9411 and are illustrated in Fig. 12.6. At low  $x \lesssim 10^{-4}$ , the hadronic final state is emitted backwards,  $\theta_h > 135^\circ$ ,  
 9412 with energies of a few GeV to a maximum of  $E_e$ . Lines at constant  $y$  at low  $x$  are approximately at  
 9413  $y = 1 - E'_e/E_e$  and  $E'_e + E_h = E_e$ , i.e.  $y = E_h/E_e$ . Final state physics at lowest  $x \lesssim 3 \cdot 10^{-6}$  requires access  
 9414 to the backward region within a few degrees of the beam pipe (Fig. 12.6). This is the high  $y$  region in which  
 9415 the longitudinal structure function is measured.

the first 1.5 m to say 80 cm but one would still like to have a sizable tracker length for achieving some sagitta to determine the charge of the scattered electron and perhaps arrive at an overall backward detector length of about 2.5 m. While this is an interesting reduction one loses the lowest  $x$  corner which opens  $\propto E_e$ . The access to lowest  $x$  in the DIS region is a fundamental part of the LHeC physics program and thus the about  $179^\circ$  design requirement has been kept. There are reasons to take data with reduced  $E_e$  as for  $F_L$ , thus the LHeC detector will access the region below  $1 \text{ GeV}^2$  too.

### LHeC - hadronic final state kinematics

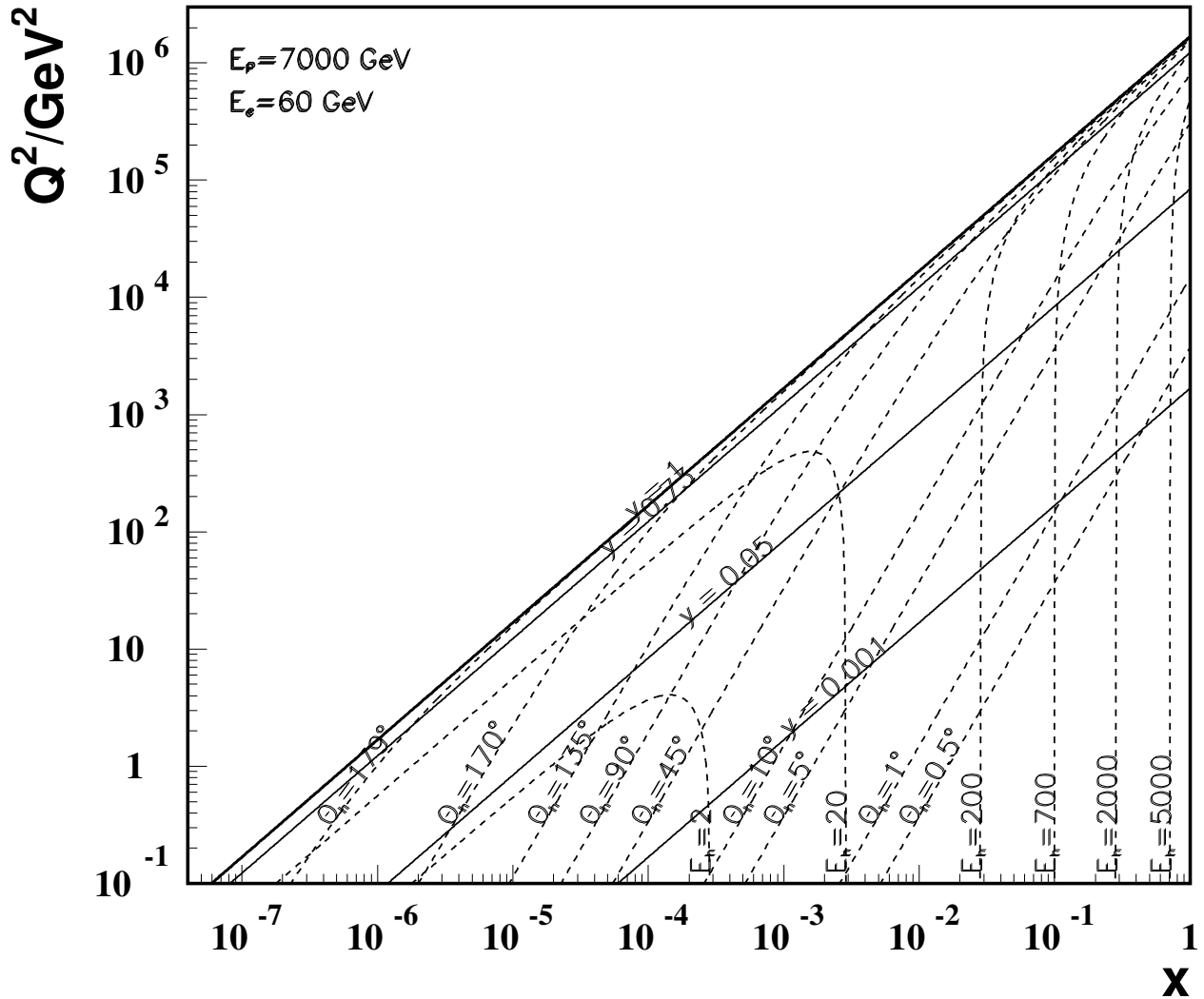


Figure 12.6: Kinematics of hadronic final state detection at the LHeC. Lines of constant energy and angle of the hadronic final state are drawn, as represented by simple kinematics of the struck quark. One easily recognizes that the most demanding region is the large  $x$  domain, where very high energetic final state particles are scattered close to the (forward) direction of the proton beam. The barrel region, of about  $90 \pm 45^\circ$ , is rather modest in its requirements. At low  $x$  the final state is not very energetic,  $E_h + E'_e \simeq E_e$ , and scattered into the backward detector region.

9416 The  $x$  range accessed with the barrel calorimeter region, of  $\theta_h$  between  $135^\circ$  and  $45^\circ$ , is typically around  
 9417  $10^{-4}$  and smaller than a decade for each  $Q^2$ , as can be seen in Fig. 12.6. The hadronic energies in this  
 9418 part do not exceed typically 200 GeV. The detector part which covers this region is quite large but the  
 9419 requirements are modest. One might even be tempted to consider a two-arm spectrometer only. However,  
 9420 the measurement of missing transverse energy and the importance of using the longitudinal momentum  
 9421 conservation for background and radiative correction reductions, with the  $E - p_z$  criterion, demand the  
 9422 detector to be hermetic and complete.

9423 For the measurement of the hadronic final state the forward detector is most demanding. Due to the  
 9424 high luminosity, the large  $x$  region will be populated and a unique physics program at large  $x$  and high  $Q^2$   
 9425 may be pursued. In this region the relative systematic error increases like  $1/(1-x)$  towards large  $x$ , see  
 9426 below this section. At high  $x$  and not extreme  $Q^2$  the  $Q^2(x, E_h)$  line degenerates to a line  $x = E_h/E_p$  as  
 9427 can be derived from Eq. 12.7 and be seen in Fig. 12.6. High  $x$  coverage thus demands the registration of up  
 9428 to a few TeV of energy close to the beam pipe, i.e. a dedicated high resolution calorimeter is mandatory for  
 9429 the region below about  $5 - 10^\circ$  extending to as small angles as possible. A minimum angle cut  $\theta_{h,min}$  in the  
 9430 forward region, the direction of the proton beam, would exclude the large  $x$  region from the hadronic final  
 9431 state acceptance (Fig. 12.6), along a line

$$Q^2(x, \theta_{h,min}) \simeq [2E_p x \tan^2(\theta_{h,min}/2)]^2, \quad (12.8)$$

9432 which is linear in the  $\log Q^2, \log x$  plot and depends on  $E_p$  only. Thus at  $E_p = 7$  TeV the minimum  $Q^2$   
 9433 is roughly  $(1000[100]x)^2$  at a minimum angle of  $10[1]^\circ$ . Since the dependence in Eq. 12.8 is quadratic with  
 9434  $E_p$ , lowering the proton beam energy is of considerable interest for reaching the highest possible  $x$  and  
 9435 overlapping with the large  $x$  data of previous experiments or searches for specific phenomena as intrinsic  
 9436 heavy flavour.

### 9437 12.1.5 Acceptance at the High Energy LHC

9438 Presently one considers to build a high energy (HE) LHC in the thirties with proton beam energies of  
 9439 16 TeV [737]. Such an accelerator would better be combined with an electron beam of energy exceeding the  
 9440 60 GeV, considered as default here, in order to profit from the doubled proton beam energy and to limit the  
 9441 asymmetry of the two beam energies. Choosing the 140 GeV beam mentioned above in this section as an  
 9442 example, Figure 12.7 displays the kinematics and acceptance regions for given scattering angles and energies  
 9443 of the electron (dashed green and red) and of the hadronic final state (black, dotted and dashed dotted).  
 9444 The cms energy in this case is enhanced by about a factor of five. The maximum  $Q^2$  reaches  $10 \text{ TeV}^2$ , which  
 9445 is  $10^6$  times higher than the typical momentum transfer squared covered by the pioneering DIS experiment  
 9446 at SLAC. The kinematic constraints in terms of angular acceptance would be similar to the present detector  
 9447 design as can be derived from the  $Q^2, x$  plot. At very high  $x$  ( $Q^2$ ) the energy  $E_h$  ( $E'_e$ ) to be registered would  
 9448 be doubled. With care in the present design, one would probably be able to use the main LHeC detector  
 9449 components also in the HE phase of the LHC.

### 9450 12.1.6 Energy Resolution and Calibration

9451 The LHeC detector is dedicated to most accurate measurements of the strong and electroweak interaction  
 9452 and to the investigation of new phenomena. The calorimetry therefore requires:

- 9453 • Optimum scale calibrations, as for the measurement of the strong coupling constant. This is much  
 9454 helped by the redundant kinematic reconstruction and kinematic relations, as  $E'_e \simeq E_e$  at low  $Q^2$ ,  
 9455  $E'_e + E_h \simeq E_e$  at small  $x$ , the double angle reconstruction [738] of  $E'_e$  and the transverse momentum  
 9456 balance of  $p_T^e$  and  $p_T^h$ . From the experience with H1 and the much increased statistics it is assumed  
 9457 that  $E'_e$  may be calibrated to  $0.1 - 0.5\%$  and  $E_h$  to  $1 - 2\%$  accuracy. The latter precision will be most  
 9458 crucial in the forward, high  $x$  part of the calorimeter because the uncertainties diverge  $\propto 1/(1-x)$   
 9459 towards large  $x$ .



## Kinematics at HE-LHeC

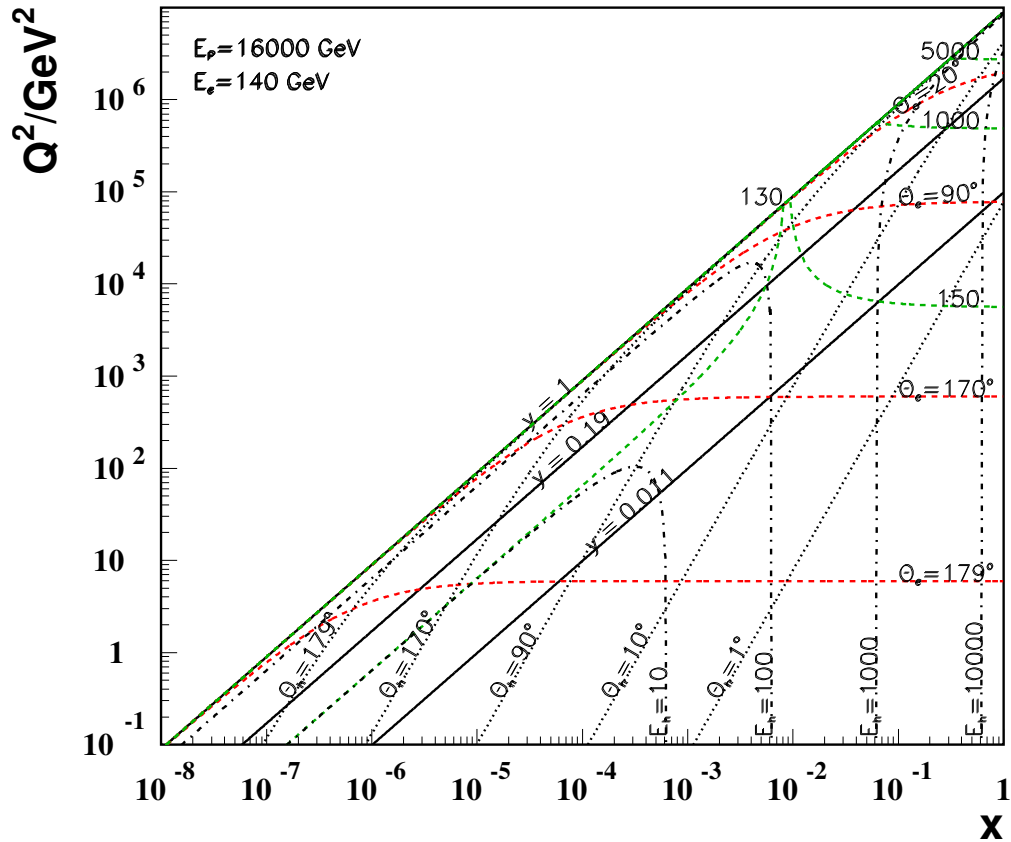


Figure 12.7: Scattered electron and hadronic final state kinematics for the HE-LHC at  $E_p = 16$  TeV coupled with a 140 GeV electron beam. Lines of constant scattering angles and energies are plotted. The line  $y = 0.011$  defines the edge of the HERA kinematics and  $y = 0.19$  defines the edge of the default machine considered in this report ( $E_e = 60$  GeV and  $E_p = 7$  TeV).

- 9460 • High resolution, for the reconstruction of multi-jet final states as from the  $H \rightarrow b\bar{b}$  decay. This is  
 9461 a particular challenge for the forward calorimeter. While detailed simulations are still ongoing one  
 9462 may assume that  $(10 - 15)/\sqrt{E/GeV}$  % resolutions for  $E'_e$  and  $(40 - 50)/\sqrt{E/GeV}$  % for  $E_h$  are  
 9463 appropriate, with small linear terms. These requirements are very similar to the ATLAS detector  
 9464 which quotes electromagnetic resolutions of  $10/\sqrt{E/GeV} \oplus 0.007$  % and hadronic energy resolutions of  
 9465  $50/\sqrt{E/GeV} \oplus 0.03$  %. The basic electromagnetic calorimeter choice for the LHeC can be for Liquid  
 9466 Argon (LAr)<sup>4</sup>. The hadronic calorimeter is outside the magnets and serving also for the magnetic flux  
 9467 return may be built as a tile calorimeter with the additional advantage of supporting the whole detector.  
 9468 The first year of operating the ATLAS combined LAr/TileCal calorimeter has been encouraging. Some  
 9469 special calorimeters are needed in the small angle forward region ( $\theta \lesssim 5^\circ$ ) where the deposited energies  
 9470 are extremely large, and also in the backward region ( $\theta \geq 135^\circ$ ) where the electron detection of modest  
 9471 energy is a special task.

<sup>4</sup>In H1 very good experience has been collected with the longterm stability of the LAr calorimeter. A special demand is the low noise performance because the measurements at small inelasticity  $y$  are crucial for reaching large Bjorken  $x$ . In this region a small misidentified deposition of energy in the backward part of the detector can spoil the measurement at low  $y \lesssim 0.01$ , as can be seen from Eq. 12.4.

9472  
9473  
9474  
9475

- Good electron-hadron separation, as for the electron identification at high  $y$  and low  $Q^2$  (backwards) or high  $Q^2$  (in the extreme forward direction). This is a requirement on the segmentation of the calorimeters and on building trackers in front also of the forward and backward calorimeters to support the energy measurements and the electron identification in particular.

9476

Obviously the calorimetry needs to be hermetic for the identification of the charged current process and good measurement of  $E_{T,miss}$ . These considerations are also summarised in Tab.12.1.

region of detector approximate angular range / degrees	backward 179 - 135	barrel 135 -45	forward 45-1
scattered electron energy/GeV	3-100	10-400	50-5000
$x_e$	$10^{-7} - 1$	$10^{-4} - 1$	$10^{-2} - 1$
elm scale calibration in %	0.1	0.2	0.5
elm energy resolution $\delta E/E$ in % $\cdot \sqrt{E/GeV}$	10	15	15
hadronic final state energy/GeV	3-100	3-200	3-5000
$x_h$	$10^{-7} - 10^{-3}$	$10^{-5} - 10^{-2}$	$10^{-4} - 1$
hadronic scale calibration in %	2	1	1
hadronic energy resolution in % $\cdot \sqrt{E/GeV}$	60	50	40

Table 12.1: Summary of calorimeter kinematics and requirements for the default design energies of  $60 \times 7000 \text{ GeV}^2$ , see text. The forward (backward) calorimetry has to extend to  $1^\circ$  ( $179^\circ$ ).

9477

9478

### 12.1.7 Tracking Requirements

9479

The tracking detector has to enable

9480  
9481  
9482  
9483  
9484  
9485

- Accurate measurements of the transverse momenta and polar angles
- Secondary vertexing in a maximum polar angle acceptance range
- Resolution of complex, multiparticle and highly energetic final states in forward direction
- Charge identification of the scattered electron
- Distinction of neutral and charged particle production
- Measurement of vector mesons, as the  $J/\psi$  or  $\Upsilon$  decay into muon pairs

9486

The transverse momentum resolution in a solenoidal field can be approximated by

$$\frac{\delta p_T}{p_T^2} = \frac{\Delta}{0.3BL^2} \cdot \sqrt{\frac{720}{N+4}} \quad (12.9)$$

9487  
9488  
9489  
9490  
9491  
9492  
9493  
9494  
9495

where  $B$  is the field strength,  $\Delta$  is the spatial hit resolution and  $L$  the track length in the plane transverse to the beam direction, and  $N$  being the number of measurements on a track, which enters as prescribed in [739]. As an example, for  $B = 3.5 \text{ T}$ ,  $\Delta = 10 \mu\text{m}$ ,  $N = 4 + 5$  and  $L = 0.42 \text{ m}$  one obtains a transverse momentum measurement accuracy of about  $3 \cdot 10^{-4}$ . A simulation, using the LICTOY program [740], of the transverse momentum, transverse impact parameter and polar angle resolutions is shown in Fig. 12.8. One can see that the estimate following Eq. 12.9 is approximately correct for larger momenta where the multiple scattering becomes negligible. This momentum resolution, in terms of  $\delta p_T/p_T^2$  is about ten times better than the one achieved with the H1 central drift chamber. It is similar to the ATLAS momentum resolution for central tracks and thus considered to be adequate for the enlarged momenta at LHeC as compared to

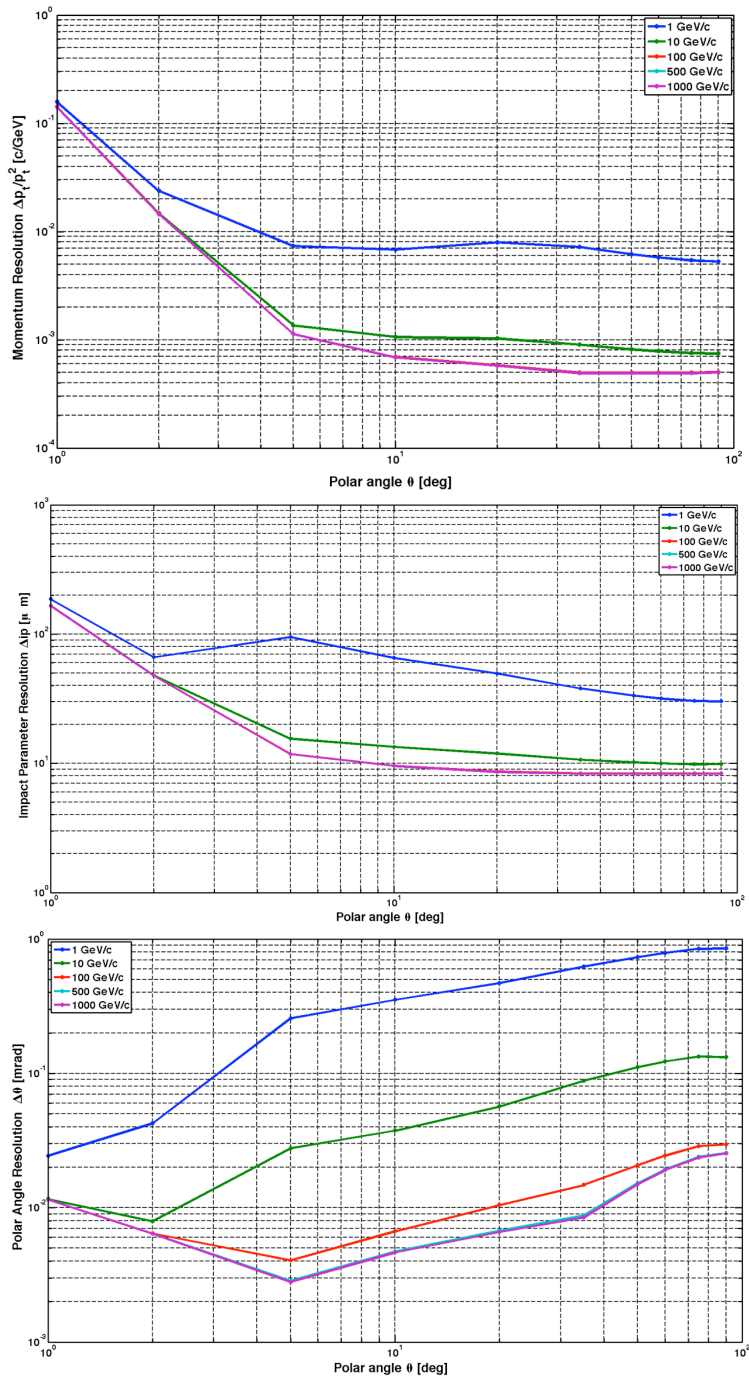


Figure 12.8: Transverse momentum (top), impact parameter (middle) and polar angle (bottom) measurement resolutions as function of the polar angle for the default detector design for four values of track transverse momentum.

HERA and the goal of high precision vertex tagging. One finds that the impact parameter resolution, for high momenta, is a factor of eight improved over the H1 or ZEUS result.

In backward direction, a main tracking task is to determine the charge of the scattered electron or positron, which has momenta  $E'_e \leq E_e$ , down to a few GeV for DIS at high  $y \simeq 1 - E'_e/E_e$ . With a beam spot as accurate as about  $10 \times 30 \mu\text{m}^2$  and the beam pipe radius of a few cm only, the backward Silicon strip tracker will allow a precise  $E/p$  determination when combined with the backward calorimeter, even better than has been achieved with the H1 backward silicon detector [68].

In the forward region,  $\theta < 5^\circ$ , as may be deduced from Figs. 12.5, 12.6, the hadronic final state, for all  $Q^2$ , and the scattered electron, when scattered "back" at high  $Q^2$ , are very energetic. This requires a dedicated calorimeter. Depending on the track path and momentum, the track sagitta becomes very small, for example about  $10 \mu\text{m}$  for a 1 TeV track momentum and a 1 m track length. In such extreme cases of high momenta, the functionality of the tracker will be difficult to achieve: the sagitta becoming small means that there will be limits to the transverse momentum measurement while the ability to distinguish photons and electrons will be compromised by the high probability of showering and conversion when the pipe is passed under very small angles. A forward tracker yet is considered to be useful down to small angles for the reconstruction of the event structure, the rejection of beam induced background and the reconstruction of forward going muons. This region requires detailed simulation studies in a next phase of the project.

### 12.1.8 Particle Identification Requirements

The requirements on the identification of particles focus on the identification of the scattered electron, a reliable missing energy measurement and precision tracking for measuring the decay of charm and beauty particles, the latter rather on a statistical basis than individually. Classic measurements as the identification of the  $D$  meson from the  $K\pi\pi$  decay with a slow pion or the identification of  $B$  production from high  $p_T$  leptons require a very precise track detector. The tracker should determine some  $dE/dX$  properties but there is no attempt to distinguish strange particles, as kaons from pions, as the measurement of the strange quark distribution is traced back to charm tagging in CC events. The identification of muons, apart from some focus on the forward and backward direction, is similar to that of  $pp$  detectors. In addition a number of taggers is foreseen to tag

- electrons scattered near the beam pipe in backward direction to access low  $Q^2$  events and control the photoproduction background;
- photons scattered near the beam pipe in backward direction to measure the luminosity from Bethe Heitler scattering;
- protons scattered in forward direction to measure diffractive DIS in  $ep$  scattering and to tag the spectator proton in  $en$  scattering in electron-deuteron runs;
- neutrons scattered in forward direction to measure pion exchange in  $ep$  scattering and to tag the spectator neutron in  $ep$  scattering in electron-deuteron runs;
- deuterons scattered in forward direction in order to discover diffraction in lepton-nucleus scattering.

From the perspective of particle identification therefore no unusual requirements are derived. One needs a state of the art tracker with a very challenging forward part and a tagger system with the deuteron as a new component in forward direction.

### 12.1.9 Summary of the Requirements on the LHeC Detector

The considerations discussed in this chapter along with the constraints from machine operation and the physics program let to following main items for the detector design.

1. The LHeC experiment has to be operated in parallel to the other LHC experiments and has to be set up in accordance to CERN regulations.

- 9540 2. The detector realization requires a modular design and construction with the assembly process done in  
9541 parallel partly at surface level and partly in the experimental area following the LHC machine running  
9542 and maintenance periods.
- 9543 3. The beam pipe will host the electron beam along with the two LHC counter rotating proton beams.  
9544 The non interacting proton/ion beam has to bypass the IP region guided through the same beam pipe  
9545 housing the electron and interacting proton/ion beam.
- 9546 4. The detector should be modular and flexible to accommodate the high acceptance as well as the high  
9547 luminosity running foreseen for the two main physics programs. The flexibility should accommodate  
9548 reducing/enhancing the energy asymmetry of the beams - section 13.3.
- 9549 5. The detector design can profit from the experience at HERA and the LHC and will be based on the  
9550 recent detector developments in order to meet the ambitious physics requirements, summarized in pre-  
9551 vious chapter, using settled technology, avoiding extended R&D programs and being of comparatively  
9552 reasonable cost.
- 9553 6. Mechanics/services have to be optimized minimizing the amount of material in sensitive regions of the  
9554 experimental setup.
- 9555 7. The detector has to be operated in a high luminosity environment  $L$ . High  $\bar{L}$  is anticipated with small  
9556 beam spot sizes ( $\sigma_x \approx 30\mu m$ ,  $\sigma_y \approx 16\mu m$ ), small  $\beta^*$  and relatively large IP angles (see acc. part). On  
9557 the other hand  $\beta^*$  has to be chosen to eliminate effects of parasitic bunch crossings. The machine and  
9558 detector requirements near the IP is an optimization problem.
- 9559 8. The detector must experience acceptable backgrounds. The design has to be background insensitive as  
9560 far as possible and the machine has to incorporate masks, shielding's and an appropriate optics design  
9561 that minimizes background sources and a vacuum profile that reduces backgrounds.
- 9562 9. It might be necessary to have insertable/removable shielding protecting the detector against injection  
9563 and poor machine performance.
- 9564 10. Special Interaction Region (IR) instrumentation for tuning of the machine with respect to background  
9565 and luminosity is needed. Radiation detectors e.g. near mask and tight apertures are useful for fast  
9566 identification of background sources. Fast bunch related informations are useful for beam optimization  
9567 in that context.
- 9568 11. Good vertex resolution for decay particle secondary vertex tagging is required, which implies a small  
9569 radius and thin beam pipe optimized in view of synchrotron radiation and background production -  
9570 see section 9.9.
- 9571 12. The detector will have one solenoid in its default version building a homogenous field in the tracking  
9572 area of 3.5 T extending over  $z = +370cm, -200cm$ . Solenoid options are described in section 13.2.
- 9573 13. The tracking and calorimetry in the forward and backward direction has to be set up such that the  
9574 extreme asymmetry of the production kinematics are taken into account by layout and choice of  
9575 technology for the detector design and ensure high efficiency measurements. The detectors have to be  
9576 radiation hard.
- 9577 14. Very forward/backward detectors have to be set up to access the diffractive produced events and  
9578 measuring the luminosity with high precision, respectively - chapter 14.

## Chapter 13

# Central Detector

Following the considerations of the physics requirements and the technical and operational constraints outlined in chapter 12.1, a detector design for high precision and large acceptance Deep Inelastic Scattering is presented. The detectors for the Linac-Ring or the Ring-Ring options are nearly identical: the two notable differences are the dipoles in the Linac-Ring case for separating the  $e$  and the  $p$  beams and the larger beam pipe due to the wider synchrotron radiation fan. For practical reasons of this report the more complicated Linac-Ring detector has been chosen as the baseline, termed version A. This evidently affects the solenoid-dipole configuration and the inner shape of the tracker but is of no severe concern. For the Ring-Ring case the luminosity may be maximised by inserting focussing quadrupoles near to the IP. This causes the inner detector to be designed modular such that a transition could be made between the two phases, with the quadrupoles to achieve maximum luminosity and without, to ensure maximum polar angle acceptance <sup>1</sup>.

### 13.1 Basic Detector Description

The LHeC detector is asymmetric in design, reflecting the beam energy asymmetry and reducing cost. It is a general purpose  $4\pi$  detector, which consists of an inner silicon tracker, with extended forward and backward parts, surrounded by an electromagnetic calorimeter, which is separated from the hadronic calorimeter by a solenoid with 3.5 T field incorporating dipoles, in the Linac-Ring case, Fig. 13.1, or not, in the Ring-Ring case, Fig. 13.2. The hadron calorimeter is enclosed in a muon tracker system, not shown here but discussed in section 13.7. The main detector is complemented by hadron tagging detectors in the forward direction and a polarimeter and luminosity measurement system backwards, as is also presented below. Its longitudinal extension is determined by the need to cover polar angles down to  $1^\circ$  at the given beam pipe dimension. Its radial size is mainly determined by the requirement of full energy containment of hadronic showers in the calorimeter.

The dipoles for the Linac-Ring IR cannot be of a too large radius to act on the beam and be affordable. Their bulk material should also not compromise tracking and electromagnetic energy measurements and thus have to be placed outside the electromagnetic calorimeter, chosen to be Liquid Argon. The solenoid cost scales, as discussed above (see Eq.12.1), approximately with its radius which in absolute allows tens of millions CHF to be economised, with the solenoid placed inside the hadronic calorimeter also considering the cost of the 10 kt of iron needed for shielding. In order to minimize cost and material, it appears appropriate to foresee a single cryostat housing the electromagnetic calorimeter and the solenoid and dipole magnets. This leads also to some modification of the forward and backward calorimeter inserts, which can be seen

---

<sup>1</sup>The very recent optics design results suggest that there is only a factor of two difference between the luminosity achievable with and without the quadrupoles. That is not enough to justify considering two measurement phases, in particular having in mind that such a transition, as happened at HERA, may take much more time than one would estimate beforehand. If the Ring-Ring solution was chosen, therefore, it would most likely only require one unchanged main detector configuration. The baseline considered here would be fully adequate for this case, with less complication of the magnets and a narrower pipe.

9610 comparing the Linac-Ring Fig. 13.1 with the Ring-Ring Fig. 13.2. Since for the physics performance it is  
 9611 evidently advantageous to place the solenoid outside the hadronic calorimeter, this option, termed B, has  
 9612 also been studied and is discussed in section 13.2. The radius of the large coil would be about 2.5 m which  
 9613 still compares well with for example the H1 and the CMS coils but is an option for the Ring-Ring machine  
 design only and not the baseline currently.

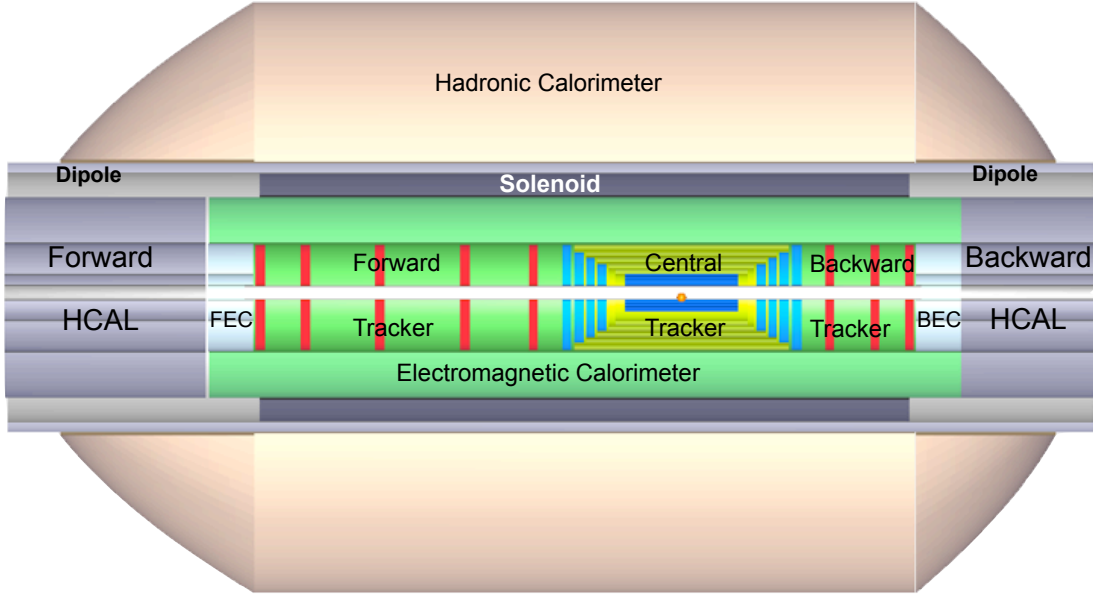


Figure 13.1: Schematic  $rz$  view of the detector design for the Linac-Ring machine option showing the characteristic dipole and solenoid placement between the electromagnetic and the hadronic calorimeters. The proton beam, from the right, collides with the electron beam, from the left, at the IP which is surrounded by a central tracker system complemented by large forward and backward tracker telescopes followed by sets of calorimeters. The detector as sketched here, i.e. without the muon tracking system, has a radius of 2.6 m and extends from about  $z = -3.6$  m to  $z = +5.9$  m in the direction of the proton beam.

9614 The Ring-Ring configuration possibly requires separate data taking phases with maximum polar angle  
 9615 acceptance, for physics at low and high  $x$ , and with ultimate luminosity, for electroweak physics and the search  
 9616 for rare phenomena. Correspondingly, the LHeC inner detector is designed here with a modular structure as  
 9617 is illustrated in Figs. 13.3 and 13.4 which show the detector without and with the low  $\beta$  quadrupoles inserted  
 9618 to accommodate for either configuration, respectively. This requires the removal of the forward/backward  
 9619 tracking setup (shown in red in Fig. 13.3) and the subsequent reinstallation of the external forward/backward  
 9620 electromagnetic and hadronic calorimeter plugins near to the vertex. The high luminosity apparatus would  
 9621 have a polar angle acceptance coverage of about  $8^\circ$ - $172^\circ$  for an estimated gain in luminosity of slightly  
 9622 higher than a factor of two with respect to the large acceptance configuration. The Ring-Ring and Linac-  
 9623 Ring detectors also differ due to the different optics and the beam pipe geometry.

9624 In the Ring-Ring design the  $e$  and  $p/A$  beams collide with a small non-zero crossing angle, large enough  
 9625 to avoid parasitic crossings, which for a 25 ns bunch crossing occur at  $\pm 3.75$  m from the IP. Additional  
 9626 masks are used to shield the inner part of the detector from synchrotron radiation generated upstream of  
 9627 the detector.  
 9628

9629 For the Linac-Ring design, the dipole field in the detector area which allow for head-on collisions and  
 9630 provide the required separation, produces additional synchrotron radiation which has to pass through the  
 9631 interaction region requiring a larger beam pipe. This difference results in a factor of two wider extension of  
 9632 the horizontal beam pipe in the outer region in the Linac-Ring case, which in this regard is the unfavorable

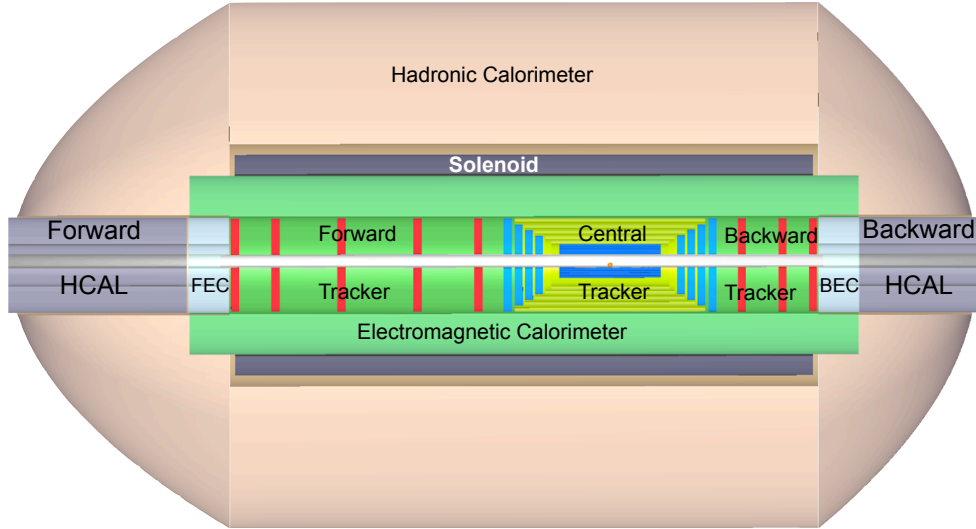


Figure 13.2: Schematic  $rz$  view of the detector design for the Ring-Ring machine option. Note that the outer part of the forward and backward calorimeters ends at smaller radii, as compared to the Linac-Ring case, since there are no dipole magnets foreseen.

9633 solution but unavoidable and necessary fully containing the synchrotron radiation fan. The radius of the  
 9634 circular part has been chosen according to tentative choices of the LHC upgrade beam pipe dimensions.

9635 According to a first estimate of the synchrotron radiation and an initial placement of masks, shielding  
 9636 the Ring-Ring detector from direct and backscattered photons, the beam pipe geometries have been chosen  
 9637 as shown in Fig. 13.5 for the Ring-Ring case and in Fig. 13.6 for the Linac-Ring case.

9638 As already mentioned, the necessity to register particle production down to  $1$  and  $179^\circ$  poses severe  
 9639 constraints on the material and the thickness of the pipe. In the design as shown here, a beryllium pipe  
 9640 would have  $3.0$  ( $1.5$ ) mm thickness in the Linac-Ring (Ring-Ring) case. An extensive R&D program is  
 9641 needed aiming for higher stability of the beam pipe at given dimensions and for thinner/lighter beam wall  
 9642 construction resulting in higher transparency for all final state particles. This R&D program is necessary  
 9643 regardless of which machine option for the LHeC facility is selected. It may also turn out to be advantageous  
 9644 to use a trumpet shaped beampipe when this problem gets revisited in a more advanced phase of the LHeC  
 9645 design when more detailed simulations will be available and results of pipe material developments become  
 9646 known.

9647 In order to ensure optimal polar angle acceptance, the innermost subdetector dimensions have to be  
 9648 adapted to the beam pipe shape. Fig. 13.7 illustrates the configuration that a circular silicon tracker would  
 9649 imply and the corresponding acceptance losses. These can be reduced as shown in Fig. 13.8 if the detector  
 9650 acceptance follows as close as possible the elliptic-circular shape of the pipe. Electrons scattered at high  
 9651 polar angle, corresponding to small  $Q^2 \sim 1 \text{ GeV}^2$ , will only be registered in the inner part of the azimuthal  
 9652 angle region for the nominal electron beam energy. As had been shown in chapter 12.1 (Eq. 12.6), the lowering  
 9653 of the electron beam energy effectively reduces the strong requirement of measuring up to about  $179^\circ$ , at  
 9654 the expense however, of a somewhat reduced acceptance towards lowest Bjorken  $x$ .

9655 The optimum configuration of the inner detector will be revisited when the choice between the Linac-Ring  
 9656 and the Ring-Ring option is made. It represents in any case one of the most challenging problems to be  
 9657 solved for the LHeC.



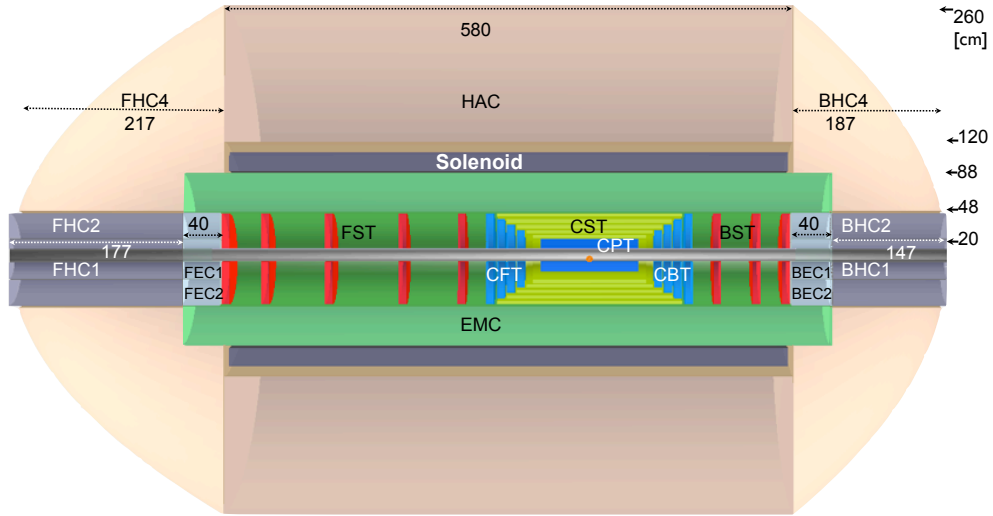


Figure 13.3: An  $rz$  cross section and dimensions of the main detector (muon detector not shown) for the Ring-Ring detector version (no dipoles) extending the polar angle acceptance to about  $1^\circ$  in forward and  $179^\circ$  in backward direction.

Detector Module	Abbreviation
Central Silicon Tracker	CST
Central Pixel Tracker	CPT
Central Forward Tracker	CFT
Central Backward Tracker	CBT
Forward Silicon Tracker	FST
Backward Silicon Tracker	BST
Electromagnetic Barrel Calorimeter	EMC
Hadronic Barrel Calorimeter	HAC
Hadronic Barrel Calorimeter Forward	FHC4
Hadronic Barrel Calorimeter Backward	BHC4
Forward Electromagnetic Calorimeter Insert 1/2	FEC1/FEC2
Backward Electromagnetic Calorimeter Insert 1/2	BEC1/BEC2
Forward Hadronic Calorimeter Insert 1/2	FHC1/FHC2
Backward Hadronic Calorimeter Insert 1/2	BHC1/BHC2

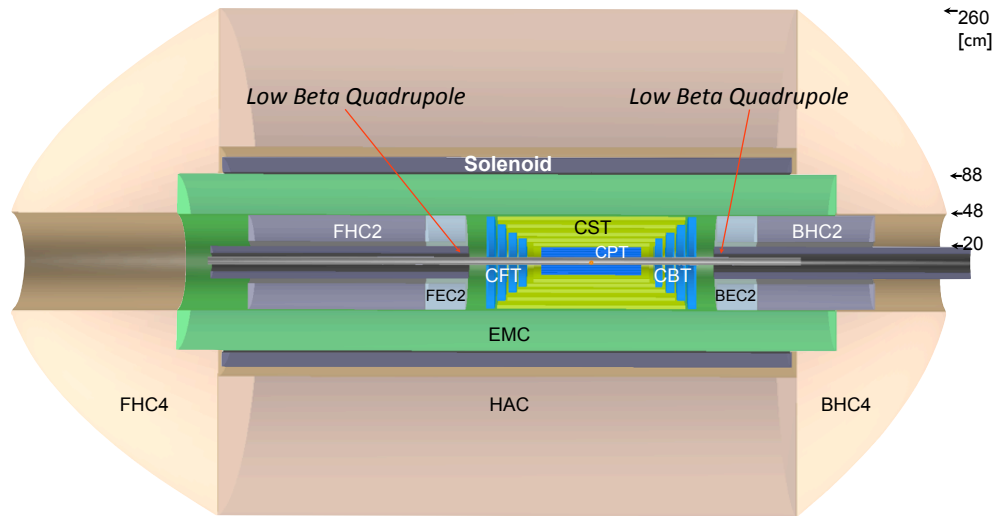


Figure 13.4: An  $rz$  cross section and dimensions of the main detector (muon detector not shown) for the Ring-Ring detector version (no dipoles) in which the luminosity is maximised by replacing the forward and backward tracker telescopes by focusing, low  $\beta$  quadrupole magnets at  $\pm 1.2$  m away from the nominal interaction point. The polar angle acceptance is thus reduced to about  $8 - 172^\circ$ . As compared to the high acceptance detector (Fig. 13.3), the outer forward/backward calorimeter inserts have been moved nearer to the interaction point.

RR - Inner Dimensions  
 Circular(x)=2.2cm; Elliptical(-x)=-5.5, y=2.2cm

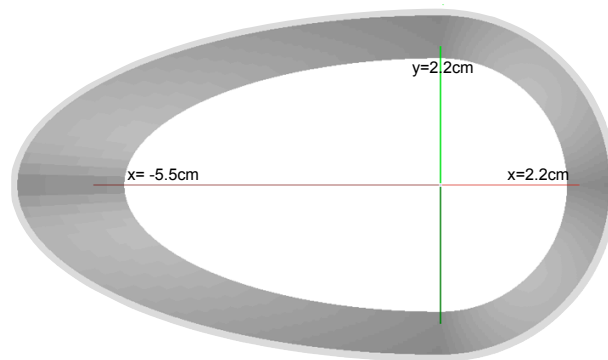


Figure 13.5: Perspective drawing of the beam pipe and its dimensions in the ring-ring configuration. The dimensions consider a 1 cm safety margin around the synchrotron radiation envelope with masks (not shown) for primary synchrotron radiation suppression placed at  $z = 6, 5, 4$  m.

LR - Inner Dimensions  
 Circular(x)=2.2cm; Elliptical(-x)=-10., y=2.2cm

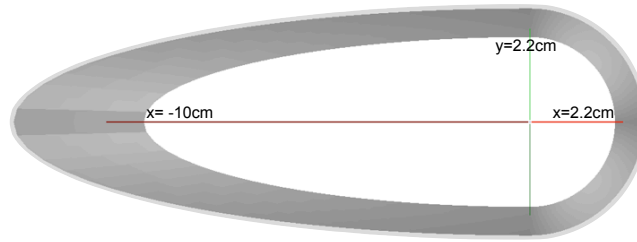


Figure 13.6: Perspective drawing of the beam pipe and its dimensions in the linac-ring configuration. The dimensions consider a 1 cm safety margin around the synchrotron radiation envelope.

### 13.1.1 Baseline Detector Layout

The baseline configuration (A) of the main detector has the solenoid in between the two calorimeters, combined with a dipole field in the Linac-Ring case. The configuration B makes sense only for the Ring-Ring machine design since an outer dipole would be a bad practice for that functionality and a second cryostat with inner dipole between electromagnetic and hadronic calorimeter is bad practice as well, obviously. The main detector is subdivided into a central barrel and the forward and backward end-cap regions, which differ in their design because the forward region sees the remnant and the highly energetic ( $E_h \lesssim E_p$ ) jet from the struck quark while the backward region sees the scattered electron of energy  $E'_e \leq E_e$ . The detector configuration is sketched in Fig. 13.9 with component abbreviations and some dimensions given. More detailed dimensions are given in Fig. 13.10.

For the purpose of this design, technologies had to be chosen in line with the detector requirements, see Sect. 12.1, and based on an evaluation of the technologies available or under development for the LHC experiments or foreseen for a linear collider detector. Due to its compactness and proven technological feasibility, the complete inner tracker is considered to be made of silicon. This allows to keep the radius of the magnets small, about 1 m. Based on experience with H1 and ATLAS the EMC is chosen to be a Liquid Argon (LAr) Calorimeter. The superconducting dipoles (light grey in Fig. 13.9) are placed in a common cryostat with the detector solenoid (dark grey) and the LAr EMC (green). The use of common cryostat is optimum for reducing the amount of material present in front of the hadronic barrel calorimeter. The HAC is an iron-scintillator tile calorimeter, which also guides the return flux of the magnetic field, as in ATLAS [741, 742]. In the baseline design (A) the muon detectors are placed outside of the magnetic field with the function of tagging muons, the momentum of which is determined mainly by the inner tracker.

For the Ring-Ring machine, in order to maximize the luminosity, extra focusing magnets must be placed near to the interaction point <sup>2</sup>. This would mean replacing the FST and the BST tracking detectors by the low- $\beta$  quadrupoles (see Fig. 13.4), at the expense of loosing about  $8^\circ$  of polar angle acceptance. The modular design of the forward and backward trackers and the corresponding calorimeter modules allow the trackers to be mounted/unmounted and the calorimeter inserts to be moved in and out of position as required. The inner electromagnetic and hadronic endcap inserts, FEC1/BEC1 and FHC1/BHC1, respectively, will be removed allowing the insertion of the low  $\beta$ -magnets and only partially put back in. Particular attention is needed for the mechanical support structures of the quadrupoles. The structure must ensure the stability of reproducible beam steering, while interfering as little as possible with the detector. The presence of strong focussing magnets close to the interaction point was one issue experienced during HERA2 running [743].

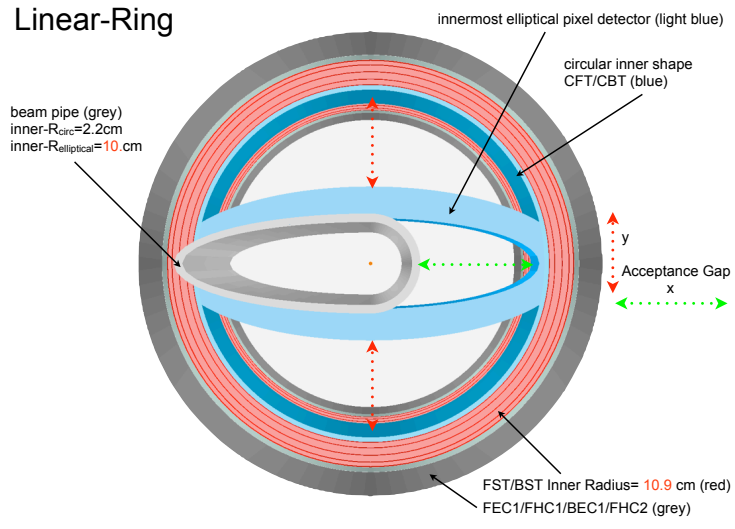


Figure 13.7: Linac-Ring beam pipe design and acceptance gaps due to deviations of inner shapes of the forward/backward tracking detectors FST/BST (circular) and the innermost central pixel detector layer (elliptical) from the pipe shape.

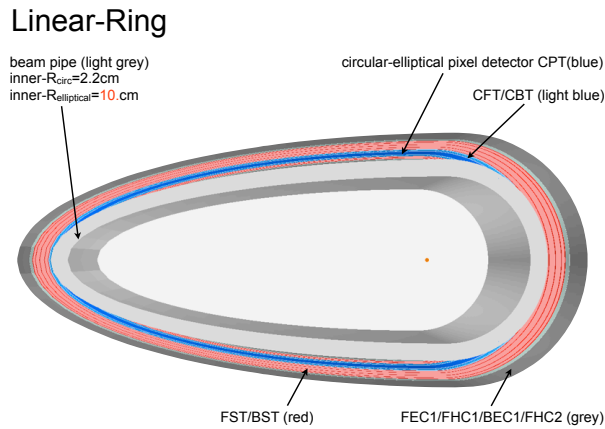


Figure 13.8: Beam pipe design for Linac-Ring and optimized circular-elliptical shape following the beam pipe for all adjacent detector parts.

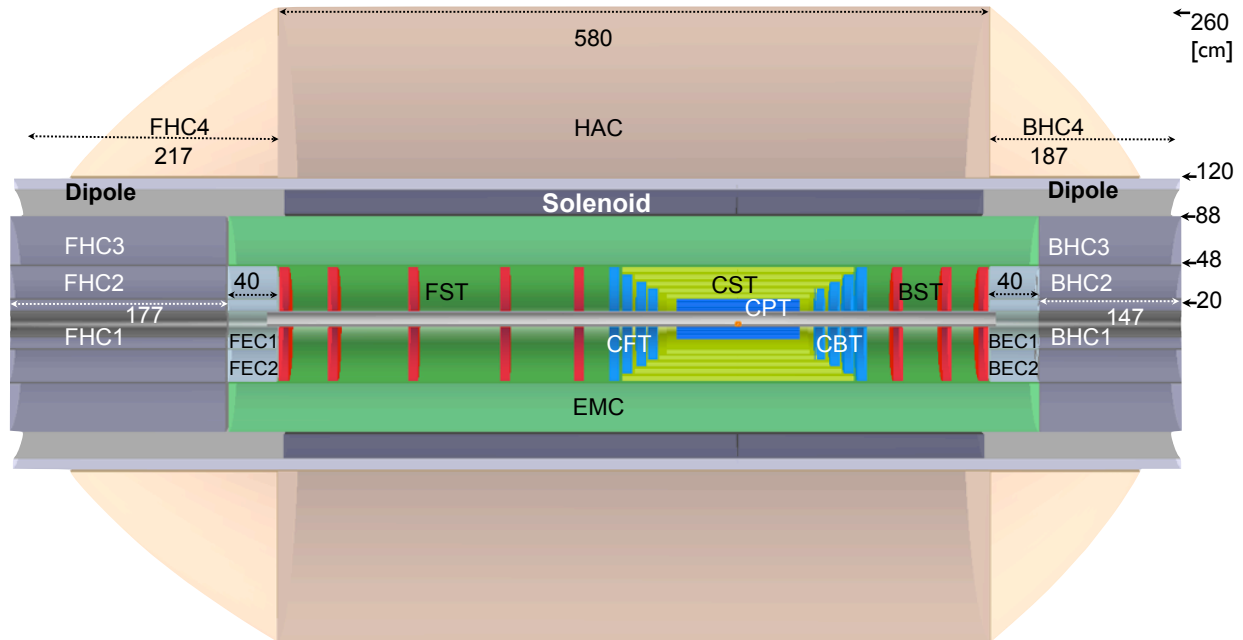


Figure 13.9: An  $rz$  cross section of the LHeC detector in its baseline configuration (A). In the central barrel, the following components are considered: a central silicon pixel detector (CPT); silicon tracking detectors (CST,CFT/CBT) of different technology; an electromagnetic calorimeter (EMC) surrounded by the magnets and followed by a hadronic calorimeter (HAC). Not shown is the muon detector. The electron at low  $Q^2$  is scattered into the backward silicon tracker (BST) and its energy measured in the BEC and BHC calorimeters. In the forward region similar components are placed for tracking (FST) and calorimetry (FEC, FHC).

### 13.1.2 An Alternative Solenoid Placement - Option B

The configuration A is determined by the intention to keep the detector ‘small’: it uses the HAC as flux return for an inside solenoid which, for the Linac-Ring case, is combined with long dipoles. This is not ideal for the hadronic energy measurement. Therefore a second configuration (B) has been considered, to much less detail, in which the solenoid is placed outside the HAC. Option B might be of interest only for the Ring-Ring case as otherwise, the requirement of the bending dipoles to be placed right after the EMC would anyhow compromise the design requiring anyhow similar cryogenics and support structures as in option A.

In considering a solenoid around the HAC one finds, as from the CMS geometry, that the return iron would be massive, of order 10000 tons, and extend by several meters further out in radius, which may pose problems when one has the IP2 cavern in mind. One then is lead to consider using a second solenoid for an active flux return, which gives a good muon momentum reconstruction. A strong magnetic field of 3.5 T covering the barrel calorimeter (HAC) leads to a better separation of charged hadron induced showers in the HAC area compared to the sole fringe field effect in case of the inner solenoid baseline design A. The HAC would have to be designed very carefully as there would be no muon-iron return yoke following for catching shower tails. A warm EMC design with no need for a cryostat would become an option worth considering. Also extending the tracker by an extra more conventional layer of tracking chambers in front of the EMC would be an interesting possibility, with which the amount and radius of the Silicon detector may be somewhat reduced.

An overview of the detector configuration B is given in Fig.13.11. A two solenoid configuration is proposed as an innovative solution with many advantages. A similar design was proposed earlier for the 4<sup>th</sup>

<sup>2</sup>See chapter ?? for an evaluation of that possibility.

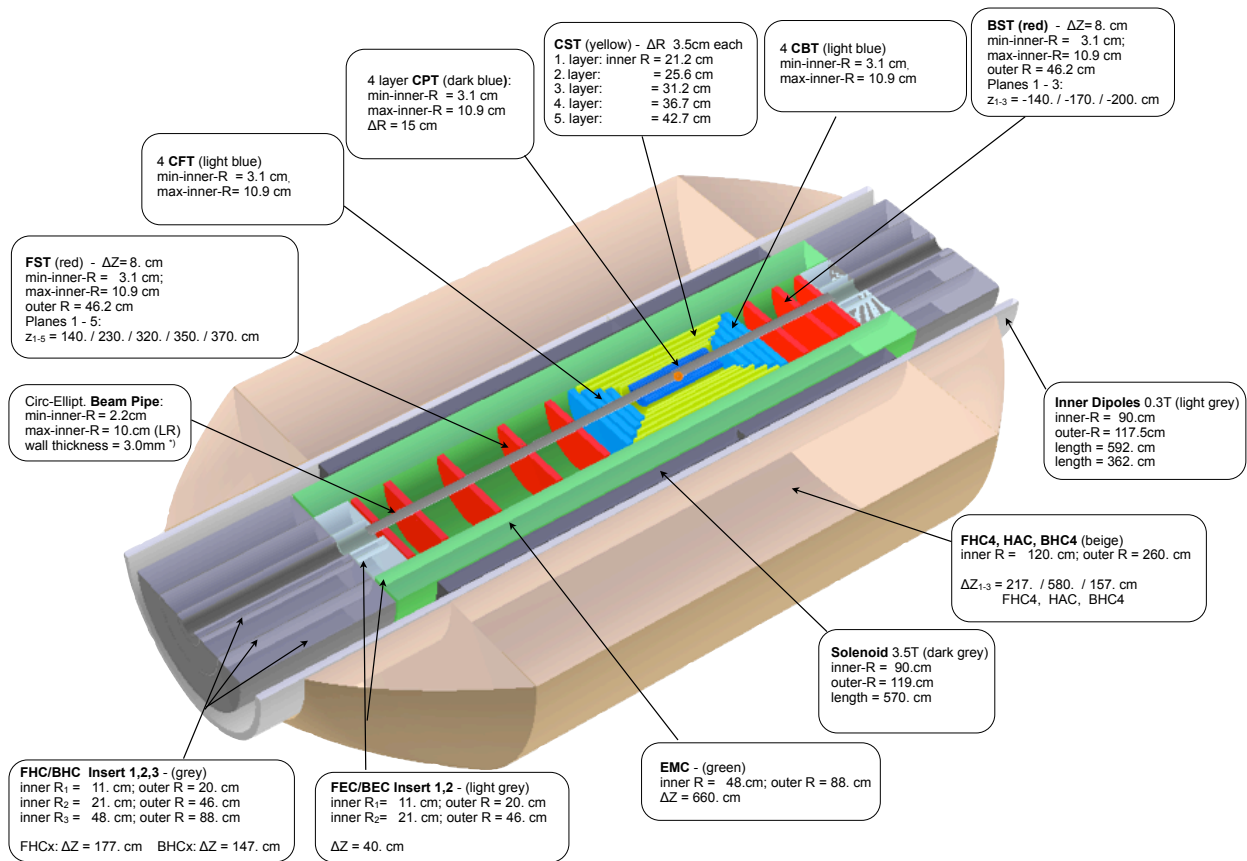


Figure 13.10: View of the baseline detector configuration (A) with some dimensions for each of the main detector components.

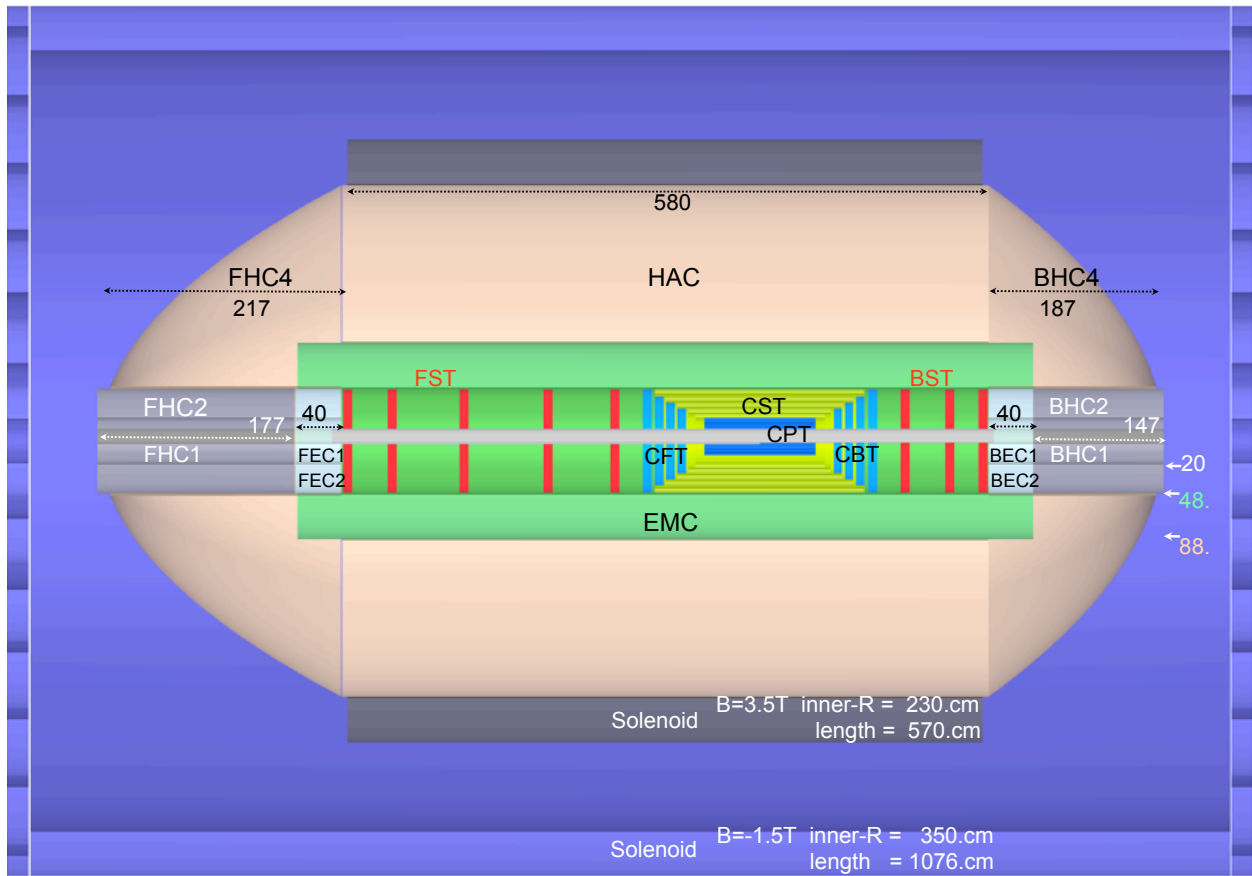


Figure 13.11: An  $rz$  cross section of the LHeC detector, option B, in which the solenoid is placed outside the HAC. A compensating larger solenoid is considered, see text. The muon detector is not shown but would be placed inside the second solenoid. The overall dimensions of this detector configuration are about 11 m length and 8 m diameter.

9709 Concept for an ILC Detector [735]. The second outer solenoid keeps the overall dimensions of the detector  
9710 limited. A detailed consideration of option B has not been intended at this stage of the project, however,  
9711 the statement is made that the option B magnet system is technically feasible and can be chosen if physics  
9712 arguments require to do so and the required extra budget is made available.

## 9713 13.2 Magnet Design

9714 The principle magnet configuration in the Linac-Ring baseline option is introduced and the principle design  
9715 of solenoid and dipole magnets as well as their cryogenic services are described. In section 13.2.5, the twin  
9716 solenoid system option (detector option B) providing 3.5 T in the entire calorimeter space in combination  
9717 with a 1.5 T space for a high precision muon tracking detector is addressed briefly.

### 9718 13.2.1 Magnets configuration

9719 The LHeC magnet system provides a 3.5 T solenoid with a free bore of 1.8 m and a coil length of 5.7 m  
9720 for the bending of the particles produced in the collisions. The bore is dimensioned to provide space for  
9721 the Pixel (CPT) and Strip (CST) detectors as well as the electromagnetic Liquid Argon calorimeter (EMC)  
9722 immersed in a magnetic field while the hadronic tile calorimeter (HAC) and muon tagging detectors are left  
9723 outside. The layout of the magnets in the baseline detector is shown in Figure 13.12. The iron present in  
9724 the hadronic calorimeter also provides the return path for the solenoid magnetic field. In the Linac-Ring  
9725 option also a set of 18 m long e-beam bending dipoles are required that provide 0.3 T on axis, a plus and  
9726 a minus dipole of 9 m length each, respectively. The first dipole is to bring the e-beam into the collision  
9727 point and the second to guide the beam away after the collision point. In the Ring-Ring option this set is  
9728 obsolete. The Linac-Ring option obviously is more demanding and thus taken as the reference design and  
9729 presented here. The introduction of the set of dipoles requires choosing a radial position and radial gap  
9730 for these coils. Since cryogenic space is required for the solenoid as well, an elegant solution is to combine  
9731 within the detector volume the dipoles and the solenoid in one cryostat, thereby minimizing the total radial  
9732 gap as well as maximizing particle transparency. A second combination of cryogenic objects can be made  
9733 by also housing the liquid argon electromagnetic calorimeter in the same cryostat which would reduce the  
9734 radial built up of material significantly. Since a combination is easier the separate option is more demanding  
9735 and therefore engineered and described here. Since the set of dipoles is 18 m long to provide the 2·2.5 Tm  
9736 magnetic field integral, and the detector is 10 m long, each of the two dipoles are split in two sections. The  
9737 inner superconducting sections sit with the solenoid in the same cryostat and the outer normal conducting  
9738 iron based electromagnetic sections with much smaller bore of 0.3 m are positioned on the beam line at  
9739 either side of the detectors, see Figure 13.12.

### 9740 13.2.2 Detector Solenoid

9741 The conceptual design of the solenoid is presented and where necessary some details on the dipoles are  
9742 mentioned as well. The position of the solenoid with respect to the other detector components and the  
9743 envelopes respected have been shown before in Figure 13.9. The longitudinal section of the LHeC baseline  
9744 detector for the default detector configuration and the Linac-Ring option are shown; indicated are the  
9745 position of the 3.5 T solenoid and the 0.3 T inner superconducting dipole sections. Solenoid and dipoles are  
9746 on a common support cylinder and housed in a single cryostat with a free bore of 1.8 m and extending along  
9747 the entire detector with a length of  $\approx 10$  m.

9748 The design of the solenoid is based on the very successful experience with the many detector magnets built  
9749 over the past 30 years, in particular the most recent ATLAS and CMS solenoids [744], [745], [746], [747].  
9750 The dimensions of the LHeC solenoid (3.5 T, 5.7 m long and 0.96 m inner radius) are about those of the  
9751 ATLAS solenoid (2.0 T, 5.3 m long with 1.25 m radius) while it has to provide the magnetic field of the much  
9752 larger CMS solenoid. Since the requested magnetic field is 1.75 times higher than in the ATLAS solenoid a



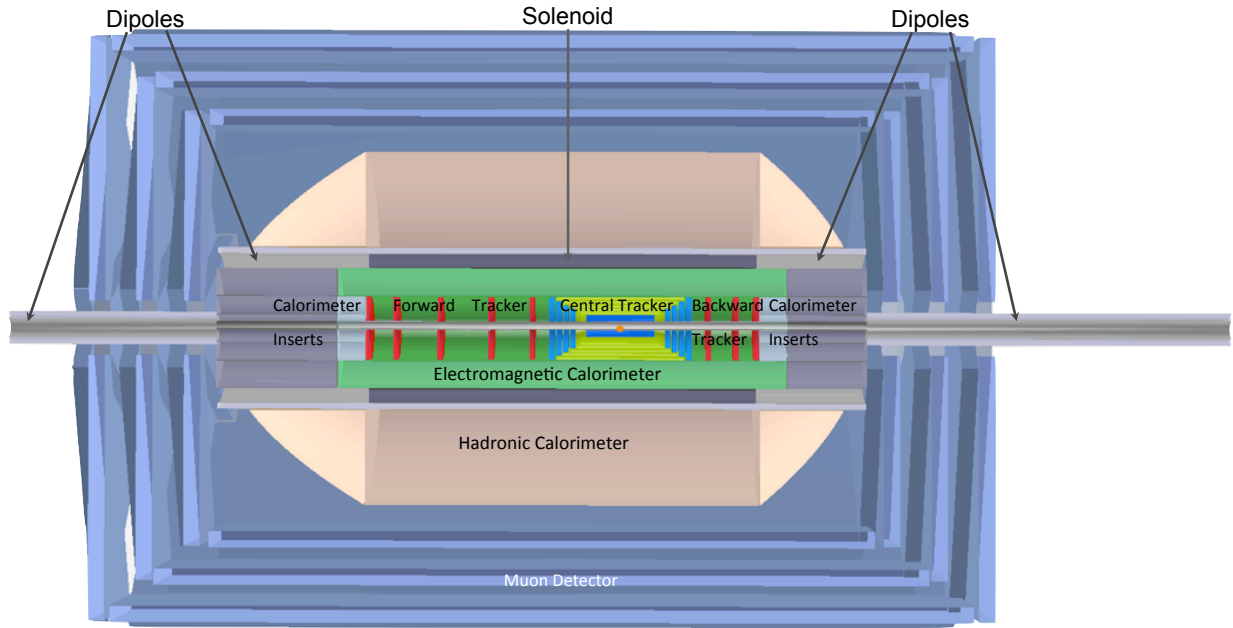


Figure 13.12: Configuration of the solenoid and electron beam bending dipoles in the baseline Linac-Ring detector. Longitudinal r-z section showing the position to solenoid and the two dipoles, each split in two sections, a superconducting inner section incorporated with the solenoid in one cryostat and a normal conducting iron based outer section magnet with smaller bore.

9753 double layer coil will be needed. Using well established design codes with proven records on earlier detector  
 9754 magnets, the main solenoid parameters are determined and are listed in Table 13.1.

9755 The solenoid is wound in two layers internally in an Al5083 alloy support cylinder with 30 mm wall  
 9756 thickness and a length of about 6 m. When finished two extensions cylinders are flanged to the central  
 9757 solenoid section at either end for supporting the inner superconducting dipole sections, see Figure 13.13. In  
 9758 this way the solenoid can be produced as a 6 m long coil unit in a company, transported to the integration  
 9759 site where the adjacent sections are coupled and the dipoles sections can be introduced.

9760 The magnetic field generated by the system of solenoid and internal dipoles is shown in Figure 13.13.  
 9761 The peaks in magnetic field in the solenoid and dipole windings as results of their combined operation at  
 9762 nominal current are 3.9 and 2.6 T respectively. The  $B_z$  and  $B_y$  components of the magnetic field are shown  
 9763 in Figure 13.14.

9764 The superconductor used for the solenoid is an Al stabilized NbTi/Cu Rutherford cable based on state-of-  
 9765 the-art NbTi strands featuring 3000 A/mm<sup>2</sup> critical current density at 5 T and 4.2 K. A 20 strands Rutherford  
 9766 cable carries the nominal current of 10 kA which is 30% of its critical current.

9767 The conductor has a comfortable temperature margin of 2.0 K when operating the coil with a forced  
 9768 Helium flow enabling 4.6 K in the solenoid windings. The high purity Al used for the co-extrusion of Al  
 9769 and cable is mechanically reinforced by micro-alloying with either Ni or Zn, or another qualified material, a  
 9770 technology qualified for the ATLAS solenoid. Two conductor units of 5.4 km would be perfect, corresponding  
 9771 to the two layers in the coil windings. Eventually internal splices are acceptable and can be made reliably  
 9772 by overlapping a full turn and performing welding on the two adjacent thin edges of the conductors.

9773 The conductor insulation is a double layer of 0.3 mm thick polyimide/glass tape (or similar product) featuring  
 9774 a high breakdown voltage of more than 2 kV and robustness for coil winding damage in order to limit the  
 9775 risk of turn-to-turn shorts. Coil winding can be performed either using the wet winding technique with  
 9776 pre-impregnated tape or a vacuum impregnation technique may be applied. Both techniques are appropriate  
 9777 provided fully qualified with the coil winding contractor.

Property	Parameter	value	unit	
Dimensions	Cryostat inner radius	0.900	m	
	Length	10.000	m	
	Outer radius	1.140	m	
	Coil windings inner radius	0.960	m	
	Length	5.700	m	
	Thickness	60.0	mm	
	Support cylinder thickness	0.030	m	
	Conductor section, Al-stabilized NbTi/Cu + insulation	$30.0 \times 6.8$	$mm^2$	
	Length	10.8	km	
	Superconducting cable section, 20 strands	$12.4 \times 2.4$	$mm^2$	
	Superconducting strand diameter Cu/NbTi ratio = 1.25	1.24	mm	
	Masses	Conductor windings	5.7	t
		Support cylinder, solenoid section + dipole sections	5.6	t
Total cold mass		12.8	t	
Cryostat including thermal shield		11.2	t	
Total mass of cryostat, solenoid and small parts		24	t	
Electro-magnetics		Central magnetic field	3.50	T
	Peak magnetic field in windings (dipoles off)	3.53	T	
	Peak magnetic field in solenoid windings (dipoles on)	3.9	T	
	Nominal current	10.0	kA	
	Number of turns, 2 layers	1683		
	Self-inductance	1.7	H	
	Stored energy	82	MJ	
	E/m, energy-to-mass ratio of windings	14.2	kJ/kg	
	E/m, energy-to-mass ratio of cold mass	9.2	kJ/kg	
	Charging time	1.0	hour	
	Current rate	2.8	A/s	
	Inductive charging voltage	2.3	V	
	Margins	Coil operating point, nominal / critical current	0.3	
Temperature margin at 4.6 K operating temperature		2.0	K	
Cold mass temperature at quench (no extraction)		$\sim 80$	K	
Mechanics	Mean hoop stress	$\sim 55$	MPa	
	Peak stress	$\sim 85$	MPa	
Cryogenics	Thermal load at 4.6 K, coil with 50% margin	$\sim 110$	W	
	Radiation shield load width 50% margin	$\sim 650$	W	
	Cooling down time / quench recovery time	4 and 1	day	
	Use of liquid helium	$\sim 1.5$	g/s	

Table 13.1: Main parameters of the baseline LHeC Solenoid providing 3.5 T in a free bore of 1.8 m.

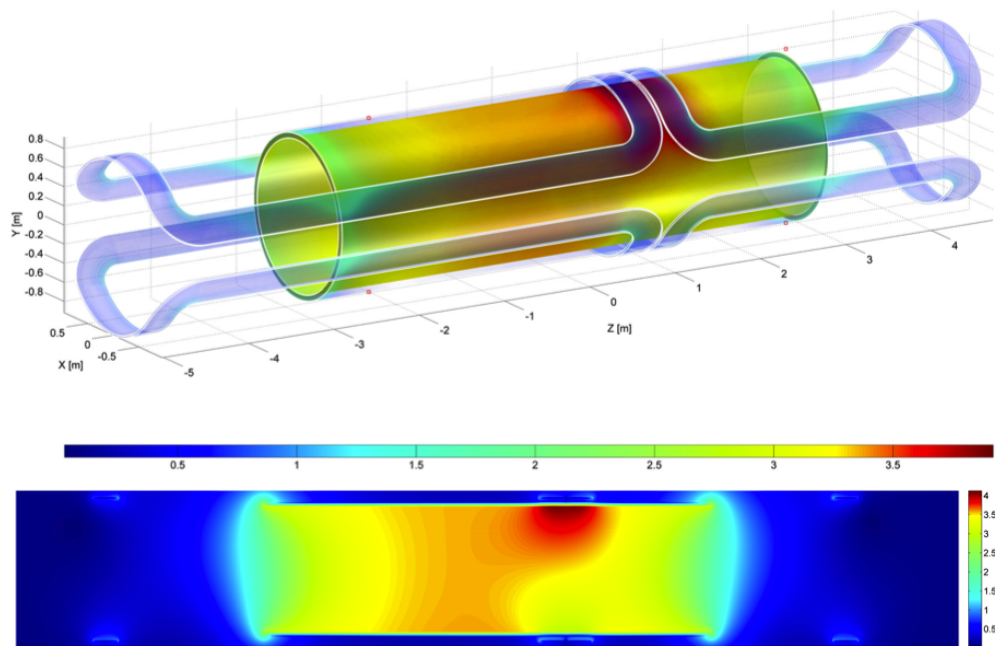


Figure 13.13: Magnetic field of the magnet system of solenoid and the two internal superconducting dipoles at nominal currents (effect of iron ignored). The position of the peak magnetic field of 3.9 T is local due to the adjacent current return heads on top of the solenoid where all magnetic fields add up.

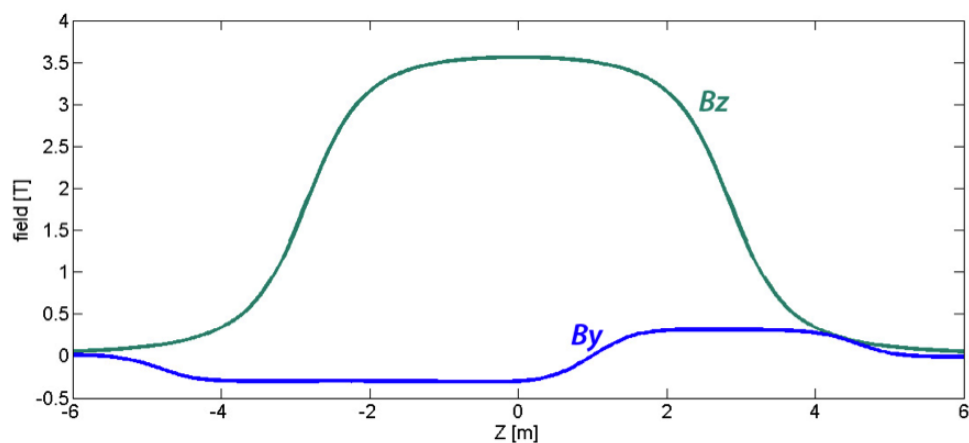


Figure 13.14: Magnetic field components  $B_z$  (solenoid) and  $B_y$  (set of internal dipoles) on the beam axis across 12 m in  $z$ . Note, the magnetic field of the external electromagnets are not included here.

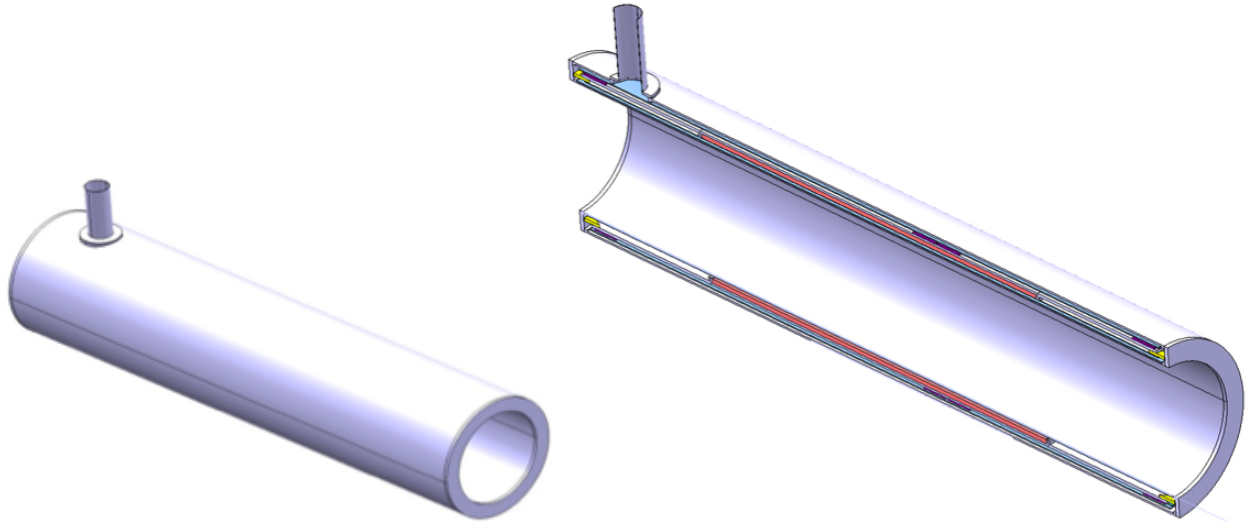


Figure 13.15: Cryostat of the magnet system. Left: the integrated cryostat, and right: longitudinal cut through the cryostat comprising a single cold mass of solenoid and internal superconducting dipole sections.

9778 Once the solenoid windings are finished and delivered to the coil integration site, the dipole coil sections  
 9779 are inserted in slots milled into the outer surface of the support cylinder, see section 13.2.3. The four dipole  
 9780 upper and lower coil sections are separately produced as flat racetrack coils and then bent onto the fully  
 9781 assembled support cylinder. Next all interconnections and bus connections to the current leads are laid down  
 9782 and the cold mass is inserted in the cryostat.

9783 The cryostat design is shown in Figure 13.15. The cold mass is supported from the cryostat with a system of  
 9784 triangle brackets, a proven technique providing a very compact solution [744], [745]. The cryostat is equipped  
 9785 with thermal shields and multi-layer super-insulation in the usual way.

9786 The coil windings of both solenoid and dipole sections are cooled by conduction by forced flow liquid helium  
 9787 circulating in 14 mm sized cooling tubes that are attached to the outer surface of the integrated support  
 9788 cylinder. The two layer winding pack of 60 mm radial built and fully bonded to the support cylinder is  
 9789 sufficiently thin to warrant a thermal gradient in the winding pack of less than 0.1 K. The total radial  
 9790 material built of essentially Al alloys is about 150 mm featuring an acceptable effective radiation thickness.  
 9791 Quench protection of the solenoid with 82 MJ stored energy in a cold mass with 9 kJ/kg can be done  
 9792 safely. The stored energy is absorbed by the cold mass enthalpy (no energy extraction) and the cold mass  
 9793 temperature will raise to a safe 80 K level. Heat drains are incorporated in the coil windings to accelerate  
 9794 quench propagation and in addition an active heater system will implemented for the same purpose.

### 9795 13.2.3 Detector integrated e-beam bending dipoles

9796 The two e-beam bending dipoles are positioned symmetrically around the beams intersection point. As  
 9797 outlined before each 9 m long dipole is split into a superconducting section integrated with the central  
 9798 solenoid and a normal conducting iron based electro-magnet positioned around the beam outside the main  
 9799 detector envelope. The external dipole magnets are conventional and will not be further detailed here. The  
 9800 principle parameters of the superconducting dipole sections are listed in Table 13.2.

### 9801 13.2.4 Cryogenics for magnets and calorimeter

9802 The cryogenic operating conditions are achieved by circulating forced flow two-phase helium in cooling pipes  
 9803 attached to the Al-alloy coil support cylinder. Electric powering of the solenoid and dipole magnets at 10  
 9804 and 2 kA, respectively, is through two pairs of low-loss high-temperature superconducting current leads. The

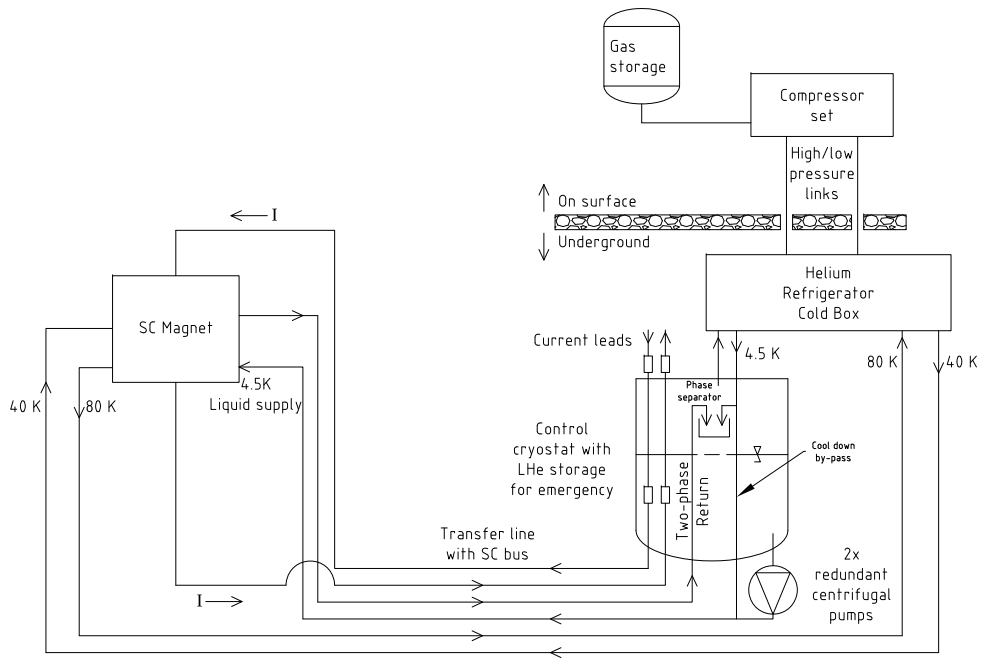


Figure 13.16: Principle cryogenic flow scheme for the cooling of the superconducting magnets.

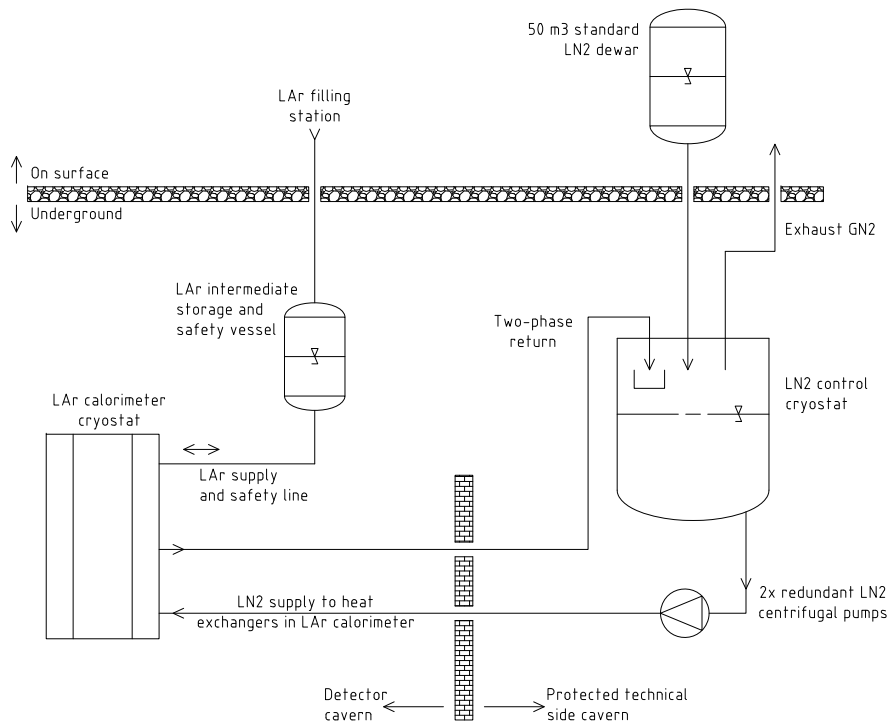


Figure 13.17: Principle cryogenic flow scheme for the cooling of the liquid argon calorimeter.

	Plus coil	Minus coil	
Magnetic field on axis	0.3		T
Peak magnetic field in windings (solenoid off)	0.7		T
Peak magnetic field in windings (solenoid on)	2.6		T
Dipole length (including external sections)	9.0		m
Field integral internal section (sc dipole)	1.6	1.0	Tm
Field integral external section (iron magnet)	1.1	1.7	Tm
Operating current	2.0		kA
Stored Energy	1.9	1.2	MJ
Coil inductance	0.50		H
Coil inner / outer radius	1.042/1052		m
Coil length	6.00	3.70	m
NbTi/Cu conductor diameter (12 strands Rutherford cable)	2.0		mm
Conductor length	5.4	3.6	km

Table 13.2: Main design parameters of the set of superconducting electron beam bending dipoles.

9805 current leads are housed in a separate service cryostat installed at distance in a side cavern, a non-radiation  
9806 environment. The service cryostat contains a larger amount of helium sufficient for a safe 1-2 hours ramp  
9807 down in the case of refrigerator failure as well as to maintain the magnets at operating temperature for a  
9808 few hours. Redundant centrifugal pumps provide for circulation of the slightly sub-cooled liquid helium to  
9809 the magnets. The two-phase return flow is brought to a phase separator in the service cryostat. A combined  
9810 superconducting link and helium transfer line connects the service cryostat with the current leads and helium  
9811 buffer to the magnets. For this circuit static and dynamic losses of the magnets and transfer lines have to be  
9812 taken into account, which are about 85 W. With 50% contingency the losses amount to 130 W. For reasons  
9813 of flow stability the vapor quality of the return flow shall not exceed 10%.

9814 The mass flow rate of the pump is calculated to 65 g/s maximum. We assume a thermo-hydraulic efficiency of  
9815 the pump of 35%, a value based on measurements on already running similar systems. The pump introduces  
9816 an additional 40 W to the system.

9817 The refrigerator is at proximity to the cryostat and the compressor set is installed on surface. The expected  
9818 modest thermal loss of the magnet system and its proximity cryogenics like service cryostat and transfer lines  
9819 amounts to some 200 W@4.5 K. The estimated overall system loss suggest a small sized standard refrigerator  
9820 in the class of 300 to 400 W@4.5 K. The thermal load of the system is summarized in Table 13.3. Figure 13.16  
9821 shows the simplified flow scheme of the helium cryogenic system.

Component heat load at temperature	4.5 K	20-300 K	40-80 K
Magnets static	45 W		430 W
Magnets dynamic	30 W		
Transfer line/bus static	10 W		150 W
Valve box cryostat static	10 W		150 W
Helium pump static	40 W		
Current leads static		1.0 g/s	
Sums with and extra 50% contingency	200 W	1.5 g/s	1100 W

Table 13.3: Thermal load of the cryogenics system including magnets and helium distribution.

9822 A liquid Argon calorimeter is envisaged as part of an EMC. As mentioned before, it can be installed

9823 in a separate cryostat or preferably share the cryostat with the solenoid. In the latter case the systems  
9824 compactness is increased and the inner thermal shield can be omitted. The calorimeter will have an overall  
9825  $18\text{ m}^3$  volume from which approximately  $12\text{ m}^3$  will be slightly sub-cooled liquid argon. Cooling is with two-  
9826 phase liquid nitrogen in longitudinal pipe runs and its circulation is provided by two redundant small sized  
9827 liquid nitrogen pumps. The liquid nitrogen is supplied from a standard dewar on surface to an intermediate  
9828 cryostat which serves also as the phase separator. For the liquid argon filling, a line connects from the surface  
9829 to an intermediate dewar from which it is transferred to the LAr cryostat in the detector. This dewar also  
9830 serves as emergency volume in the case of vacuum loss or leak problems to which the liquid argon can be  
9831 transferred from the cryostat. Figure 13.17 shows the functional principle of the Argon cooling units.

9832 The cooling principles of both cryogenic systems proposed in this paper are based on previous design and  
9833 experience from the much more complex ATLAS detector cryogenics.

### 9834 13.2.5 Twin Solenoid System

9835 Being written.

## 9836 13.3 Tracking Detector

9837 The constraints given by the magnet system (dipole/solenoid) force the tracking detectors to be kept as  
9838 small as possible in radius.

9839 According to equation 12.9, the momentum resolution is proportional to  $1/L^2$  and is therefore limited  
9840 by the tracker radius. For a given magnetic field strength, the only other parameters left to improve are  
9841 the intrinsic detector resolution,  $\Delta$ , and the number of points sampled along the track trajectory. The  
9842 forward/backward tracking extensions provide additional measurement points in these regions. Hence, a  
9843 balance of number of track points (number of sensitive detector layers), material economy and costs must  
9844 be found.

9845 The design adopted here is an all-Silicon detector, with very high resolution. The readout scheme must  
9846 be such that a signal weighting using analog information is possible without losing the advantages of digital  
9847 signal processing and on-chip zero suppression. All of the components need power and cooling, influencing  
9848 the material budget of the tracker system which should be kept as low as possible. The technology used  
9849 must be advanced at the industrial level, radiation hard and relatively cheap. A good candidate are n\_in\_p  
9850 single sided sensors [748].

9851 In the following, the layout of a tracker system for the baseline detector configuration A is defined, along  
9852 with the design criteria and possible solutions for a tracker which provides high resolution impact parameter  
9853 measurement, momentum determination (as far as possible) and optimal support of the calorimetry.

### 9854 13.3.1 Tracking Detector - Baseline Layout

9855 The tracking detectors (Fig. 13.22) inside the electromagnetic calorimeter are all-Silicon devices. The tracker  
9856 covers the pseudorapidity range  $-4.8 < \eta < 5.5$  and is located inside the solenoidal field of 3.5T. Addition-  
9857 ally a dipole field of 0.3T, resulting from the steering dipoles required for the Linac-Ring configuration, is  
9858 superimposed.

9859 The tracker is subdivided into central (CPT, CST, CFT/CBT) and forward/backward parts (FST, BST).  
9860 Fig. 13.18 shows the tracker configuration for LHeC operation at maximal acceptance in the baseline (A)  
9861 detector design. More details are summarized in Tab. 13.4<sup>3</sup>. The shape of the CPT and the inner dimensions  
9862 of all near-beam detectors have been chosen to maximise detector acceptance by measuring as close to the  
9863 beam-line as possible (see Fig. 13.19 which shows the  $xy$  view of the circular-elliptical CPT and the cylindrical  
9864 CST detectors).

---

<sup>3</sup>The item *project area* in table 13.4 describes the area which has to be equipped with appropriate Si-sensors (e.g. single-sided or double-sided sensors). An alternative would be the usage of Si-Gas detectors providing track segment information instead of track points, e.g. in the CST cylinders (Ref. [749], [750], [751])

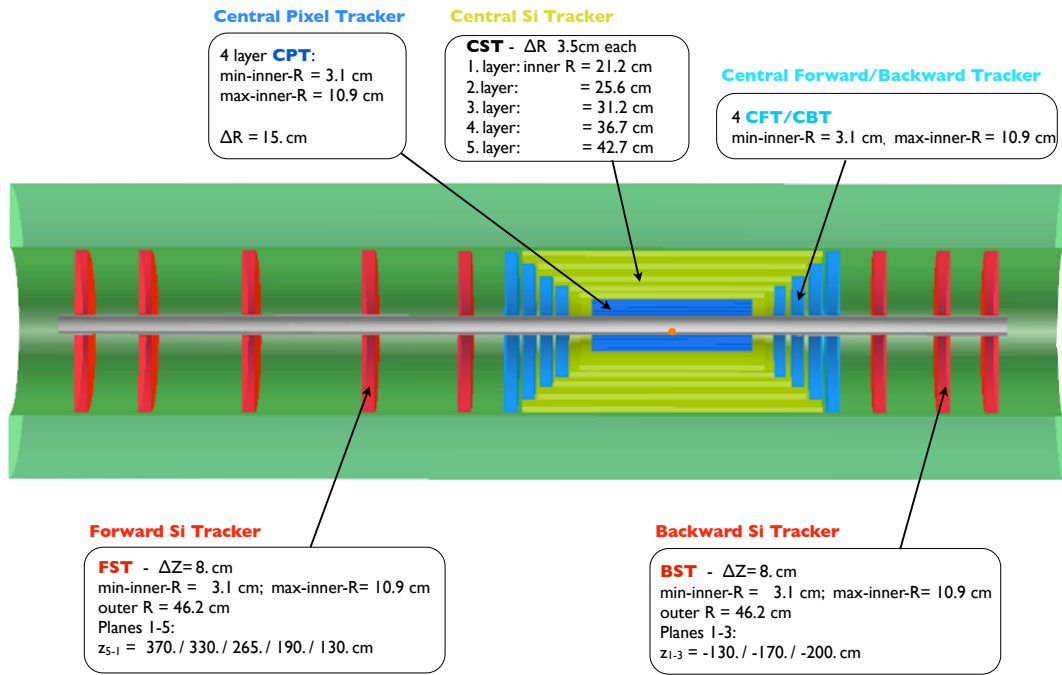


Figure 13.18: Tracker and barrel Electromagnetic-Calorimeter  $rz$  view of the baseline detector (Linac-Ring case).

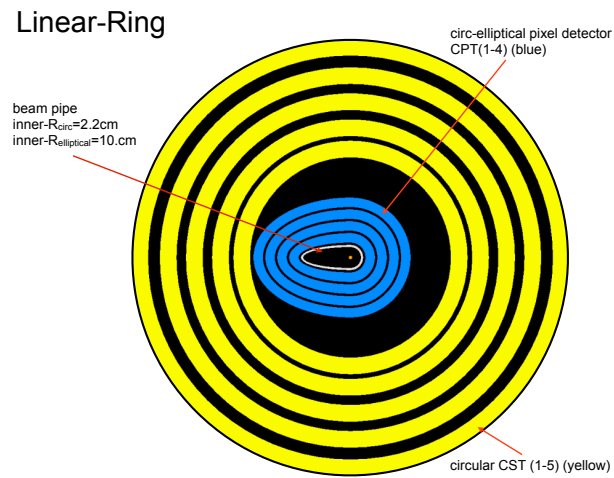


Figure 13.19: XY cut away view of the Central Pixel (CPT) and Central Strixel Tracker (CST) (Linac-Ring layout).



Central Barrel	CPT1	CPT2	CPT3	CPT4	CST1	CST2	CST3	CST4	CST5
Min. Radius $R$ [cm]	3.1	5.6	8.1	10.6	21.2	25.6	31.2	36.7	42.7
Min. Polar Angle $\theta$ [°]	3.6	6.4	9.2	12.0	20.0	21.8	22.8	22.4	24.4
Max. $ \eta $	3.5	2.9	2.5	2.2	1.6	1.4	1.2	1.0	0.8
$\Delta R$ [cm]	2	2	2	2	3.5	3.5	3.5	3.5	3.5
$\pm z$ -length [cm]	50	50	50	50	58	64	74	84	94
Project Area [m <sup>2</sup> ]	1.4				8.1				
Central Endcaps	CFT4	CFT3	CFT2	CFT1		CBT1	CBT2	CBT3	CBT4
Min. Radius $R$ [cm]	3.1	3.1	3.1	3.1		3.1	3.1	3.1	3.1
Min. Polar Angle $\theta$ [°]	1.8	2.0	2.2	2.6		177.4	177.7	178	178.2
at $z$ [cm]	101	90	80	70		-70	-80	-90	-101
Max./Min. $\eta$	4.2	4.0	3.9	3.8		-3.8	-3.9	-4.0	-4.2
$\Delta z$ [cm]	7	7	7	7		7	7	7	7
Project Area [m <sup>2</sup> ]	1.8					1.8			
Fwd/Bwd Planes	FST5	FST4	FST3	FST2	FST1		BST1	BST2	BST3
Min. Radius $R$ [cm]	3.1	3.1	3.1	3.1	3.1		3.1	3.1	3.1
Min. Polar Angle $\theta$ [°]	0.48	0.54	0.68	0.95	1.4		178.6	178.9	179.1
at $z$ [cm]	370	330	265	190	130		-130	-170	-200
Max./Min. $\eta$	5.5	5.4	5.2	4.8	4.5		-4.5	-4.7	-4.8
Outer Radius $R$ [cm]	46.2	46.2	46.2	46.2	46.2		46.2	46.2	46.2
$\Delta z$ [cm]	8	8	8	8	8		8	8	8
Project Area [m <sup>2</sup> ]	3.3						2.0		

Table 13.4: Summary of tracker dimensions. The 4 Si-Pixel-Layers CPT1-CPT4 (resolution of  $\sigma_{\text{pix}} \approx 8\mu\text{m}$ ) are positioned as close to the beam pipe as possible. Si-strixel (CST1-CST5) (resolution of  $\sigma_{\text{strixel}} \approx 12\mu\text{m}$ ) form the central barrel layers. An alternative is the 2\_in\_1 single sided Si-strip solution for these barrel cylinders ( $\sigma_{\text{strip}} \approx 15\mu\text{m}$ ) [752]. The endcap Si-strip detectors CFT/CBT(1-4) complete the central tracker. The tracker inserts, 5 wheels of Si-Strip detectors in forward direction (FST) and 3 wheels in backward direction (BST), are based on single sided Si-strip detectors of 2\_in\_1-design ( $\sigma_{\text{strip}} \approx 15\mu\text{m}$ ). They have to be removed in case of high luminosity running for the Ring-Ring option of the accelerator configuration (see Fig. 13.4).

9865 **13.3.2 Performance**

9866 Some results of preliminary tracker performance simulations using the LicToy-2.0 program [740] for the  
 9867 tracker setup (see table 13.4 and Fig. 13.20), and with parameters given in table 13.5 are summarised in  
 Fig. 13.21. The detector performance is very good, as expected. For  $1^\circ$  tracks the bending solenoidal field

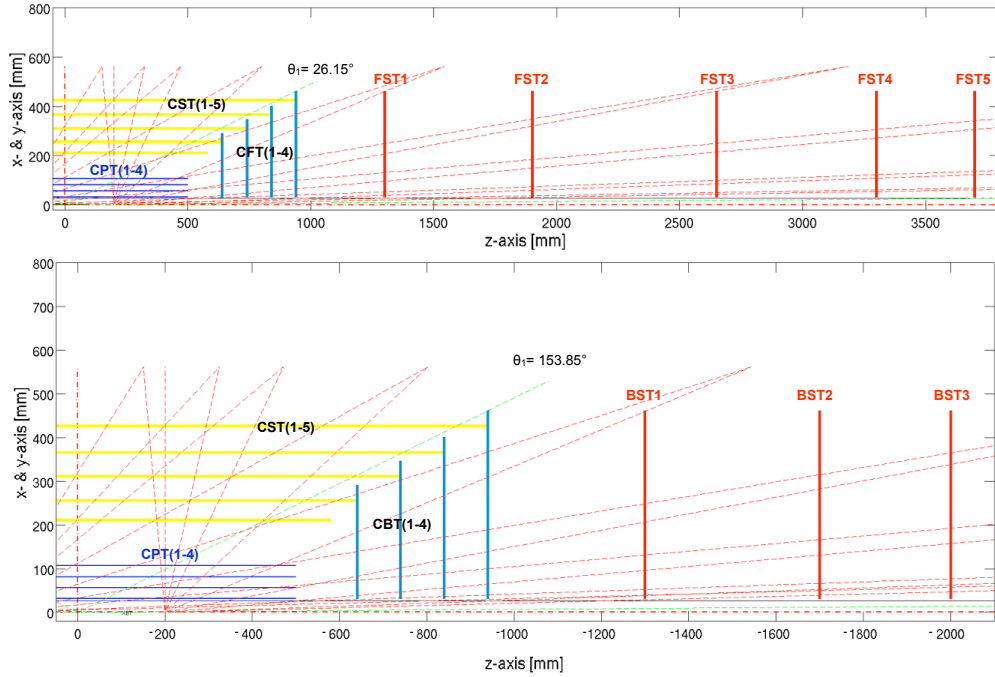


Figure 13.20: LicToy2.0 tracker design of the central/forward FST(top) and central/backward direction BST(bottom).

9868 component (0.36T) is of the same order as the dipole field and the resulting track sagitta only reaches the  
 9869  $mm$  range when particles of momentum  $< 100$  GeV have a track length of 250cm (see Fig.13.18). The  
 9870 tracker described here measures  $1^\circ$  tracks over a distance of  $\approx 180$ cm, and therefore high momentum tracks  
 9871 will have a poor momentum determination. Nevertheless, the position information can be used to match a  
 9872 track to a calorimeter deposit with high precision.  
 9873

9874 The backward measurement is characterised by even shorter track lengths and in this case the analysis  
 9875 has to rely on the energy measurement in the calorimeters matched to a well defined track. Thanks to  
 9876 the much reduced particle flux in the backward direction due to kinematics, the performance and precision  
 9877 achievable is expected to be higher. Very low  $Q^2$ /low  $x$  processes will be more easily accessible by reducing the  
 9878 electron beam energy, thus measuring at larger angles in the backward direction (see Fig. 12.3 and Fig. 12.4  
 9879 and discussion in chapter 12.1).

9880 **13.3.3 Tracking detector design criteria and possible solutions**

9881 The experience of former attempts for an optimal detector design suggest that some criteria should be  
 9882 discussed as early as possible.

9883 The main items to consider [748, 753] are discussed in the following.

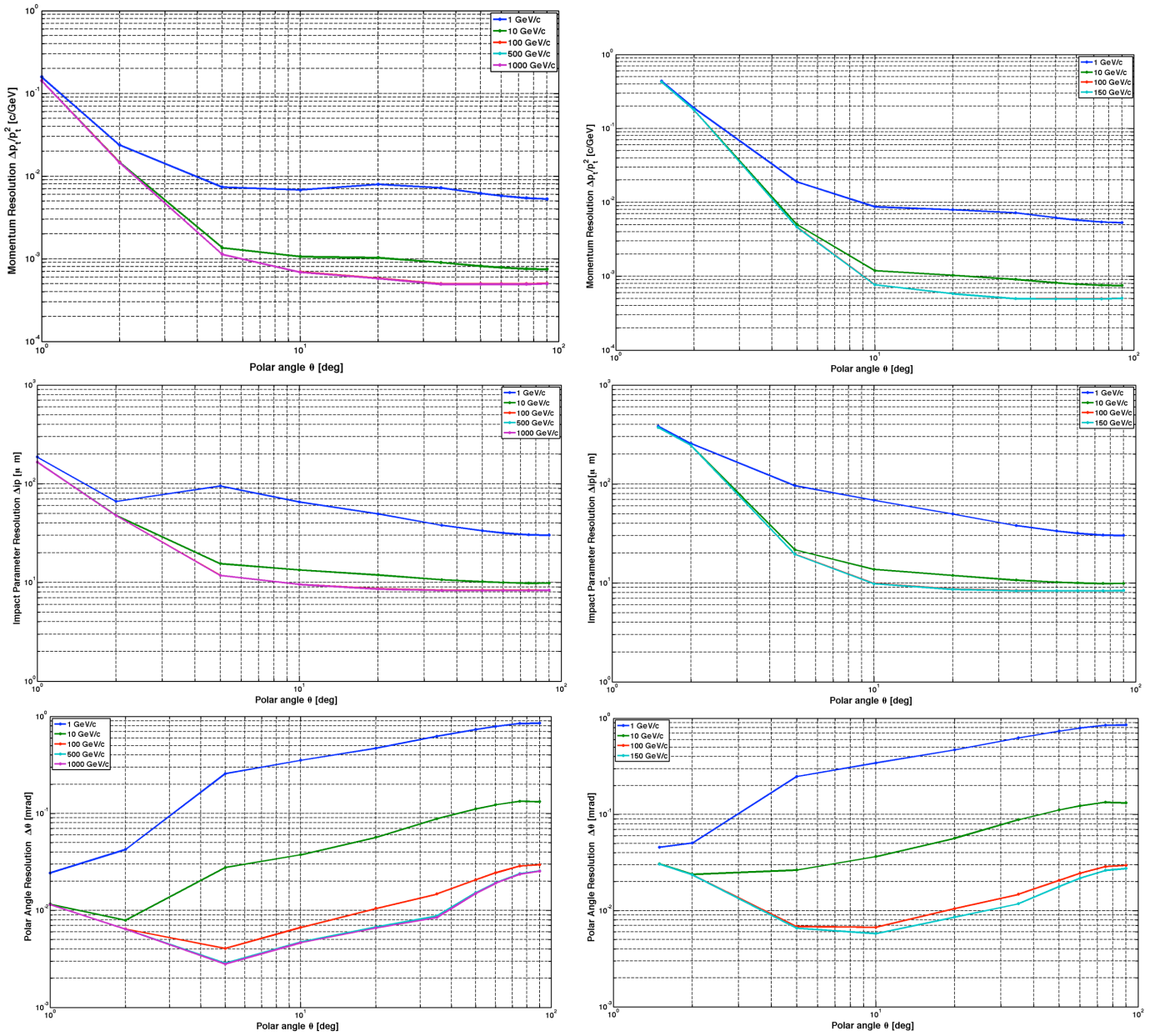


Figure 13.21: Scaled momentum, impact parameter and polar angle resolution as function of polar angle  $\theta$  resulting from tracker design simulation using LiCToy2 for the FST(left) and BST(right) side. Tracker setup used as shown in Fig. 13.20.

Parameters	
B	3.5T
$X/X_0^{\text{beampipe}}$	0.002
$X/X_0^{\text{det-parts}}$	0.005
efficiency	0.99%
Minimal inner radius	3.15cm
$\sigma_{\text{CPT}}$	8 $\mu\text{m}$
$\sigma_{\text{CST,CFT,CBT}}$	12 $\mu\text{m}$
$\sigma_{\text{FST,BST}}$	15 $\mu\text{m}$

Table 13.5: The main parameters assumed in the tracking simulation.

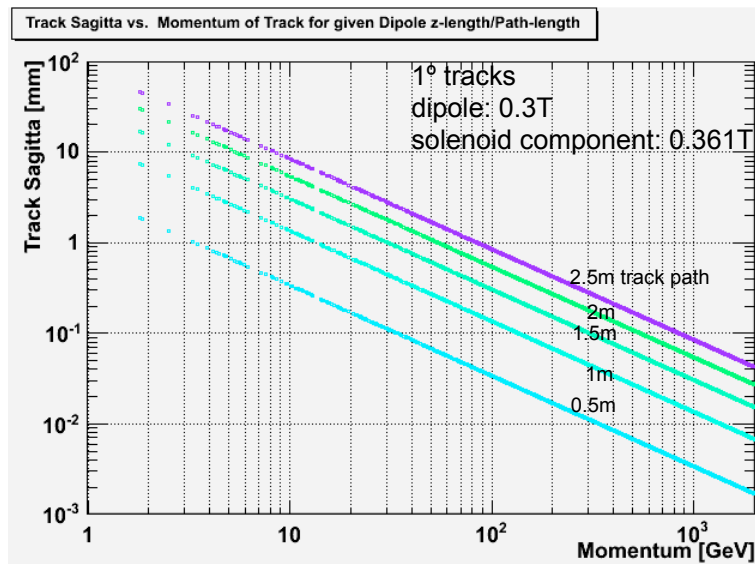


Figure 13.22: Track Sagitta vs. Momentum of  $1^\circ$  tracks in a superposed dipole/solenoidal field.

9884 **Optimising cost for all components**

9885 The technology developments for HL-LHC/ILC experiments [754–767] should be used as far as possible  
9886 while relying on existing technologies because of time constraints. The sensors, integrated electronics, read-  
9887 out/trigger circuitry, mechanics, cooling, etc. available today have to be used in order to meet the goal of  
9888 installation in the early 2020’s.

9889 **Choice of sensor type**

9890 The default tracker design is based on the silicon microstrip detector technology developed for the experiments  
9891 at LHC, ILC, TEVATRON, b-factories etc. within the last 20 years. The final decision for sensor types  
9892 (pixel, strixel, strip) depend on many factors and will be taken according to their functionality.

9893 **Radiation hardness** The expected radiation load is defined and influenced by the interaction rate (25ns),  
9894 luminosity ( $\approx 10^{33} \text{ cm}^{-2} \text{ s}^{-1}$ ), particle rate per angle interval, fluence  $n_{eq}$  and ionisation dose. Some data  
9895 will be better defined after evaluation of more detailed simulations. Specifically the radiation impact on  
9896 tracker wheels, calorimeter inserts and the inner tracker-barrel layer has to be studied. The tools for those  
9897 simulations are being prepared. First estimates are discussed in section 13.8 in more detail, but there is  
9898 as yet no indication for extremely high radiation load into the detectors adjacent to the beam pipe. The  
9899 expected levels are far below what the LHC experiments have to withstand.

9900 A side remark is related to the active parts of the forward/backward calorimeter. For safety reasons those  
9901 calorimeter inserts should be equipped with radiation hard silicon-based sensors according to LHC/HL-LHC  
9902 standards. Relatively small in volume but still large in terms of layer area  $\mathcal{O}(\text{m}^2)$ , the use of Si-strip/Si-pad  
9903 based calo-inserts might turn out as a sizeable investment which is anyhow needed in order to guarantee  
9904 for a stable performance and a sufficient detector lifetime. A final decision will only be possible after more  
9905 detailed **FLUKA** [768, 769] simulations are complete.

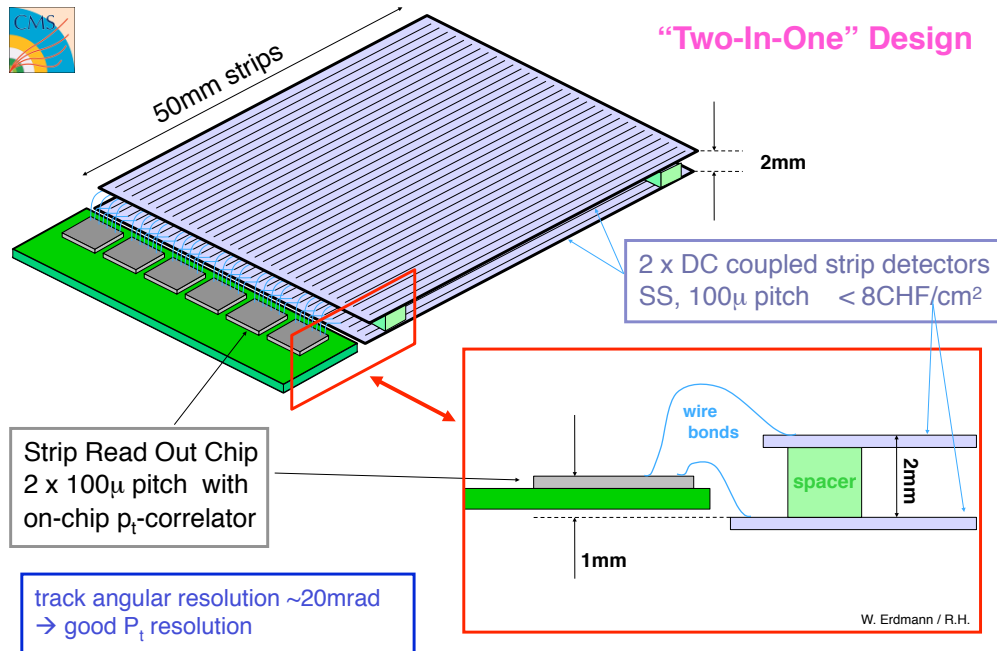


Figure 13.23: Layout of the 2\_in\_1 strip sensor design used as  $p_t$ -trigger setup for the CMS experiment.

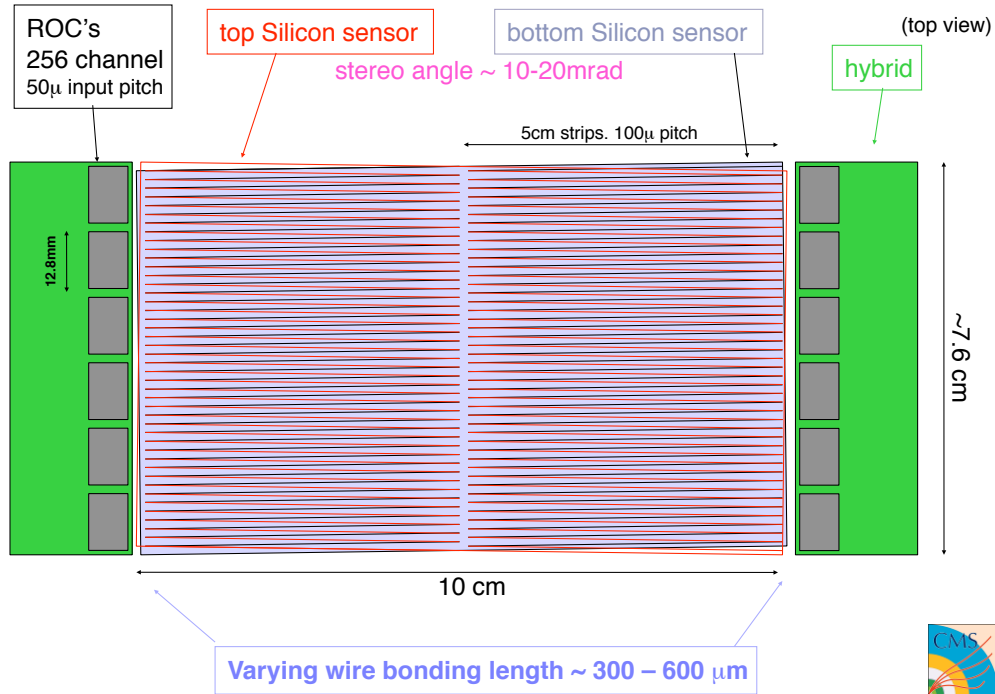


Figure 13.24: Layout of the 2\_in\_1 strip sensor design used as tracker module. Double use of e.g. power and cooling for the two strip wafer.

9906 **Trigger** The trigger capabilities of the tracking system is yet to be defined and will have a direct impact  
 9907 on sensor choice, associated electronics and arrangement. It is possible that very recent developments of  
 9908 3D integration semiconductor layers interconnected to form monolithic unities of sensor&electronic circuitry  
 9909 would be available in time for installation in the 2020's, but conventional wire bonded or bump bonded  
 9910 solutions may be more cost efficient and rely on components available today. For example, the 2\_in\_1 strip  
 9911 sensor design  $p_t$ -trigger discussed by the CMS upgrade design group [752], shown in Fig. 13.23, would have  
 9912 a direct impact on a muon-trigger definition. The sensor, hybrid and readout modules are available and  
 9913 interconnected by wire bonds. The 2\_in\_1 sensor design is a very elegant way of saving resources when  
 9914 designing a tracker, as shown in Fig. 13.24

9915 **Front-end** Candidates of readout chips attached to the sensors are e.g. the ATLAS FE-I4 ( $50\mu m * 250\mu m$ )  
 9916 [748] and CMS ROC ( $100\mu m * 150\mu m$ ) [754]). The sensor pitch has to be matched and the electronics scheme  
 9917 defined beforehand.

### 9918 Powering and cooling

9919 The size of the largest stave structure to be installed (half z-length  $\approx 94cm$ ) is smaller than the stave length  
 9920 used e.g. by ATLAS ( $\approx 120cm$ ). Powering and cooling per stave are therefore less demanding than for the  
 9921 current LHC installations. Minimisation of cooling directly reduces the material budget; cooling is related  
 9922 to power consumption issues and it may be a criterion for technology selection. A decision on the powering  
 9923 concept is needed (serial, parallel powering). It will depend on the template chosen for readout and services.  
 9924 An obvious solution is to re-apply the scheme used by a current LHC experiment in line with the sensor,  
 9925 electronics & readout option selected.

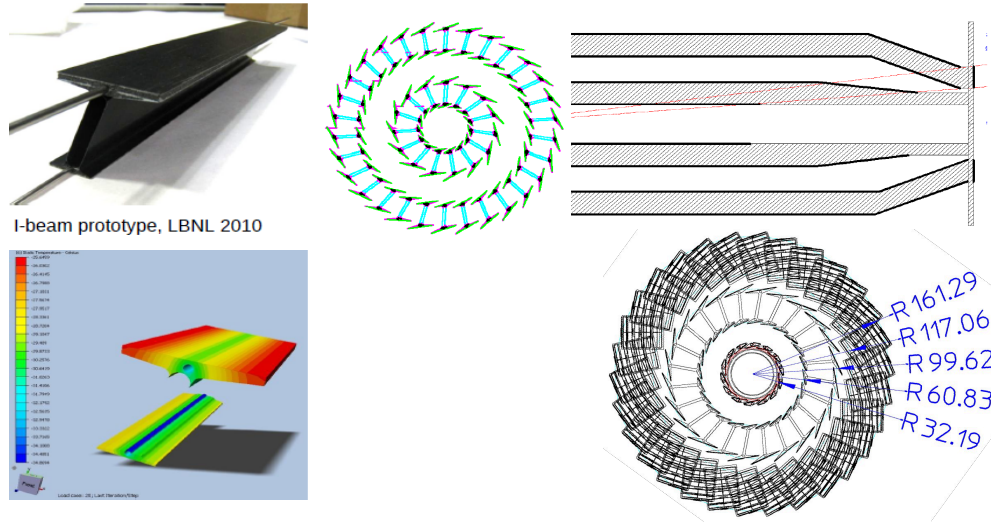


Figure 13.25: Proposed mechanics and sensor layout for the ATLAS pixel upgrade.

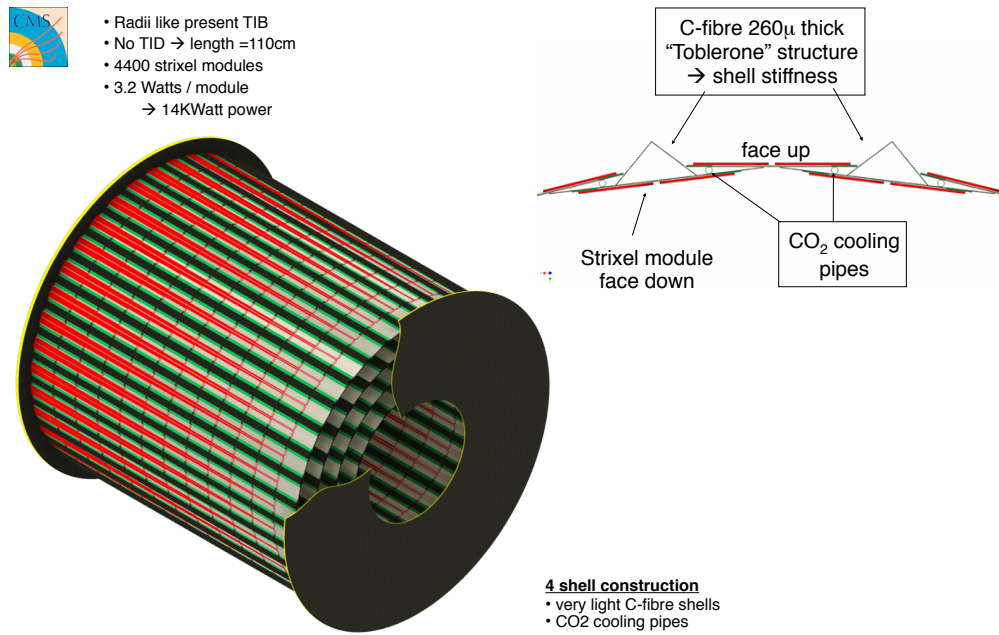


Figure 13.26: Proposed mechanics layout for the CMS inner barrel tracker upgrade.

Inner & outer ring of blades

CO<sub>2</sub> tubes embedded in half disk support:

- support cylinder:
  - Carbon carbon
  - Grooves for cooling tube
  - Stainless steel tube:
    - 1.8mm OD, 100 $\mu$ m wall

Blades:

- all identical
- Rotated by 20° radial
- Tilted by 12° (inner ring)
- 2 modules per blade ( $\phi$  overlap)
- individually replaceable

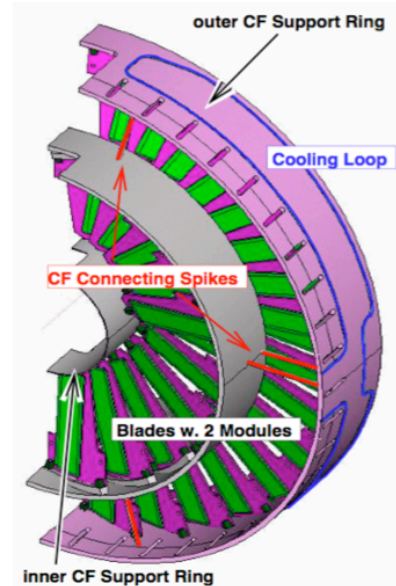
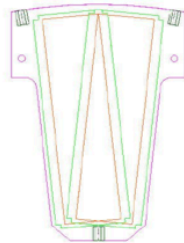


Figure 13.27: Proposed mechanics layout for the CMS tracker wheel upgrade.

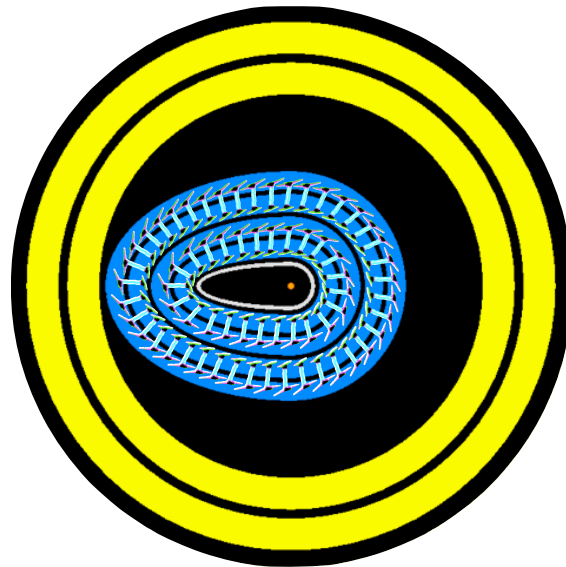


Figure 13.28: Artist view of the pixel sensor arrangement using the double-I ATLAS layout as template (Fig. 13.25).



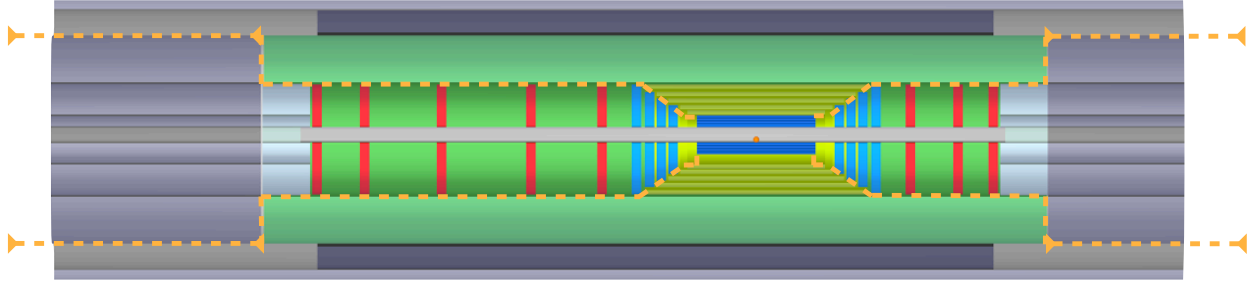


Figure 13.29: Path of services for all tracking detectors (shown in orange). The services are integrated into support structures whenever possible

### 9926 Mechanical support

9927 The mechanical support and cooling elements have to be chosen to minimise the material budget and hence  
 9928 minimise the impact of multiple-scattering on track resolution by the tracker material. Rigid but very light  
 9929 mechanics in connection with improved sensor arrangement, incorporation of cooling systems and all other  
 9930 services into the support structure are the main design criteria for HL-LHC upgrade projects for e.g. ATLAS  
 9931 and CMS - this is also the case for LHeC.

9932 In Figs. 13.25, 13.26 and 13.27, possible mechanical solutions for the ATLAS [748, 770] and CMS [752]  
 9933 tracker upgrades in the barrel and forward/backward tracker regions are shown. These designs may serve as  
 9934 templates for the LHeC detector. As an example, an artist's view in Fig. 13.28 shows an implementation of  
 9935 the double-I ATLAS pixel arrangement into a 4 layer pixel structure for the LHeC detector. The goal is the  
 9936 design of a tracker which is in the range  $\approx 1.5 - 2\%X_0$  in terms of radiation lengths.

### 9937 Readout

9938 Possible paths for the IN/OUT services of the LHeC tracking detectors are sketched in Fig. 13.29. The cables  
 9939 and tubes are integrated into the support structures of the sub-detectors as far as possible. Optimisation of  
 9940 detector readout reduces the cost and material impact of cables. An example is discussed in detail for the  
 9941 ATLAS/CMS HL-LHC opto-link upgrade in Ref. [771]. The front end electronics buffer depth will depend  
 9942 on bunch crossing rate (25ns) and the trigger/readout speed capability.

### 9943 Radiation detectors

9944 Special Interaction Region instrumentation for tuning of the machine in order to minimise background and  
 9945 optimise luminosity is needed. Radiation detectors, e.g. near mask and tight apertures, are useful for  
 9946 fast identification of background sources. Fast bunch related informations are collected efficiently e.g. by  
 9947 dedicated diamond detectors, e.g. for CMS [772-775].

## 9948 13.4 Calorimetry

9949 The LHeC calorimetry has to fulfill the requirements described in 12.1. The goal is a powerful level 1  
 9950 trigger and a detector able to resolve shower development in three-dimensional space with no or minimal  
 9951 punch through. High transverse and longitudinal segmentation are necessary along with a good matching to  
 9952 tracking detectors for particle identification and separation of neutral and charged particles. The calorimetry  
 9953 needs to be hermetic in order to provide a good measurement of the total transverse energy in the charged  
 9954 current process. These considerations are summarised in Tab. 12.1.

9955 The baseline design foresees a modular structure of independent electromagnetic (EMC) and hadronic  
 9956 (HAC) calorimeter components. In order to fully contain electromagnetic showers, the EMC must provide

9957  $\sim 25 - 30X_0$ . The design of the EMC modules will vary when moving from the very forward region, where  
 9958 energies up to  $\mathcal{O}(1\text{TeV})$  are expected, to the barrel and the backward region, where an accurate and precise  
 9959 measurement of the scattered electron with energy  $\mathcal{O}(60\text{ GeV})$  is paramount.

9960 In the baseline design, the EMC is surrounded by the solenoid coil which provides the magnetic field for  
 9961 momentum measurement in the tracking. The hadronic calorimetry comes next and has sufficient depth in  
 9962 order to precisely measure jets over the full energy range, while providing the granularity in a projective  
 9963 modular design such that it can faithfully separate multiple jet events. The forward part of the HAC will  
 9964 need to provide up to  $10\lambda_I$  to guarantee containment of energies up to a few TeV.

9965 In the next sections the baseline design for the EMC and HAC components is presented and discussed  
 9966 along with a comparison of technologies and the experience from other HEP detectors e.g. [776], [777], [778],  
 9967 [779], [780]. A brief summary of ongoing R&D into new technologies which could extend the precision and  
 9968 scope of the detector are briefly addressed.

### 9969 13.4.1 The Barrel Electromagnetic Calorimeter

9970 In the barrel region ( $2.8 < \eta < -2.3$ ), a Liquid Argon calorimeter (LAr) with *accordion-shaped* electrodes,  
 9971 as is currently in use by ATLAS [781], is proposed. The principle of LAr sampling calorimetry is to arrange  
 9972 many layers of passive material, in this case lead ( $X_0=0.56\text{ cm}$ ), alternated with layers of active material,  
 9973 here LAr with  $X_0=14.0\text{ cm}$ . The choice of Liquid Argon follows from its intrinsic properties of excellent  
 9974 linearity, stability in time and radiation tolerance [782–789]. A LAr calorimeter would provide the required  
 9975 energy resolution, detector granularity and projective design. The detector, with an outer diameter of 88 cm,  
 9976 would share the same cryostat as the main solenoid which in the case of a Linac-Ring design would include  
 9977 the bending dipoles. The performance of the LAr calorimetry system has been extensively addressed [781]  
 9978 and here only specific design issues and detector simulation will be discussed.

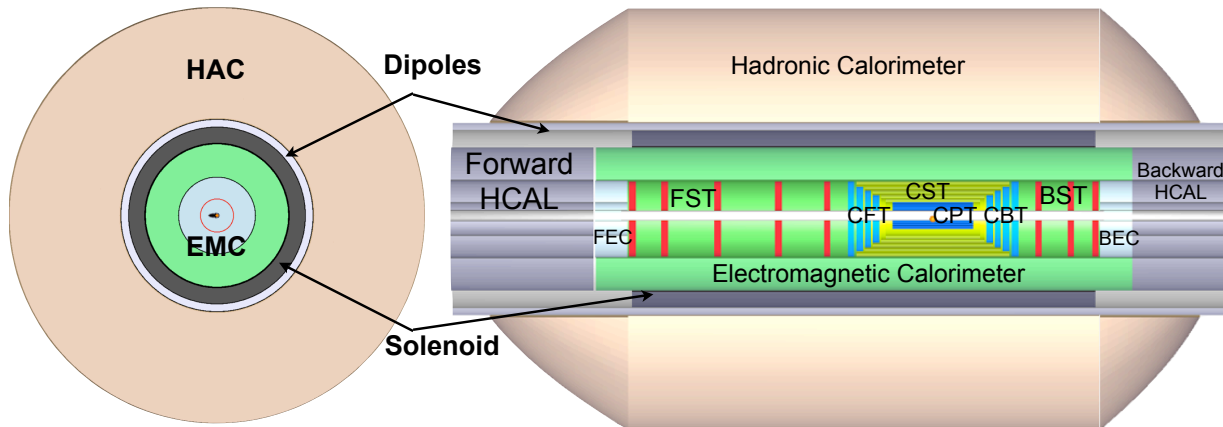


Figure 13.30:  $x$ - $y$  and  $r$ - $z$  view of the LHeC Barrel EM calorimeter (green).

9979 Fig. 13.30 shows a  $x$ - $y$  and  $r$ - $z$  view of the LHeC Barrel EM calorimeter. The layout allows the extraction  
 9980 of detector signals without significantly degrading the high-frequency components which are vital for fast  
 9981 shaping. The flexibility in the longitudinal and transverse segmentation, and the possibility of implementing  
 9982 a section with narrow strips to measure the shower shape in its initial development, represent additional  
 9983 advantages. It is worth noting that due to the asymmetric design, the projective structure is not fully  
 9984 symmetric as the calorimeter and the solenoid centre are shifted forward with respect to the interaction  
 9985 point.

9986 Fig. 13.31 shows a detail of the accordion-electrode structure. A basic cell consists of an absorber plate,  
 9987 a liquid argon gap, a readout electrode and a second liquid argon gap. The mean thickness of the liquid  
 9988 argon gap is constant along the whole barrel and along the calorimeter depth. The readout granularity

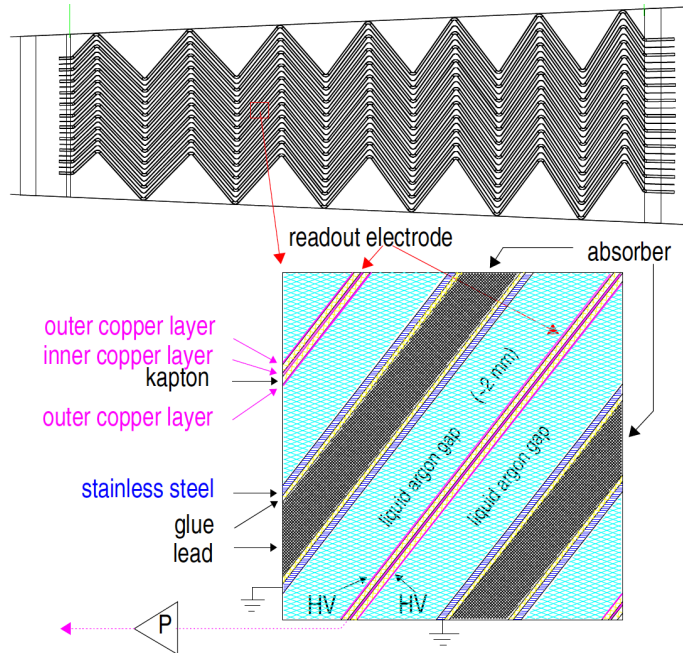


Figure 13.31: Longitudinal view of one cell of the ATLAS LAr Calorimeter, showing the accordion structure.

9989 is subdivided into 3 cylindrical sections of increasing size in  $\Delta\eta \times \Delta\phi$ . As shown in Fig. 13.32, the first  
 9990 sampling section of the EMC would have a very fine granularity ( $\Delta\eta \times \Delta\phi = 0.003 \times 0.1$ ), to optimize the  
 9991 ability to separate photons from  $\pi^0$  energy deposits. The second sampling section, mainly devoted to energy  
 9992 measurement, would have a granularity of about  $0.025 \times 0.025$ , and the final sampling section has a slightly  
 9993 coarser granularity of  $\Delta\eta \times \Delta\phi = 0.050 \times 0.025$ .

### 9994 13.4.2 The Hadronic Barrel Calorimeter

9995 The baseline hadronic calorimeter in the barrel region is a sampling calorimeter using steel and scintillating  
 9996 tiles as absorber and active material, respectively [790]. The *Tile Calorimeter* would provide the required  
 9997 mechanical stability for the inner LAr and Magnet cryostat along with the iron required for the return flux  
 9998 of the solenoidal field, as is also the case in ATLAS [781].

9999 The Tile calorimeter consists of a cylindrical structure with inner and outer radius of 120 and 260 cm  
 10000 respectively (Tab. 13.6). The central HAC barrel part is 580 cm in length along the beam axis. Endcaps  
 10001 extend the calorimetry further in the forward and backward direction in order to guarantee sufficient energy  
 10002 containment. The detector cylinder would be built of several independent wedges along the azimuthal  
 10003 direction while the modularity and segmentation may vary depending on the machine design.

10004 The Tile calorimeter forms the shell of the inner part of the LHeC detector. Once the barrel and the  
 10005 extended barrels are assembled, all of the sub-detectors apart from the muon system will be placed inside of  
 10006 it. The massive iron structure is rigid enough to support their weight, in particular the liquid argon cryostat  
 10007 and the solenoid.

10008 The absorber structure is a laminate of steel plates of various dimensions, connected to a massive struc-  
 10009 tural element referred to as a girder. The highly periodic structure of the system allows the construction of a  
 10010 large detector by assembling smaller sub-modules together. Since the mechanical assembly is completely in-  
 10011 dependent from the optical instrumentation, the design is simple and cost effective. Simplicity has also been  
 10012 the guideline for the light collection scheme: the fibres are coupled radially to the tiles along the external  
 10013 faces of each module. The laminated structure of the absorber allows for channels in which the fibres run.

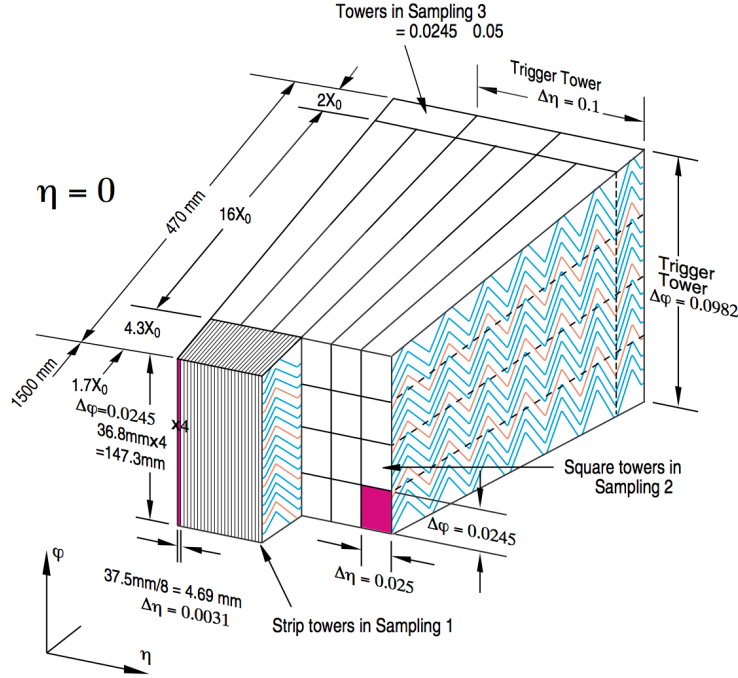


Figure 13.32: 3D view of the accordion structure of the ATLAS LAr Calorimeter

10014 The use of fibres for the readout allows a layered cell read-out to be used, creating a projective geometry  
 10015 for triggering and energy reconstruction. A compact electronics read-out is housed in the girder of each  
 10016 module. Finally, the scintillating tiles are read out in two separate photomultipliers, providing the required  
 10017 redundancy.

10018 The granularity of the Tile Calorimeter is important to finely match the electromagnetic LAr calorimeter  
 10019 in front and correct for the dead material of the magnet complex. The proposed hadronic segmentation for  
 10020 the cells behind the electromagnetic section, will allow an efficient hadron leakage cut, needed for electron  
 10021 and photon identification. A reasonable longitudinal segmentation, especially around the maximum depth  
 10022 of the shower, favours an appropriate weighting technique to restore, at the level of 1-2%, the linearity of  
 10023 the energy response to hadrons, which is intrinsically non-linear because of the non-compensating nature  
 10024 of the calorimeter. At the highest energies, the resolution of the calorimetry is dominated by the constant  
 10025 term, for which the largest contribution comes from the detector non-linearity and calibration. An attempt  
 10026 is made to keep the constant term below the 2% level.

10027 with the same granularity

### 10028 13.4.3 Endcap Calorimeters

10029 Calorimetry in the forward and backward direction at the LHeC is of extreme importance: in the forward  
 10030 region for the measurement of the hadronic final state, and in the backward region for the measurement  
 10031 of the low energy scattered electron. Here, a good  $e/h$  separation is also important to suppress hadronic  
 10032 background.

10033 As seen in Fig. 13.60, the very forward and to a lesser extent the backward parts of the calorimeter are  
 10034 exposed to high levels of particle radiation and must therefore be radiation hard by design. Synchrotron  
 10035 radiation and any further background radiation must also be tolerated in addition.

10036 Fig. 13.9 shows in detail the endcap calorimeters for the Ring-Ring design. The two-phase experimental  
 10037 program requires the endcaps to be modular as these components will either be moved along the beam

E-Calo Parts	FEC1	FEC2		EMC		BEC2	BEC1
Min. Inner radius $R$ [cm]	3.1	21		48		21	3.1
Min. polar angle $\theta$ [°]	0.48	3.2		6.6/168.9		174.2	179.1
Max. pseudorapidity $\eta$	5.5	3.6		2.8/-2.3		-3.	-4.8
Outer radius [cm]	20	46		88		46	20
$z$ -length [cm]	40	40		660		40	40
Volume [m <sup>3</sup> ]	0.3			11.3		0.3	
H-Calo Parts barrel			FHC4	HAC	BHC4		
Inner radius [cm]			120	120	120		
Outer radius [cm]			260	260	260		
$z$ -length [cm]			217	580	157		
Volume [m <sup>3</sup> ]			121.2				
H-Calo Parts Inserts	FHC1	FHC2	FHC3		BHC3	BHC2	BHC1
Min. inner radius $R$ [cm]	11	21	48		48	21	11
Min. polar angle $\theta$ [°]	0.43	2.9	6.6		169.	175.2	179.3
Max/min pseudorapidity $\eta$	5.6	3.7	2.9		-2.4	-3.2	-5.
Outer radius [cm]	20	46	88		88	46	20
$z$ -length [cm]	177	177	177		117	117	117
Volume [m <sup>3</sup> ]	4.2				2.8		

Table 13.6: Summary of calorimeter dimensions.

The electromagnetic barrel calorimeter is currently represented by the barrel part EMC (LAr-Pb module); the setup reaches  $X_0 \approx 25$  radiation length) and the movable inserts forward FEC1, FEC2 (Si-W modules ( $X_0 \approx 30$ ) and the backward BEC1, BEC2 (Si-Pb modules;  $X_0 \approx 25$ ).

The hadronic barrel parts are represented by FHC4, HAC, BHC4 ( forward, central and backward - Scintillator-Fe Tile modules;  $\lambda_I \approx 8$  interaction length) and the movable inserts FHC1, FHC2, FHC3 (Si-W modules;  $\lambda_I \approx 10$ ), BHC1, BHC2, BHC3 (Si-Cu modules,  $\lambda_I \approx 8$ ) see Fig. 13.9.

10038 line or completely removed to allow the placement of the strong focussing magnets for the high luminosity  
 10039 phase. The relevant dimensions and specifications are summarised in Tab. 13.6. For the Linac-Ring design,  
 10040 where no additional magnets along the beam line will be required, the subcomponents FHC2/FHC3 and  
 10041 BHC2/BHC3, can be combined into single modules.

10042 The restrictive geometry of the insert calorimeters requires a non-conventional and challenging design  
 10043 based on previous developments [791–798]. Tungsten ( $W$ ) is considered as the absorber material, in particular  
 10044 for the forward inserts, because of its very short radiation length and large absorption to radiation length  
 10045 ratio. About 26 cm of tungsten will absorb electromagnetic showers completely and will contain the hadronic  
 10046 shower to a large extent and over a large range of energy ( $\approx 30X_0 + \approx 10\lambda_I$ ). The electromagnetic and  
 10047 hadronic sections can be combined to minimise boundary effects. An alternative to tungsten for the hadronic  
 10048 absorber is copper ( $Cu$ ).

10049 Simulations have been performed to compare the different absorbers. Since the backward inserts have  
 10050 looser requirements, the material for the absorbers are lead ( $Pb$ ) for the electromagnetic part and copper  
 10051 for the hadronic. For the Ring-Ring option, where no dipole field along the beampipe is required, a more  
 10052 economical choice of steel ( $Fe$ ) instead of copper can be considered. The active signal sensors for both the  
 10053 forward and backward calorimeters have been chosen to be silicon-strip (electromagnetic fwd/bwd parts)  
 10054 and silicon-pad (hadronic fwd/bwd parts).

## 10055 13.5 Calorimeter Simulation

10056 In this section preliminary results on simulations of the barrel and endcap calorimeters are illustrated. The  
 10057 detector components presented in 13.4.1, 13.4.2, 13.4.3 have been simulated using **GEANT4.9.2** [799] with  
 10058 single and multiple particle events along with full  $e-p$  events from the **QGSP-3.3** [800] physics list. The  
 10059 Quark-Gluon String Precompound (**QGSP**) is based on theory-driven models and uses the quark-gluon-  
 10060 string model for interactions and a pre-equilibrium decay model for fragmentation.

10061  
 10062 The detector geometry, including the various layers of active, absorbing and support material were coded  
 10063 and inserted in the simulation. Energy resolutions for electromagnetic and hadronic deposits were studied  
 10064 along with concepts for optimal trigger and signal reconstruction. Particular attention was put into the key  
 10065 features and the construction constraints of the detector, namely the beam optics and the magnets (the  
 10066 solenoid and the Linac-Ring dipoles). Where a similar design from an existing or developing detector are  
 10067 available, the results are presented complemented by referenced studies.

10068  
 10069 The energy resolution of a calorimeter is parameterized by the following quadratic sum:

$$\frac{\sigma_E}{E} = \frac{a}{\sqrt{E}} \oplus b \quad (13.1)$$

10070 where  $E$  is the particle energy in  $GeV$ ,  $a$  is the stochastic term, which is arising from fluctuations in the  
 10071 number of signal producing processes,  $b$  is the constant term, which describes imperfections in calorimeter  
 10072 construction, fluctuations in longitudinal energy containment, non-uniformities in signal collection etc. A  
 10073 third term  $c$  (left out here) is often also added which would represent the noise in experimental data de-  
 10074 scription. The energy deposition of primary and secondary particles in the calorimeter was obtained using  
 10075 **GEANT4**, and fitted to extract  $a$  and  $b$ . Effects due to the readout process were not considered at this  
 10076 stage.

10077  
 10078 Each energy distribution was fitted with a Gaussian,  $\pm 2\sigma$  around the mean and the energy depended  
 10079 resolution was calculated using those mean values fitted. An example of the energy distribution and Gaus-  
 10080 sian fit applied is shown in Fig. 13.33. The  $a$  and  $b$  parameters are then calculated from the fit of  $\sigma/E$ .

10081

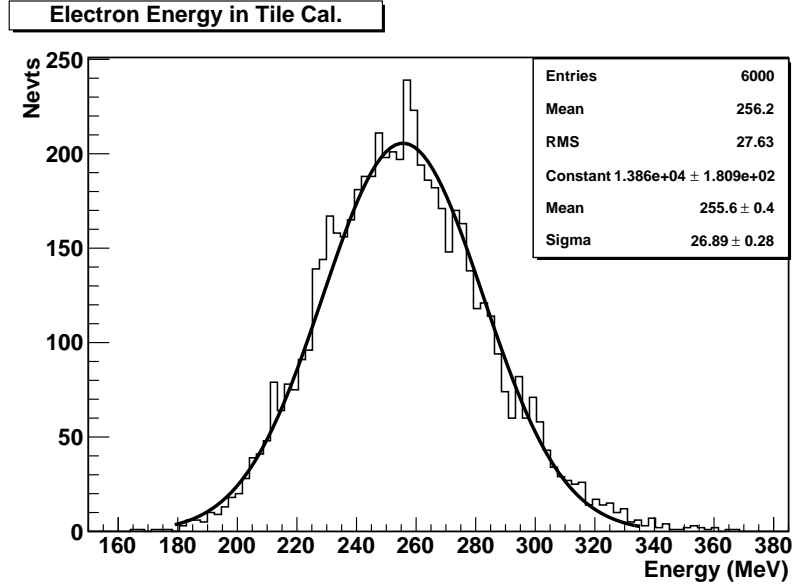


Figure 13.33: Example for a pion energy distribution and the Gaussian fit. The resulting  $\sigma$  and mean values are estimated for pions of an incident angle  $\theta = 70^\circ$  and 10 GeV energy.

### 10082 13.5.1 The Barrel LAr Calorimeter Simulation

10083 A simplified layout, adapted from the ATLAS LAr calorimeter [781], has been implemented in a **GEANT4**  
 10084 simulation and used to extract the main characteristics of the LHeC barrel electromagnetic calorimeter.

10085 The accordion shaped absorber sheets are 2.2 mm thick lead layers interspersed with 3.8 mm wide gaps  
 10086 filled with liquid argon. In the present model the electrodes which in the case for ATLAS are  $2 \times 0.275$  mm  
 10087 thick, were not considered. Both absorber and the liquid argon gap have an accordion fold length of 40.1 mm  
 10088 and 13 bend angles of  $90^\circ$ . A total of 62 absorber sheets each 250 cm wide in  $z$ -direction have been incorpo-  
 10089 rated into the simulation (Fig. 13.35-left). A 20 GeV incident single electron showering in the stack is shown  
 10090 in Fig. 13.35-right. The energy resolution for electrons was obtained from the ratio of the mean and the  
 10091 standard deviation of the electron response, both obtained by fitting a Gaussian to the energy spectrum.  
 10092 Figure 13.36 shows the energy resolution for electrons of energy between 10 and 400 GeV. These results are  
 10093 in agreement with [789]. In the simulation the energy deposited in the active material is normalized to the  
 10094 energy of the incident particle.

### 10095 13.5.2 The Barrel Tile Calorimeter Simulation

Tile Rows	Height of Tiles in Radial Direction	Scintillator Thickness
1-3	97 mm	3 mm
4-6	127 mm	3 mm
7-11	147 mm	3 mm
$x$ -depth	1407 mm	

Table 13.7: Longitudinal (into  $x$ -direction) segmentation of the hadronic tile calorimeter (HAC).

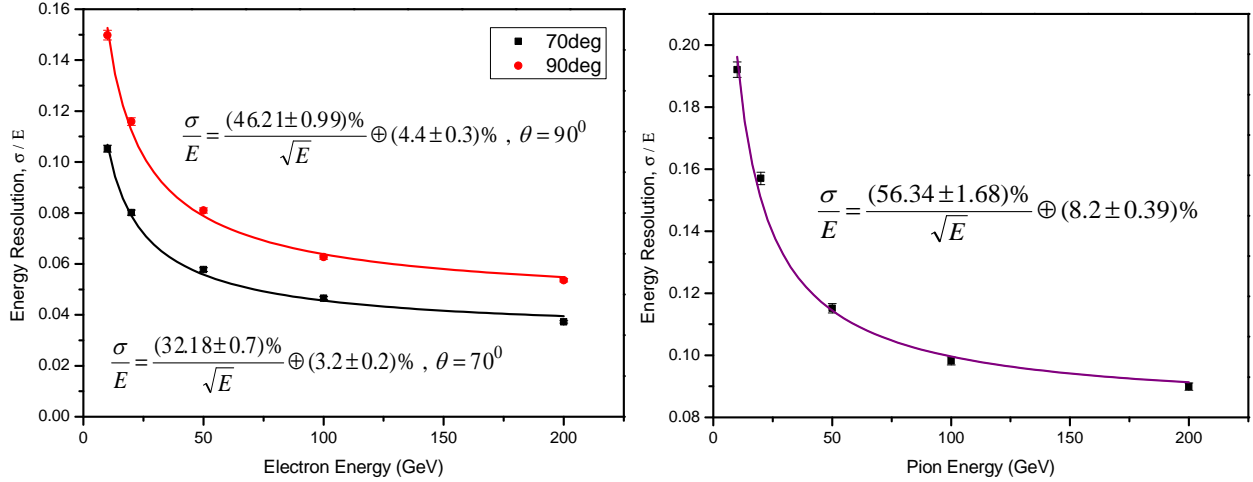


Figure 13.34: Tile Calorimeter energy resolution for electrons at  $\theta = 70^\circ$  and  $90^\circ$  (left) and for pions at  $\theta = 90^\circ$  (right).

10096 The HAC is a scintillator-steel tile calorimeter: 4 mm thick steel plates are interspaced by 3 mm thick  
 10097 scintillator tiles. The tiles are placed in planes perpendicular to the  $z$ -direction. The absorber structure  
 10098 consist of 262 repeated periods, each of which spans 19 mm in  $z$  and consist of 16 mm of steel and 3 mm  
 10099 of scintillator tile. 11 transverse rows of tiles are used in a module. The total interaction depth of the  
 10100 HAC prototype correspond to  $\lambda_I = 7$ . The longitudinal segmentation of the HAC module is described in  
 10101 Tab. 13.7. In this section the performance of the hadron calorimeter alone has been investigated. in the  
 10102 later sections the combined use of EMC and HAC parts has been studied. The energy resolution of the tile  
 10103 calorimeter was simulated with electrons and pions within the energy range 3-200 GeV (Fig. 13.34). The  
 10104 obtained stochastic term values are consistent with results obtained for ATLAS [789]. The response to  
 10105 electrons show the general good resolution such that any leakage from the electromagnetic calorimetry in  
 10106 front of HAC would be resolved safely.

### 10107 13.5.3 Combined Liquid Argon and Tile Calorimeter Simulation

10108 The combined system (accordion and tile calorimeter) has been studied. The effect of the dead material due  
 10109 to the magnet and the cryostat between the EMC and HAC has been studied in first approximation. The  
 10110 energy resolution of the combined system has been simulated. The effect of the solenoid and the cryostat  
 10111 infrastructure has been simulated by adding a thick Aluminum layer (14 cm) in between EMC and HAC.  
 10112 The study has been performed with particles in a wide range of energy and for different incident angle in  
 10113 order to obtain information about the detector response for particles entering the calorimeters at different  
 10114  $z$ . The hadronic shower simulations have been obtained in the energy range 3 GeV-200 GeV. First results of  
 10115 the energy resolutions as a function of energy for pions are shown in Fig. 13.37.

### 10116 13.5.4 Lead-Scintillator Electromagnetic Option

10117 Along with the baseline liquid argon calorimeter, a more conservative option, not requiring a dedicated  
 10118 cryogenic system, has been considered for the barrel electromagnetic calorimetry. For this purpose a  
 10119 lead-scintillator sampling calorimeter, composed of  $20 \times 0.85$  cm thick  $Pb$  layers interspaced by 4 mm plas-  
 10120 tic scintillator plates was setup for simulation. The radiation length of this systems correspond to  $30X_0$   
 10121 ( $X_0(Pb) = 0.56$  cm). All dimensions of the calorimeter systems have been kept according to the default solu-  
 10122 tion summarized in Tab. 13.6.



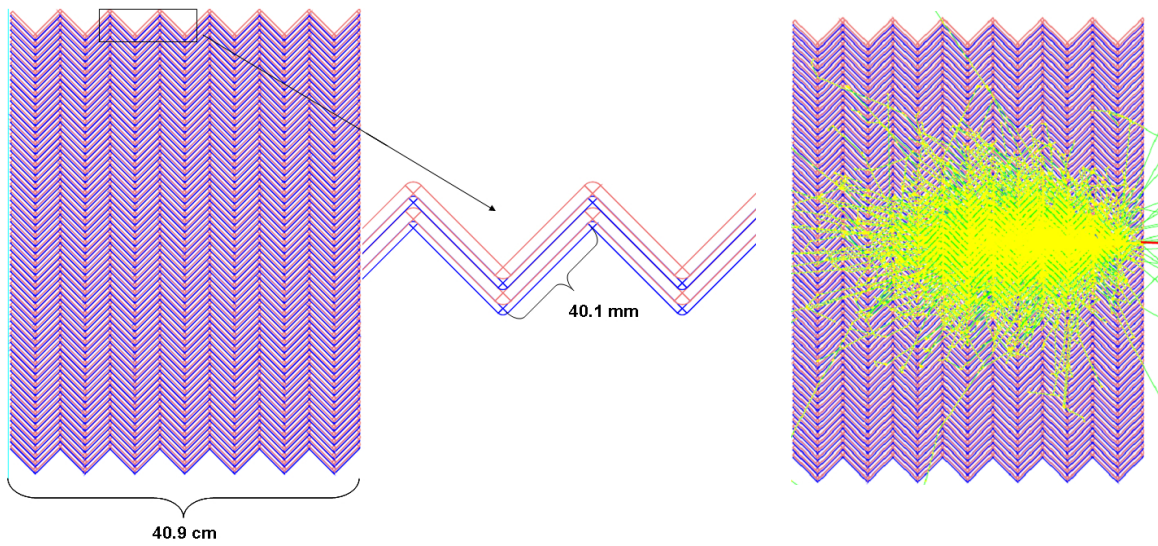


Figure 13.35: View of the parallel geometry accordion calorimeter (left) and simulation of a single electron shower with initial energy of 20 GeV (right).

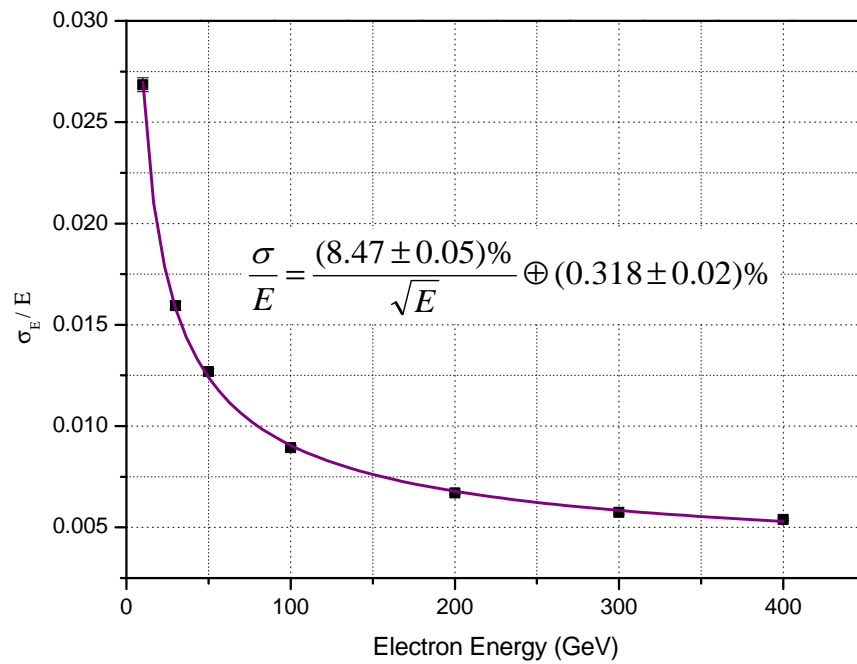


Figure 13.36: LAr accordion calorimeter energy resolution for electrons between 10 and 400 GeV.

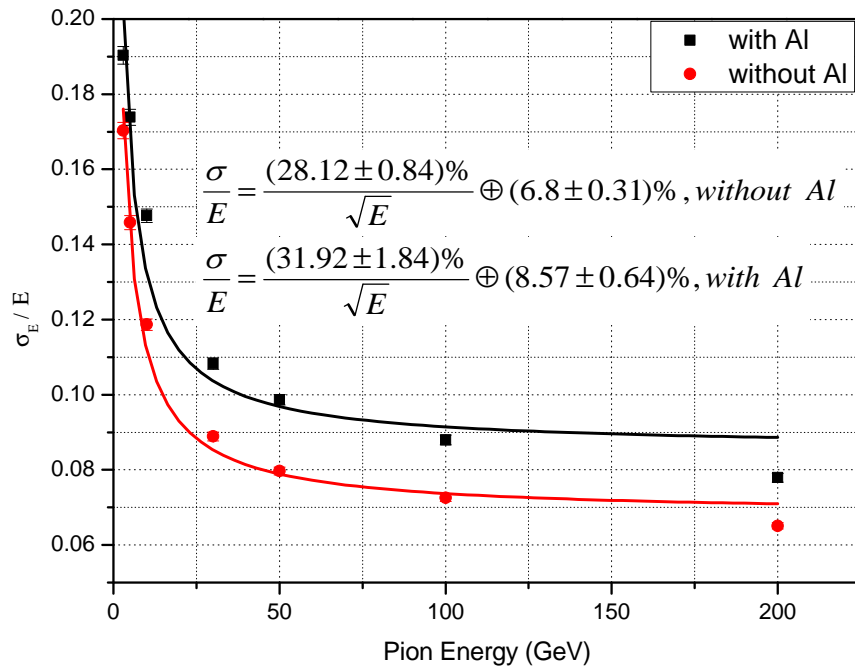


Figure 13.37: Accordion and Tile Calorimeter energy resolution for pions with and without 14cm Al block.

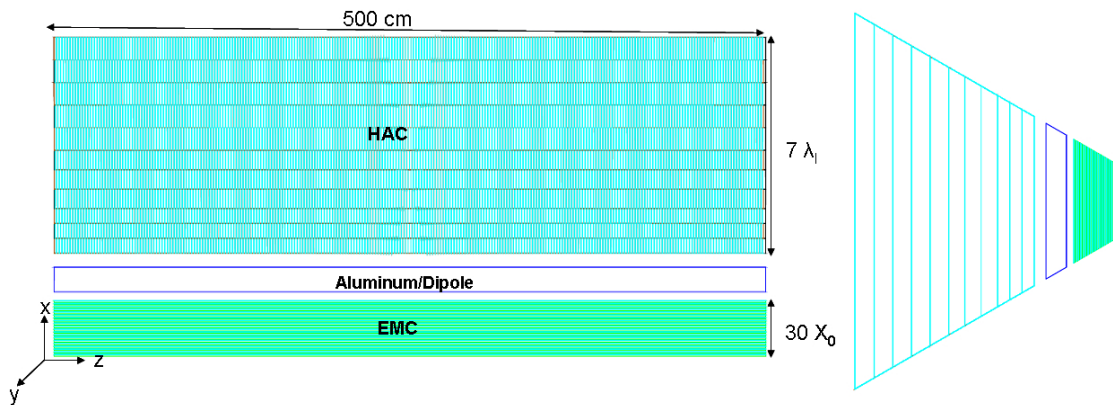


Figure 13.38: Simulation - barrel calorimeter module EMC/solenoid-dipole-system( $\propto 16$  cm Al-block)/HAC.

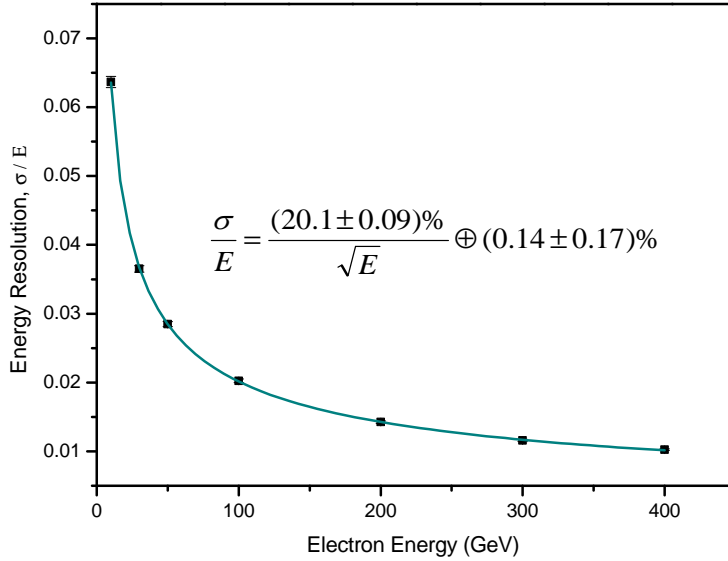


Figure 13.39: EM-Calorimeter energy resolution for electrons at  $\theta = 90^\circ$ .

10123 The lead-scintillator EMC stack was placed 30 cm in front of the HAC. Again an aluminum block of 16 cm  
 10124 was inserted between EMC and HAC representing the magnet/cryostat system as illustrated in Fig. 13.38.  
 10125 The sketched module would be one out of 6 azimuthal segments of the complete barrel EMC and HAC. The  
 10126 energy resolution of the electromagnetic lead-scintillator calorimeter as obtained with electrons of 10-400 GeV  
 10127 is shown in Fig. 13.39.

10128 As the energy loss for electrons and pions differs in shape, normalization and depth, it is worth looking  
 10129 in more detail into their shower profiles when traversing the calorimeter. At detector level, this information,  
 10130 if available, can be used to identify and discriminate particles and improve the energy resolution. High  
 10131 granularity, necessary to separate jets and energy deposits coming from different products, along with a  
 10132 longitudinal segmentation and software reweighting are essential.

10133 Longitudinal and transverse shower profiles have been studied with electrons and pions of different energies.  
 10134 The detector structure set up here for first test only and non projective designed but the comparison of studies  
 10135 with electrons and pions sent into the calorimeter system with incident angles between  $30^\circ$  and  $90^\circ$  are of  
 10136 some interest for studying shower profile properties. The effective calorimeter depth is larger for particles  
 10137 with  $\theta \neq 90^\circ$  (37 cm for the EMC and 140 cm for the barrel HAC in case of perpendicular impact). The  
 10138 longitudinal shower profiles for electrons and pions are summarized in Fig. 13.40 and Fig. 13.41. They show  
 10139 the mean deposited energy as a function of the calorimeter stack depth. The longitudinal shower profile of  
 10140 electrons is shorter than for pions as expected. The energy deposition of the electrons has its maximum in  
 10141 the EMC (Fig. 13.40). The leakage into the hadronic part of the calorimeter system is small and sums up  
 10142 to  $\mathcal{O}(10)$  MeV. Pions penetrate deeper into the calorimeter and the maximum of energy deposition is seen  
 10143 consistently in the HAC region (Fig. 13.41-right). Less energy deposition occurs in the region between 37  
 10144 and 67 cm because of the aluminum layer which represents the cryostat-wall, the solenoid and the dipole  
 10145 magnet structures. The containment of the hadronic showers is complete.

10146 Transverse profiles are usually expressed as a function of the transverse coordinates and are integrated  
 10147 over the longitudinal coordinate. Fig. 13.42 shows the transverse shower profiles for electrons and pions.  
 10148 Since the electromagnetic showers are compact, the electromagnetic energy is deposited relatively close to  
 10149 the core of the shower. As expected the hadronic profiles show a larger transverse spread.

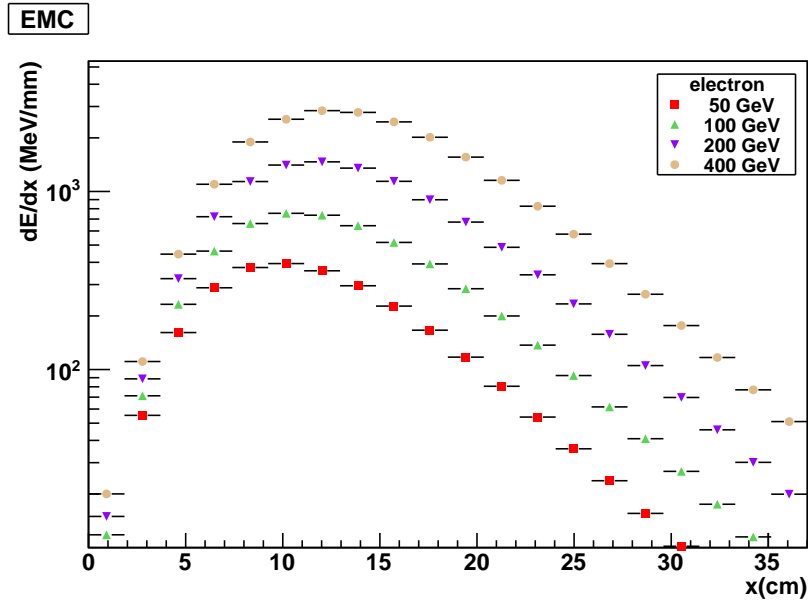


Figure 13.40: Electron longitudinal shower profile for EMC at various energies. Only the statistical uncertainties are shown.

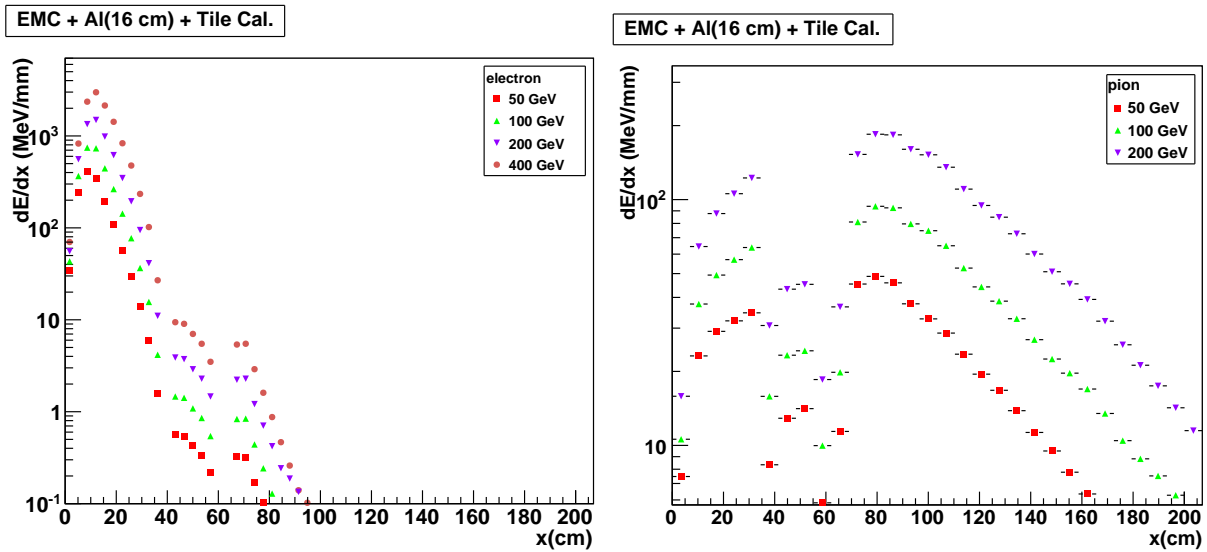


Figure 13.41: Electron (left) and Pion (right) longitudinal shower profile for the EMC/solenoid-dipole-system (Al-block)/HAC at various energies.

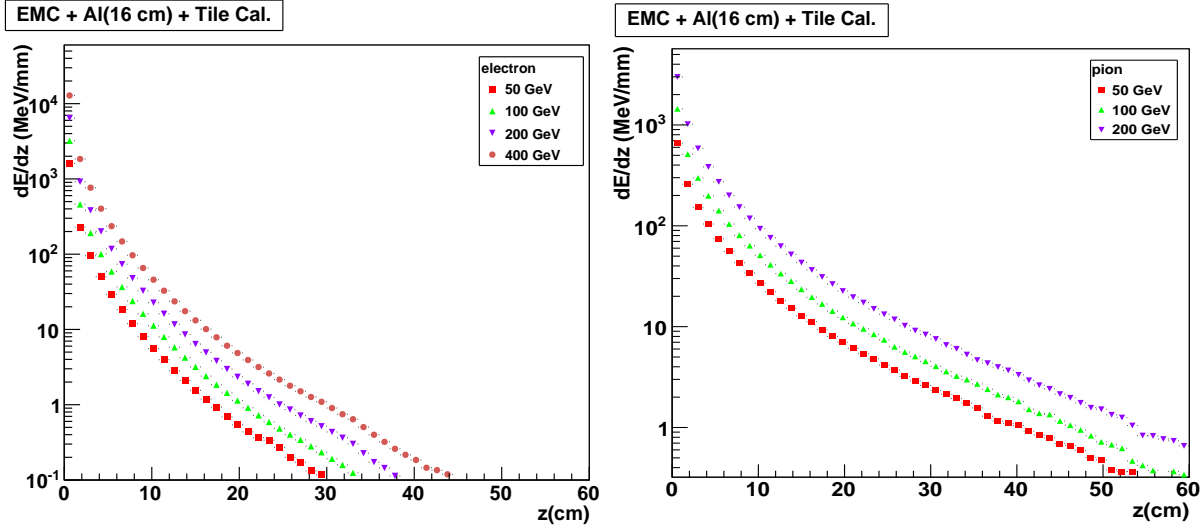


Figure 13.42: Energy deposit and transverse shower profiles for electron (left) and pion (right).

### 13.5.5 Forward and Backward Inserts Calorimeter Simulation

The very important forward/backward instrumentation for calorimetric measurement has been chosen such that from the point of view of performance and availability of the technology all currently known boundary conditions could be met. More detailed studies towards a technical design will clarify open issues. The details of the stack constructions are summarized in Table 13.8. The following options have been considered for the insert calorimeters:

- The forward electromagnetic calorimeter (FEC) inserts (i.e. FEC1 and FEC2) are tungsten-silicon sampling calorimeters for compact and radiation hard stack design matching the tracking system towards the interaction point with high granularity.
- The forward hadronic calorimeter (FHC) inserts (i.e. FHC1, FHC2 and FHC3) have been simulated using two different absorber materials, Copper (*Cu*) and Tungsten (*W*). Using *W* only would make the forward insert calorimeters FEC&FHC very homogenous. The electromagnetic and the hadronic part could be combined in the same compartment. On the other hand using *Cu* is probably more economical.
- The backward electromagnetic calorimeter (BEC) inserts (i.e. BEC1 and BEC2) are lead-silicon sampling calorimeters, with silicon as sensitive media because of the synchrotron radiation risk, specifically in the backward direction. The energy of particles, predominantly the "kinematical peak electrons" scattered backward, is expected to be low enough such that a smaller integrated radiation length  $X_0$  installed and the use of *Pb* as absorber material is justified.
- The backward hadronic calorimeter (BHC) inserts (i.e. BHC1, BHC2 and BHC3) have been setup as copper-silicon sampling calorimeters.

The BEC, BHC and BEC&BHC composite calorimeter are generally structured as their forward electromagnetic and hadronic calorimeter counterparts sketched in Figure 13.43.

The lateral size of a shower is due to the multiple scattering of electrons and positrons and characterized by the Molière radius ( $\rho_M$ ) of the setup. The lateral development of the electromagnetic showers initiated by electrons or photons scales with the Molière radius. The Molière radii of tungsten and lead are  $\rho_M=0.9327$  cm

Calorimeter Module	Layer	Absorber	Thickness	Instrumented Gap	Total Depth
FEC <sub>(W-Si)</sub> <b>30X<sub>0</sub></b>	1-25	1.4 mm	16 cm	5 mm	35.5 cm
	26-50	2.8 mm	19.5 cm		
FHC <sub>(W-Si)</sub> <b>10λ<sub>I</sub></b>	1-15	1.2 cm	39 cm	14 mm	165 cm
	16-31	1.6 cm	48 cm		
	32-46	3.8 cm	78 cm		
FHC <sub>(Cu-Si)</sub> <b>10λ<sub>I</sub></b>	1-10	2.5 cm	30 cm	5 mm	165 cm
	11-20	5 cm	55 cm		
	21-30	7.5 cm	80 cm		
BEC <sub>(Pb-Si)</sub> <b>25X<sub>0</sub></b>	1-25	1.8 mm	17 cm	5 mm	39 cm
	26-50	3.8 mm	22 cm		
BHC <sub>(Cu-Si)</sub> <b>7.9λ<sub>I</sub></b>	1-15	2.0 cm	39.75 cm	6.5 mm	145.35 cm
	16-27	3.5 cm	49.8 cm		
	28-39	4.0 cm	55.8 cm		

Table 13.8: Layer material choice and dimension of electromagnetic and hadronic calorimeter modules simulated.  $X_0$  denotes the radiation length and  $\lambda_I$  the interaction length for the whole stack, respectively. Additional to each absorber layer, layers are placed inside the gap describing the instrumentation (support and readout, respectively): Si-sensors (525 $\mu$ m), Si-support structures (FR4; 0.65 mm) and Kapton based circuits (1.15 mm). Constants used:  $X_0(W)=0.3504$  cm,  $\lambda_I(W)=9.946$  cm,  $\lambda_I(Cu)=15.06$  cm and  $X_0(Pb) = 0.5612$  cm.

Calorimeter Module (Composition)	Parameterized Energy Resolution
Electromagnetic Response	
FEC <sub>(W-Si)</sub>	$\frac{\sigma_E}{E} = \frac{(14.0 \pm 0.16)\%}{\sqrt{E}} \oplus (5.3 \pm 0.049)\%$
BEC <sub>(Pb-Si)</sub>	$\frac{\sigma_E}{E} = \frac{(11.4 \pm 0.5)\%}{\sqrt{E}} \oplus (6.3 \pm 0.1)\%$
Hadronic Response	
FEC <sub>(W-Si)</sub> & FHC <sub>(W-Si)</sub>	$\frac{\sigma_E}{E} = \frac{(45.4 \pm 1.7)\%}{\sqrt{E}} \oplus (4.8 \pm 0.086)\%$
FEC <sub>(W-Si)</sub> & FHC <sub>(Cu-Si)</sub>	$\frac{\sigma_E}{E} = \frac{(46.0 \pm 1.7)\%}{\sqrt{E}} \oplus 6.1 \pm 0.073)\%$
BEC <sub>(Pb-Si)</sub> & BHC <sub>(Cu-Si)</sub>	$\frac{\sigma_E}{E} = \frac{(21.6 \pm 1.9)\%}{\sqrt{E}} \oplus (9.7 \pm 0.4)\%$

Table 13.9: Energy resolution parameterization for electrons in the electromagnetic stacks (FEC/BEC) and for pions in the composite FEC&FHC and BEC&BHC stack structures, respectively. For each stack structure, the energy range used in the fits is:

- FEC<sub>(W-Si)</sub>: 1 GeV-5 TeV electrons,
- BEC<sub>(Pb-Si)</sub>: 3 GeV-100 GeV electrons,
- FEC<sub>(W-Si)</sub> & FHC<sub>(Cu-Si)</sub> and FEC<sub>(W-Si)</sub> & FHC<sub>(W-Si)</sub>: 50 GeV-1 TeV pions,
- BEC<sub>(Pb-Si)</sub> & BHC<sub>(Cu-Si)</sub>: 3 GeV-100 GeV pions.

The energy resolution spectra from the simulation are summarized in Figs. 13.44 and 13.45.

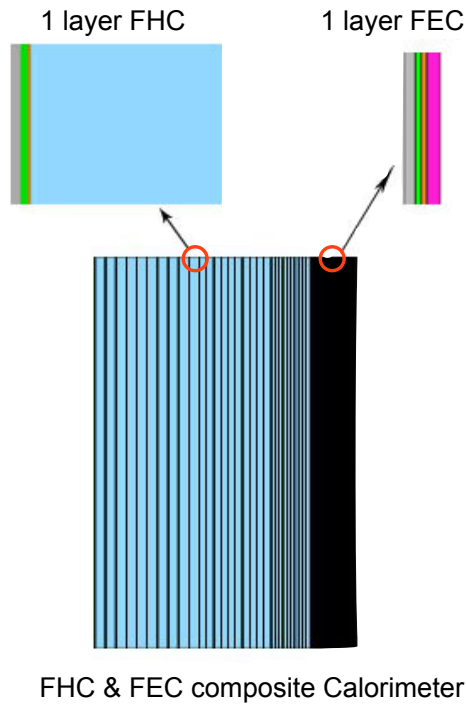


Figure 13.43: Cross section in  $rz$  of FHC+FEC. Color coding: the absorber of the FHC is in blue. The absorber of the FEC is in pink. The silicon detectors, silicon support and kapton circuits of FEC and FHC are in brown, green and gray respectively.

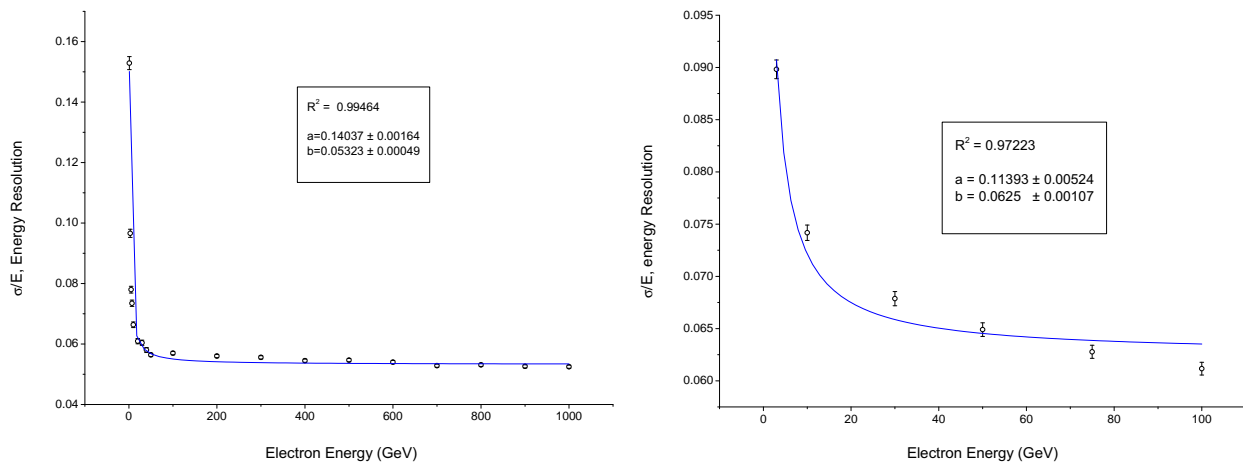


Figure 13.44: Energy resolution spectra for electrons in the energy range 1 GeV-1 TeV in the FEC<sub>(w-si)</sub> (left) and for electrons (energy range 3 GeV-100 GeV) in the BEC<sub>(Pb-Si)</sub> stacks (right).

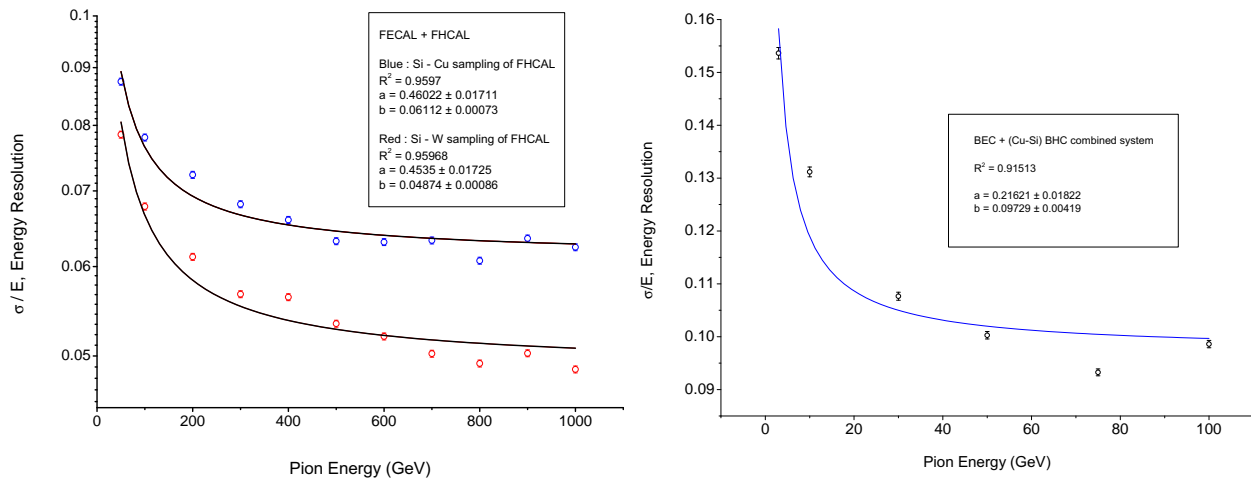


Figure 13.45: Comparison of energy resolution spectra for pions (energy range 50 GeV-1 TeV) in  $FEC_{(W-Si)}$ & $FHC_{(Cu-Si)}$  and  $FEC_{(W-Si)}$ & $FHC_{(W-Si)}$  composite system, respectively (left) and energy resolution spectrum for pions (energy range 3 GeV-100 GeV) in the  $BEC_{(Pb-Si)}$ & $BHC_{(Cu-Si)}$  composite system (right).

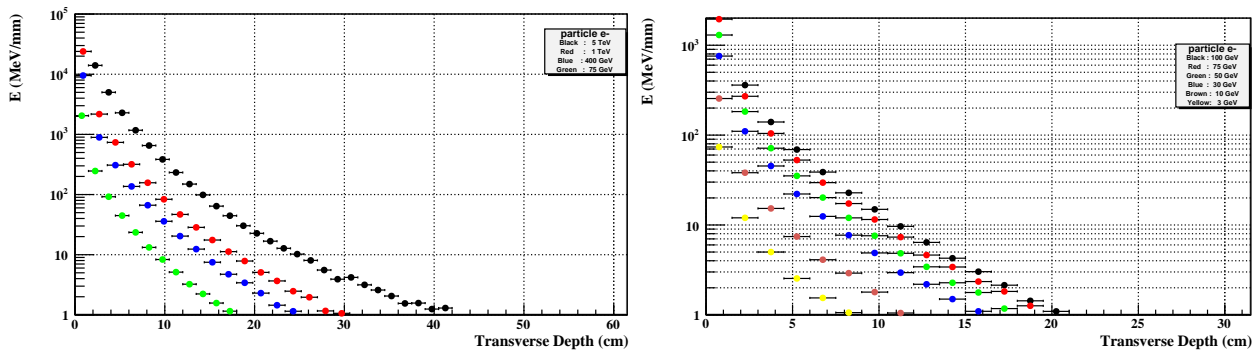


Figure 13.46: Comparison of transverse shower profiles for electrons with energies 75 GeV-5 TeV on  $FEC_{(W-Si)}$  (left) and 3 GeV-100 GeV on  $BEC_{(Pb-Si)}$  (right).



10176 and  $\rho_M=1.602$  cm [64], respectively. <sup>4</sup>  $\rho_M$  has to be low enough to separate showers, thus that argument is  
 10177 in favour of  $W$  specifically for the construction of the forward insert calorimeters (Fig. 13.46).

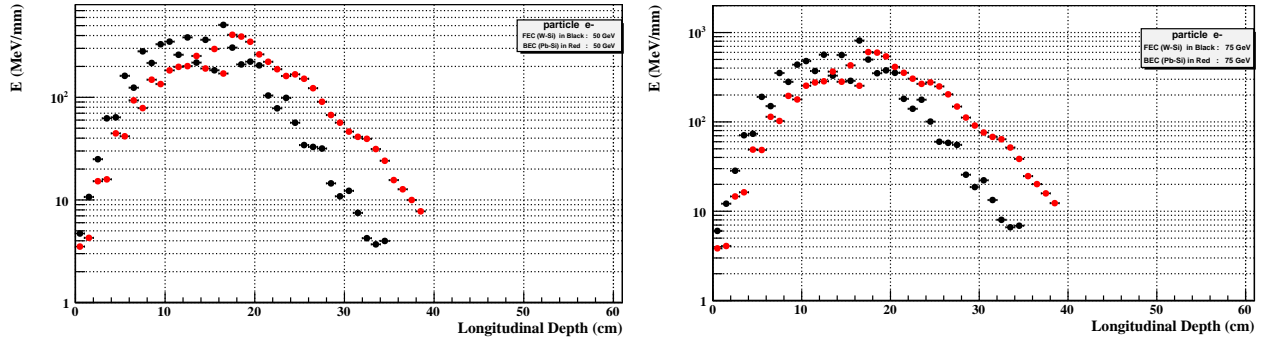


Figure 13.47: Comparison of average energy deposition as a function of longitudinal shower extension for electrons energies of 50 GeV (left) and 75 GeV (right) in  $FEC_{(W-Si)}$  (black) and  $BEC_{(Pb-Si)}$  (red).

10178 The simulated maximum longitudinal shower profiles for electrons in the FEC and BEC (Fig 13.47) are  
 10179 in agreement with former results [801]. In average 99.4% and 98.8% of the incident energy for simulated  
 10180 electron energies in the range of 1 GeV-1 TeV for  $FEC_{(W-Si)}$  and 3 GeV-100 GeV for  $BEC_{(Pb-Si)}$ , respec-  
 10181 tively, are contained in the electromagnetic calorimeters. Thus the high energy electromagnetic showers are  
 10182 sufficiently well contained in the  $30X_0^{FEC}$  and  $25X_0^{BEC}$  stack construction, respectively, taking into account  
 10183 the considerably lower energies expected in backward direction.

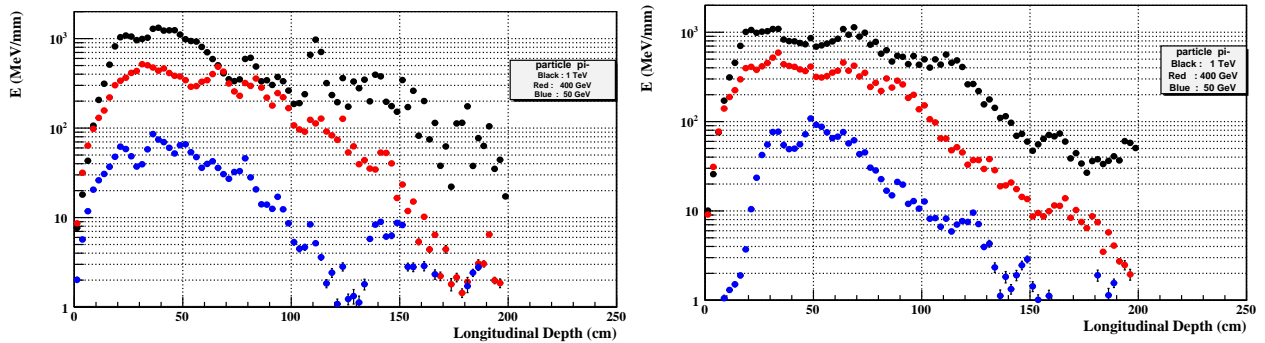


Figure 13.48: Average energy deposition as a function of depth for pions in the energy range 50 GeV-1 TeV in the  $FEC_{(W-Si)}$  &  $FHC_{(W-Si)}$  system (left) and in the  $FEC_{(W-Si)}$  &  $FHC_{(Cu-Si)}$  composite stack system (right).

10184 The longitudinal distribution of the hadronic calorimeters and shower maxima of the longitudinal dis-  
 10185 tribution scales with the nuclear interaction length  $\lambda_I$ . For copper  $\lambda_I$  is by  $\approx 51\%$  larger than for tungsten.  
 10186 Indeed we observed that showers in the  $FHC_{(W-Si)}$  stack (Fig. 13.48-left) reaches the energy deposition  
 10187 maximum already earlier in the calorimeter, i.e. at smaller depth values. That effect is more pronounced for  
 10188 lower energetic pions (Fig. 13.49-left). The thickness of  $10\lambda_I$  provides sufficient containment of the hadronic  
 10189 cascades for precision measurements both of jet properties and of  $E_T^{miss}$ . The overall containment when  
 10190 using  $FHC_{(W-Si)}$  instead of  $FHC_{(Cu-Si)}$  for the configurations described in Tab. 13.9 seems to be better.

10191 Some leakage for the hadronic calorimetry ( $BEC_{(Pb-Si)}$  &  $BHC_{(Cu-Si)}$ ) in the backward direction has  
 10192 been observed. This is not too worrisome as the main focus in the backward direction is the analysis of

<sup>4</sup>The Molière radius,  $\rho_M$ , is the radius of a cylinder containing on average 90% of the electromagnetic shower's energy deposition.

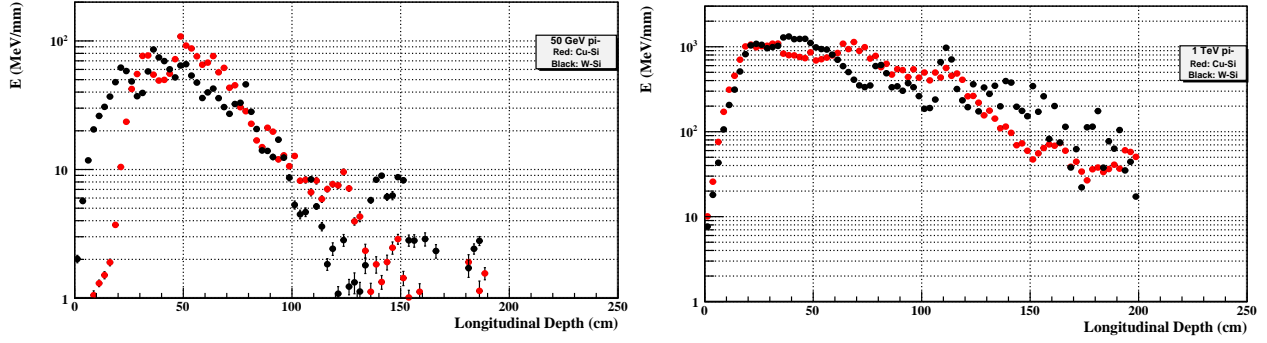


Figure 13.49: Comparison of  $FEC_{(W-Si)}$  &  $FHC_{(Cu-Si)}$  (red) and  $FEC_{(W-Si)}$  &  $FHC_{(W-Si)}$  (black) stack systems in terms of average energy depositions as a function of stack depth for pions of energy 50 GeV (left) and the same comparison for pions with energy 1 TeV (right).

10193 the electromagnetic component of the  $e^\pm p/e^\pm A$  scattering. It should be mentioned that important design  
 10194 details which will affect the performance of the real calorimeter are not defined yet. Two of these are the  
 10195 granularity definitions which have to be optimized for shower separation, and the impact of the dead regions  
 10196 coming from the cabling and the mechanical infrastructure, which is unavoidable and introducing losses in  
 10197 terms of energy measurement [802], [803]. A detailed simulation will take that into account.

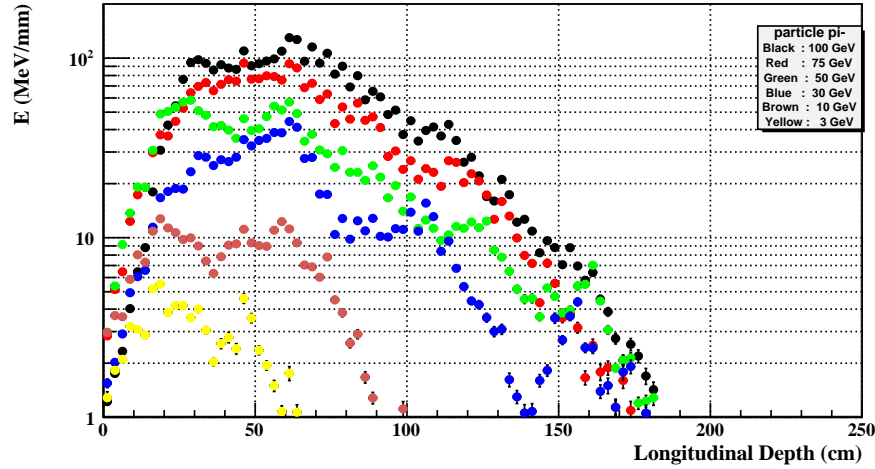


Figure 13.50: Average energy deposition as a function of depth for pions in the energy range 3 GeV-100 GeV incident on the  $BEC_{(Pb-Si)}$  &  $BHC_{(Cu-Si)}$  composite system.

## 10198 13.6 Calorimeter Summary

10199 At the LHeC different calorimeter approaches are required following the asymmetric interaction region and  
 10200 energy imbalance of the interacting beams.

10201 High energy jets with energy up to few TeV are expected in the forward region requiring radiation hard  
 10202 design, a high granularity and depth of up to  $10 \lambda_I$  and in a very compact space. More relaxed are the  
 10203 requirements in the barrel and backward region.

10204 The choice of the sampling calorimetry for all calorimeter parts is motivated by the good experience from  
10205 past experiments and from the LHC along with considerations on the available technologies, their costs and  
10206 the detector dimensions.

10207 In the barrel region, the need for a precise match to the tracking system and the ability to separate mul-  
10208 tijet events pushes toward a solution which allows for a high energy linearity and a high readout granularity  
10209 as obtainable for liquid argon. The use of a compensating calorimeter, as was for instance the uranium  
10210 calorimeter of ZEUS, would allow to reduce the  $e/h$  energy fluctuations and provide an absolute energy  
10211 measurement, but only hardly and at high manufacturing expense, provide the required granularity. More-  
10212 over software compensation and energy-reweighting for a linear response of the electromagnetic/hadronic  
10213 calorimeter is nowadays well established (H1/ATLAS).

10214 **Particle-Flow Calorimeter** [804–806] as presently being designed for the future ILC, have very specific  
10215 construction requirements making at present their choice also not suitable for the LHeC. Some of these  
10216 aspects are the powering scheme and the related duty cycle which follows from the large number of channels  
10217 involved, the required cooling, the large dimensions and costs.

10218 As already mentioned very challenging appears the design in the forward and backward endcaps especially  
10219 at small angle. In these regions the momentum measured by the tracking system is also less precise due to  
10220 the almost parallel magnetic field and the higher multiple scattering due to an effective larger beampipe and  
10221 infrastructure the particles have to cross. The silicon-absorber based inserts in the forward and backward  
10222 directions will have to be compact and efficiently matched to the tracking devices in front. In any case the  
10223 projective design of the calorimeter stack cells has to be ensured making use of signal weighting for good  
10224 space resolutions (of the order of 1 mm).

10225 An alternative approach would be the implementation of the **Double Readout Calorimeter** concept [807]  
10226 <sup>5</sup>. The dual readout calorimeters measure each shower twice and in two different ways. The major compo-  
10227 nent,  $dE/dx$  contributions of all charged particles ( $e^\pm, \pi^\pm, K^\pm$ , spallation p, recoil p, nuclear fragments, etc.),  
10228 is measured in scintillating material and the electromagnetic part, predominantly coming from subshowers  
10229 from  $\pi^0 \rightarrow \gamma\gamma$  decays, is measured by the Čerenkov light generated in clear fibres/plates by the relativistic  
10230  $e^\pm$  passing through [808]. Making use of a obviously constant ratio of  $(e/h)_C$  (for Čerenkov light emit-  
10231 ting material) and  $(e/h)_S$  (for Scintillation light emitting material), respectively, the energy response of the  
10232 calorimeter to electrons  $e$  and to hadrons  $h$  at all energies can be controlled by construction with convincing  
10233 results [809] [808].

10234  
10235 The preliminary simulations and the results shown indicate the validity of the proposed design concepts as  
10236 a baseline solution for the given dimensions of the LHeC detector. A more elaborated design will be possible  
10237 as soon as general decisions on the accelerator concept and therefore magnet design have been taken.

## 10238 13.7 Muon Detector

10239 Muon detection is an important aspect of the physics program covered by the LHeC. In particular the muon  
10240 detector can improve the scope and the spectrum of measurements, here only a few are listed:

- 10241 • Higgs decay, leptoquarks, lepton flavor violation
- 10242 • PDF fits from semileptonic decay of hadrons and heavy flavors.
- 10243 • Vector meson production

10244 The penetrative power of muons would be exploited by several layers of muon chambers ensuring good  
10245 tracking resolution and hermetic coverage, in particular towards small angles in the forward and backward  
10246 regions. These regions, particular challenging for central tracking detector due to the accelerator infrastruc-  
10247 ture, are more accessible at larger distance from the interaction region as is done for travelling minimum  
10248 ionizing particles as muons are.

---

<sup>5</sup>using plates/fibres in the double readout calorimeter stack for both signal components which are radiation hard

10249 Fig. 13.51 shows the muon polar distributions at the LHeC coming from the decay elastic  $ep \rightarrow J/\psi \rightarrow$   
 10250  $\mu^+\mu^-$  production. The improvement by enlarging the coverage towards small angles is evident as shown in  
 10251 Fig. 13.52 where the coverage as a function of the  $\gamma p$  system center of mass energy  $W$  is shown for the cases  
 10252 of  $10^\circ$  and  $1^\circ$  detector acceptance.

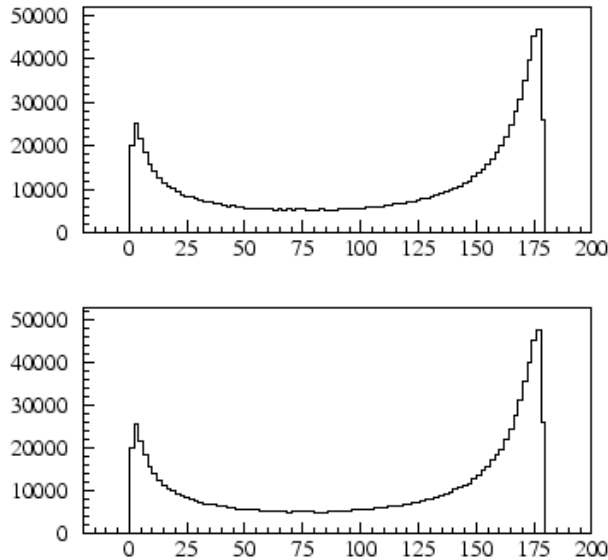


Figure 13.51: Distribution for  $J/\psi$  with  $E_e = 50$  GeV. Polar angle of positive (top) and negative (bottom) muon respectively.

### 10253 13.7.1 Muon detector design

10254 The LHeC main detector will be surrounded by multiple layers of muon detectors. Fig. 13.53 shows a 3d  
 10255 view of the baseline detector (option A). Three muon double detector layers mechanically attached to an  
 10256 iron structure which could provide either the return flux of residual B field from the inner solenoid or an  
 10257 additional field from warm magnets.

10258 Following the state of the art of present muon detector as implemented in the LHC experiments and  
 10259 in similar high energy physics experiments, several options providing the required tracking resolution, rate  
 10260 sustainability and prompt trigger and readout are available.

10261 The two LHC general purpose detectors, ATLAS and CMS, combine Drift Tubes and Cathode Strip  
 10262 Chambers for precision measurements along with with Resistive Plates Chambers and Thin Gap Chambers  
 10263 for Trigger and second coordinate measurements [810, 811]. A similar approach can be considered for the  
 10264 LHeC muon detector with 2 or 3 superlayers each one composed of a double layer of 2d trigger detector and  
 10265 a precision measurement as shown in Fig.13.54.

10266 Other technologies (as for instance micromegas [812], etc.) along with further developments of the  
 10267 existing ones (thin gap RPC [813], smaller monitored drift tubes [814], thin strip TGC [815, 816]), might also  
 10268 be considered for the LHeC. It is anyhow evident that the requirements from the LHC would also satisfy the  
 10269 running at the LHeC where backgrounds and luminosity are expected to be lower.

10270 To provide at this stage a complete design of the muon detector is beyond the scope of this document  
 10271 as too many options are available and depend on the choices to be taken in the accelerator and the main  
 10272 detector design. Only a few options are discussed below with the aim to demonstrate, for the baseline design,  
 10273 the feasibility and scope of a detector using available technologies. More studies and design optimization  
 10274 will follow in the next steps.

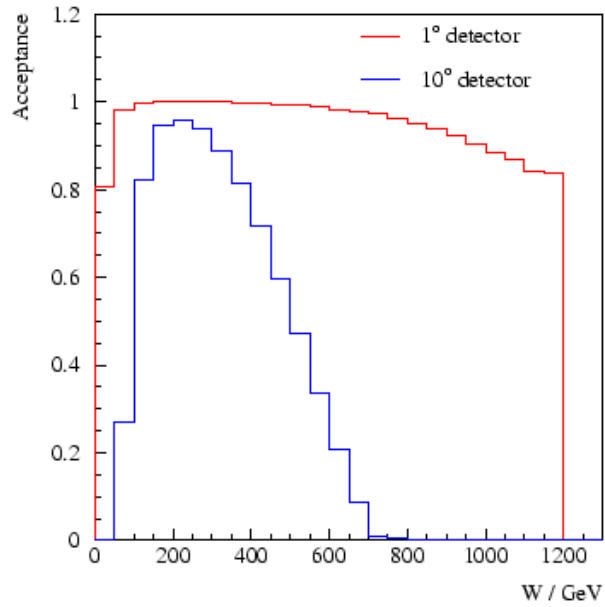


Figure 13.52: Acceptance for  $J/\psi$  with  $E_e = 50$  GeV as a function of  $W$ , the center of mass energy of the  $\gamma p$  system. A detector with larger coverage both in the forward and in the rear region allows for measurements on a much wider  $W$  range.

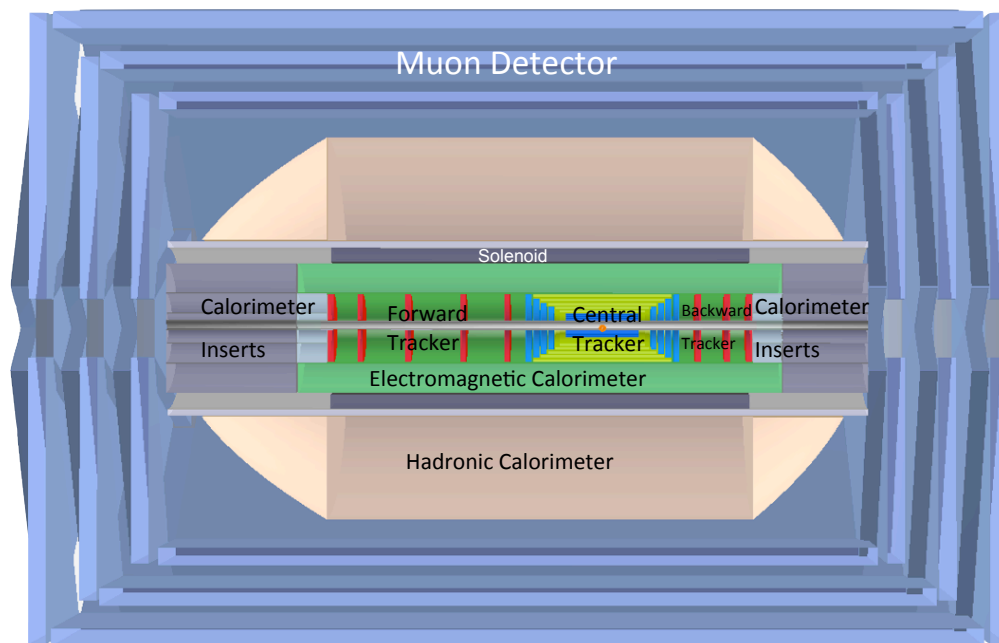


Figure 13.53: A full view of the baseline detector in the  $r$ - $z$  plane with all components shown. The detector dimensions are  $\approx 14$  m in  $z$  with a diameter of  $\approx 9$  m.

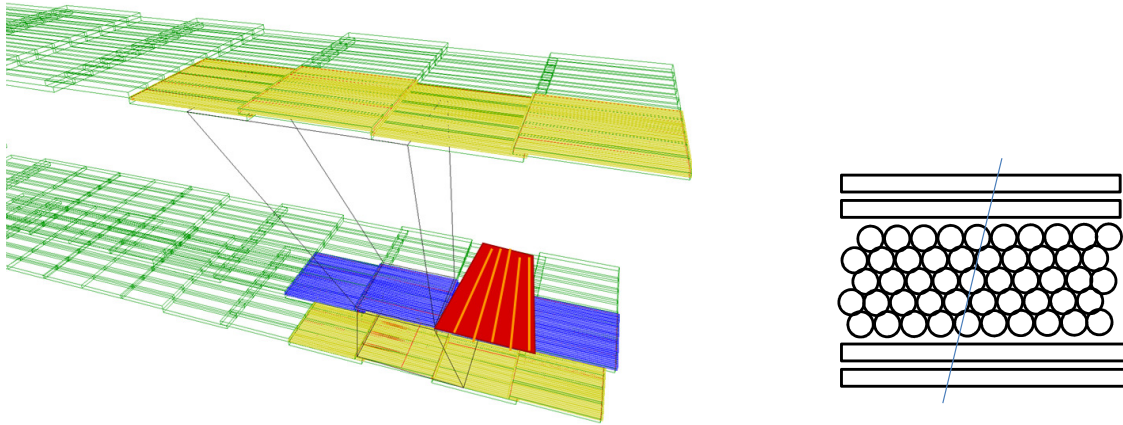


Figure 13.54: Artist 3d view of the projective arrangement of the layers barrel muon chambers (left). A schematic view of the cross section of one of the chambers which include a double layer of  $\eta\phi$  trigger measurement used also for level one triggering along with the precision measurement obtained by drift tubes

### 13.7.2 The LHeC muon detector options

Neglecting for the moment the detector technologies to be used, depending on the experimental weight the muon detector will have within the LHeC detector, few different approaches satisfying increasing requirements can be considered.

1. Muon tagging
2. Combined muon momentum measurement
3. Standalone momentum measurement

With “muon tagging” (1) we indicate a muon detector built with at least 2 layers of muon chambers that provide  $\eta\phi$  measurement and a fast coincidence for trigger purposes. No additional magnetic field would be set up and the muon detector, using only the return flux of the central solenoid would be able to provide only a very rough estimate of the particle momentum. The multiple layers and the fast detector response would allow a pointing trigger to reject non prompt particles. Muon Momentum measurements would be done using mainly the tracking detector and possibly complemented by the energy deposits in the calorimeter (that have to be compatible with those of a minimum ionizing particle) and the muon tag.

The next step (2) would be to enhance the muon momentum measurement by adding an extra magnetic field, embedding the muon chambers in an iron yoke. The amount of iron and the size of the yoke can be optimized in order maximize the resolution in the energy range required.

Both options (1) and (2) can be considered for the baseline design option A and. It is worth noticing that for low energy muons (as expected in the barrel and rear region) an instrumented yoke might not be required as the momentum resolution of the tracking system will be far superior. For muon momenta of 20 GeV and above the presence of an additional magnetic field or an instrumented iron yoke could improve especially in the forward and backward region, where the momentum resolution is worse due to the solenoidal field being parallel to the beamline.

Although the presence of an iron mass serves four good purposes, namely:

- return the magnetic flux
- serve as a hadron ( $\pi^\pm, K, p, n$ ) particle filter so that predominantly  $\mu^\pm$  emerge at a large radius

- 10301 • provide excellent mechanical support for all detector systems, especially the massive calorimeter
- 10302 • serve as a radiation shield for the area and the electronics

10303 as soon as the solenoid field and its size increase, the required shielding also increases proportionally and its  
 10304 density, weight and costs pose important limitations which might be overcome by the use of a twin solenoid  
 10305 system as discussed in 13.2.5.

10306 This novel approach which would guarantee a “standalone momentum measurement ” (3). The outer  
 10307 solenoid allows for a very smooth and constant field in an iron free region. As shown in Fig. 13.55, the muon  
 10308 detector is immersed in a strong constant field ( $\sim 1.5$  T) which would allow precise momentum measurement  
 10309 of momenta up to 500 GeV with  $\delta p/p$   $x.x$ . A strong advantage of an air muon spectrometer is the significant  
 10310 reduction of the the uncertainty due to multiple Coulomb scattering. Additionally, the use of forward  
 10311 and backward coils can improve the field quality also in the endcap regions allowing the field to line up  
 10312 transversely to the beam line, for an improved longitudinal momentum measurement.

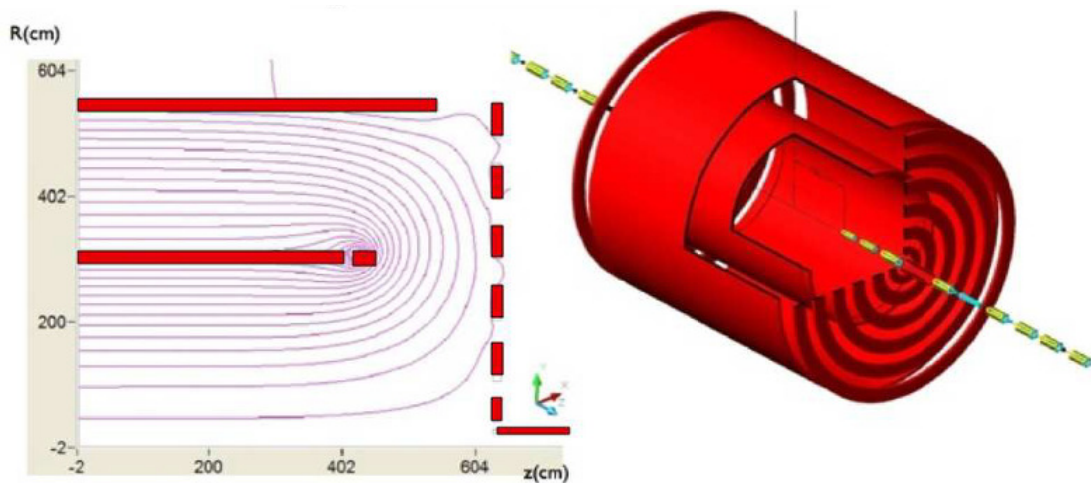


Figure 13.55: Magnetic field lines for the dual solenoid and wall of coil [817]. The whole detector is enclosed in a second return solenoid; forward and rear coils which allow for a smooth field at the detector muon encaps

### 10313 13.7.3 Forward Muon Extensions

10314 Detection of muons in the forward hemisphere is extremely relevant at the LHeC where the kinematics of  
 10315 important physical phenomena (production of heavy flavours, high  $x$  physics, leptoquarks etc.) requires a  
 10316 coverage down to the smallest possible angle with respect to the beam axis. Since the tracking momentum  
 10317 resolution deteriorates at small angles an independent measurement in the forward region would provide a  
 10318 completely independent tool for the measurement of the muon momentum.

10319 Given the high particle, and specifically, muons flux expected in the forward region, the use of a dedicated  
 10320 forward muon toroid would allow the measurement of muon charge and momentum. In Fig.13.56 a sketch of a  
 10321 possible design for a “small” forward muon toroid is given. For the baseline detector A, a more conventional,  
 10322 iron based solution (as in HERA for H1 and ZEUS) could be adopted incorporated or located outside of the  
 10323 the muon iron-yoke. The option of an air core forward toroid combined, either with the option A detector  
 10324 inside the iron yoke system or in the larger twin solenoid option B would even more enhance the forward  
 10325 muon momentum resolution especially for very small angles with respect to the beam line.

10326 The insertion of a forward air core based toroid closer to the central tracking system was also consid-  
10327 ered and rejected as the bulk material of the required coils, located between the tracking planes and the  
10328 calorimeters would compromise the calorimetry measurements.

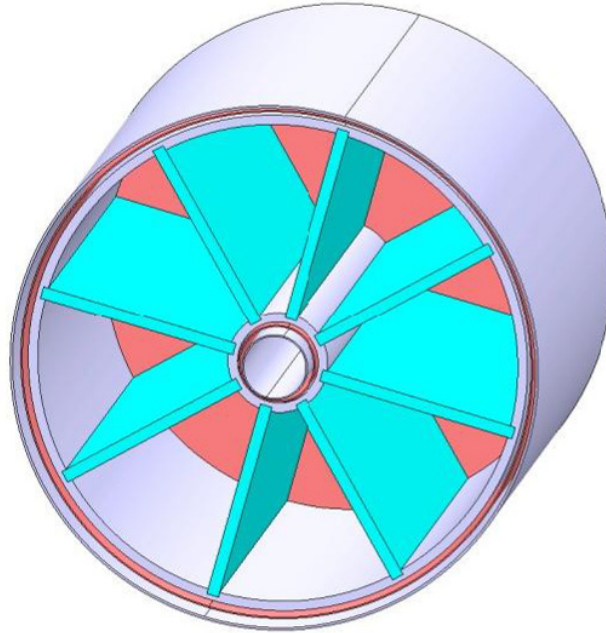


Figure 13.56: CAD drawing for a 2T air core toroid with 20 cm bore and a size about 1 m<sup>3</sup>

#### 10329 **13.7.4 Muon Detector Summary**

10330 Several options for the LHeC muon detector are available.

10331 These range from a simple muon tagging detector which, combined with the baseline detector A would  
10332 already be sufficient for a clean muon trigger, allowing to remove beam gas background and non pointing  
10333 tracks. The precision of the momentum resolution would depend mostly on the main detector (tracking and  
10334 calorimetry) which anyhow would degrade at small forward and backward angle.

10335 Improvements by means of a iron yoke and conventional forward muon toroids would allow improved  
10336 performance especially for higher momenta and for muon spectroscopy in the forward region. The experience  
10337 from HERA indicate that a solution lacking of a standalone muon trigger could be acceptable for most of  
10338 the physics program.

10339 The ultimate design nevertheless appears to be the the twin solenoid option. This more challenging  
10340 design, shown in Fig.13.57 naturally follows the option B of the baseline design: the larger main solenoid is  
10341 located outside of the hadronic calorimeter and together with a second active shielding solenoid provides a  
10342 wide material free region for precise standalone muon momentum measurement. The higher energies available  
10343 in the forward region and the interesting physics channels also push for a leading edge design towards use  
10344 of additional forward muon toroid. The detector acceptance for the muon channel physics could be largely  
10345 extended.

### 10346 **13.8 Event and Detector Simulations**

10347 Minimum bias events in the LHeC Detector have been simulated using the **GEANT4** Toolkit [799]. In  
10348 addition **ROOT** [818], **GDML** [819], **AIDA** [820] and **Pythia6** [130] have also been incorporated. A **ROOT**



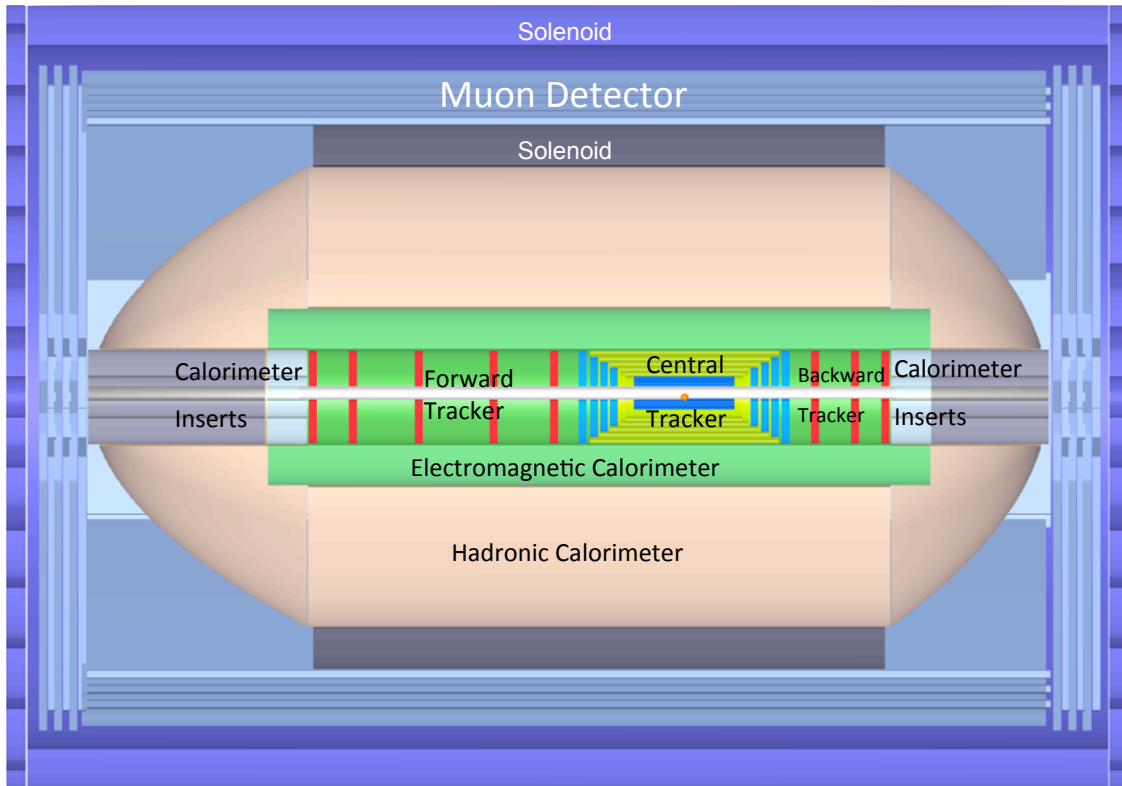


Figure 13.57: The option B of the LHeC baseline detector. The larger solenoid surrounds the hadronic calorimetry. The volume outside the solenoid is filled with an approximately uniform magnetic field of 1.5 T and is instrumented with 3 multilayers of muon chambers.

10349 macro has been written which gives a general description of the LHeC Detector geometry and materials. This  
 10350 description is then transported from **ROOT** to **GEANT4** in XML format via **GDML**. A **Pythia6** program  
 10351 has also been used to create minimum bias ep events. **Pythia6** outputs the events in HEPEVT format. This  
 10352 is then run through a subroutine to produce a format readable by **GEANT4**. The actual simulations are  
 10353 completed natively in **GEANT4** once the geometry, materials and events are loaded. The Analysis is done  
 10354 with **ROOT** (and the Java Analysis Studio **JAS** [820] ) which is interfaced to **GEANT4** via **AIDA**. The  
 10355 flow of these simulations is outlined in Figure 13.58.

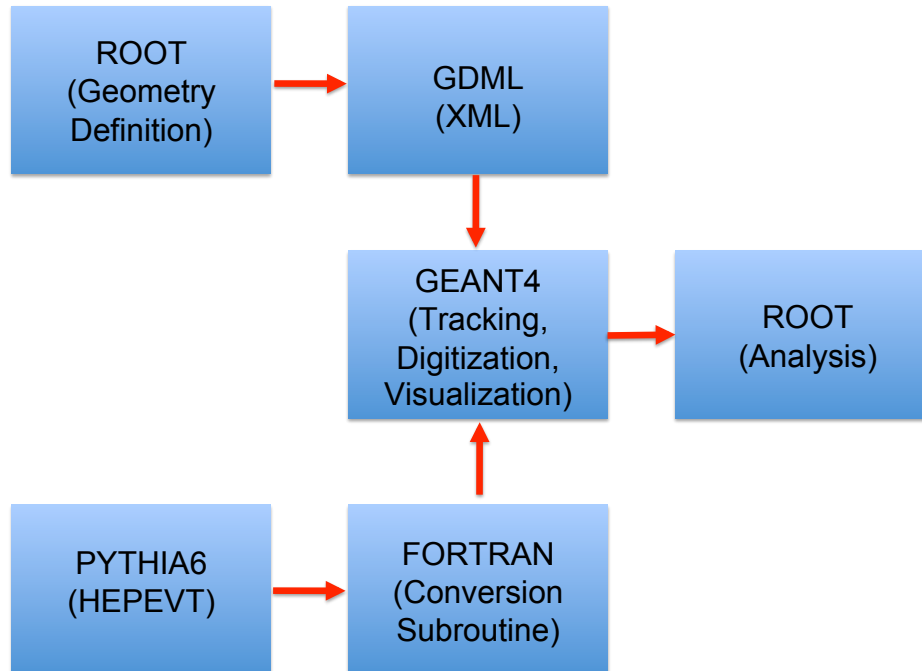


Figure 13.58: Simulation Framework Flow Chart

### 10356 13.8.1 Pythia6

10357 The **Pythia6**( [130]) event used in the **GEANT4** simulations contains  $\gamma^*P$  interactions convoluted with the  
 10358  $\gamma/e^-$  flux. This setup contains non vanishing cross sections including semihard QCD, elastic scattering,  
 10359 single/double diffractive among others (The listed interactions dominate  $\sigma_{tot}$ ). In order for the events to be  
 10360 minimum bias no restrictions are placed on the W or  $Q^2$  range.

10361 Table 13.10 gives the **Pythia6** parameters used for the minimum bias events. The logarithm of the  
 10362 variables W and  $Q^2$  are given. Since these variables obey amplitudes given by  $P(x) \propto \frac{1}{x^2}$  then  $P(\text{Log}(x)) \propto$   
 10363  $e^{-x^2}$  showing that Log(x) produces mean and rms values following normal statistics.

10364 The tools available for ep event generation are not current. The frontier of high energy physics is focused  
 10365 on hadron collisions due to the LHC. The numerous problems present in a new energy scale require developers  
 10366 to focus in this area. This results in a lack of development of event generation tools for a new energy scale of  
 10367 ep collisions. This is the reason we are using **Pythia6** as opposed to its C++ successor. Although it works  
 10368 fine for an approximation it would be advantageous to have development here.

10369 The parameters used to scale the results of the simulation in order to find annual quantities are given in  
 10370 Table 13.11.

Characteristic	Value
$Log(W)_{mean}$ [GeV]	2.09
$Log(W)_{rms}$ [GeV]	0.55
$Log(Q^2)_{mean}$ [ $GeV^2$ ]	-4.98
$Log(Q^2)_{rms}$ [ $GeV^2$ ]	3.15
Electron Energy [GeV]	60
Proton Energy [GeV]	7000

Table 13.10: Pythia6 Parameters

Characteristic	Value
Total Cross Section [ $mb$ ]	0.0686
Luminosity [ $mb^{-1}s^{-1}$ ]	$10^6$
$\frac{dN}{dt}$ [int/yr]	$2.57 \times 10^{12}$

Table 13.11: Scaling Parameters

### 10371 13.8.2 1 MeV Neutron Equivalent

10372 In order to find the 1 MeV Neutron Equivalent one must find the appropriate displacement damage functions  
 10373 [D(E)] for the particles. By scaling the damage functions by the reciprocal of D(n, 1 MeV) one arrives at  
 10374 a weight which will turn a fluence of random particles into the 1 MeV Neutron Equivalent fluence. D(E) is  
 10375 not only dependent on particle type but also on the material in which the particles are traversing. The D(E)  
 10376 functions used in the simulations can be found in Figure 13.59 [821].

10377 In order to find the 1 MeV Neutron Equivalent fluence through the tracking portion of the detector scoring  
 10378 was incorporated into the **GEANT4** simulations. A user defined scorer was used that would calculate the  
 10379 number of hits on the surface of a detector component, weight the hits according to the appropriate damage  
 10380 functions and finally divide the sum of these weighted hits by the inner surface area of the detector component.  
 10381 The flux was then scaled by the number of events per year using the mentioned scaling parameters given in  
 10382 Table 13.11. The total 1 MeV Neutron Equivalent fluences are given in Table 13.12.

10383 A different approach was used in order to find the 1 MeV Neutron Equivalent fluence distribution in  
 10384  $R_{polar}$  and  $Z$ . In order to retain data generated on the event level instead of the run level a set up of  
 10385 Sensitive Detectors [SD] must be initialized that will measure user defined quantities for traversing particles.  
 10386 The entire tracking region was set as one SD, with each hit containing the position information, and the  
 10387 current  $D(E)$  value of the given track. A 2D histogram is generated for the variables  $R_{polar}$  and  $Z$ . The  
 10388 intensity (each hit weighted by its  $D(E)$  value) is then scaled by the number of events in the run, the number  
 10389 of events per year, and a fluence weighting function. This function divides the number of entries in each bin  
 10390 by the average surface area the bin represents (i.e.  $2\pi R_{mean}\Delta Z$  where  $R_{mean}$  is the mean R value which  
 10391 the bin spans and  $\Delta Z$  is the width of the  $Z$  bins). By this weighting process the resulting 2D histogram  
 10392 (Figure 13.60) displays the 1 MeV Neutron Equivalent Fluence in  $\frac{cm^{-2}}{year}$ .

### 10393 13.8.3 Nearest Neighbor

10394 The **Geant4** simulations were also used to find the resolution required in the forward tracking. Firstly, the  
 10395 flux through the surface of CFT1, CFT4, FST1, and FST5 was found. A minimization algorithm is then  
 10396 used to find the nearest neighboring hit at the  $Z = constant$  surface for each hit. This distance scale is  
 10397 characteristic of the resolution required for the tracking component in question. The nearest neighboring  
 10398 hit distribution is calculated on the event level. This implies that only the hits from the same event are  
 10399 compared. This will have to be studied further to take pileup into account, however information on the event

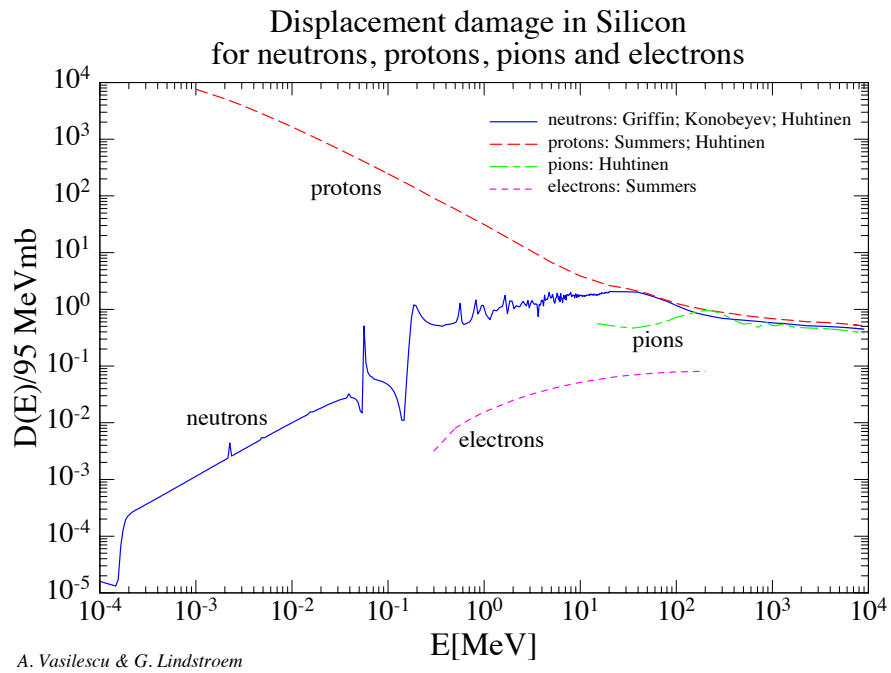


Figure 13.59: Displacement Damage for various particles in Silicon

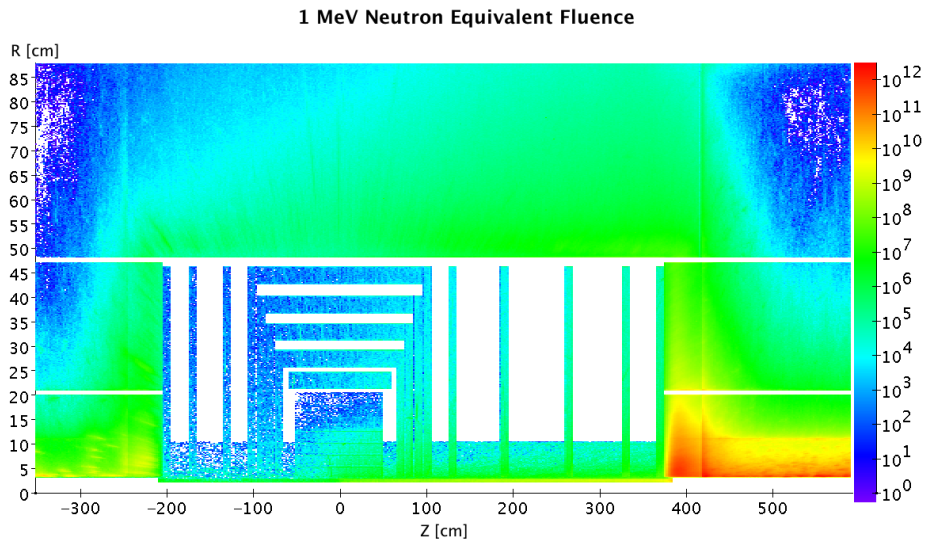


Figure 13.60: 1 MeV Neutron Equivalent Fluence [ $\text{cm}^{-2}/\text{year}^{-1}$ ].

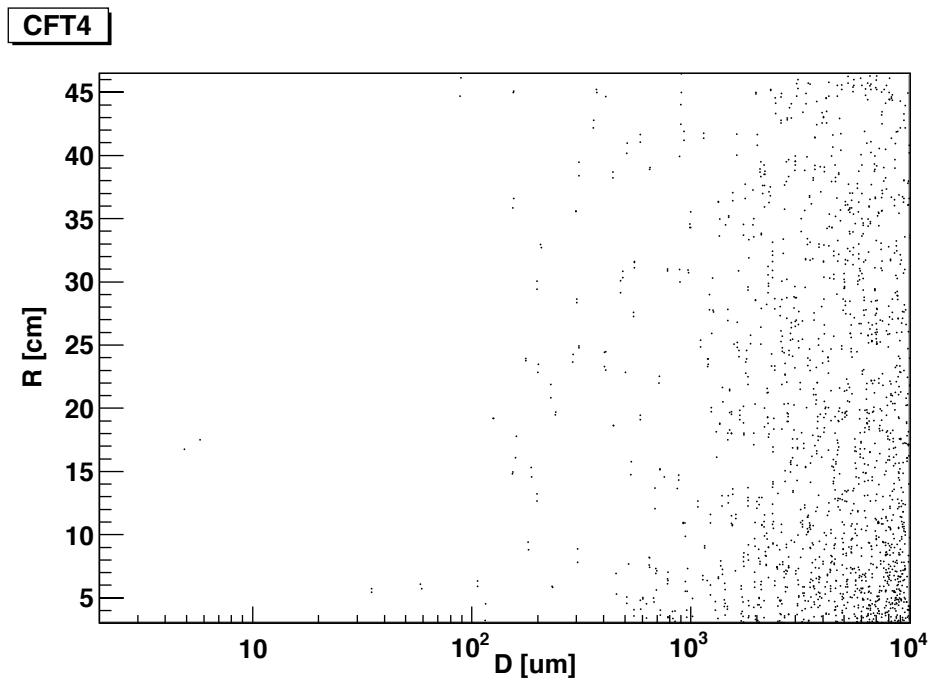


Figure 13.61: Nearest Neighbor distribution for CFT4

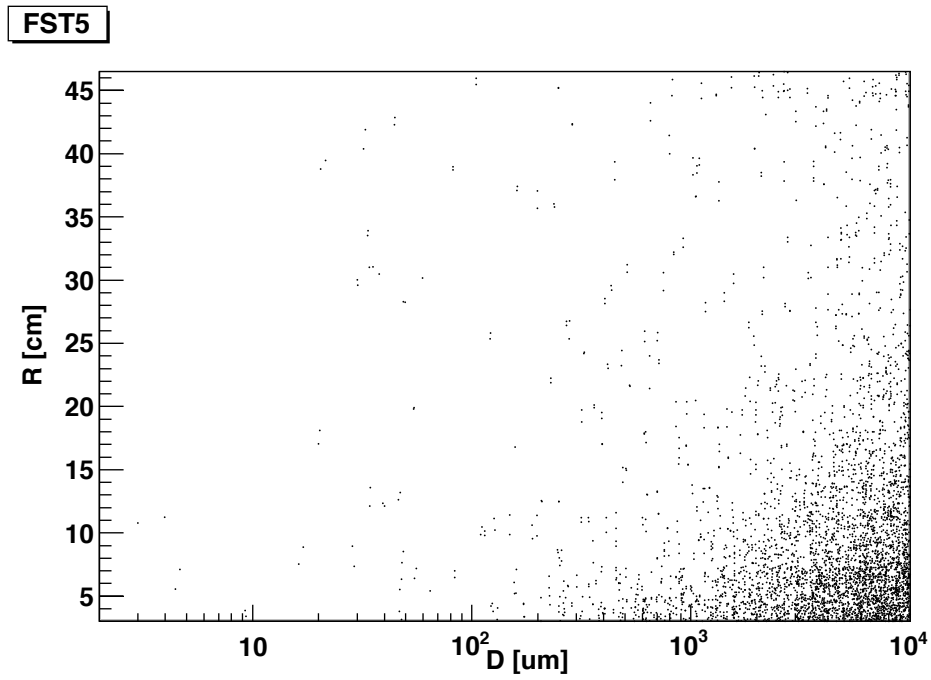


Figure 13.62: Nearest Neighbor distribution for FST5

Central Barrel			
Region	$\Delta Z$ [cm]	$R_{min}$ [cm]	Fluence [ $\frac{N}{cm^2 yr}$ ]
CPT1	100	3.1	$1.38 \times 10^{10}$
CPT2	100	5.6	$9.99 \times 10^9$
CPT3	100	8.1	$8.26 \times 10^9$
CPT4	100	10.6	$7.25 \times 10^9$
CST1	116	21.2	$6 \times 10^9$
CST2	128	25.6	$5.66 \times 10^9$
CST3	148	31.2	$5.38 \times 10^9$
CST4	168	36.7	$5.25 \times 10^9$
CST5	188	42.7	$5.16 \times 10^9$
Central Endcaps			
Region	Z [cm]	$\Delta R$ [cm]	Fluence [ $\frac{N}{cm^2 yr}$ ]
CFT1	70	26	$8 \times 10^9$
CFT2	80	31.6	$7.42 \times 10^9$
CFT3	90	37.1	$7.08 \times 10^9$
CFT4	101	43.1	$6.93 \times 10^9$
CBT1	-70	26	$2.77 \times 10^9$
CBT2	-80	31.6	$2.48 \times 10^9$
CBT3	-90	37.1	$2.26 \times 10^9$
CBT4	-101	43.1	$2.09 \times 10^9$
Fwd/Bwd Planes			
Region	Z [cm]	$\Delta R$ [cm]	Fluence [ $\frac{N}{cm^2 yr}$ ]
FST1	130	43.1	$8.2 \times 10^9$
FST2	190	43.1	$1.14 \times 10^{10}$
FST3	265	43.1	$1.63 \times 10^{10}$
FST4	330	43.1	$2.29 \times 10^{10}$
FST5	370	43.1	$2.75 \times 10^{10}$
BST1	-130	43.1	$1.96 \times 10^9$
BST2	-170	43.1	$1.91 \times 10^9$
BST3	-200	43.1	$1.99 \times 10^9$

Table 13.12: 1 MeV Neutron Equivalent Fluence

10400 level is a nice approximation. The nearest neighbor distribution for CFT4 is shown in Figure 13.61 and for  
10401 FST5 in Figure 13.62. The x axis contains the value of the nearest neighbor for each hit in terms of  $\mu m$  while  
10402 the y axis contains R in terms of cm. A required resolution of 10 or less  $\mu m$  would require pixel detectors  
10403 instead of strip detectors. The CFT4 and FST5 Figures display a very low hit density in this area. The  
10404 percentage of hits with  $D < 10 \mu m$  for the four tracking components in question are given in Table 13.13.

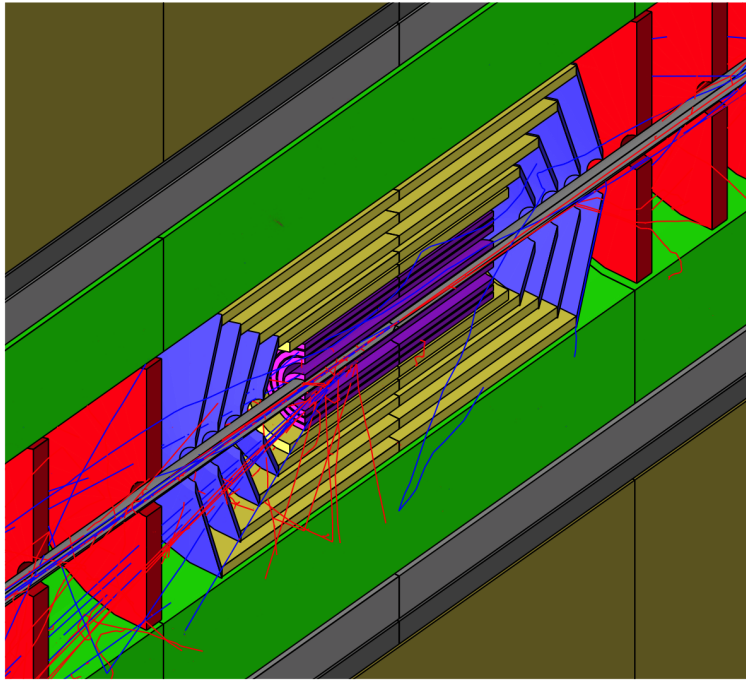


Figure 13.63: G4 Event

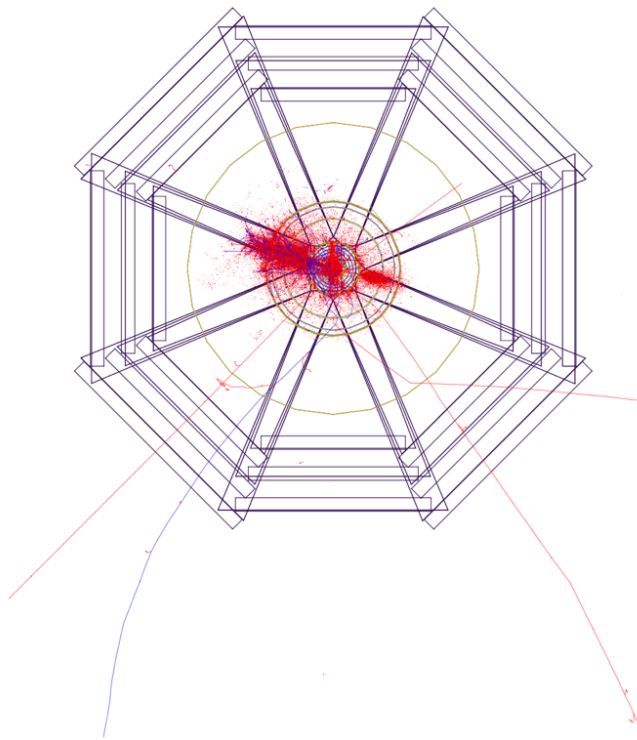


Figure 13.64: Leptoquark Event XY

Tracking Component	Hits under 10 $\mu m$ [%]
CFT1	0.18
CFT4	0.23
FST1	0
FST5	0.1

Table 13.13: Nearest Neighbor under 10  $\mu m$

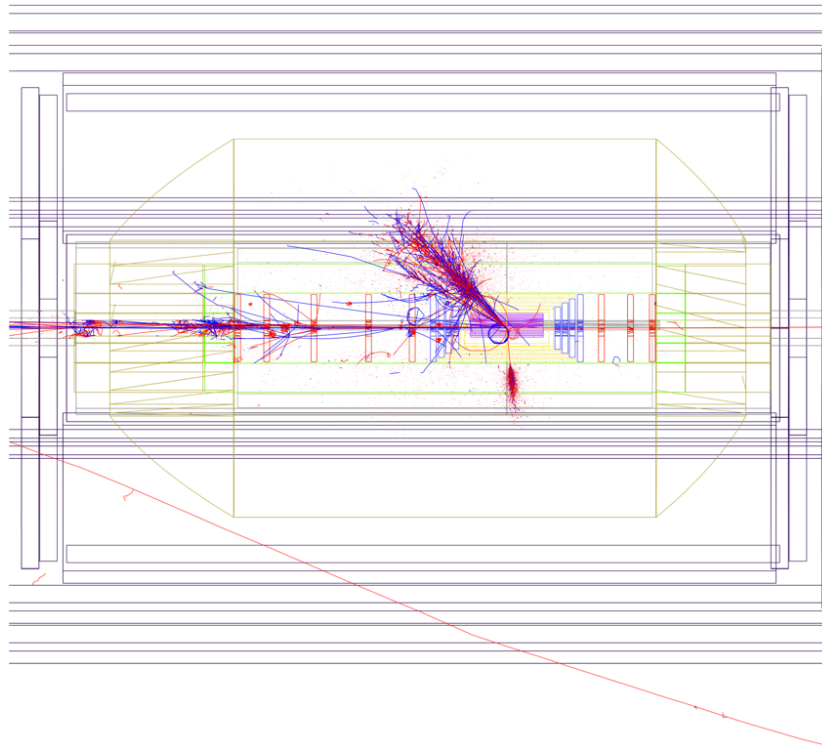


Figure 13.65: Leptoquark Event RZ

#### 10405 13.8.4 Cross Checking

10406 DAWN was used for visualization of the detector. This was able to produce clear pictures which was one  
 10407 way to make sure the translation of geometry from **ROOT** to **GEANT4** went as expected. An event in the  
 10408 central tracking region is presented in Figure 13.63.

10409 In addition to the minimum bias events, **Pythia6** was also used to create some Leptoquark events. This  
 10410 was one method of checking the **Pythia6** input (i.e. that the events produced describe the given kinematic  
 10411 range and cross sections available). However it was also utilized to determine the detector response at various  
 10412 kinematic ranges. Since  $\sigma_{EM} \propto \frac{1}{Q^4}$  The minimum bias events have very low  $Q^2$  and therefore very forward  
 10413 jets, which leaves almost no activity in the barrel HCAL. By looking at some high  $Q^2$  events it is possible  
 10414 to see the response of the hadronic calorimetry in the barrel region, making sure it is showering correctly.  
 10415 Some pictures of the Leptoquark events are given in Figure 13.64 and Figure 13.65.



### 10416 13.8.5 Future Goals

10417 There are many goals still to be accomplished by the LHeC Detector Simulations. The set up needs to be  
10418 modified to include a detailed calorimeter description. Currently e.g. the forward/backward calorimeter  
10419 volumes contain a mixture of FR4, Kapton, Active and Passive material which is weighted according to a  
10420 realistic set up. This design must be replaced with a realistic setup of the calorimeters. This also needs  
10421 to be done for the tracking which is currently composed of single silicon pieces instead of smaller modules.  
10422 The majority of the work in making these changes comes from the required read out geometry and sensitive  
10423 detector set up that would be required for analysis of a complicated geometrical structure. This also might  
10424 require a restructuring of the simulation package. Since the detector description was done first in **ROOT**,  
10425 **GDML** was an option to allow utilizing **GEANT4** without recoding the geometry. However if the geometry  
10426 will significantly change then this might benefit from being done natively in **GEANT4**. Of course the  
10427 Geometry needs to be iterated until it actually describes the exact detector (service pipes, read out, etc...).  
10428 However this will come with the TDR.

10429 Finally the stability of the simulations needs to be assessed. Eventually a complex multifunctional  
10430 detector simulation package needs to be produced. This is best done by wrapping numerous simulation  
10431 toolkits into a single package utilizing **ROOT**, such as **AliROOT** [822], [823], [824] or **ILCROOT** [825].  
10432 The LHeC simulations at some point need to make a shift towards creating a package like this, in order to  
10433 promote greater functionality and greater accessibility.

## Chapter 14

# Forward and Backward Detectors

In this chapter forward and backwards detector are presented. These detector are located from few tens of meters from the interaction point up to several hundreds in order to provide specific information not accessible to the main detector. Main focus are the measurements of

- the instantaneous luminosity (Section 14.1)
- the electron or positron beam polarization (Section 14.2)
- very forward diffractive nucleons (Section ??,14.4)

The placement of dedicated taggers both forward and backwards along the beampipe, as discussed in Section 14.1 will provide also additional means to trigger and select data for specific analyses.

### 14.1 Luminosity Measurement and Electron Tagging

Luminosity measurement is an important issue for any collider experiment. At the LHeC, where precision measurements constitute a significant part of the physics programme, the design requirement is  $\delta\mathcal{L} = 1\%$ .

In addition to an accurate determination of integrated luminosity,  $\mathcal{L}$ , for the normalisation of physics cross sections, the luminosity system should allow for fast beam monitoring with a typical statistical precision of 1%/sec for tuning and optimisation of  $ep$ -collisions and to provide good control of the mid-term variations of instantaneous luminosity,  $L$ .

Rich experience gained by H1 [826,827] and ZEUS [828,829] Collaborations at HERA was used in the design studies of the luminosity system for the LHeC. In particular, one important lesson to be learnt from HERA is to prepare several alternative methods for luminosity determination.

For the LHeC we consider both Linac-Ring (LR) and Ring-Ring (RR) options as well as high  $Q^2$  ( $10^\circ - 170^\circ$  acceptance) and low  $Q^2$  ( $1^\circ - 179^\circ$  acceptance) detector setups. This spans over a wide range of instantaneous luminosity<sup>1</sup>  $L = (10^{32} - 2 \cdot 10^{33})\text{cm}^{-2}\text{s}^{-1}$ . Hence suitable processes for the three tasks outlined above should have the following minimal visible cross sections<sup>2</sup>:

- fast monitoring ( $\delta\mathcal{L} = 1\%/sec \Rightarrow 10\text{ kHz}$ ) -  $\sigma_{\text{vis}} \gtrsim 100\mu\text{b}$ ,
- mid-term control ( $\delta\mathcal{L} = 0.5\%/hour \Rightarrow 10\text{ Hz}$ ) -  $\sigma_{\text{vis}} \gtrsim 100\text{nb}$ ,
- physics sample normalisation ( $\delta\mathcal{L} = 0.5\%/week \Rightarrow 0.1\text{ Hz}$ ) -  $\sigma_{\text{vis}} \gtrsim 1\text{nb}$ .

<sup>1</sup>This also takes into account exponential reduction of  $L$  during the data taking in every luminosity fill.

<sup>2</sup>Statistical error has to be small in comparison with total error  $\delta L_{\text{tot}}$  in order not to spoil overall accuracy.

10461 The best candidate for luminosity determination is the purely electromagnetic *bremstrahlung reaction*  $ep \rightarrow$   
 10462  $e\gamma + p$  shown in Figure 14.1a, which has a large and precisely known cross section. Depending on the photon  
 10463 emission angle it is called either Bethe-Heitler process (collinear emission) or QED Compton scattering (wide  
 10464 angle bremsstrahlung). In addition, Neutral Current DIS events in a well understood  $(x, Q^2)$  range can be  
 10465 used for the *relative* normalisation and mid-term yield control.

10466 While QED Compton and NC DIS processes can be measured in the main detector dedicated ‘tunnel  
 10467 detectors’ are required to register Bethe-Heitler events. For the latter, additional challenges as compared  
 10468 to HERA are related to the LHeC specifics: non-zero beam crossing angle in IP for RR option, and severe  
 10469 aperture limitation for LR option. Finally, for the high luminosity LHeC running one should not forget  
 10470 about significant pileup ( $L/\text{bunch}$  is  $\sim 2 - 3$  times bigger as compared to HERA-II running).

### 10471 14.1.1 Options

10472 The huge rate of ‘zero angle’ electrons and photons from Bethe-Heitler reaction<sup>3</sup> makes a dedicated luminosity  
 10473 system in the tunnel ideal for fast monitoring purposes. However, it is usually very sensitive to the details  
 10474 of the beam optics at the IP, may suffer from synchrotron radiation (SR) and requires, for accurate absolute  
 10475 normalisation, a large and precisely known geometrical acceptance which is often difficult to ensure. On  
 10476 the contrary, the main detector has stable and well known acceptance and is safely shielded against SR.  
 10477 Therefore, although QED Compton events in the detector acceptance have significantly smaller rates they  
 10478 may be better suited for overall global normalisation of the physics samples. Thus the two methods are  
 10479 complementary, having very different systematics and providing useful redundancy and cross check for the  
 10480 luminosity determination.

10481 To evaluate the main LHeC detector acceptance for NC DIS events and for the elastic QED Compton  
 10482 process DJANGO [830] and COMPTON [831] event generators were used respectively. Different options for  
 10483 dedicated luminosity detectors in the LHC tunnel have been studied with help of the special H1LUMI program  
 10484 package [832], which contains Monte Carlo generation of the ‘collinear’ photons and electrons from various  
 10485 processes (Bethe-Heitler reaction, quasi-real photoproduction, e-beam scattering on the rest gas) as well as  
 10486 a simple tracking through the beamline.<sup>4</sup>

### 10487 14.1.2 Use of the Main LHeC Detector

10488 To estimate visible cross sections for NC DIS and elastic QED Compton events a typical HERA analysis  
 10489 strategy was used. That is: safe fiducial cuts against energy leakage over the backward calorimeter boundaries  
 10490 at small radii, safe  $(Q^2, y)$  cuts for NC DIS events to restrict measurement to the phase space where  $F_2$  is  
 10491 known to good precision of  $1 - 2\%$  and the  $F_L$  contribution is negligible, and elasticity cuts for QEDC events  
 10492 to reject the less precisely known inelastic contribution. In addition basic cuts against major backgrounds  
 10493 were applied (photoproduction in case of NC DIS and DVCS, elastic VM production and low mass diffraction  
 10494 in case of QED Compton).

10495 The visible NC DIS cross section,  $\sigma_{\text{vis}}^{\text{DIS}}(Q^2 > 10\text{GeV}^2, 0.05 < y < 0.6) \simeq 10$  nb for  $10^\circ$  setup and  $\simeq 150$   
 10496 nb for  $1^\circ$  setup. This corresponds to a  $10 - 15$  Hz rate which is comfortable enough for mid-term yield  
 10497 control.

10498 For elastic QED Compton events, the visible cross section,  $\sigma_{\text{vis}}^{\text{QEDC}} \simeq 0.03$  nb for  $10^\circ$  setup and  $\simeq 3.5$  nb  
 10499 for  $1^\circ$  setup. Hence while for the latter sufficiently high rate is possible even for  $L = 10^{32}\text{cm}^{-2}\text{s}^{-1}$ , in case  
 10500 of ‘high  $Q^2$ ’ setup the QEDC event rate is  $4 - 5$  times smaller, thus only providing acceptable statistical  
 10501 precision for large samples, of the order  $0.5\%$ /month.

10502 In order to improve this a special small dedicated calorimeter could eventually be added after the strong  
 10503 focusing quadrupole, at  $z = -6\text{m}$ . Such ‘QEDC tagger’ should consist of two movable stations approaching  
 10504 the beam-pipe from the top and the bottom in the vertical direction, as sketched in Figure 14.1b. This way  
 10505 detector sections will be safe with respect to SR fan confined in the median plane. The visible elastic QED

<sup>3</sup>Total cross section,  $\sigma_{BH} \simeq 870$  mb for  $60 \times 7000$  GeV<sup>2</sup>  $ep$  collisions at the LHeC.

<sup>4</sup>The tracking has been performed by interfacing H1LUMI to GEANT3 [833] having LHeC beamline implemented up to  $\sim 110\text{m}$  from the IP.

10506 Compton cross section for such a device is  $4.3 \pm 0.2$  nb which significantly improves statistics for the luminosity  
 10507 measurement. The angular acceptance of the ‘QEDC tagger’ corresponds to the range  $\theta = 0.5^\circ - 1^\circ$  which  
 10508 lies outside the tracking acceptance. Therefore calorimeter sections should be supplemented by small silicon  
 10509 detectors in order to make it possible to reconstruct the event vertex from the final state containing only  
 10510 one electron and one photon. These silicon trackers are also useful for  $e/\gamma$  separation and rejection of the  
 10511 potential background. Actual dimensions and parameters of this optional ‘QEDC tagger’ requires extra  
 10512 design studies.

### 10513 14.1.3 Dedicated Luminosity Detectors in the tunnel

10514 In case of the RR-option which implies non-zero crossing angle for early  $e/p$  beam separation, the dominant  
 10515 part of the Bethe-Heitler photons will end up at  $z \simeq -22$ m, between electron and proton beam-pipes (see  
 10516 Figure 14.1c). This is the hottest place where also a powerful SR flux must be absorbed. On the first glance  
 10517 this makes luminosity monitoring based upon the bremsstrahlung photons impossible.

10518 There is however an interesting possibility. SR absorber needs good cooling system. The most natural  
 10519 cooling utilises circulating water. This cooling water can be used at the same time as an active media for  
 10520 Čerenkov radiation from electromagnetic showers initiated by the energetic Bethe-Heitler photons. The idea  
 10521 is based on two facts:

- 10522 1. The dominant part of the SR spectrum lies below the Čerenkov threshold for water,  $E_{\text{thr}} = 260$  keV,  
 10523 and hence will not produce light signal. Low intensity tail of the energetic synchrotron photons can be  
 10524 further suppressed by few radiation lengths of the absorber material in front of the water volume.
- 10525 2. Water is absolutely radiation resistant media and hence such simple Čerenkov counter can stand any  
 10526 dose without performance deterioration.

10527 The Čerenkov light can be collected and read out by two photo-multipliers as sketched on Figure 14.1d.  
 10528 The geometric acceptance depends on the details of the  $e$ -beam optics. For the actual RR design with the  
 10529 crossing angle  $\sim 1$  mrad the acceptance to the Bethe-Heitler photons is up to 90%, thus allowing fast and  
 10530 reliable luminosity monitoring with 3 – 5% systematic uncertainty.

10531 Of course, such an active SR absorber is not a calorimeter with good energy resolution, but just a simple  
 10532 counter. It is worth noting, that similar water Čerenkov detector has been successfully used in the H1  
 10533 Luminosity System during HERA-I operation.

10534 In case of LR-option, electrons collide with protons head-on, with zero crossing angle. This makes  
 10535 the situation very similar to HERA, where Bethe-Heitler photons travel along the proton beam direction  
 10536 and can be caught at around  $z = -120$ m, after the first proton bending dipole. Essential difference is  
 10537 that unlike HERA, LHC protons are deflected horizontally at this place rather than vertically. Thus the  
 10538 luminosity detector should be placed in the median plane next to the interacting proton beam,  $p_1$ , as shown  
 10539 on Figure 14.1e. In this case energy measurement with good resolution is not a problem, so major uncertainty  
 10540 will come from the knowledge of the limited geometric acceptance. This limitation is defined by the proton  
 10541 beam-line aperture, in particular by the aperture of the quadrupoles Q1-Q3 of the low-beta proton triplet.  
 10542 Moreover, it might be necessary to split D1 dipole into two parts in order to provide escape path for the  
 10543 photons with sufficient aperture. First estimates show that the geometric acceptance of the Photon Detector  
 10544 up to 95% is possible at the nominal beam conditions. HERA experience tells, that the uncertainty can be  
 10545 estimated as  $\delta A = 0.1 \cdot (1 - A)$  leading to the total luminosity error of  $\delta L = 1\%$  in this case.

### 10546 14.1.4 Small angle Electron Tagger

10547 The Bethe-Heitler reaction can be tagged not only by detecting a final state photon, but also by detecting the  
 10548 outgoing electron. Since all other competing processes have much smaller cross sections measuring inclusive  
 10549 rate of the scattered electrons under zero angle will provide a clean enough sample for luminosity monitoring.  
 10550 The remaining small background (mainly due to off-momentum electrons from  $e$ -beam scattering on the rest  
 10551 gas) can be precisely controlled and statistically subtracted using non-colliding (*pilot*) electron bunches.

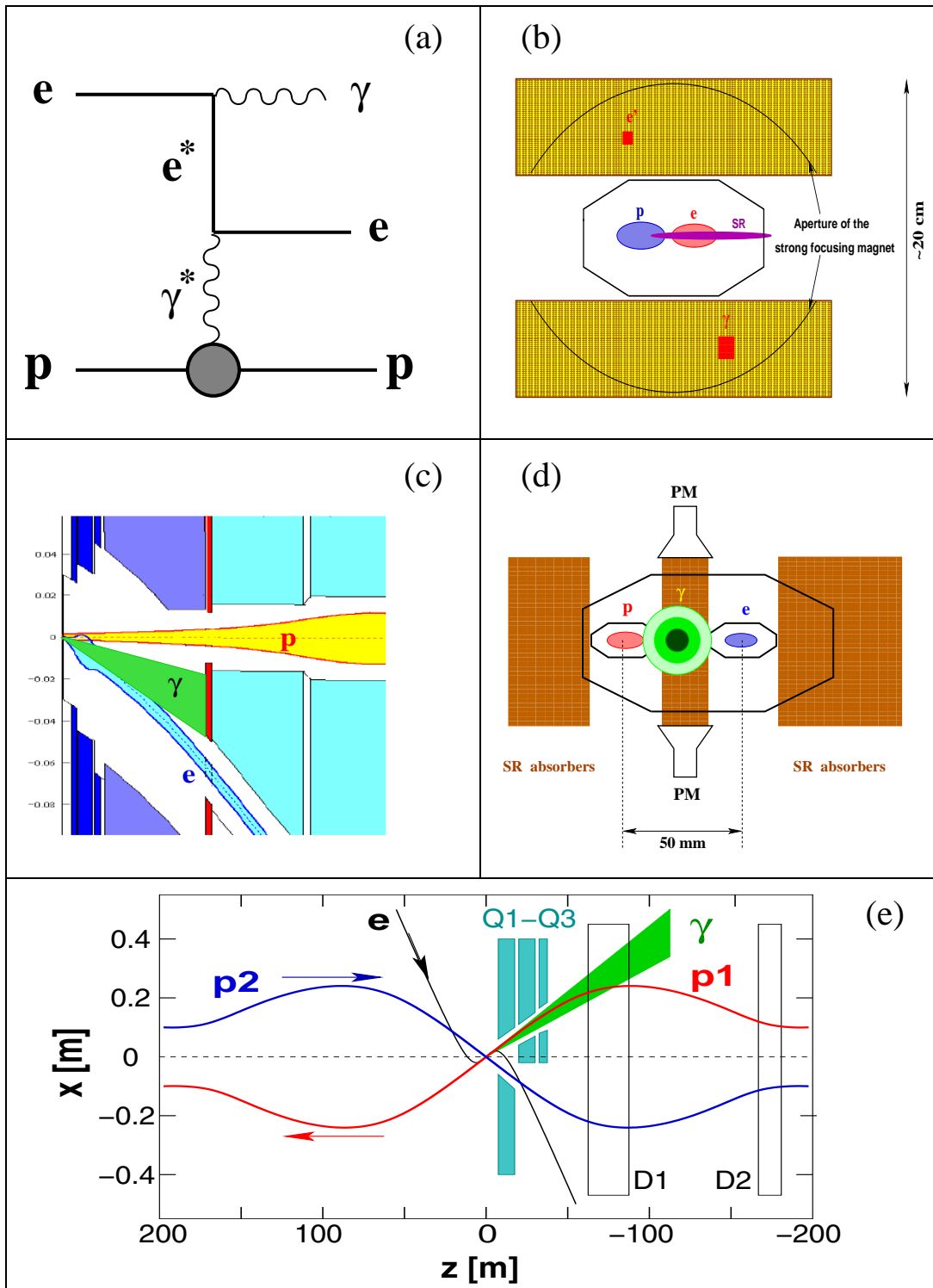


Figure 14.1: Options for the luminosity monitoring at the LHeC. (a) Feynman diagram for QEDC ( $\gamma^*$  pole) or BH ( $\gamma^*$ ,  $e^*$  poles) processes; (b) QEDC tagger at  $z = -6\text{m}$ ; (c,d) active SR absorber at  $z = -22\text{m}$  for RR-option (circles show 1-, 2- and 3- $\sigma$  contours for BH photons); (e) schematic view for the LR-option with 3- $\sigma$  fan of BH photons.

10552  
10553  
10554  
10555  
10556

In order to determine the best positions for the Electron taggers the LHeC beamline simulation has been performed in the vicinity of the Interaction Region for the RR-option. Several positions for the  $e$ -tagger stations were tried:<sup>5</sup>  $z = -14\text{m}$ ,  $-22\text{m}$  and  $-62\text{m}$ . As one can see on the top part of Figure 14.2 all places provide reasonable acceptances, reaching approximately (20 – 25)% at the maximum. However,  $z = -14\text{m}$  and  $z = -22\text{m}$  most likely will suffer from SR flux, making  $e$ -tagger operation problematic at those positions.

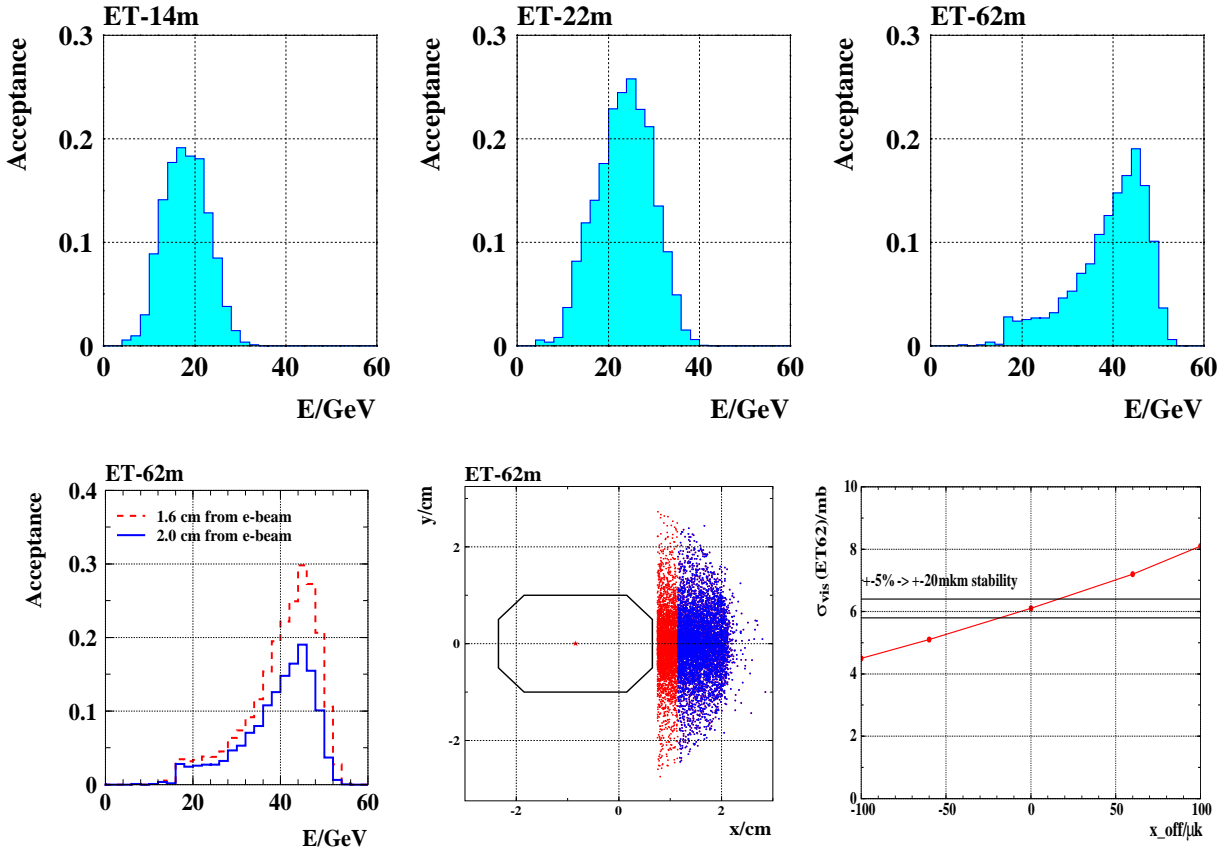


Figure 14.2: Top: acceptances of the  $e$ -taggers for Bethe-Heitler events at different  $z$ -positions from IP (RR-option). Bottom: variations in the acceptance of the  $e$ -tagger at  $z = -62\text{m}$  as a function of its position with respect to the  $e$ -beam axis and on the horizontal offset of the beam orbit at the IP.

10557  
10558  
10559  
10560  
10561  
10562  
10563  
10564  
10565  
10566

The most promising position for the Electron tagger is at  $z = -62\text{m}$ . The actual acceptance strongly depends both on the distance of the sensitive detector volume from the  $e$ -beam axis and on the details of the electron optics at the IP, such as beam tilt or small trajectory offset, as illustrated on the bottom part of Figure 14.2. Therefore a precise independent monitoring of beam optics and accurate position measurement of the  $e$ -tagger are required in order to control geometrical acceptance to a sufficient precision. For example, instability in the horizontal trajectory offset at IP,  $x_{\text{off}}$ , of  $\pm 20\mu\text{m}$  leads to the systematic uncertainty of 5% in the visible cross section,  $\sigma_{\text{vis}}(ET62)$ .

It is fair to note, that the magnetic field of the main LHeC detector was not taken into account in the simulation. The influence of this field is expected to be very small and will not alter basic conclusions of this section. Also, for the LR-option a similar acceptance is expected, although it may differ in shape somewhat.

<sup>5</sup>For the station at  $z = -14\text{m}$  the electron dipole magnet should be split into two parts, while the region around  $z = -62\text{m}$  has sufficiently comfortable place for the Electron tagger, before the  $e$ -beam is bended vertically.

10567  
10568  
10569  
10570  
10571  
10572

In order to demonstrate that the ideas described in Sec. 14.1.3 and 14.1.4 are realistic a typical example of the online rates variations for the H1 Luminosity System at HERA is shown on Figure 14.3. The system utilised all three types of the detectors discussed above: a total absorption electromagnetic calorimeter for the Bethe-Heitler photons (PD), a water Čerenkov counter (VC) and the Electron tagger (ET6). One can see, that online luminosity estimate by every of those detectors is well within 5% in spite of significant changes in the acceptance due to electron beam tilt jumps and adjustments at the IP.

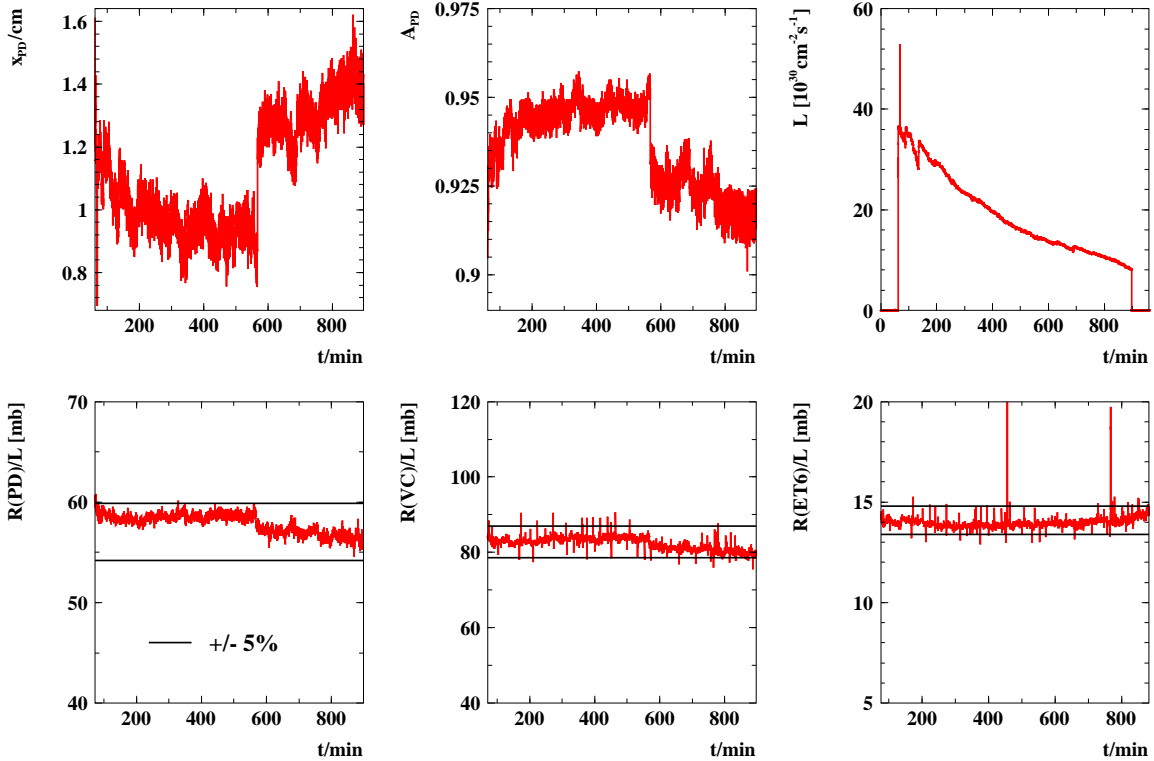


Figure 14.3: Online H1 Lumi System acceptance and rates variations in a typical HERA luminosity fill.

10573

### 14.1.5 Summary and Open Questions

10574  
10575  
10576

Accurate luminosity measurement at the LHeC is highly non-trivial task. As follows from HERA experience unexpected surprises are possible, hence it is important to consider several scenarios from the beginning and to prepare alternative methods for luminosity determination.

10577  
10578

Statistical precision and systematic uncertainties for different methods of luminosity measurement are summarised in Table 14.1.

10579  
10580  
10581  
10582  
10583

Precise determination of integrated luminosity,  $\mathcal{L}$ , is possible with the main detector utilising the QEDC process.  $\delta\mathcal{L} = 1.5 - 2\%$  is within reach. Further improvement requires in particular more accurate theoretical calculation of the elastic QED Compton cross section, with  $\delta\sigma_{el}^{QEDC} \lesssim 0.5\%$ . To enhance statistical precision a dedicated QEDC tagger at  $z = -6m$  might be useful. This device could also be used to access very low  $Q^2$  region, interpolating between DIS and photoproduction regimes.

10584  
10585

Fast instantaneous luminosity monitoring is challenging, but several options do exist which are based upon detection of the photons and/or electrons from the Bethe-Heitler process.

Method	Stat. error	Syst.error	Systematic error components	Application
BH ( $\gamma$ )	0.05%/sec	1–5%	$\sigma(E \gtrsim 10\text{GeV})$ acceptance, $A$ $E$ -scale, pileup	0.5% 10%(1– $A$ ) 0.5 – 4% Monitoring, tuning, short term variations
BH ( $e$ )	0.2%/sec	3–6%	$\sigma(E \gtrsim 10\text{GeV})$ acceptance background $E$ -scale	0.5% 2.5 – 5% 1% 1% Monitoring, tuning, short term variations
QEDC	0.5%/week	1.5%	$\sigma$ (el/inel) acceptance vertex eff. $E$ -scale	1% 1% 0.5% 0.3% Absolute $\mathcal{L}$ , global normalisation
NC DIS	0.5%/h	2.5%	$\sigma$ ( $y < 0.6$ ) acceptance vertex eff. $E$ -scale	2% 1% 1% 0.3% Relative $\mathcal{L}$ , mid-term variations

Table 14.1: Dominant systematics for various methods of luminosity measurement.

- 10586 • Photon Detector at  $z = 110\text{m}$  for LR option requires properly shaped proton beam-pipe at  $z =$   
10587  $-68 - 120\text{m}$  from IP2.
  - 10588 • In case of RR option Bethe-Heitler photons can be detected using a water Čerenkov counter integrated  
10589 with SR absorber at  $z = -22\text{m}$ .
  - 10590 • Electron tagger at  $z = -62\text{m}$  is very promising for both LR and RR schemes. It can be used not only  
10591 for luminosity monitoring, but also to enhance photoproduction physics capabilities and to provide  
10592 extra control of the  $\gamma p$  background to DIS, by tagging quasi-real photoproduction events.
- 10593 Good monitoring of the  $e$ -optics at the IP is required to control acceptances of the tunnel detectors to a  
10594 level of 2 – 5%.

## 10595 14.2 Polarimeter

The most powerful technique to measure the polarisation of the electrons and positrons of LHeC is Compton polarimetry. At high electron beam energies, this technique has been successfully used in the past at SLC [834] and at HERA [835] for example. The experimental setup consists of a laser beam which scatters off the electron/positron beam, and a calorimeter to measure the scattered gamma ray. At SLC, the scattered electron was also measured in a dedicated spectrometer. From the kinematics of Compton scattering one can get the expression for the maximum scattered photon energy:

$$E_{\gamma,max} \approx E_0 \frac{x}{1+x}$$

and the minimum scattered electron energy

$$E_{e,min} \approx E_0 \frac{1}{1+x},$$

10596 where  $E_0$  is the electron/positron beam energy and  $x = 4kE_0/m_e^2$  with  $k$  being the laser photon beam  
10597 energy. At LHeC and for a  $\approx 1\mu\text{m}$  laser beam wavelength, one gets  $E_{\gamma,max} \approx 29\text{GeV}$  and  $E_{e,min} \approx 31\text{GeV}$ .



10598 Providing that the laser beam is circularly polarised, the electron/positron beam longitudinal polarisation is  
10599 obtained from a fit to the scattered photon and/or to the electron energy spectrum. From an experimental  
10600 point of view, both measurements can be complementary since the high energy region of the scattered  
10601 photon energy spectrum is sensitive to the electron/positron beam longitudinal polarisation, whereas it is  
10602 the opposite for the scattered electron/positron energy spectrum. Indeed, the high measurement precision of  
10603 SLC was achieved thanks to the measurement of the scattered electrons. The measurement of both scattered  
10604 photon and electron/positron spectra was therefore foreseen for a very high precision polarimetry at future  
10605 electron-positron high energy colliders [262, 836].

10606 For LHeC, we may follow the work done for the future linear colliders [836]. In order to reach the per  
10607 mille level on the longitudinal polarisation measurement, one may measure both the scattered photon and  
10608 electron energy spectra.

### 10609 **14.2.1 Polarisation from the scattered photons**

10610 The photons are scattered within a very narrow cone of half aperture  $\approx 1/\gamma$ . It is therefore impossible  
10611 to distinguish the photons reaching the calorimeter. As for the extraction of the longitudinal polarisation  
10612 from the scattered photon beam energy, one may then distinguish three dynamical regimes [837]. The  
10613 single and few scattered photons regimes, where one can extract the polarisation from a first principle fit  
10614 to the scattered photon energy spectrum; the multi-photon regime where the central limit theorem holds  
10615 for the energy spectra and where the longitudinal polarisation is extracted from an asymmetry between the  
10616 average scattered energies corresponding to a circularly left and right laser beam polarisation [838]. Both  
10617 regimes have positive and negative experimental features. In the single and few photon regimes the energy  
10618 spectra exhibits kinematical edges which allow an in situ calibration of the detector energy response but  
10619 the physical accelerator photon background which is difficult to model precisely, e.g. synchrotron radiation,  
10620 limits the final precision on the polarisation measurement [837]. In the multi-photon regime, the background  
10621 is negligible since it is located at low energy but one cannot measure the energy calibration of the detector  
10622 in situ and one must rely on some high energy extrapolation of calibrations obtained at low energy [838]  
10623 (e.g. for 100 scattered photon/bunch the deposited energy in the calorimeter would be more than 1TeV at  
10624 LHeC). However, the laser technology has improved in the last ten years and one can consider at present  
10625 a very stable pulsed laser beam with adjustable pulse energy allowing to operate in single, few and multi  
10626 photon regimes. In this way, one can calibrate the calorimeter in situ and optimise the dynamical regime, a  
10627 multi-photon regime as close as possible to the few photon regime, in order to minimise the final uncertainty  
10628 on the polarisation measurement.

### 10629 **14.2.2 Polarisation from the scattered electrons**

10630 The nice feature of the scattered electron/positron is that one can use a magnetic spectrometer to distinguish  
10631 them from each other. Following [836] one may carefully design a Compton interaction region in order to  
10632 implement a dedicated electron spectrometer followed by a segmented electron detector in order to measure  
10633 the scattered electron angular spectrum, itself related to the electron energy spectrum. A precise particle  
10634 tracking is needed but this experimental method also allows a precise control of the systematic uncertainties  
10635 [834].

10636 Common to both techniques is the control and measurement of the laser beam polarisation. it was shown  
10637 in [839] that a few per mille precision can be achieved in an accelerator environment. Therefore, with a  
10638 redundancy in measuring the electron/positron beam longitudinal polarisation from both the electron and  
10639 photon scattered energy spectra, a final precision at the per mille level will be reachable at LHeC.

## 10640 **14.3 Zero Degree Calorimeter**

10641 The goal of the Zero Degree Calorimeter (ZDC) is to measure the energies and angles of the very forward  
10642 particles. At HERA experiments, H1 and ZEUS, the forward neutral particles scattered at polar angles

10643 below 0.75 mrad were measured in the dedicated Forward Neutron Calorimeters (FNC) [498,840]. The LHC  
10644 experiments, CMS, ATLAS, ALICE and LHCf, have the ZDC calorimeters for detection of forward neutral  
10645 particles [841–845], ALICE has also the ZDC calorimeter for the measurements of spectator protons (as an  
10646 illustration, a photo of the neutron calorimeter of ALICE experiment [841,842] is shown in Figure 14.4).

10647 The ZDC calorimeter will be an important addition to the future LHeC experiment as many physics  
10648 measurements in  $ep$ ,  $ed$  and  $eA$  collisions can be made possible with the installation of the ZDC.

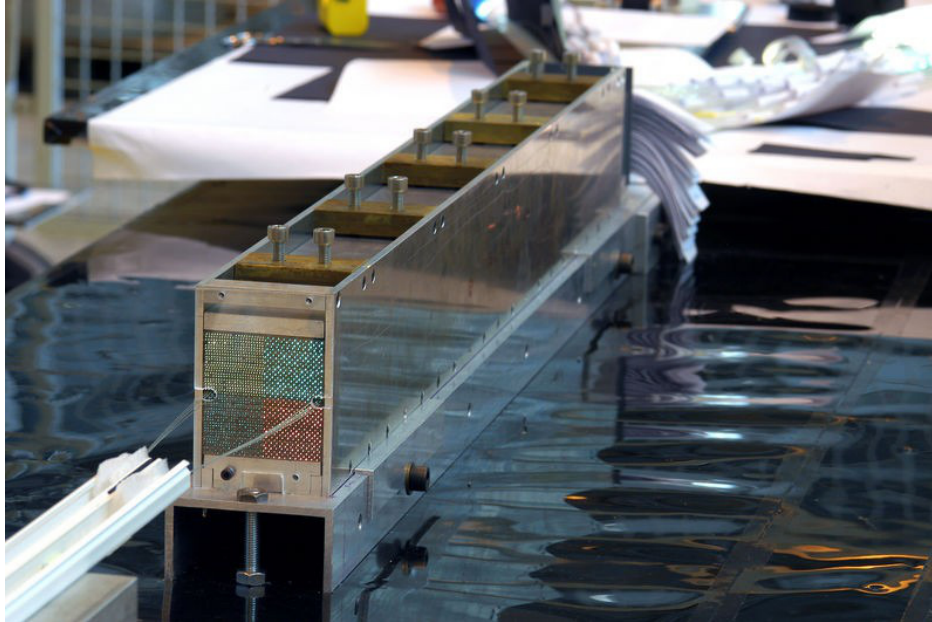


Figure 14.4: Photo of the Zero Degree Neutron Calorimeter of ALICE experiment [841].

### 10649 14.3.1 ZDC detector design

10650 The position of the Zero Degree Calorimeter in the tunnel and the overall dimensions depend mainly on the  
10651 space available for the installation. At the LHC the beams are deflected by two separating dipoles. These  
10652 dipoles also deflect the spectator protons, separating them from the neutrons and photons, which scatter at  
10653  $\sim 0^\circ$ .

10654 The geometry, technical specifications and proposed design of ZDC detectors are to large extent similar  
10655 to the ZDCs of the LHC experiments. There the ZDC calorimeter for detection of neutral particles are  
10656 placed at  $z = 115 - 140$  m in a 90 mm narrow space between two beam pipes. In the case of the LHeC, the  
10657 ZDC calorimeter can be placed in the space available at about 90 – 100 m next to the interacting proton  
10658 beam pipe, as indicated in Figure 14.5.

10659 Below the general considerations for the design are presented. In order to finalise the study of the  
10660 geometry of detectors, a detailed simulation of the LHeC interaction region and the beamline must be  
10661 performed.

### 10662 14.3.2 Neutron Calorimeter

10663 The design of the ZDC has to satisfy the various technical issues. Detector has to be capable of detecting  
10664 neutrons and photons produced with scattering angles up to 0.3 mrad or more and energies between some  
10665 hundreds GeV to the proton beam energy (7 TeV) with a reasonable resolution of few percents. It must  
10666 be able to distinguish hadronic and electromagnetic showers (i.e. separate neutrons from photons) and to

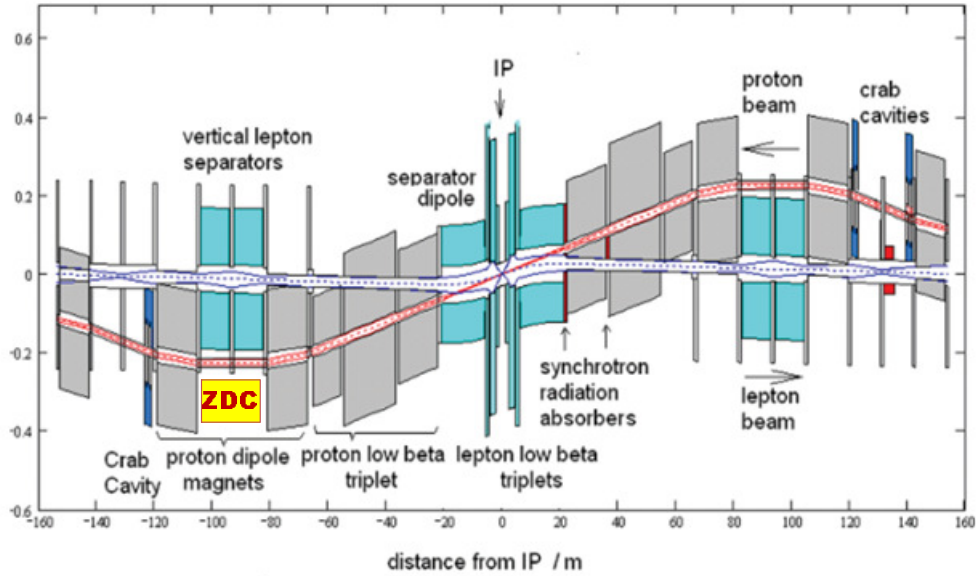


Figure 14.5: Schematic layout of the LHeC interaction region. The possible position of the ZDC is indicated.

10667 distinguish showers from two or more particles entering the detector (i.e. needs position resolution of  $\mathcal{O}(1\text{mm})$   
 10668 or better). The ZDC will be operating in a very hard radiation environment, therefore it has to be made of  
 10669 radiation resistant materials.

10670 The neutron ZDC can be built as a longitudinally segmented tungsten-quartz calorimeter. In this design,  
 10671 ZDC will contain the electromagnetic and hadronic sections. The electromagnetic section with 1.5-2 nuclear  
 10672 interaction lengths,  $\lambda_I$ , and fine granularity is needed for precise determination of the position of the impact  
 10673 point, discrimination of the electromagnetic and hadronic showers and separation of the showers from two or  
 10674 more particles entering the detector. The hadronic section of the ZDC can be built with coarser sampling,  
 10675 which gives an increase of average density and, consequently, the increase of effective nuclear interaction  
 10676 length. The total depth of the calorimeter will be about 8-9  $\lambda_I$ , which contains more than 90% of hadronic  
 10677 shower of  $\mathcal{O}(\text{TeV})$  energies. Since the different parts of calorimeter undergo different intensity of radiation  
 10678 (higher for front part), it is advantageous to have longitudinal segmentation of 3-4 identical sections, which  
 10679 will allow the control of the change of energy response due to radiation damage. Comparison of the energy  
 10680 spectrum from the showers which start in different sections can be used for correction of changes in energy  
 10681 response.

10682 One of the possibilities to build a compact calorimeter with good radiation resistance is to use tungsten  
 10683 absorbers and quartz fibres, similar to the one operated by CMS Experiment [844] (a schematic view is  
 10684 shown in Fig.14.6). The principle of operation is based on the detection of Cherenkov light produced by  
 10685 the shower's charged particles in the fibres. Using tungsten as a passive material allows the construction  
 10686 of compact devices. (One can also consider option to use THGEM, thick gaseous electron multipliers,  
 10687 as an active media [?, 847].) These detectors are proven to be fast ( $\sim$ few ns) and radiation hard. The  
 10688 tungsten-quartz technology is used in ZDC calorimeters implemented by the CMS, ATLAS and ALICE  
 10689 experiments [841, 843, 844]. However, these calorimeters based on the detection of Cherenkov light are  
 10690 sensitive mainly to the electromagnetic component of the hadronic shower. Therefore, they are highly non-  
 10691 compensating and the energy resolution is not very high, e.g. the hadronic energy resolution for the CMS  
 10692 ZDC is  $\sigma(E)/E \approx 176\%/\sqrt{E[\text{GeV}]} \oplus 8\%$  [?].

10693 An interesting new solution for the ZDC calorimeter is offered by the Dual Readout calorimetry technique,  
 10694 which is currently being developed within the DREAM/RD52 Project [?]. In this approach the detector is  
 10695 equipped with both scintillating and quartz fibers, which are sensitive to the different components of the

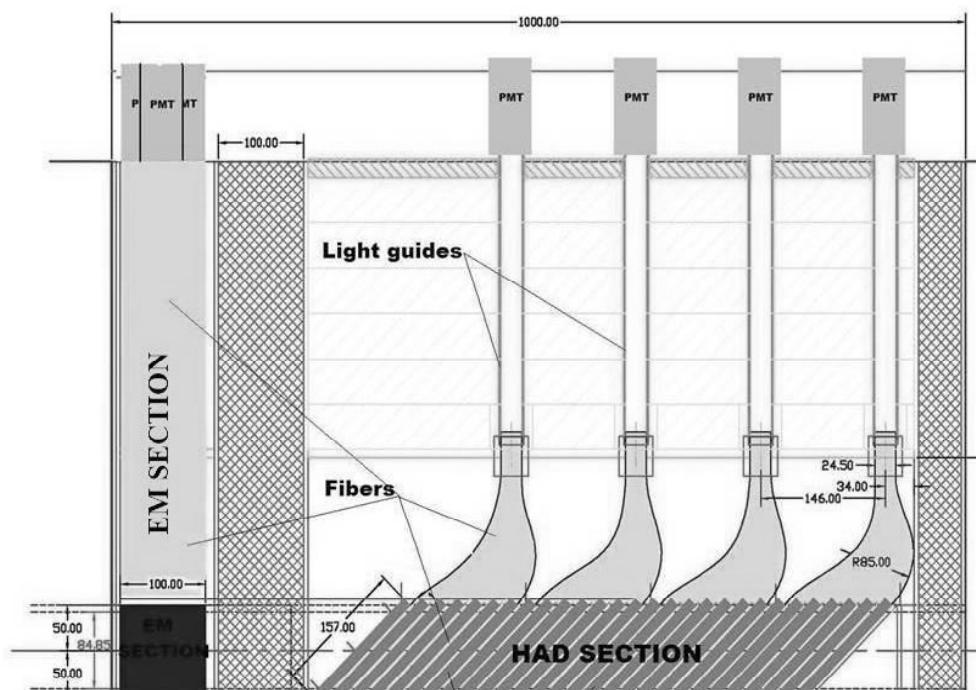


Figure 14.6: A side view of the CMS ZDC calorimeter with electromagnetic section in front and hadronic section behind.

10696 hadron shower. Hadron showers developing in this detector generate signals in both types of fibres and these  
 10697 signals provide complementary information about these showers. With this method, the dominant source of  
 10698 fluctuations contributing to the hadronic energy resolution can be eliminated, since it allows a measurement  
 10699 of the electromagnetic energy fraction event-by-event [?]. The ZDC calorimeter for LHeC detector can be  
 10700 built using tungsten absorber and SiPM readout. The readout can be made on the both ends of fibres, which  
 10701 will give a handle on the effects of radiation damage in the scintillating fibres, The discrimination between  
 10702 neutrons and photons will be possible using the time structure of the signals. With the prototype tested by  
 10703 DREAM Collaboration, the depth resolutions of the order of 10 cm has been reached, which is sufficient to  
 10704 distinguish between neutrons and photons in such longitudinally unsegmented calorimeter [?, ?].

### 10705 14.3.3 Proton Calorimeter

10706 In addition to the ZDC calorimeter for measurement of neural particles at  $0^\circ$ , a proton calorimeter positioned  
 10707 externally to the outgoing proton beam can be installed for the measurement of spectator protons from  $eD$   
 10708 and  $eA$  scattering produced at zero degree. In analogy to ALICE experiment [841, 842], this detector can  
 10709 be positioned at about a same distance from the interaction point as neutron ZDC. The size of proton  
 10710 ZDC has to be small, due to the few cm small size of spectator proton spot, but sufficient to obtain shower  
 10711 containment. This calorimeter will be made using the same technique as the neutron ZDC.

### 10712 14.3.4 Calibration and monitoring

10713 After initial calibration of the ZDCs with test-beams, it is essential to have regular online and offline control  
 10714 of the stability of the response, in particular due to hard radiation and temperature environment. The

10715 stability of the gain of the PMTs and the radiation damage in fibres can be monitored using the laser or  
 10716 LED light pulses. The stability of absolute calibration can be monitored using the interactions of the proton  
 10717 beam and residual gas molecules in the beam-pipe and comparison with the results of Monte Carlo simulation  
 10718 based on pion exchange, as used at HERA [498,840]. A useful tool for absolute energy calibration will be the  
 10719 reconstruction of invariant masses, e.g.  $\pi^0 \rightarrow 2\gamma$  or  $\Lambda, \Delta \rightarrow n\pi^0$ , with decay particles produced at very small  
 10720 opening angles and reconstructed in ZDC. This will however require the possibility to reconstruct several  
 10721 particles in the ZDC within the same event.

10722 The ZDC detector will be made of two calorimeters: one for the measurement of neutral particles at  
 10723  $0^\circ$  and another one positioned externally to the outgoing proton beam for the measurement of spectator  
 10724 protons from  $eD$  and  $eA$  scattering.

## 10725 14.4 Forward Proton Detection

10726 In diffractive interactions between protons or between an electron and a proton, the proton may survive a  
 10727 hard collision and be scattered at a low angle  $\theta$  along the beam line while losing a small fraction  $\xi$  ( $\sim 1\%$ )  
 10728 of its energy. The ATLAS and CMS collaborations have investigated the feasibility to install detectors along  
 10729 the LHC beam line to measure the energy and momentum of such diffractively scattered protons [848]. Since  
 10730 the proton beam optics is primarily determined by the shape of the accelerator - which will not change for  
 10731 proton arm of the LHeC - the conclusions reached in this R&D study are still relevant for an LHeC detector.

In such a setup, diffractively scattered protons are separated from the nominal beam when traveling  
 through dipole magnets with a slightly lower momentum. This spectroscopic behavior of the accelerator is  
 described by the energy dispersion function,  $D_x$ , which, when multiplied with the actual energy loss,  $\xi$ , gives  
 the additional offset of the trajectory followed by the off-momentum proton:

$$x_{\text{offset}} = D_x \times \xi.$$

10732 The acceptance window in  $\xi$  is therefore determined by the closest possible approach of the proton  
 10733 detectors to the beam for low  $\xi$  and by the distance of the beam pipe walls from the nominal proton  
 10734 trajectory for high  $\xi$ . The closest possible approach is often taken to be equal to  $12\sigma$  with  $\sigma$  equal to the  
 10735 beam width at a specific point. At the point of interest, 420m from the interaction point, the beam width  
 10736 is approximately equal to  $250 \mu\text{m}$ . On the other hand, the typical LHC beam pipe radius at large distances  
 10737 from the interaction point is approximately 2 cm. Even protons that have lost no energy, will eventually  
 10738 hit the beam pipe wall if they are scattered at large angles. This therefore fixes the maximally allowed  
 10739 four-momentum-transfer squared  $t$ , which is approximately equal to the square of the transverse momentum  
 10740  $p_T$  of the scattered proton at the interaction point.

10741 At 420 m from the interaction point, the dispersion function at the LHC reaches 1.5 m, which results in an  
 10742 optimal acceptance window for diffractively scattered protons (roughly  $0.002 < \xi < 0.013$ ). The acceptance  
 10743 as function of  $\xi$  and  $t$  is shown in Fig. 14.7, using the LHC proton beam optics [849]. The small corrections  
 10744 to be applied for the LHeC proton beam optics are not considered to be relevant for the description of the  
 10745 acceptance.

10746 When the proton's position and angle w.r.t. the nominal beam can be accurately measured by the  
 10747 detectors, it is in principle possible to reconstruct the initial scattering angles and momentum loss of the  
 10748 proton at the interaction point. Even with an infinitesimally small detector resolution, the intrinsic beam  
 10749 width and divergence will still imply a lower limit on the resolution of the reconstructed kinematics. As the  
 10750 beam is typically maximally focussed at the interaction point in order to obtain a good luminosity, it will  
 10751 be the beam divergence that dominates the resolution on reconstructed variables.

10752 Figure 14.8 shows the relation between position and angle w.r.t. the nominal beam and the proton  
 10753 scattering angle and momentum loss in both the horizontal and vertical plane as obtained from the LHC  
 10754 proton beam optics [849]. Clearly, in order to distinguish angles and momentum losses indicated by the  
 10755 curves in Fig. 14.8, the detector must have a resolution better than the distance between the curves.

10756 As stated above, protons with the same momentum loss and scattering angles will still end up at different  
 10757 positions and angles due to the intrinsic width and divergence of the beam. Lower limits on the resolution

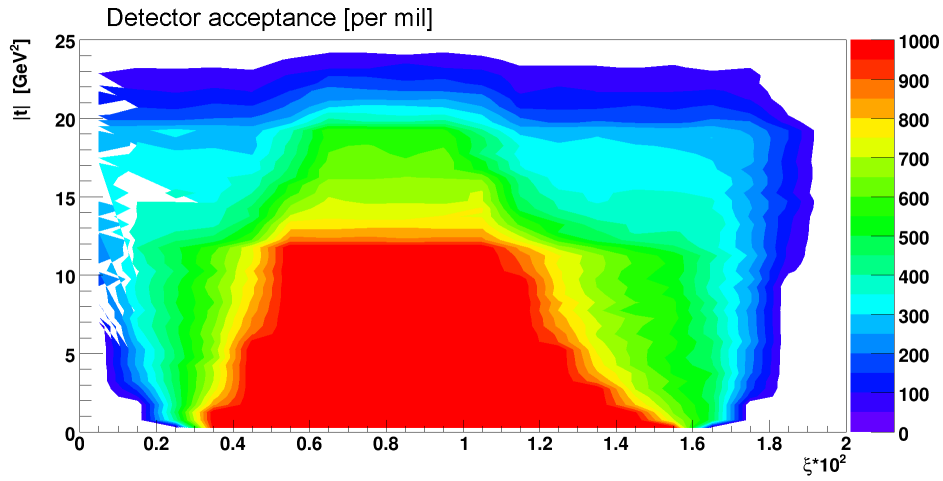


Figure 14.7: The acceptance for a proton detector placed at 420m from the interaction point is shown as function of the momentum loss  $\xi$  and the fourmomentum-transfer squared  $t$ . The color legend runs from 0‰(no acceptance) to 1000‰(full acceptance).

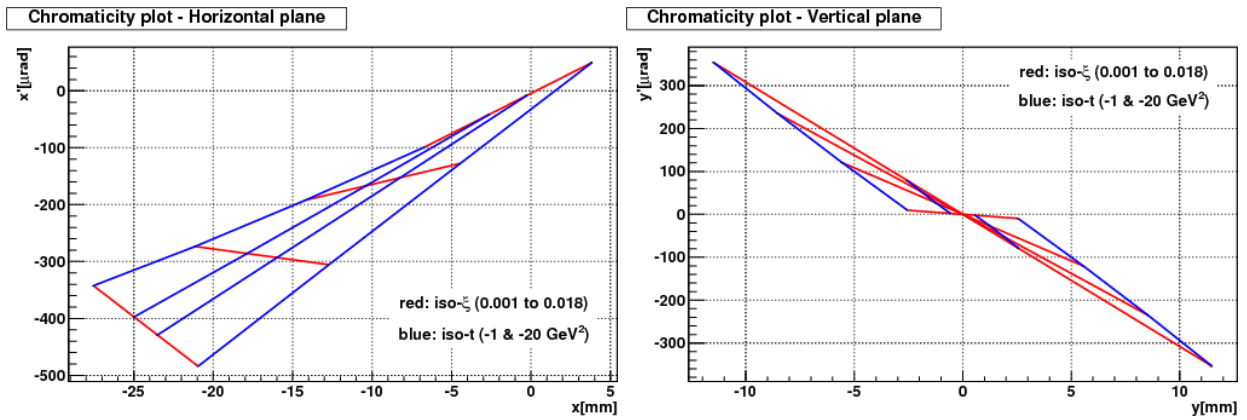


Figure 14.8: Lines of constant  $\xi$  and  $t \approx (1 - \xi)E_{\text{beam}}\theta^2$  are shown in the plane of proton position and angle w.r.t. the nominal proton beam in the horizontal (left) and vertical (right) plane.

10758 of reconstructed kinematics can therefore be determined. These are typically of the order of 0.5‰ for  $\xi$  and  
 10759 0.2  $\mu\text{rad}$  for the scattering angle  $\theta$ . Figure 14.9 shows the main dependences of the resolution on  $\xi$ ,  $t$  and  
 10760 the azimuthal scattering angle  $\phi$ .

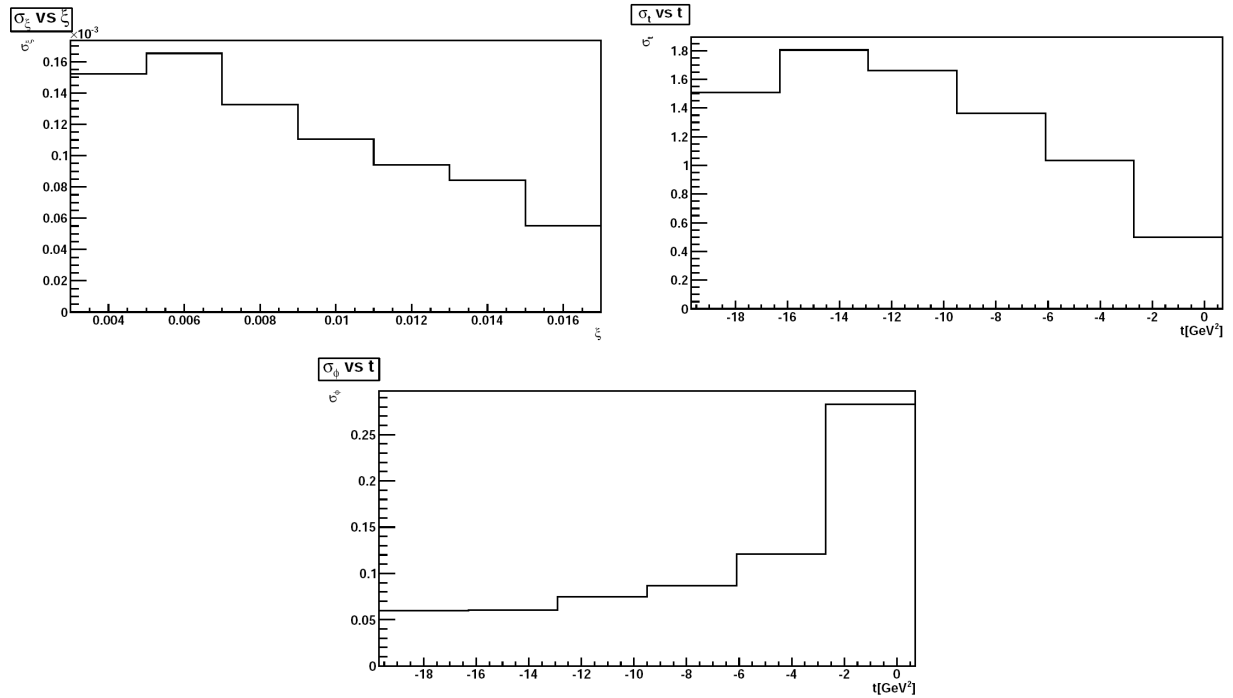


Figure 14.9: The lower limit due to the intrinsic beam width and divergence on the resolution of kinematic variables is shown for  $\xi$  as function  $\xi$  (top left),  $t$  as function  $t$  (top right) and  $\phi$  as function of  $t$  (bottom).

10761 A crucial issue in the operation of near-beam detectors is the alignment of the detectors w.r.t. the  
 10762 nominal beam. Typically, such detectors are retracted when beams are injected and moved close to the  
 10763 beam only when the accelerator conditions are declared to be stable. Also the beam itself, may not always  
 10764 be reinjected at the same position. It is therefore important to realign the detectors at for each accelerator  
 10765 run and to monitor any drifts during the run. At HERA, a kinematic peak method was used for alignment:  
 10766 as the reconstructed scattering angles depend on the misalignment, one may extract alignment constants  
 10767 by required that the observed cross section is maximal for forward scattering. In addition, this alignment  
 10768 procedure may be cross-checked by using a physics process with a exclusive system produced in the central  
 10769 detector such that the proton kinematics is fixed by applying energy-momentum conservation to the full set  
 10770 of final state particles. The feasibility of various alignment methods at the LHeC remains to be studied.

10771

## Part V

10772

# Summary



The summary will be added when the referee process is completed.

# 10774 Acknowledgement

10775 The authors express their gratitude to the CERN directorate, the CERN SPC, to ECFA, NuPECC, several  
10776 members of the Scientific Advisory Committee and their home institutions for their support, interest and  
10777 help in this development. We wish to thank many colleagues, engineers, experimentalist and theorists, for  
10778 their contributions to the design report and interesting discussions.

# Bibliography

- 10780 [1] A. Vera et al., *5D tiny black holes and perturbative saturation*, Talk at the LHeC Workshop at Divonne 08,  
10781 <http://cern.ch/lhec>.
- 10782 [2] G. Altarelli, B. Mele, and R. Ruckl, *Physics of ep collisions in the TeV energy range*, . Presented at ECFA-CERN  
10783 Workshop on Feasibility of Hadron Colliders in LEP Tunnel, Lausanne and Geneva, Switzerland, 1984.
- 10784 [3] A. Febel, H. Gerke, M. Tigner, H. Wiedemann, and B. Wiik, *The proposed desy proton-electron colliding beam*  
10785 *experiment. (talk)*, IEEE Trans.Nucl.Sci. **20** (1973) 782–785.
- 10786 [4] B. Wiik et al., *PROPER - ep with PETRA*, DESY preprint **38** (1977).
- 10787 [5] J. R. Ellis, B. Wiik, and K. Hubner, *CHEEP: AN e-p FACILITY IN THE SPS*, CERN Yellow Report NN (1978).
- 10788 [6] SLAC-LBL Collaboration, M. Allen et al., *Particle Physics with electron-positron-proton beams*, SLAC-146 (1972).
- 10789 [7] J. T. Kamae et al., *Tristan ep Working Group Report*, UTPN-165, University of Tokyo (1980).
- 10790 [8] E. Blackmore et al., *Electron - proton collisions at Fermilab*, Fermilab-Proposal-0703 (1981).
- 10791 [9] A. Verdier, *An e p insertion for LHC and LEP*, Proc. Aachen LHC Workshop, CERN-90-10-B, 820-823 (1990).
- 10792 [10] W. Bartel, *e p experiments in LEP/LHC interaction regions*, Proc. Aachen LHC Workshop, CERN-90-10-B, B 824-832  
10793 (1990).
- 10794 [11] R. Ruckl, *e p physics at LEP x LHC*, Proc. Aachen LHC Workshop, CERN-90-10-B, MPI-PAE-PTH-76-90 (1990).
- 10795 [12] E.Keil, *LHC ep Option*, LHC Report 93, CERN (1996).
- 10796 [13] P. Grosse-Wiesmann, *Colliding a Linear Electron Beam with a Storage Ring Beam*, NIM A **274** (1989) 21.
- 10797 [14] M. Tigner, B. Wiik, and F. Willeke, *An Electron - proton collider in the TeV range*, Proc. PAC IEEE, 2910-2912, San  
10798 Francisco (1991).
- 10799 [15] U. Katz, A. Levy, M. Klein, and S. Schlenstedt, *Physics and experimentation at a linear electron positron collider. Vol.*  
10800 *4: The THERA book. Electron proton scattering at  $s^{**}(1/2)$  approx. 1-TeV, 445p.*, .
- 10801 [16] D. Schulte and F. Zimmermann, *QCD explorer based on LHC and CLIC-1*, . Prepared for 9th European Particle  
10802 Accelerator Conference (EPAC 2004), Lucerne, Switzerland, 5-9 Jul 2004.
- 10803 [17] J. B. Dainton, M. Klein, P. Newman, E. Perez, and F. Willeke, *Deep inelastic electron nucleon scattering at the LHC*,  
10804 JINST **1** (2006) P10001, [arXiv:hep-ex/0603016](http://arxiv.org/abs/hep-ex/0603016).
- 10805 [18] M. Klein, *Physics at HERA and beyond*, AIP Conf.Proc. **792** (2005) 1065–1076.
- 10806 [19] M. Breidenbach, J. I. Friedman, H. W. Kendall, E. D. Bloom, D. Coward, et al., *Observed Behavior of Highly Inelastic*  
10807 *electron-Proton Scattering*, Phys.Rev.Lett. **23** (1969) 935–939.
- 10808 [20] E. D. Bloom, D. Coward, H. DeStaebler, J. Drees, G. Miller, et al., *High-Energy Inelastic e p Scattering at 6-Degrees*  
10809 *and 10-Degrees*, Phys.Rev.Lett. **23** (1969) 930–934.
- 10810 [21] LHeC Collaboration, M. Klein, *Status of the LHeC Design*, Reports to ECFA 2008-2010, ICFA 2008,  
10811 <http://cern.ch/lhec>.
- 10812 [22] *NuPECC Long Range Plan 2010*. <http://www.nupecc.org/>.
- 10813 [23] S. Myers, *Invited Talk at ICHEP, Paris*, 2010.
- 10814 [24] F. Wilczek, *Talk at the 50 Years of the PS Nobel Prize Winner Colloquium, CERN*, 2009.
- 10815 [25] H. Geiger and E. Marsden, *On a Diffuse Reflection of the  $\alpha$  Particles*, Proc. Royal Society **A82** (1909) 495–500.
- 10816 [26] E. Rutherford, *The scattering of the  $\alpha$  and  $\beta$  Particles by Matter and the Structure of the Atom*, Philosophical  
10817 Magazine, Series 6 **21** (1911) 669–688.
- 10818 [27] R. Hofstadter and R. McAllister, *ELECTRON SCATTERING FROM THE PROTON*, Phys.Rev. **98** (1955) 217–218.
- 10819 [28] D. J. Gross and F. Wilczek, *Ultraviolet behaviour of non-abelian gauge theories*, Phys. Rev. Lett. **30** (1973) 1343–1346.

- 10820 [29] H. D. Politzer, *Reliable perturbative results for strong interactions?*, Phys. Rev. Lett. **30** (1973) 1346–1349.
- 10821 [30] R. Feynman, *Photon-hadron interactions*, . New York, 1973.
- 10822 [31] H. Fritzsch, M. Gell-Mann, and H. Leutwyler, *Advantages of the Color Octet Gluon Picture*, Phys.Lett. **B47** (1973)  
10823 365–368.
- 10824 [32] M. Froissart, *Fundamental Theoretical Questions, Rapporteurs Talk at the Rochester Conference, Berkeley*, 1966.
- 10825 [33] V. N. Gribov and L. N. Lipatov, *Deep inelastic ep scattering in perturbation theory*, Sov. J. Nucl. Phys. **15** (1972)  
10826 438–450.
- 10827 [34] Y. L. Dokshitzer, *Calculation of the structure functions for Deep Inelastic scattering and  $e^+e^-$  annihilation by  
10828 perturbation theory in Quantum Chromodynamics. (In Russian)*, Sov. Phys. JETP **46** (1977) 641–653.
- 10829 [35] G. Altarelli and G. Parisi, *Asymptotic Freedom in Parton Language*, Nucl. Phys. **B126** (1977) 298.
- 10830 [36] S. Moch, J. Vermaseren, and A. Vogt, *The Three loop splitting functions in QCD: The Nonsinglet case*, Nucl.Phys.  
10831 **B688** (2004) 101–134, [arXiv:hep-ph/0403192](#) [hep-ph].
- 10832 [37] A. Vogt, S. Moch, and J. Vermaseren, *The Three-loop splitting functions in QCD: The Singlet case*, Nucl.Phys. **B691**  
10833 (2004) 129–181, [arXiv:hep-ph/0404111](#) [hep-ph].
- 10834 [38] H1 and ZEUS Collaboration, F. Aaron et al., *Combined Measurement and QCD Analysis of the Inclusive  $e^+p$   
10835 Scattering Cross Sections at HERA*, JHEP **1001** (2010) 109, [arXiv:0911.0884](#) [hep-ex].
- 10836 [39] F. Schrempp, *Instanton-induced processes: An Overview*, [arXiv:hep-ph/0507160](#) [hep-ph].
- 10837 [40] L. Lipatov, *Effective action for the Regge processes in gravity*, [arXiv:1105.3127](#) [hep-th]. \* Temporary entry \*.
- 10838 [41] e. Ioffe, Boris Lazarevich, e. Fadin, Victor Sergeevich, and e. Lipatov, Lev Nikolaevich, *Quantum chromodynamics:  
10839 Perturbative and nonperturbative aspects*, .
- 10840 [42] A. De Rujula, *Charm is found*, . Proceedings of XVIII ICHEP Conference, Tbilissi, 1976.
- 10841 [43] A. Salam, *The Unconfined Quarks and Gluons*, . Proceedings of XVIII ICHEP Conference, Tbilissi, 1976.
- 10842 [44] J. L. Hewett and T. G. Rizzo, *Low-Energy Phenomenology of Superstring Inspired  $E(6)$  Models*, Phys. Rept. **183**  
10843 (1989) 193.
- 10844 [45] J. C. Pati and A. Salam, *Lepton Number as the Fourth Color*, Phys. Rev. **D10** (1974) 275–289.
- 10845 [46] L. Susskind, *Dynamics of Spontaneous Symmetry Breaking in the Weinberg-Salam Theory*, Phys.Rev. **D20** (1979)  
10846 2619–2625.
- 10847 [47] E. Farhi and L. Susskind, *Technicolor*, Phys. Rept. **74** (1981) 277.
- 10848 [48] B. Andersson, G. Gustafson, G. Ingelman, and T. Sjostrand, *Parton Fragmentation and String Dynamics*, Phys. Rept.  
10849 **97** (1983) 31–145.
- 10850 [49] A. Glazov, S. Moch, and V. Radescu, *Parton Distribution Uncertainties using Smoothness Prior*, Phys.Lett. **B695**  
10851 (2011) 238–241, [arXiv:1009.6170](#) [hep-ph].
- 10852 [50] J. Kuti and V. F. Weisskopf, *Inelastic lepton - nucleon scattering and lepton pair production in the relativistic quark  
10853 parton model*, Phys.Rev. **D4** (1971) 3418–3439.
- 10854 [51] S. Brodsky, P. Hoyer, C. Peterson, and N. Sakai, *The Intrinsic Charm of the Proton*, Phys.Lett. **B93** (1980) 451–455.
- 10855 [52] M. Krasny, F. Dydak, F. Fayette, W. Placzek, and A. Siodmok,  $\Delta M_W \leq 10 MeV/c^2$  at the LHC: a forlorn hope?,  
10856 Eur.Phys.J. **C69** (2010) 379–397, [arXiv:1004.2597](#) [hep-ex].
- 10857 [53] K. Kovarik, I. Schienbein, F. Olness, J. Yu, C. Keppel, et al., *Nuclear corrections in neutrino-nucleus DIS and their  
10858 compatibility with global NPDF analyses*, Phys.Rev.Lett. **106** (2011) 122301, [arXiv:1012.0286](#) [hep-ph].
- 10859 [54] D. Mueller, D. Robaschik, B. Geyer, F. M. Dittes, and J. Horejsi, *Wave functions, evolution equations and evolution  
10860 kernels from light-ray operators of QCD*, Fortschr. Phys. **42** (1994) 101, [arXiv:hep-ph/9812448](#).
- 10861 [55] A. V. Belitsky and A. V. Radyushkin, *Unraveling hadron structure with generalized parton distributions*, Phys. Rept.  
10862 **418** (2005) 1–387, [arXiv:hep-ph/0504030](#).
- 10863 [56] V. N. Gribov, *Interaction of gamma quanta and electrons with nuclei at high-energies*, Sov. Phys. JETP **30** (1970)  
10864 709–717.
- 10865 [57] M. Tigner, *A possible apparatus for electron clashing-beam experiments*, Nuovo Cim. **37** (1965) 1228–1231.
- 10866 [58] M. Klein and T. Riemann, *Electroweak interactions probing the nucleon structure*, Z.Phys. **C24** (1984) 151.
- 10867 [59] E. Derman, *Tests for a weak neutral current in  $ln$  to  $l+$  anything at high energy*, Phys.Rev. **D7** (1973) 2755–2775.
- 10868 [60] J. Callan, Curtis G. and D. J. Gross, *High-energy electroproduction and the constitution of the electric current*,  
10869 Phys.Rev.Lett. **22** (1969) 156–159.
- 10870 [61] G. Altarelli and G. Martinelli, *Transverse Momentum of Jets in Electroproduction from Quantum Chromodynamics*,  
10871 Phys.Lett. **B76** (1978) 89.

- 10872 [62] A. Argento, A. Benvenuti, D. Bollini, G. Bruni, T. Camporesi, et al., *Measurement of the interference structure*  
10873 *function  $xG(3)(x)$  in muon - nucleon scattering*, Phys.Lett. **B140** (1984) 142.
- 10874 [63] A. Arbuzov, D. Y. Bardin, J. Blumlein, L. Kalinovskaya, and T. Riemann, *Hector 1.00: A Program for the calculation*  
10875 *of QED, QCD and electroweak corrections to  $e p$  and lepton+-  $N$  deep inelastic neutral and charged current scattering*,  
10876 Comput.Phys.Commun. **94** (1996) 128–184, arXiv:hep-ph/9511434 [hep-ph].
- 10877 [64] Particle Data Group Collaboration, K. Nakamura, *Review of particle physics*, J. Phys. **G37** (2010) 075021.
- 10878 [65] J. Blumlein and M. Klein, *On the cross calibration of calorimeters at  $e p$  colliders*, Nucl. Instrum. Meth. **A329** (1993)  
10879 112–116.
- 10880 [66] M. Klein, *Scenarios and Measurements with the LHeC*, Talk given at the LHeC Meeting at DIS 2009, Madrid, Spain,  
10881 April 2009.
- 10882 [67] ZEUS Collaboration, S. Chekanov et al., *Measurement of the Longitudinal Proton Structure Function at HERA*,  
10883 Phys.Lett. **B682** (2009) 8–22, arXiv:0904.1092 [hep-ex].
- 10884 [68] F. Aaron, C. Alexa, V. Andreev, S. Backovic, A. Baghdasaryan, et al., *Measurement of the Inclusive  $e\pm p$  Scattering*  
10885 *Cross Section at High Inelasticity  $y$  and of the Structure Function  $FL$* , Eur.Phys.J. **C71** (2011) 1579, arXiv:1012.4355  
10886 [hep-ex].
- 10887 [69] M. Botje, *QCDNUM manual*. <http://www.nikhef.nl/~h24/qcdnum/>. <http://www.nikhef.nl/~h24/qcdnum/>.
- 10888 [70] E. Rizvi and T. Sloan,  *$x F^{**}(\gamma Z)(3)$  in charged lepton scattering*, Eur.Phys.J.direct **C3** (2001) N2,  
10889 arXiv:hep-ex/0101007 [hep-ex].
- 10890 [71] HERMES Collaboration, A. Airapetian et al., *Measurement of Parton Distributions of Strange Quarks in the Nucleon*  
10891 *from Charged-Kaon Production in Deep-Inelastic Scattering on the Deuteron*, Phys. Lett. **B666** (2008) 446–450,  
10892 arXiv:0803.2993 [hep-ex].
- 10893 [72] U. Baur and J. van der Bij, *Top quark production at HERA*, Nucl.Phys. **B304** (1988) 451.
- 10894 [73] H. Fritzsch and D. Holtmannspotter, *The Production of single  $t$  quarks at LEP and HERA*, Phys. Lett. **B457** (1999)  
10895 186–192, arXiv:hep-ph/9901411.
- 10896 [74] C. Pascaud, *CFNS*, Talk given at DIS 2011, Newport News, USA, April 2011.
- 10897 [75] G. Brandt, *Single top production of diquarks at LHeC*, Talk given at the 1st CERN-ECFA Workshop on the LHeC,  
10898 Divonne-les-Bains, France, 1-3 September 2008.
- 10899 [76] CMS Collaboration, S. Chatrchyan et al., *Measurement of the  $t$ -channel single top quark production cross section in  $pp$*   
10900 *collisions at  $\sqrt{s} = 7$  TeV*, arXiv:1106.3052 [hep-ex]. \* Temporary entry \*.
- 10901 [77] S. Alekhin, J. Blumlein, P. Jimenez-Delgado, S. Moch, and E. Reya, *NNLO Benchmarks for Gauge and Higgs Boson*  
10902 *Production at TeV Hadron Colliders*, Phys. Lett. **B697** (2011) 127–135, arXiv:1011.6259 [hep-ph].
- 10903 [78] J. A. M. Vermaseren, A. Vogt, and S. Moch, *The third-order QCD corrections to deep-inelastic scattering by photon*  
10904 *exchange*, Nucl. Phys. **B724** (2005) 3–182, arXiv:hep-ph/0504242.
- 10905 [79] I. Bierenbaum, J. Blumlein, and S. Klein, *Mellin Moments of the  $O(\alpha^{**3}(s))$  Heavy Flavor Contributions to*  
10906 *unpolarized Deep-Inelastic Scattering at  $Q^{**2} \gg m^{**2}$  and Anomalous Dimensions*, Nucl.Phys. **B820** (2009) 417–482,  
10907 arXiv:0904.3563 [hep-ph].
- 10908 [80] J. Blumlein, H. Bottcher, and A. Guffanti, *Non-singlet QCD analysis of deep inelastic world data at  $O(\alpha(s)^{**3})$* ,  
10909 Nucl.Phys. **B774** (2007) 182–207, arXiv:hep-ph/0607200 [hep-ph].
- 10910 [81] M. Gluck, E. Reya, and C. Schuck, *Non-singlet QCD analysis of  $F(2)(x, Q^{**2})$  up to NNLO*, Nucl.Phys. **B754** (2006)  
10911 178–186, arXiv:hep-ph/0604116 [hep-ph].
- 10912 [82] S. Alekhin, J. Blumlein, S. Klein, and S. Moch, *The 3, 4, and 5-flavor NNLO Parton from Deep-Inelastic-Scattering*  
10913 *Data and at Hadron Colliders*, Phys.Rev. **D81** (2010) 014032, arXiv:0908.2766 [hep-ph].
- 10914 [83] P. Jimenez-Delgado and E. Reya, *Dynamical NNLO parton distributions*, Phys. Rev. **D79** (2009) 074023,  
10915 arXiv:0810.4274 [hep-ph].
- 10916 [84] A. D. Martin, W. J. Stirling, R. S. Thorne, and G. Watt, *Uncertainties on  $\alpha_s$  in global PDF analyses and*  
10917 *implications for predicted hadronic cross sections*, Eur. Phys. J. **C64** (2009) 653–680, arXiv:0905.3531 [hep-ph].
- 10918 [85] S. Alekhin, J. Blumlein, and S.-O. Moch, *Update of the NNLO PDFs in the 3-, 4-, and 5-flavour scheme*, PoS  
10919 **DIS2010** (2010) 021, arXiv:1007.3657 [hep-ph].
- 10920 [86] S. Bethke, *The 2009 World Average of  $\alpha(s)$* , Eur.Phys.J. **C64** (2009) 689–703, arXiv:0908.1135 [hep-ph].
- 10921 [87] J. Blumlein, S. Riemersma, W. van Neerven, and A. Vogt, *Theoretical uncertainties in the QCD evolution of structure*  
10922 *functions and their impact on  $\alpha-s(M(Z)^{**2})$* , Nucl.Phys.Proc.Suppl. **51C** (1996) 97–105, arXiv:hep-ph/9609217  
10923 [hep-ph].
- 10924 [88] S. J. Brodsky, *Novel QCD Phenomenology at the LHeC*, arXiv:1106.5820 [hep-ph]. LHeC-Note-2011-002 PHY and  
10925 SLAC-PUB-14487.

- 10926 [89] P. Baikov and K. Chetyrkin, *New four loop results in QCD*, Nucl.Phys.Proc.Suppl. **160** (2006) 76–79.
- 10927 [90] M. Buza, Y. Matiounine, J. Smith, and W. van Neerven, *Charm electroproduction viewed in the variable flavor number*  
10928 *scheme versus fixed order perturbation theory*, Eur.Phys.J. **C1** (1998) 301–320, arXiv:hep-ph/9612398 [hep-ph].
- 10929 [91] S. Alekhin and S. Moch, *Heavy-quark deep-inelastic scattering with a running mass*, Phys. Lett. **B699** (2011) 345–353,  
10930 arXiv:1011.5790 [hep-ph].
- 10931 [92] T. Gehrmann, M. Jaquier, and G. Luisoni, *Hadronization effects in event shape moments*, Eur.Phys.J. **C67** (2010)  
10932 57–72, arXiv:0911.2422 [hep-ph].
- 10933 [93] R. Abbate, M. Fickinger, A. H. Hoang, V. Mateu, and I. W. Stewart, *Thrust at N3LL with Power Corrections and a*  
10934 *Precision Global Fit for  $\alpha_s(m_Z)$* , Phys.Rev. **D83** (2011) 074021, arXiv:1006.3080 [hep-ph].
- 10935 [94] M. Virchaux and A. Milsztajn, *A Measurement of  $\alpha_s$  and higher twists from a QCD analysis of high statistics F-2*  
10936 *data on hydrogen and deuterium targets*, Phys.Lett. **B274** (1992) 221–229.
- 10937 [95] H1 Collaboration, C. Adloff et al., *Deep-inelastic inclusive e p scattering at low x and a determination of  $\alpha_s$* , Eur.  
10938 Phys. J. **C21** (2001) 33–61, arXiv:hep-ex/0012053.
- 10939 [96] R. Wallny, *A Measurement of the Gluon Distribution in the Proton and of the Strong Coupling Constant  $\alpha_s$  from*  
10940 *Inclusive Deep-Inelastic Scattering*, H1 PhD Thesis 2001, Zurich, Switzerland,2001.
- 10941 [97] A. Martin, W. Stirling, R. Thorne, and G. Watt,  *$\alpha_s$  in MSTW Analyses*, Talk given in [99], February 2011.
- 10942 [98] S. Lionetti, R. D. Ball, V. Bertone, F. Cerutti, L. Del Debbio, et al., *Precision determination of  $\alpha_s$  using an unbiased*  
10943 *global NLO parton set*, arXiv:1103.2369 [hep-ph].
- 10944 [99] S. Bethke et al., *Workshop on Precision Measurements on  $\alpha_s$* , MPI Munich, Germany, February, 2011.
- 10945 [100] T. Kluge, *Prospects of  $\alpha_s$  Determinations in DIS*, Talks given at the CERN-ECFA-NuPECC Workshops on the  
10946 LHeC, Divonne-les-Bains, France, September 2008/09.
- 10947 [101] BCDMS Collaboration, A. Benvenuti et al., *A comparison of the structure functions F2 of the proton and the neutron*  
10948 *from Deep Inelastic muon scattering at high Q\*\*2*, Phys.Lett. **B237** (1990) 599.
- 10949 [102] BCDMS Collaboration, A. C. Benvenuti et al., *A High Statistics Measurement of the Deuteron Structure Functions*  
10950 *F(2) (x, Q\*\*2) and R from Deep Inelastic Muon Scattering at High Q\*\*2*, Phys. Lett. **B237** (1990) 592.
- 10951 [103] European Muon Collaboration, J. Aubert et al., *Measurements of the nucleon structure functions F2n in deep inelastic*  
10952 *muon scattering from deuterium and comparison with those from hydrogen and iron*, Nucl.Phys. **B293** (1987) 740.
- 10953 [104] T. A. et al., *eD Scattering with H1, A Letter of Intent DESY 03-194*, .
- 10954 [105] T. A. et al., *A New experiment For HERA, MPP-2003-62*, .
- 10955 [106] T. Greenshaw and M. Klein, *The Future of lepton nucleon scattering: A Summary of the Durham Workshop, December*  
10956 *2001*, J.Phys.G **G28** (2002) 2503–2508, arXiv:hep-ex/0204032 [hep-ex].
- 10957 [107] I. Schienbein, J. Yu, K. Kovarik, C. Keppel, J. Morfin, et al., *PDF Nuclear Corrections for Charged and Neutral*  
10958 *Current Processes*, Phys.Rev. **D80** (2009) 094004, arXiv:0907.2357 [hep-ph].
- 10959 [108] L. Frankfurt, V. Guzey, and M. Strikman, *Nuclear shadowing in inclusive and tagged deuteron structure functions and*  
10960 *extraction of F(2)\*\*p - F(2)\*\*n at small x from electron-deuteron collider data*, Mod.Phys.Lett. **A21** (2006) 23–40,  
10961 arXiv:hep-ph/0601123 [hep-ph].
- 10962 [109] T. Hobbs, J. Londergan, D. Murdock, and A. Thomas, *Testing Partonic Charge Symmetry at a High-Energy Electron*  
10963 *Collider*, Phys.Lett. **B698** (2011) 123–127, arXiv:1101.3923 [hep-ph].
- 10964 [110] S. J. Brodsky and B. Chertok, *The Asymptotic Form-Factors of Hadrons and Nuclei and the Continuity of Particle*  
10965 *and Nuclear Dynamics*, Phys.Rev. **D14** (1976) 3003–3020.
- 10966 [111] V. A. Matveev and P. Sorba, *Is Deuteron a Six Quark System?*, Lett.Nuovo Cim. **20** (1977) 435.
- 10967 [112] S. J. Brodsky, C.-R. Ji, and G. Lepage, *Quantum Chromodynamic Predictions for the Deuteron Form-Factor*,  
10968 Phys.Rev.Lett. **51** (1983) 83.
- 10969 [113] R. Arnold, B. Chertok, E. Dally, A. Grigorian, C. Jordan, et al., *Measurement of the electron-Deuteron Elastic*  
10970 *Scattering Cross-Section in the Range 0.8 GeV\*\*2 <math>j q\*\*2 <math>j 6 GeV\*\*2, Phys.Rev.Lett. **35** (1975) 776.*
- 10971 [114] G. R. Farrar, K. Huleihel, and H.-y. Zhang, *Deuteron form-factor*, Phys.Rev.Lett. **74** (1995) 650–653.
- 10972 [115] B. W. Harris and J. Smith, *Charm quark and D\*+- cross sections in deeply inelastic scattering at HERA*, Phys. Rev.  
10973 **D57** (1998) 2806–2812, arXiv:hep-ph/9706334.
- 10974 [116] S. Frixione, M. L. Mangano, P. Nason, and G. Ridolfi, *Total Cross Sections for Heavy Flavour Production at HERA*,  
10975 Phys. Lett. **B348** (1995) 633–645, arXiv:hep-ph/9412348.
- 10976 [117] S. Frixione, P. Nason, and G. Ridolfi, *Differential distributions for heavy flavor production at HERA*, Nucl. Phys. **B454**  
10977 (1995) 3–24, arXiv:hep-ph/9506226.
- 10978 [118] J. Binnewies, B. A. Kniehl, and G. Kramer, *Inclusive B meson production in e+ e- and p anti-p collisions*, Phys. Rev.  
10979 **D58** (1998) 034016, arXiv:hep-ph/9802231.

- 10980 [119] J. Binnewies, B. A. Kniehl, and G. Kramer, *Coherent description of  $D^{*+}$ - production in  $e^+ e^-$  and low-  $Q^{*2}$   $e p$*   
10981 *collisions*, Z. Phys. **C76** (1997) 677–688, [arXiv:hep-ph/9702408](#).
- 10982 [120] B. A. Kniehl, G. Kramer, and M. Spira, *Large  $p(T)$  photoproduction of  $D^{*+}$ - mesons in  $e p$  collisions*, Z. Phys. **C76**  
10983 (1997) 689–700, [arXiv:hep-ph/9610267](#).
- 10984 [121] M. Cacciari and M. Greco, *Charm Production via Fragmentation*, Z. Phys. **C69** (1996) 459–466, [arXiv:hep-ph/9505419](#).
- 10985 [122] G. Kramer and H. Spiesberger, *Inclusive photoproduction of  $D^*$  mesons with massive charm quarks*, Eur. Phys. J. **C38**  
10986 (2004) 309–318, [arXiv:hep-ph/0311062](#).
- 10987 [123] B. A. Kniehl, G. Kramer, I. Schienbein, and H. Spiesberger, *Inclusive  $D^{*+}$ - production in  $p$  anti- $p$  collisions with*  
10988 *massive charm quarks*, Phys. Rev. **D71** (2005) 014018, [arXiv:hep-ph/0410289](#).
- 10989 [124] S. Catani, M. Ciafaloni, and F. Hautmann, *Glueon contributions to small  $x$  heavy flavor production*, Phys. Lett. **B242**  
10990 (1990) 97.
- 10991 [125] S. Catani, M. Ciafaloni, and F. Hautmann, *High-energy factorization and small  $x$  heavy flavor production*, Nucl. Phys.  
10992 **B366** (1991) 135–188.
- 10993 [126] A. Belyaev, J. Pumplin, W.-K. Tung, and C. P. Yuan, *Uncertainties of the inclusive Higgs production cross section at*  
10994 *the Tevatron and the LHC*, JHEP **01** (2006) 069, [arXiv:hep-ph/0508222](#).
- 10995 [127] S. J. Brodsky, J. C. Collins, S. D. Ellis, J. F. Gunion, and A. H. Mueller, *INTRINSIC CHEVROLETS AT THE SSC*, .
- 10996 [128] B. Harris, J. Smith, and R. Vogt, *Reanalysis of the EMC charm production data with extrinsic and intrinsic charm at*  
10997 *NLO*, Nucl.Phys. **B461** (1996) 181–196, [arXiv:hep-ph/9508403](#) [[hep-ph](#)].
- 10998 [129] M. Franz, M. V. Polyakov, and K. Goeke, *Heavy quark mass expansion and intrinsic charm in light hadrons*, Phys.Rev.  
10999 **D62** (2000) 074024, [arXiv:hep-ph/0002240](#) [[hep-ph](#)].
- 11000 [130] T. Sjostrand, S. Mrenna, and P. Z. Skands, *PYTHIA 6.4 Physics Manual*, JHEP **05** (2006) 026, [arXiv:hep-ph/0603175](#).
- 11001 [131] J. Pumplin et al., *New generation of parton distributions with uncertainties from global QCD analysis*, JHEP **07** (2002)  
11002 012, [arXiv:hep-ph/0201195](#).
- 11003 [132] H. Jung, *Hard diffractive scattering in high-energy  $e p$  collisions and the Monte Carlo generator RAPGAP*, Comp.  
11004 Phys. Commun. **86** (1995) 147–161.
- 11005 [133] CTEQ Collaboration, H. L. Lai et al., *Global QCD analysis of parton structure of the nucleon: CTEQ5 parton*  
11006 *distributions*, Eur. Phys. J. **C12** (2000) 375–392, [arXiv:hep-ph/9903282](#).
- 11007 [134] G. Ingelman, A. Edin, and J. Rathsman, *LEPTO 6.5 - A Monte Carlo Generator for Deep Inelastic Lepton-Nucleon*  
11008 *Scattering*, Comput. Phys. Commun. **101** (1997) 108–134, [arXiv:hep-ph/9605286](#).
- 11009 [135] H1 and Z. Collaborations, *Combination of  $F_2^{cc}$  from DIS measurements at HERA*, Preliminary measurements  
11010 H1prelim-09-171,ZEUS-prel-09-015.
- 11011 [136] H1 Collaboration, F. D. Aaron et al., *Measurement of the Charm and Beauty Structure Functions using the H1 Vertex*  
11012 *Detector at HERA*, Eur. Phys. J. **C65** (2010) 89–109, [arXiv:0907.2643](#) [[hep-ex](#)].
- 11013 [137] J. Pumplin, H. L. Lai, and W. K. Tung, *The charm parton content of the nucleon*, Phys. Rev. **D75** (2007) 054029,  
11014 [arXiv:hep-ph/0701220](#).
- 11015 [138] D0 Collaboration, V. Abazov et al., *Measurement of  $\gamma + b + X$  and  $\gamma + c + X$  production cross sections in*  
11016  *$p$  anti- $p$  collisions at  $s^{*2}(1/2) = 1.96$ -TeV*, Phys.Rev.Lett. **102** (2009) 192002, [arXiv:0901.0739](#) [[hep-ex](#)].
- 11017 [139] S. J. Brodsky, B. Kopeliovich, I. Schmidt, and J. Soffer, *Diffractive Higgs production from intrinsic heavy flavors in the*  
11018 *proton*, Phys.Rev. **D73** (2006) 113005, [arXiv:hep-ph/0603238](#) [[hep-ph](#)].
- 11019 [140] P. Aurenche, M. Fontannaz, and J. P. Guillet, *New NLO parametrizations of the parton distributions in real photons*,  
11020 Eur. Phys. J. **C44** (2005) 395–409, [arXiv:hep-ph/0503259](#).
- 11021 [141] W. K. Tung et al., *Heavy quark mass effects in deep inelastic scattering and global QCD analysis*, JHEP **02** (2007) 053,  
11022 [arXiv:hep-ph/0611254](#).
- 11023 [142] T. Kneesch, B. A. Kniehl, G. Kramer, and I. Schienbein, *Charmed-Meson Fragmentation Functions with Finite-Mass*  
11024 *Corrections*, Nucl. Phys. **B799** (2008) 34–59, [arXiv:0712.0481](#) [[hep-ph](#)].
- 11025 [143] M. Gluck, E. Reya, and A. Vogt, *Photonic parton distributions*, Phys. Rev. **D46** (1992) 1973–1979.
- 11026 [144] M. Klasen and G. Kramer, *Inclusive two-jet production at HERA: Direct and resolved cross sections in next-to-leading*  
11027 *order QCD*, Z. Phys. **C76** (1997) 67–74, [arXiv:hep-ph/9611450](#).
- 11028 [145] S. Catani and M. H. Seymour, *A general algorithm for calculating jet cross sections in NLO QCD*, Nucl. Phys. **B485**  
11029 (1997) 291–419, [arXiv:hep-ph/9605323](#).
- 11030 [146] D. Stump et al., *Inclusive jet production, parton distributions, and the search for new physics*, JHEP **10** (2003) 046,  
11031 [arXiv:hep-ph/0303013](#).
- 11032 [147] J. Pumplin, A. Belyaev, J. Huston, D. Stump, and W. K. Tung, *Parton distributions and the strong coupling:*  
11033 *CTEQ6AB PDFs*, JHEP **02** (2006) 032, [arXiv:hep-ph/0512167](#).

- 11034 [148] T. Gehrmann and E. W. N. Glover, *Two-Loop QCD Helicity Amplitudes for (2+1)-Jet Production in Deep Inelastic*  
11035 *Scattering*, Phys. Lett. **B676** (2009) 146–151, arXiv:0904.2665 [hep-ph].
- 11036 [149] A. Daleo, A. Gehrmann-De Ridder, T. Gehrmann, and G. Luisoni, *Antenna subtraction at NNLO with hadronic initial*  
11037 *states: initial-final configurations*, JHEP **01** (2010) 118, arXiv:0912.0374 [hep-ph].
- 11038 [150] S. Frixione, Z. Kunszt, and A. Signer, *Three jet cross-sections to next-to-leading order*, Nucl. Phys. **B467** (1996)  
11039 399–442, arXiv:hep-ph/9512328.
- 11040 [151] S. Frixione, *A General approach to jet cross-sections in QCD*, Nucl. Phys. **B507** (1997) 295–314,  
11041 arXiv:hep-ph/9706545.
- 11042 [152] M. Gluck, E. Reya, and A. Vogt, *Parton structure of the photon beyond the leading order*, Phys. Rev. **D45** (1992)  
11043 3986–3994.
- 11044 [153] K. J. Eskola, H. Paukkunen, and C. A. Salgado, *EPS09 - a New Generation of NLO and LO Nuclear Parton*  
11045 *Distribution Functions*, JHEP **04** (2009) 065, arXiv:0902.4154 [hep-ph].
- 11046 [154] S. D. Ellis and D. E. Soper, *Successive combination jet algorithm for hadron collisions*, Phys. Rev. **D48** (1993)  
11047 3160–3166, arXiv:hep-ph/9305266.
- 11048 [155] H1 Collaboration, C. Adloff et al., *Measurement of inclusive jet cross-sections in photoproduction at HERA*, Eur. Phys.  
11049 J. **C29** (2003) 497–513, arXiv:hep-ex/0302034.
- 11050 [156] S. Frixione and G. Ridolfi, *Jet photoproduction at HERA*, Nucl. Phys. **B507** (1997) 315–333, arXiv:hep-ph/9707345.
- 11051 [157] V. M. Budnev, I. F. Ginzburg, G. V. Meledin, and V. G. Serbo, *The Two photon particle production mechanism.*  
11052 *Physical problems. Applications. Equivalent photon approximation*, Phys. Rept. **15** (1975) 181–281.
- 11053 [158] T. H. Bauer, R. D. Spital, D. R. Yennie, and F. M. Pipkin, *The Hadronic Properties of the Photon in High-Energy*  
11054 *Interactions*, Rev. Mod. Phys. **50** (1978) 261.
- 11055 [159] J. M. Butterworth and M. Wing, *High energy photoproduction*, Rept. Prog. Phys. **68** (2005) 2773–2828,  
11056 arXiv:hep-ex/0509018.
- 11057 [160] L. Frankfurt, V. Guzey, M. McDermott, and M. Strikman, *Revealing the black body regime of small  $x$  DIS through final*  
11058 *state signals*, Phys. Rev. Lett. **87** (2001) 192301, arXiv:hep-ph/0104154.
- 11059 [161] T. C. Rogers and M. I. Strikman, *Hadronic interactions of ultra-high energy photons with protons and light nuclei in*  
11060 *the dipole picture*, J. Phys. **G32** (2006) 2041–2063, arXiv:hep-ph/0512311.
- 11061 [162] ZEUS Collaboration, S. Chekanov et al., *Measurement of the photon proton total cross section at a center-of-mass*  
11062 *energy of 209-GeV at HERA*, Nucl. Phys. **B627** (2002) 3–28, arXiv:hep-ex/0202034.
- 11063 [163] H1 Collaboration, S. Aid et al., *Measurement of the total photon-proton cross-section and its decomposition at 200-GeV*  
11064 *center-of-mass energy*, Z. Phys. **C69** (1995) 27–38, arXiv:hep-ex/9509001.
- 11065 [164] G. M. Vereshkov, O. D. Lalakulich, Y. F. Novoseltsev, and R. V. Novoseltseva, *Total cross section for photon nucleon*  
11066 *interaction in the energy range  $\sqrt{s} = 40\text{-GeV} - 250\text{-GeV}$* , Phys. Atom. Nucl. **66** (2003) 565–574.
- 11067 [165] Z. Collaboration, *Measurement of the energy dependence of the total photon-proton cross section at HERA*, Phys.Lett.  
11068 **B697** (2011) 184–193, arXiv:1011.1652 [hep-ex]. \* Temporary entry \*.
- 11069 [166] R. M. Godbole, A. Grau, G. Pancheri, and Y. N. Srivastava, *Total photoproduction cross-section at very high energy*,  
11070 Eur. Phys. J. **C63** (2009) 69–85, arXiv:0812.1065 [hep-ph].
- 11071 [167] M. M. Block and F. Halzen, *Evidence for the saturation of the Froissart bound*, Phys. Rev. **D70** (2004) 091901,  
11072 arXiv:hep-ph/0405174.
- 11073 [168] M. M. Block and F. Halzen, *New evidence for the saturation of the Froissart bound*, Phys. Rev. **D72** (2005) 036006,  
11074 arXiv:hep-ph/0506031.
- 11075 [169] M. M. Block, E. M. Gregores, F. Halzen, and G. Pancheri, *Photon - proton and photon-photon scattering from nucleon-*  
11076 *nucleon forward amplitudes*, Phys. Rev. **D60** (1999) 054024, arXiv:hep-ph/9809403.
- 11077 [170] H. Flacher, M. Goebel, J. Haller, A. Hocker, K. Monig, et al., *Gfitter - Revisiting the Global Electroweak Fit of the*  
11078 *Standard Model and Beyond*, Eur.Phys.J. **C60** (2009, see <http://gfitter.desy.de/>) 543–583, arXiv:0811.0009  
11079 [hep-ph].
- 11080 [171] J. Erler, *The Mass of the Higgs Boson in the Standard Electroweak Model*, Phys.Rev. **D81** (2010) 051301,  
11081 arXiv:1002.1320 [hep-ph].
- 11082 [172] P. Gambino, *The top priority: Precision electroweak physics from low to high energy*, Int. J. Mod. Phys. **A19** (2004)  
11083 808–820, arXiv:hep-ph/0311257.
- 11084 [173] M. Davier, A. Hoecker, B. Malaescu, and Z. Zhang, *Reevaluation of the Hadronic Contributions to the Muon  $g-2$  and to*  
11085  *$\alpha(MZ)$* , Eur.Phys.J. **C71** (2011) 1515, arXiv:1010.4180 [hep-ph].
- 11086 [174] S. Haywood, P. Hobson, W. Hollik, Z. Kunszt, G. Azuelos, et al., *Electroweak physics*, hep-ph/0003275 ,  
11087 arXiv:hep-ph/0003275 [hep-ph].



- 11088 [175] K. Rabbertz, *QCD and Electroweak Physics at LHC*, PoS **RADCOR2009** (2010) 016, [arXiv:1002.3628](#) [hep-ph].
- 11089 [176] S. <http://www.jlab.org/qweak/>, , .
- 11090 [177] S. <http://hallaweb.jlab.org/12GeV/Moller/>, , .
- 11091 [178] R. Cashmore, E. Elsen, B. A. Kniehl, and H. Spiesberger, *Electroweak physics at HERA: Introduction and summary*, [arXiv:hep-ph/9610251](#) [hep-ph].
- 11093 [179] H1 and ZEUS Collaboration, Z. Zhang, *Electroweak and beyond the Standard Model results from HERA*, Nucl.Phys.Proc.Suppl. **191** (2009) 271–280, [arXiv:0812.4662](#) [hep-ex].
- 11094 [180] H1 Collaboration, A. Aktas et al., *A Determination of electroweak parameters at HERA*, Phys.Lett. **B632** (2006) 35–42, [arXiv:hep-ex/0507080](#) [hep-ex].
- 11097 [181] H1 Collaboration, Z.-Q. Zhang, *Combined electroweak and QCD fits including NC and CC data with polarised electron beam at HERA-2*, PoS **DIS2010** (2010) 056.
- 11099 [182] D0 Collaboration Collaboration, V. Abazov et al., *Measurement of  $\sin^2 \theta_{\text{eff}}^{\ell}$  and Z-light quark couplings using the forward-backward charge asymmetry in  $p\bar{p} \rightarrow Z/\gamma^* \rightarrow e^+e^-$  events with  $\mathcal{L} = 5.0 \text{ fb}^{-1}$  at  $\sqrt{s} = 1.96 \text{ TeV}$* , Phys.Rev.D (2011), [arXiv:1104.4590](#) [hep-ex]. \* Temporary entry \*.
- 11102 [183] E. Salvioni, A. Strumia, G. Villadoro, and F. Zwirner, *Non-universal minimal Z' models: present bounds and early LHC reach*, JHEP **1003** (2010) 010, [arXiv:0911.1450](#) [hep-ph].
- 11104 [184] J. Erler and P. Langacker, *Indications for an extra neutral gauge boson in electroweak precision data*, Phys.Rev.Lett. **84** (2000) 212–215, [arXiv:hep-ph/9910315](#) [hep-ph].
- 11106 [185] R. Barbier, C. Berat, M. Besancon, M. Chemtob, A. Deandrea, et al., *R-parity violating supersymmetry*, Phys.Rept. **420** (2005) 1–202, [arXiv:hep-ph/0406039](#) [hep-ph].
- 11108 [186] M. Carpentier and S. Davidson, *Constraints on two-lepton, two quark operators*, Eur.Phys.J. **C70** (2010, and refs. therein) 1071–1090, [arXiv:1008.0280](#) [hep-ph].
- 11110 [187] J. Erler, A. Kurylov, and M. J. Ramsey-Musolf, *The Weak charge of the proton and new physics*, Phys.Rev. **D68** (2003) 016006, [arXiv:hep-ph/0302149](#) [hep-ph].
- 11112 [188] C. Prescott, W. Atwood, R. Cottrell, H. DeStaebler, E. L. Garwin, et al., *Further Measurements of Parity Nonconservation in Inelastic electron Scattering*, Phys.Lett. **B84** (1979) 524.
- 11114 [189] E. A. Paschos and L. Wolfenstein, *Tests for neutral currents in neutrino reactions*, Phys. Rev. **D7** (1973) 91–95.
- 11115 [190] J. Blumlein, M. Klein, and T. Riemann, *Testing the electroweak standard model at HERA*, .
- 11116 [191] A. Czarnecki and W. J. Marciano, *Polarized Moller scattering asymmetries*, Int.J.Mod.Phys. **A15** (2000) 2365–2376, [arXiv:hep-ph/0003049](#) [hep-ph].
- 11118 [192] J. A. Bagger and M. E. Peskin, *Exotic processes in high-energy ep collisions*, Phys. Rev. **D31** (1985) 2211.
- 11119 [193] R. J. Cashmore et al., *Exotic phenomena in high-energy ep collisions*, Phys. Rept. **122** (1985) 275–386.
- 11120 [194] G. Jarlskog, (Ed. ) and D. Rein, (Ed. ), *ECFA Large Hadron Collider Workshop, Aachen, Germany, 4-9 Oct 1990: Proceedings.1*, . CERN-90-10-V-1.
- 11122 [195] G. Kopp, D. Schaile, M. Spira, and P. M. Zerwas, *Bounds on radii and magnetic dipole moments of quarks and leptons from LEP, SLC and HERA*, Z. Phys. **C65** (1995) 545–550, [arXiv:hep-ph/9409457](#).
- 11124 [196] A. F. Zarnecki, *Leptoquarks and Contact Interactions at LeHC*, [arXiv:0809.2917](#) [hep-ph].
- 11125 [197] E. Eichten, K. D. Lane, and M. E. Peskin, *New Tests for Quark and Lepton Substructure*, Phys. Rev. Lett. **50** (1983) 811–814.
- 11127 [198] R. Ruckl, *Probing lepton and quark substructure in polarized e- + N scattering*, Nucl. Phys. **B234** (1984) 91.
- 11128 [199] P. Haberl, F. Schrempp, and H. U. Martyn, *Contact interactions and new heavy bosons at HERA: A Model independent analysis*, . In \*Hamburg 1991, Proceedings, Physics at HERA, vol. 2\* 1133-1148. (see HIGH ENERGY PHYSICS INDEX 30 (1992) No. 12988).
- 11131 [200] A. F. Zarnecki, *Global analysis of eeqq contact interactions and future prospects for high-energy physics*, Eur. Phys. J. **C11** (1999) 539–557, [arXiv:hep-ph/9904334](#).
- 11133 [201] C. T. Hill and E. H. Simmons, *Strong dynamics and electroweak symmetry breaking*, Phys. Rept. **381** (2003) 235–402, [arXiv:hep-ph/0203079](#).
- 11135 [202] W. Buchmuller, R. Ruckl, and D. Wyler, *Leptoquarks in lepton quark collisions*, Phys. Lett. **B191** (1987) 442–448.
- 11136 [203] B. Schrempp, *Leptoquarks and leptogluons at HERA: Theoretical perspectives*, . In \*Hamburg 1991, Proceedings, Physics at HERA, vol. 2\* 1034-1042. (see HIGH ENERGY PHYSICS INDEX 30 (1992) No. 12988).
- 11138 [204] S. Davidson, D. C. Bailey, and B. A. Campbell, *Model independent constraints on leptoquarks from rare processes*, Z. Phys. **C61** (1994) 613–644, [arXiv:hep-ph/9309310](#).
- 11140 [205] M. Leurer, *A Comprehensive study of leptoquark bounds*, Phys. Rev. **D49** (1994) 333–342, [arXiv:hep-ph/9309266](#).

- 11141 [206] A. Belyaev, C. Leroy, R. Mehdiev, and A. Pukhov, *Leptoquark single and pair production at LHC with*  
11142 *CalchEP/CompHEP in the complete model*, JHEP **09** (2005) 005, arXiv:hep-ph/0502067.
- 11143 [207] D0 Collaboration, V. M. Abazov et al., *Search for pair production of first-generation leptoquarks in  $p\bar{p}$  collisions at*  
11144  *$\sqrt{s}=1.96$  TeV*, Phys. Lett. **B681** (2009) 224–232, arXiv:0907.1048 [hep-ex].
- 11145 [208] T. A. Collaboration, *Search for pair production of first or second generation leptoquarks in proton-proton collisions at*  
11146  *$\sqrt{s}=7$  TeV using the ATLAS detector at the LHC*, arXiv:1104.4481 [hep-ex]. \* Temporary entry \*.
- 11147 [209] CMS Collaboration, S. Chatrchyan et al., *Search for First Generation Scalar Leptoquarks in the  $evjj$  channel in  $pp$*   
11148 *collisions at  $\sqrt{s} = 7$  TeV*, arXiv:1105.5237 [hep-ex]. \* Temporary entry \*.
- 11149 [210] A. Belyaev and A. Pukhov.
- 11150 [211] A. Pukhov, *Calchep 2.3: MSSM, structure functions, event generation, 1, and generation of matrix elements for other*  
11151 *packages*, arXiv:hep-ph/0412191.
- 11152 [212] S. Ovin, X. Rouby, and V. Lemaitre, *Delphes, a framework for fast simulation of a generic collider experiment*,  
11153 arXiv:0903.2225 [hep-ph].
- 11154 [213] H. Harari, *A Schematic Model of Quarks and Leptons*, Phys. Lett. **B86** (1979) 83.
- 11155 [214] H. Fritzsch and G. Mandelbaum, *Weak Interactions as Manifestations of the Substructure of Leptons and Quarks*,  
11156 Phys. Lett. **B102** (1981) 319.
- 11157 [215] O. W. Greenberg and J. Sucher, *A Quantum Structure Dynamic Model of Quarks, Leptons, Weak Vector Bosons, and*  
11158 *Higgs Mesons*, Phys. Lett. **B99** (1981) 339.
- 11159 [216] R. Barbieri, R. N. Mohapatra, and A. Masiero, *Compositeness and a Left-Right Symmetric Electroweak Model Without*  
11160 *Broken Gauge Interactions*, Phys. Lett. **B105** (1981) 369–374.
- 11161 [217] U. Baur and K. H. Streng, *Colored lepton mass bounds from  $p$  anti- $p$  collider data*, Phys. Lett. **B162** (1985) 387.
- 11162 [218] A. Celikel, M. Kantar, and S. Sultansoy, *A search for sextet quarks and leptogluons at the LHC*, Phys. Lett. **B443**  
11163 (1998) 359–364.
- 11164 [219] S. S. M. Sahin and S. Turkoz, *Resonant production of color octet electrons at the LHeC*, . CERN-LHeC-Note-2010-015  
11165 PHY.
- 11166 [220] H. Harari, *Composite models for quarks and leptons*, Phys. Rept. **104** (1984) 159.
- 11167 [221] N. T. E. Sauvan, *Single production of excited fermions at LHeC*, . CERN-LHeC-Note-2010-011 PHY.
- 11168 [222] O. J. P. Eboli, S. M. Lietti, and P. Mathews, *Excited leptons at the CERN Large Hadron Collider*, Phys. Rev. **D65**  
11169 (2002) 075003, arXiv:hep-ph/0111001.
- 11170 [223] E. M. Gregores, M. C. Gonzalez-Garcia, and S. F. Novaes, *Discriminating new physics scenarios at NLC: The Role of*  
11171 *polarization*, Phys. Rev. **D56** (1997) 2920–2927, arXiv:hep-ph/9703430.
- 11172 [224] H1 Collaboration, F. D. Aaron et al., *Search for Excited Electrons in  $ep$  Collisions at HERA*, Phys. Lett. **B666** (2008)  
11173 131–139, arXiv:0805.4530 [hep-ex].
- 11174 [225] H1 Collaboration, F. D. Aaron et al., *A Search for Excited Neutrinos in  $e-p$  Collisions at HERA*, Phys. Lett. **B663**  
11175 (2008) 382–389, arXiv:0802.1858 [hep-ex].
- 11176 [226] H1 Collaboration, F. D. Aaron et al., *Search for Excited Quarks in  $ep$  Collisions at HERA*, Phys. Lett. **B678** (2009)  
11177 335–343, arXiv:0904.3392 [hep-ex].
- 11178 [227] OPAL Collaboration, G. Abbiendi et al., *Search for charged excited leptons in  $e^+e^-$  collisions at  $s^{1/2} = 183\text{-}209\text{-GeV}$*   
11179 *, Phys. Lett. **B544** (2002) 57–72*, arXiv:hep-ex/0206061.
- 11180 [228] DELPHI Collaboration, J. Abdallah et al., *Determination of the  $e^+e^- \rightarrow \gamma\gamma$  ( $\gamma$ ) cross-section at*  
11181 *LEP 2*, Eur. Phys. J. **C37** (2004) 405–419, arXiv:hep-ex/0409058.
- 11182 [229] D0 Collaboration, V. M. Abazov et al., *Search for excited electrons in  $p\bar{p}$  collisions at  $\sqrt{s} = 1.96\text{-TeV}$* , Phys. Rev. **D77**  
11183 (2008) 091102, arXiv:0801.0877 [hep-ex].
- 11184 [230] K. Hagiwara, D. Zeppenfeld, and S. Komamiya, *Excited Lepton Production at LEP and HERA*, Z. Phys. **C29** (1985)  
11185 115.
- 11186 [231] F. Boudjema, A. Djouadi, and J. L. Kneur, *Excited fermions at  $e^+e^-$  and  $eP$  colliders*, Z. Phys. **C57** (1993) 425–450.
- 11187 [232] U. Baur, M. Spira, and P. M. Zerwas, *Excited quark and lepton production at hadron colliders*, Phys. Rev. **D42** (1990)  
11188 815–824.
- 11189 [233] T. Kohler, *Exotic processes at HERA: The Event generator COMPOS*, . In \*Hamburg 1991, Proceedings, Physics at  
11190 HERA, vol. 3\* 1526-1541. (see HIGH ENERGY PHYSICS INDEX 30 (1992) No. 12988).
- 11191 [234] M. Spira. private communication.
- 11192 [235] C. Berger and P. Kandel, *A new generator for wide angle bremsstrahlung*, . Prepared for Workshop on Monte Carlo  
11193 Generators for HERA Physics (Plenary Starting Meeting), Hamburg, Germany, 27-30 Apr 1998.

- 11194 [236] A. C. et al., *Production of the Fourth SM Family Fermions at the Large Hadron Electron Collider*, .  
11195 CERN-LHeC-Note-2010-016 PHY.
- 11196 [237] J. A. Aguilar-Saavedra, *A minimal set of top anomalous couplings*, Nucl. Phys. **B812** (2009) 181–204, arXiv:0811.3842  
11197 [hep-ph].
- 11198 [238] Particle Data Group Collaboration, C. Amsler et al., *Review of particle physics*, Phys. Lett. **B667** (2008) 1.
- 11199 [239] The ATLAS Collaboration, G. Aad et al., *Expected Performance of the ATLAS Experiment - Detector, Trigger and  
11200 Physics*, arXiv:0901.0512 [hep-ex].
- 11201 [240] *ATLAS detector and physics performance. Technical design report. Vol. 2*, . CERN-LHCC-99-15.
- 11202 [241] T. Han, K. Whisnant, B. L. Young, and X. Zhang, *Searching for  $t \rightarrow c g$  at the Fermilab Tevatron*, Phys. Lett. **B385**  
11203 (1996) 311–316, arXiv:hep-ph/9606231.
- 11204 [242] E. Malkawi and T. M. P. Tait, *Top-Charm Strong Flavour-Changing Neutral Currents at the Tevatron*, Phys. Rev. **D54**  
11205 (1996) 5758–5762, arXiv:hep-ph/9511337.
- 11206 [243] T. M. P. Tait and C. P. Yuan, *Anomalous  $t$ - $c$ - $g$  coupling: The connection between single top production and top decay*,  
11207 Phys. Rev. **D55** (1997) 7300–7301, arXiv:hep-ph/9611244.
- 11208 [244] T. Han, M. Hosch, K. Whisnant, B.-L. Young, and X. Zhang, *Single top quark production via FCNC couplings at  
11209 hadron colliders*, Phys. Rev. **D58** (1998) 073008, arXiv:hep-ph/9806486.
- 11210 [245] T. M. P. Tait and C. P. Yuan, *Single top quark production as a window to physics beyond the standard model*, Phys.  
11211 Rev. **D63** (2001) 014018, arXiv:hep-ph/0007298.
- 11212 [246] J. J. Liu, C. S. Li, L. L. Yang, and L. G. Jin, *Single top quark production via SUSY-QCD FCNC couplings at the  
11213 CERN LHC in the unconstrained MSSM*, Nucl. Phys. **B705** (2005) 3–32, arXiv:hep-ph/0404099.
- 11214 [247] J. J. Liu, C. S. Li, L. L. Yang, and L. G. Jin, *Next-to-leading order QCD corrections to the direct top quark production  
11215 via model-independent FCNC couplings at hadron colliders*, Phys. Rev. **D72** (2005) 074018, arXiv:hep-ph/0508016.
- 11216 [248] J.-j. Cao, G.-l. Liu, J. M. Yang, and H.-j. Zhang, *Top-quark FCNC productions at LHC in topcolor-assisted technicolor  
11217 model*, Phys. Rev. **D76** (2007) 014004, arXiv:hep-ph/0703308.
- 11218 [249] J. J. Cao et al., *SUSY-induced FCNC top-quark processes at the Large Hadron Collider*, Phys. Rev. **D75** (2007)  
11219 075021, arXiv:hep-ph/0702264.
- 11220 [250] P. M. Ferreira, R. B. Guedes, and R. Santos, *Combined effects of strong and electroweak FCNC effective operators in  
11221 top quark physics at the CERN LHC*, Phys. Rev. **D77** (2008) 114008, arXiv:0802.2075 [hep-ph].
- 11222 [251] J. M. Yang, *Probing New Physics from Top Quark Processes at LHC: A Mini Review*, Int. J. Mod. Phys. **A23** (2008)  
11223 3343, arXiv:0801.0210 [hep-ph].
- 11224 [252] X.-F. Han, L. Wang, and J. M. Yang, *Top quark FCNC decays and productions at LHC in littlest Higgs model with  
11225  $T$ -parity*, arXiv:0903.5491 [hep-ph].
- 11226 [253] J. Cao, Z. Heng, L. Wu, and J. M. Yang,  *$R$ -parity violating effects in top quark FCNC productions at LHC*, Phys. Rev.  
11227 **D79** (2009) 054003, arXiv:0812.1698 [hep-ph].
- 11228 [254] V. F. Obraztsov, S. R. Slabospitsky, and O. P. Yushchenko, *Search for anomalous top quark interaction at LEP-2  
11229 collider*, Phys. Lett. **B426** (1998) 393–402, arXiv:hep-ph/9712394.
- 11230 [255] T. Han and J. L. Hewett, *Top charm associated production in high-energy  $e^+e^-$  collisions*, Phys. Rev. **D60** (1999)  
11231 074015, arXiv:hep-ph/9811237.
- 11232 [256] J.-j. Cao, Z.-h. Xiong, and J. M. Yang, *SUSY-induced top quark FCNC processes at linear colliders*, Nucl. Phys. **B651**  
11233 (2003) 87–105, arXiv:hep-ph/0208035.
- 11234 [257] J. A. Aguilar-Saavedra, *Top flavor-changing neutral interactions: Theoretical expectations and experimental detection*,  
11235 Acta Phys. Polon. **B35** (2004) 2695–2710, arXiv:hep-ph/0409342.
- 11236 [258] A. T. Alan and A. Senol, *Single top production at HERA and THERA*, Europhys. Lett. **59** (2002) 669–673,  
11237 arXiv:hep-ph/0202119.
- 11238 [259] A. A. Ashimova and S. R. Slabospitsky, *The Constraint on FCNC Coupling of the Top Quark with a Gluon from ep  
11239 Collisions*, Phys. Lett. **B668** (2008) 282–285, arXiv:hep-ph/0604119.
- 11240 [260] H1 Collaboration, F. D. Aaron et al., *Search for Single Top Quark Production at HERA*, Phys. Lett. **B678** (2009)  
11241 450–458, arXiv:0904.3876 [hep-ex].
- 11242 [261] O. Cakir and S. A. Cetin, *Anomalous single top quark production at the CERN LHC*, J. Phys. **G31** (2005) N1–N8.
- 11243 [262] G. A. Moortgat-Pick et al., *The role of polarized positrons and electrons in revealing fundamental interactions at the  
11244 linear collider*, Phys. Rept. **460** (2008) 131–243, arXiv:hep-ph/0507011.
- 11245 [263] S. Sultansoy, *Linac-ring type colliders: Second way to TeV scale*, Eur. Phys. J. **C33** (2004) s1064–s1066,  
11246 arXiv:hep-ex/0306034.
- 11247 [264] S. F. Sultanov, *Prospects of the future  $e p$  and gamma  $p$  colliders: Luminosity and physics*, . IC/89/409.

- 11248 [265] S. I. Alekhin et al., *Physics at gamma p colliders of TeV energies*, Int. J. Mod. Phys. **A6** (1991) 21–40.
- 11249 [266] A. K. Ciftci, S. Sultansoy, S. Turkoz, and O. Yavas, *Main parameters of TeV energy gamma p colliders*, Nucl. Instrum. Meth. **A365** (1995) 317–328.
- 11251 [267] A. K. Ciftci, S. Sultansoy, and O. Yavas, *TESLA\*HERA based gamma p and gamma A colliders*, Nucl. Instrum. Meth. **A472** (2001) 72–78, [arXiv:hep-ex/0007009](#).
- 11253 [268] H. Aksakal, A. K. Ciftci, Z. Nergiz, D. Schulte, and F. Zimmermann, *Conversion efficiency and luminosity for gamma proton colliders based on the LHC-CLIC or LHC-ILC QCD Explorer scheme*, Nucl. Instrum. Meth. **A576** (2007) 287–293, [arXiv:hep-ex/0612041](#).
- 11256 [269] I. T. Cakir, O. Cakir, and S. Sultansoy, *Anomalous Single Top Production at the Large Hadron electron Collider Based gamma p Collider*, Phys. Lett. **B685** (2010) 170–173, [arXiv:0911.4194 \[hep-ph\]](#).
- 11258 [270] CMS Collaboration, G. L. Bayatian et al., *CMS technical design report, volume II: Physics performance*, J. Phys. **G34** (2007) 995–1579.
- 11260 [271] O. Cakir, *Anomalous production of top quarks at CLIC + LHC based  $\gamma p$  colliders*, J. Phys. **G29** (2003) 1181–1192, [arXiv:hep-ph/0301116](#).
- 11262 [272] R. Ciftci, *Production of Excited Quark at  $\gamma p$  Collider Based on the Large Hadron Electron Collider*, . CERN-LHeC-Note-2010-017 PHY.
- 11264 [273] O. Çakır and M. Şahin, *Diquarks in  $\gamma p$  Collisions at LHeC*, . CERN-LHeC-Note-2010-012 PHY.
- 11265 [274] CMS Collaboration, V. Khachatryan et al., *Search for Dijet Resonances in 7 TeV pp Collisions at CMS*, Phys. Rev. Lett. **105** (2010) 211801, [arXiv:1010.0203 \[hep-ex\]](#).
- 11267 [275] A. Atre, M. Carena, T. Han, and J. Santiago, *Heavy Quarks Above the Top at the Tevatron*, Phys. Rev. **D79** (2009) 054018, [arXiv:0806.3966 \[hep-ph\]](#).
- 11269 [276] A. Atre et al., *Model-Independent Searches for New Quarks at the LHC*, [arXiv:1102.1987 \[hep-ph\]](#).
- 11270 [277] O.Cakir, *Single Production of Fourth Family Quarks at LHeC*, . CERN-LHeC-Note-2010-013 PHY.
- 11271 [278] M. Dührssen, *Measurement of Higgs boson parameters at the LHC*, Czech. J. Phys. **55** (2005) B145–B152.
- 11272 [279] J. M. Butterworth, A. R. Davison, M. Rubin, and G. P. Salam, *Jet substructure as a new Higgs search channel at the LHC*, Phys. Rev. Lett. **100** (2008) 242001, [arXiv:0802.2470 \[hep-ph\]](#).
- 11274 [280] T. Han and B. Mellado, *Higgs Boson Searches and the Hbbar Coupling at the LHeC*, Phys. Rev. **D82** (2010) 016009, [arXiv:0909.2460 \[hep-ph\]](#).
- 11276 [281] B. Jager, *Next-to-leading order QCD corrections to Higgs production at a future lepton-proton collider*, Phys.Rev. **D81** (2010) 054018, [arXiv:1001.3789 \[hep-ph\]](#).
- 11278 [282] J. Blumlein, G. van Oldenborgh, and R. Ruckl, *QCD and QED corrections to Higgs boson production in charged current e p scattering*, Nucl.Phys. **B395** (1993) 35–59, [arXiv:hep-ph/9209219 \[hep-ph\]](#).
- 11280 [283] J. Alwall et al., *MadGraph/MadEvent v4: The New Web Generation*, JHEP **09** (2007) 028, [arXiv:0706.2334 \[hep-ph\]](#).
- 11281 [284] PGS. <http://www.physics.ucdavis.edu/~conway/research/software/pgs/pgs4-general.htm>.
- 11282 [285] T. Plehn, D. L. Rainwater, and D. Zeppenfeld, *Determining the structure of Higgs couplings at the LHC*, Phys. Rev. Lett. **88** (2002) 051801, [arXiv:hep-ph/0105325](#).
- 11284 [286] T. Regge, *Introduction to complex orbital momenta*, Nuovo Cim. **14** (1959) 951.
- 11285 [287] V. N. Gribov, *A Reggeon diagram technique*, Sov. Phys. JETP **26** (1968) 414–422.
- 11286 [288] H. D. I. Abarbanel, J. B. Bronzan, R. L. Sugar, and A. R. White, *Reggeon Field Theory: Formulation and Use*, Phys. Rept. **21** (1975) 119–182.
- 11288 [289] J. C. Collins, D. E. Soper, and G. F. Sterman, *Factorization of Hard Processes in QCD*, Adv. Ser. Direct. High Energy Phys. **5** (1988) 1–91, [arXiv:hep-ph/0409313](#).
- 11290 [290] Y. L. Dokshitzer, *Calculation of the Structure Functions for Deep Inelastic Scattering and e+ e- Annihilation by Perturbation Theory in Quantum Chromodynamics*, Sov. Phys. JETP **46** (1977) 641–653.
- 11292 [291] L. V. Gribov, E. M. Levin, and M. G. Ryskin, *Semihard Processes in QCD*, Phys. Rept. **100** (1983) 1–150.
- 11293 [292] A. H. Mueller, *Small x Behavior and Parton Saturation: A QCD Model*, Nucl. Phys. **B335** (1990) 115.
- 11294 [293] J. Jalilian-Marian, A. Kovner, A. Leonidov, and H. Weigert, *The Wilson renormalization group for low x physics: Towards the high density regime*, Phys. Rev. **D59** (1999) 014014, [arXiv:hep-ph/9706377](#).
- 11296 [294] I. Balitsky, *Operator expansion for high-energy scattering*, Nucl. Phys. **B463** (1996) 99–160, [arXiv:hep-ph/9509348](#).
- 11297 [295] Y. V. Kovchegov, *Small-x F2 structure function of a nucleus including multiple pomeron exchanges*, Phys. Rev. **D60** (1999) 034008, [arXiv:hep-ph/9901281](#).
- 11299 [296] M. Froissart, *Asymptotic behavior and subtractions in the Mandelstam representation*, Phys. Rev. **123** (1961) 1053–1057.
- 11300

- 11301 [297] A. Martin, *Unitarity and high-energy behavior of scattering amplitudes*, Phys. Rev. **129** (1963) 1432–1436.
- 11302 [298] E. A. Kuraev, L. N. Lipatov, and V. S. Fadin, *The Pomeron singularity in Nonabelian Gauge Theories*, Sov. Phys. JETP **45** (1977) 199–204.
- 11304 [299] I. I. Balitsky and L. N. Lipatov, *The Pomeron singularity in Quantum Chromodynamics*, Sov. J. Nucl. Phys. **28** (1978) 822–829.
- 11306 [300] V. N. Gribov, *Glauber corrections and the interaction between high-energy hadrons and nuclei*, Sov. Phys. JETP **29** (1969) 483–487.
- 11308 [301] N. Armesto, A. B. Kaidalov, C. A. Salgado, and K. Tywoniuk, *A unitarized model of inclusive and diffractive DIS with  $Q^2$ -evolution*, Phys. Rev. **D81** (2010) 074002, arXiv:1001.3021 [hep-ph].
- 11309 [302] N. Armesto, A. B. Kaidalov, C. A. Salgado, and K. Tywoniuk, *Nuclear shadowing in Glauber-Gribov theory with  $Q^2$ -evolution*, Eur. Phys. J. **C68** (2010) 447–457, arXiv:1003.2947 [hep-ph].
- 11310 [303] A. H. Mueller and J.-w. Qiu, *Gluon Recombination and Shadowing at Small Values of  $x$* , Nucl. Phys. **B268** (1986) 427.
- 11311 [304] J. Bartels and M. Wusthoff, *The Triple Regge limit of diffractive dissociation in deep inelastic scattering*, Z. Phys. **C66** (1995) 157–180.
- 11315 [305] L. D. McLerran and R. Venugopalan, *Computing quark and gluon distribution functions for very large nuclei*, Phys. Rev. **D49** (1994) 2233–2241, arXiv:hep-ph/9309289.
- 11316 [306] L. D. McLerran and R. Venugopalan, *Gluon distribution functions for very large nuclei at small transverse momentum*, Phys. Rev. **D49** (1994) 3352–3355, arXiv:hep-ph/9311205.
- 11317 [307] L. D. McLerran and R. Venugopalan, *Green's functions in the color field of a large nucleus*, Phys. Rev. **D50** (1994) 2225–2233, arXiv:hep-ph/9402335.
- 11318 [308] J. Jalilian-Marian, A. Kovner, and H. Weigert, *The Wilson renormalization group for low  $x$  physics: Gluon evolution at finite parton density*, Phys. Rev. **D59** (1999) 014015, arXiv:hep-ph/9709432.
- 11321 [309] A. Kovner, J. G. Milhano, and H. Weigert, *Relating different approaches to nonlinear QCD evolution at finite gluon density*, Phys. Rev. **D62** (2000) 114005, arXiv:hep-ph/0004014.
- 11322 [310] H. Weigert, *Unitarity at small Bjorken  $x$* , Nucl. Phys. **A703** (2002) 823–860, arXiv:hep-ph/0004044.
- 11323 [311] E. Iancu, A. Leonidov, and L. D. McLerran, *Nonlinear gluon evolution in the color glass condensate. I*, Nucl. Phys. **A692** (2001) 583–645, arXiv:hep-ph/0011241.
- 11324 [312] E. Ferreiro, E. Iancu, A. Leonidov, and L. McLerran, *Nonlinear gluon evolution in the color glass condensate. II*, Nucl. Phys. **A703** (2002) 489–538, arXiv:hep-ph/0109115.
- 11325 [313] T. Altinoluk, A. Kovner, M. Lublinsky, and J. Peressutti, *QCD Reggeon Field Theory for every day: Pomeron loops included*, JHEP **03** (2009) 109, arXiv:0901.2559 [hep-ph].
- 11326 [314] F. Gelis, E. Iancu, J. Jalilian-Marian, and R. Venugopalan, *The Color Glass Condensate*, Ann.Rev.Nucl.Part.Sci. **60** (2010) 463–489, arXiv:1002.0333 [hep-ph].
- 11327 [315] Y. V. Kovchegov and H. Weigert, *Triumvirate of Running Couplings in Small- $x$  Evolution*, Nucl.Phys. **A784** (2007) 188–226, arXiv:hep-ph/0609090 [hep-ph].
- 11328 [316] I. Balitsky and G. A. Chirilli, *Next-to-leading order evolution of color dipoles*, Phys. Rev. **D77** (2008) 014019, arXiv:0710.4330 [hep-ph].
- 11329 [317] E. Iancu, A. Mueller, and S. Munier, *Universal behavior of QCD amplitudes at high energy from general tools of statistical physics*, Phys.Lett. **B606** (2005) 342–350, arXiv:hep-ph/0410018 [hep-ph].
- 11330 [318] Y. V. Kovchegov, J. Kuokkanen, K. Rummukainen, and H. Weigert, *Subleading- $N(c)$  corrections in non-linear small- $x$  evolution*, Nucl.Phys. **A823** (2009) 47–82, arXiv:0812.3238 [hep-ph].
- 11331 [319] A. Dumitru and J. Jalilian-Marian, *Forward dijets in high-energy collisions: Evolution of QCD  $n$ -point functions beyond the dipole approximation*, Phys.Rev. **D82** (2010) 074023, arXiv:1008.0480 [hep-ph].
- 11332 [320] C. Marquet and H. Weigert, *New observables to test the Color Glass Condensate beyond the large- $N_c$  limit*, Nucl.Phys. **A843** (2010) 68–97, arXiv:1003.0813 [hep-ph].
- 11333 [321] Y. Hatta, E. Iancu, C. Marquet, G. Soyez, and D. Triantafyllopoulos, *Diffusive scaling and the high-energy limit of deep inelastic scattering in QCD at large  $N(c)$* , Nucl.Phys. **A773** (2006) 95–155, arXiv:hep-ph/0601150 [hep-ph].
- 11334 [322] S. Munier, *Quantum chromodynamics at high energy and statistical physics*, Phys.Rept. **473** (2009) 1–49, arXiv:0901.2823 [hep-ph]. \* Temporary entry \*.
- 11335 [323] S. Catani and F. Hautmann, *High-energy factorization and small  $x$  deep inelastic scattering beyond leading order*, Nucl. Phys. **B427** (1994) 475–524, arXiv:hep-ph/9405388.
- 11336 [324] F. Caola, S. Forte, and J. Rojo, *Deviations from NLO QCD evolution in inclusive HERA data*, Phys. Lett. **B686** (2010) 127–135, arXiv:0910.3143 [hep-ph].

- 11354 [325] V. S. Fadin and L. N. Lipatov, *BFKL pomeron in the next-to-leading approximation*, Phys. Lett. **B429** (1998) 127–134,  
11355 [arXiv:hep-ph/9802290](#).
- 11356 [326] M. Ciafaloni and G. Camici, *Energy scale(s) and next-to-leading BFKL equation*, Phys. Lett. **B430** (1998) 349–354,  
11357 [arXiv:hep-ph/9803389](#).
- 11358 [327] G. Altarelli, R. D. Ball, and S. Forte, *An anomalous dimension for small  $x$  evolution*, Nucl. Phys. **B674** (2003)  
11359 459–483, [arXiv:hep-ph/0306156](#).
- 11360 [328] G. Altarelli, R. D. Ball, and S. Forte, *Perturbatively stable resummed small  $x$  evolution kernels*, Nucl. Phys. **B742**  
11361 (2006) 1–40, [arXiv:hep-ph/0512237](#).
- 11362 [329] G. Altarelli, R. D. Ball, and S. Forte, *Small  $x$  Resummation with Quarks: Deep-Inelastic Scattering*, Nucl. Phys. **B799**  
11363 (2008) 199–240, [arXiv:0802.0032 \[hep-ph\]](#).
- 11364 [330] M. Ciafaloni, D. Colferai, G. P. Salam, and A. M. Stasto, *Renormalisation group improved small- $x$  Green's function*,  
11365 Phys. Rev. **D68** (2003) 114003, [arXiv:hep-ph/0307188](#).
- 11366 [331] M. Ciafaloni, D. Colferai, G. P. Salam, and A. M. Stasto, *The gluon splitting function at moderately small  $x$* , Phys.  
11367 Lett. **B587** (2004) 87–94, [arXiv:hep-ph/0311325](#).
- 11368 [332] M. Ciafaloni, D. Colferai, G. P. Salam, and A. M. Stasto, *A matrix formulation for small- $x$  singlet evolution*, JHEP **08**  
11369 (2007) 046, [arXiv:0707.1453 \[hep-ph\]](#).
- 11370 [333] J. C. Collins, *Proof of factorization for diffractive hard scattering*, Phys. Rev. **D57** (1998) 3051–3056,  
11371 [arXiv:hep-ph/9709499](#).
- 11372 [334] F. Low, *A Model of the Bare Pomeron*, Phys. Rev. **D12** (1975) 163.
- 11373 [335] S. Nussinov, *Colored Quark Version of Some Hadronic Puzzles*, Phys. Rev. Lett. **34** (1975) 1286.
- 11374 [336] K. J. Golec-Biernat and M. Wusthoff, *Saturation effects in deep inelastic scattering at low  $Q^{*2}$  and its implications on*  
11375 *diffraction*, Phys. Rev. **D59** (1998) 014017, [arXiv:hep-ph/9807513](#).
- 11376 [337] K. J. Golec-Biernat and M. Wusthoff, *Saturation in diffractive deep inelastic scattering*, Phys. Rev. **D60** (1999) 114023,  
11377 [arXiv:hep-ph/9903358](#).
- 11378 [338] N. Armesto, *Nuclear shadowing*, J. Phys. **G32** (2006) R367–R394, [arXiv:hep-ph/0604108](#).
- 11379 [339] L. Frankfurt, M. Strikman, and C. Weiss, *Small- $x$  physics: From HERA to LHC and beyond*, Ann. Rev. Nucl. Part. Sci.  
11380 **55** (2005) 403–465, [arXiv:hep-ph/0507286](#).
- 11381 [340] E. Iancu, K. Itakura, and S. Munier, *Saturation and BFKL dynamics in the HERA data at small  $x$* , Phys. Lett. **B590**  
11382 (2004) 199–208, [arXiv:hep-ph/0310338](#).
- 11383 [341] J. R. Forshaw and G. Shaw, *Gluon saturation in the colour dipole model?*, JHEP **12** (2004) 052, [arXiv:hep-ph/0411337](#).
- 11384 [342] A. M. Stasto, K. J. Golec-Biernat, and J. Kwiecinski, *Geometric scaling for the total  $\gamma^* p$  cross-section in the low*  
11385  *$x$  region*, Phys. Rev. Lett. **86** (2001) 596–599, [arXiv:hep-ph/0007192](#).
- 11386 [343] N. Armesto, C. A. Salgado, and U. A. Wiedemann, *Relating high-energy lepton hadron, proton nucleus and nucleus*  
11387 *nucleus collisions through geometric scaling*, Phys. Rev. Lett. **94** (2005) 022002, [arXiv:hep-ph/0407018](#).
- 11388 [344] C. Marquet and L. Schoeffel, *Geometric scaling in diffractive deep inelastic scattering*, Phys. Lett. **B639** (2006)  
11389 471–477, [arXiv:hep-ph/0606079](#).
- 11390 [345] V. Goncalves and M. Machado, *Geometric scaling in inclusive charm production*, Phys.Rev.Lett. **91** (2003) 202002,  
11391 [arXiv:hep-ph/0307090 \[hep-ph\]](#).
- 11392 [346] L. McLerran and M. Praszalowicz, *Saturation and Scaling of Multiplicity, Mean  $p_T$  and  $p_T$  Distributions from 200*  
11393 *GeV  $lt \sqrt{s} lt 7$  TeV*, Acta Phys.Polon. **B41** (2010) 1917–1926, [arXiv:1006.4293 \[hep-ph\]](#).
- 11394 [347] F. Caola and S. Forte, *Geometric Scaling from GLAP evolution*, Phys. Rev. Lett. **101** (2008) 022001, [arXiv:0802.1878](#)  
11395 [\[hep-ph\]](#).
- 11396 [348] N. N. Nikolaev and B. G. Zakharov, *Colour transparency and scaling properties of nuclear shadowing in deep inelastic*  
11397 *scattering*, Z. Phys. **C49** (1991) 607–618.
- 11398 [349] N. Nikolaev and B. G. Zakharov, *Pomeron structure function and diffraction dissociation of virtual photons in*  
11399 *perturbative QCD*, Z. Phys. **C53** (1992) 331–346.
- 11400 [350] A. H. Mueller and B. Patel, *Single and double BFKL pomeron exchange and a dipole picture of high-energy hard*  
11401 *processes*, Nucl. Phys. **B425** (1994) 471–488, [arXiv:hep-ph/9403256](#).
- 11402 [351] A. H. Mueller, *Unitarity and the BFKL pomeron*, Nucl. Phys. **B437** (1995) 107–126, [arXiv:hep-ph/9408245](#).
- 11403 [352] M. L. Good and W. D. Walker, *Diffraction dissociation of beam particles*, Phys. Rev. **120** (1960) 1857–1860.
- 11404 [353] A. H. Mueller, *Parton saturation: An overview*, [arXiv:hep-ph/0111244](#).
- 11405 [354] J. Bartels, K. J. Golec-Biernat, and H. Kowalski, *A modification of the saturation model: DGLAP evolution*, Phys.  
11406 Rev. **D66** (2002) 014001, [arXiv:hep-ph/0203258](#).

- 11407 [355] H. Kowalski and D. Teaney, *An impact parameter dipole saturation model*, Phys. Rev. **D68** (2003) 114005,  
11408 [arXiv:hep-ph/0304189](#).
- 11409 [356] H. Kowalski, L. Motyka, and G. Watt, *Exclusive diffractive processes at HERA within the dipole picture*, Phys. Rev.  
11410 **D74** (2006) 074016, [arXiv:hep-ph/0606272](#).
- 11411 [357] A. D. Martin, R. G. Roberts, W. J. Stirling, and R. S. Thorne, *Uncertainties of predictions from parton distributions. I:  
11412 Experimental errors. ((T))*, Eur. Phys. J. **C28** (2003) 455–473, [arXiv:hep-ph/0211080](#).
- 11413 [358] A. D. Martin, W. J. Stirling, R. S. Thorne, and G. Watt, *Update of Parton Distributions at NNLO*, Phys. Lett. **B652**  
11414 (2007) 292–299, [arXiv:0706.0459](#) [[hep-ph](#)].
- 11415 [359] P. M. Nadolsky et al., *Implications of CTEQ global analysis for collider observables*, Phys. Rev. **D78** (2008) 013004,  
11416 [arXiv:0802.0007](#) [[hep-ph](#)].
- 11417 [360] G. Watt, A. D. Martin, W. J. Stirling, and R. S. Thorne, *Recent Progress in Global PDF Analysis*, [arXiv:0806.4890](#)  
11418 [[hep-ph](#)].
- 11419 [361] A. Martin, W. Stirling, R. Thorne, and G. Watt, *Parton distributions for the LHC*, Eur.Phys.J. **C63** (2009) 189–285,  
11420 [arXiv:0901.0002](#) [[hep-ph](#)].
- 11421 [362] H.-L. Lai, J. Huston, Z. Li, P. Nadolsky, J. Pumplin, et al., *Uncertainty induced by QCD coupling in the CTEQ global  
11422 analysis of parton distributions*, Phys.Rev. **D82** (2010) 054021, [arXiv:1004.4624](#) [[hep-ph](#)].
- 11423 [363] R. D. Ball et al., *A first unbiased global NLO determination of parton distributions and their uncertainties*, Nucl. Phys.  
11424 **B838** (2010) 136–206, [arXiv:1002.4407](#) [[hep-ph](#)].
- 11425 [364] J. R. Forshaw, R. Sandapen, and G. Shaw, *Further success of the colour dipole model*, JHEP **11** (2006) 025,  
11426 [arXiv:hep-ph/0608161](#).
- 11427 [365] H.-L. Lai, M. Guzzi, J. Huston, Z. Li, P. M. Nadolsky, et al., *New parton distributions for collider physics*, Phys.Rev.  
11428 **D82** (2010) 074024, [arXiv:1007.2241](#) [[hep-ph](#)].
- 11429 [366] R. D. Ball and R. K. Ellis, *Heavy quark production at high-energy*, JHEP **05** (2001) 053, [arXiv:hep-ph/0101199](#).
- 11430 [367] S. Marzani, R. D. Ball, V. Del Duca, S. Forte, and A. Vicini, *Higgs production via gluon-gluon fusion with finite top  
11431 mass beyond next-to-leading order*, Nucl. Phys. **B800** (2008) 127–145, [arXiv:0801.2544](#) [[hep-ph](#)].
- 11432 [368] S. Marzani, R. D. Ball, V. Del Duca, S. Forte, and A. Vicini, *Finite-top-mass effects in NNLO Higgs production*, Nucl.  
11433 Phys. Proc. Suppl. **186** (2009) 98–101, [arXiv:0809.4934](#) [[hep-ph](#)].
- 11434 [369] S. Marzani and R. D. Ball, *High Energy Resummation of Drell-Yan Processes*, Nucl. Phys. **B814** (2009) 246–264,  
11435 [arXiv:0812.3602](#) [[hep-ph](#)].
- 11436 [370] S. Marzani and R. D. Ball, *Drell-Yan processes in the high-energy limit*, [arXiv:0906.4729](#) [[hep-ph](#)].
- 11437 [371] G. Diana, *High-energy resummation in direct photon production*, Nucl. Phys. **B824** (2010) 154–167, [arXiv:0906.4159](#)  
11438 [[hep-ph](#)].
- 11439 [372] G. Diana, J. Rojo, and R. D. Ball, *High energy resummation of direct photon production at hadronic colliders*,  
11440 Phys.Lett. **B693** (2010) 430–437, [arXiv:1006.4250](#) [[hep-ph](#)].
- 11441 [373] S. Forte, G. Altarelli, and R. D. Ball, *Can we trust small  $x$  resummation?*, Nucl. Phys. Proc. Suppl. **191** (2009) 64–75,  
11442 [arXiv:0901.1294](#) [[hep-ph](#)].
- 11443 [374] M. Dittmar et al., *Parton Distributions*, [arXiv:0901.2504](#) [[hep-ph](#)].
- 11444 [375] J. Rojo, G. Altarelli, R. D. Ball, and S. Forte, *Towards small  $x$  resummed DIS phenomenology*, [arXiv:0907.0443](#)  
11445 [[hep-ph](#)].
- 11446 [376] J. Rojo and F. Caola, *Parton distributions and small- $x$  QCD at the Large Hadron Electron Collider*, [arXiv:0906.2079](#)  
11447 [[hep-ph](#)].
- 11448 [377] C. Salgado, J. Alvarez-Muniz, F. Arleo, N. Armesto, M. Botje, et al., *Proton-Nucleus Collisions at the LHC: Scientific  
11449 Opportunities and Requirements*, [arXiv:1105.3919](#) [[hep-ph](#)]. \* Temporary entry \*.
- 11450 [378] D. G. d’Enterria, *Quarkonia photoproduction at nucleus colliders*, Nucl.Phys.Proc.Suppl. **184** (2008) 158–162,  
11451 [arXiv:0711.1123](#) [[nucl-ex](#)].
- 11452 [379] D. d’Enterria, *Forward jets physics in ATLAS, CMS and LHCb*, [arXiv:0911.1273](#) [[hep-ex](#)].
- 11453 [380] R. Ichou and D. d’Enterria, *Sensitivity of isolated photon production at TeV hadron colliders to the gluon distribution  
11454 in the proton*, Phys.Rev. **D82** (2010) 014015, [arXiv:1005.4529](#) [[hep-ph](#)].
- 11455 [381] LHCb Collaboration, F. de Lorenzi et al. Proceedings of DIS2010.
- 11456 [382] J. M. Jowett, *The LHC as a Nucleus-Nucleus Collider*, J.Phys.G **G35** (2008) 104028, [arXiv:0807.1397](#) [[nucl-ex](#)]. \*  
11457 Temporary entry \*.
- 11458 [383] P. Quiroga-Arias, J. G. Milhano, and U. A. Wiedemann, *Testing nuclear parton distributions with pA collisions at the  
11459 TeV scale*, Phys.Rev. **C82** (2010) 034903, [arXiv:1002.2537](#) [[hep-ph](#)].

- 11460 [384] K. Eskola, V. Kolhinen, and R. Vogt, *Obtaining the nuclear gluon distribution from heavy quark decays to lepton pairs in  $pA$  collisions*, Nucl.Phys. **A696** (2001) 729–746, arXiv:hep-ph/0104124 [hep-ph].
- 11461
- 11462 [385] F. Arleo and T. Gousset, *Measuring gluon shadowing with prompt photons at RHIC and LHC*, Phys.Lett. **B660** (2008) 181–187, arXiv:0707.2944 [hep-ph].
- 11463
- 11464 [386] H. Paukkunen and C. A. Salgado, *Constraints for the nuclear parton distributions from  $Z$  and  $W$  production at the LHC*, JHEP **1103** (2011) 071, arXiv:1010.5392 [hep-ph].
- 11465
- 11466 [387] A. Baltz, G. Baur, D. d’Enterria, L. Frankfurt, F. Gelis, et al., *The Physics of Ultrapерipheral Collisions at the LHC*, Phys.Rept. **458** (2008) 1–171, arXiv:0706.3356 [nucl-ex].
- 11467
- 11468 [388] BRAHMS Collaboration, I. Arsene et al., *On the evolution of the nuclear modification factors with rapidity and centrality in  $d + Au$  collisions at  $s(NN)^{1/2} = 200\text{-GeV}$* , Phys.Rev.Lett. **93** (2004) 242303, arXiv:nucl-ex/0403005 [nucl-ex].
- 11469
- 11470
- 11471 [389] B. Kopeliovich, J. Nemchik, I. Potashnikova, M. Johnson, and I. Schmidt, *Breakdown of QCD factorization at large Feynman  $x$* , Phys.Rev. **C72** (2005) 054606, arXiv:hep-ph/0501260 [hep-ph].
- 11472
- 11473 [390] STAR Collaboration, E. Braidot, *Suppression of Forward Pion Correlations in  $d+Au$  Interactions at STAR*, arXiv:1005.2378 [hep-ph].
- 11474
- 11475 [391] L. Frankfurt and M. Strikman, *Energy losses in the black disc regime and correlation effects in the STAR forward pion production in  $d Au$  collisions*, Phys.Lett. **B645** (2007) 412–421, arXiv:nucl-th/0603049 [nucl-th].
- 11476
- 11477 [392] J. L. Albacete and C. Marquet, *Azimuthal correlations of forward di-hadrons in  $d+Au$  collisions at RHIC in the Color Glass Condensate*, Phys.Rev.Lett. **105** (2010) 162301, arXiv:1005.4065 [hep-ph].
- 11478
- 11479 [393] PHENIX Collaboration, A. Adare et al., *Suppression of back-to-back hadron pairs at forward rapidity in  $d+Au$  Collisions at  $\sqrt{s_{NN}} = 200\text{ GeV}$* , arXiv:1105.5112 [nucl-ex]. \* Temporary entry \*.
- 11480
- 11481 [394] F. Arleo et al., *Photon physics in heavy ion collisions at the LHC*, arXiv:hep-ph/0311131.
- 11482
- 11483 [395] STAR Collaboration, B. Abelev et al., *Three-particle coincidence of the long range pseudorapidity correlation in high energy nucleus-nucleus collisions*, Phys.Rev.Lett. **105** (2010) 022301, arXiv:0912.3977 [hep-ex].
- 11484
- 11485 [396] CMS Collaboration, V. Khachatryan et al., *Observation of Long-Range Near-Side Angular Correlations in Proton-Proton Collisions at the LHC*, JHEP **1009** (2010) 091, arXiv:1009.4122 [hep-ex].
- 11486
- 11487 [397] CMS Collaboration, S. Chatrchyan et al., *Long-range and short-range dihadron angular correlations in central PbPb collisions at a nucleon-nucleon center of mass energy of 2.76 TeV*, arXiv:1105.2438 [nucl-ex]. \* Temporary entry \*.
- 11488
- 11489 [398] A. Dumitru, K. Dusling, F. Gelis, J. Jalilian-Marian, T. Lappi, et al., *The Ridge in proton-proton collisions at the LHC*, Phys.Lett. **B697** (2011) 21–25, arXiv:1009.5295 [hep-ph].
- 11490
- 11491 [399] N. Armesto, *Predictions for the heavy-ion programme at the Large Hadron Collider*, arXiv:0903.1330 [hep-ph].
- 11492
- 11493 [400] ALICE Collaboration, K. Aamodt et al., *Charged-particle multiplicity density at mid-rapidity in central Pb-Pb collisions at  $\sqrt{s_{NN}} = 2.76\text{ TeV}$* , Phys.Rev.Lett. **105** (2010) 252301, arXiv:1011.3916 [nucl-ex]. \* Temporary entry \*.
- 11494
- 11495 [401] ALICE Collaboration, J. Nystrand, *Photon-Induced Physics with Heavy-Ion Beams in ALICE*, Nucl.Phys.Proc.Suppl. **179-180** (2008) 156–161, arXiv:0807.0366 [nucl-ex].
- 11496
- 11497 [402] M. Arneodo, *Nuclear effects in structure functions*, Phys. Rept. **240** (1994) 301–393.
- 11498
- 11499 [403] D. F. Geesaman, K. Saito, and A. W. Thomas, *The nuclear EMC effect*, Ann. Rev. Nucl. Part. Sci. **45** (1995) 337–390.
- 11500
- 11501 [404] A. Accardi et al., *Hard probes in heavy ion collisions at the lhc: pdfs, shadowing and pa collisions*, arXiv:hep-ph/0308248.
- 11502
- 11503 [405] D. de Florian and R. Sassot, *Nuclear parton distributions at next to leading order*, Phys. Rev. **D69** (2004) 074028, arXiv:hep-ph/0311227.
- 11504
- 11505 [406] M. Hirai, S. Kumano, and T. H. Nagai, *Determination of nuclear parton distribution functions and their uncertainties at next-to-leading order*, Phys. Rev. **C76** (2007) 065207, arXiv:0709.3038 [hep-ph].
- 11506
- 11507 [407] V. Guzey and M. Strikman, *Color fluctuation approximation for multiple interactions in leading twist theory of nuclear shadowing*, Phys. Lett. **B687** (2010) 167–173, arXiv:0908.1149 [hep-ph].
- 11508
- 11509 [408] K. J. Eskola, V. J. Kolhinen, and C. A. Salgado, *The scale dependent nuclear effects in parton distributions for practical applications*, Eur. Phys. J. **C9** (1999) 61–68, arXiv:hep-ph/9807297.
- 11510
- 11511 [409] H. Paukkunen and C. A. Salgado, *Compatibility of neutrino DIS data and global analyses of parton distribution functions*, JHEP **07** (2010) 032, arXiv:1004.3140 [hep-ph].
- 11512
- 11513 [410] A. Accardi et al., *Hard probes in heavy ion collisions at the LHC: Jet physics*, arXiv:hep-ph/0310274.
- 11514
- 11515 [411] M. Bedjidian et al., *Hard probes in heavy ion collisions at the LHC: Heavy flavor physics*, arXiv:hep-ph/0311048.
- 11516
- 11517 [412] M. Gyulassy and L. McLerran, *New forms of QCD matter discovered at RHIC*, Nucl. Phys. **A750** (2005) 30–63, arXiv:nucl-th/0405013.



- 11513 [413] D. G. d'Enterria, *Quark-gluon matter*, J. Phys. **G34** (2007) S53–S82, [arXiv:nucl-ex/0611012](#).
- 11514 [414] T. Lappi, *Initial conditions of heavy ion collisions and high energy factorization*, Acta Phys. Polon. **B40** (2009)  
11515 1997–2012, [arXiv:0904.1670 \[hep-ph\]](#).
- 11516 [415] A. Accardi, F. Arleo, W. K. Brooks, D. D'Enterria, and V. Muccifora, *Parton Propagation and Fragmentation in QCD*  
11517 *Matter*, Riv. Nuovo Cim. **032** (2010) 439–553, [arXiv:0907.3534 \[nucl-th\]](#).
- 11518 [416] ALICE Collaboration, K. Aamodt et al., *Suppression of Charged Particle Production at Large Transverse Momentum*  
11519 *in Central Pb–Pb Collisions at  $\sqrt{s_{NN}} = 2.76$  TeV*, Phys.Lett. **B696** (2011) 30–39, [arXiv:1012.1004 \[nucl-ex\]](#). \*  
11520 Temporary entry \*.
- 11521 [417] Atlas Collaboration, G. Aad et al., *Observation of a Centrality-Dependent Dijet Asymmetry in Lead-Lead Collisions at*  
11522  *$\sqrt{s(NN)} = 2.76$  TeV with the ATLAS Detector at the LHC*, Phys.Rev.Lett. **105** (2010) 252303, [arXiv:1011.6182](#)  
11523 [\[hep-ex\]](#). \* Temporary entry \*.
- 11524 [418] CMS Collaboration, S. Chatrchyan et al., *Observation and studies of jet quenching in PbPb collisions at*  
11525 *nucleon-nucleon center-of-mass energy = 2.76 TeV*, [arXiv:1102.1957 \[nucl-ex\]](#). \* Temporary entry \*.
- 11526 [419] The NNPDF Collaboration, R. D. Ball et al., *Precision determination of electroweak parameters and the strange content*  
11527 *of the proton from neutrino deep-inelastic scattering*, Nucl. Phys. **B823** (2009) 195–233, [arXiv:0906.1958 \[hep-ph\]](#).
- 11528 [420] K. Golec-Biernat and A. M. Stasto,  *$F_L$  proton structure function from the unified DGLAP/BFKL approach*, Phys.  
11529 Rev. **D80** (2009) 014006, [arXiv:0905.1321 \[hep-ph\]](#).
- 11530 [421] J. L. Albacete, N. Armesto, J. G. Milhano, and C. A. Salgado, *Non-linear QCD meets data: A global analysis of lepton-*  
11531 *proton scattering with running coupling BK evolution*, Phys. Rev. **D80** (2009) 034031, [arXiv:0902.1112 \[hep-ph\]](#).
- 11532 [422] The NNPDF Collaboration, and others, *Reweighting NNPDFs: the W lepton asymmetry*, [arXiv:1012.0836 \[hep-ph\]](#).
- 11533 [423] NNPDF Collaboration, R. D. Ball et al., *A determination of parton distributions with faithful uncertainty estimation*,  
11534 Nucl. Phys. **B809** (2009) 1–63, [arXiv:0808.1231 \[hep-ph\]](#).
- 11535 [424] J. Jowett. Private communication.
- 11536 [425] N. Armesto, *A simple model for nuclear structure functions at small x in the dipole picture*, Eur. Phys. J. **C26** (2002)  
11537 35–43, [arXiv:hep-ph/0206017](#).
- 11538 [426] PHENIX Collaboration, S. S. Adler et al., *Centrality dependence of pi0 and eta production at large transverse*  
11539 *momentum in  $s(NN)^{1/2} = 200$ -GeV d + Au collisions*, Phys. Rev. Lett. **98** (2007) 172302,  
11540 [arXiv:nucl-ex/0610036](#).
- 11541 [427] S. J. Brodsky, I. Schmidt, and J.-J. Yang, *Nuclear antishadowing in neutrino deep inelastic scattering*, Phys.Rev. **D70**  
11542 (2004) 116003, [arXiv:hep-ph/0409279 \[hep-ph\]](#).
- 11543 [428] E. R. Cazaroto, F. Carvalho, V. P. Goncalves, and F. S. Navarra, *Constraining the nuclear gluon distribution in eA*  
11544 *processes at RHIC*, Phys. Lett. **B669** (2008) 331–336, [arXiv:0804.2507 \[hep-ph\]](#).
- 11545 [429] N. Armesto, H. Paukkunen, C. A. Salgado, and K. Tywoniuk, *Nuclear effects on the longitudinal structure function at*  
11546 *small x*, Phys.Lett. **B694** (2010) 38–43, [arXiv:1005.2035 \[hep-ph\]](#).
- 11547 [430] A. Bruni, X. Janssen, and P. Marage, *Exclusive Vector Meson Production and Deeply Virtual Compton Scattering at*  
11548 *HERA*, Proceedings of the HERA-LHC Workshops, 2006-8, eds. Jung, de Roeck, DESY-PROC-2009-02 (2009) 427,  
11549 2009.
- 11550 [431] A. D. Martin, C. Nockles, M. G. Ryskin, and T. Teubner, *Small x gluon from exclusive J/psi production*, Phys. Lett.  
11551 **B662** (2008) 252–258, [arXiv:0709.4406 \[hep-ph\]](#).
- 11552 [432] A. Caldwell and H. Kowalski, *Investigating the gluonic structure of nuclei via J/psi scattering*, Phys. Rev. **C81** (2010)  
11553 025203.
- 11554 [433] S. Munier, A. M. Stasto, and A. H. Mueller, *Impact parameter dependent S-matrix for dipole proton scattering from*  
11555 *diffractive meson electroproduction*, Nucl. Phys. **B603** (2001) 427–445, [arXiv:hep-ph/0102291](#).
- 11556 [434] K. Goeke, M. V. Polyakov, and M. Vanderhaeghen, *Hard Exclusive Reactions and the Structure of Hadrons*, Prog. Part.  
11557 Nucl. Phys. **47** (2001) 401–515, [arXiv:hep-ph/0106012](#).
- 11558 [435] M. Diehl, *Generalized parton distributions*, Phys. Rept. **388** (2003) 41–277, [arXiv:hep-ph/0307382](#).
- 11559 [436] S. J. Brodsky, L. Frankfurt, J. F. Gunion, A. H. Mueller, and M. Strikman, *Diffractive leptonproduction of vector mesons*  
11560 *in QCD*, Phys. Rev. **D50** (1994) 3134–3144, [arXiv:hep-ph/9402283](#).
- 11561 [437] J. C. Collins, L. Frankfurt, and M. Strikman, *Factorization for hard exclusive electroproduction of mesons in QCD*,  
11562 Phys. Rev. **D56** (1997) 2982–3006, [arXiv:hep-ph/9611433](#).
- 11563 [438] M. Burkardt, *Impact parameter dependent parton distributions and off-forward parton distributions for zeta -z 0*,  
11564 Phys. Rev. **D62** (2000) 071503, [arXiv:hep-ph/0005108](#).
- 11565 [439] T. Rogers, V. Guzey, M. Strikman, and X. Zu, *Determining the proximity of gamma\* N scattering to the black body*  
11566 *limit using DIS and J/psi production*, Phys. Rev. **D69** (2004) 074011, [arXiv:hep-ph/0309099](#).

- 11567 [440] H. Kowalski, T. Lappi, and R. Venugopalan, *Nuclear enhancement of universal dynamics of high parton densities*,  
11568 Phys. Rev. Lett. **100** (2008) 022303, [arXiv:0705.3047 \[hep-ph\]](#).
- 11569 [441] L. Frankfurt, M. Strikman, and C. Weiss, *Dijet production as a centrality trigger for pp collisions at CERN LHC*,  
11570 Phys. Rev. **D69** (2004) 114010, [arXiv:hep-ph/0311231](#).
- 11571 [442] H1 Collaboration, F. D. Aaron et al., *Diffraction Dijet Photoproduction in ep Collisions at HERA*, Eur. Phys. J. **C70**  
11572 (2010) 15–37, [arXiv:1006.0946 \[hep-ex\]](#).
- 11573 [443] L. Frankfurt, C. E. Hyde, M. Strikman, and C. Weiss, *Generalized parton distributions and rapidity gap survival in*  
11574 *exclusive diffractive pp scattering*, Phys. Rev. **D75** (2007) 054009, [arXiv:hep-ph/0608271](#).
- 11575 [444] M. Deile et al., *13th International Conference on Elastic and Diffractive Scattering (Blois Workshop) - Moving*  
11576 *Forward into the LHC Era*, [arXiv:1002.3527 \[hep-ph\]](#).
- 11577 [445] ZEUS Collaboration, S. Chekanov et al., *Exclusive electroproduction of J/psi mesons at HERA*, Nucl. Phys. **B695**  
11578 (2004) 3–37, [arXiv:hep-ex/0404008](#).
- 11579 [446] H1 Collaboration, A. Aktas et al., *Elastic J/psi production at HERA*, Eur. Phys. J. **C46** (2006) 585–603,  
11580 [arXiv:hep-ex/0510016](#).
- 11581 [447] H1 Collaboration, F. D. Aaron et al., *Measurement of Deeply Virtual Compton Scattering and its t-dependence at*  
11582 *HERA*, Phys. Lett. **B659** (2008) 796–806, [arXiv:0709.4114 \[hep-ex\]](#).
- 11583 [448] ZEUS Collaboration, S. Chekanov et al., *A measurement of the Q<sup>2</sup>, W and t dependences of deeply virtual Compton*  
11584 *scattering at HERA*, JHEP **05** (2009) 108, [arXiv:0812.2517 \[hep-ex\]](#).
- 11585 [449] C. Marquet and B. Wu, *Exclusive vs. diffractive vector meson production in DIS at small x or off nuclei*,  
11586 [arXiv:0908.4180 \[hep-ph\]](#).
- 11587 [450] T. Lappi and H. Mantysaari, *Incoherent diffractive J/Psi-production in high energy nuclear DIS*, (2010) ,  
11588 [arXiv:1011.1988 \[hep-ph\]](#).
- 11589 [451] W. Horowitz, *Measuring the Gluon Density in e + A Collisions: KLN CGC, DGLAP Glauber, or Neither?*,  
11590 [arXiv:1102.5058 \[hep-ph\]](#). \* Temporary entry \*.
- 11591 [452] L. Frankfurt, M. Strikman, D. Treleani, and C. Weiss, *Evidence for color fluctuations in the nucleon in high- energy*  
11592 *scattering*, Phys. Rev. Lett. **101** (2008) 202003, [arXiv:0808.0182 \[hep-ph\]](#).
- 11593 [453] J. Bartels, K. J. Golec-Biernat, and K. Peters, *On the dipole picture in the nonforward direction*, Acta Phys. Polon.  
11594 **B34** (2003) 3051–3068, [arXiv:hep-ph/0301192](#).
- 11595 [454] C. Marquet, R. B. Peschanski, and G. Soyez, *Exclusive vector meson production at HERA from QCD with saturation*,  
11596 Phys.Rev. **D76** (2007) 034011, [arXiv:hep-ph/0702171 \[HEP-PH\]](#).
- 11597 [455] M. G. Ryskin, *Diffractive J / psi electroproduction in LLA QCD*, Z. Phys. **C57** (1993) 89–92.
- 11598 [456] P. Newman, *Low x and Diffractive Physics at a Large Hadron electron Collider*, . In Proceedings of the 13th  
11599 International (Blois) Conference on Elastic and Diffractive Scattering, EDS’09, CERN, 2009, p182.
- 11600 [457] B. List and A. Mastroberardino, *DIFVIM: A Monte Carlo generator for diffractive processes in ep scattering*,  
11601 Proceedings of the Workshop on Monte Carlo Generators for HERA Physics, DESY-PROC-1992-02 (1999) 396, 1999.
- 11602 [458] J. R. Forshaw, R. Sandapen, and G. Shaw, *Colour dipoles and rho, Phi electroproduction*, Phys. Rev. **D69** (2004)  
11603 094013, [arXiv:hep-ph/0312172](#).
- 11604 [459] ZEUS Collaboration, S. Chekanov et al., *Exclusive photoproduction of J/psi mesons at HERA*, Eur. Phys. J. **C24**  
11605 (2002) 345–360, [arXiv:hep-ex/0201043](#).
- 11606 [460] ZEUS Collaboration, J. Breitweg et al., *Measurement of elastic Upsilon photoproduction at HERA*, Phys. Lett. **B437**  
11607 (1998) 432–444, [arXiv:hep-ex/9807020](#).
- 11608 [461] H1 Collaboration, C. Adloff et al., *Elastic photoproduction of J/psi and Upsilon mesons at HERA*, Phys. Lett. **B483**  
11609 (2000) 23–35, [arXiv:hep-ex/0003020](#).
- 11610 [462] ZEUS Collaboration, S. Chekanov et al., *Exclusive photoproduction of upsilon mesons at HERA*, Phys. Lett. **B680**  
11611 (2009) 4–12, [arXiv:0903.4205 \[hep-ex\]](#).
- 11612 [463] B. E. Cox, J. R. Forshaw, and R. Sandapen, *Diffractive upsilon production at the LHC*, JHEP **06** (2009) 034,  
11613 [arXiv:0905.0102 \[hep-ph\]](#).
- 11614 [464] E. Perez, L. Schoeffel, and L. Favart, *MILOU: A Monte-Carlo for deeply virtual Compton scattering*,  
11615 [arXiv:hep-ph/0411389 \[hep-ph\]](#).
- 11616 [465] L. Frankfurt, A. Freund, and M. Strikman, *Diffractive exclusive photoproduction in DIS at HERA*, Phys.Rev. **D58**  
11617 (1998) 114001, [arXiv:hep-ph/9710356 \[hep-ph\]](#).
- 11618 [466] H1 Collaboration, F. Aaron et al., *Deeply Virtual Compton Scattering and its Beam Charge Asymmetry in e+-*  
11619 *Collisions at HERA*, Phys.Lett. **B681** (2009) 391–399, [arXiv:arXiv:0907.5289 \[hep-ex\]](#).
- 11620 [467] Fermilab Tagged Photon Spectrometer Collaboration, M. D. Sokoloff et al., *An Experimental Study of the a-Dependence*  
11621 *of J/psi Photoproduction*, Phys. Rev. Lett. **57** (1986) 3003.

- 11622 [468] E665 Collaboration, M. R. Adams et al., *Measurement of nuclear transparencies from exclusive rho0 meson production*  
11623 *in muon - nucleus scattering at 470-GeV*, Phys. Rev. Lett. **74** (1995) 1525–1529.
- 11624 [469] L. Frankfurt, V. Guzey, and M. Strikman, *Leading twist nuclear shadowing phenomena in hard processes with nuclei*,  
11625 [arXiv:1106.2091 \[hep-ph\]](#).
- 11626 [470] B. Nicolescu, *Recent advances in odderon physics*, [arXiv:hep-ph/9911334 \[hep-ph\]](#).
- 11627 [471] C. Ewerz, *The Odderon in quantum chromodynamics*, [arXiv:hep-ph/0306137 \[hep-ph\]](#).
- 11628 [472] J. Bartels, *High-Energy Behavior in a Nonabelian Gauge Theory. 1.  $T(n,m)$  in the Leading Log Normal  $S$*   
11629 *Approximation*, Nucl.Phys. **B151** (1979) 293.
- 11630 [473] J. Bartels, *High-Energy Behavior in a Nonabelian Gauge Theory. 2. First Corrections to  $T(n,m)$  Beyond the Leading*  
11631 *LNS Approximation*, Nucl.Phys. **B175** (1980) 365.
- 11632 [474] J. Kwiecinski and M. Praszalowicz, *Three Gluon Integral Equation and Odd  $c$  Singlet Regge Singularities in QCD*,  
11633 Phys.Lett. **B94** (1980) 413.
- 11634 [475] R. Janik and J. Wosiek, *Solution of the odderon problem*, Phys.Rev.Lett. **82** (1999) 1092–1095, [arXiv:hep-th/9802100](#)  
11635 [\[hep-th\]](#).
- 11636 [476] J. Bartels, L. Lipatov, and G. Vacca, *A New odderon solution in perturbative QCD*, Phys.Lett. **B477** (2000) 178–186,  
11637 [arXiv:hep-ph/9912423 \[hep-ph\]](#).
- 11638 [477] H1 Collaboration, C. Adloff et al., *Search for odderon induced contributions to exclusive pi0 photoproduction at HERA*,  
11639 Phys.Lett. **B544** (2002) 35–43, [arXiv:hep-ex/0206073 \[hep-ex\]](#).
- 11640 [478] J. Czyzewski, J. Kwiecinski, L. Motyka, and M. Sadzikowski, *Exclusive eta(c) photoproduction and electroproduction at*  
11641 *HERA as a possible probe of the odderon singularity in QCD*, Phys.Lett. **B398** (1997) 400–406, [arXiv:hep-ph/9611225](#)  
11642 [\[hep-ph\]](#).
- 11643 [479] S. J. Brodsky, J. Rathsman, and C. Merino, *Odderon-Pomeron interference*, Phys.Lett. **B461** (1999) 114–122,  
11644 [arXiv:hep-ph/9904280 \[hep-ph\]](#).
- 11645 [480] A. Kaidalov, *Diffraction Production Mechanisms*, Phys.Rept. **50** (1979) 157–226.
- 11646 [481] K. A. Goulianos, *Diffraction Interactions of Hadrons at High-Energies*, Phys. Rept. **101** (1983) 169.
- 11647 [482] G. Ingelman and P. E. Schlein, *Jet Structure in High Mass Diffraction Scattering*, Phys. Lett. **B152** (1985) 256.
- 11648 [483] A. Donnachie and P. V. Landshoff, *Diffraction Deep Inelastic Lepton Scattering*, Phys. Lett. **B191** (1987) 309.
- 11649 [484] G. Wolf, *Review of High Energy Diffraction in Real and Virtual Photon Proton scattering at HERA*, Rept. Prog. Phys.  
11650 **73** (2010) 116202, [arXiv:0907.1217 \[hep-ex\]](#).
- 11651 [485] H1 Collaboration, A. Aktas et al., *Diffraction deep-inelastic scattering with a leading proton at HERA*, Eur. Phys. J.  
11652 **C48** (2006) 749–766, [arXiv:hep-ex/0606003](#).
- 11653 [486] ZEUS Collaboration, S. Chekanov et al., *Deep inelastic scattering with leading protons or large rapidity gaps at HERA*,  
11654 Nucl. Phys. **B816** (2009) 1–61, [arXiv:0812.2003 \[hep-ex\]](#).
- 11655 [487] F. Aaron et al., *Measurement of the Diffraction Deep-Inelastic Scattering Cross Section with a Leading Proton at*  
11656 *HERA*, [arXiv:1010.1476 \[hep-ex\]](#).
- 11657 [488] H1 Collaboration, A. Aktas et al., *Measurement and QCD analysis of the diffraction deep- inelastic scattering*  
11658 *cross-section at HERA*, Eur. Phys. J. **C48** (2006) 715–748, [arXiv:hep-ex/0606004](#).
- 11659 [489] J. Blumlein and D. Robaschik, *On the scaling violations of diffraction structure functions: Operator approach*, Phys.  
11660 Lett. **B517** (2001) 222–232, [arXiv:hep-ph/0106037](#).
- 11661 [490] H1 Collaboration, A. Aktas et al., *Dijet Cross Sections and Parton Densities in Diffraction DIS at HERA*, JHEP **10**  
11662 (2007) 042, [arXiv:0708.3217 \[hep-ex\]](#).
- 11663 [491] ZEUS Collaboration, S. Chekanov et al., *A QCD analysis of ZEUS diffraction data*, Nucl. Phys. **B831** (2010) 1–25,  
11664 [arXiv:0911.4119 \[hep-ex\]](#).
- 11665 [492] A. D. Martin, M. G. Ryskin, and G. Watt, *Diffraction parton distributions from perturbative QCD*, Eur. Phys. J. **C44**  
11666 (2005) 69–85, [arXiv:hep-ph/0504132](#).
- 11667 [493] H1 Collaboration, A. Aktas et al., *Tests of QCD factorisation in the diffraction production of dijets in deep-inelastic*  
11668 *scattering and photoproduction at HERA*, Eur. Phys. J. **C51** (2007) 549–568, [arXiv:hep-ex/0703022](#).
- 11669 [494] H1 Collaboration, A. Aktas et al., *Diffraction open charm production in deep-inelastic scattering and photoproduction*  
11670 *at HERA*, Eur. Phys. J. **C50** (2007) 1–20, [arXiv:hep-ex/0610076](#).
- 11671 [495] P. Newman, *Deep Inelastic Scattering at the TeV Energy Scale and the LHeC Project*, Nucl. Phys. Proc. Suppl. **191**  
11672 (2009) 307–319, [arXiv:0902.2292 \[hep-ex\]](#).
- 11673 [496] J. Bartels, J. R. Ellis, H. Kowalski, and M. Wusthoff, *An analysis of diffraction in deep-inelastic scattering*, Eur. Phys.  
11674 J. **C7** (1999) 443–458, [arXiv:hep-ph/9803497](#).
- 11675 [497] H. Collaboration, *Measurement of the Diffraction Longitudinal Structure Function at HERA*, . in litt.

- 11676 [498] H1 Collaboration, F. D. Aaron et al., *Measurement of Leading Neutron Production in Deep- Inelastic Scattering at*  
11677 *HERA*, Eur. Phys. J. **C68** (2010) 381–399, [arXiv:1001.0532 \[hep-ex\]](#).
- 11678 [499] G. Watt and H. Kowalski, *Impact parameter dependent colour glass condensate dipole model*, Phys. Rev. **D78** (2008)  
11679 014016, [arXiv:0712.2670 \[hep-ph\]](#).
- 11680 [500] V. A. Abramovsky, V. N. Gribov, and O. V. Kancheli, *Character of inclusive spectra and fluctuations produced in*  
11681 *inelastic processes by multi-pomeron exchange*, Yad. Fiz. **18** (1973) 595–616.
- 11682 [501] L. Frankfurt and M. Strikman, *Diffraction at HERA, color opacity and nuclear shadowing*, Eur. Phys. J. **A5** (1999)  
11683 293–306, [arXiv:hep-ph/9812322](#).
- 11684 [502] L. Frankfurt, V. Guzey, and M. Strikman, *Leading twist nuclear shadowing: A user's guide*, Phys. Rev. **D71** (2005)  
11685 054001, [arXiv:hep-ph/0303022](#).
- 11686 [503] H. Abramowicz, L. Frankfurt, and M. Strikman, *Interplay of hard and soft physics in small  $x$  deep inelastic processes*,  
11687 ECONF **C940808** (1994) 033, [arXiv:hep-ph/9503437](#).
- 11688 [504] N. Armesto, A. Capella, A. Kaidalov, J. Lopez-Albacete, and C. Salgado, *Nuclear structure functions at small  $x$  from*  
11689 *inelastic shadowing and diffraction*, Eur.Phys.J. **C29** (2003) 531–540, [arXiv:hep-ph/0304119 \[hep-ph\]](#).
- 11690 [505] K. Tywoniuk, I. Arsene, L. Bravina, A. Kaidalov, and E. Zabrodin, *Gluon shadowing in the Glauber-Gribov model at*  
11691 *HERA*, Phys. Lett. **B657** (2007) 170–175, [arXiv:0705.1596 \[hep-ph\]](#).
- 11692 [506] L. Frankfurt, V. Guzey, and M. Strikman, *Leading twist coherent diffraction on nuclei in deep inelastic scattering at*  
11693 *small  $x$  and nuclear shadowing*, Phys. Lett. **B586** (2004) 41–52, [arXiv:hep-ph/0308189](#).
- 11694 [507] C. Marquet, *A Unified description of diffractive deep inelastic scattering with saturation*, Phys.Rev. **D76** (2007)  
11695 094017, [arXiv:0706.2682 \[hep-ph\]](#).
- 11696 [508] H. Kowalski, T. Lappi, C. Marquet, and R. Venugopalan, *Nuclear enhancement and suppression of diffractive structure*  
11697 *functions at high energies*, Phys. Rev. **C78** (2008) 045201, [arXiv:0805.4071 \[hep-ph\]](#).
- 11698 [509] J. Collins and H. Jung, *Need for fully unintegrated parton densities*, [arXiv:hep-ph/0508280](#).
- 11699 [510] J. C. Collins and D. E. Soper, *Back-To-Back Jets in QCD*, Nucl. Phys. **B193** (1981) 381.
- 11700 [511] J. C. Collins and D. E. Soper, *Parton Distribution and Decay Functions*, Nucl. Phys. **B194** (1982) 445.
- 11701 [512] J. C. Collins, *What exactly is a parton density?*, Acta Phys. Polon. **B34** (2003) 3103, [arXiv:hep-ph/0304122](#).
- 11702 [513] J. Collins, *Rapidity divergences and valid definitions of parton densities*, PoS **LC2008** (2008) 028, [arXiv:0808.2665](#)  
11703 [\[hep-ph\]](#).
- 11704 [514] X.-d. Ji, J.-p. Ma, and F. Yuan, *QCD factorization for semi-inclusive deep-inelastic scattering at low transverse*  
11705 *momentum*, Phys. Rev. **D71** (2005) 034005, [arXiv:hep-ph/0404183](#).
- 11706 [515] M. Ciafaloni, *Coherence Effects in Initial Jets at Small  $q^{*2} / s$* , Nucl. Phys. **B296** (1988) 49.
- 11707 [516] S. Catani, F. Fiorani, and G. Marchesini, *QCD Coherence in Initial State Radiation*, Phys.Lett. **B234** (1990) 339.
- 11708 [517] S. Catani, F. Fiorani, and G. Marchesini, *Small  $x$  Behavior of Initial State Radiation in Perturbative QCD*, Nucl.Phys.  
11709 **B336** (1990) 18.
- 11710 [518] G. Marchesini, *QCD coherence in the structure function and associated distributions at small  $x$* , Nucl.Phys. **B445**  
11711 (1995) 49–80, [arXiv:hep-ph/9412327 \[hep-ph\]](#).
- 11712 [519] I. Balitsky, *High-energy QCD and Wilson lines*, [arXiv:hep-ph/0101042](#).
- 11713 [520] J. C. Collins, *Foundations of Perturbative QCD*. Cambridge University Press, Cambridge, 2011. To be published.
- 11714 [521] S. Aybat and T. C. Rogers, *TMD Parton Distribution and Fragmentation Functions with QCD Evolution*,  
11715 [arXiv:1101.5057 \[hep-ph\]](#). \* Temporary entry \*.
- 11716 [522] J. C. Collins and A. Metz, *Universality of soft and collinear factors in hard- scattering factorization*, Phys. Rev. Lett.  
11717 **93** (2004) 252001, [arXiv:hep-ph/0408249](#).
- 11718 [523] F. Landry, R. Brock, P. M. Nadolsky, and C. P. Yuan, *Tevatron Run-1 Z boson data and Collins-Soper-Sterman*  
11719 *resummation formalism*, Phys. Rev. **D67** (2003) 073016, [arXiv:hep-ph/0212159](#).
- 11720 [524] J. C. Collins, D. E. Soper, and G. F. Sterman, *Transverse Momentum Distribution in Drell-Yan Pair and W and Z*  
11721 *Boson Production*, Nucl. Phys. **B250** (1985) 199.
- 11722 [525] C. Marquet, B.-W. Xiao, and F. Yuan, *Semi-inclusive Deep Inelastic Scattering at small  $x$* , Phys. Lett. **B682** (2009)  
11723 207–211, [arXiv:0906.1454 \[hep-ph\]](#).
- 11724 [526] F. Dominguez, B.-W. Xiao, and F. Yuan,  *$kt$ -factorization for Hard Processes in Nuclei*, Phys. Rev. Lett. **106** (2011)  
11725 022301, [arXiv:1009.2141 \[hep-ph\]](#).
- 11726 [527] H1 Collaboration, A. Aktas et al., *Inclusive dijet production at low Bjorken- $x$  in deep inelastic scattering*, Eur. Phys. J.  
11727 **C33** (2004) 477–493, [arXiv:hep-ex/0310019](#).

- 11728 [528] A. J. Askew, D. Graudenz, J. Kwiecinski, and A. D. Martin, *Dijet production at HERA as a probe of BFKL dynamics*, Phys. Lett. **B338** (1994) 92–97, [arXiv:hep-ph/9407337](#).
- 11729
- 11730 [529] J. Kwiecinski, A. D. Martin, and A. M. Stasto, *Predictions for dijet production in DIS using small  $x$  dynamics*, Phys. Lett. **B459** (1999) 644–648, [arXiv:hep-ph/9904402](#).
- 11731
- 11732 [530] A. Szczurek, N. N. Nikolaev, W. Schafer, and J. Speth, *Mapping the proton unintegrated gluon distribution in dijets correlations in real and virtual photoproduction at HERA*, Phys. Lett. **B500** (2001) 254–262, [arXiv:hep-ph/0011281](#).
- 11733
- 11734 [531] M. Hansson and H. Jung, *Towards precision determination of  $uPDFs$* , [arXiv:0707.4276 \[hep-ph\]](#).
- 11735 [532] F. Hautmann and H. Jung, *Angular correlations in multi-jet final states from  $kt$ -dependent parton showers*, JHEP **10** (2008) 113, [arXiv:0805.1049 \[hep-ph\]](#).
- 11736
- 11737 [533] J. Bartels, C. Ewerz, H. Lotter, and M. Wusthoff, *Azimuthal distribution of quark - anti-quark jets in DIS diffractive dissociation*, Phys.Lett. **B386** (1996) 389–396, [arXiv:hep-ph/9605356 \[hep-ph\]](#).
- 11738
- 11739 [534] J. Bartels, H. Jung, and M. Wusthoff, *Quark - anti-quark gluon jets in DIS diffractive dissociation*, Eur.Phys.J. **C11** (1999) 111–125, [arXiv:hep-ph/9903265 \[hep-ph\]](#).
- 11740
- 11741 [535] L. Lonnblad, *ARIADNE version 4: A Program for simulation of QCD cascades implementing the color dipole model*, Comput.Phys.Commun. **71** (1992) 15–31.
- 11742
- 11743 [536] H. Jung et al., *The CCFM Monte Carlo generator CASCADE 2.2.0*, Eur. Phys. J. **C70** (2010) 1237–1249, [arXiv:1008.0152 \[hep-ph\]](#).
- 11744
- 11745 [537] A. H. Mueller, *Parton distributions at very small  $x$  values*, Nucl. Phys. Proc. Suppl. **18C** (1991) 125–132.
- 11746 [538] A. H. Mueller, *Jets at LEP and HERA*, J. Phys. **G17** (1991) 1443–1454.
- 11747 [539] H1 Collaboration, S. Aid et al., *Transverse energy and forward jet production in the low  $x$  regime at HERA*, Phys. Lett. **B356** (1995) 118–128, [arXiv:hep-ex/9506012](#).
- 11748
- 11749 [540] H1 Collaboration, C. Adloff et al., *Forward jet and particle production at HERA*, Nucl. Phys. **B538** (1999) 3–22, [arXiv:hep-ex/9809028](#).
- 11750
- 11751 [541] H1 Collaboration, A. Aktas et al., *Forward jet production in deep inelastic scattering at HERA*, Eur. Phys. J. **C46** (2006) 27–42, [arXiv:hep-ex/0508055](#).
- 11752
- 11753 [542] ZEUS Collaboration, J. Breitweg et al., *Forward jet production in deep inelastic scattering at HERA*, Eur. Phys. J. **C6** (1999) 239–252, [arXiv:hep-ex/9805016](#).
- 11754
- 11755 [543] ZEUS Collaboration, J. Breitweg et al., *Measurement of the  $E(T_{jet})^{*2}/Q^{*2}$  dependence of forward-jet production at HERA*, Phys. Lett. **B474** (2000) 223–233, [arXiv:hep-ex/9910043](#).
- 11756
- 11757 [544] ZEUS Collaboration, S. Chekanov et al., *Forward jet production in deep inelastic  $e p$  scattering and low- $x$  parton dynamics at HERA*, Phys. Lett. **B632** (2006) 13–26, [arXiv:hep-ex/0502029](#).
- 11758
- 11759 [545] J. Kwiecinski, S. C. Lang, and A. D. Martin, *Single particle spectra in deep inelastic scattering as a probe of small  $x$  dynamics*, Eur. Phys. J. **C6** (1999) 671–680, [arXiv:hep-ph/9707240](#).
- 11760
- 11761 [546] J. Kwiecinski, A. D. Martin, and J. J. Outhwaite, *Small  $x$  QCD effects in DIS with a forward jet or a forward  $\pi^0$* , Eur. Phys. J. **C9** (1999) 611–622, [arXiv:hep-ph/9903439](#).
- 11762
- 11763 [547] G. Bottazzi, G. Marchesini, G. P. Salam, and M. Scorletti, *Small- $x$  one-particle-inclusive quantities in the CCFM approach*, JHEP **12** (1998) 011, [arXiv:hep-ph/9810546](#).
- 11764
- 11765 [548] H. Jung, *CCFM prediction on forward jets and  $F_2$ : Parton level predictions and a new hadron level Monte Carlo generator CASCADE*, [arXiv:hep-ph/9908497](#).
- 11766
- 11767 [549] H. Jung, *CCFM prediction for  $F_2$  and forward jets at HERA*, Nucl. Phys. Proc. Suppl. **79** (1999) 429–431, [arXiv:hep-ph/9905554](#).
- 11768
- 11769 [550] H. Jung and G. P. Salam, *Hadronic final state predictions from CCFM: The hadron- level Monte Carlo generator CASCADE*, Eur. Phys. J. **C19** (2001) 351–360, [arXiv:hep-ph/0012143](#).
- 11770
- 11771 [551] O. Kepka, C. Royon, C. Marquet, and R. B. Peschanski, *Next-leading BFKL effects in forward-jet production at HERA*, Phys. Lett. **B655** (2007) 236–240, [arXiv:hep-ph/0609299](#).
- 11772
- 11773 [552] J. Bartels, V. Del Duca, and M. Wusthoff, *Azimuthal dependence of forward jet production in DIS in the high-energy limit*, Z.Phys. **C76** (1997) 75–79, [arXiv:hep-ph/9610450 \[hep-ph\]](#).
- 11774
- 11775 [553] A. Sabio Vera and F. Schwennsen, *Azimuthal decorrelation of forward jets in Deep Inelastic Scattering*, Phys. Rev. **D77** (2008) 014001, [arXiv:0708.0549 \[hep-ph\]](#).
- 11776
- 11777 [554] J. Kwiecinski, A. D. Martin, P. J. Sutton, and K. J. Golec-Biernat, *QCD predictions for the transverse energy flow in deep inelastic scattering in the HERA small  $x$  regime*, Phys. Rev. **D50** (1994) 217–225, [arXiv:hep-ph/9403292](#).
- 11778
- 11779 [555] K. J. Golec-Biernat, J. Kwiecinski, A. D. Martin, and P. J. Sutton, *Transverse energy flow at HERA*, Phys. Lett. **B335** (1994) 220–225, [arXiv:hep-ph/9405400](#).
- 11780

- 11781 [556] N. H. Brook et al., *A comparison of deep inelastic scattering Monte Carlo event generators to HERA data*,  
11782 [arXiv:hep-ex/9912053](#).
- 11783 [557] G. P. Salam and G. Soyez, *A practical Seedless Infrared-Safe Cone jet algorithm*, JHEP **05** (2007) 086,  
11784 [arXiv:0704.0292 \[hep-ph\]](#).
- 11785 [558] Y. L. Dokshitzer, V. A. Khoze, A. H. Mueller, and S. I. Troyan, *Basics of perturbative QCD*, . Editions Frontieres 1991,  
11786 274p.
- 11787 [559] D. de Florian, R. Sassot, and M. Stratmann, *Global analysis of fragmentation functions for pions and kaons and their  
11788 uncertainties*, Phys.Rev. **D75** (2007) 114010, [arXiv:hep-ph/0703242 \[HEP-PH\]](#).
- 11789 [560] D. de Florian, R. Sassot, and M. Stratmann, *Global analysis of fragmentation functions for protons and charged  
11790 hadrons*, Phys.Rev. **D76** (2007) 074033, [arXiv:0707.1506 \[hep-ph\]](#).
- 11791 [561] A. M. Stasto, *Physics of ultrahigh energy neutrinos*, Int. J. Mod. Phys. **A19** (2004) 317–340, [arXiv:astro-ph/0310636](#).
- 11792 [562] J. K. Becker, *High-energy neutrinos in the context of multimessenger physics*, Phys. Rept. **458** (2008) 173–246,  
11793 [arXiv:0710.1557 \[astro-ph\]](#).
- 11794 [563] E. Zas, *Neutrino Detection with Inclined Air Showers*, New J. Phys. **7** (2005) 130, [arXiv:astro-ph/0504610](#).
- 11795 [564] N. Armesto, C. Merino, G. Parente, and E. Zas, *Charged Current Neutrino Cross Section and Tau Energy Loss at  
11796 Ultra-High Energies*, Phys. Rev. **D77** (2008) 013001, [arXiv:0709.4461 \[hep-ph\]](#).
- 11797 [565] T. L. Team, *LEP Design Report, Vol.III, LEP2*, CERN-AC/96-01-LEP2 (1996) .
- 11798 [566] K. Hirata and E. Keil, *Barycentre motion of beams due to beam-beam interaction in asymmetric ring colliders*, Nuclear  
11799 Instruments and Methods in Physics Research Section A: Accelerators, Spectrometers, Detectors and Associated  
11800 Equipment **292** (1990) no. 1, 156 – 168.  
11801 <http://www.sciencedirect.com/science/article/B6TJM-470F1H3-M/2/ff1b42fa7c847256a9e6c3245d3335d5>.
- 11802 [567] *Private Communication with Sylvain Weisz*, .
- 11803 [568] U. Schneckloth, *Boundary Conditions for the Interaction Region Design*, talk given at the 1st CERN-ECFA-NuPECC  
11804 Workshop on the LHeC, Divonne-les-Bains, France, 1-3 September 2008.
- 11805 [569] M. Bieler, E. Gianfelice-Wendt, G. Hoffstaetter, B. Holzer, S. Levonian, et al., *Recent and past experiences with  
11806 beam-beam effects at HERA*, . Workshop On Beam-Beam Effects In Large Hadron Colliders.
- 11807 [570] F. Zimmermann, R. Brinkmann, J. Feikes, S. Herb, A. Piwinski, et al., *First experience with the asymmetric beam-beam  
11808 interaction in the 1991 luminosity runs of HERA*, .
- 11809 [571] J. Rossbach and R. Brinkmann, *HERA Straight Sections for Head-On Electron-Proton Interactions*, IEEE  
11810 Trans.Nucl.Sci. **32** (1985) 1647–1649.
- 11811 [572] R. Appleby, *IRSYN*, (2010) .
- 11812 [573] S. Russenschuck, *Magnet Options for Q1 and Q2 (Ring-Ring and Linac-Ring, 3<sup>rd</sup> CERN-ECFA-NuPECC Workshop  
11813 on the LHeC* (2010) .
- 11814 [574] N. Bernard, *Analytic Method to Calculate the Power Produced by Synchrotron Radiation in a Quadrupole Magnet*,  
11815 CERN LHeC Note 2 (2010) .
- 11816 [575] H. Wiedemann, *Synchrotron Radiation*, Springer-Verlag Berlin Heidelberg (2003) .
- 11817 [576] I. B. et al., *Study of beam-induced backgrounds in the ZEUS detector from 2002 HERA running*, (2002) .
- 11818 [577] S. Russenschuck, *Private Communication*, (2010) .
- 11819 [578] E. Young, S. Henderson, R. Littauer, B. McDaniel, T. Pelaia, et al., *Collisions of Resonantly Coupled Round Beams at  
11820 the Cornell Electron Positron Storage Ring (CESR)*, .
- 11821 [579] D. Brandt, W. Herr, M. Meddahi, and A. Verdier, *Is LEP beam-beam limited at its highest energy?*, .
- 11822 [580] R. e. a. Alemany, *Head-on beam-beam tune shifts with high brightness beams in the LHC*, CERN-ATS-Note-2011-029 MD.
- 11823 [581] M. Meddahi, *Effets faisceau-faisceau dans le collisionneur proton-antiproton du SPS*, . PhD Thesis, Universite de Paris  
11824 VII.
- 11825 [582] M. Bassetti and G. Erskine, *Closed Expression for the electrical field of a two-dimensional Gaussian charge*,  
11826 CERN-ISR-TH/80-06.
- 11827 [583] R. e. a. Alemany, *Test of Luminosity leveling with separated collisions*, CERN-ATS-Note-2011-028 MD.
- 11828 [584] *LHC beam-beam studies webpage*. <http://lhc-beam-beam.web.cern.ch/lhc-beam-beam/>.
- 11829 [585] J. Jowett, *Heavy Ions in 2011 and Beyond*, . Chamonix 2011 Workshop on LHC Performance, Chamonix, France,  
11830 CERN-ATS-2011-005.
- 11831 [586] E. Benedikt, M., E. Collier, P., E. Mertens, V., E. Poole, J., and E. Schindl, K., *LHC Design Report. 3. The LHC  
11832 injector chain*, . CERN-2004-003-V-3.

- 11833 [587] E. Bruning, Oliver S., E. Collier, P., E. Lebrun, P., E. Myers, S., E. Ostojic, R., et al., *LHC Design Report. 1. The LHC*  
11834 *Main Ring*, . CERN-2004-003-V-1.
- 11835 [588] J. e. a. Stovall, *On the Feasibility of Accelerating Deuterons in Linac4*, CERN-sLHC-Project-Note-0032 (2011) .
- 11836 [589] C. Hill, D. Kuchler, R. Scrivens, and F. Wenander, *Studies on ECR4 for the CERN ion program*, Rev.Sci.Instrum. **73**  
11837 (2002) 564–566.
- 11838 [590] D. Barber and G. Ripken in *Handbook of Accelerator Physics and Engineering*, A. Chao and M. Tigner, eds. World  
11839 Scientific, first ed., 2006. third printing.
- 11840 [591] D. Barber et al., *Several articles*, in *Proc. ICFA Workshop on Quantum Aspects of Beam Physics*. World Scientific,  
11841 Monterey, CA, USA, 1999.
- 11842 [592] A. Sokolov and I. Ternov Sov. Phys. Dokl. **8** (1964) no. 12, 1203.
- 11843 [593] J. Jackson, *Classical Electrodynamics*. Wiley & Sons, third ed., 1998.
- 11844 [594] Y. Derbenev and A. Kondratenko Sov. Phys. JETP **37** (1973) 968.
- 11845 [595] S. Mane Phys. Rev. **A36** (1987) 105–130.
- 11846 [596] G. Hoffstätter, M. Vogt, and D. Barber Phys. Rev. ST Accel. Beams **11** (1999) no. 2, 114001.
- 11847 [597] D. Barber, G. Hoffstätter, and M. Vogt in *Proc. 14th Int. Spin Physics Symp.* AIP Conf. Proc. 570 (2001), 2000.
- 11848 [598] V. Baier and V. Katkov Sov. Phys. JETP **25** (1967) 944.
- 11849 [599] V. Baier, V. Katkov, and V. Strakhovenko Sov. Phys. JETP **31** (1970) 908.
- 11850 [600] R. Assmann et al. in *Proc. Part. Accel. Conf.*, p. 2999 and page 3002. New York, NY, USA, 1999.
- 11851 [601] D. Barber et al. Phys. Lett. **343B** (1995) 436.
- 11852 [602] S. Mane Nucl.Inst.Meth. **A292** (1990) 52.
- 11853 [603] S. Mane Nucl.Inst.Meth. **A321** (1992) 21.
- 11854 [604] D. Barber. SLICKTRACK is the extended version of SLICK [605] which includes Monte-Carlo spin-orbit tracking using  
11855 the mathematical structures of SLICK.
- 11856 [605] D. Barber. SLICK is a thick lens version of SLIM [590] by D.P. Barber using the formalism of [850].
- 11857 [606] Y. Derbenev and H. Grote Tech. Rep. SL/Note 95-37, CERN, 1995.
- 11858 [607] B. Montague Physics Reports **113** (1984) .
- 11859 [608] D. Forkel-Wirth, *Radioprotection issues after 20 years of LHC operation*, . EUCARD-HE-LHC'10 AccNet  
11860 miniworkshop on the HE-LHC, Valetta, Malta, 2010, tbp.
- 11861 [609] *LHC data base LHCLJ-3U0014*, .
- 11862 [610] *LHC data base LHCLJ-3U0012*, .
- 11863 [611] *LHC-LJ-EC-0002*, .
- 11864 [612] P. Bandyopadhyay and C. Segre, *Mucal on the web*. <http://www.csrri.iit.edu/mucal.html>.
- 11865 [613] K. Wittenburg, *The PIN-diode beam loss monitor system at HERA*, . AIP Conference Proceedings Volume 546, 9th  
11866 Beam Instrumentation Workshop, Boston, MA, USA.
- 11867 [614] K. Aulenbacher, B. Aune, J. Aysto, J. Baldy, e. Burkhardt, H., et al., *ELFE at CERN: Conceptual design report*, .
- 11868 [615] D. Brandt and A. Hofmann, *Does a high Q(s) raise the maximum intensity to be accumulated in LEP?*, .
- 11869 [616] <http://www-conf.slac.stanford.edu/facetusers/spring2010/Instrument.asp>. Nominal FACET Beam Parameters,  
11870 Spring 2010 User workshop.
- 11871 [617] CERN-LEP/TH/83-29. <http://cdsweb.cern.ch/record/98881>. LEP Design Report. Vol. 1. The LEP Injector Chain.
- 11872 [618] CERN-LEP/84-01. <http://cdsweb.cern.ch/record/102083>. LEP Design Report. Vol. 2. The LEP Main Ring.
- 11873 [619] CERN-AC/96-01. <http://cdsweb.cern.ch/record/314187>. LEP Design Report. Vol. 3. LEP 2.
- 11874 [620] V. Litvinenko, *LHeC with 100% Energy Recovery Linac*, 2nd CERN-ECFA-NuPECC Workshop on the LHeC,  
11875 Divonne-les-Bains, 1–3 September 2009 (2009) .
- 11876 [621] F. Ruggiero and F. Zimmermann, *Luminosity Optimization near the Beam-Beam Limit by Increasing Bunch Length or*  
11877 *Crossing Angle*, PRST-AB **5** (2002) 061101.
- 11878 [622] F. Zimmermann et al., *Linac-LHC ep Collider Options*, Proc. EPAC'08 Genoa (2008) 2847–2849.
- 11879 [623] D. Schulte, *LHeC Ring-Linac Lattice and Beam Dynamics*, 3rd CERN-ECFA-NuPECC LHeC Workshop  
11880 Chavannes-de-Bogis, December 2010 (2010) .
- 11881 [624] F. Zimmermann, K. Thompson, and R. Helm, *Electron-Electron Luminosity in the Next Linear Collider*,  
11882 Int. J. Mod. Phys. A **13** (1998) 2443–2454.

- 11883 [625] H. Braun et al., *CLIC 2008 Parameters*, CLIC-Note-764 (2008) .
- 11884 [626] N. Phinney, N. Toge, and N. Walker, *LC Reference Design Report Volume 3 - Accelerator*, (2007) , [arXiv:0712.2361](https://arxiv.org/abs/0712.2361)  
11885 [physics.acc-ph].
- 11886 [627] F. Gerigk et al., *Conceptual Design of the SPL II*, CRN-2006-006 (2006) .
- 11887 [628] C. Mayes and G. Hoffstaetter, *Cornell Energy Recovery Linac Lattice and Layout*, Proc. IPAC'10 Kyoto (2010) .
- 11888 [629] V. Litvinenko, *Future Electron-Hadron Colliders*, Proc. IPAC'10 Kyoto (2010) .
- 11889 [630] G. Neil, *Free Electron Lasers from THz to X-rays*, Invited Talk at UPHUK4, Bodrum, Turkey, 30 August 2010 (2010) .
- 11890 [631] Linnecar, T. and Tückmantel, J., , Private communication, 28 May 2008 (2008) .
- 11891 [632] O. Napoly, , Private communication, 6th EuCARD Steering Meeting, Malta, 12–13 October 2010. (2010) .
- 11892 [633] E. Ciapala, *RF for the LHeC*, 3rd CERN-ECFA-NuPECC LHeC Workshop Chavannes-de-Bogis, December 2010 (2010)  
11893 .
- 11894 [634] J. Tuckmantel, , Comment at 2nd RFTech meeting, PSI, Villigen, 2–3 December 2010 (2010) .
- 11895 [635] V. Litvinenko and I. Ben-Zvi, , Private communications (2010) .
- 11896 [636] I. Ben-Zvi, , Private communications, 16 November 2010 (2010) .
- 11897 [637] D. Tommasini, *RR+RL Magnets*, 3rd CERN-ECFA-NuPECC LHeC Workshop Chavannes-de-Bogis, December 2010  
11898 (2010) .
- 11899 [638] J. Skrabacz, *Optimizing Cost and Minimizing Energy Loss in the Recirculating Race-Track Design of the LHeC*  
11900 *Electron Linac*, CERN-AB-Note-2008-043 (2008) .
- 11901 [639] A. Bogacz, *LHeC Recirculator with Energy Recovery – Beam Optics Choices*, JLAB-TN-10-040 (2010) .
- 11902 [640] D. Schulte and F. Zimmermann, , Private discussions (2010) .
- 11903 [641] D. Schulte, , Private communication (2010) .
- 11904 [642] D. Schulte and F. Zimmermann, *QCD Explorer Based on LHC and CLIC-1*, Proc. EPAC'04, Lucerne,  
11905 CERN-AB-2004-079, and CLIC Note 608 (2004) .
- 11906 [643] K. Ohmi, R. Calaga, W. Hofle, R. Tomas, and F. Zimmermann, *Beam-Beam Effects with External Noise in LHC*,  
11907 Proc. PAC07, Albuquerque (2007) 1496.
- 11908 [644] F. Zimmermann et al., *First Bunch Length Studies in the SLC South Final Focus*, Proc. EPAC 1998 Stockholm (1998)  
11909 487.
- 11910 [645] C. Adolphsen et al., *Pulse-to-Pulse Stability Issues at the SLC*, Proc. IEEE PAC 1995 Dallas (1995) .
- 11911 [646] P. Chen and K. Yokoya, *Disruption Effects from the Interaction of Round  $e+e-$  Beams*, Phys. Rev. D **38** (1988) 987.
- 11912 [647] M. Yamamoto, M. and Kuwahara, *Superlattice Photocathode Development for Low Emittance*, Photocathode Physics for  
11913 Photoinjectors Workshop, BNL, October 2010 (2010) .
- 11914 [648] I. Bailey, *A Helical Undulator Based Positron Source for the International Linear Collider*, Proc. PoS HEP2005 (2006)  
11915 368.
- 11916 [649] S. Araki et al., *Conceptual Design of a Polarised Positron Source Based on Laser Compton Scattering*,  
11917 CARE/ELAN-Document-2005-013, CLIC Note 639, KEK Preprint 2005-60, LAL 05-94 (2005) , [physics/0509016](https://arxiv.org/abs/physics/0509016).
- 11918 [650] F. Zimmermann et al., *Stacking Simulations for Compton Positron Sources of Future Linear Colliders*, Proc. PAC'09  
11919 Vancouver (2009) .
- 11920 [651] V. Litvinenko, *Recirculating Linac*, 2nd CERN-ECFA-NuPECC workshop on LHeC, Divonne-les-Bains (2009) .
- 11921 [652] I. Ginzburg, G. Kotkin, V. Serbo, and V. Telnov, *Colliding  $\gamma e$  and  $\gamma\gamma$  Beams Based on the Single Pass Accelerators (of*  
11922 *VLEPP Type)*, Nucl. Instr. & Meth. **205** (1983) 47.
- 11923 [653] H. Burkhardt and V. Telnov, *CLIC 3-TeV Photon Collider Options*, CERN-SL-2002-013-AP, CLIC-Note-508 (2002) .
- 11924 [654] T. N. D. Group, *NLC Zeroth-Order Design Report for the Next Linear Collider, Appendix B*, LBNL-5424, SLAC-474,  
11925 Appendix B (1996) .
- 11926 [655] V. Telnov, *Principles of Photon Colliders*, NIM A **355** (1995) 3–18.
- 11927 [656] Klemz, G. and Mönig, K. and Will, I. , *Design Study of an Optical Cavity for a Future Photon-Collider at ILC*, NIM A  
11928 **564** (2006) 212.
- 11929 [657] H. Aksakal, Z. Nergiz, et al.,  *$\gamma p$  Option for LHeC*, Draft Note, October 2010 (2010) .
- 11930 [658] K. Yokoya, *CAIN: A Computer Simulation Code for the Interaction of Electron, Positron, Gamma Beams and Strong*  
11931 *Lasers*, available at <http://lcdev.kek.jp/yokoya/CAIN> (2010) .
- 11932 [659] C. Johnstone, *Local chromaticity correction of the LHC*, PAC97 (1997) .



- 11933 [660] S. Fartoukh, *Optics Challenges and Solutions for the LHC Insertion Upgrade Phase I*, LHC Project Report 0038  
11934 (2010) .
- 11935 [661] S. Fartoukh, *Towards the LHC Upgrade using the LHC well-characterized technology*, LHC Project Report 0049 (2010) .
- 11936 [662] P. Raimondi and A. Seryi, *Novel Final Focus Design for Future Linear Colliders*, Phys. Rev. Lett. **86** (2001) .
- 11937 [663] A. Gaddi, *Passive isolation*, Presented in IWLC 2010 (2010) .
- 11938 [664] A. Verdier, *Alignment optics for LHC*, LHC Project Note 325 (2003) .
- 11939 [665] D. Schulte, *Beam-Beam Simulations with GUINEA-PIG*, ICAP98 (1998) .
- 11940 [666] A. Bogacz, *LHeC Recirculator with Energy Recovery Beam Optics Choices*, CERN-LHeC-Note-2010-009 ACC,  
11941 JLAB-TN-10-040 (2010) .
- 11942 [667] Y. Hao, K. D., V. Litvinenko, V. Ptitsyn, D. Trbojevic, and N. Tsoupas, *ERL Option for LHeC*,  
11943 CERN-LHeC-Note-2010-010 ACC (2010) .
- 11944 [668] D. Schulte, *Multi-bunch calculations in the CLIC main linac*, PAC2009 Vancouver (2009) .
- 11945 [669] D. Schulte, *Simulation package based on PLACET*, Proceedings PAC01, Chicago (2001) .
- 11946 [670] *International Linear Collider Reference Design Report*, ILC-Report-2007-001 (2007) .
- 11947 [671] I. Bazarov and G. Hoffstaetter, *Multi-pass Beam-breakup: Theory and Calculation*, EPAC2004 Lucerne (2004) .
- 11948 [672] D. Schulte, , to be published .
- 11949 [673] M. Schuh, , private communication .
- 11950 [674] F. Zimmermann, J. Byrd, A. Chao, S. Heifets, M. Minty, T. Raubenheimer, J. Seeman, S. G., and J. Thomson,  
11951 *Experiments on the fast beam-ion instability at the ALS*, Report SLAC-PUB-7617 (1997) .
- 11952 [675] G. Hoffstaetter and M. Liepe, , NIM A **557** (2006) 205–212.
- 11953 [676] N. Hilleret, , Private communication .
- 11954 [677] B. Holzer, , Private communication .
- 11955 [678] V. Baglin, , Private communication .
- 11956 [679] F. Zimmermann et al., *CAIN: A Computer Simulation Code for the Interaction of Electron, Positron, Gamma Beams  
11957 and Strong Lasers*, 3rd CERN-ECFA-NuPECC Workshop on the LHeC, <http://www.lhec.org.uk>, Nov. 12-13, 2010.  
11958 (2010) .
- 11959 [680] L. Thomas, , Phil. Mag, **3** (1927) 1.
- 11960 [681] I. Alekseev et al., *Design Manual - Polarized Proton Collider at RHIC*, Nucl. Inst. and Meth. A **499** (2003) 392.
- 11961 [682] V. Ptitsin, *Symmetric Designs for Helical Spin Rotators at RHIC*, AGS/RHIC/SN No. 5 (1996) .
- 11962 [683] *Topical Meeting on Positrons for the LHeC, May 2011*. <http://cern.ch/lhec>.
- 11963 [684] E. Bulyak, J. Urakawa, and F. Zimmermann, *Asymmetric laser radiant cooling in storage rings (report mop064)*, .  
11964 <http://www.bnl.gov/pac11/>. In *PAC 2011, New York, U.S.A., March 28 – April 1, 2011*.
- 11965 [685] O. e. a. Dadoun, *Study of an hybrid positron source using channeling for CLIC*, CLIC Note 808.
- 11966 [686] P. Sievers. Private communication.
- 11967 [687] P. collaboration, *Options for polarized  $e^+$ . Compton ring.*, . In *CLIC RDR, chapter 2*.
- 11968 [688] E. Bulyak., *Optimal  $\gamma \rightarrow e^+$  conversion target for Compton sources.*, . In *report at ALCPG11, Eugene, Oregon U.S.A.*  
11969 *21/03/2011*.
- 11970 [689] T. E. et al, *Optics Letters, Vol. 35 No. 2, January 15, 2010*, .
- 11971 [690] V. B. et al., *Nuclear Instruments and Methods in Physics Research A 608*, .
- 11972 [691] I. P. et al., *Optics Letters, Vol. 35, No. 12, June 15, 2010*, .
- 11973 [692] F. Zomer, *Mighty Laser*, . ANR project ANR-08-BLAN-0280-01; publication currently under writing.
- 11974 [693] T. Erber, *High-Energy Electromagnetic Conversion Processes in Intense Magnetic Fields*, . Reviews of Modern  
11975 Physics, vol. 38, no. 4.
- 11976 [694] P. Chen and R. Palmer, *Coherent Pair Creation as a positron source for Linear Colliders*, . SLAC-PUB-5966.
- 11977 [695] C. B. et al, *Studies of Nonlinear QED in collisions of 46.6 GeV Electrons with Intense Laser Pulses*, .  
11978 Phys.Rev.D60:092004.
- 11979 [696] H. Braun, *Private communication*, .
- 11980 [697] R. Ostojic and T. Taylor, *Conceptual design of a 70 mm aperture quadrupole for the LHC insertions*, . IEEE  
11981 Transactions on Applied Superconductivity.

- 11982 [698] M. Tawada, H. Nakayama, and K. Satoh, *Special quadrupole magnets for KEKB interaction region*, . Proceedings of  
11983 EPAC 2000, Vienna.
- 11984 [699] R. Gupta, *Modular Program and Modular Design for LARP Quadrupoles*, . Magnet Note, Superconducting Magnet  
11985 Division, Brookhaven National Laboratory.
- 11986 [700] S. Russenschuck, *Field computation for accelerator magnets: Analytical and numerical methods for electromagnetic  
11987 design and optimization*, .
- 11988 [701] J. e. a. Parrell, *High Field Nb<sub>3</sub>Sn conductor development at Oxford Superconductor Technology*, . IEEE Transactions on  
11989 Applied Superconductivity.
- 11990 [702] A. Devred, E. Baynham, M. Chorowski, P. Fabbriatore, E. Garcia-Tabares, et al., *A Strategy for European  
11991 superconducting accelerator magnet R&D aimed at LHC luminosity upgrade*, .
- 11992 [703] *Conceptual design of the SPL II, a high-power superconducting H- linac at CERN*, . CERN (series) 2006-006.
- 11993 [704] F. e. a. Gerigk, *Choice of the optimum beta for the SPL cavities*, . CERN-sLHC-Project-Note-0001.
- 11994 [705] W. Weingarten, *Performance of superconducting cavities as required for the SPL*, . CERN-AB-2008-063.
- 11995 [706] *Some Aspects of 704 MHz Superconducting RF Cavities*. <http://cern.ch/rcalaga/PUBS/THPP0003.pdf>.
- 11996 [707] G. Neil, *Worldwide ERL R&D Overview Including JLAMP, BNL, and Cornell ERLs, Proceedings of LINAC10*.  
11997 <http://accelconf.web.cern.ch/AccelConf/LINAC2010/papers/tu103.pdf>.
- 11998 [708] F. e. a. Zimmermann, *The Large Hadron-Electron Collider (LHeC) at the LHC*, Proc PAC'09 Vancouver 4233–4235.  
11999 <http://accelconf.web.cern.ch/AccelConf/PAC2009/papers/fr1pbc05.pdf>.
- 12000 [709] F. e. a. Zimmermann, *Designs for a Linac-Ring LHeC*, Proc. IPAC'10 Kyoto 1611–1613.  
12001 <http://accelconf.web.cern.ch/AccelConf/IPAC10/papers/tu039.pdf>.
- 12002 [710] V. Litvinenko, *Designs for a Linac-Ring LHeC*, 3rd CERN-ECFA-NuPECC LHeC Workshop Chavannes-de-Bogis,  
12003 December 2010 .
- 12004 [711] R. e. a. Calaga, *in the proceedings of CARE-HHH08, Chavannes-de-Bogis, 2008*, .
- 12005 [712] R. e. a. Calaga, *in the proceeding of the LHC performance workshop 2010, Chamonix, 2010*, .
- 12006 [713] D. Brandt, H. Burkhardt, M. Lamont, S. Myers, and J. Wenninger, *Accelerator physics at LEP*, Rept.Prog.Phys. **63**  
12007 (2000) 939–1000.
- 12008 [714] B. Dehning, A. Melissinos, F. Perrone, C. Rizzo, and G. von Holtey, *Scattering of high-energy electrons off thermal  
12009 photons*, Phys.Lett. **B249** (1990) 145–148.
- 12010 [715] C. Yin Vallgren, A. Ashraf, S. Calatroni, P. Chiggiato, P. Costa Pinto, et al., *Low Secondary Electron Yield Carbon  
12011 Coatings for Electron-cloud Mitigation in Modern Particle Accelerators*, .
- 12012 [716] C. Hauviller, *Development of composite tubes for experimental vacuum chambers of colliders*, .
- 12013 [717] V. Parma and U. Wagner, *SPL Cryogenic System Studies*, CERN Presentation 2008.
- 12014 [718] B. Petersen. Private communication, Bernd Petersen, DESY.
- 12015 [719] S. Claudet, G. Ferlin, F. Miller, and L. Taviani, *1.8 K Refrigeration units for the LHC: Performance Assessment of  
12016 Pre-series Units*, . ICEC 2004, Beijing.
- 12017 [720] M. Barnes, F. Caspers, L. Ducimetiere, N. Garrel, and T. Kroyer, *The beam screen for the LHC injection kicker  
12018 magnets*, .
- 12019 [721] E. Carlier, U. Jansson, R. Jung, V. Mertens, S. Péraire, et al., *The LEP beam dumping system*, .
- 12020 [722] R. Appleby, L. Keller, T. W. Markiewicz, A. Seryi, D. Walz, et al., *The International linear collider beam dumps*,  
12021 [arXiv:physics/0601103](https://arxiv.org/abs/physics/0601103) [physics].
- 12022 [723] J. Amann, R. Arnold, A. Seryi, D. Walz, K. Kulkarni, et al., *Design of an 18 MW Beam Dump for 500 GeV  
12023 Electron/Positron Beams at an ILC*, .
- 12024 [724] S. Myers, *LHC: Machine Status and Prospects for the Short, Medium and Long Term*, , Invited Plenary Talk at EPS,  
12025 **Grenoble, July 2011**.
- 12026 [725] M. Klein, *The High Luminosity Design study for the LHC*, [Https://espace.cern.ch/hl-lhc/default.aspx](https://espace.cern.ch/hl-lhc/default.aspx).
- 12027 [726] E. Ciapala. Private communication, Edmund Ciapala, CERN, BE-RF group.
- 12028 [727] A. Yamamoto. <http://www.fnal.gov/directorate/ILCPAC/ILCPACNov2010/Yamamoto---cavityindustrialization.pdf>.  
12029 Talk at ILC-PAC Eugene November 2010.
- 12030 [728] V. Mertens. Private communication, Volker Mertens, CERN, TE-ABT group.
- 12031 [729] J. Osborne. Private communication, John Osborne, CERN, GS-SE group.
- 12032 [730] *The XFEL construction calendar*. <http://www.xfel.eu/projekt/kalender/>.

- 12033 [731] M. Peininger. [www.cockcroft.ac.uk/events/CSSA/presentations/Michael\%20Peiniger.pdf](http://www.cockcroft.ac.uk/events/CSSA/presentations/Michael\%20Peiniger.pdf). Talk at Cockcroft  
12034 Institute seminar April 2011.
- 12035 [732] R. Ruber. [www.isv.uu.se/~ziemann/teaching/ht10/ESS.pdf](http://www.isv.uu.se/~ziemann/teaching/ht10/ESS.pdf). Uppsala University.
- 12036 [733] *LINAC4 Project Page*. <http://linac4-project.web.cern.ch/linac4-project/>.
- 12037 [734] R. Ischebeck. [www.cockcroft.ac.uk/events/eslsxvi/proceedings/psixfelischebeck.pdf](http://www.cockcroft.ac.uk/events/eslsxvi/proceedings/psixfelischebeck.pdf). Talk given at the Sixteenth  
12038 European Synchrotron Light Source workshop, England, Daresbury Laboratory, Crockcroft Institute, November 2008.
- 12039 [735] A. Mazzacane, *The 4th concept detector for the ILC*, Nucl.Instrum.Meth. **A617** (2010) 173–176.
- 12040 [736] M. Klein and R. Yoshida, *Collider Physics at HERA*, Prog.Part.Nucl.Phys. **61** (2008) 343–393, [arXiv:0805.3334](https://arxiv.org/abs/0805.3334)  
12041 [hep-ex].
- 12042 [737] e. Pire, Bernard, e. Cirelli, Marco, e. Colas, Paul, e. Djouadi, Abdelhak, e. Lounis, Abdenour, et al., *High energy*  
12043 *physics. Proceedings, 35th International Conference, ICHEP 2010, Paris, France, July 22-28, 2010*, .
- 12044 [738] e. Buchmuller, W. and e. Ingelman, G., *Physics at HERA. Proceedings, Workshop, Hamburg, Germany, October 29-30,*  
12045 *1991. Vol. 1-3*, .
- 12046 [739] R. Gluckstern, *Uncertainties in track momentum and direction, due to multiple scattering and measurement errors*,  
12047 Nucl.Instrum.Meth. **24** (1963) 381–389.
- 12048 [740] M. Regler, W. Mitaroff, M. Valentan, R. Fruhwirth, and R. Hofler, *The 'LiC Detector Toy' program*, J.Phys.Conf.Ser.  
12049 **119** (2008) 032034.
- 12050 [741] P. Adragna, C. Alexa, K. Anderson, A. Antonaki, A. Arabidze, et al., *Measurement of pion and proton response and*  
12051 *longitudinal shower profiles up to 20 nuclear interaction lengths with the ATLAS tile calorimeter*, Nucl.Instrum.Meth.  
12052 **A615** (2010) 158–181.
- 12053 [742] ATLAS Collaboration, G. Aad et al., *The ATLAS Experiment at the CERN Large Hadron Collider*, JINST **3** (2008)  
12054 S08003.
- 12055 [743] B. Holzer, , Private communication .
- 12056 [744] ATLAS Collaboration Collaboration, *ATLAS central solenoid: Technical design report*, . Hardcopy at DESY.
- 12057 [745] ATLAS Collaboration Collaboration, *ATLAS magnet system: Technical design report*, . Hardcopy at DESY.
- 12058 [746] *CMS, the Compact Muon Solenoid. Muon technical design report*, .
- 12059 [747] CMS Collaboration Collaboration, G. Acquistapace et al., *CMS, the magnet project: Technical design report*, .
- 12060 [748] P. Allport, "Conventional Silicon Pixel/Strip Tracker", talk at 3rd CERN-ECFA-NuPECC Workshop on LHeC,  
12061 Chavannes-de-Bogis, Switzerland, 12. November 2010. <http://indico.cern.ch/getFile.py/access?contribId=50&sessionId=9&resId=0&materialId=slides&confId=105142>.  
12062
- 12063 [749] E. Koffeman, *Gossip: Gaseous pixels*, Nucl.Instrum.Meth. **A582** (2007) 858–860.
- 12064 [750] H. van der Graaf, "Gossip and GridPix at LHeC", talk at 3rd CERN-ECFA-NuPECC Workshop on LHeC,  
12065 Chavannes-de-Bogis, Switzerland, 12. November 2010.  
12066 <http://indico.cern.ch/materialDisplay.py?contribId=51&sessionId=9&materialId=slides&confId=105142>.
- 12067 [751] H. van der Graaf, *Gaseous detectors*, Nucl.Instrum.Meth. **A628** (2011) 27–30.
- 12068 [752] R. Horisberger, "Tracking at Phase II, Pixel, Strixel & Strips", CMS Tracker Week, La Biodola, Isola d'Elba 27. May  
12069 2010.
- 12070 [753] R. Horisberger, "Considerations for future Large Pixel Systems", talk CMS Pixel Detector Upgrade Workshop, FNAL  
12071 10. October 2006.
- 12072 [754] J. Brau, *The Science and Challenges for Future Detector Development in High Energy Physics*, .
- 12073 [755] N. Wermes, "Silicon Pixel Detectors for Tracking", talk at 1st CERN-ECFA Workshop on LHeC, Divonne-les-Bains,  
12074 France, 1-3 September 2008.  
12075 <http://indico.cern.ch/contributionDisplay.py?sessionId=19&contribId=63&confId=31463>.
- 12076 [756] ATLAS and CMS Collaboration, N. Hessey, *Overview and electronics needs of ATLAS and CMS high luminosity*  
12077 *upgrades*, . <http://indico.cern.ch/getFile.py/access?contribId=140&sessionId=21&resId=0&materialId=paper&confId=21985>.  
12078
- 12079 [757] M. Nessi, "The Detector Upgrade and the Requirements on the Upgrade Scenarios".  
12080 <http://cdsweb.cern.ch/record/1304568>.
- 12081 [758] C. Haber, "Lecture Silicon Detectors: Principles and Technology", talk at TIPP, Chicago, USA, June 2011. <https://indico.cern.ch/getFile.py/access?contribId=529&sessionId=25&resId=0&materialId=slides&confId=102998>.  
12082
- 12083 [759] D. Christian, "Semiconductor Detectors Overview", talk at TIPP, Chicago, USA, June 2011. <https://indico.cern.ch/getFile.py/access?contribId=527&sessionId=22&resId=1&materialId=slides&confId=102998>.  
12084

- 12085 [760] S. Cihanger, "Silicon sensor R&D for an upgraded CMS Tracker in HL-LHC", talk at TIPP, Chicago, USA, June  
12086 2011. [https://indico.cern.ch/getFile.py/access?contribId=107&sessionId=22&resId=0&materialId=slides\](https://indico.cern.ch/getFile.py/access?contribId=107&sessionId=22&resId=0&materialId=slides&confId=102998)  
12087 [&confId=102998](https://indico.cern.ch/getFile.py/access?contribId=107&sessionId=22&resId=0&materialId=slides&confId=102998).
- 12088 [761] A. Affolder, "Silicon Strip Detectors for the ATLAS sLHC Upgrade", talk at TIPP, Chicago, USA, June 2011.  
12089 [https://indico.cern.ch/getFile.py/access?contribId=31&sessionId=22&resId=1&resmaterialId=slides\](https://indico.cern.ch/getFile.py/access?contribId=31&sessionId=22&resId=1&resmaterialId=slides&confId=102998)  
12090 [&confId=102998](https://indico.cern.ch/getFile.py/access?contribId=31&sessionId=22&resId=1&resmaterialId=slides&confId=102998).
- 12091 [762] A. Macchiolo, "Performance of Silicon n-in-p Pixel Detectors irradiated up to  $5^{15} n_{eq}/cm^2$  for the future ATLAS  
12092 Upgrades", talk at TIPP, Chicago, USA, June 2011. [https://indico.cern.ch/getFile.py/access?contribId=33&sessionId=22&resId=0&materialId=slides\](https://indico.cern.ch/getFile.py/access?contribId=33&sessionId=22&resId=0&materialId=slides&confId=102998)  
12093 [&confId=102998](https://indico.cern.ch/getFile.py/access?contribId=33&sessionId=22&resId=0&materialId=slides&confId=102998).
- 12094 [763] U. Parzefall, "Silicon for High-Luminosity Tracking Detectors - Recent RD50 Results", talk at TIPP, Chicago, USA,  
12095 June 2011. [https://indico.cern.ch/getFile.py/access?contribId=203&sessionId=22&resId=3&materialId=](https://indico.cern.ch/getFile.py/access?contribId=203&sessionId=22&resId=3&materialId=slides&confId=102998)  
12096 [slides&confId=102998](https://indico.cern.ch/getFile.py/access?contribId=203&sessionId=22&resId=3&materialId=slides&confId=102998).
- 12097 [764] I. Rubinskiy, "An EUDET/AIDA pixel beam telescope for detector development", talk at TIPP, Chicago, USA, June  
12098 2011. [https://indico.cern.ch/getFile.py/access?contribId=25&sessionId=22&resId=0&materialId=slides\](https://indico.cern.ch/getFile.py/access?contribId=25&sessionId=22&resId=0&materialId=slides&confId=102998)  
12099 [&confId=102998](https://indico.cern.ch/getFile.py/access?contribId=25&sessionId=22&resId=0&materialId=slides&confId=102998).
- 12100 [765] M. Bomben, "Recent progress of the ATLAS Planar Pixel Sensor R&D Project", talk at TIPP, Chicago, USA, June  
12101 2011. [https://indico.cern.ch/getFile.py/access?contribId=436&sessionId=22&resId=0&materialId=slides\](https://indico.cern.ch/getFile.py/access?contribId=436&sessionId=22&resId=0&materialId=slides&confId=102998)  
12102 [&confId=102998](https://indico.cern.ch/getFile.py/access?contribId=436&sessionId=22&resId=0&materialId=slides&confId=102998).
- 12103 [766] M. Mikuz, "Diamond for high energy radiation and particle detection", talk at TIPP, Chicago, USA, June 2011.  
12104 [https://indico.cern.ch/getFile.py/access?contribId=463&sessionId=22&resId=1&materialId=slides\](https://indico.cern.ch/getFile.py/access?contribId=463&sessionId=22&resId=1&materialId=slides&confId=102998)  
12105 [&confId=102998](https://indico.cern.ch/getFile.py/access?contribId=463&sessionId=22&resId=1&materialId=slides&confId=102998).
- 12106 [767] A. Mac Raighne, "3D pixel devices; design, production and characterisation in test beams", talk at TIPP, Chicago,  
12107 USA, June 2011. [https://indico.cern.ch/getFile.py/access?contribId=249&sessionId=22&resId=1\](https://indico.cern.ch/getFile.py/access?contribId=249&sessionId=22&resId=1&materialId=slides&confId=102998)  
12108 [&materialId=slides&confId=102998](https://indico.cern.ch/getFile.py/access?contribId=249&sessionId=22&resId=1&materialId=slides&confId=102998).
- 12109 [768] A. Ferrari, P. Sala, A. Fasso, and J. Ranft, *FLUKA: A multi-particle transport code (Program version 2005)*, .
- 12110 [769] G. Battistoni, S. Muraro, P. R. Sala, F. Cerutti, A. Ferrari, et al., *The FLUKA code: Description and benchmarking*,  
12111 *AIP Conf.Proc.* **896** (2007) 31–49.
- 12112 [770] M. Garcia-Sciveres, "ATLAS pixels for 2017/18", talk at ACES 2011 Workshop, CERN 9. March 2011.
- 12113 [771] K.K.Gan, F.Vasey, T.Weidberg "Lessons Learned and to be Learned from LHC", talk at Joint ATLAS-CMS Working  
12114 Group on Opto-Electronics for SLHC, Report from Sub-Group A, Joint ATLAS/CMS NOTE,  
12115 *ATL-COM-ELEC-2007-001*. <https://edms.cern.ch/document/882775/3.8>.
- 12116 [772] A. Bell, E. Castro, R. Hall-Wilton, W. Lange, W. Lohmann, et al., *Fast Beam Conditions Monitor BCM1F for the*  
12117 *CMS Experiment*, *Nucl.Instrum.Meth.* **A614** (2010) 433–438, [arXiv:0911.2480](https://arxiv.org/abs/0911.2480) [physics.ins-det].
- 12118 [773] L. Fernandez Hernandez, D. Chong, R. Gray, C. Ilgner, A. Macpherson, et al., *Development of a CVD diamond beam*  
12119 *condition monitor for CMS at the Large Hadron Collider*, *Nucl.Instrum.Meth.* **A552** (2005) 183–188.
- 12120 [774] A. Macpherson, *Beam Condition Monitoring and radiation damage concerns of the experiment*, talk at ICHEP 2010,  
12121 Paris, France, .
- 12122 [775] D. Chong, L. Fernandez-Hernando, R. Gray, C. J. Ilgner, A. Oh, et al., *Validation of synthetic diamond for a beam*  
12123 *condition monitor for the Compact Muon Solenoid experiment*, *IEEE Trans.Nucl.Sci.* **54** (2007) 182–185.
- 12124 [776] D. Green, *How physics defines the LHC environment and detectors*, *Int.J.Mod.Phys.* **A25** (2010) 1279–1313.
- 12125 [777] J. Freeman, *Innovations for the CMS HCAL*, *Int.J.Mod.Phys.* **A25** (2010) 2421–2436.
- 12126 [778] L. Mandelli, *The ATLAS electromagnetic calorimeters: Features and performance*, *Int.J.Mod.Phys.* **A25** (2010)  
12127 1739–1760.
- 12128 [779] P. Bloch, *The CMS electromagnetic calorimeter: Crystals and APD productions*, *Mod.Phys.Lett.* **A25** (2010)  
12129 1027–1045.
- 12130 [780] K. Anderson, T. Del Prete, E. Fullana, J. Huston, C. Roda, et al., *TileCal: The hadronic section of the central ATLAS*  
12131 *calorimeter*, *Int.J.Mod.Phys.* **A25** (2010) 1981–2003.
- 12132 [781] ATLAS Collaboration, A. Airapetian et al., *ATLAS calorimeter performance Technical Design Report*, .
- 12133 [782] H1 Collaboration, A. Babaev, *Performance of the H1 liquid argon calorimeter*, .
- 12134 [783] H1 Collaboration, I. Abt et al., *The H1 detector at HERA*, *Nucl.Instrum.Meth.* **A386** (1997) 310–347.
- 12135 [784] M. Fleischer, M. Keller, K. Meier, O. Nix, G. Schmidt, et al., *Performance and upgrade of H1 calorimeters: LAr*  
12136 *calorimeter, SpaCal and VLQ*, .
- 12137 [785] C. Issever, *The calibration of the H1 liquid argon calorimeter*, .
- 12138 [786] H1 collaboration Collaboration, C. Schwanenberger, *The Jet calibration in the H1 liquid argon calorimeter*,  
12139 [arXiv:physics/0209026](https://arxiv.org/abs/physics/0209026) [physics].

- 12140 [787] J. Seehafer, *Simulation of hadronic showers in the H1 liquid argon calorimeter with the simulation programs GHEISHA*  
12141 *and CALOR*, .
- 12142 [788] C. Kiesling, A. Dubak, and B. Olivier, *The liquid argon jet trigger of the H1 experiment at HERA*, Nucl.Instrum.Meth.  
12143 **A623** (2010) 513–515.
- 12144 [789] ATLAS Electromagnetic Barrel Liquid Argon Calorimeter Group Collaboration, B. Aubert et al., *Construction,*  
12145 *assembly and tests of the ATLAS electromagnetic barrel calorimeter*, Nucl.Instrum.Meth. **A558** (2006) 388–418.
- 12146 [790] O. Gildemeister, F. Nessi-Tedaldi, and M. Nessi, *An economic concept for a barrel hadron calorimeter with iron*  
12147 *scintillator sampling and WLS-fiber readout*, .
- 12148 [791] I. Golutvin, B. Borgia, F. Carminati, M. Della Negra, S. Giani, et al., *A Silicon hadron calorimeter module operated in*  
12149 *a strong magnetic field with VLSI readout for LHC*, .
- 12150 [792] OPAL Collaboration, B. Anderson et al., *The OPAL silicon - tungsten calorimeter front end electronics*, IEEE  
12151 Trans.Nucl.Sci. **41** (1994) 845–852.
- 12152 [793] J. Adams, G. Bashindzhagian, V. Zatsepin, M. Merkin, M. Panasyuk, et al., *The silicon matrix as a charge detector for*  
12153 *the ATIC experiment*, Instrum.Exp.Tech. **44** (2001) 455–461.
- 12154 [794] V. Zatsepin, J. Adams, H. Ahn, G. Bashindzhagian, K. Batkov, et al., *Experience of application of silicon matrix as a*  
12155 *charge detector in the ATIC experiment*, .
- 12156 [795] V. Bonvicini, M. Boezio, E. Haslum, D. Matveev, M. Pearce, et al., *New concepts in silicon calorimetry for space*  
12157 *experiments*, Nucl.Instrum.Meth. **A518** (2004) 186–187.
- 12158 [796] V. Bonvicini, A. Vacchi, V. Dzhordzhadze, R. Seto, E. Kistenev, et al., *Silicon-tungsten calorimeter for the forward*  
12159 *direction in the PHENIX experiment at RHIC*, IEEE Trans.Nucl.Sci. **52** (2005) 874–878.
- 12160 [797] D. Strom "Silicon Tungsten Calorimetry", talk at SLAC Meeting, 8 January 2004.
- 12161 [798] D. M. Strom, R. Frey, M. Breidenbach, D. Freytag, N. Graf, et al., *Fine grained silicon-tungsten calorimetry for a*  
12162 *linear collider detector*, IEEE Trans.Nucl.Sci. **52** (2005) 868–873.
- 12163 [799] GEANT4 Collaboration, S. Agostinelli et al., *GEANT4: A Simulation toolkit*, Nucl.Instrum.Meth. **A506** (2003)  
12164 250–303.
- 12165 [800] A. Kaidalov and K. Ter-Martirosian, *Pomeron as Quark-Gluon Strings and Multiple Hadron Production at SPS*  
12166 *Collider Energies*, Phys.Lett. **B117** (1982) 247–251.
- 12167 [801] M. Barbi "Calorimetry - 3rd course", talk at TRIUMF Summer Institute, July 2007.
- 12168 [802] C. Leroy and P. Rancoita, *Physics of cascading shower generation and propagation in matter: Principles of*  
12169 *high-energy, ultrahigh-energy and compensating calorimetry*, Rept.Prog.Phys. **63** (2000) 505–606.
- 12170 [803] G. Barbiellini, G. Cecchet, J. Hemery, F. Lemeilleur, C. Leroy, et al., *Energy resolution and longitudinal shower*  
12171 *development in a Si/ W electromagnatic calorimeter*, Nucl.Instrum.Meth. **A235** (1985) 55.
- 12172 [804] J.-C. Brient and H. Videau, *The Calorimetry at the future e+ e- linear collider*, arXiv:hep-ex/0202004 [hep-ex].
- 12173 [805] V. Morgunov, *Calorimetry design with energy-flow concept (imaging detector for high-energy physics)*, .
- 12174 [806] S. R. Magill, *Innovations in ILC detector design using a particle flow algorithm approach*, New J.Phys. **9** (2007) 409.
- 12175 [807] R. Wigmans, *Recent results from the DREAM project*, J.Phys.Conf.Ser. **160** (2009) 012018.
- 12176 [808] J. Hauptman, *Particle physics experiments at high energy colliders*, .
- 12177 [809] G. Gaudio and R. Wigmans, *Dual-Readout Calorimetry for High-Quality Energy Measurements*,  
12178 CERN-SPSC-2011-021/SPSC-SR-086/June 2011.
- 12179 [810] G. Mikenberg, *The ATLAS muon spectrometer*, Mod.Phys.Lett. **A25** (2010) 649–667.
- 12180 [811] F. Gasparini, *The CMS muon detector: From the first thoughts to the final design*, Int.J.Mod.Phys. **A25** (2010)  
12181 3121–3154.
- 12182 [812] J. Burnens, R. de Oliveira, G. Glonti, O. Pizzirusso, V. Polychronakos, et al., *A spark-resistant bulk-micromegas*  
12183 *chamber for high-rate applications*, arXiv:1011.5370 [physics.ins-det]. \* Temporary entry \*.
- 12184 [813] R. Santonico et al., *A new generation of RPCs to be used as muon trigger detectors at the super-LHC*, .  
12185 <http://indico.cern.ch/materialDisplay.py?contribId=427&sessionId=16&materialId=slides&confId=102998>.
- 12186 [814] B. Bittner, J. Dubbert, S. Horvat, M. Kilgenstein, O. Kortner, et al., *Development of precision muon drift tube*  
12187 *detectors for the high-luminosity upgrade of the LHC*, Nucl.Phys.Proc.Suppl. **215** (2011) 143–146.
- 12188 [815] N. Amram, G. Bella, Y. Benhammou, M. A. Diaz, E. Duchovni, E. Etzion, A. Hershenhorn, A. Klier, N. Lupu,  
12189 G. Mikenberg, D. Milstein, Y. Munves, O. Sasaki, M. Shoa, V. Smakhtin, and U. Volkman, *Position resolution and*  
12190 *efficiency measurements with large scale Thin Gap Chambers for the super LHC*, Nuclear Instruments and Methods in  
12191 Physics Research Section A: Accelerators, Spectrometers, Detectors and Associated Equipment **628** (2011) no. 1, 177 –  
12192 181. <http://www.sciencedirect.com/science/article/pii/S0168900210015019>. VCI 2010 - Proceedings of the 12th  
12193 International Vienna Conference on Instrumentation.

- 12194 [816] V. Smakhtin, G. Mikenberg, A. Klier, Y. Rozen, E. Duchovni, E. Kajamovitz, and A. Hershenhorn, *Thin Gap Chamber*  
12195 *upgrade for SLHC: Position resolution in a test beam*, Nuclear Instruments and Methods in Physics Research Section  
12196 A: Accelerators, Spectrometers, Detectors and Associated Equipment **598** (2009) no. 1, 196 – 200.  
12197 <http://www.sciencedirect.com/science/article/pii/S0168900208012242>. Instrumentation for Colliding Beam Physics  
12198 - Proceedings of the 10th International Conference on Instrumentation for Colliding Beam Physics.
- 12199 [817] Fourth (“4th”) Detector Collaboration, G. Drobychev et al., *Letter of Intent from the Fourth Detector (“4th”)*  
12200 *Collaboration at the International Linear Collider*, . <http://www.4thconcept.org/4LoI.pdf>.
- 12201 [818] R. Brun and F. Rademakers, *ROOT - An Object Oriented Data Analysis Framework*, *Proceedings AIHENP’96*  
12202 *Workshop, Lausanne, Sep. 1996*, Nucl. Inst. & Meth. in Phys. Res. A **389** (1997) 81–86.
- 12203 [819] R. Chytracsek, J. McCormick, W. Pokorski, and S. G., *Geometry Description Markup Language for Physics Simulation*  
12204 *and Analysis Applications*, IEEE Trans. Nucl. Sci. **Vol. 53, Issue: 5, Part 2** 2892–2896.
- 12205 [820] V. V. Serbo, *Status of AIDA and JAS 3*, Nuclear Instruments and Methods in Physics Research Section A:  
12206 Accelerators, Spectrometers, Detectors and Associated Equipment **502** (2003) no. 2-3, 663 – 665.  
12207 <http://www.sciencedirect.com/science/article/pii/S0168900203005370>. Proceedings of the VIII International  
12208 Workshop on Advanced Computing and Analysis Techniques in Physics Research.
- 12209 [821] A. Vasilescu and L. G., *Displacement damage in Silicon for neutrons, protons, pions, and electrons*, .  
12210 <http://sesam.desy.de/members/gunnar/NIEL-allr.ps>.
- 12211 [822] F. Carminati and A. Morsch, *Simulation in ALICE*, [arXiv:physics/0306092](https://arxiv.org/abs/physics/0306092) [physics]. On behalf of the ALICE  
12212 Offline Project.
- 12213 [823] ALICE Collaboration, I. Hrivnacova et al., *The Virtual Monte Carlo*, [arXiv:cs/0306005](https://arxiv.org/abs/cs/0306005) [cs-se].
- 12214 [824] ALICE Collaboration, I. Gonzalez Caballero, F. Carminati, A. Morsch, and I. Hrivnacova, *ALICE experience with*  
12215 *GEANT4*, [arXiv:physics/0306025](https://arxiv.org/abs/physics/0306025) [physics].
- 12216 [825] J. Hauptman, *Particle Identification in 4th*, [arXiv:0812.3571](https://arxiv.org/abs/hep-ex/0812.3571) [hep-ex].
- 12217 [826] H1 Collaboration, T. Ahmed et al., *Experimental Study of Hard Photon Radiation Processes at HERA*, Z. Phys. **C66**  
12218 (1995) 529–542.
- 12219 [827] V. Andreev et al., *The new H1 luminosity system for HERA II*, Nucl. Instrum. Meth. **A494** (2002) 45–50.
- 12220 [828] ZEUS Luminosity Group Collaboration, J. Andruszkow et al., *Luminosity measurement in the ZEUS experiment*, Acta  
12221 Phys. Polon. **B32** (2001) 2025–2058.
- 12222 [829] ZEUS Collaboration, S. D. Paganis, *The upgraded luminosity system for the ZEUS experiment*, Int. J. Mod. Phys.  
12223 **A16S1C** (2001) 1147–1149.
- 12224 [830] G. A. Schuler and H. Spiesberger, *DJANGO: The Interface for the event generators HERACLES and LEPTO*, . In  
12225 \*Hamburg 1991, Proceedings, Physics at HERA, vol. 3\* 1419-1432. (see HIGH ENERGY PHYSICS INDEX 30 (1992)  
12226 No. 12988).
- 12227 [831] A. Courau and P. Kessler, *QED Compton scattering in high-energy electron - proton collisions*, Phys. Rev. **D46** (1992)  
12228 117–124.
- 12229 [832] S. Levonian, *H1LUMI - A Fast Simulation Package for the H1 Luminosity System*, . H1 internal note h1-0493-287  
12230 (1993); <http://www.desy.de/~levonian/papers/H1lumi.pdf>.
- 12231 [833] R. Brun, M. Caillat, M. Maire, G. N. Patrick, and L. Urban, *The GEANT3 electromagnetic shower program and a*  
12232 *comparison with the EGS3 code*, . CERN-DD/85/1.
- 12233 [834] SLD Collaboration Collaboration, R. King, *A Precise measurement of the left-right asymmetry of Z boson production at*  
12234 *the SLAC Linear Collider*, Nucl.Phys.Proc.Suppl. **37B** (1994) 23–31.
- 12235 [835] D. Barber, H. Bremer, M. Boge, R. Brinkmann, W. Bruckner, et al., *The HERA polarimeter and the first observation*  
12236 *of electron spin polarization at HERA*, Nucl.Instrum.Meth. **A329** (1993) 79–111.
- 12237 [836] S. Boogert, M. Hildreth, D. Kafer, J. List, K. Monig, et al., *Polarimeters and Energy Spectrometers for the ILC Beam*  
12238 *Delivery System*, JINST **4** (2009) P10015, [arXiv:0904.0122](https://arxiv.org/abs/0904.0122) [physics.ins-det].
- 12239 [837] S. Baudrand, M. Bouchel, V. Brisson, R. Chiche, M. Jacquet, et al., *A High Precision Fabry-Perot Cavity Polarimeter*  
12240 *at HERA*, JINST **5** (2010) 06005, [arXiv:1005.2741](https://arxiv.org/abs/1005.2741) [physics.ins-det].
- 12241 [838] M. Beckmann, A. Borissov, S. Brauksiepe, F. Burkart, H. Fischer, et al., *The Longitudinal polarimeter at HERA*,  
12242 Nucl.Instrum.Meth. **A479** (2002) 334–348, [arXiv:physics/0009047](https://arxiv.org/abs/physics/0009047) [physics].
- 12243 [839] V. Brisson, R. Chiche, M. Jacquet, C. Pascaud, V. Soskov, et al., *Per Mill Level Control of the Circular Polarisation of*  
12244 *the Laser Beam for a Fabry-Perot Cavity Polarimeter at HERA*, JINST **5** (2010) 06006, [arXiv:1005.2742](https://arxiv.org/abs/1005.2742)  
12245 [physics.ins-det].
- 12246 [840] ZEUS FNC Group Collaboration, S. Bhadra et al., *Design and test of a forward neutron calorimeter for the ZEUS*  
12247 *experiment*, Nucl. Instrum. Meth. **A394** (1997) 121–135, [arXiv:hep-ex/9701015](https://arxiv.org/abs/hep-ex/9701015).
- 12248 [841] R. Arnaldi et al., *The Zero Degree Calorimeters for the ALICE Experiment*, Nucl. Instrum. Meth. **A581** (2007)  
12249 397–401.

- 12250 [842] ALICE Collaboration, N. De Marco et al., *Commissioning and calibration of the zero degree calorimeters for the ALICE*  
12251 *experiment*, J. Phys. Conf. Ser. **160** (2009) 012060.
- 12252 [843] A. Collaboration, *Zero degree calorimeters for ATLAS*, . CERN-LHCC-2007-01.
- 12253 [844] O. Grachov et al., *Commissioning of the CMS zero degree calorimeter using LHC beam*, [arXiv:1008.1157](#)  
12254 [[physics.ins-det](#)].
- 12255 [845] LHCf Collaboration, O. Adriani et al., *The LHCf detector at the CERN Large Hadron Collider*, JINST **3** (2008) S08006.
- 12256 [846] A. Breskin et al., *The THGEM: A thick robust gaseous electron multiplier for radiation detectors*, Nucl. Instrum. Meth.  
12257 **A623** (2010) 132–134.
- 12258 [847] V. Inshakov et al., *Development of detector active element based on thgem*, [arXiv:0906.4441](#) [[physics.ins-det](#)].
- 12259 [848] FP420 R and D Collaboration Collaboration, M. Albrow et al., *The FP420 R&D Project: Higgs and New Physics with*  
12260 *forward protons at the LHC*, JINST **4** (2009) T10001, [arXiv:0806.0302](#) [[hep-ex](#)].
- 12261 [849] P. Taels, *Studie van de acceptantie en resolutie van een protonspectrometer bij de LHeC*, . University of Antwerp  
12262 Bachelor thesis.
- 12263 [850] H. Mais and G. Ripken Tech. Rep. 83-62, DESY, 1983. Modern notation: replace  $\vec{n}$  by  $\vec{n}_0$ .

## 12264 Chapter 15

# 12265 Appendix

### 12266 15.1 Scientific Advisory Committee

12267 Guido Altarelli (Roma)  
12268 Sergio Bertolucci (CERN)  
12269 Stan Brodsky (SLAC)  
12270 Allen Caldwell (MPI Muenchen) - Chair  
12271 Swapan Chattopadhyay (Cockcroft Institute)  
12272 John Dainton (Liverpool)  
12273 John Ellis (CERN)  
12274 Jos Engelen (NWO)  
12275 Joel Feltesse (Saclay)  
12276 Roland Garoby (CERN)  
12277 Rolf Heuer (CERN)  
12278 Roland Horisberger (PSI)  
12279 Young-Kee Kim (Fermilab)  
12280 Aharon Levy (Tel Aviv)  
12281 Lev Lipatov (St. Petersburg)  
12282 Karlheinz Meier (Heidelberg)  
12283 Richard Milner (MIT)  
12284 Joachim Mnich (DESY)  
12285 Steve Myers (CERN)  
12286 Guenther Rosner (Glasgow)  
12287 Alexander N. Skrinsky (INP Novosibirsk)  
12288 Anthony Thomas (JLab)  
12289 Steve Vigdor (Brookhaven)  
12290 Ferdinand Willeke (Brookhaven)  
12291 Frank Wilczek (MIT)  
12292



12293

## 15.2 Steering Committee

12294 Oliver Bruening(CERN)  
12295 John Dainton (Liverpool)  
12296 Albert De Roeck (CERN)  
12297 Stefano Forte (Milano)  
12298 Max Klein (Liverpool) - Chair  
12299 Paul Laycock (Liverpool)  
12300 Paul Newman (Birmingham)  
12301 Emmanuelle Perez (CERN)  
12302 Wesley Smith (Wisconsin)  
12303 Bernd Surrow (MIT)  
12304 Katsuo Tokushuku (KEK)  
12305 Urs Wiedemann (CERN)  
12306 Frank Zimmermann (CERN)

12307 **15.3 Working Group Convenors**

12308 **Accelerator Design**

12309 Oliver Bruening (CERN)  
12310 John Dainton (Liverpool)  
12311

12312 **Interaction Region**

12313 Bernhard Holzer(CERN)  
12314 Uwe Schneekloth (DESY)  
12315 Pierre van Mechelen (Antwerpen)  
12316

12317 **Detector Design**

12318 Peter Kostka (DESY)  
12319 Alessandro Polini (Bologna)  
12320 Rainer Wallny (Zurich)  
12321

12322 **New Physics at Large Scales**

12323 Georges Azuelos (Montreal)  
12324 Emmanuelle Perez (CERN)  
12325 Georg Weiglein (Hamburg)  
12326

12327 **Precision QCD and Electroweak**

12328 Olaf Behnke (DESY)  
12329 Paolo Gambino (Torino)  
12330 Thomas Gehrmann (Zurich)  
12331 Claire Gwenlan (Oxford)  
12332

12333 **Physics at High Parton Densities**

12334 Néstor Armesto (Santiago de Compostela)  
12335 Brian A. Cole (Columbia)  
12336 Paul R. Newman (Birmingham)  
12337 Anna M. Stasto (PennState)

12338

## 15.4 CERN Referees

12339

### Ring Ring Design

12340

Kurt Huebner (CERN)

12341

Alexander N. Skrinsky (INP Novosibirsk)

12342

Ferdinand Willeke (BNL)

12343

### Linac Ring Design

12344

Reinhard Brinkmann (DESY)

12345

Andy Wolski (Cockcroft)

12346

Kaoru Yokoya (KEK)

12347

### Energy Recovery

12348

Georg Hoffstaetter (Cornell)

12349

Ilan Ben Zvi (BNL)

12350

### Magnets

12351

Neil Marks (Cockcroft)

12352

Martin Wilson (CERN)

12353

### Interaction Region

12354

Daniel Pitzl (DESY)

12355

Mike Sullivan (SLAC)

12356

### Detector Design

12357

Philippe Bloch (CERN)

12358

Roland Horisberger (PSI)

12359

### Installation and Infrastructure

12360

Sylvain Weisz (CERN)

12361

### New Physics at Large Scales

12362

Cristinel Diaconu (IN2P3 Marseille)

12363

Gian Giudice (CERN)

12364

Michelangelo Mangano (CERN)

12365

### Precision QCD and Electroweak

12366

Guido Altarelli (Roma)

12367

Vladimir Chekelian (MPI Munich)

12368

Alan Martin (Durham)

12369

### Physics at High Parton Densities

12370

Alfred Mueller (Columbia)

12371

Raju Venugopalan (BNL)

12372

Michele Arneodo (INFN Torino)